

Horst Köppel  
David R. Yarkony  
Heinz Barentzen  
*Editors*

SPRINGER SERIES IN CHEMICAL PHYSICS 97

# The Jahn-Teller Effect

Fundamentals and Implications  
for Physics and Chemistry



Springer



Springer Series in  
**CHEMICAL PHYSICS**

---

*Series Editors:* A. W. Castleman, Jr. J. P. Toennies K. Yamanouchi W. Zinth

The purpose of this series is to provide comprehensive up-to-date monographs in both well established disciplines and emerging research areas within the broad fields of chemical physics and physical chemistry. The books deal with both fundamental science and applications, and may have either a theoretical or an experimental emphasis. They are aimed primarily at researchers and graduate students in chemical physics and related fields.

For further volumes:  
<http://www.springer.com/series/676>

Horst Köppel  
David R. Yarkony  
Heinz Barentzen  
(Eds.)

# **The Jahn-Teller Effect**

## **Fundamentals and Implications for Physics and Chemistry**

With 350 Figures



## Professor Horst Köppel

Universität Heidelberg  
Theoretische Chemie  
Im Neuenheimer Feld 229  
69120 Heidelberg  
Germany  
E-Mail: horst.koepfel@pci.uni-heidelberg.de

## Professor Heinz Barentzen

MPI für Festkörperforschung  
Heisenbergstr. 1  
70569 Stuttgart  
Germany  
E-mail: h.barentzen@fkf.mpg.de

## Professor David R. Yarkony

Johns Hopkins University  
Department of Chemistry  
3400 N. Charles Street  
Baltimore MD 21218  
USA  
E-Mail: yarkony@jhu.edu

### *Series Editors:*

## Professor A.W. Castleman, Jr.

Department of Chemistry, The Pennsylvania State University  
152 Davey Laboratory, University Park, PA 16802, USA

## Professor J.P. Toennies

Max-Planck-Institut für Strömungsforschung  
Bunsenstrasse 10, 37073 Göttingen, Germany

## Professor K. Yamanouchi

University of Tokyo, Department of Chemistry  
Hongo 7-3-1, 113-0033 Tokyo, Japan

## Professor W. Zinth

Universität München, Institut für Medizinische Optik  
Öttingerstr. 67, 80538 München, Germany

ISSN 0172-6218

ISBN 978-3-642-03431-2

e-ISBN 978-3-642-03432-9

DOI 10.1007/978-3-642-03432-9

Springer Heidelberg Dordrecht London New York

Library of Congress Control Number: 2009938946

© Springer-Verlag Berlin Heidelberg 2009

This work is subject to copyright. All rights are reserved, whether the whole or part of the material is concerned, specifically the rights of translation, reprinting, reuse of illustrations, recitation, broadcasting, reproduction on microfilm or in any other way, and storage in data banks. Duplication of this publication or parts thereof is permitted only under the provisions of the German Copyright Law of September 9, 1965, in its current version, and permission for use must always be obtained from Springer. Violations are liable to prosecution under the German Copyright Law.

The use of general descriptive names, registered names, trademarks, etc. in this publication does not imply, even in the absence of a specific statement, that such names are exempt from the relevant protective laws and regulations and therefore free for general use.

*Cover design:* SPi Publisher Services

Printed on acid-free paper

Springer is part of Springer Science+Business Media (www.springer.com)

# Preface

The Jahn–Teller (JT) effect continues to be a paradigm for structural instabilities and dynamical processes in molecules and in the condensed phase. While the basic theorem, first published in 1937, had to await experimental verification for 15 years, the intervening years saw rapid development, initially in the theoretical arena, followed increasingly by experimental work on molecules and crystals. The International Jahn–Teller Symposium was established in the mid-1970s, to foster the exchange of ideas between researchers in the field. Among the many important developments in the field, we mention cooperative phenomena in crystals, the general importance of pseudo-Jahn–Teller (PJT) couplings for symmetry-lowering phenomena in molecular systems, nonadiabatic processes at conical intersections of potential energy surfaces and extensions of the basic theory in relation to the discovery of fullerenes and other icosahedral systems.

It is the objective of this volume to provide the interested reader with a collection of tutorial reviews by leading researchers in the field. These reviews provide a comprehensive overview of the current status of the field, including important recent developments. This volume is targeted at both the non-expert scientist as well as the expert who wants to expand his/her knowledge in allied areas. It is intended to be a complement to the existing excellent textbooks in the field. Guided by the idea of tutorial reviews, we provide here short introductory remarks to the various sections, as they appear in the table of contents. These are followed by a brief characterization of the individual papers to make their basic contents, as well as their interrelation, more transparent.

## *1. Jahn–Teller Effect and Vibronic Interactions: General Theory*

The first set of reviews deals with general formal aspects of the theory, its range of application and implementation. While the original formulation of the JT theorem applies to orbitally degenerate electronic states, it was later recognized that similar mechanisms for structural instabilities are operative also in nondegenerate states (PJT effect). In the first paper of this volume, Bersuker emphasizes the even more general implications of the JT and related couplings, by demonstrating that they may affect ground state structural properties, even when operative in the excited state manifold (hidden JT effect). This may be associated with spin-crossover effects and orbital disproportionation. The following two papers (by Ceulemans and Lijnen, and

by Breza) address group theoretical aspects. A desire has sometimes been expressed to gain more insight into the nature of the JT theorem than is afforded by the original proof (which consists in enumerating all topologically distinct realizations of all molecular point groups). This goal is indeed achieved in the article by Ceulemans and Lijnen. Poluyanov and Domcke advocate the use of the microscopic Breit-Pauli operator for the spin-orbit coupling rather than the phenomenological form often adopted. They point out that the resulting dependence of the spin-orbit coupling on the nuclear coordinates can lead to novel effects, of relevance to molecular spectra. Sato and coworkers present a scheme for analyzing vibronic coupling constants in terms of densities, which allows them to investigate their local properties and visualize their electronic origin. Finally, an efficient method to compute multimode JT coupling constants with density functional theory is presented by Zlatař et al. The approach uses information from the JT distorted structure, which is decomposed into contributions from the various relevant normal modes.

## *2. Conical Intersections and Nonadiabatic Dynamics in Molecular Processes*

Conical intersections can be considered generalizations of the JT intersections in less symmetric cases, the latter being also conical in shape owing to the presence of the linear coupling terms predicted by the JT theorem. In molecular physics, conical intersections have emerged in the past one or two decades as paradigms for nonadiabatic excited-state dynamics, triggering a plethora of studies of elementary photophysical and photochemical processes. The article by Blancafort et al. reports on modern developments in the characterization of conical intersections by *ab initio* techniques. Their second-order analysis shows, for example, how to distinguish between minima and saddle points in the subspace of electronic degeneracy and to identify photochemically active coordinates. The paper by Bouakline et al. presents a quantum dynamical analysis of the smallest JT active system, triatomic hydrogen. This prototypical reactive scattering system is subject to geometric phase effects which, however, almost completely cancel out in the integral cross section. On the other hand, strong nonadiabatic couplings/geometric phase effects govern the upper-cone resonances (Rydberg states) of the system. The papers by Faraji et al. and by Reddy and Mahapatra present multimode quantum dynamical treatments of JT and PJT systems with more than two intersecting potential energy surfaces. Pronounced effects of the couplings in the spectral intensity distribution and in femtosecond (fs) internal conversion processes are identified. A systematic dependence of the phenomena on the (fluoro) substituents as well as the importance for the photostability of hydrocarbons is demonstrated. In the article by McKinlay and Paterson, similar phenomena, including nonadiabatic photodissociation processes and fs pump-probe spectroscopy, are discussed for transition metal complexes, thus providing a bridge between the JT effect and photochemistry.

## *3. Impurities; Spectroscopy of Transition Metal Complexes*

Transition metal complexes have represented, for a long time, the archetypical system for which the JT effect plays a crucial role, especially with regard to crystal field splitting and spin-orbit interaction (Ham effect). This affects optical as well

as EPR spectra of 3d group ions, for example. In the review by Brik and Avram these are studied for various coordination sites using an effective Hamiltonian formalism. Useful relations for the Ham reduction factors are derived, and the JT parameters obtained from the Ham effect are compared with those obtained from the JT-distorted minima of the potential energy surfaces. Tregenna-Piggott and Riley present in their review a very pedagogic introduction to the Exe JT effect, and the Ham effect as one of its consequences. Applications to various types of spectra of different transition metal complexes underline the usefulness of the theoretical concepts. Garcia-Fernandez et al. address the question of structural instabilities of doped materials and their type and origin. They argue, and present convincing evidence, that these are frequently not due to differences in atomic sizes (as is often assumed in the literature) but rather to vibronic coupling, that is, the PJT effect. Finally in their review, Reinen and Atanasov analyze in their review, the effects of JT coupling on the changes from a high-spin to a low-spin electronic ground state in hexacoordinate fluoride complexes of Mn(III), Co(III), Ni(III) and Cu(III), an aspect which is frequently ignored in the literature on spin-crossover systems. In particular, the strong links to coordination and solid state chemistry are set out in this contribution.

#### *4. Fullerenes and Fullerides*

In the mid 1980s and subsequent years, the discovery of C<sub>60</sub> and other fullerenes opened a route to the analysis of JT systems with higher than threefold degeneracies (G and H irreducible representations). This led to substantial developments from the point of view of pure theory as well as applications. This volume includes two important papers in this area. Structural aspects of fulleride salts, i.e. fullerene anions in various charge states in the solid state, are covered by Klupp and Kamaras. Evidence, based mostly on infrared spectroscopy, is used to discuss issues including static vs. dynamic JT effect, unusual phases, and relation to conductivity. The review by Hands et al. addresses the further complication of fullerenes being adsorbed on surfaces. The lowering in symmetry due to the surface interactions is considered, as well as the rather slow time-scale of the experimental technique of scanning tunneling microscopy proposed. Detailed simulations of the corresponding images shed useful light on their possible significance in establishing the presence and shape of JT distortions.

#### *5. Jahn–Teller Effect and Molecular Magnetism*

Molecular magnetism concerns the synthesis, characterization and application of molecular-based materials that possess the typical properties of magnets – slow relaxation, quantum tunneling and blocking of the magnetization at low temperatures (single molecular magnets (SMM)). It is an interdisciplinary research field which requires the combined efforts (cooperation) of chemists, molecular and solid state physicists, as well as theoreticians (quantum chemists). This is the point where the JT effect enters into the game. The magnetic properties of SMMs are affected by the structural influences caused by vibronic coupling and these influences are further manifested in the optical band shapes, the interactions between magnetic molecules

with degenerate ground states (cooperative JT effect), and the dynamical JT and PJT effects (which impact upon the magnetic relaxation and spin coherence times). In their review, Tsukerblat, Klokishner and Palii address these points in spin-frustrated systems with threefold symmetry, mixed valence systems, photoswitchable spin systems, and magnetic molecules which undergo tautomeric transformations leading to long-lived (metastable) states. The Jahn–Teller effect plays a crucial role in magnetic clusters built up from magnetic centers in orbitally degenerate ground states. Using a combination of ligand field theory and density functional theory Atanasov and Comba show how small structural changes due to Jahn–Teller activity and/or structural strains induce a dramatic lowering of the magnetic anisotropy. The same authors also show for the first time, using cyanide-bridged systems as model examples, how one can deduce the parameters of the spin Hamiltonian from first principles.

### *6. The Cooperative Jahn–Teller Effect and Orbital Ordering*

It has long been recognized for JT crystals, i.e., crystals containing a JT center in each unit cell, that the intrinsic instability of JT complexes against distortions may give rise to an effective interaction between JT ions, mediated by the surrounding ligands of the ions. Below a critical temperature, this interaction may lead to the cooperative JT effect (CJTE), a structural phase transition where the whole crystal distorts. There are two main approaches to the CJTE, differing in the form of the effective ion–ion interaction. Kaplan’s review is partly based on Kanamori’s treatment, who generated this interaction by the transformation from local vibrational modes to phonons. This treatment, in combination with the canonical Hamiltonian shift transformation and a subsequent mean-field approximation, is the most popular approach to the CJTE. Although this concept, also referred to as virtual phonon exchange, has led to impressive results for some simpler systems, it cannot be applied to systems characterized by the Exe JT effect because of insurmountable technical difficulties. Such systems are conveniently treated by means of an alternative approach, developed by Thomas and co-workers and described in Polinger’s article. This method assumes a bilinear lattice-dynamical interaction between the normal coordinates belonging to nearest-neighbor cells. However, the main emphasis of this article lies in a detailed comparison of the CJTE with the orbital-ordering (or Kugel–Khomskii) approach. A typical example of the orbital-ordering approach is presented in Ishihara’s review. The main emphasis of this article is on the intrinsic orbital frustration effect, meaning that no orbital configuration exists, whereby the bond energies in all equivalent directions are simultaneously minimized. It is shown that the orbital frustration effect leads to several nontrivial phenomena in strongly correlated systems with orbital degrees of freedom. The influence of the CJTE and of JT impurities on material properties is elucidated in the reviews by Gudkov and Lucovsky. The review by Gudkov deals mainly with the influence of JT impurities on the elastic moduli and ultrasonic wave attenuation in diluted crystals. The elastic-wave technique broadens the facilities of JT spectroscopy in its low-energy part and provides new information, mostly about the properties of the ground state and its tunneling splitting. That the JT effect even plays an important role in semiconductor technology is convincingly demonstrated in Lucovsky’s article. Here the CJTE

manifests itself in the group IVB transition-metal oxides, designed as replacement gate dielectrics for advanced metal-oxide-semiconductor devices.

### *7. Jahn–Teller Effect and High-Tc Superconductivity*

The explanation of high-temperature superconductivity (HTSC) in copper oxides (cuprates) is one of the most difficult problems in modern physics. The undoped cuprates are antiferromagnetic Mott insulators, where the insulating behavior is caused by a strong on-site Coulomb repulsion. HTSC arises upon hole doping, whereupon the originally immobile electrons in the half-filled conduction band become mobile. The basic problem is to find the proper mechanism for the formation of Cooper pairs, the necessary ingredient of all superconductors. There are mainly two antagonistic views on the problem amounting to the question of whether the participation of phonons is indispensable for the pair formation or whether the electrons alone can do the job. The review by Miranda Mena tries to answer this question by gathering all available evidence in favor of electron–phonon mechanisms such as (bi)polarons and JT (bi)polarons. Seen in this perspective, the article gives a fair account of the state of the art in HTSCs. A more detailed theory of JT polarons and bipolarons with application to the fullerene superconductors is presented in the article by Hori and Takada. In addition to offering a thorough mathematical analysis, the authors also make the interesting observation that, for stronger coupling, JT polarons acquire a smaller effective mass than the Holstein polaron. Such a reduction of the polaron effective mass is essential for the existence of superconductivity, as the polaron mass increases with increasing coupling so that, for sufficiently strong coupling, the polaron becomes immobile and cannot contribute to the electric current. These remarks apply, in particular, to Koizumi’s work, which proposes that the doped holes become small polarons and not, as is supposed in all electron-based theories of HTSC, constituents of Zhang–Rice singlets. As the mobility of the polarons is very limited, a novel mechanism is required to facilitate a macroscopic electric current. The author solves the problem by a loop current generation around each spin vortex due to the spin Berry phase. The macroscopic current is then the collection of all these loop currents.

This set of tutorial reviews has been created on the occasion of the 19th International Jahn–Teller Symposium, held in Heidelberg, University Campus, 25–29 August 2008. The volume does not, however, reflect directly the conference contents. Full coverage of the 46 oral presentations given at the meeting (plus a similar number of posters) was not attempted. Conversely, the 27 papers collected here go into considerably more depth than would be normal for a proceedings volume. We hope that this volume constitutes a valuable reference, for beginners and experts alike.

Heidelberg  
Stuttgart  
Baltimore  
May 2009

*H. Köppel*  
*H. Barentzen*  
*D.R. Yarkony*

# Acknowledgments

D. R. Yarkony acknowledges the support of NSF grant CHE-0513952. The editors are indebted to M. Atanasov for helpful comments.

# Contents

## **Part I Jahn–Teller Effect and Vibronic Interactions: General Theory**

<b>Recent Developments in the Jahn–Teller Effect Theory .....</b>	<b>3</b>
Isaac B. Bersuker	

<b>Electronic Degeneracy and Vibrational Degrees of Freedom: The Permutational Proof of the Jahn–Teller Theorem .....</b>	<b>25</b>
Arnout Ceulemans and Erwin Lijnen	

<b>Group-Theoretical Analysis of Jahn–Teller Systems.....</b>	<b>51</b>
Martin Breza	

<b>Spin–Orbit Vibronic Coupling in Jahn–Teller and Renner Systems .....</b>	<b>77</b>
Leonid V. Poluyanov and Wolfgang Domcke	

<b>Vibronic Coupling Constant and Vibronic Coupling Density .....</b>	<b>99</b>
Tohru Sato, Ken Tokunaga, Naoya Iwahara, Katsuyuki Shizu, and Kazuyoshi Tanaka	

<b>A New Method to Describe the Multimode Jahn–Teller Effect Using Density Functional Theory .....</b>	<b>131</b>
Matija Zlatar, Carl-Wilhelm Schl�pfer, and Claude Daul	

## **Part II Conical Intersections and Nonadiabatic Dynamics in Molecular Processes**

<b>Second-Order Analysis of Conical Intersections: Applications to Photochemistry and Photophysics of Organic Molecules.....</b>	<b>169</b>
Llu�s Blancafort, Benjamin Lasorne, Michael J. Bearpark, Graham A. Worth, and Michael A. Robb	



<b>Influence of the Geometric Phase and Non-Adiabatic Couplings on the Dynamics of the <math>\text{H}+\text{H}_2</math> Molecular System</b> .....	201
Foudhil Bouakline, Bruno Lepetit, Stuart C. Althorpe, and Aron Kuppermann	

<b>Multi-Mode Jahn–Teller and Pseudo-Jahn–Teller Effects in Benzenoid Cations</b> .....	239
Shirin Faraji, Etienne Gindensperger, and Horst Köppel	

<b>On the Vibronic Interactions in Aromatic Hydrocarbon Radicals and Radical Cations</b> .....	277
V. Sivaranjana Reddy and S. Mahapatra	

<b>The Jahn–Teller Effect in Binary Transition Metal Carbonyl Complexes</b> .....	311
Russell G. McKinlay and Martin J. Paterson	

### **Part III Impurities; Spectroscopy of Transition Metal Complexes**

<b>Jahn–Teller Effect for the 3d Ions (Orbital Triplets in a Cubic Crystal Field)</b> .....	347
M.G. Brik, N.M. Avram, and C.N. Avram	

<b>Constructing, Solving and Applying the Vibronic Hamiltonian</b> .....	371
Philip L.W. Tregenna-Piggott and Mark J. Riley	

<b>Instabilities in Doped Materials Driven by Pseudo Jahn–Teller Mechanisms</b> .....	415
P. García-Fernández, A. Trueba, J.M. García-Lastra, M.T. Barriuso, M. Moreno, and J.A. Aramburu	

<b>The Influence of Jahn–Teller Coupling on the High-Spin/Low-Spin Equilibria of Octahedral <math>\text{M}^{\text{III}}\text{L}_6</math> Polyhedra (<math>\text{M}^{\text{III}} : \text{Mn} - \text{Cu}</math>), with <math>\text{NiF}_6^{3-}</math> as the Model Example</b> .....	451
D. Reinen and M. Atanasov	

### **Part IV Fullerenes and Fullerides**

<b>Following Jahn–Teller Distortions in Fulleride Salts by Optical Spectroscopy</b> .....	489
G. Klupp and K. Kamarás	

<b>Jahn–Teller Effects in Molecules on Surfaces with Specific Application to C<sub>60</sub></b> .....	517
Ian D. Hands and Janette L. Dunn, Catherine S.A. Rawlinson, and Colin A. Bates	

## **Part V Jahn-Teller Effect and Molecular Magnetism**

<b>Jahn–Teller Effect in Molecular Magnetism: An Overview</b> .....	555
Boris Tsukerblat, Sophia Klokishner, and Andrew Palii	

<b>The Effect of Jahn–Teller Coupling in Hexacyanometalates on the Magnetic Anisotropy in Cyanide-Bridged Single-Molecule Magnets</b> .....	621
Mihail Atanasov and Peter Comba	

## **Part VI The Cooperative Jahn-Teller Effect and Orbital Ordering**

<b>Cooperative Jahn–Teller Effect: Fundamentals, Applications, Prospects</b> .....	653
Michael Kaplan	

<b>Orbital Ordering Versus the Traditional Approach in the Cooperative Jahn–Teller Effect: A Comparative Study</b> .....	685
Victor Polinger	

<b>Frustration Effect in Strongly Correlated Electron Systems with Orbital Degree of Freedom</b> .....	727
Sumio Ishihara	

<b>Ultrasonic Consequences of the Jahn–Teller Effect</b> .....	743
Vladimir Gudkov	

<b>Long Range Cooperative and Local Jahn-Teller Effects in Nanocrystalline Transition Metal Thin Films</b> .....	767
Gerald Lucovsky	

## **Part VII Jahn-Teller Effect and High-T<sub>c</sub> Superconductivity**

<b>Jahn–Teller Polarons, Bipolarons and Inhomogeneities. A Possible Scenario for Superconductivity in Cuprates</b> .....	811
Joaquin Miranda Mena	

<b>Polarons and Bipolarons in Jahn–Teller Crystals .....</b>	<b>841</b>
Chishin Hori and Yasutami Takada	
<b>Vibronic Polarons and Electric Current Generation by a Berry Phase in Cuprate Superconductors .....</b>	<b>873</b>
Hiroyasu Koizumi	
<b>Index .....</b>	<b>907</b>

# List of Contributors

**Stuart C. Althorpe** Department of Chemistry, University of Cambridge, Cambridge CB2 1EW, UK

**J.A. Aramburu** Departamento de Ciencias de la Tierra y Física de la Materia Condensada, Universidad de Cantabria, 39005 Santander, Spain, antonio.aramburu@unican.es

**Mihail Atanasov** Institute of General and Inorganic Chemistry, Bulgarian Academy of Sciences, Acad.Georgi Bontchev Str., Bl.11, 1113 Sofia, Bulgaria, mihail.atanasov@aci.uni-heidelberg.de  
and

Anorganisch-Chemisches Institut, Universität Heidelberg, Im Neuenheimer Feld 270, 69120 Heidelberg, Germany

and

Chemistry Department, Philipps-University, Hans-Meerwein-Strasse, 35043 Marburg, Germany

**C.N. Avram** Department of Physics, West University of Timisoara, Bvd.V. Parvan 4, Timisoara 300223, Romania

**N.M. Avram** Department of Physics, West University of Timisoara, Bvd. V. Parvan 4, Timisoara 300223, Romania

and

Academy of Romanian Scientists, Splaiul Independentei 54, 050094 Bucharest, Romania

**M.T. Barriuso** Departamento de Física Moderna, Universidad de Cantabria, 39005 Santander, Spain

**Colin A. Bates** School of Physics and Astronomy, University of Nottingham, Nottingham, NG7 2RD, UK

**Michael J. Bearpark** Department of Chemistry, Imperial College London, London SW7 2AZ, UK

**Isaac B. Bersuker** Institute for Theoretical Chemistry, The University of Texas at Austin, Austin, TX 78712, USA, bersuker@cm.utexas.edu

**Lluís Blancafort** Institut de Química Computacional and Parc Científic i Tecnològic, Universitat de Girona, 17071 Girona, Spain, lluis.blancafort@udg.edu

**Foudhil Bouakline** Department of Chemistry, University of Cambridge, Cambridge CB2 1EW, UK, foudhil.bouakline@googlemail.com

**Martin Breza** Department of Physical Chemistry, Slovak Technical University, 81237 Bratislava, Slovakia, martin.breza@stuba.sk

**M.G. Brik** Institute of Physics, University of Tartu, Riia Street 142, 51014 Tartu, Estonia

**Arnout Ceulemans** Department of Chemistry and INPAC Institute for Nanoscale Physics and Chemistry, Katholieke Universiteit Leuven, Celestijnenlaan 200F, 3001 Leuven, Belgium, Arnout.Ceulemans@chem.kuleuven.be

**Peter Comba** Anorganisch-Chemisches Institut, Universität Heidelberg, Im Neuenheimer Feld 270, 69120, Heidelberg, Germany, peter.comba@aci.uni-heidelberg.de

**Claude Daul** Department of Chemistry, University of Fribourg, Fribourg, Switzerland, claude.daul@unifr.ch

**Wolfgang Domcke** Department of Chemistry, Technische Universität München, 85747 Garching, Germany, wolfgang.domcke@ch.tum.de

**Janette L. Dunn** School of Physics and Astronomy, University of Nottingham, Nottingham, NG7 2RD, UK, Janette.Dunn@nottingham.ac.uk

**Shirin Faraji** Theoretische Chemie, Universität Heidelberg, Im Neuenheimer Feld 229, 69120 Heidelberg, Germany

**P. García-Fernández** Departamento de Ciencias de la Tierra y Física de la Materia Condensada, Universidad de Cantabria, 39005 Santander, Spain

**J.M. García-Lastra** Departamento de Física de Materiales, Facultad de Químicas, Universidad del País Vasco, 20018 San Sebastián, Spain

**Etienne Gindensperger** Laboratoire de Chimie Quantique, Institut de Chimie UMR 7177, CNRS/Université de Strasbourg, 4 rue Blaise Pascal, B.P. 1032, 67070 Strasbourg Cedex, France

**Vladimir Gudkov** Ural State Technical University, 19, Mira st., Ekaterinburg 620002, Russia, gudkov@imp.uran.ru

**Ian D. Hands** School of Physics and Astronomy, University of Nottingham, Nottingham, NG7 2RD, UK

**Chishin Hori** Institute for Solid State Physics, University of Tokyo, 5-1-5 Kashiwanoha, Kashiwa, Chiba 277-8581, Japan, chori@issp.u-tokyo.ac.jp

**Sumio Ishihara** Department of Physics, Tohoku University, Sendai 980-8578, Japan, ishihara@cmpt.phys.tohoku.ac.jp

**Naoya Iwahara** Department of Molecular Engineering, Graduate School of Engineering, Kyoto University, Nishikyo-ku, Kyoto 615-8510, Japan, iwaharanaoya@t03.mbox.media.kyoto-u.ac.jp

**K. Kamarás** Research Institute for Solid State Physics and Optics, Hungarian Academy of Sciences, Budapest, Hungary, kamaras@szfki.hu

**Michael Kaplan** Chemistry Department, Simmons College, 300 The Fenway, Boston, MA 02115, USA, michael.kaplan@simmons.edu

and

Physics Department, Simmons College, 300 The Fenway, Boston, MA 02115, USA

**Sophia Klokishner** Institute of Applied Physics of the Academy of Sciences of Moldova, Academy str. 5, Kishinev, 2028, Moldova

**G. Klupp** Research Institute for Solid State Physics and Optics, Hungarian Academy of Sciences, Budapest, Hungary, klupp@szfki.hu

**Hiroyasu Koizumi** Institute of Materials Science, University of Tsukuba, Tsukuba, Ibaraki 305-8573, Japan, koizumi@ims.tsukuba.ac.jp

**Horst Köppel** Theoretische Chemie, Universität Heidelberg, Im Neuenheimer Feld 229, 69120 Heidelberg, Germany, Horst.Koeppel@pci.uni-heidelberg.de

**Aron Kuppermann** Division of Chemistry and Chemical Engineering, California Institute of Technology, Pasadena, CA 91125, USA, aron@caltech.edu

**Benjamin Lasorne** CTMM, Institut Charles Gerhardt, UMR 5253, CC 1501, Université Montpellier II, 34095 Montpellier Cédex 5, France

**Bruno Lepetit** Université de Toulouse, UPS, Laboratoire Collisions Agrégats Réactivité, IRSAMC, 31062 Toulouse, France

and

CNRS, UMR 5589, 31062 Toulouse, France, bruno.lepetit@irsamc.ups-tlse.fr

**Erwin Lijnen** Department of Chemistry and INPAC Institute for Nanoscale Physics and Chemistry, Katholieke Universiteit Leuven, Celestijnenlaan 200F, 3001 Leuven, Belgium, Erwin.Lijnen@chem.kuleuven.be

**Gerald Lucovsky** Department of Physics, North Carolina State University, Raleigh, NC 27695-8202, USA, lucovsky@ncsu.edu

**S. Mahapatra** School of Chemistry, University of Hyderabad, Hyderabad-500046, India, smsc@uohyd.ernet.in

**Russell G. McKinlay** School of Engineering and Physical Sciences, Heriot-Watt University, Edinburgh, Scotland, EH14 4AS

**Joaquin Miranda Mena** Departamento de Física Aplicada, CINVESTAV-Mérida, Mérida, 97300, México, miranda.joaquin@gmail.com

**M. Moreno** Departamento de Ciencias de la Tierra y Física de la Materia Condensada, Universidad de Cantabria, 39005 Santander, Spain

**Andrew Palii** Institute of Applied Physics of the Academy of Sciences of Moldova, Academy str.5, Kishinev 2028, Moldova

**Martin J. Paterson** School of Engineering and Physical Sciences, Heriot-Watt University, Edinburgh, Scotland, EH14 4AS, m.j.paterson@hw.ac.uk

**Victor Polinger** Department of Chemistry, University of Washington, Seattle, WA 98195-17001, USA  
and  
Bellevue College, 3000 Landerholm Circle SE, Science Div., L-200, Bellevue, WA 98007, USA, polinv@u.washington.edu

**Leonid V. Poluyanov** Institute of Chemical Physics, Russian Academy of Sciences, Chernogolovka, Moscow 14232, Russian Federation

**Catherine S.A. Rawlinson** School of Physics and Astronomy, University of Nottingham, Nottingham, NG7 2RD, UK

**D. Reinen** Chemistry Department, Philipps-University, Hans-Meerwein-Strasse, 35043 Marburg, Germany, reinen@chemie.uni-marburg.de

**Mark J. Riley** School of Chemistry and Molecular Biosciences, University of Queensland, St. Lucia, QLD, 4072, Australia, m.riley@uq.edu.au

**Michael A. Robb** Department of Chemistry, Imperial College London, London SW7 2AZ, UK

**Tohru Sato** Fukui Institute for Fundamental Chemistry, Kyoto University, Kyoto, Japan  
and

Department of Molecular Engineering, Graduate School of Engineering, Kyoto University, Nishikyo-ku, Kyoto 615-8510, Japan, tsato@scl.kyoto-u.ac.jp

**Carl-Wilhelm Schl pfer** Department of Chemistry, University of Fribourg, Fribourg, Switzerland, Carl-Wilhelm.Schlaepfer@unifr.ch

**Katsuyuki Shizu** Department of Molecular Engineering, Graduate School of Engineering, Kyoto University, Nishikyo-ku, Kyoto 615-8510, Japan, katsuyuki@21emon.mbox.media.kyoto-u.ac.jp

**V. Sivaranjana Reddy** School of Chemistry, University of Hyderabad, Hyderabad-500046, India, ch05ph07@uohyd.ernet.in

**Yasutami Takada** Institute for Solid State Physics, University of Tokyo, 5-1-5 Kashiwanoha, Kashiwa, Chiba 277-8581, Japan, takada@issp.u-tokyo.ac.jp

**Kazuyoshi Tanaka** Department of Molecular Engineering, Graduate School of Engineering, Kyoto University, Nishikyo-ku, Kyoto 615-8510, Japan, a51053@sakura.kudpc.kyoto-u.ac.jp

**Ken Tokunaga** Research and Development Center for Higher Education, Kyushu University, Ropponmatsu, Fukuoka 810-8560, Japan, tokunaga@rche.kyushu-u.ac.jp

**Philip L.W. Tregenna-Piggott** Laboratory for Neutron Scattering, ETH Zürich and Paul Scherrer Institut, CH-5232 Villigen PSI, Switzerland, philip.tregenna@psi.ch

**A. Trueba** Departamento de Ciencias de la Tierra y Física de la Materia Condensada, Universidad de Cantabria, 39005 Santander, Spain

**Boris Tsukerblat** Department of Chemistry, Ben-Gurion University of the Negev, PO Box 653, 84105 Beer-Sheva, Israel, tsuker@bgu.ac.il

**Graham A. Worth** School of Chemistry, University of Birmingham, Edgbaston, Birmingham B15 2TT, UK

**Matija Zlatar** Department of Chemistry, University of Fribourg, Fribourg, Switzerland  
and  
Center for Chemistry, IHTM, University of Belgrade, Belgrade, Serbia, matija.zlatar@unifr.ch, matijaz@chem.bg.ac.rs



**Part I**  
**Jahn-Teller Effect and Vibronic**  
**Interactions: General Theory**

# Recent Developments in the Jahn–Teller Effect Theory

## The Hidden Jahn–Teller Effect

Isaac B. Bersuker

**Abstract** In a review paper an updated formulation of the Jahn–Teller (JT) effect (JTE) (including proper JT, pseudo JT, and Renner–Teller (RT) effects) is given based on the latest achievements in this field, including the conclusion that the JTE is the only source of instability and distortion of *any* polyatomic system from its high-symmetry configuration. Together with the statement in particle physics that “symmetry breaking is always associated with a degeneracy” the extended formulation of the JTE leads us to the speculation that *Nature tends to avoid degeneracies*. In the updated formulation the presence of two or more electronic states, degenerate or within a limited energy gap, that mix strongly enough under nuclear displacements is the necessary and sufficient condition of instability. Distinguished from the usually considered electron–vibrational (electron–phonon) interaction in which one electronic state interacts with totally symmetric vibrations, the JTE, mixing two or more electronic states, involves also low-symmetry displacements.

It is shown that if in the global minimum of the adiabatic potential energy surface (APES) the polyatomic system is distorted from its high-symmetry configuration, while the electronic term in the latter is neither degenerate nor pseudo degenerate, and hence there is no apparent JTE or pseudo-JTE (PJTE), the distortion is due to these effects in the higher excited states. This is possible when the JT stabilization energy is larger than the energy gap to the ground state. Since the JT origin of the distortion is not seen explicitly from the calculation of the ground state, we call it *hidden JTE* (HJTE). There are two kinds of HJTE: (1) induced by proper JTE in an excited state, and (2) produced by the PJTE which mixes two excited states. Both types of HJTE are confirmed by ab initio calculations of a variety of molecular systems. While the first type of HJTE is more “accidental” (ozone,  $\text{O}_3$ , is shown to be a nice example), the second type occurs in  $e^2$  and  $t^3$  electron configurations and it is accompanied by orbital disproportionation, making the spin state in the global minimum different from that of the high-symmetry configuration. This in turn results in two minima of the APES with relatively close energies, but different electronic states and spin, and a spin crossover between the two minima. With the PJTE and HJTE included, the role of excited states in the analysis of structure and properties of molecular systems in the ground state becomes most important. It can be said that no full treatment of polyatomic systems is possible without involving excited states, even when the properties in the ground state are considered.

## 1 Introduction: An Updated View on the Formulation and the Meaning of the Jahn–Teller Effect

The Jahn–Teller effect (JTE) (including proper JTE, pseudo JTE (PJTE), and Renner–Teller effects (RTE)) in its present understanding is a local feature of *any* polyatomic system which describes its properties in high-symmetry configurations with respect to nuclear displacements from this configuration [1]. This understanding is essentially enlarged and much different from that introduced by E. Teller [2] based on a discussion with L. Landau [3]. The new achievements in this field so far did not reach the layman physicists and chemists and are not introduced in textbooks; the latter continue to treat the JTE as a small effect of instability and spontaneous distortion relevant to specific situations of electronic degeneracy in nonlinear molecules, which is not entirely true. In the modern formulation (see below) the JTE is possible, in principle, in any polyatomic systems without a priori exceptions.

If not restricted to the special case of electronic degeneracy, interactions of electronic states with nuclear displacements that constitute the basis of the JTE look like the well known general electron-vibrational (in molecules) and electron–phonon (in crystals) interactions. In fact, however, JT vibronic couplings are different from the general cases, and the difference is due to the different number of electronic states involved in the interaction with vibrations. In the usual approach the interaction of one electronic nondegenerate (usually ground) state or band with vibrations is considered, and therefore it is nonzero for totally symmetric vibrations only. Distinguished from this general case the JTE involves necessarily *two or more electronic states (bands)*, degenerate or with a limited energy gap between them (pseudodegenerate), which allow for interaction also with low-symmetry nuclear displacements. The latter may produce peculiar (unusual) adiabatic potential energy surfaces (APES) with conical intersections, instabilities, distortions, and pseudorotations, and a variety of important observable properties, jointly termed JTE.

Since two or more electronic states and low-symmetry nuclear displacements are present in any quantum polyatomic system with more than two atoms, there are no a priori exceptions from possible occurrence of JTE in such systems. The question is only that, depending on the system parameters, the JTE may be small, and it may be unobservable directly. For nuclear configurations with zero energy gaps between the interacting electronic states (exact degeneracy) the APES has no minimum due to the JTE, but if the vibronic coupling constants are small, there is only splitting of vibrational frequencies and no structural instability. This is true also for weak RTE. The weak PJTE just softens (lowers the vibrational frequency of) the state under consideration in the direction of the active coordinate, but in many cases this softening cannot be observed directly as we don't know the primary frequency without the PJT interaction (still there are indirect indications of the PJTE in this case, too). The strong PJTE results in instability and distortions which can be observed directly via a variety of consequences for observable properties [1]. The latter may be qualitatively different for JT, PJT, and RT effects, respectively.

This modern understanding of the JTE is based on the latest achievements of the theory. In the primary (“primitive”) formulation based on the JT theorem [2] in which only exact degeneracy and the interaction with only linear terms of vibronic coupling were taken into account, the JTE states that *in electronic degenerate states of nonlinear molecular systems the nuclear configuration is unstable with respect to low-symmetry distortions that remove the degeneracy*. The limitation of linear vibronic coupling resulted in the exclusion of linear molecules, making them an exception from the JTE; with the inclusion of quadratic terms of vibronic coupling, linear molecules in degenerate states may become unstable (this is the RTE), similar to the JTE<sup>1</sup>).

The limitation of exact degeneracy was first removed by Opik and Pryce [4], but they assumed that the degeneracy is lifted by a small perturbation transforming the point of degeneracy into an avoided crossing, for which the JTE remains, albeit slightly modified. The idea was essentially extended much later to include interactions with any excited states (with large energy gaps) and to show that this interaction is of fundamental importance, as it is the only source of instabilities and distortions in polyatomic systems in nondegenerate states. Because of its extreme importance and to introduce some denotations used below, we bring here a simple formulation of the PJTE.

Consider the APES of a two-level system with the ground state 1 and excited state 2 and an energy gap  $\Delta$  between them, which interact (mix) under the symmetrized nuclear displacement  $Q_\Gamma$ . Using perturbation theory with respect to the linear vibronic coupling term  $(\partial H/\partial Q_\Gamma)_0$   $Q_\Gamma$  we easily obtain [1] that the primary curvature (the curvature without vibronic coupling) of the ground state  $K_0^\Gamma$ ,

$$K_0^\Gamma = \langle 1 | (\partial^2 H / \partial Q_\Gamma^2)_0 | 1 \rangle \quad (1)$$

is lowered by the amount  $(F_\Gamma^{12})^2 / \Delta_{12}$ ,

$$K^\Gamma = K_0^\Gamma - (F_\Gamma^{12})^2 / \Delta_{12} \quad (2)$$

where  $F_\Gamma^{12}$  is the PJT vibronic coupling constant,

$$F_\Gamma^{12} = \langle 1 | (\partial H / \partial Q_\Gamma)_0 | 2 \rangle \quad (3)$$

---

<sup>1</sup> The above formulation of the JTE without the exception of linear molecules was given first by L. Landau in a discussion with E. Teller of his student’s (Renner’s) work on the linear CO<sub>2</sub> molecule [3]. Since in the linear vibronic coupling approximation linear molecules are exceptions from the JTE, Teller claimed that in this case Landau was wrong and that “this was the only argument” he “won in discussions with Landau”. It turns out that Teller did not win this argument, because when the full vibronic coupling is taken into account (as was implied in Landau’s statement) linear molecules are not exceptions.

Similarly, for a multilevel problem in the linear approximation,

$$K^\Gamma = K_0^\Gamma - \sum_j (F_\Gamma^{1j})^2 / \Delta_{1j} \quad (4)$$

At the point of extremum of the APES in the  $Q_\Gamma$  direction,

$$\langle 1 | (\partial H / \partial Q_\Gamma)_0 | 1 \rangle = 0 \quad (5)$$

(we call this point high-symmetry configuration) the curvature  $K^\Gamma$  coincides with the force constant; the latter is thus a sum of two terms:

$$K^\Gamma = K_0^\Gamma + K_v^\Gamma \quad (6)$$

where  $K_0^\Gamma$  after (1) is the rigidity of the system with regard to  $Q_\Gamma$  displacements of the nuclei in the fixed electron distribution, while the negative PJT vibronic coupling contribution  $K_v^\Gamma$  stands for the softening of the system in this direction due to electrons partly following the nuclei.

If

$$|K_v^\Gamma| > K_0^\Gamma \quad (7)$$

(or for a two-level system  $\Delta < F_\Gamma^2 / K_0^\Gamma$ ), the force constant (5) is negative and the system is unstable in the direction  $Q_\Gamma$ .

Thus the condition (7) is sufficient to make the system unstable. But is it a necessary condition? In other words, can the system become unstable beyond the condition (7), that is, can the inequality  $K_0^\Gamma < 0$  be realized? We succeeded to show [5, 6] that at the extrema points (5) the inequality

$$K_0^\Gamma > 0 \quad (8)$$

*always* holds, meaning that the PJT coupling to the appropriate excited states is the only possible source of instability of the ground state high-symmetry configuration (5) (a similar statement can be formulated for the instability of excited states). This means also that the condition  $|K_v^\Gamma| > K_0^\Gamma$  is both necessary and sufficient for instability of the systems.

For atoms the condition (8) is trivial. Indeed, since the charge distribution around the nucleus obeys the condition of minimum energy, any displacement of the nucleus in the fixed electron cloud (equivalent to the displacement of the latter with respect to the fixed nucleus) will increase the energy. This argumentation does not hold for molecules, because when there are two or more nuclei, the energy minimum of charge distribution for fixed nuclei is not an energy minimum with regard to nuclear displacements; the latter may decrease the nuclear repulsion. Nevertheless, it was shown both analytically and by *ab initio* calculations [5, 7] that the condition (8) at the points (5) is valid *always*.

Thus, with these proofs two important additions to the previous traditional understanding of the JTE emerged: (1) Any polyatomic system may be subject to the JTE, and (2) if there are instabilities and distortions of high-symmetry configurations, they are due to, and only to the JTE. Together with the previously achieved understanding of the role of quadratic terms of the vibronic coupling, the extended formulation of the JTE that includes the latest achievements in this field is as follows [1, 8]:

*The necessary and sufficient condition of instability of high-symmetry configurations of any polyatomic system (lack of minimum of the APES) is the presence of two or more electronic states, degenerate or nondegenerate, that are interacting sufficiently strongly under the nuclear displacements in the direction of instability, the twofold spin degeneracy being an exception.*

This formulation may be regarded as a general law of instability of polyatomic systems. As compared with the previous formulations of the JTE this general law does not restrict the instability to exact degeneracies or near-degeneracies and excludes other mechanism of instability. The only restriction is the requirement of “high-symmetry configurations” in the sense of (5). The meaning of this requirement is that the system should be force-equilibrated; if there is no extremum of the APES, the system is unstable for other reasons not related to the JTE (e.g., classical electrostatic repulsion). The twofold spin degeneracy is an obvious exception from the JTE since, in accordance with the Kramers theorem, only magnetic interactions can remove this degeneracy, whereas the vibronic coupling is electrostatic.

The consequences of the extended formulation of the JTE in the form of a general law are vast, both for fundamental understanding of the origin of molecular and solid state structure and its applications [1]. In particular, it leads directly to the conclusion that all structural symmetry breakings in molecular systems and condensed matter are triggered by the JTE [9]. Together with the statement in particle physics that “symmetry breaking is always associated with degeneracy” [10] we may speculate that *Nature tends to avoid degeneracies*. In molecular systems and condensed matter, avoiding degeneracies is realized via the JTE.

The statement “Nature tends to avoid degeneracies” should be understood in the sense that any degeneracy will be removed, provided there are degrees of freedom to do it. In the absence of such appropriate degrees of freedom the degeneracy could remain. So far we did not find such examples when the degeneracy remains. For instance, in an isolated system in a degenerate electronic E state, the degeneracy will be removed by the JTE, but the double degeneracy of the ground vibronic level in the free molecule at first sight seems to remain. However, it will be removed by the Coriolis interaction. Another example is the Kramers twofold spin degeneracy mentioned above, which can be lifted only in the presence of magnetic fields, and therefore seems to remain in the absence of external perturbations. However, even in this case there seem to be the magnetic field of the nuclei which formally removes the degeneracy.

As for practical applications of the extended JTE, they are numerous and continuously increasing, involving such important fields as molecular shapes, stereochemistry, chemical activation and mechanism of chemical reactions, al-range

spectroscopy, electron-conformational changes in biology, impurity physics, lattice formation, phase transitions, etc. [1].

## 2 Hidden JTE: General Considerations

The generalized formulation of the JTE given in the previous section raises some questions that require special explanation. If the instability of any polyatomic system is of JT origin, why are there systems with no apparent electronic degeneracy or pseudo-degeneracy, which are unstable in the high-symmetry configuration and stable in configurations of lower symmetry? In other words, there are stable molecular systems in low-symmetry configurations for which the nearest high-symmetry configuration has no degenerate ground state and no low-lying excited states, and hence no apparent JTE. Recent developments in JTE theory cast light on this question.

As shown below, it turns out that in all cases when the JT origin of distortions is not seen explicitly, the instability is still due to the JTE, but the latter is “hidden” in the excited states of the high-symmetry configurations. For any fixed nuclear configuration one can define the ground and excited electronic states, but by changing the nuclear configuration a crossover of the electronic energy levels may take place which interchanges the ground and excited states, so that the former excited state becomes the ground state in the changed nuclear geometry. This is what happens with the hidden JTE.

Usually, exploring molecular shapes, the nuclear configuration at the global minimum of the APES is sought for, but no much attention is paid to the problem of the *origin* of this configuration. If the geometry of the system in the global minimum has lower symmetry than the nearest possible higher symmetry configuration, the latter should be unstable *due to JTE in the ground or excited states*. The latter case (excited-state JTE in the high-symmetry configuration) can be traced back from the distorted configuration by searching the APES and revealing the electronic level crossover. The examples in the next Sections explain this situation in more detail.

Hidden JTE (HJTE) cases can be divided into two kinds (Fig. 1):

1. The distorted ground state configuration is due to a strong JTE in the excited state of the high-symmetry configuration, with a stabilization energy  $E_{JT}$  larger than the energy gap  $\Delta$  to the ground state (Fig. 1a).

For an excited state  $E \otimes e$  problem the condition that its distortion will produce a global minimum is  $(F_E^2/2K_E) > \Delta$ , where  $F_E$  and  $K_E$  are the vibronic coupling and primary force constants, respectively. For a  $T \otimes (e + t_2)$  problem the corresponding conditions are either  $(F_E^2/2K_E) > \Delta$  when  $e$  distortions are advantageous, or  $(2F_T^2/3K_T) > \Delta$  in case of  $t_2$  distortions.

2. The distorted ground state configuration is due to a strong PJT mixing of two excited states of the high-symmetry configuration with an energy gap  $\Delta_{12}$  and a

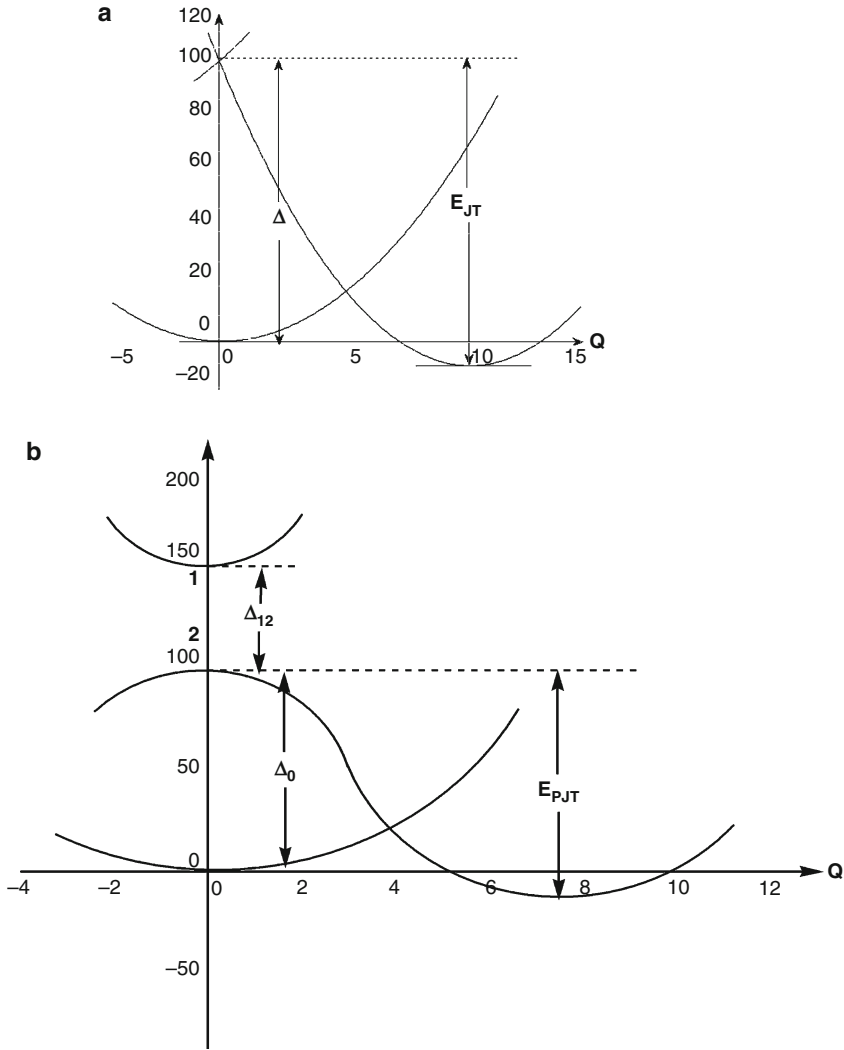


**Fig. 1** Illustration of two cases of hidden JTE: **(a)** Excited state JTE overcomes the energy gap to the ground state producing a global minimum with a distorted configuration (the ground state A is nondegenerate); **(b)** PJTE between two excited states produces a global minimum with a distorted configuration

stabilization energy  $E_{\text{PJT}}$  larger than  $\Delta_0$  (Fig. 1b). The condition that the excited state PJT distorted configuration produces a global minimum of the APES is thus [1]

$$(F_{\Gamma}^{12})^2/2K_0 - \Delta_{12} + \Delta_{12}^2 K_0/2(F_{\Gamma}^{12})^2 > \Delta_0 \quad (9)$$



In contrast to the JT case, where the possible distortion is restricted by the JT active modes only, the PJT-induced distortion may be of any kind, depending on the symmetries of the mixing states. Another distinguished feature of the excited-state PJT-induced distortion is that it leads to orbital disproportionation discussed in Sect. 4.

### 3 Hidden JTE Generated by Excited JT States

The first type of hidden JTE defined above is generated by an excited state with a strong JTE. A straightforward example of such a hidden JTE, the ozone molecule  $O_3$ , was considered recently [11]. Ab initio calculations of the electronic structure of this molecule were performed by a number of authors. Figure 2 shows some of the results obtained by means of high-level ab initio calculations for the ground state with geometry optimization [12–14].

The APES of  $O_3$  has three equivalent minima (Fig. 2a) in which the molecule was shown to have a distorted (obtuse) triangular configuration, and a central minimum at higher energy for the undistorted regular triangular geometry. Figure 2b shows the cross section of the surface along one of the minima. The electronic ground state of this molecule is not degenerate, neither at the undistorted nor the distorted nuclear configurations, so there is no JTE in the ground state, nor are there low-lying excited states to justify an assumption of a PJTE. Nevertheless, we see explicitly the distortions. So where is the JT origin of these distortions?

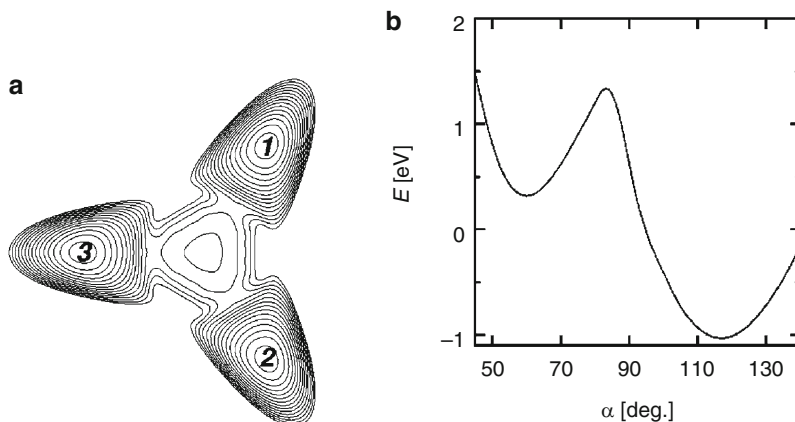


**Fig. 2** Ab initio calculations for the ground state APES of the ozone molecule [12–14]: (a) equipotential contours showing three minima of three equivalent obtuse-triangular distortions and a shallow minimum (in the centre) of the undistorted regular-triangular configuration [12]; (b) cross section of the APES along one of the minima [13, 14] ( $\alpha$  is the angle at the distinguished oxygen atom in the isosceles configuration)

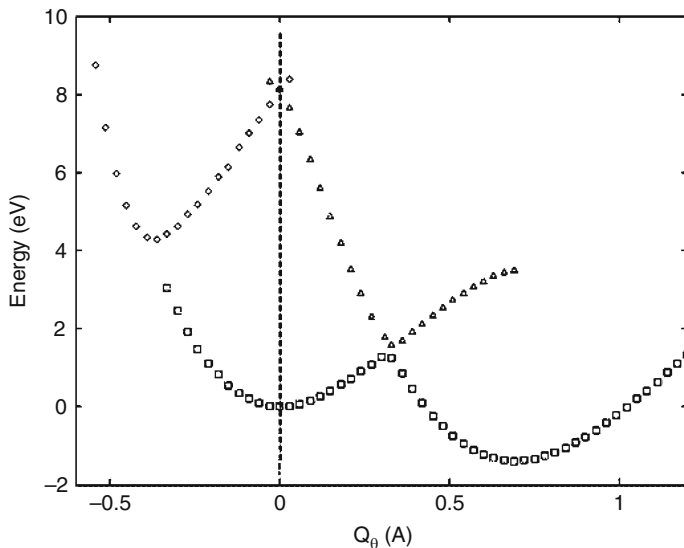


**Fig. 3** Cross-section of the APES of the ozone molecule along the  $Q_\theta$  component of the double degenerate  $e$  mode obtained by numerical ab initio calculations including the highly excited  $E$  state, explicitly demonstrating that the ground-state distorted configurations are due to the JTE in the excited state [11]. The global minimum is at  $Q_\theta = 0.69 \text{ \AA}$  and the  $E$ – $A$  avoided crossing takes place at  $Q_\theta \sim 0.35 \text{ \AA}$

To answer this question, ab initio electronic structure calculations including excited states were performed [11]. The results for the cross section along one of the minima are shown in Fig. 3. In comparison with Fig. 2b we see that there is an excited state, which for the undistorted configuration is an  $E$  term, and the global minimum for the distorted configuration is just a component of this degenerate term in the  $E \otimes e$  problem that produces the three minima of the APES (the interaction with the ground  $A$  term at the crossing is very weak). In this picture, the JT origin of the three equivalent distorted configurations is seen explicitly as originating from the strong JTE in the excited state, with essential contribution of quadratic terms of the vibronic coupling.

Note that the energy gap from the ground  $A$  state to the excited  $E$  state in the undistorted configuration is relatively large,  $\sim 8.5 \text{ eV}$ , so the “classical” thinking of the JTE as a small structural deviation from the configuration of the degenerate state could not apprehend such an effect of distortion with  $Q_\theta = 0.69 \text{ \AA}$  and with a stabilization energy of more than  $9 \text{ eV}$  (in our early ab initio calculations [7] we encountered cases of strong PJTE between states with energy gaps of  $10$ – $15 \text{ eV}$ ). The paradigm of the JTE as resulting in small distortions should be eliminated. The JT distortions may be of any size as *all* the distortions are of JT nature.

To reveal the JT origin of the distortions is not the end of the story: the authors of the above electronic structure calculations of  $\text{O}_3$  (or any other ab initio calculations with geometry optimization that result in distorted configurations) may argue that

it is nice to know the origin of the minima, but this does not change the validity of their results on the geometry of the system (the global minimum) and vibrational frequencies (the curvature of the minimum). With regard to the interpretation of the numerical results this would be wrong judgment. Indeed, if the minima are of JT origin, the properties of the system should bear all the features of the JTE that produced them. In particular, in the case of the ozone molecule the minima emerge as a result of the JT  $E \otimes e$  problem for which the wavefunctions and energy levels should be subject to the topological (Berry) phase, which may drastically change the results. The differences include first of all the ordering and spacing of the vibronic energy levels, their ground state degeneracy, and fractional (semi-integer) quantum numbers of the vibrations when the Berry phase is included [1], which in turn change the spectroscopic and thermodynamic properties. With the Berry phase included, the ordering of the vibronic energy levels is:

$$E, A_{1(2)}, A_{2(1)}, E, E, A_{1(2)}, A_{2(1)}, E, E, A_{1(2)}, A_{2(1)}, \dots$$

and their quantum numbers are fractional, whereas if the Berry phase is ignored we have:

$$A_1, E, E, A_{1(2)}, A_{2(1)}, E, E, A_{1(2)}, A_{2(1)}, E, E, \dots$$

and the quantum numbers are integer. Thus by revealing the hidden JTE, the JT origin of the distorted global minimum configuration, we get the correct observable spectroscopic and thermodynamic properties of the system, which are essentially different from those obtained by electronic structure calculations of the ground state.

Of particular interest are the fractional (half-integer) quantum numbers of the vibronic energy levels as they influence directly the spectroscopic properties, e.g., the Coriolis splitting of the ground state. For a triangular  $X_3$  (symmetric top) molecule the rotational energy is given by the following approximate expression [15]:

$$E = BJ(J + 1) - (B - C)K_c^2 \pm 2C\zeta K_c \quad (10)$$

where  $B$  and  $C$  are the rotational constants (the  $C$  axis is perpendicular to the  $X_3$  plan),  $J$  and  $K_c$  are the rotational quantum numbers of a symmetric top, and the last term describes the Coriolis interactions with the Coriolis constant  $\zeta$ . For strong JTE or PJTE the effective Coriolis constant can be taken equal to the quantum number  $m$  of the vibronic level [1, 12]. It emerges from (10) that the Coriolis splitting equals  $4mCK_c$ , and for integer values of  $m$  it will differ essentially from those for half-integer  $m$ . Moreover, the ground vibronic state with  $m = 0$  should not be split by the Coriolis interaction, whereas it should be split in the state with fractional quantization where  $m = \pm 1/2$ .

## 4 Hidden JTE Generated by PJT Coupling of Two Excited States

The second type of hidden JTE formulated in Sect. 2 is even more “hidden” than the first type above. The best examples of this kind of JTE induced by PJT coupling between two excited states are in systems with half-filled closed shells of degenerate  $e$  and  $t$  orbitals, meaning electronic  $e^2$  and  $t^3$  configurations. Indeed in the ground state, according to Hund’s rule, the electronic configurations have the highest possible spin,  $^3A$  in  $e^2$  and  $^4A$  in  $t^3$ , as in  $(e_\theta \uparrow; e_\varepsilon \uparrow)$  and  $(t_x \uparrow; t_y \uparrow; t_z \uparrow)$ , respectively. Since the charge distribution in these configurations is totally symmetric with respect to the geometry of the system and the electronic states are nondegenerate, no JTE is expected in these ground states. Other distributions of the electrons on these orbitals result in excited terms with lower spin,  $^1E$  and  $^1A$  in  $e^2$ , and  $^2E, ^2T_1$  and  $^2T_2$  in  $t^3$ . In accordance with the earlier (primitive) formulation of the JT theorem, the nuclear configuration (geometry) of the system in the excited degenerate states should be unstable. Unexpectedly, it was shown [16–19] that, *in violation of the earlier formulation of the JTE*, all these states are non-JT, meaning that the totally symmetric charge distribution of the  $e^2$  and  $t^3$  electron configurations is not violated by the electron interactions in the excited states. Since the spin of the latter is different from that in the ground state, there is no PJT interaction between them either. Nevertheless many of these systems are distorted in the ground state. So where is the JTE in these systems?

Analyzing this situation it was found that, in systems with electronic  $e^2$  configurations, there is a strong PJTE between the two excited states  $^1E$  and  $^1A$ , approximately twice as strong as the expected JTE in the same system with just one  $e$  electron [16]. The possibility of such a PJTE, in general, was indicated earlier [17–19], but it was not comprehended that it may produce a global minimum with a distorted configuration. Calculations including the  $E$ – $A$  PJT mixing of excited states of  $\text{Na}_3$  were performed to explain its two-photon ionization spectra [20].

Consider, for example, the triangular molecule  $\text{Si}_3$  with  $D_{3h}$  symmetry. Experimental spectroscopic data indicate that, similar to  $\text{O}_3$ , this molecule in its ground state has a distorted (obtuse triangular) configuration with  $C_{2v}$  symmetry. Figure 4 illustrates some results of ab initio MRCI/cc-pqzt calculations of the electronic structure of this molecule (including excited states) and the APES in the cross-section along the mode of distortion ( $Q_\theta$  coordinate) [16]. We see that the electronic ground state in the undistorted geometry is a spin triplet  $^3A'_2$ , while the excited states are singlets  $^1E'$  and  $^1A'$ , with a very small JTE in the  $^1E'$  state (which cannot overcome the energy gap to the ground state to produce the global distortion as in the  $\text{O}_3$  case), but a strong PJTE ( $^1E' + ^1A'$ )  $\otimes e'$ . In the direction of the distortion, one of the components of the  $^1E'$  term is stabilized by the strong PJT coupling with the excited  $^1A'_1$  state and crosses the ground triplet state of the undistorted configuration to produce the global minimum with a distorted geometry. The latter is in agreement with the experimental data on infrared spectra [21, 22]. The small JTE in the  $^1E'$  state is due to the “contamination” of the non-JT pure  $e^2$  configuration with other

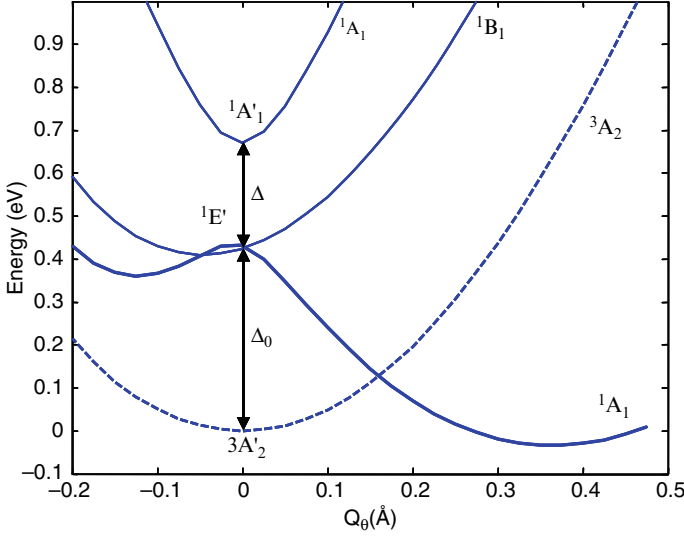


**Fig. 4** Cross section of the APES along the  $Q_\theta$  coordinate for the terms arising from the electronic  $e^2$  configuration of  $\text{Si}_3$  [16]. Its main features are (as predicted by the theory): a very weak JTE in the excited  $E$  state, a strong PJTE between the  $A$  component of this state and the higher  $A$  state producing the global minimum with a distorted configuration, and a second conical intersection along  $Q_\theta$  (with two more equivalent intersections in the full  $e$  space). The spin-triplet state is shown by dashed line

(non- $e^2$ ) configurations in the process of ab initio calculations with configuration interaction.

Figure 4 shows also one of the additional conical intersections in the  $Q_\theta$  direction, and there are two other equivalent intersections in the  $e$  space of the distortions in accordance with the JTE theory for the  $E \otimes e$  problem [1]. Because of these additional conical intersections there are no Berry phase implications in this case: the transition between the minima along the lowest barriers goes around four conical intersections instead of one [23, 24].

The PJTE in excited states of systems with electronic  $e^2$  configurations, which produce global minima with distorted geometries and orbital disproportionation (see below), was confirmed also by ab initio calculations of a series of molecular systems from different classes, including  $\text{Si}_3\text{C}$ ,  $\text{Si}_4$ ,  $\text{Na}_4^-$ , and  $\text{CuF}_3$  [16].

Moving to systems with half-closed-shell electronic  $t^3$  configurations, we find a similar totally symmetric charge distribution in all their states, ground and excited (including degenerate states), which makes all of them non-JT, in violation of the primitive formulation of the JTE. Again, in these cases there is a strong PJTE that mixes two excited states, with the result that the lower one is pushed down to overcome the energy gap to the ground state and to produce a global minimum with a distorted configuration. For the electronic  $t_2^3$  configuration the energy terms are  $^4A_2$  (usually the ground state),  $^2E$ ,  $^2T_1$  and  $^2T_2$  (the results for  $t_1^3$  are similar), and the strong PJT problem under consideration is  $(^2T_1 + ^2T_2) \otimes e$ .

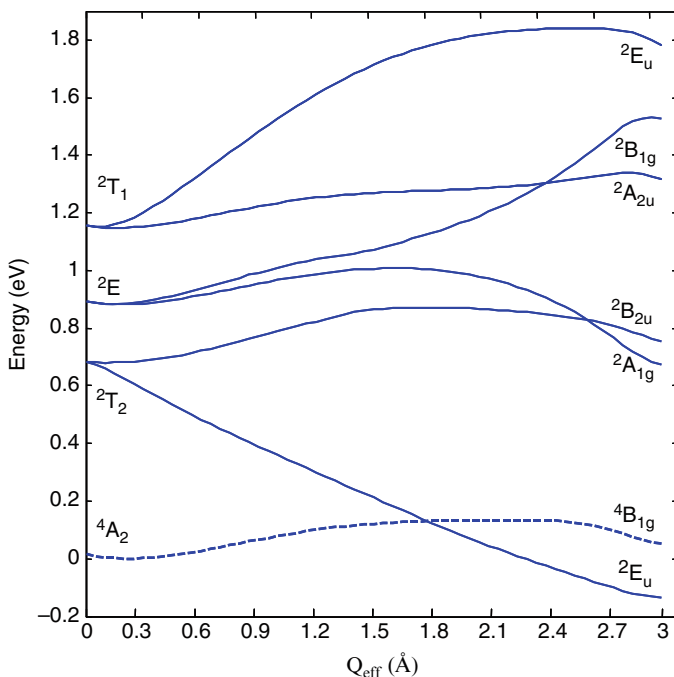


**Fig. 5** Cross-section of the APES of  $\text{Na}_4^-$  along the  $e$ -mode distortion transforming the system from tetrahedral ( $Q_{\text{eff}} = 0$ ) to square-planar geometry due to the  $(T_1 + T_2) \otimes e$  PJT coupling

Consider the example of the  $\text{Na}_4^-$  cluster [16]. In its high-symmetry configuration the four sodium atoms are arranged in a tetrahedron. The four 3s valence orbitals in this conformation form  $a_1$  and  $t_2$  symmetrised orbitals. In the  $\text{Na}_4^-$  system the valence electronic configuration is  $a_1^2 t_2^3$ , producing electronic terms  $^4A_2$ ,  $^2T_1$ ,  $^2E$  and  $^2T_2$  from the  $t_2^3$  configuration. CASSCF calculations of the electronic structure of this system in the ground and excited states as a function of the tetragonal  $e$  displacements using the  $cc\text{-}pvtz$  basis set and the  $s$  valence orbitals of Na as the active space are illustrated in Fig. 5.

As expected from the general theory [16], there are no significant JT distortions in any of the states formed by the  $t_2^3$  configuration, but there is a strong PJTE of the type  $(^2T_1 + ^2T_2) \otimes e$  that pushes down one of the components of the  $^2T_2$  term, making it the absolute minimum, in which the tetrahedron is distorted in the  $e$  direction. We have thus a spin-quadruplet ground state in the undistorted tetrahedral configuration and a spin-doublet state in the distorted global minimum with the shape of a rhombus.

The  $t_{1u}^3$  configuration was also explored in the fullerene anions  $\text{C}_{60}^{3-}$ . For this system the orbital disproportionation (see Sect. 5) was first revealed by Ceulemans, Chibotaru, and Cimpoesu [25, 26] by direct estimation of the electron interactions in the distorted configuration in order to explain the origin of conductivity in the alkaline-doped fullerenes  $\text{A}_3\text{C}_{60}$ .

## 5 PJT-Induced Orbital Disproportionation and Spin-Crossover

Analyzing the wavefunctions in the distorted configurations in the general case of electronic  $e^2$  configurations it was shown [16] that the distortion induced by the PJT mixing of two excited states is accompanied by *orbital disproportionation* of the type  $(|\varepsilon \uparrow; \varepsilon \downarrow\rangle - |\theta \uparrow; \theta \downarrow\rangle) \rightarrow |\theta \uparrow; \theta \downarrow\rangle$ , meaning that in the distorted geometry the two electrons occupy one  $e$  orbital with opposite spins, instead of the proportionate distribution of the two electrons on the two orbitals in the undistorted configuration. The ab initio calculations for  $\text{Si}_3$  fully confirm this prediction [16]. The orbital disproportionation provides for a transparent physical picture on why and how the distortion takes place. The wavefunctions of the excited singlet terms  $^1A_1$  and  $^1E$  before PJT mixing are:

$$^1A_1 = \frac{1}{\sqrt{2}}(|\varepsilon \uparrow; \varepsilon \downarrow\rangle + |\theta \uparrow; \theta \downarrow\rangle) \quad (11)$$

$$^1E_\theta = \frac{1}{\sqrt{2}}(|\varepsilon \uparrow; \varepsilon \downarrow\rangle - |\theta \uparrow; \theta \downarrow\rangle) \quad (12)$$

$$^1E_\varepsilon = \frac{1}{\sqrt{2}}(|\theta \uparrow; \varepsilon \downarrow\rangle + |\theta \downarrow; \varepsilon \uparrow\rangle) \quad (13)$$

In all these states the charge distribution is symmetrical with respect to the  $\theta$  and  $\varepsilon$  components. Due to the PJTE the  $^1E_\theta$  component mixes with the  $^1A_1$  function to result in their linear combination, which in the case of sufficiently strong vibronic coupling produces a disproportionate distribution of either  $|\varepsilon \uparrow; \varepsilon \downarrow\rangle$  or  $|\theta \uparrow; \theta \downarrow\rangle$  [16]. In any of these cases the charge distribution is nontotally symmetric and distorts the high-symmetry configuration. In other words, if the PJTE conditions are met, it is more energetically convenient for the system to pair its electrons in the same orbital and distort the nuclear framework than to remain symmetrical and high-spin under Hund's rule.

A quite similar effect takes place in the case of electron configurations  $t^3$ . In this case the PJT strong vibronic mixing of two excited states  $^2T_1$  and  $^2T_2$  results in a lower orbitally disproportionate component of the type  $|t_x \uparrow; t_z \downarrow; t_z \uparrow\rangle$ , while the ground quadruplet state  $^4A_2$  corresponds to the Hund's rule distribution  $|t_x \uparrow; t_y \uparrow; t_z \uparrow\rangle$ .

As follows from these results, orbital disproportionation in systems with half-closed-shell electronic configurations is producing a distorted configuration with a lower spin than that of the high-symmetry geometry. For the  $e^2$  configuration this results in a transition from the high-spin (HS) triplet  $^3A$  state to the low-spin (LS) singlet state  $^1A$ , while for  $t^3$  this transition is from the quadruplet (HS = 3/2) to the doublet (LS = 1/2) state. Since the formation of the LS minimum is induced by the PJT distortion originating from an excited electronic state, the two states, HS undistorted and LS distorted, coexist in two minima of the APES, which may be close in energy. Between these two minima there may be a crossing between the two states of different spin, a *spin crossover*. The results of ab initio calculations in [16],

some of which are presented in Figs. 4–6, show explicitly the spin crossover that takes place in the specific molecules under consideration. It may take place in any molecular system with electronic  $e^2$  or  $t^3$  configurations, meaning molecules with at least one threefold axis of symmetry and an appropriate number of electrons.

The spin-crossover phenomenon is known to take place in cubic coordination systems of transition metal compounds (TMC) with electronic configurations  $d^4$ – $d^7$  that may produce either HS or LS complexes, subject to the strength of the ligand field [27–30]. For some values of the latter the two electronic configurations, high-spin and low-spin, may be close in energy so they can cross over as a function of the breathing mode of the system (metal–ligand distance). This spin crossover has been known for a long time and has been the subject of intensive study for over two decades because, in principle, systems with two spin-states may serve as molecular materials for electronics [28, 30]). However, the observation of the two states and transitions between them under perturbations (required for such materials) encounters essential difficulties because of fast radiationless transitions between them (very short lifetime of the higher-energy state due to its fast relaxation to the lower one). So far the two spin states in TMC have been observed only for some compounds in optical  $LS \rightarrow HS$  excitations at low temperatures ( $<50$  K), and mostly as a cooperative effect in solids. They are not observed at higher temperatures because of their poor separation in space and fast relaxation due to the relatively high spin–orbital interaction in the metal [28, 30].

The crossover and orbital disproportionation induced by the PJTE are essentially different from the spin crossover in transition metal compounds (TMC) produced by the strength of the ligand field. Indeed, (1) the PJT-induced spin crossover takes place in a variety of molecular systems, small to moderate, organic and inorganic, as well as in metal-containing molecules, as illustrated on a series of molecular systems taken as examples [16]; (2) the HS–LS intersystem relaxation rate in the PJT case is expected to be much lower than in TMC because the two spin states have different nuclear configurations, distorted and undistorted, producing a significant barrier between them and a small Franck–Condon factor, while the spin–orbital interaction in light-atom molecules is smaller by orders of magnitude than in TMC; (3) based on these considerations (followed by numerical estimates) it can be assumed that in the PJT-induced spin-crossover the switch between the two states (in both directions) under perturbations can be observed as a single-molecule phenomenon and at relatively high temperatures. The molecule  $Si_4$  (Fig. 6) seems to be an appropriate candidate for testing this effect.

For the molecular systems above, for which numerical calculations were carried out, numerical estimates for the positions of the two minima on the APES, their energies and the point of crossover of the terms with different spin are given in Table 1, with the notations shown in Fig. 7. The values of the energy barriers are corrected for zero-point vibrational energies. We see that the spin-crossover parameter values vary in considerably large ranges. Preliminary estimates show that the relaxation rate in some of these systems is by several orders of magnitude lower than in TMC. Since the number and the variety of molecules with  $e^2$  and  $t^3$  electronic configurations are practically unlimited, we may hope that systems with required



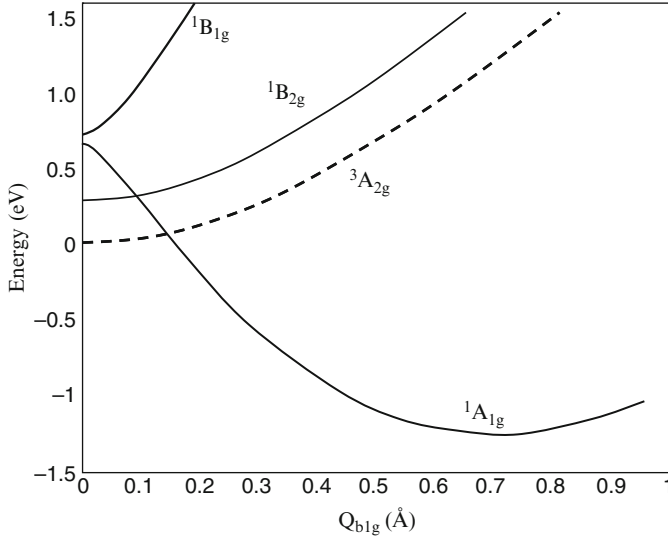


**Fig. 6** Cross-section of the APES of  $\text{Si}_4$  along the  $b_1$ -mode that distorts the system from square-planar to rhombic geometry due to the  $(^1A_1 + ^1B_1) \otimes e$  PJT coupling between two excited states

**Table 1** The parameters of the JT spin-crossover in several systems

	Method	$\Delta_{\text{ex}}$ (eV)	$\delta_{\text{HS}}$ (eV)	$\delta_{\text{LS}}$ (eV)
$\text{Si}_3\text{C}$	CASPT2/cc-pvtz	2.180	-0.148	2.031
$\text{Na}_4$	MRCI/cc-pvtz	0.367	-0.020	0.364
$\text{Si}_4$	CASPT2/cc-pvtz	1.341	0.004	1.241
$\text{Na}_4^-$	CASPT2/cc-pvtz	0.141	0.107	0.251
$\text{Si}_3$	MRCI/cc-pqtz	0.132	0.062	0.194
$\text{CuF}_3$	CASPT2/Roos	0.190	0.541	0.712
$\text{C}_{60}^{3-}$	DFT (LDA) [31–33]	0.157	-0.004	-0.001

$\Delta_{\text{ex}}$  is the energy difference between the ground states of the high-spin and low-spin configurations, and  $\delta_{\text{HS}}$  and  $\delta_{\text{LS}}$  are the respective energy barriers, the energy difference between the minima and the crossing point between the two spin states (Fig. 7). All the energies are corrected for zero-point vibrational energies

combinations of these parameter values in specific limits and with low relaxation rates are feasible. This *JT single-molecule spin crossover* is a new phenomenon that may also have applications in novel materials for electronics.

## 6 Role of Excited States in Rationalization and Prediction of Molecular and Solid State Properties

The extended formulation of the JTE above – the law of instability – states that the necessary and sufficient condition for instability of the high-symmetry configuration of any polyatomic system is the presence of two or more electronic states

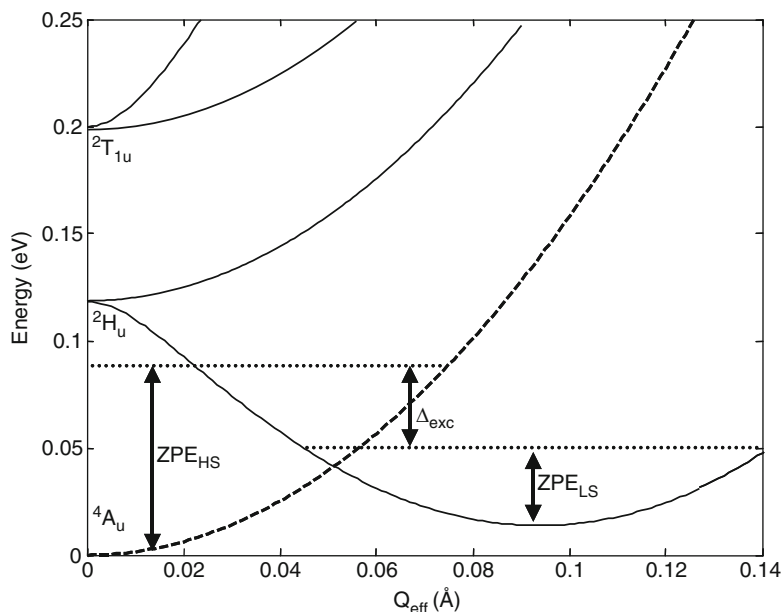


**Fig. 7** Cross-section of the APES of  $C_{60}^{3-}$  along the *effective mode* that takes the system from the undistorted high-spin minimum to the distorted low-spin minimum due to the multimode  $(H_u + T_{1u}) \otimes h_g$  PJT coupling [31–33]. The zero-point energies (ZPE) along *this mode* (which are different from the global ZPE) show that the lowest vibronic state associated with the electronic spin-doublet state is lower than that of the spin-quadruplet state

that interact sufficiently strong under the nuclear displacements in the direction of instability. Configurational instabilities are present in a vast majority of processes in chemistry, physics, and biology, including, e.g., transition states of chemical reactions, conformational changes in biology, phase transitions in physics, etc. (for examples see [1]). In all these situations, the possible instabilities (their trigger mechanisms) are controlled by the *two or more electronic states*; there is no instability within just one electronic state.

If the ground state in the high-symmetry configuration is degenerate (meaning it has two or more electronic states), it may produce the instability by itself. More often, the electronic ground state is nondegenerate, and then the instability is possible *only* if there are appropriate excited states that produce the necessary PJT interaction. In this way we get a general approach to (a tool for) solving molecular and solid state problems in which the excited states assume a key role: they determine both the possibility and the direction of instability (e.g., the mechanism of the elementary step of a chemical reaction, starting at its transition state).

The role of excited states in the instability of the ground state comes out clearly from the practice of *ab initio* calculations. Indeed, it is well known that in general, one cannot get instability and energy barriers without including some representation of the corresponding excited states in the basis set or in the singles of configuration

interaction. The negative PJT contribution of the excited states to the curvature of the APES of the ground state, resulting in its instability, was confirmed also directly by means of *ab initio* calculations for specific molecular systems (see, e.g., in [1, 7, 34, 35]). A direct probe of the role of excited atomic states (in the basis sets) in producing the instability of the ground state was performed recently [36]. The  $\text{CaF}_2$  molecule was shown by *ab initio* calculations to have a bent geometry in its ground state due to the PJT instability of the linear configuration, in which the main contribution to the PJTE is due to the excited states formed mainly by the excited atomic  $d$  states of Ca [37]. Based on this information, one can predict that by excluding the atomic  $d$  states from the basis set there will be no instability. Indeed, *ab initio* CCSD(T) calculations with a F-cc-pvtz basis set yield a bent configuration for  $\text{CaF}_2$  in the ground state, with an angle  $\alpha = 154^\circ$  and interatomic distance  $R = 2.006 \text{ \AA}$  when the full basis set is involved, and a linear configuration with  $\alpha = 180^\circ$  and  $R = 2.059 \text{ \AA}$  if the excited atomic  $d$  states are excluded from the basis set [36].

The role of the JTE is most important in interpretation (rationalization) of experimental results including results of *ab initio* calculations. With regard to the latter the JTE may serve as a general (based on first principles) analytical model for understanding and generalizations. In the majority of cases the results of *ab initio* calculations are published “as they are” with discussion of methods used and accuracies achieved in comparison with other similar calculations, which is an important problem by itself, also because they yield necessary numbers good for comparison with the experimental data. But very rarely the question is raised why the results are “as they are”, meaning what is the origin of the molecular characteristics obtained from the calculations. As an illustrative example we mention the results of a recent paper entitled: *Why are some  $\text{ML}_2$  molecules ( $\text{M} = \text{Ca, Sr, Ba}$ ;  $\text{L} = \text{H, F, Br}$ ) bent while others are linear?* [37]. While the *ab initio* calculations only yield that some of these molecules are linear and others are bent, the analysis of the results from the point of view of the PJTE shows convincingly what is the difference in the electronic structure of the atoms that makes the molecular geometry different. Indeed, Fig. 8 shows the MO scheme for such  $\text{ML}_2$  molecules, from which it is seen that the PJT mixing of the HOMO  $\sigma_u$ , formed mainly by the ligand orbitals, with the unoccupied  $\pi_g$  orbitals, formed by mainly central atomic  $d$  orbitals, may produce the odd (bending) nuclear displacements. Obviously, both the energy gap between these states  $\Delta$  and the vibronic coupling constant  $F$  are specific for the atoms M and L, and only some of them obey the condition of instability (7) [37].

Another example is the prediction of possible noncentrosymmetric linear configurations of  $\text{YX}_2$  molecules as a result of the PJT mixing of the electronic state under consideration with a higher-energy state of opposite parity. Such a configuration with two nonequivalent Y–X bonds to two equivalent atoms X seems to be unreasonable, but the bonding interpretation of the PJTE [38] suggest that under certain conditions the additional covalency on  $\pi$  bonding gained by the shortening of one of the Y–X bonds is larger than the loss on distorted (stressed)  $\sigma$  bond, and two such bonds cannot be formed simultaneously. The two minima of the APES with nonequivalent Y–X bonds in each of them and a dipole moment of the molecule was found in the lowest excited  $^2\Pi_u$  state of  $\text{CuCl}_2$  [38], and there is

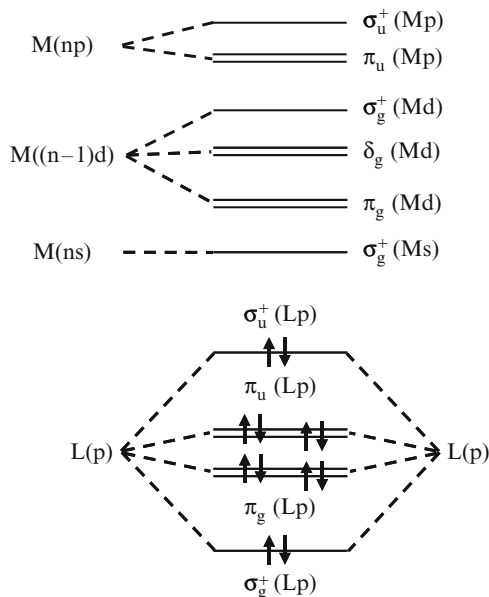


**Fig. 8** Molecular orbital (MO) scheme of the valence states in the  $ML_2$  molecules. Shown in parenthesis are the main atomic orbital contributions to the MOs

reasonable confidence that this is not the only case of such PJT-predicted distorted configurations.

Another illustration of the role of the JTE in rationalization of the results of *ab initio* calculations is the APES (discussed above) of the ground and first two excited states of the  $Si_3$  molecule the cross section of which is shown in Fig. 4 [16]. Presently, just the picture of this APES and the numerical values of its parameters, without further rationalization, may not be sufficiently informative, even for a journal publication; the only model to fully explain this picture is the JTE. The picture reveals a very weak JTE in the excited  $^1E'$  state in combination with the PJTE on the two excited states  $^1E'$  and  $^1A_1'$  accompanied by orbital disproportionation (and no Berry phase factor) which together provide for a sufficiently full understanding of the results of the *ab initio* calculations.

## 7 Conclusions

In this review paper we give an updated formulation of the JTE, which states, in essence, that structural instabilities of high-symmetry configurations of any poly-atomic system are due to and only to sufficiently strong mixing of two or more electronic states (degenerate or with a limited energy gap) by nuclear displacements. This means that if the symmetry of the stable (global minimum) nuclear

configuration of a molecular system is lower than the nearest highest possible symmetry, the latter is unstable due to, and only to the JTE. Based on this understanding, we introduce the hidden JTE (HJTE): if for distorted systems there is no apparent JTE in the undistorted configuration, it is hidden in its excited states. Two qualitatively different cases can be distinguished: (1) the distortion is due to a strong JTE in one of the excited states of the undistorted configuration, and (2) it is created by a strong PJTE mixing two excited states of the latter. Examples with ab initio calculations illustrate both cases. An interesting consequence of the hidden PJTE is that it results in orbital disproportionation and the spin-crossover phenomenon. In general, excited electronic states cannot be ignored in any full analysis of molecular properties (even in the ground state), and the JTE is the unique model that allows for a reasonable rationalization of experimental and computational results.

## References

1. I.B. Bersuker, *The Jahn Teller Effect*, (Cambridge University Press, Cambridge, UK, 2006)
2. H.A. Jahn E. Teller, Proc. Roy. Soc. Lond. A **161**, 220 (1937)
3. E. Teller, in *The Jahn-Teller Effect in Molecules and Crystals*, ed. by R. Englman (Wiley, London, 1972), Foreword
4. U. Öpik M.H.L. Pryce, Proc. R. Soc. Lond. A **238**, 425 (1957)
5. I.B. Bersuker, Nouv. J. Chim. **4**, 139 (1980); Teor. Eksp. Khim. **16**, 291 (1980)
6. I.B. Bersuker, Pure Appl. Chem. **60**, 1167 (1988); Fiz. Tverdogo Tela **30**, 1738 (1988)
7. I.B. Bersuker, N.N. Gorinchoi, V.Z. Polinger, Teor. Chim. Acta **66**, 161 (1984)
8. I.B. Bersuker, in *Fundamental World of Quantum Chemistry*, vol. 3, ed. by E.J. Brandas, E.S. Kryachko (Kluwer, Dordrecht, 2004), p. 257
9. I.B. Bersuker, Adv. Quant. Chem. **44**, 1 (2003)
10. S. Weinberg, *Quantum theory of Fields*, (Cambridge University Press, Cambridge, 1995), Ch. 11
11. P. Garcia-Fernandez, I.B. Bersuker, J.E. Boggs, Phys. Rev. Lett. **96**, 163005 (2006)
12. D. Babikov, B.K. Kendrick, R.B. Walker, R.T. Pack, P. Fleurat-Lesard, R. Schinke, J. Chem. Phys. **118**, 6298 (2003)
13. R. Siebert, P. Fleurat-Lessard, R. Schinke, M. Bittererová, S.C. Farantos, J. Chem. Phys. **116**, 9749 (2002)
14. R. Schinke, P. Fleurat-Lessard, J. Chem. Phys. **121**, 5789 (2004)
15. G. Herzberg, *Electronic Spectra and Electronic Structure of Polyatomic Molecules*, (Van Nostrand, Toronto, 1966)
16. P. Garcia-Fernandez, I.B. Bersuker, J.E. Boggs, J. Chem. Phys. **125**, 104102 (2006)
17. A. Ceulemans, Chem. Phys. **66**, 169 (1982)
18. A. Ceulemans, D. Beyens, L.G. Vanquickenborne, J. Am. Chem. Soc. **104**, 2988 (1982)
19. A. Ceulemans, Top. Curr. Chem. **171**, 27 (1994)
20. R. Meiswinkel, H. Koppel, Chem. Phys. **144**, 117 (1990)
21. J.S. Li, R.J. van Zee, W. Weltner Jr., K. Raghavachari, Chem. Phys. Lett. **243**, 275 (1995)
22. J. Fulara, P. Freivogel, M. Grutter, J.P. Maier, J. Phys. Chem. **100**, 18042 (1996)
23. W. Zwanziger, E.R. Grant, J. Chem. Phys. **87**, 2954 (1987)
24. H. Koizumi, I.B. Bersuker, Phys. Rev. Lett. **83**, 3009 (1999)
25. L.F. Chibotaru, A. Ceulemans, Phys. Rev. B **53**, 15522 (1996)
26. A. Ceulemans, L.F. Chibotaru, F. Cimpoesu, Phys. Rev. Lett. **78**, 3725 (1997)
27. H.A. Goodwin, Coord. Chem. Rev. **18**, 293 (1976)
28. A. Hauser, Top. Curr. Chem. **234**, 155 (2004)

29. E.K. Barefield, D.B. Busch, S.M. Nelson, *Q. Rev. Chem. Soc.* **22**, 457 (1968)
30. O. Kahn, C.J. Martinez, *Science* **279** 5347, (1998)
31. M. Lüders, A. Bordosi, N. Manini, A. Dal Corso, M. Fabrizio, E. Tossatti, *Phil. Mag. B* **82**, 1611 (2002)
32. N. Manini, A. Dal Corso, M. Fabrizio, E. Tossatti, *Phil. Mag. B* **81**, 793 (2001)
33. M. Lüders, N. Manini, P. Gattari, E. Tosatti, *Eur. Phys. J. B* **35**, 57 (2003)
34. I.B. Bersuker, N.B. Balabanov, D. Pekker, J.E. Boggs, *J. Chem. Phys.* **117**, 10478 (2002)
35. B. Bersuker, V.Z. Polinger, N.N. Gorinchoi, *J. Struct. Chem. (Theochem)* **5**, 369 (1992)
36. P. Garcia-Fernandez, I.B. Bersuker, unpublished
37. P. Garcia-Fernandez, I.B. Bersuker, J.E. Boggs, *J. Phys. Chem. A* **111**, 10409 (2007)
38. W. Zou, I.B. Bersuker, J.E. Boggs, *J. Chem. Phys.* **129**, 114107 (2008)

# Electronic Degeneracy and Vibrational Degrees of Freedom: The Permutational Proof of the Jahn–Teller Theorem

Arnout Ceulemans and Erwin Lijnen

**Abstract** In 1937 Jahn and Teller stated their remarkable theorem that all non-linear nuclear configurations are unstable for an orbitally degenerate electronic state. The original demonstration of this theorem was by exhaustive verification for all non-trivial cases. Since then several authors have presented theoretical treatments that offer formal proofs. None of these however succeeds to attain a real insight into the origin of the theorem, nor does there appear to exist a general proof that covers all point groups in a uniform way. For a clear understanding of the Jahn–Teller theorem a different starting point is needed, based on the question: What is the origin of electronic degeneracy? According to Group Theory the existence of an  $n - 1$  fold degeneracy is related to the existence of a set of  $n$  identical sites which form a doubly transitive orbit of a symmetry group. Using the symmetric groups this permutational character of electronic degeneracies can be turned into a transparent proof for the Jahn–Teller theorem. The presentation of this proof is preceded by introductory sections which explain the principal group-theoretical concepts that come into play. The proof is followed by an application to the fivefold degenerate irreducible representation in the icosahedral group. This quintuplet degeneracy can be described by the  $S_6$  permutation group, which gives rise to extra selection rules. The embedding of the icosahedral group in  $S_6$  is discussed, and the relevance of this group-theoretical scheme for the Jahn–Teller interactions in icosahedral shells is demonstrated. The extension to the hyperoctahedron in 4D space is also discussed.

## 1 Introduction

The Jahn–Teller theorem states that ‘a configuration of a polyatomic molecule for an electronic state having orbital degeneracy cannot be stable with respect to all displacements of the nuclei unless in the original configuration all the nuclei lie on a straight line’ [1]. In the original paper of 1937 verification of the theorem was by enumeration of all possible cases. In the words of Teller, ‘this was not a proof that a

mathematician would enjoy.’<sup>1</sup> Nevertheless up till now the original procedure is still considered to be the most practical and useful way to introduce the theorem [2]. Several authors have presented more general proofs, which however lack transparency and do not yield additional insights into the strong connection between distortions and degeneracy. In the present paper we will first review these treatments and then develop a different point of view which leads to a concise permutational proof.

## 2 Existing Proofs of the Jahn–Teller Theorem

The first attempt to clarify the physical basis of the Jahn–Teller theorem was due to Ruch, [3] in an introductory presentation to the 1957 annual meeting of the Bunsen–Gesellschaft in Kiel, which was organised by H. Hartmann. Ruch discussed the general connection between symmetry and chemical bonding, and also touched upon the Jahn–Teller effect in transition-metal complexes. He explained that degeneracy can always be related to the existence of a higher than twofold rotational axis and a wave function which is not totally symmetric under a rotation around this axis. Provided that the wave function is real the electron densities for such a wave function are bound to be anisotropic. The combination of an anisotropic distribution of the electron cloud and a symmetric nuclear frame leads to electrostatic distortion forces where the nuclear frame adapts itself to the anisotropic attraction force.

Strictly speaking the densities of the electronic cloud on the sites of the atomic nuclei, the so-called *on-site* density, need not be different for different components of a degenerate wave function. A simple counter-example is a  $T_{1u}$  orbital level in a cubic cluster. Let  $|\sigma_i\rangle$  denote a  $\sigma$ -type atomic orbital on a given site  $i$ . The symmetry adapted linear combinations (SALC’s) of these basis orbitals are given by (see Fig. 1):

$$\begin{aligned} |T_{1u}x\rangle &= \frac{1}{2\sqrt{2}} (|\sigma_1\rangle - |\sigma_2\rangle - |\sigma_3\rangle + |\sigma_4\rangle + |\sigma_5\rangle + |\sigma_6\rangle - |\sigma_7\rangle - |\sigma_8\rangle) \\ |T_{1u}y\rangle &= \frac{1}{2\sqrt{2}} (|\sigma_1\rangle + |\sigma_2\rangle - |\sigma_3\rangle - |\sigma_4\rangle - |\sigma_5\rangle + |\sigma_6\rangle + |\sigma_7\rangle - |\sigma_8\rangle) \\ |T_{1u}z\rangle &= \frac{1}{2\sqrt{2}} (|\sigma_1\rangle + |\sigma_2\rangle + |\sigma_3\rangle + |\sigma_4\rangle - |\sigma_5\rangle - |\sigma_6\rangle - |\sigma_7\rangle - |\sigma_8\rangle). \quad (1) \end{aligned}$$

Clearly all three components have the same on-site densities. What differs are the *inter-site* or overlap matrix elements. The importance of these inter-site contributions is confirmed by a recent analysis of the vibronic coupling density functional [4]. Parenthetically we note that a function which has the same on-site

---

<sup>1</sup> Historical note by Edward Teller in R. Englman, *The Jahn–Teller effect in molecules and crystals* (Wiley, London, 1972). See also: B. R. Judd, in: *Vibronic Processes in Inorganic Chemistry*, C. D. Flint (ed.) Nato ASI series C288, pp. 79–101 (Kluwer, Dordrecht, 1989)



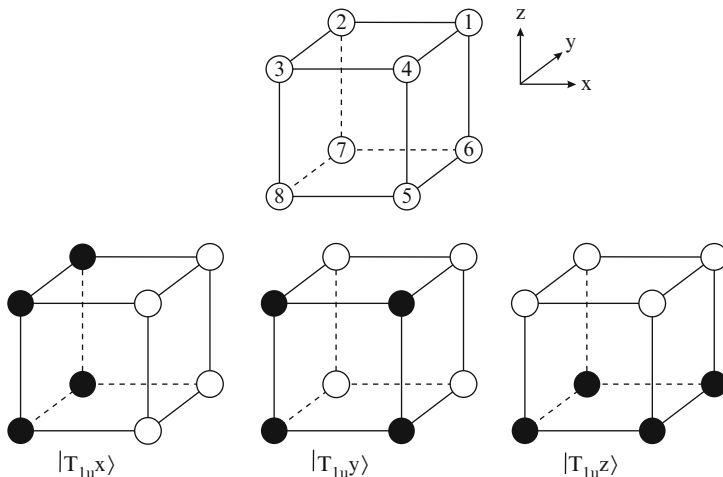


**Fig. 1** SALC's for the  $T_{1u}$  representation of the cube

density on all equivalent atomic sites is called 'equidistributive'. In fact as we have shown elsewhere, [5] for all degeneracies of the cubic groups a degeneracy basis can always be constructed with equidistributive components, provided the use of complex component functions is allowed. For some icosahedral degeneracies more intricate cases may occur where the wave functions have to be of quaternionic form.

In 1968 Ruch and Schönhofer cast the qualitative arguments in a more formal proof [6]. The authors expressed the hope that the proof would yield additional insight. This hope did not really materialize because the proof was not very transparent, one of the reasons being that it was not illustrated with an actual example. In order to obtain a better understanding of this proof we try to apply it to a practical example of a  ${}^2T_{2g}$  state in an octahedral complex, as would be the case for a  $(d)^1$  transition-metal ion such as  $\text{Ti}^{3+}$  surrounded by six ligands. The site symmetry group of a ligand in an octahedron is  $C_{4v}$ . In this site symmetry group the  $T_{2g}$  symmetry of the electronic level transforms as  $B_2 + E$ . The argument then runs as follows: since the electronic level is threefold degenerate and the site-symmetry group only allows non-degenerate and twofold degenerate irreducible representations at least one of the components of the electronic level has to transform as a non-degenerate irreducible representation of the site group. This is indeed the case for the  $B_2$  representation. The electronic density at the site transforms as the direct product  $B_2 \otimes B_2 = A_1$  and thus is totally symmetric. This implies that the electronic level will always yield a non-zero vibronic coupling matrix element with the radial displacement of the ligand at that site. The proof continues to show that this condition is sufficient to claim vibronic instability of the octahedral triplet level. The radial distortions of the octahedron induce a distortion space of the following symmetry:

$$\Gamma(A_1 C_{4v} \uparrow O_h) = a_{1g} + t_{1u} + e_g. \quad (2)$$

According to the Jahn–Teller theorem the active modes for an orbital multiplet are given by the non-totally symmetric part of the symmetrized direct product of the electronic degeneracy:

$$[T_{2g} \otimes T_{2g}] - a_{1g} = e_g + t_{2g}. \quad (3)$$

Square brackets denote the symmetrized part of the direct square. Two aspects of the formal proof are noteworthy. Firstly, as in the qualitative argument the proof only considers the on-site densities. As a result for the  $T_{2g}$  level the vibronic coupling resides with the radial distortions of the octahedron only, as described by the antisymmetric stretch of  $e_g$  symmetry which is the common symmetry in the above equations. However the 1937 Jahn–Teller treatment yielded a stronger result in that it showed *both* active modes to be present in an octahedral complex with six ligands. As we know  $T_{2g}$  electrons preferentially couple with tangential bending modes of  $t_{2g}$  symmetry rather than with radial  $e_g$  distortions, which coincide with nodal planes of the  $T_{2g}$  orbitals. Secondly, although the derivation is no longer by discrete enumeration the proof still rests on the consideration of several separate cases, depending on whether the index  $n$  in the cyclic site group  $C_{nv}$  is equal to 2 or larger than two, and whether the electronic degeneracy is even or odd.

In 1971 a different proof was provided by Blount in the Journal of Mathematical Physics [7]. Blount mentions that after the completion of his proof he learned about the work of Ruch and Schönhofer. He further notes that, although both treatments are closely connected, his approach ‘uses the basic ideas in a more direct fashion and reveals more clearly the distinction between general and special features’ (quoted from [7]). Indeed the 1971 proof calculates directly by means of the standard character theory the overlap between the direct square of the electronic irrep and the normal distortion modes. In line with Ruch and Schönhofer, Blount also subduces this expression to the site groups which leave individual atoms invariant. The proof then splits into several cases depending on whether the subduction of the electronic irrep is reducible or not. The irreducible case occurs when the atoms are lying on a threefold axis and urges Blount to consider the cubic and icosahedral groups separately. Interestingly Blount has also considered possible symmetry breaking in higher dimensions. He argued that already in 4D there appear symmetries where the JT theorem is not obeyed. We will illustrate an example of the hypercube in more details later. This may not be too surprising in view of the fact that also linear 1D structures constitute exceptions to the theorem.

Further rather indirect proofs have been given by Raghavacharyulu [8] and most recently by Pupyshev [9].

In the present work we will approach the problem from a different point of view, and start from the causes for electronic degeneracies. So we will ask ourselves the question: *Why is it that certain point groups contain degenerate irreps?* According to group theory the necessary and sufficient condition is that the group has at least two generators which do not commute. For a proper understanding of the Jahn–Teller effect this algebraic condition is not very useful, and we will find a

more inspiring answer in the theory of induction. Before we can proceed to the actual proof, we collect various group-theoretical propositions that will introduce the reader to the necessary mathematical background that is required for the subsequent proof. For a more intuitive chemical perspective on the present proof, we refer the interested reader to our recent contribution to the commemorative accounts of the Chemical Society of Japan [10].

### 3 Group-Theoretical Propositions

#### 3.1 Transitive Left Cosets

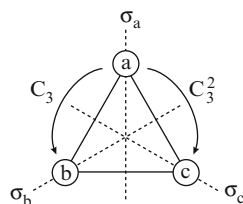
Degeneracy starts from equivalence. A simple way to demonstrate that two objects are equivalent is when the permutation of the two objects is symmetry allowed. Consider a simple triatomic molecule with the shape of a regular triangle. The relevant point group in two dimensions is limited to  $C_{3v}$ . The equivalence of the three nuclei is demonstrated by symmetry operations which permute nuclei that are identical and occupy equivalent positions in space. The set of the three nuclei that are connected in this way is called an *orbit*. Symmetry operations are said to act *transitively* on the elements of the orbit, i.e. they send every element over into every other element of the same orbit. The *stabilizer* of a given nucleus  $\langle a \rangle$  in the molecule is the subgroup  $H_a \subset G$  which leaves the site  $\langle a \rangle$  invariant. In the case of a triangle the stabilizer of a nucleus is a  $C_s$  subgroup. This corresponds to the site groups in the previous proofs. The total group may be expanded in left cosets of this subgroup, according to the general formula:

$$G = \sum_r g_r H, \quad (4)$$

where  $g_r$  is a coset generator or representative. The number of cosets is equal to the quotient of the group orders,  $n = |G|/|H| = 3$ . For our example, using the notation in Fig. 2 the coset expansion of  $C_{3v}$  over  $C_s$  reads:

$$C_{3v} = \{E, \sigma_a\} + \{C_3, \sigma_b\} + \{C_3^2, \sigma_c\}. \quad (5)$$

**Fig. 2** Triatomic configuration with  $C_{3v}$  symmetry together with the corresponding symmetry labels



It is easily seen that the coset distribution reflects the generation of the triangle from the starting point on  $\langle a \rangle$ . The first coset is the set of all elements which map  $\langle a \rangle$  onto itself, the second collects all elements which map  $\langle a \rangle$  onto  $\langle b \rangle$ , and the third contains the elements which send  $\langle a \rangle$  over into  $\langle c \rangle$ . There is thus a one-to-one mapping between the cosets and the elements of the orbit. The cosets thus really represent equivalent sites, and they too form an orbit. Through the coset expansion the geometric concept of equivalent nuclei may be turned into a purely group theoretical concept. We may now pass from a nuclear orbit to an electronic function space by decorating each site with an orbital which is totally symmetric under the respective stabilizer. The space of these basis functions transforms as the orbit of the nuclei, and its symmetry representation is called the *positional* representation [11, 12]. Again we may free ourselves of a particular set of nuclei and think of the positional representation as the transitive representation of the orbit of cosets of a particular site group. We will denote this orbit as  $\Omega(H \subset G)$ , and its representation as  $\Gamma_\Omega$ . In the language of induction theory this positional or orbit representation corresponds to the induced representation from the totally symmetric subgroup representation:

$$\Gamma_\Omega = \Gamma(A' C_s \uparrow C_{3v}). \quad (6)$$

Although  $\Gamma_\Omega$  describes a set of equivalent elements, it is not degenerate, since it can be further reduced into invariant subspaces. For the case of a triangle this representation gives rise to two irreducible representations (irreps) of  $C_{3v}$ .

$$\text{Triangle: } \Gamma_\Omega = A_1 + E. \quad (7)$$

Indeed the sum or trace of the elements of the orbit is certainly invariant under any group action, and thus always constitutes the totally symmetric root,  $A_1$ . In the present case the traceless remainder space with dimension 2 is in fact twofold degenerate. This is not always the case though. Already in a square this is no longer true as the positional representation of the four quadrangular sites, after subtraction of the  $A_1$  irrep, further decomposes into  $E + B_1$  irreps. The essential difference between the triangle and the square is that in the triangle the three sites are *equidistant*. This will prove to be a general result: a configuration of  $n$  equivalent sites gives rise to a degeneracy space of dimension  $n - 1$ , provided all sites are equidistant.

### 3.2 Doubly Transitive Orbits

As we have already indicated, in a group theoretical treatment the geometric concept of equivalent nuclei is generalized to the concept of equivalent site symmetries, which together constitute the orbit of cosets of a given subgroup. This is an essential point of the present treatment which allows us to make abstraction of the particular nuclear configuration and reformulate the problem entirely in group-theoretical terms. At this point we take a different route as compared to the first proof by Ruch

and Schönhofer, where the sites are identified as atomic nuclei. Let us consider equivalence inside the orbit  $\Omega(H \subset G)$ . In precise terms the orbit is *singly transitive*, meaning that there always exists a symmetry operation in  $G$  which can map a given coset  $g_r H$  onto any other coset  $g_s H$ . To define degenerate irreps however a stronger criterion is needed, which requires the orbit of cosets to be *doubly transitive*. This means that any ordered pair of cosets can be mapped on any other ordered pair, i.e.:

$$\begin{aligned} \forall g_r H, g_s H, g_u H, g_v H \in \Omega(H \subset G) \Rightarrow \\ \exists x \in G : x g_r H = g_u H \wedge x g_s H = g_v H. \end{aligned} \quad (8)$$

This criterion is a rigorous group theoretical translation of the intuitive concept of equal distances between all sites. As an example in a square there are no symmetry elements that will turn a pair of opposite sites into a pair of adjacent sites, which reflects the fact that the inter-site distances between opposite and adjacent sites are different. In contrast in a tetrahedron all vertices are equidistant and the six possible pairs or bonds can indeed be permuted. For the representation of a doubly transitive orbit the following theorem was proven by Hall: [13]

**Theorem 1.** *A doubly transitive permutation representation of a group  $G$  over the complex field is the sum of the identical representation and an absolutely irreducible representation [13].*

This theorem provides a connection between a degenerate irrep of dimension  $n - 1$  and the existence of an orbit of  $n$  equivalent and equidistant sites. We will express this result as follows:

$$\Gamma_\Omega = \Gamma_0 + \Gamma_{n-1}, \quad (9)$$

where the elements of the orbit are seen to transform according to the direct sum of two irreps:  $\Gamma_0$  which is the totally symmetric irrep of  $G$ , and an irrep  $\Gamma_{n-1}$ , which represents a degeneracy of dimension  $n - 1$ , i.e. one less than the dimension of the orbit. A legitimate example is the threefold degenerate  $T_2$  irrep in a tetrahedron, which arises through the doubly transitive orbit of the  $C_{3v}$  subgroups:

$$\text{Tetrahedron: } \Gamma_\Omega = \Gamma(A_1 C_{3v} \uparrow T_d) = A_1 + T_2. \quad (10)$$

A useful corollary, which was known to the Luleks, [14] reads:

**Corollary 1.** *The orbit of the cosets of a subgroup  $H$  of group  $G$ ,  $\Omega(H \subset G)$ , can only be doubly transitive for  $H$  a maximal subgroup of  $G$ .*

A subgroup  $H$  is maximal if there are no intermediate subgroups between  $H$  and  $G$  in the branching scheme of  $G$ . A proof of this corollary is presented in the Appendix.

A case in point is the pentagonal subgroup  $D_{5d}$  of the icosahedral point group. This subgroup is a maximal subgroup, and the six pentagonal directions are ‘equidistant’, in the sense that any pair of them can be mapped onto any other pair. Induction then yields the five-fold degenerate H representation:

$$\text{Icosahedron: } \Gamma_{\Omega} = \Gamma (A_1 D_{5d} \uparrow I_h) = A_{1g} + H_g. \quad (11)$$

Note that the opposite is not necessarily true, e.g. the orbit of a maximal subgroup is not necessarily doubly transitive. A case in point in icosahedral symmetry is the trigonal subgroup  $D_{3d}$ . This is a maximal subgroup, but its orbit is not doubly transitive. In fact an icosahedron has ten trigonal sites which are however not all equidistant. Induction from  $D_{3d}$  yields three irreps:

$$\text{Icosahedron: } \Gamma_{\Omega} = \Gamma (A_1 D_{3d} \uparrow I_h) = A_{1g} + G_g + H_g. \quad (12)$$

It is also important to remind that double transitivity implies the mapping of all *ordered* pairs. As an example if the symmetry of the triangle is limited to  $C_3$  only, the double transitivity is lost, since this group does not allow odd permutations that are needed to switch the ordering of pairs. As a result the  $E$  irrep is split into two complex conjugate one-dimensional irreps.

$$\Gamma_{\Omega} = \Gamma (A C_1 \uparrow C_3) = A + E_+ + E_-. \quad (13)$$

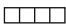




### 3.3 All-Transitive Orbits

When an ordered set of *all*  $n$  elements of a given orbit can be mapped onto any differently ordered set of these elements the orbit is *all-transitive* and the corresponding symmetry group will be isomorphic to the symmetric group,  $S_n$  which contains all permutations of  $n$  elements. In a ‘molecular’ sense, symmetric groups describe the symmetry of a set of  $n$  equivalent equidistant nuclei, which is a so-called simplex. The  $n$ -simplex is the elementary building block of a  $n - 1$  dimensional Euclidean space. The whole space can be tessellated in a lattice of such simplex unit cells. We have already encountered the triangle and tetrahedron as the simplexes of 2D and 3D space respectively. Their symmetry groups are isomorphic to symmetric groups:

$$\begin{aligned} C_{3v} &\sim S_3 \\ T_d &\sim S_4. \end{aligned} \quad (14)$$

The stabilizer of a vertex in a simplex, i.e. the group of all elements of  $S_n$  which leave a given vertex invariant, is the maximal subgroup  $S_{n-1}$ . The set of all vertices thus will transform as the induced representation of a totally symmetric irrep of the site group in the parent group. Since this representation is certainly doubly

**Table 1** Isomorphism relations between the elements of the groups  $T_d$  and  $S_4$ 

		$T_d$ $S_4$	$E$ $1^4$	$8C_3$ $1^13^1$	$3C_2$ $2^2$	$6S_4$ $4^1$	$6\sigma_d$ $1^22^1$
$A_1$	(4)		1	1	1	1	1
$A_2$	(1 <sup>4</sup> )		1	1	1	-1	-1
$E$	(2 <sup>2</sup> )		2	-1	2	0	0
$T_1$	(2, 1 <sup>2</sup> )		3	0	-1	1	-1
$T_2$	(3, 1)		3	0	-1	-1	1

transitive, the theorem applies and the positional space contains a totally symmetric representation, denoted as  $(n)$ , and a  $n - 1$  fold degenerate traceless irrep,  $\Gamma_{n-1}$ , which in the symmetric group is denoted as  $(n - 1, 1)$ :

$$\Gamma_{\Omega} = \Gamma((n - 1) S_{n-1} \uparrow S_n) = (n) + (n - 1, 1). \quad (15)$$

The isomorphism between  $T_d$  and  $S_4$  provides a simple illustration to become familiar with the formal description of permutational groups. A permutational operation on four elements can be characterized as a sequence of cyclic permutations, e.g. a threefold axis running through atom 1 will map 1 onto itself and produce a cyclic permutation of the remaining three atoms. It is therefore denoted as  $(3, 1)$ . All threefold elements have the same cycle structure and in view of the complete transitivity of the set thus must belong to the same symmetry classes. In this way the elements of  $T_d$  can easily be identified as  $S_4$  operators, as shown in Table 1. The irreps themselves are also denoted as partitions of  $n$ , indicated between parentheses. Pictorially these partitions may be denoted by Young tableaux, as also indicated in the character table.

We may put the numbers from 1 to 4 in the Young tableaux in strictly increasing order, such that the number sequence in any row and in any column always increases. The number of ways in which this is possible gives the dimension of the corresponding irreducible representation. The important advantage of the symmetric group over the point groups is that the direct product rules as well as the corresponding Clebsch–Gordan coefficients can be obtained by general combinatorial formulae which apply to all symmetric groups [15]. As an example, the following product rules apply:

$$(n-1, 1) \otimes (n-1, 1) = [(n) + (n-1, 1) + (n-2, 1^2)] + \{(n-2, 2)\}, \quad (16)$$

where square and round brackets denote the symmetrized and antisymmetrized products respectively.

## 4 Electronic Degeneracy

In the previous section the existence of a  $n-1$  fold degeneracy was shown to be related to the presence of a set of  $n$  identical molecular sites, which are symmetry equivalent and equidistant from each other. In these cases the molecular point group can be considered to be a subgroup of the symmetric group  $S_n$ .

$$G \subset S_n. \quad (17)$$

The combinatorial structure of this parent group offers a closed form expression of the connection between permutational degeneracy and internal motion. This forms the basis of our proof.

### 4.1 Construction of a Degeneracy Basis

The theorem by Hall and its corollary provides us with a general tool to describe degenerate irreps of finite groups. The procedure proceeds as follows: one finds all maximal subgroups of a given group and then verifies if the orbit  $\Omega(H \subset G)$  is doubly transitive. If this is the case, the theorem states the existence of a degenerate irrep,  $\Gamma_{n-1}$ , with dimension  $n-1$ . This link between  $\Omega$  and  $\Gamma_{n-1}$  provides at once a carrier space which is singly and doubly transitive. This carrier space is a degeneracy basis, i.e. it defines a purely permutational description of the degeneracy manifold. Indeed for any function space,  $|\Phi\rangle$ , which transforms as  $\Gamma_{n-1}$ , symmetry lowering or subduction from  $G$  to  $H_a$  will yield exactly one component which is totally symmetric in the subgroup. Let us denote this component as  $|\phi_a\rangle$ , and define the other components by applying the coset generators to it, as follows:

$$g_r |\phi_a\rangle = |\phi_r\rangle. \quad (18)$$

The set  $|\Phi\rangle = \{|\phi_i\rangle\}_{i=1,n}$  forms a carrier space which is in one to one correspondence with the elements of the orbit  $\Omega(H \subset G)$ . An orthogonal basis set for  $|\Phi\rangle$  may then always be defined by forming the  $n-1$  traceless combinations of these  $n$  components. As an example in the case of a tetrahedron an arbitrary function space, transforming as  $T_2$ , will have exactly one component which is totally symmetric under a  $C_{3v}$  subgroup, and which we will label as  $|\phi_a\rangle$ . Four such components can be formed, one for each trigonal site. The  $T_2$  basis may then be expressed (up to



**Fig. 3** The threefold degenerate  $T_2$  representation and the tetrahedron

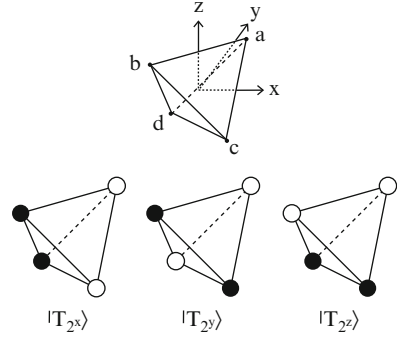


**Table 2** Degeneracies in the cubic and icosahedral groups

$D_3$	$\Gamma(A_1 C_2 \uparrow D_3) = A_1 + E$
$O$	$\Gamma(A_1 D_4 \uparrow O) = A_1 + E$
	$\Gamma(A_1 D_3 \uparrow O) = A_1 + T_1$
	$\Gamma(A_2 D_3 \uparrow O) = A_2 + T_2$
$I$	$\Gamma(A T \uparrow I) = A_1 + G$
	$\Gamma(A_1 D_5 \uparrow I) = A_1 + H$

a common normalizer) as three orthogonal traceless combinations of this standard basis (cf. Fig. 3):

$$\begin{aligned}
 |T_2x\rangle &= \frac{1}{2} (|\phi_a\rangle - |\phi_b\rangle + |\phi_c\rangle - |\phi_d\rangle) \\
 |T_2y\rangle &= \frac{1}{2} (|\phi_a\rangle - |\phi_b\rangle - |\phi_c\rangle + |\phi_d\rangle) \\
 |T_2z\rangle &= \frac{1}{2} (|\phi_a\rangle + |\phi_b\rangle - |\phi_c\rangle - |\phi_d\rangle).
 \end{aligned} \tag{19}$$

Extension of this method to the alternative tetrahedral threefold degenerate irrep  $T_1$  is straightforward. This irrep is formed in the same way as  $T_2$  but starting from the antisymmetric  $A_2$  representation in the  $C_{3v}$  subgroup, hence:

$$\Gamma(A_2 C_{3v} \uparrow T_d) = A_2 + T_1. \tag{20}$$

When this method is applied to the point group degeneracies, a distinction must be made between spherical-like point groups, which include the cubic and icosahedral families, and the cylindrical-like point groups which contain the cyclic and dihedral families. The application to the first class is shown in Table 2. In this case nearly all degeneracies stem from doubly transitive orbits of maximal subgroups. The only exceptions are the threefold degenerate irreps in the icosahedral point group. These would require the presence of a maximal subgroup of order 30 which is not available in  $I_h$ .

On the other hand for the cylindrical-like point groups only the simplest case with triangular symmetry, obeys the equidistance criterion required by the present construction. This case is included in Table 2 as  $D_3$ . In summary the expansion of a degenerate manifold in a permutational carrier space based on maximal subgroups can be executed for all degenerate irreps of the cubic and icosahedral groups, except for the T irreps in the icosahedron. For the cyclic groups double transitivity does not exist, except for the triangle. However in this case there is the additional feature that single transitivity is of a cyclic nature, requiring only one generator. So here too the concept of a permutational carrier space will simplify the analysis. This aspect will be developed in Sect. 6.1.

## 4.2 Construction of the Jahn–Teller Hamiltonian

At present we have found that for the degenerate point group irreps which are listed in the table the basis functions can be expressed by means of a carrier space which exactly matches the orbit of a maximal subgroup of the point group, and counts  $|G|/|H| = n$  elements. The one-particle Hamiltonian operating in this carrier space can easily be constructed as follows:

$$H = k \sum_{i < j} (|\phi_i\rangle\langle\phi_j| + |\phi_j\rangle\langle\phi_i|), \quad (21)$$

where as previously the  $i$  and  $j$  components refer to elements of the orbit  $\Omega$  ( $H \subset G$ ). Since this orbit is doubly transitive the interaction parameter  $k$  does not depend on the pair indices. The Hamiltonian contains  $n(n-1)/2$  symmetrized inter-site operators. As the theorem states the  $\Gamma_\Omega$  representation of the carrier space corresponds to the direct sum  $\Gamma_0 + \Gamma_{n-1}$ . The symmetrized square of this direct sum not only covers the symmetries of the inter-site operators but also of the on-site diagonal operators of type  $|\phi_i\rangle\langle\phi_i|$ . The latter transform as the representation of  $\Gamma_\Omega$  itself. The inter-site operators thus span the symmetrized square of the positional representation minus  $\Gamma_\Omega$ :

$$\begin{aligned} \Gamma_H &= [\Gamma_\Omega \otimes \Gamma_\Omega] - \Gamma_\Omega \\ &= [(\Gamma_0 + \Gamma_{n-1}) \otimes (\Gamma_0 + \Gamma_{n-1})] - \Gamma_\Omega \\ &= [\Gamma_{n-1} \otimes \Gamma_{n-1}]. \end{aligned} \quad (22)$$

Note in the second line of this equation that symmetrization of the direct square gives rise to only one cross-term. This equation expresses the standard Jahn–Teller result that time-even interactions in a degeneracy space transform according to the symmetrized square (indicated by square brackets) of the corresponding irrep. This square can be further resolved, into a non-distortive totally symmetric part and the proper Jahn–Teller part.

We will now take this result to the parent symmetric group, which describes the permutation of all the sites. In this group the sites transform as  $(n - 1, 1)$  and the inter-site operators span the symmetrized square of  $(n - 1, 1)$ , hence:

$$\Gamma_H = [(n - 1, 1) \otimes (n - 1, 1)]. \quad (23)$$

This square can be further resolved, yielding:

$$\Gamma_H = (n) + (n - 1, 1) + (n - 2, 2). \quad (24)$$

The non-totally symmetric interactions which can appear in the degenerate  $(n - 1, 1)$  irrep thus will transform as  $(n - 1, 1) + (n - 2, 2)$ .

So far the analysis has lead to the concept of a carrier space which links the degeneracy to a doubly transitive orbit of cosets of maximal subgroups. Interactions in this space are expressed as transition operators between the cosets. The final part of the treatment should bring in the vibrational degrees of freedom which are responsible for the Jahn–Teller activity.

## 5 Vibrational Degrees of Freedom

### 5.1 Symmetric Group Analysis

Having identified the symmetries of the electronic distortion operators, we now determine the symmetries of the nuclear degrees of freedom. These are defined as the direct product of the positional representation with the symmetry of the translations [12, 16]. The  $n$ -simplex is situated in a  $(n - 1)$ -dimensional space and thus will exhibit  $(n - 1)$  translations. The corresponding irrep is denoted as  $\Gamma_T$ . One easily realizes that this will correspond to the  $(n - 1, 1)$  irrep: from the center of the simplex one can move in  $n$  different directions, but the vectorial sum of all these directions amounts to zero, hence the translational space has one degree of freedom less than the number of sites. The direct product can be decomposed in a standard way as follows:

$$\Gamma_\Omega \otimes \Gamma_T = (n) + 2(n - 1, 1) + (n - 2, 2) + (n - 2, 1^2). \quad (25)$$

These degrees of freedom also contain the so-called external degrees of freedom: translations and rotations. The rotations, described by  $\Gamma_R$ , transform as the anti-symmetrized square of the translations. One thus has for the external modes:

$$\begin{aligned} \Gamma_T &= (n - 1, 1) \\ \Gamma_R &= \{\Gamma_T \otimes \Gamma_T\} = (n - 2, 1^2). \end{aligned} \quad (26)$$

Finally the symmetries of the internal or vibrational degrees of freedom are obtained by subtracting the external modes from the space of nuclear motions:

$$\Gamma_{\Omega} \otimes \Gamma_T - \Gamma_T - \Gamma_R = (n) + (n-1, 1) + (n-2, 2). \quad (27)$$

Clearly this symmetry shows a perfect match with the symmetry of the interaction Hamiltonian, as obtained in (24).

$$\Gamma_{\Omega} \otimes \Gamma_T - \Gamma_T - \Gamma_R \equiv \Gamma_H. \quad (28)$$

This expression is the central result of our paper and the most concise expression of the Jahn–Teller theorem. It shows that the time-even interactions in a degenerate irrep based on a simplex of  $n$  nuclei are in one-to-one correspondence with the vibrational degrees of freedom of that simplex. Another way to express this is that the bonds between the sites form a complete set of internal coordinates. In 3D this reflects the Cauchy theorem that ‘in a convex polyhedron with rigid faces the angles between the faces will also be rigid’ [17, 18].

As in the original treatment of Jahn and Teller our result attributes the vibronic instability to the terms in the Hamiltonian which are linear in the nuclear displacements. Higher order contributions will of course occur as well but they cannot be responsible for the conical instability at the high symmetry origin.

## 5.2 Extensions to Other Symmetries and irreps

The case of a perfect match which we have considered in the previous section reveals the intimate connection between degeneracy and vibrational degrees of freedom. In the simplex this connection attains a one-to-one correspondence. In more complex frames the connection is often disguised by the presence of additional inactive modes. In fact five possible situations can occur, depending on the relationship between the space of normal modes and the space of JT interactions. The symmetries of the non-totally symmetric vibronic interactions will be denoted as  $\Gamma_{JT}$ , while the symmetries of the non-totally symmetric normal modes will be denoted as  $\Gamma_{NM}$ . The five possible set relations between these two sets are:

1.  $\Gamma_{JT} = \Gamma_{NM}$
  2.  $\Gamma_{JT} \subset \Gamma_{NM}$
  3.  $\Gamma_{JT} \cap \Gamma_{NM} = \emptyset$
  4.  $\Gamma_{JT} \cap \Gamma_{NM} \neq \emptyset$
  5.  $\Gamma_{JT} \supset \Gamma_{NM}$ .
- (29)

The first case describes the perfect match of both spaces, which as we have seen occurs for the  $(n-1, 1)$  irrep of the  $n$ -simplex.

The usual JT effect in 3D point groups exemplifies the second case,  $\Gamma_{JT} \subset \Gamma_{NM}$ . These cases involve molecules that are more involved than the simplexes, which implies that the site which is stabilized by a maximal subgroup contains more nuclei than the one that is considered in the simplex. As a result all the possible JT interaction symmetries are represented *at least* by one normal mode, but in addition the space of vibrational modes also contains inactive modes. A case in point are centrosymmetric molecules where only *gerade* modes can be JT active, the odd modes are found in the remainder space  $\Gamma_{NM} - \Gamma_{JT}$ .

The third case,  $\Gamma_{JT} \cap \Gamma_{NM} = 0$ , constitutes an exception to the Jahn–Teller theorem since it states that none of the normal modes has the right symmetry to couple with the degeneracy. As we know this occurs in linear molecules. More examples can be found in higher dimensions.

The remaining cases offer the intriguing possibility that not all of the vibronic operators that are required for the coupling between the sites have a counterpart in the space of normal modes. This does not occur in point group symmetries, although in practice coupling to some modes may be so weak that it can be neglected, thus giving rise to partial Jahn–Teller activity. Again in higher symmetric groups examples of these cases may be found. They occur for degenerate irreps that do not subduce one-dimensional subrepresentations when symmetry is lowered to the maximal subgroup of the site symmetry. This implies that the electronic structure on the sites is of a composite nature.

## 6 Applications

### 6.1 2D: Cylindrical Symmetry

As we have indicated before, apart from the triangle, orbits which correspond to the sites of higher polygons are not doubly transitive. In this case Halls theorem cannot be used. However as was already alluded to in the original proof of Jahn and Teller, for such cylindrical like structures, there is a general generic treatment, which in its simplest form only is based on the cyclic generator structure of these polygons. In a  $n$ -cycle symmetry eigenfunctions can always be written as cyclic waves running over the sites, with some angular momentum  $\lambda$ , i.e.:

$$\Psi_\lambda = \sum_k \exp(\lambda \frac{2\pi ki}{n}) |k\rangle, \quad (30)$$

where  $\lambda$  is an integer ring quantum number, which characterizes the symmetry of this function. When the function is rotated over an angle of  $2\pi/n$  a phase factor of  $\exp(-\lambda \frac{2\pi i}{n})$  appears. Unless  $\lambda = n/2$ , this wave function will always have a complex conjugate counterpart which has the same electronic density over the sites, and thus will be degenerate. This implies that the vibronic instability resides in the

electronic operator connecting  $\Psi_\lambda$  and  $\Psi_{-\lambda}$ . It is given by:

$$|\Psi_{-\lambda}\rangle\langle\Psi_\lambda| = \sum_{k,k'} \exp(\lambda \frac{2\pi(k+k')i}{n}) |k\rangle\langle k'|. \quad (31)$$

When this operator is rotated over the angle  $2\pi/n$  a phase is built up which equals  $\exp(-2\lambda \frac{2\pi i}{n})$ , hence the operator runs twice as fast as the wavefunctions. Its symmetry is therefore characterized by the ring quantum number  $2\lambda$ .

A convenient set of internal normal modes is offered by the set of all edges of the polygon. The set of  $n$ -edges transforms as the regular representation, thus it offers a complete set of all irreducible representations of the cyclic generator. As a result this set will always contain the symmetry of the active operator.

## 6.2 3D: The Icosahedral Quintuplet

The fivefold degenerate representation of the icosahedral group is the highest possible orbital degeneracy within the 3D point groups. As indicated in (11), this fivefold degeneracy originates from the presence of six equivalent and equidistant pentagonal directions in the icosahedron (labeled  $A$  to  $F$  in Fig. 5). The mere existence of this quintuplet is remarkable in itself and can be related to a unique property of its parental symmetric group  $S_6$ . The symmetric group  $S_6$  stands out in the family of symmetric groups  $S_n$  as it is the only member which has two non-equivalent maximal subgroups of type  $S_{n-1}$  ( $S_5$ ) [19]. As the icosahedral group  $I \cong A_5 \subset S_5 \subset S_6$ , this will lead to two separate branches in the subgroup lattice leading to inequivalent icosahedral embeddings as indicated in Fig. 4. To fully understand these two embeddings, it is helpful to take a closer look at the exact structure of their intermediate  $S_5$  subgroups.

A first type of  $S_5$  subgroup can easily be seen to originate from fixing one of the elements of  $S_6$  and acting fully transitive on the remaining five elements. This type of  $S_{n-1}$  subgroup is common to all  $S_n$  groups, but clearly not the one we are interested in as it does not act doubly transitive, not even singly transitive, on the set of six pentagonal directions. The icosahedral quintuplet therefore originates from a second and unexpected branch in the subgroup lattice of  $S_6$ . In this branch the embedding of  $I$  into  $S_6$  is mediated by a second type of  $S_5$  subgroup (see Table 3) which acts doubly transitive on the six pentagonal directions. The actual elements of

**Fig. 4** Branching scheme of the symmetric group  $S_6$  showing two separate branches leading to inequivalent  $I$  subgroups

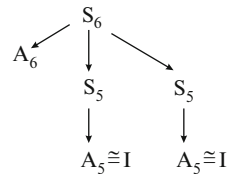


**Fig. 5** The icosahedron showing the six equidistant pentagonal directions A to F and the three generators of (32)

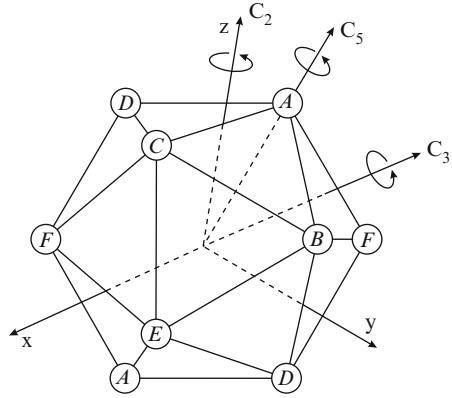


**Table 3** Embedding of the icosahedral group  $I$  into the symmetric group  $S_6$

$S_6$	1	15	40	45	90	120	144	15	90	40	120
	$1^6$	$1^4 2^1$	$1^3 3^1$	$1^2 2^2$	$1^2 4^1$	$1^1 2^1 3^1$	$1^1 5^1$	$2^3$	$2^1 4^1$	$3^2$	$6^1$
$S_5$	1			15	30		24	10		20	20
	$1^6$			$1^2 2^2$	$1^2 4^1$		$1^1 5^1$	$2^3$		$3^2$	$6^1$
$I \cong A_5$	$E$			$15C_2$			$12C_5$			$20C_3$	
							$12C_5^2$				

this icosahedral subgroup can easily be deduced using the three generators depicted in Fig. 5:

$$\begin{aligned}
 C_5 &\rightarrow (A)(B, F, E, D, C) \\
 C_3 &\rightarrow (A, B, F)(C, D, E) \\
 C_2 &\rightarrow (A, C)(B, D)(E)(F).
 \end{aligned} \tag{32}$$

In order to generate the intermediate  $S_5$  subgroup it suffices to add one of its uneven permutations to the generators of  $I$ . As seen from Table 3 the uneven permutations constitute three classes:  $6^1$ ,  $2^3$  and  $1^2 4^1$  with respectively 30, 10 and 20 elements. Prototypical examples are:

$$\begin{aligned}
 6^1 &\rightarrow (A, C, F, E, D, B) \\
 2^3 &\rightarrow (A, E)(C, D)(F, B) \\
 1^2 4^1 &\rightarrow (A)(B)(C, D, F, E).
 \end{aligned} \tag{33}$$

The action of these elements can be clarified by means of the icosahedral embedding of Fig. 5. From the 120 possible  $6^1$  elements existing within  $S_6$ , only those encircling a ‘supertriangle’ of the icosahedron survive within  $S_5$ . A supertriangle is by definition composed of a triangular face of the icosahedron together with its three neighboring faces. The  $6^1$  element listed above for instance originates

from encircling the supertriangle  $AFD$  in Fig. 5 (in an anticlockwise direction). Obviously the number of such supertriangles coincides with the number of triangular faces of the icosahedron therefore leading to exactly twenty elements of type  $6^1$ . Notice that the chosen sense of rotation is immaterial as the set of permutations generated by clockwise rotations would be exactly the same due to the inversion symmetry of Fig. 5. The ten elements of the class  $2^3$  are now easily identified as cubes of these  $6^1$  elements. The squares of the  $6^1$  elements do not constitute a new class. They are of even type and coincide nicely with the twenty  $C_3$  rotations of the icosahedral group. The last uneven class  $1^24^1$  consists of elements which fix two pentagonal directions and cyclicly permute the remaining four elements. Only thirty from a total of ninety such elements survive in the subduction from  $S_6$  to  $S_5$ . They correspond to those elements for which the four non-fixed elements encircle two neighboring triangles on the surface of the icosahedron. For the listed  $1^24^1$  element for instance the fourcycle  $(C, D, F, E)$  encircles the neighboring triangles  $CDF$  and  $FEC$ .

In previous work we have shown how this embedding of the icosahedron in  $S_6$  can be used to resolve the product multiplicity in the icosahedral  $H \otimes (g + 2h)$  Jahn–Teller problem [10, 20]. In the context of atomic spectroscopy, Judd and Lo have made use of the  $S_6$  connection to explain some puzzling degeneracies in the spectroscopic terms of  $d^3$  [21].

As a further illustration we will demonstrate here the use of this embedding to resolve a multiplicity case for the symmetry coordinates of a vibrating icosahedron [22]. An icosahedral cage with twelve atoms has 30 internal modes. Since the icosahedron is a deltahedron, the stretchings of the 30 edges form a non-redundant set of internal coordinates. The corresponding symmetry representations are given by:

$$\Gamma_{NM} = a_g + t_{1u} + t_{2u} + g_g + g_u + 2h_g + h_u. \quad (34)$$

For the even modes, displacements of opposite edges are equal. If two opposite edges are being squeezed simultaneously, two pentagonal directions approach each other. In this way the 15 pairs of opposite edges correspond to the 15 edges of the  $S_6$  simplex, consisting of the six pentagonal directions. Hence the 15 gerade symmetry coordinates will transform in  $S_6$  as  $(6) + (5, 1) + (4, 2)$ , exactly as described in (27). Using the embedding relations in Table 3, the following subduction relations between the  $S_6$  and  $I_h$  labels can be found:

$$\begin{aligned} (6) &\rightarrow A_g \\ (5, 1) &\rightarrow H_g \\ (4, 2) &\rightarrow G_g + H_g. \end{aligned} \quad (35)$$

This subduction shows that the two equisymmetric  $h_g$  cluster deformations may be distinguished by a different  $S_6$  parentage. The construction of the modes with  $(5, 1)$  and  $(4, 2)$  parentage proceeds as follows. One first defines a carrier space of  $H_g$  symmetry, based on the six pentagonal sites. The components of this space are labeled  $\theta, \epsilon, \xi, \eta, \zeta$ .



$$\begin{aligned}
|\theta\rangle &= \frac{1}{2}(-|A\rangle + |D\rangle - |E\rangle + |F\rangle) \\
|\epsilon\rangle &= \frac{1}{\sqrt{12}}(|A\rangle - 2|B\rangle - 2|C\rangle + |D\rangle + |E\rangle + |F\rangle) \\
|\xi\rangle &= \frac{1}{\sqrt{2}}(|D\rangle - |F\rangle) \\
|\eta\rangle &= \frac{1}{\sqrt{2}}(-|A\rangle + |E\rangle) \\
|\zeta\rangle &= \frac{1}{\sqrt{2}}(-|B\rangle + |C\rangle).
\end{aligned} \tag{36}$$

Then these components are coupled using Clebsch–Gordan coefficients for the  $H \otimes H = 2H$  direct product. In view of the product multiplicity in this coupling, two independent sets of coefficients exists. The coefficients which we have published before are based on a product multiplicity separation which obeys the  $S_6$  parentage [23]. The published  $a$  and  $b$  coefficients correspond to the (4, 2) and (5, 1) Young tableaux resp. Hence by using these components we obtain at once the desired permutational multiplicity separation. Upon coupling only the off-diagonal terms are kept, since these correspond to the inter-site distances. Here we will limit ourselves to present the normalized coordinates for pentagonal and trigonal distortion modes. In the coordinate frame of Fig. 5, the  $h_g$ -symmetry components which are totally symmetric along the pentagonal  $C_5$  direction, corresponding to site  $A$ , are given by:

$$\begin{aligned}
Q_{5,1} &= \frac{1}{\sqrt{30}}(2r_{AB} + 2r_{AC} + 2r_{AD} + 2r_{AE} + 2r_{AF} \\
&\quad - r_{BC} - r_{BD} - r_{BE} - r_{BF} - r_{CD} - r_{CE} - r_{CF} - r_{DE} - r_{DF} - r_{EF}) \\
Q_{4,2} &= \frac{1}{\sqrt{10}}(-r_{BC} + r_{BD} + r_{BE} - r_{BF} - r_{CD} + r_{CE} + r_{CF} \\
&\quad - r_{DE} + r_{DF} - r_{EF}).
\end{aligned} \tag{37}$$

Here the  $r$  variables denote the distance between two pentagonal directions, which correspond to the simultaneous activation of the two edges connecting the atoms along these directions. Note that the  $Q_{5,1}$  coordinate corresponds to a pure pentagonal squashing mode: the icosahedron is elongated along the  $A$  direction, and simultaneously compressed around its waist. The  $Q_{4,2}$  mode behaves differently. This mode does not involve the apical  $A$  site. The two pentagonal rings forming the tropics around the waist are compressed, while the 10 edges in between those rings are elongated. The components which gives rise to a trigonal distortion oriented along the  $C_3$  direction in Fig. 5 are given by:

$$\begin{aligned}
Q_{5,1} &= \frac{1}{\sqrt{6}}(r_{AB} + r_{AF} + r_{BF} - r_{CD} - r_{CE} - r_{DE}) \\
Q_{4,2} &= \frac{1}{\sqrt{18}}(2r_{AD} + 2r_{BE} + 2r_{CF} - r_{AB} - r_{AF} - r_{BF} - r_{CD} - r_{CE} - r_{DE}).
\end{aligned}
\tag{38}$$

Here the roles are switched. Now the  $Q_{4,2}$  mode describes a pure trigonal squash, which elongates the icosahedron along the  $C_3$  direction. The  $Q_{5,1}$  behaves differently: three sites  $A, B, F$  are pushed away from each other while the three remaining sites  $C, D, E$  approach each other.

### 6.3 4D: The Hyperoctahedron

Blount indicated that in higher dimensions the Jahn–Teller theorem not necessarily holds [7]. We will illustrate this here for the case of the hyperoctahedron, which is a 4D polytope. The symmetry of this structure can easily be constructed by straightforward generalization of the octahedral group in 3D. A 3D octahedron is composed of six vertices, arranged symmetrically around the origin along the three Cartesian directions, i.e. at:  $\pm x, \pm y, \pm z$ . The 48 operations of the group  $O_h$  corresponds to all interchanges of these six vertices that obey the following rules:

- All transpositions of vertices on the same axis, e.g.  $(+x) \leftrightarrow (-x)$
- All permutations of the three directions, e.g.  $(\pm x) \leftrightarrow (\pm y) \leftrightarrow (\pm z)$

The first rule gives rise to a group of eight elements corresponding to  $Z_2^3$ , where  $Z_2$  is the cyclic group of order two. The corresponding point group is the  $D_{2h}$  normal subgroup of the octahedron. The second rule consists of 6 permutations of three objects, as described by the symmetric group  $S_3$ . The combination of both gives rise to a so-called wreath product of  $Z_2^3$  and  $S_3$ , which is isomorphic to  $O_h$ :

$$O_h = Z_2^3 \times S_3. \tag{39}$$

The elements of the octahedral group will permute the six vertices and as such be part of the full permutation group  $S_6$ . The octahedral group is a subgroup of  $S_6$ , since not all permutations are in accordance with the rules, e.g. it is not allowed by the rules to interchange  $(+x)$  and  $(+z)$ , without simultaneously interchanging  $(-x)$  and  $(-z)$ .

This presentation of the octahedral symmetry group can directly be extended to the hyperoctahedron [24, 25]. This will be a 4D polytope, formed by eight vertices, distributed evenly over the four Cartesian directions, i.e.  $\pm x, \pm y, \pm z, \pm u$ . The hyperoctahedral group, commonly denoted as  $W_4$  from the German *Würfel* which signifies dice, is given by:

$$W_4 = Z_2^4 \times S_4. \tag{40}$$

This group contains 384 elements. It contains 20 classes, which may be labeled by a combination of the labels from the parent symmetry group  $S_8$  and the permutational subgroup  $S_4$ . The corresponding character table is available from the literature and will be reproduced in Table 4 for convenience [25]. In order to obtain the normal modes of the hyperoctahedron we first derive the positional representation of the eight vertices. Since the  $S_8$  labels refer to permutations of the eight vertices, the character of the positional representation will simply correspond to the number of 1-cycles in each class. These numbers indeed indicate how many vertices are left invariant by the symmetry operations in that class. The symmetry of the translations can also easily be derived, since it must correspond to a 4-dimensional irrep, which subduces the  $T_{1u}$  symmetry in the  $O_h$  subgroup. The only irrep with these properties is  $\Gamma_1^{(4)}$ . The antisymmetrized square of this irrep is equal to  $\Gamma_1^{(6)}$  and corresponds to the symmetry of the rotational degrees of freedom. Hence one has for the normal modes:

$$\begin{aligned}\Gamma_\Omega &= \Gamma_1^{(1)} + \Gamma_1^{(3)} + \Gamma_1^{(4)} \\ \Gamma_\Omega \otimes \Gamma_1^{(4)} - \Gamma_T - \Gamma_R &= \Gamma_1^{(1)} + \Gamma_1^{(3)} + \Gamma_1^{(4)} + \Gamma_3^{(6)} + \Gamma_1^{(8)}.\end{aligned}\quad (41)$$

There are two twofold degenerate irreducible representations,  $\Gamma_i^{(2)}, i = 1, 2$ . Their squares both yield the same result:

$$\Gamma_i^{(2)} \times \Gamma_i^{(2)} = \{\Gamma_3^{(1)}\} + [\Gamma_1^{(1)} + \Gamma_1^{(2)}]. \quad (42)$$

It is immediately clear that the non-totally symmetric part of the symmetrized square, which transforms as  $\Gamma_1^{(2)}$  is not contained in the normal modes of the hyperoctahedron. This simply signifies that there are no Jahn–Teller distortions in this case. The twofold degenerate irreps of the hyperoctahedron thus constitute a 4D example of an exception, exactly as the 1D case. The subgroup structure of  $W_4$  may be invoked to explain this result. In order to obtain a twofold degenerate irrep by a double transitive orbit one would need a subgroup of one third of the total group order, i.e. 128. Clearly  $W_4$  does not contain such a subgroup. Since the total order is given by  $2^4 \times 4!$ , a subgroup of order 128 can only be obtained by the wreath product of  $Z_2^4$  with a subgroup of  $S_4$  that would have to be of order 8. But  $S_4$  does not contain such a subgroup, hence  $W_4$  cannot be divided in an orbit of rank 3.

Even more interesting results can be obtained for irreducible representations of dimension three:  $\Gamma_i^{(3)}, i = 1, 3$ . In this case the antisymmetrised and symmetrised parts of the square are given by:

$$\Gamma_i^{(3)} \times \Gamma_i^{(3)} = \{\Gamma_1^{(6)}\} + [\Gamma_1^{(1)} + \Gamma_1^{(3)} + \Gamma_2^{(6)}]. \quad (43)$$

This case corresponds to the fifth possibility in (29) which does not occur in lower dimensions and exemplifies a partial overlap between the Jahn–Teller modes and the normal modes. In order to destroy the symmetry of this level one would need modes of type  $\Gamma_1^{(3)}$  and  $\Gamma_2^{(6)}$ . A glance at the normal modes of the hyperoctahedron



shows that only the first one of these is included in the normal modes. No distortion operators exist with  $\Gamma_2^{(6)}$  symmetry, hence the degeneracy can only be partially lifted.

## 7 Epikernel Principle and Dynamic Symmetry

The permutational proof also elucidates two important general properties of JT potentials: the epikernel principle, and the symmetry of the dynamic ground state.

The epikernel principle was originally proposed as a simple rule to predict the preferential symmetry of a Jahn–Teller distortion [26]. Later on it was rationalized using the technique of the isostationary function [27]. Epikernels are those subgroups of the point group that occur in the distortion space formed by the Jahn–Teller active coordinates. The lowest subgroup of the epikernel set is called the kernel. A Jahn–Teller distortion cannot lower the symmetry of a compound below the kernel symmetry. As an example an  $e_g$  vibration of an octahedron cannot lower the symmetry below the kernel group  $D_{2h}$ , which is a normal subgroup of  $O_h$ . Thus any modal point in the twofold distortion space will at least have orthorhombic symmetry. In addition the  $e_g$  distortion space contains three preferential directions where a tetragonal symmetry axis is conserved. Along these directions the symmetry is  $D_{4h}$  which is an epikernel of the distortion space. According to the epikernel principle stable minima on a Jahn–Teller distortion prefer epikernel rather than kernel points. According to the present proof this principle is a natural consequence of the structure of electronic degeneracies. A degeneracy is built on a doubly transitive orbit, and as we have seen such an orbit is based on *maximal* subgroups of a group. These naturally correspond to the maximal epikernels. The Jahn–Teller coordinates correspond to the intersite interactions between these epikernel directions.

When dynamics is taken into account the Jahn–Teller distortion starts to move inside the nuclear frame, and the complex gradually runs through all equivalent sites of the orbit on which the degeneracy is built. According to Bersuker and Pollinger the ground state of such a system has a dynamic symmetry which as a rule exhibits the same type of degeneracy as the electronic symmetry which was at the origin of the Jahn–Teller effect [28]. The connection with the present proof is obvious: an electronic  $n - 1$ -fold degeneracy is based on an orbit of  $n$  sites, which correspond to the stable minima of the JT potential. In the symmetric group based on permutations of these minima, the eigenvectors span the positional representation of these minima, and thus will transform as the totally symmetric representation, and the  $(n - 1)$  basic vector irrep, which is precisely the symmetry of the electronic degeneracy. When the coupling to the  $(n - 2, 2)$  modes becomes more important the symmetry of the dynamic ground state may change, and this behavior indeed may occur in the icosahedral quintuplet case, with dominant trigonal coupling [29]. (See also [30])

## 8 Conclusion

In this treatment we have searched the underlying common structure that unites all Jahn–Teller problems. The starting point has been the important theorem by Hall, which relates the existence of an  $(n - 1)$ -fold degeneracy to a doubly transitive orbit of  $n$  elements. This yields a simple permutational proof for nearly all cubic and icosahedral degeneracies as well for the degeneracies in a triangle. Exceptional cases are the  $T_1$  and  $T_2$  irreps in an icosahedron for which no doubly transitive orbit exist, since there is no subgroup of rank 4 in the icosahedral group. Apart from the triangle, higher order polygons, which all belong to subgroups of cylindrical symmetry, also do not contain doubly transitive orbits.

The induction processes which we have used in the present treatment were mainly limited to inductions from totally symmetric roots in the subgroups. Induction from non-totally symmetric subgroup irreps sometimes give rise to interesting alternative constructions of degeneracies, which may clarify the kaleidoscope structure [31] of the icosahedral  $T$  irreps, and allow extensions into spin degeneracies.

**Acknowledgements** A.C. is indebted to Prof. T. Lulek (Rzeszów) for pointing out Halls theorem, and to Prof. H. Köppel (Heidelberg) for interesting discussions. This work was supported by the Flemish Government through the concerted action scheme. E.L. is research fellow from the National Science Fund FWO.

## Appendix

In this appendix we prove the corollary to the theorem of Hall that the orbit of the cosets of a subgroup  $H$  of group  $G$  can only be doubly transitive for  $H$  a maximal subgroup of  $G$ . To this end we consider a further subgroup  $S \subset H$ , and examine if the orbit of cosets of  $S$  can be doubly transitive. Let  $g_r$  and  $h_\rho$  denote cosets representatives of  $H$  in  $G$ , and  $S$  in  $H$  resp., i.e.:

$$\begin{aligned} G &= \sum_r^{|G|/|H|} g_r H \\ H &= \sum_\rho^{|H|/|S|} h_\rho S. \end{aligned} \tag{44}$$

The cosets of  $S$  in  $G$  may then be generated by the product of both types of generators:

$$G = \sum_{r, \rho}^{|G|/|S|} g_r h_\rho S. \tag{45}$$

Elements of this orbit are thus labeled by double labels  $(r, \rho)$ . If we want this orbit to be doubly transitive the elements of  $G$  should be able to effectuate any mapping between pairs of such labels. It can easily be shown that this is not the case. Take for example the case where  $g_r$  is the unit element  $e$ , and consider the initial pair  $(e, \rho), (e, \sigma)$ . Both these cosets thus belong to  $H$ . Now we wonder if there would exist an element  $g_x$  that maps this pair onto a pair  $(e, \rho'), (r, \sigma')$ . In this target pair the first coset stays in  $H$ , but the second is outside  $H$ .

$$? \exists g_x : g_x h_\rho S = h_{\rho'} S \quad \wedge \quad g_x h_\sigma S = g_r h_{\sigma'} S \quad (46)$$

Clearly such an element cannot be found. Indeed from the first requirement it follows that  $g_x$  must be in  $H$ , while the second condition places  $g_x$  outside  $H$ . Hence only maximal subgroups can have doubly transitive cosets.

## References

1. H.A. Jahn, E. Teller, Proc. R. Soc. **A161** 220 (1937)
2. I.B. Bersuker, *The Jahn-Teller Effect* (Cambridge University Press, Cambridge, 2006)
3. E. Ruch, Z. Elektrochemie **61** 913 (1957)
4. T. Sato, K. Tokunaga, N. Iwahara, K. Shizu, K. Tanaka. in: *The Jahn-Teller Effect – Advances and Perspectives. Springer series in Chemical Physics* (Springer, Berlin, 2009)
5. A. Ceulemans, P. W. Fowler, M. Szopa, Math. Proc. R. Ir. Acad. **98A** 139 (1998)
6. E. Ruch, A. Schönhofer, Theor. Chim. Acta (Berl.) **3** 291 (1965)
7. E.I. Blount, J. Math. Phys. **12** 1890 (1971)
8. I.V.V. Raghavacharyulu. J. Phys. C Solid State Phys. **6** L455 (1973)
9. V.I. Pupyshev, Int. J. Quantum Chem. **107** 1446 (2007)
10. A. Ceulemans, E. Lijnen, Bull. Chem. Soc. Jpn. **80** 1229 (2007)
11. T. Lulek, Acta Physica Pol. **A57** 407 (1980)
12. A. Ceulemans, Mol. Phys. **54** 161 (1985)
13. M. Hall, *The Theory of Groups* (Macmillan, New York, 1959)
14. B.Lulek, T. Lulek, J. Phys. A: Math. Gen. **17** 3077, 1984
15. M. Hamermesh, *Group Theory and its Application To Physical Problems* (Addison-Wesley, Reading MA, 1962)
16. T. Lulek, M. Szopa, J. Phys. A: Math. Gen. **23** 677, (1990)
17. A. Ceulemans, P.W. Fowler, Nature **353** 52, 1991
18. A.L. Cauchy, J. Ecole Impériale Polytech. **19** 87 (1813)
19. B. Newton, B. Benesh, J. Algebra **304** 1108 (2006)
20. E. Lijnen, A. Ceulemans, Europhys. Lett. **80** 67006 (2007)
21. E. Lo, B.R. Judd, Phys. Rev. Lett. **82** 3224 (1999)
22. A. Ceulemans, B.C. Titeca, L.F. Chibotaru, I. Vos, P.W. Fowler, J. Phys. Chem. A **105** 8284 (2001)
23. P.W. Fowler, A. Ceulemans, Mol. Phys. **54** 767 (1985)
24. P. W. Fowler, A. Rassat, A. Ceulemans, J. Chem. Soc. Faraday Trans. **92** 4877, (1996)
25. M. Baake, B. Gemünden, R. Oedinger, J. Math. Phys. **23** 944 (1982)
26. A. Ceulemans, L.G. Vanquickenborne, Struct. Bonding (Berlin) **71** 125 (1989)
27. A. Ceulemans, J. Chem. Phys. **87** 5374 (1987)
28. I.B. Bersuker, V.Z. Polinger, *Vibronic Interactions in Molecules and Crystals* (Springer, Berlin, 1989)

29. C.P. Moate, M.C.M. O'Brien, J.L. Dunn, C.A. Bates, Y.M. Liu, V.Z. Polinger, Phys. Rev. Lett. **77** 4362 (1996)
30. F.S. Ham, C.H. Leung, *The Unpublished Work of F.S. Ham on the Jahn–Teller Effect*. (Trinity Enterprise Inc, Saint-John NB, 2008)
31. B.R. Judd, E.Lo, J. Phys. B **32** 1073 (1999)



# Group-Theoretical Analysis of Jahn–Teller Systems

Martin Breza

**Abstract** The problem of searching the stable structures obtained by the symmetry descent of high-symmetric non-linear parent systems in a degenerate electronic state (except an accidental and Kramers degeneracy) due to Jahn–Teller effect is solved by a group-theoretical treatment. The basic terms of group theory (especially of point groups of symmetry) and potential energy surfaces are explained. The methods of epikernel principle (based on Jahn–Teller active coordinates obtained by the first order perturbation theory) and step-by-step descent in symmetry (based on a consecutive split of the degenerate electronic state due to a symmetry descent) are explained. Both methods are illustrated by several examples and their results are compared with the structures obtained by high-level quantum-chemical calculations. The method of step-by-step descent in symmetry seems to be more complete.

## 1 Introduction

In the history of modern science there are many examples that the physical interpretations of the formulas obtained by the mathematical formalism of quantum physics need not be straightforward. Therefore new attempts to their reinterpretation are unavoidable. The original complete formulation of Jahn–Teller (JT) theorem [1, 2] is somewhat lengthy (and thus not well-known):

*A configuration of a polyatomic molecule for an electronic state having orbital degeneracy cannot be stable with respect to all displacements of the nuclei unless in the original configuration the nuclei all lie on a straight line. . . . if the total electronic state of orbital and spin motion is degenerate, then a non-linear configuration of the molecule will be unstable unless the degeneracy is the special twofold one (discussed by Kramers in 1930) which can occur only when the molecule contains an odd number of electrons. The additional instability caused by the spin degeneracy alone, however, is shown to be very small and its effect for all practical purposes negligible. The possibility of spin forces stabilizing a non-linear configuration which is unstable owing to orbital degeneracy. . . is not possible except perhaps for molecules containing heavy atoms for which the spin forces are large.*

Therefore its shortened formulation “*any nonlinear arrangement of atomic nuclei in degenerate electron state (except Kramers degeneracy [3]) is unstable*” is of general use. The authors evidently supposed that this degeneracy is caused by the nuclear configuration symmetry as manifested by the published proofs of JT theorem [4–8] as well. On the other hand, the recent extended understanding of Jahn–Teller effect (JTE) includes both degenerate and pseudodegenerate states (pseudo-JTE), both non-linear and linear (Renner–Teller effect) nuclear arrangements, as well as all the conical intersections of energy hypersurfaces corresponding to various electronic states. Within such a treatment “... *the JT theory is an approach to (a tool for) general understanding and solving of molecular and crystal problems, which is in principle applicable to any system with more than two atoms.*” [9].

Our study is based on the original formulation of JT theorem and deals with the symmetry conditioned orbitally degenerate electronic states – i.e. without considering the accidental and Kramers (or spin) degeneracy. As a consequence of this theorem a stable nuclear configuration of lower symmetry in nondegenerate electronic state is formed. It is evident that this nondegenerate electronic state is obtained by splitting the parent degenerate electronic state. The problem of obtaining the stable geometries of JT systems can be solved analytically using perturbation theory treatment for small systems only. For large systems a group-theoretical treatment is necessary which can be based either on the distortion (JT active coordinate) or on the electronic state symmetry.

## 2 Point Groups of Symmetry

Symmetry properties of a molecule (molecular ion) are described by its symmetry point group. This group is a collection of its symmetry operations  $\mathbf{R}$  (group elements) which must satisfy group postulates. There are several types of the symmetry operations [10]:

1. The identity  $\mathbf{E}$
2. Rotation  $\mathbf{C}_n^k$  through an angle  $2\pi k/n$  about the  $n$ -fold rotation axis  $\mathbf{C}_n$  ( $\mathbf{C}_n$  with maximal  $n$  denotes a principal axis which should be coincident with a cartesian  $z$  axis, the rotational axes perpendicular to the principal axis are denoted by primes).
3. Inversion  $\mathbf{i}$  of all points through the origin of coordinates.
4. Reflection  $\sigma$  of all points in a mirror plane  $\sigma$  ( $\sigma_v$  - a mirror plane containing the principal axis,  $\sigma_h$  - a mirror plane normal to the principal axis,  $\sigma_d$  - a dihedral mirror plane containing the principal axis and bisecting the angles between  $\mathbf{C}_2'$  axes).
5. Improper rotation-reflection operation  $\mathbf{S}_n^k$  is the rotation about the improper axis  $\mathbf{S}_n$  through an angle  $2\pi k/n$ , combined with reflection  $k$  times in a plane normal to this axis.

where  $n$  and  $k$  are integers (for  $k = 1$  the superscript is omitted).

**Table 1** Character table of  $D_{3h}$ ,  $C_{3v}$ ,  $C_{2v}$  and  $C_2$  point groups [10]

$D_{3h}$	$E$	$2C_3$	$3C_2'$	$\sigma_h$	$2S_3$	$3\sigma_v$
$A_1'$	+1	+1	+1	+1	+1	+1
$A_2'$	+1	+1	-1	+1	+1	-1
$E'$	+2	-1	0	+2	-1	0
$A_1''$	+1	+1	+1	-1	-1	-1
$A_2''$	+1	+1	-1	-1	-1	+1
$E''$	+2	-1	0	-2	+1	0

$C_{3v}$	$E$	$2C_3$	$3\sigma_v$
$A_1$	+1	+1	+1
$A_2$	+1	+1	-1
$E$	+2	-1	0

$C_{2v}$	$E$	$C_2$	$\sigma_v$	$\sigma_v'$
$A_1$	+1	+1	+1	+1
$A_2$	+1	+1	-1	-1
$B_1$	+1	-1	+1	-1
$B_2$	+1	-1	-1	+1

$C_s$	$E$	$\sigma_h$
$A'$	+1	+1
$A''$	+1	-1

The number of elements (operations) in a group is known as the order of the group (symbol  $h$ ). A subgroup consists of a set of the elements within a group which, on their own, constitute a group. The order of the parent group (supergroup) is an integer multiple of the orders of each of its subgroups [10].

Each symmetry point group is represented by a Schönflies symbol consisting of a capital letter and usually one or two suffixes [10]. Its properties are described by a character table (see Table 1 for  $D_{3h}$ ,  $C_{3v}$ ,  $C_{2v}$  and  $C_2$  point groups). The table headline contains group operations  $\mathbf{R}$  (more exactly - the corresponding symmetry elements  $R$ ). The first column contains the symbols of irreducible representations (IRs) describing the symmetry of molecular orbitals, electronic states, symmetric coordinates, vibrations and so on (usually the electronic states are denoted by capital letters and the remaining quantities by small letters). The effect of symmetry operations  $\mathbf{R}$  on IRs is described by their characters  $\chi(\mathbf{R})$  in the remaining columns. The first line under the headline belongs to full-symmetric IR which is not changed by any symmetry operation (all characters equal to +1). Thus the full-symmetric vibration cannot change the point group of a molecule. One-dimensional (or non-degenerate) IRs are denoted by symbols  $A$  (symmetric to the rotation about the principal axis,  $\chi(C_n) = +1$ ) or  $B$  (antisymmetric to the rotation about the principal axis,  $\chi(C_n) = -1$ ). Degenerate (multidimensional) IRs are denoted by symbols  $E$  for two-dimensional IRs,  $T$  (or  $F$ ) for three-dimensional,  $G$  (or  $U$ ) for four-dimensional IRs,  $H$  (or  $V$ ) for five-dimensional IRs and so on (see their characters

for the identity operation  $E$ ). Their characters are the traces (the sums of diagonal elements) of multidimensional transformation matrices of their components. Where appropriate, primes (') and double primes (") indicate symmetry (') or anti-symmetry (") with respect to a horizontal mirror plane  $\sigma_h$ ,  $g$  and  $u$  subscripts denote symmetry ( $g$ ) or anti-symmetry ( $u$ ) with respect to an inversion center, etc.

By removing two  $C_3$  rotations ( $2C_3$ , implying both the  $2S_3$  improper rotations,  $2C_2'$  rotations and  $2\sigma_v$  reflections removal) of  $D_{3h}$  group (dimension  $h = 12$ ) we obtain the point group  $C_{2v}$  of lower dimension ( $h = 4$ ) which is a subgroup of  $D_{3h}$  (be careful -  $C_3$  principal axis of  $D_{3h}$  and  $C_2$  principal axis of  $C_{2v}$  must be coincident with cartesian  $z$  axis,  $\sigma_h$  mirror plane of  $D_{3h}$  is transformed into  $\sigma_v'$  plane of  $C_{2v}$ ). The relations between their IRs may be obtained by the comparison of the characters in  $E$ ,  $C_2'$ ,  $\sigma_v$  and  $\sigma_h$  headed columns of  $D_{3h}$  with the corresponding values for  $C_{2v}$ . We may see that the double-degenerate  $E'$  ( $E''$ ) type IR of  $D_{3h}$  is split into  $A_1$  and  $B_2$  ( $A_2$  and  $B_1$ ) type IRs of  $C_{2v}$  as may be seen from the sum of their characters. On the other hand, the  $C_{3v}$  group obtained by removing  $C_2'$ ,  $\sigma_h$  and  $S_3$  operations from  $D_{3h}$  group preserves the double degeneracy (an analogous characters comparison shows that  $E'$  and  $E''$  type IRs of  $D_{3h}$  correspond to  $E$  type IR of  $C_{3v}$ ).

We may see that all  $A_2''$  characters of  $D_{3h}$  which are in the  $E$ ,  $C_3$  and  $\sigma_v$  headed columns (the corresponding operations constitute the  $C_{3v}$  group) are equal to  $+1$ . It means that these symmetry operations are conserved during any nuclear displacement (such as vibrations) described by IR  $A_2''$  of  $D_{3h}$  group. The subgroup formed in this way is called kernel or kernel subgroup  $K(G, \Lambda)$  where  $G$  is the parent group and  $\Lambda$  denotes the IR of this displacement [11]. In our case this relation is described by the formula

$$C_{3v} = K(D_{3h}, a_2'') \quad (1)$$

For full-symmetric IRs the kernel group is identical with the parent group

$$D_{3h} = K(D_{3h}, a_1') \quad (2)$$

A degenerate (multidimensional) representation describes the symmetry of a set of coordinates (such as vibrations). The elements of this set are called the components of the representation and span a multidimensional distortion space [10]. Because the degeneracy leaves the direction of the distortion unspecified, one has to scan all directions of the distortion space. A minimal subgroup of symmetry elements, which must be conserved in any case, consists of those symmetry operations that leave all distortions invariant and is said to form the kernel  $K(G, \Lambda)$  of the degenerate representation  $\Lambda$ . The kernel of the degenerate mode may be obtained from the character tables by collecting all symmetry operations with the same characters as the identity operation [11]. In the case of  $D_{3h}$  group for  $E'$  type IR with all characters equal to  $+2$  we obtain

$$C_s(\sigma_h) = K(D_{3h}, e') \quad (3)$$

( $C_s(\sigma_h)$  denotes the kernel subgroup with  $\sigma_h$  mirror plane of  $D_{3h}$  being preserved).

Such a subgroup, which is preserved in a part of distortion space only, is termed an epikernel  $E(G, \Lambda)$  of degenerate representation  $\Lambda$  in parent group  $G$  [11]. Hence

$$C_{2v} = E(D_{3h}, e') \quad (4)$$

Clearly epikernels are intermediate subgroups between the parent group and the kernel group.

$$G \supset E(G, L) \supset K(G, L) \quad (5)$$

There are often several epikernels corresponding to the same  $G$  and  $\Lambda$  [11]. Representations of higher dimensions may give rise to a chain of subgroups between the parent group and its kernel (lower and higher ranking epikernels). These epikernels can represent independent ways of symmetry lowering, leading to the kernel group along different paths. Kernels and epikernels of selected point groups and degenerate IRs are presented in Table 2.

Analogously the reducible representations (consisting of several IRs) may be treated [11]. The kernels of individual IRs become epikernels of the sum (reducible) representation. In our case

$$C_1 = K(D_{3h}, e' \oplus a_2'') \quad (6)$$

and  $C_{3v}$ ,  $C_{2v}$  and  $C_s(\sigma_h)$  are epikernels,  $E(D_{3h}, e' \oplus a_2'')$ .

Finally it must be mentioned that cyclic groups such as  $C_n$ ,  $S_n$ ,  $C_{nh}$ ,  $n > 2$ , and the tetrahedral groups  $T$  and  $T_h$  contain non-degenerate complex representations which always occur in degenerate pairs with conjugate characters and hence form a reducible space of dimension two [10, 11]. Their kernel may be easily determined from their character sets. However, since both irreducible components have complex conjugate transformational properties, it is impossible to find an epikernel subgroup which leaves one component invariant while transforming the other one.

### 3 Potential Energy Surface

The conception of potential energy surface (PES) is used in physics and chemistry for the description of structures, dynamics, spectroscopy, and reactivity [13]. It is generally connected with the adiabatic or Born–Oppenheimer approximation (APES). For an atoms arrangement (molecules or ions) it may be understood as the total energy (i.e. the electronic energy with an internuclear repulsion contribution) function of its nuclear coordinates. There are several PESs corresponding to the same molecular/ionic system in various charge, electronic and spin states (usually denoted as ground and excited states). This treatment is based on the picture of the molecules/ions movement on a PES and their transitions between various PESs depending on the system temperature and external fields.

**Table 2** Kernel,  $K(G, \Lambda)$ , and epikernel,  $E(G, \Lambda)$ , subgroups of some parent groups,  $G$ , for degenerate representations,  $\Lambda$ . [11, 12]

$G$	$\Lambda$	$K(G, \Lambda)$	$E(G, \Lambda)$
Doubly degenerate representations			
$C_{3v}$	$e$	$C_l$	$C_s$
$C_{4v}$	$e$	$C_l$	$C_s(\sigma_v), C_s(\sigma_d)$
$C_{5v}$	$e_1, e_2$	$C_l$	$C_s$
$C_{6v}$	$e_1$	$C_l$	$C_s(\sigma_v), C_s(\sigma_d)$
	$e_2$	$C_2$	$C_{2v}$
$D_3$	$e$	$C_l$	$C_2$
$D_4$	$e$	$C_l$	$C_2(C_2'), C_2(C_2'')$
$D_5$	$e_1, e_2$	$C_l$	$C_2$
$D_6$	$e_1$	$C_l$	$C_2(C_2'), C_2(C_2'')$
	$e_2$	$C_2(C_6^3)$	$D_2$
$D_7$	$e_1, e_2, e_3$	$C_l$	$C_2$
$D_{3h}$	$e'$	$C_s(\sigma_h)$	$C_{2v}$
	$e''$	$C_l$	$C_2, C_s(\sigma_v)$
$D_{4h}$	$e_g$	$C_i$	$C_{2h}(C_2'), C_{2h}(C_2'')$
	$e_u$	$C_s(\sigma_h)$	$C_{2v}(C_2'), C_{2v}(C_2'')$
$D_{5h}$	$e_1', e_2'$	$C_s(\sigma_h)$	$C_{2v}$
	$e_1'', e_2''$	$C_l$	$C_2, C_s(\sigma_v)$
$D_{6h}$	$e_{1g}$	$C_i$	$C_{2h}(C_2'), C_{2h}(C_2'')$
	$e_{1u}$	$C_s(\sigma_h)$	$C_{2v}(C_2'), C_{2v}(C_2'')$
	$e_{2g}$	$C_{2h}(C_6^3)$	$D_{2h}$
	$e_{2u}$	$C_2(C_6^3)$	$C_{2v}(\sigma_v), D_2$
$D_{2d}$	$e$	$C_l$	$C_2(C_2'), C_s(\sigma_d)$
$D_{3d}$	$e_g$	$C_i$	$C_{2h}$
	$e_u$	$C_l$	$C_2, C_s$
$D_{4d}$	$e_1, e_3$	$C_l$	$C_2(C_2'), C_s$
	$e_2$	$C_2(C_4^2)$	$C_{2v}, D_2$
$D_{5d}$	$e_{1g}, e_{2g}$	$C_i$	$C_{2h}$
	$e_{1u}, e_{2u}$	$C_l$	$C_2, C_s$
$T_d$	$e$	$D_2$	$D_{2d}$
$O$	$e$	$D_2(C_4^2)$	$D_4$
$O_h$	$e_g$	$D_{2h}(C_4^2)$	$D_{4h}$
	$e_u$	$D_2(C_4^2)$	$D_4, D_{2d}$
Triply degenerate representations			
$T$	$t$	$C_l$	$C_2, C_3$
$T_h$	$t_g$	$C_i$	$C_{2h}, S_6$
	$t_u$	$C_l$	$C_{2v}, C_3$
$T_d$	$t_1$	$C_l$	$C_3, S_4, C_s$
	$t_2$	$C_l$	$C_{3v}, C_{2v}, C_s$
$O$	$t_1$	$C_l$	$C_4, C_2, C_3$
	$t_2$	$C_l$	$D_3, D_2, C_2$
$O_h$	$t_{1g}$	$C_i$	$S_6, C_{4h}, C_{2h}(C_2)$

(continued)

**Table 2** (*continued*)

$G$	$\Lambda$	$K(G, \Lambda)$	$E(G, \Lambda)$
	$t_{2g}$	$C_i$	$D_{3d}, D_{2h}(C_4^2, C_2), C_{2h}(C_2)$
	$t_{1u}$	$C_i$	$C_{3v}, C_{4v}, C_{2v}(C_2), C_s(\sigma_d), C_s(\sigma_v)$
	$t_{2u}$	$C_i$	$D_3, D_{2d}(C_4^2, C_2),$ $C_{2v}(C_2), C_2(C_2), C_s(\sigma_h)$
Fourfold degenerate representations			
$I_h$	$g_g$	$C_i$	$T_h, D_{3d}, S_6, C_{2h}$
Fivefold degenerate representations			
$I_h$	$h_g$	$C_i$	$D_{5d}, D_{3d}, D_{2h}, C_{2h}$

PES extremal points are of special interest. The stable structure of atomic nuclei corresponds to a PES minimum whereas its first order saddle point corresponds to a transition state for the transition between neighboring minima. At low temperatures and if the energy barriers between PES minima are sufficiently high, a single structure may be observed. This is the case of a static JTE. Dynamic JTE corresponds to the situation when the structure is permanently changed along the pathways between several minima and as a result only the averaged structure of higher symmetry is observed.

The type of any PES extremal point may be determined by the corresponding energy Hessian (the matrix of cartesian second derivatives of the energy). All its eigenvalues must be positive for PES minima whereas its single negative eigenvalue corresponds to the 1st order saddle point. As we will show later, the group theory is able to predict the symmetry of these extremal points of PES.

## 4 Jahn–Teller Active Coordinate

JT active coordinate originates in the 1st order perturbation theory with the Taylor expansion of the perturbation operator being restricted to linear members [13]. For the nuclear coordinate  $Q_k$  we demand non-zero value of the 1st order perturbation matrix element

$$H_{ij}^{(1)} = \langle \Psi_i^0 | \partial \mathbf{H} / \partial Q_k | \Psi_j^0 \rangle Q_k \neq 0 \quad (7)$$

in the space of non-perturbed wavefunctions  $\Psi_i^0$ . If we denote  $\Gamma_i$ ,  $\Gamma_k$  and  $\Gamma_j$  the representations of  $\Psi_i^0$ ,  $Q_k$  and  $\Psi_j^0$ , respectively ( $\mathbf{H}$  operator is full-symmetric), the integral

$$\langle \Psi_i^0 | \partial \mathbf{H} / \partial Q_k | \Psi_j^0 \rangle \quad (8)$$

may be non-zero only if the direct product  $\Gamma_{ikj}$  (reducible representation, in general)

$$\Gamma_{ikj} = \Gamma_i^* \otimes \Gamma_k \otimes \Gamma_j \quad (9)$$

contains full-symmetric IR within the point group of the unperturbed system (the asterisk denotes the complex conjugated value) [10]. Alternatively  $\Gamma_k$  must be contained in the direct product of the representations of both wavefunctions.

$$\Gamma_k \subset \Gamma_i \otimes \Gamma_j \quad (10)$$

In the case of degenerate perturbation theory both wavefunctions  $\Psi_i^0$  and  $\Psi_j^0$  correspond to the components  $\Gamma_{\gamma_i}$  and  $\Gamma_{\gamma_j}$  of the same multidimensional  $\Gamma$  representation. If accounting for hermicity of this matrix element,

$$H_{ij}^{(1)} = H_{ji}^{(1)} \quad (11)$$

the  $\Gamma_k$  representation of JT active coordinate  $Q_k$  must be contained in the symmetric direct product of the IRs of the degenerate wavefunction [10].

$$\Gamma_k \subset [\Gamma \otimes \Gamma]^+ = [\Gamma^2]^+ \quad (12)$$

The characters of the representation  $\Gamma_{ij} = \Gamma_i \otimes \Gamma_j$  are obtained by multiplying the corresponding characters of the contributing representations for the same symmetry operation  $\mathbf{R}$  [10]

$$\phi_{ij}(\mathbf{R}) = \phi_i(\mathbf{R}) \cdot \phi_j(\mathbf{R}) \quad (13)$$

The characters of the symmetric direct product representation  $[\Gamma^2]^+$  of dimension  $n(n+1)/2$  (where  $n$  is the dimension of  $\Gamma$ ) for the symmetry operation  $\mathbf{R}$  are defined as

$$\chi_{\Gamma}^+ = \{[\chi_{\Gamma}(\mathbf{R})]^2 + \chi_{\Gamma}(\mathbf{R}^2)\}/2 \quad (14)$$

where  $\chi_{\Gamma}(\mathbf{R}^2)$  is the character of the  $\mathbf{R}^2$  operation (see Table 3) [10].

Analogously, the characters of antisymmetric direct product  $[\Gamma^2]^-$  of dimension  $n(n-1)/2$  is defined as follows [10]

$$\chi_{\Gamma}^- = \{[\chi_{\Gamma}(\mathbf{R})]^2 - \chi_{\Gamma}(\mathbf{R}^2)\}/2 \quad (15)$$

Using perturbation theory treatment the analytical formula for APES of a JT system may be obtained. Its extremal points are determined by the extrema condition

**Table 3** Symmetry operations  $\mathbf{R}$  and their squares  $\mathbf{R}^2$  [10]

$R$	$R^2$	$R$	$R^2$
$E$	$E$	$\sigma$	$E$
$C_2$	$E$	$i$	$E$
$C_3$	$C_3^2$	$S_3$	$C_3^2$
$C_4$	$C_2$	$S_4$	$C_2$
$C_5$	$C_5^2$	$S_5$	$C_5^2$
$C_6$	$C_3$	$S_6$	$C_3$



$$\partial E / \partial Q_k = 0 \quad k = 1, 2 \dots \quad (16)$$

where  $E$  is the total energy of the perturbed system. The energy difference between the energy of the unperturbed system and the energy of PES minimum (stable configuration) is called the JT stabilization energy. Here it must be mentioned that at least two JT active coordinates are necessary for the adequate description of the PES of JT systems (at least two energy minima must be obtained).

Alternatively, the method of Öpik and Pryce [14] using eigenvectors may be used to obtain PES extremal point coordinates.

The problem of obtaining the stable geometries of JT systems can be solved analytically for small systems only. For large systems a group-theoretical treatment is necessary. This may be based on JT active coordinates or a degenerate electronic state split.

## 5 Epikernel Principle

Several theoretical methods ranging from simple model treatments to extensive ab initio calculations have been used to calculate the JT stabilization energies and JT distortions for a variety of JT systems. Based on these results Liehr [15] conjectured that the symmetry of the stable JT geometry would be the highest which is yet compatible with the loss of the initial electronic degeneracy. A more general and more precise description of the symmetry characteristics of JT instabilities is based on the concept of kernels and epikernels. Ceulemans et al. [10, 16, 17] formulated the following epikernel principle for the  $\Lambda$  representations of JT active coordinates:

*Extremum points on a JT energy surface prefer epikernels; they prefer maximal epikernels to the lower ranking ones. As a rule stable minima are to be found with the structures of maximal epikernel symmetry.*

For double electronic degeneracy it may be further specified:

*Extremum points on a JT PES for an orbital doublet will coincide with epikernel configurations. If the distortion space conserves only one type of epikernel, minima and saddle points will be found on opposite sides of the same epikernel distortion. If the distortion space conserves two types of epikernels, minima and saddle points will be characterized by different epikernel symmetries.*

Since kernel  $K(G, \Lambda)$  is a subgroup of epikernel  $E(G, \Lambda)$ , kernel extrema (if they exist) will be more numerous than epikernel extrema of a given type. In order to be stationary at all these equivalent points, the JT PES must be of considerable complexity. Only higher order term in the perturbation expansion (7) are able to generate non-symmetrical extrema. However – from a perturbational point of view – the dominance of higher order terms over the first (and second) order contributions is (extremely) unlikely. This rationalizes the epikernel principle as well.

## 6 Step-by-step Descent in Symmetry

An alternative treatment to PES extrema of JT systems is based on their electronic degeneracy removal with a symmetry decrease [13, 18–22]. This method has been developed for PES minima but it is applicable to PES saddle points as well (e.g. the double electronic degeneracy of ideal  $[\text{CuX}_6]^{4-}$  octahedron is removed in both elongated and compressed  $[\text{CuX}_6]^{4-}$  bipyramids of  $D_{4h}$  symmetry independent of corresponding to PES minima or saddle points). This treatment also uses the above mentioned Liehrs's principle [15] that the symmetry of the stable JT geometry would be the highest which is yet compatible with the loss of the initial electronic degeneracy.

The method of step-by-step descent in symmetry supposes that the driving force of JT distortion is the (geometry conditioned) electronic degeneracy (more exactly – the lifting of the degeneracy in the first order of the nuclear displacements, analogously to the “repulsion” of pseudodegenerate electronic states) and its removal is connected with an energy decrease. During this process, some symmetry elements of the system are removed and a new symmetry group arises which is an immediate subgroup of the original (parent) group before the distortion. If the electronic state (described by its IR) of the system in the immediate subgroup is non-degenerate (one-dimensional IR), the symmetry descent stops because the distortion mode is not coupled with electronic degeneracy anymore (there is no driving force). Otherwise further symmetry elements are to be removed and the JT symmetry descent continues till a non-degenerate electronic state is obtained. The relations between IRs describing the electronic states within the same symmetry descent path are determined by group-subgroup relations. As several ways of symmetry descent (due to different symmetry elements removal) are possible (the parent group has several immediate subgroups), several symmetry descent paths may exist for the system in a degenerate electronic state.

This problem is relatively simple in the case of double electronic degeneracy where only the complete degeneracy removal is possible. Consequently, the JT stable groups may correspond to both PES minima and saddle points (and other PES extremal points as well). On the other hand, a partial degeneracy removal is possible in the systems with higher than double electronic degeneracy (e.g. the triple degenerate electronic state of ideal  $[\text{CuX}_4]^{2-}$  tetrahedron is split into the double degenerate and the non-degenerate ones in  $[\text{CuX}_4]^{2-}$  pyramids of  $C_{3v}$  symmetry). The sign of the splitting (the energy difference of the electronic states after splitting) is inverted when the distortion mode is applied in the opposite direction (e.g. elongated or compressed  $[\text{CuX}_4]^{2-}$  pyramids of  $C_{3v}$  symmetry). If either the non-degenerate or degenerate electronic states may be obtained within the same symmetry descent (depending on the direction of the distortion mode only) then the same symmetry group may be either JT stable or JT unstable, respectively, for various chemical systems. JT unstable groups cannot correspond to PES minima but might correspond to other PES extrema types. Consequently, two types of PES saddle (or extremal) points may be distinguished – JT stable and JT unstable.

Schemes 1–6 contain the possible JT symmetry descent paths for the most important point groups of symmetry. The symbols in each rectangle denote a point group (upper line) and the IR describing the electronic state (bottom line). The paths connect the bottom side of rectangles with the upper side of the rectangles in the next level. The rectangles corresponding to JT stable groups and IRs are the end points of these paths (no path at the rectangle bottom side). For the JT unstable group the path continues at the bottom side of its rectangle. The arrows at these lines indicate that the path continues in another Scheme containing the rectangle with the same group and IR symbols.

## 7 Applications

### 7.1 Cyclopropenyl Radical

A very simple JT system of cyclo- $C_3H_3$  has been frequently studied till the 1980s at various levels of theory but its more sophisticated studies including electron correlation are very rare. Unfortunately, it is a typical system with electronic structure and optimal geometry depending on fine effects. Recent B3LYP geometry optimization of cyclopropenyl radical [23] leads to planar structures of  $C_{2v}$  symmetry. The “obtuse” triangular structures in  $^2A_2$  electronic state are stable whereas the “acute” ones in  $^2B_1$  electronic state of higher energy correspond to the PES saddle points between them (Table 4).

The existence of these structures may be explained by the JT distortion of a parent  $D_{3h}$  structure in  $^2E'$  or  $^2E''$  electronic states. The symmetry of JT active coordinates may be obtained from the symmetric direct product within  $D_{3h}$  group

$$[(E')^2]^+ = [(E'')^2]^+ = A_1 \oplus E' \quad (17)$$

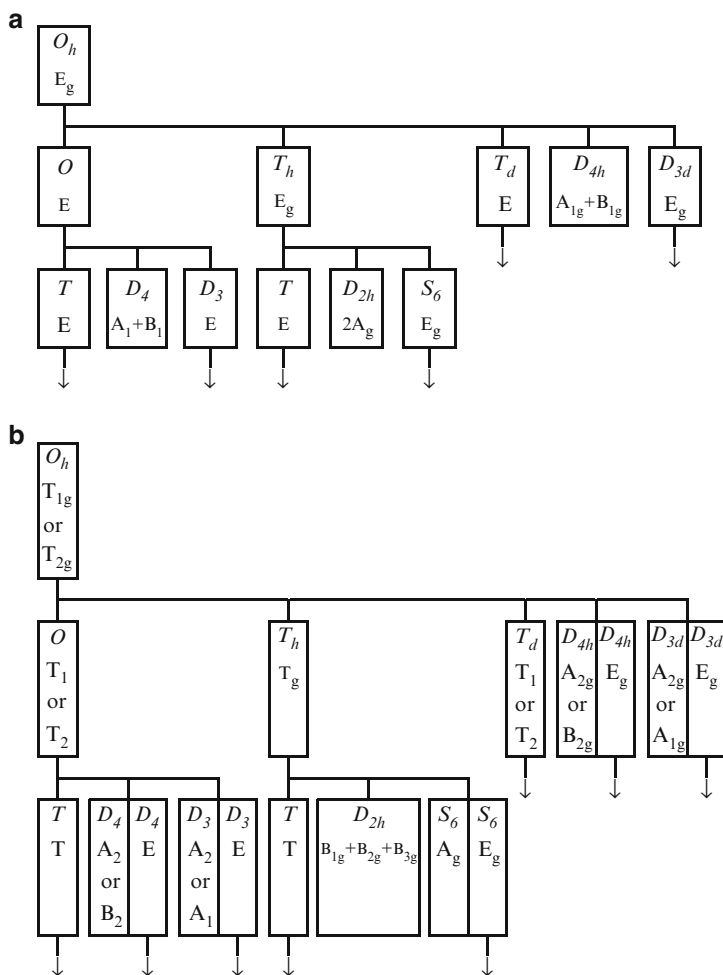
According to the epikernel principle for  $e'$  distortion (see Table 2)

$$E(D_{3h}, e') = C_{2v} \quad (18)$$

$$K(D_{3h}, e') = C_s(\sigma_h) \quad (19)$$

**Table 4** Symmetry, electronic state, relative energy ( $\Delta E$ ) and number of imaginary vibrations ( $N_{\text{imag}}$ ) for MP2/cc-pVTZ optimized structures of cyclo- $C_3H_3$  radical [23]

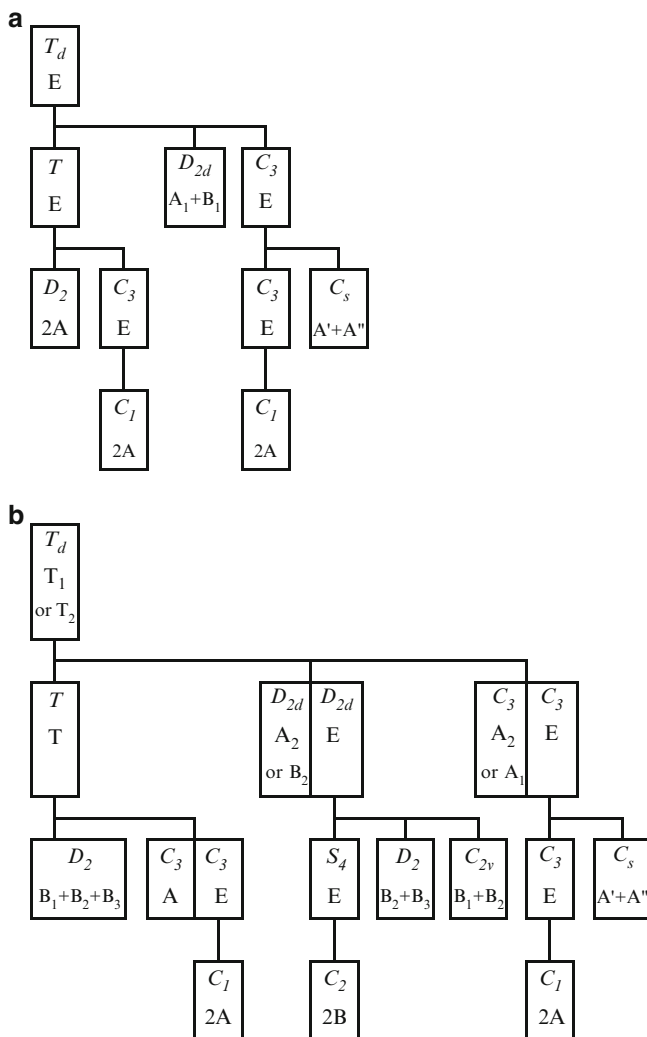
Symmetry	El. state	$\Delta E [kJ/mol]$	$N_{\text{imag}}$	Remark
$D_{3h}$	$^2E''$	0	2	
$C_{2v}$	$^2B_1$	−68.2	1	“acute”
$C_{2v}$	$^2A_2$	−69.2	3	“obtuse”
$C_s$	$^2A''$	−81.2	1	“obtuse”, two H out-of-plane
$C_s$	$^2A'$	−104.6	0	“acute”, single H out-of-plane



**Scheme 1** JT symmetry descent paths of  $O_h$  parent group and its subgroups (upper lines in rectangles) for IRs (bottom lines in rectangles)  $E_g$  (**a**),  $T_{1g}$  and  $T_{2g}$  (**b**). Analogous schemes may be obtained for ungerade IRs ( $E_u$ ,  $T_{1u}$ ,  $T_{2u}$ ) replacing subscripts g by the u ones where appropriate. For continuation see Schemes 2 ( $T_d$  and  $T$  groups), 4 ( $S_6$  group) and 6 ( $D_{3d}$  and  $D_3$  groups)

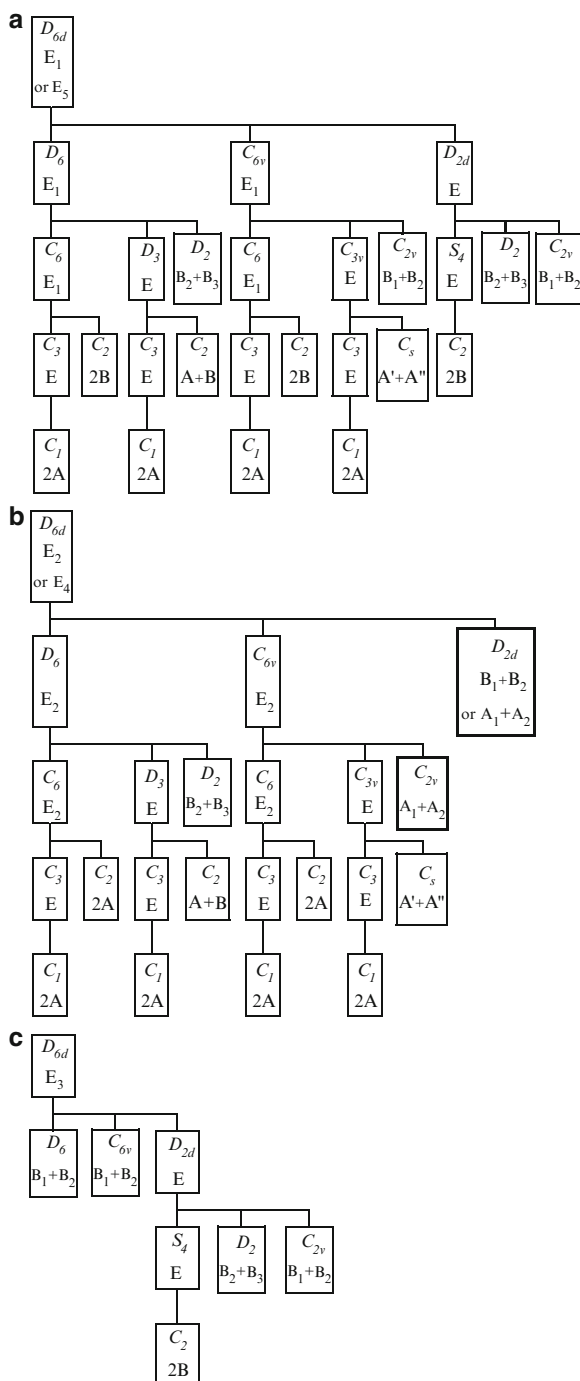
Thus the B3LYP obtained  $C_{2v}$  structures are epikernels of the parent group in agreement with the epikernel principle.

According to the method of step-by-step descent in symmetry,  $C_{2v}$  is a JT stable immediate subgroup of  $D_{3h}$  parent group for  $^2E'$  or  $^2E''$  electronic states (Scheme 6b). The above mentioned  $^2A_2$  and  $^2B_1$  electronic states of  $C_{2v}$  structures [23] are obtained by splitting the  $^2E''$  degenerate one of the  $D_{3h}$  parent group. A symmetry descent to other JT stable groups such as  $C_s$ ,  $C_2$  or  $C_1$  mediated by some JT unstable groups containing  $C_3$  rotation axis is possible as well.

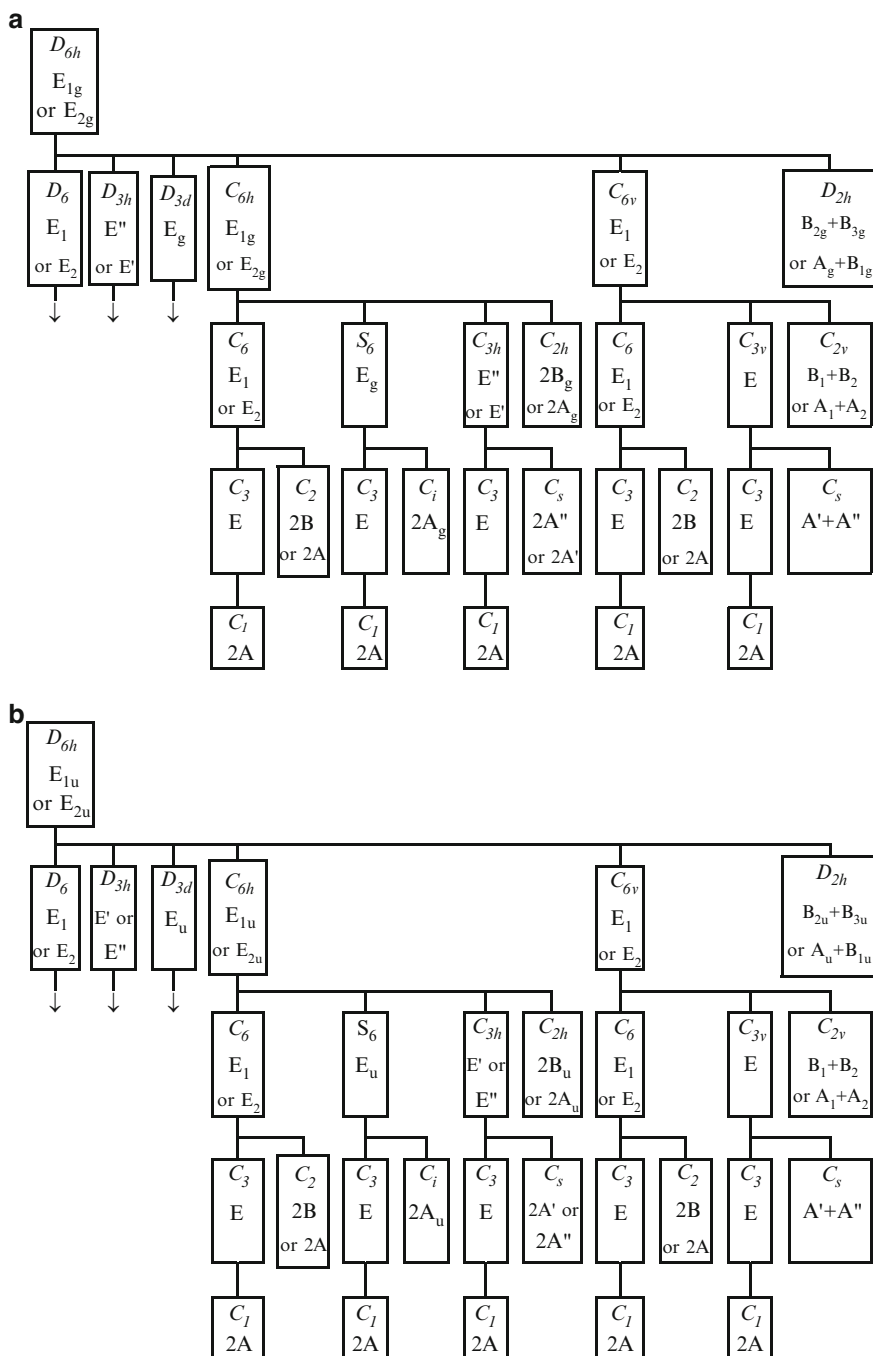


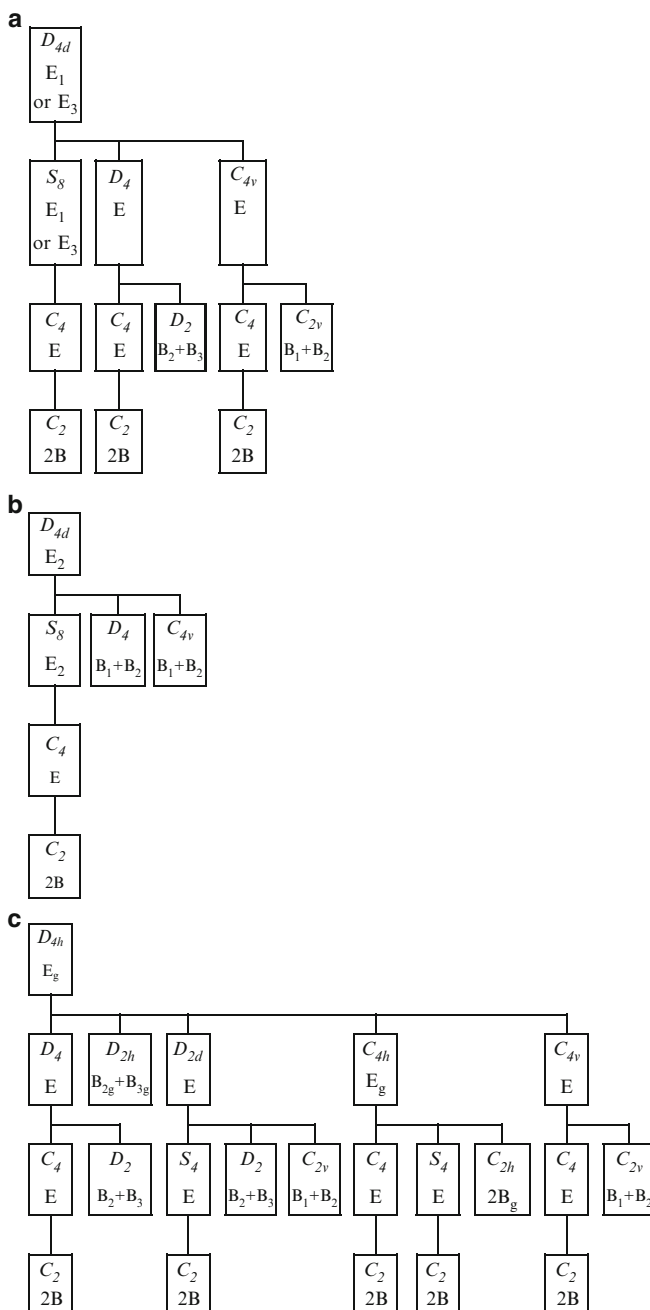
**Scheme 2** JT symmetry descent paths of  $T_d$  parent group and its subgroups (upper lines in rectangles) for IRs (bottom lines in rectangles) E (**a**),  $T_1$  and  $T_2$  (**b**)

We performed MP2/cc-pVTZ geometry optimization of cyclo- $C_3H_3$  radical using Gaussian03 software [24]. We have found  $C_s$  stable structure ( $^2A'$  electronic state) and PES saddle points of  $C_{2v}$  ( $^2B_1$  and  $^2A_2$  electronic states) and  $C_s$  ( $^2A''$  electronic state) symmetries (see Table 4 and Fig. 1) in agreement with step-by-step descent method (because the original  $\sigma_h$  plane of the parent  $D_{3h}$  group is not conserved in the non-planar cyclopropenyl radical). Two symmetry descent paths of Scheme 6b may be employed:



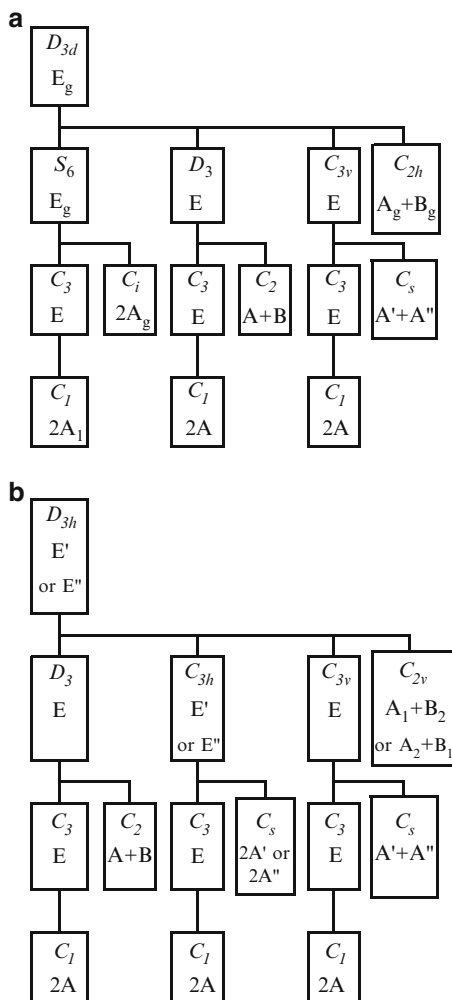
**Scheme 3** JT symmetry descent paths of  $D_{6d}$  parent group and its subgroups (upper lines in rectangles) for IRs (bottom lines in rectangles)  $E_1$  and  $E_5$  (**a**),  $E_3$  and  $E_4$  (**b**) and  $E_3$  (**c**)





**Scheme 5** JT symmetry descent paths of  $D_{4d}$  parent group and its subgroups (upper lines in rectangles) for IRs (bottom lines in rectangles)  $E_1$  and  $E_3$  (**a**) and  $E_2$  (**b**) and of  $D_{4h}$  (**c**) parent groups and its subgroups (upper lines in rectangles) for IR  $E_g$  (bottom lines in rectangles). Analogous  $D_{4h}$  scheme may be obtained for ungerade IRs ( $E_u$ ) replacing subscripts g by the u ones where appropriate





**Scheme 6** JT symmetry descent paths of  $D_{3d}$  (a) and  $D_{3h}$  (b) parent groups and their subgroups (upper lines in rectangles) for two-dimensional IRs (bottom lines in rectangles). Analogous  $D_{3d}$  scheme may be obtained for ungerade IRs ( $E_u$ ) replacing subscripts g by the u ones where appropriate

$$D_{3h}(E'') \rightarrow C_{2v}(A_2) \text{ or } C_{2v}(B_1) \quad (20)$$

$$D_{3h}(E'') \rightarrow C_{3v}(E) \rightarrow C_s(A') \text{ or } C_s(A'') \quad (21)$$

It must be mentioned that  $C_2$  structures have been obtained using MP2/cc-pVDZ treatment which are not predicted by epikernel principle for the  $e'$  type JT coordinate (these are possible for the  $e''$  one only). Nevertheless, further theoretical studies using larger basis sets and more exact methods are desirable.

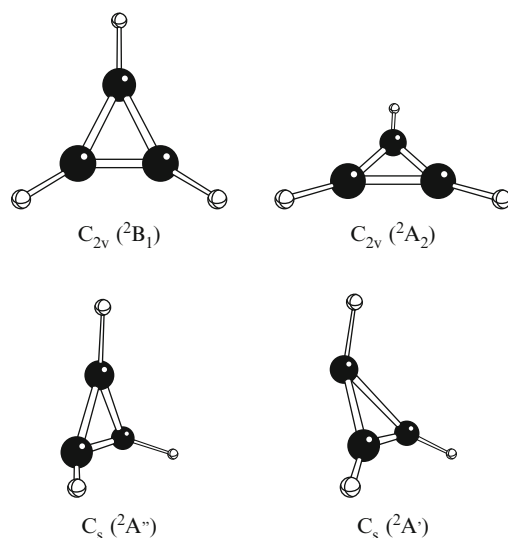


**Fig. 1** MP2/cc-pVTZ optimized structures of cyclopropenyl radical (electronic states in parentheses)

## 7.2 Coronene Anion

Sato and coworkers [25–27] investigated the electronic and geometric structure of the coronene monoanion,  $C_{24}H_{12}^-$  (Fig. 2). ESR observation in solution exhibited no JT effect down to 183 K. JT distorted structure was obtained using HF/6–31G\*\* calculation. The optimized structure of the monoanionic state has  $C_{2h}$  symmetry ( $^2B_g$  electronic state) for the energy minimum (JT stabilization energy of 297 meV) and  $D_{2h}$  for the transition structures (energy barrier of ca 0.2 meV between  $C_{2h}$  minima).

The symmetric direct product within  $D_{6h}$  symmetry group

$$[E_{ij}^2]^+ = A_{1g} \oplus E_{2g} \quad i = 1 \text{ or } 2, j = u \text{ or } g \quad (22)$$

indicates JT active coordinates of  $e_{2g}$  symmetry for any degenerate electronic state. According to the epikernel principle

$$E(D_{6h}, e_{2g}) = D_{2h} \quad (23)$$

$$K(D_{6h}, e_{2g}) = C_{2h}(C_6^3) \quad (24)$$

It has been mentioned [25–27] that the optimized structure of the monoanionic state of coronene does not have (epikernel)  $D_{2h}$  symmetry expected from the epikernel principle but has (kernel)  $C_{2h}$  symmetry. Hence the JT distortion of coronene monoanion is an exception for the epikernel principle. This is because the epikernel

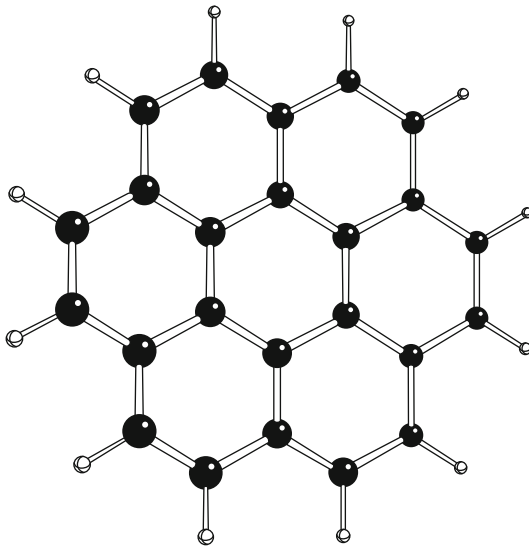


**Fig. 2** Structure of coronene

principle does not take higher-order terms into consideration. It is necessary to extend the epikernel principle to include higher-order anharmonic terms (the anharmonic terms up to sixth order are necessary to obtain the minimum structure with  $C_{2h}$  symmetry).

The application of the method of step-by-step descent in symmetry to the  $D_{6h}$  parent symmetry group for all the possible degenerate electronic states may be seen in Scheme 4 [21]. Among its immediate subgroups, only the  $D_{2h}$  one is JT stable.

$$D_{6h} \rightarrow D_{2h} \quad (25)$$

The remaining groups preserve double electron degeneracy and are subjects to further JT symmetry descent (moreover, the  $D_6$  symmetry group is not feasible for coronene). There are two possible ways to JT stable  $C_{2h}$  group in  ${}^2B_g$  electronic state:

$$D_{6h}({}^2E_{1g} \text{ or } {}^2E_{2g}) \rightarrow C_{6h}({}^2E_{1g} \text{ or } {}^2E_{2g}) \rightarrow C_{2h}({}^2B_g) \quad (26)$$

$$D_{6h}({}^2E_{1g} \text{ or } {}^2E_{2g}) \rightarrow D_{3d}({}^2E_g) \rightarrow C_{2h}({}^2B_g) \quad (27)$$

More detailed analysis of the PES of coronene monoanion is desirable. It is evident that at least JT stable structures of  $D_{2h}$  and  $C_{2h}$  groups in alternate electronic states should be found (compare cyclo- $C_3H_3$  in Chap. 7.1).

### 7.3 Spirobifluorene Anion

The lowest unoccupied molecular orbital of neutral spirobifluorene (Fig. 3) of  $D_{2d}$  point group is of  $e$  symmetry. Consequently, the single electron addition leads to an anion in double degenerate  ${}^2E$  electronic state and the system undergoes to a symmetry descent [22, 28]. B3LYP/6-31 + G\* geometry optimization leads to a  $C_{2v}$  stable geometry in  ${}^2B_2$  electronic state with two perpendicular non-equivalent planar fluorene units. Within additional investigations, a transition structure of  $D_2$  symmetry in  ${}^2B_2$  electronic state (the fluorene units are non-planar but equivalent) has been found and further geometry optimizations are in progress.

The symmetric direct product

$$[E^2]^+ = A_1 \oplus B_1 \oplus B_2 \quad (28)$$

indicates JT active coordinates of  $b_1$  or  $b_2$  symmetries. According to the epikernel principle

$$K(D_{2d}, b_1) = D_2 \quad (29)$$

$$K(D_{2d}, b_2) = C_{2v} \quad (30)$$

$$K(D_{2d}, b_1 + b_2) = C_2 \quad (31)$$

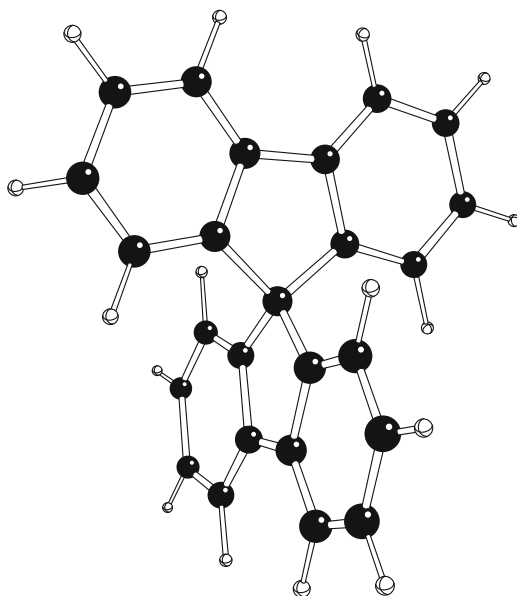


**Fig. 3** Structure of spirobifluorene

The method of step-by-step descent in symmetry indicates two descent paths to JT stable immediate subgroups of  $D_{2d}$  (see Scheme 5d) [22]

$$D_{2d}({}^2E) \rightarrow C_{2v}({}^2B_2) \quad (32)$$

$$D_{2d}({}^2E) \rightarrow D_2({}^2B_2) \quad (33)$$

The remaining descent path consists of two steps

$$D_{2d}({}^2E) \rightarrow S_4({}^2E) \rightarrow C_2({}^2B) \quad (34)$$

but the final  $C_2$  structure has not been found yet.

Finally, an absolute agreement between the results of epikernel principle and step-by-step symmetry descent method may be concluded.

## 7.4 $B_4^+$

Yang and coworkers [29] performed a QCISD/6–311G\* study of  $B_4^+$  isomers. For this cation, the  $D_{2h}$  (rectangle and rhombus),  $D_{4h}$ ,  $C_{2v}$  (planar and nonplanar) and  $D_{3h}$  structures were fully optimized. The obtained structures are presented in Table 5 (for atom numbering see Fig. 4). Calculated harmonic vibrational frequencies indicate that  $D_{4h}$  and rectangle  $D_{2h}$  structures (i.e. B2 and B3 models) do not correspond to stable configurations (single imaginary frequency of  $b_{3g}$  and  $b_{1g}$  symmetry, respectively) and they should be PES saddle points of  $B_4^+$ . However, it must be mentioned that their energies as well as geometries are so similar that they might be equal within the calculation errors. Unfortunately, there have been presented no data on optimization procedure accuracy and this problem cannot be resolved.

Yang and coworkers [29] suppose that the optimal  $B_4^+$  geometries are a consequence of a JT distortion of their parent structures of  $D_{4h}$  or  $T_d$  symmetries in degenerate electronic states. The authors explain both non-planar and planar  $C_{2v}$  structures (A and C models) as a consequence of JT distortions of the ideal  $B_4^+$  tetrahedron in triple degenerate electronic state as the epikernel for  $t_2$  JT active coordinate (see Table 5).

$$[T_1^2]^+ = [T_2^2]^+ = A_1 \oplus E \oplus T_2 \quad (35)$$

and for JT active coordinate of  $t_2$  symmetry we obtain

$$E(T_d, t_2) = C_{2v} \quad (36)$$

Similar conclusions on rhombic and rectangular  $D_{2h}$  structures as JT perturbed  $B_4^+$  squares ( $D_{4h}$  group) in double degenerate electronic state (B1–B3 models) as the kernel of  $b_{1g}$  or  $b_{2g}$  JT active coordinate have been done.

**Table 5** The symmetries, geometries and energies of the  $B_4^+$  structures optimized at QCISD/6-311G\* level of theory [29]

Model	Symmetry	Electronic state	Bond lengths (Å)	Bond angles (°)	Energy (a.u.)
Non-planar systems:					
A	$C_{2v}$	$^2B_1$	$R_{12} = R_{13} = R_{34} = R_{24} = 1.7326$ $R_{32} = 1.5636$ $R_{41} = 1.5718$	$\angle 142 = \angle 143 = 63.02$ $\angle 123 = \angle 132 = 63.18$	-98.4197752
Planar systems:					
B1	$D_{2h}$	$^2A_g$	$R_{12} = R_{23} = R_{34} = R_{41} = 1.5691$	$\angle 123 = \angle 143 = 80.85$ $\angle 214 = \angle 234 = 99.15$	-98.4597205
B2	$D_{4h}$	${}^{1/2}A_{1g}$	$R_{12} = R_{23} = R_{34} = R_{41} = 1.5643$	$\angle 123 = \angle 143 = 90.0$ $\angle 214 = \angle 234 = 90.0$	-98.4591652
B3	$D_{2h}$	$^2A_g$	$R_{12} = R_{43} = 1.5647$ $R_{23} = R_{41} = 1.5648$	$\angle 123 = \angle 143 = 90.0$ $\angle 214 = \angle 234 = 90.0$	-98.4591648
C	$C_{2v}$	$^2A_1$	$R_{12} = 1.5956$ $R_{23} = R_{24} = 1.5892$	$\angle 123 = \angle 124 = 116.79$ $\angle 423 = 126.42$	-98.3697939

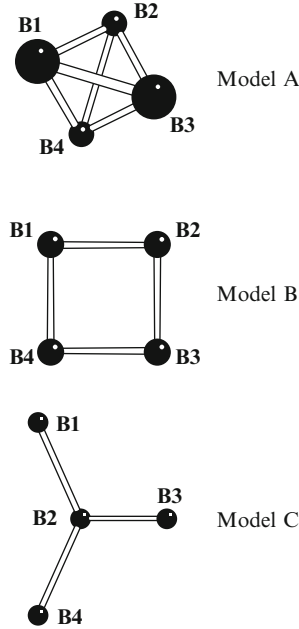


**Fig. 4** High-symmetric structures of  $B_4^+$

$$[E_g^2]^+ = [E_u^2]^+ = A_{1g} \oplus B_{1g} \oplus B_{2g} \quad (37)$$

For  $b_{1g}$  and  $b_{2g}$  JT active coordinates we obtain the kernel groups

$$K(D_{4h}, b_{1g}) = D_{2h}(C_2') \quad (38)$$

$$K(D_{4h}, b_{2g}) = D_{2h}(C_2'') \quad (39)$$

which are not in full agreement with the corresponding energies in Table 5 (B2 and B3 models).

However, the above explanation cannot be fully correct [20]. Non-linear  $B_4^+$  clusters of the highest symmetry (before JT distortion) may be divided into three groups (see Fig. 4):

1. Non-planar tetrahedral ( $T_d$  symmetry group) – A model
2. Square planar ( $D_{4h}$  symmetry group) – B model
3. Regular triangular ( $D_{3h}$  symmetry group) – C model

Because no group-subgroup relations hold for these groups, no JT distortion can transform between them and they must be treated separately (different parent groups for JT descent paths).

Possible symmetry groups originating in JT symmetry descent of parent  $T_d$  group with triple electron degeneracy ( $^2T_1$  or  $^2T_2$  electronic state for  $B_4^+$  cluster) in (36) formally agree with the epikernel principle but it does not hold for the

corresponding electronic states implied by symmetry descent paths (Scheme 2b).  $C_{2v}$  symmetry group with  ${}^2B_1$  electronic state is JT stable as the end-point of the symmetry descent path via JT unstable  $D_{2d}$  group

$$T_d({}^2T_2) \rightarrow D_{2d}({}^2E) \rightarrow C_{2v}({}^2B_1) \text{ or } C_{2v}({}^2B_2) \quad (40)$$

Thus the planar  $C_{2v}$  structure (C model) in  ${}^2A_1$  electronic state cannot be explained by JT symmetry descent from parent  $T_d$  group.

It is evident that  ${}^2A_g$  electronic state of  $D_{2h}$  symmetry group cannot arise due to JT effect (by splitting  ${}^2E_g$  electronic state of  $D_{4h}$  group) because it is not allowed by the symmetry descent path (see Scheme 5c)

$$D_{4h}({}^2E_g) \rightarrow D_{2h}({}^2B_{2g}) \text{ or } D_{2h}({}^2B_{3g}) \quad (41)$$

Alternatively, possible  ${}^2E_u$  electronic state of  $D_{4h}$  can be split into the ungerade ones of  $D_{2h}$  group (subscript  $u$ ).

Moreover,  ${}^2A_{1g}$  electronic state of  $D_{4h}$  symmetry group is non-degenerate (despite being a saddle point and not a PES minimum) and thus JT inactive. Consequently, B1–B3 model structures cannot be explained by JT effect.

Planar  $C_{2v}$  structure with  ${}^1A_1$  electronic state (C model) cannot be explained by JT symmetry descent from parent  $T_d$  group and must be explained by JT symmetry descent of parent  $D_{3h}$  symmetry group (see Fig. 4) with double electron degeneracy by the symmetry descent path (Scheme 6b)

$$D_{3h}({}^2E' \text{ or } {}^2E'') \rightarrow C_{2v}({}^2A_1) \text{ or } C_{2v}({}^2B_2) \quad (42)$$

This is in agreement with the epikernel principle since

$$[(E')^2]^+ = [(E'')^2]^+ = A_1 \oplus E' \quad (43)$$

and for JT active coordinate of  $e'$  symmetry we obtain

$$E(D_{3h}, e') = C_{2v} \quad (44)$$

Finally it may be concluded that only non-planar (A model) and planar (C model)  $C_{2v}$  structures of  $B_4^+$  may be explained by JT effect. The electronic states of the remaining structures indicate that they cannot originate in a degenerate electronic state of the parent JT group. Their existence should be explained by other effects (probably also of vibronic character such as pseudo-JT effect). It has been clearly demonstrated that the treatment based on JT active coordinates may often lead to incorrect results and accounting for electronic state symmetry is necessary.



## 8 Conclusions

This study deals with group-theoretical analysis of JT systems, especially with the prediction of the symmetries of the structures caused by JTE. Two alternative treatments based on JT active coordinates and on the step-by-step splitting degenerate electronic states are explained and their results are compared within several examples. Despite producing equal results for some low-dimensional groups, both treatments have their advantages and shortages.

The method of epikernel principle seems to be incomplete due to its restriction to the 1st order perturbation theory and linear extension of the perturbation potential. Using more complete perturbation may produce the results comparable with the other method on account of higher elaborateness. The JT caused loss of planarity or of symmetry center in JT systems can be explained by pseudo-JT mechanisms only. Another problem is the applicability to the groups with complex characters ( $C_n$ ,  $S_n$ , and  $C_{nh}$  for  $n > 2$ ,  $T$  and  $T_h$ ).

The method of step-by-step symmetry descent does not explain the mechanisms that are responsible for JT distortions. Some opponents argue that its predictions are far too wide on account of selectivity (“all is possible”). On the other hand, this treatment is based exclusively on group theory and does not account for any approximations used in the recent solutions of Schrödinger equation. Chemical thermodynamics does not solve the problems of chemical kinetics but nobody demands to do it as well. Thus we cannot demand this theory to solve also the mechanistic problems despite the epikernel principle solves it. The problem of too wide predictions can be reduced by minimizing the numbers and lengths of symmetry descent paths (see the applications in this study).

Finally it may be concluded that both the above mentioned treatments should be used jointly in all studies dealing with JTE problems. The group-theoretical treatments enable to extend the applications from molecular systems (described by point groups) up to crystals and phase transitions (described by space groups). Further studies in this field should bring valuable results and solve the recent theoretical problems as well.

**Acknowledgements** Slovak Grant Agency VEGA (Project No. 1/0127/09) is acknowledged for financial support. This work has benefited from the Center of Excellence Program of the Slovak Academy of Sciences in Bratislava, Slovakia (COMCHEM, Contract no. II/1/2007).

## References

1. H.A. Jahn, E. Teller, *Proc. Roy. Soc. London A* **161**, 220 (1937)
2. H.A. Jahn, *Proc. Roy. Soc. London A* **164**, 117 (1938)
3. H.A. Kramers, *Kon. Acad. Wet. Amsterdam* **33**, 959 (1930) (The Kramers degeneracy theorem states that the energy levels of systems with an odd number of electrons remain at least doubly degenerate in the presence of purely electric fields (i.e. no magnetic fields))
4. E. Ruch, *Z. Elektrochemie* **61**, 913 (1957)
5. E. Ruch, A. Schönhofer, *Theoret. Chim. Acta (Berl.)* **3**, 291 (1965)

6. E.I. Blount, J. Math. Phys. **12**, 1890 (1971)
7. I.V.V. Raghavacharyulu, J. Phys. C **6**, L455 (1973)
8. V.I. Pupyshev, Int. J. Quantum Chem. **107**, 1446 (2006)
9. I.B. Bersuker, The Jahn–Teller Effect, Cambridge University Press, London (2006)
10. J.A. Salthouse, M.J. Ware, *Point Group Character Tables and Related Data*. (Cambridge University Press, London, 1972)
11. A. Ceulemans, L.G. Vanquickenborne, Struct. Bonding **71**, 125 (1989)
12. V. Janovec, V. Kopský, in *International Tables for Crystallography, Vol. D: Physical Properties of Crystals* ed. by H. Wondratschek, U. Müller (Springer, New York, 2004), pp. 350–361
13. R. Boča, M. Breza, P. Pelikán, Struct. Bonding **71**, 57 (1989)
14. U. Öpik, M.H.L. Pryce, Proc. Roy. Soc. A **238**, 425 (1957)
15. A.D. Liehr, Progr. Inorg. Chem. **5**, 385 (1963)
16. A. Ceulemans, D. Beyens, L.G. Vanquickenborne, J. Am. Chem. Soc. **106**, 5824 (1984)
17. A. Ceulemans, J. Chem. Phys. **87**, 5374 (1987)
18. P. Pelikán, M. Breza, Chem. Zvesti **39**, 255 (1985)
19. M. Breza, Acta Crystallogr. B **46**, 573 (1990)
20. M. Breza, J. Mol. Struct.-THEOCHEM **618**, 165 (2002)
21. M. Breza, Chem. Phys. **291**, 207 (2003)
22. K. Matuszová, M. Breza, T. Pálszegi, J. Mol. Struct.-THEOCHEM **851**, 277 (2008)
23. G. Katzer, A.F. Sax, J. Chem. Phys. **117**, 8219 (2002)
24. M.J. Frisch et al., *Gaussian 03, Revision C.1.1*. (Gaussian Inc., Pittsburgh, PA, 2003)
25. T. Sato, H. Tanaka, A. Yamamoto, Y. Kuzumoto, K. Tokunaga, Chem. Phys. **287** 91 (2003)
26. T. Sato, A. Yamamoto, H. Tanaka: Chem. Phys. Lett. **326**, 573 (2000)
27. T. Sato, A. Yamamoto, T. Yamabe: J. Phys. Chem. A **104**, 130 (2000)
28. V. Lukeš, R. Šolc, F. Milota, J. Sperling, H.F. Kauffmann, Chem. Phys. **349**, 226 (2008)
29. C.I. Yang, Z.H. Zhang, T.Q. Ren, R. Wang, Z.H. Zhu, J. Mol. Struct. (THEOCHEM) **583**, 63 (2002)

# Spin–Orbit Vibronic Coupling in Jahn–Teller and Renner Systems

Leonid V. Poluyanov and Wolfgang Domcke

**Abstract** A systematic analysis of spin–orbit coupling effects in Jahn–Teller and Renner systems is presented. The spin–orbit coupling is described by the microscopic Breit–Pauli operator. In contrast to most previous work for molecules and crystals, the spin–orbit operator is treated in the same manner as the electrostatic Hamiltonian, that is, the Breit–Pauli operator is expanded in powers of normal-mode displacements at the reference geometry, matrix elements are taken with diabatic electronic states, and symmetry selection rules are used to determine the non-vanishing matrix elements. Choosing trigonal systems, tetrahedral systems and linear molecules as examples, it is shown how the generalized symmetry group of the spin–orbit operator can be determined. The vibronic Hamiltonians including spin–orbit coupling up to first order in the vibrational displacements are derived. It is shown that there exist linear vibronic-coupling terms of relativistic origin which are particularly relevant in systems where the vibronic coupling by the electrostatic Hamiltonian arises in second (or higher) order in the vibrational coordinates.

## 1 Introduction

The term “vibronic coupling” subsumes all phenomena which arise from the mixing of degenerate or nearly degenerate electronic states by nuclear displacements from a reference geometry. The most well-known examples of vibronic coupling are the Renner effect in linear molecules and the Jahn–Teller (JT) effect in non-linear molecules. In these cases, the electronic degeneracy arises as a consequence of symmetry. The basic concepts of vibronic coupling in molecules and crystals, including the Renner and JT effects, have been worked out by the pioneers of molecular and solid-state spectroscopy during the first half and around the middle of the 20th century [1–8].

The basic ingredients of vibronic-coupling theory can be summarized as follows:

- (a) Representation of the (non-relativistic) electronic Hamiltonian in a basis of diabatic electronic states.

- (b) Expansion of the electronic Hamiltonian in powers of normal-mode displacements at the reference geometry.
- (c) Use of symmetry selection rules for the determination of the non-vanishing matrix elements.

Diabatic electronic states (previously termed “crude adiabatic states”) are defined as slowly varying functions of the nuclear geometry in the vicinity of the reference geometry [9–11]. The final vibronic-coupling Hamiltonian is obtained by adding the nuclear kinetic-energy operator which is assumed to be diagonal in the diabatic representation.

Spin–orbit (SO) coupling lifts, in general, the degeneracy of electronic states in open-shell systems. It is therefore essential to take SO-coupling effects into account in molecules and complexes containing second-row or heavier atoms.

Herein, we shall be concerned with systems for which the SO interaction can be considered as a relatively weak perturbation of the non-relativistic Hamiltonian. In this case, the electronic Hamiltonian can be written as the sum of the electrostatic Hamiltonian  $H_{\text{ES}}$  and the SO operator  $H_{\text{SO}}$

$$H = H_{\text{ES}} + H_{\text{SO}} \quad (1)$$

$H_{\text{ES}}$  may be chosen, for example, as the restricted open-shell Hartree-Fock (ROHF) Hamiltonian of the many-electron system.

SO coupling is a relativistic effect. The theory of the interaction of the magnetic moments of the electron spin and the orbital motion in one- and two-electron atoms has been formulated independently by Heisenberg and Pauli [12, 13], shortly before the advent of the four-component Dirac theory of the electron [14]. Breit later has added the retardation correction [15]. The resulting Breit-Pauli SO operator, which can more elegantly be derived from the Dirac equation via a Foldy-Wouthuysen transformation [16], was thus well known for atoms since the early 1930s [17].

Surprisingly, the theoretical analysis of the extensive spectroscopic data for molecules and crystals in the 1940s and 1950s did not make use of the microscopic Breit-Pauli operator, but rather relied on various empirical effective SO operators. For impurity centers in crystals, for example, atom-like SO operators

$$H_{\text{SO}} = AL \cdot S \quad (2)$$

have exclusively been employed, assuming atomic Russell–Saunders coupling and an empirically adjustable effective SO constant  $A$ . For linear molecules, on the other hand, the empirical SO operator introduced by Pople [18]

$$H_{\text{SO}} = AL_z S_z \quad (3)$$

is in widespread use until today. These empirical expressions treat SO coupling as an atomic property and neglect any dependence of the SO interaction on the nuclear geometry. While this approximation may be justified for partially occupied inner shells of an impurity atom in a rigid crystal, it is expected to be inadequate

for valence orbitals of molecules, atomic clusters and multi-center transition-metal complexes, in particular when large-amplitude nuclear motions are involved. In quantum chemistry, on the other hand, all-electron treatments of the SO operator have been in use since the 1970s [19]. Matrix elements of the Breit-Pauli operator with non-relativistic electronic wave functions can nowadays routinely be calculated with several *ab initio* electronic-structure packages [20–22]. This is another motivation to base the description of SO coupling on the Breit-Pauli operator rather than empirical expressions like (2) or (3) [23, 24].

Having said this, it is obvious that the SO operator should be treated in exactly the same manner as the non-relativistic Hamiltonian, that is,

- (a) Representation of the Breit-Pauli operator in a basis of (non-relativistic) diabatic electronic states.
- (b) Expansion of the Breit-Pauli operator in powers of normal-mode displacements at the reference geometry.
- (c) Use of symmetry selection rules (including time-reversal symmetry) to determine the non-vanishing matrix elements.

The use of non-relativistic basis functions in (a) requires that the SO interaction can be considered as a relatively weak perturbation of the non-relativistic Hamiltonian, which typically is the case for second- and third-row atoms and transition metals. For systems with heavier atoms, two-component relativistic electronic basis functions should be employed or the analysis should be based on the four-component Dirac-Coulomb Hamiltonian.

## 2 Symmetry Properties of the Spin–Orbit Operator: A Tutorial

The symmetry operations which commute with the non-relativistic (electrostatic) Hamiltonian  $H_{\text{ES}}$  of a given system do not necessarily commute with the Breit-Pauli operator  $H_{\text{SO}}$ . It is therefore appropriate to analyse the group of symmetry operators of  $H_{\text{SO}}$  for each particular point-group symmetry of the electrostatic Hamiltonian.

In this section, we discuss, as a tutorial, the simplest example of the JT effect, that is, a single unpaired electron in the field of three identical nuclei which form an equilateral triangle ( $D_{3h}$  symmetry).

For the purpose of symmetry analysis, the electrostatic Hamiltonian can be written as (in atomic units)

$$H_{\text{ES}} = -\frac{1}{2}\nabla^2 - e\Phi(\mathbf{r}) \quad (4)$$

where

$$\Phi(\mathbf{r}) = \sum_{k=1}^3 \frac{q}{r_k} \quad (5)$$

and

$$r_k = |\mathbf{r} - \mathbf{R}_k|. \quad (6)$$

Here  $\mathbf{r}$  is the radius vector of the single unpaired electron,  $\mathbf{R}_k$ ,  $k = 1, 2, 3$ , denote the positions of the nuclei, and  $q$  is the effective charge of the three identical nuclei.

The Breit-Pauli Hamiltonian of this system is [17]

$$H_{\text{SO}} = -ig_e\beta_e^2q\mathbf{S}\sum_{k=1}^3\frac{1}{r_k^3}(\mathbf{r}_k \times \nabla) \quad (7)$$

where

$$\mathbf{S} = \frac{1}{2}(\mathbf{i}\sigma_x + \mathbf{j}\sigma_y + \mathbf{k}\sigma_z), \quad (8)$$

$\sigma_x, \sigma_y, \sigma_z$  are the Pauli spin matrices,

$$\beta_e = \frac{e\hbar}{2m_e c} \quad (9)$$

is the Bohr magneton,  $g_e = 2.0023$  is the  $g$ -factor of the electron, and  $\mathbf{i}, \mathbf{j}, \mathbf{k}$  are the Cartesian unit vectors.

It is seen that the Breit-Pauli operator has the structure of (2) for each atomic center, but depends explicitly on the distances  $r_k$  of the unpaired electron from the atomic centers, defined in (6). While the magnetic interaction energy is  $\sim r_k^{-2}$  and thus of shorter range than the electrostatic interaction, it can nevertheless result in a non-negligible dependence of the SO operator on the nuclear coordinates. This effect is neglected when the empirical SO operators (2) or (3) are employed.

It is useful for the symmetry analysis to write the Breit-Pauli operator (7) in determinantal form

$$H_{\text{SO}} = \frac{1}{2}ig_e\beta_e^2 \begin{vmatrix} \sigma_x & \sigma_y & \sigma_z \\ \Phi_x & \Phi_y & \Phi_z \\ \frac{\partial}{\partial x} & \frac{\partial}{\partial y} & \frac{\partial}{\partial z} \end{vmatrix}, \quad (10)$$

where  $\Phi$  is given by (5) and

$$\Phi_x = \frac{\partial \Phi}{\partial x}, \quad \text{etc.} \quad (11)$$

Since  $H_{\text{SO}}$  contains the Pauli spin matrices, each of the usual spatial symmetry operations of the  $D_{3h}$  point group has to be supplemented by a unitary  $2 \times 2$  matrix which operates on the spin matrices. Let  $X_n$  denote one of the symmetry operations of  $D_{3h}$ ; the corresponding operation in the extended symmetry group is defined as

$$Z_n = X_n U_n^\dagger \quad (12)$$

where

$$U_n U_n^\dagger = 1_2 \quad (13)$$

and  $1_2$  denotes the two-dimensional unit matrix. The invariance condition of the Hamiltonian is

$$Z_n H_{\text{SO}} Z_n^{-1} = H_{\text{SO}}. \quad (14)$$

The task is to find the appropriate  $2 \times 2$  matrix  $U_n$  for each of the twelve  $X_n$  of the group  $D_{3h}$  and to verify the group axioms for the set  $\{Z_n\}$ . Equation (14) is evidently fulfilled for  $H_{\text{ES}}$  if the  $X_n$  are the operations of the point group of  $H_{\text{ES}}$ .

As is outlined in Appendix A, the  $U_n$  can straightforwardly be determined, making use of the determinantal form (10) of  $H_{\text{SO}}$ . In particular, an associated unitary  $2 \times 2$  matrix can be found for each of the 12 elements of  $D_{3h}$ . The resulting group of order 24, the so-called spin double group  $D'_{3h}$ , is the symmetry group of the SO operator (10).

In addition,  $H_{\text{SO}}$  is time-reversal invariant. The time-reversal operator for a single electron is the antiunitary operator (up to an arbitrary phase factor) [25]

$$\tau = -i\sigma_y \hat{c}c = \begin{pmatrix} 0 & -1 \\ 1 & 0 \end{pmatrix} \hat{c}c, \quad (15)$$

where  $\hat{c}$  denotes the operation of complex conjugation. The full symmetry group  $G$  of  $H_{\text{SO}}$  of (10) is thus

$$G = D'_{3h} \otimes (1, \tau) \quad (16)$$

of order 48. The operations of  $D'_{3h}$  commute with  $\tau$ .

### 3 Jahn–Teller and Spin–Orbit Coupling in Trigonal Systems

The  $E \times E$  JT effect, where a doubly degenerate vibrational mode lifts the degeneracy of a doubly degenerate electronic state, is presumably the most extensively investigated vibronic-coupling problem in molecular and solid-state spectroscopy, see [26–28] for reviews.

We consider a single unpaired electron in the field of three equivalent nuclear centers forming an equilateral triangle ( $D_{3h}$  symmetry). A pair of electronic basis functions transforming as  $x$  and  $y$  in  $D_{3h}$  symmetry is

$$\psi_x = 6^{-1/2} [2\chi(\mathbf{r}_1) - \chi(\mathbf{r}_2) - \chi(\mathbf{r}_3)] \quad (17a)$$

$$\psi_y = 2^{-1/2} [\chi(\mathbf{r}_2) - \chi(\mathbf{r}_3)], \quad (17b)$$

where the  $\chi(\mathbf{r}_k)$  are atom-centered basis functions. Introducing the spin of the electron, we have four non-relativistic spin–orbital basis functions

$$\begin{aligned}
\psi_x^+ &= \psi_x \alpha \\
\psi_y^+ &= \psi_y \alpha \\
\psi_x^- &= \psi_x \beta \\
\psi_y^- &= \psi_y \beta
\end{aligned} \tag{18}$$

where  $\alpha(\beta)$  represent the spin projection  $1/2(-1/2)$  of the electron. The time-reversal operator  $\tau$  acts on these spin orbitals as follows:

$$\begin{aligned}
\tau \psi_x^+ &= \psi_x^- \hat{c} \hat{c}, \quad \tau \psi_x^- = -\psi_x^+ \hat{c} \hat{c}, \\
\tau \psi_y^+ &= \psi_y^- \hat{c} \hat{c}, \quad \tau \psi_y^- = -\psi_y^+ \hat{c} \hat{c}.
\end{aligned} \tag{19}$$

The representation of the operator  $\tau$  is thus the  $4 \times 4$  matrix

$$\tau = \begin{pmatrix} 0 & 0 & 1 & 0 \\ 0 & 0 & 0 & 1 \\ -1 & 0 & 0 & 0 \\ 0 & -1 & 0 & 0 \end{pmatrix} \hat{c} \hat{c}. \tag{20}$$

Note that  $\tau^2 = -1_4$ , as is required for an odd-electron system [25].

The vibrational displacements are described in terms of dimensionless normal coordinates  $Q_x$ ,  $Q_y$  of a degenerate vibrational mode of  $E$  symmetry. The electrostatic Hamiltonian is expanded at the reference geometry in powers of  $Q_x$ ,  $Q_y$  up to second order

$$H_{\text{ES}} = H_0 + H_x Q_x + H_y Q_y + \frac{1}{2} H_{xx} Q_x^2 + \frac{1}{2} H_{yy} Q_y^2 + H_{xy} Q_x Q_y \tag{21}$$

where

$$\begin{aligned}
H_0 &= H_{\text{ES}}(0) \\
H_x &= \left( \frac{\partial H_{\text{ES}}}{\partial Q_x} \right)_0 \\
H_{xy} &= \left( \frac{\partial^2 H_{\text{ES}}}{\partial Q_x \partial Q_y} \right)_0.
\end{aligned} \tag{22}$$

$H_0$  transforms totally symmetric,  $H_x(H_y)$  transforms as  $Q_x(Q_y)$ ,  $H_{xy}$  transforms as  $Q_x Q_y$ , etc.

The electrostatic vibronic matrix is obtained by taking matrix elements of the Hamiltonian (21) with the electronic wave functions  $\psi_x$ ,  $\psi_y$ . The well-known result is [26–28]



$$H_{\text{ES}} = \frac{1}{2}\omega(Q_x^2 + Q_y^2)1_2 + \begin{pmatrix} \kappa Q_x + \frac{1}{2}g(Q_x^2 - Q_y^2) & \kappa Q_y - g Q_x Q_y \\ \kappa Q_y - g Q_x Q_y & -\kappa Q_x - \frac{1}{2}g(Q_x^2 - Q_y^2) \end{pmatrix} \quad (23)$$

where  $\omega$  is the vibrational frequency of the  $E$  mode and  $\kappa(g)$  denotes the linear (quadratic) JT coupling constant. Obviously,  $H_{\text{ES}}$  is independent of the spin projection.

To obtain the SO vibronic matrix,  $H_{\text{SO}}$  is expanded in analogy to (21).

$$H_{\text{SO}} = h_0 + h_x Q_x + h_y Q_y + \dots \quad (24)$$

Assuming that the SO coupling is weak compared to the electrostatic interactions, we terminate the expansion after the first order. The individual SO operators in (24) can be written as

$$\begin{aligned} h_0 &= h^x \sigma_x + h^y \sigma_y + h^z \sigma_z \\ h_x &= h_x^x \sigma_x + h_x^y \sigma_y + h_x^z \sigma_z \\ h_y &= h_y^x \sigma_x + h_y^y \sigma_y + h_y^z \sigma_z \end{aligned} \quad (25)$$

with

$$\begin{aligned} h^x &= ig_e \beta_e^2 q \left( \frac{\partial \Phi}{\partial y} \frac{\partial}{\partial z} - \frac{\partial \Phi}{\partial z} \frac{\partial}{\partial y} \right) \\ h^y &= ig_e \beta_e^2 q \left( \frac{\partial \Phi}{\partial z} \frac{\partial}{\partial x} - \frac{\partial \Phi}{\partial x} \frac{\partial}{\partial z} \right) \\ h^z &= ig_e \beta_e^2 q \left( \frac{\partial \Phi}{\partial x} \frac{\partial}{\partial y} - \frac{\partial \Phi}{\partial y} \frac{\partial}{\partial x} \right) \end{aligned} \quad (26)$$

and

$$\begin{aligned} h_x^x &= \left( \frac{\partial h_x}{\partial Q_x} \right)_0 \\ h_y^x &= \left( \frac{\partial h_x}{\partial Q_y} \right)_0, \text{ etc.} \end{aligned} \quad (27)$$

Using the results of Sect. 2 and Appendix A, it is straightforward to calculate the matrix elements of  $H_{\text{SO}}$  with the basis functions (18). The result is

$$H_{\text{SO}} = i \begin{pmatrix} 0 & \Delta_z & 0 & \Delta_x - i\Delta_y \\ -\Delta_z & 0 & -\Delta_x + i\Delta_y & 0 \\ 0 & \Delta_x + i\Delta_y & 0 & -\Delta_z \\ -\Delta_x - i\Delta_y & 0 & \Delta_z & 0 \end{pmatrix} \quad (28)$$

where  $\Delta_x$ ,  $\Delta_y$ ,  $\Delta_z$  are real constants. It can easily be verified that  $H_{\text{SO}}$  of (28) commutes with the time-reversal operator of (20).

When transformed to complex-valued spatial electronic basis functions

$$\psi_{\pm} = \frac{1}{\sqrt{2}} (\psi_x \pm i\psi_y) \quad (29)$$

and expressed in terms of complex-valued normal-mode displacements

$$Q_{\pm} = \varrho e^{\pm i\phi} = Q_x \pm iQ_y, \quad (30)$$

$H_{\text{ES}}$  takes the more familiar form

$$H_{\text{ES}} = \frac{1}{2} \omega \varrho^2 1_2 + \begin{pmatrix} 0 & X \\ X^* & 0 \end{pmatrix} \quad (31)$$

with

$$X = \kappa \varrho e^{i\phi} + \frac{1}{2} g \varrho^2 e^{-2i\phi}. \quad (32)$$

$H_{\text{SO}}$  of (28) becomes

$$H_{\text{SO}} = \begin{pmatrix} \Delta_z & 0 & \Delta_x - i\Delta_y & 0 \\ 0 & -\Delta_z & 0 & -\Delta_x + i\Delta_y \\ \Delta_x + i\Delta_y & 0 & -\Delta_z & 0 \\ 0 & -\Delta_x - i\Delta_y & 0 & \Delta_z \end{pmatrix}. \quad (33)$$

The SO vibronic matrix (33), which does not depend on the nuclear geometry (within first order in  $\varrho$ ), can be transformed to diagonal form by a unitary  $4 \times 4$  matrix  $S$  [29], yielding

$$S^\dagger H_{\text{SO}} S = \begin{pmatrix} \Delta & 0 & 0 & 0 \\ 0 & -\Delta & 0 & 0 \\ 0 & 0 & -\Delta & 0 \\ 0 & 0 & 0 & \Delta \end{pmatrix} \quad (34)$$

with

$$\Delta = \sqrt{\Delta_x^2 + \Delta_y^2 + \Delta_z^2}. \quad (35)$$

The electrostatic vibronic matrix is invariant with respect to  $S$ . The final form of the  ${}^2E \times E$  JT Hamiltonian is thus [29]

$$H = \left( T_N + \frac{1}{2} \omega \varrho^2 \right) 1_4 + \begin{pmatrix} \Delta & X & 0 & 0 \\ X^* & -\Delta & 0 & 0 \\ 0 & 0 & -\Delta & X \\ 0 & 0 & X^* & \Delta \end{pmatrix}. \quad (36)$$

Equation (36) agrees with previous results, which have been derived in a more heuristic manner [30–32]. The adiabatic electronic potential-energy surfaces (that is, the eigenvalues of  $(H - T_N 1_4)$  are doubly degenerate (Kramers degeneracy). The adiabatic electronic wave functions carry nontrivial geometric phases which depend on the radius of the loop of integration [29–32].

It should be noted that the SO operator is nondiagonal in the diabatic spin–orbital electronic basis which usually is employed to set up the  $E \times E$  JT Hamiltonian, see (28, 33). The (usually *ad hoc* assumed) diagonal form of  $H_{\text{SO}}$  is obtained by the unitary transformation  $S$  which mixes spatial orbitals and spin functions of the electron. In this transformed basis, the electronic spin projection is thus no longer a good quantum number.

When electronic states with more than one unpaired electron (triplet states, quartet states, etc.) are considered, the two-electron part of the Breit-Pauli operator becomes relevant. For a many-electron system with  $D_{3h}$  symmetry, the complete Breit-Pauli operator reads

$$H_{\text{SO}} = \sum_k H_{\text{SO}}^{(k)} + \sum_{k < l} H_{\text{SO}}^{(kl)}, \quad (37)$$

$$H_{\text{SO}}^{(k)} = -ig_e \beta_e^2 q \mathbf{S}_k \sum_{n=1}^3 \frac{1}{r_{kn}^3} (\mathbf{r}_{kn} \times \nabla_k), \quad (38)$$

$$H_{\text{SO}}^{(kl)} = ig_e \beta_e^2 \frac{1}{r_{kl}^3} [\mathbf{S}_k [\mathbf{r}_{kl} \times (\nabla_k - 2\nabla_l)] + \mathbf{S}_l [\mathbf{r}_{kl} \times (\nabla_l - 2\nabla_k)]] \quad (39)$$

with

$$\mathbf{S}_k = \frac{1}{2} (\mathbf{i}\sigma_x^{(k)} + \mathbf{j}\sigma_y^{(k)} + \mathbf{k}\sigma_z^{(k)}). \quad (40)$$

The two-electron terms arise from the magnetic interaction of the spin of electron  $k$  with the orbital angular momentum of electron  $l$ . It should be noted that  $H_{\text{SO}}$  is a two-electron operator in the electronic coordinate space, but is a one-electron operator in spin space.  $H_{\text{SO}}^{(kl)}$  can be written in determinantal form analogous to (10).

The generalization of the time-reversal operator for the case of several unpaired electrons is

$$\tau = \prod_k \begin{pmatrix} 0 & -1 \\ 1 & 0 \end{pmatrix}_k \hat{c}. \quad (41)$$

where the index  $k$  enumerates the electrons. Starting from (37–41), the JT–SO Hamiltonians of  ${}^3E$ ,  ${}^4E$  and  ${}^5E$  states of trigonal systems have been elaborated in [33].

## 4 Jahn–Teller and Spin–Orbit Coupling in Tetrahedral Systems

The well-known JT selection rules for tetrahedral systems are [2]

$$[E]^2 = A + E \quad (42)$$

$$[T_{1,2}]^2 = A + E + T_2. \quad (43)$$

In electronic states of  $T_1$  and  $T_2$  symmetry, the  $E$  mode as well as the  $T_2$  mode are JT active. In electronic states of  $E$  symmetry, only the  $E$  mode is JT active. The vibrational modes of a four-atomic tetrahedral system ( $X_4$ ) are of  $A$ ,  $E$  and  $T_2$  symmetries.

The most common JT effects in tetrahedral systems are of the type  ${}^2T_{1,2} \times T_2$  and  ${}^2E \times E$  [26–28]. In this section, we consider the novel problem of SO induced JT activity of the  $T_2$  mode in a  ${}^2E$  state.

According to (42), the  $T_2$  mode is not JT active (in first order) in  ${}^2E$  states. However, the matrix elements of the SO operator with non-relativistic electronic wave functions vanish for a  ${}^2E$  state in  $T_d$  symmetry. It is then essential to take account of the leading nonvanishing terms in the Taylor expansion of the matrix elements of the SO operator. As shown below, these are of first order of vibrational displacements of  $T_2$  symmetry, which implies the existence of a purely relativistic  $E \times T$  JT effect [34]. Linear  $E \times T$  vibronic coupling is not accounted for by the JT selection rules [2]; it is, therefore, a novel type of JT effect.

Let  $\mathbf{R}_k$ ,  $k = 1, 2, 3, 4$ , denote the radius vectors from the origin to the four corners of the tetrahedron, and  $R_{km} = |\mathbf{R}_k - \mathbf{R}_m|$  the length of the four edges. Symmetry-adapted displacements transforming as  $x$ ,  $y$  and  $z$  in the  $T_d$  point group are

$$\begin{aligned} S_x &= \frac{1}{\sqrt{2}} (R_{12} - R_{34}) \\ S_y &= \frac{1}{\sqrt{2}} (R_{14} - R_{23}) \\ S_z &= \frac{1}{\sqrt{2}} (R_{13} - R_{24}). \end{aligned} \quad (44)$$

Let us define

$$\begin{aligned} \mathbf{r}_k &= \mathbf{r} - \mathbf{R}_k, \\ r_k &= |\mathbf{r}_k|, \end{aligned} \quad (45)$$

where  $\mathbf{r}$  is the radius vector of single electron under consideration. Defining atomic  $p$  orbitals at the four centers

$$\begin{aligned}
\chi_x^{(k)} &= x_k f(r_k) \\
\chi_y^{(k)} &= y_k f(r_k) \\
\chi_z^{(k)} &= z_k f(r_k),
\end{aligned} \tag{46}$$

where  $f(r)$  is an arbitrary radial function, two degenerate molecular orbitals transforming as the  $E$  representation can be constructed with the projection-operator technique [25]

$$\begin{aligned}
\psi_a(\mathbf{r}) &= \frac{1}{\sqrt{2^3}} \left( -\chi_y^{(1)} + \chi_z^{(1)} + \chi_y^{(2)} - \chi_z^{(2)} + \chi_y^{(3)} + \chi_z^{(3)} \right) \\
\psi_b(\mathbf{r}) &= \frac{1}{2\sqrt{6}} \left( 2\chi_x^{(1)} + 2\chi_x^{(2)} - 2\chi_x^{(3)} - 2\chi_x^{(4)} - \chi_y^{(1)} + \chi_y^{(2)} \right. \\
&\quad \left. + \chi_y^{(3)} - \chi_y^{(4)} - \chi_z^{(1)} + \chi_z^{(2)} - \chi_z^{(3)} + \chi_z^{(4)} \right).
\end{aligned} \tag{47}$$

Taylor expansion of the electrostatic Hamiltonian

$$H_{\text{ES}} = -\frac{1}{2}\nabla^2 - e\Phi(\mathbf{r}), \tag{48}$$

$$\Phi(\mathbf{r}) = \sum_{k=1}^4 \frac{q}{r_k}, \tag{49}$$

up to second order in the  $T_2$  normal coordinates  $Q_x$ ,  $Q_y$ ,  $Q_z$  at the tetrahedral reference geometry and evaluation of the matrix elements with the electronic basis functions (47) yields the electrostatic vibronic matrix

$$H_{\text{ES}} = \frac{1}{2}\omega R^2 1_2 + \frac{1}{2}g \begin{pmatrix} -2Q_x^2 + Q_y^2 + Q_z^2 & \sqrt{3}(Q_y^2 - Q_z^2) \\ \sqrt{3}(Q_y^2 - Q_z^2) & 2Q_x^2 - Q_y^2 - Q_z^2 \end{pmatrix} \tag{50}$$

where

$$R^2 = Q_x^2 + Q_y^2 + Q_z^2. \tag{51}$$

As predicted by the JT selection rule (42), the electrostatic JT coupling is zero in first order of  $\mathbf{Q}$ . Equation (50) describes the quadratic JT coupling of the  $T_2$  mode in an electronic state of  $E$  symmetry.

The Breit-Pauli Hamiltonian for a single unpaired electron in the field of four identical atomic centers reads

$$H_{\text{SO}} = -ig_e\beta_e^2\mathbf{S} \sum_{k=1}^4 \frac{q}{r_k^3} (\mathbf{r}_k \times \nabla) \tag{52}$$

in analogy to (7). The Breit-Pauli operator (52) can be written in compact form as

$$\begin{aligned}
H_{SO} &= i g_e \beta_e^2 \mathbf{S} \left[ \nabla \Phi \times \nabla \right] \\
&= \frac{1}{2} i g_e \beta_e^2 \begin{vmatrix} \sigma_x & \sigma_y & \sigma_z \\ \Phi_x & \Phi_y & \Phi_z \\ \partial/\partial x & \partial/\partial y & \partial/\partial z \end{vmatrix}
\end{aligned} \tag{53}$$

where  $\Phi(\mathbf{r})$  is given by (49) and

$$\Phi_x = \partial \Phi / \partial x, \quad \text{etc.}$$

$H_{SO}$  is time-reversal invariant. The time-reversal operator for a single electron is the anti-unitary operator (up to an arbitrary overall phase factor) [15]

$$\tau = -i \sigma_y \hat{c} \hat{c} = \begin{pmatrix} 0 & -1 \\ 1 & 0 \end{pmatrix} \hat{c} \hat{c}, \tag{54}$$

where  $\hat{c} \hat{c}$  denotes the operation of complex conjugation of spatial wave functions.

Using the methods discussed in the tutorial (Sect. 2), the group of symmetry operations of  $H_{SO}$  can be constructed explicitly. As is shown in Appendix B, the symmetry group of  $H_{SO}$  of (53) is  $T'_d$ , the spin double group of the tetrahedral rotation group.  $T'_d$  is of order 48.  $T'_d$  also is the symmetry group of the total Hamiltonian  $H = H_{ES} + H_{SO}$ .

Expansion of  $H_{SO}$  in powers of  $Q_x$ ,  $Q_y$ ,  $Q_z$  up to first order, analogous to (24–27) and calculation of the matrix elements with the basis of spin orbitals

$$\begin{aligned}
\psi_a^+ &= \psi_a(\mathbf{r}) \alpha \\
\psi_b^+ &= \psi_b(\mathbf{r}) \alpha \\
\psi_a^- &= \psi_a(\mathbf{r}) \beta \\
\psi_b^- &= \psi_b(\mathbf{r}) \beta
\end{aligned} \tag{55}$$

yields (see [34] for more details)

$$H_{SO} = i\gamma \begin{pmatrix} 0 & Q_z & Q_x - iQ_y & 0 \\ -Q_z & 0 & 0 & -Q_x + iQ_y \\ -Q_x - iQ_y & 0 & 0 & Q_z \\ 0 & Q_x + iQ_y & -Q_z & 0 \end{pmatrix}. \tag{56}$$

Including the nuclear kinetic-energy operator  $T_N$ , the final JT Hamiltonian of the  ${}^2E$  state (up to second order in  $\mathbf{Q}$  for the electrostatic part and up to first order in  $\mathbf{Q}$  for the SO part) is thus given by

$$H = (T_N + \frac{1}{2}\omega R^2)1_4 + \quad (57)$$

$$\begin{pmatrix} \frac{1}{2}g(-2Q_x^2 + Q_y^2 + Q_z^2) & i\gamma Q_z + \frac{\sqrt{3}}{2}g(Q_y^2 - Q_z^2) & i\gamma(Q_x - iQ_y) & 0 \\ -i\gamma Q_z + \frac{\sqrt{3}}{2}g(Q_y^2 - Q_z^2) & \frac{1}{2}g(2Q_x^2 - Q_y^2 - Q_z^2) & 0 & -i\gamma(Q_x + iQ_y) \\ -i\gamma(Q_x + iQ_y) & 0 & \frac{1}{2}g(2Q_x^2 - Q_y^2 - Q_z^2) & i\gamma Q_z + \frac{\sqrt{3}}{2}g(Q_y^2 - Q_z^2) \\ 0 & i\gamma(Q_x + iQ_y) & -i\gamma Q_z + \frac{\sqrt{3}}{2}g(Q_y^2 - Q_z^2) & \frac{1}{2}g(-2Q_x^2 + Q_y^2 + Q_z^2) \end{pmatrix}.$$

The adiabatic electronic potentials (the eigenvalues of  $(H - T_N 1_4)$ ) are given by

$$V_{1,2} = \frac{1}{2}\omega R^2 - W \quad (58a)$$

$$V_{3,4} = \frac{1}{2}\omega R^2 + W \quad (58b)$$

where

$$W = \left[ \gamma^2 R^2 + \frac{3}{4}g^2 (Q_y^2 - Q_z^2)^2 + \frac{1}{4}g^2 (2Q_x^2 - Q_y^2 - Q_z^2)^2 \right]^{\frac{1}{2}}. \quad (59)$$

The adiabatic potentials (58) are doubly degenerate, as it must be for a spin 1/2 system (Kramers degeneracy). For small displacements from  $\mathbf{Q} = 0$ , (58) simplifies to

$$V_{1,2} = \frac{1}{2}\omega R^2 - \gamma R \quad (60a)$$

$$V_{3,4} = \frac{1}{2}\omega R^2 + \gamma R. \quad (60b)$$

Equation (60) represents a “Mexican Hat” in four-dimensional space (the energy as a function of three nuclear coordinates). The JT splitting parameter  $\gamma$  is of purely relativistic origin, that is, it arises from the SO operator, see (56). The adiabatic electronic eigenfunctions carry nontrivial geometric phases which have been discussed in [34].

## 5 Renner and Spin–Orbit Coupling in Linear Molecules

As is well known, linear molecules represent an exception of the JT theorem. The degeneracy of  $\Pi$  electronic states is lifted in second order of the bending amplitude, the degeneracy of  $\Delta$  electronic states is lifted in fourth order, etc., see [35–38] for reviews.

The electrons of a linear molecule move in an electrostatic field which has cylindrical symmetry. Therefore, the electronic Hamiltonian commutes with the projection of the sum of the orbital and spin angular momenta on the symmetry axis

$$[H_{\text{ES}} + H_{\text{SO}}, j_z] = 0 \quad (61)$$

where

$$j_z = -i \frac{\partial}{\partial \theta} + \frac{1}{2} \sigma_z. \quad (62)$$

Here  $\theta$  is the azimuthal angle in electronic space and  $\sigma_z$  is the corresponding Pauli matrix. As a consequence of (61, 62), the symmetry group of  $H_{SO}$  is a continuous group with group parameter  $\varepsilon$  and the symmetry operations

$$J_\varepsilon = e^{i\varepsilon j_z} = \exp\left(\varepsilon \frac{\partial}{\partial \theta}\right) e^{i\varepsilon \sigma_z/2} = C_\varepsilon U_\varepsilon^{-1}, \quad (63)$$

where  $C_\varepsilon$  is the rotation by the angle  $\varepsilon$  around the  $z$  axis and

$$U_\varepsilon^{-1} = \begin{pmatrix} e^{\frac{i\varepsilon}{2}} & 0 \\ 0 & e^{-\frac{i\varepsilon}{2}} \end{pmatrix}. \quad (64)$$

Note the analogy of (63) with the definition (12) in the case of a discrete symmetry group.

In addition to the cylindrical symmetry, the Hamiltonian is time-reversal invariant, that is, it commutes with the time-reversal operator  $\tau$  of (15). The symmetry group of  $H_{SO}$  is  $C'_{\infty v}$ , the spin double group of  $C_{\infty v}$ .

Let us consider a single unpaired electron in the field of the three nuclei of a linear triatomic molecule,

$$H_{ES} = -\frac{1}{2} \nabla^2 - e \Phi(\mathbf{r}) \quad (65)$$

with

$$\Phi(\mathbf{r}) = \sum_{k=1}^3 \frac{q_k}{r_k} \quad (66)$$

where the  $q_k$ ,  $k = 1, 2, 3$ , are effective nuclear charges. The SO operator  $H_{SO}$  is given by (10) with  $\Phi(\mathbf{r})$  of (66).

For a  $^2\Pi$  state, the appropriate spin-orbital basis functions are

$$\begin{aligned} \psi_{\frac{3}{2}} &= \pi(\varrho, z) e^{i\theta} \alpha \\ \psi_{-\frac{1}{2}} &= \pi(\varrho, z) e^{-i\theta} \alpha \\ \psi_{\frac{1}{2}} &= \pi(\varrho, z) e^{i\theta} \beta \\ \psi_{-\frac{3}{2}} &= \pi(\varrho, z) e^{-i\theta} \beta \end{aligned} \quad (67)$$

where  $\varrho, z, \theta$  are the cylindrical coordinates of the electron and it is assumed that  $\pi(\varrho, z)$  is real.

The derivation of the relativistic Renner Hamiltonian of a  $^2\Pi$  state has been described in detail in [39]. The result is



$$H = (T_N + \frac{1}{2}\omega\varrho^2)1_4 + \begin{pmatrix} 0 & d\varrho e^{i\chi} & \frac{1}{2}g\varrho^2 e^{2i\chi} & 0 \\ d\varrho e^{-i\chi} & \zeta & 0 & \frac{1}{2}g\varrho^2 e^{2i\chi} \\ \frac{1}{2}g\varrho^2 e^{-2i\chi} & 0 & \zeta & -d\varrho e^{i\chi} \\ 0 & \frac{1}{2}g\varrho^2 e^{-2i\chi} & -d\varrho e^{-i\chi} & 0 \end{pmatrix}. \quad (68)$$

Here  $\varrho$  and  $\chi$  are radial and angular components of the dimensionless bending coordinate, respectively,  $\omega$  is the harmonic bending frequency,  $\zeta$  is the SO splitting of the  $^2\Pi$  state and  $g$  is the well-known non-relativistic Renner coupling constant. The new result of this analysis is the linear (in the bending amplitude) coupling constant  $d$ , which arises from the Breit-Pauli operator and is therefore of relativistic origin. This coupling term is absent when the approximate SO operator (3) is employed.

The adiabatic potential-energy surfaces and adiabatic electronic eigenfunctions of the Hamiltonian (68) have been analyzed in detail in [39]. Since the degeneracy of the  $^2\Pi$  state is lifted already in zeroth order in  $\varrho$  by the SO splitting  $\zeta$ , the linear coupling term does not lead to a JT-like conical intersection of the adiabatic energy surfaces. The linear coupling term has a significant effect, however, on the adiabatic electronic wave functions which acquire nontrivial geometric phase factors [39].

The experimentally observable effects of the linear relativistic Renner coupling are perturbations in the vibronic spectra of  $^2\Pi$  states. Since  $d\varrho e^{i\chi}$  couples zero-order energy levels which differ by one quantum of the bending mode, the effects are maximal for  $\zeta \approx \omega$ . These perturbations have previously been observed in the Renner spectra of triatomic radicals, such as NCO, NCS and GeCH [40–42] and have been termed “Sears resonances” [42]. Another signature of the linear relativistic vibronic coupling is intensity transfer to vibronic levels with an odd number of quanta of the bending mode [43, 44].

The analysis of the relativistic Renner coupling has been extended to  $^3\Pi$  states, including the two-electron part of the Breit-Pauli operator, thus generalizing previous result of Hougen [45, 46]. Other extensions of the theory are  $\Sigma - \Pi$  coupling in the doublet manifold [47] and SO coupling in a half-filled  $\pi$  shell, as found, for example, in carbenes [48].

## 6 Summary

It is the intention of this chapter to point out that it is feasible and worthwhile to treat the SO coupling operator on an equal footing with the non-relativistic Hamiltonian in JT and Renner systems. Considering tetrahedral systems and linear molecules as examples, it has been shown that the microscopic SO operator can give rise to novel vibronic-coupling terms which are linear in the vibrational coordinates. These relativistic coupling terms are particularly relevant in systems where the vibronic coupling by the electrostatic Hamiltonian arises in second (or higher) order in the vibrational coordinates, as is the case for the Renner effect in linear molecules or the  $E \times T$  JT effect in tetrahedral systems. These interesting phenomena are dis-

carded when the SO coupling is approximated by an atom-like operator which is independent of the nuclear coordinates.

There exists a rich variety of essentially untouched vibronic-coupling phenomena in molecules and clusters containing heavy atoms. Since the SO-induced vibronic-coupling parameters can conveniently be computed with *ab initio* electronic-structure methods, these novel phenomena can be explored irrespective of the availability of experimental spectroscopic data.

**Acknowledgements** The collaboration of the authors has continuously been supported by the Deutsche Forschungsgemeinschaft since 8 years.

## Appendix A: Symmetry Group of the Spin–Orbit Operator of Triangular $X_3$ Systems

Consider, as an example, the operation  $C_3^2 = C_3^{-1}$  (rotation by  $4\pi/3$ ) of the  $D_{3h}$  point group:

$$\begin{pmatrix} x' \\ y' \\ z' \end{pmatrix} = C_3^2 \begin{pmatrix} x \\ y \\ z \end{pmatrix} = \begin{pmatrix} -\frac{1}{2}x - \frac{\sqrt{3}}{2}y \\ \frac{\sqrt{3}}{2}x - \frac{1}{2}y \\ z \end{pmatrix}. \quad (69)$$

The partial derivatives transform as follows:

$$\begin{aligned} \frac{\partial}{\partial x'} &= -\frac{1}{2} \frac{\partial}{\partial x} - \frac{\sqrt{3}}{2} \frac{\partial}{\partial y} \\ \frac{\partial}{\partial y'} &= \frac{\sqrt{3}}{2} \frac{\partial}{\partial x} - \frac{1}{2} \frac{\partial}{\partial y} \\ \frac{\partial}{\partial z'} &= \frac{\partial}{\partial z}. \end{aligned} \quad (70)$$

With the definition (12), the invariance condition (14) takes the form

$$\begin{vmatrix} \sigma_x & \sigma_y & \sigma_z \\ \Phi_x & \Phi_y & \Phi_z \\ \frac{\partial}{\partial x} & \frac{\partial}{\partial y} & \frac{\partial}{\partial z} \end{vmatrix} = \begin{vmatrix} U^{-1}\sigma_x U & U^{-1}\sigma_y U & U^{-1}\sigma_z U \\ -\frac{1}{2}\Phi_x - \frac{\sqrt{3}}{2}\Phi_y & \frac{\sqrt{3}}{2}\Phi_x - \frac{1}{2}\Phi_y & \Phi_z \\ -\frac{1}{2}\frac{\partial}{\partial x} - \frac{\sqrt{3}}{2}\frac{\partial}{\partial y} & \frac{\sqrt{3}}{2}\frac{\partial}{\partial x} - \frac{1}{2}\frac{\partial}{\partial y} & \frac{\partial}{\partial z} \end{vmatrix}. \quad (71)$$

Expansion of the determinants and comparison of left and right sides yields the equations

$$\begin{aligned}
\sigma_z U &= U \sigma_z \\
\sigma_x U &= -\frac{1}{2} U \sigma_x - \frac{\sqrt{3}}{2} U \sigma_y \\
\sigma_y U &= \frac{\sqrt{3}}{2} U \sigma_x - \frac{1}{2} U \sigma_y.
\end{aligned} \tag{72}$$

The general nontrivial solution is

$$U = e^{-2i\phi} \begin{pmatrix} 1 & 0 \\ 0 & \varepsilon \end{pmatrix} \tag{73}$$

where  $\varepsilon = e^{2\pi i/3}$  and  $\phi$  is an arbitrary phase phactor. The generalization of the  $C_3^2$  point-group operation is thus

$$Z_3^2 = e^{2i\phi} C_3^2 \begin{pmatrix} 1 & 0 \\ 0 & \varepsilon^* \end{pmatrix}. \tag{74}$$

The analogous calculation for  $C_3$  yields

$$Z_3 = e^{i\phi} C_3 \begin{pmatrix} 1 & 0 \\ 0 & \varepsilon \end{pmatrix}. \tag{75}$$

A rotation by  $2\pi$  around the  $z$ -axis must change the sign of the electronic wave function [49]:

$$Z_3^3 = Z_3^2 Z_3 = Z_3 Z_3^2 = -1_2 \tag{76}$$

which yields

$$\phi = \pm \frac{\pi}{3}. \tag{77}$$

The generalized operator of reflection on the horizontal plane ( $\sigma_h$ ),  $Z_h$ , must fulfill [49]

$$Z_h^2 = -1, \tag{78}$$

which has the solution

$$Z_h = \pm i \sigma_h \begin{pmatrix} 1 & 0 \\ 0 & -1 \end{pmatrix}. \tag{79}$$

With (74, 75, 79) we have the generalization of improper rotations

$$\bar{Z}_3 = Z_h Z_3 = (\pm i) e^{\pm i\pi/3} S_3 \begin{pmatrix} 1 & 0 \\ 0 & -\varepsilon \end{pmatrix} \tag{80}$$

$$\bar{Z}_3^{(2)} = Z_h Z_3^2 = (\pm i) e^{\pm 2i\pi/3} S_3^{(2)} \begin{pmatrix} 1 & 0 \\ 0 & -\varepsilon^* \end{pmatrix}. \tag{81}$$

**Table 1** The symmetry operations of the spin double group  $D'_{3h}$ . Abbreviation:  $\epsilon = e^{\frac{2\pi i}{3}}$ 


---

1. $I = E1_2$ (the identity)
2. $Z_h = i\sigma_h \begin{pmatrix} 1 & 0 \\ 0 & -1 \end{pmatrix}$
3. $Z_3 = e^{-i\pi/3} C_3 \begin{pmatrix} 1 & 0 \\ 0 & \epsilon \end{pmatrix}$
4. $Z_3^2 = e^{-2i\pi/3} C_3^2 \begin{pmatrix} 1 & 0 \\ 0 & \epsilon^* \end{pmatrix}$
5. $\bar{Z}_3 = Z_h Z_3 = ie^{-i\pi/3} S_3 \begin{pmatrix} 1 & 0 \\ 0 & -\epsilon \end{pmatrix}$
6. $\bar{Z}_3^{(2)} = Z_h Z_3^2 = ie^{-2i\pi/3} S_3^{(2)} \begin{pmatrix} 1 & 0 \\ 0 & -\epsilon^* \end{pmatrix}$
7. $Z_2^a = C_2^a \begin{pmatrix} 0 & -1 \\ 1 & 0 \end{pmatrix}$
8. $Z_2^b = e^{i\pi/3} C_2^b \begin{pmatrix} 0 & 1 \\ -\epsilon^* & 0 \end{pmatrix}$
9. $Z_2^c = e^{i\pi/3} C_2^c \begin{pmatrix} 0 & -\epsilon^* \\ 1 & 0 \end{pmatrix}$
10. $Z_v^a = i\sigma_v^a \begin{pmatrix} 0 & 1 \\ 1 & 0 \end{pmatrix}$
11. $Z_v^b = e^{-i\pi/6} \sigma_v^b \begin{pmatrix} 0 & 1 \\ \epsilon^* & 0 \end{pmatrix}$
12. $Z_v^c = e^{-i\pi/6} \sigma_v^c \begin{pmatrix} 0 & \epsilon^* \\ 1 & 0 \end{pmatrix}$

---

The generalized  $C_2$  rotations and reflections on vertical planes ( $\sigma_v$ ) are obtained analogously. The final list of generalized symmetry operators is given in Table 1. The other 12 symmetry operators are defined as

$$Z_{12+k} = -Z_k, \quad k = 1 \cdots 12. \quad (82)$$

The signs ( $\pm$ ) in (79, 80, 81) have been chosen to obtain a closed group multiplication table.

## Appendix B: Symmetry Properties of $H_{SO}$ in Tetrahedral Systems

For simplicity and brevity, we consider the pure rotational subgroup  $T$  of the tetrahedral point group  $T_d$ . The extension of the analysis to  $T_d$  is straightforward.

We want to find the complete set of symmetry operators  $Z_n$  for which

$$Z_n H_{SO} Z_n^{-1} = H_{SO}. \quad (83)$$

The general form of symmetry operators of spin 1/2 systems is

$$Z_n = C_n U_n^\dagger \quad (84)$$

where  $C_n$  are spatial operations and the  $U_n$  are unitary  $2 \times 2$  matrices acting on the spin functions  $\alpha, \beta$ .

The invariance condition for  $H_{SO}$  is

$$\begin{aligned} Z_n H_{SO} Z_n^{-1} &= \\ &= \frac{1}{2} i g_e \beta_e^2 \begin{vmatrix} U_n^{-1} \sigma_x U_n & U_n^{-1} \sigma_y U_n & U_n^{-1} \sigma_z U_n \\ C_n \Phi_x & C_n \Phi_y & C_n \Phi_z \\ C_n \frac{\partial}{\partial x} & C_n \frac{\partial}{\partial y} & C_n \frac{\partial}{\partial z} \end{vmatrix} \\ &= \frac{1}{2} i g_e \beta_e^2 \begin{vmatrix} \sigma_x & \sigma_y & \sigma_z \\ \Phi_x & \Phi_y & \Phi_z \\ \frac{\partial}{\partial x} & \frac{\partial}{\partial y} & \frac{\partial}{\partial z} \end{vmatrix}. \end{aligned} \quad (85)$$

By straightforward, although lengthy, calculations one can verify that the 12 symmetry operators given in Table 2 fulfill (85). The set  $\bar{T}$  of the operators in Table 2 is

**Table 2** The set  $\bar{T}$  of symmetry operators of  $H = H_{es} + H_{SO}$  in tetrahedral symmetry. Abbreviations:  $\nu = 2^{-1/2}$ ,  $e^\pm = e^{\pm \frac{i\pi}{4}}$

1. $I = E1_2$ (identical transformation)		
2. $Z_2^x = iC_2^x \begin{pmatrix} 0 & 1 \\ 1 & 0 \end{pmatrix}$	$Z_2^{x^2} = -I$	
3. $Z_2^y = iC_2^y \begin{pmatrix} 0 & -i \\ i & 0 \end{pmatrix}$	$Z_2^{y^2} = -I$	
4. $Z_2^z = iC_2^z \begin{pmatrix} 1 & 0 \\ 0 & -1 \end{pmatrix}$	$Z_2^{z^2} = -I$	
5. $Z_3^a = e^+ C_3^a \begin{pmatrix} \nu & \nu \\ i\nu & -i\nu \end{pmatrix}$	$Z_3^{a^3} = -I$	
6. $Z_3^b = e^- C_3^b \begin{pmatrix} \nu & -\nu \\ i\nu & i\nu \end{pmatrix}$	$Z_3^{b^3} = -I$	
7. $Z_3^c = e^+ C_3^c \begin{pmatrix} \nu & -\nu \\ -i\nu & -i\nu \end{pmatrix}$	$Z_3^{c^3} = -I$	
8. $Z_3^d = e^- C_3^d \begin{pmatrix} \nu & \nu \\ -i\nu & i\nu \end{pmatrix}$	$Z_3^{d^3} = -I$	
9. $Z_3^{a^2} = iC_3^{a^2} \begin{pmatrix} \nu e^+ & \nu e^- \\ \nu e^+ & -\nu e^- \end{pmatrix}$	$= -(Z_3^a)^{-1}$	
10. $Z_3^{b^2} = -iC_3^{b^2} \begin{pmatrix} \nu e^- & -\nu e^+ \\ -\nu e^- & -\nu e^+ \end{pmatrix}$	$= -(Z_3^b)^{-1}$	
11. $Z_3^{c^2} = iC_3^{c^2} \begin{pmatrix} \nu e^+ & -\nu e^- \\ -\nu e^+ & -\nu e^- \end{pmatrix}$	$= -(Z_3^c)^{-1}$	
12. $Z_3^{d^2} = -iC_3^{d^2} \begin{pmatrix} \nu e^- & \nu e^+ \\ \nu e^- & -\nu e^+ \end{pmatrix}$	$= -(Z_3^d)^{-1}$	

not closed with respect to multiplication. To obtain a group of symmetry operators, we need the additional element  $-I$ .

The direct product set

$$T' = \bar{T} \otimes (I, -I) \quad (86)$$

is a group of order 24. It is the pure rotational double group of tetrahedral spin  $1/2$  systems [25, 49].

The full rotational symmetry group includes the time-reversal operator  $\tau$ . It is given by

$$G = T' \otimes (I, \tau) = \bar{T} \otimes (I, -I) \otimes (I, \tau). \quad (87)$$

$G$  is of order 48.

## References

1. E. Renner, Z. Phys. **92**, 172 (1934)
2. H. Jahn, E. Teller, Proc. Roy. Soc. (London) A **161**, 220 (1937)
3. H. Jahn, Proc. Roy. Soc. (London) A **164**, 117 (1938)
4. H. Sponer, E. Teller, Rev. Mod. Phys. **13**, 75 (1941)
5. W. Moffit, A. Liehr, Phys. Rev. **106**, 1195 (1956)
6. W. Moffit, W. Thorson, Phys. Rev. **108**, 1251 (1957)
7. U. Öpik, M. Pryce, Proc. Roy. Soc. (London) A **238**, 425 (1957)
8. H. Longuet-Higgins, U. Öpik, M. Pryce, R. Sack, Proc. Roy. Soc. (London) A **244**, 1 (1958)
9. W. Lichten, Phys. Rev. **131**, 229 (1963)
10. F.T. Smith, Phys. Rev. **179**, 111 (1969)
11. V. Sidis, Adv. At. Mol. Phys. **26**, 161 (1989)
12. W. Heisenberg, Z. Physik **39**, 514 (1926)
13. W. Pauli, Z. Physik **43**, 601 (1927)
14. P. Dirac, Proc. Roy. Soc. (London) A **117**, 610 (1928)
15. G. Breit, Phys. Rev. **34**, 553 (1929)
16. L. Foldy, S. Wouthuysen, Phys. Rev. **78**, 29 (1950)
17. H. Bethe, E. Salpeter, *Quantum Mechanics for One- and Two-Electron Atoms* (Springer, Berlin, 1957)
18. J. Pople, Mol. Phys. **3**, 16 (1960)
19. S.R. Langhoff, C.W. Kern, *Modern Theoretical Chemistry*, vol. 4 (Plenum, New York, 1977)
20. B. Heß, C. Marian, U. Wahlgren, O. Gropen, Chem. Phys. Lett. **251**, 365 (1996)
21. B. Heß, C. Marian, S. Peyerimhoff, *Modern Electronic Structure Theory (Part I)* (World Scientific, Singapore, 1995), p. 152
22. D. Fedorov, M. Gordon, J. Chem. Phys. **112**, 5611 (2000)
23. R.A. Young, Jr., D.R. Yarkony, J. Chem. Phys. **125**, 234301 (2006)
24. M.S. Schuurman, D.E. Weinberg, D.R. Yarkony, J. Chem. Phys. **127**, 104309 (2007)
25. E. Wigner, *Group Theory* (Academic, New York, 1959)
26. M. Sturge, Solid State Phys. **20**, 91 (1967)
27. R. Englman, *The Jahn-Teller Effect* (Wiley, New York, 1972)
28. I. Bersuker, *The Jahn-Teller Effect* (Cambridge University Press, Cambridge, 2006)
29. W. Domcke, S. Mishra, L. Poluyanov, Chem. Phys. **322**, 405 (2006)
30. A. Stone, Proc. Roy. Soc. (London) A **351**, 141 (1976)
31. H. Koizumi, S. Sugano, J. Chem. Phys. **102**, 4472 (1995)
32. J. Schön, H. Köppel, J. Chem. Phys. **108**, 1503 (1998)
33. L. Poluyanov, W. Domcke, Chem. Phys. **352**, 125 (2008)

34. L. Poluyanov, W. Domcke, J. Chem. Phys. **129**, 224102 (2008)
35. G. Duxbury, *Molecular Spectroscopy: Specialist Periodical Report*, vol. 3 (Chemical Society, London, 1975)
36. A. Merer, C. Jungen, *Molecular Spectroscopy: Modern Research*, vol. 2 (Academic, New York, 1976)
37. J. Brown, F.J. rgensen, Adv. Chem. Phys. **52**, 117 (1983)
38. M. Perić, S. Peyerimhoff, Adv. Chem. Phys. **124**, 583 (2002)
39. L. Poluyanov, W. Domcke, Chem. Phys. **301**, 111 (2004)
40. F. Northrup, T. Sears, Mol. Phys. **71**, 45 (1990)
41. F. Northrup, T. Sears, J. Chem. Phys. **91**, 762 (1989)
42. S.G. He, H. Li, T. Smith, D. Clouthier, A. Merer, J. Chem. Phys. **119**, 10115 (2003)
43. S. Mishra, V. Vallet, L. Poluyanov, W. Domcke, J. Chem. Phys **123**, 124104 (2005)
44. S. Mishra, V. Vallet, L. Poluyanov, W. Domcke, J. Chem. Phys **124**, 044317 (2006)
45. J. Hougen, J. Chem. Phys. **36**, 1874 (1962)
46. S. Mishra, L. Poluyanov, W. Domcke, J. Chem. Phys. **126**, 134312 (2007)
47. S. Mishra, W. Domcke, L. Poluyanov, Chem. Phys. **327**, 457 (2006)
48. I. Sioutis, S. Mishra, L. Poluyanov, W. Domcke, J. Chem. Phys. **128**, 124318 (2008)
49. L. Landau, E. Lifshitz, *Quantum Mechanics* (Nauka, Moscow, 1974)

# Vibronic Coupling Constant and Vibronic Coupling Density

Tohru Sato, Ken Tokunaga, Naoya Iwahara, Katsuyuki Shizu,  
and Kazuyoshi Tanaka

**Abstract** The definition of vibronic coupling is given with emphasis on its difference from non-adiabatic coupling. We present one of the methods for calculation of the vibronic coupling constant and vibronic coupling density analysis that enables us to investigate the local properties of vibronic coupling. Some applications of vibronic coupling density are presented. Vibronic couplings in fullerene ions still contain some unresolved problems as targets for the calculations. Studies on vibronic couplings in fullerene ions are reviewed.

## 1 Introduction: Definition of Vibronic Coupling Constant

The Jahn–Teller effect [7–9, 25] originates from vibronic coupling [19]. In this chapter, we discuss the definition of vibronic coupling with emphasis on its difference from non-adiabatic coupling.

### 1.1 The Vibronic Hamiltonian

We consider a molecule that consists of  $M$  nuclei whose configurations are denoted by  $\mathbf{R} = (\mathbf{R}_1, \dots, \mathbf{R}_A, \dots, \mathbf{R}_M)$  and  $N$  electrons whose configurations are denoted by  $\mathbf{r} = (\mathbf{r}_1, \dots, \mathbf{r}_i, \dots, \mathbf{r}_N)$ , where  $\mathbf{R}_A = (X_A, Y_A, Z_A)$  and  $\mathbf{r}_i = (x_i, y_i, z_i)$  in the Cartesian coordinate system. Masses of an electron and a nucleus  $A$  are denoted by  $m_e$  and  $M_A$ , respectively.

A Hamiltonian is written as

$$\mathcal{H}(\mathbf{r}, \mathbf{R}) = \mathcal{T}_n(\mathbf{R}) + \mathcal{T}_e(\mathbf{r}) + \mathcal{U}_{ee}(\mathbf{r}) + \mathcal{U}_{ne}(\mathbf{r}, \mathbf{R}) + \mathcal{U}_{nn}(\mathbf{R}), \quad (1)$$

$$= \mathcal{T}_n(\mathbf{R}) + \mathcal{T}_e(\mathbf{r}) + \mathcal{U}(\mathbf{r}, \mathbf{R}), \quad (2)$$

where, using

$$\nabla_A^2 = \frac{\partial^2}{\partial X_A^2} + \frac{\partial^2}{\partial Y_A^2} + \frac{\partial^2}{\partial Z_A^2}, \quad (3)$$

$$\nabla_i^2 = \frac{\partial^2}{\partial x_i^2} + \frac{\partial^2}{\partial y_i^2} + \frac{\partial^2}{\partial z_i^2}, \quad (4)$$



$\mathcal{T}_n$  is a kinetic energy operator

$$\mathcal{T}_n(\mathbf{R}) = \sum_{A=1}^M -\frac{\hbar^2}{2M_A} \nabla_A^2, \quad (5)$$

and  $\mathcal{T}_e$  is an kinetic energy operator

$$\mathcal{T}_e(\mathbf{r}) = \sum_{r=1}^N -\frac{\hbar^2}{2m_e} \nabla_r^2. \quad (6)$$

$\mathcal{U}_{ee}(\mathbf{r})$  is an potential energy operator

$$\mathcal{U}_{ee}(\mathbf{r}) = \sum_{i=1}^N \sum_{j>i}^N \frac{e^2}{4\pi\epsilon_0 r_{ij}}, \quad (7)$$

where  $e$  is the elementary charge,  $\epsilon_0$  the permittivity of vacuum, and  $r_{ij} = |\mathbf{r}_i - \mathbf{r}_j|$ .  $\mathcal{U}_{ne}(\mathbf{r}, \mathbf{R})$  is a potential energy operator

$$\mathcal{U}_{ne}(\mathbf{r}, \mathbf{R}) = \sum_{A=1}^M \sum_{i=1}^N -\frac{Z_A e^2}{4\pi\epsilon_0 R_{iA}}, \quad (8)$$

where  $Z_A$  is the nuclear charge,  $R_{iA} = |\mathbf{r}_i - \mathbf{R}_A|$ .  $\mathcal{U}_{nn}(\mathbf{R})$  is a potential energy operator

$$\mathcal{U}_{nn}(\mathbf{R}) = \sum_{A=1}^M \sum_{B>A}^M \frac{Z_A Z_B e^2}{4\pi\epsilon_0 R_{AB}}, \quad (9)$$

where  $R_{AB} = |\mathbf{R}_A - \mathbf{R}_B|$ .

We assume the molecular system is in a state  $R$  with a stationary nuclear configuration  $\mathbf{R}_0$ . We call the state  $R$  and nuclear configuration  $\mathbf{R}_0$  *reference state* and *reference configuration*, respectively. A change in the state  $R \rightarrow S$ , for example, an ionization or excitation, gives rise to a vibronic interaction that results in a structural change  $\mathbf{R}_0 \rightarrow \mathbf{R}$ . The structural change  $\Delta\mathbf{R} = \mathbf{R} - \mathbf{R}_0$  can be expressed by the mass-weighted normal coordinates of vibrational motions  $\mathbf{Q} = (Q_1, \dots, Q_\alpha, \dots, Q_{3M-5 \text{ or } 3M-6})$ . Normal coordinates are defined in the Appendix.

If  $\Delta\mathbf{R}$  is small, the Hamiltonian of a deformed molecule  $S$ , or Hamiltonian can be expanded around the reference configuration  $\mathbf{R}_0$  as a Taylor series in terms of the normal coordinates as

$$\begin{aligned} \mathcal{H}(\mathbf{r}, \mathbf{Q}) = & \mathcal{T}_n(\mathbf{Q}) + \mathcal{T}_e(\mathbf{r}) + \mathcal{U}(\mathbf{r}, \mathbf{R}_0) + \sum_{\alpha} \left( \frac{\partial \mathcal{U}}{\partial Q_{\alpha}} \right)_{\mathbf{R}_0} Q_{\alpha} \\ & + \frac{1}{2} \sum_{\alpha} \sum_{\beta} \left( \frac{\partial^2 \mathcal{U}}{\partial Q_{\alpha} \partial Q_{\beta}} \right)_{\mathbf{R}_0} Q_{\alpha} Q_{\beta} + \cdots, \end{aligned} \quad (10)$$

$$\begin{aligned} = & \sum_{\alpha} -\frac{\hbar^2}{2} \left( \frac{\partial^2}{\partial Q_{\alpha}^2} \right) + \mathcal{T}_e(\mathbf{r}) + \mathcal{U}(\mathbf{r}, \mathbf{R}_0) + \sum_{\alpha} \mathcal{V}_{\alpha} Q_{\alpha} \\ & + \frac{1}{2} \sum_{\alpha} \sum_{\beta} \mathcal{W}_{\alpha\beta} Q_{\alpha} Q_{\beta} + \cdots. \end{aligned} \quad (11)$$

This is called the Herzberg–Teller expansion. The fourth term in the last line describes a vibronic coupling. The electronic part of the vibronic operator is defined by

$$\mathcal{V}_{\alpha} = \left( \frac{\partial \mathcal{U}}{\partial Q_{\alpha}} \right)_{\mathbf{R}_0}. \quad (12)$$

The fifth term in the last line describes a vibronic coupling. The electronic part of the vibronic operator is defined by

$$\mathcal{W}_{\alpha\beta} = \left( \frac{\partial^2 \mathcal{U}}{\partial Q_{\alpha} \partial Q_{\beta}} \right)_{\mathbf{R}_0}. \quad (13)$$

Furthermore, the  $l$ th order vibronic coupling can be written as

$$\frac{1}{l!} \mathcal{U}_{\alpha_1 \dots \alpha_l}^{(l)} Q_{\alpha_1} \cdots Q_{\alpha_l} = \frac{1}{l!} \left( \frac{\partial^l \mathcal{U}}{\partial Q_{\alpha_1} \cdots \partial Q_{\alpha_l}} \right)_{\mathbf{R}_0} Q_{\alpha_1} \cdots Q_{\alpha_l}. \quad (14)$$

## 1.2 Electronic Bases and Adiabatic Approximations

We will discuss an electronic basis, the electronic basis on which the Jahn–Teller theory is based, and compare it with another electronic basis, the electronic basis. Since non-adiabatic coupling in Jahn–Teller effect has a different meaning from that in the Born–Oppenheimer basis, we will also discuss adiabatic approximations in these electronic bases.

A wavefunction or vibronic wavefunction  $\Psi(\mathbf{r}, \mathbf{Q})$  is a solution of the Schrödinger equation for the molecular Hamiltonian

$$\mathcal{H}(\mathbf{r}, \mathbf{Q}) \Psi(\mathbf{r}, \mathbf{Q}) = E \Psi(\mathbf{r}, \mathbf{Q}), \quad (15)$$

where  $E$  is the total energy of the system. To obtain the exact  $\Psi$  is very difficult. However, because  $M_A$  is much larger than  $m_e$ ,  $m_e/M_A \approx 10^{-3}$ , the motion of electrons can be regarded as being in a fixed nuclear framework  $\mathbf{R}_0$ . In other words, when one is concerned with the electronic motion, the kinetic energy can be

neglected. This is called the *adiabatic approximation*. As we will discuss later, some adiabatic approximations are possible, depending upon the choice of the electronic basis used to expand the vibronic wavefunction.

The electronic basis is obtained from the eigenvalue problem of an Hamiltonian which is defined as

$$\mathcal{H}_e(\mathbf{r}; \mathbf{R}) = \mathcal{T}_e(\mathbf{r}) + \mathcal{U}(\mathbf{r}, \mathbf{R}) = \mathcal{T}_e(\mathbf{r}) + \mathcal{U}_{ee}(\mathbf{r}) + \mathcal{U}_{ne}(\mathbf{r}, \mathbf{R}) + \mathcal{U}_{nn}(\mathbf{R}). \quad (16)$$

Note that the nuclear-nuclear potential is included in the electronic Hamiltonian in this chapter. In the electronic Hamiltonian, the nuclear coordinates are given from outside the problem.

An electronic wavefunction  $\varphi(\mathbf{r}; \mathbf{R})$  is a solution of the electronic Hamiltonian  $\mathcal{H}_e(\mathbf{r}; \mathbf{R})$ :

$$\mathcal{H}_e(\mathbf{r}; \mathbf{R})\varphi_m(\mathbf{r}; \mathbf{R}) = E_m(\mathbf{R})\varphi_m(\mathbf{r}; \mathbf{R}), \quad (17)$$

where  $E_m$  is the electronic energy of an electronic state  $m$ . For the reference nuclear configuration, the wavefunction  $\varphi_m(\mathbf{r}; \mathbf{R}_0)$  satisfies

$$\mathcal{H}_e(\mathbf{r}; \mathbf{R}_0)\varphi_m(\mathbf{r}; \mathbf{R}_0) = E_m(\mathbf{R}_0)\varphi_m(\mathbf{r}; \mathbf{R}_0). \quad (18)$$

The two Hamiltonians in (17) and (18) have the following relationship:

$$\begin{aligned} \mathcal{H}_e(\mathbf{r}; \mathbf{R}) &= \mathcal{T}_e(\mathbf{r}) + \mathcal{U}(\mathbf{r}; \mathbf{R}) = \mathcal{T}_e(\mathbf{r}) + \mathcal{U}(\mathbf{r}; \mathbf{R}_0) + \Delta\mathcal{U}(\mathbf{r}; \mathbf{R}), \\ &= \mathcal{H}_e(\mathbf{r}; \mathbf{R}_0) + \Delta\mathcal{U}(\mathbf{r}; \mathbf{Q}), \end{aligned} \quad (19)$$

where

$$\Delta\mathcal{U}(\mathbf{r}; \mathbf{Q}) = \sum_{\alpha\Gamma\gamma} \mathcal{V}_{\alpha\Gamma\gamma} \mathcal{Q}_{\alpha\Gamma\gamma} + \frac{1}{2} \sum_{\alpha\Gamma\gamma} \sum_{\beta\Gamma'\gamma'} \mathcal{W}_{\alpha\Gamma\gamma\beta\Gamma'\gamma'} \mathcal{Q}_{\alpha\Gamma\gamma} \mathcal{Q}_{\beta\Gamma'\gamma'} + \cdots, \quad (20)$$

where the mode  $\alpha$  is expressed along with its representation  $\Gamma$  and line  $\gamma$ .

If a single  $e$  mode  $(Q_{E\theta}, Q_{E\epsilon})$  is considered, for instance,  $\{Q_E \times Q_E\}_{A_1} = Q_{E\theta}^2 + Q_{E\epsilon}^2$  transforms as the  $A_1$  representation, and  $(\{Q_E \times Q_E\}_{E\theta}, \{Q_E \times Q_E\}_{E\epsilon}) = (Q_{E\theta}^2 - Q_{E\epsilon}^2, 2 Q_{E\theta} Q_{E\epsilon})$  as the lines  $\theta$  and  $\epsilon$  of the  $E$  representation, respectively. Thus the quadratic terms in (20) can be rewritten as

$$\begin{aligned} &\frac{1}{2} \{ \mathcal{W}_{E\theta E\theta} Q_{E\theta} Q_{E\theta} + \mathcal{W}_{E\theta E\epsilon} Q_{E\theta} Q_{E\epsilon} + \mathcal{W}_{E\epsilon E\theta} Q_{E\epsilon} Q_{E\theta} \\ &\quad + \mathcal{W}_{E\epsilon E\epsilon} Q_{E\epsilon} Q_{E\epsilon} \} \\ &= \frac{1}{2} \{ \mathcal{W}_{A_1} (Q_{E\theta}^2 + Q_{E\epsilon}^2) + \mathcal{W}_{E\theta} (Q_{E\theta}^2 - Q_{E\epsilon}^2) + \mathcal{W}_{E\epsilon} (2 Q_{E\theta} Q_{E\epsilon}) \}, \end{aligned} \quad (21)$$

where

$$\mathcal{W}_{A_1} = \frac{1}{2} (\mathcal{W}_{E\theta E\theta} + \mathcal{W}_{E\epsilon E\epsilon}) = \{ \mathcal{W}_{EE} \}_{A_1}, \quad (22)$$

$$\mathcal{W}_{E\theta} = \frac{1}{2}(\mathcal{W}_{E\theta E\theta} - \mathcal{W}_{E\epsilon E\epsilon}) = \{\mathcal{W}_{EE}\}_{E\theta}, \quad (23)$$

and

$$\mathcal{W}_{E\epsilon} = \mathcal{W}_{E\theta E\epsilon} = \mathcal{W}_{E\epsilon E\theta} = \{\mathcal{W}_{EE}\}_{E\epsilon}. \quad (24)$$

Using tensor convolutions  $\{Q_{\Gamma_1} \times Q_{\Gamma_2}\}_{\Gamma_\gamma}$  and  $\{\mathcal{W}_{\Gamma_1 \Gamma_2}\}_{\Gamma_\gamma}$ , (20) is written in a general form as

$$\begin{aligned} \Delta\mathcal{U}(\mathbf{r}; \mathbf{R}) &= \sum_{\alpha\Gamma_\gamma} \mathcal{V}_{\alpha\Gamma_\gamma} Q_{\alpha\Gamma_\gamma} \\ &+ \frac{1}{2} \sum_{\alpha\Gamma_\gamma} \sum_{\alpha'\Gamma'_\gamma} \sum_{\alpha''\Gamma''_\gamma} \{\mathcal{W}_{\alpha'\Gamma'_\gamma \alpha''\Gamma''_\gamma}\}_{\alpha\Gamma_\gamma} \{Q_{\alpha'\Gamma'_\gamma} \times Q_{\alpha''\Gamma''_\gamma}\}_{\alpha\Gamma_\gamma} + \dots \end{aligned} \quad (25)$$

The wavefunction can be represented using the two electronic bases  $\{\varphi(\mathbf{r}; \mathbf{R})\}$  and  $\{\varphi(\mathbf{r}; \mathbf{R}_0)\}$ . One is

$$\Psi(\mathbf{r}, \mathbf{Q}) = \sum_m \chi_m^{CA}(\mathbf{Q}) \varphi_m(\mathbf{r}; \mathbf{R}_0). \quad (26)$$

In this representation, the molecular wavefunction is expanded using the electronic wavefunctions with the configuration fixed at the reference configuration  $\mathbf{R}_0$ . This representation is called a *crude adiabatic (CA) representation* and the basis  $\{\varphi_m(\mathbf{r}; \mathbf{R}_0)\}$  the *electronic basis*. The other representation, the *Born–Oppenheimer (BO) representation*, is defined as

$$\Psi(\mathbf{r}, \mathbf{Q}) = \sum_m \chi_m^{BO}(\mathbf{Q}) \varphi_m(\mathbf{r}; \mathbf{R}), \quad (27)$$

where the *electronic basis*  $\{\varphi_m(\mathbf{r}; \mathbf{R})\}$  is obtained from the electronic Schrödinger equation (17). It should be noted that the dependence of nuclear coordinates is included both in the nuclear function  $\chi_m^{BO}(\mathbf{Q})$  and in the electronic function  $\varphi_m(\mathbf{r}; \mathbf{R})$ . Furthermore, as long as each basis is complete, these expansions are equivalent. The Hamiltonian is based on the CA representation.

### 1.2.1 Crude Adiabatic Approximation

In the CA representation, the wavefunction  $\chi_m^{CA}(\mathbf{Q})$  satisfies the following coupled equations

$$\begin{aligned} &[T_n(\mathbf{Q}) + E_m(\mathbf{R}_0) + \langle \varphi_m(\mathbf{r}; \mathbf{R}_0) | \Delta\mathcal{U}(\mathbf{r}; \mathbf{Q}) | \varphi_m(\mathbf{r}; \mathbf{R}_0) \rangle] \chi_m^{CA}(\mathbf{Q}) \\ &+ \sum_{n \neq m} \langle \varphi_m(\mathbf{r}; \mathbf{R}_0) | \Delta\mathcal{U}(\mathbf{r}; \mathbf{Q}) | \varphi_n(\mathbf{r}; \mathbf{R}_0) \rangle \chi_n^{CA}(\mathbf{Q}) = \epsilon \chi_m^{CA}(\mathbf{Q}). \end{aligned} \quad (28)$$

It should be noted that the kinetic energy

$$T_n(Q) = \left( \sum_{\alpha} -\frac{\hbar^2}{2} \frac{\partial^2}{\partial Q_{\alpha}^2} \right) \delta_{nm} \quad (29)$$

is diagonal in this representation, since the electronic wavefunction  $\varphi_m(\mathbf{r}; \mathbf{R}_0)$  is independent of  $Q_{\alpha}$ . This is an advantage of the CA representation.

When the off-diagonal coupling, the last term in the left-hand-side of (28), can be neglected

$$\langle \varphi_m(\mathbf{r}; \mathbf{R}_0) | \Delta \mathcal{U}(\mathbf{r}; \mathbf{Q}) | \varphi_n(\mathbf{r}; \mathbf{R}_0) \rangle = 0, \quad (30)$$

the coupled equations (28) may be decoupled as

$$[T_n(Q) + E_m(\mathbf{R}_0) + \langle \varphi_m(\mathbf{r}; \mathbf{R}_0) | \Delta \mathcal{U}(\mathbf{r}; \mathbf{R}) | \varphi_m(\mathbf{r}; \mathbf{R}_0) \rangle] \chi_m^{CAA}(Q) = \epsilon_m^{CA} \chi_m^{CAA}(Q), \quad (31)$$

which is equivalent for the molecular wavefunction to be put as a simple product

$$\Psi(\mathbf{r}, \mathbf{Q}) \approx \Phi_m^{CA}(\mathbf{r}, \mathbf{Q}) = \chi_m^{CAA}(\mathbf{Q}) \varphi_m(\mathbf{r}; \mathbf{R}_0). \quad (32)$$

This is called a *crude adiabatic (CA) approximation*. The CA approximation is valid if

$$\hbar\omega \ll |E_n - E_m|, \quad (33)$$

which is not fulfilled when the electronic state is degenerate or pseudo-degenerate. The degenerate case, or the Jahn–Teller case, will be discussed later.

## 1.2.2 Born–Oppenheimer Approximation

In the BO representation, the nuclear kinetic energy matrix is not diagonal because of the nuclear coordinate dependence of the wavefunction. The off-diagonal elements of the nuclear kinetic energy are *non-adiabatic couplings*. In order to discuss the relationship between vibronic coupling and non-adiabatic coupling, we present the Born–Oppenheimer approximation.

Since  $\mathcal{T}_n(\mathbf{Q})$  acts on  $\chi_m^{BO}(\mathbf{Q})\varphi_m(\mathbf{r}; \mathbf{R})$  as

$$\begin{aligned} \mathcal{T}_n(\mathbf{Q}) \left[ \chi_m^{BO}(\mathbf{Q}) \varphi_m(\mathbf{r}; \mathbf{R}) \right] &= \left[ \mathcal{T}_n(\mathbf{Q}) \chi_m^{BO}(\mathbf{Q}) \right] \varphi_m(\mathbf{r}; \mathbf{R}) + [\mathcal{T}_n(\mathbf{Q}) \varphi_m(\mathbf{r}; \mathbf{R})] \chi_m^{BO}(\mathbf{Q}) \\ &\quad - \hbar^2 \sum_{\alpha} \left[ \frac{\partial \chi_m^{BO}(\mathbf{Q})}{\partial Q_{\alpha}} \right] \left[ \frac{\partial \varphi_m(\mathbf{r}; \mathbf{R})}{\partial Q_{\alpha}} \right], \end{aligned} \quad (34)$$

the equation for the wavefunction is

$$\begin{aligned} &[T_n(\mathbf{Q}) + E_m(\mathbf{Q}) + \langle \varphi_m(\mathbf{r}; \mathbf{R}) | \mathcal{T}_n(\mathbf{Q}) | \varphi_m(\mathbf{r}; \mathbf{R}) \rangle] \chi_m^{BO}(\mathbf{Q}) \\ &+ \sum_{n \neq m} \left[ \langle \varphi_m(\mathbf{r}; \mathbf{R}) | \mathcal{T}_n(\mathbf{Q}) | \varphi_n(\mathbf{r}; \mathbf{R}) \rangle - \hbar^2 \sum_{\alpha} \left\langle \varphi_m(\mathbf{r}; \mathbf{R}) \left| \frac{\partial}{\partial Q_{\alpha}} \right| \varphi_n(\mathbf{r}; \mathbf{R}) \right\rangle \frac{\partial}{\partial Q_{\alpha}} \right] \\ &\times \chi_n^{BO}(\mathbf{Q}) \end{aligned}$$

$$= \epsilon \chi_m^{BO}(\mathbf{Q}). \quad (35)$$

When the off-diagonal couplings in (35) can be ignored

$$\langle \varphi_m(\mathbf{r}; \mathbf{R}) | \mathcal{T}_n(\mathbf{Q}) | \varphi_n(\mathbf{r}; \mathbf{R}) \rangle = 0 \quad (36)$$

and

$$\left\langle \varphi_m(\mathbf{r}; \mathbf{R}) \left| \frac{\partial}{\partial Q_\alpha} \right| \varphi_n(\mathbf{r}; \mathbf{R}) \right\rangle = 0, \quad (37)$$

the coupled equations in (35) can be decoupled as

$$[T_n(\mathbf{Q}) + E_m(\mathbf{Q}) + \langle \varphi_m(\mathbf{r}; \mathbf{R}) | \mathcal{T}_n(\mathbf{Q}) | \varphi_m(\mathbf{r}; \mathbf{R}) \rangle] \chi_m^{BHA}(\mathbf{Q}) = \epsilon \chi_m^{BHA}(\mathbf{Q}). \quad (38)$$

The approximation with (36) and (37) is called a *Born–Huang (BH) approximation*. In this approximation, the molecular wavefunction is written as

$$\Psi(\mathbf{r}, \mathbf{Q}) \approx \Phi_m^{BH}(\mathbf{r}, \mathbf{Q}) = \chi_m^{BHA}(\mathbf{Q}) \varphi_m(\mathbf{r}; \mathbf{R}). \quad (39)$$

When the diagonal element of the nuclear kinetic energy in (38) can be neglected

$$\langle \varphi_m(\mathbf{r}; \mathbf{R}) | \mathcal{T}_n(\mathbf{Q}) | \varphi_m(\mathbf{r}; \mathbf{R}) \rangle = 0, \quad (40)$$

the decoupled (38) is

$$[T_n(\mathbf{Q}) + E_m^{BO}(\mathbf{Q})] \chi_m^{BOA}(\mathbf{Q}) = \epsilon \chi_m^{BOA}(\mathbf{Q}). \quad (41)$$

This is a *BO approximation*. The BO vibronic wavefunction is written as

$$\Psi(\mathbf{r}, \mathbf{Q}) \approx \Phi_m^{BO}(\mathbf{r}, \mathbf{Q}) = \chi_m^{BOA}(\mathbf{Q}) \varphi_m(\mathbf{r}; \mathbf{R}). \quad (42)$$

It should be noted that the BO potential  $E^{BO}(\mathbf{Q})$  does not contain information on the CA potential  $\langle \varphi_m(\mathbf{r}; \mathbf{R}) | \Delta \mathcal{U}(\mathbf{r}, \mathbf{Q}) | \varphi_n(\mathbf{r}; \mathbf{R}) \rangle$ .

The off-diagonal couplings neglected in (36) and (37) are *non-adiabatic couplings* [16]

$$\Lambda_{mn}(\mathbf{Q}) = -\hbar^2 \sum_{\alpha} \left[ A_{mn}^{(\alpha)}(\mathbf{Q}) \frac{\partial}{\partial Q_{\alpha}} + \frac{1}{2} B_{mn}^{(\alpha)}(\mathbf{Q}) \right], \quad (43)$$

where

$$A_{mn}^{(\alpha)}(\mathbf{Q}) = \left\langle \varphi_m(\mathbf{r}; \mathbf{R}) \left| \frac{\partial}{\partial Q_{\alpha}} \right| \varphi_n(\mathbf{r}; \mathbf{R}) \right\rangle, \quad (44)$$

and

$$B_{mn}^{(\alpha)}(\mathbf{Q}) = \left\langle \varphi_m(\mathbf{r}; \mathbf{R}) \left| \frac{\partial^2}{\partial Q_\alpha^2} \right| \varphi_n(\mathbf{r}; \mathbf{R}) \right\rangle. \quad (45)$$

Although the nuclear kinetic part in the CA representation is diagonal, an adiabatic approximation is possible for Jahn–Teller systems, as we will discuss later. Therefore, a non-adiabatic coupling can also be defined in the CA representation. The meaning of the non-adiabatic coupling depends upon the adiabatic approximation assumed. In the CA representation, we should distinguish between vibronic couplings and non-adiabatic couplings.

The CA basis is usually employed in the vibronic coupling theory. The remaining sections of this chapter are based on the CA representation.

### 1.3 Vibronic Coupling Constant and Jahn–Teller Hamiltonian

From (20) and (28), the coupled equations for the nuclear wavefunction are

$$\begin{aligned} & \left[ T_n(Q) + E_m(\mathbf{R}_0) + \sum_{\alpha} (V_{\alpha})_{mm} Q_{\alpha} + \frac{1}{2} \sum_{\alpha, \beta} (W_{\alpha\beta})_{mm} Q_{\alpha} Q_{\beta} + \cdots \right] \chi_m^{CA}(Q) \\ & + \sum_{n \neq m} \left[ \sum_{\alpha} (V_{\alpha})_{mn} Q_{\alpha} + \frac{1}{2} \sum_{\alpha, \beta} (W_{\alpha\beta})_{mn} Q_{\alpha} Q_{\beta} + \cdots \right] \chi_n^{CA}(Q) = \epsilon \chi_m^{CA}(Q), \end{aligned} \quad (46)$$

where the vibronic coupling is defined by

$$V_{\alpha} = (\langle \varphi_m(\mathbf{r}; \mathbf{R}_0) | \mathcal{V}_{\alpha} | \varphi_n(\mathbf{r}; \mathbf{R}_0) \rangle) = \left( \int d^{3N} \mathbf{r} \varphi_m^*(\mathbf{r}; \mathbf{R}_0) \mathcal{V}_{\alpha}(\mathbf{r}) \varphi_n(\mathbf{r}; \mathbf{R}_0) \right), \quad (47)$$

and the vibronic coupling is defined by

$$W_{\alpha\beta} = (\langle \varphi_m(\mathbf{r}; \mathbf{R}_0) | \mathcal{W}_{\alpha\beta} | \varphi_n(\mathbf{r}; \mathbf{R}_0) \rangle) \quad (48)$$

$$= \left( \int d^{3N} \mathbf{r} \varphi_m^*(\mathbf{r}; \mathbf{R}_0) \mathcal{W}_{\alpha\beta}(\mathbf{r}) \varphi_n(\mathbf{r}; \mathbf{R}_0) \right). \quad (49)$$

These matrix elements are called the vibronic coupling, respectively.

These matrix elements can be reduced with the aid of group theory. To show the symmetry species of the vibrational mode and electronic state explicitly, we express the normal coordinate and electronic states as  $Q_{\alpha\overline{\Gamma\gamma}}$ ,  $|m\Gamma\gamma\rangle$ , and  $|n\Gamma'\gamma'\rangle$ , respectively. Equation (47) is rewritten as

$$(V_{\alpha\overline{\Gamma\gamma}})_{n\Gamma'\gamma', m\Gamma\gamma} = \langle n\Gamma'\gamma' | \mathcal{V}_{\alpha\overline{\Gamma\gamma}} | m\Gamma\gamma \rangle. \quad (50)$$

This integral is nonzero if and only if  $\bar{\Gamma} \in \Gamma' \times \Gamma$ . Furthermore, according to the Wigner–Eckart theorem, the matrix element (50) can be reduced as

$$\langle n\Gamma' \gamma' | \mathcal{V}_{\alpha\bar{\Gamma}} | m\Gamma \gamma \rangle = \langle n\Gamma' || \mathcal{V}_{\alpha\bar{\Gamma}} || m\Gamma \rangle \langle \Gamma' \gamma' | \Gamma \gamma \bar{\Gamma} \gamma \rangle = \mathbf{V}_{\alpha\bar{\Gamma}}^{n\Gamma', m\Gamma} \langle \Gamma' \gamma' | \Gamma \gamma \bar{\Gamma} \gamma \rangle, \quad (51)$$

where  $\langle \Gamma' \gamma' | \Gamma \gamma \bar{\Gamma} \gamma \rangle$  is the Clebsch–Gordan coefficient, which depends only on the symmetry, and  $\mathbf{V}_{\alpha\bar{\Gamma}}^{n\Gamma', m\Gamma} = \langle n\Gamma' || \mathcal{V}_{\alpha\bar{\Gamma}} || m\Gamma \rangle$  is the reduced matrix element, which is independent of  $\gamma$ ,  $\gamma'$ , or  $\bar{\gamma}$ . Thus, if  $(\mathbf{V}_{\alpha\bar{\Gamma}\gamma_1})_{n\Gamma'\gamma'_1, m\Gamma\gamma_1}$  is known, one can calculate another constant  $(\mathbf{V}_{\alpha\bar{\Gamma}\gamma_2})_{n\Gamma'\gamma'_2, m\Gamma\gamma_2}$  using the table of Clebsch–Gordan coefficients. For the diagonal element, the vibronic coupling constant  $\mathbf{V}_{\alpha\bar{\Gamma}}^{m\Gamma, m\Gamma}$  is nonzero if and only if the symmetric product of  $\Gamma$ ,  $[\Gamma^2]$  contains  $\bar{\Gamma}$ . For a non-degenerate state,  $\Gamma \times \Gamma = A_1$ , where  $A_1$  is a totally symmetric representation. Therefore, the distortions are totally symmetric in a non-degenerate electronic state. As for a degenerate state, the symmetric product contains some non-totally symmetric representations that cause Jahn–Teller distortions.

The diagonal part of the linear vibronic coupling constants has a clear physical meaning: the force along the normal mode  $\bar{\Gamma}$  from the field produced by the electronic state  $\Gamma$ .

When the electronic state  $m$  is neither degenerate nor pseudo-degenerate, the CA approximation is valid; neglecting the higher order terms,

$$\begin{aligned} & \left[ T_n(Q) + E_m(\mathbf{R}_0) + \sum_{\alpha} (\mathbf{V}_{\alpha})_{mm} Q_{\alpha} + \frac{1}{2} \sum_{\alpha, \beta} (\mathbf{W}_{\alpha\beta})_{mm} Q_{\alpha} Q_{\beta} \right] \chi_m^{CAA}(Q) \\ & = \epsilon \chi_m^{CAA}(Q). \end{aligned} \quad (52)$$

After making a rotation of the normal coordinates, (52) can be separated to remove the cross terms  $Q_{\alpha} Q_{\beta}$  as follows:

$$\begin{aligned} & \left[ E_m(\mathbf{R}_0) + \sum_{\alpha} \left\{ -\frac{\hbar^2}{2} \frac{\partial^2}{\partial Q_{\alpha}^2} + (\mathbf{V}_{\alpha})_{mm} Q_{\alpha} + \frac{1}{2} (\mathbf{W}_{\alpha\alpha})_{mm} Q_{\alpha}^2 \right\} \right] \chi_m^{CAA}(Q) \\ & = \epsilon \chi_m^{CAA}(Q), \end{aligned} \quad (53)$$

where the matrix elements and the normal coordinates are redefined. The solution is a collection of the displaced harmonic oscillator the potential of which is written as

$$V_{\alpha} Q_{\alpha} + \frac{1}{2} \omega_{\alpha}^2 Q_{\alpha}^2 = \frac{1}{2} \omega_{\alpha}^2 \left( Q_{\alpha} + \frac{V_{\alpha}}{\omega_{\alpha}^2} \right)^2 - \frac{V_{\alpha}^2}{2\omega_{\alpha}^2}, \quad (54)$$

where  $V_{\alpha} = (\mathbf{V}_{\alpha})_{mm}$  and  $\omega_{\alpha}^2 = (\mathbf{W}_{\alpha\alpha})_{mm}$ . Therefore, because of the vibronic couplings, the potential minimum is shifted by  $\{\dots, Q_{\alpha} = -V_{\alpha}/\omega_{\alpha}^2, \dots\}$ , and the total energy is stabilized by



$$\Delta\epsilon = \sum_{\alpha} \frac{V_{\alpha}^2}{2\omega_{\alpha}^2}. \quad (55)$$

As mentioned previously,  $V_{\alpha}$  is non-zero if the mode  $\alpha$  is totally symmetric. This stabilization energy is sometimes called the *reorganization energy*.

When the electronic state  $\Gamma$  is  $n_{\Gamma}$ -fold degenerate, ignoring the couplings between the electronic states outside the degenerate manifold and the higher order of  $Q_{\alpha}$  in (46), we obtain

$$\begin{aligned} & \left( T_n(Q) \delta_{\gamma\gamma'} + E_{\Gamma}(\mathbf{R}_0) \delta_{\gamma\gamma'} + \sum_{\alpha} (V_{\alpha})_{\gamma\gamma'} Q_{\alpha} + \frac{1}{2} \sum_{\alpha, \beta} (W_{\alpha\beta})_{\gamma\gamma'} Q_{\alpha} Q_{\beta} \right) \\ & \left( \chi_{\gamma'}^{CAA}(Q) \right) = \epsilon \left( \chi_{\gamma'}^{CAA}(Q) \right), \quad (\gamma, \gamma' = 1, \dots, n_{\Gamma}). \end{aligned} \quad (56)$$

For example, in a triangular molecule  $X_3$ , if the electronic state belongs to an  $E$  representation and only a doubly degenerate  $e$  mode is considered, we can obtain the following Jahn–Teller effect with the quadratic vibronic coupling

$$\begin{aligned} & \left[ \left\{ E_E(\mathbf{R}_0) - \frac{\hbar^2}{2} \left( \frac{\partial^2}{\partial Q_{\theta}^2} + \frac{\partial^2}{\partial Q_{\epsilon}^2} \right) + \frac{1}{2} W_{A_1} (Q_{\theta}^2 + Q_{\epsilon}^2) \right\} \begin{pmatrix} 1 & 0 \\ 0 & 1 \end{pmatrix} \right. \\ & \quad \left. + V_E \begin{pmatrix} Q_{\theta} & -Q_{\epsilon} \\ -Q_{\epsilon} & -Q_{\theta} \end{pmatrix} + W_E \begin{pmatrix} Q_{\theta}^2 - Q_{\epsilon}^2 & 2Q_{\theta}Q_{\epsilon} \\ 2Q_{\theta}Q_{\epsilon} & -(Q_{\theta}^2 - Q_{\epsilon}^2) \end{pmatrix} \right] \begin{pmatrix} \chi_{\theta}(Q_{\theta}, Q_{\epsilon}) \\ \chi_{\epsilon}(Q_{\theta}, Q_{\epsilon}) \end{pmatrix} \\ & = \epsilon \begin{pmatrix} \chi_{\theta}(Q_{\theta}, Q_{\epsilon}) \\ \chi_{\epsilon}(Q_{\theta}, Q_{\epsilon}) \end{pmatrix}. \end{aligned} \quad (57)$$

When the quadratic coupling  $W_E$  is negligible, we obtain

$$\begin{aligned} & \left[ \left\{ E_E(\mathbf{R}_0) - \frac{\hbar^2}{2} \left( \frac{\partial^2}{\partial Q_{\theta}^2} + \frac{\partial^2}{\partial Q_{\epsilon}^2} \right) + \frac{1}{2} W_{A_1} (Q_{\theta}^2 + Q_{\epsilon}^2) \right\} \begin{pmatrix} 1 & 0 \\ 0 & 1 \end{pmatrix} \right. \\ & \quad \left. + V_E \begin{pmatrix} Q_{\theta} & -Q_{\epsilon} \\ -Q_{\epsilon} & -Q_{\theta} \end{pmatrix} \right] \begin{pmatrix} \chi_{\theta}(Q_{\theta}, Q_{\epsilon}) \\ \chi_{\epsilon}(Q_{\theta}, Q_{\epsilon}) \end{pmatrix} = \epsilon \begin{pmatrix} \chi_{\theta}(Q_{\theta}, Q_{\epsilon}) \\ \chi_{\epsilon}(Q_{\theta}, Q_{\epsilon}) \end{pmatrix}. \end{aligned} \quad (58)$$

This is the *dynamic linear  $E \otimes e$  problem*.

## 1.4 Adiabatic Approximation in Dynamic Jahn–Teller System

In some situations, especially in the BO approximation, the term *vibronic coupling* is identical to non-adiabatic coupling. In the Jahn–Teller theory, however, the concept of vibronic coupling is different from that of non-adiabatic coupling. To clarify the difference, we discuss the adiabatic approximation in the  $E \otimes e$  dynamic Jahn–Teller problem [27] in the strong coupling limit [32]. In this subsection, we employ

dimensionless quantities  $k = V_E / \sqrt{\hbar\omega_E^3}$ . Equation (58) is rewritten in the complex basis

$$|+\rangle = \frac{1}{\sqrt{2}}(|\theta\rangle + i|\epsilon\rangle), \quad |-\rangle = \frac{1}{\sqrt{2}}(|\theta\rangle - i|\epsilon\rangle) \quad (59)$$

as

$$\left[ -\frac{1}{2} \left\{ \left( \frac{\partial^2}{\partial Q_\theta^2} + \frac{\partial^2}{\partial Q_\epsilon^2} \right) - (Q_\theta^2 + Q_\epsilon^2) \right\} \hat{\sigma}_0 + k \begin{pmatrix} 0 & Q_\theta - iQ_\epsilon \\ Q_\theta + iQ_\epsilon & 0 \end{pmatrix} \right] \Psi = \epsilon \Psi, \quad (60)$$

where  $\hat{\sigma}_0$  is the  $2 \times 2$  unit matrix, and

$$\Psi = \begin{pmatrix} \chi_+(Q_\theta, Q_\epsilon) \\ \chi_-(Q_\theta, Q_\epsilon) \end{pmatrix} = \chi_+(Q_\theta, Q_\epsilon)|+\rangle + \chi_-(Q_\theta, Q_\epsilon)|-\rangle. \quad (61)$$

Transforming the equation into the polar coordinate  $Q_\theta = \rho \cos \phi$  and  $Q_\epsilon = \rho \sin \phi$  yields

$$\left[ \left\{ -\frac{1}{2\rho} \frac{\partial}{\partial \rho} \left( \rho \frac{\partial}{\partial \rho} \right) - \frac{1}{2\rho^2} \frac{\partial^2}{\partial \phi^2} + \frac{1}{2} \rho^2 \right\} \hat{\sigma}_0 + k\rho \begin{pmatrix} 0 & e^{-i\phi} \\ e^{i\phi} & 0 \end{pmatrix} \right] \Psi = \epsilon \Psi. \quad (62)$$

Substituting  $\Psi = \Phi / \sqrt{\rho}$  to remove the first derivative, we obtain

$$\left[ \left\{ -\frac{1}{2} \frac{\partial^2}{\partial \rho^2} - \frac{1}{8\rho^2} + \frac{\hat{L}_z^2}{2\rho^2} + \frac{1}{2} \rho^2 \right\} \hat{\sigma}_0 + k\rho \begin{pmatrix} 0 & e^{-i\phi} \\ e^{i\phi} & 0 \end{pmatrix} \right] \Phi = \epsilon \Phi, \quad (63)$$

where  $\hat{L}_z = -i \partial / \partial \phi$  is a vibrational angular momentum operator. The potential matrix can be diagonalized using a unitary transformation

$$\hat{S} = \frac{1}{\sqrt{2}} \begin{pmatrix} \exp(-i\frac{\phi}{2}) & \exp(-i\frac{\phi}{2}) \\ \exp(i\frac{\phi}{2}) & -\exp(i\frac{\phi}{2}) \end{pmatrix}. \quad (64)$$

We obtain the transformed equations as

$$\left[ \left( -\frac{1}{2} \frac{\partial^2}{\partial \rho^2} + \frac{1}{2} \rho^2 - \frac{1}{8\rho^2} \right) \hat{\sigma}_0 + \frac{1}{2\rho^2} \left( \hat{L}_z - \frac{1}{2} \hat{\sigma}_x \right)^2 + k\rho \begin{pmatrix} 1 & 0 \\ 0 & -1 \end{pmatrix} \right] \Phi' = \epsilon \Phi', \quad (65)$$

where  $\hat{\sigma}_r$  ( $r = x, y, z$ ) is a Pauli matrix,

$$\Phi' = \hat{S}^\dagger \Phi. \quad (66)$$

After a variable separation

$$\Phi'(\rho, \phi) = \frac{1}{\sqrt{2\pi}} e^{ij\phi} \chi(\rho), \quad (67)$$

where  $j$  is an eigenvalue of the vibronic angular momentum operator  $\hat{J} = \hat{L}_z + \hat{\sigma}_z/2$ ,  $j = \pm 1/2, \pm 3/2, \pm 5/2, \dots$ , we obtain the equations for the radial function  $\chi(\rho)$ ,

$$\left[ \left( -\frac{1}{2} \frac{d^2}{d\rho^2} + \frac{j^2}{2\rho^2} + \frac{1}{2} \rho^2 \right) \hat{\sigma}_0 - \frac{j}{2\rho^2} \hat{\sigma}_x + k \rho \hat{\sigma}_z \right] \chi = \epsilon \chi. \quad (68)$$

In the strong coupling limit, neglecting the off-diagonal coupling  $-\frac{j}{2\rho^2} \hat{\sigma}_x$ , the equations are decoupled as

$$\begin{aligned} \left( -\frac{1}{2} \frac{d^2}{d\rho^2} + \frac{j^2}{2\rho^2} + \frac{1}{2} \rho^2 - |k| \rho \right) \chi_- &= \epsilon_- \chi_-, \\ \left( -\frac{1}{2} \frac{d^2}{d\rho^2} + \frac{j^2}{2\rho^2} + \frac{1}{2} \rho^2 + |k| \rho \right) \chi_+ &= \epsilon_+ \chi_+. \end{aligned} \quad (69)$$

This is an *adiabatic approximation in the dynamic Jahn–Teller problem*. The wavefunction is expressed by

$$|\pm, n, j\rangle = \psi_{\pm}^{\text{ad}}(\mathbf{r}) e^{ij\phi} \frac{\chi_{\pm, n}(\rho)}{\sqrt{2\pi\rho}}. \quad (70)$$

The analytical solution of the decoupled equation (69) is discussed in reference [32].

The non-adiabatic coupling between the lower sheet  $\epsilon_-$  and upper sheet  $\epsilon_+$  is calculated from

$$\langle \chi_- | \left( -\frac{j}{2\rho^2} \right) | \chi_+ \rangle. \quad (71)$$

We can find that the non-adiabatic coupling in the BO approximation is different from that in the dynamic Jahn–Teller theory.

## 2 Calculation Method

Vibronic coupling constants have been evaluated from the BO potentials [8]. Here, we present another calculation method employing (47). This method has an advantage: we can analyze a local property of vibronic coupling using the vibronic coupling density, which we will define in Sect. 3.

In this section, before we present the calculation method, we will discuss the spatial symmetry breaking of wavefunctions (Sect. 2.1) and the violation of the Hellmann–Feynman theorem (Sect. 2.2). We will define an atomic vibronic coupling

constant (Sect. 2.4) which is useful for the vibronic coupling density analysis, and summarize other forms of vibronic coupling (Sect. 2.5).

## 2.1 Symmetry of Electronic Wavefunction at the Degenerate Point

The eigenfunctions of the electronic Hamiltonian (16) is usually obtained from the variational method

$$\delta E [\varphi(\mathbf{r}; \mathbf{R})] = 0, \quad (72)$$

where

$$E [\varphi(\mathbf{r}; \mathbf{R})] = \langle \varphi(\mathbf{r}; \mathbf{R}) | \mathcal{H}_e(\mathbf{r}; \mathbf{R}) | \varphi(\mathbf{r}; \mathbf{R}) \rangle. \quad (73)$$

When the electronic state is degenerate at  $\mathbf{R}_0$ , the spatial symmetry of the wavefunctions are destroyed which gives rise to artificial level splitting [10, 34]. For example, for the  $X^2E_1''$  state in cyclopentadienyl radical  $C_5H_5$ , the two states that should be degenerate give rise to an energy splitting of 6.9 meV using the ROHF method [34]. The DFT calculation also yields an energy splitting of 0.8 meV (ROB3LYP). Furthermore, the symmetry of the ROHF wavefunction is broken, which results in a wrong symmetry of the vibronic coupling matrix in the atomic unit as

$$V_{e'_2(3)\theta} = \begin{pmatrix} 0.0009413247 & 0.0000000000 \\ 0.0000000000 & -0.0009764159 \end{pmatrix}, \quad (74)$$

where the absolute values of the diagonal elements should be the same because of the Wigner–Eckart theorem and Clebsch–Gordan coefficients [34]. In the Jahn–Teller problem, symmetry of the wavefunction is crucial. The wavefunction without the symmetry breaking should be employed to calculate the vibronic coupling.

The symmetry breaking originates from the expectation value (73). If the wavefunction  $\varphi(\mathbf{r}; \mathbf{R}_0)$  is one of the degenerate states under the symmetry of the point group  $\mathcal{G}$ , the integrand  $\varphi^*(\mathbf{r}; \mathbf{R}_0) \mathcal{H}_e(\mathbf{r}; \mathbf{R}_0) \varphi(\mathbf{r}; \mathbf{R}_0)$  is reducible as, for example,  $E \times A_1 \times E = A_1 + A_2 + E$  for doubly degenerate wavefunctions. This signifies that the integrand is not totally symmetric and has a coordinate dependence under the symmetry operation  $R \in \mathcal{G}$ , which is an artifact that causes the symmetry breaking.

In order to recover the correct symmetry in the integrand for the degenerate case, we apply the projection operator of the totally symmetric species for the integrand. The projection operator is defined by

$$P^{A_1} = \frac{1}{|\mathcal{G}|} \sum_{R \in \mathcal{G}} R, \quad (75)$$

where  $|\mathcal{G}|$  is the order of the point group  $\mathcal{G}$ , which yields

$$P^{A_1} : E[\varphi_{\Gamma\gamma}] \mapsto \sum_{\gamma', \gamma''} \left( \frac{1}{|\mathcal{G}|} \sum_{R \in \mathcal{G}} D_{\gamma\gamma'}^{\Gamma}(R)^* D_{\gamma''\gamma}^{\Gamma}(R) \right) \langle \varphi_{\Gamma\gamma'} | \mathcal{H}_e | \varphi_{\Gamma\gamma''} \rangle, \quad (76)$$

$$= \frac{1}{n_{\Gamma}} \sum_{\gamma', \gamma''} \delta_{\gamma', \gamma''} \langle \varphi_{\Gamma\gamma'} | \mathcal{H}_e | \varphi_{\Gamma\gamma''} \rangle, \quad (77)$$

$$= \frac{1}{n_{\Gamma}} \sum_{\gamma'} E[\varphi_{\Gamma\gamma'}], \quad (78)$$

where  $D^{\Gamma}(R)$  is the matrix representation of  $R$  in the irreducible representation  $\Gamma$ , and the orthogonality theorem of the matrix representation is applied [24]. The result is the state-averaged energy with equal weights. This form of the expectation value is a starting point of the general restricted Hartree–Fock (GRHF) method [13] and state-averaged multi-configuration self-consistent field (SA-MCSCF) method [23]. The GRHF and SA-CASSCF calculations for the cyclopentadienyl radical yield the wavefunction with the correct symmetry [5, 34].

## 2.2 The Hellmann–Feynman Theorem

According to the Hellmann–Feynman theorem [18, 22], when a Hamiltonian depends on a parameter  $\lambda$ , the derivative of the energy with respect to  $\lambda$  is equal to the expectation value of the derivative of the Hamiltonian with respect to  $\lambda$ ,

$$\frac{\partial E(\lambda)}{\partial \lambda} = \left\langle \varphi(\lambda) \left| \frac{\partial \mathcal{H}(\lambda)}{\partial \lambda} \right| \varphi(\lambda) \right\rangle. \quad (79)$$

In the formal derivation of this chapter, we apply this theorem taking  $Q_{\alpha}$  as a parameter  $\lambda$  in the following form,

$$\left( \frac{\partial E(\mathbf{R})}{\partial \mathbf{R}} \right)_{\mathbf{R}_0} = \left\langle \varphi(\mathbf{r}; \mathbf{R}_0) \left| \left( \frac{\partial \mathcal{H}_e(\mathbf{r}; \mathbf{R})}{\partial \mathbf{R}} \right)_{\mathbf{R}_0} \right| \varphi(\mathbf{r}; \mathbf{R}_0) \right\rangle. \quad (80)$$

Although this theorem can be applied for exact wavefunction, conventional LCAO wavefunctions do not satisfy this theorem. There are two methods for deriving wavefunctions that fulfil the Hellmann–Feynman theorem: (1) Gaussian basis set with their derivatives [30] and (2) a floating basis [40]. Figure 1 shows the l.h.s and r.h.s. of (80) for the hydrogen molecule anion using (a) 6-31G and (b) 6-31G with their first derivatives. It is found that the wavefunction using the conventional basis function does not satisfy the theorem.

Sometimes the Hellmann–Feynman theorem has been assumed for wavefunctions with the conventional basis functions to evaluate vibronic coupling constants.

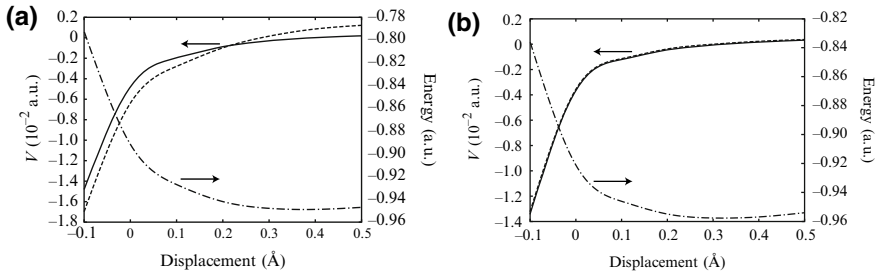


**Fig. 1** Vibronic coupling constant (solid line) and energy gradient (dotted line) of hydrogen molecule anion using the ROHF method with the basis set (a) 6-31G and (b) 6-31G with their first derivatives. The electronic energy (dashed line) is shown against the displacement from the equilibrium geometry of the neutral molecule

Such an approach has two pitfalls: one is the symmetry breaking of wavefunction, and the other is the violation of the Hellmann–Feynman theorem [35].

### 2.3 Calculation of Vibronic Coupling Constants

In this subsection, the electronic wavefunction  $\varphi(\mathbf{r}; \mathbf{R}_0)$  is denoted by

$$|\varphi\rangle = \sum_K |K\rangle C_K, \quad (81)$$

where  $|K\rangle$  is a Slater determinant, and  $K$  designates the occupation of spin orbitals  $|m\rangle$ . The vibronic coupling constant can be calculated from the diagonal element

$$\langle\varphi|\mathcal{V}_\alpha|\varphi\rangle = \sum_{K,L} C_L^* C_K \langle L|\mathcal{V}_\alpha|K\rangle. \quad (82)$$

Since the vibronic coupling is a sum of the one-electron operators  $v_\alpha(\mathbf{r}_i)$ , the matrix element over Slater determinants can be deduced using the following rule [36]:

$$1. |K\rangle = |\cdots mn \cdots\rangle$$

$$\langle K|\mathcal{V}_\alpha|K\rangle = \sum_{m \in K} \langle m|v_\alpha|m\rangle,$$

$$2. |K\rangle = |\cdots mn \cdots\rangle, \quad |L\rangle = |\cdots pn \cdots\rangle \quad (m \neq p)$$

$$\langle K|\mathcal{V}_\alpha|L\rangle = \langle m|v_\alpha|p\rangle,$$

$$3. |K\rangle = |\cdots mn \cdots\rangle, \quad |L\rangle = |\cdots pq \cdots\rangle \quad (m \neq p, n \neq q)$$

$$\langle K | \mathcal{V}_\alpha | L \rangle = 0.$$

The diagonal vibronic coupling constant over the Slater determinant  $|K\rangle$  is given by a sum of *vibronic coupling* [7] as

$$\langle K | \mathcal{V}_\alpha | K \rangle = \sum_{j \in \text{occ}} q_j \langle \psi_j | v_\alpha | \psi_j \rangle, \quad (83)$$

where  $\psi_j$  is a space orbital and  $q_j$  an occupation number. In some cases, for Jahn–Teller modes, the summation over fully occupied degenerate orbitals does not contribute to vibronic coupling because of the symmetry of the Clebsch–Gordan coefficients. On the other hand, it should be noted that for totally symmetric modes, all the occupied orbitals contribute to vibronic coupling [34, 35, 37].

The orbital vibronic coupling constant is calculated from

$$\langle \psi_j | v_\alpha | \psi_j \rangle = \sum_r \sum_s c_j^{r*} c_j^s \langle r | \mathbf{v}_\alpha | s \rangle = \sum_A \sum_r \sum_s c_j^{r*} c_j^s (\mathbf{M}\mathbf{u}^\alpha)_A \cdot \langle r | \mathbf{v}_A | s \rangle, \quad (84)$$

where  $c_j^s$  denotes a molecular orbital coefficient,  $r, s$  denote basis functions,

$$v_\alpha(\mathbf{r}_i) = \sum_{A=1}^M (\mathbf{M}\mathbf{u}^\alpha)_A \cdot \mathbf{v}_A(\mathbf{r}_i), \quad (85)$$

$$\mathbf{v}_A(\mathbf{r}_i) = \left[ \frac{\partial}{\partial \mathbf{R}_A} \left( \sum_{B=1}^M \frac{Z_B e^2}{4\pi\epsilon_0 |\mathbf{r}_i - \mathbf{R}_B|} \right) \right]_{\mathbf{R}_0} = \left[ -\frac{Z_A e^2 (\mathbf{r}_i - \mathbf{R}_A)}{4\pi\epsilon_0 |\mathbf{r}_i - \mathbf{R}_A|^3} \right]_{\mathbf{R}_0}. \quad (86)$$

$\mathbf{M}\mathbf{u}^\alpha$  is defined in the Appendix.

## 2.4 Atomic Vibronic Coupling Constant

An *atomic vibronic coupling constant* (AVCC) [33] is defined by

$$V_\alpha^A = \left\{ \left\langle \varphi(\mathbf{r}; \mathbf{R}_0) \left| \left( \frac{\partial \mathcal{U}_{ne}}{\partial \mathbf{R}_A} \right)_{\mathbf{R}_0} \right| \varphi(\mathbf{r}; \mathbf{R}_0) \right\rangle + \frac{\partial \mathcal{U}_{nn}}{\partial \mathbf{R}_A} \right\} \cdot \frac{\mathbf{u}_\alpha^A}{\sqrt{M_A}}, \quad (87)$$

which gives the vibronic coupling constant as the summation over  $A$ ,

$$V_\alpha = \sum_{A=1}^M V_\alpha^A. \quad (88)$$

The AVCC has been applied for the vibronic couplings in a carrier-transport material of organic light-emitting diodes (OLED) [33]. We can explain the reason why that material has small vibronic couplings. In one of the phenyl amines, e.g. TPD, although the vibronic coupling density is strongly localized on the nitrogen atoms, the large distributions around the nitrogen atoms are cancelled, because they are distributed almost symmetrically around the atoms with opposite signs [33].

## 2.5 Other Forms of the Vibronic Constant and Their Units

The vibronic coupling constant is expressed in other forms depending upon the definition of the variables or operators of vibrations.

Here we consider the simplest Hamiltonian

$$H = E_0 - \frac{\hbar^2}{2} \frac{\partial^2}{\partial Q_\alpha^2} + \frac{\omega^2}{2} Q_\alpha^2 + V_\alpha Q_\alpha = E_0 + \frac{1}{2} P_\alpha^2 + \frac{\omega^2}{2} Q_\alpha^2 + V_\alpha Q_\alpha. \quad (89)$$

In the form, the Hamiltonian can be written as

$$H = E_0 c^\dagger c + \hbar\omega_\alpha \left( b_\alpha^\dagger b_\alpha + \frac{1}{2} \right) + \lambda_\alpha c^\dagger c (b_\alpha^\dagger + b_\alpha), \quad (90)$$

where  $c^\dagger$  and  $c$  are the creation and annihilation operators of the one-electron state, respectively.  $b_\alpha^\dagger$  and  $b_\alpha$  are the creation and annihilation operators of the vibrational state with vibrational energy  $\hbar\omega$ , respectively.  $\lambda_\alpha$  is the electron-vibration coupling constant, the dimension of which is in energy. Since  $b_\alpha^\dagger$  and  $b_\alpha$  have the following relationship

$$Q_\alpha = \left( \frac{\hbar}{2\omega_\alpha} \right)^{\frac{1}{2}} (b_\alpha^\dagger + b_\alpha), \quad P_\alpha = i \left( \frac{\hbar\omega_\alpha}{2} \right)^{\frac{1}{2}} (b_\alpha^\dagger - b_\alpha), \quad (91)$$

$$\lambda_\alpha = \left( \frac{\hbar}{2\omega_\alpha} \right)^{\frac{1}{2}} V_\alpha. \quad (92)$$

The vibronic coupling is defined by

$$g_\alpha = \frac{\lambda_\alpha}{\hbar\omega_\alpha} = \frac{V_\alpha}{\sqrt{2\hbar\omega^3}}, \quad (93)$$

which is a measure of the strength of the vibronic coupling. The Hamiltonian becomes

$$H = E_0 c^\dagger c + \hbar\omega_\alpha \left[ \left( b_\alpha^\dagger b_\alpha + \frac{1}{2} \right) + g_\alpha c^\dagger c (b_\alpha^\dagger + b_\alpha) \right]. \quad (94)$$



The Rys–Huang factor is another measure of the coupling strength, which is defined by

$$S_\alpha = \frac{\Delta E_\alpha}{\hbar\omega_\alpha} = \frac{V_\alpha^2}{2\hbar\omega^3} = \frac{1}{2}g_\alpha^2, \quad (95)$$

where  $\Delta E_\alpha$  is the reorganization energy of the mode  $\alpha$ , which is equal to the Jahn–Teller stabilization energy  $E_{JT}$  in the degenerate state.  $S_\alpha$  signifies the stabilization energy measured by the vibrational energy.

The atomic unit of the linear vibronic coupling constant  $V_\alpha$  is  $E_h/(m_e^{\frac{1}{2}}a_0) = m_e^{\frac{3}{2}}e^6/(32\pi^3\epsilon_0^3\hbar^4)$ , where  $a_0$  is the Bohr radius,  $a_0 = 4\pi\epsilon_0\hbar^2/m_e e^2$ , and  $E_h$  is the Hartree energy  $E_h = e^2/4\pi\epsilon_0 a_0$ .  $\lambda_\alpha$  in (91) is in the energy unit. The atomic unit of  $\lambda_\alpha$  is  $E_h$ .

### 3 Vibronic Coupling Density

We will now define the vibronic coupling density [34, 35, 37] which enables us to analyze a local property of vibronic coupling.

The vibronic coupling is defined by

$$\mathcal{V}_\alpha = \left( \frac{\partial \mathcal{U}(\mathbf{r}, \mathbf{R})}{\partial Q_\alpha} \right)_{\mathbf{R}_0} = \left( \frac{\partial \mathcal{U}_{ne}(\mathbf{r}, \mathbf{R})}{\partial Q_\alpha} \right)_{\mathbf{R}_0} + \left( \frac{\partial \mathcal{U}_{nn}(\mathbf{R})}{\partial Q_\alpha} \right)_{\mathbf{R}_0}. \quad (96)$$

Note that, for a non-totally symmetric mode,

$$\left( \frac{\partial \mathcal{U}_{nn}(\mathbf{R})}{\partial Q_\alpha} \right)_{\mathbf{R}_0} = 0 \quad (\text{non-totally symmetric mode}). \quad (97)$$

The nuclear-electronic part is

$$\left( \frac{\partial \mathcal{U}_{ne}(\mathbf{r}, \mathbf{R})}{\partial Q_\alpha} \right)_{\mathbf{R}_0} = \left[ \frac{\partial}{\partial Q_\alpha} \left( \sum_A \sum_i \frac{Z_A e^2}{4\pi\epsilon_0 |\mathbf{r}_i - \mathbf{R}_A|} \right) \right]_{\mathbf{R}_0} = \sum_i v_\alpha(\mathbf{r}_i), \quad (98)$$

where the one-electron operator  $v_\alpha(\mathbf{r}_i)$  is defined by

$$v_\alpha(\mathbf{r}_i) = \sum_A \left[ \frac{\partial}{\partial Q_\alpha} \left( \frac{Z_A e^2}{4\pi\epsilon_0 |\mathbf{r}_i - \mathbf{R}_A|} \right) \right]_{\mathbf{R}_0}. \quad (99)$$

The reference nuclear configuration  $\mathbf{R}_0$  satisfies

$$\left\langle \varphi^R(\mathbf{r}, \mathbf{R}_0) \left| \left( \frac{\partial \mathcal{U}_{ne}(\mathbf{r}, \mathbf{R})}{\partial Q_\alpha} \right)_{\mathbf{R}_0} \right| \varphi^R(\mathbf{r}, \mathbf{R}_0) \right\rangle + \left( \frac{\partial \mathcal{U}_{nn}(\mathbf{R})}{\partial Q_\alpha} \right)_{\mathbf{R}_0} = 0 \quad (100)$$

for the electronic wavefunction  $\varphi^R(\mathbf{r}, \mathbf{R}_0)$  of the reference state  $R$ . Thus,

$$V_\alpha = \left\langle \varphi^S(\mathbf{r}, \mathbf{R}_0) \left| \mathcal{V}_\alpha \right| \varphi^S(\mathbf{r}, \mathbf{R}_0) \right\rangle, \quad (101)$$

$$\begin{aligned} &= \left\langle \varphi^S(\mathbf{r}, \mathbf{R}_0) \left| \left( \frac{\partial \mathcal{U}_{ne}(\mathbf{r}, \mathbf{R})}{\partial Q_\alpha} \right)_{\mathbf{R}_0} \right| \varphi^S(\mathbf{r}, \mathbf{R}_0) \right\rangle \\ &\quad - \left\langle \varphi^R(\mathbf{r}, \mathbf{R}_0) \left| \left( \frac{\partial \mathcal{U}_{ne}(\mathbf{r}, \mathbf{R})}{\partial Q_\alpha} \right)_{\mathbf{R}_0} \right| \varphi^R(\mathbf{r}, \mathbf{R}_0) \right\rangle. \end{aligned} \quad (102)$$

Since  $\mathcal{V}_\alpha$  is a sum of the one-electron operators  $v_\alpha$ ,

$$\langle \varphi(\mathbf{r}, \mathbf{R}_0) | \mathcal{V}_\alpha | \varphi(\mathbf{r}, \mathbf{R}_0) \rangle = \frac{1}{N} \sum_i^N \int d^3 \mathbf{r}_i \rho(\mathbf{r}_i) v_\alpha(\mathbf{r}_i) = \int d^3 \mathbf{r}_i \rho(\mathbf{r}_i) v_\alpha(\mathbf{r}_i), \quad (103)$$

where  $\rho^S(\mathbf{r}_1)$  is the electron density of the electronic function  $\varphi^S(\mathbf{r}, \mathbf{R}_0)$  with  $N_S$ -electrons:

$$\rho^S(\mathbf{r}_1) = N_S \int d^3 \mathbf{r}_2 \cdots \int d^3 \mathbf{r}_N \varphi^{S*}(\mathbf{r}, \mathbf{R}_0) \varphi^S(\mathbf{r}, \mathbf{R}_0). \quad (104)$$

Therefore

$$V_\alpha = \int d^3 \mathbf{r}_i \rho^S(\mathbf{r}_i) v_\alpha(\mathbf{r}_i) - \int d^3 \mathbf{r}_i \rho^R(\mathbf{r}_i) v_\alpha(\mathbf{r}_i) = \int d^3 \mathbf{r}_i \Delta \rho(\mathbf{r}_i) v_\alpha(\mathbf{r}_i), \quad (105)$$

where

$$\Delta \rho(\mathbf{r}_i) = \rho^S(\mathbf{r}_i) - \rho^R(\mathbf{r}_i) \quad (106)$$

is the electron density difference between the systems  $S$  and  $R$ . We define *vibronic coupling density* as

$$\eta_\alpha(\mathbf{r}_i) = \Delta \rho(\mathbf{r}_i) v_\alpha(\mathbf{r}_i). \quad (107)$$

The integration of the vibronic coupling density over the three-dimensional space yields the vibronic coupling

$$V_\alpha = \int d^3 \mathbf{r}_i \eta_\alpha(\mathbf{r}_i). \quad (108)$$

## 4 Applications of Vibronic Coupling Density Analysis

### 4.1 Structures

The physical meaning of the diagonal element of vibronic coupling is a force. A change in the electronic state causes a force to act between nuclei and gives rise to a

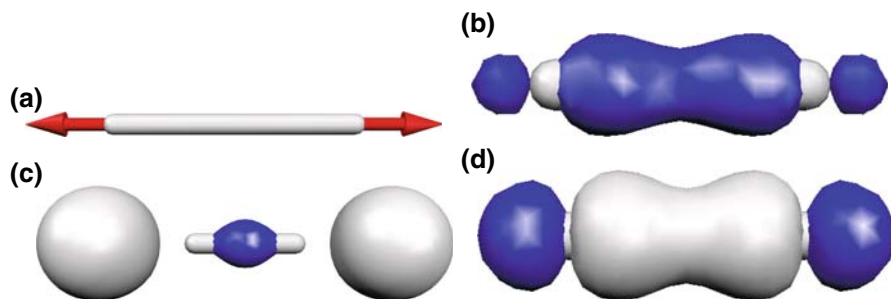


**Fig. 2** Vibronic coupling density analysis for hydrogen molecule anion (ROHF/6-31G with first derivatives). (a) Vibrational mode, (b) vibronic coupling density  $\eta$ , (c) electron density difference  $\Delta\rho$  and (d) potential derivative  $v$ . The blue and grey surfaces denote negative and positive densities, respectively

geometry change. Therefore, we can understand the structural change by analyzing the vibronic coupling density.

As an example, the vibronic coupling density for a hydrogen molecule anion is shown in Fig. 2. It is well-known that when a neutral hydrogen molecule acquires an electron, the chemical bond will be elongated, since the additional electron occupies the anti-bonding LUMO. The vibronic coupling density analysis reveals this driving force. From Fig. 2(b), it is seen that most of the negative vibronic coupling density occurs in the bond region. The vibronic coupling density is a product between the electron density difference  $\Delta\rho$  and the potential derivative  $v$ . In Fig. 2(c), it should be noted that small negative  $\Delta\rho$  occurs in the bond region. This is because the additional electron distribution, which is represented by the grey surfaces in Fig. 2(c), polarizes orbitals occupied by the other electrons. The negative  $\Delta\rho$  couples with the positive potential derivative  $v$ . The orbital polarization due to anionization or orbital relaxation plays a crucial role in vibronic coupling.

The importance of orbital relaxation can be observed in  $\pi$  electron systems. Figure 3 shows the vibronic coupling density analysis for the ethylene anion. Since ethylene has 12 vibrational modes, the results are shown for a reaction mode, which we will define later. Anionization of ethylene also gives rise to an elongation of the double bond. The additional electron occupies the anti-bonding  $\pi$  LUMO. However, as shown in Fig. 3 (a), a negative vibronic coupling density occurs near the carbon atoms in the molecular plane as well, which means that the  $\sigma$  electrons also couple with the bond-elongation motion (Fig. 3 (c)). The additional  $\pi$  electron polarizes the other  $\sigma$  orbitals. This results in the negative  $\Delta\rho$  as shown in Fig. 3 (b).

These simple examples clearly show that orbital relaxation is crucial in vibronic coupling. Therefore, variationally optimized wavefunctions should be employed for vibronic coupling calculations. The frozen orbital approximation is not suitable for calculation [35].

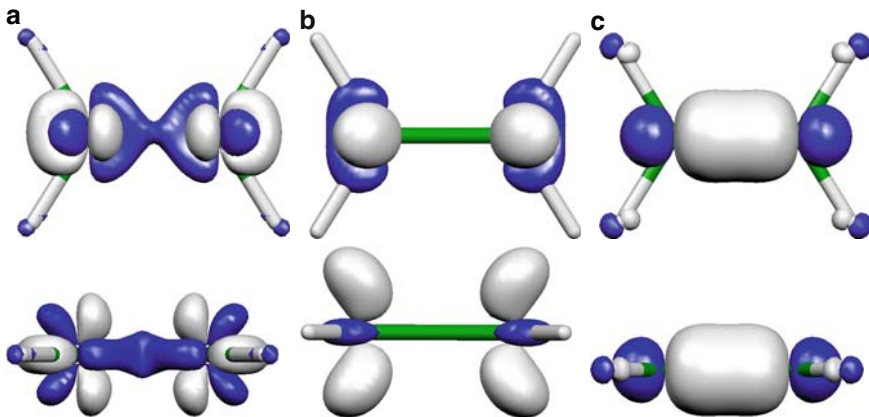


**Fig. 3** Vibronic coupling density for the reaction mode of ethylene anion (ROHF/6-31G+ first derivatives). (a) Vibronic coupling density, (b) electron density difference, and (c) potential derivative

## 4.2 Relationship to Fukui Function and Nuclear Fukui Function

In this subsection, we consider an  $N$ -electron system as system  $R$  and an  $(N + 1)$ -electron system as system  $S$ .

According to the Hohenberg–Kohn theorem, a ground state electronic energy within the BO approximation is a functional of the electron density  $\rho(\mathbf{r}_i)$  and the potential  $u(\mathbf{r}_i)$ :

$$E[\rho, u] = F[\rho] + U[\rho, u], \quad (109)$$

where

$$u(\mathbf{r}_i) = \sum_{A=1}^M -\frac{Z_A e^2}{4\pi\epsilon_0 |\mathbf{r}_i - \mathbf{R}_A|}, \quad (110)$$

$$F[\rho] = \langle \varphi | \mathcal{T}_e + \mathcal{U}_{ee} | \varphi \rangle = T_e[\rho] + U_{ee}[\rho], \quad (111)$$

and

$$U[\rho] = U_{ne}[\rho, u] + U_{nn}[u] \quad (112)$$

with

$$U_{ne}[\rho, u] = \int \rho(\mathbf{r}_i) u(\mathbf{r}_i) d^3 \mathbf{r}_i \quad (113)$$

and

$$U_{nn}[u] = \frac{1}{2} \sum_B' \int u(\mathbf{r}_i) Z_B \delta(\mathbf{r}_i - \mathbf{R}_B) d^3 \mathbf{r}_i. \quad (114)$$

$\sum_B'$  signifies a summation of  $B$  avoiding  $\mathbf{R}_B - \mathbf{R}_A = 0$  in the denominator. The total differential of  $E[\rho, u]$  is

$$dE = \int \left( \frac{\delta E}{\delta \rho} \right) d\rho(\mathbf{r}_i) d^3\mathbf{r}_i + \int \left( \frac{\delta E}{\delta u} \right) du(\mathbf{r}_i) d^3\mathbf{r}_i, \quad (115)$$

$$= \mu dN + \int \rho(\mathbf{r}_i) du(\mathbf{r}_i) d^3\mathbf{r}_i. \quad (116)$$

The chemical potential  $\mu$  is defined by

$$\mu = \left( \frac{\partial E}{\partial N} \right)_u. \quad (117)$$

The total differential of the chemical potential  $\mu = \mu[N, u]$  is

$$d\mu = \left( \frac{\partial \mu}{\partial N} \right)_u dN + \int \left[ \frac{\delta \mu}{\delta u(\mathbf{r}_i)} \right]_N du(\mathbf{r}_i) d^3\mathbf{r}_i. \quad (118)$$

An absolute hardness  $\eta$  and Fukui function  $f(\mathbf{r}_i)$  are defined by

$$2\eta = \left( \frac{\partial \mu}{\partial N} \right)_u \quad (119)$$

and

$$f(\mathbf{r}_i) = \left[ \frac{\delta \mu}{\delta u(\mathbf{r}_i)} \right]_N = \left[ \frac{\partial \rho(\mathbf{r}_i)}{\partial N} \right]_u. \quad (120)$$

Therefore,

$$d\mu = 2\eta dN + \int f(\mathbf{r}_i) du(\mathbf{r}_i) d^3\mathbf{r}_i. \quad (121)$$

The Fukui function is approximated by the electron density difference using the finite difference method,

$$f(\mathbf{r}_i) = \left[ \frac{\partial \rho(\mathbf{r}_i)}{\partial N} \right]_u \approx \rho^S(\mathbf{r}_i) - \rho^R(\mathbf{r}_i) = \Delta\rho(\mathbf{r}_i). \quad (122)$$

Furthermore, if the frozen orbital approximation is applicable,

$$f(\mathbf{r}_i) \approx \rho_{frontier}(\mathbf{r}_i), \quad (123)$$

where  $\rho_{frontier}(\mathbf{r}_i)$  is the frontier electron density.

Since a deformation of the potential  $\delta u$  can be expressed in terms of a set of changes of the normal coordinates  $\{dQ_1, \dots, dQ_\alpha, \dots, dQ_{3M-5} \text{ or } 3M-6\}$ , the total differential of energy can be written as

$$dE = \mu dN + \sum_{\alpha} \left( \frac{\partial U}{\partial Q_{\alpha}} \right)_N dQ_{\alpha}. \quad (124)$$

Furthermore, for the chemical potential

$$d\mu = 2\eta dN + \sum_{\alpha} \left( \frac{\partial \mu}{\partial Q_{\alpha}} \right)_N dQ_{\alpha}. \quad (125)$$

From the mixed derivative of  $E$  with respect to  $N$  and  $Q_{\alpha}$ , the Maxwell relation can be obtained. Assuming  $E$  is continuous with respect to  $N$  and  $Q_{\alpha}$ ,

$$\left[ \frac{\partial}{\partial N} \left( \frac{\partial E}{\partial Q_{\alpha}} \right)_N \right]_{\mathbf{R}_0} = \left[ \frac{\partial}{\partial Q_{\alpha}} \left( \frac{\partial E}{\partial N} \right)_{\mathbf{R}_0} \right]_N = \left( \frac{\partial \mu}{\partial Q_{\alpha}} \right)_N. \quad (126)$$

For the left-hand-side, according to the Hellmann-Feynman theorem,

$$\left( \frac{\partial E}{\partial Q_{\alpha}} \right)_N = \left\langle \varphi \left| \frac{\partial \mathcal{U}}{\partial Q_{\alpha}} \right| \varphi \right\rangle = \int \rho(\mathbf{r}_i) v(\mathbf{r}_i) d^3 \mathbf{r}_i + \left( \frac{\partial U_{nn}}{\partial Q_{\alpha}} \right)_{\mathbf{R}_0} = V_{\alpha}(N). \quad (127)$$

Thus we obtain the Maxwell relation as

$$\left( \frac{\partial V_{\alpha}}{\partial N} \right)_{\mathbf{R}_0} = \left( \frac{\partial \mu}{\partial Q_{\alpha}} \right)_N. \quad (128)$$

The left-hand-side can be approximated using the finite-difference method,

$$\left( \frac{\partial V_{\alpha}}{\partial N} \right)_{\mathbf{R}_0} \approx V_{\alpha}(N+1) - V_{\alpha}(N) = V_{\alpha}, \quad (129)$$

since  $\mathbf{R}_0$  is a reference stationary point. Therefore,

$$\left( \frac{\partial \mu}{\partial Q_{\alpha}} \right)_N = V_{\alpha} = \int \eta_{\alpha}(\mathbf{r}_i) d^3 \mathbf{r}_i. \quad (130)$$

Thus, the vibronic coupling constant  $V_{\alpha}$  can be regarded as a change in the chemical potential against the deformation  $dQ_{\alpha}$ .

From (125), we obtain

$$d\mu = 2\eta dN + \sum_{\alpha} \int \eta_{\alpha}(\mathbf{r}_i) d^3 \mathbf{r}_i dQ_{\alpha}. \quad (131)$$

Instead of the normal modes, when we concentrate on a certain reaction path mode that can be expressed as

$$dQ_{\alpha} = \lambda_{\alpha} ds, \quad (132)$$

$$\lambda_{\alpha} = V_{\alpha} / \sqrt{\sum_{\alpha} V_{\alpha}^2}, \quad (133)$$

where  $\lambda_{\alpha}$  describes the contribution of the mode  $\alpha$  to the reaction path  $s$ . Equation (131) can be written as

$$d\mu = 2\eta dN + \int \eta_s(\mathbf{r}_i) ds d^3\mathbf{r}_i, \quad (134)$$

where

$$\eta_s(\mathbf{r}_i) = \sum_{\alpha} \lambda_{\alpha} \eta_{\alpha}(\mathbf{r}_i). \quad (135)$$

Comparing (134) with (121), we can again obtain

$$\eta_s(\mathbf{r}_i) = f(\mathbf{r}_i) \frac{du}{ds} \approx \Delta\rho(\mathbf{r}_i) v_s(\mathbf{r}_i). \quad (136)$$

In order to predict a reactive region that gives a large  $|d\mu|$ , it is necessary but not sufficient condition for Fukui function  $f(\mathbf{r}_i)$  to take a large value in the reactive region. The potential derivative  $v_s(\mathbf{r}_i)$  also plays an important role in  $|d\mu|$ . Consequently, the vibronic coupling density for the reactive mode  $s$  can be a chemical reactivity index that can predict a large  $|d\mu|$  region.

For example, Fig. 4 shows the vibronic coupling density of the naphthalene cation for the reaction mode  $s$ , which is defined by the steepest direction. We can find that the vibronic coupling density has a large value near the  $\alpha$ -carbons. This means that the motion of the  $\alpha$ -carbon couples with the hole. This is consistent with the prediction of the frontier orbital theory.

Using the nuclear Fukui function [6, 15] defined by

$$\phi_{XA} = -\left(\frac{\partial U}{\partial X_A}\right)_N, \quad \phi_{YA} = -\left(\frac{\partial U}{\partial Y_A}\right)_N, \quad \phi_{ZA} = -\left(\frac{\partial U}{\partial Z_A}\right)_N, \quad (137)$$

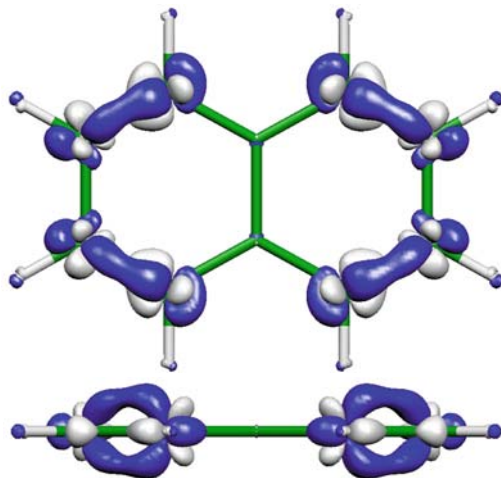


**Fig. 4** Vibronic coupling density of the naphthalene cation. Blue and grey surfaces denote negative and positive densities, respectively

the total differential of the chemical potential is written as

$$d\mu = 2\eta dN - \sum_A (\phi_{XA} dX_A + \phi_{YA} dY_A + \phi_{ZA} dZ_A). \quad (138)$$

The mass-weighted normal coordinate (see Appendix) is expressed in terms of the nuclear coordinate  $\mathbf{R}$  as

$$Q_\alpha = \sum_A \mathbf{A}_{\alpha X_A} X_A + \mathbf{A}_{\alpha Y_A} Y_A + \mathbf{A}_{\alpha Z_A} Z_A. \quad (139)$$

Therefore,

$$d\mu = 2\eta dN + \sum_\alpha V_\alpha \sum_A (\mathbf{A}_{\alpha X_A} dX_A + \mathbf{A}_{\alpha Y_A} dY_A + \mathbf{A}_{\alpha Z_A} dZ_A), \quad (140)$$

and

$$\phi_{XA} = - \sum_\alpha V_\alpha \mathbf{A}_{\alpha X_A}, \quad \phi_{YA} = - \sum_\alpha V_\alpha \mathbf{A}_{\alpha Y_A}, \quad \phi_{ZA} = - \sum_\alpha V_\alpha \mathbf{A}_{\alpha Z_A}. \quad (141)$$

The relationship between the Jahn-Teller system and the Fukui function has been discussed by Balawender *et al.* [6].

## 5 Vibronic Coupling in Fullerene Ions and Future Prospects

Since  $C_{60}$  has  $I_h$  symmetry with fivefold degenerate  $h_u$  HOMO levels and threefold degenerate  $t_{1u}$  LUMO levels, the Jahn-Teller effect occurs in the anionic or cationic states. For example, as the electronic state of  $C_{60}^-$  has  $T_{1u}$  symmetry, two  $a_g$  and eight  $h_g$  vibrational modes couple to the  $T_{1u}$  state. In the case of  $C_{60}^+$ , the electronic state has  $H_u$  symmetry and the vibrational modes that couple to the  $H_u$  electronic state are two  $a_g$ , six  $g_g$  and eight  $h_g$  modes [14]. To understand the Jahn-Teller effect in  $C_{60}$  ions, the vibronic coupling constants have been estimated using experimental and theoretical methods [20].

Gunnarsson *et al.* measured photoemission spectra of  $C_{60}^-$  in the gas phase and extracted the vibronic coupling constants (Tables 1 and 2) [21]. To estimate the vibronic coupling constants, they diagonalized the model Hamiltonian numerically and calculated the photoemission spectrum [9, 27]. The wavefunction of the harmonic oscillators were used as a basis. The cut-off of the occupation number of each harmonic oscillator state was five. Their model Hamiltonian included the vibronic couplings of two  $a_g$  modes and eight  $h_g$  modes. The diagonalization of the model Hamiltonian was performed with some approximations. First, they assumed  $T = 0$  because the vibrational temperature  $\sim 200$  K is lower than the temperature of the lowest-frequency vibrational mode  $\sim 400$  K. Then they neglected



the emitted electron by using the sudden approximation and assuming that the dipole matrix elements do not depend on the final state. The Gaussian function was used to take the width of the spectrum into consideration. In addition, because of the difficulty in determining all vibronic coupling with no ambiguity, they also used the calculated vibronic coupling constants of the two  $a_g$  modes using the LDA [4]. Their fit agrees well with the photoemission spectrum in low energy region.

Using a similar method, Alexandrov and Kabanov also estimated the vibronic coupling constants from the photoemission spectrum obtained by Gunnarsson *et al.* (Tables 1 and 2) [1]. Their Hamiltonian includes the linear vibronic coupling of the  $a_g(2)$  mode and eight  $h_g$  modes. The cut-off of the occupation number of each harmonic oscillator state was four. They considered not only vibronic coupling but also polaron-exciton coupling by adding a spectral function shifted by the energy of an exciton ( $\simeq 0.5$  eV) to the spectral function:

$$I(\omega) = I_{pol}(\omega) + \alpha I_{pol}(\omega + \omega_{ex}), \quad (142)$$

where  $I(\omega)$  is the total spectral function,  $I_{pol}$  is a spectral function derived by diagonalizing the model Hamiltonian,  $\alpha$  is the polaron-exciton coupling constant and  $\omega_{ex}$  is the energy of an exciton. A Gaussian function was used for the width of the spectrum. Furthermore, they include the damping of an exciton  $\gamma_{ex} \simeq 580 \text{ cm}^{-1}$  in the second term.

They found that the fit to the low and high energy regions of the photoemission spectrum was good. They concluded that the vibronic coupling of the  $a_g(2)$  mode is stronger than the value given by Gunnarsson *et al.* and, contrary to the results by Gunnarsson *et al.*, the vibronic coupling of the high-frequency  $h_g(7)$  and  $h_g(8)$  modes is negligible. However, this difference is due to the ambiguity in determining the coupling constants. Alexandrov and Kabanov might have overestimated the coupling constant of the  $a_g(2)$  mode.

The photoemission spectra of  $C_{60}$  have also been measured [11, 12] and calculated [29] using the calculated coupling constants [28]. Manini *et al.* used a model Hamiltonian that includes the linear vibronic coupling of two  $a_g$ , six  $g_g$  and eight  $h_g$  modes. They used the sudden approximation and assumed a thermal equilibrium and performed a DFT calculation using the LDA [28] to obtain the vibronic coupling constants in  $C_{60}^+$ . The calculated photoemission spectrum was in good agreement with the experimental spectrum.

Manini *et al.* also calculated the vibronic coupling constants in  $C_{60}^-$  using the same method (Tables 1 and 2). Although their results for  $C_{60}^+$  agreed with the photoemission spectrum, the stabilization energy of  $C_{60}^-$  was smaller than the experimental value [1, 21].

The vibronic coupling constants have been estimated from the Raman spectra of  $K_3C_{60}$  [42] and neutron spectroscopy [31] using Allen's formula [2, 3]. However, the Jahn-Teller effect is not considered in Allen's formula [21], and the density of states at the Fermi level per spin and molecule used in the formula is not precisely known.

As described above, there are two problems in determining the vibronic coupling constants in  $C_{60}$  ions. The first problem involves the analysis of experiments, where ambiguity remains. Second, the agreements of the vibronic coupling constants and Jahn-Teller stabilization energies derived from experiments and theoretical calculations are not good. Therefore, the calculation of the vibronic coupling constants in  $C_{60}$  ions is still an unsolved problem.

Better experimental spectra should be used to estimate the vibronic coupling constants. Recently, a high resolution photoemission spectra has been obtained by Wang *et al.* [41]. However, these authors did not estimate the vibronic coupling constants. Since they measured the spectrum at low temperature, its widths are narrower than those obtained by Gunnarsson *et al.*, and the fine structures can be clearly observed. These results show that a better estimation of the coupling constants is possible.

Experimental values should be compared with reliable calculated values. From our point of view, as presented in the previous sections, the following three important points are involved in the calculation of vibronic coupling constants in Jahn-Teller molecules. (1) Symmetry of the wavefunction: when the spatial symmetry of the wavefunction is broken, the Wigner-Eckert theorem is no longer satisfied. In addition, potential surfaces split at the Jahn-Teller crossing point. As a result, the absolute values of the vibronic coupling constants become smaller. (2) Hellmann-Feynman theorem: when the wavefunction is not variationally optimized, it does not satisfy the Hellmann-Feynman theorem. Accordingly, the energy gradient is not equal to the vibronic coupling constant. (3) Orbital relaxation: frozen orbital approximation is not valid for vibronic coupling calculations.

**Table 1** Vibronic coupling  $k = v/\sqrt{\hbar\omega^3}$  in  $C_{60}$  anions. The coupling constant  $V$ , is same as  $I_E$  defined in [26]

Mode	[21] <sup>a</sup>	[1] <sup>a</sup>	[28] <sup>b</sup>	[4] <sup>c</sup>	[42] <sup>d</sup>	[39] <sup>e</sup>	[17] <sup>f</sup>
$a_g(1)$	0.14	0.000	0.157	0.14			
$a_g(2)$	0.42	0.806	0.340	0.42			
$h_g(1)$	0.82	0.852	0.412	0.32	1.31	0.33	0.20
$h_g(2)$	0.94	0.925	0.489	0.36	0.67	0.15	0.41
$h_g(3)$	0.42	0.506	0.350	0.20	0.17	0.12	0.10
$h_g(4)$	0.47	0.474	0.224	0.19	0.19	0.00	0.31
$h_g(5)$	0.33	0.283	0.193	0.16	0.09	0.22	0.10
$h_g(6)$	0.20	0.028	0.138	0.25	0.09	0.00	0.12
$h_g(7)$	0.34	0.000	0.315	0.37	0.16	0.45	0.28
$h_g(8)$	0.38	0.000	0.289	0.38	0.14	0.25	0.21

<sup>a</sup> Extracted values from the photoemission spectra in  $C_{60}^-$ .

<sup>b</sup> Calculated values in  $C_{60}^-$  using LDA.

<sup>c</sup> Calculated values of  $a_g$  modes in  $C_{60}^-$  and of  $h_g$  modes in  $K_3C_{60}$  using LDA.

<sup>d</sup> Raman scattering experiment in  $K_3C_{60}$ .

<sup>e</sup> Calculated values in  $C_{60}^-$  using MNDO.

<sup>f</sup> Calculated values in  $C_{60}^{3-}$  using LDA.

**Table 2** Vibronic coupling and Jahn-Teller stabilization energy in  $C_{60}$  anions ( $10^{-4}$  a.u.). The relationship between the dimensionless vibronic coupling constant  $k$  and the vibronic coupling constant  $V$  in a.u. is  $k = V/\sqrt{\hbar\omega^3}$ .  $E_{JT}$  is defined as  $E_{JT} = V^2/2\omega^2$

Mode	[21] <sup>a</sup>	[1] <sup>a</sup>	[28] <sup>b</sup>	[4] <sup>c</sup>	[42] <sup>d</sup>	[39] <sup>e</sup>	[17] <sup>f</sup>
$a_g(1)$	0.15	0.000	0.171	0.14			
$a_g(2)$	2.33	4.419	1.942	2.31			
$h_g(1)$	0.36	0.370	0.169	0.15	0.57	0.14	0.07
$h_g(2)$	0.84	0.822	0.423	0.36	0.58	0.14	0.33
$h_g(3)$	0.77	0.931	0.655	0.39	0.30	0.22	0.13
$h_g(4)$	0.99	0.993	0.479	0.41	0.41	0.00	0.62
$h_g(5)$	1.15	1.003	0.703	0.57	0.33	0.93	0.34
$h_g(6)$	0.85	0.122	0.611	1.10	0.38	0.00	0.49
$h_g(7)$	1.78	0.000	1.702	1.88	0.86	2.82	1.42
$h_g(8)$	2.29	0.000	1.779	2.08	0.82	1.73	1.20
$E_{JT}$	32.4	23.13	14.06	15.0	18.1	12.3	8.21

<sup>a</sup> Extracted values from the photoemission spectra in  $C_{60}^-$ .

<sup>b</sup> Calculated values in  $C_{60}^-$  using LDA.

<sup>c</sup> Calculated values of  $a_g$  modes in  $C_{60}^-$  and of  $h_g$  modes in  $K_3C_{60}$  using LDA.

<sup>d</sup> Raman scattering experiment in  $K_3C_{60}$ .

<sup>e</sup> Calculated values in  $C_{60}^-$  using MNDO.

<sup>f</sup> Calculated values in  $C_{60}^{3-}$  using LDA.

## 6 Conclusion

Vibronic coupling density analysis provides a local picture of vibronic coupling. With help of this analysis, we can design a new molecule with desired vibronic couplings, e.g. a small vibronic coupling in the case of carrier-transport materials. The precise calculation of the vibronic coupling constant and vibronic coupling density analysis will enable us to realize the engineering of vibronic coupling: *vibronics* [38].

## Appendix: Normal Mode

The displacement from the equilibrium geometry  $\mathbf{R}_0$  is written as

$$\Delta\mathbf{R} = (\dots, X_{Ax}, X_{Ay}, X_{Az}, \dots) = (\dots, X_{Ar}, \dots) = \mathbf{X}, \quad (r = x, y, z). \quad (143)$$

The conjugate momentum is defined by  $P_{Ar} = -i\hbar\partial/\partial X_{Ar}$ . The Hessian matrix is the second derivatives of  $E(\mathbf{R})$  with respect to the displacement,

$$K_{Ar, Bs} = \left( \frac{\partial^2 E(\mathbf{R})}{\partial X_{Ar} \partial X_{Bs}} \right)_{\mathbf{R}_0}. \quad (144)$$

The Hamiltonian is written as

$$\mathcal{H}_{vib} = \frac{1}{2} \left[ \sum_{A=1}^M \sum_{r=x,y,z} \frac{P_{Ar}^2}{M_A} + \sum_{A=1}^M \sum_{r=x,y,z} \sum_{B=1}^M \sum_{s=x,y,z} X_{Ar} K_{Ar,Bs} X_{Bs} \right]. \quad (145)$$

Passing from  $\mathbf{X}$  to the mass-weighted coordinate  $\mathbf{X}' = (\dots, \sqrt{M_A} X_{Ar}, \dots)$ , the Hamiltonian becomes

$$H_{vib} = \frac{1}{2} \left[ \mathbf{P}'^t \mathbf{P}' + \mathbf{X}'^t \mathbf{K}' \mathbf{X}' \right], \quad (146)$$

where  $\mathbf{P}' = (\dots, P_{Ar}/\sqrt{M_A}, \dots)$ , and  $(\mathbf{K}')_{Ar,Bs} = K_{Ar,Bs}/\sqrt{M_A M_B}$ .

Since Hessian  $\mathbf{K}'$  is a real symmetric matrix, its eigenvalue problem

$$\mathbf{K}' \mathbf{u}^\alpha = \omega_\alpha^2 \mathbf{u}^\alpha \quad (147)$$

yields real eigenvalues  $\omega_\alpha^2$  and orthonormal eigenvectors, or *normal modes*  $\mathbf{u}^\alpha$ ,  $\mathbf{u}^\alpha \cdot \mathbf{u}^\beta = \delta_{\alpha\beta}$ . The displacement can be expressed by

$$\mathbf{X}' = \sum_{\alpha} \mathbf{u}^\alpha Q_{\alpha}, \quad (148)$$

where  $Q_{\alpha}$  is a *mass-weighted normal coordinate*. Using the normal coordinate, the potential term becomes

$$\mathbf{X}'^t \mathbf{K}' \mathbf{X}' = \sum_{\alpha} (\mathbf{u}^\alpha)^t Q_{\alpha} \mathbf{K}' \sum_{\beta} \mathbf{u}^\beta Q_{\beta} = \sum_{\alpha,\beta} \delta_{\alpha\beta} \omega_{\beta}^2 Q_{\alpha} Q_{\beta} = \sum_{\alpha} \omega_{\alpha}^2 Q_{\alpha}^2. \quad (149)$$

The kinetic term becomes

$$\sum_{Ar} P_{Ar}'^2 = \sum_{\alpha} -\hbar^2 \frac{\partial^2}{\partial Q_{\alpha}^2}, \quad (150)$$

since  $\mathbf{u}^\alpha$  is orthonormal. Thus the vibrational Hamiltonian is written as

$$H_{vib} = \frac{1}{2} \sum_{\alpha} \left[ -\hbar^2 \frac{\partial^2}{\partial Q_{\alpha}^2} + \omega_{\alpha}^2 Q_{\alpha}^2 \right]. \quad (151)$$

In the  $\mathbf{X}$  coordinate,

$$\mathbf{X} = \mathbf{M} \mathbf{X}' = \sum_{\alpha} \mathbf{M} \mathbf{u}^\alpha Q_{\alpha}, \quad (152)$$

where  $\mathbf{M}$  is a diagonal matrix with  $(\mathbf{M})_{Ar,Ar} = 1/\sqrt{M_A}$ . The displacement for the mode  $\alpha$  can be rewritten as

$$\mathbf{Mu}^\alpha Q_\alpha = \mathbf{v}^\alpha Q_\alpha = \frac{\mathbf{v}^\alpha}{|\mathbf{v}^\alpha|} |\mathbf{v}^\alpha| Q_\alpha = \frac{\mathbf{v}^\alpha}{|\mathbf{v}^\alpha|} q_\alpha, \quad (153)$$

where  $\mathbf{v}^\alpha = \mathbf{Mu}^\alpha$  is not normalized, and  $q_\alpha = (1/\sqrt{\mu_\alpha}) Q_\alpha$ . The *reduced mass*  $\mu_\alpha$  is defined by

$$\mu_\alpha = \frac{1}{|\mathbf{v}^\alpha|^2} = \frac{1}{|\mathbf{Mu}^\alpha|^2}. \quad (154)$$

**Acknowledgements** TS gratefully acknowledges Prof. Arnout Ceulemans and Prof. Liviu F. Chibotaru for valuable discussions on the dynamic Jahn-Teller problem and vibronic couplings in fullerene ions. Numerical calculation was partly performed in the Supercomputer Laboratory of Kyoto University and Research Center for Computational Science, Okazaki, Japan. This work was supported by Grant-in-Aid for Scientific Research (C) (20550163), Priority Areas “Molecular theory for real system” (20038028) from Japan Society for the Promotion of Science (JSPS), and the JSPS-FWO (Fonds voor Wetenschappelijk Onderzoek-Vlaanderen) Joint Research Project.

## References

1. A.S. Alexandrov, V.V. Kabanov, JETP Lett. **62** 937 (1995).
2. P.B. Allen, Phys. Rev. B **6** 2577 (1972)
3. P.B. Allen, Solid State Commun. **14** 937 (1974)
4. V.P. Antropov, O. Gunnarsson, A.I. Liechtenstein, Phys. Rev. B **48** 7651 (1993)
5. B.E., Applegate, T.A., Miller, T.A., Barckholtz, J. Chem. Phys. **114** 4855 (2001)
6. R. Balawender, F.D. Proft, P. Geerlings, J. Chem. Phys. **114** 4441 (2001)
7. I.B. Bersuker, The Jahn-Teller Effect and Vibronic Interactions in Modern Chemistry (Plenum, New York, 1984)
8. I.B. Bersuker, The Jahn-Teller Effect (Cambridge University Press, Cambridge, 2006)
9. I.B. Bersuker, V.Z. Polinger, Vibronic Interactions in Molecules and Crystals. (Springer, Berlin, 1989)
10. W. Borden, E. Davidson, Acc. Chem. Res. **29**(2) 67 (1996)
11. P.A. Brühwiler, A.J. Maxwell, P. Baltzer, S. Andersson, D. Arvanitis, L. Karlsson, N. Mårtensson, Chem. Phys. Lett. **279**, 85 (1997)
12. S.E. Canton, A.J. Yench, E. Kukk, J.D. Bozek, M.C.A. Lopes, G. Snell, N. Berrah, Phys. Rev. Lett. **89** 045502 (2002)
13. R. Carbo, J.M. Riera, A General SCF Theory (Springer, Berlin, 1978)
14. C.C. Chancey, M.C.M. O'Brien, The Jahn-Teller Effect in  $C_{60}$  and Other Icosahedral Complexes (Princeton University Press, Princeton, 1997)
15. M.H. Cohen, J. Chem. Phys. **101** 8988 (1994)
16. W. Domcke, D.R. Yarkony, H. Köppel, (eds.) Conical Intersections: Electronic Structure, Dynamics, and Spectroscopy. (World Scientific, Singapore, 2003)
17. J.C.R. Faulhaber, D.Y.K. Ko, P.R. Briddon, Phys. Rev. B **48** 661 (1993)
18. R. Feynman, Phys. Rev. **56** 340 (1939)
19. G. Fischer, Vibronic Coupling : The Interaction between the Electronic and Nuclear Motions. (Academic, London, 1984)
20. O. Gunnarsson, Rev. Mod. Phys. **69** 575 (1997)
21. O. Gunnarsson, H. Handschuh, P.S. Bechthold, B. Kessler, G. Ganteför, W. Eberhardt, Phys. Rev. Lett. **74** 1875 (1995)
22. H. Hellmann, Einführung in die Quantenchemie. (Franz Deuticke, Leipzig, 1937)
23. H. Hinze, J. Chem. Phys. **59** 6424 (1973)

24. T. Inui, Y. Tanabe, Y. Onodera, *Group Theory and Its Applications in Physics*. (Springer, Berlin, 1996)
25. H.A. Jahn, E. Teller, *Proc. R. Soc. Lond. Ser. A* **161** 220 (1937)
26. M. Lannoo, G.A. Baraff, M. Schlüter, D. Tomanek, vacancy. *Phys. Rev. B* **44** 12106 (1991)
27. H.C. Longuet-Higgins, U. Öpik, M.H.L. Pryce, R.A. Sack, *Proc. R. Soc. Lond. Ser. A* **244**, 1 (1958)
28. N. Manini, A.D. Carso, M. Fabrizio, E. Tosatti, *Philos. Mag. B* **81** 793 (2001)
29. N. Manini, P. Gattari, E. Tosatti, *Phys. Rev. Lett.* **91** 196402 (2003)
30. H. Nakatsuji, K. Kanda, T. Yonezawa, *Chem. Phys. Lett.* **75** 340 (1980)
31. K. Prassides, C. Christides, M.J. Rosseinsky, J. Tomkinson, D.W. Murphy, R.C. Haddon, *Europhys. Lett.* **19** 629 (1992)
32. T. Sato, L.F. Chibotaru, A. Ceulemans, *J. Chem. Phys.* **122** 054104 (2005)
33. T. Sato, K. Shizu, T. Kuga, K. Tanaka, H. Kaji, *Chem. Phys. Lett.* **458** 152 (2008)
34. T. Sato, K. Tokunaga, K. Tanaka, *J. Chem. Phys.* **124** 024314 (2006)
35. T. Sato, K. Tokunaga, K. Tanaka, *J. Phys. Chem. A* **112** 758 (2008)
36. A. Szabo, N.S. Ostlund, *Modern Quantum Chemistry: Introduction to Advanced Electronic Structure Theory*. (McGraw-Hill, New York, 1989)
37. K. Tokunaga, T. Sato, K. Tanaka, *J. Chem. Phys.* **124** 154303 (2006)
38. K. Tokunaga, T. Sato, K. Tanaka, *J. Mol. Struct.* **838** 116 (2007)
39. C.M. Varma, J. Zaanen, K. Raghavachari, *Science* **254** 989 (1991)
40. W.C. Johnson Jr, O.E. Weigang Jr. *J. Chem. Phys.* **63** 2135 (1975)
41. X. Wang, H. Woo, L. Wang, *J. Chem. Phys.* **123** 051106 (2005)
42. J. Winter, H. Kuzmany, *Phys. Rev. B* **53** 655 (1996)

# A New Method to Describe the Multimode Jahn–Teller Effect Using Density Functional Theory

Matija Zlatar, Carl-Wilhelm Schl pfer, and Claude Daul

**Abstract** A new method for the analysis of the adiabatic potential energy surfaces of Jahn–Teller (JT) active molecules is presented. It is based on the analogy between the JT distortion and reaction coordinates. Within the harmonic approximation the JT distortion can be analysed as the linear combination of all totally symmetric normal modes in the low symmetry minimum energy conformation. Contribution of the normal modes to the distortion, their energy contribution to the JT stabilisation energy, the forces at high symmetry cusp and detailed distortion path can be estimated quantitatively. This approach gives direct insight into the coupling of electronic structure and nuclear displacements. Further more, it is reviewed how multideterminantal DFT can be applied for the calculation of the JT parameters. As examples the results for  $\text{VCl}_4$ , cyclopentadienyl radical and cobaltocene are given.

## 1 Introduction

The Jahn–Teller (JT) theorem states that a molecule with a degenerate electronic ground state spontaneously distorts along non-totally symmetric vibrational coordinates. This removes the degeneracy and lowers the energy. At the point of electronic degeneracy the Born–Oppenheimer (BO) [18], or adiabatic, approximation breaks down and there is vibronic coupling between electronic states and nuclear motion. The theory underlying the JT and related effects, is well known and documented in detail [15]. It is based on a perturbation expression of the potential energy surface near the point of electronic degeneracy. The coefficients in the expression of potential energy are called vibronic coupling coefficients, and they have a physical meaning. One of the goals in the analysis of JT systems is the determination of these parameters, and rationalizing the microscopic origin of the problem.

Despite the big advance in various experimental techniques used to study the JT effect, it is not sufficient to understand the latter based only on experimental data. Computational methods are, thus, necessary to get deeper insight into the system under study and to predict the properties of unknown ones. Traditional first principles methods can still be used even where non-adiabatic effects are important, if the BO approximation is reintroduced by the perturbation approach. Density

Functional Theory (DFT) is the most common theoretical method in quantum chemistry today, but there are still erroneous beliefs that it is not able to handle degenerate states. E.g. Bersuker [14] and Kaplan [49] emphasised that DFT techniques are not adequate to reproduce vibronic effects. In contrary, DFT can be applied to both, degenerate and excited states, as formally proved by the reformulation of the original Hohenberg–Kohn theorems—constrained search method and finite temperature DFT [63]. Further more, Kohn–Sham (KS) DFT, as the most common practical way of using DFT, is based on the equations equivalent and fully compatible with equations used in wave-function based methods. Conventional single determinant DFT has been extended to handle the multiplet problem [27, 84]. A method based on this multideterminantal DFT, for the study of the JT systems was developed in our group [21] and reviewed in this article. The theory behind the DFT is well elaborated and will not be presented in this review. The reader interested in this subject is referred to a several good and comprehensive reviews or books e.g. [31, 51, 63] and to the references therein.

The JT effect is dictated by the molecular symmetry. Group theory allows identifying the symmetry of the JT distortion, which is for simple molecules usually determined by one single normal coordinate that satisfies the symmetry requirements. In complex molecules, the JT distortion is a superposition of many different normal coordinates. In the JT semantics this is called the multimode problem. In this review the treatment of this problem using DFT recently proposed by us [86] is presented. The essence of our proposition is to express JT active distortion as a linear combination of all totally symmetric normal modes in the low symmetry minimum energy conformation. It is based on the fact that JT distortion is analogous to a reaction coordinate. The reaction coordinate belongs to the totally symmetric irreducible representation of the molecular point group of the energy minimum conformation, as proved by Bader [9–11] and Pearson [64, 65]. This is so even if a complicated nuclear motion is considered for the reaction coordinate. The JT distortion can always be written as a sum of totally symmetric normal modes. A detailed analysis of the different contributions of the normal modes is of interest, because it gives direct insight into the coupling of electronic structure and nuclear movements. This is of a particular interest in various fields of chemistry, e.g. in coordination, bioinorganic, material chemistry, or in discussing reaction mechanisms.

This review is organized in the following way. In Sect. 2 the vibronic coupling theory used in this work will be presented, with an emphasise on the different aspects and meaning of vibronic coupling constants. Several simple examples are given to show how the group theory is used for a qualitative discussion. In Sect. 3 we show how DFT can be applied for the calculation of the JT parameters. Section 4 contains some particular examples from our work as illustration of the concepts discussed in Sects. 2 and 3. They are tetrachlorovanadium(IV) ( $\text{VCl}_4$ ) in 4.1, cyclopentadienyl radical ( $\text{C}_5\text{H}_5$ ) in 4.2, and cobaltocene ( $\text{CoCp}_2$ ) in 4.3. In the Sect. 5 our model for the analysis of the multimode JT effect is described in detail. Finally, conclusions and perspectives are given in Sect. 6. In Sect. 7 computational details are reported.



## 2 Relevant Theory of JT Effect

Vibronic coupling theory has been applied to explain Electron Paramagnetic Resonance (EPR), Raman and UV/VIS spectra of some JT-active molecules. Model Hamiltonians were used to fit to the experiments. Some of the early work on various aspects of the vibronic coupling was done by e.g. van Vleck [77], Öpyk and Pryce [62], Longuet-Higgins [25, 56, 57], Liehr [55, 60], Herzberg [41, 42], etc. For the historical development, details about vibronic coupling theory and various application until year 2006 reader is referred to the book by I. B. Bersuker [46] and to the references therein. We would like to emphasize the works of Bader [9–11] and Pearson [64, 65] on the symmetry of reaction coordinates in addition, because it is crucial in our discussion of the multimode problem, as shown in our recent paper [86] and in Sect. 5 of this review.

Consider a  $N$ -atomic molecule in the high-symmetry (HS) nuclear configuration,  $\mathbf{R}_{\text{HS}}$ , in point-group  $G_{\text{HS}}$ .  $\mathcal{H}^{\text{HS}}$  is the electronic Hamilton operator, which defines the electronic structure. The molecule has  $3N - 6$  normal coordinates  $\mathbf{Q}_{\text{HS}k}$ ,  $k = 1, \dots, 3N - 6$  ( $3N - 5$  in the case of linear molecules),<sup>1</sup> which can be classified according to the corresponding irreps,  $\Gamma_{\text{HS}k}^{\text{vib}}$ , of the point-group  $G_{\text{HS}}$ .<sup>2</sup> In order to discuss the potential energy surface, the electronic Hamiltonian,  $\mathcal{H}$ , is expanded as a Taylor series around the HS point  $\mathbf{R}_{\text{HS}}$ , along the orthonormal  $\mathbf{Q}_{\text{HS}k}$ :

$$\mathcal{H} = \mathcal{H}^{\text{HS}} + \sum_{k=1}^{3N-6} \left( \frac{\partial V}{\partial \mathbf{Q}_{\text{HS}k}} \right)_{\text{HS}} \mathbf{Q}_{\text{HS}k} + \frac{1}{2} \sum_{k,l=1}^{3N-6} \left( \frac{\partial^2 V}{\partial \mathbf{Q}_{\text{HS}k} \partial \mathbf{Q}_{\text{HS}l}} \right)_{\text{HS}} \mathbf{Q}_{\text{HS}k} \mathbf{Q}_{\text{HS}l} + \dots \quad (1)$$

$$\mathcal{H} = \mathcal{H}^{\text{HS}} + \mathcal{W}. \quad (2)$$

$\mathcal{W}$  represents vibronic operator (JT Hamiltonian) and is a perturbation on the  $\mathcal{H}^{\text{HS}}$ .

Next, consider that the ground state eigenfunction of  $\mathcal{H}^{\text{HS}}$  with energy,  $E^0$ , is  $f$ -fold degenerate,  $\Psi_i^{\text{HS},0} = |\Gamma_{\text{HS}}^{\text{elect}} m_i\rangle$ .  $\Gamma_{\text{HS}}^{\text{elect}}$  is irrep of the ground state and  $m_i$  the component,  $i = 1, \dots, f$ . This leads to an  $f$ -fold JT effect. The matrix elements,  $H_{ij}$ , of  $\mathcal{H}$  within the basis functions  $\Psi_i^{\text{HS},0}$ , are given, according to the conventional second-order perturbation theory, where 0 designate the ground state, and  $p$  excited states:

<sup>1</sup> As it will be described in Sect. 5 our analysis of the multimode JT effect is based on the normal-coordinate analysis from the low symmetry points, contrary to the conventional vibronic-coupling theory. Therefore we distinguish between the normal coordinates in the HS conformation,  $\mathbf{Q}_{\text{HS}k}$ , and the normal coordinates in the stable low symmetry (LS) conformation  $\mathbf{Q}_k$ .

<sup>2</sup> In general discussions label of the irreducible representation is  $\Gamma$ . To differentiate between the symmetry of electronic states and vibrations, irreps of point groups  $G_{\text{HS}}$  and  $G_{\text{LS}}$  we add subscript and superscript, e.g.  $\Gamma_{\text{HS}}^{\text{elect}}$ ,  $\Gamma_{\text{HS}}^{\text{vib}}$  etc. In particular examples Mulliken symbols are used, e.g.  $A_1$ ,  $B_2$  etc. Electronic states are labelled with upper-case letters, e.g.  $^2E$ , while one-electron orbitals with lower-case, e.g. configuration  $e^{0.5}e^{0.5}$ . Symmetry of the normal modes are denoted also with lower case letters, e.g.  $a_1$  vibration, or in general as  $\gamma$ .

$$H_{ij} = E^0 \delta_{ij} + \sum_{i,j=1}^f \langle \Psi_i^{\text{HS},0} | \mathcal{W} | \Psi_j^{\text{HS},0} \rangle + \sum_{i=1}^f \sum_{p \neq 0} \frac{|\langle \Psi_i^{\text{HS},0} | \mathcal{W} | \Psi_j^{\text{HS},p} \rangle|^2}{E^0 - E^p} + \dots \quad (3)$$

This formulation defines potential energy surface around  $\mathbf{R}_{\text{HS}}$  (or in general around any point  $\mathbf{R}_X$ ) and allows a discussion of the Jahn–Teller (JT) effect [47], the pseudo-Jahn–Teller (PJT) effect [9–11, 46, 64, 65], the Renner–Teller (RT) effect [46, 66] as well as the chemical reactivity [9–11, 64, 65], with the same formalism [46]. Keeping the terms up to second order in  $\mathbf{Q}_{\text{HSk}}$ :

$$\begin{aligned} H_{ij} = & E^0 \delta_{ij} + \sum_{k=1}^{3N-6} \sum_{i,j=1}^f \underbrace{\langle \Psi_i^{\text{HS},0} | \left( \frac{\partial V}{\partial \mathbf{Q}_{\text{HSk}}} \right)_{\text{HS}} | \Psi_j^{\text{HS},0} \rangle}_{F_{ij}^k} \mathbf{Q}_{\text{HSk}} \\ & + \frac{1}{2} \sum_{k=1}^{3N-6} \sum_{i=1}^f \underbrace{\langle \Psi_i^{\text{HS},0} | \left( \frac{\partial^2 V}{\partial \mathbf{Q}_{\text{HSk}}^2} \right)_{\text{HS}} | \Psi_i^{\text{HS},0} \rangle}_{K_0} \mathbf{Q}_{\text{HSk}}^2 \\ & + \frac{1}{2} \sum_{k,l=1; k \neq l}^{3N-6} \sum_{i,j=1; i \neq j}^f \underbrace{\langle \Psi_i^{\text{HS},0} | \left( \frac{\partial^2 V}{\partial \mathbf{Q}_{\text{HSk}} \partial \mathbf{Q}_{\text{HSl}}} \right)_{\text{HS}} | \Psi_j^{\text{HS},0} \rangle}_{G_{ij}^{kl}} \mathbf{Q}_{\text{HSk}} \mathbf{Q}_{\text{HSl}} \\ & + \sum_{k=1}^{3N-6} \sum_{i=1}^f \sum_{p \neq 0} \underbrace{\frac{|\langle \Psi_i^{\text{HS},0} | \left( \frac{\partial V}{\partial \mathbf{Q}_{\text{HSk}}} \right)_{\text{HS}} | \Psi_j^{\text{HS},p} \rangle|^2}{E^0 - E^p}}_{R_{ip}} \mathbf{Q}_{\text{HSk}}^2. \end{aligned} \quad (4)$$

The matrix elements in (4) are vibronic coupling constants, thus (4) can be rewritten as:

$$\begin{aligned} H_{ij} = & E^0 \delta_{ij} + \sum_{k=1}^{3N-6} \sum_{i,j=1}^f F_{ij}^k \mathbf{Q}_{\text{HSk}} + \frac{1}{2} \sum_{k=1}^{3N-6} \sum_{i=1}^f K_0 \mathbf{Q}_{\text{HSk}}^2 \\ & + \frac{1}{2} \sum_{k,l=1; k \neq l}^{3N-6} \sum_{i,j=1; i \neq j}^f G_{ij}^{kl} \mathbf{Q}_{\text{HSk}} \mathbf{Q}_{\text{HSl}} + \sum_{k=1}^{3N-6} \sum_{i=1}^f \sum_{p \neq 0} R_{ip} \mathbf{Q}_{\text{HSk}}^2 \end{aligned} \quad (5)$$

The definition of the vibronic coupling constants is given in (6), (7), (8) and (9):

$$\text{The terms} \quad F_{ij}^k = \langle \Psi_i^{\text{HS},0} | \left( \frac{\partial V}{\partial \mathbf{Q}_{\text{HSk}}} \right)_{\text{HS}} | \Psi_j^{\text{HS},0} \rangle \quad (6)$$

are the linear vibronic coupling constants;

$$\text{The terms} \quad G_{ij}^{kl} = \langle \Psi_i^{\text{HS},0} | (\frac{\partial^2 V}{\partial \mathbf{Q}_{\text{HSk}} \partial \mathbf{Q}_{\text{HSI}}})_{\text{HS}} | \Psi_j^{\text{HS},0} \rangle \quad (7)$$

are the quadratic vibronic coupling constants;

$$\text{The terms} \quad G_{ii}^{kk} = K_0 = \langle \Psi_i^{\text{HS},0} | (\frac{\partial^2 V}{\partial \mathbf{Q}_{\text{HSk}}^2})_{\text{HS}} | \Psi_i^{\text{HS},0} \rangle \quad (8)$$

are the harmonic force constants at HS point;

$$\text{The terms} \quad R_{ip} = \frac{1}{2} K_v = \frac{|\langle \Psi_i^{\text{HS},0} | (\frac{\partial V}{\partial \mathbf{Q}_{\text{HSk}}})_{\text{HS}} | \Psi_i^{\text{HS},p} \rangle|^2}{E^0 - E^p} \quad (9)$$

are the electronic relaxation.

The complexity of (4) is reduced by symmetry rules, which allow identifying the non zero vibronic coupling constants. The Hamiltonian is invariant under all symmetry operations of the corresponding point group. Therefore, the operator  $\partial V / \partial \mathbf{Q}_{\text{HSk}}$  is transforming according to the irreducible representation  $\Gamma_{\text{HSk}}^{\text{vib}}$  of the normal coordinate  $\mathbf{Q}_{\text{HSk}}$ . The operator  $\partial^2 V / \partial \mathbf{Q}_{\text{HSk}} \partial \mathbf{Q}_{\text{HSI}}$  represents a basis for the reducible representation obtained by direct product  $\Gamma_{\text{HSk}}^{\text{vib}} \otimes \Gamma_{\text{HSI}}^{\text{vib}} \subset \Gamma_r$ .<sup>3</sup> Hence, the matrix elements in (4) are only different from zero for  $\Gamma_{\text{HSk}}^{\text{vib}} \subset \Gamma_{\text{HS}}^{\text{elect}} \otimes \Gamma_{\text{HSI}}^{\text{elect}}$  or in the case of the quadratic vibronic coupling constants for  $\Gamma_{\text{HSk}}^{\text{vib}} \otimes \Gamma_{\text{HSI}}^{\text{vib}} \subset \Gamma_{\text{HS}}^{\text{elect}} \otimes \Gamma_{\text{HS}}^{\text{elect}}$ .

The slope of the potential energy along the direction  $\mathbf{Q}_{\text{HSk}}$ , is given by the diagonal linear vibronic constant,  $F_{ii}^k$ .  $F_{ii}^k$  represents the force, which moves the nuclei and leads to a change of the structure. These terms are zero at any stationary point on the potential energy surface. If the ground state is nondegenerate the integral will vanish unless  $\mathbf{Q}_{\text{HSk}}$  is totally symmetric. Therefore for a system with a non-degenerate ground state, the potential energy surface shows only a gradient along totally symmetric distortions. As a consequence, for any non stationary point, the point group does not change along any reaction path [65]. If the ground state is degenerate,  $\mathbf{Q}_{\text{HSk}}$  might be a basis for a non-totally symmetric representation. This is a case if  $\mathbf{Q}_{\text{HSk}}$  belongs to one of the irreps which is a component of the direct product  $\Gamma_{\text{HS}}^{\text{elect}} \otimes \Gamma_{\text{HS}}^{\text{elect}}$ . The spontaneous distortion along these non-totally symmetric normal coordinates,  $\mathbf{Q}_{\text{HSk}}$ , leads to a descent in symmetry and removes the degeneracy of the ground state. When the symmetry is lowered,  $\Psi_i^{\text{HS},0}$  is no longer degenerate, and the  $F_{ii}^k$  will be zero unless the  $\mathbf{Q}_{\text{HSk}}$  becomes totally symmetric in the new point group. The movement of nuclei that were non-totally symmetric in the  $G_{\text{HS}}$ , must now become totally symmetric. The point group  $G_{\text{LS}}$  of the minimum on

<sup>3</sup> Totally symmetric component of the direct product  $\Gamma_{\text{HSk}}^{\text{vib}} \otimes \Gamma_{\text{HSI}}^{\text{vib}}$  yields the harmonic force constant,  $K_0$ , which is separate term in (4).

the potential energy surface, can be predicted by looking at the correlation tables for the symmetry descent, e.g. in [7]. The point group  $G_{LS}$  is the one in which the mode becomes totally symmetric. If there are several possibilities for a descent in symmetry,  $G_{LS}$  of the minimal energy conformation is the highest one with lifted degeneracy according to the epikernal principle [23, 24, 46]. Jahn and Teller [47] examined all degenerate terms of the symmetry point groups of non-linear molecules, and showed that there is always at least one non-totally symmetric vibration for which the  $F_{ij}^k \neq 0$ . This holds even for double groups, in this case  $\Psi_i^{HS,0}$  is a Kramers doublet. This is the physical basis of the (first order) JT effect. The JT problems are classified according to the symmetry types of the electronic states and the vibrations that are coupled,  $\Gamma \otimes \gamma$  [46]. For example,  $E \otimes e$  JT problem denotes, coupling of the degenerate electronic state of irrep  $E$ , by a degenerate vibration of irrep  $e$ . Since the slope of the potential surface at the high symmetry configuration,  $\mathbf{R}_{HS}$ , is nonzero, this conformation corresponds not to a stationary point. It represents a cusp of the potential energy surface obtained in conventional DFT.

The curvature of the potential energy surface in the direction  $\mathbf{Q}_{HSk}$  at  $\mathbf{R}_{HS}$ , is measured by the force constant,  $K_k = K_0 + K_v$  [46]. The diagonal matrix elements of the second derivative of the potential energy operator, are the primary or nonvibronic force constants,  $K_0$  [46].  $K_0$  is always different from zero and positive [46, 70]. It represents a restoring force that tends to bring the system back to the more symmetrical situation. HS configuration represents the most stable configuration of the molecule, if the vibronic coupling is ignored, as it minimizes electron–electron repulsion.

The electronic relaxation,  $R_{ip} = \frac{1}{2}K_v$ , depicts the coupling of the ground state with excited states. This term is always negative, due to the nominator  $E^0 - E^P$ . Generally it is different from zero, because there is always some excited states, of the same irrep as the ground state. It becomes increasingly important when the ground and the excited states are close in energy. It is referred to as the vibronic force constant,  $K_v$  [46]. It is responsible for: (1) the negative curvature along the reaction coordinate of the potential energy surface at a transition state [65] (2) for the pseudo-Jahn–Teller effect [46, 65], configurational instability of polyatomic species with nondegenerate electronic states; (3) for the avoided crossing between the states of the same symmetry; (4) for the softening of the ground state curvature at the energy minimum conformation; and (5) it contributes to the anharmonicity of the vibrations. In practice, in the analysis of JT systems, this term is usually neglected, or added to the total, observed force constant  $K_k$ .

The quadratic constants,  $G_{ij}^{kl}$ , in non linear molecules influence the shape of the potential energy surfaces. This is true for the higher order terms, e.g. cubic, and terms  $R_{ip}$  (PJT terms) also. Discussion of the various terms contributing to the warping of the potential energy surface can be found in e.g. [39]. For linear molecules the linear vibronic constants are always zero because the non-totally symmetric vibrations are odd and the degenerate states are even. The quadratic terms however are nonzero, and this may lead to instability of the linear configurations in case of a sufficiently strong coupling. This is physical basis of the RT effect [46, 66].

As we see, the complexity of (4) is already reduced by symmetry rules, which allow us to identify the non zero vibronic coupling constants. Moreover, the application of the Wigner–Eckart theorem [33, 81] yields a further reduction of the complexity for degenerate irreducible representations.

$$\langle \Psi_i^{\text{HS},0} | (\frac{\partial V}{\partial \mathbf{Q}_{\text{HSk}}}) | \Psi_j^{\text{HS},0} \rangle = C \begin{pmatrix} \Gamma_{\text{HS}}^{\text{elect}} & \Gamma_{\text{HSk}}^{\text{vib}} & \Gamma_{\text{HS}}^{\text{elect}} \\ m_i & m_k & m_j \end{pmatrix} \langle \Psi_{\Gamma_{\text{HS}}}^{\text{HS},0} | (\frac{\partial V}{\partial \mathbf{Q}_{\Gamma_{\text{HSk}}}}) | \Psi_{\Gamma_{\text{HS}}}^{\text{HS},0} \rangle \quad (10)$$

where  $C \begin{pmatrix} \Gamma_{\text{HS}}^{\text{elect}} & \Gamma_{\text{HSk}}^{\text{vib}} & \Gamma_{\text{HS}}^{\text{elect}} \\ m_i & m_k & m_j \end{pmatrix}$  are the coupling coefficients of the point group of the molecule at the high symmetry point,  $G_{\text{HS}}$ , and  $\langle \Psi_{\Gamma_{\text{HS}}}^{\text{HS},0} | (\frac{\partial V}{\partial \mathbf{Q}_{\Gamma_{\text{HSk}}}}) | \Psi_{\Gamma_{\text{HS}}}^{\text{HS},0} \rangle$  is reduced matrix-element that only depends upon irreps and not upon their components.

In the case of the quadratic matrix elements,  $G_{ij}^{\text{kl}}$ , the Wigner–Eckart theorem [33, 81] might be applied similarly to the previous case, where the summations run over all  $\Gamma_r$  and their components  $m_r$ :

$$\langle \Psi_i^{\text{HS},0} | (\frac{\partial V^2}{\partial \mathbf{Q}_{\text{HSk}} \partial \mathbf{Q}_{\text{HSI}}}) | \Psi_j^{\text{HS},0} \rangle = \langle \Psi_{\Gamma_{\text{HS}}}^{\text{HS},0} | (\frac{\partial V^2}{\partial \mathbf{Q}_{\Gamma_{\text{HSk}}} \partial \mathbf{Q}_{\Gamma_{\text{HSI}}}}) | \Psi_{\Gamma_{\text{HS}}}^{\text{HS},0} \rangle \sum_{\Gamma_r, m_r} C \begin{pmatrix} \Gamma_{\text{HS}}^{\text{elect}} & \Gamma_r & \Gamma_{\text{HS}}^{\text{elect}} \\ m_i & m_r & m_j \end{pmatrix} C \begin{pmatrix} \Gamma_{\text{HSk}}^{\text{vib}} & \Gamma_r & \Gamma_{\text{HSI}}^{\text{vib}} \\ m_k & m_r & m_l \end{pmatrix}. \quad (11)$$

Thus, only one reduced matrix element has to be calculated or determined experimentally, because the coupling coefficients are known. This simplifies the interpretation considerably. E.g. in the case of a  $E \otimes e$  JT problem the potential energy surface is determined by only three reduced matrix elements, corresponding to the parameters  $F$ ,  $G$ ,  $K$  [46].

In order to show how the theory given above can be applied, few simple examples are shown. Numerical results obtained from the DFT calculation on these systems are given later, Sect. 4.

The ground electronic state of eclipsed cobaltocene ( $\text{CoCp}_2$ ) or cyclopentadienyl radical ( $\text{C}_5\text{H}_5$ ), with  $D_{5h}$  symmetry is  $^2E_1''$ , with a single electron (hole) in the doubly degenerate orbital,  $e_1''$ . Using group theory it is easy to show that the distortion coordinate is  $e_2'$  ( $E_1'' \otimes E_1'' \subset A_1' + [A_2'] + E_2'$ ), and the descent in symmetry goes to  $C_{2v}$ . The electronic state will split into  $A_2$  and  $B_1$ , while the degenerate JT active distortion  $e_2'$  splits into  $a_1$  and  $b_2$ . Let us analyse the problem in the space of the two components  $Q_a$  and  $Q_b$  of  $e_2'$  ( $Q_a$  is of  $a_1$  symmetry in  $C_{2v}$ , and  $Q_b$  is of  $b_2$  symmetry). The JT active distortion is the totally symmetric reaction coordinate,  $a_1$ , in  $C_{2v}$ . The modes of  $b_2$  symmetry allow mixing of the two electronic states emerging from the degenerate ground state. The second order vibronic coupling constant,  $G_{ij}^{\text{kl}}$  is zero, because in the direct product  $E_2' \otimes E_2' \subset A_1' + [A_2'] + E_1'$  there are no

**Table 1** Coupling coefficients for the  $D_5$  group

vib.	el.state component	$E_1 \times E_1$			
		$AA$	$AB$	$BA$	$BB$
$e_2$	$b$	0	$-\frac{1}{\sqrt{2}}$	$-\frac{1}{\sqrt{2}}$	0
	$a$	$\frac{1}{\sqrt{2}}$	0	0	$-\frac{1}{\sqrt{2}}$

terms of  $E'_2$  symmetry able to interact with the  $E''_1$  electronic wavefunctions. There is no warping of the Mexican hat. The totally symmetric component of  $E'_2 \otimes E'_2$  representation yields the harmonic force field constant,  $K$ . Using Wigner–Eckart theorem [33, 81] and the coupling coefficients for the  $D_{5h}$  point group, Table 1. it is easy to see that the following integrals vanish:

$$\langle \Psi_A | \frac{\partial V}{\partial \mathbf{Q}_a} | \Psi_B \rangle = \langle \Psi_B | \frac{\partial V}{\partial \mathbf{Q}_a} | \Psi_A \rangle = \langle \Psi_A | \frac{\partial V}{\partial \mathbf{Q}_b} | \Psi_A \rangle = \langle \Psi_B | \frac{\partial V}{\partial \mathbf{Q}_b} | \Psi_B \rangle = 0 \quad (12)$$

and the remaining integrals are:

$$\begin{aligned} F &= \langle \Psi_A | \frac{\partial V}{\partial \mathbf{Q}_a} | \Psi_A \rangle = -\langle \Psi_B | \frac{\partial V}{\partial \mathbf{Q}_a} | \Psi_B \rangle = -\langle \Psi_A | \frac{\partial V}{\partial \mathbf{Q}_b} | \Psi_B \rangle = -\langle \Psi_B | \frac{\partial V}{\partial \mathbf{Q}_b} | \Psi_A \rangle \\ &= \frac{1}{\sqrt{2}} \langle \Psi_{E''_1} | \frac{\partial V}{\partial \mathbf{Q}_{E'_2}} | \Psi_{E'_1} \rangle. \end{aligned} \quad (13)$$

Potential energy as a function of a distortion along  $\mathbf{Q}_a$  and  $\mathbf{Q}_b$  is:

$$E = E^0 + \frac{1}{2} K (\mathbf{Q}_a^2 + \mathbf{Q}_b^2) \pm F [(\mathbf{Q}_a^2 + \mathbf{Q}_b^2)]^{\frac{1}{2}}. \quad (14)$$

The energy change along  $\mathbf{Q}_a$ , or  $\mathbf{Q}_b$  or along any linear combination is the same. In this expression only quadratic forms of  $\mathbf{Q}_a$  and  $\mathbf{Q}_b$  are present, thus the energy of a distortion along  $-\mathbf{Q}_a$  is the same energy as along  $\mathbf{Q}_a$ , thus only the other component of the degenerate state is stabilized. The potential energy surface has a Mexican-hat shape, without any warping. Energy change is the same in all directions in the two dimensional space spanned by these two coordinates.

In the case of CoCp<sub>2</sub> there are six different  $e'_2$  modes and in the case of C<sub>5</sub>H<sub>5</sub> four and each of them will be characterized with one pair of parameters  $F$  and  $K$ .

The quadratic vibronic constants of the  $e'_1$  normal coordinates are not zero even if the linear ones are zero because in the  $D_{5h}$  point group  $E'_1 \otimes E'_1 \subset A'_1 + [A'_2] + E'_2$ . In HS, thus the first order and the second order JT effect are separated. As one component of  $e'_1$  becomes in LS totally symmetric too, they will also mix and contribute to the totally symmetric JT coordinate. Thus, we see that considering only one normal coordinate is not enough to describe the JT effect even in this simple case. In the subsequent sections we will address this problem again, and propose how to analyse which is the contribution of the different vibrations to the total distortion of a molecule, and which of them are the most important driving force for the distortion.

Next, let see how group theory can be used in determining the symmetry properties of the JT distortions in a tetrahedral,  $T_d$ , molecule with an  $E$  ground electronic state, e.g.  $\text{VCl}_4$ , Sect. 4.1. The symmetry of the JT active vibration is determined as  $E \otimes E \subset A_1 + [A_2] + E$ . This is another example of an  $E \otimes e$  JT problem. Symmetry lowering is  $T_d \rightarrow D_{2d}$ . In lower symmetry  $e$  vibration splits into  $a_1 + b_1$ . Only one component of the degenerate vibration is JT active. JT distortion is along the totally symmetric reaction coordinate,  $a_1$ , in  $D_{2d}$ . The potential along the direction of the JT inactive vibrations is parabolic with a minimum for the high symmetry conformation. In this case quadratic vibronic coupling constant is different from zero, as there is always  $E$  terms present in the direct product of  $E \otimes E$ , and the potential energy surface has a famous Mexican-hat-like form, with three equivalent minima and three equivalent transition states. The distortion along  $+\mathbf{Q}_{a_1}$  and  $-\mathbf{Q}_{a_1}$  are not identical. The energy of the two different states is not the same.

### 3 DFT Calculation of the JT Ground State Properties

As seen in the Sect. 2, JT effect is governed by the symmetry properties of  $G_{\text{HS}}$  and  $G_{\text{LS}}$  point groups of the studied molecule. The information from group theory can be used for a qualitative discussion. This does not tell anything about the degree of the distortion or how big the energy gain is due to the descent in symmetry. These questions are of fundamental importance to characterize JT systems. To answer them it is necessary either to perform the experiment, and fit the results to the proposed model, or to carry out a computational study.

The vibronic coupling constants discussed in Sect. 2 define the potential energy surface. A qualitative cut through the potential energy surface, along JT active vibration  $\mathbf{Q}_a$  is given in Fig. 1. The figure indicates how the parameters  $E_{\text{JT}}$  (the JT stabilization energy),  $\Delta$  (the warping barrier),  $R_{\text{JT}}$  (the JT radius) and  $E_{\text{FC}}$  (the

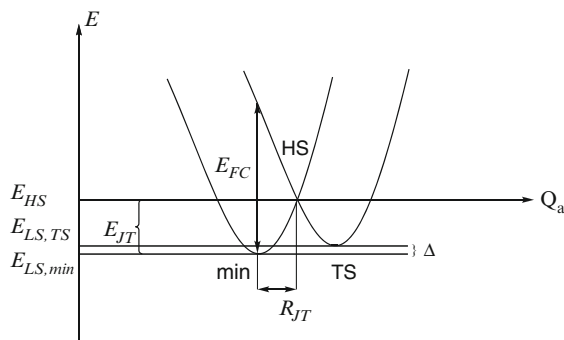


**Fig. 1** Qualitative cross section through the potential energy surface, along JT active vibration  $\mathbf{Q}_a$ ; Definition of the JT parameters – the JT stabilisation energy,  $E_{\text{JT}}$ , the warping barrier,  $\Delta$ , the JT radius,  $R_{\text{JT}}$ , the energy of the vertical Frank–Condon transition,  $E_{\text{FC}}$

Frank–Condon transition) define the potential energy surface. The meaning of the parameters is clear – energy stabilization due to the JT effect is given by the value of  $E_{\text{JT}}$  (or alternatively by  $E_{\text{FC}} = 4E_{\text{JT}}$ ), and direction and magnitude of the distortion by the  $R_{\text{JT}}$ .

Using non-empirical methods it is, at least in principle, easy to calculate this alternative set of parameters. They are connected to the set of parameters discussed in previous Sect. 2, e.g. for the  $E \otimes e$  JT problem using following expressions, (15), (16), (17):

$$E_{\text{JT}} = \frac{F^2}{2(K - 2|G|)}. \quad (15)$$

$$\Delta = \frac{4E_{\text{JT}}|G|}{K + 2|G|}, \quad (16)$$

$$R_{\text{JT}}^{\text{min}} = \frac{|F|}{K - 2|G|} \quad R_{\text{JT}}^{\text{TS}} = -\frac{|F|}{K + 2|G|}, \quad (17)$$

Similar expressions, for other type of JT problems can be found in [46].

DFT is the modern alternative to the wave-function based ab initio methods and allows to obtain accurate results at low computational cost, that also helps to understand the chemical origin of the effect. DFT, like Hartree–Fock (HF) methods, exploit molecular symmetry which is crucial in the case of computational studies of the JT effect. It also includes correlation effects into the Hamiltonian via the exchange-correlation functional. HF and many-body perturbation methods are found to perform poorly in the analysis of JT systems for obvious reasons, at contrast to the methods based on DFT, or multiconfigurational SCF and coupled cluster based methods [73]. The later are very accurate but have some drawbacks, mainly the very high computational cost that limits the applications to the smaller systems only. Another drawback is the choice of the active space which involves arbitrariness.

In order to get the JT parameters, it is necessary to know geometries and energies of HS and LS points. For the LS points, as they are in non-degenerate electronic ground state, at least formally, this is straightforward. Electronic structure of the HS point, on the other hand, must be represented with at least two Slater determinants, consequently, using a single determinant DFT is troublesome. Wang and Shwarz [79], or Baerends [69] pointed out that a single determinant KS–DFT is deficient in the description of (near) degeneracy correlation. In a non-empirical approach to calculate the JT distortion using DFT [21] it was proposed to use average of configuration (AOC) calculation to generate the electron density. This is a SCF calculation where the electrons of degenerate orbitals are distributed equally over the components of the degenerate irreps leading to a homogeneous distribution of electrons with partial occupation, in order to retain the  $A_1$  symmetry of the total density in the HS point group. E.g. for  $e^1$  configuration this will mean to place 0.5 electrons into each of the two  $e$  orbitals. This calculation yields the geometry of the high symmetry species.



The idea of fractional occupation numbers was introduced by Slater [71], already in 1969. This approach is not limited for the JT systems, e.g. it was explored by Dunlap and Mei [32] for molecules, by Filatov and Shaik [36] for diradicals, and is also used for calculations of solids and metal clusters [8]. It rests on a firm basis in cases when the ground state density has to be represented by a weighted sum of single determinant densities [53, 79]. One should remember that molecular orbitals (MO) themselves have no special meaning. Thus, using partial occupation is just a way of obtaining electron density of a proper symmetry (HS).

Although, AOC calculation gives us geometry of a HS point, using simply the energy obtained in this way would be erroneous. AOC calculation is giving too low energy. The JT stabilization energy is not simply the energy difference between the HS and the LS species. This is due to the self interaction error (SIE) present in the approximate exchange–correlation functionals used in practical DFT (approximate DFT), unless special forms are taken into account. This is sometimes referred as overestimation of the delocalisation by approximate DFT. Zhang and Yang [83] showed that SIE in case of delocalized states with non integer number of electrons, e.g. in HS point, is much bigger than in case of localized ones, where an integer number of electrons is present, e.g. in LS point. SIE will always artificially stabilize the energy of systems having fractional number of electrons compared to the corresponding ones with integer number of electrons. It is also worthwhile to stress that relative stability of the states with partial occupation relative to the ones with integer occupation (delocalized vs. localized) is of interest not only in study of JT systems as such, but also in the field of chemical reactivity or mixed valence compounds.

To solve this problem and to obtain  $E_{JT}$ , a multideterminantal DFT approach is applied. We need two types of DFT calculations: (1) a single-point calculation imposing the high symmetry on the nuclear geometry and the low symmetry on the electron density. This is achieved by introducing an adequate occupation scheme of the MOs. This gives the energy of a Slater determinant with an integer electron orbital occupancy. (2) A geometry optimization in the lower symmetry.  $E_{JT}$  is the difference in these two energies. To obtain the energies of the degenerate states at HS one needs to evaluate the energies of all possible single determinants with integer occupations in HS geometry. Thus, both steps will be repeated for all the possible combinations of electronic states in  $G_{LS}$ . The energy of vertical (Franck–Condon) transition  $E_{FC}$ , is easily obtained in promoting the unpaired electron from the ground state to the first excited state for the ground state geometry. Our computational recipe, for the case of  $VCl_4$  is schematically drawn in Fig. 2.

In order to discuss the JT distortion on the adiabatic potential surface we define a vector  $\mathbf{R}_{JT}$  as the vector given by the displacements of the atoms from the high symmetry point defined by the  $\mathbf{R}_{HS}$ . The JT radius,  $R_{JT}$  is given by the length of the distortion vector between the high symmetry and the minimum energy configuration.

$$\mathbf{R}_{JT} = \mathbf{R}_{HS} - \mathbf{R}_{LS} = R_{JT}\mathbf{u} \quad (18)$$

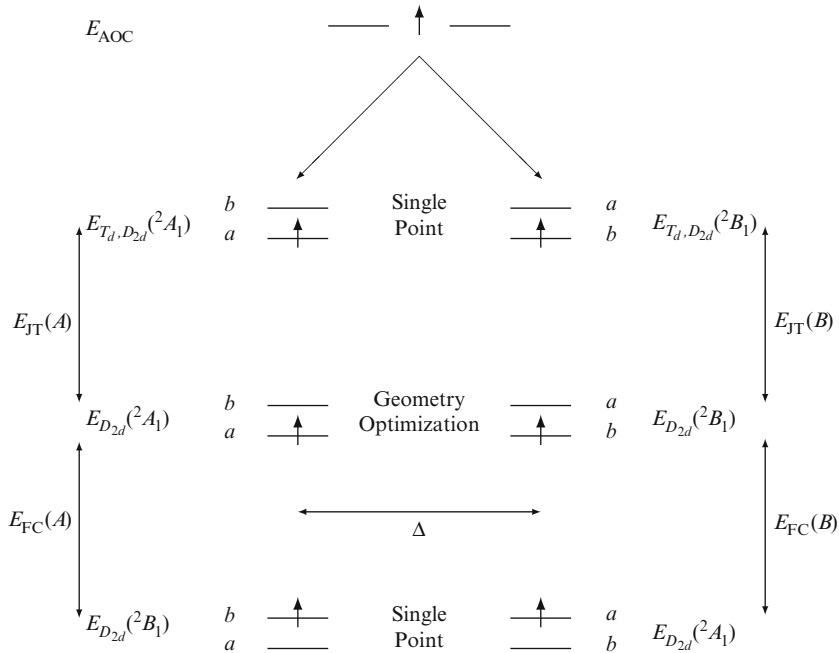


**Fig. 2** Schematic representation of the calculation recipe in  $T_d$  point group –  $VCl_4$

Let us summarize our calculation recipe:

1. AOC geometry optimization with fractional orbital occupation. This yields the HS geometry  $\mathbf{R}_{HS}$
2. Geometry optimization with the different LS electron distributions. This yields the different LS geometries  $\mathbf{R}_{LS,min}$  and  $\mathbf{R}_{LS,TS}$ , and the different energies  $E_{LS,min}$  and  $E_{LS,TS}$  that correspond to the minimum and to the transition state on the potential energy surface respectively
3. Single point calculation with fixed nuclear geometry  $\mathbf{R}_{HS}$  and different LS electron distributions with an integer SD occupations, resulting the energies  $E_{HS,LS,min}$  and  $E_{HS,LS,TS}$ . Energies for the different distributions should be equal
4. Single point calculation of the excited states with  $\mathbf{R}_{LS}$  to obtain  $E_{FC}$ .

Combination of the calculated energies yield the JT parameters,  $E_{JT}$ ,  $\Delta$ ,  $E_{FC}$ .

$$E_{JT,min} = E_{HS,LS,min} - E_{LS,min}, \quad (19)$$

$$E_{JT,TS} = E_{HS,LS,TS} - E_{LS,TS}, \quad (20)$$

$$\Delta = E_{LS,min} - E_{LS,TS} = E_{JT,min} - E_{JT,TS}. \quad (21)$$

Within a harmonic approximation the JT distortion is given as a linear combination of displacements along all,  $N_{a_1}$ , totally symmetric normal coordinates in the

LS conformation. The linear coefficients, or the weighting factors,  $w_{\text{HS}k}$ , define the contribution of each of these normal modes,  $\mathbf{Q}_k$ , to the distortion.

$$\mathbf{R}_{\text{JT}} = \sum_{k=1}^{N_{a1}} w_{\text{HS}k} \mathbf{Q}_k. \quad (22)$$

Each of the totally symmetric normal modes contributes the energy  $E_k$  to the JT stabilisation, and  $E_{\text{JT}}$  can be expressed as the sum of these energy contributions, (23). Force at HS point, which drives the nuclei along  $\mathbf{Q}_k$  to the minimum is given by  $\mathbf{F}_{\text{HS}k}$  (24).<sup>4</sup>

$$E_{\text{JT}} = \sum_{k=1}^{N_{a1}} E_k = \frac{1}{2} \sum_{k=1}^{N_{a1}} w_{\text{HS}k}^2 \mathbf{Q}_k^2 \lambda_k, \quad (23)$$

$$\mathbf{F}_{\text{HS}k} = w_{\text{HS}k} \lambda_k \mathbb{M}^{1/2} \mathbf{Q}_k. \quad (24)$$

Detailed discussion of this analysis is given in the Sect. 5.

## 4 Applications

In this section we present the applications of DFT to discuss JT distortions. The results demonstrate that the computational recipe, described previously, Sect. 3, allows the calculation of the JT parameters, which are in good agreement with the experimental results. In this section, results of the analysis of the multimode JT effect are presented too.

### 4.1 Tetrachlorovanadium(IV), $\text{VCl}_4$

Among the simplest of the JT molecules is  $\text{VCl}_4$ , a tetrahedral molecule with a  $d^1$  configuration. It is characterized by a small JT effect. The method of calculation of the JT parameters using DFT was first developed on this system in our group [21] and it shows some important features.

In  $T_d$  point group, a single electron occupies  $e$  orbital. The electronic ground state is  ${}^2E$ . After the symmetry descent to  $D_{2d}$  the later splits into  ${}^2A_1$  and  ${}^2B_1$ . In order to obtain JT parameters calculation recipe discussed in Sect. 3 is applied. Calculation method is summarized in Fig. 2 and results are given in Table 2.

---

<sup>4</sup> In (23) and (24) eigenvectors  $\mathbf{Q}_k$ , of the Hessian obtained in the LS minimum are expressed in generalized (mass-weighted) displacement coordinates, with eigenvalues  $\lambda_k$ ;  $\mathbb{M}$  is a diagonal  $3N \times 3N$  matrix with atomic masses in triplicates as elements  $(m_1, m_1, m_1, m_2, \dots, m_N)$ .

**Table 2** Results of the DFT calculations performed to analyse the JT effect of  $\text{VCl}_4$ ; energies (LDA) are given in eV; the JT parameters  $E_{JT}$  and  $\Delta$  are given in  $\text{cm}^{-1}$  and  $R_{JT}$  in  $(\text{amu})^{1/2}\text{\AA}$

Occupation	State	Geometry	Energy
$e^{0.5}e^{0.5}$	${}^2E$	$T_d$	-21.7470
$b_1^0a_1^1$	${}^2A_1$	$T_d$	-21.6074
$a_1^0b_1^1$	${}^2B_1$	$T_d$	-21.6084
$b_1^0a_1^1$	${}^2A_1$	$D_{2d}$	-21.6137
$a_1^0b_1^1$	${}^2B_1$	$D_{2d}$	-22.6134
$E_{JT}$	${}^2A_1$		50.8
$E_{JT}$	${}^2B_1$		40.3
$\Delta$			10.5
$R_{JT}$	${}^2A_1$		0.10
$R_{JT}$	${}^2B_1$		0.10

As a starting point the geometry of  $\text{VCl}_4$  has been optimized in  $T_d$  symmetry using an AOC calculation. This means that both  $e$  orbitals carry 0.5 electron leading to a totally symmetric electron distribution. The second step is to carry out a calculation with fixed  $T_d$  geometry occupying selectively one of the two degenerate orbitals. Finally a geometry optimization in  $D_{2d}$  symmetry is performed, corresponding to both  ${}^2A_1$  and  ${}^2B_1$  electronic ground states, leading to two different geometries and energies. Only due to the imposal of different electron distribution in two  $D_{2d}$  cases, the calculations give rise to the simulation of the JT distortion. The results of this calculation are shown in Table 2.

We notice that the energies  $E({}^2A_1, T_d)$  and  $E({}^2B_1, T_d)$  are not equal. This inequality is due to the nature of the numerical integration grid involved in DFT calculations [28]. This is generally observed also if symmetry arguments impose equal energy. In this cases energy difference between two is negligible, e.g. in the case of cobaltocene (see Sect. 4.3). From the Table 2 it is evident why the two calculations with  $T_d$  nuclear geometries and  $D_{2d}$  electron densities have been performed. Comparing the final energies in LS with the one obtained from AOC calculation in  $T_d$  would give a misleading result, that there is no JT effect. The electron distribution in the nondistorted  $\text{VCl}_4$  is different from that in distorted one. The electron interaction term in the total energy is also different. In order to compare the two LS geometries with one in the HS, the unpaired electron needs to be distinguishably placed in one of the two  $e$  orbitals, as done in our calculation scheme.

Within  $3N - 6 = 9$  normal modes only one pair of  $e$  and one  $a_1$  modes have non zero linear vibronic coupling constant. Thus this can be the simplest case of the multimode problem, with possibly two JT active vibrations. Applying our method for the analysis of the different contributions of the normal coordinates, Sect. 5, we find that the contribution of the  $e$  mode to the distortion is more than 99%, which is in agreement with usual consideration of  $\text{VCl}_4$  system as an ideal, single mode problem. This also justifies full potential energy surface calculation along the JT active component of the degenerate vibration,  $\mathbf{Q}_a$  for both electronic states. In the

case of simple molecules, e.g. tetrahedral  $\text{VCl}_4$ , it is possible to have analytical expression for the displacements, which can be found in e.g. [46].

This vibration is illustrated in Fig. 3, potential energy surface calculation along it on Fig. 4, and the Mexican-hat-like plot on Fig. 5.

In summary this shows that DFT calculations for this simple molecule, with a relatively small JT effect, yields results in good agreement with the experiments [4, 16, 48, 61].  $E_{\text{JT}} = 50.8 \text{ cm}^{-1}$  is obtained by the DFT calculation and the

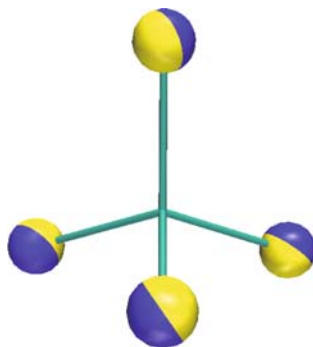


**Fig. 3** Vibrational energy distribution representation of the JT active vibration of  $\text{VCl}_4$ . The different colours indicate the direction of the displacement vector; the volume of the spheres is proportional to the contribution made by the individual nuclei to the energy of the vibrational mode

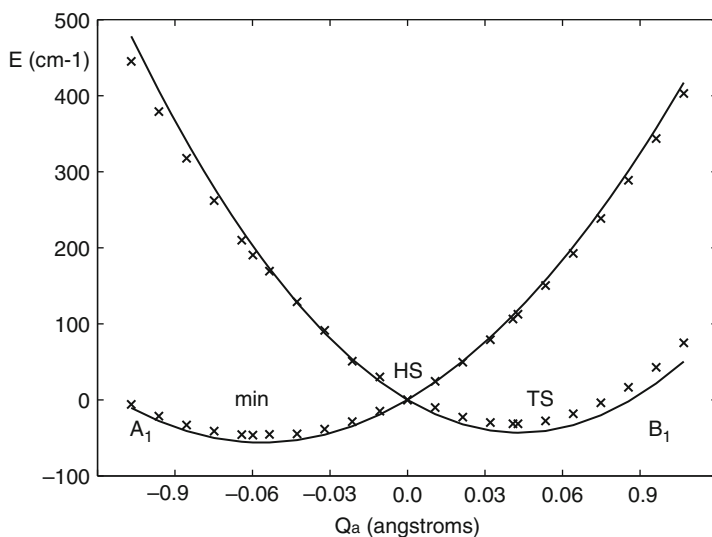


**Fig. 4**  $\text{VCl}_4$  potential energy surface calculation along the JT active vibration  $Q_a$  (Å) (times) and least square fitting of the data (minus); energies are given in  $\text{cm}^{-1}$  relative to the HS point

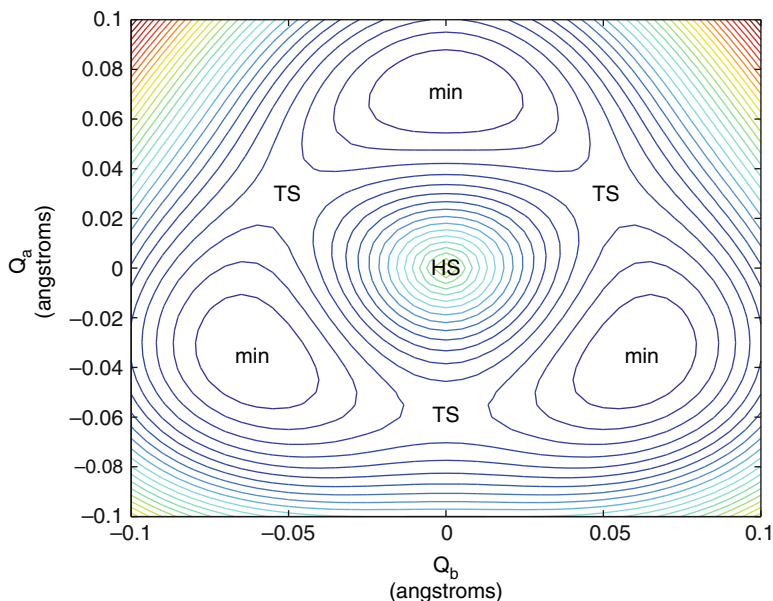


**Fig. 5** VCl<sub>4</sub> Mexican-hat-like contour plot of the adiabatic potential energy in the space of  $Q_a$  and  $Q_b$  components of the JT active  $e$  vibration

experimental value lies between 30 and 80  $\text{m}^{-1}$  [4, 16, 48, 61]. These results confirm the dynamic character of the JT effect.

## 4.2 Cyclopentadienyl Radical

Cyclopentadienyl radical is one of the most studied JT active molecules, both experimentally and theoretically. Theoretical works trace back to Andy Liehr in 1956 [54]. They span many different methods [5, 12, 17, 26, 43, 45, 50, 54, 59, 72, 85] during the years. The values of  $E_{JT}$  obtained are summarised in Table 3. The JT effect was discussed using various models, (1) the classical perturbation model as in the work of Liehr [54] (2) models based on the analysis of spectra as in the works of Miller et al. [5, 6] or Stanton et al. [45], (3) Valence Bond (VB) model [85], or (4) vibronic coupling density analysis [67]. Somehow surprisingly there was to our knowledge no attempt to use DFT to analyse the JT effect in this system up to now. As it can be seen from the Table 3 our multideterminantal DFT approach gives the value of 1,253  $\text{cm}^{-1}$  for  $E_{JT}$  which is in excellent agreement with the experimental one of 1,237  $\text{cm}^{-1}$  [6]. The various other theoretical methods give different results ranging from 495 to 5,072  $\text{cm}^{-1}$ . Studies of Miller et al. [5, 6] who used complete active space methods ( $E_{JT} = 2147 \text{cm}^{-1}$ ) and dispersed fluorescence spectroscopy ( $E_{JT} = 1237 \text{cm}^{-1}$ ), as well as fitting of ab initio calculations to the spectra

**Table 3** Summary of various computational methods used to study the JT effect in  $C_5H_5$ ;  $E_{JT}$  is given in  $cm^{-1}$ 

Method <sup>a</sup> /Basis set	$E_{JT}$
Semiempirical-MO [54]	560
Semiempirical-MO [72]	728
Semiempirical-MO [43]	495
HF/STO-3G [59]	5,072
CI/STO-3G [17]	2,484
HF/6-311+G* [26]	1,452
MP2/6-311+G* [26]	3,065
MP4/6-311+G* [26]	2,581
CCSD/6-311+G* [26]	1,613
CCSD(T)/6-311+G* [26]	1,613
CASSCF/cc-PVDZ [12]	2,139
CASSCF/6-31G* [5]	2,147/1,463
CASSCF/cc-PVDZ [50]	1,665
CISD/cc-PVDZ [85]	2,553
EOMIP-CCSD/DZP [45]	1,581
DFT(LDA)/TZP <sup>b</sup>	1,253
DFT(PW91)/TZP <sup>b</sup>	1,326
Exp. [6]	1237

<sup>a</sup>Acronyms used for the calculation methods: *HF* Hartree–Fock; *CI* Configuration Interaction; *MPN* Møller–Plesset Perturbation Theory of order N for electron correlation; *CCSD(T)* Coupled Cluster Single, Double (Triple) excitations; *CASSCF* Complete-Active-Space SCF; *CISD* Single and Double excitations, single reference CI method; *EOMIP–CCSD* Equation-of-motion ionization potential coupled-cluster single, double excitations; *LDA* Local Density Approximation; *PW91* Generalized Gradient Approximation in the form given by Perdew–Wang

<sup>b</sup>Multideterminantal DFT – this work

( $E_{JT} = 1,463cm^{-1}$ ) are considered to be benchmark results for the determination of the JT parameters. They also identified three dominant normal modes necessary to explain their results. These were recently confirmed by Stanton et al. using Equation-of-motion ionization potential coupled–cluster (EOMIP–CCSD) calculations [45]. Thus, this system is a good test case for both our multideterminantal DFT approach in studies of the JT effect and for our model of the analysis of the multimode JT effect.

The ground electronic state of  $C_5H_5$  in  $D_{5h}$  symmetry is  ${}^2E_1''$ , with three electrons occupying the doubly degenerate orbital (one hole). Using group theory it is easy to show, see Sect. 2 that the distortion coordinate is  $e_2'$ . The descent in symmetry goes to  $C_{2v}$ . The electronic state  ${}^2E_1''$  splits into  ${}^2A_2$  and  ${}^2B_1$  and the JT active distortion  $e_2'$  splits into  $a_1$  and  $b_2$ . The results of the DFT calculation are summarised in the Table 4.

The difference in the JT energies for the different electronic states is only  $3.2cm^{-1}$ . This confirms results of the analysis by group theory, see Sect. 2, that

**Table 4** Results of the DFT calculations performed to analyse the JT effect of  $C_5H_5$ ; energies (LDA) are given in eV; the JT parameters  $E_{JT}$  and  $\Delta$  are given in  $cm^{-1}$  and  $R_{JT}$  in  $(amu)^{1/2}\text{\AA}$ 

Occupation	State	Geometry	Energy
$e^{0.75}e^{0.75}$	$^2E$	$D_{5h}$	-64.6740
$b_1^2a_1^1$	$^2A_1$	$D_{5h}$	-64.6529
$a_1^2b_1^1$	$^2B_1$	$D_{5h}$	-64.6523
$b_1^2a_1^1$	$^2A_1$	$C_{2v}$	-64.8079
$a_1^2b_1^1$	$^2B_1$	$C_{2v}$	-64.8077
$E_{JT}$	$^2A_1$		1,250.2
$E_{JT}$	$^2B_1$		1,253.4
$\Delta$			3.2
$R_{JT}$	$^2A_1$		0.17
$R_{JT}$	$^2B_1$		0.18

**Table 5** Analysis of the JT multimode problem in  $C_5H_5$  radical by LS totally symmetric normal modes in harmonic approximation. Frequencies of normal modes are in  $cm^{-1}$  as obtained from ADF [1,40,76] calculations; contribution of the normal mode  $Q_k$  to the  $R_{JT}$  is given by  $w_k$  (linear coefficients in (22));  $c_k$  linear coefficients ( $w_k$ ) normalized to 1;  $E_k$  energy contribution of  $Q_k$  to the  $E_{JT}$  calculated in harmonic approximation, (23) in  $cm^{-1}$ ;  $F_k$  force along  $Q_k$  at HS point, calculated in harmonic approximation, (24) in  $10^3N$ ; experimental value  $E_k^{exp}$ , and two theoretical values  $E_k^{t1}$  and  $E_k^{t2}$  in  $cm^{-1}$  from [5,6].  $E_{JT}(DFT)$ , in  $cm^{-1}$ , from multideterminantal DFT, this work

$Q_k$	$\tilde{\nu}_k$ in $C_{2v}$	Assignment	HS-irrep	$w_k$	$c_k$	$E_k$	$F_k$	$E_k^{exp}$	$E_k^{t1}$	$E_k^{t2}$	$E_{JT}(DFT)$
1	831	C-C-C bend	$e_2'$	0.0738	0.2419	247.5	28.5	166	155	245	
2	937	C-C-H bend	$e_1'$	0.0374	0.0621	30.9	9.9				
3	1040	C-C-H bend	$e_2'$	0.1083	0.5218	247.9	29.0	594	360	509	
4	1127	C-C stretch	$a_1'$	0.0043	0.0008	1.6	2.6				
5	1349	C-C stretch	$e_1'$	-0.0276	0.0339	43.8	19.1				
6	1482	C-C stretch	$e_2'$	0.0560	0.1393	665.3	73.0	477	959	1387	
7	3120	C-H stretch	$e_2'$	0.0020	0.0002	0.5	2.9				
8	3140	C-H stretch	$e_1'$	-0.0012	0.0001	0.1	2.1				
9	3165	C-H stretch	$a_1'$	0.0014	0.0001	0.1	2.5				
$E_{JT}$						1,238		1,237	1,474	2,141	1,253

the quadratic coupling constant,  $G_{ij}^{kl}$  is zero, and there is no warping of the Mexican hat. In order to analyse multimode character of the JT distortion in  $C_5H_5$  we express the distortion as a linear combination of all totally symmetric normal modes in the LS energy minimum. Details of the procedure will be given later in Sect. 5, and only the results are presented in Table 5.

We are able to identify the three most important vibrations contributing to the JT distortion, vibrations 1, 3 and 6, in agreement with previous studies [5,6]. Comparing our results to the experimental one we may note that vibrations 3 and 6 are contributing approximately the same amount to the  $E_{JT}$ . While the other authors considered only those three normal modes, in our model all vibrations that can contribute to the JT distortion are included. Our model is completely theoretical without



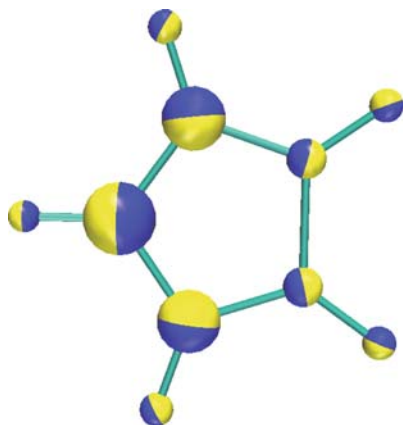


**Fig. 6a** vibration 1 (C-C-C bend)

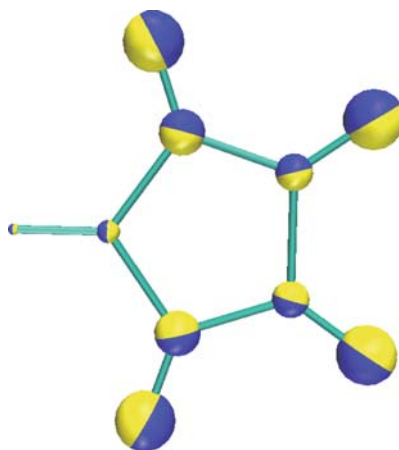


**Fig. 6b** vibration 3 (C-C-H bend)

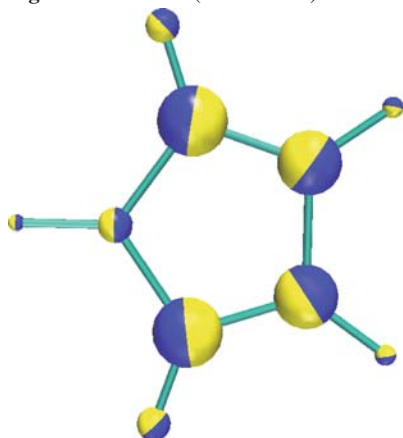


**Fig. 6c** vibration 6 (C-C stretch)

**Fig. 6** Vibrational energy distribution representation of the three most important  $a_1$  vibrations in  $C_{2v}$  symmetry of  $C_5H_5$ , corresponding to the three  $e'_2$  JT active vibrations in  $D_{5h}$  symmetry. The different colours indicate the direction of the displacement vector; the volume of the spheres is proportional to the contribution made by the individual nuclei to the energy of the vibrational mode

any fitting to the experimental data. Three most dominant vibrations are presented in the Fig. 6.

Vibrations 1, 3, 6 contribute 90% to the JT distortion. Vibrations 2 and 5, which correspond to the  $e'_1$  irreps in  $D_{5h}$  around 10%. They are JT active in the second order, and accordingly not negligible. This is because the vibrations are all of the same type, in plane ring deformation, as the ones corresponding to the  $e'_2$ , C-C-C bend and C-C stretch, thus influencing the C-C bonding in a similar way.

### 4.3 Cobaltocene

The high symmetry conformation of metallocenes can be either  $D_{5h}$  if the two rings are eclipsed or  $D_{5d}$  if the two rings are staggered. In both cases the symmetry arguments are the same as for an intermediate structure of  $D_5$  symmetry. The ground electronic state of cobaltocene in  $D_{5h}$  symmetry is  ${}^2E_1''$ ,  ${}^2E_{1g}$  in  $D_{5d}$ , with a single electron in the doubly degenerate orbital. Using group theory it is easy to show, see Sect. 2 that the distortion coordinates are of  $e_2'$  irreps in the eclipsed and of  $e_{2g}$  in the staggered conformation, and the descent in symmetry goes to  $C_{2v}$  and  $C_{2h}$  respectively. The electronic states will split in  $D_{5h}$   $E_1''$  into  $A_2$  and  $B_1$ , in  $D_{5d}$   $E_{1g}$  into  $A_g$  and  $B_g$ . Respectively, the JT active distortion  $e_2'$  splits into  $a_1$  and  $b_2$  and  $e_{2g}$  into  $a_g$  and  $b_g$ .

This system is more complicated than the previous ones, because an internal rotation of the rings is present. Our study [86] showed that this rotation does not influence the JT distortion. In the low symmetry,  $C_{2v}$  for the eclipsed,  $C_{2h}$  for the staggered conformation, the structure of the rings is nearly identical. This strongly suggests that the energy barrier for the rotation of the rings is small compared to the  $E_{JT}$ . This was verified calculating the energy profile for the ring rotation. The energy barrier for the internal rotation of the rings, from eclipsed to staggered conformation, is estimated to be around  $240\text{ cm}^{-1}$  in both high and low symmetries, similar to the energy for the rotation of the rings in ferrocene [13]. Cobaltocene in  $D_{5h}$  symmetry is approximately  $160\text{ cm}^{-1}$  more stable than in  $D_{5d}$ . This is in agreement with results of previous DFT calculations on metallocenes [75, 82]. The energy difference between the low symmetry conformations  $C_{2v}$  and  $C_{2h}$  obtained by descent in symmetry from  $D_{5h}$  and  $D_{5d}$  is similar. This is summarised in the Fig. 7.

Cobaltocene has been subject of wide research [3, 4, 22, 34, 52, 58, 74, 80], but only recently a detailed analysis [86] of the JT distortion has been carried out. Calculations were done for both the eclipsed and the staggered conformations, giving similar results. In this paper we will present only the results for the more stable of the two, i.e. for the eclipsed case. Details for both eclipsed and staggered conformation can be found in [86]. As already indicated in previous Sect. 3, DFT produces a totally symmetric electron distribution if each  $e_1''$  orbital carries 0.5 electrons. There are two distinct ways to accommodate the single electron in  $C_{2v}$  symmetry, i.e.  $a_2^1 b_1^0$  ( ${}^2A_2$  electronic state) or  $b_1^1 a_2^0$  ( ${}^2B_1$  electronic state). One of the states is stabilized by a distortion along  $+\mathbf{R}_{JT}$ , the other along  $-\mathbf{R}_{JT}$ . Thus, DFT calculations corresponding to both of these occupations, as well as to the  $G_{HS} = D_{5h}$  and  $G_{LS} = C_{2v}$  geometries, are carried out, leading to the values of JT stabilization energies,  $E_{JT}(A)$  and  $E_{JT}(B)$ . Results are tabulated in Table 6.

The JT stabilization energy is  $814.2\text{ cm}^{-1}$  in good agreement with the value of  $1050\text{ cm}^{-1}$  estimated from the solid state EPR [4, 22]. The experimental results strongly depend on the diamagnetic host matrix, thus making experimental determination of the JT parameters difficult. The JT energies for the different electronic states are almost exactly the same, the difference is only  $0.7\text{ cm}^{-1}$ , smaller

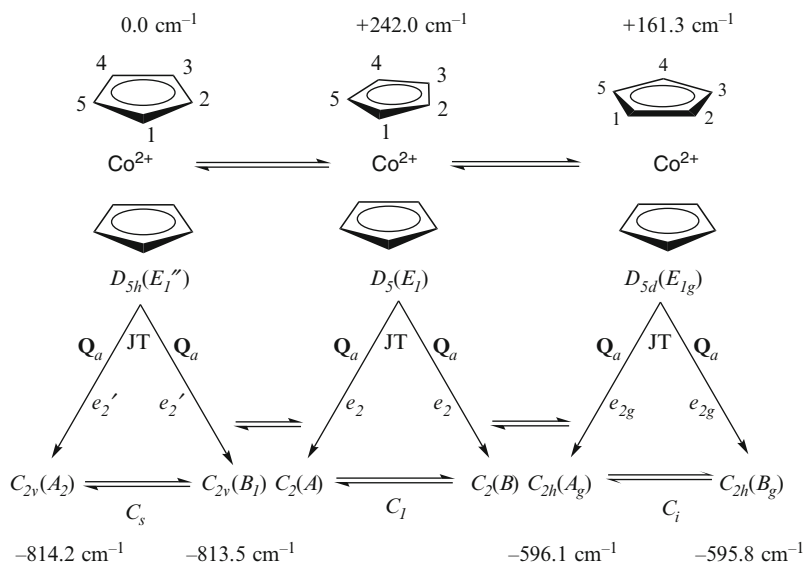


**Fig. 7** Summary of the JT effect in cobaltocene. Symmetries of the corresponding geometries, electronic states and normal coordinates, numbering of C atoms in the cyclopentadienyl rings, as well as the relative energies of the different structures is given

**Table 6** Results of the DFT calculations performed to analyse the JT effect of cobaltocene; energies (LDA) are given in eV; the JT parameters  $E_{JT}$  and  $\Delta$  are given in cm<sup>-1</sup> and  $R_{JT}$  in (amu)<sup>1/2</sup>Å

Occupation	State	Geometry	Energy
$e^{0.5}e^{0.5}$	${}^2E$	<i>D</i> <sub>5h</sub>	-142.28971
$a_2^0b_1^0$	${}^2A_2$	<i>D</i> <sub>5h</sub>	-142.26105
$b_1^1a_2^0$	${}^2B_1$	<i>D</i> <sub>5h</sub>	-142.26113
$a_2^1b_1^0$	${}^2A_2$	<i>C</i> <sub>2v</sub>	-142.36200
$b_1^1a_2^0$	${}^2B_1$	<i>C</i> <sub>2v</sub>	-142.36199
$E_{JT}$	${}^2A_2$		814.2
$E_{JT}$	${}^2B_1$		813.5
$\Delta$			0.7
$R_{JT}$	${}^2A_2$		0.35
$R_{JT}$	${}^2B_1$		0.35

then the precision of the calculations. As expected, based on group theoretical considerations, Sect. 2, there is no warping of the potential energy surface.

Cobaltocene is an another example of the multimode JT system. There are six pairs of  $e_2'$  vibrations which are first order JT active, four  $a_1'$  and six pairs of  $e_1'$  vibrations which are second order JT active. They become all totally symmetric in *C*<sub>2v</sub> symmetry (one component of each pair in the case of the degenerate vibrations). Thus in *C*<sub>2v</sub> symmetry we have 16 totally symmetric vibrations. As already pointed

**Table 7** Analysis of the JT multimode problem in cobaltocene by LS totally symmetric normal modes in harmonic approximation. Frequencies of normal modes are in  $\text{cm}^{-1}$  as obtained from ADF [1,40,76] calculations; contribution of the normal mode  $\mathbf{Q}_k$  to the  $\mathbf{R}_{\text{JT}}$  is given by  $w_k$  (linear coefficients in (22));  $c_k$  linear coefficients ( $w_k$ ) normalized to 1;  $E_k$  energy contribution of  $\mathbf{Q}_k$  to the  $E_{\text{JT}}$  calculated in harmonic approximation, (23) in  $\text{cm}^{-1}$ ;  $F_k$  force along  $\mathbf{Q}_k$  at HS point, calculated in harmonic approximation, (24) in  $10^3\text{N}$ ;  $E_{\text{JT}}(\text{DFT})$ , in  $\text{cm}^{-1}$ , from multideterminantal DFT [86]

$\mathbf{Q}_k$	$\tilde{\nu}_k$ in $C_{2v}$	Assignment	HS-irrep	$w_k$	$c_k$	$E_k$	$F_k$	$E_{\text{JT}}(\text{DFT})$
1	153	skeletal bending	$e'_1$	0.0035	0.0003	0.02	0.1	
2	292	ring–metal stretch	$a'_1$	−0.0172	0.0080	1.95	1.6	
3	405	ring tilt	$e'_1$	0.0097	0.0025	0.03	4.2	
4	587	out-of-plane ring deformation	$e'_2$	−0.1550	0.6495	475.49	48.2	
5	762	C-H wagging	$a'_1$	−0.0147	0.0058	2.11	2.0	
6	825	C-H wagging	$e'_1$	−0.0181	0.0082	4.12	3.8	
7	830	in-plane ring distortion	$e'_2$	−0.0621	0.1044	118.86	32.4	
8	869	C-H wagging	$e'_2$	−0.0657	0.1166	66.22	17.4	
9	976	C-H bending	$e'_1$	0.0084	0.0019	1.44	3.1	
10	1031	in-plane C–H bending	$e'_2$	0.0547	0.0809	55.77	15.5	
11	1126	ring breathing mode (C–C stretch)	$a'_1$	0.0002	0.0000	0.00	0.3	
12	1367	C–C stretch	$e'_2$	0.0209	0.0118	47.86	35.9	
13	1397	C–C stretch	$e'_1$	0.0185	0.0093	34.15	30.0	
14	3136	C–H stretch	$e'_2$	−0.0017	0.0001	0.46	3.5	
15	3148	C–H stretch	$e'_1$	−0.0009	0.0000	0.13	1.9	
16	3166	C–H stretch	$a'_1$	−0.0002	0.0000	0.00	0.4	
$E_{\text{JT}}$						808.6		814.2

out in order to analyse JT distortion in terms of the contribution of different normal coordinates, we express the distortion as a linear combination of all totally symmetric normal modes in the low symmetry ( $C_{2v}$ ) minimum energy conformation. The result is given in Table 7. Assignment of the vibrations is given according to the normal coordinate analysis of the ferrocene and ruthenocene [2, 13, 20, 68].

The main contribution to the JT distortion arises from the four  $e'_2$  type vibrations (labelled as 4, 7, 8 and 10 in Table 7). They contribute to about 95% of the total JT distortion vector. The four vibrations are: the out-of-plane ring distortion, 4, the in-plane ring distortion, 7, the C–H wagging (the out-of-plane C–H bending), 8, and in-plane C–H bending, 10. These vibrations are illustrated in Fig. 8, using the vibrational energy distribution representation [44]. The analysis shows, that the contribution of low energy skeletal vibrations (1 to 3) and the high energy vibrations (C–H stretch 14 to 16) is almost negligible. The JT important  $e'_2$  vibrations, and hence the JT distortion, is predominantly located in the five–member rings. The main contribution is the out-of-plane deformation of cyclopentadienyl ring (vibration 4). This is expected because this normal coordinate minimizes antibonding interactions between the cyclopentadienyl ring orbitals and the single occupied metal  $d$  orbital. The symmetry of the electronic ground state in HS point directs

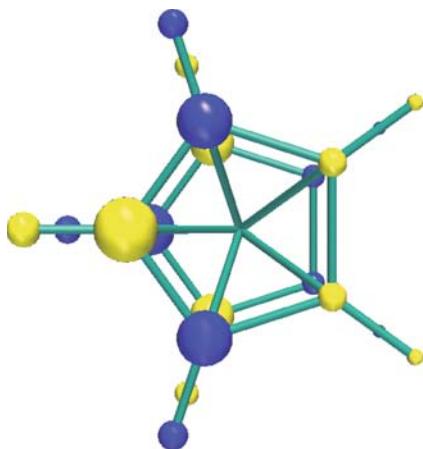


**Fig. 8a** vibration 4 (out-of-plane ring deformation)

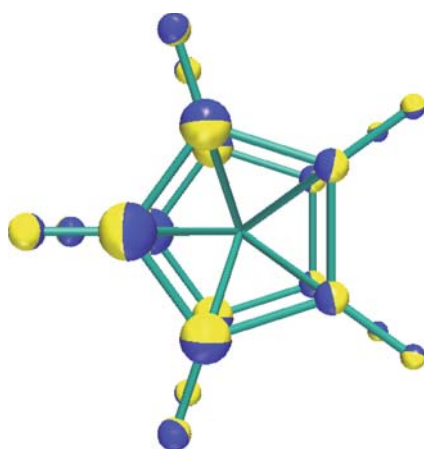


**Fig. 8b** vibration 7 (in-plane ring distortion)

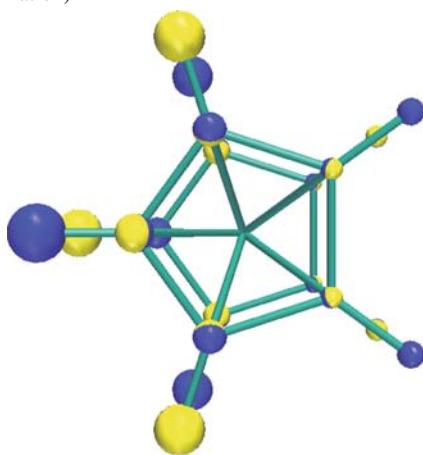


**Fig. 8c** vibration 8 (C-H wagging)

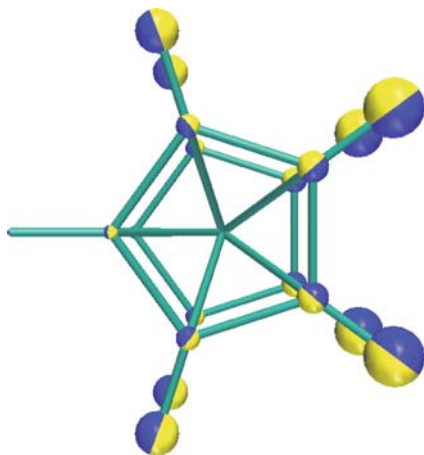


**Fig. 8d** vibration 10 (in-plane C-H bending)

**Fig. 8** Vibrational energy distribution representation of the four most important  $a_1$  vibrations in  $C_{2v}$  symmetry of cobaltocene, corresponding to the four  $e'_2$  vibrations in  $D_{5h}$  symmetry. The different colours indicate the direction of the displacement vector; the volume of the spheres is proportional to the contribution made by the individual nuclei to the energy of the vibrational mode

the distortion in a way of perturbing the aromaticity of the two rings. The multimode analysis gives a direct insight into microscopic origin of the distortion and into counterplay between the energy gain due to the JT effect and energy loss due to the out-of-plane distortion of the ligands.

$e'_1$  vibrations, that are JT active in second order only are almost not contributing, except the C–C stretch, vibration 13. The situation is different when comparing to

the  $C_5H_5$ , 4.2. This is due to the fact that in cobaltocene  $e'_2$  and  $e'_1$  vibrations are of different type,  $e'_2$  are located in the ligands, while  $e'_1$  are mainly skeletal deformations. In  $C_5H_5$  they are of the same kind, thus influencing bonding in an analogous way.

$E_{JT}$  calculated from the LS normal coordinate analysis is in the excellent agreement with previously calculated one using multideterminantal approach. In  $C_5H_5$  both the JT electronic deformation and nuclear displacements are localized in the rings, while in  $CoCp_2$  the first is localized on the central metal ion and the latter on the Cp rings. In  $C_5H_5$  contributions originating from the second order JT active vibrations,  $e'_1$ , are consequently not negligible.

The mixing of the totally symmetric vibrations in lower symmetry is expected to increase with increasing deviation from the high symmetry geometry. It is interesting to see how the composition of the distortion vector changes along the minimal energy path. The latter is defined as the steepest descent path [37, 38], down from the JT, HS, cusp to the local energy minimum, LS. The former is easily calculated using the Intrinsic Reaction Coordinate (IRC) algorithm as implemented by Deng and Ziegler [29, 30] in the ADF program package [1, 40, 76]. There is a complete analogy between the JT distortion and chemical reaction paths, thus it is possible to use the same algorithms previously developed for the analysis of reaction paths. The JT distortion path is totally symmetric reaction path in the LS potential energy surface, connecting HS, JT cusp, and LS energy minimum. The high symmetry point has a nonzero gradient, thus, the first step is computed in direction of the steepest descent and not in the direction of a negative Hessian eigenvector as usually in IRC calculations starting from the transition states. The path is then computed by taking steps of adequate size and by optimizing all atomic coordinates orthogonal to it. During the calculation  $C_{2v}$  symmetry is conserved, and it is taken into account that one electronic state corresponds to the forward path, and the other to the backward path. IRC calculations for the eclipsed conformation of the rings are summarized in Fig. 9 together with the direct path. It can be seen that these two ways are not significantly different. Changes of the contributions of the four dominant vibrations along the IRC path are represented in Fig. 10.

The significance of different normal coordinates is not the same at the beginning step and at the minimum. Figure 10 shows that the composition of the distortion vector changes along the minimal energy path. In the beginning, the contribution of in-plane C-H bending, 10, is also important, but as the distortion deviates from the high symmetry point its contribution decreases. The opposite is true for the lowest energy  $e'_2$  vibration 4, the out-of-plane ring deformation, which is indeed the most important one. The contribution of C-H wagging is also becoming more important. On the first sight, it might be surprising, that the softest of the four modes makes the largest contribution. This indicates that the distortion along the corresponding normal coordinate is larger than for any other one. One can see that the first point along the IRC path is already giving 2/3 of the JT stabilisation. Thus, although IRC calculation gives the information that different contributions change along the reaction path, the information from the first, infinitesimally small, step is missing. This is due to the fact that IRC algorithm is implemented to locate the minima, reactants

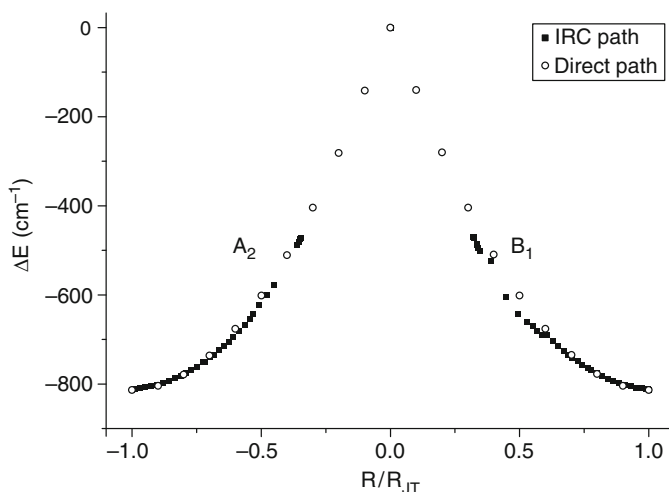


**Fig. 9** IRC calculation (*filled squares*) and direct path (*open circles*) from the high symmetry cusp, in  $C_{2v}$  symmetry (eclipsed conformation of the rings); forward direction correspond to the  $^2B_1$  electronic state and backward direction to the  $^2A_2$  electronic state; energies are given in  $\text{cm}^{-1}$  relative to the HS point

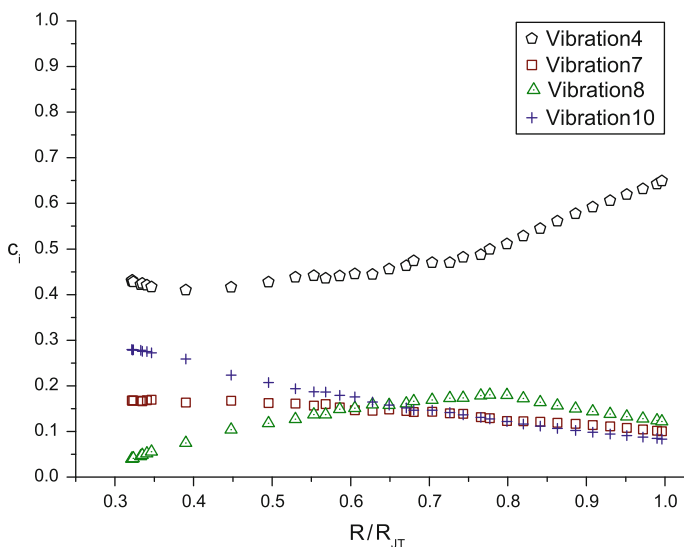


**Fig. 10** Changes in the composition of the distortion vector – contribution of the four most important vibrations to the  $\mathbf{R}_{JT}$ , given as  $c_k$  (linear coefficients in (22) normalized to 1) along the minimal energy (IRC) path

and products, in the fastest way, and due to the fact that in chemical reactions there is bond formation and bond breaking, thus the distortions are much bigger than in the JT cases. This information is obtained from the calculation of the forces at the

HS point as done by our multimode analysis, Table 7. Vibration 4 is clearly dominating one, while forces along harder vibrations 7, 8 and 10 are smaller and of comparable size. This can be also seen from the values  $c_k$ ,  $E_k$  and IRC calculations. The importance of the vibration 12 (also corresponding to the  $e'_2$  irrep in HS) and 13 (corresponding to the  $e'_1$  irrep in HS) is small but still contributing to the distortion. They contribute each around 1% to the distortion, and each around 5% to the  $E_{JT}$ , but with not negligible forces at HS point.

## 5 Analysis of the Multimode JT Effect at the Stationary Point of Low Symmetry

As shown in the Sect. 2, the JT theorem predicts a spontaneous distortion of the high symmetry configuration. Group theory allows finding the irreducible representation of the non-totally symmetric vibrations in the HS conformation, which are JT active and remove the degeneracy and lead to a stabilization of the system by lowering the symmetry. The irreducible representations of the active modes,  $\Gamma_{HS}^{vib}$  are given by the direct product  $\Gamma_{HS}^{elect} \otimes \Gamma_{HS}^{elect} \subset A_1 + \Gamma_{HS}^{vib}$  in  $G_{HS}$ .  $G_{LS}$ , the point group of the minimum energy conformation is defined by the requirement that the irreps of the active modes become totally symmetric upon descent in symmetry and application of the epikernal principle [23, 24, 46].

JT distortion,  $\mathbf{R}_{JT}$  represents a displacement of the nuclei from the HS conformation to the LS energy minimum on the  $3N - 6$  dimensional potential energy surface. The minimum is localized by energy minimization constraining the structure to  $G_{LS}$ , using well developed algorithms as implemented in standard computational chemistry program packages. The difference between the HS cusp and the LS conformation of minimal energy defines the  $\mathbf{R}_{JT}$ . The path from the cusp to the minimum conformation is a reaction coordinate. This has been often overlooked. Therefore, the symmetry rules developed by Bader [9–11] and Pearson [64, 65] can be applied. The JT distortion is defined by the symmetry of the electronic states, as pointed out above and represents a totally symmetric reaction coordinate in  $G_{LS}$ . Any displacement on the potential energy surface, also  $\mathbf{R}_{JT}$ , has to be totally symmetric and consequently a superposition of the totally symmetric normal coordinates. The number of the later is  $N_{a_1}$ , in general smaller than  $3N - 6$ .

Within the harmonic approximation,  $3N - 6$  dimensional potential energy surface has a simple mathematical form. Because the displacement of the nuclei must be totally symmetric in the  $G_{LS}$ , the potential energy surface is defined as a superposition of  $N_{a_1} \leq 3N - 6$  totally symmetric orthogonal oscillators in LS. In other words the JT distortion is given as a linear combination of displacements along all totally symmetric normal modes in the LS minimum energy conformation. Using this approach it is possible to estimate the contribution of the different normal modes to the  $\mathbf{R}_{JT}$  in a complex system.  $N_{a_1}$  is in general larger than the number of JT active,  $\gamma_{JT}$ , vibrations, which spans  $\Gamma_{HS}^{vib}$ . Because they are of the same symmetry they contribute all to the JT distortion. Especially the  $a_1$  modes in  $G_{HS}$  mix into



the  $\gamma_{JT}$  vibrations, because they never change upon descent in symmetry and they are always present in the direct product  $\Gamma_{HS}^{elect} \otimes \Gamma_{HS}^{elect}$ . An example is the  $E \otimes e$  problem in  $T_d$  point group discussed for  $VCl_4$  in Sect. 4.1. In this case only one component of the angle deformation of  $e$  symmetry is JT active. It changes to  $a_1$  in  $D_{2d}$ . In the lower symmetry it might mix with the  $a_1$  stretch vibration which is not JT active in  $T_d$ . In many situations other irreps, which are not JT active in HS become totally symmetric upon descent in symmetry, and therefore contribute also to the JT distortion. This is found in the case of the JT  $D_{5h} \rightarrow C_{2v}$  distortion<sup>5</sup> already discussed for  $C_5H_5$  radical and  $CoCp_2$ , Sects. 4.2 and 4.3. The normal coordinates that are basis of the  $e'_2$ ,  $e'_1$  and  $a'_1$  irreducible representations in  $D_{5h}$  become  $a_1$  in  $C_{2v}$ .  $e'_2$ s are JT active in first order, while  $e'_1$  are active in second order.

The choice of the LS geometry as the reference point is in contrast to the usual treatment of the JT effect. This point corresponds to a energy minimum and has the property that the Hessian of the energy is positive semi-definite<sup>6</sup> and thus can be used to obtain the harmonic vibrational modes without any complications. As already pointed, the totally symmetric subset of vibrations is used to represent potential energy surface of the JT distortion in a harmonic approximation. The HS point in contrary is a cusp on the potential energy surface, the gradients—first derivatives of energy over nuclear displacements, are discontinuous and not zero, hence this point is inappropriate for a normal coordinate analysis. Conventional quantum chemistry program packages do not allow to use other points than stationary ones as a reference point in the frequency calculations. Thus, frequency calculations in the HS point will need the implementation of special algorithms into the conventional quantum chemistry packages, e.g. ADF. Of course one can use the results of the normal coordinate analysis of a similar JT-nonactive molecule (e.g. with one electron more or less), but this is an unnecessary approximation. Such a calculation, however, yields no gradients along the JT active modes, which are the essential ingredient of the JT distortions, the force, which drives the molecule out of the high symmetry conformation. In the HS point  $a_1$  and  $\gamma_{JT}$  normal coordinates do not interact, which is not the case in the LS point, as they are then all of the same symmetry. This allows us to obtain different contribution from the simple linear equation, (29). Furthermore, it is always possible to correlate normal modes of LS to HS ones, thus having connection to the usual treatment based on perturbation theory in HS.

Based on this consideration it is straight forward to analyse the multimode problem using generalized displacement coordinates,  $q_k$  ( $k = 1 \dots 3N$ ), around the low symmetry (LS) energy minimum as a origin ( $q_{LSk} = 0$ ,  $k = 1 \dots 3N$ ):

$$q_1 = \sqrt{m_1} \Delta x_1, \quad q_2 = \sqrt{m_1} \Delta y_1, \quad \dots, \quad q_{3N} = \sqrt{m_N} \Delta z_N \quad (25)$$

<sup>5</sup> This can be applied of course also for the  $D_{5d}$  and  $D_5$  point groups.

<sup>6</sup> The square matrix of second-order partial derivatives of a potential energy over the nuclear displacements, Hessian,  $\mathbb{H}$ , is positive semi-definite if  $\mathbf{Q}^T \mathbb{H} \mathbf{Q} \geq 0$  for any arbitrary vector  $\mathbf{Q}$ .

$\Delta x_n, \Delta y_n, \Delta z_n$  are Cartesian displacements from the origin, and  $m_n$  are masses of atoms. Every point  $\mathbf{X}$  in our conformational space can be represented using this generalized coordinates relative to the origin, by a  $3N$  dimensional vector  $\mathbf{R}_X$ :

$$\mathbf{R}_X = \begin{bmatrix} q_{X1} \\ q_{X2} \\ q_{X3} \\ \vdots \\ q_{X3N-2} \\ q_{X3N-1} \\ q_{X3N} \end{bmatrix} = \begin{bmatrix} \sqrt{m_1} & & & & & & \\ & \sqrt{m_1} & & & & & \\ & & \sqrt{m_1} & & & & \\ & & & \ddots & & & \\ & \mathbf{0} & & & \sqrt{m_N} & & \mathbf{0} \\ & & & & & \sqrt{m_N} & \\ & & & & & & \sqrt{m_N} \end{bmatrix} \begin{bmatrix} \Delta x_1 \\ \Delta y_1 \\ \Delta z_1 \\ \vdots \\ \Delta x_N \\ \Delta y_N \\ \Delta z_N \end{bmatrix} \quad (26)$$

$$\mathbf{R}_X = \mathbb{M}^{1/2} \Delta \mathbf{r}_X \quad (27)$$

The HS point is given by the vector  $\mathbf{R}_{HS}$ :

$$\mathbf{R}_{HS} = \begin{bmatrix} q_{HS1} \\ \vdots \\ q_{HS3N} \end{bmatrix} \quad (28)$$

Consider  $q_{HS1}, q_{HS2}, \dots, q_{HS3N}$ . This is equivalent to say that the JT distortion is equal to  $\mathbf{R}_{HS}$ ,  $\mathbf{R}_{JT} = \mathbf{R}_{HS}$ , with elements  $q_{HSk}$ .

As the result of the DFT frequency calculations in LS, we have  $N_{a_1}$  totally symmetric normal coordinates  $\mathbf{Q}_k$  ( $k = 1 \dots N_{a_1}$ ), which are the eigenvectors of the Hessian. The corresponding eigenvalues are  $\lambda_k = (2\pi \nu_k)^2$ ,  $\nu_k$  is a frequency of a normal mode which is connected to the wave numbers,  $\tilde{\nu}_k$ , that are usually used, by a simple relation  $\nu_k = \tilde{\nu}_k c$ , where  $c$  is the speed of light. The normal modes are displacement vectors in generalized displacement coordinates, i.e.:

$$\mathbf{Q}_k = \begin{bmatrix} \Delta q_{k1} \\ \vdots \\ \Delta q_{k3N} \end{bmatrix} \quad (29)$$

Within the harmonic approximation it is possible to express the JT distortion in terms of LS totally symmetric normal coordinates:

$$\mathbf{R}_{JT} = \sum_{k=1}^{N_{a_1}} w_{HSk} \mathbf{Q}_k \quad (30)$$

In matrix form this yields:

$$\mathbf{R}_{\text{JT}} = \begin{bmatrix} q_{\text{HS}1} \\ \vdots \\ q_{\text{HS}3N} \end{bmatrix} = \begin{bmatrix} \Delta q_{11} & \dots & \Delta q_{N_{a_1}1} \\ & \ddots & \\ \Delta q_{13N} & \dots & \Delta q_{N_{a_1}3N} \end{bmatrix} \begin{bmatrix} w_{\text{HS}1} \\ \vdots \\ w_{\text{HS}N_{a_1}} \end{bmatrix} = [\mathbf{Q}_1, \mathbf{Q}_2, \dots, \mathbf{Q}_{N_{a_1}}] \begin{bmatrix} w_{\text{HS}1} \\ \vdots \\ w_{\text{HS}N_{a_1}} \end{bmatrix} \quad (31)$$

$$\mathbf{R}_{\text{JT}} = \mathbf{Q} \mathbf{w}_{\text{HS}} \quad (32)$$

This linear problem can be easily solved to get weighting factors  $w_{\text{HS}k}$ . They represent the contribution of the displacements along the different totally symmetric normal coordinates to the  $\mathbf{R}_{\text{JT}}$ .

$$\mathbf{w}_{\text{HS}} = (\mathbf{Q}^T \mathbf{Q})^{-1} \mathbf{Q}^T \mathbf{R}_{\text{JT}} \quad (33)$$

The weighting can be normalized to 1, which is more informative as  $c_k$  are giving the information of the percentage contribution of each normal mode to the  $\mathbf{R}_{\text{JT}}$ :

$$c_k = \frac{w_k^2}{w_1^2 + w_2^2 + \dots + w_{N_{a_1}}^2} \quad (34)$$

The same treatment is possible for any point  $\mathbf{R}_X$  on the potential energy surface:

$$\mathbf{R}_X = \mathbf{Q} \mathbf{w}_X \quad (35)$$

Alternatively to the method described in Sect. 2, in this harmonic model,  $E_{\text{JT}}$  is expressed as the sum of the energy contributions of the totally symmetric normal modes.

$$E_{\text{JT}} = \sum_{k=1}^{N_{a_1}} E_k = \frac{1}{2} \sum_{k=1}^{N_{a_1}} w_{\text{HS}k}^2 \mathbf{Q}_k^2 \lambda_k \quad (36)$$

Thus each normal mode contributes the energy  $E_k$  to the JT stabilisation.

$$E_k = 2\pi^2 w_{\text{HS}k}^2 \nu_k^2 |\mathbf{Q}_k|^2 \quad (37)$$

Similarly one can get the potential gradient along each normal coordinate at any point  $\mathbf{R}_X$ , which is the force,  $\mathbf{F}_{Xk}$ , which drives the nuclei along each coordinate to the minimum.  $\mathbf{F}_{Xk}$  is defined as derivative of energy over Cartesian coordinates which yields (38).

$$\mathbf{F}_{Xk} = w_{Xk} \lambda_k \mathbb{M}^{1/2} \mathbf{Q}_k \quad (38)$$

In the HS point this will lead information which normal mode has the steepest descent indicating the main driving force for the JT distortion from the HS to the LS. The total distortion force at a given point is given as the sum of the individual forces, which allows determination of the minimal energy distortion path.

$$\mathbf{F}_X = \sum_k \mathbf{F}_{Xk} \quad (39)$$

As a conclusion, the simple analytical form of the potential energy surface allows to calculate the minimal energy path, step by step from HS to the LS energy minimum. It is obvious that along the path the contributions of the different modes will change. At HS only JT active modes contribute. After the first step the symmetry is lowered and the other modes as mentioned will mix in. This allows getting very detailed picture on the interaction between the deformation of the electron distribution and the displacements of the nuclei.

It must be mentioned that the  $3N - 6$  normal coordinates in LS are not identical with the normal coordinates in HS. The correlation between the two systems is however straight forward. There is a unitary transformation between the normal coordinates of HS and LS points:

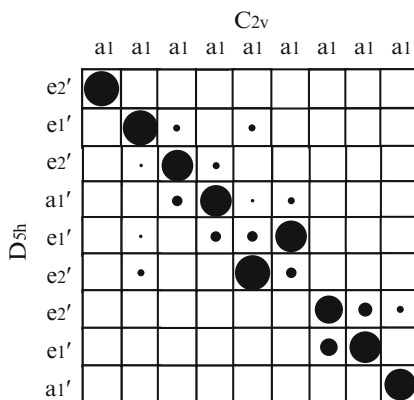
$$\left[ \mathbf{Q}_{1\text{HS}}, \mathbf{Q}_{2\text{HS}}, \dots, \mathbf{Q}_{N_{a_1}\text{HS}} \right] = \left[ \mathbf{Q}_1, \mathbf{Q}_2, \dots, \mathbf{Q}_{N_{A_1}} \right] \begin{bmatrix} r_{11} & \dots & r_{1N_{a_1}} \\ \vdots & & \vdots \\ r_{3N_1} & \dots & r_{3NN_{a_1}} \end{bmatrix} \quad (40)$$

The visual inspection can be used for small molecules, but for larger molecules this is impossible. Alternatively, it is possible to use the method developed by Hug [44], for the comparison of nuclear motions of structurally similar fragments of molecules. We applied it for the correlation of the normal modes of the same molecule in different conformations belonging to different point groups. Using the idea of similarity of the two normal coordinates it is possible to correlate the HS and LS normal coordinates quantitatively. Furthermore it allows using as a reference molecule (HS) a similar molecule which is not JT active, e.g. cyclopentadienyl anion or ferrocene, thus bypassing difficulties in obtaining the normal coordinates of the HS cusp. Hug's program allows pictorial representation of the unitary transformation matrix as shown in Fig. 11 for  $\text{C}_5\text{H}_5$ , or in matrix form with numerical values of the similarities, as shown in Table 8 for  $\text{CoCp}_2$ . Identical modes have the value of 1, while orthogonal value 0. In schematic representation a circle with a diameter equal to the square which contains it means a value of 1.

## 6 Conclusions and Perspectives

In this paper a new DFT based method for the qualitative and quantitative analysis of the adiabatic potential energy surfaces of JT active molecules is presented. It is shown how DFT can be successfully applied for the calculation of the JT parameters, and thus be a useful tool in understanding the JT effect and related phenomena. The performance of the model has been evaluated for tetrachlorovanadium(IV) ( $\text{VCl}_4$ ), an example of ideal, single mode problem; cyclopentadienyl radical ( $\text{C}_5\text{H}_5$ ) and bis(cyclopentadienyl)cobalt(II) (cobaltocene,  $\text{CoCp}_2$ ) as examples of the multimode problems. The JT parameters obtained using DFT are in excellent agreement with

**Fig. 11** Representation of the similarities of the vibrations in cyclopentadienyl anion (rows),  $D_{5h}$ , and radical (columns),  $C_{2v}$ ; A circle with a diameter equal to the square which contains it means a value of 1; vibrations are ordered by increasing energy



experiment. In addition the importance of the analysis of the multimode JT effect is shown.

JT effect is controlled by the molecular symmetry. Displacements of the nuclei from the JT unstable HS configuration to the LS minimum on the potential energy surface is a totally symmetric reaction coordinate in the  $G_{LS}$  point group. This aspect was often neglected so far. This analogy allows application of the fundamental symmetry rule for reaction coordinates, that it belongs to the totally symmetric irreducible representation of the LS point group of the molecule. Thus, within the harmonic approximation, the distortion can be analysed as the linear combination of totally symmetric normal modes of the LS minimum. This model allows quantifying the contribution of all possible normal modes, their energy contribution to the  $E_{JT}$ , the forces at the HS cusp and the detailed distortion path.

There is a sophisticated counterplay between the electronic distortion due to the JT effect, mainly localized on the central metal ion, and the distortion of the ligand conformation in metal complexes. This can lead to a surprising result, e.g. that in  $C_5H_5$  the JT distortion does not break the planarity in contrast to the situation in  $CoCp_2$ . In  $C_5H_5$  the ring accepts an en-allyl conformation, whereas in the complex we find a non planar dien conformation. Similar cases are expected in various JT active chelate complexes. Using our method for the multimode analysis presented in this paper, one can get direct insight into the interaction between electronic structure and the nuclear movements. This is of great significance in various fields, not only in the larger JT systems, but also in the systems like spin-crossover compounds, mixed valence compounds, photochemical reactions etc.

## 7 Computational Details

The DFT calculations reported in this work have been carried out using the Amsterdam Density Functional program package, ADF2007.01 [1, 40, 76]. The local density approximation (LDA) characterized by the Vosko-Willk-Nusair (VWN)



[78] parametrization have been used for the geometry optimizations. Triple zeta (TZP) Slater-type orbital (STO) basis set have been used for all atoms. All calculations were spin-unrestricted with strict criteria for convergence: energy  $10^{-4}$  Hartrees; gradients  $10^{-4}$  Hartree/Å; changes in Cartesian coordinates  $10^{-4}$  Å; and for numerical integration ten significant digits are used. Analytical harmonic frequencies were calculated [19, 46], and were analysed with the aid of PyVib2 1.1 [35]. Vibrations are illustrated using the vibrational energy distribution representation [44]. The different colours indicate the direction of the displacement vector, while the volumes of the spheres are proportional to the contribution made by the individual nuclei to the energy of the vibrational mode. The Intrinsic Reaction Coordinate method [37, 38] as implemented in ADF has been used [29, 30]. The initial direction of the path is chosen by computing the gradient at the high symmetry configuration. Matlab scripts for the calculation of the coupling coefficients for any point group (Wigner-Eckart theorem) and for the calculation of the weighting factors,  $w_{\chi k}$  in (35), can be obtained from authors upon request.

**Acknowledgements** This work was supported by the Swiss National Science Foundation and the Serbian Ministry of Science (Grant No. 142017G). We thank all the past and present members of our group for their contribution and the valuable discussions.

## References

1. (2007) Adf2007.01. SCM, Theoretical Chemistry, Vrije Universiteit Amsterdam, The Netherlands, <http://www.scm.com>
2. D.M. Adams, W.S. Fernando, *J Chem Soc. Dalton Trans.* **22** 2507 (1972)
3. J.H. Ammeter, J.D. Swalen, *J. Chem. Phys.* **57** 678 (1972)
4. J.H. Ammeter, L. Zoller, J. Bachmann, P. Baltzer, E. Gamp, R. Bucher, E. Deiss, *Helv. Chim. Acta* **64** 1063 (1981)
5. B.E. Applegate, T.A. Miller, *J. Chem. Phys.* **114** 4855 (2001)
6. B.E. Applegate, A.J. Bezant, T.A. Miller, *J. Chem. Phys.* **114** 4869 (2001)
7. P.W. Atkins, M.S. Child, C.S.G. Phillips, *Tables for Group Theory* (Oxford University Press, Oxford, 1970)
8. F.W. Averill, G.S. Painter, *Phys. Rev. B* **46**(4) 2498 (1992)
9. R.F.W. Bader, *Mol. Phys.* **3** 137 (1960)
10. R.F.W. Bader *Can. J. Chem.* **40** 1164 (1962)
11. R.F.W. Bader, A.D. Bandrauk, *J. Chem. Phys.* **49** 1666 (1968)
12. M.J. Bearpark, M.A. Robb, N. Yamamoto, *Spectrochim. Acta A* **55** 639 (1999)
13. A. Berces, T. Ziegler, *Top. Curr. Chem.* **182** 41 (1996)
14. I.B. Bersuker, *J Comp. Chem.* **18**(2) 260 (1997)
15. I.B. Bersuker, *The Jahn–Teller Effect* (Cambridge University Press, Cambridge, 2006)
16. F.A. Blankenship, R.L. Belford, *J. Chem. Phys.* **36** 633 (1962)
17. W.T. Borden, E.R. Davidson, *J. Am. Chem. Soc.* **101** 3771 (1979)
18. M. Born, R. Oppenheimer, *Ann. Phys.* **84** 457 (1927)
19. A. Brces, R.M. Dickson, L. Fan, H. Jacobsen, D. Swerhone, T. Ziegler, *Comput. Phys. Commun.* **100** 247 (1997)
20. J. Brunvoll, S.J. Cyvin, L. Schäfer *J. Organomet. Chem.* **11** 459 (1971).
21. R. Bruyndonckx, C. Daul, P.T. Manoharan, E. Deiss, *Inorg. Chem.* **36** 4251 (1997)
22. R. Bucher, *Esr-untersuchungen an jahn-teller-aktiven sandwichkomplexen*. PhD thesis, ETH Zuerich, 1977

23. A. Ceulemans, L.G. Venquickenborne, *Struct. Bonding* **71** 125 (1989)
24. A. Ceulemans, D. Beyens, L.G. Venquickenborne, *J. Am. Chem. Soc.* **106** 5824 (1984)
25. M.S. Child, H.C. Longuet-Higgins, *Proc. R. Soc. Lond. Ser. A* **254**(1041) 259 (1961)
26. C. Cunha, S. Canuto, *J. Mol. Struct: THEOCHEM* **464** 73 (1999)
27. C. Daul, *Int. J. Quant. Chem.* **52** 867 (1994)
28. C.A. Daul, K. Doclo, C.A. Stückl *Recent Advances in Density Functional Methods, Part II* (World Scientific Company, Singapore, 1997), chap On the Calculation of Multiplets
29. L. Deng, T. Ziegler, *Int. J. Quant. Chem.* **52** 731 (1994)
30. L. Deng, T. Ziegler, L. Fan, *J. Chem. Phys.* **99** 3823 (1993)
31. R.M. Dreizler, E.K.U. Gross, *Density Functional Theory, an Approach to Quantum Many-Body Problem* (Springer, Berlin, 1990)
32. B.I. Dunlap, W.N. Mei, *J. Chem. Phys.* **78** 4997 (1983)
33. C. Eckart, *Rev. Mod. Phys.* **2** 305 (1930)
34. H. Eicher, *Phys. Rev. A* **40** 1637 (1989)
35. M. Fedorovsky, Pyvib2, a program for analyzing vibrational motion and vibrational spectra. <http://pyvib2.sourceforge.net>, 2007
36. M. Filatov, S. Shaik, *Chem. Phys. Lett.* **304** 429 (1999)
37. K. Fukui, *J. Phys. Chem.* **74** 4161 (1970)
38. K. Fukui, *Acc. Chem. Res.* **14** 363 (1981)
39. P. Garcia-Fernandez, I.B. Bersuker, J.A. Aramburu, M.T. Barriuso, M. Moreno, *Phys. Rev. B* **71** 184 117–1–10 (2005)
40. C.F. Guerra, J.G. Snijders, G. te Velde, E.J. Baerends, *Theor. Chem. Acc.* **99** 391 (1998)
41. G. Herzberg, *Molecular Spectra and Molecular Structure III. Electronic Spectra and Electronic Structure of Polyatomic Molecules* (Van Nostrand Reinhold Company, Princeton, 1966)
42. G. Herzberg, E. Teller, *Z. Phys. Chem. B* **21** 410 (1933)
43. W.D. Hobey, A.D. McLachlan, *J. Chem. Phys.* **33** 1965 (1960)
44. W. Hug, M. Fedorovsky, *Theor. Chem. Acc.* **119** 113 (2008)
45. T. Ichino, S.W. Wren, K.M. Vogelhuber, A.J. Gianola, W.C. Lineberger, J.F. Stanton *J. Chem. Phys.* **129** 084 310–084 319 (2008)
46. H. Jacobsen, A. Brces, D. Swerhone, T. Ziegler, *Comput. Phys. Commun.* **100** 263 (1997)
47. H.A. Jahn, E. Teller, *Proc R Soc Lond. Ser. A* **161** 220 (1937)
48. R.B. Johannesen, G.A. Candela, T. Tsang, *J. Chem. Phys.* **48** 5544 (1968)
49. I.G. Kaplan, *J. Mol. Struct.* **838** 39 (2007)
50. J.H. Kiefer, R.S. Tranter, H. Wang, A.F. Wagner, *Int. J. Chem. Kin.* **33** 834 (2001)
51. W. Koch, M.C. Holthausen, *A Chemis's Guide to Density Functional Theory* (Wiley-VCH, New York, 2001)
52. E. König, R. Schnakig, S. Kremer, *Chem. Phys.* **27** 331 (1978)
53. M. Levy, *Phys. Rev. A* **26** 1200 (1982)
54. A.D. Liehr, *Z. Phys. Chem.* **9** 338 (1956)
55. A.D. Liehr, *J. Phys. Chem.* **67** 389 (1963)
56. H.C. Longuet-Higgins, *Proc. R. Soc. Lond. Ser. A* **344**(1637) 147 (1975)
57. H.C. Longuet-Higgins, U. Öpik, M.H.L. Pryce, R.A. Sack, *Proc. R. Soc. Lond. Ser. A* **244**(1236) 1 (1958)
58. N. Matsuzawa, J. Seto, D. Dixon, *J. Phys. Chem. A* **101** 9391 (1997)
59. R. Meyer, F. Grof, T. Ha, H.H. Gunthard, *Chem. Phys. Lett.* **66** 65 (1979)
60. W. Moffitt, A.D. Liehr, *Phys. Rev.* **106**(6) 1195 (1957)
61. Y. Morino, H. Uehara, *J. Chem. Phys.* **45** 4543 (1966)
62. U. Öpik, M.H.L. Pryce, *Proc. R. Soc. Lond. Ser. A* **238**(1215) 425 (1957)
63. R.G. Parr, W. Yang, *Density-Functional Theory of Atoms and Molecules* (Oxford University Press, Oxford, 1989)
64. R.G. Pearson, *J. Am. Chem. Soc.* **91**(18) 4947 (1969)
65. R.G. Pearson, *Symmetry Rules for Chemical Reactions* (Wiley-Interscience, New York, 1976)
66. R. Renner, *Z. Phys. A* **92** 172 (1934)
67. T. Satoa, K. Tanaka, K. Tokunaga, *J. Chem. Phys.* **124** 124 (2006)
68. L. Schäfer, J. Brunvoll, S.J. Cyvin, *J. Mol. Struct.* **11** 459 (1972)



69. P.R.T. Schipper, O.V. Gritsenko, E.J. Baerends, *Theor. Chim. Acc.* **99** 329 (1998)
70. J. Simons, *Energetic Principles of Chemical Reactions* (Jones and Bartlett, Boston, 1983)
71. J.C. Slater, J.B. Mann, T.M. Wilson, J.H. Wood, *Phys. Rev.* **184** 672 (1969)
72. L.C. Snyder, *J. Chem. Phys.* **33** 619 (1960)
73. J.F. Stanton, *J. Chem. Phys.* **115** 10382 (2001)
74. A. Stebler, A. Furrer, J.H. Ammeter, *Inorg. Chem.* **23** 3493 (1984)
75. M. Swart, *Inorg. Chim. Acta* **360** 179 (2007)
76. G. te Velde, F.M. Bickelhaupt, S.J.A van Gisbergen, C.F. Guerra, E.J. Baerends, J.G. Snijders, T. Ziegler, *J. Comput. Chem.* **22** 931 (2001)
77. J.H. van Vleck, *J. Chem. Phys.* **7** 72 (1939)
78. S. Vosko, L. Wilk, M. Nusair, *Can. J. Phys.* **58** 1200 (1980)
79. S.G. Wang, H.E. Schwarz, *J. Chem. Phys.* **105** 4641 (1996)
80. J. Weber, A. Goursot, E. Pénigault, J.H. Ammeter, J. Bachmann, *J. Am. Chem. Soc.* **104** 1491
81. E.P. Wigner, (1930) *Gruppentheorie* (Vieweg, Braunschweig, 1930)
82. Z.F. Xu, Y. Xie, W.L. Feng, H.F. SchaeferIII, *J. Phys. Chem. A* **107** 2176 (1997)
83. Y. Zhang, W. Yang, *J. Chem. Phys.* **109** 2604 (1998)
84. T. Ziegler, A. Rauk, E.J. Baerends, *Theor. Chim. Acta* **43** 261 (1977)
85. S. Zilberg, Y. Haas, *J. Am. Chem. Soc.* **124** 10683 (2002)
86. M. Zlatar, C.W. Schlöpfer, E.P. Fowe, C. Daul, *Pure Appl. Chem.* **81** 1397 (2009)

**Part II**  
**Conical Intersections and Nonadiabatic**  
**Dynamics in Molecular Processes**

# Second-Order Analysis of Conical Intersections: Applications to Photochemistry and Photophysics of Organic Molecules

Lluís Blancafort, Benjamin Lasorne, Michael J. Bearpark,  
Graham A. Worth, and Michael A. Robb

**Abstract** Analysis of the space of conical intersection is crucial for the understanding of photochemical and photophysical processes of molecules. This chapter presents our methodology to characterize the critical points of conical intersection and discusses applications to static and dynamic studies. The intersection space is treated as an analog of a Born-Oppenheimer surface. When second-order effects are taken into account (differences between the nuclear Hessians of the intersection states), the seam of intersection lies along curved coordinates, and the critical points are characterized with the second derivatives of the seam energy along these coordinates. This methodology is presented for a simplified three-coordinate model, and the generalization to a multidimensional problem is applied to the study of the intersection space in fulvene, which lies along a double bond isomerization coordinate. Our second-order analysis can also be used for the systematic selection of nuclear coordinates for quantum dynamics with a reduced number of modes. This selection scheme is applied to a quantum dynamics study of the photochemistry of benzene, where we study the competition between unreactive decay and formation of a pre-fulvenic product. Our study allows us to propose the vibrational modes that have to be stimulated to control the photochemistry.

## 1 Introduction: Conical Intersection Seams as Analogs of Born-Oppenheimer Surfaces

The importance of conical intersections (crossings between potential energy surfaces of the same multiplicity) in photochemistry and photophysics has been known for a long time [1–4]. In the last two decades, more detailed knowledge about their role has been obtained from theoretical studies of a large number of excited-state processes, and this progress has gone hand in hand with the development of more sophisticated and accurate experimental techniques. However the conical intersection structures are not isolated points on the potential energy surface but belong to the so-called intersection space, a range of nuclear geometries over which the two surfaces intersect along a seam. The focus of this chapter is the characterization of

this space to improve our understanding of excited-state processes. For this purpose the intersection space is considered as an analog of a Born-Oppenheimer surface: it contains minima and saddle points that can be characterized by frequency calculations and are interconnected. In this context, we will concentrate on several points: the first one is the mathematical treatment required for the characterization of the intersection critical points. This treatment provides the basis for the analogy with a Born-Oppenheimer surface, because it makes it possible that different conical intersection structures belong to the same seam, even if the degenerate states are different for the two structures. We will also show that second-order effects are essential to characterize the structures, and in this respect our approach goes beyond the treatment of conical intersections centered on linear effects. Moreover, the mathematical treatment is based on the quadratic vibronic Hamiltonian approach [5, 6], and we hope to provide a link between the study of Jahn–Teller and related systems and our approach to photochemistry (see also several chapters in [3] for basics and applications of the vibronic Hamiltonian approach). This analysis is applied to the study of the seam of intersection of fulvene. As a further application we will show how the analysis can be used to generate optimal reduced sets of coordinates for quantum dynamics studies of excited-state processes.

The signature of conical intersections in excited-state processes is usually related to the observation of short excited-state lifetimes of tens of picoseconds or less, since the intersection provides a funnel of fast access to the ground state. This is the case when the conical intersection is accessible from the Franck-Condon region without significant energy barriers. We call a seam of conical intersection “extended” when a large portion of the intersection space is energetically accessible. This occurs when some directions drawn from the minimum conical intersection point correspond to a region of degeneracy with a flat energy profile. The presence of such an extended seam of intersection favors the decay and has an influence on the quantum yields and the branching ratios of the possible photoproducts. One early example where the importance of the extended intersection space was studied is fulvene [7], where there are two minimum energy intersections on the potential energy surface that differ in the torsion of the methylene substituent: a planar intersection and one where the methylene group is twisted by  $90^\circ$  with respect to the plane of the ring (Fig. 1). In this case, dynamics calculations showed that the decay to the ground state can take place at intermediate geometries between the two intersections, suggesting that they are connected by a seam. Other early examples of seams of intersection include the triatomic systems  $\text{H}_2\text{Cl}^+$  [8], dimethyl sulfide [9], hydroxylamine [10], ozone [11, 12],  $\text{AlH}_2$  [13], and  $\text{BH}_2$  [14], as well as ketene [15]. Seams of intersection were also suggested to be involved in the photochemistry of ethylene [16–18] and other alkenes [19]. More recently, seams of conical intersection were mapped in detail for the minimal model of the retinal chromophore, the pentadieniminium cation, where the seam lies along the torsion coordinate of the central double bond (Fig. 2) [20], and for related polyenes [21]. In these cases and in fulvene, the intersection seam lies along the photochemical *Z-E* isomerization coordinate, and the quantum yield of the photoisomerization depends on the segment of the seam preferred for the

**Fig. 1** Schematic representation of the  $S_1$  potential energy surfaces of fulvene, where the  $S_0/S_1$  conical intersection seam is represented by a *dashed line* (reprinted with permission from [7])

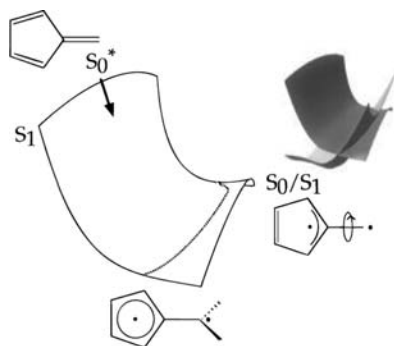
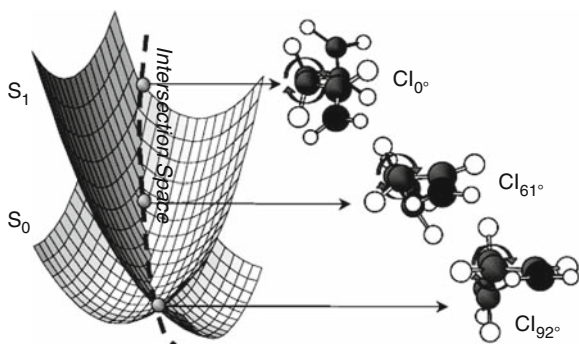


**Fig. 2** Schematic representation of the  $S_1/S_0$  conical intersection seam along the torsion coordinate of the central bond of the minimal retinal chromophore model pentadieniminium cation (reprinted with permission from [20])



decay. It is clear that a detailed characterization of the extended seam is necessary to understand these excited-state processes.

One of the key points of our analytical approach is the concept of a ‘curved’ seam as opposed to a straight line of intersection. The curvature is caused by second-order effects, i.e., the differences between the Hessians of the intersecting states (second derivatives of the energy with respect to nuclear coordinates). A treatment of the seam curvature similar to ours has been presented recently by Yarkony [22], focused on a global description of the seam. In our case, the curvature has to be considered explicitly for the characterization of the critical points on the seam. To facilitate the approach of the reader, we begin with a simplified model that includes only three coordinates and allows us to present these concepts in a graphical way, together with the mathematical formulation. This model will then be generalized to multidimensional cases.

Our model starts with the well-known picture of conical intersections and their associated branching space vectors (Fig. 3) [2, 23–26]. Thus, at a point of conical intersection there are two coordinates along which the degeneracy is lifted ( $Q_{x_1}$  and  $Q_{x_2}$ ). These coordinates lie along the gradient difference and interstate coupling vectors, which form the so-called branching space of the intersection (see below for a definition of these vectors). The rest of the coordinates form the so-called intersection space. The conical shape of the intersection along the branching space

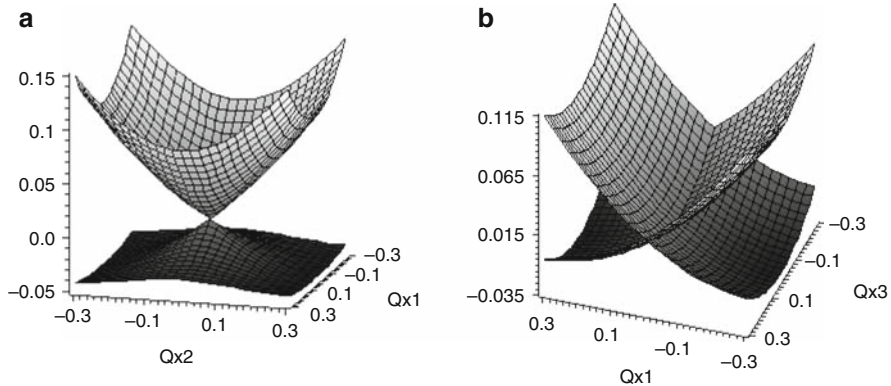


**Fig. 3** First-order conical intersection picture: plot of the 3-coordinate model potential energy surface (3) along coordinates  $Q_{x_1}$  and  $Q_{x_2}$  (a) and  $Q_{x_1}$  and  $Q_{x_3}$  (b). Parameter values:  $a = b = c = 0.2$ ;  $\alpha = 0.2$ ;  $\beta = 0.25$

coordinates was derived in 1937 by Teller [1], who used the theorem established by von Neumann and Wigner in 1929 [27]. According to von Neumann and Wigner, two parameters have to be adjusted to obtain the degeneracy of two eigenvalues for a real Hermitian matrix (the electronic Hamiltonian, when magnetic effects can be ignored). To illustrate this result for a two-state problem, we follow Teller and write the elements of the energy matrix  $\mathbf{W}^1$  as a function of two branching space coordinates  $Q_{x_1}$  and  $Q_{x_2}$  and a coordinate  $Q_{x_3}$  that belongs to the intersection space:

$$\mathbf{W}^1(\mathbf{Q}) = (aQ_{x_1}^2 + bQ_{x_2}^2 + cQ_{x_3}^2)\mathbf{I} + \begin{bmatrix} \alpha Q_{x_1} & \beta Q_{x_2} \\ \beta Q_{x_2} & -\alpha Q_{x_1} \end{bmatrix} \quad (1)$$

$\mathbf{W}^1$  has the form of a Taylor expansion of the energy along the coordinates, and in (1) the quadratic terms are equal for the two states. The second summand gives rise to the energy split along the two branching space coordinates. We call this the *linear* or *first-order* conical intersection picture (see the superscript on  $\mathbf{W}^1$ ) because the terms that lift the degeneracy are linear terms along  $Q_{x_1}$  and  $Q_{x_2}$ . In contrast to this, displacements along the intersection space modes do not lift the degeneracy. Thus, the intersection space forms an  $(N - 2)$ -dimensional subspace (also called a hyperline) of the  $N$ -dimensional potential energy surface, where  $N = 3n - 6$  and  $n$  is the number of atoms. Applying the theorem of von Neumann and Wigner, the degeneracy occurs when the two diagonal elements of the matrix are equal and the off-diagonal term is zero:

$$\begin{aligned} \alpha Q_{x_1} &= -\alpha Q_{x_1}, \\ \beta Q_{x_2} &= 0. \end{aligned} \quad (2)$$

Moreover, the energy eigenvalues of  $\mathbf{W}^1$  are:

$$E_{A,B}(\mathbf{Q}) = (aQ_{x_1}^2 + bQ_{x_2}^2 + cQ_{x_3}^2) \pm \sqrt{(\alpha Q_{x_1})^2 + (\beta Q_{x_2})^2}. \quad (3)$$

The plot of (3) along  $Q_{x_1}$  and  $Q_{x_2}$  (keeping  $Q_{x_3} = 0$ ) shows the double cone shape of the surface (Fig. 3a). At the tip of the double cone ( $Q_{x_1} = Q_{x_2} = 0$ ) the two conditions of von Neumann and Wigner (Eq. 2) are fulfilled, and the two eigenvalues are equal. In turn, the seam of intersection is a straight line along  $Q_{x_3}$  as shown by a plot of the energies along  $Q_{x_1}$  and  $Q_{x_3}$  (Fig. 3b).

The first-order picture described up to now has some limitations. First, displacements along the intersection space coordinates usually induce a small lifting of the degeneracy between the two states. This behavior is shown schematically in Fig. 4a. The degeneracy is lifted at second order because the two states have different second derivatives along the intersection space coordinates, i.e., different Hessians. Second, a conceptual difficulty appears when the relationship between the branching space and the seam coordinates is considered. As we will show below for fulvene, different conical intersection critical points are found for different values of a coordinate (bond inversion in fulvene) that corresponds to one of the branching space vectors of the intersections (the gradient difference). Thus, a rectilinear displacement along the branching space vectors can retain degeneracy when combined with other displacements. Although counterintuitive, this merely is a consequence of the curved nature of the intersection space, which induces a continuous mixing of the branching and intersection space coordinates that have been defined at a given intersection point. In other words, rectilinear directions where degeneracy is lifted or retained are a first-order description only, and higher-order terms are needed to go beyond an infinitesimal displacement.

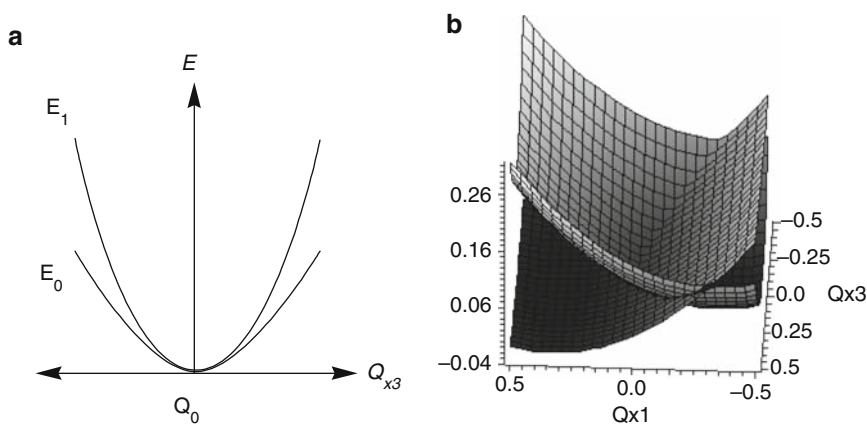


**Fig. 4** Second-order conical intersection picture: plot of the 3-coordinate model potential energy surface (5) along coordinate  $Q_{x_3}$  (a) and coordinates  $Q_{x_1}$  and  $Q_{x_3}$  (b). Parameter values:  $a = b = c = 0.2$ ;  $\alpha = 0.2$ ;  $\beta = 0.25$ ;  $\delta\gamma = 0.25$

Our analysis explains these observations by going beyond the first-order picture and taking the second-order degeneracy lifting terms along the intersection space modes into account [28–31]. Thus, we include an additional term in the energy difference matrix (the non-diagonal matrix of (1)) which reflects the different second derivatives of the two states along the intersection space mode  $Q_{x_3}$ :

$$\mathbf{W}^2(\mathbf{Q}) = (aQ_{x_1}^2 + bQ_{x_2}^2 + cQ_{x_3}^2) \mathbf{I} + \begin{bmatrix} \alpha Q_{x_1} + \delta\gamma Q_{x_3}^2 & \beta Q_{x_2} \\ \beta Q_{x_2} & -(\alpha Q_{x_1} + \delta\gamma Q_{x_3}^2) \end{bmatrix}. \quad (4)$$

The term  $\delta\gamma$  corresponds to the difference between the second derivatives of the two states along the intersection space coordinate. Similar terms can appear along  $Q_{x_1}$  and  $Q_{x_2}$ , but they are neglected here for simplicity. Diagonalization of  $\mathbf{W}^2$ , where the superscript stands for degeneracy lifting up to second order, gives the following expression for the energy of the two states:

$$E_{A,B}(\mathbf{Q}) = (aQ_{x_1}^2 + bQ_{x_2}^2 + cQ_{x_3}^2) \pm \sqrt{(\alpha Q_{x_1} + \delta\gamma Q_{x_3}^2)^2 + (\beta Q_{x_2})^2}. \quad (5)$$

The plot of the energy along  $Q_{x_1}$  and  $Q_{x_3}$  in the second order picture is shown in Fig. 4b. In this case, the seam of intersection is a curved line. The energy degeneracy is kept by combined displacements along  $Q_{x_1}$  and  $Q_{x_3}$ , and the first condition of von Neumann and Wigner (Equation 2) becomes:

$$f_1(Q_{x_1}, Q_{x_3}) = 2\alpha Q_{x_1} + 2\delta\gamma Q_{x_3}^2 = 0. \quad (6)$$

This constrained relationship between the two rectilinear coordinates  $Q_{x_1}$  and  $Q_{x_3}$  defines implicitly the locus of the seam in the plane  $(Q_{x_1}, Q_{x_3})$  (the complementary equation being  $f_2(Q_{x_2}) = \beta Q_{x_2} = 0$ , i.e.,  $Q_{x_2} = 0$ , in the full three-dimensional space). The graph of the seam is a parabola given by the explicit equation

$$Q_{x_1} = -\frac{\delta\gamma}{\alpha} Q_{x_3}^2. \quad (7)$$

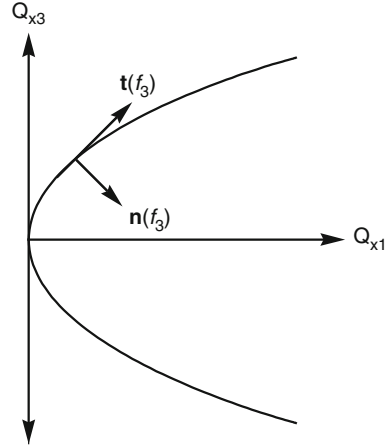
Only one degree of freedom,  $f_3$ , is needed to parameterize this curve, and we call it parabolic coordinate. Here, it is convenient to make this parameter equal to  $Q_{x_3}$ , such that the seam is defined parametrically as

$$\begin{aligned} Q_{x_1}(f_3) &= -\frac{\delta\gamma}{\alpha} f_3^2, \\ Q_{x_3}(f_3) &= f_3. \end{aligned} \quad (8)$$

Substitution of  $f_3$  in (5), together with the second condition of (2) ( $Q_{x_2} = 0$ ), gives the same energy for the two states:



**Fig. 5** Second-order model of conical intersection. Projection of the seam on the  $(Q_{x_1}, Q_{x_3})$ -plane



$$E_{\text{seam}}(f_3) = -a \left( \frac{\delta\gamma}{\alpha} \right)^2 f_3^4 + c f_3^2 \quad (9)$$

Although equal in value to the rectilinear coordinate  $Q_{x_3}$ , the parameter  $f_3$  can be treated as a curvilinear coordinate that follows the infinitesimal displacement of a point on the seam along the local tangent vector to the curve,  $\mathbf{t}(f_3)$ . This moving frame is completed by the normal vector,  $\mathbf{n}(f_3)$ . At the expansion point (origin of the frame:  $f_3 = 0$ ), the normal and tangent vectors to the seam are parallel to  $\hat{\mathbf{x}}_1$  and  $\hat{\mathbf{x}}_3$  (unit vectors), respectively. However, away from that point, these vectors are different and combine  $\hat{\mathbf{x}}_1$  and  $\hat{\mathbf{x}}_3$  because the seam is curved (Fig. 5).

At any point on the seam referred by  $f_3$ , the local tangent vector,

$$\mathbf{t}(f_3) = \frac{\partial Q_{x_1}(f_3)}{\partial f_3} \hat{\mathbf{x}}_1 + \frac{\partial Q_{x_3}(f_3)}{\partial f_3} \hat{\mathbf{x}}_3 = -\frac{2\delta\gamma}{\alpha} f_3 \hat{\mathbf{x}}_1 + \hat{\mathbf{x}}_3, \quad (10)$$

gives the direction followed by the seam as the curvilinear coordinate  $f_3$  increases its value at first order. This shows how, at the central point of the expansion,  $\mathbf{t}(f_3)$  is parallel to  $\hat{\mathbf{x}}_3$ , while it changes its direction and mixes with  $\hat{\mathbf{x}}_1$  as one moves away from this point. The normal vector is obtained by taking the gradient of the constraint on the energy difference (Equation (6)):

$$\mathbf{n}(f_3) = \frac{\partial f_1(Q_{x_1}, Q_{x_3})}{\partial Q_{x_1}} \hat{\mathbf{x}}_1 + \frac{\partial f_1(Q_{x_1}, Q_{x_3})}{\partial Q_{x_3}} \hat{\mathbf{x}}_3 = 2\alpha \hat{\mathbf{x}}_1 + 4\delta\gamma f_3 \hat{\mathbf{x}}_3. \quad (11)$$

It is orthogonal to  $\mathbf{t}(f_3)$  and also changes its direction along the seam. Being orthogonal to the seam, it is one of the two vectors spanning the branching space and is parallel to  $\hat{\mathbf{x}}_1$  at the origin. It is identified with the local gradient-difference vector that thus satisfies  $\mathbf{x}_1(f_3) = 2\alpha \hat{\mathbf{x}}_1 + 4\delta\gamma f_3 \hat{\mathbf{x}}_3$ . In the model defined in (4), the local interstate coupling vector satisfies  $\mathbf{x}_2(f_3) = \beta \hat{\mathbf{x}}_2$  everywhere, but this could change

too if higher-order terms were to be added to the model. The change of direction of  $\mathbf{t}(f_3)$  along the seam explains how the seam can be found at finite displacements that involve partly the direction of the branching space as calculated at the origin. Reciprocally, because the seam usually is curved, the local branching space must rotate with respect to the original one to stay orthogonal to the seam at any point, possibly within the intersection space as defined at the origin.

Before we generalize the second-order picture to a multidimensional problem, it is useful to comment on some relevant consequences of this picture for our further analysis. The previous development gives a mathematical justification of how the branching space vectors of the conical intersection change along the seam. Therefore it is possible that two different conical intersections belong to the same seam, even though they have a different branching space. Based on this, it is convenient to consider the seam of intersection as the analog of a Born-Oppenheimer surface, which can contain different minima that are connected to each other by transition structures and reaction paths. Following this analogy, the optimized points of conical intersection can be characterized as minima or ‘transition structures’ on the seam. For this purpose we use the analog of the Hessian, the so-called intersection-space Hessian (see details below [30]). Because of the curved nature of the seam, the differentiation to calculate the Hessian has to be carried out along the curvilinear set of coordinates  $\{f_i\}$ . This procedure is the central point of the next section.

## 2 Intersection Space Hessian for the Analysis of Conical Intersections

In this section we generalize the second-order analysis required to calculate the intersection space Hessian. For further details, the reader is referred to [30]. Before we derive the general expression, we discuss the parametrization of the Hamiltonian with *ab initio* calculations (CASSCF in our case). The relationship between the energy Hamiltonian and the *ab initio* calculations is not trivial because the Hamiltonian is usually expressed in a diabatic basis, where the states have a fixed electronic character and are coupled by the off-diagonal elements of the Hamiltonian. In contrast to this, the CASSCF calculations yield adiabatic states which are optimized for the geometry of choice. Although this issue has been discussed before (see, e.g., [5, 24, 32–34]; see also [35] for a recent review of adiabatic-diabatic transformations), it is helpful in the present context to go through the essential points. For the sake of simplicity, we assume for now an exact and complete, ideal two-level model. A more general derivation is given in the Appendix.

We first define a suitable electronic basis. In what follows,  $\mathbf{Q}_0$  represents the geometry of a conical intersection between  $S_0$  and  $S_1$  chosen as a reference point. The two degenerate electronic wave functions,  $|\Psi_0\rangle$  and  $|\Psi_1\rangle$ , are the result of an electronic structure calculation at the state-averaged CASSCF level at the reference point. For any geometry  $\mathbf{Q}$ , the first two singlet adiabatic states will be noted  $|S_0; \mathbf{Q}\rangle$  and  $|S_1; \mathbf{Q}\rangle$ , where the semicolon is used to emphasize that the electronic states are

parametrized by the nuclear geometry  $\mathbf{Q}$ . At the reference point,  $|\Psi_0\rangle = |S_0; \mathbf{Q}_0\rangle$  and  $|\Psi_1\rangle = |S_1; \mathbf{Q}_0\rangle$ . If the adiabatic states  $|S_0; \mathbf{Q}\rangle$  and  $|S_1; \mathbf{Q}\rangle$  do not change their character significantly in the region of interest, apart from mixing  $|\Psi_0\rangle$  and  $|\Psi_1\rangle$  with each other, then  $|\Psi_0\rangle$  and  $|\Psi_1\rangle$  provide a suitable basis set of trivial diabatic states (they do not vary with  $\mathbf{Q}$ ) for describing  $|S_0; \mathbf{Q}\rangle$  and  $|S_1; \mathbf{Q}\rangle$  in the vicinity of  $\mathbf{Q}_0$ , usually called the ‘crude adiabatic’ basis set [36]. In practice, this description is not valid because such a basis set is far from complete. More general quasidiabatic states must be introduced to account for second-order mixing with more excited electronic states  $|\Psi_J\rangle$  ( $J > 1$ ) when  $\mathbf{Q}$  varies. This point is further discussed in the Appendix.

The matrix elements of the Hamiltonian matrix in the diabatic representation are:

$$H_{IJ}(\mathbf{Q}) = \langle \Psi_I | \hat{H}(\mathbf{Q}) | \Psi_J \rangle = \langle S_I; \mathbf{Q}_0 | \hat{H}(\mathbf{Q}) | S_J; \mathbf{Q}_0 \rangle, \quad (12)$$

where  $\hat{H}(\mathbf{Q})$  is the clamped-nucleus Hamiltonian operator (at this stage, this is the actual operator, not any finite matrix representation of it). At the reference geometry  $\mathbf{Q}_0$ , where the states are known, the corresponding matrix,  $\mathbf{H}(\mathbf{Q}_0)$ , is diagonal:

$$\mathbf{H}(\mathbf{Q}_0) = \begin{bmatrix} H_{00}(\mathbf{Q}_0) & H_{01}(\mathbf{Q}_0) \\ H_{01}(\mathbf{Q}_0) & H_{11}(\mathbf{Q}_0) \end{bmatrix} = \begin{bmatrix} E_0(\mathbf{Q}_0) & 0 \\ 0 & E_1(\mathbf{Q}_0) \end{bmatrix}, \quad (13)$$

where real-valued electronic wave functions are assumed. In the diabatic basis set, a displacement  $\delta\mathbf{Q}$  from  $\mathbf{Q}_0$  gives rise to non-zero off-diagonal elements and to different diagonal elements:

$$\mathbf{H}(\mathbf{Q}_0 + \delta\mathbf{Q}) = \begin{bmatrix} E_0(\mathbf{Q}_0) & 0 \\ 0 & E_1(\mathbf{Q}_0) \end{bmatrix} + \begin{bmatrix} \delta H_{00} & \delta H_{01} \\ \delta H_{01} & \delta H_{11} \end{bmatrix}. \quad (14)$$

The energy at the displaced point can be obtained from diagonalization of this Hamiltonian. When the reference geometry is a conical intersection,  $E_0(\mathbf{Q}_0) = E_1(\mathbf{Q}_0)$ , the energy splitting caused by finite displacements is:

$$\Delta E(\mathbf{Q}_0 + \delta\mathbf{Q}) = \sqrt{(\delta H_{11} - \delta H_{00})^2 + 4\delta H_{01}^2}. \quad (15)$$

We now introduce two functions of the coordinates  $\mathbf{Q}$ :

$$\begin{aligned} f_1(\mathbf{Q}) &= H_{11}(\mathbf{Q}) - H_{00}(\mathbf{Q}), \\ f_2(\mathbf{Q}) &= H_{01}(\mathbf{Q}). \end{aligned} \quad (16)$$

Using the generalized coordinates  $f_1$  and  $f_2$ , the energy difference becomes:

$$\Delta E(\mathbf{Q}_0 + \delta\mathbf{Q}) = \sqrt{\delta f_1^2 + 4\delta f_2^2}. \quad (17)$$

To second order,  $\delta f_1$  and  $\delta f_2$  can be expressed as energies with a Taylor expansion of the form:

$$\begin{aligned}\delta f_1 &= \sum_i [\partial_{x_i} f_1]_0 \delta Q_{x_i} + \frac{1}{2} \sum_{ij} [\partial_{x_i} \partial_{x_j} f_1]_0 \delta Q_{x_i} \delta Q_{x_j}, \\ \delta f_2 &= \sum_i [\partial_{x_i} f_2]_0 \delta Q_{x_i} + \frac{1}{2} \sum_{ij} [\partial_{x_i} \partial_{x_j} f_2]_0 \delta Q_{x_i} \delta Q_{x_j},\end{aligned}\quad (18)$$

where  $[\partial_j]_0$  stands for the local partial derivative  $\partial/\partial Q_{x_j}|_{\mathbf{Q}=\mathbf{Q}_0}$ . The derivatives of  $f_1$  and  $f_2$  at the expansion point refer to the diabatic states (see (16)). However, the diabatic states,  $|\Psi_0\rangle$  and  $|\Psi_1\rangle$ , are equal to the adiabatic states,  $|S_0; \mathbf{Q}_0\rangle$  and  $|S_1; \mathbf{Q}_0\rangle$ , at that point, and because the Hellmann-Feynman theorem is valid in the ideal two-state case (see Appendix for a more general discussion), the local first derivatives of the energies are the same in both representations. Thus the linear component of the gradient is:

$$\begin{aligned}[\partial_{x_i} f_1]_0 &= [\partial_{x_i} (H_{11} - H_{00})]_0 \\ &= \langle \Psi_1 | [\partial_{x_i} \hat{H}]_0 | \Psi_1 \rangle - \langle \Psi_0 | [\partial_{x_i} \hat{H}]_0 | \Psi_0 \rangle \\ &= \langle S_1; \mathbf{Q}_0 | [\partial_{x_i} \hat{H}]_0 | S_1; \mathbf{Q}_0 \rangle - \langle S_0; \mathbf{Q}_0 | [\partial_{x_i} \hat{H}]_0 | S_0; \mathbf{Q}_0 \rangle \\ &= [\partial_{x_i} \Delta E]_0.\end{aligned}\quad (19)$$

At the same time, the derivative of the coupling can also be obtained from the *ab initio* wave functions,

$$\begin{aligned}[\partial_{x_i} f_2]_0 &= [\partial_{x_i} H_{01}]_0 \\ &= \langle \Psi_0 | [\partial_{x_i} \hat{H}]_0 | \Psi_1 \rangle \\ &= \langle S_0; \mathbf{Q}_0 | [\partial_{x_i} \hat{H}]_0 | S_1; \mathbf{Q}_0 \rangle.\end{aligned}\quad (20)$$

In practice, at the CASSCF level, the Hellmann-Feynman theorem is not valid in this form because the basis set is truncated. However, it can be applied when the states (kets) are replaced by the configuration-interaction vectors, and the Hamiltonian operator by its matrix representation in the space of the configuration-state functions (see Appendix). In this case, the terms in the Taylor expansion of the energy Hamiltonian can still be obtained from *ab initio* calculations at the expansion point. Moreover, the expansion can be simplified by choosing the appropriate coordinate basis set. Here we use the so-called intersection-adapted coordinates introduced by Ruedenberg [25]. This basis set is formed by the two branching space coordinates and the complementary  $N - 2$  intersection space coordinates. The first branching space coordinate is the direction of the gradient difference vector, and the second one that of the interstate coupling vector (also known as the *gh* vectors [37]). The definition of these vectors at the center of the expansion, in Cartesian coordinates, noted  $\xi_{i\gamma}$ , is:

$$\begin{aligned} x_1^{(i\gamma)}(\mathbf{Q}_0) &= [\partial_{\xi_{i\gamma}} \Delta E]_0, \\ x_2^{(i\gamma)}(\mathbf{Q}_0) &= \langle \Psi_0 | [\partial_{\xi_{i\gamma}} \hat{H}]_0 | \Psi_1 \rangle. \end{aligned} \quad (21)$$

Once again, the operational application of this development to CASSCF wave functions means that the states (kets) are replaced by the configuration-interaction vectors, and the Hamiltonian operator by its matrix representation in the space of the configuration-state functions (see Appendix).

We now introduce a pair of mass-weighted nuclear coordinates,  $Q_{x_1}$  and  $Q_{x_2}$ , (see Section 1) that describe mass-weighted rectilinear displacements along  $\hat{\mathbf{x}}_1(\mathbf{Q}_0)$  and  $\hat{\mathbf{x}}_2(\mathbf{Q}_0)$ , respectively. This basis set is the most convenient one for the present analysis because it simplifies the degeneracy-lifting terms of (17). The expansions for  $\delta f_1$  and  $\delta f_2$  in this basis are:

$$\begin{aligned} \delta f_1 &= [\partial_{x_1} f_1]_0 \delta Q_{x_1} + \frac{1}{2} \sum_{ij} [\partial_{x_i} \partial_{x_j} f_1]_0 \delta Q_{x_i} \delta Q_{x_j}, \\ \delta f_2 &= [\partial_{x_2} f_2]_0 \delta Q_{x_2} + \frac{1}{2} \sum_{ij} [\partial_{x_i} \partial_{x_j} f_2]_0 \delta Q_{x_i} \delta Q_{x_j}. \end{aligned} \quad (22)$$

The total energy expansion is obtained by adding the terms that are equal for the two states to (15). When finite displacements are considered, the expansion of the energy around the intersection in intersection-adapted coordinates becomes:

$$E_{0,1}(\mathbf{Q}) = \pm \frac{1}{2} \sqrt{\left( \sum_{i=1,2} \lambda_i Q_{x_i} + \sum_{i=3}^N \lambda_i Q_{x_i} + \frac{1}{2} \sum_{i,j=1}^N \omega_{ij} Q_{x_i} Q_{x_j} \right)^2 + 4 \left( \kappa^{01} Q_{x_1} + \frac{1}{2} \sum_{i,j=1}^N \eta_{ij}^{01} Q_{x_i} Q_{x_j} \right)^2} \quad (23)$$

where the second term is zero at an optimized point of intersection because the gradient is zero along the intersection space coordinates [38].

In the notation introduced in (23),  $\lambda_i$  are the projections of the average gradient of the two states along the branching space coordinates and the intersection space coordinates;  $\delta\kappa$  and  $\kappa^{01}$  are the length of the gradient difference and interstate coupling vectors (i.e.,  $[\partial_{x_1} f_1]_0$  and  $[\partial_{x_2} f_2]_0$ );  $\omega_{ij}$  and  $\delta\gamma_{ij}$  are the elements of the average and difference Hessians between the two states, respectively; and  $\eta_{ij}^{01}$  are the second-order couplings (all terms evaluated at the expansion point). If we assume a small, but non-zero energy difference, these terms read:

$$\begin{aligned} \lambda_i &= \frac{1}{2} [\partial_{x_i} (E_1 + E_0)]_0, \\ \delta\kappa &= [\partial_{x_i} (E_1 - E_0)]_0, \\ \kappa^{01} &= \langle \Psi_0 | [\partial_{x_2} \hat{H}]_0 | \Psi_1 \rangle, \\ \omega_{ij} &= \frac{1}{2} [\partial_{x_i} \partial_{x_j} (E_1 + E_0)]_0, \\ \delta\gamma_{ij} &= [\partial_{x_i} \partial_{x_j} (E_1 - E_0)]_0 - 4 \frac{(\kappa^{01})^2}{\Delta E(\mathbf{Q}_0)} \delta_{i2} \delta_{j2}, \\ \eta_{ij}^{01} &= \langle \Psi_0 | [\partial_{x_i} \partial_{x_j} \hat{H}]_0 | \Psi_1 \rangle + \frac{\kappa^{01} \delta\kappa}{\Delta E(\mathbf{Q}_0)} \delta_{i2} \delta_{j1}, \end{aligned} \quad (24)$$

where  $\delta_{ij}$  is the Kronecker symbol. The validity and practical meaning of these expressions are detailed in the Appendix. Here we merely point out that the linear terms come from the same derivation as (19) and (20), while the quadratic terms contain the Hellmann-Feynman-like terms as well as additional contributions due to second-order Jahn–Teller couplings within and from out of the two-level model subspace (see Appendix and Section 4). Thus, the effect of second-order mixing of the two intersecting states with higher-lying states is contained indirectly in the state-averaged CASSCF Hessians used for the parametrization. In its turn, the second-order mixing within the two-level subspace is included in the two terms divided by  $\Delta E(\mathbf{Q}_0)$ . These terms become ill-defined if  $\Delta E(\mathbf{Q}_0)$  tends to zero, i.e., at a conical intersection. However, they do not cause any problem in our analysis because the Hessian that we consider is projected out of the branching space [30]. In other words, (24) is used in practice for  $ij \neq 11, 12, 21, 22$ .

If the expansion of  $f_1$  and  $f_2$  is truncated at first order, one obtains the analog of (3), and the energy splitting occurs only along the branching space vectors. If the second-order terms are included, one obtains the analog of (5). In this case, the conditions of von Neumann and Wigner that define the intersection space are:

$$\begin{aligned} \delta\kappa Q_{x_1} + \frac{1}{2} \sum_{i,j=1}^N \delta\gamma_{ij} Q_{x_i} Q_{x_j} &= 0, \\ \kappa^{01} Q_{x_2} + \frac{1}{2} \sum_{i,j=1}^N \eta_{ij}^{01} Q_{x_i} Q_{x_j} &= 0. \end{aligned} \quad (25)$$

Following the approach described for the three-coordinate model, we now define the curvilinear coordinates that fulfill these conditions. To simplify the mathematical treatment, it is convenient to neglect the second-order terms that involve the branching space modes, i.e., the  $\delta\gamma_{ij}$  and  $\eta_{ij}^{01}$  terms with  $i$  or  $j < 3$  are set to zero (projection out of the branching space, as mentioned earlier). In this case it is possible to define the  $N - 2$  parabolic intersection coordinates  $\{f_i\}$  that fulfill the following conditions:

$$\begin{aligned} f_i &= Q_{x_i} \quad (i \geq 3), \\ Q_{x_1} &= -\frac{\sum_{i,j=3}^N \delta\gamma_{ij} f_i f_j}{2\delta\kappa}, \\ Q_{x_2} &= -\frac{\sum_{i,j=3}^N \eta_{ij}^{01} f_i f_j}{2\kappa^{01}}. \end{aligned} \quad (26)$$

Substitution of the expressions of (26) in (23) yields the following expression, truncated to second order:

$$E_{\text{seam}}(\mathbf{f}) = \sum_{i,j \geq 3} -\frac{\lambda_1}{4\delta\kappa} \delta\gamma_{ij} f_i f_j - \frac{\lambda_2}{4\kappa^{01}} \delta\eta_{ij}^{01} f_i f_j + \frac{\omega_{ij}}{4} f_i f_j \quad (27)$$

Equation (27) gives the energy of the intersection seam along the  $N - 2$  curvilinear coordinates. The critical points on the seam can then be characterized with the help of the intersection-space Hessian, the matrix of second derivatives of the seam energy with respect to the curvilinear coordinates  $\{f_i (i \geq 3)\}$ :

$$H_{ij}^{IS} = [\partial_{f_i} \partial_{f_j} E_{seam}]_0 = \frac{1}{2} \left( \omega_{ij} - \frac{\lambda_1}{\delta\kappa} \delta\gamma_{ij} - \frac{\lambda_2}{\kappa^{01}} \eta_{ij}^{01} \right) \quad (28)$$

The eigenvectors of the intersection-space Hessian after diagonalization form a set of parallel vectors to the curvilinear intersection space coordinates  $\{f_i\}$  at the expansion point. These eigenvectors are called the seam normal modes. The eigenvalues give the second derivatives of the energy along these coordinates, and with this it is possible to calculate the intersection-space frequencies, i.e., the analogs of the frequencies at a critical point on a Born-Oppenheimer surface. Structures with imaginary intersection-space frequencies are saddle points on the seam that are connected to intersections with lower energy.

The terms that appear in the intersection-space Hessian are obtained from the analytical, state-averaged complete active space self-consistent field (CASSCF) gradients and second derivatives as they are implemented in the GAUSSIAN program [39, 40]. The use of state-averaged orbitals requires the solution of the coupled-perturbed multiconfigurational self-consistent field (MCSCF) equations, and this limits the calculations to an active space of 8 orbitals or less. For the second-order terms in (28), we use the  $N - 2$  dimensional Hessians obtained by projecting the branching space from the full Hessians of the two states, similar to the reaction-path Hamiltonian [29, 41]. The  $\omega_{ij}$  and  $\delta\gamma_{ij}$  terms are the average and difference of the projected Hessians, respectively. For the  $\eta_{ij}^{01}$  terms we make use of the fact that rotation of the adiabatic states  $\Psi_0$  and  $\Psi_1$  by  $45^\circ$  interchanges the Hessian difference and second-order coupling terms. Thus, the rotated states are:

$$\Psi_{\pm} = \frac{1}{\sqrt{2}} (\Psi_0 \pm \Psi_1) \quad (29)$$

Taking into account that the average Hessian of the rotated and unrotated states is the same, the second-order couplings for the unrotated states can be obtained from the average Hessian and the Hessian of one of the rotated states, using for example (30):

$$\eta_{ij}^{01} = \gamma_{ij}^+ - \frac{1}{2}\omega_{ij} \quad (30)$$

In the next section we will present an example of how the intersection-space Hessian has been applied for the analysis of the seam of intersection of fulvene, a non-fluorescent hydrocarbon. However before that we comment on some points regarding our use of the two-state energy Hamiltonian. This Hamiltonian (or versions including a larger number of states) has been commonly used for the dynamic treatment of Jahn-Teller and symmetry allowed intersections [3, 5]. There are two main differences with respect to our development. First, we use intersection-space adapted coordinates, rather than the normal modes of a related minimum, such as the ground-state minimum in excited-state problems or the neutral system in radical cations. In the latter case there are linear degeneracy-lifting terms along all the modes of a given symmetry, while in intersection-space adapted coordinates the expansion is simplified because the linear terms appear by definition only along two coordinates. The second difference concerns our use of CASSCF *ab initio*

calculations for the parametrization. The dynamics calculations require a relatively large part of the potential energy surface, and the Hamiltonian is usually fitted to the surfaces calculated at a high level of theory. However in our analysis we are interested in the local properties at the intersection, which are derived from the analytical CASSCF gradients and second derivatives. Our approach suffers therefore from the limitations of this method, i.e., the lack of dynamic correlation. However our scheme requires the analytical quantities, because some of the terms cannot be obtained from finite-difference approaches. At present we are therefore bound to use the CASSCF method, which gives qualitatively good results unless ionic states are involved, to calculate the second derivatives with state-average orbitals. Still it is possible to improve the level of theory in specific applications. For example, quantum dynamics on benzene have been carried selecting the normal modes from a second-order CASSCF analysis and parametrizing the surface with CASPT2 [42].

### 3 Second-Order Analysis at an Intersection: Intersection Space of Fulvene

Fulvene is a non-fluorescent hydrocarbon [43]. The lack of fluorescence indicates fast internal conversion of the excited state to the ground state via a conical intersection. In an early CASSCF study, two distinct critical points on the  $S_1/S_0$  seam were located which differed in the torsion angle of the methylene group: a planar intersection ( $\mathbf{CI}_{\text{Plan}}$ ), where the methylene group lies in the ring plane, and one where the methylene is perpendicular to the ring ( $\mathbf{CI}_{\text{Perp}}$ ) (Fig. 6). The existence of a seam of intersection that connects both structures along the methylene torsion coordinate was suggested by semiclassical dynamics calculations with a surface hopping algorithm, where the trajectories decayed to the ground states at all methylene torsion angles. This seam has been characterized with CASSCF(6,6)/cc-pvdz calculations and our second-order analysis [28, 44, 45].

Fulvene is a good example for our analysis because it is symmetric, and the different conical intersections can be located as symmetry-restricted minima with a standard conical intersection optimization algorithm [38]. In a first approximation, fulvene can be treated with the three-state model described in the first section. The resulting picture is shown in Fig. 6a. Figure 6a is a qualitative plot of the energy along two modes. The first one is the gradient difference vector at  $\mathbf{CI}_{\text{Plan}}$  and  $\mathbf{CI}_{\text{Perp}}$  (stretching of the methylenic bond and inversion of the ring bond lengths) and corresponds to  $Q_{x_1}$  in (4) and (5). The second mode ( $Q_{x_3}$  in (4) and (5)) is the intersection space mode with a largest curvature difference between the two states, i.e., largest  $\delta\gamma$  value, and corresponds to the methylene torsion (see the calculated frequencies of the two states at  $\mathbf{CI}_{\text{Plan}}$  and  $\mathbf{CI}_{\text{Perp}}$  in Table IV of [28]). The two intersections, of  $C_{2v}$  symmetry, are therefore connected along the two coordinates by a seam of  $C_2$  symmetry, and the minimum on this segment has a torsion angle of  $63^\circ$  ( $\mathbf{CI}_{63}$ ). The connection between the three structures was proved by constrained optimizations along the torsion coordinate and by the analog of intrinsic reaction



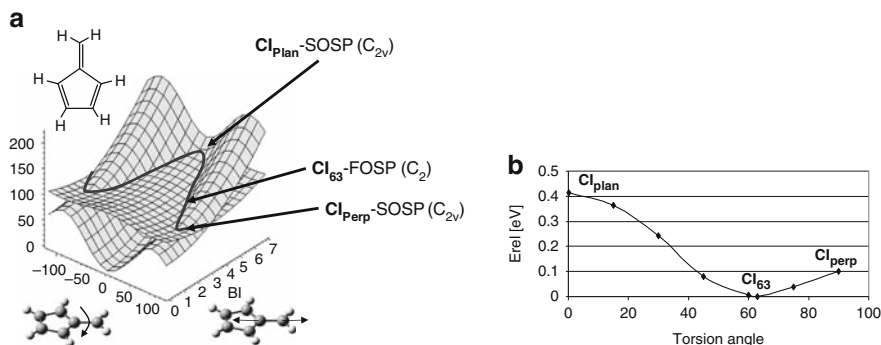


**Fig. 6** Sketch of the  $S_1/S_0$  conical intersection seam in fulvene along the methylene torsion and bond inversion coordinates (a) and energy profile along the seam (b) (adapted with permission from [44])

coordinate calculations in the intersection space (see the energy profile in Fig. 6b). The difference between the sketch of the fulvene surface (Fig. 6a) and the general plot along  $Q_{x_1}$  and  $Q_{x_3}$  (Fig. 4b) is that Fig. 6a contains three minima of intersection, so that the local topology shown in Fig. 4 is contained three times in the global sketch of Fig. 6a, around the minima.

The changes in the direction of the seam and gradient difference coordinates that were discussed in Section 1 for the three-coordinate model (Fig. 5) can now be illustrated with the help of Fig. 6a. Thus, at  $\text{CI}_{\text{Plan}}$  and  $\text{CI}_{\text{Perp}}$  the tangent to the seam is parallel to the torsion, but along the seam it becomes a combination of the torsion with the stretching, as discussed with the help of (10). At the same time, the gradient difference vector, which is locally orthogonal to the seam, also changes its direction. At the  $C_{2v}$  structures it is the bond stretching coordinate, but along the rest of the seam segment it is a combination of the stretching with the torsion mode (see (11)). Also the topology of the intersection changes along the seam from sloped at  $\text{CI}_{\text{plan}}$  to peaked at  $\text{CI}_{\text{perp}}$ .

A more detailed characterization of the intersection space is based on the intersection-space Hessian analysis, which has guided us in the search for further intersection minima. The picture delivered by this analysis is consistent with the one based on the Hessian difference between the states and the three-coordinate model. Thus,  $\text{CI}_{\text{Plan}}$  and  $\text{CI}_{\text{Perp}}$ , of  $C_{2v}$  symmetry, are second-order saddle points on the intersection space along the methylene torsion and pyramidalization coordinates. In turn,  $\text{CI}_{63}$ , of  $C_2$  symmetry, is a first-order saddle point in the seam with a small imaginary frequency (methylene pyramidalization). The global intersection-space minimum  $\text{CI}_{\text{Min}}$  is a close-lying structure of  $C_1$  symmetry. In a similar way, following the pyramidalization mode from  $\text{CI}_{\text{Plan}}$  a further conical intersection,  $\text{CI}_{\text{Pyr}}$  of  $C_s$  symmetry has been found. This intersection has an imaginary intersection-space frequency along the torsion coordinate, and optimization of a structure distorted along this coordinate leads to  $\text{CI}_{\text{Min}}$ . Overall, the connection of the different critical points (see Fig. 7) confirms the validity of the analogy between the saddle points

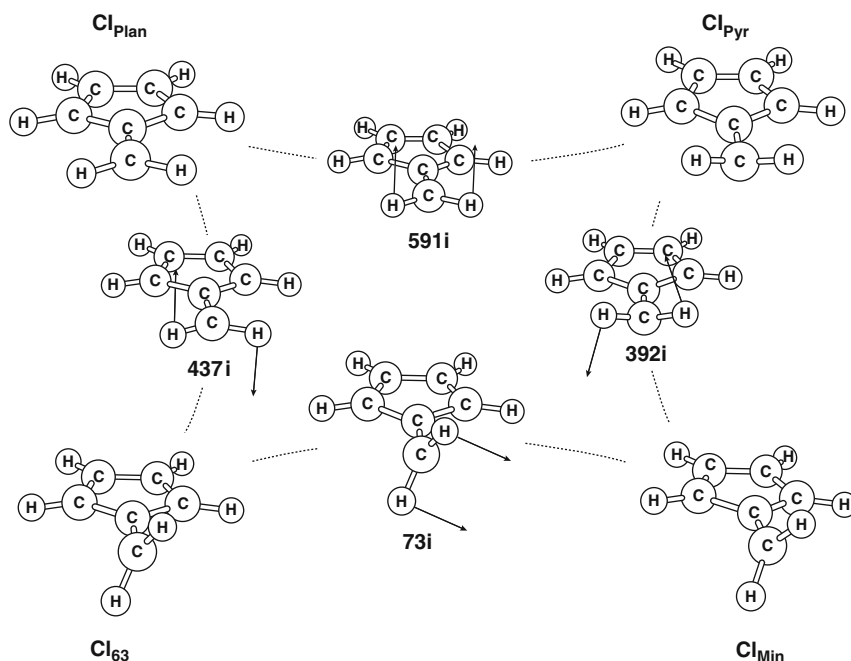


**Fig. 7** Schematic representation of the conical intersection seam in fulvene along the torsion and pyramidalization modes, including the critical points, the seam normal modes that connect the different structures and the imaginary frequencies in  $\text{cm}^{-1}$  (displacement vectors shown only for the hydrogen atoms) (reprinted with permission from [45])

on the seam and those on a Born-Oppenheimer surface. The second-order saddle point connects two first-order saddle points with each other, and these in turn are connected to a lower-energy global minimum.

## 4 Generation of Active Coordinates for Quantum Dynamics in Non-adiabatic Photochemistry

In addition to the analysis of the topology of a conical intersection, the quadratic expansion of the Hamiltonian matrix can be used as a new practical method to generate a subspace of active coordinates for quantum dynamics calculations. The cost of quantum dynamics simulations grows quickly with the number of nuclear degrees of freedom, and quantum dynamics simulations are often performed within a subspace of active coordinates (see, e.g., [46–50]). In this section we describe a method which enables the *a priori* selection of these important coordinates for a photochemical reaction. Directions that reduce the adiabatic energy difference are expected to lead faster to the conical intersection seam and will be called ‘photoactive modes’. The efficiency of quantum dynamics run in the subspace of these reduced coordinates will be illustrated with the photochemistry of benzene [31, 51–53].

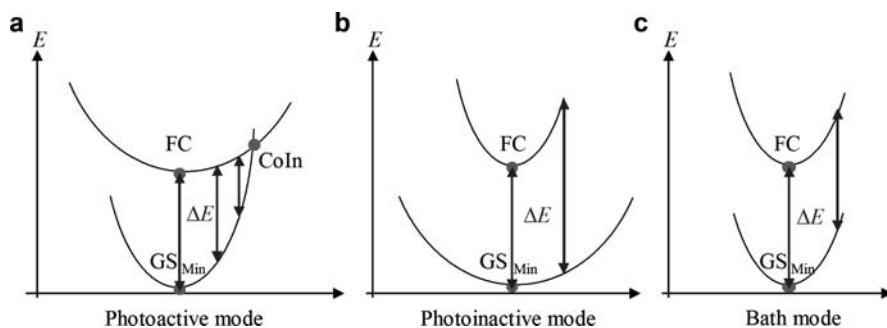


**Fig. 8** Three classes of normal modes: photoactive mode (a); photoinactive mode (b); bath mode (c) (reprinted with permission from [31])

### 4.1 Intuitive Definition of the Photoactive Coordinates

As mentioned in Sections 1 and 2, the degeneracy of the adiabatic PESs at a conical intersection point is lifted at first order along the branching-plane coordinates,  $Q_{x_1}$  and  $Q_{x_2}$ , defined at the apex of the double cone. These coordinates can be generalized to any other point where the energy gap is not zero, in order to characterize the local variations of the adiabatic energy difference and non-adiabatic coupling between two electronic states. In particular,  $Q_{x_1}$  and  $Q_{x_2}$  can be defined at the Franck-Condon (FC) point (geometry of the ground-state PES minimum) for getting information on the early stage of the dynamics of the photochemical process after absorption of light. We call this coordinates the ‘pseudo-branching plane’. The energy-difference Hessian projected onto the space orthogonal to the plane  $(Q_{x_1}, Q_{x_2})$  can be evaluated to get information about the second-order variation of the energy difference within the complementary coordinate space. The  $N - 2$  eigenvectors of this projected energy-difference Hessian can be classified according to the magnitude and sign of the corresponding eigenvalues. As shown in Fig. 8, three types of projected energy-difference normal modes must be distinguished.

Three one-dimensional cuts of two PESs are plotted in the space orthogonal to the pseudo-branching plane in Fig. 8. A generic case involving two singlet electronic states,  $S_0$  and  $S_1$ , is considered. All coordinates measure rectilinear displacements of the nuclei with respect to the FC point along the normal modes of the projected energy-difference Hessian. The  $S_0$  gradient is zero, and the gradient difference reduces to the  $S_1$  gradient. The projected modes are therefore orthogonal to the gradient of  $S_1$ , and the FC point appears as an excited-state minimum along those coordinates.

The first class of modes makes the energy difference decrease (negative eigenvalues of the projected energy-difference Hessian, using the excited-minus-ground-state convention), and we call them ‘photoactive modes’ (Fig. 8a). The modes along which the energy difference increases (positive eigenvalues) are called ‘photoinactive modes’ (Fig. 8b). Finally, those eigenvectors where the energy difference does

not significantly change (almost zero eigenvalues), are called ‘bath modes’ (Fig. 8c). To reach the conical intersection point from the ground-state minimum (CoIn and  $GS_{\text{Min}}$  in Fig. 8, respectively) and undergo internal conversion, the system must reduce the energy difference to access the seam of conical intersection. The most important directions are thus  $\mathbf{x}_1$  and the additional photoactive modes. In addition,  $\mathbf{x}_2$  is the direction that increases the interstate coupling, and it must be added to the subspace to take account of non-adiabatic effects.

In a quantum dynamics picture, the center of the wavepacket starting around the Franck-Condon region will follow mostly the negative direction of  $Q_{x_1}$  (driving force equal to the negative of the  $S_1$  gradient). Also, it will spread along photoactive modes (see Fig. 8a), thus leading to an increase of the probability density for larger absolute values of the corresponding coordinates, and contract along photoinactive modes (see Fig. 8b). Bath modes, with a near-zero eigenvalue (see Fig. 8c), will not play any significant role in the dynamics. The wavepacket will stay similar to the ground vibrational state along such directions, which can be neglected in a first approach using reduced dimensionality techniques.

## 4.2 Formal Definition of the Photoactive Coordinates

The analysis of the photochemical activity of nuclear coordinates is now presented in more details. Most of the formalism has been presented in [31]. The analysis presented in Section 2 is generalized here to the ground-state equilibrium geometry (i.e., FC point in the excited state), where the energy difference is not zero.

Using the same notations as in Section 2, the positive difference between the adiabatic potential energies within a two-level approximation varies with  $\delta\mathbf{Q}$  according to

$$\Delta E(\mathbf{Q}_0 + \delta\mathbf{Q}) = \sqrt{[\Delta E(\mathbf{Q}_0) + \delta f_1]^2 + 4\delta f_2^2}. \quad (31)$$

As opposed to a conical intersection,  $f_1(\mathbf{Q}_0) = \Delta E(\mathbf{Q}_0) > 0$  at the FC point. However with quasidiabatic states  $f_2(\mathbf{Q}_0) = 0$ . As a consequence, the second-order variation of the adiabatic energy difference satisfies

$$\delta\Delta E = \Delta E(\mathbf{Q}_0 + \delta\mathbf{Q}) - \Delta E(\mathbf{Q}_0) \approx \delta f_1 + 2\frac{(\delta f_2)^2}{\Delta E_0}, \quad (32)$$

where  $\Delta E_0 = \Delta E(\mathbf{Q}_0)$ . The second term in (32) characterizes a second-order Jahn–Teller effect, also called pseudo-Jahn–Teller (see, e.g., [54] and [55]). Note that the formula with the square-root is valid only within a two-level approximation. In practice, additional second-order Jahn–Teller contributions can arise from other  $f_2$ -like terms involving couplings with higher electronic states (see Appendix). Using non-degenerate perturbation theory to second order would lead to the correct expression of (32) with all the terms that arise from an actual MCSCF calculation.

In what follows, we assume the energy gaps with higher electronic states large enough to neglect such contributions for the sake of simplicity.

Using intersection-adapted coordinates, the quadratic approximation, in other words the local harmonic approximation, of the adiabatic energy difference for a finite displacement around  $\mathbf{Q}_0$  reads thus

$$\begin{aligned} \Delta E(\mathbf{Q}) \approx & \Delta E_0 + [\partial_{x_1} f_1]_0 Q_{x_1} + \frac{1}{2} \sum_{i,j} [\partial_{x_i} \partial_{x_j} f_1]_0 Q_{x_i} Q_{x_j} \\ & + 2 \frac{[\partial_{x_2} f_2]_0}{\Delta E_0} Q_{x_2}^2 \end{aligned} \quad (33)$$

The quadratic expansions of  $f_1$  and  $\Delta E$  differ only by a supplementary term due to  $f_2$ , which alters the curvature along  $Q_{x_2}$  in the Hessian of  $\Delta E$ . As mentioned above, this term is the signature of the second-order Jahn–Teller effect. It is always positive and leads to the increase (sometimes referred to as exaltation) of the corresponding  $S_1$  curvature along the direction of the non-adiabatic coupling at the FC geometry. Taking the influence of higher electronic states into account would modify the second derivatives of  $\Delta E$  with respect to the quasidiabatic  $f_1$ -contribution along other directions: those of the corresponding non-adiabatic couplings with respect to the higher electronic states.

Neglecting bilinear couplings between branching-plane and intersection-space coordinates as in the approximation used in the solution of (25) leads to

$$\begin{aligned} \Delta E(\mathbf{Q}) \approx & \Delta E_0 + \delta\kappa Q_{x_1} + \frac{1}{2} \delta\gamma_{11} Q_{x_1}^2 + \frac{1}{2} \sum_{i,j>2} \delta\gamma_{ij} Q_{x_i} Q_{x_j} \\ & + \frac{1}{2} \left[ \delta\gamma_{22} + \frac{4(\kappa^{01})^2}{\Delta E_0} \right] Q_{x_2}^2, \end{aligned} \quad (34)$$

where the notations of (24) were used. In practice, the corresponding reduced  $(N-2) \times (N-2)$  matrix block  $(\delta\gamma_{ij})$ , with  $i, j > 2$ , is calculated as the mass-weighted Hessian of  $f_1$  or  $\Delta E$  projected out of the branching plane [29, 41]. Further, choosing the intersection-space coordinates  $Q_{x_i}$  ( $i > 2$ ) as mass-weighted displacements along the eigenvectors of the projected difference Hessian [56] with eigenvalues  $\delta\gamma_{ii} = {}^{is}\lambda_i$  leads to a simplified form:

$$\begin{aligned} \Delta E(\mathbf{Q}) \approx & \Delta E_0 + \delta\kappa Q_{x_1} + \frac{1}{2} \delta\gamma_{11} Q_{x_1}^2 + \frac{1}{2} \sum_{i>2} {}^{is}\lambda_i Q_{x_i}^2 \\ & + \frac{1}{2} \left[ \delta\gamma_{22} + \frac{4(\kappa^{01})^2}{\Delta E_0} \right] Q_{x_2}^2, \end{aligned} \quad (35)$$

i.e., the equation of a paraboloid with a slope along  $Q_{x_1}$  only. Thus, the eigenvectors form the normal modes and the eigenvalues are the normal curvatures (force constants) of the energy difference  $\Delta E$  within the intersection space ( $N-2$  dimensions). The classification of the modes in terms of their photochemical activity discussed above is based on the magnitude and sign of the  $N-2$  eigenvalues,  ${}^{is}\lambda_i$  ( $i > 2$ ).

### 4.3 Application to Benzene

In the photochemistry of benzene, the so-called channel 3 represents a well-known decay route along which fluorescence is quenched above a vibrational excess of  $3000\text{ cm}^{-1}$  [57]. The decay takes place through a ‘prefulvenic’ conical intersection characterized by an out of plane bending [52, 58] and results in the formation of benzvalene and fulvene. The purpose of this study is to find distinct radiationless decay pathways that could be selected by exciting specific combinations of photoactive modes in the initial wavepacket created by a laser pulse. For this, we carry out quantum dynamics simulations on potential energy surfaces of reduced dimension, using the analysis outlined above for the choice of the coordinates.

The numerical result of this analysis applied to benzene is illustrated in Fig. 9. Calculations were performed with a CASSCF of six electrons spread over six  $\pi$  molecular orbitals at the 6–31 G\* level. The special set of energy-difference-adapted coordinates,  $Q_{x_i}$ , was compared to the original coordinates,  $Q_i^0$ , i.e., the traditional 30 normal modes calculated at the  $S_0$  equilibrium geometry ( $D_{6h}$ ), labeled following the Wilson scheme of frequency numbering [59]. A common feature of the  $Q_{x_i}$  coordinates compared to the  $Q_i^0$  coordinates is that they tend to decouple the H motions ( $s$  CH stretching,  $\beta$  HCC bending, and  $\gamma$  CCCH wagging) from the  $C_6$ -ring motions. Other than that, both sets are actually quite similar. This confirms that Duschinsky rotations are not large for them except for modes 14 and 15 [60–62].

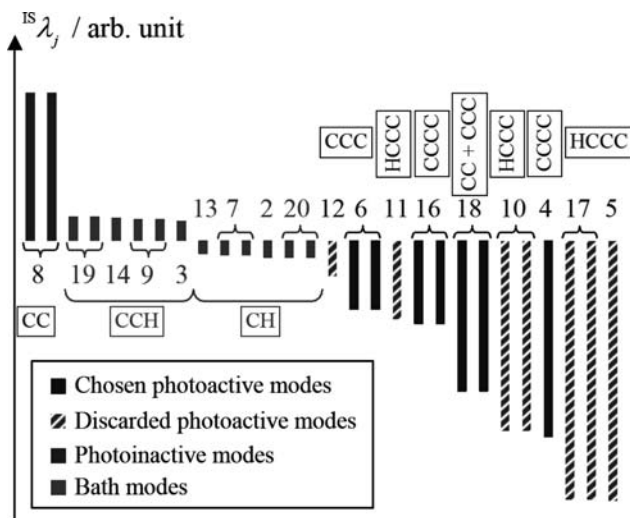


**Fig. 9** Eigenvalues of the energy-difference Hessian computed at the Franck-Condon point of benzene in the 28-dimensional space orthogonal to the pseudo-branching plane. The labels refer to the most similar normal modes of  $S_0$  benzene (Wilson’s convention). The dominant local motions are indicated in boxes (reprinted with permission from [31])

The gradient-difference mode corresponding to coordinate  $Q_{x_1}$  involves mostly the  $a_{1g}$  mode 1, the totally symmetric breathing (the remaining contribution being carried only by mode 2 by symmetry).  $S_0$  is  $A_{1g}$  and  $S_1$  is  $B_{2u}$  at the FC point, so the interstate-coupling mode corresponding to coordinate  $Q_{x_2}$  combines the two  $b_{2u}$  modes and mainly 15, the Kékulé mode, well-known for the exaltation of the  $S_1$  frequency [63, 64]. On Fig. 9, the  $N - 2$   $Q_{x_i}$  coordinates are labeled with the corresponding main components in terms of  $Q_i^0$  coordinates. Twelve modes are of no interest (bath modes): the six  $s$  CH stretching modes and the six  $\beta$  HCC bending modes. As a first approximation, they involve independent motion of the six H nuclei with respect to the  $C_6$ -ring. In contrast, the photoactive modes (large negative value of  $^{18}\lambda_i$ ) describe deformations of the  $C_6$ -ring: three out-of-plane  $\delta$  CCCC ring-puckering modes (torsions), six out-of-plane  $\gamma$  CCCH wagging modes and nine in-plane modes mixing  $t$  CC stretching and  $\alpha$  CCC bending. There is only one degenerate pair of photoinactive modes, similar to the pair 8 ( $e_{2g}$   $t$  CC stretching).

This selection scheme was supported by an analysis of the evolution of the non-totally-symmetric-mode frequencies along a totally symmetric deformation [31]. Also, chemical intuition suggests that  $\delta$  CCCC ring-puckering modes are more relevant than  $\gamma$  CCCH wagging modes in order to change the shape of the  $C_6$ -ring and allow electronic configurations to become degenerate. These considerations led to the selection of seven modes (see Fig. 10) among the 14 photoactive modes previously identified: three out-of-plane modes – the  $b_{2g}$  mode 4 and the  $e_{2u}$  pair 16 ( $\delta$  CCCC motions) – as well as four in-plane skeletal deformations of the  $C_6$ -ring – the  $e_{2g}$  pair 6 and the  $e_{1u}$  pair 18. These modes were included in the quantum dynamics calculations.

Quantum dynamics simulations were run within a nine-dimensional model subspace including the nine most important modes displayed on Fig. 10 and a five-dimensional model including only the pseudo-branching-plane modes 1 and 15, and the three out-of-plane photoactive modes 4, 16x, and 16y [31, 53]. The results were interpreted with regard to the topological features of the extended seam of conical intersection and their influence on the photoreactivity. This is illustrated with Fig. 11.

The calculations were run using the DD-vMCG approach [65–69]. This method uses an expansion of the wavepacket on a time-dependent basis set of Gaussian functions. A local harmonic approximation of the PESs is calculated on the fly along the trajectory followed by the center of each Gaussian function. A diabatic picture is used to represent the pair of coupled electronic states. The dynamics code is implemented in a development version of the Heidelberg MCTDH package [70] and is currently interfaced with a development version of the GAUSSIAN program [40]. The same theoretical level as in the static analysis was used.

Simulations were started with a Franck-Condon Gaussian wavepacket placed on  $S_1$  at  $t = 0$  and approximated by a harmonic product of 1D Gaussian functions with parameters based on a normal frequency analysis at  $Q_0$ . We focused on discriminating photophysical internal conversion (regeneration of  $S_0$  benzene)

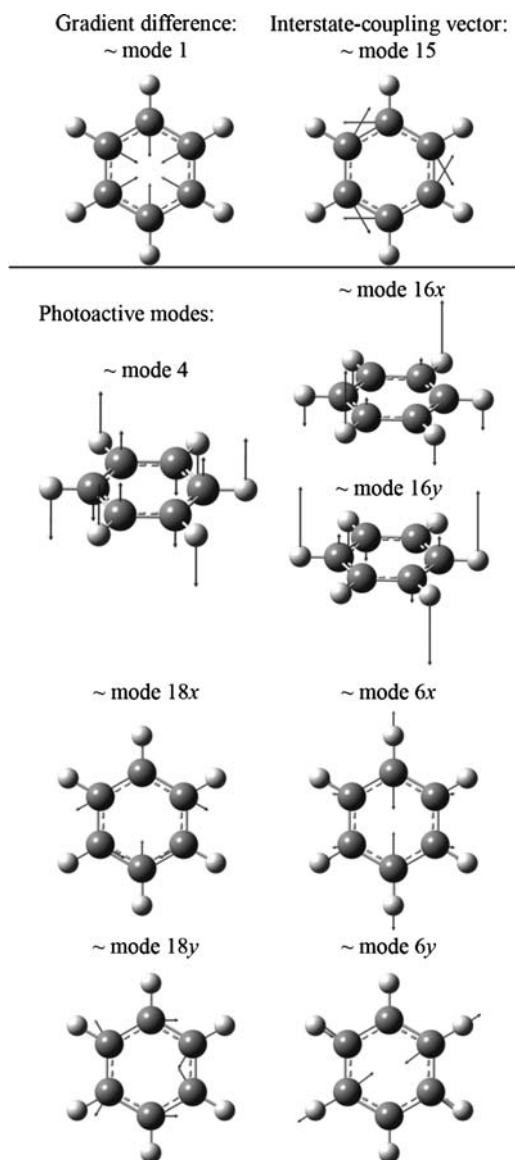


**Fig. 10** The nine dominant motions for the photochemistry of benzene (the labels refer to the most similar normal modes of  $S_0$  benzene following Wilson's convention) (adapted with permission from [31])

from photochemical internal conversion (production of  $S_0$  prefulvene) by stimulating specific combinations of photoactive modes. For this, an additional mean momentum was given to the initial wavepacket, with components of higher or lower magnitude along the five or nine coordinates of the reduced model subspace.



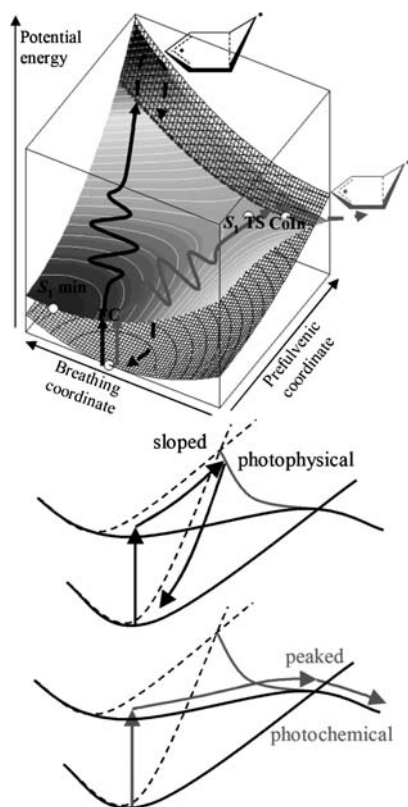


**Fig. 11** Schematic representation of two trajectories starting from the benzene  $S_1$  FC point with different initial momenta. The light grey trajectory goes through a peaked region of the seam and describes a photochemical event, whereas the dark grey trajectory goes through a sloped region and describes a photophysical event (adapted with permission from [53])

The calculations with a minimal five-dimensional model provided relevant insights on the photoreactivity of benzene. The accessible part of the seam of conical intersection (see Fig. 11) has a ‘prefulvenic’ shape reached by displacements along modes 4, 16x and 16y, and it is parallel to the breathing coordinate (mode 1). In brief, we identified two important features that control the photochemistry. First, a specific combination of modes 4 and mode 16x must be activated to force the system to follow a prefulvenic coordinate (see Fig. 11) and reach the prefulvenoid geometries that belong to the seam of conical intersection. Second, as the accessible part of the seam is extended along the breathing coordinate, the selectivity can be modulated by changing the excitation of this mode in the initial wavepacket. For example, no excitation of mode 1 led to the system crossing the seam in a sloped region, thus inducing a photophysical behavior. Choosing the excitation of mode 1 for the wavepacket to cross the seam around the lowest-energy point gave rise to a counter-reactive bobsled effect, where the system was bounced back toward the

reactant because of the shape of the  $S_1$  energy landscape, even if the seam is peaked in this region. Finally, the most efficient way to induce a photochemical behavior proved to be an intermediate case, where the wavepacket was driven to pass near the  $S_1$  transition structure and continue toward a region of the seam still peaked but higher than the lowest-energy point. Therefore, we have been able to prove that various initial excitations can lead to different photochemical products. In addition to that, inclusion of other photoactive modes improved the results by making the system more flexible and improving the PES description in regions relevant for the photochemical pathways.

## 5 Conclusions and Outlook

Our second-order analysis of conical intersections can be applied to the characterization of seams of intersection in molecules and the generation of active coordinates for non-adiabatic quantum dynamics. For the seam characterization, we have presented one example where the relevant seam segment lies along a double-bond isomerization coordinate, and the two degenerate states essentially retain their character along the seam. However studies on other molecules show that the concept of the continuous seam is much broader than what we have presented for fulvene. Along a connected seam it is possible to find conical intersections which differ in the associated reactivity and/or in the degenerate states. One such example is butadiene [30], where the seam includes two conical intersections that mediate the double bond isomerizations and one that leads to cycloadduct formation. A further example is *o*-hydroxybenzaldehyde [71], where the relevant seam of intersection contains several conical intersections associated with hydrogen transfer, double bond isomerization and cycloaddition. In this case, the change in reactivity is associated to a change in the character of the degenerate states, i.e., the excited state changes from  $\pi$ ,  $\pi^*$  to  $n$ ,  $\pi^*$ . The mathematical basis to justify the complexity of the seam in these cases is the theoretical development outlined in Sections 1 and 2 gives. Apart from the interest in improving our mechanistic understanding of the studied photochemical processes, there are two more general questions related to the study of these complex seams. The first one is if, as it has been shown in Section 3 for fulvene, a simple three-coordinate model is enough to describe the seam, or at least its more relevant part. The other question is whether all conical intersections in a molecule may be connected [72]. The examples of butadiene and *o*-hydroxybenzaldehyde shows that this is possible, although the question seems difficult to answer in a general, rigorous way (see also recent work on disjoint intersection spaces [73, 74]). Moreover, we have recently improved the algorithms for the study of seam segments [75], and this opens the way for a better characterization of the seams and an improvement of our knowledge about them.

The generation of active coordinates for non-adiabatic dynamics is related with our interest in laser-driven control. The optimal control of photochemical reactions is based on shaped laser pulses designed to generate photoproducts selectively.

Theoretical rationalization can help the preconditioning of the laser pulse by predicting which vibrations have to be stimulated by an optimized laser pulse to enhance radiationless decay and change the branching ratio in favor of a selected target. In the context of theory-assisted optimal control, it is essential to establish systematic methods to select such active coordinates. In this work, we have proposed a new approach based on the local, second-order properties of the energy difference rather than the sole energy of the excited state. We have identified the most relevant vibrations that have to be excited in benzene to creating ground-state prefulvene. We have confirmed this approach by quantum dynamics simulations, and we hope that it will prove fruitful in the future.

**Acknowledgements** M. A. R. and B. L. gratefully acknowledge financial support by EPSRC (Grant No. EP/F028296/1). L.B. acknowledges support from Projects No. CTQ2005–04563/BQU and CTQ2008–06696/BQU from the Spanish Ministerio de Ciencia e Innovacin. G. A. W. acknowledges funding from the EPSRC and thanks Irene Burghardt for her work in developing the vMCG method.

## Appendix: Quadratic Expansion for MCSCF Wavefunctions

In this appendix we generalise the expressions of the ‘diabatic’ quantities first introduced in Sec. 2 for the ideal case of an exact two-level problem to a more realistic description. In a normal situation, the Hamiltonian has an infinite number of eigenstates, and there is no finite number of strictly diabatic states [76] that can describe a given pair of adiabatic states [77–80]. Instead, one can define a unitary transformation of the adiabatic states generating two quasidiabatic states characterised by a residual non-adiabatic coupling, as small as possible, but never zero (see, e.g., [5, 24, 32–35]). In practice, the electronic Hilbert space is always truncated to a finite number of configurations. In what follows, we consider the case of MCSCF wavefunctions and make use of ‘generalised crude adiabatic’ states adapted to this.

At  $\mathbf{Q} = \mathbf{Q}_0$ , the adiabatic state number  $J$  is known as an MCSCF expansion:

$$|S_J; \mathbf{Q}_0\rangle = \sum_L C_L^{(J)}(\mathbf{Q}_0) |\Phi_L; \mathbf{Q}_0\rangle, \quad (\text{A.1})$$

which represents the best variational solution to the electronic problem within the truncated Hilbert space spanned by the configuration state functions (CSFs),  $\{|\Phi_L; \mathbf{Q}_0\rangle\}$ . In this subspace, the configuration-interaction (CI) vectors,  $\mathbf{C}^{(J)}(\mathbf{Q}_0)$ , are the ‘exact’ eigenstates of the finite matrix of the clamped-nucleus Hamiltonian,  $\hat{H}(\mathbf{Q}_0)$ , in the CSF representation:

$$\mathbf{H}^{\text{CSF}}(\mathbf{Q}_0) \mathbf{C}^{(J)}(\mathbf{Q}_0) = E_J(\mathbf{Q}_0) \mathbf{C}^{(J)}(\mathbf{Q}_0), \quad (\text{A.2})$$

where  $H_{KL}^{\text{CSF}}(\mathbf{Q}_0) = \langle \Phi_K; \mathbf{Q}_0 | \hat{H}(\mathbf{Q}_0) | \Phi_L; \mathbf{Q}_0 \rangle$ . In principle, the finite system of secular equations, (A.2), can be solved exactly by a numerical diagonalisation method for a given set of CSFs. No further discussion will be made here about how

the molecular orbitals on which the CSFs are constructed are optimised. We will just assume that the CSF Hamiltonian matrix and its first and second derivatives with respect to  $\mathbf{Q}$  can be calculated.

The two-level adiabatic Hamiltonian matrix is diagonal at  $\mathbf{Q} = \mathbf{Q}_0$ :

$$\mathbf{H}^{\text{adia}}(\mathbf{Q}_0) = \begin{bmatrix} E_0(\mathbf{Q}_0) & 0 \\ 0 & E_1(\mathbf{Q}_0) \end{bmatrix}, \quad (\text{A.3})$$

where  $H_{IJ}^{\text{adia}}(\mathbf{Q}_0) = \langle S_I; \mathbf{Q}_0 | \hat{H}(\mathbf{Q}_0) | S_J; \mathbf{Q}_0 \rangle$ . The first-order non-adiabatic coupling vector at the reference geometry is defined as:

$$\mathbf{g}_{IJ}(\mathbf{Q}_0) = \langle S_I; \mathbf{Q}_0 | [\nabla | S_J; \mathbf{Q} \rangle]_0, \quad (\text{A.4})$$

where  $[\nabla]_0$  stands for the local gradient, with components  $\partial/\partial Q_i|_{\mathbf{Q}=\mathbf{Q}_0}$ . Differentiating (A.1) and using the product rule gives rise to two contributions:

$$\begin{aligned} \mathbf{g}_{IJ}^{\text{CI}}(\mathbf{Q}_0) &= \sum_L C_L^{(I)*}(\mathbf{Q}_0) [\nabla C_L^{(J)}(\mathbf{Q})]_0, \\ \mathbf{g}_{IJ}^{\text{CSF}}(\mathbf{Q}_0) &= \sum_{K,L} C_K^{(I)*}(\mathbf{Q}_0) \langle \Phi_K; \mathbf{Q}_0 | [\nabla | \Phi_L; \mathbf{Q} \rangle]_0 C_L^{(J)}(\mathbf{Q}_0), \end{aligned} \quad (\text{A.5})$$

where the first term exhibits explicit variation of the CI coefficients, and the second one explicit variation of the CSFs (through molecular-orbital coefficients and atomic-orbital overlaps). Note that, in practice, the derivatives of the CI coefficients and the orbital coefficients depend implicitly on each other when calculated. In most MCSCF applications, the latter term is neglected because the CSFs vary smoothly, and often less rapidly, than the CI coefficients. It may also be canceled out by a suitable rotation of the active orbitals [81, 82].

By definition, the adiabatic states are eigenstates at any value of  $\mathbf{Q}$ . At first-order, this implies:

$$[\nabla H_{IJ}^{\text{adia}}(\mathbf{Q})]_0 = [\nabla E_J(\mathbf{Q})]_0 \delta_{IJ}, \quad (\text{A.6})$$

where  $\delta_{IJ}$  is the Kronecker delta. Using:

$$[\nabla \langle S_I; \mathbf{Q} | S_J; \mathbf{Q} \rangle]_0 = \mathbf{g}_{JI}^{\text{CI}*}(\mathbf{Q}_0) + \mathbf{g}_{IJ}^{\text{CI}}(\mathbf{Q}_0) = \mathbf{0}, \quad (\text{A.7})$$

and (A.2) further leads to:

$$\begin{aligned} \mathbf{g}_{01}^{\text{CI}}(\mathbf{Q}_0) &= \frac{\sum_{K,L} C_K^{(0)*}(\mathbf{Q}_0) [\nabla H_{KL}^{\text{CSF}}(\mathbf{Q})]_0 C_L^{(1)}(\mathbf{Q}_0)}{\Delta E(\mathbf{Q}_0)}, \\ [\nabla V_J(\mathbf{Q})]_0 &= \sum_{K,L} C_K^{(J)*}(\mathbf{Q}_0) [\nabla H_{KL}^{\text{CSF}}(\mathbf{Q})]_0 C_L^{(J)}(\mathbf{Q}_0), \end{aligned} \quad (\text{A.8})$$

where  $\Delta E(\mathbf{Q}_0) = E_1(\mathbf{Q}_0) - E_0(\mathbf{Q}_0)$ . Differentiating the secular system, (A.2), leads to Hellmann-Feynman-like relationships in the CI space because the CI vectors,  $\mathbf{C}^{(J)}(\mathbf{Q}_0)$ , are the exact eigenvectors of the truncated CSF matrix representation of the Hamiltonian,  $\mathbf{H}^{\text{CSF}}(\mathbf{Q}_0)$ . Note that the Hellmann-Feynman theorem does not apply to the states,  $|S_J; \mathbf{Q}_0\rangle$ , since they are approximate eigenstates of the exact operator,  $\hat{H}(\mathbf{Q}_0)$ .

Eq. (A.9) shows how the branching-plane vectors are calculated in practice from CI difference and transition densities as well as the CSF first-derivative density:

$$\begin{aligned} \mathbf{x}_1(\mathbf{Q}_0) &= [\nabla \Delta E(\mathbf{Q})]_0 = \sum_{K,L} \left[ \rho_{KL}^{(11)}(\mathbf{Q}_0) - \rho_{KL}^{(00)}(\mathbf{Q}_0) \right] [\nabla H_{KL}^{\text{CSF}}(\mathbf{Q})]_0, \\ \mathbf{x}_2(\mathbf{Q}_0) &= \Delta E(\mathbf{Q}_0) \mathbf{g}_{01}^{\text{CI}}(\mathbf{Q}_0) = \sum_{K,L} \rho_{KL}^{(01)}(\mathbf{Q}_0) [\nabla H_{KL}^{\text{CSF}}(\mathbf{Q})]_0, \end{aligned} \quad (\text{A.9})$$

where  $\rho_{KL}^{(IJ)}(\mathbf{Q}) = C_K^{(I)*}(\mathbf{Q}) C_L^{(J)}(\mathbf{Q})$ . At a conical intersection, the energy difference is zero. Although the first-order non-adiabatic coupling,  $\mathbf{g}_{01}^{\text{CI}}(\mathbf{Q}_0)$ , diverges, the interstate-coupling vector,  $\mathbf{x}_2(\mathbf{Q}_0)$ , is a finite quantity. The ‘pseudo-branching-space’ vectors introduced in Sec. 4 are defined as in (A.9) but at geometries where the energy difference is not zero. As opposed to (21), in which the states (kets) were frozen and the Hamiltonian (operator),  $\hat{H}(\mathbf{Q})$ , was differentiated, here, only the CI coefficients are frozen and the Hamiltonian matrix,  $\mathbf{H}^{\text{CSF}}(\mathbf{Q}) = [\langle \Phi_K; \mathbf{Q} | \hat{H}(\mathbf{Q}) | \Phi_L; \mathbf{Q} \rangle]$ , is differentiated, which involves differentiation of the CSFs.

It is clear from (A.8) and (A.9) that the gradient difference and derivative coupling in the adiabatic representation can be related to Hamiltonian derivatives in a quasidiabatic representation. In the two-level approximation used in Section 2, the ‘crude adiabatic’ states are trivial diabatic states. In practice (see (A.9)), the fully frozen states at  $\mathbf{Q}_0$  are not convenient because the CSF basis set  $\{|\Phi_L; \mathbf{Q}\rangle\}$  is not complete and the states may not be expanded in a CSF basis set evaluated at another value of  $\mathbf{Q}$  (this would require an infinite number of states). However, generalized crude adiabatic states are introduced for multiconfiguration methods by freezing the expansion coefficients but letting the CSFs relax as in the adiabatic states:

$$|S_J^{\text{ca}(\mathbf{Q}_0)}; \mathbf{Q}\rangle = \sum_L C_L^{(J)}(\mathbf{Q}_0) |\Phi_L; \mathbf{Q}\rangle. \quad (\text{A.10})$$

This implies that the adiabatic states at the displaced geometry,  $|S_J; \mathbf{Q}\rangle$ , are related to the generalized crude adiabatic states by a mere rotation of the CI coefficients.

As a result, the generalized crude adiabatic representation of the clamped-nucleus Hamiltonian satisfies:

$$\begin{aligned} \mathbf{x}_1(\mathbf{Q}_0) &= [\nabla H_{11}^{\text{ca}(\mathbf{Q}_0)}(\mathbf{Q})]_0 - [\nabla H_{00}^{\text{ca}(\mathbf{Q}_0)}(\mathbf{Q})]_0, \\ \mathbf{x}_2(\mathbf{Q}_0) &= [\nabla H_{01}^{\text{ca}(\mathbf{Q}_0)}(\mathbf{Q})]_0, \end{aligned} \quad (\text{A.11})$$

At a conical intersection, the branching plane is invariant through any unitary transformation within the two electronic states and any such combination of degenerate states is still a solution. Thus, the precise definition of the two vectors in (A.9) or (A.11) is not unique and depends on an arbitrary rotation within the space of the CI coefficients (i.e., between the generalized crude adiabatic states), unless the states have different symmetries (then  $\mathbf{x}_1$  is totally symmetric and  $\mathbf{x}_2$  breaks the symmetry).

In this basis set, any finite displacement  $\delta\mathbf{Q}$ , such as  $\mathbf{Q} = \mathbf{Q}_0 + \delta\mathbf{Q}$ , gives rise to non-zero off-diagonal elements and to different diagonal elements:

$$\mathbf{H}^{\text{ca}(\mathbf{Q}_0)}(\mathbf{Q}_0 + \delta\mathbf{Q}) = \begin{bmatrix} E_0(\mathbf{Q}_0) & 0 \\ 0 & E_1(\mathbf{Q}_0) \end{bmatrix} + \begin{bmatrix} \delta H_{00}^{\text{ca}(\mathbf{Q}_0)} & \delta H_{01}^{\text{ca}(\mathbf{Q}_0)} \\ \delta H_{01}^{\text{ca}(\mathbf{Q}_0)} & \delta H_{11}^{\text{ca}(\mathbf{Q}_0)} \end{bmatrix}, \quad (\text{A.12})$$

approximated at first-order as:

$$\begin{bmatrix} \delta H_{00}^{\text{ca}(\mathbf{Q}_0)} & \delta H_{01}^{\text{ca}(\mathbf{Q}_0)} \\ \delta H_{01}^{\text{ca}(\mathbf{Q}_0)} & \delta H_{11}^{\text{ca}(\mathbf{Q}_0)} \end{bmatrix} \approx \begin{bmatrix} -\frac{1}{2}\delta\mathbf{Q} \cdot \mathbf{x}_1(\mathbf{Q}_0) & \delta\mathbf{Q} \cdot \mathbf{x}_2(\mathbf{Q}_0) \\ \delta\mathbf{Q} \cdot \mathbf{x}_2(\mathbf{Q}_0) & \frac{1}{2}\delta\mathbf{Q} \cdot \mathbf{x}_1(\mathbf{Q}_0) \end{bmatrix}, \quad (\text{A.13})$$

where the dot denotes the scalar or dot product. Note that the electronic wavefunctions are assumed to be real-valued. With respect to the kinetic energy of the nuclei, the generalized crude adiabatic states form a quasidiabatic basis set, and their non-fully diabatic character is attributed to the residual term  $\mathbf{g}_{IJ}^{\text{CSF}}(\mathbf{Q}_0)$  in (A.4) and (A.5) (see, e.g., [35] and references therein). In other words, these states cancel out the main CI contribution to the first-order non-adiabatic coupling exactly. From now on, we will refer to them as ‘the’ quasidiabatic basis set.

The  $(2 \times 2)$  diabatic Hamiltonian matrix,  $\mathbf{H}(\mathbf{Q})$ , introduced in Sec. 2 (see (14)) is to be understood in practice as being equal to the matrix  $\mathbf{H}^{\text{ca}(\mathbf{Q}_0)}(\mathbf{Q})$ . In addition, the two-level square-root formula (see, e.g., (15) or (35)) is given only as a guideline for better understanding the concepts involved here. In practice the adiabatic energies are actually obtained by diagonalising the larger CSF Hamiltonian matrix, the CSFs being “equally optimal” for  $|S_0; \mathbf{Q}\rangle$  and  $|S_1; \mathbf{Q}\rangle$  in a state-averaged CASSCF calculation (they actually minimize a weighted average of the eigenvalues  $E_0(\mathbf{Q})$  and  $E_1(\mathbf{Q})$ ).

The parameters for the second-order expansion of the matrix  $\mathbf{H}(\mathbf{Q})$  can be obtained from state-averaged CASSCF calculations, provided the coupled-perturbed-MCSCF equations can be solved for the system under study. For the first-order terms, there is a simple correspondence between the adiabatic and quasidiabatic expressions of  $\mathbf{x}_1$  and  $\mathbf{x}_2$ , as illustrated in (A.9) and (A.11). However, the second derivatives have to include mixing of the two states with each other and with higher-lying electronic states. At a conical intersection this problem can be addressed using second-order degenerate perturbation theory, as developed by Mead [32]. Here we use a different approach. We derive the expressions for a non-degenerate case and approximate the result for the degenerate case by projecting the

ill-defined terms out of the Hessian. Thus, for the non-degenerate case the adiabatic constraint at second order reads:

$$[\nabla \otimes \nabla H_{IJ}^{\text{adia}}(\mathbf{Q})]_0 = [\nabla \otimes \nabla E_J(\mathbf{Q})]_0 \delta_{IJ}, \quad (\text{A.14})$$

where  $\otimes$  denotes the tensor or cross product, and  $[\nabla \otimes \nabla]_0$  stands for the local Hessian, with components  $\partial^2/\partial Q_i \partial Q_j|_{\mathbf{Q}=\mathbf{Q}_0}$  ( $\otimes$  transforms two vectors,  $\mathbf{u} = [u_i]$  and  $\mathbf{v} = [v_i]$ , into a tensor that can be represented by a dyadic matrix,  $\mathbf{u} \otimes \mathbf{v} = [u_i v_j]$ ). After some algebra, one gets

$$\begin{aligned} [\nabla \otimes \nabla H_{IJ}^{\text{adia}}(\mathbf{Q})]_0 &= \sum_{K,L} C_K^{(I)*}(\mathbf{Q}_0) [\nabla \otimes \nabla H_{KL}^{\text{CSF}}(\mathbf{Q})]_0 C_L^{(J)}(\mathbf{Q}_0) \\ &\quad + [E_I(\mathbf{Q}_0) - E_J(\mathbf{Q}_0)] [\nabla \otimes \mathbf{g}_{IJ}^{\text{Cl}}(\mathbf{Q})]_0 \\ &\quad + \sum_M [E_M(\mathbf{Q}_0) - E_I(\mathbf{Q}_0)] \mathbf{g}_{MJ}^{\text{Cl}}(\mathbf{Q}_0) \otimes \mathbf{g}_{IM}^{\text{Cl}}(\mathbf{Q}_0) \\ &\quad + \sum_M [E_M(\mathbf{Q}_0) - E_J(\mathbf{Q}_0)] \mathbf{g}_{IM}^{\text{Cl}}(\mathbf{Q}_0) \otimes \mathbf{g}_{MJ}^{\text{Cl}}(\mathbf{Q}_0) \\ &\quad + \left\{ [\nabla E_I(\mathbf{Q})]_0 - [\nabla E_J(\mathbf{Q})]_0 \right\} \otimes \mathbf{g}_{IJ}^{\text{Cl}}(\mathbf{Q}_0) \\ &\quad + \mathbf{g}_{IJ}^{\text{Cl}}(\mathbf{Q}_0) \otimes \left\{ [\nabla E_I(\mathbf{Q})]_0 - [\nabla E_J(\mathbf{Q})]_0 \right\}, \quad (\text{A.15}) \end{aligned}$$

where use was made of (A.2) and:

$$[\nabla \otimes \nabla \langle S_I; \mathbf{Q} | S_J; \mathbf{Q} \rangle]_0 = [\nabla \otimes \mathbf{g}_{JI}^{\text{Cl}*}(\mathbf{Q})]_0 + [\nabla \otimes \mathbf{g}_{IJ}^{\text{Cl}}(\mathbf{Q})]_0 = \mathbf{0}, \quad (\text{A.16})$$

with:

$$\begin{aligned} [\nabla \otimes \mathbf{g}_{IJ}^{\text{Cl}}(\mathbf{Q})]_0 &= - \sum_M \mathbf{g}_{IM}^{\text{Cl}}(\mathbf{Q}_0) \otimes \mathbf{g}_{MJ}^{\text{Cl}}(\mathbf{Q}_0) \\ &\quad + \sum_K C_K^{(I)*}(\mathbf{Q}_0) [\nabla \otimes \nabla C_K^{(J)}(\mathbf{Q})]_0, \quad (\text{A.17}) \end{aligned}$$

$$\left( [\nabla \otimes \mathbf{g}_{IJ}^{\text{Cl}}(\mathbf{Q})]_0 \text{ is the matrix of elements } \partial/\partial Q_i g_{IJ,j}^{\text{Cl}}(\mathbf{Q}) \Big|_{\mathbf{Q}=\mathbf{Q}_0} \right).$$

In contrast with first derivatives, second derivatives involve couplings with all states (sums over  $M$  in (A.15)) that correspond to a second-order Jahn–Teller effect. Such contributions from higher-lying states ( $M \geq 2$ ) do not exist in a pure two-level model (see Sec. 2), but they are part of the actual MCSCF calculation, where the number of eigenstates is equal to the number of CSFs. Limiting the values of  $M$  to 0 and 1 leads to:

$$\begin{aligned} [\nabla \otimes \nabla E_0(\mathbf{Q})]_0 &= \left[ \nabla \otimes \nabla H_{00}^{\text{ca}(\mathbf{Q}_0)}(\mathbf{Q}) \right]_0 \\ &\quad - 2 [E_1(\mathbf{Q}_0) - E_0(\mathbf{Q}_0)] \mathbf{g}_{01}^{\text{Cl}}(\mathbf{Q}_0) \otimes \mathbf{g}_{01}^{\text{Cl}}(\mathbf{Q}_0), \end{aligned}$$

$$\begin{aligned}
[\nabla \otimes \nabla E_1(\mathbf{Q})]_0 &= \left[ \nabla \otimes \nabla H_{11}^{\text{ca}(\mathbf{Q}_0)}(\mathbf{Q}) \right]_0 \\
&\quad + 2[E_1(\mathbf{Q}_0) - E_0(\mathbf{Q}_0)] \mathbf{g}_{01}^{\text{Cl}}(\mathbf{Q}_0) \otimes \mathbf{g}_{01}^{\text{Cl}}(\mathbf{Q}_0), \\
\mathbf{0} &= \left[ \nabla \otimes \nabla H_{01}^{\text{ca}(\mathbf{Q}_0)}(\mathbf{Q}) \right]_0 \\
&\quad + [E_0(\mathbf{Q}_0) - E_1(\mathbf{Q}_0)] [\nabla \otimes \mathbf{g}_{01}^{\text{Cl}}(\mathbf{Q})]_0 \\
&\quad + \left\{ [\nabla E_0(\mathbf{Q})]_0 - [\nabla E_1(\mathbf{Q})]_0 \right\} \otimes \mathbf{g}_{01}^{\text{Cl}}(\mathbf{Q}_0) \\
&\quad + \mathbf{g}_{01}^{\text{Cl}}(\mathbf{Q}_0) \otimes \left\{ [\nabla E_0(\mathbf{Q})]_0 - [\nabla E_1(\mathbf{Q})]_0 \right\}, \quad (\text{A.18})
\end{aligned}$$

which yields:

$$\begin{aligned}
\left[ \nabla \otimes \nabla \frac{H_{00}^{\text{ca}(\mathbf{Q}_0)}(\mathbf{Q}) + H_{11}^{\text{ca}(\mathbf{Q}_0)}(\mathbf{Q})}{2} \right]_0 &= \frac{[\nabla \otimes \nabla E_0(\mathbf{Q})]_0 + [\nabla \otimes \nabla E_1(\mathbf{Q})]_0}{2}, \\
\left[ \nabla \otimes \nabla \frac{H_{11}^{\text{ca}(\mathbf{Q}_0)}(\mathbf{Q}) - H_{00}^{\text{ca}(\mathbf{Q}_0)}(\mathbf{Q})}{2} \right]_0 &= \frac{1}{2} [\nabla \otimes \mathbf{x}_1(\mathbf{Q})]_0 - 2 \frac{\mathbf{x}_2(\mathbf{Q}_0) \otimes \mathbf{x}_2(\mathbf{Q}_0)}{E_1(\mathbf{Q}_0) - E_0(\mathbf{Q}_0)}, \\
\left[ \nabla \otimes \nabla H_{01}^{\text{ca}(\mathbf{Q}_0)}(\mathbf{Q}) \right]_0 &= [\nabla \otimes \mathbf{x}_2(\mathbf{Q})]_0 + \frac{\mathbf{x}_2(\mathbf{Q}_0) \otimes \mathbf{x}_1(\mathbf{Q}_0)}{E_1(\mathbf{Q}_0) - E_0(\mathbf{Q}_0)}, \quad (\text{A.19})
\end{aligned}$$

and in turn (24) and (33) if a non-zero energy difference is assumed (the degenerate case is discussed after (24)). Second-order Jahn–Teller couplings with higher-lying states are part of the adiabatic second derivatives. Strictly speaking, they should be removed to define the quasidiabatic second derivatives. Here, we assume their effect is small enough (or similar enough on both states), and we incorporate them in the quasidiabatic Hessians to produce an effective two-level model.

## References

1. E. Teller, *J. Phys. Chem.* **41**, 109–116 (1937)
2. F. Bernardi, M. Olivucci, M.A. Robb, *Chem. Soc. Rev.* **25**, 321–328 (1996)
3. W. Domcke, D.R. Yarkony, H. Köppel (eds.), *Conical Intersections: Electronic Structure, Dynamics & Spectroscopy. Advanced Series in Physical Chemistry, 15.* (World Scientific, Singapore, 2004)
4. L. Blancafort, F. Ogliaro, M. Olivucci, M.A. Robb, M.J. Bearpark, A. Sinicropi, in *Computational Methods in Photochemistry*, ed. by A.G. Kutateladze (Taylor & Francis, Boca Raton, FL, 2005), pp. 31–110
5. H. Köppel, W. Domcke, L.S. Cederbaum, *Adv. Chem. Phys.* **57**, 59–246 (1984)
6. T.A. Barckholtz, T.A. Miller, *Int. Rev. Phys. Chem.* **17**, 435–524 (1998)
7. M.J. Bearpark, F. Bernardi, M. Olivucci, M.A. Robb, B.R. Smith, *J. Am. Chem. Soc.* **118**, 5254–5260 (1996)
8. P.J. Kuntz, W.N. Whitton, I. Paidarova, R. Polak, *Can. J. Chem.* **72**, 939–946 (1994)
9. M.R. Manaa, D.R. Yarkony, *J. Am. Chem. Soc.* **116**, 11444–11448 (1994)
10. H. Hettema, D.R. Yarkony, *J. Chem. Phys.* **102**, 8431–8439 (1995)



11. G.J. Atchity, K. Ruedenberg, A. Nanayakkara, *Theor. Chem. Acc.* **96**, 195–204 (1997)
12. J. Ivanic, G.J. Atchity, K. Ruedenberg, *J. Chem. Phys.* **107**, 4307–4317 (1997)
13. G. Chaban, M.S. Gordon, D.R. Yarkony, *J. Phys. Chem. A* **101**, 7953–7959 (1997)
14. M.S. Gordon, V.A. Glezakou, D.R. Yarkony, *J. Chem. Phys.* **108**, 5657–5659 (1998)
15. D.R. Yarkony, *J. Phys. Chem. A* **103**, 6658–6668 (1999)
16. L. Freund, M. Klessinger, *Int. J. Quantum Chem.* **70**, 1023–1028 (1998)
17. M. Ben-Nun, T.J. Martinez, *Chem. Phys.* **259**, 237–248 (2000)
18. M. Barbatti, J. Paier, H. Lischka, *J. Chem. Phys.* **121**, 11614–11624 (2004)
19. S. Wilsey, K.N. Houk, *J. Am. Chem. Soc.* **124**, 11182–11190 (2002)
20. A. Migani, M.A. Robb, M. Olivucci, *J. Am. Chem. Soc.* **125**, 2804–2808 (2003)
21. A. Migani, A. Sinicropi, N. Ferre, A. Cembran, M. Garavelli, M. Olivucci, *Faraday Disc.* **127**, 179–191 (2004)
22. D.R. Yarkony, *J. Chem. Phys.* **123**, 204101 (2005)
23. E.R. Davidson, *J. Am. Chem. Soc.* **99**, 397–402 (1977)
24. M. Desouter-Lecomte, C. Galloy, J.C. Lorquet, M.V. Pires, *J. Chem. Phys.* **71**, 3661–3672 (1979)
25. G.J. Atchity, S.S. Xantheas, K. Ruedenberg, *J. Chem. Phys.* **95**, 1862–1876 (1991)
26. D.R. Yarkony, *Rev. Mod. Phys.* **68**, 985–1013 (1996)
27. J. von Neumann, E. Wigner, *Phys. Z.* **30**, 467–470 (1929)
28. M.J. Paterson, M.J. Bearpark, M.A. Robb, L. Blancafort, *J. Chem. Phys.* **121**, 11562–11571 (2004)
29. M.J. Paterson, M.J. Bearpark, M.A. Robb, L. Blancafort, G.A. Worth, *Phys. Chem. Chem. Phys.* **7**, 2100–2115 (2005)
30. F. Sicilia, L. Blancafort, M.J. Bearpark, M.A. Robb, *J. Phys. Chem. A* **111**, 2182–2192 (2007)
31. B. Lasorne, F. Sicilia, M.J. Bearpark, M.A. Robb, G.A. Worth, L. Blancafort, *J. Chem. Phys.* **128**, 124307 (2008)
32. C.A. Mead, *J. Chem. Phys.* **78**, 807–814 (1983)
33. W. Domcke, C. Woywod, M. Stengle, *Chem. Phys. Lett.* **226**, 257–262 (1994)
34. C. Woywod, W. Domcke, A.L. Sobolewski, H.J. Werner, *J. Chem. Phys.* **100**, 1400–1413 (1994)
35. B.N. Papas, M.S. Schuurman, D.R. Yarkony, *J. Chem. Phys.* **129** (2008)
36. H.C. Longuet-Higgins, in *Advances in Spectroscopy*, ed. by W.B. Thompson (Wiley Interscience, New York, 1961), p. 429
37. D.R. Yarkony, *Acc. Chem. Res.* **31**, 511–518 (1998)
38. M.J. Bearpark, M.A. Robb, H.B. Schlegel, *Chem. Phys. Lett.* **223**, 269–274 (1994)
39. N. Yamamoto, T. Vreven, M.A. Robb, M.J. Frisch, H.B. Schlegel, *Chem. Phys. Lett.* **250**, 373–378 (1996)
40. M.J. Frisch, G.W. Trucks, H.B. Schlegel et al., *Gaussian03, Revision E.01*. (Gaussian, Inc, Pittsburgh, PA, 2008)
41. W.H. Miller, N.C. Handy, J.E. Adams, *J. Chem. Phys.* **72**, 99–112 (1980)
42. S.N. Parker, R.S. Minns, T.J. Penfold, G.A. Worth, H.H. Fielding, *Chem. Phys. Lett.* **469**, 43–47 (2009)
43. J.E. Kent, P.J. Harman, M.F. Odwyer, *J. Phys. Chem.* **85**, 2726–2730 (1981)
44. M.J. Bearpark, L. Blancafort, M.J. Paterson, *Mol. Phys.* **104**, 1033–1038 (2006)
45. F. Sicilia, M.J. Bearpark, L. Blancafort, M.A. Robb, *Theor. Chem. Acc.* **118**, 241–251 (2007)
46. F. Gatti, Y. Justum, M. Menou, A. Nauts, X. Chapuisat, *J. Mol. Spectrosc.* **181**, 403–423 (1997)
47. D. Lauvergnat, A. Nauts, *J. Chem. Phys.* **116**, 8560–8570 (2002)
48. F. Gatti, *Chem. Phys. Lett.* **373**, 146–152 (2003)
49. E. Gindensperger, I. Burghardt, L.S. Cederbaum, *J. Chem. Phys.* **124**, 144103 (2006)
50. D. Lauvergnat, E. Baloitcha, G. Dive, M. Desouter-Lecomte, *Chem. Phys.* **326**, 500–508 (2006)
51. I.J. Palmer, I.N. Ragazos, F. Bernardi, M. Olivucci, M.A. Robb, *J. Am. Chem. Soc.* **115**, 673–682 (1993)
52. A.L. Sobolewski, C. Woywod, W. Domcke, *J. Chem. Phys.* **98**, 5627–5641 (1993)

53. B. Lasorne, M.J. Bearpark, M.A. Robb, G.A. Worth, *J. Phys. Chem. A* **112**, 13017–13027 (2008)
54. S. Shaik, A. Shurki, D. Danovich, P.C. Hiberty, *J. Am. Chem. Soc.* **118**, 666–671 (1996)
55. L. Blancafort, M. Sola, *J. Phys. Chem. A* **110**, 11219–11222 (2006)
56. A.G. Baboul, H.B. Schlegel, *J. Chem. Phys.* **107**, 9413–9417 (1997)
57. K.E. Wilzbach, A.L. Harkness, L. Kaplan, *J. Am. Chem. Soc.* **90**, 1116–1118 (1968)
58. M. Olivucci, I.N. Ragazos, F. Bernardi, M.A. Robb, *J. Am. Chem. Soc.* **115**, 3710–3721 (1993)
59. E.B. Wilson, *Phys. Rev.* **45**, 706 (1934)
60. F. Metz, M.J. Robey, E.W. Schlag, F. Dorr, *Chem. Phys. Lett.* **51**, 8–12 (1977)
61. G. Orlandi, P. Palmieri, R. Tarroni, F. Zerbetto, M.Z. Zgierski, *J. Chem. Phys.* **100**, 2458–2464 (1994)
62. A. Bernhardsson, N. Forsberg, P.A. Malmqvist, B.O. Roos, L. Serrano-Andres, *J. Chem. Phys.* **112**, 2798–2809 (2000)
63. S. Shaik, A. Shurki, D. Danovich, P.C. Hiberty, *J. Am. Chem. Soc.* **118**, 666–671 (1996)
64. L. Blancafort, M. Sola, *J. Phys. Chem. A* **110**, 11219–11222 (2006)
65. G.A. Worth, P. Hunt, M.A. Robb, *J. Phys. Chem. A* **107**, 621–631 (2003)
66. G.A. Worth, M.A. Robb, I. Burghardt, *Faraday Disc.* **127**, 307–323 (2004)
67. B. Lasorne, M.J. Bearpark, M.A. Robb, G.A. Worth, *Chem. Phys. Lett.* **432**, 604–609 (2006)
68. G.A. Worth, M.A. Robb, B. Lasorne, *Mol. Phys.* **106**, 2077–2091 (2008)
69. B. Lasorne, G.A. Worth, in *Multidimensional Quantum Dynamics: MCTDH Theory and Applications*, ed. by H.D. Meyer, F. Gatti, G.A. Worth (Wiley-VCH, Weinheim, 2009)
70. G.A. Worth, I. Burghardt, *Chem. Phys. Lett.* **368**, 502–508 (2003)
71. A. Migani, L. Blancafort, A.D. DeBellis, M.A. Robb, *J. Am. Chem. Soc.* **130**, 6932–6933 (2008)
72. J.D. Coe, M.T. Ong, B.G. Levine, T.J. Martinez, *J. Phys. Chem. A* **112**, 12559–12567 (2008)
73. J.J. Dillon, D.R. Yarkony, *J. Chem. Phys.* **126** (2007)
74. M.S. Schuurman, D.R. Yarkony, *J. Chem. Phys.* **126** (2007)
75. F. Sicilia, L. Blancafort, M.J. Bearpark, M.A. Robb, *J. Chem. Theory Comput.* **4**, 257–266 (2008)
76. F.T. Smith, *Phys. Rev.* **179**, 111 (1969)
77. M. Baer, *Chem. Phys.* **15**, 49–57 (1976)
78. C.A. Mead, D.G. Truhlar, *J. Chem. Phys.* **77**, 6090–6098 (1982)
79. B.K. Kendrick, C.A. Mead, D.G. Truhlar, *Chem. Phys. Lett.* **330**, 629–632 (2000)
80. T. Vertesi, E. Bene, A. Vibok, G.J. Halasz, M. Baer, *J. Phys. Chem. A* **109**, 3476–3484 (2005)
81. B.H. Lengsfeld, P. Saxe, D.R. Yarkony, *J. Chem. Phys.* **81**, 4549–4553 (1984)
82. P. Saxe, B.H. Lengsfeld, D.R. Yarkony, *Chem. Phys. Lett.* **113**, 159–164 (1985)

# Influence of the Geometric Phase and Non-Adiabatic Couplings on the Dynamics of the $\text{H} + \text{H}_2$ Molecular System

Foudhil Bouakline, Bruno Lepetit, Stuart C. Althorpe,  
and Aron Kuppermann

**Abstract** The effects of the geometric phase and non-adiabatic coupling induced by the conical intersection between the two lowest electronic potential energy surfaces are investigated for the  $\text{H} + \text{H}_2$  collision and  $\text{H}_3$  predissociation. The strongest effect of the geometric phase at all collision energies is a significant change in the ortho  $\rightarrow$  ortho and para  $\rightarrow$  para differential cross-sections, which is due to a sign change in the interference between reactive and non reactive contributions. This is caused by the indistinguishability of the three interacting atoms. At high energies (3.5 eV above collision threshold and more), a significant dynamical effect appears in the differential cross-sections. This effect is related to a sign change in the interference between two dynamical paths (direct and looping contributions) connecting reagents to products. Both these symmetry and dynamical effects almost completely disappear in the integral cross-sections. Electronic non-adiabatic couplings are efficient in turning the bound states supported by the cone of the first excited electronic adiabatic potential into resonances which have significant effects only on transitions between excited reagents and products. The study of the decay of these resonances provides clues for the understanding of the experimental results in the predissociation of Rydberg states of  $\text{H}_3$ .

## 1 General Introduction

The  $\text{H} + \text{H}_2$  molecular system with its isotopic variants has been a benchmark in the development of chemical reaction dynamics in the gas phase [1–29] and continues to serve as a prototype in theoretical as well as experimental advances in this field [30–41]. One particular importance of this system is its well characterized (Jahn–Teller) conical intersection (CI) seam [42–46] connecting the electronic ground-state potential energy surface (PES) to the first excited state surface by a hyperline passing through all the nuclear equilateral triangle geometries. Such topologies (CI) are ubiquitous in polyatomic molecules and play a major role in their spectroscopy, photochemistry and also reactivity [47,48]. At a CI, the Born–Oppenheimer approximation stipulating that electronic and nuclear motions are separable breaks down, giving rise to what we call non-adiabatic chemistry. Molecular systems which

exhibit such topologies can easily hop between electronic states through the funnel of the CI. As a result, the correct description of molecular spectroscopy and dynamics in the presence of a CI requires all non-adiabatic couplings between the conically intersecting PES to be taken into account [47–50].

Another quantum effect resulting from the presence of a CI is the geometric phase (GP) [42, 51] which occurs even if the nuclear motion is confined to the lower electronic state and avoids the neighbourhood of the intersection. The GP is the sign change acquired by the electronic wave function when the nuclei complete an odd number of loops around the CI. Because the total wave function must be single valued, the GP produces a corresponding sign change in the boundary condition of the nuclear wave function [52, 53], which may affect the spectroscopy and the reactivity of the system whenever the nuclear wave function encircles the CI. The impact of non-adiabatic couplings between the degenerate electronic states and the geometric phase on molecular spectra has been observed and is well understood. For instance, it is well-known [54] that the GP shifts the spectrum of a bound state system by altering the pattern of nodes in the nuclear wave function; recent calculations and experiments have reproduced such GP effects in detail [53–58]. However, our understanding of such effects in nonbound systems, especially the GP, have only started to become clear recently, owing to a series of calculations and experiments on the  $\text{H} + \text{H}_2 \rightarrow \text{H}_2 + \text{H}$  exchange reaction [7–41] and also on the predissociation dynamics of the upper cone states of the  $\text{H}_3$  molecular system [37, 59–63].

The first work on the effect of the GP in this system was done by Mead [7], who showed that the GP changes the sign of the interference term between the inelastic and reactive scattering contributions to the fully symmetrized cross sections of the hydrogen-exchange reaction. His prediction was confined to nuclear wave functions which do not encircle the CI when unsymmetrized so that the GP effects can be predicted entirely using symmetry arguments. Later work considered more general GP effects where the unsymmetrized nuclear wave function may encircle the CI. Kuppermann and co-workers [8–12] were the first to perform GP quantum reactive scattering calculations on the hydrogen-exchange reaction and its isotopologues using multivalued basis functions, predicting strong geometric phase effects in state-to-state scattering observables. Subsequent theoretical calculations without the inclusion of the GP revealed excellent agreement with experiment [5, 26–29]. This finding stimulated further theoretical work by Kendrick [13–15], who performed time-independent calculations including the GP using the Mead–Truhlar vector potential approach, where he found that the GP effects were small and only appeared at total energies higher than 1.8 eV above the  $\text{H}_3$  potential minimum. However, an unexpected result was that these effects appear in state-to-state reaction probabilities but completely cancel out on summing over all partial wave contributions to give the corresponding state-to-state integral cross sections (ICS). The GP effects also cancel out on summing over a limited number of partial waves ( $0 \leq J \leq 10$ ) in the low-impact parameter state-to-state differential cross sections (DCS). Subsequent work of Juanes-Marcos et al. [30, 31], using a completely different theoretical approach to solve the nuclear Schrödinger equation via wave packet propagation for total energies below the energetic minimum of the CI seam,

confirmed these results and extended them to higher impact parameters. They found that the fully converged DCS do show small GP effects, which cancel on integrating over all the scattering angles to give the ICS. Recently, Bouakline et al. [39] extended these calculations to total energies up to 4.5 eV above the ground state potential minimum. At total energies above 3.5 eV, many of the state-to-state reaction probabilities show strong GP effects. These effects survive the coherent sum over partial waves to produce features in the state-to-state DCS which could be detected in an experiment with an angular resolution of  $20^\circ$ . However, these effects almost completely cancel out in the ICS, thus continuing a trend observed at lower energies.

In addition to these calculations, Althorpe and co-workers [31, 32] were able to explain these observations using topological arguments, originally introduced by Schulman [64, 65], Laidlaw and De Witt [66] in Feynman path integral treatments of the Aharonov–Bohm effect. Althorpe [32, 34, 35] demonstrated that the nuclear wave function can be split into two components, each of which contains all the Feynman paths that loop in a given sense around the CI. In  $\text{H}+\text{H}_2$ , these components correspond to paths that pass over, respectively, one and two transition states. The interference between these two components governs the extent to which state-to-state scattering attributes are affected by the GP. This topological approach also predicts that the two mechanisms scatter their products into opposite hemispheres, which causes the GP to dephase very efficiently in the state-to-state integral cross sections. We should notice that the GP effects in  $\text{H} + \text{H}_2$  predicted by theory have defeated any experimental measurement, as all the experiments on the hydrogen-exchange reaction were carried out at energies below the energy minimum of the CI seam and only on its isotopic variants.

In parallel to this work on the  $\text{H}+\text{H}_2$  reaction, bound states contained in the upper cone on the first excited PES were investigated. It was shown that it is crucial to include the geometric phase in this calculation to obtain correct bound state energies [67]. These bound states turn into resonances which can predissociate by vibronic couplings when non adiabatic couplings between the upper and lower PES are taken into account. While the GP effect in the hydrogen-exchange reaction still awaits experimental confirmation, strong non-adiabatic effects due to the coupling between the two degenerate electronic states emerged from the experiment of Bruckmeier et al. [59, 68] probing Rydberg emission spectra of  $\text{H}_3$  and its isotopomers. These cone-states generate a broad bimodal structure in UV spectra [68], well reproduced by time dependent wavepacket calculations involving the two coupled electronic states [60, 61]. The vibronic coupling was shown to have a strong effect and to provide quasi bound states with lifetimes of the order of 10 fs.

These strong non-adiabatic effects observed in the cone-states of the upper sheet contrast with the absence of any significant effect in the  $\text{H}+\text{H}_2$  reactive collision. For instance, Mahapatra et al. [69] examined the role of these effects in the  $\text{H} + \text{H}_2$  ( $v=0, j=0$ ) reaction probability for  $J = 0$  and found negligible nonadiabatic coupling effects in the initial state selected probability. Subsequently, Mahapatra and co-workers [70] reported initial state-selected ICS and thermal rate constants of  $\text{H} + \text{H}_2(\text{HD})$  for total energies up to the three body dissociation. Again, they

found nonadiabatic effects to be small for  $\text{H} + \text{H}_2$  and substantial for  $\text{H} + \text{HD}$  in the case of channel specific dynamics, but to cancel in the overall reaction. Similar results on the lack of the contribution of the upper surface to the dynamics were obtained by Ghosal et al. [71] for the  $\text{D} + \text{H}_2(v=0, j=0)$  reaction. Varandas and co-workers [72] examined these effects by looking at state-to-state dynamics of the  $\text{H} + \text{D}_2(v=0, j=0) \rightarrow \text{HD}(v'=3, j') + \text{D}$  for energies below the energy minimum of the CI seam, and found a minor effect of the surface coupling on rotational distributions as well as on initial state-selected total reaction probabilities and ICS. Recent work by Bouakline et al. [39] confirmed these results and extended them to total energies well above the lowest point of the conical intersection seam (up to 4.5 eV), yet the contribution of the excited state to the state-to-state reactive scattering is found to be very small. However, recent work by Mahapatra et al. [73] and Lepetit et al. [37] show that the importance of the non-adiabatic coupling in the dynamics of the  $\text{H}_3$  system strongly depends on the reagent rotation and vibration, suggesting that exciting the reagent promotes such non-adiabatic effects.

In this contribution, we review the implication of the aforementioned GP and non-adiabatic effects in the scattering and predissociation dynamics of the  $\text{H}_3$  system.

## 2 Basic Concepts on Non-Adiabatic and Geometric Phase Effects

Most of our knowledge about molecules, their spectroscopy and reaction dynamics is due to the Born–Oppenheimer approximation, which states that the nuclear and electronic motions are completely decoupled owing to the large ratio of the nuclear mass to the electron mass whereas the forces exerted on them are the same (thus ensuring that the nuclei move much more slowly than the electrons). In other words, the electronic wave functions instantaneously adjust to the slow motion of the nuclei leading to a distortion of the electronic states but not to transitions between them [47–49]. As a result, the nuclear motion proceeds on the potential energy surface of a single electronic state independently of the other electronic states. This adiabatic approximation is based on the assumption that the nuclear kinetic energy is small relative to the energy gap between the electronic state energies, which obviously fails when electronic states are degenerate. In this section, we briefly summarise the origin of the breakdown of the Born–Oppenheimer approximation in the presence of a conical intersection, where two electronic states touch and the degeneracy is lifted to the first order of nuclear motion distortions.

For a general molecular system, the non-relativistic molecular Hamiltonian can be written as:  $\text{H} = \text{T}_n + \text{T}_e + \text{U}(\mathbf{r}, \mathbf{R})$ , where  $\text{T}_n$  and  $\text{T}_e$  are the kinetic energy operator for the nuclei and the electrons respectively, and  $\text{U}(\mathbf{r}, \mathbf{R})$  is the total potential energy operator for the electrons and nuclei.  $\mathbf{r}$  and  $\mathbf{R}$  denote a set of electronic

and nuclear coordinates respectively. We start by solving the electronic Schrödinger equation for clamped nuclear configurations

$$H_e(\mathbf{r}, \mathbf{R})\Phi_i(\mathbf{r}, \mathbf{R}) = V_i(\mathbf{R})\Phi_i(\mathbf{r}, \mathbf{R}), \quad (1)$$

where  $H_e(\mathbf{r}, \mathbf{R}) = T_e + U(\mathbf{r}, \mathbf{R})$ . The electronic eigenvectors  $\Phi_i(\mathbf{r}, \mathbf{R})$  and eigenvalues  $V_i(\mathbf{R})$  (usually called potential energy surfaces) parametrically depend on the nuclear coordinates  $\mathbf{R}$ . To solve the Schrödinger equation for the total molecular Hamiltonian, we expand the total molecular wave function  $\Psi$  in the basis of the electronic eigenfunctions

$$\Psi(\mathbf{r}, \mathbf{R}) = \sum_i \Phi_i(\mathbf{r}, \mathbf{R})\chi_i(\mathbf{R}), \quad (2)$$

where  $\chi_i(\mathbf{R})$  are nuclear wavefunctions. This expansion is exact provided the electronic set  $\Phi_i(\mathbf{r}, \mathbf{R})$  is complete. To get the nuclear wave functions, we substitute the total molecular wave function into the total Schrödinger equation, and after simple manipulations, we get the Schrödinger equation governing the nuclear motion

$$[T_n + V_i(\mathbf{R})]\chi_i(\mathbf{R}) + \sum_j \Lambda_{ij}\chi_j(\mathbf{R}) = E\chi_i(\mathbf{R}), \quad (3)$$

where the matrix elements  $\Lambda_{ij}$  are called non-adiabatic couplings, describing the dynamical interaction between the nuclear and electronic motions. They are given by

$$\Lambda_{ij} = -\frac{1}{2M}[2\mathbf{F}_{ij} \cdot \nabla + G_{ij}], \quad (4)$$

where  $M$  is an averaged nuclear mass and  $\mathbf{F}_{ij}$  and  $G_{ij}$  are given in the bra and ket notation by

$$\begin{aligned} \mathbf{F}_{ij}(\mathbf{R}) &= \langle \Phi_i(\mathbf{r}, \mathbf{R}) | \nabla \Phi_j(\mathbf{r}, \mathbf{R}) \rangle \\ G_{ij}(\mathbf{R}) &= \langle \Phi_i(\mathbf{r}, \mathbf{R}) | \nabla^2 \Phi_j(\mathbf{r}, \mathbf{R}) \rangle, \end{aligned} \quad (5)$$

where the integration is carried out over the electronic coordinates. Neglecting the off-diagonal nonadiabatic couplings  $\Lambda_{ij} (i \neq j)$  and retaining only the diagonal terms  $\Lambda_{ii}$  (called the adiabatic correction) leads to what we know as the adiabatic approximation. In the case of H<sub>3</sub>,  $\Lambda_{ii}$  can be easily calculated with some approximations using normal mode coordinates [74] giving the simple form [69]

$$\Lambda_{ii} = \frac{\hbar^2}{8m_H Q^2}, \quad (6)$$

where  $m_H$  is the mass of the hydrogen nucleus and  $Q$  is the radial coordinate of the degenerate normal mode in the D<sub>3h</sub> point group. It turned out that the inclusion of

this term is essential to correctly describe the dynamics at energies above the energy minimum of the CI seam, as we can see below.

The adiabatic approximation is based on the assumption that the off-diagonal non-adiabatic couplings  $\Lambda_{ij}$  are very small in magnitude compared to the nuclear kinetic energy and the energy separation between the electronic states. However, simple derivation of  $\mathbf{F}_{ij}$  leads to

$$\mathbf{F}_{ij}(\mathbf{R}) = \frac{\langle \Phi_i(\mathbf{r}, \mathbf{R}) | \nabla H_e | \Phi_j(\mathbf{r}, \mathbf{R}) \rangle}{V_i(\mathbf{R}) - V_j(\mathbf{R})}. \quad (7)$$

It is very clear from this expression that if two electronic states get closer in energy, the derivative coupling becomes substantial and the adiabatic approximation for the involved electronic states is expected to break down. Particularly, in the case of a conical intersection of the two PES  $V_i(\mathbf{R})$  and  $V_j(\mathbf{R})$ , the derivative coupling diverges at the intersection point and the adiabatic approximation is meaningless. In this case, to correctly describe the spectroscopy and the dynamics of such molecules, all non-adiabatic couplings must be taken into account.

Another subtle consequence of conical intersections is the geometric phase effect [42, 51], which occurs even when the dynamics is confined to low energies avoiding the neighbourhood of the CI. It is the result of transporting the electronic wave function on a closed loop around the CI. This leads to a sign change in the electronic wave function when it returns to its initial position

$$\Phi_e(\alpha + 2\pi) = -\Phi_e(\alpha), \quad (8)$$

where  $\alpha$  is any internal angular nuclear coordinate describing motion around the CI. Hence, as the total molecular wave function must be single valued, the GP effect also influences nuclear dynamics by, either imposing a corresponding sign change in the nuclear wave function upon completion of a closed loop around the CI [9, 52], or introducing extra terms in the nuclear Hamiltonian if the electronic wave function is multiplied by a complex phase factor [52] to make it single-valued, as we can see below. Furthermore, such a sign change must be taken into account for molecules with two or more identical nuclei to satisfy the correct Bose–Fermi statistics under an interchange of any two identical nuclei [7, 14] even if the nuclear wave function does not dynamically encircle the CI as we will see in Sect. 3.1.

### 3 Theory and Computational Methods

In this section, we give the reader the necessary theoretical and computational ingredients used to compute scattering and predissociation dynamics observables with an emphasis on how to include the GP and non-adiabatic couplings.



### 3.1 *Incorporation of the Geometric Phase*

To satisfy the GP boundary condition, one can proceed through three different ways, each one suitable with the basis and coordinates used to represent the Hamiltonian and the wavefunctions. The first one [8] requires the expansion of the wavefunction in terms of basis functions that themselves satisfy the GP boundary condition. This method is very efficient when using hyperspherical coordinates since they allow an easy inclusion of the full permutation symmetries as well as the correct description of the phase of the nuclear wavefunction in the presence of a conical intersection. However, the double-valued boundary conditions are very difficult to implement in Jacobi coordinates, thus making this method inefficient for the time dependent wave packet propagation approach (usually using Jacobi coordinates) since it will not allow the nuclear wavefunction to be represented in terms of a simple grid. The second method uses the vector potential approach of Mead and Truhlar [52], in which single-valued complex electronic wavefunctions satisfying the GP boundary condition are used, and this introduces an additional vector potential in the nuclear Hamiltonian. This method is very robust numerically and can be implemented in both Jacobi and hyperspherical coordinates. The last method [39, 49, 50] includes both electronic states within the diabatic representation framework, in which the GP is implicitly taken into account through the adiabatic–diabatic mixing angle. Among all these methods, the two diabatic surfaces method is the most exact and numerically robust since it not only includes the GP but also all the non-adiabatic couplings. However, it is numerically more expensive and clearly inefficient if we are dealing with low energies where the system is confined to the lower adiabatic surface and the coupling to the upper surface is not needed. In what follows, we present succinctly the three different approaches mentioned above.

#### 3.1.1 **Boundary Condition Approach**

##### **A. Symmetry Considerations**

Let us consider a pseudo-rotation  $\mathcal{R}$  of the system, which we start for convenience at an acute (principal vertex angle smaller than  $60^\circ$ ) isosceles triangular configuration.  $\mathcal{R}$  is defined to allow the principal vertex atom to move on a circle centered on the vertex of the equilateral triangular configuration and finally to return to its initial position. Application of  $\mathcal{R}$  keeps the rovibronic wavefunction unchanged, but in the GP case, the electronic wavefunction is changed to its opposite and so does the nuclear wavefunction, if we allow these functions to be multivalued. This GP requirement can be implemented simply if an appropriate coordinate system is chosen to parameterize the system. One possible choice is the row orthonormal hyperspherical coordinate system defined in details in [75]. We give here only a brief account and refer the reader to this paper for more details. These coordinates are dependent on the clustering scheme for the three particles, labelled  $\lambda$ . These coordinates consist in three Euler angles  $(a_\lambda, b_\lambda, c_\lambda)$  which rotate a space fixed frame to

a body fixed one attached to the principal axes of inertia of the system  $Gx^{I\lambda}y^{I\lambda}z^{I\lambda}$ , and in three internal coordinates  $(\rho, \theta, \delta_\lambda)$ .  $\rho$  is the hyperspherical radius which describes the global size of the system, whereas  $\theta$  and  $\delta_\lambda$  are two angles which describe the shape of the molecular triangle.  $\theta \in [0, \pi/4]$  is defined such that  $\theta = 0$  corresponds to collinear configurations of the three atoms and  $\theta = \pi/4$  correspond to equilateral triangular configurations.  $\theta$  does not depend on the clustering scheme chosen (i.e. it is a kinematic rotation invariant) whereas  $\delta_\lambda$  is changed by a simple additive constant.  $\delta_\lambda$  is the angle which plays the role of  $\alpha$  in (8).  $\delta_\lambda = 0, \pi/3$  and  $2\pi/3 \pmod{\pi}$  correspond to obtuse isosceles configurations (principal vertex angle larger than  $60^\circ$ ) whereas  $\delta_\lambda = \pi/6, \pi/2$  and  $5\pi/6 \pmod{\pi}$  correspond to acute isosceles configurations. The two sets of coordinates  $(a_\lambda, b_\lambda, c_\lambda, \delta_\lambda)$  and  $(\pi + a_\lambda, \pi - b_\lambda, \pi - c_\lambda, \pi + \delta_\lambda)$  correspond to the same physical configuration with two body frames corresponding to opposite  $x^{I\lambda}$  and  $z^{I\lambda}$  axes. This suggests two possible definitions for the range allowed for  $\delta_\lambda$ . One possibility is to allow  $\delta_\lambda$  to be in the range  $[0, 2\pi]$ , as was first suggested in [76]. If we call  $I_{\mathcal{R}}$  the operation in coordinate space which corresponds to  $\mathcal{R}$ , then:

$$I_{\mathcal{R}} : (a_\lambda, b_\lambda, c_\lambda, \delta_\lambda) \rightarrow (\pi + a_\lambda, \pi - b_\lambda, \pi - c_\lambda, \pi + \delta_\lambda). \quad (9)$$

The presence of the GP is implemented by the condition:  $I_{\mathcal{R}}\chi_{nuc} = -\chi_{nuc}$ .

Another possibility is to restrict the range of  $\delta_\lambda$  to  $[0, \pi]$ , as done in [75]. This provides a one-to-one correspondence between physical configurations and coordinates. In this case, the pseudo-rotation  $I_{\mathcal{R}}$  is the identity operator in the coordinate space. However, the description of the physical pseudo-rotation  $\mathcal{R}$  in coordinate space is more complex. When the system subjected to  $\mathcal{R}$  reaches obtuse isosceles configurations, a discontinuous change of the Euler angles between  $(a_\lambda, b_\lambda, c_\lambda)$  and  $(\pi + a_\lambda, \pi - b_\lambda, \pi - c_\lambda)$  occurs (corresponding to a change in the orientation of the principal axes of inertia between  $Gx^{I\lambda}y^{I\lambda}z^{I\lambda}$  and  $G - x^{I\lambda}y^{I\lambda} - z^{I\lambda}$ , which is also the effect of the inversion operator), as well as a similar discontinuous change of the  $\delta_\lambda$  angle between 0 and  $\pi$ . In this case, the GP condition is implemented by boundary conditions on the nuclear part of the wavefunction:

$$\chi_{nuc}(a_\lambda, b_\lambda, c_\lambda, \rho, \theta, \delta_\lambda = 0) = -\chi_{nuc}(\pi + a_\lambda, \pi - b_\lambda, \pi - c_\lambda, \rho, \theta, \delta_\lambda \rightarrow \pi). \quad (10)$$

We now consider the case of three identical atoms and we show how to compute wavefunctions which are bases for the irreducible representations of the permutation group  $S_3$ . In addition to the identity, this group contains three binary permutations and two cyclic permutations, but all its elements can be generated from the binary permutation  $\hat{\sigma}_1$  of the two atoms different from  $\lambda$  as well as one of the two cyclic permutations  $\hat{C}^+$ .

Table 1 shows the effect of these two operations on the coordinates [77]. If the convention  $\delta_\lambda \in [0, \pi]$  is chosen, then the action of the operations depend on the value of  $\delta_\lambda$ . However, the action of the operations become independent of  $\delta_\lambda$  if

**Table 1** Action of the binary permutation  $\hat{\sigma}_1$  and cyclic one  $\hat{C}^+$ , as well as the  $I_{\mathcal{R}}$  operator which corresponds to a deformation  $\mathcal{R}$  which encircles the conical intersection, on the Euler and  $\delta_\lambda$  angles. Two possible choices for the range of the angle  $\delta_\lambda$  are shown. The one dimensional irreducible representations of the double group associated to  $S_3$  [78] can be used to label the wavefunction in the case  $\delta_\lambda \in [0, 2\pi]$ . If we now choose the convention  $\delta_\lambda \in [0, \pi]$ , the effect of the operations depend on the values of  $\delta_\lambda$ . The wavefunctions are labelled by the irreducible representation to which they belong when extended to  $[0, 2\pi]$

	$\hat{\sigma}_1$	$\hat{C}^+$	$I_{\mathcal{R}}$
$\delta_\lambda \in [0, \pi]$	$[0, \pi]$	$[0, 2\pi/3]$	$[2\pi/3, \pi]$
	$(a_\lambda, b_\lambda, \pi + c_\lambda, \pi - \delta_\lambda)$	$(\pi + a_\lambda, \pi - b_\lambda, \pi - c_\lambda, \pi/3 + \delta_\lambda)$	$(a_\lambda, b_\lambda, c_\lambda, \delta_\lambda - 2\pi/3)$
$A_1$	1	1	1
$A_2$	-1	1	1
$\bar{A}_1$	1	-1	1
$\bar{A}_2$	-1	-1	1
$\delta_\lambda \in [0, 2\pi]$	$[0, 2\pi]$	$[0, 2\pi]$	$[0, 2\pi]$
	$(a_\lambda, b_\lambda, \pi + c_\lambda, \pi - \delta_\lambda \bmod 2\pi)$	$(a_\lambda, b_\lambda, c_\lambda, \delta_\lambda - 2\pi/3 \bmod 2\pi)$	$(a_\lambda, b_\lambda, c_\lambda, \delta_\lambda + \pi \bmod 2\pi)$
$A_1$	1	1	1
$A_2$	-1	1	1
$\bar{A}_1$	1	1	-1
$\bar{A}_2$	-1	1	-1

the extended range  $\delta_\lambda \in [0, 2\pi]$  is chosen. In this case, the pseudo-rotation operation  $I_{\mathcal{R}}$  has to be added to the group and the double group associated to  $S_3$  has to be used. In addition to the usual one dimensional irreducible representations  $A_1$  and  $A_2$  of  $S_3$ , two new one dimensional representations, labelled  $\bar{A}_1$  and  $\bar{A}_2$ , have to be considered, and the effect of the operations on the corresponding wavefunctions is shown on Table 1. Even if the definition domain is restricted to  $\delta_\lambda \in [0, \pi]$ , the irreducible representation labels of the double group can be kept for the wavefunction.

In the case of H<sub>3</sub> (three fermions with 1/2 nuclear spin), the electronuclear wavefunction without nuclear spin part belongs to the  $A_2$  and E irreducible representations of the permutation group of the nuclei for quartet and doublet nuclear spin states respectively. The adiabatic electronic wavefunction subjected to the GP condition belongs to the  $\bar{A}_1$  and  $\bar{A}_2$  irreducible representations of the double group of  $S_3$ , for the ground and first excited electronic states respectively. The nuclear wavefunction without nuclear spin must also belong to irreducible representations of the double group. For instance, an  $\bar{A}_2$  nuclear wavefunction combined with the ground  $\bar{A}_1$  electronic state provides an  $A_2$  electronuclear wavefunctions appropriate for quartet nuclear spins. The symmetry properties of the nuclear wavefunction can be implemented easily in the frame of the hyperspherical formalism, as described now.

## B. Hyperspherical Formalism

The Hamiltonian of the system in this coordinate system reads[75]:

$$H = -\frac{\hbar^2}{2\mu}\rho^{-5}\frac{\partial}{\partial\rho}\rho^5\frac{\partial}{\partial\rho} + \frac{\hat{\Lambda}^2}{2\mu\rho^2} + V(\rho, \theta, \delta_\lambda), \quad (11)$$

where  $\hat{\Lambda}$  is the grand canonical angular momentum,  $\mu$  the 3-body reduced mass of the system, and  $V(\rho, \theta, \delta_\lambda)$  the Born–Oppenheimer electronic potential. We will discuss in Sect. 3.2 the necessary changes to go beyond this single electronic state formalism. The nuclear wavefunction of the system,  $\chi^{\text{JM}\Pi\Gamma}$ , is labeled by the nuclear total angular momentum,  $J$ , its projection onto a space-fixed axis,  $M$ , the parity under inversion through the nuclear center of mass,  $\Pi$  ( $=0$  or  $1$ ), and the irreducible representation  $\Gamma$  of the double group associated to  $S_3$  to which it belongs. It is obtained by expansion on a basis of  $N_s$  surface functions,  $\phi_i^{\text{JM}\Pi\Gamma}$  ( $i = 1, N_s$ ), which are eigenfunctions of the fixed  $\rho$  Hamiltonian,

$$\left( \frac{\hat{\Lambda}^2}{2\mu\rho^2} + V(\rho, \theta, \delta_\lambda) \right) \phi_i^{\text{JM}\Pi\Gamma}(\Omega; \rho) = \epsilon_i^{\text{J}\Pi}(\rho) \phi_i^{\text{JM}\Pi\Gamma}(\Omega; \rho), \quad (12)$$

where  $\Omega$  refers to the set of five angles ( $a_\lambda, b_\lambda, c_\lambda, \theta, \delta_\lambda$ ). The coefficients of this expansion are solutions of a set of coupled ordinary differential equations [79] which provide the desired scattering matrix elements once appropriate boundary conditions are enforced.

Equation (12) is solved by expanding the surface functions on a basis of principal-axes-of-inertia hyperspherical harmonics  $F^{\text{JnLJ}}_{\text{Md}}^{\text{D}}(\Omega)$ . These harmonics [80, 81] are simultaneous eigenfunctions of the square of the nuclear angular momentum operator, its projection on a space fixed axis and the inversion operator, and are labeled by the corresponding quantum numbers  $J$ ,  $M$  and  $\Pi$ . They are also eigenfunctions of the grand canonical angular momentum squared,  $\hat{\Lambda}^2$ , as well as of an internal hyperangular momentum operator,  $\hat{L} = -i\hbar\frac{\partial}{\partial\delta}$ ,

$$\hat{\Lambda}^2 F^{\text{JnLJ}}_{\text{Md}}^{\text{D}}(\Omega) = n(n+4)\hbar^2 F^{\text{JnLJ}}_{\text{Md}}^{\text{D}}(\Omega), \quad (13)$$

$$\hat{L} F^{\text{JnLJ}}_{\text{Md}}^{\text{D}}(\Omega) = L\hbar F^{\text{JnLJ}}_{\text{Md}}^{\text{D}}(\Omega). \quad (14)$$

The quantum numbers  $n, J, L, M$  and  $\Pi$  are all integers and satisfy the following constraints:

$$\begin{aligned} n &\geq 0, & 0 &\leq J \leq n, \\ -J &\leq M \leq J, & -n &\leq L \leq n. \end{aligned} \quad (15)$$

The integer superscript  $D$  gives the number of linearly independent harmonics having the same values of the five quantum numbers, and the integer  $d$  indicates

which of these degenerate harmonics is being considered. The irreducible representation  $\Gamma$  is not an explicit index for the hyperspherical harmonics because the irreducible representation is implicit through appropriate choices for  $n$  and  $L$ . Both  $n$  and  $L$  are integer with the same parity dictated by  $\Pi$  and the existence or not of the GP :  $(-1)^n = (-1)^L = \pm(-1)^\Pi$ , the  $+$  corresponding to the case without the GP and  $-$  to the GP case. Without the GP,  $A_1$  and  $A_2$  are obtained as even (for  $(-1)^\Pi = 1$ ) or odd (for  $(-1)^\Pi = -1$ ) multiples of 3, the situation being reversed in the GP case.

In practice, hyperspherical harmonics are obtained by an expansion over simple trigonometric functions. This procedure has been published in [33] for the four body case, and can be simplified easily for the three body case. In short, the hyperspherical harmonics  $F_{M_d}^{\Pi n L J}(\Omega)$  can be expanded in Wigner rotation matrices. The coefficients of these expansions are homogeneous polynomials of degree  $n$  in  $\cos \theta$  and  $\sin \theta$  [80], which can be transformed to linear combinations of basis functions  $\cos(m\theta)$  and  $\sin(m\theta)$ ,  $m$  being an integer smaller or equal to  $n$ . The appropriate choice of the trigonometric functions is dependent on the internal symmetries [33] of the harmonics. This trigonometric basis provides a mathematically exact and finite expansion for the harmonics. The kinetic energy operator is expressed in matrix form in the product basis of the trigonometric functions and of the Wigner rotation matrices. Since this basis is non orthogonal and has linear dependencies, we use singular value decomposition to generate a smaller orthonormal basis. The expression of the kinetic energy operator in this reduced basis is diagonalized to provide the desired harmonics. Individually, each basis function does not satisfy appropriate boundary conditions at the poles of the kinetic energy operator ; however, the numerically generated linear combination of these functions which constitutes the harmonics does.

Although this formalism is presented here in the context of collisional problems, it is important to notice that it applies equally well to bound state problems [82, 83].

### 3.1.2 Vector Potential Approach

Mead and Truhlar [52] introduced an elegant way of incorporating the geometric phase effect, namely the vector potential approach. In this method, the real electronic wave function  $\Phi(\alpha)$ , where  $\alpha$  is any internal angular coordinate describing the motion around the CI, is multiplied by a complex phase factor  $c(\alpha)$  to ensure the single-valuedness of the new complex electronic wave function:

$$c(\alpha + 2\pi)\Phi(\alpha + 2\pi) = c(\alpha)\Phi(\alpha). \quad (16)$$

A simple choice of the phase factor is given by

$$c(\alpha) = e^{i(l/2)\alpha}, \quad (17)$$

where  $l$  must be odd so that (16) is satisfied. All odd values of  $l$  take into account the GP and give the same physical wavefunction since different wavefunctions corresponding to different values of  $l$  only differ in an overall phase factor. Similarly, all even values give the same physical wave function obeying normal (non-GP) boundary conditions. By analogy with electromagnetic vector potentials, we can say that different odd (or even) values of  $l$  are related by a gauge transformation.

When the complex phase factor takes the form of (2), the Laplacian of the nuclear Hamiltonian is modified according to

$$-\nabla^2 \rightarrow (-i\nabla - \mathbf{A}) \cdot (-i\nabla + \mathbf{A}), \quad (18)$$

where the vector potential  $\mathbf{A}$  is given by

$$\mathbf{A} = -\frac{l}{2}\nabla\alpha. \quad (19)$$

Thus, the vector potential approach yields single-valued nuclear wave functions by adding a vector potential  $\mathbf{A}$  to the nuclear kinetic energy operator, making it very practical to include the GP effect into the wave packet calculation, since one may use the same coordinate system and grid basis functions as in the normal boundary conditions. Besides its easy numerical implementation, this method highlights the analogy of the effect of the GP on a nuclear wave function with the effect of a magnetic solenoid on an encircling electron (which does not overlap the solenoid) called the Aharonov–Bohm (AB) effect [52–54]. Thus, one can apply the results derived from the AB effect to explain the effect of the GP on a nuclear wave function encircling the CI as we will see in the next sections.

It is now straightforward to include the GP in nuclear dynamics calculations by just using (18) and adding the extra terms that result from it to the nuclear Hamiltonian. As in most wave packet calculations on reactive scattering, we employ a Jacobi coordinate system defined by three coordinates ( $R$ ,  $r$  and  $\gamma$ ) where  $R$  is the length of the A-BC molecular axis,  $r$  is the BC bond length and  $\gamma$  is the angle between the intermolecular axis and the BC bond. In this coordinate system, the kinetic energy operator splits into three parts:  $\hat{T} = \hat{T}_R + \hat{T}_r + \hat{T}_{\text{ang}}$ , each containing a derivative term in just one of the Jacobi coordinates ( $R$ ,  $r$ ,  $\gamma$ ) and hence involves just one component of the vector potential,

$$A_x(R, r, \gamma) = -\frac{l}{2} \frac{\partial \alpha(R, r, \gamma)}{\partial x}, \quad (20)$$

where  $x$  denotes, respectively,  $R$ ,  $r$  and  $\gamma$ . Note that the angle  $\alpha$  (describing the motion around the CI) is a function of all three of the coordinates, and so is the vector potential  $\mathbf{A}$ . The first term in  $\hat{T}$  is given by:

$$\hat{T}_R = -\frac{\hbar^2}{2\mu_R} \frac{\partial^2}{\partial R^2}, \quad (21)$$

where  $\mu_R$  is the reduced mass associated with the R coordinate. Application of (18) changes the second derivative operator (with respect to R) according to

$$\begin{aligned} -\frac{\partial^2}{\partial R^2} &\rightarrow \left(-i\frac{\partial}{\partial R} - A_R\right) \left(-i\frac{\partial}{\partial R} - A_R\right) \\ &\rightarrow -\frac{\partial^2}{\partial R^2} + A_R^2 + i\left(\frac{\partial}{\partial R} A_R + A_R \frac{\partial}{\partial R}\right). \end{aligned} \quad (22)$$

This operator is diagonal in all but the R grid basis functions (denoted  $|k\rangle$ ), and its matrix elements change according to

$$\begin{aligned} \langle k|R|k'\rangle &\rightarrow \langle k|R|k'\rangle + \frac{\hbar^2}{2\mu_R} \{ \delta_{kk'} A_R(R_k, r_l, \gamma_m)^2 \\ &\quad + i\langle k|\frac{\partial}{\partial R}|k'\rangle [A_R(R_k, r_l, \gamma_m) + A_R(R_{k'}, r_l, \gamma_m)] \}, \end{aligned} \quad (23)$$

where  $R_k$  denotes the value of R at the kth grid point;  $r_l$  and  $\gamma_m$  are the values of r and  $\gamma$  at the lth and mth grid points respectively. Note that this expression was derived by keeping the operator in the symmetric form of (22), and by acting outwards with the first derivative operators, on the bra and the ket. This approach (as opposed to taking the second derivative of the ket) yields a grid matrix which is exactly hermitian and this is essential for keeping the unitarity of the propagator.

The second term in  $\hat{T}_r$  has exactly the same form as  $\hat{T}_R$  (with r in place of R) and produces an exactly analogous change in the matrix elements between the r-grid basis functions  $|l\rangle$ .

The most complicated changes are those produced in the angular part of the kinetic energy operator ( $\hat{T}_{ang}$ ). This operator can further be split into three terms [84]:

$$\hat{T}_{ang} = \hat{T}_{ang}^{(1)} + \hat{T}_{ang}^{(2)} + \hat{T}_{ang}^{(3)}, \quad (24)$$

which are given by

$$\begin{aligned} \hat{T}_{ang}^{(1)} &= \frac{\hat{\mathbf{J}}^2 - 2\hat{\mathbf{J}}_z^2}{2\mu_R R^2} \\ \hat{T}_{ang}^{(2)} &= \left( \frac{1}{2\mu_R R^2} + \frac{1}{2\mu_r r^2} \right) \hat{\mathbf{J}}^2 \\ \hat{T}_{ang}^{(3)} &= -\frac{\hat{\mathbf{J}} \cdot \hat{\mathbf{j}} + \hat{\mathbf{j}} \cdot \hat{\mathbf{J}}}{2\mu_R R^2}, \end{aligned} \quad (25)$$

where  $\mu_r$  is the reduced mass associated with the r coordinate. The term  $\hat{T}_{ang}^{(1)}$  contains the total angular momentum operators  $\hat{\mathbf{J}}^2$  and  $\hat{J}_z^2$  which do not operate on the internal degrees of freedom, and are thus unchanged by (18). The term  $\hat{T}_{ang}^{(2)}$  contains the BC angular momentum operator, which involves a  $\gamma$ -derivative operator. As a result, (18) will change this operator in a similar way as it did to  $\hat{T}_R$  and  $\hat{T}_r$ . Thus the matrix elements of  $\hat{T}_{ang}^{(2)}$  are diagonal in all but the  $\gamma$ -grid basis functions  $|m\rangle$  and change according to

$$\begin{aligned} \langle m | \hat{T}_{\text{ang}}^{(2)} | m' \rangle &\rightarrow \langle m | \hat{T}_{\text{ang}}^{(2)} | m' \rangle + \hbar^2 \left( \frac{1}{2\mu_R R_k^2} + \frac{1}{2\mu_r r_l^2} \right) \{ \delta_{mm'} A_\gamma(R_k, r_l, \gamma_m)^2 \\ &\quad + i \langle m | \frac{\partial}{\partial \gamma} | m' \rangle [A_\gamma(R_k, r_l, \gamma_m) + A_\gamma(R_k, r_l, \gamma_{m'})] \}. \end{aligned} \quad (26)$$

The operator  $\hat{T}_{\text{ang}}^{(3)}$  contains the cross-terms that give rise to the Coriolis coupling that mixes states with different  $\Omega$  which is the quantum number of the projection of the total angular momentum operator  $\hat{\mathbf{J}}$  on the intermolecular axis. This term contains first derivative operators in  $\gamma$ , and its matrix elements change on application of (18) according to

$$\begin{aligned} \langle mJ\Omega | \hat{T}_{\text{ang}}^{(3)} | m'J'\Omega' \rangle &\rightarrow \langle mJ\Omega | \hat{T}_{\text{ang}}^{(3)} | m'J'\Omega' \rangle + \frac{i\hbar^2}{2\mu_R R_k^2} \times \\ &\quad \times \{ \delta_{\Omega\Omega'+1} C_{J\Omega'}^+ \langle m\Omega | m'\Omega' \rangle A_\gamma(R_k, r_l, \gamma_{m'}) \\ &\quad - \delta_{\Omega'\Omega+1} C_{J\Omega}^+ \langle m\Omega | m'\Omega' \rangle A_\gamma(R_k, r_l, \gamma_m) \}, \end{aligned} \quad (27)$$

where the coefficients  $C_{ab}^\mp$  are given by  $C_{ab}^\mp = \sqrt{a(a+1) - b(b \mp 1)}$ .

To apply the above equations to  $\text{H} + \text{H}_2$ , an expression of the vector potential  $\mathbf{A}(\mathbf{R}, \mathbf{r}, \gamma)$  is needed, this can be obtained from (19) once the angle  $\alpha(\mathbf{R}, \mathbf{r}, \gamma)$  has been specified. As mentioned before, this angle can be chosen in a free way provided that  $\alpha = 0 \rightarrow 2\pi$  describes a closed path around the conical intersection. The angle  $\alpha$  is chosen to be the pseudo-rotation polar angle of the  $D_{3h}$  doubly degenerate normal mode, which is given by [30]:

$$\alpha(\mathbf{R}, \mathbf{r}, \gamma) = \tan^{-1} \left( \frac{d^2 R^2 - r^2/d^2}{2Rr \cos \gamma} \right), \quad (28)$$

$d$  is a dimensionless scaling factor equal to  $\sqrt{2/\sqrt{3}}$  for  $\text{H} + \text{H}_2$ . Notice that the  $\alpha$  used here is related to the angle  $\delta_\lambda$  defined in Sect. 3.1.1 by a simple factor of 2.

### 3.2 Coupled-Surface Calculations

In this section, we describe an approach which, in addition to the implicit inclusion of the GP, takes into account all the non-adiabatic couplings between the two conically intersecting electronic surfaces. In this case, within the adiabatic representation, the nuclear Hamiltonian has the following form:

$$H^{\text{ad}} = T_n \mathbf{1} + \begin{pmatrix} \Lambda_{11} & \Lambda_{12} \\ \Lambda_{21} & \Lambda_{22} \end{pmatrix} + \begin{pmatrix} V_g & 0 \\ 0 & V_{\text{ex}} \end{pmatrix}, \quad (29)$$

where  $V_g$  and  $V_{\text{ex}}$  are the ground and excited adiabatic electronic state potentials,  $T_n$  is the nuclear kinetic energy operator,  $\Lambda_{ij} (i \neq j)$  are the derivative coupling elements between the adiabatic electronic states and  $\Lambda_{ii}$  is the adiabatic correction given by (6). Wave packet propagation in the adiabatic picture is numerically



cumbersome, because the electronic wave functions become discontinuous as the system approaches the CI, thus introducing a singularity in the off-diagonal coupling term. In addition, to account for the geometric phase effect, the GP boundary condition must be enforced on both surfaces.

To overcome these numerical problems, one can convert to an approximately diabatic representation of the wave function via the unitary transformation [85, 86]:

$$H^d = U^\dagger H^{ad} U, \quad (30)$$

where the transformation matrix is given by

$$U = \begin{pmatrix} \cos(\alpha/2) & \sin(\alpha/2) \\ -\sin(\alpha/2) & \cos(\alpha/2) \end{pmatrix}. \quad (31)$$

The adiabatic–diabatic mixing angle  $\alpha$  must be chosen so as to remove the off-diagonal coupling term [50]. It has been demonstrated that, with the diabaticization scheme using the angle  $\alpha$  given by (28), the singular derivative coupling terms are eliminated and the residual derivative couplings become vanishingly small [87]. Thus the kinetic derivative couplings are removed and transformed into smooth potential energy couplings [60, 61] giving rise to the following form of the nuclear Hamiltonian

$$H^d = T_n \begin{pmatrix} 1 & 0 \\ 0 & 1 \end{pmatrix} + \begin{pmatrix} V_{11} & V_{12} \\ V_{21} & V_{22} \end{pmatrix}. \quad (32)$$

The approximation in this quasi-diabatic approach is known to be quite accurate [69], and the diabatic Hamiltonian is much easier to implement in the coupled-surface wave packet propagation. In addition, apart from the inclusion of the off-diagonal couplings, thus allowing hops between the two electronic states, the GP is included exactly through the adiabatic–diabatic mixing angle  $\alpha$  [47]. This quasi-diabatic approach has been used for the H + H<sub>2</sub> scattering dynamics presented in this contribution.

The  $U$  matrix given by (31) is in fact a low order approximation of the true transformation matrix. A higher precision analytical model using double many-body expansion method has been obtained in [88]. More recently, numerical *ab initio* first derivative non adiabatic couplings for the conically intersecting states were obtained by analytic gradient techniques and a fit to these results [45]. This coupling can be decomposed into a longitudinal part (zero curl) and a transverse part (zero divergence). At conical intersection geometry, the longitudinal part is singular, whereas the transverse part is not. The longitudinal part can be expressed as the gradient of a mixing angle between adiabatic states. This mixing angle can be obtained by solving a three dimensional Poisson equation [89]. The resulting adiabatic-to-diabatic transformation eliminates the contribution of the longitudinal part, and minimizes that of the transverse part which cannot be forced to vanish. This refined version

of diabatic potentials and couplings has been used for the predissociation dynamics study presented in the next section.

Symmetry properties of the nuclear wavefunction are different in the diabatic and adiabatic representations. The pair of adiabatic electronic states (see (1)) belong to the  $\bar{A}_1$  and  $\bar{A}_2$  irreducible representations of the double group of  $S_3$ . The diabatic states obtained from the adiabatic ones by applying the  $\mathbf{U}$  matrix form a basis for the two dimensional irreducible representation  $E$  of  $S_3$ . For quartet nuclear spin states, the electronuclear wavefunction, nuclear spin part excluded, must belong to the  $A_2$  irreducible representation. This requires the nuclear wavefunction (without nuclear spin) to be of the same  $E$  symmetry as the electronic one, because of the identity:  $E \times E = A_1 + A_2 + E$ . For doublet spin states, the  $E$  electronuclear wavefunction (nuclear spin excluded) is obtained with an  $A_1$  or  $A_2$  nuclear wavefunction, combined with the  $E$  electronic ones.

We should note that using only the two lowest conically intersecting electronic states in the expansion of the total molecular wavefunction as described above is a very good approximation for the energy range considered here (i.e. below the three body dissociation energy limit). Indeed, the first excited states above the two lowest conically intersecting ones are Rydberg states with  $^2A'_1$  and  $^2A''_2$  symmetries and  $2sa'_1$  and  $2pa''_2$  outer orbitals [63]. The corresponding minima of these potentials, occurring at equilateral triangular geometries, are close to the potential energy minimum of the molecular ion  $H_3^+$ . The energies of these minima are approximately 0.5 and 0.6 eV above the three body dissociation energy limit and the lowest  $H_3$  rovibrational states for the  $2sa'_1$  and  $2pa''_2$  potentials have been detected experimentally at 0.97 and 1.09 eV above this limit [63]. All results presented in this review correspond to energies below the three body dissociation energy limit and thus can safely be obtained with a two electronic state model.

### 3.3 Inelastic and Reactive Quantum Scattering

In this section, we summarise the necessary theoretical ingredients to compute experimental observables in molecular collision events [2, 90]. We assume that the reader is familiar with the concept of scattering wave functions and boundary conditions. To simplify the description, we consider atom-diatom collisions of the type  $A + BC(n) \rightarrow A + BC(n'), AC(n') + B, AB(n') + C$ , where  $n = (\nu, j, k)$  is a collective quantum number describing the vibration( $\nu$ ) and rotation( $j$ ) of the reagent diatom (with  $k$  representing the projection of  $\hat{\mathbf{j}}$  on the initial relative velocity vector of the reactants), and  $n' = (\nu', j', k')$  is similarly defined for the products. The nuclear wave functions describing this molecular system is expanded in terms of the total angular momentum  $\hat{\mathbf{J}}$  eigenfunctions  $D_{kk'}^J(\theta, \eta, \chi)$  [91] where  $(\theta, \eta, \chi)$  are the three Euler angles, and takes the following form [2, 90]:

$$\Psi_n(\mathbf{R}, \mathbf{r}, \gamma; \theta, \eta, \chi | E) = \frac{1}{2k_n R} \sum_{Jk'} (2J+1) D_{kk'}^J(\theta, \eta, \chi) F_{Jnk'}(\mathbf{R}, \mathbf{r}, \gamma | E), \quad (33)$$

where  $E$  is the total energy,  $\hbar k_n$  is the magnitude of the initial (A-BC) approach momentum, and  $(R, r, \gamma)$  are Jacobi coordinates which can be defined in either the reactant or product arrangements.

To calculate any scattering attribute, we must take the asymptotic limit ( $R \rightarrow \infty$ ) of the components  $F_{Jnk'}(R, r, \gamma|E)$  of the nuclear wavefunction [2–66, 69–74, 76, 77, 84–87, 89, 90, 92–94, 104]

$$F_{Jnk'}(R, r, \gamma|E) \rightarrow \sum_{j'v'} \sqrt{\frac{k_{n'}}{k_n}} \Theta_{j'k'}(\gamma) \psi_{v'}(r) e^{ik_{n'}R} S_{n' \leftarrow n}(J, E), \quad (34)$$

where  $\Theta_{j'k'}(\gamma)$  and  $\psi_{v'}(r)$  are the rotational and vibrational wave functions of the product diatomic molecule. The aim of the calculation is thus to find the reactive scattering  $S$  matrix elements ( $S_{n' \leftarrow n}(J, E)$ ), which determine the  $J$  partial wave probability for a molecule to undergo a transition from its initial state ( $n$ ) to its final one ( $n'$ ), given by  $P_{n' \leftarrow n}(J, E) = |S_{n' \leftarrow n}(J, E)|^2$ .

However, this measure of the scattered product at a given value of  $J$  (equivalently, at a fixed classical impact parameter) is not an experimental observable, and therefore one needs to sum up the different contributions of different impact parameters leading to reaction to be able to compare theory to experiment. By coherently summing different  $S$  matrix elements corresponding to different values of  $J$ , one obtains the scattering amplitude given by the expression

$$f_{n' \leftarrow n}(\theta, E) = \frac{1}{2ik_n} \sum_J (2J+1) d_{kk'}^J(\pi - \theta) S_{n' \leftarrow n}(J, E), \quad (35)$$

where  $d_{kk'}^J(\pi - \theta)$  is a reduced Wigner rotation matrix. The scattering amplitude is all what we need to compute experimental scattering observables such as state-to-state DCS and ICS, respectively given by

$$\begin{aligned} \frac{d\sigma'_{n' \leftarrow n}}{d\Omega}(\theta, E) &= \frac{1}{2j+1} |f_{n' \leftarrow n}(\theta, E)|^2 \\ \sigma'_{n' \leftarrow n}(E) &= \frac{2\pi}{2j+1} \int_0^\pi |f_{n' \leftarrow n}(\theta, E)|^2 \sin\theta d\theta, \end{aligned} \quad (36)$$

which measure the amount of the scattered products in the direction  $\theta$  and in the overall space, respectively.

Note that different scattering observables could be obtained whether we use continuity or GP boundary conditions as we will see later. So far, we have treated the atoms as distinguishable particles, and one needs to incorporate the particle exchange symmetry for identical particles (as in the case of  $H + H_2$ ) to get the correct physically measurable cross sections. This can be done by the technique of postantisymmetrization, by which the cross sections are calculated as if the atoms are distinguishable to get the distinguishable atom cross sections which are then properly antisymmetrized to obtain the physical ones. The resulting expressions for the indistinguishable-particle differential cross sections are given by [2, 14].

$$\begin{aligned}
\frac{d\sigma'_{n \leftarrow n}}{d\Omega} &= \frac{1}{2j+1} [|\tilde{f}_{n' \leftarrow n}^N + \tilde{f}_{n' \leftarrow n}^R|^2 + 2|\tilde{f}_{n' \leftarrow n}^R|^2], & \text{for } j \text{ and } j' \text{ odd (i.e., ortho} \rightarrow \text{ortho)} \\
\frac{d\sigma'_{n \leftarrow n}}{d\Omega} &= \frac{1}{2j+1} |\tilde{f}_{n' \leftarrow n}^N - \tilde{f}_{n' \leftarrow n}^R|^2, & \text{for } j \text{ and } j' \text{ even (i.e., para} \rightarrow \text{para)} \\
\frac{d\sigma'_{n \leftarrow n}}{d\Omega} &= \frac{3}{2j+1} |\tilde{f}_{n' \leftarrow n}^R|^2, & \text{for } j \text{ even and } j' \text{ odd (i.e., para} \rightarrow \text{ortho)} \\
\frac{d\sigma'_{n \leftarrow n}}{d\Omega} &= \frac{1}{2j+1} |\tilde{f}_{n' \leftarrow n}^R|^2, & \text{for } j \text{ odd and } j' \text{ even (i.e., ortho} \rightarrow \text{para)}
\end{aligned} \tag{37}$$

where  $\tilde{f}^R$  and  $\tilde{f}^N$  denote the reactive and the nonreactive scattering amplitudes, respectively. The presence or absence of the GP is expected to change the relative sign of  $\tilde{f}_{n' \leftarrow n}^R$  with respect to  $\tilde{f}_{n' \leftarrow n}^N$  [7]. It is clear from (37) that this changes the sign of the interference term between the reactive and nonreactive contributions, and thus may produce different results whether the GP is included or not. Equivalent distinguishable-particle expressions for the ICS can be obtained in the same manner [2, 14].

### 3.4 Predissociation Dynamics

The upper potential sheet has a minimum for equilateral triangular configurations of the nuclei and is known to support bound states when coupling to the lower sheet is neglected [67]. When this coupling is included, these bound states turn into resonances which are expected to be short lived because of the strong electronic non-adiabatic couplings for near equilateral triangular configurations. In fact, these resonances can be viewed from two equivalent points of view. One possibility is to consider them as predissociating vibrational states, another to view them as collisional complexes. In the latter case, their positions and widths can be obtained from the Smith lifetime matrix formalism [95]. If we call  $\mathbf{S}$  the scattering matrix for the  $\text{H}+\text{H}_2$  collision involving all inelastic and reactive open channels, then the lifetime matrix is defined by:  $\mathbf{Q} = -i\hbar\mathbf{S}^\dagger(d\mathbf{S}/dE)$ . In the vicinity of a resonance, one eigenvalue of the  $\mathbf{Q}$  matrix is a Lorentzian function of energy. The energy of its maximum is the resonance energy and the value of the maximum provides the resonance lifetime. The corresponding eigenvector at resonance energy provides the product state distribution of the resonance decay.

## 4 Applications

In this section, we report the implication of the aforementioned effects, namely the geometric phase and non-adiabatic couplings between the two lowest coupled electronic surfaces, in the  $\text{H}+\text{H}_2$  exchange reaction as well as in the predissociation dynamics of  $\text{H}_3$  Rydberg states.

## 4.1 The Hydrogen-Exchange Reaction

Here we investigate the effect of the GP and non-adiabatic effects on state-to-state scattering attributes of the reaction  $\text{H}_\text{A} + \text{H}_\text{B}\text{H}_\text{C} \rightarrow \text{H}_\text{A} + \text{H}_\text{B}\text{H}_\text{C}, \text{H}_\text{A}\text{H}_\text{C} + \text{H}_\text{B}, \text{H}_\text{A}\text{H}_\text{B} + \text{H}_\text{C}$ . To compute state-to-state reaction probabilities, DCS and ICS, we solve the time-dependent Schrödinger equation using Jacobi coordinates. To overcome the coordinate problem relevant to reactive scattering (that is the AC+B arrangement being difficult to represent in A+BC coordinates and vice versa), we use the reactant-product decoupling (RPD) [96] method in its further refined partitioned form [97–101]. This method will allow us to decouple the nuclear dynamics Schrödinger equation into separate reactant, strong-interaction and product regions, permitting different coordinates to be used in each region and using absorbing and reflecting potentials to transform between reagent and product Jacobi coordinates. In the single-surface calculations, we used the BKMP2 ground state potential energy surface of Boothroyd et al. [44], and in the diabatic coupled-surface calculations we used the same surface for the ground electronic state and the DMBE potential energy surface [16] for the excited electronic state. A small correction term was added to the DMBE surface to ensure that the vertices of the upper and lower cones touched at every point along the CI seam.

The parameters used in our calculations on the hydrogen-exchange reaction can be found in ([39]). Different tests were carried out to ensure the convergence of the results with respect to these different parameters. The calculations were repeated for all partial waves in the range  $J = 0 - 55$  to yield state-to-state cross sections converged to 5% over the whole energy range.

### 4.1.1 Effect of the Adiabatic Correction on State-to-State Scattering Observables

Before exploring the effects of the geometric phase and of the off-diagonal non-adiabatic couplings on the  $\text{H} + \text{H}_2$  exchange-reaction, we first investigate the importance of the diagonal non-Born–Oppenheimer correction  $\Lambda_{ii}$  given by (6) (which is usually ignored in single-surface calculations) on the reaction dynamics. To gauge this effect, single-surface non-GP calculations were performed by including and excluding this term.

Figures 1 and 2 illustrate this effect on state-to-state reaction probabilities and DCS respectively. It is clear from both figures that the inclusion of  $\Lambda_{ii}$  has no effect on the dynamics for total energies below about 2.3 eV, where the wave packet has insufficient energy to approach the conical intersection and experience the adiabatic correction which has the form of a spike centered around the CI. However, at energies above these, the inclusion of the correction term makes a significant contribution to the dynamics as can be seen from Fig. 1. The inclusion of  $\Lambda_{ii}$  not only changes the probabilities, but even experimental scattering observables such as the DCS as illustrated by Fig. 2, in which the adiabatic correction tends to reduce the rotational temperature of the  $\text{H}_2$  products, and the amount of sideways scattering

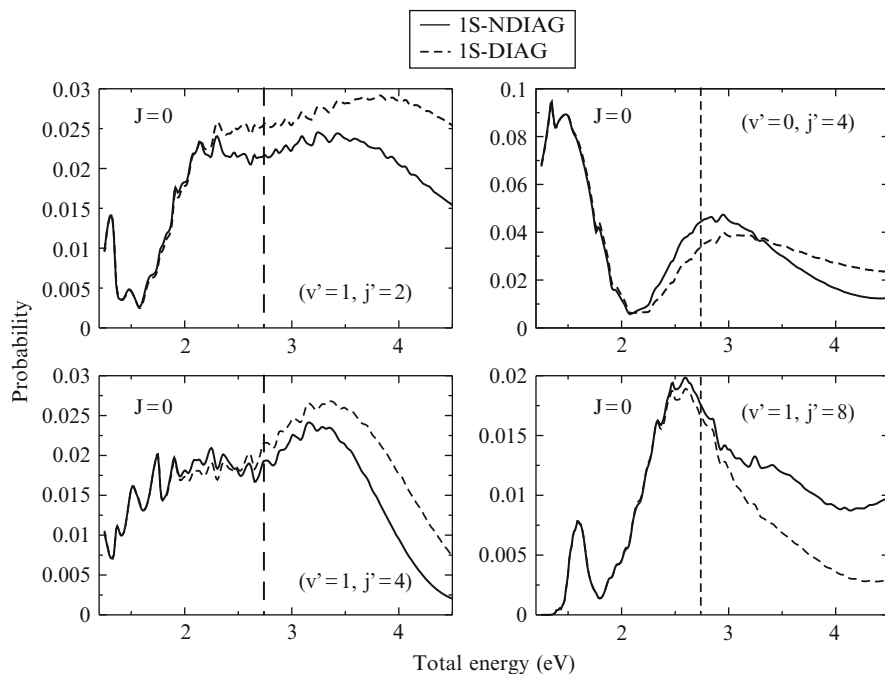


**Fig. 1**  $\text{H} + \text{H}_2(v = 0, j = 0) \rightarrow \text{H}_2(v', j') + \text{H}$  state-to-state non-GP reaction probabilities computed without (1S-NDIAG) and with (1S-DIAG) the inclusion of the diagonal non-Born–Oppenheimer term using the lower adiabatic PES. The *dashed vertical line* indicates the energetic minimum of the CI seam. Reprinted with permission from [39]. Copyright (2008) by the American Institute of Physics

in favour of forward and backward scattering. Comparable effects were observed for most of the state-to-state reaction probabilities and DCS. Clearly, it is essential to include the diagonal non-Born–Oppenheimer correction when computing scattering observables of the hydrogen exchange-reaction in single-surface calculations at energies above about 2.3 eV. So, in the remainder of the results on reactivity, this correction is included either explicitly when using the adiabatic single-surface calculations (for both GP and non-GP calculations) or implicitly in the diabatic coupled-surface picture.

#### 4.1.2 Low Energy Regime: Particle-Exchange Symmetry Geometric Phase Effect

To distinguish the effect of the geometric phase from that of non-adiabatic population transfer between the two coupled electronic surfaces on the reactivity of the  $\text{H} + \text{H}_2$  system, we first confine the dynamics to the electronic ground state by exploring total energies below 1.8 eV (far below the energy minimum of the CI seam occurring at 2.74 eV), where it is well known that non-adiabatic off-diagonal

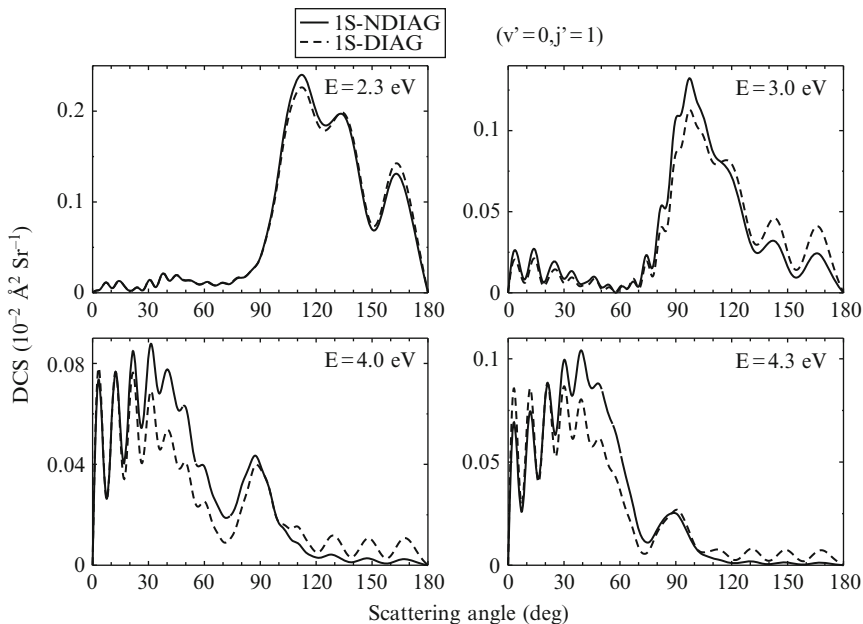


**Fig. 2**  $\text{H} + \text{H}_2(v = 0, j = 0) \rightarrow \text{H}_2(v', j') + \text{H}$  state-to-state non-GP DCS for four different total energies computed without (1S-NDIAG) and with (1S-DIAG) the inclusion of the diagonal non-Born–Oppenheimer term using the lower adiabatic PES. Reprinted with permission from [39]. Copyright (2008) by the American Institute of Physics

elements vanish. Three sets of calculations, ignoring the GP effect and including it explicitly (by artificially changing the sign of the reactive S matrix) and implicitly with the vector potential approach, were performed. Distinguishable-particle scattering amplitudes were obtained and then antisymmetrized to obtain the physical cross sections to be compared to the experimental ones.

Figure 3 illustrates the effect of the geometric phase on Pauli-antisymmetrized DCS for para–para transitions. From this figure, we notice that the results obtained by including the GP either implicitly or explicitly are indistinguishable. This suggests that, at these low energies, the sole effect of the GP is a change in the sign of the reactive scattering matrix elements and of the associated scattering amplitudes leaving the absolute value of their real and imaginary parts unchanged. As a result, the DCS obtained by ignoring the GP are exactly the same as those including this effect for para–ortho and ortho–para transitions (so are the corresponding ICS), because only the reactive part of the wave function contributes to these transitions, the inelastic part being zero by symmetry [2] (see (37)). However, for para–para (and ortho–ortho) transitions, the inclusion of the GP induces significant changes in the DCS as can be seen in Fig. 3 showing some para–para transitions, where the two curves including and excluding the GP exhibit pronounced oscillations which are out of phase with each other. A maximum in one curve corresponds to a minimum in another and vice versa. This out of phase behaviour in the DCS is a trivial result of

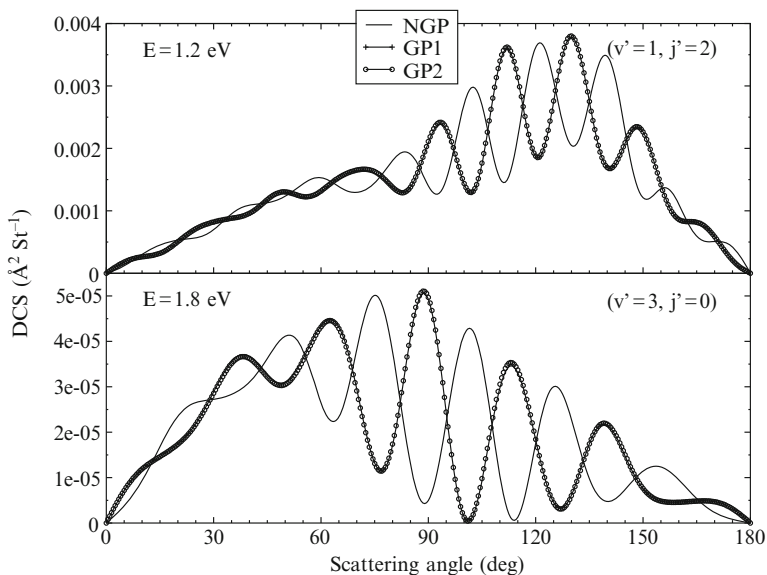


**Fig. 3**  $\text{H} + \text{H}_2(v = 0, j = 0) \rightarrow \text{H}_2(v', j') + \text{H}$  para–para state-to-state Pauli-antisymmetrized DCS for two different total energies computed by excluding (NGP) and including the geometric phase explicitly (GP1), by artificially changing the sign of the reactive scattering amplitude, and implicitly (GP2) with the vector potential approach

the interference between the reactive and nonreactive scattering amplitudes as the GP solely changes the sign of this interference term as (37) suggests. The integration of this interference term over the scattering angle vanishes, which is why the GP effect cancels out in the integral cross section as shown in Fig. 4. Indeed, these oscillations come from the crossed term  $2\text{Re}(f_{n, \leftarrow n}^{\text{N}} f_{n, \leftarrow n}^{\text{R}})$  which adds to or subtracts from the other contributions to the DCS according to the presence or absence of the GP. This term is a sufficiently fast function of the scattering angle to provide a negligible contribution after integration. To summarise, the inclusion of the GP resulting from particle-exchange symmetry of identical nuclei in  $\text{H}_3$ , at energies far below the energetic minimum of the CI, only introduces a sign change in the scattering amplitude reactive part, thus leaving para–ortho (and also ortho–para) transitions DCS unchanged, and inducing a phase shift in the oscillations of the DCS for para–para (and ortho–ortho) transitions when compared with those computed with normal boundary conditions.

#### 4.1.3 High Energy Regime: Geometric Phase and Non-Adiabatic Couplings Effects

When the total energy increases and reaches the intersection region of the CI, the resulting GP effect is more complicated as the wave packet may encircle the CI [7]. In the remaining parts of this section, we focus the study on reactive scattering



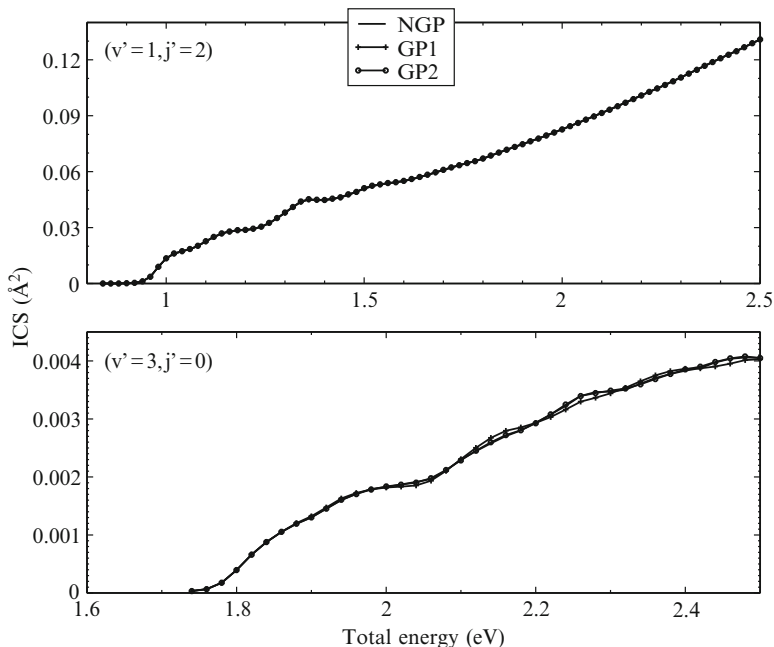


**Fig. 4**  $\text{H} + \text{H}_2(v = 0, j = 0) \rightarrow \text{H}_2(v', j') + \text{H}$  state-to-state Pauli-antisymmetrized ICS computed by excluding (NGP) and including the geometric phase explicitly (GP1), by artificially changing the sign of the reactive scattering amplitude, and implicitly (GP2) with the vector potential approach

and investigate the high energy regime in which the GP effect due to encircling wave functions may become significant. To distinguish this later effect from the one produced by symmetry, we ignore cyclic permutation symmetry of the nuclei whose effect was studied before, and thus only para–ortho and ortho–para scattering observables correspond to the experimentally measurable ones. In addition to the GP, we investigate all non-adiabatic effects since at these energies the coupling to the upper sheet of the potential energy surface must be included in the calculations.

### A. State-to-State Reaction Probabilities and ICS

We compare state-to-state reaction probabilities and ICS obtained by three sets of calculations, two of them using the ground electronic state PES in which the GP is either included (1S-GP) or excluded (1S-NGP), and the last one includes all of the nonadiabatic effects using the two coupled diabatic surfaces (2S-DIABATIC).

The extent to which state-to-state reaction probabilities are affected by the GP and the off-diagonal couplings can be gauged from Fig. 5, in which the three calculations for  $\text{H} + \text{H}_2(v = 0, j = 0) \rightarrow \text{H}_2(v' = 2, j = 1) + \text{H}$  are compared. This figure shows that the result of one surface including the GP reproduces almost

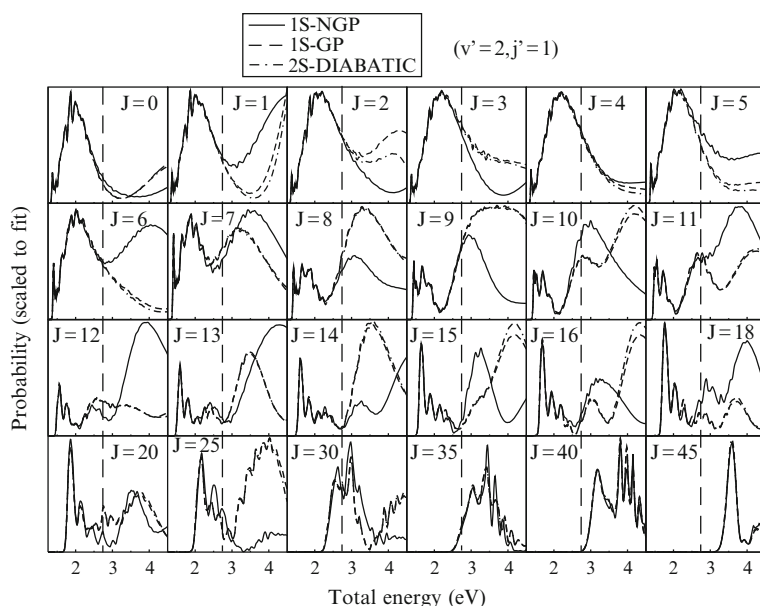


**Fig. 5**  $\text{H} + \text{H}_2(v = 0, j = 0) \rightarrow \text{H}_2(v' = 2, j' = 1) + \text{H}$  state-to-state reaction probabilities computed using the lower adiabatic PES including the diagonal non-Born–Oppenheimer term without (1S-NGP) and with (1S-GP) the GP, and using the coupled diabatic surfaces (2S-DIABATIC). The dashed vertical line indicates the energetic minimum of the CI seam. Reprinted with permission from [39]. Copyright (2008) by the American Institute of Physics

exactly the coupled-surface result, that is the contribution of the upper surface to the state-to-state reaction probabilities for the specified initial rovibrational state of the reactant is very small, and may be neglected to a good approximation. Hence, the large effects shown in this figure which appear at high energies are caused mainly by the geometric phase, which are very strong especially for energies above 3.5 eV. The same effects were observed for almost all the final rovibrational states of the products [39].

However, upon summing up the different probabilities over  $J$  to obtain the integral cross sections, all the GP effects almost completely cancel out as shown in Figs. 6 and 7 even at high energies, thus continuing a trend observed in the earlier work of Kendrick [13–15] and Juanes-Marcos et al. [30, 31]. Some of the state-to-state ICS do retain small GP effects (e.g. the  $v' = 0$  ICS at 4.3 eV), but these effects are much smaller than the GP effects in the corresponding state-to-state reaction probabilities. The origin of this cancellation will be discussed further in Sect. 5.

## B. State-to-State Differential Cross Sections

Now, we examine whether the strong GP effects present in many of the state-to-state reaction probabilities survive the coherent sum over partial waves to appear in the

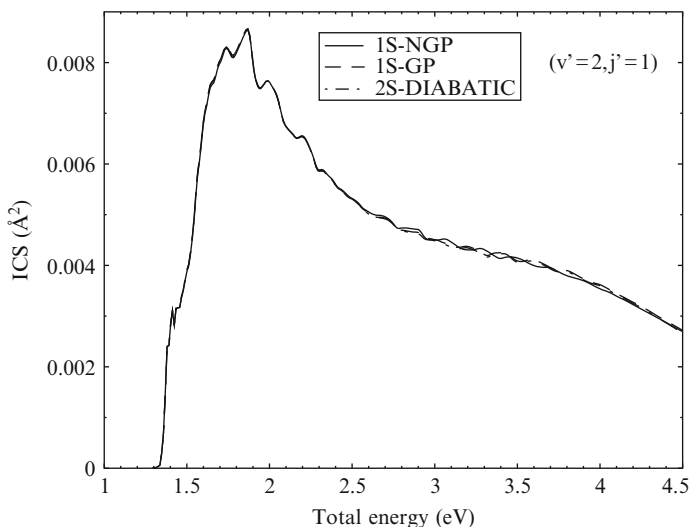


**Fig. 6**  $\text{H} + \text{H}_2(v = 0, j = 0) \rightarrow \text{H}_2(v' = 2, j' = 1) + \text{H}$  state-to-state ICS computed using the lower adiabatic PES including the diagonal non-Born–Oppenheimer term without (1S-NGP) and with (1S-GP) the GP, and using the coupled diabatic surfaces (2S-DIABATIC)

state-to-state DCS. The effect of the GP on the DCS corresponding to the probabilities in Fig. 5 is shown in Fig. 8. At energies below 3.5 eV, the GP slightly shifted the phase of the rapidly oscillating part of the DCS at high impact parameters, as we can see in the forward part of the DCS at a total energy of 2.3 eV. However, at energies above 3.5 eV, we find that the much stronger GP effects in the individual partial waves survive as large GP effects in the corresponding DCS. This is illustrated in Fig. 8 for a total energy of 4.3 eV where the inclusion of the GP splits the broad single peak centred around  $80^\circ$  into a double peak producing a shift of  $15^\circ$  in the DCS, thus requiring relatively low resolution to measure it experimentally. Comparable strong GP effects are found in most of the other state-to-state DCS [39].

## 4.2 Predissociation Dynamics of Rydberg States of $\text{H}_3$

Figure 9 compares transitions probabilities for zero total angular momentum  $J$  resulting from (2S-DIABATIC) and (1S-GP) calculations with initial and final states chosen to be representative of two cases : (A) initial and/or final states have low rovibrational excitation, (B) initial and final states have both high rovibrational excitation. In case (A), both (2S-DIABATIC) and (1S-GP) results almost coincide, even for energies close to the three body dissociation limit. Case (A) corresponds to the kind of transitions already considered in Sect. 4.1 where it was shown that it is valid to use the single rovibrational wavefunction associated to the ground electronic state

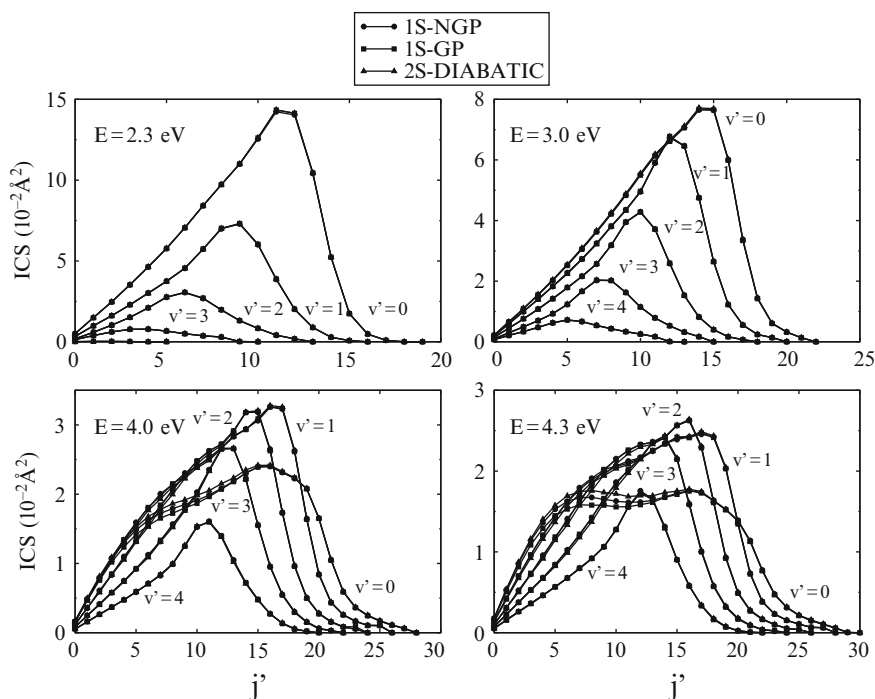


**Fig. 7** Product ro-vibration distributions for  $\text{H}+\text{H}_2(v=0, j=0)$  for different total energies computed using the lower adiabatic PES including the diagonal non-Born–Oppenheimer term without (1S-NGP) and with (1S-GP) the GP, and using the coupled diabatic surfaces (2S-DIABATIC). Reprinted with permission from [39]. Copyright (2008) by the American Institute of Physics

even for energies well above the one of the conical intersection minimum. However, in case (B), broad resonance profiles appear on the (2S-DIABATIC) results that are not present on the (1S-GP) ones. In this case, for energies near and above 4 eV, the presence of the excited adiabatic potential significantly influences the reaction dynamics and must be included in the calculation.

The main difference between (2S-DIABATIC) and (1S-GP) results is the appearance of broad Fano profiles on the (2S-DIABATIC) transition probabilities, which suggests that the upper adiabatic PES can support resonances which do not exist in the single ground adiabatic surface calculation. This can be investigated further with the lifetime matrix formalism described in Sect. 3.4. Smith lifetime matrices for the (2S-DIABATIC) case differ from the (1S-GP) ones only by the appearance of Lorentzian-shape eigenvalues near and above 4 eV.

These extra eigenvalues are shown as a function of energy for both  $A_1$  and  $A_2$  symmetries of the rovibronic wavefunction in Fig. 10. There are two maxima near 4.41 and 4.62 eV for  $A_1$  symmetry, 4.49 and 4.70 eV for  $A_2$  symmetry. They correspond to resonances with lifetimes close to 15 fs for  $A_1$  symmetry and 10 fs for  $A_2$  symmetry. Resonances with similar lifetimes have been computed in [60, 61] and detected experimentally in [68]. The energies of the bound rovibrational states

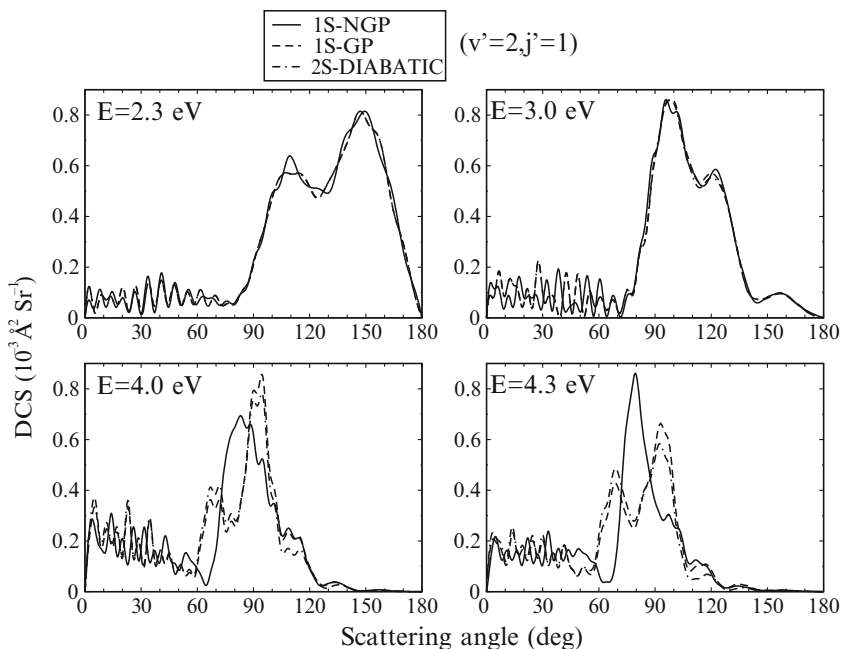


**Fig. 8**  $\text{H} + \text{H}_2(v = 0, j = 0) \rightarrow \text{H}_2(v' = 2, j' = 1) + \text{H}$  state-to-state DCS for four different total energies computed using the lower adiabatic PES including the diagonal non-Born–Oppenheimer term without (1S-NGP) and with (1S-GP) the GP, and using the coupled diabatic surfaces (2S-DIABATIC)

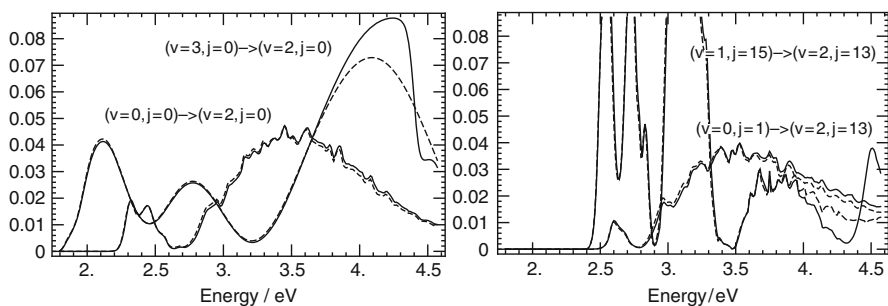


**Fig. 9**  $J = 0$  transition probabilities for  $A_1$  (left) and  $A_2$  (right) symmetries of the rovibronic wavefunction. The particular transitions chosen are representative examples of two cases: (a): the initial and/or final states have low vibrational excitation, (b): the initial and final states both have significant vibrational excitation. Case (A) transitions are:  $\text{H} + \text{H}_2(v = 0, j = 0) \rightarrow \text{H} + \text{H}_2(v = 2, j = 0)$  for  $A_1$  symmetry and:  $\text{H} + \text{H}_2(v = 0, j = 1) \rightarrow \text{H} + \text{H}_2(v = 2, j = 13)$  for  $A_2$  symmetry. Case (B) transitions are:  $\text{H} + \text{H}_2(v = 3, j = 0) \rightarrow \text{H} + \text{H}_2(v = 2, j = 0)$  for  $A_1$  symmetry and:  $\text{H} + \text{H}_2(v = 1, j = 15) \rightarrow \text{H} + \text{H}_2(v = 2, j = 13)$  for  $A_2$  symmetry. Continuous and dashed lines correspond to results obtained with two coupled diabatic (2S-Diabatic) and one single adiabatic (1S-GP) electronic states respectively

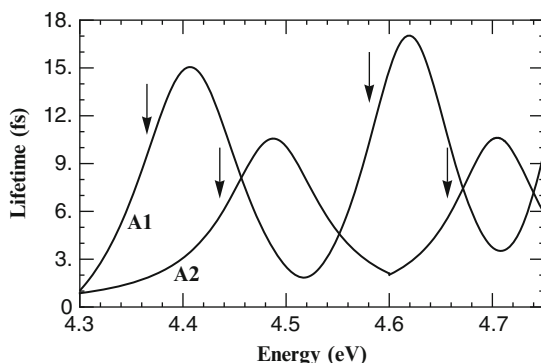


**Fig. 10** Smith lifetimes for  $A_1$  and  $A_2$  rovibronic wavefunctions. The vertical arrows indicate the energies of the bound states on the upper electronic potential energy surface, with adiabatic corrections

associated to the excited adiabatic electronic potential (and including the diagonal adiabatic correction) are also shown on Fig. 10 as vertical arrows. There is a clear correlation between bound and resonant state energies which allows us to interpret the scattering resonances as bound rovibrational states on the excited electronic potential coupled to the continuum by electronic non-adiabatic couplings.

These resonances can be classified using the quantum numbers  $v_1$  for the hyper-radial motion and  $v_2^l$  for the two dimensional bending motion [67].  $l$  is the vibrational angular momentum such that  $(v_2 - l)/2$  is the number of nodes of the wavefunction along  $\theta$ . Both  $v_2$  and  $l$  are half integers and integers in the cases with and without GP respectively. The pairs of resonances appearing on Figs. 9 and 10 correspond to  $v_2 = 1 = 3/2$  and  $v_1 = 0$  and 1. The vibrational angular momentum plays a crucial role for the lifetime of the resonance. Indeed, it provides an effective centrifugal potential which expels the wavefunction away from the equilateral triangular configuration region  $\theta = \pi/4$  [82]. It prevents the nuclear wavefunction from being exposed to the large non-adiabatic electronic couplings in this region which even diverge for  $\theta = \pi/4$ . The stability of the resonances is thus expected to increase with  $l$ . This was checked by comparing the lifetimes of the resonances extracted from a calculation performed for the E irreducible representation with the ones performed for  $A_1$  and  $A_2$ . Resonances for the E symmetry correspond to  $v_2 = 1 = 1/2$  [67] and were found to have lifetimes shorter than the ones for  $A_1$  and  $A_2$  ( $l = 1/2$ ) and limited to a few femtoseconds only, as expected. This vibrational stabilization mechanism is a particular case of Slonczewski resonances [102].

Figure 11 shows the product state distributions after decay of the  $A_1$  and  $A_2$  resonances at 4.41 and 4.49 eV respectively. In both cases,  $H + H_2$  decay products have significant internal energy : for the  $A_1$  symmetry, 41% of the available energy appears as rovibrational energy, and 51% for the  $A_2$  case. Thus, these resonances decay exclusively into excited rovibrational states and were not observed on previously computed reactive scattering transitions probabilities and cross-sections

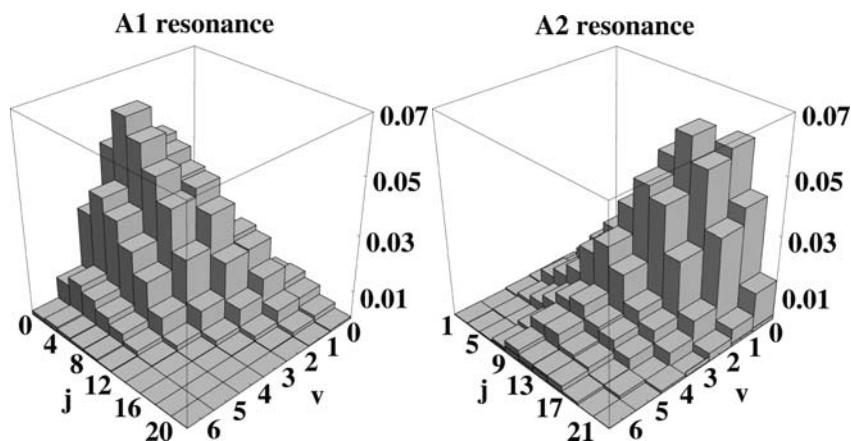


**Fig. 11** Population of the different  $\text{H}+\text{H}_2(v, j)$  channels in the decay of the  $A_1$  and  $A_2$  resonances at 4.41 and 4.49 eV respectively

[60, 61, 70] which were performed for low excitation either of the reactants or of the products. In our reaction probabilities, these resonances display significant intensities only for transitions between simultaneously excited reactants and products.

Internal energy partitioning between vibration and rotation is very different for  $A_1$  and  $A_2$  symmetries : 18% of the internal energy goes into rotation for the  $A_1$  symmetry, in contrast with 50% for the  $A_2$  symmetry. This reflects itself in the product state distributions of Fig. 11, which have a maximum for low rotational quantum number  $j$  in the  $A_1$  symmetry, but for  $j$  near 15 for the  $A_2$  case.

Interpretation of these results requires the knowledge of the nodal structure of the vibrational wavefunction which is strongly influenced by the presence of the geometric phase. For the case without GP,  $A_1$  vibrational wavefunctions have no nodal surface prescribed by nuclear permutation symmetry, whereas  $A_2$  vibrational wavefunctions have nodal surfaces imposed by nuclear permutation symmetry for both acute (principal vertex angle smaller than  $60^\circ$ ) and obtuse isosceles configurations. For the GP case,  $\bar{A}_1$  ( $\bar{A}_2$ ) vibrational wavefunctions have nodal planes for obtuse (acute) isosceles configurations and maxima for acute (obtuse) configurations, respectively [37, 58]. Loosely speaking,  $\bar{A}_1$  and  $\bar{A}_2$  vibrational wavefunctions therefore have dominant acute and obtuse isosceles characters, respectively. For near acute isosceles configurations, the decay mechanism is an abstraction one, in which one atom departs from the two others without providing significant rotational excitation.  $\bar{A}_1$  resonances thus decay into products with little rotational excitation, in agreement with the result of Fig. 11. On the contrary, for  $\bar{A}_2$  obtuse isosceles vibrational wavefunctions, the decay mechanism is an insertion one, where the atom initially close to the principal vertex of the isosceles triangle is pushed towards the two others. This motion provides a bending excitation of the triatom, which turns into rotational energy as the system departs from isosceles configurations,

which correspond to an electronic potential crest and a saddle point for collinear geometries. Consequently, fragments arising from  $A_2$  resonances have significant rotational excitation, as shown in Fig. 11. The strong differences in product state distributions are therefore the direct consequence of the nodal structure imposed on the vibrational wavefunction by the GP. A similar nodal structure analysis is used in [58] to explain the impact of the geometric phase on the cyclic- $N_3$  vibrational spectra.

## 5 Topological Interpretation of the Geometric Phase Effect in the Dynamics of $H_3$

From the results shown above, it is clear that the GP effect on the  $H + H_2$  reaction at low energies (below 1.8 eV) is only observable for para–para and ortho–ortho transitions due to symmetry considerations. The GP introduces a sign change in the reactive scattering amplitude [7], thus changing the sign of the interference term between the reactive and nonreactive parts of the total nuclear wavefunction. This is the origin of the phase shift observed in the oscillations of the DCS computed with and without the inclusion of the GP. The highly oscillatory behaviour of the interference term as a function of the scattering angle is the reason for an almost complete cancellation of the GP in the ICS. Analysing the GP effects at high energies for para–ortho and ortho–para transitions is a different task, since the wave function only involves a reactive part, the nonreactive one being zero by symmetry.

In this section, to explain the observed results in this later energy regime, we summarise a topological approach originally introduced by Schulman [64, 65, 104], and Laidlaw and De Witt [66] in Feynman path integral treatments of the Aharonov–Bohm effect, in which an electron encircles a magnetic solenoid but does not overlap with it, thus acquiring a geometric phase. They showed that the electronic wave function can be split into two components, each of which contains all the Feynman paths that loop in a given sense around the solenoid. Althorpe and co-workers [31, 32, 34] demonstrated that the nuclear wave function encircling the CI can be split, in a similar way, into two components, the even and odd looping ones. In  $H+H_2$ , they correspond to paths that pass over, respectively, one (1-TS) and two (2-TS) transition states, as shown in Fig. 12.

The approach is extremely simple to apply, since the non-GP and GP scattering amplitudes are given by:

$$\begin{aligned} f_N(\theta) &= \frac{1}{\sqrt{2}}[f_{1-TS}(\theta) + f_{2-TS}(\theta)] \\ f_G(\theta) &= \frac{1}{\sqrt{2}}[f_{1-TS}(\theta) - f_{2-TS}(\theta)] \end{aligned} \quad (38)$$



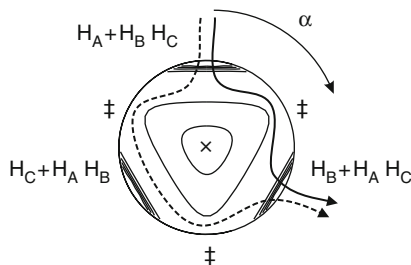


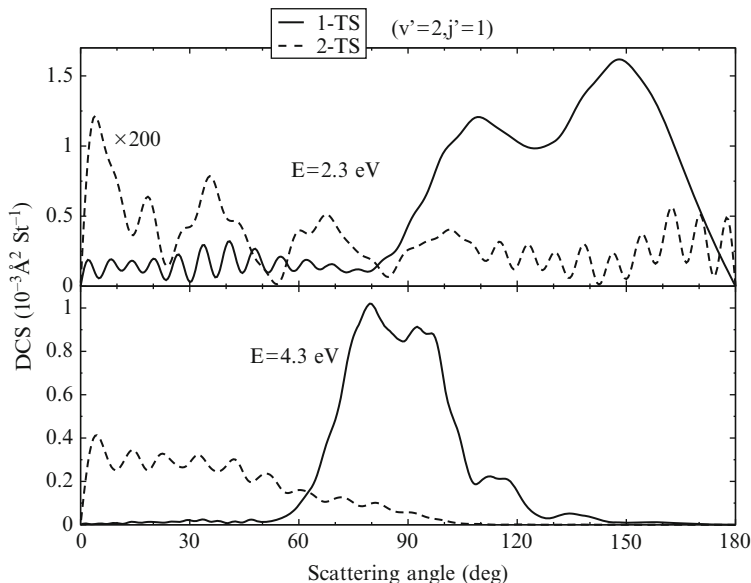
**Fig. 12** Schematic representation of the 1-TS (solid) and 2-TS (dashed) reaction paths in the reaction  $H_A + H_B H_C \rightarrow H_A H_C + H_B$ . The  $H_3$  potential energy surface is represented using the hyperspherical coordinate system of Kuppermann [103] for a fixed value of the hyper-radius  $\rho$ , in which the equilateral-triangle geometry of the CI is in the centre ( $\times$ ) and the linear transition states ( $\ddagger$ ) are on the perimeter of the circle. The angle  $\alpha$  is the internal angular coordinate which describes motion around the CI

Hence the 1-TS and 2-TS contributions to the amplitudes can be obtained from

$$\begin{aligned} f_{1-TS}(\theta) &= \frac{1}{\sqrt{2}}[f_N(\theta) + f_G(\theta)] \\ f_{2-TS}(\theta) &= \frac{1}{\sqrt{2}}[f_N(\theta) - f_G(\theta)] \end{aligned} \quad (39)$$

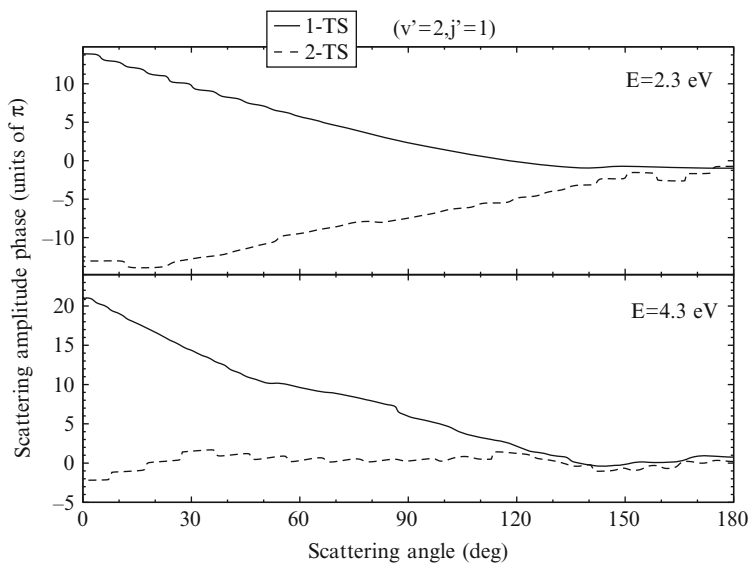
This approach is rigorous, provided the 1-TS paths cannot be continuously deformed into 2-TS paths. (In the language of topology, the 1-TS and 2-TS paths are then different ‘homotopes’). At energies below about 2.5 eV, this criterion is satisfied because there is an energetically inaccessible region of space surrounding the CI seam. This region acts as an obstacle when one tries to deform a 1-TS path into a 2-TS path. (In the language of topology, this region makes the space occupied by the nuclear wave function ‘multiply connected’.) At first sight, this condition would appear to relax at energies above the CI seam (2.74 eV) since the wave packet has enough energy to access points along the CI seam, and hence there is no obstacle to discriminate between the 1-TS and 2-TS paths. However, we recently showed that the topological approach originally developed for dynamics confined to the lower surface can be easily applied to a coupled-surface system, with no essential modifications [105]. Thus, the topological approach described by (38–39) is justified for the whole range of energies.

Figure 13 shows the resulting direct and looping DCS for ( $v' = 2, j' = 1$ ) at two different total energies (2.3 and 4.3 eV), which were obtained by substituting  $f_{1-TS}(\theta)$  and  $f_{2-TS}(\theta)$  into the standard formula of the DCS given by (36). At the lower of the two energies, the 1-TS products scatter mainly in the backward hemisphere and the 2-TS products scatter mainly in the forward hemisphere; also, the 2-TS contribution is negligible at this energy (for clarity, the 2-TS DCS shown on the figure is 200 times the computed one). As a result, the interference between the direct and looping scattering amplitudes is very small and thus no appreciable difference between the GP and non-GP is observed. However, at higher energies, the amount of the products traversing 1-TS and 2-TS are of the same order of magnitude



**Fig. 13**  $\text{H} + \text{H}_2(v = 0, j = 0) \rightarrow \text{H}_2(v' = 2, j' = 1) + \text{H}$  state-to-state DCS for two different total energies obtained by extracting direct (1-TS) and looping (2-TS) contributions to the GP and non-GP scattering amplitudes. For clarity, the 2-TS DCS are shown multiplied by a factor of 200 for an energy of 2.3 eV

and their scattering amplitudes do interfere. This is clearly shown in Fig. 13 for a total energy of 4.3 eV, where the two direct and looping scattering amplitudes considerably interfere for sideways-approach geometries thus leading to significant differences between the GP and non-GP DCS as we can see in Fig. 8. The topological approach developed above can also be used to explain why the GP effects cancel out in the ICS. To do so, we plot in Fig. 14 the phases of the 1-TS and 2-TS scattering amplitudes corresponding to the DCS of Fig. 13 as a function of the scattering angle  $\theta$ . At a total energy of 2.3 eV, the slopes of these phases depend in opposite senses on  $\theta$ . From semiclassical scattering theory [94, 106], this implies that the 1-TS and 2-TS paths scatter their products with opposite spatial angular momentum, into positive (nearside) and negative (farside) deflection angles respectively. As discussed in [30, 31, 34], this tendency is observed for most final states at these lower energies, including those states for which noticeable GP effects appear in the DCS. As a result, the interference term  $[f_{1\text{-TS}}(\theta) * f_{2\text{-TS}}(\theta)]$  between the two scattering mechanisms is highly oscillatory, integrates over  $\theta$  to a very small value, and thus cancels in the ICS any GP effects that did survive in the DCS. At higher energies, as for 4.3 eV given in Fig. 14, the slopes of the 1-TS and 2-TS phases no longer have opposite dependencies on  $\theta$ . However, the phase dependencies are still sufficiently different to give efficient cancellation of the GP effects at these energies. This cancellation is not as efficient as at lower energies, and there are some



**Fig. 14** Phases of  $\text{H} + \text{H}_2(v = 0, j = 0) \rightarrow \text{H}_2(v' = 2, j' = 1, \Omega' = 0) + \text{H}$  direct (1-TS) and looping (2-TS) scattering amplitudes

final states in which a very small residual GP effect remains in the ICS, as can be seen in the  $v' = 0$  integral cross sections at 4.3 eV (Fig. 7).

## 6 Conclusions and Perspectives

In this contribution, we investigated the effects of the geometric phase and non-adiabatic couplings between the two lowest conically intersecting potential energy surfaces of the  $\text{H} + \text{H}_2$  system on state-to-state reactive and inelastic scattering as well as on predissociation of the quasibound states of the upper cone. These studies showed that non-adiabatic effects (including the GP) play a significant role in the dynamics of this system. Neglecting these effects will sometimes lead to incompatible results with experimentally measurable observables, especially at high energies.

As for state-to-state reactive scattering, the first conclusion concerns the diagonal adiabatic correction, yet ignored in almost all quantum dynamics calculations, where its inclusion makes an important contribution to the dynamics by changing significantly state-to-state probabilities and also differential cross sections at high energies (above about 3 eV). These energies are well above the lowest point on the conical intersection seam, yet the contribution of the excited state to the state-to-state reactive scattering is found to be very small. In fact, we obtain accurate predictions of the state-to-state reaction probabilities and cross sections employing

just the ground state surface, with inclusion of the diagonal non-Born–Oppenheimer correction and the geometric phase GP. These results extend the earlier results of Mahapatra et al. [69, 70] who found a similar lack of participation of the excited state in the initial state-selected reaction probabilities and integral cross sections. This result should be taken carefully as it only concerns the case where the reactant  $\text{H}_2$  is initially in low excited states. For transitions involving excitation of both reagents and products, we have shown that the resonances associated to the excited PES play a significant role in the dynamics and should be included. On the other hand, even for the reagent in low excited states, the geometric phase effect is found to be very significant. At low energies, the GP effect is clearly observable for para–para (and correspondingly ortho–ortho) transitions, a consequence of a cyclic permutation symmetry of the nuclei leading to a sign change in the interference of the reactive and nonreactive parts of the nuclear wave function. For these transitions, inclusion of the GP produces out of phase oscillations in the DCS with respect to those computed with normal boundary conditions. However, the GP effects for para–ortho and ortho–para transitions on the DCS are too limited to be confirmed experimentally, and this is due to the lack of the encirclement of the CI at these low energies. At high energies (above 3.5 eV), GP effects are strong on state-to-state reaction probabilities, and these effects survive in many state-to-state differential cross sections. A low angular experimental resolution (about  $20^\circ$ ) would be sufficient to observe them. However, for the whole energy range, the GP effects cancel almost completely in the state-to-state ICS, owing to efficient dephasing when integrating over  $\theta$ . Thus, state-to-state rates can be computed reliably on the ground state Born–Oppenheimer surface, with the complete neglect of all non-adiabatic terms except for the diagonal non-Born–Oppenheimer correction term.

The study of the predissociation mechanism of the resonances supported by the first excited electronic potential opens the way for a theoretical interpretation of the ongoing experiments on the predissociation of Rydberg states of  $\text{H}_3$  [62, 63]. For the predissociation from the  $2s, ^2A'_1$  state in its ground bending mode, most of the available energy is equally shared by two of the three atoms. This corresponds to three lobes with maxima for obtuse isosceles configurations on the Dalitz plots of [62, 63]. Configurations with equal sharing of the energy between the three atoms have a low probability of occurrence which gives a minimum at the center of the Dalitz plot. The situation is opposite for predissociation from the  $2p, ^2A''_2$  state in its ground bending mode : equal sharing of energy between the three atoms now has a high occurrence probability (maximum at the center of the Dalitz plots [62, 63]). Configurations where one atom carries most of the energy also have a high probability of occurrence and produce secondary lobes with maxima for acute isosceles configurations on the Dalitz plots. These systematic effects do not depend on the choice of the symmetric stretch excitation of the predissociating state and they are equally valid for hydrogen and deuterium. A theoretical analysis [37] has shown that the symmetry of the different electronic states and in particular the geometric phase plays a crucial role in the interpretation of these experimental data. The different computational methods described in the present paper could be used to obtain quantitative agreement with experimental data.

In addition to the investigation of the influence of the GP on the reactivity of the  $\text{H} + \text{H}_2$  system, a topological approach developed by one of the authors [32] to explain this effect was presented. This approach used a simple topological argument to extract reaction paths with different senses from a nuclear wave function that encircles a conical intersection. In the  $\text{H} + \text{H}_2$  system, these senses correspond to paths that cross one or two transition states, and their interference dictates the importance of the GP in state-to-state probabilities and DCS. These two sets of paths scatter their products into different regions of space, which causes an almost complete cancellation of the geometric phase effect in the ICS. The analysis should generalize to other direct reactions and estimate the likely magnitude of GP effects by modeling the dynamics of the even- and odd-looping reaction paths around the CI using classical trajectories methods [107–110].

**Acknowledgements** F.B. and S.C.A. acknowledge a grant from the U.K. Engineering and Physical Sciences Research Council, B.L. acknowledges an allocation of computer time at the IDRIS computer center and A.K. a grant from the US National Science Foundation.

## References

1. F. London, *Z. Elektrochem.* **35** 552 (1929)
2. G.C. Schatz, A. Kuppermann, *J. Chem. Phys.* **65** 4642 and 4668 (1976)
3. D.G. Truhlar, R.E. Wyatt, *Ann. Rev. Phys. Chem.* **27** 1 (1976)
4. G.C. Schatz, *Ann. Rev. Phys. Chem.* **39** 317 (1988)
5. F. Fernández-Alonso R.N. Zare, *Annu. Rev. Phys. Chem.* **53** 67 (2002)
6. F.J. Aoiz, V.J. Herrero, V. Sáez Rábanos, *J. Chem. Phys.* **94** 7991 (1991)
7. C.A. Mead, *J. Chem. Phys.* **72** 3839 (1980)
8. B. Lepetit, A. Kuppermann, *Chem. Phys. Lett.* **166** 581 (1990)
9. Y.M. Wu, A. Kuppermann, B. Lepetit, *Chem. Phys. Lett.* **186** 319 (1991)
10. A. Kuppermann, Y.-S.M. Wu, *Chem. Phys. Lett.* **205** 577 (1993)
11. A. Kuppermann, Y.-S.M. Wu, *Chem. Phys. Lett.* **241** 229 (1995)
12. A. Kuppermann, Y.-S.M. Wu, *Chem. Phys. Lett.* **349** 537 (2001)
13. B.K. Kendrick, *J. Chem. Phys.* **112** 5679 (2000)
14. B.K. Kendrick, *J. Phys. Chem. A* **107** 6739 (2003)
15. B.K. Kendrick, *J. Chem. Phys.* **118** 10502 (2003)
16. A.J.C. Varandas, L.P. Viegas, *Chem. Phys. Lett.* **367** 625 (2003)
17. J.C. Juanes-Marcos, S.C. Althorpe, *Chem. Phys. Lett.* **381** 743 (2003)
18. J.C. Juanes-Marcos, S.C. Althorpe, *Faraday Discuss.* **127** 115 (2004)
19. R.-F. Lu, T.-S. Chu, Y. Zhang, K.-L. Han, A.J.C. Varandas, J.Z.H. Zhang, *J. Chem. Phys.* **125** 133108 (2006)
20. K. Koszinowski, N.T. Goldberg, A.E. Pomerantz, R.N. Zare, J.C. Juanes-Marcos, S.C. Althorpe, *J. Chem. Phys.* **123** 054306 (2005)
21. A.E. Pomerantz, F. Ausfelder, R.N. Zare, S.C. Althorpe, F.J. Aoiz, L. Bañares, J.F. Castillo, *J. Chem. Phys.* **120** 3244 (2004)
22. F. Ausfelder, A.E. Pomerantz, R.N. Zare, S.C. Althorpe, F.J. Aoiz, L. Bañares, J.F. Castillo, *J. Chem. Phys.* **120** 3255 (2004)
23. S.C. Althorpe, F. Fernández-Alonso, B.D. Bean, J.D. Ayers, A.E. Pomerantz, R.N. Zare, E. Wrede, *Nature (London)* **416** 67 (2002)
24. S.A. Harich, D. Dai, C.C. Wang, X. Yang, S.D. Chao, R.T. Skodje, *Nature (London)* **419** 281 (2002)

25. D. Dai, C.C. Wang, S.A. Harich, X. Wang, X. Yang, S.D. Chao, R.T. Skodje, *Science* **300** 1730 (2003)
26. F. Fernández-Alonso, B.D. Bean, R.N. Zare, F.J. Aoiz, L. Baares, J.F. Castillo, *J. Chem. Phys.* **115** 4534 (2001)
27. E. Wrede, L. Schnieder, K.H. Welge, F.J. Aoiz, L. Bañares, J.F. Castillo, B. Martínez-Haya, V.J. Herrero, *J. Chem. Phys.* **110** 9971 (1999)
28. E. Wrede, L. Schnieder, *J. Chem. Phys.* **107** 786 (1997)
29. E. Wrede, L. Schnieder, K.H. Welge, F.J. Aoiz, L. Bañares, V.J. Herrero, *Chem. Phys. Lett.* **265** 129 (1997)
30. J.C. Juanes-Marcos, S.C. Althorpe, *J. Chem. Phys.* **122** 204324 (2005)
31. J.C. Juanes-Marcos, S.C. Althorpe, E. Wrede, *Science* **309** 1227 (2005)
32. S.C. Althorpe, *J. Chem. Phys.* **124** 084105 (2006)
33. B. Lepetit, D. Wang, A. Kuppermann, *J. Chem. Phys.* **125** 133505 (2006)
34. J.C. Juanes-Marcos, S.C. Althorpe, E. Wrede, *J. Chem. Phys.* **126** 044317 (2007)
35. S.C. Althorpe, J.C. Juanes-Marcos, E. Wrede, *Adv. Chem. Phys.* **138** 1-42 (2008)
36. K. Koszinowski, N.T. Goldberg, J. Zhang, R.N. Zare, F. Bouakline, S.C. Althorpe, *J. Chem. Phys.* **127** 124315 (2007)
37. B. Lepetit, R. Abrol, A. Kuppermann, *Phys. Rev. A* **76** 040702(R) (2007)
38. J.C. Juanes-Marcos, A.J. Varandas, S.C. Althorpe, *J. Chem. Phys.* **128** 211101 (2008)
39. F. Bouakline, S.C. Althorpe, D. Peláez Ruiz, *J. Chem. Phys.* **128** 124322 (2008)
40. S.J. Greaves, E. Wrede, N.T. Goldberg, J. Zhang, D.J. Miller, R.N. Zare, *Nature* **454** 91 (2008)
41. N.T. Goldberg, J. Zhang, K. Koszinowski, F. Bouakline, S.C. Althorpe, R.N. Zare, *Proc. Natl. Acad. Sci. U.S.A.* **105** 18194 (2008)
42. G. Herzberg, H.C. Longuet-Higgins, *Discuss. Faraday Soc.* **35** 77 (1963)
43. A.J.C. Varandas, F.B. Brown, C.A. Mead, D.G. Truhlar, N.C. Blais, *J. Chem. Phys.* **86** 6258 (1987)
44. A.I. Boothroyd, W.J. Keogh, P.G. Martin, M.R. Peterson, *J. Chem. Phys.* **104** 7139 (1996)
45. R. Abrol, A. Shaw, A. Kuppermann, D.R. Yarkony, *J. Chem. Phys.* **115** 4640 (2002)
46. C.R. Evenhuis, X. Lin, D.H. Zhang, D. Yarkony, M.A. Collins, *J. Chem. Phys.* **123** 134110 (2005)
47. A. Kuppermann, in *Dynamics of Molecules and Chemical Reactions*, ed. by R.E. Wyatt, J.Z.H. Zhang (Dekker, New York, 1996), pp 411-472
48. *Conical Intersections: Electronic Structure, Dynamics and Spectroscopy*, ed. by W. Domcke, D.R. Yarkony, H. Köppel (World Scientific, River Edge, NJ, 2003)
49. G.A. Worth, L.S. Cederbaum, *Annu. Rev. Phys. Chem.* **55** 127 (2004)
50. A. Kuppermann, R. Abrol, in *The Role of Degenerate States in Chemistry*, *Adv. Chem. Phys.* **124**, ed. by M. Baer, G.D. Billing (Wiley, New York, 2002), pp 283-322
51. M.V. Berry, *Proc. R. Soc. London Ser. A* **392** 45 (1984)
52. C.A. Mead, D.G. Truhlar, *J. Chem. Phys.* **70** 2284 (1979)
53. C.A. Mead, *Rev. Mod. Phys.* **64** 51 (1992)
54. M.S. Child, *Adv. Chem. Phys.* **124** 1 (2002)
55. B.K. Kendrick, *Phys. Rev. Lett.* **79** 2431 (1997)
56. H. von Busch, V. Dev, H.-A. Eckel, S. Kasahara, J. Wang, W. Demtröder, P. Sebald, W. Meyer, *Phys. Rev. Lett.* **81** 4584 (1998)
57. B.E. Applegate, T.A. Barckholtz, T.A. Miller, *Chem. Soc. Rev.* **32** 38 (2003)
58. D. Babikov, B.K. Kendrick, P. Zhang, K. Morokuma, *J. Chem. Phys.* **122** 044315 (2005)
59. R. Bruckmeier, Ch. Wunderlich, H. Figger, *Phys. Rev. Lett.* **72** 2550 (1994)
60. S. Mahapatra, H. Köppel, *J. Chem. Phys.* **109** 1721 (1998)
61. S. Mahapatra, H. Köppel, *Phys. Rev. Lett.* **81** 3116 (1998)
62. C. Laperle, J. Mann, T. Clemens, R. Continetti, *Phys. Rev. Lett.* **93** 153202 (2004)
63. U. Galster, F. Baumgartner, U. Müller, H. Helm, M. Jungen, *Phys. Rev. A* **72** 062506 (2005)
64. L.S. Schulman, *Techniques and Applications of Path Integration* (Wiley, New York, 1981)
65. L.S. Schulman, *Phys. Rev.* **176** 1558 (1968)
66. M.G.G. Laidlaw, C.M. De Witt, *Phys. Rev. D* **3** 1375 (1971)
67. B. Lepetit, Z. Peng, A. Kuppermann, *Chem. Phys. Lett.* **166** 572 (1990)

68. D. Azinovic, R. Bruckmeier, Ch. Wunderlich, H. Figger, G. Theodorakopoulos, I. Petsalakis, 69. S. Mahapatra, H. Köppel, L.S. Cederbaum, *J. Phys. Chem. A* **105** 2321 (2001)
70. B. Jayachander Rao, R. Padmanaban, S. Mahapatra *Chem. Phys.* **333** 135 (2007)
71. S. Ghosal, B. Jayachander Rao, S. Mahapatra, *J. Chem. Sci.* **119** 401 (2007)
72. R.-F. Lu, T.-S. Chu, Y. Zhang, K.-L. Han, A.J.C. Varandas, J.Z.H. Zhang, *J. Chem. Phys.* **125** 133108 (2006)
73. B. Jayachander Rao, S. Mahapatra, *Indian J. Phys.* **81** 1003 (2007)
74. T.C. Thompson, G. Izmirlian, Jr., S.J. Lemon, D.G. Truhlar, C.A. Mead, *J. Chem. Phys.* **82** 5597 (1985)
75. A. Kuppermann, *J. Phys. Chem.* **100** 2621 (1996)
76. R.T. Pack, G.A. Parker, *J. Chem. Phys.* **87** 3888 (1987)
77. F. Karlický, B. Lepetit, R. Kalus, I. Paidarová, F.X. Gadéa, *J. Chem. Phys.* **128** 124303 (2008)
78. M. Hamermesh, *Group Theory and its Application to Physical Problems* (Addison-Wesley, Reading, MA, 1962)
79. A. Kuppermann, *Isr. J. Chem.* **43** 229 (2003)
80. D. Wang, A. Kuppermann, *J. Phys. Chem. A* **107** 7290 (2003)
81. A. Kuppermann, *J. Phys. Chem. A* **110** 809 (2006)
82. F. Karlický, B. Lepetit, R. Kalus, F.X. Gadéa, *J. Chem. Phys.* **126** 174305 (2007)
83. L. Velilla, B. Lepetit, A. Aguado, J.A. Beswick, M. Paniagua, *J. Chem. Phys.* **129** 084307 (2008)
84. J. Tennyson, B.T. Sutcliffe, *J. Chem. Phys.* **77** 4061 (1982)
85. C.A. Mead, D.G. Truhlar, *J. Chem. Phys.* **77** 6090 (1982)
86. H. Köppel, *Faraday Discuss.* **127** 35 (2004)
87. A. Thiel, H. Köppel, *J. Chem. Phys.* **110** 9371 (1999)
88. A.J.C. Varandas, F.B. Brown, C.A. Mead, D.G. Truhlar, N.C. Blais, *J. Chem. Phys.* **86** 6258 (1987)
89. R. Abrol, A. Kuppermann, *J. Chem. Phys.* **116** 1035 (2005)
90. S.C. Althorpe, D.C. Clary, *Annu. Rev. Phys. Chem.* **54** 493 (2003)
91. R.N. Zare, *Angular Momentum* (Wiley, New York, 1988)
92. W.H. Miller, *J. Chem. Phys.* **50** 407 (1969)
93. D. Neuhauser, M. Baer, R.S. Judson, D.J. Kouri, *J. Chem. Phys.* **90** 5882 (1989)
94. M.S. Child, *Molecular Collision Theory* (Dover, New York, 1996)
95. F.T. Smith, *Phys. Rev.* **118** 349 (1960)
96. T. Peng, J.Z.H. Zhang, *J. Chem. Phys.* **105** 6072 (1996)
97. S.C. Althorpe, D.J. Kouri, D.K. Hoffman, *J. Chem. Phys.* **107** 7816 (1997)
98. S.C. Althorpe, *J. Chem. Phys.* **114** 1601 (2001)
99. S.C. Althorpe, *J. Chem. Phys.* **117** 4623 (2002)
100. S.C. Althorpe, *J. Chem. Phys.* **121** 1175 (2004)
101. S.C. Althorpe, *Int. Rev. Phys. Chem.* **121** 1175 (2004)
102. J.C. Slonczewski, *Phys. Rev.* **131** 1596 (1963)
103. A. Kuppermann, *Chem. Phys. Lett.* **32** 374 (1975)
104. L. S. Schulman, *J. Math. Phys.* **12**, 304 (1971)
105. S.C. Althorpe, T. Stecher, F. Bouakline, *J. Chem. Phys.* **129** 214117 (2008)
106. A.J. Dobbyn, P. McCabe, J.N.L. Connor, J.F. Castillo, *Phys. Chem. Chem. Phys.* **1** 1115 (1999) *Phys. Rev. A* **58** 1115 (1998)
107. D.G. Truhlar, J.T. Muckerman, in *Atom-Molecule Collision Theory*, ed. by R.B. Bernstein (Plenum, New York, 1979)
108. F.J. Aoiz, V.J. Herrero, V. Sáez Rábanos, *J. Chem. Phys.* **94** 7991 (1991)
109. L. Bonnet, J.-C. Rayez, *Chem. Phys. Lett.* **277** 183 (1997)
110. L. Bonnet, J.-C. Rayez, *Chem. Phys. Lett.* **397** 106 (2004)

# Multi-Mode Jahn–Teller and Pseudo-Jahn–Teller Effects in Benzenoid Cations

Shirin Faraji, Etienne Gindensperger, and Horst Köppel

**Abstract** The multi-state multi-mode vibronic interactions in the benzene radical cation and some of its fluorinated derivatives are surveyed from a theoretical point of view. While the parent system is a prototypical example for the multi-mode dynamical Jahn–Teller effect, partial fluorination leads to a reduction of symmetry and a ‘disappearance’ of the Jahn–Teller effect. Nevertheless, strong vibronic interactions prevail also there and lead to marked effects in the spectral intensity distributions and to an ultrafast electronic population dynamics. These phenomena have been analyzed theoretically in our group by means of a well-established vibronic coupling scheme, combined with an *ab initio* quantum dynamical approach (namely, *ab initio* coupled cluster calculations for the underlying potential energy surfaces and coupling constants, and the so-called MCTDH wavepacket propagation technique for the nuclear motion). The results are presented and discussed, putting emphasis on their dependence on the respective system, especially the degree of fluorination. They shed new light on the substitutional effects on vibronic interactions and demonstrate the degree of sophistication that can be achieved nowadays in their theoretical treatment.

## 1 Introduction and Historical Background

The Jahn–Teller (JT) effect [1–3] and vibronic interactions [4–8] are among the key factors governing excited-state dynamics in molecular systems. An important aspect is the reduction in symmetry [3,6,9] occurring through the coupling between the different potential energy surfaces. Historically, this was in fact the main perspective of the theorem of Jahn and Teller [1,3,5], which provided a mechanism for structural instabilities of molecules and solids, through the incompatibility of spatial degeneracy of the electronic wavefunction and stationarity of the associated potential energy surfaces (except for accidental degeneracy and linear molecules). This field is still actively explored in many current investigations as is testified by several other articles in the present volume. Another important aspect, more in the focus of the present article, is the nonadiabatic nature of the nuclear motion near degeneracies of potential energy surfaces [7, 10–15], such as occur by virtue of symmetry in



the JT case. Especially through the seminal work of Longuet-Higgins et al. [16–18], the degeneracy was recognized to require a coupled-surface treatment of the nuclear motion, thus taking nonadiabatic interactions into account on an equal footing with the vibrational motion. Coupled-surface dynamics was indeed studied in numerous papers on different JT systems from various viewpoints later on (see for example [19–28] and references therein). In addition to the degeneracy itself, the existence of linear coupling terms as implied by the JT theorem leads to a double-cone shape of the JT split potential energy surfaces near the point of symmetry-induced degeneracy, as soon as several JT active degrees of freedom are considered. From a more modern perspective, this makes the JT intersections a special case of conical intersections [6, 7, 10–15, 17]. Conical intersections have now emerged as paradigms for nonadiabatic excited-state dynamics [5–7, 10, 12–15], and are considered responsible for a wide range of phenomena in areas like spectroscopy, reactive scattering, photophysics and photochemistry.

Apart from systematic studies and individual examples, it is of considerable interest to have available a set of related molecules which can serve as a means to vary one or several system parameters and thus establish their impact on the vibronic interactions in general and on the nonadiabatic coupling effects in particular. One such class of systems has proven to be the radical cations of the five-membered heterocycles furan, pyrrole and thiophene [29]. Here, the variation of the first two vertical ionization potentials (more precisely, their difference) in the series provides a parameter to change the energetic location of the conical intersection of the corresponding potential energy surfaces (PES). This tunes the energy range where strong nonadiabatic coupling effects occur, which nicely shows up in their respective photoelectron spectra [29].

Another useful class of systems in this context is provided by benzene, its radical cation and their halo derivatives. They represent a prototype family of molecules for the multi-mode dynamical JT effect and associated vibronic interactions [30–42]. The relevant molecular point groups are  $D_{6h}$  for the unsubstituted or ‘parent’ systems and  $D_{3h}$  for the 1,3,5 symmetrically substituted derivatives, like halobenzenes or halobenzene cations [41–63]. This makes these systems representatives of the  $E \otimes e$  dynamical JT effect [1, 5, 14], where a doubly degenerate electronic state (E) interacts with doubly degenerate (e) vibrational modes. In addition, pseudo-Jahn–Teller (PJT) [5, 14, 34, 64–67] interactions with nearby nondegenerate states come into play which immediately enlarges the vibronic system beyond the most commonly treated two-state problem and leads to multi-state vibronic interactions. For less symmetric substitutions [41, 53, 62, 63, 68–73], there is generally no JT effect possible ‘any more’, and the question arises how this affects the vibronic dynamics, whether the effects vanish altogether or whether there are only quantitative (possibly minor) changes. Furthermore, for the family of fluorobenzene cations, there is a marked dependence of their emission properties on the degree of fluorination: the monofluoro benzene cation, like the parent cation itself [43, 74, 75], shows no emission, while for a threefold and higher degree of fluorination generally emissive species are obtained [43–50]. The doubly fluorinated benzene cations appear to be at the borderline, and the emissive properties depend on the particular isomer [43].

This is indicative of characteristic energy shifts of the relevant electronic states of the cations similar as indicated above for the five-membered heterocycles.

In the past several years, following earlier studies more limited in scope, we have conducted a rather comprehensive set of theoretical investigations on the benzene cation and its mono- and difluoro derivatives [30, 31, 60–62, 68, 69]. This serves to analyze not only the multi-mode dynamical JT and PJT effect in the unsubstituted species, but also the changes that occur upon reduction in symmetry. In addition, multi-state vibronic interactions with 4–5 strongly coupled PES, the energetic shifts that occur upon fluorination and their impact on the interstate couplings, on the spectroscopic properties, and, also on the fluorescence dynamics, have been elucidated. The investigations are all based on *ab initio* quantum dynamics, employing coupled-cluster [76–78] calculations for the coupling constants and underlying PES, and wavepacket propagation techniques with typically ten vibrational degrees of freedom for the nuclear motion (the latter relying on the powerful multiconfiguration time-dependent Hartree (MCTDH) method [79–82]). The conceptual framework is provided by the well-established linear vibronic coupling approach [6, 14, 83], augmented by characteristic quadratic coupling terms. By a careful analysis, much of the available spectroscopic information on these species is well reproduced, and useful insight is obtained on the different fluorescence properties of the various benzene cation derivatives.

In the present review we survey these studies and results, with special emphasis on the relations between the various systems treated. The latter applies to the electronic structural data as well as to the dynamical behaviour and their interrelation. We focus on the vibronic structure of various spectral bands and on the femtosecond population dynamics in the coupled electronic manifolds. Preliminary data on a trifluoro derivative are also included. As a by-product we hope to demonstrate the types of quantum-dynamical calculations that are feasible nowadays and thus give an idea about possible future applications and developments in the field.

## 2 Theoretical Framework: Vibronic Hamiltonians

We are focusing on the five lowest electronic states of the benzene cation and its fluoro derivatives, namely the mono-, di- (three different isomers) and tri- (1,2,3-isomer) fluorobenzene cations. These states lie, for all six cations, in the energy range from 9 to 13–14 eV above the electronic ground state of the respective neutral species. They give rise to the low energy band systems of the experimental photoelectron spectra [70].

At the equilibrium geometries of the neutrals, the symmetry assignments of these cationic doublet states, ordered by ascending vertical ionization potentials, are as follows. The obvious notations  $\text{Bz}^+$ ,  $\text{F-Bz}^+$ , 1, 2, 1, 3, 1, 4 and 1, 2, 3 correspond to the benzene, mono-fluorobenzene, ortho-, meta-, para-difluorobenzene isomers and 1,2,3-trifluorobenzene, respectively. (The numbers refer to the position of the

fluorine atoms on the hexagonal arrangement of carbon atoms):

$Bz^+ (D_{6h})$	$F-Bz^+ (C_{2v})$	1,2 ( $C_{2v}$ )	1,3 ( $C_{2v}$ )	1,4 ( $D_{2h}$ )	1,2,3 ( $C_{2v}$ )
$\tilde{X}^2 E_{1g}(\pi)$	$\tilde{X}^2 B_1(\pi)$	$\tilde{X}^2 B_1(\pi)$	$\tilde{X}^2 A_2(\pi)$	$\tilde{X}^2 B_{3g}(\pi)$	$\tilde{X}^2 B_1(\pi)$
	$\tilde{A}^2 A_2(\pi)$	$\tilde{A}^2 A_2(\pi)$	$\tilde{A}^2 B_1(\pi)$	$\tilde{A}^2 B_{2g}(\pi)$	$\tilde{A}^2 A_2(\pi)$
$\tilde{B}^2 E_{2g}(\sigma)$	$\tilde{B}^2 B_1(\pi)$	$\tilde{B}^2 B_1(\pi)$	$\tilde{B}^2 B_1(\pi)$	$\tilde{B}^2 B_{1u}(\pi)$	$\tilde{B}^2 B_1(\pi)$
$\tilde{C}^2 A_{2u}(\pi)$	$\tilde{C}^2 B_2(\sigma)$	$\tilde{C}^2 A_1(\sigma)$	$\tilde{C}^2 A_1(\sigma)$	$\tilde{C}^2 B_{1g}(\sigma)$	$\tilde{C}^2 B_2(\sigma)$
	$\tilde{D}^2 A_1(\sigma)$	$\tilde{D}^2 B_2(\sigma)$	$\tilde{D}^2 B_2(\sigma)$	$\tilde{D}^2 B_{3u}(\sigma)$	$\tilde{D}^2 A_1(\sigma)$

The symbols in parentheses refer to the character of the underlying orbitals out of which ionization takes place. Note that the  $\tilde{X}^2 E_{1g}$  and  $\tilde{B}^2 E_{2g}$  states of the benzene cation are both doubly degenerate by symmetry, leading to a total of five electronic component states as well [84, 85]. These degeneracies will be lifted due to Jahn–Teller and pseudo Jahn–Teller interactions.

In order to study the vibronic dynamics and spectra resulting from the coupled electronic and vibrational motion of the various species we use the same approach throughout this work: the vibronic coupling (VC) model [6, 14, 83]. This model relies on the use of a (quasi-)diabatic representation of the electronic states. Contrary to the usual adiabatic electronic basis, the off-diagonal matrix elements which generate the couplings within the electronic manifold arise from the potential energy part of the Hamiltonian, rather than from the nuclear kinetic energy. This has the tremendous advantage to get rid off the singularities in the derivative couplings at degeneracies of electronic states. Indeed, diabatic functions are usually smooth functions of the nuclear coordinates  $\mathbf{Q}$  [86–91]. As a consequence, the potential energy matrix elements in the diabatic basis can be expanded in a Taylor series in  $\mathbf{Q}$  and only low-order terms retained. Truncating the series after the first-order terms defines the *linear vibronic coupling* model (LVC), while including second-order terms leads to the – as a short-hand notation – *quadratic vibronic coupling* model (QVC), and so forth.

The total vibronic potential energy matrix  $\mathbf{W}^{tot}(\mathbf{Q})$  is derived by splitting each of its elements  $W_{\alpha\beta}^{tot}(\mathbf{Q})$  into a part  $V_0(\mathbf{Q})$  describing the initial electronic state – the ground state of the neutral species in our case – and the changes  $W_{\alpha\beta}(\mathbf{Q})$  induced by the ionization. Here,  $\alpha$  and  $\beta$  labels the electronic states of the cations. We have:

$$W_{\alpha\beta}^{tot}(\mathbf{Q}) = V_0(\mathbf{Q}) \delta_{\alpha\beta} + W_{\alpha\beta}(\mathbf{Q}). \quad (1)$$

Defining  $\mathbf{Q}$  as the set of dimensionless normal coordinates  $\{Q_i\}$  of the (model) harmonic ground state potential  $V_0(\mathbf{Q})$  with frequencies  $\omega_i$ , we obtain [6, 14]:

$$W_{\alpha\alpha}(\mathbf{Q}) = E_\alpha + \sum_i (\kappa_i^{(\alpha)} Q_i + \sum_j g_{ij}^{(\alpha)} Q_i Q_j + \dots) \quad (2)$$

$$W_{\alpha\neq\beta}(\mathbf{Q}) = \sum_i \lambda_i^{(\alpha\beta)} Q_i + \dots \quad (3)$$

In (2),  $E_\alpha$  corresponds to the vertical IP for the state  $\alpha$ . This is due to our particular choice of the diabatic states, chosen to coincide with the adiabatic ones at the center of the Franck–Condon zone,  $\mathbf{Q} = \mathbf{0}$ . The quantities  $\kappa_i^{(\alpha)}$  and  $\lambda_i^{(\alpha\beta)}$  are the intrastate and interstate (linear) coupling constants, respectively, and similarly for the  $g_{ij}^{(\alpha)}$ , etc.

In the present study, the LVC model has shown to be sufficient for the study of the benzene cation. However, for its fluoro derivatives it was needed to go beyond, and some diagonal second-order contributions ( $g_{ii}^{(\alpha)}$ ) have been included. All other second order terms (bilinear on- and off-diagonal couplings) are not included in the present treatment. The inclusion of the  $g_{ii}^{(\alpha)}$  couplings for some of the totally symmetric modes has a strong impact on the energetics of the intersection seams, as will be discussed in more details in Sect. 4.1, and their inclusion is compulsory to properly describe the electronic population dynamics [62].

The full VC Hamiltonian is obtained by adding the kinetic energy  $T_N = \sum_i P_i^2 \omega_i / 2$  and  $V_0 = \sum_i \omega_i Q_i^2 / 2$ :

$$\mathbf{H} = (T_N + V_0) \mathbf{1} + \mathbf{W}(\mathbf{Q}), \quad (4)$$

with  $P_i$  the conjugated momentum of  $Q_i$  and  $\mathbf{1}$  the identity matrix in the electronic space. We note that the form of the kinetic energy is an additional assumption here because derivative couplings cannot be completely removed in general [92], but are nevertheless expected to be small if the quasi-diabatic basis is constructed properly. The explicit forms of the VC Hamiltonians corresponding to the various cations of interest are presented in the two following subsections.

## 2.1 $E \otimes e$ Jahn–Teller and $(E \oplus A) \otimes e$ Pseudo Jahn–Teller Hamiltonian for the Benzene Cation

The case of the benzene cation deserves particular attention compared to its fluoro derivatives to be presented next, because of the occurrence of JT and PJT effects which complicate the set up of the vibronic Hamiltonian. For a detailed derivation of the latter we refer to [30].

The benzene molecule belongs to the  $D_{6h}$  molecular point group. Among its 30 vibrational modes, 21 are planar and 9 lead to out-of-plane motion. They belong to the following symmetry species [93]:

$$\begin{aligned} B_z^+: \Gamma_{vib} = & 2A_{1g} \oplus 1A_{2g} \oplus 1A_{2u} \oplus 2B_{1u} \oplus 2B_{2g} \oplus 2B_{2u} \oplus 1E_{1g} \oplus 3E_{1u} \\ & \oplus 4E_{2g} \oplus 2E_{2u}. \end{aligned} \quad (5)$$

In applying the VC Hamiltonian, (4), one has the following general symmetry selection rule for the linear ( $\kappa$  and  $\lambda$ ) contributions:

$$\Gamma_\alpha \otimes \Gamma_\beta \supset \Gamma_i. \quad (6)$$

This equation states that the irreducible representation of the vibrational mode  $i$  must be contained in the direct product of the irreducible representations of the electronic states  $\alpha$  and  $\beta$  in order to contribute. The most important modes which have been used in the subsequent treatment of the vibronic coupling in  $Bz^+$  are collected in Table 3, using the Wilson notation [94].

For the nondegenerate  $\tilde{C}$  state, only totally symmetric vibrations ( $\nu_1$  and  $\nu_2$ ) can possess non-vanishing  $\kappa$ 's. For the doubly degenerate states  $\tilde{X}$  and  $\tilde{B}$  in addition the four doubly-degenerate  $E_{2g}$  modes ( $\nu_6 - \nu_9$ ) can contribute, recovering the well-known result that these modes are JT active in  $Bz^+$ .

For the off-diagonal contributions to the vibronic potential matrix, application of group theory gives:

$$E_{1g} \otimes E_{2g} = B_{2g} + E_{1g}; \quad E_{1g} \otimes A_{2u} = E_{1u}; \quad E_{2g} \otimes A_{2u} = E_{2u}, \quad (7)$$

where, on the right hand sides, irreducible representations containing no modes of the benzene cations have been omitted. Note that, since the  $\tilde{X}$  and  $\tilde{C}$  states are antisymmetric with respect to reflections in the molecular plane ( $\tilde{B}$  is symmetric), the off-diagonal elements involving only one of these states contain out-of-plane vibrations, while the others not.

In order to set up the working Hamiltonian, further simplifications are done. These regard in particular the values of the couplings and/or the energetic location of the minimum of the intersection seam between the various electronic states. Details about these results are given in [30] and Sect. 4, but we anticipate them here by putting some entries to zero in the Hamiltonian. Indeed, when the minimum of the seam of intersections is too high in energy with respect to our energy range (9–14 eV), the intersection will not play a significant role. In this line, the 3  $E_{1u}$  modes which couple the  $\tilde{X}$  and  $\tilde{C}$  states according to the group theory are neglected, and the corresponding entries in the Hamiltonian are put to zero. The LVC potential energy matrix for the benzene cation thus reads [30]:

$$\mathbf{W}_{Bz^+} = \begin{pmatrix} E_X + \kappa_{A_{1g}}^{(X)} \mathbf{Q} + \lambda_{E_{2g}}^{(X)} \mathbf{Q}_x & \lambda_{E_{2g}}^{(X)} \mathbf{Q}_y & \lambda_{E_{1g}}^{(XB)} \mathbf{Q}_x & \lambda_{E_{1g}}^{(XB)} \mathbf{Q}_y + \lambda_{B_{2g}}^{(XB)} \mathbf{Q} & 0 \\ \lambda_{E_{2g}}^{(X)} \mathbf{Q}_y & E_X + \kappa_{A_{1g}}^{(X)} \mathbf{Q} - \lambda_{E_{2g}}^{(X)} \mathbf{Q}_x & \lambda_{E_{1g}}^{(XB)} \mathbf{Q}_y - \lambda_{B_{2g}}^{(XB)} \mathbf{Q} & -\lambda_{E_{1g}}^{(XB)} \mathbf{Q}_x & 0 \\ \lambda_{E_{1g}}^{(XB)} \mathbf{Q}_x & \lambda_{E_{1g}}^{(XB)} \mathbf{Q}_y - \lambda_{B_{2g}}^{(XB)} \mathbf{Q} & E_B + \kappa_{A_{1g}}^{(B)} \mathbf{Q} + \lambda_{E_{2g}}^{(B)} \mathbf{Q}_x & \lambda_{E_{2g}}^{(B)} \mathbf{Q}_y & \lambda_{E_{2u}}^{(BC)} \mathbf{Q}_y \\ \lambda_{E_{1g}}^{(XB)} \mathbf{Q}_y + \lambda_{B_{2g}}^{(XB)} \mathbf{Q} & -\lambda_{E_{1g}}^{(XB)} \mathbf{Q}_x & \lambda_{E_{2g}}^{(B)} \mathbf{Q}_y & E_B + \kappa_{A_{1g}}^{(B)} \mathbf{Q} - \lambda_{E_{2g}}^{(B)} \mathbf{Q}_x & \lambda_{E_{2u}}^{(BC)} \mathbf{Q}_x \\ 0 & 0 & \lambda_{E_{2u}}^{(BC)} \mathbf{Q}_y & \lambda_{E_{2u}}^{(BC)} \mathbf{Q}_x & E_C + \kappa_{A_{1g}}^{(C)} \mathbf{Q} \end{pmatrix} \quad (8)$$

where

$$\kappa_{\Gamma_i}^{(\alpha)} \mathbf{Q} = \sum_{i \in \Gamma_i} \kappa_i^{(\alpha)} Q_i \quad \text{and} \quad \lambda_{\Gamma_i}^{(\alpha\beta)} \mathbf{Q} = \sum_{i \in \Gamma_i} \lambda_i^{(\alpha\beta)} Q_i, \quad (9)$$

with  $\Gamma_i$  being the irreducible representation to which the mode  $i$  belongs. The other quantities entering (9) are defined in (2) and (3). In (8), the additional indices  $x$  and  $y$  of  $\mathbf{Q}$  identify, whenever appropriate, the two components of the doubly degenerate modes. For these modes, the on- and off-diagonal contributions have the same magnitude (denoted by  $\lambda$ ), but not always the same sign. The relative signs of these contributions are of crucial importance for the JT Hamiltonians, and require a careful derivation. The details are given in [30].

## 2.2 Multi-State Vibronic Hamiltonians for the Fluorobenzene Cations

The mono-, di- and tri- (1,2,3-isomer) fluorobenzene cations belong to the  $C_{2v}$  or  $D_{2h}$  molecular point groups. They contain only nondegenerate irreducible representations, and thus no symmetry-induced degeneracies occur. The tedious analysis of the relative signs of coupling elements required for  $Bz^+$  [30] is therefore absent here. The 30 modes of the fluorinated benzene cations belong to the following symmetry species [52, 70, 73, 95]:

$$F - Bz^+ : \Gamma_{vib} = 11A_1 \oplus 3A_2 \oplus 6B_1 \oplus 10B_2, \quad (10)$$

$$1, 2 : \Gamma_{vib} = 11A_1 \oplus 5A_2 \oplus 4B_1 \oplus 10B_2, \quad (11)$$

$$1, 3 : \Gamma_{vib} = 11A_1 \oplus 3A_2 \oplus 6B_1 \oplus 10B_2, \quad (12)$$

$$1, 4 : \Gamma_{vib} = 6A_g \oplus 2A_u \oplus 5B_{1g} \oplus 3B_{1u} \oplus 1B_{2g} \oplus 5B_{2u} \oplus 3B_{3g} \oplus 5B_{3u}, \quad (13)$$

$$1, 2, 3 : \Gamma_{vib} = 11A_1 \oplus 3A_2 \oplus 6B_1 \oplus 10B_2. \quad (14)$$

By using the LVC model, augmented by purely quadratic couplings only for totally symmetric modes (thus adding QVC contributions) the symmetry-selection rule, (6), can be directly applied to deduce the vibronic Hamiltonian matrices for the description of the five lowest  $\tilde{X} - \tilde{D}$  doublet states of these fluorobenzene cations. We shall not write down all five matrices here, but rather provide the basic features regarding their QVC Hamiltonian. The general form of the QVC potential energy matrix,  $\mathbf{W}_{fluoro}$ , for the above mentioned fluorobenzene cations is depicted below:

$$\mathbf{H} = (T_N + V_0) \mathbf{1} + \mathbf{W}_{fluoro}, \quad (15)$$

$$\mathbf{W}_{fluoro} =$$

$$\begin{pmatrix} E_X + \kappa^{(X)}\mathbf{Q} + \mathbf{g}^{(X)}\mathbf{Q}^2 & \lambda^{(XA)}\mathbf{Q} & 0 & 0 & 0 \\ \lambda^{(XA)}\mathbf{Q} & E_A + \kappa^{(A)}\mathbf{Q} + \mathbf{g}^{(A)}\mathbf{Q}^2 & 0 & \lambda^{(AC)}\mathbf{Q} & 0 \\ 0 & 0 & E_B + \kappa^{(B)}\mathbf{Q} + \mathbf{g}^{(B)}\mathbf{Q}^2 & \lambda^{(BC)}\mathbf{Q} & \lambda^{(BD)}\mathbf{Q} \\ 0 & \lambda^{(AC)}\mathbf{Q} & \lambda^{(BC)}\mathbf{Q} & E_C + \kappa^{(C)}\mathbf{Q} + \mathbf{g}^{(C)}\mathbf{Q}^2 & \lambda^{(CD)}\mathbf{Q} \\ 0 & 0 & \lambda^{(BD)}\mathbf{Q} & \lambda^{(CD)}\mathbf{Q} & E_D + \kappa^{(D)}\mathbf{Q} + \mathbf{g}^{(D)}\mathbf{Q}^2 \end{pmatrix},$$

**Table 1** Symmetry species ( $j$ ) of the various vibrational modes entering the elements of the  $5 \times 5$  vibronic Hamiltonian matrices for the mono-fluorobenzene (F-Bz<sup>+</sup>), 1, 2-, 1, 3-, 1, 4- difluorobenzene and 1,2,3-trifluorobenzene cations. The entries not appearing at all, e.g.  $\lambda^{(AD)}$ , are zero. See text for details

Interstate coupling	F-Bz <sup>+</sup>	1,2	1,3	1,4	1,2,3
$\lambda^{(XA)}$	$B_2$	$B_2$	$B_2$	$B_{1g}$	$B_2$
$\lambda^{(AC)}$	$B_1$	$A_2$	$B_1$	$B_{3g}$	$B_1$
$\lambda^{(BC)}$	$A_2$	$B_1$	$B_1$	$A_u$	$A_2$
$\lambda^{(BD)}$	$B_1$	$A_2$	$A_2$	$B_{2g}$	$B_1$
$\lambda^{(CD)}$	$B_2$	$B_2$	$B_2$	$B_{2u}$	$B_2$

where the quantities  $\kappa^{(\alpha)}$  and  $\lambda^{(\alpha\beta)}$  are given by (9), and the quadratic terms by:

$$\mathbf{g}^{(\alpha)} \mathbf{Q}^2 = \sum_{i \in A_1(A_g)} g_{ii}^{(\alpha)} Q_i^2. \quad (16)$$

The details about the construction of the Hamiltonian matrices, as well as their explicit form, can be found in [62] and [68, 69] for the mono- and di-fluorobenzene cations, respectively. All the modes which appear in the diagonal elements of the matrix  $\mathbf{W}_x$  are totally symmetric modes. The symmetry of the vibrational modes which enter in the off-diagonal elements, for all the compounds, are provided in Table 1. As is well known [6], the nonadiabatic dynamics described by the above vibronic coupling Hamiltonian is essentially controlled by the energies of the minima of the various diabatic surfaces as well as of the various conical intersection seams [6, 14, 83]. The determination of the seam minima in the presence of quadratic couplings are discussed in the appendix of [62]. In (15), some of the off-diagonal entries are put to zero, because the subsequent electronic structure calculations reveal only negligible interactions between the corresponding electronic states. In particular, some conical intersections are so high in energy ( $\geq 0.5$  eV higher than the vertical IP of the highest-energy electronic state) that they are inaccessible to the nuclear motions for the excitation energies considered here – see the discussion in [68] and Sect. 4. Therefore, only those terms which will be found to be significant for the dynamics are included. The electronic states can be divided into two groups:  $\tilde{X} - \tilde{A}$  and  $\tilde{B} - \tilde{D}$ , resembling in part the strongly JT coupled states of the parent cation. These groups of states appear clearly in the experimental photoelectron spectrum as two separated band systems exhibiting strong mixing of their underlying states [70]. The coupling between these two groups of states is found to be significant only for one pair of states among them, namely between the  $\tilde{A}$  and  $\tilde{C}$  states.

The most important modes included in the subsequent calculations, together with the values for the frequency and coupling constants, are collected in Table 3 below.

### 3 Computational Methods

#### 3.1 *Ab initio Electronic Structure Calculations*

In order to determine the various coupling parameters entering the vibronic coupling Hamiltonian, (8), (15), and provide a solid basis for the dynamical calculations, *ab initio* electronic structure calculations have been performed. In case of the parent cation,  $\text{Bz}^+$ , two methods have been applied [30]. In the first method, called outer valence Greens function (OVGF) method, the ionization potentials are determined directly, i.e. without forming the energy difference of electronic states of ionic and neutral species [96–98]. The OVGF method accounts for reorganisation and correlation effects in a balanced way without giving up the quasi-particle picture for ionization. It leads to an improved description of vibrational structures in PE-spectra [96,99,100] as long as satellite lines are not important in the spectrum. The quantity  $V_0(\mathbf{Q})$  has been determined, in the harmonic approximation, at the MP2 level of theory, which thus also serves to define the normal coordinates used in the OVGF calculations. The calculations were performed using the Gaussian program package [101]. In addition to the OVGF calculations, the calculations at the Coupled Cluster level using the so called EOMIP–CCSD (Equation-of-Motion Ionization Potential Coupled Clusters Singles and Doubles) method (also known as Coupled-Cluster Greens Function method) [76, 77] have also been performed. Here again the ionization potentials are determined directly. The relation of this method to the OVGF method was discussed in detail by Nooijen and Snijders [102]. In short: while in EOMIP–CCSD the infinite order summations are performed by solving the Coupled Cluster equations, in OVGF the so-called Dyson’s equations are used. EOMIP–CCSD is considered to be less approximative than OVGF. However, EOMIP–CCSD is more expensive since no perturbational truncation is involved. Therefore we have also applied the second order approximation to EOMIP–CCSD known under different names (EOMIP–CCSD(2), EOMIP–MBPT(2) and MBPT(2)-GF) [103, 104]. This approximate version has been extensively tested and it has been shown not to introduce substantial error in the energy of ionized states, but somewhat less expensive than OVGF [30, 103]. A standard DZP [105] basis set has been employed for both sets of calculations.

For the first fluoro derivative,  $\text{F-Bz}^+$ , the MP2 method has been employed for ground state geometry optimization and vibrational frequency analysis. Ionization potentials and ionic state energies have been determined by means of the equation-of-motion coupled-cluster (EOM–CCSD) method [76,77]. Comparison calculations have also been performed using the perturbative treatment [104] of the double excitations [EOM–CCSD(2)], and good agreement with the full CCSD results has been obtained. For both the EOMIP–CCSD and the EOMIP–CCSD(2) surfaces, the TZ2P basis has been employed [106]. This basis consists of the triple zeta set of Dunning [107] augmented by polarization functions as given in [106, 108].

For higher fluoro derivatives, namely di- and 1,2,3-trifluoro derivatives we have also employed the coupled-clusters singles and doubles (CCSD) method with TZ2P



one-particle basis set for ground state geometry optimization and vibrational frequency analysis in the ACES electronic structure package [109]. Ionization potentials and ionic state energies have been determined by means of the EOMIP–CCSD method [76, 77] implemented in the local version of the ACES program system [109]. In all the ab initio calculations, the ground state structural parameters thus obtained agree very well with available literature data [41, 71, 110–112].

Formally, the various coupling constants can be computed by using analytic gradient techniques or finite displacements along the various normal coordinates entering (8), (15). While for the totally symmetric modes first derivatives are needed, the computation of the off-diagonal or inter-state coupling constants requires the second derivatives, or a least-squares fitting procedure using the eigenvalues of an appropriate coupling matrix. For the totally symmetric modes one simply has

$$\kappa_i^{(\alpha)} = \frac{\partial \Delta V_\alpha(\mathbf{Q})}{\partial Q_i} \big|_{\mathbf{Q}=\mathbf{0}}, \quad (17)$$

where the derivative is to be taken at the Franck–Condon zone centre (reference geometry)  $\mathbf{Q} = \mathbf{0}$  [6] and  $\Delta V$  denotes eigenvalue of  $\mathbf{W}_{\text{fluoro}}$  in (15). The quadratic coupling terms,  $g_i^{(\alpha)}$ , are computed as follows;

$$\mathbf{g}_i^{(\alpha)} = \frac{\partial^2 \Delta V_\alpha(\mathbf{Q})}{\partial Q_i^2} \big|_{\mathbf{Q}=\mathbf{0}}. \quad (18)$$

For the inter-state coupling constants, displacement along a single normal coordinate  $Q_i$  usually leads to a coupling of two component states only, with a  $2 \times 2$  coupling matrix  $W_{eff}^{\alpha\beta}$  of the following form [6]:

$$W_{eff}^{\alpha\beta}(Q_i) = \begin{pmatrix} E_\alpha & \lambda_i^{\alpha\beta} Q_i \\ \lambda_i^{\alpha\beta} Q_i & E_\beta \end{pmatrix}. \quad (19)$$

The difference  $\Delta V_{\alpha\beta}$  of eigenvalues of this  $2 \times 2$  matrix is:

$$\Delta V_{\alpha\beta} = \sqrt{(E_\alpha - E_\beta)^2 + 4(\lambda_i^{\alpha\beta} Q_i)^2}, \quad (20)$$

from which one easily deduces [6]:

$$\lambda_i^{\alpha\beta} = \sqrt{\frac{1}{8} \frac{\partial^2 (\Delta V_{\alpha\beta})^2}{\partial Q_i^2}} \big|_{\mathbf{Q}=\mathbf{0}}. \quad (21)$$

The above (17), (18) are evaluated numerically using finite difference technique and values of the normal coordinate displacements  $Q_i = 0.5, 1.0, 1.5$  and  $2.0$ . Displacement along a single normal coordinate usually leads to a coupling of two component states, as stated above. This is, however, not always the case and

sometimes more than one electronic state couples with a particular state. In particular, we have to consider a three-states problem and consequently a  $3 \times 3$  coupling matrix. To this end we have used least-squares fitting for the eigenvalues of the following coupling matrix with respect to the ab initio data points, (again we use displacements mentioned above to reproduce the inter-state coupling constants for all coupled states simultaneously):

$$W_{eff}^{\alpha\beta\gamma}(Q_i) = \begin{pmatrix} E_\alpha & 0 & \lambda_i^{\alpha\gamma} Q_i \\ 0 & E_\beta & \lambda_i^{\beta\gamma} Q_i \\ \lambda_i^{\alpha\gamma} Q_i & \lambda_i^{\beta\gamma} Q_i & E_\gamma \end{pmatrix}. \quad (22)$$

This was the case for the vibrational modes of  $A_2$  symmetry in the 1,2-difluorobenzene,  $B_1$ ,  $A_2$  symmetries in the case of the 1,3-difluorobenzene and 1,2,3-trifluorobenzene cations. As stated in Table 1 the interactions between some electronic states are negligible which appear as zero entries in the off-diagonal terms of (15), (8). But one should note that in case of a  $3 \times 3$  coupling matrix the imperceptible coupling between two electronic states may have an important effect on the coupling of the other two electronic states.

### 3.2 Quantum Dynamical Simulations

To calculate numerically the quantum dynamics of the various cations in time-dependent domain, we shall use the multiconfiguration time-dependent Hartree method (MCTDH) [79–82, 113, 114]. This method for propagating multidimensional wave packets is one of the most powerful techniques currently available. For an overview of the capabilities and applications of the MCTDH method we refer to a recent book [114]. Additional insight into the vibronic dynamics can be achieved by performing time-independent calculations. To this end Lanczos algorithm [115, 116] is a very suitable algorithm for our purposes because of the structural sparsity of the Hamiltonian secular matrix and the matrix-vector multiplication routine is very efficient to implement [6].

#### 3.2.1 The Multiconfiguration Time-Dependent Hartree (MCTDH) Method

The MCTDH method [79–82, 113, 114] uses a time development of the wavefunction expanded in a basis of sets of variationally optimized time-dependent functions called single-particle functions (SPFs). A set of SPFs is used for each particle, where each particle represents a coordinate or a set of coordinates called combined mode. Indeed, when some modes are strongly coupled, and when there are many degrees of freedom, it is more efficient to combine sets of coordinates together as a

“particle” with a multi-dimensional coordinate  $q_\kappa = (Q_i, Q_j, \dots)$  [117]. Consequently, the number of particles,  $p$ , must be distinguished from the total number of modes included in the calculation.

The MCTDH wavefunction ansatz for  $N$  modes combined as  $p$  particles is the multiconfigurational expansion

$$\Psi(q_1, \dots, q_p, t) = \sum_{j_1}^{n_1} \dots \sum_{j_p}^{n_p} A_{j_1 \dots j_p}(t) \prod_{\kappa=1}^p \varphi_{j_\kappa}^{(\kappa)}(q_\kappa, t) = \sum_J A_J \phi_J, \quad (23)$$

where  $n_\kappa$  is the number of SPFs for the  $\kappa$ th particle and where the third identity defines the multi-index  $J = (j_1 \dots j_p)$  and the configuration  $\phi_J = \varphi_{j_1}^{(1)} \varphi_{j_2}^{(2)} \dots \varphi_{j_p}^{(p)}$ .

To obtain the set of coupled equations of motion for the coefficients and SPFs, the Dirac–Frenkel variational principle is used. Dividing the Hamiltonian into parts that act only on a given particle (separable or correlated term),

$$H(q_1, \dots, q_p) = \sum_{\kappa=1}^p h_\kappa(q_\kappa) + H_R(q_1, \dots, q_p), \quad (24)$$

one obtains the equations of motion [80–82]:

$$i \dot{A}_J = \sum_L \langle \phi_J | H_R | \phi_L \rangle A_L \quad (25)$$

$$i \dot{\varphi}_a^{(\kappa)} = h_\kappa \varphi_a^{(\kappa)} + (1 - P^{(\kappa)}) \sum_{b,c} \rho_{ab}^{(\kappa)-1} \mathcal{H}_{bc}^{(\kappa)} \varphi_c^{(\kappa)}. \quad (26)$$

Here  $\mathcal{H}_{bc}^{(\kappa)} = \langle \Psi_b^{(\kappa)} | H_R | \Psi_c^{(\kappa)} \rangle$  is the mean-field matrix operator, with the “single-hole function”  $\Psi_a^{(\kappa)}$

$$\Psi_a^{(\kappa)} = \langle \varphi_a^{(\kappa)} | \Psi \rangle \quad (27)$$

$$= \sum_{j_1}^{n_1} \dots \sum_{j_{\kappa-1}}^{n_{\kappa-1}} \sum_{j_{\kappa+1}}^{n_{\kappa+1}} \dots \sum_{j_p}^{n_p} A_{j_1 \dots j_{\kappa-1} a j_{\kappa+1} \dots j_p} \times \varphi_{j_1}^{(1)} \dots \varphi_{j_{\kappa-1}}^{(\kappa-1)} \varphi_{j_{\kappa+1}}^{(\kappa+1)} \dots \varphi_{j_p}^{(p)}, \quad (28)$$

which collects all the terms in the wavefunction which would contain the  $a$ th function of the  $\kappa$ th particle.  $P^{(\kappa)} = \sum_a |\varphi_a^{(\kappa)} \rangle \langle \varphi_a^{(\kappa)}|$  is the projector on the set of SPFs for the  $\kappa$ th particle, and  $\rho^{(\kappa)}$  is the reduced density matrix defined by  $\rho_{ab}^{(\kappa)} = |\Psi_a^{(\kappa)} \rangle \langle \Psi_b^{(\kappa)}|$ . These equations of motion are general, and can be used to treat the dynamics of nonadiabatic systems [81, 113, 118]. The efficiency of the MCTDH method for vibronically coupled systems is even improved by writing the wavefunction as a sum of several wavefunctions – one for each electronic state [81, 117]:

$$\Psi(t) = \sum_{\alpha}^{n_s} \Psi_{\alpha}(t) |\alpha\rangle = \sum_{\alpha}^{n_s} \sum_{J_{\alpha}} A_{J_{\alpha}}^{(\alpha)} \phi_{J_{\alpha}}^{(\alpha)} |\alpha\rangle, \quad (29)$$

where  $n_s$  is the number of electronic states, and  $J_{\alpha}$  is the multi-index for the configurations used to describe the wavefunction on the state  $\alpha$ . This form of the MCTDH wavefunction has the advantage to allow for a separate optimization of the SPFs for each electronic state, and therefore fewer coefficients are needed in the wavefunction expansion. This choice is employed in this work.

The solution of the equations of motion requires the computation of the mean-fields at every time-step. The efficiency of the MCTDH method thus demands their fast evaluation, and necessitates to avoid the explicit calculation of high-dimensional integrals. Using the form of the Hamiltonian given by (24), we readily see that the evaluation of the mean-fields for the separable terms needs only integrals over a single particle at a time. However, for the correlated part of the Hamiltonian,  $H_R$  of (24), the mean-fields may involve integrals of the full dimensionality of the problem. This correlated term can, however, be written as a sum of products of single-particle Hamiltonians, rendering the evaluation of the mean-fields faster:

$$H_R = \sum_{r=1}^s c_r \prod_{\kappa=1}^p h_r^{(\kappa)}, \quad (30)$$

where  $h_r^{(\kappa)}$  operates on the  $\kappa$ -th particle only and where the  $c_r$  are numbers.

Interestingly, the LVC and QVC Hamiltonians of Sect. 4 are already in this form, allowing a powerful use of the MCTDH method and enabling us to include as many as 10 to 13 modes in the dynamics.

### 3.2.2 Calculated Quantities

In this review, we shall present and discuss spectra at various resolutions, time-dependent electronic populations and reduced densities.

Spectra,  $P(E)$ , can be obtained directly from a time-dependent treatment as the Fourier transform of the autocorrelation function  $C(t)$ , assuming a direct transition from the initial to the final states within the framework of Fermi's golden rule [6, 119]:

$$P(E) \propto \int e^{iEt} C(t) dt, \quad (31)$$

with:

$$C(t) = \langle \Psi(0) | \Psi(t) \rangle = \left\langle 0 \left| \tau^{\dagger} e^{-iHt} \tau \right| 0 \right\rangle \quad (32)$$

$$= \langle \Psi(t/2)^* | \Psi(t/2) \rangle. \quad (33)$$

In (32),  $|0\rangle$  is the vibrational ground state of the initial electronic state – the ground state of the neutral species in our case –, and  $\tau^\dagger$  is the vector of individual transition matrix element  $\tau_\alpha$  between the initial state and the final electronic states labelled by  $\alpha$ . The autocorrelation function  $C(t)$  measures the overlap between this time-evolving wave-packet and the initial one, and its Fourier transform gives the corresponding spectrum according to (31). The scalar product involving the vector  $\tau$  of transition matrix elements implies a summation over various partial spectra, each being proportional to  $|\tau_\alpha|^2$  (different final electronic states). The total spectrum can thus be obtained in two equivalent ways: (1) by exciting initially all electronic states, or (2) by summing partial ‘single-state’ spectra obtained after excitation of only one electronic state at a time. Equation (33), which is valid here because our Hamiltonians are symmetric and the initial wavepackets are real [120, 121], and allows us to reduce the propagation time by a factor of two.

Due to the finite propagation time  $T$  of the wavepackets, the Fourier transformation causes artifacts known as the Gibbs phenomenon [122]. In order to reduce this effect, the autocorrelation function is first multiplied by a damping function  $\cos^2(\pi t/2T)$  [81, 123]. Furthermore, to simulate the experimental line broadening, the autocorrelation functions will be damped by an additional multiplication with a Gaussian function  $\exp[-(t/\tau_d)^2]$ , where  $\tau_d$  is the damping parameter. This multiplication is equivalent to a convolution of the spectrum with a Gaussian with a full width at half maximum (FWHM) of  $4(\ln 2)^{1/2}/\tau_d$ . The convolution thus simulates the resolution of the spectrometer used in experiments, plus intrinsic line broadening effects.

The two other quantities we shall evaluate are the time-evolving (diabatic) electronic populations,  $P_\alpha(t)$ , and two-dimensional reduced densities  $\rho_\alpha(Q_i, Q_j, t)$  for the electronic state  $\alpha$ . These quantities are defined as follows, using the wavefunction given by (29):

$$P_\alpha(t) = \langle \Psi_\alpha(t) | \Psi_\alpha(t) \rangle, \quad (34)$$

$$\rho_\alpha(Q_i, Q_j, t) = \int \Psi_\alpha^*(t) \Psi_\alpha(t) \prod_{l \neq i, j} dQ_l. \quad (35)$$

All these quantities will be exploited in the following to decipher the dynamical properties of the benzene cation and its fluoro derivatives.

## 4 Electronic Structure Results

### 4.1 Vertical Ionization Potentials and Coupling Constants

To provide a proper basis for the understanding of the dynamical results in Sect. 5, we first discuss the underlying potential energy surfaces and their changes upon fluorination. We start here with the key quantities, the vertical ionization potentials

**Table 2** Comparison of the ab initio (IPa) and adjusted data (IPb) for vertical IPs of the benzene radical cation and its fluoro derivatives

		$\tilde{X}$	$\tilde{A}$	$\tilde{B}$	$\tilde{C}$	$\tilde{D}$
Bz <sup>+</sup>	Symmetry	<b>E<sub>1g</sub></b>		<b>E<sub>2g</sub></b>	<b>A<sub>2u</sub></b>	
	IPb	9.45		11.84	12.44	
	IPa	9.27		12.15	12.61	
F-Bz <sup>+</sup>	Symmetry	<b>B<sub>1</sub></b>	<b>A<sub>2</sub></b>	<b>B<sub>1</sub></b>	<b>B<sub>2</sub></b>	<b>A<sub>1</sub></b>
	IPb	9.435	9.83	12.295	12.34	12.85
	IPa	9.45	9.85	12.82	12.57	13.25
1,2	Symmetry	<b>B<sub>1</sub></b>	<b>A<sub>2</sub></b>	<b>B<sub>1</sub></b>	<b>A<sub>1</sub></b>	<b>B<sub>2</sub></b>
	IPb	9.4	9.8	12.3	12.6	13.1
	IPa	9.39	9.81	12.84	12.88	13.40
1,3	Symmetry	<b>A<sub>2</sub></b>	<b>B<sub>1</sub></b>	<b>B<sub>1</sub></b>	<b>A<sub>1</sub></b>	<b>B<sub>2</sub></b>
	IPb	9.6	9.9	12.5	13.1	13.3
	IPa	9.44	9.82	12.79	13.06	13.50
1,4	Symmetry	<b>B<sub>3g</sub></b>	<b>B<sub>2g</sub></b>	<b>B<sub>1u</sub></b>	<b>B<sub>1g</sub></b>	<b>B<sub>3u</sub></b>
	IPb	9.40	10.05	12.35	12.75	13.55
	IPa	9.25	10.04	12.77	12.74	13.70
1,2,3	Symmetry	<b>B<sub>1</sub></b>	<b>A<sub>2</sub></b>	<b>B<sub>1</sub></b>	<b>B<sub>2</sub></b>	<b>A<sub>1</sub></b>
	IPb	...	...	...	...	...
	IPa	9.73	9.78	12.96	13.48	13.59

(IPs) and coupling constants, and present the former in tabular form in Table 2 and as a correlation diagram in Fig. 1. The figure displays, in addition, schematic drawings of the molecular orbitals corresponding to the first two IPs to visualize their bonding properties and correlation in the series.

In Table 2 are listed two sets of vertical IPs for every species (except 1,2,3-trifluorobenzene). The set labelled IPa represents ab initio results obtained through EOM-CCSD calculations as described above. These are considered accurate calculations which nevertheless require minor adjustment for a better comparison with experiment [70]. The latter has been achieved in [31, 62, 68, 69] by a careful analysis of PE spectroscopic data, and the details are not repeated here. The adjusted numbers are collected as IPb in Table 2 and are seen to deviate by typically 0.1–0.2 eV from the pure ab initio data (IPa) which is considered quite satisfactory. The *B*<sub>1</sub> state (generally 3rd state according to the adjusted IPs) of the fluoroderivatives represents an exception in that larger shifts, of the order of 0.5 eV occur here, leading to an interchange of the  $\tilde{B}$  and  $\tilde{C}$  states for monofluoro and 1,4-difluorobenzene. On the other hand, these states are quite close either before or after the readjustment. The labelling of electronic states reported in Table 2 is according to the adjusted IPs in order to have a coherent nomenclature in the series (see scheme on p. 242 and Eq. (15)). Note that for the  $\tilde{B}$  and  $\tilde{C}$  states of mono- and 1,4-difluorobenzene this deviates from our earlier work [62, 68, 69] where we have followed the ordering of the ab initio IPs in that labelling.

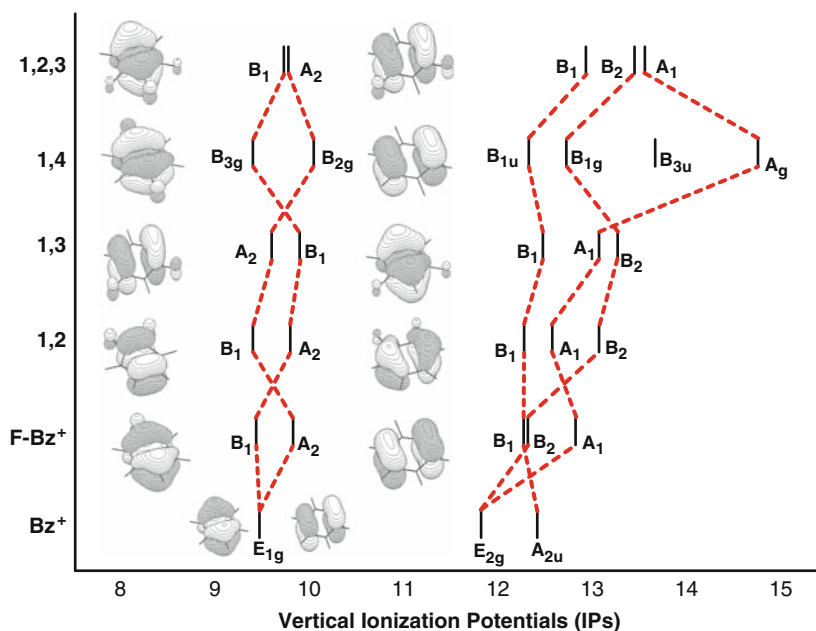


**Fig. 1** Correlation of lowest ionization potentials between the benzene, mono-, di- and trifluoro derivatives according to the adjusted IPs for details see the text)

While the numbers of Table 2 are needed for a quantitative reference, the main results are visualized more easily from Fig. 1. First, the underlying molecular orbitals show a characteristic behaviour in the figure. Whereas for benzene one can see the familiar components of the degenerate HOMO of  $E_{1g}$  symmetry, for all the fluoro derivatives this degeneracy is necessarily lifted, although the key features remain similar for all cases studied. The analogous bonding properties of the various component MOs provide the basis for the correlation lines of the corresponding IPs. It is seen that their symmetries change owing to a different location of the various symmetry elements in the different isomers. Also, the energetic ordering of the components of the same symmetry changes, which can be attributed to the different number (and strength) of the C–F antibonding interactions. For example, for monofluoro benzene the HOMO has one, the HOMO-1 has no C–F antibonding contribution. For 1,2- and 1,3-difluoro benzene both MOs have two C–F antibonding interactions, but of different strength, as indicated by the different MO coefficients at the F atoms. The size of the energetic splitting is considerably larger for the 1,4-difluorobenzene than for the other cases, owing to the (*two*) C–F antibonding interactions in the HOMO and HOMO-1. Conversely, the situation is opposite for the 1,2,3-trifluorobenzene isomer where the different numbers and strengths compensate each other and the splitting becomes rather small.

The situation is similar for the  $E_{2g}$  derived IPs and the underlying MOs. They are of  $B_2$  and  $A_1$  symmetry ( $B_{1g}$  and  $A_g$  in case of 1,4-difluorobenzene), and the

nodal properties can similarly be related to those of the degenerate HOMO-1 of benzene, although the details are more complicated (not shown here for the sake of brevity). Their energetic splitting is again largest for the 1,4-difluoro isomer. As a consequence, the higher ( $A_g$ ) state is out of the energy range under consideration and has been skipped in Table 2 and will also be ignored in the subsequent treatment. More important proves to be their systematic increase with increasing fluorination. This holds in absolute energy as well as in relation to the second  $\pi$ -type IP, which corresponds to the state of  $A_{2u}$  symmetry in the benzene radical cation and the higher one of  $B_1$  symmetry in the fluoro derivatives ( $B_{1u}$  symmetry for the 1,4-difluoro isomer). This energetic increase is known in the literature as perfluoro-effect [55], and seen here to lead to an interchange of the energetic ordering of the  $E_{2g}$  and  $A_{2u}$  derived ionization processes. This will be seen below to play a crucial role for the nonadiabatic interactions in the cations and their change upon fluorination.

Before proceeding, we briefly address Table 3 which collects selected vibrational and vibronic coupling constants. These are defined in relation to the vibronic Hamiltonians of (8), (15) and have been obtained *ab initio* without further readjustment. Out of the many coupling constants computed in this way, we present only a few first order couplings which are large and correspond to vibrational modes that can be correlated between the various fluoro derivatives and the parent cation.

Mode 1 denotes the totally symmetric C–C stretching mode of  $Bz^+$  while the modes 6a–8a, 6b–8b derive from the doubly degenerate  $E_{2g}$  modes 6–8 of  $Bz^+$  (they are to be considered as components of these doubly degenerate modes for the parent cation, but distinct modes with similar displacement patterns for the fluoro derivatives). The similarity of the vibrational frequencies throughout the series is noted (Table 3a). The same holds for the coupling constants for the  $\tilde{X}$ ,  $\tilde{A}$  states (corresponding to the  $E_{1g}$  state of  $Bz^+$ , see Table 3b) and also for the coupling constants of the  $E_{2g}$  – derived states (see Table 3c).

## 4.2 Potential Energy Surfaces and Conical Intersections

The sets of coupling constants and the Hamiltonians, (8), (15) define the high-dimensional potential energy surfaces of the lowest five electronic states of the various cations treated. Typically 6–8 totally symmetric modes and 8–10 non-totally symmetric modes are found to have non-negligible coupling constants in the  $C_{2v}$  systems; in the two cases with higher symmetry these numbers apparently decrease, e.g. to 3 relevant totally symmetric modes for the 1,4-difluoro isomer. Only few selected constants are included in Table 3 and we refer to the original papers for full details [62, 68, 69].

Although the multidimensional PES for the totally symmetric modes are harmonic oscillators, we emphasize that (pronounced) anharmonicity of the adiabatic PES comes into play as soon as non-totally symmetric modes are included [6]. The minima of the diabatic PES can be determined by retaining only the totally



**Table 3** Frequencies and coupling constants of important vibrational modes of the benzene radical cations and its fluoro derivatives. (a) Vibrational frequencies

Mode No.	Bz <sup>+</sup>	F-Bz <sup>+</sup>	1,2	1,3	1,4
1	0.1257	–	0.097	0.0929	0.1080
6a	0.0757	0.0643	0.0722	0.0658	0.0566
7a	0.1497	0.1548	0.1586	–	0.1600
8a	0.2055	0.2021	0.2071	0.2072	0.2076
6b	0.0757	0.077	0.0688	0.0642	0.0804
7b	0.1497	–	–	0.1212	–
8b	0.2055	0.203	0.2069	0.2069	0.2071

(b) The  $\tilde{X} - \tilde{A}$  set of electronic states ( $\tilde{X}$  state in case of Bz<sup>+</sup>)

Mode		Bz <sup>+</sup>	F-Bz <sup>+</sup>	1,2	1,3	1,4
1	$\kappa^{(X)}$	0.0888	–	0.019	0.025	0.030
	$\kappa^{(A)}$	–	–	–0.035	–0.057	–0.022
6a	$\kappa^{(X)}$	0.0744	0.091	0.087	0.089	0.094
	$\kappa^{(A)}$	–	–0.055	–0.056	–0.044	–0.047
7a	$\kappa^{(X)}$	0.0764	–0.083	0.016	–	–0.1390
	$\kappa^{(A)}$	–	–0.147	0.018	–	–0.201
8a	$\kappa^{(X)}$	0.1643	0.176	0.203	–0.193	–0.205
	$\kappa^{(A)}$	–	–0.125	–0.120	0.136	0.098
6b	$\lambda^{(XA)} = \kappa^{(X)}$		0.075	0.056	0.078	0.073
7b	$\lambda^{(XA)} = \kappa^{(X)}$		–	–	0.024	–
8b	$\lambda^{(XA)} = \kappa^{(X)}$		0.158	0.160	0.166	0.157

(c) The  $\tilde{C} - \tilde{D}$  set of electronic states ( $\tilde{B}$  state in case of Bz<sup>+</sup>)

Mode		Bz <sup>+</sup>	F-Bz <sup>+</sup>	1,2	1,3	1,4
1	$\kappa^{(C)}$	0.0031	–	–0.041	–0.107	0.076
	$\kappa^{(D)}$	–	–	0.022	0.053	0.049
6a	$\kappa^{(C)}$	0.1163	–0.048	–0.051	–0.046	0.014
	$\kappa^{(D)}$	–	0.093	0.110	0.056	0.070
7a	$\kappa^{(C)}$	0.0991	–0.067	–0.085	–	–0.209
	$\kappa^{(D)}$	–	–0.080	0.158	–	–0.069
8a	$\kappa^{(C)}$	0.3276	0.301	0.272	–0.298	–0.011
	$\kappa^{(D)}$	–	–0.257	–0.251	0.077	0.092
6b	$\lambda^{(CD)} = \kappa^{(B)}$		0.086	0.070	0.051	–
7b	$\lambda^{(CD)} = \kappa^{(B)}$		–	–	0.037	–
8b	$\lambda^{(CD)} = \kappa^{(B)}$		0.273	0.199	0.275	–

symmetric modes, and the corresponding energies are listed as the diagonal entries in Table 4. Comparing with the vertical IPs of Table 2, one can infer stabilization energies of typically 0.2–0.4 eV for the various electronic states. These minimum energies derive from the quadratic coupling scheme underlying (2), (15) and can be compared with numbers obtained from a full geometry optimization. Agreement is found to within typically 0.01–0.02 eV (with very few exceptions) and taken to

indicate the applicability of the quadratic coupling scheme adopted [68,69]. Further evidence comes from the potential energy curves along the various normal modes which have been computed for various displacements to extract the coupling constants. These are generally very well represented by the model curves [68], so that the coupling scheme can be taken to faithfully represent the actual situation in these systems.

These multidimensional PES imply a rich variety of different conical intersections in the various cations. For every pair of states (in a given system) the minimum energy of intersection has been computed according to expressions developed earlier [6], and the result is included as the corresponding off-diagonal entry in Table 4. There are various low-energy curve crossings (conical intersections) within the  $\tilde{X}$ - $\tilde{A}$  sets of states on one hand and within the  $\tilde{B}$ - $\tilde{C}$ - $\tilde{D}$  sets of states on the other hand. The minimum energy intersections are generally high for pairs of states from different sets, see Table 4. However, there is always one such pair with a low-energy curve crossing, namely the  $\tilde{A}$  and  $\tilde{C}$  states of the fluoro benzene cations. To test the possible importance of higher-order coupling terms and thus be even more precise in the location of the minimum of the intersection seams, unrestricted searches for these minima might be useful as recently proposed in [124, 125]. A preliminary calculation already yielded encouraging results.

**Table 4** Summary of important electronic energies, for the interacting states of the fluorobenzene radical cations including the quadratic coupling terms (QVC). The diagonal values represent the minima of the diabatic potential energies, off-diagonal entries are minima of the corresponding intersection seams. Three dots (...) indicate missing results

Benzene						mono-fluorobenzene					
	$\tilde{X}$	$\tilde{X}$	$\tilde{B}$	$\tilde{B}$	$\tilde{C}$		$\tilde{X}$	$\tilde{A}$	$\tilde{B}$	$\tilde{C}$	$\tilde{D}$
$\tilde{X}$	9.27	9.27	11.58	11.58	...	$\tilde{X}$	9.22	9.69	>16	12.84	>14
$\tilde{X}$	9.27	9.27	11.58	11.58	...	$\tilde{A}$		9.69	>15	12.29	>14
$\tilde{B}$			11.42	11.42	12.27	$\tilde{B}$			12.22	12.24	12.45
$\tilde{B}$			11.42	11.42	12.27	$\tilde{C}$				11.91	12.58
$\tilde{C}$					12.25	$\tilde{D}$					12.43
1,2-difluorobenzene						1,3-difluorobenzene					
	$\tilde{X}$	$\tilde{A}$	$\tilde{B}$	$\tilde{C}$	$\tilde{D}$		$\tilde{X}$	$\tilde{A}$	$\tilde{B}$	$\tilde{C}$	$\tilde{D}$
$\tilde{X}$	9.15	9.61	>16	>13	>13	$\tilde{X}$	9.35	9.70	>16	>14	>13
$\tilde{A}$		9.61	>16	12.70	>13	$\tilde{A}$		9.69	>16	13.67	>13
$\tilde{B}$			12.12	12.28	12.60	$\tilde{B}$			12.32	12.67	12.89
$\tilde{C}$				12.16	12.76	$\tilde{C}$				12.64	13.04
$\tilde{D}$					12.57	$\tilde{D}$					12.88
1,4-difluorobenzene						1,2,3-fluorobenzene					
	$\tilde{X}$	$\tilde{A}$	$\tilde{B}$	$\tilde{C}$	$\tilde{D}$		$\tilde{X}$	$\tilde{A}$	$\tilde{B}$	$\tilde{C}$	$\tilde{D}$
$\tilde{X}$	9.11	9.92	>16	>14	>16	$\tilde{X}$	9.45	9.62	>16	>15	>16
$\tilde{A}$		9.88	>16	13.09	>16	$\tilde{A}$		9.52	>16	14.85	>16
$\tilde{B}$			12.17	12.39	14.61	$\tilde{B}$			12.76	13.14	13.22
$\tilde{C}$				12.31	13.46	$\tilde{C}$				13.13	13.39
$\tilde{D}$					13.43	$\tilde{D}$					13.22

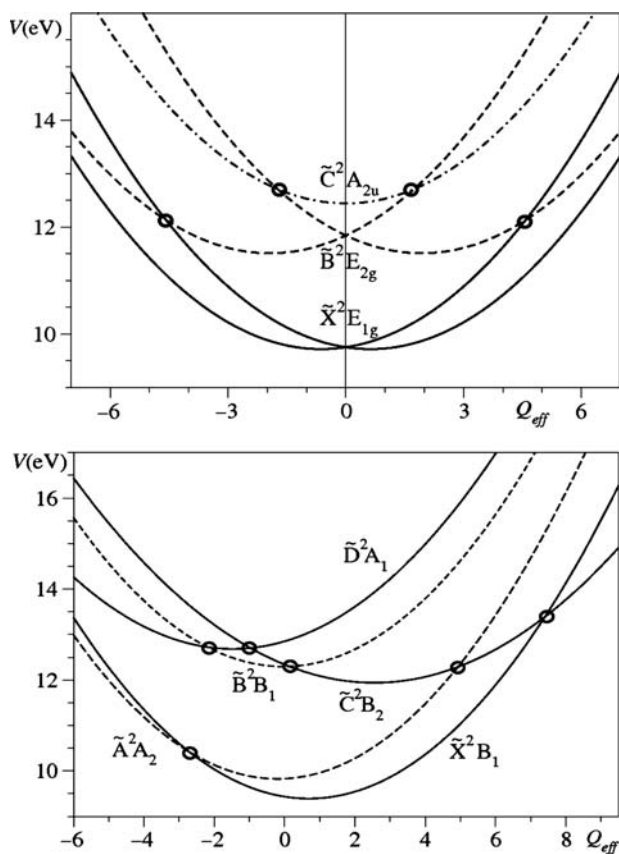


**Fig. 2** Representative cuts through the potential energy surfaces of  $\text{Bz}^+$  (upper panel or a) and its mono fluoro derivative,  $\text{F-Bz}^+$  (lower panel or b). The upper panel shows the results for the linear vibronic coupling model, while in the lower one the quadratic coupling terms are also included. In both panels the effective coordinate connects the centre of the Franck–Condon zone to the minimum of the intersection seam between the  $\tilde{A}$  and  $\tilde{C}$  states of  $\text{F-Bz}^+$ , and between the  $\tilde{X}$  and  $\tilde{B}$  states of the parent cation (within the subspace of JT active coordinates)

The  $\tilde{X}$ – $\tilde{A}$  conical intersections in the fluoro derivatives are the analogue of the JT conical intersection in the  $\tilde{X}^2E_{1g}$  state of the parent cation  $\text{Bz}^+$  (see also below). The latter is not indicated explicitly in Table 4 because only a single data row and column is provided for this doubly degenerate state (same as for the  $\tilde{B}^2E_{2g}$  state). We mention in passing that the diagonal entries have a slightly different meaning for this symmetric system in that the JT stabilization energy is included there (i.e. not only totally symmetric modes contribute).

To better visualize the situation, we present in Fig. 2 representative cuts through the PES of the benzene cation (Fig. 2a) as well as the monofluoro derivative (Fig. 2b). A linear combination of the normal coordinates of the JT active modes  $\nu_6 - \nu_8$  is chosen for the benzene cation and one of the totally symmetric modes for the monofluoro benzene cation. Both are defined to minimize the energy of the conical intersection between the  $\tilde{A}$  and  $\tilde{C}$  states of the monofluoro derivative, and between the  $\tilde{X}$  and  $\tilde{B}$  states of the parent cation (within the subspace of JT active coordinates). For the parent cation one identifies a low-energy inter-state curve crossing which is mediated by the multimode JT effect in the two degenerate electronic states. The latter is reflected by the symmetric crossing between the two lowest ( ${}^2E_{1g}$ ) potential energy curves in Fig. 2a which actually represents a cut through the multidimensional JT split PES in this state. These are the well-known Mexican hat PES of the  $E \otimes e$  JT effect. They are recovered also from the  ${}^2E_{2g}$  state curves in the figure.

We emphasize the analogy between the states exhibiting the  $\tilde{X}$ - $\tilde{B}$  crossing in  $Bz^+$  and the  $\tilde{A}$ - $\tilde{C}$  crossing in the monofluoro (as well as the other fluorinated) derivatives. This is apparent by inspecting Fig. 1 which shows that the electronic states indeed correlate with each other, e.g. by analogous bonding properties of the molecular orbitals. As a by-product there is indeed only one low-energy crossing between the PES from the two different sets ( $\tilde{X}$ - $\tilde{A}$  and  $\tilde{B}$ - $\tilde{C}$ - $\tilde{D}$ ) of electronic states (fluorobenzene cations), just as there is only one such pair of crossings between the  $\tilde{B}$ - $\tilde{C}$  states PES and those of the  $\tilde{X}$  state surfaces of  $Bz^+$ .

Figure 2 illustrates two main trends in the series of molecules. First, by the asymmetric substitution the JT effect in the parent cation ‘disappears’ in the fluoro derivatives; nevertheless, the shapes of their lowest two PES still resemble those of the parent cation, regarding the opposite slopes, the rather small energetic splitting at the origin  $Q = 0$ , and the presence of a low-energy conical intersection; therefore this has also been termed a replica of the JT intersection in  $Bz^+$ . This topological, or more ‘physical’ effect is complemented by the second, more ‘chemical’ effect, caused by the energetic increase of the second  $\pi$ -type IP by fluorination. This trend, already mentioned in relation to Fig. 1 above, is specially related to the substituents (F) atom and manifests itself in a growing separation of the  $\tilde{X}$ - $\tilde{A}$  and the  $\tilde{B}$ - $\tilde{C}$ - $\tilde{D}$  sets of states in Fig. 2. While the effect is rather moderate in Fig. 2b, it increases upon increasing fluorination and thus leads to a higher energy of the corresponding intersection, see Table 4 (also called inter-set crossing or intersection below). These two trends, caused by the substitution in general and fluorination in particular, will provide useful guidelines in the discussion of the dynamical results in Sect. 5.

Finally we point out that the results for the inter-set crossings depend crucially on the inclusion of the quadratic coupling constants for the totally symmetric modes. The latter lower them energetically, thus making them accessible to the nuclear motion following photoionization. They are included in the results of the present sub-section and also in all dynamical calculations on the fluoro derivatives reported below.

## 5 Quantum Dynamical Results

As stated above, the quantum dynamical calculations of this work focus on the vibronic structure of electronic transitions into the interacting sets of states (time-independent quantities) and on the electronic populations following such transitions (time-dependent quantities).

### 5.1 Photoelectron and mass analyzed threshold ionization (MATI) spectra

We start with the photoelectron spectroscopic studies on the benzene cation, and present in Fig. 3 the theoretical [126] and experimental [85] spectral intensity distributions for the first band, corresponding to the transition to the  $\tilde{X}^2E_{1g}$  ground electronic state of  $Bz^+$ . The computation follows the lines described above in Sects. 4,3, using ab initio data for the frequencies and coupling constants, and the Lanczos scheme for the solution of the vibronic eigenvalue problem. Given the good agreement between theory and experiment, the system is apparently very well described by the theoretical approach. Note that the two hot bands in Fig. 3 are not covered by the theoretical spectrum which has been computed for temperature  $T = 0$ . The vibronic structure reflects the multimode dynamical JT effect in the degenerate electronic state, as indicated by the two lowest (JT split) potential energy curves of Fig. 2a. The  $a_{1g}$  mode  $\nu_1$  (symmetric C–C stretching) and the linearly JT active  $e_{2g}$  modes  $\nu_6$ – $\nu_8$  are found to be noticeably excited in the band. (It should be remembered that the Wilson numbering is adopted here for easier correlation with the vibrational modes of the fluorinated derivatives. In our earlier work we have used Herzberg's notation [31, 126], where, for examples, the  $e_{2g}$  modes  $\nu_6$ ,  $\nu_7$ ,  $\nu_8$  are numbered as  $\nu_{18}$ ,  $\nu_{17}$ ,  $\nu_{16}$ , respectively.)

We point out that similar analyses and results have been performed and obtained also by other authors [33, 35, 38–40]. The spectral lines at 86 meV and 123 meV excitation energy in the theoretical spectrum correspond to excitation of the modes  $\nu_6$  and  $\nu_1$ , respectively. The first spacing deviates from the harmonic frequency of mode  $\nu_6$  in Table 3 because of the JT effect, while the second coincides with that of mode  $\nu_1$  because of the linear coupling scheme adopted. For higher excitation energies the lines represent an intricate mixture of the various modes because of the well-know nonseparability of modes in the multi-mode dynamical JT effect. Overall, the excitation of the various modes can be characterized as moderately weak. The total JT stabilization energy amounts to  $\sim 930\text{ cm}^{-1}$  and is dominated by the contribution of mode  $\nu_6$ . The barrier to pseudorotation is of the order of  $10\text{ cm}^{-1}$  only, consistent with the fact that the theoretical spectrum of Fig. 3 is obtained within the LVC scheme (see Sect. 2.1 above).

Because of limited space we confine ourselves here to the presentation of this single prototypical multi-mode dynamical JT system. However, investigations along

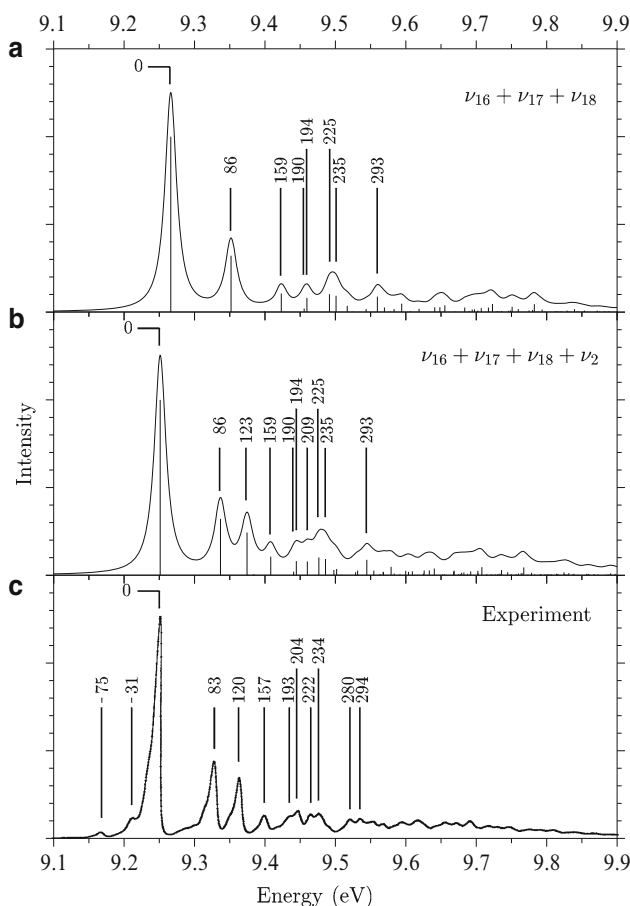


**Fig. 3** Comparison of experimental and theoretical results for the  $\tilde{X}$  band of the PE spectrum of benzene. (a) JT spectrum (with modes  $\nu_{16}$ – $\nu_{18}$ . (b) Same as (a) but with the additional mode,  $\nu_2$ . (c) Experimental PE spectrum. The numbering of the modes is according to Herzberg's notation (in Wilson notation, adopted otherwise in their work, these are the modes  $\nu_8$ – $\nu_6$ , respectively, while  $\nu_2$  is denoted as  $\nu_1$ )

similar lines, though more sophisticated in detail, have been performed also for the higher-energy bands of the photoelectron spectrum of benzene [31, 126]. These comprise, in particular, the strongly coupled  ${}^2E_{2g}$  and  ${}^2A_{2u}$  states, corresponding to the three higher-energy potential curves in Fig. 2a. Here, in addition to the multimode JT effect in the  ${}^2E_{2g}$  state, also strong PJT interactions with the nearby, nondegenerate  ${}^2A_{2u}$  state arise. The interplay between both coupling mechanisms leads to complex triple intersections between the underlying PES and to a combination of different types of nonadiabatic coupling effects in the corresponding PE spectral bands. Furthermore, the crossing between the  $\tilde{X}$ - and  $\tilde{B}$ -type PES (see Fig. 2a) and its implications on the nuclear dynamics have been addressed. While its impact on

the spectral intensity distribution proves to be only minor, the time-dependent electronic populations are affected strongly, see below. Finally, we mention that similar studies have been conducted also on the higher-energy  $^2E_{1u}$  and  $^2B_{2u}$  states of  $Bz^+$ , and the experimental PE spectrum in this energy range could be well reproduced in this way [31, 34, 85].

How are these features affected by the partial fluorination and the accompanying symmetry reduction? Figure 4 displays in comparison the experimental [71] MATI spectrum of 1,2-difluorobenzene and the theoretical [69] first PE band(s) of the same species. The associated PES turn out to be represented by cuts very similar to those in Fig. 2b. The dominating feature for low energies is the progression in mode  $\nu_{6a}$ . This agrees with experiment where this mode is labelled no.  $\nu_{10}$  according to Mulliken. Recalling that the analogous mode  $\nu_6$  was seen to dominate also the JT effect in the parent cation, we see that there is a structural similarity between

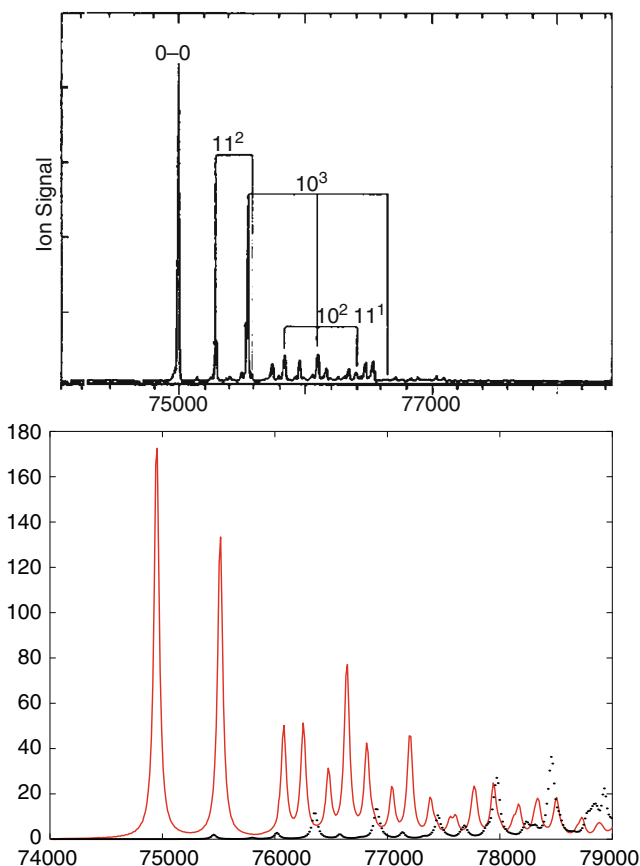


**Fig. 4** Comparison of first two calculated [69] bands of 1,2-difluorobenzene vs. experimental MATI spectrum [71] (*upper panel*). The energy units are in  $\text{cm}^{-1}$ . The two contributing bands  $\tilde{X}$  (*full line*) and  $\tilde{A}$  (*dotted line*) are drawn separately

the systems regarding the most active vibrational modes. For higher energies the vibrational excitation strength in the MATI spectrum is generally weaker than in the calculated spectrum. The experimental and theoretical intensities are, however, not directly comparable because the excitation is resonant through an intermediate state in the MATI spectrum, but assumed to be direct from the ground state of neutral fluorobenzene in the calculation. The resonant excitation in the MATI spectrum may be the reason why almost no spectral lines are observed above  $77,000\text{ cm}^{-1}$  excitation energy, where the  $\tilde{A}$  state spectral intensity is predicted to start in the calculation. This is somewhat unfortunate, because the theoretical spectral profile exhibits there marked irregularities characteristic for strong nonadiabatic couplings, and no vibrational quantum numbers can be assigned there any more. The latter is attributed to a low-energy conical intersection, visible as the curve crossing between the two lowest potential energy curves in Fig. 2b. As discussed in Sect. 4.2 the latter is the counterpart of the JT intersection in the  ${}^2E_{1g}$  ground state of  $\text{Bz}^+$ . Due to the resulting asymmetry of the lowest PES of the fluoro derivative, this is  $\sim 3,500\text{ cm}^{-1}$  above its ground state minimum, almost four times the JT stabilization energy in  $\text{Bz}^+$  mentioned above. The latter gives rise to an adiabatic energy regime (namely below the intersection) which allows an assignment of quantum numbers in the experimental MATI spectrum. Within the energy range of the  $\tilde{A}$  state the nonadiabatic effects dominate, and in this sense the  $\tilde{X}$ - $\tilde{A}$  system of states in the 1,2-difluoro derivative can be said to be a replica of the JT system in the parent cation. The analogy is further underlined by noting that also the dominating coupling modes  $\nu_{6b}$  and  $\nu_{8b}$  (see Table 3b) correlate with the JT active modes in  $\text{Bz}^+$ , (more explicitly, with their ‘other’ cartesian component, different from the one correlating with the totally symmetric modes  $\nu_{6a}$  and  $\nu_{8a}$ ). Very similar situations prevail in the monofluoro and 1,3-difluoro derivatives, which emphasizes the trend in the series [62, 68, 69, 71, 73]. Only for the 1,4-difluoro [68, 69, 72, 73, 127] isomer there is a larger vertical  $\tilde{X}$ - $\tilde{A}$  energy gap which leads to a larger adiabatic energy regime and weakens the analogy with the other fluorobenzene cations (see Table 4). For the 1,2,3-trifluoro case on the other hand, while the trend regarding the higher energy states is enhanced (see below), the  $\tilde{X}$ - $\tilde{A}$  energy gap is found to be very small which renders the situation again very similar to that in the parent cation.

The nonadiabatic coupling effects manifest themselves as irregularities in the spectral structures of Figs. 3 and 4. They are moderate because of relatively low excitation energies involved and a resulting rather sparse level structure. The effects are typically stronger when the excitation energies increase and so does the vibronic level density. Under low-to-moderate resolution a diffuse spectral profile results, because the highly irregular and very dense individual spectral lines cannot be resolved any more. An example is given in Fig. 5 which displays all 5 PE spectral bands of the monofluoro benzene cation [62].

The experimental and the upper theoretical panel show this diffuse structure with typically one ‘bump’ appearing for every electronic state (although for the states 3 and 4 they overlap so heavily that only a single one emerges, that is, only four ‘bumps’ result in total for the five electronic states). The lower panel with higher resolution gives an impression of the highly complex, irregular and dense underlying



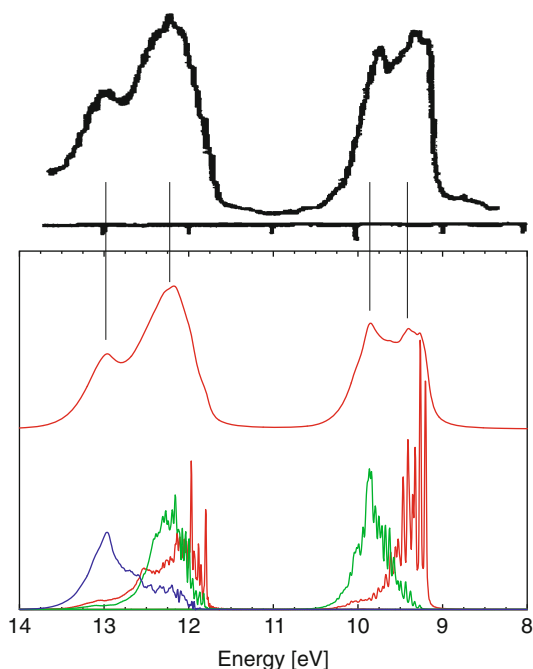


**Fig. 5** Comparison of theoretical[62] (*lower panel*) and experimental (*upper panel*) [70] photoelectron spectra of fluorobenzene. The linewidths of the theoretical spectra are FWHM=132 meV (*upper curve*) and 16 meV (*lower curve*). In the higher-resolution theoretical spectrum, the various electronic bands are drawn separately. Their ordering is (from *right to left*)  $\tilde{X}^2B_1$ ,  $\tilde{A}^2A_2$ ,  $\tilde{B}^2B_1$ ,  $\tilde{C}^2B_2$ , and  $\tilde{D}^2A_1$

line structure; it is not fully resolved even here because the resolution is still too limited except for the low-energy spectral regimes. (The calculation has been carried out here using the MCTDH scheme so that the spectral envelope is computed, no individual spectral lines.) This situation has been found typical for nonadiabatic motion on conically intersecting PES and is generalized here to multiply intersecting surfaces as displayed in Fig. 2. This holds especially for the three higher lying PES of the  $\tilde{B}$ - $\tilde{C}$ - $\tilde{D}$  states. The (coupled)  $\tilde{X}$ - $\tilde{A}$  state motion is affecting the coupled  $\tilde{B}$ - $\tilde{C}$ - $\tilde{D}$  state motion only weakly regarding the spectrum (as stated for benzene above). The importance of the coupling between the  $\tilde{X}$ - $\tilde{A}$  and  $\tilde{B}$ - $\tilde{C}$ - $\tilde{D}$  sets of states for the electronic population dynamics will be documented below.

## 5.2 Time-Dependent Electronic Population Dynamics

The theoretical studies of the spectral intensity distributions are complemented, and the insight gained is essentially augmented, by time-dependent investigations of the nonadiabatic nuclear dynamics. Here it should be recalled that the information

encoded in the spectrum is basically limited by the overlap with the initial wave packet, generated in the FC type transition at time  $t = 0$ , according to (31), (32). Furthermore it is inversely proportional to the available spectral resolution (see Sect. 3.2.2). In the case of photoelectron spectroscopy the latter alone amounts to typically several tens of femtoseconds. The full time-dependent wave-packet is apparently free of these limitations, and often the electronic populations alone carry substantial further information on the vibronic dynamics. All the results presented in this section have been computed using the MCTDH algorithm.

### The Benzene Radical Cation

In the preceding section we discussed the nonadiabatic coupling effects associated with the JT intersection in the  $\tilde{X}^2E_{1g}$  state, and with the JT and PJT intersections within/between the  $\tilde{B}^2E_{2g}$  and  $\tilde{C}^2A_{2u}$  states. Figure 2a reveals the further intriguing feature of a low-energy curve crossing between the  $\tilde{X}^2E_{1g}$  and  $\tilde{B}^2E_{2g}$  JT split PES of  $Bz^+$ . While this was found to have little impact on the spectral intensity distribution, it proves to be crucial for the time-dependent electronic populations [31]. Figure 6 shows the probability of being located on either the  $\tilde{X}$ ,  $\tilde{B}$  or  $\tilde{C}$  states of  $Bz^+$  after an initial vertical excitation to the highest of the PES in Fig. 2a. All five PES in the figure, that is, the JT effects in the two degenerate states and the PJT couplings between them, are included in the calculation. Given the degeneracies of the vibrational modes, this amounts to 10 nonseparable degrees of freedom and a size of the underlying ‘primitive grid’ (see Sect. 3.2 for more details) of  $10^{12}$  basis functions. This is reduced to  $\sim 10^6$  time-dependent single particle functions by the MCTDH contraction effect [81], thus rendering the calculations numerically feasible at all.

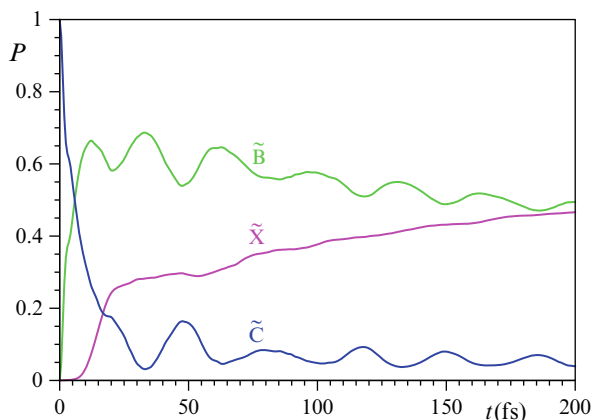


**Fig. 6** Population dynamics of the coupled  $\tilde{X}$  -  $\tilde{B}$  -  $\tilde{C}$  states of  $Bz^+$  for an initial wavepacket located on the  $\tilde{C}$  surface

The figure displays a femtosecond  $\tilde{B}/\tilde{C}$  population dynamics with an initial  $\tilde{C}-\tilde{B}$  nonradiative transition (i.e. internal conversion driven by the nonadiabatic interaction) of the order of 20 fs. This is roughly the same as that of the subsequent oscillations (30 fs) which in turn almost coincides with the period of the C–C stretching mode 1 (33 fs). This behaviour is typical for 2-state systems with conically intersecting PES, and reflects their ‘tuning’ behaviour along the normal coordinate of the C–C stretching mode. Nevertheless, the initial population decay is particularly fast here owing to the proximity of the intersection to the FC-point  $Q = 0$ . It turns out to be even faster when monitored in the adiabatic representation rather than in the diabatic one as done here [128].

The aforementioned features remain indeed the same when restricting the treatment to the two excited ( $\tilde{B}^2E_{2g}$  and  $\tilde{C}^2A_{2u}$ ) states. Including the coupling to the ground state leads additionally to an increase of the  $\tilde{X}$  state population on the order of 100–200 fs (and apparently to an accompanying decrease of the excited-state population). This directly reflects the  $\tilde{B}-\tilde{X}$  intersection visible as the curve crossing in Fig. 2a. We emphasize that this occurs (in this energy range) only by virtue of the multi-mode JT effect in the two degenerate electronic states, and the totally symmetric modes  $\nu_1$  and  $\nu_2$  are insufficient in this respect. This was a novel finding when first established in the literature [31, 129].

The time-scale in question (100–200 fs) does not render these nonadiabatic coupling effects of major importance for the photoelectron spectrum, see above. However, the associated nonradiative decay mechanism is crucial in understanding the fluorescence behaviour of  $Bz^+$ , which does not exhibit emission although the  $\tilde{C}-\tilde{X}$  transition is dipole-allowed. The sub-picosecond decay  $\tilde{B} / \tilde{C} - \tilde{X}$  documented in Fig. 6 is so fast that fluorescence cannot compete and the quantum yield is reduced below the detection threshold of  $\sim 10^{-4}$ . Further details on the fluorescence properties and their dependence on fluorination will be discussed in the Sect. 5.3 below. The details of the high-dimensional, multi-state dynamics underlying Fig. 6 are still far from understood, and their investigation is to be pursued in future work. Some aspects have been explored in [128], such as a comparison between adiabatic and diabatic electronic populations or the inspection of nuclear probability densities in suitable subspaces. Interestingly the suppression of the electronic and vibrational degeneracies does not affect the electronic populations very much. Also, the difference between the oscillatory  $\tilde{C}/\tilde{B}$  electronic populations on one hand and the monotonously increasing  $\tilde{X}$  state population on the other hand is noteworthy in the figure. This can be traced back to the different movement of the time-dependent wave packet regarding the various seams of conical intersections. Figure 7 shows suitable snapshots (contour lines) of the wave packet moving on the  $\tilde{B}$  state PES after the initial  $\tilde{C}-\tilde{B}$  nonradiative transition. The seams of intersection with the  $\tilde{C}$  and  $\tilde{X}$  state PES are indicated as straight lines, and the energy contours for the various PES are also included. As one can see, the wave packet crosses (at least partly) the  $\tilde{B}-\tilde{C}$  seam of intersections several times during its movements. The  $\tilde{B}-\tilde{X}$  seam, on the other hand is only approached, not crossed, and the distance from the seam changes only weakly during the movement of the wave packet. The

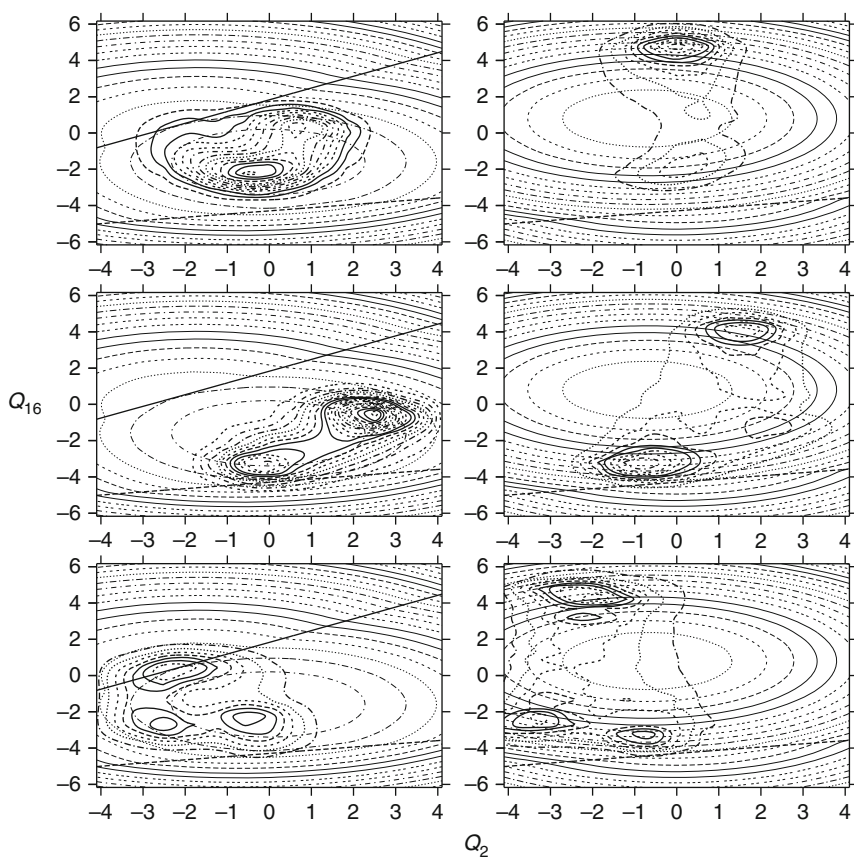


**Fig. 7** Diatomic reduced densities on the  $\tilde{B}$  and  $\tilde{X}$  surfaces (left and right panels, respectively) at  $t = 24, 33$  and  $51$  fs (from top to bottom). The solid (dashes) straight lines represent the seams of  $\tilde{C}-\tilde{B}$ -( $\tilde{B}-\tilde{X}$ ) conical intersections whose minima are located at  $Q_2 = -2.166, Q_8 = 0.430$  ( $Q_2 = 0.697, Q_8 = -4.127$ )

oscillatory behaviour of the electronic populations has indeed been correlated in earlier work with analogous oscillations of the adiabatic-to-diabatic mixing angle, and the latter in turn with those of the energy gap of the (diabatic) potential energy surfaces. Figure 6 shows nicely, indeed, that the  $\tilde{B}-\tilde{C}$  energy gap is a strongly oscillatory function of time whereas the  $\tilde{B}-\tilde{X}$  energy gap is not. This provides a simple rationale for the different behaviour of the electronic populations. For more details and further aspects of this entangled electronic and nuclear motion we refer to the original work [128].

## The Fluorobenzene Radical Cations

A further avenue of analysis is opened by partial substitution of hydrogens by fluoro-atoms, here mono-, di- and 1,2,3-fluorobenzene cations. Through the reduction of the molecular symmetry (without any symmetry-enforced degeneracies of the electronic states or vibrational modes) the JT effect formally disappears in these systems. One question of immediate interest is, whether in the absence of the JT effect in these derivatives, nevertheless some signatures of the JT-related dynamics remain. We recall first of all, that according to Fig. 2b there is a grouping of the electronic states into two sets, the first set comprising the  $\tilde{X}$  and  $\tilde{A}$  states, the second comprising the  $\tilde{B}-\tilde{C}-\tilde{D}$  states. This splitting has been also found for the difluoro isomers and 1,2,3-trifluorobenzene and correspond to the  $\tilde{X}$  and  $\tilde{B}-\tilde{C}$  states in the parent cation, respectively. To avoid an excessive number of drawings, we confine ourselves to the results of the wavepacket located initially in a coherent superposition of the three higher excited,  $\tilde{B}-\tilde{C}-\tilde{D}$ , electronic states. This again amounts to a broadband excitation, of sufficiently large coherence width to equally excite all PE spectral bands in the 12–14 eV energy range. The details about the initial preparation of the wavepacket on different intermediate states can be found in [62] and [68, 69] for the mono- and di-fluorobenzene cations, respectively. Results are presented in Fig. 8. As for the  $Bz^+$  we see a reach population dynamics proceeding on the fs time

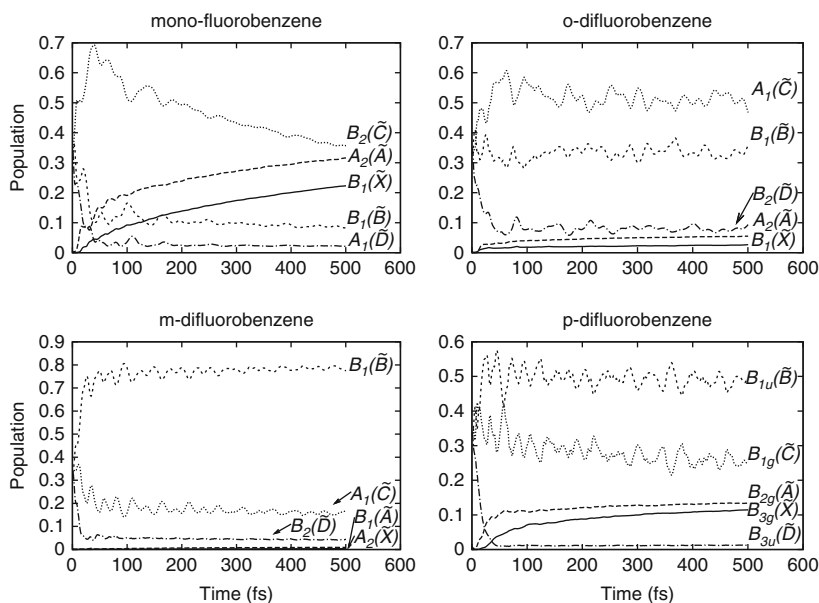


**Fig. 8** Electronic population dynamics of fluorobenzene isomers for initial preparation of the cation in a coherent superposition of the three higher excited electronic states. Results obtained with the adjusted IPs reported in Table 2

scale. Generally all five states become populated to a significant extent owing to the higher initial energy of the wave packet. The  $\tilde{D}$  state always becomes least likely populated as expected from its high energy. Its decrease in the series 1,2-, 1,3- and 1,4-difluorobenzene cations can be rationalized by density of states arguments and the increase of the diabatic minimum of this state in the same series (see Table 4). The diabatic minima for the  $\tilde{B}$  and  $\tilde{C}$  states also help to understand their different populations in Fig. 8: it is always the lower-energy state (at the diabatic minimum) which is more likely populated for long propagation times. This explains the different relative  $\tilde{B}$  and  $\tilde{C}$  state populations in the mono, 1,3- and 1,4- isomers, and their near equality in the 1,2- case. (Regarding the state numbering for the monofluoro and 1,4-difluorobenzene, we adhere to the ordering defined by the *adjusted* vertical IPs according to Table 1. For the ab initio values of the IPs the labelling  $\tilde{B}$  and  $\tilde{C}$  should be interchanged)

Of further interest is the transfer of population from the  $\tilde{B}$ - $\tilde{C}$ - $\tilde{D}$  to the  $\tilde{X}$ - $\tilde{A}$  group of states. As pointed out above, these two sets of states are far apart energetically in the center of the FC zone, but nevertheless interconnected through one conical intersection (namely  $\tilde{A}$ - $\tilde{C}$  states) which is low (mono, 1,2- and 1,4- isomers) or moderately high (1,3- and 1,2,3- isomers) in energy. This energetic trend, seen in Table 4, is again reflected in the population curves of Fig. 8. There the combined  $\tilde{X}/\tilde{A}$  population after  $\sim 500$  fs propagation time amounts to only  $\sim 3$  % for 1,3-difluorobenzene, but to  $\sim 50$ ,  $\sim 10$  % and  $\sim 25$  % for the mono, 1,2- and 1,4-difluorobenzene cations, respectively. Preliminary results of 1,2,3-trifluorobenzene reveal no population transfer to  $\tilde{X}$ - $\tilde{A}$  sets. The minimum energies of the intersections seams are 13.67, 12.29, 12.70 and 13.09 eV in the same series. Thus the difference between the 1,3- isomer, on one hand, and the mono, 1,2- and 1,4- isomers, on the other hand, is well reflected by these energetic data. The average populations stay fairly constant after  $\sim 100$  fs in the case of 1,2- and 1,3-difluorobenzene, but show a gradual decrease ( $\tilde{B}/\tilde{C}$ ) and increase ( $\tilde{X}/\tilde{A}$ ) for the mono and 1,4-difluorobenzene cations. The reason for this difference remains unclear at present, as is the case for the different oscillatory or fluctuating time dependences of the various populations. Apparently, the underlying complex and multidimensional dynamics still awaits a more detailed analysis and understanding. Some of this was explored recently for the parent cation,  $\text{Bz}^+$  [128]. The general trends of the electronic populations, and their relations to the respective energetic quantities, remain the same also for state-specific preparation of the initial wave-packet, and also for the purely ab initio vertical IPs.

### 5.3 Relation to fluorescence dynamics

Another more chemical line of reasoning is related to the ‘re-appearance’ of fluorescence for most of the fluoro derivatives with three or more fluorine atoms. There has been a plethora of work on emission spectra of halobenzene cations, with a goal of disclosing structural and dynamic properties of these species to a higher resolution

than is possible with PE spectroscopy. Emission spectra revealed many details on the electronic and geometrical structure, e.g. of trifluoro and hexafluoro benzene cations and their deuterated isotopomers [32, 43–51]. (For sufficiently symmetric structures this included, in particular, the study of the Jahn–Teller effect as an important vibronic phenomenon). Clear emission, nevertheless, is only observed for at least threefold fluorination of the parent cation,  $\text{Bz}^+$ . Only one of the three difluorobenzene cations, the 1,3-isomer, has been found to emit weakly [43]. For the monofluoro derivative, as for  $\text{Bz}^+$  itself [74, 75], no emission could be detected [43], imposing an upper limit for the quantum yield of fluorescence of  $10^{-4}$ – $10^{-5}$ . Given typical radiative lifetimes of  $10^{-8}$  s, these low quantum yields imply a sub-picosecond timescale for the radiationless deactivation of the electronically excited radical cations. The question arises whether and how the expected weakening of the inter-state coupling effects shows up in these species. For the parent system  $\text{Bz}^+$  itself, a detailed mechanism could be established in terms of the multimode dynamical JT effect in the  $\tilde{X}$  and  $\tilde{B}$  electronic states, which leads to a low-energy conical intersection between the corresponding potential energy surfaces (see subsection 5.2). Also it has been conjectured that the stabilization of the  $e_{2g}$  ( $\sigma$ ) orbital by fluorination leads to an increase of the corresponding ionization potential and a corresponding increase of the (minimum energy of) conical intersection, thus weakening the vibronic interactions and rendering the excited states long lived to make emission eventually (*i.e.*, for a sufficient degree of fluorination) observable [43].

This earlier conjecture is fully confirmed, regarding the general trends upon fluorination, by the present mechanism and results. The radiationless deactivation in the  $\text{Bz}^+$  is not a direct one (from the state where dipole-allowed transitions are possible, the  $\tilde{C}$  state, to the ground state) but involving the  $\tilde{B}$  state as an intermediate [30, 75]. Already for the monofluoro derivative, the two IPs deriving from the  $\sigma$  orbital of benzene (the  $\tilde{B}$  and  $\tilde{D}$  states of monofluoro benzene) are sufficiently high in energy so that their energetic ordering with the  $\pi$ -type IP is interchanged [53, 61, 62, 70]. For the three difluoro isomers and 1,2,3-trifluorobenzene, the shifts in energy are correspondingly more pronounced (see Table 2 and Fig. 1). Note that for the *ab initio* values of the IPs the labelling  $\tilde{B}$  and  $\tilde{C}$  should be interchanged for F- $\text{Bz}^+$  and 1,4-difluorobenzene cations. Correspondingly, already for the monofluoro derivative the  $\tilde{D}$ – $\tilde{X}$  internal conversion, competing with the strongly dipole-allowed transition, is much slower than in the parent cation [61, 62]. In the difluoro isomers and 1,2,3-trifluorobenzene this decay is further slowed down owing to the higher-energy vertical IPs and conical intersections as discussed above. A quantitative determination of the fluorescence quantum yield would require detailed consideration of longer time dynamics, which is beyond the scope of the present work. It should also be pointed out that the difluoro isomers represent a difficult case in that they are at the ‘borderline’ of either fluorescing or not, and differences between them will be quantitative rather than qualitative [69].

Nevertheless, the present electronic populations allow to draw important conclusions on the different emission properties of these six systems. As seen from Fig. 8 the internal conversion to the  $\tilde{X} + \tilde{A}$  states is indeed slowest, and inefficient also on an absolute scale, for the 1,3- isomer. We find it intriguing that emission has indeed

been observed for this species, but not for the others. For the  $\text{F-Bz}^+$  and 1,4 isomer, on the other hand the  $\tilde{X} + \tilde{A}$  populations keep increasing after 500 fs and may be expected to dominate after several ps. This behaviour is expected to suppress fluorescence, in accord with the experimental results. Only for the 1,2- isomer the situation is somewhat less clear. However, other modes, not included in the present treatment, may further enhance the  $\tilde{X} + \tilde{A}$  populations and thus be consistent with the absence of fluorescence in the ortho isomer.

Additional evidence comes from the consideration of the dipole transition matrix elements. As mentioned above, the transition from the  $\sigma$ -type state of the benzene cation to the ground state is dipole forbidden [30,75]. For the difluoro derivatives the molecular symmetry is reduced and the selection rules are relaxed [69]. Given that the components of the electric dipole operator transform (in the  $C_{2v}$  point group) as:

$$\Gamma_{\mu} = A_1 + B_1 + B_2, \quad (36)$$

one sees that there is always one component of the  $\sigma$ -type ( $\tilde{C} + \tilde{D}$ ) states that has a finite dipole matrix element for transitions to one component of the lower  $\pi$ -type ( $\tilde{X} + \tilde{A}$ ) states, at least for the  $C_{2v}$  molecular point group. All relevant dipole transition matrix elements for the states in question and all fluoro derivatives considered in the present study, using the same method (EOM-CCSD/TZ2P) are listed in Table 5. One sees that there are indeed nonzero entries due to the reduction in symmetry. However they are all smaller by 2–3 orders of magnitude than those for the  $\tilde{B} - (\tilde{X} + \tilde{A})$  transition corresponding to the dipole-allowed transition in the case of  $\text{Bz}^+$ . Thus, the  $\pi$ -type electronic state is the ‘emitting’ state also for the fluorobenzene cations. Its total oscillator strength is almost the same for all five systems. Comparing again the various populations of Fig. 8 we find that the  $\tilde{B}$  state of 1,3-difluorobenzene is indeed more populated after 300–500 fs (probability 0.75–0.8) than the  $\tilde{B}$  state of 1,2-, 1,4-difluorobenzene and  $\text{F-Bz}^+$  (probability  $\sim 0.35$ ,  $\sim 0.45$ – $0.5$  and  $\sim 0.1$ , respectively). Thus, according to both criteria (dipole matrix elements and purely energetic grounds) we find that the conditions to find emission are most favorable for the 1,3- isomer. According to our preliminary results of 1,2,3-trifluorobenzene, there is no population transfer to the  $\tilde{X}$ - $\tilde{A}$  set regarding the high energy seam minima of the conical intersections connecting the  $\tilde{X}$ - $\tilde{A}$  and  $\tilde{B}$ - $\tilde{C}$ - $\tilde{D}$  sets. This agrees with the observations [43]. It demonstrates that the internal conversion mechanism considered here, namely multiple conical intersections involving one of the  $\sigma$ -type electronic states of benzene and its fluoro derivatives, is of key importance to the fluorescence dynamics in this family of compounds.

## 6 Summary and Outlook

In this article we have given an overview over our theoretical studies on the multi-mode multi-state vibronic interactions in the benzene cation and several of its fluoro derivatives. These are all associated with multiple conical intersections between the



**Table 5** Oscillator strengths of electronic dipole transitions between the five lowest electronic states of the fluorinated benzene cations. An empty entry (—) means that the quantity vanishes by symmetry

		$\tilde{\mathbf{B}}$	$\tilde{\mathbf{C}}$	$\tilde{\mathbf{D}}$
<i>Mono</i>	$\tilde{\mathbf{X}}$	0.0935	—	0.000
	$\tilde{\mathbf{A}}$	0.0552	0.000	—
1, 2	$\tilde{\mathbf{X}}$	0.0999	0.0001	—
	$\tilde{\mathbf{A}}$	0.0644	—	0.0001
1, 3	$\tilde{\mathbf{X}}$	0.1002	—	0.0002
	$\tilde{\mathbf{A}}$	0.0641	0.000	—
1, 4	$\tilde{\mathbf{X}}$	0.1282	—	—
	$\tilde{\mathbf{A}}$	0.0474	—	0.000
1, 2, 3	$\tilde{\mathbf{X}}$	0.0889	—	0.000
	$\tilde{\mathbf{A}}$	0.0907	0.0002	—

underlying PES, which are in turn related to the JT effects in degenerate states (in the parent cation), to the PJT effects involving degenerate and nondegenerate states (in the parent cation) or to vibronic coupling effects involving nearby nondegenerate states (in the – less symmetric – fluoro derivatives). Typical nonadiabatic effects like complex spectral structures and an ultrafast electronic population decay have been identified and thus been generalized from the familiar case of two to several interacting states, with multiple conical intersections. We point out that in such situations the coupling modes are generally different for different pairs of interacting states, and the topologies of the high-dimensional conical intersections become also correspondingly complex.

Apart from the multi-state nature of the vibronic coupling, it is their evolution in the series of related molecules that has been of considerable interest in this work. The more physical and more chemical effects of partial fluorination have been distinguished. The former consist in the reduction of symmetry which leads to the disappearance of the JT effect in the mono- and difluoro, and in the 1,2,3-trifluoro derivatives. Here we have demonstrated that this leads to quantitative, rather than qualitative, changes and transforms the JT effect in the parent cation to more generic vibronic coupling problems, with strong interactions and nonadiabatic effects remaining, at least for higher vibronic energies. The latter, more chemical effect consists in a systematic increase of the  $\sigma$ -type vertical IPs in the fluorinated derivatives which leads to a corresponding increase of the conical intersection between the two lower and the three higher electronic states of the radical cations. This weakens the accompanying interactions and the strength of the electronic population transfer of these higher states to the two lowest states. It nicely correlates with the appearance of emission for increasing fluorination of the cations. It also corroborates the present mechanism for the interaction of the emissive ( $\pi$ ) state with the electronic ground state: there is no significant direct coupling between these states, which could indeed not explain the dependence on fluorination, but only an indirect coupling through the  $\sigma$  states which explains the observed trends.

Computationally, the present approach rests on the QVC coupling scheme in conjunction with coupled-cluster electronic structure calculations for the vibronic Hamiltonian, and on the MCDTH wave packet propagation method for the nuclear dynamics. In combination, these are powerful tools for studying such systems with 10–20 nuclear degrees of freedom. (This holds especially in view of so-called multi-layer MCTDH implementations which further enhance the computational efficiency [130, 131].) If the LVC or QVC schemes are not applicable, related variants of constructing diabatic electronic states are available [132, 133], which may extend the realm of application from the present spectroscopic and photophysical also to photochemical problems. Their feasibility and further applications remain to be investigated in future work.

**Acknowledgements** The authors are grateful to Prof. L. S. Cederbaum, Prof. H.-D. Meyer, Dr. I. Bâldea and Dr. E. Gromov for useful discussions. This work has been supported financially by the Deutsche Forschungsgemeinschaft through the Graduiertenkolleg 850 ‘Modeling of Molecular Properties’.

## References

1. R. Englman, *The Jahn-Teller Effect in Molecules and Crystals* (Wiley-Interscience, New York, 1972)
2. I.B. Bersuker, *The Jahn–Teller Effect* (Cambridge University Press, Cambridge, 2006)
3. H.A. Jahn, E. Teller, Proc. R. Soc. Lond. Ser. A **161** 220 (1937)
4. G. Fischer, *Vibronic Coupling* (Academic, San Diego CA, 1984)
5. I.B. Bersuker, *Vibronic Interactions in Molecules and Crystals* (Springer, Berlin, 1989)
6. H. Köppel, W. Domcke, L.S. Cederbaum, Adv. Chem. Phys. **57** 59 (1984)
7. M. Klessinger, J. Michl, *Excited States and Photochemistry of Organic Molecules* (VCH Publishers, New York, 1995)
8. T.A. Barckholtz, T. Miller, Int. Rev. Phys. Chem. **17** 435 (1998)
9. E.R. Davidson, W.T. Borden, J. Phys. Chem. **87** 4783 (1983)
10. D.R. Yarkony, Rev. Mod. Phys. **68** 985 (1996)
11. D.R. Yarkony, Acc. Chem. Res. **31** 511 (1998)
12. F. Bernardi, M. Olivucci, M. Robb, Chem. Soc. Rev. **25** 321 (1996)
13. Y. Haas, M. Klessinger, S. Zilberg, Chem. Phys. **259** 121 (2000)
14. W. Domcke, D.R. Yarkony, H. Köppel (eds.), *Conical Intersections: Electronic Structure, Dynamics and Spectroscopy* (Word Scientific, Singapore, 2004)
15. M. Robb, F. Bernardi, M. Olivucci, Pure Appl. Chem. **67** 783 (1995)
16. H.C. Longuet-Higgins, U. Öpik, M.H. Pryce, R.A. Sack, Proc. R. Soc. A **244** 1 (1958)
17. G. Herzberg, H.C. Longuet-Higgins, Discuss. Faraday Soc. **35** 77 (1963)
18. H.C. Longuet-Higgins, Adv. Spectrosc. **3** 429 (1961)
19. B.R. Judd, J. Chem. Phys. **67** 1174 (1977)
20. H. Köppel, W. Domcke, W. von Niessen, L.S. Cederbaum, Mol. Phys. **35** 1283 (1978)
21. C. Woywod, S. Scharfe, R. Krawczyk, W. Domcke, H. Köppel, J. Chem. Phys. **118** 5880 (2003)
22. J. Schmidt-Klügmann, H. Köppel, S. Schmatz, P. Botschwina, Chem. Phys. Lett. **369** 21 (2003)
23. N. Sakamoto, J. Phys. Soc. Jpn **51** 1516 (1982)
24. H. Barentzen, O.E. Polansky, J. Chem. Phys. **68** 4398 (1978)
25. H. Barentzen, G. Olbrich, M.C.M.O. Brien, J. Phys. A **14** 111 (1981)

26. J.C. Slonczewski, Phys. Rev. **15** 1596 (1963)
27. M.C.M. O'Brien, S.N. Evangelou, Solid State Commun. **36** 29 (1980)
28. S. Faraji, H. Köppel, W. Eisfeld, S. Mahapatra, Chem. Phys. **347** 110 (2008)
29. A.B. Trofimov, H. Köppel, J. Schirmer, J. Chem. Phys. **109** 1025 (1998)
30. M. Döschel, H. Köppel, P. Szalay, J. Chem. Phys. **117** 2645 (2002)
31. H. Köppel, I.M. Döschel, Baldea, H.D. Meyer, P. Szalay, J. Chem. Phys. **117** 2657 (2002)
32. T. Miller, V.E. Bondybey, *Molecular Ions: Spectroscopy, Structure and Chemistry* (North-Holland, Amsterdam, 1983)
33. J. Eiding, R. Schneider, W. Domcke, H. Köppel, W. von Niessen, Chem. Phys. Lett. **177** 345 (1991)
34. H. Köppel, L.S. Cederbaum, W. Domcke, J. Chem. Phys. **89** 2023 (1988)
35. K. Müller-Dethlefs, J.B. Peel, J. Chem. Phys. **111** 10550 (1999)
36. H. Köppel, Chem. Phys. Lett. **205** 361 (1993)
37. M. Döschel, H. Köppel, Chem. Phys. **225** 93 (1997)
38. P.M. Johnson, J. Chem. Phys. **117** 9991 (2002)
39. P.M. Johnson, J. Chem. Phys. **117** 10001 (2002)
40. B.E. Applegate, T.A. Miller, J. Chem. Phys. **117** 10654 (2002)
41. C.H. Kwon, H.L. Kim, M.S. Kim, J. Chem. Phys. **116** 10361 (2002)
42. W. Price, A. Potts, T. Williams, Chem. Phys. Lett. **37** 17 (1976)
43. M. Allan, J.P. Maier, O. Marthaler, Chem. Phys. **26** 131 (1977)
44. C. Cossart-Magos, D. Cossart, S. Leach, Mol. Phys. **37** 793 (1979)
45. C. Cossart-Magos, D. Cossart, S. Leach, Chem. Phys. **41** 375 (1979)
46. V.E. Bondybey, T.J. Sears, J.H. English, T.A. Miller, J. Chem. Phys. **73** 2063 (1980)
47. T.J. Sears, T.A. Miller, V.E. Bondybey, J. Am. Chem. Soc. **103** 326 (1981)
48. C. Cossart-Magos, D. Cossart, S. Leach, J.P. Maier, L. Misev, J. Chem. Phys. **78** 3673 (1983)
49. G. Dujardin, S. Leach, J. Chem. Phys. **79** 658 (1983)
50. D. Klapstein, S. Leutwyler, J.P. Maier, Mol. Phys. **51** 413 (1984)
51. D. Winkoun, D. Champoulaud, G. Dujardin, S. Leach, Can. J. Phys. **62** 1361 (1984)
52. K. Walter, K. Schern, U. Boesl, J. Phys. Chem. **95** 1188 (1991)
53. R. Anand, J.E. LeClaire, P.M. Johnson, J. Phys. Chem. A **1999** 2618 (1999)
54. A. Potts, W. Price, D. Streets, T. Williams, Discuss. Faraday Soc. **54** 168 (1972)
55. C. Brundle, M. Robin, N. Kuebler, J. Am. Chem. Soc. **94** 1466 (1972)
56. D. Davies, D. Shirley, T. Thomas, J. Am. Chem. Soc. **94** 6565 (1972)
57. D. Clark, D. Kilcast, D. Adams, W. Musgrave, J. Electron Spectrosc. **1** 227 (1973)
58. R. Gilbert, C. Sandorfy, Chem. Phys. Lett. **27** 457 (1974)
59. B. Narayan, J. Murrell, Mol. Phys. **19** 169 (1970)
60. I. Bâldea, J. Franz, H. Köppel, J. Mol. Struct. **838** 94 (2007)
61. I. Bâldea, J. Franz, P. Szalay, H. Köppel, Chem. Phys. **329** 65 (2006)
62. E. Gindensperger, I. Bâldea, J. Franz, H. Köppel, Chem. Phys. **338** 207 (2007)
63. V.P. Vysotsky, G.E. Salnikov, L.N. Shchegoleva, Int. J. Quantum Chem. S **100** 469 (2004)
64. H. Köppel, in *Conical Intersections, Advanced Series in Physical Chemistry*, vol. 15, ed. by W. Domcke, D.R. Yarkony, H. Köppel (World Scientific, Singapore, 2004), pp. 429–472
65. M.H. Perrin, M. Gouterman, J. Chem. Phys. **46** 1019 (1967)
66. J.H. van der Waals, A.M.D. Berghuis, M.S. de Groot, Mol. Phys. **13** 301 (1967)
67. M.Z. Zgierski, M. Pawlikowski, J. Chem. Phys. **70** 3444 (1979)
68. S. Faraji, H. Köppel, J. Chem. Phys. **129** 074310 (2008)
69. S. Faraji, H.D. Meyer, H. Köppel, J. Chem. Phys. **129** 074311 (2008)
70. G. Bieri, L. Asbrink, W. von Niessen, J. Electron Spectrosc. Relat. Phenom. **23** 281 (1981)
71. C.H. Kwon, H.L. Kim, M.S. Kim, J. Chem. Phys. **118** 6327 (2003)
72. Y. Tsuchiya, M. Fujii, M. Ito, Chem. Phys. Lett. **168** 173 (1990)
73. Y. Tsuchiya, K. Takazawa, M. Fujii, M. Ito, J. Phys. Chem. **96** 99 (1992)
74. J.P. Maier, *Kinetics of Ion-Molecule Reactions* (Plenum Press, New York, 1979)
75. O. Braithart, E. Castellucci, G. Dujardin, S. Leach, J. Phys. Chem. **87** 4799 (1983)
76. M. Nooijen, J.G. Snijders, Int. J. Quantum Chem. S **26** 55 (1992)
77. J.F. Stanton, J. Gauss, J. Chem. Phys. **101** 8938 (1994)

78. J.F. Stanton, R.J. Bartlett, *J. Chem. Phys.* **98** 7029 (1993)
79. H.D. Meyer, U. Manthe, L.S. Cederbaum, *Chem. Phys. Lett.* **165** 73 (1990)
80. U. Manthe, H.D. Meyer, L.S. Cederbaum, *J. Chem. Phys.* **97** 3199 (1992)
81. M. Beck, A. Jäckle, G.A. Worth, H.D. Meyer, *Phys. Rep.* **324** 1 (2000)
82. H.D. Meyer, G.A. Worth, *Theor. Chem. Acc.* **109** 251 (2003)
83. H. Köppel, W. Domcke, in *Encyclopedia of Computational Chemistry*, ed. by P. von Ragué Schleyer (Wiley, New York, 1998), p. 3166
84. L. Karlsson, L. Mattsson, R. Jadrny, T. Bergmark, K. Siegbahn, *Physica Scr.* **14** 230 (1976)
85. P. Baltzer, L. Karlsson, B. Wannberg, G. Öhrwall, D.M.P. Holland, M.A. Mac Donald, M.A. Hayes, W. von Niessen, *Chem. Phys.* **224** 95 (1997)
86. H.C. Longuet-Higgins, *Proc. R. Soc. London A* **344** 147 (1975)
87. W. Lichten, *Phys. Rev.* **131**. (1963); **139**, A27 (1965); **164**, 131 (1967)
88. F.T. Smith, *Phys. Rev.* **179** 111 (1969)
89. T.F. O'Malley, *Adv. At. Mol. Phys.* **7** 223 (1971)
90. A. Thiel, H. Köppel, *J. Chem. Phys.* **110** 9371 (1999)
91. T. Pacher, L.S. Cederbaum, H. Köppel, *Adv. Chem. Phys.* **84** 293 (1993)
92. C.A. Mead, D.G. Truhlar, *J. Chem. Phys.* **77** 6090 (1982)
93. G. Herzberg, *Molecular Spectra and Molecular Structure* (Van Nostrand, New York, 1945)
94. E.B. Wilson Jr., J.C. Decius, P.C. Cross, *Molecular Vibrations* (McGraw-Hill, New York, 1955)
95. G. Lembach, B. Brutschy, *J. Phys. Chem.* **100** 19758 (1996)
96. L.S. Cederbaum, W. Domcke, *Adv. Chem. Phys.* **36** 205 (1977)
97. W. von Niessen, J. Schirmer, L.S. Cederbaum, *Comput. Phys. Rept.* **1** 57 (1984)
98. L.S. Cederbaum, *J. Phys. B* **8** 290 (1975)
99. W. von Niessen, L.S. Cederbaum, W. Domcke, *Excited States in Quantum Chemistry* (Reidel, Dordrecht, 1978), p. 183
100. J. Eiding, R. Schneider, W. Domcke, H. Köppel, W. von Niessen, *Chem. Phys. Lett.* **177** 345 (1991)
101. Gaussian94, 2nd edn. M.J. Frisch, G.W. Trucks, H.B. Schlegel, P.M.W. Gill, B.G. Johnson, M.A. Robb, J.R. Cheeseman, T. Keith, G.A. Petersson, J.A. Montgomery, K. Raghavachari, M. A. Al-Laham, V. G. Zakrzewski, J.V. Ortiz, J.B. Foresman, J. Cioslowski, B.B. Stefanov, A. Nanayakkara, M. Challacombe, C.Y. Peng, P.Y. Ayala, W. Chen, M.W. Wong, J.L. Andres, E.S. Replogle, R. Gomperts, R.L. Martin, D.J. Fox, J.S. Binkley, D.J. Defrees, J. Baker, J.P. Stewart, M. Head-Gordon and C. Gonzalez and J.A. Pople., *Gaussian, Inc.*, Wallingford CT (1994).
102. M. Nooijen, J.G. Snijders, *Int. J. Quantum Chem. S* **48** 15 (1993)
103. M. Nooijen, J.G. Snijders, *J. Chem. Phys.* **102** 1681 (1995)
104. J.F. Stanton, J. Gauss, *J. Chem. Phys.* **103** 1064 (1995)
105. T.H. Dunning, Jr., P.J. Hay, in *Methods of Electronic Structure Theory*, vol. 2, ed. by H.F. Schaefer III (Plenum Press, New York, 1977)
106. O. Christiansen, J. Stanton, J. Gauss, *J. Chem. Phys.* **108** 3987 (1998)
107. T.H. Dunning, *J. Chem. Phys.* **55** 716 (1971)
108. P. Szalay, J.F. Stanton, R.J. Bartlett, *Chem. Phys. Lett.* **193** 573 (1992)
109. J. F. Stanton, J. Gauss, J. D. Watts *et al.* ACES II Mainz-Austin-Budapest version; integral packages: MOLECULE (J. Almlöf and P. R. Taylor); PROPS (P. R. Taylor); ABACUS (T. Helgaker, H. J. Aa. Jensen, P. Jørgensen, and J. Olsen); current version see <http://www.aces2.de>
110. E.J.H.V. Schaick, H.J. Geise, F.C. Mijlthoff, G. Renes, *J. Mol. Struct.* **16** 389 (1973)
111. G.J.D. Otter, J. Gerritsen, C. MacLean, *J. Mol. Struct.* **16** 379 (1973)
112. A. Domenicano, G. Schultz, I. Harigittai, *J. Mol. Struct.* **78** 97 (1982)
113. G.A. Worth, H.D. Meyer, L.S. Cederbaum, *J. Chem. Phys.* **105** 4412 (1996)
114. H.D. Meyer, F. Gatti, G.A. Worth, *Multidimensional Quantum Dynamics: MCTDH Theory and Applications* (Wiley-VCH, Weinheim, 2009)
115. C. Lanczos, *J. Res. Nat. Bur. Stand.* **45** 255 (1950)

116. Jane K. Cullum and Ralph A. Willoughby, *Lanczos Algorithms for Large Symmetric Eigenvalue Computations*, Birkhäuser, Boston (1985)
117. G.A. Worth, H.D. Meyer, L.S. Cederbaum, J. Chem. Phys. **109** 3518 (1998)
118. U. Manthe, A.D. Hammerich, Chem. Phys. Lett. **211** 7 (1993)
119. R. Schinke, *Photodissociation Dynamics* (Cambridge University Press, Cambridge, 1991)
120. U. Manthe, H.D. Meyer, L.S. Cederbaum, J. Chem. Phys. **97** 9062 (1992)
121. V. Engel, Chem. Phys. Lett. **189** 76 (1992)
122. A.J. Jerri, *The Gibbs Phenomenon in Fourier Analysis, Splines and Wavelet Approximations* (Kluwer, New York, 1998)
123. A. Raab, G.A. Worth, H.D. Meyer, L.S. Cederbaum, J. Chem. Phys. **110** 936 (1999)
124. M. Dallos, H. Lischka, R. Shepard, D.R. Yarkony, P.G. Szalay, J. Chem. Phys. **120** 7330 (2004)
125. R.A. Young, D.R. Yarkony, J. Chem. Phys. **125** 234301 (2006)
126. H. Köppel, I. Baldea, P. Szalay, Adv. Quantum Chem. **44** 199 (2003)
127. E. Sekreta, K.S. Viswanathan, J.P. Reilly, J. Chem. Phys. **90** 5349 (1989)
128. H. Köppel, I. Baldea, J. Chem. Phys. **124** 064101 (2006)
129. H. Köppel, I. Baldea, P.G. Szalay, Adv. Quantum Chem. **44** 200 (2003)
130. H. Wang, M. Thoss, J. Chem. Phys. **107** 2126 (2003)
131. U. Manthe, J. Chem. Phys. **128** 164116 (2008)
132. H. Köppel, J. Gronki, S. Mahapatra, J. Chem. Phys. **115** 2377 (2001)
133. H. Köppel, B. Schubert, Mol. Phys. **104** 1069 (2006)

# On the Vibronic Interactions in Aromatic Hydrocarbon Radicals and Radical Cations

V. Sivaranjana Reddy and S. Mahapatra

**Abstract** The study of the fate of electronically excited radical and radical cation of aromatic hydrocarbons is an emerging topic in modern chemical dynamics. Observations like low quantum yield of fluorescence and photostability are of immediate concern to unravel the mechanism of ultrafast nonradiative internal conversion dynamics in such systems. The radical cations of polycyclic aromatic hydrocarbons (PAHs) have received considerable attention in this context and invited critical measurements of their optical spectroscopy in a laboratory, in striving to understand the enigmatic diffuse interstellar bands (DIBs).

The Born–Oppenheimer (BO) approximation breaks down owing to the feasibility of crossings of electronic states of polyatomic molecules. These crossings lead to conical intersections of electronic potential energy surfaces (PESs), which are proved to be the bottleneck in the photophysical/chemical processes in those systems. Understandably, a concurrent treatment of electronic and nuclear motions is required to explore the excited state dynamics of polyatomic systems. Motivated by the new experimental measurements, we recently carried out *ab initio* quantum dynamical studies on phenyl radical ( $\text{Ph}^\bullet$ ) and phenylacetylene radical cation ( $\text{PA}^{\bullet+}$ ) and established nonadiabatic interactions in their low-lying electronic states. These are the derivatives of the Jahn–Teller active benzene molecule, and are precursors of formation of PAHs. Employing a general vibronic coupling scheme, the ultrafast decay of their electronic states through successive conical intersections was studied by us recently. More specifically, the electronic ground  $\tilde{X}^2A_1$  state of  $\text{Ph}^\bullet$  is energetically well separated from its excited  $\tilde{A}^2B_1$  and  $\tilde{B}^2A_2$  states, and the nuclear dynamics in this state follow the adiabatic BO mechanism. In contrast, the  $\tilde{A}^2B_1$  and  $\tilde{B}^2A_2$  states are very close in energy ( $\sim 0.57$  eV spaced vertically at the equilibrium configuration of the reference phenide anion) and low-lying conical intersections are discovered which drive the nuclear dynamics via nonadiabatic paths. An ultrafast nonradiative decay rate of  $\sim 30$  fs of the  $\tilde{B}$  state is estimated. In  $\text{PA}^{\bullet+}$  both the long-lived and short-lived electronic states are discovered. The resolved structures of the vibronic bands are compared with the experimental photoelectron, mass analyzed threshold ionization and photoinduced Rydberg ionization spectroscopy data. The diffused structure of vibronic band for the  $\tilde{A}$  state of the radical cation is attributed to an ultrafast decay ( $\sim 20$  fs) to the electronic ground state.

Benchmark ab initio quantum dynamical studies are carried out for the prototypical naphthalene and anthracene radical cations of the PAH family aiming to understand the vibronic interactions and ultrafast decay of their low-lying electronic states. The broadening of vibronic bands and ultrafast internal conversion through conical intersections in the  $D_0 - D_1 - D_2$  electronic states of these species is examined in conjunction with the experimental results. The results demonstrate the crucial role of electronic nonadiabatic interactions to understand their low quantum yield of fluorescence and photostability and adds to the understanding of DIBs.

## 1 Introduction

Understanding the fate of excited electronic states continues to be a challenging problem in the current research in the photo-physics/chemistry of aromatic hydrocarbons. The crossing of electronic states of diatomic molecules is generally restricted by the von Neumann and Wigner's "non crossing rule" [1]. However, the same does not apply to polyatomic molecules due to the availability of two or more nuclear degrees of freedom. Unraveling the crossings of polyatomic molecular electronic states is a notoriously difficult task and has been considered in contemporary chemical dynamics with renewed vigor [2]. These crossings lead to the vibronic coupling of molecular electronic states and open up numerous pathways for the nuclei to move. A crucial and immediate consequence of this coupling is a breakdown of the founding adiabatic Born–Oppenheimer (BO) approximation of molecular quantum mechanics [3], endowing a concurrent motion of electrons and nuclei in polyatomic molecular systems.

The vibronic coupling, a coupling of electron and nuclear motion, is inherent to the Jahn–Teller (JT) active molecular electronic states. In this case the symmetry enforced electronic degeneracy is split by suitable symmetry-reducing nuclear vibrations [4]. The JT-split component electronic states form, what is popularly known as *conical intersections* (CIs) at the original undistorted equilibrium configuration of the molecule [5]. Besides the JT systems, symmetry allowed and accidental CIs are ubiquitous in polyatomic molecular systems [2, 6–8]. CIs of electronic PESs are established to be the paradigm of triggering strong nonadiabatic effects leading to various ultrafast molecular processes [2].

In recent years aromatic hydrocarbon radicals and radical cations occupy the center stage in the research on the structure and dynamics of excited electronic states [9–14]. In particular, the benzenoid systems and polycyclic aromatic hydrocarbons (PAHs) have received considerable attention by experimentalists because of their fundamental and practical importance in the chemistry of the earth and interstellar media. Striking efforts are being made to unravel their electronic state ordering, life time of excited electronic states and the vibrational energy level spectrum at higher energy resolution using a variety of energy and time-resolved experimental techniques [11–16].

Benchmark theoretical studies to elucidate the complex vibronic coupling in the low-lying electronic states of these systems and the mechanistic details of the nuclear dynamics are also emerging in recent years [17–21]. The large number of electronic and nuclear degrees of freedom often makes it impossible to carry out an accurate and complete theoretical study. Furthermore, owing to a mixing of different vibronic symmetries, the precise details of the vibronic bands are often difficult to decipher for strongly coupled electronic states of a large polyatomic system.

In this article we mainly focus on the central issue of vibronic coupling in the benzenoid systems viz., the phenyl radical ( $\text{Ph}^\bullet$ ) and phenylacetylene radical cation ( $\text{PA}^{\bullet+}$ ) and the lowest members of the family of the PAH radical cations viz., naphthalene ( $\text{N}^{\bullet+}$ ) and anthracene ( $\text{AN}^{\bullet+}$ ) radical cations. Consequences of this coupling for the nuclear dynamics of these systems are studied at length. The difficulties faced in the quantum mechanical treatments of these large systems are also discussed. Dynamical observables like the rich vibronic spectrum are calculated and assigned. The ultrafast nonradiative dynamics of the excited states is also studied. These observables are compared with the available experimental data to validate the established theoretical model [19–22].

Novel signature of vibronic coupling of electronic states is often borne by the observed lack of fluorescence emissions of electronically excited polyatomic molecules. Broad and diffuse vibronic spectra can finally be related to this observation. The electronic mechanism of photostability is connected to the decay of a strongly ultraviolet (UV) absorbing electronic state via a non-emissive path. Such a process is notably of immense importance in biological molecules and greatly contributes to life. A nonradiative dissipation of the absorbed UV radiation prevents the initiation of hazardous and dangerous photoreactions, particularly important for the relevant molecules constituting the DNA of living beings [23–26].

Sobolewski and Domcke have made pioneering contributions to elucidate the mechanism of photostability considering a wide variety of molecular systems of chemical and biological importance [26–30]. CIs of PESs are established to be the bottleneck in such photochemical processes [2, 31, 32]. A schematic diagram shown in Fig. 1 illustrates the mechanism of photostability. The UV photon promotes the molecule to its electronic excited state as indicated by the vertical long arrow in the diagram. The excited electronic state  $|1\rangle$  meets a second one  $|2\rangle$  (may or may not be optically bright and depends on the molecular system) which links  $|1\rangle$  and the electronic ground state  $|g\rangle$  via successive CIs. Therefore, once excited to the UV absorbing state  $|1\rangle$ , the molecule can return to its electronic ground state  $|g\rangle$  traversing through the CIs and nonradiatively dissipating the absorbed UV radiation [25, 33, 34]. Experimental evidence of negligible yield of photoproducts supports this mechanism [35].

Structural and dynamical studies have been carried out on chromophores of aromatic amino acids and bases [27, 30, 33, 36]. These aromatic biomolecules possess strongly UV absorbing short lived  $^1\pi\pi^*$  state. Short lifetime of this state is established to be caused by an optically dark  $^1\pi\sigma^*$  state which connects it to the  $S_0$  ground state via two successive CIs as illustrated in the diagram of Fig. 1. Extensive studies have also been carried out on DNA base pairs validating such a



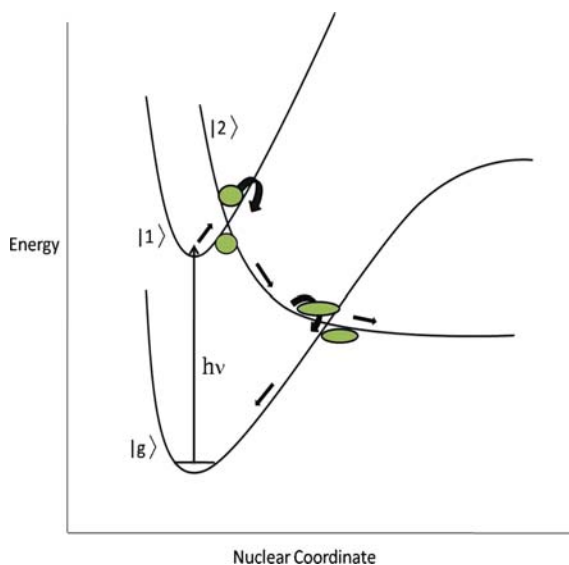


**Fig. 1** Schematic diagram of the potential energy surface crossings to illustrate the mechanism of photostability. The electronic ground state is indicated by  $|g\rangle$  and the excited states by  $|1\rangle$  and  $|2\rangle$

mechanism of photostability of the strongly UV absorbing state [37, 38]. In case of 2-aminopyridine dimer (a mimetic model of DNA base pair), enhanced deactivation of a locally excited  $^1\pi\pi^*$  state is found to be caused by an optically dark  $^1\pi\pi^*$  excited charge transfer state connecting it to the  $S_0$  ground electronic state via CIs [34]. A discussion on the photostability and the femtosecond time-resolved experiment to measure ultrafast deactivation of excited states of biologically important molecules was reviewed recently [23].

Besides above developments, photostability of electronically excited radical cations of PAHs has received increasing attention in recent years [39]. These cations are most abundant in the interstellar space, and an understanding of their UV photophysics/chemistry has become a major concern [40, 41]. The lack of fluorescence emission and the enigmatic diffuse interstellar bands (DIBs) are indicative of complex vibronic coupling and ultrafast nonradiative decay of electronic excited states of these systems. Aided by the availability of various experimental data [16, 42–47] we recently studied the photophysics/chemistry of the prototypical naphthalene and anthracene radical cations quantum mechanically [20, 22]. The complex vibronic coupling in their low-lying electronic states was established and its impact on the vibronic dynamics with regard to their photostability and possible contribution to the DIBs was discussed.

The rest of the article is organized in the following way. The basic concept of vibronic coupling is reviewed in Sect. 2. The theoretical and computational methodologies to treat the static and dynamic aspects of vibronic coupling are outlined in Sect. 3. The important findings on the vibronic dynamics of  $\text{Ph}^\bullet$ ,  $\text{PA}^{\bullet+}$ ,  $\text{N}^{\bullet+}$  and

$\text{AN}^{\bullet+}$  are highlighted in Sect. 4. Finally the summarizing remarks are presented in Sect. 5.

## 2 Vibronic Coupling: General Perspective

The concept of “vibronic coupling” perhaps dates back to the seminal and thought provoking paper of von Neumann and Wigner on the “non crossing rule” [1]. With this discovery the validity of the celebrated Born–Oppenheimer (BO) approximation of separation of electronic and nuclear motions in molecular quantum mechanics [3] became questionable. The huge difference in the electron and nuclear masses was the sole justification of this pioneering approximation. However, when molecular electronic states approach to within a quantum of vibrational energy this justification seems to become futile. To begin the discussion, let us consider a general molecular Hamiltonian written in terms of the set of electronic and nuclear coordinates  $\mathbf{q}$  and  $\mathbf{Q}$ , respectively, as

$$\mathcal{H}(\mathbf{q}, \mathbf{Q}) = T_e(\mathbf{q}) + T_N(\mathbf{Q}) + U(\mathbf{q}, \mathbf{Q}), \quad (1)$$

where  $T_e(\mathbf{q})$  and  $T_N(\mathbf{Q})$  are the kinetic energy operators of the electrons and nuclei, respectively. The quantity  $U(\mathbf{q}, \mathbf{Q})$  is the total potential energy of the electron–electron, electron–nuclear and nuclear–nuclear interactions. The BO adiabatic electronic states are obtained by setting,  $T_N(\mathbf{Q}) = 0$ , and solving the resulting electronic eigenvalue equation for fixed nuclear configuration [48]

$$[T_e(\mathbf{q}) + U(\mathbf{q}, \mathbf{Q})] \Phi_n(\mathbf{q}; \mathbf{Q}) = \mathbf{V}_n(\mathbf{Q}) \Phi_n(\mathbf{q}; \mathbf{Q}), \quad (2)$$

where  $\Phi_n(\mathbf{q}; \mathbf{Q})$  and  $\mathbf{V}_n(\mathbf{Q})$  are the BO adiabatic electronic wavefunction parametrically depending on the set of nuclear coordinates  $\mathbf{Q}$  and the adiabatic electronic PES, respectively. The full molecular wavefunction  $\Psi(\mathbf{q}, \mathbf{Q})$  can now be expressed in terms of the above adiabatic electronic functions as

$$\Psi(\mathbf{q}, \mathbf{Q}) = \sum_n \chi_n(\mathbf{Q}) \Phi_n(\mathbf{q}; \mathbf{Q}). \quad (3)$$

Substitution of (1–3) in the eigenvalue equation leads to the following coupled differential equations for the expansion coefficients  $\chi_n(\mathbf{Q})$  [48]

$$\{T_N(\mathbf{Q}) + \mathbf{V}_n(\mathbf{Q}) - E\} \chi_n(\mathbf{Q}) = \sum_m \Lambda_{nm}(\mathbf{Q}) \chi_m(\mathbf{Q}), \quad (4)$$

where

$$\Lambda_{nm}(\mathbf{Q}) = - \int d\mathbf{q} \Phi_n^*(\mathbf{q}; \mathbf{Q}) [T_N(\mathbf{Q}), \Phi_m(\mathbf{q}; \mathbf{Q})], \quad (5)$$

describes the coupling of electronic states  $n$  and  $m$  through the nuclear kinetic energy operator and defines the nonadiabatic coupling matrix of the adiabatic electronic representation. Notice that the nuclear kinetic energy operator is non-diagonal in this representation. The quantity  $\Lambda_{nm}(\mathbf{Q})$  can be recasted as [7, 49]

$$\Lambda_{nm}(\mathbf{Q}) = - \sum_i \frac{\hbar^2}{M_i} \mathbf{A}_{nm}^{(i)}(\mathbf{Q}) \frac{\partial}{\partial Q_i} - \sum_i \frac{\hbar^2}{2M_i} \mathbf{B}_{nm}^{(i)}(\mathbf{Q}), \quad (6)$$

where  $M_i$  are nuclear masses and

$$\mathbf{A}_{nm}^{(i)}(\mathbf{Q}) = \langle \Phi_n(\mathbf{q}; \mathbf{Q}) | \nabla_i | \Phi_m(\mathbf{q}; \mathbf{Q}) \rangle, \quad (7)$$

and

$$\mathbf{B}_{nm}^{(i)}(\mathbf{Q}) = \langle \Phi_n(\mathbf{q}; \mathbf{Q}) | \nabla_i^2 | \Phi_m(\mathbf{q}; \mathbf{Q}) \rangle, \quad (8)$$

are the derivative coupling vector and scalar coupling, respectively.

In the BO approximation  $\Lambda_{nm}(\mathbf{Q})$  is set to zero which holds for widely separated electronic PESs. Using the Hellmann–Feynman theorem the elements of  $\mathbf{A}_{nm}(\mathbf{Q})$  can be expressed as [7]

$$\mathbf{A}_{nm}^{(i)}(\mathbf{Q}) = \frac{\langle \Phi_n(\mathbf{q}; \mathbf{Q}) | \nabla_i \mathcal{H}_{el}(\mathbf{q}; \mathbf{Q}) | \Phi_m(\mathbf{q}; \mathbf{Q}) \rangle}{V_n(\mathbf{Q}) - V_m(\mathbf{Q})}, \quad (9)$$

where  $\mathcal{H}_{el}$  represents the electronic Hamiltonian for fixed nuclear configuration. At the intersection of the two surfaces  $V_n(\mathbf{Q}) = V_m(\mathbf{Q})$ , and the derivative coupling elements of (9) exhibit a singularity. As a result, both the electronic wavefunction and the derivative of energy become discontinuous at the point of intersection making the adiabatic representation unsuitable for the numerical simulation of nuclear dynamics. Therefore, when different electronic PESs closely approach or even intersect the derivative coupling,  $\mathbf{A}_{nm}(\mathbf{Q})$ , becomes extremely large and supersedes the large nuclear to electronic mass ratio and hence the BO approximation breaks down.

To circumvent the singularity problem the concept of complementary diabatic electronic representation was introduced [50–52]. In this representation, the diverging kinetic energy coupling is transformed into smooth potential energy couplings through a suitable unitary transformation. As a result, the nuclear kinetic energy operator assumes a diagonal form and the coupling between the electronic states is described by the off-diagonal elements of the potential energy operator. In this representation the coupled equations of motion (as compared to (4)) read [53, 54]

$$\{T_N(\mathbf{Q}) + \mathbf{U}_{nn}(\mathbf{Q}) - E\} \chi_n(\mathbf{Q}) = \sum_{m \neq n} \mathbf{U}_{nm}(\mathbf{Q}) \chi_m(\mathbf{Q}), \quad (10)$$

where  $\mathbf{U}_{nn}(\mathbf{Q})$  are the diabatic PESs and  $\mathbf{U}_{nm}(\mathbf{Q})$  are their coupling elements. The latter are give by

$$\mathbf{U}_{nm}(\mathbf{Q}) = \int d\mathbf{q} \psi_n^*(\mathbf{q}, \mathbf{Q}) [T_e + \mathbf{V}(\mathbf{q}, \mathbf{Q})] \psi_m(\mathbf{q}, \mathbf{Q}), \quad (11)$$

where  $\psi$  represents the diabatic electronic wavefunction obtained from the corresponding adiabatic  $\Phi(\mathbf{q}; \mathbf{Q})$  ones via a unitary transformation

$$\psi(\mathbf{q}; \mathbf{Q}) = \mathbf{S} \Phi(\mathbf{q}; \mathbf{Q}), \quad (12)$$

with the aid of an orthogonal transformation matrix

$$\mathbf{S}(\mathbf{Q}) = \begin{pmatrix} \cos \theta(\mathbf{Q}) & \sin \theta(\mathbf{Q}) \\ -\sin \theta(\mathbf{Q}) & \cos \theta(\mathbf{Q}) \end{pmatrix}. \quad (13)$$

The matrix  $\mathbf{S}(\mathbf{Q})$  is called the adiabatic-to-diabatic transformation (ADT) matrix and  $\theta(\mathbf{Q})$  defines the transformation angle. The required condition for such transformation is the first-order derivative couplings of (7) vanishes in the new representation for all nuclear coordinates [55, 56] i.e.,

$$\int d\mathbf{q} \psi_n^*(\mathbf{q}, \mathbf{Q}) \frac{\partial}{\partial Q_i} \psi_m(\mathbf{q}, \mathbf{Q}) = 0. \quad (14)$$

This requirement yields the following differential equations for the transformation matrix [55, 57, 58]

$$\frac{\partial \mathbf{S}}{\partial Q_i} + \mathbf{A}^{(i)} \mathbf{S} = 0, \quad (15)$$

where the elements of the first-order derivative coupling matrix  $\mathbf{A}^{(i)}$  are given by (7). A unique solution of the above equation can be obtained only when the *curl* of the derivative coupling matrix vanishes [55, 57, 58] which is difficult to achieve in practice starting from a finite subspace of electronic states [56]. Therefore, for polyatomic molecular systems rigorous diabatic electronic states do not exist [56]. For a survey of some approximate schemes to construct diabatic electronic states the readers are referred to the articles in [58–60].

In order to review the basic aspects of PES crossings let us recall a two-state electronic Hamiltonian in a diabatic representation

$$\mathcal{H}_{el}(\mathbf{Q}) = \begin{pmatrix} H_{11}(\mathbf{Q}) & H_{12}(\mathbf{Q}) \\ H_{21}(\mathbf{Q}) & H_{22}(\mathbf{Q}) \end{pmatrix}, \quad (16)$$

where  $H_{11}$  and  $H_{22}$  represent the potential energies of the two diabatic electronic states and,  $H_{12} = H_{21}$ , describes their coupling potential. We also assume that all the elements of (16) are real. On diagonalization using the ADT matrix  $\mathbf{S}$ , the electronic Hamiltonian of 16 yields the adiabatic potential energies

$$V_{1,2}(\mathbf{Q}) = \Sigma \pm \sqrt{\Delta^2 + H_{12}^2}, \quad (17)$$

where  $\Sigma = (H_{11} + H_{22})/2$  and  $\Delta = (H_{11} - H_{22})/2$ . The transformation angle  $\theta(\mathbf{Q})$  of the ADT matrix depends on the set of nuclear coordinates and can be obtained from

$$\theta(\mathbf{R}) = \frac{1}{2} \arctan [2H_{12}(\mathbf{Q})/(H_{22}(\mathbf{Q}) - H_{11}(\mathbf{Q}))]. \quad (18)$$

It can be seen from (17) that the two adiabatic surfaces exhibit a degeneracy when,  $\Delta = 0$  and  $H_{12} = 0$ . The latter quantities depend on two independent set of nuclear coordinates, not available for a diatomic molecule leading to the non crossing rule [1] unless  $H_{12}$  vanishes on symmetry ground. On the other hand, due to the availability of more than one nuclear degrees of freedom, the PESs of polyatomic molecules generally cross. It can be seen that  $V_{1,2}(\mathbf{Q})$  resembles the equation of a double cone intersecting at their vertex. This topography of intersecting PESs is popularly known as *conical intersections* (CIs) [5–8, 31, 32, 61–65]. By expanding  $H_{11}$ ,  $H_{22}$  and  $H_{12}$  in a first-order Taylor series, the quantities  $\Delta$  and  $H_{12}$  can be equated to a gradient difference and nonadiabatic coupling vectors, respectively [66]. The space spanned by these vectors defines the two-dimensional branching space in which the degeneracy of the two surfaces is lifted except at the origin. Whereas, the surfaces remain degenerate in the remaining  $N - 2$  dimensional space (when spin is not included,  $N$  is the number of nuclear degrees of freedom). The locus of the degeneracy of the two surfaces defines the seam of the CIs.

The evidence of CIs of PESs perhaps emerged from the Jahn–Teller (JT) active molecular systems [5]. In this case the symmetry required electronic degeneracy is lifted by symmetry reducing nuclear coordinates. The classic example in this category is lifting of the degeneracy of a doubly degenerate  $E$  electronic state upon distortion along a doubly degenerate  $e$  nuclear vibration and is known as  $(E \otimes e)$ -JT effect [67]. The two JT split states form CIs at the undistorted molecular configuration. For example, the electronic degeneracy of an equilateral triangular molecular system (like cyclopropane) in  $D_{3h}$  symmetry splits upon distortion to  $C_{2v}$ . The system develops new minima at the latter configuration of reduced symmetry and the JT split component states form CIs at the original  $D_{3h}$  configuration.

The CIs of a  $(E \otimes e)$ -JT system are sketched in Fig. 2. The one-dimensional cut on top is plotted along a JT active  $e$  vibrational mode. It can be seen that the degeneracy of the two surfaces is split and they form CIs at the original undistorted  $D_{3h}$  configuration. In two dimensions the CIs is an isolated point indicated by a circle around it. However, in multidimension, as illustrated by the contour diagram at the bottom plotted along a symmetric and an  $e$  vibrational mode, the surface remain degenerate at a set of points and form seam. The line drawn on the contour diagram represents such a seam and the point marked on it defines the energetic minimum on this seam.

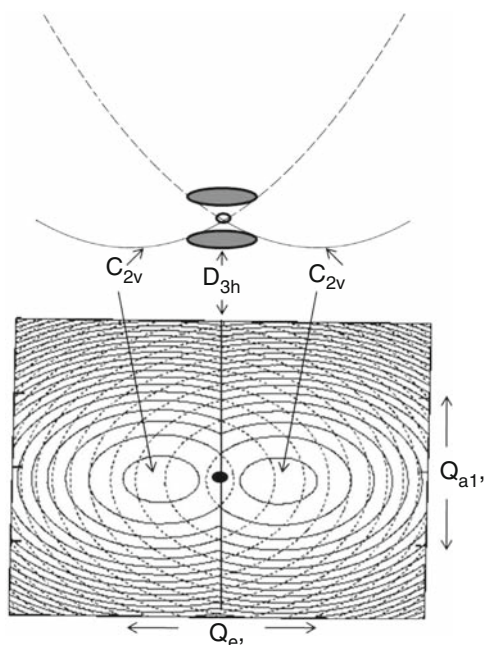


**Fig. 2** Schematic plot of  $(E \times e)$ -JT CIs of a system with  $D_{3h}$  equilibrium symmetry. Upon distortion the equilibrium symmetry breaks to  $C_{2v}$  as shown by the development of new minima on the lower adiabatic component of the JT split surface. The contour diagram is plotted along the coordinates of a JT active ( $Q_{e'}$ ) and totally symmetric ( $Q_{a1'}$ ) vibrational modes to reveal that CIs are not isolated points in space, rather the surfaces remain degenerate along a seam (see text for further details)

### 3 Outline of Theoretical and Computational Methodology

The vibronic coupling in the radical and radical cation of aromatic hydrocarbons is studied by photoionizing the corresponding anion and neutral molecules, respectively. The vibronic Hamiltonian of the final states of the ionized species is constructed in terms of the dimensionless normal coordinates of the electronic ground state of the corresponding (reference) anion or neutral species. The mass-weighted normal coordinates ( $\xi_i$ ) are obtained by diagonalizing the force field and are converted into the dimensionless form by [68]

$$Q_i = (\omega_i / \hbar)^{\frac{1}{2}} \xi_i, \quad (19)$$

where  $\omega_i$  is the harmonic frequency of the  $i$ th vibrational mode. These actually describes the normal displacement coordinates from the equilibrium configuration,  $\mathbf{Q} = 0$ , of the reference state. The vibronic Hamiltonian describing the photoinduced molecular process is then given by [7]

$$\mathcal{H} = (\mathcal{T}_N + \mathcal{V}_0)\mathbf{1}_n + \Delta\mathcal{H}. \quad (20)$$

In the above equation  $(\mathcal{T}_N + \mathcal{V}_0)$  defines the Hamiltonian for the unperturbed reference ground electronic state, with

$$\mathcal{T}_N = -\frac{1}{2} \sum_i \omega_i \left[ \frac{\partial^2}{\partial Q_i^2} \right], \quad (21)$$

and

$$\mathcal{V}_0 = \frac{1}{2} \sum_i \omega_i Q_i^2, \quad (22)$$

describing the kinetic and potential energy operators, respectively. All vibrational motions in this reference electronic state are generally, to a good approximation, assumed to be harmonic. The quantity  $\mathbf{1}_n$  is a  $(n \times n)$  (where  $n$  is the number of final electronic states) unit matrix and  $\Delta\mathcal{H}$  in (20) describes the change in the electronic energy upon ionization. This is a  $(n \times n)$  non-diagonal matrix. A diabatic electronic basis is utilized in order to construct the above Hamiltonian. This is to circumvent the stated shortcomings of the adiabatic electronic basis in the numerical application. The diagonal elements of the electronic Hamiltonian,  $\Delta\mathcal{H}$ , describe the diabatic potential energy surfaces of the electronic states and the off-diagonal elements describe their coupling surfaces. Possible coupling between the states is assessed by employing the symmetry selection rule in first-order

$$\Gamma_m \times \Gamma_{Q_i} \times \Gamma_n \supset \Gamma_A, \quad (23)$$

where  $\Gamma_m, \Gamma_n$  and  $\Gamma_{Q_i}$  refer to the irreducible representations (IREPs) of the electronic states  $m, n$  and the  $i$ th vibrational mode, respectively.  $\Gamma_A$  denotes the totally symmetric representation. According to this prescription, the totally symmetric vibrational modes are always active within a given electronic state. The elements of  $\Delta\mathcal{H}$  are expanded in a Taylor series around the reference equilibrium geometry ( $\mathbf{Q} = 0$ ) and the series is suitably truncated to best fit the *ab initio* computed electronic energies. A truncation of the series at the first-order term results the pioneering linear vibronic coupling (LVC) model of Köppel, Domcke and Cederbaum [7].

The derivatives of the electronic energies appearing in the Taylor expansion describe the coupling parameters of the vibronic Hamiltonian (see later in the text). These are determined by calculating the adiabatic potential energies as a function of the dimensionless normal coordinates by a suitable *ab initio* method. Several new developments in the electronic structure calculations of vibronically coupled systems have emerged in recent years. An exhaustive discussions on this is out of the scope of this review and the readers are referred to the [69–75]. For the reference molecule, the equilibrium geometry and the harmonic force field of the ground electronic state are routinely calculated by electronic structure methods in which the analytic gradients of energy are available. In the present case, a second-order

Møller-Plesset perturbation theory (MP2) based method is used for the purpose. For molecules which possess a closed-shell ground electronic state, the outer valence Green's function (OVGF) method has been found to be very successful in estimating the energies of their ionized states [76,77]. In this method the vertical ionization energies (VIEs) are calculated along the normal coordinates of a given vibrational mode. These VIEs plus the harmonic potential of the reference state are equated with the adiabatic potential energies ( $\mathbf{V}$ ) of the final electronic state. The latter are then fitted to the adiabatic form of the diabatic electronic Hamiltonian of (20)

$$\mathbf{S}^\dagger (\mathcal{H} - T_N 1_n) \mathbf{S} = \mathbf{V}. \quad (24)$$

Once the Hamiltonian is constructed, first principles nuclear dynamical simulations are carried out by solving the Schrödinger eigenvalue equation numerically. The spectral intensity in the photoinduced process is described by Fermi's golden rule

$$P(E) = \sum_v \left| \langle \Psi_v^f | \hat{T} | \Psi_0^i \rangle \right|^2 \delta(E - E_v^f + E_0^i), \quad (25)$$

where  $|\Psi_0^i\rangle$  is the initial vibronic ground state (reference state) with energy  $E_0^i$  and  $|\Psi_v^f\rangle$  corresponds to the (final) vibronic states of the photoionized molecule with energies  $E_v^f$ . The reference ground electronic state is approximated to be vibronically decoupled from the other states and it is given by

$$|\Psi_0^i\rangle = |\Phi_0^0\rangle |\mathbf{0}\rangle, \quad (26)$$

where  $|\Phi_0^0\rangle$  and  $|\mathbf{0}\rangle$  represent the electronic and vibrational components of the initial wavefunction, respectively. The quantity  $\hat{T}$  represents the transition dipole operator for the photoionization process.

Use of the Fourier representation of the Dirac delta function,  $\delta(x) = \frac{1}{2\pi} \int_{-\infty}^{+\infty} e^{ixt/\hbar}$ , in the golden rule equation transforms (25) into the following useful form, readily utilized in a time-dependent picture

$$P(E) \approx 2Re \int_0^\infty e^{iEt/\hbar} \langle \Psi_f(0) | \boldsymbol{\tau}^\dagger e^{-i\mathcal{H}t/\hbar} \boldsymbol{\tau} | \Psi_f(0) \rangle dt, \quad (27)$$

$$\approx 2Re \int_0^\infty e^{iEt/\hbar} C_f(t) dt. \quad (28)$$

In (27) the elements of the transition dipole matrix  $\boldsymbol{\tau}^\dagger$  is given by,  $\boldsymbol{\tau}^f = \langle \Phi^f | \hat{T} | \Phi^i \rangle$ . These elements are slowly varying function of nuclear coordinates and generally treated as constants in accordance with the applicability of the Condon approximation in a diabatic electronic basis [7,78]. The quantity  $C_f(t) = \langle \Psi_f(0) | \Psi_f(t) \rangle$ , is the time autocorrelation function of the wave packet (WP) initially prepared on the  $f$ th electronic state and,  $\Psi_f(t) = e^{-i\mathcal{H}t/\hbar} \Psi_f(0)$ .



The vibronic spectrum is calculated by numerically solving the eigenvalue equation of the vibronic Hamiltonian. In a time-independent approach, the latter is represented in a direct product basis of diabatic electronic state and one-dimensional harmonic oscillator eigenfunctions of the reference Hamiltonian ( $\mathcal{T}_N + \mathcal{V}_0$ ) [7]. The number of latter in a given application is roughly estimated from the coupling strength of the vibrational modes. The final number is however, fixed by examining the convergence behavior of the eigenvalue spectrum. The vibronic Hamiltonian expressed in a direct product harmonic oscillator basis has a sparse structure, which is then diagonalized by using the Lanczos algorithm [79]. The diagonal elements of the resulting eigenvalue matrix give the location of the vibrational levels and the relative intensities are obtained from the squared first component of the Lanczos eigenvectors [7, 54].

The matrix diagonalization approach becomes computationally impracticable with increase in the electronic and nuclear degrees of freedom. Therefore, for large molecules and with complex vibronic coupling mechanism this method often becomes unreliable. The WP propagation approach within the multi-configuration time-dependent Hartree (MCTDH) scheme has emerged as a very promising alternative tool for such situations [80–82]. This is a grid based method which utilizes discrete variable representation (DVR) combined with fast Fourier transformation and powerful integration schemes. The efficient multiset ansatz of this scheme allows for an effective combination of vibrational degrees of freedom and thereby reduces the dimensionality problem. In this ansatz the wavefunction for a nonadiabatic system is expressed as [80–82]

$$\Psi(Q_1, \dots, Q_f, t) = \Psi(R_1, \dots, R_p, t) \quad (29)$$

$$= \sum_{\alpha=1}^{\sigma} \sum_{j_1=1}^{n_1^{(\alpha)}} \dots \sum_{j_p=1}^{n_p^{(\alpha)}} A_{j_1, \dots, j_p}^{(\alpha)}(t) \prod_{k=1}^p \varphi_{jk}^{(\alpha, k)}(R_k, t) |\alpha\rangle, \quad (30)$$

Where,  $R_1, \dots, R_p$  are the coordinates of  $p$  particles formed by combining  $f$  vibrational degrees of freedom,  $\alpha$  is the electronic state index and  $\varphi_{jk}^{(\alpha, k)}$  are the  $n_k$  single-particle functions for each degree of freedom  $k$  associated with the electronic state  $\alpha$ .  $\sigma$  represents the number of electronic states. Employing a variational principle, the solution of the time-dependent Schrödinger equation is described by the time-evolution of the expansion coefficients  $A_{j_1, \dots, j_p}^{(\alpha)}$ . In this scheme all multi-dimensional quantities are expressed in terms of one-dimensional ones employing the idea of mean-field or Hartree approach. This provides the efficiency of the method by keeping the size of the basis optimally small. Furthermore, multi-dimensional single-particle functions are designed by appropriately choosing the set of system coordinates so as to reduce the number of particles and hence the computational overheads. The operational principles, successes and shortcomings of this schemes are detailed in the literature [80–82] and we do not reiterate them here. The Heidelberg MCTDH package [83] is employed to propagate WPs in the

numerical simulations discussed below. The spectral intensity is finally calculated using (27) from the time-evolved WP.

To reproduce the inherent broadening of the experimental vibronic spectrum, the stick vibronic lines obtained from the matrix diagonalization calculations are usually convoluted [7] with a Lorentzian line shape function

$$L(E) = \frac{1}{\pi} \frac{\frac{\Gamma}{2}}{E^2 + (\frac{\Gamma}{2})^2}, \quad (31)$$

with a full width at the half maximum (FWHM)  $\Gamma$ . In the time-dependent calculations, the time autocorrelation function is damped with a suitable time-dependent function before Fourier transformation. The usual choice has been a function of type

$$f(t) = \exp[-t/\tau_r], \quad (32)$$

where  $\tau_r$  represents the relaxation time. Multiplying  $C(t)$  with  $f(t)$  and then Fourier transforming it is equivalent to convoluting the spectrum with a Lorentzian line shape function (cf., (30)) of FWHM,  $\Gamma = 2/\tau_r$ .

The mechanistic details of the nonadiabatic dynamics can be best extracted from the motion of the WP in a time-dependent study, by creating a movie. The “ultra-fast” dynamics of the excited electronic states is examined by recording the diabatic (“adiabatic”) electronic populations during the entire course of the dynamics.

## 4 Representative Examples

### 4.1 Vibronic Coupling in the Phenyl Radical and Radical Cation of Phenylacetylene

The benzenoid systems,  $\text{Ph}^\bullet$  and  $\text{PA}^{\bullet+}$  are derived from the parent benzene molecule. The JT effect in the benzene radical cation ( $\text{BZ}^{\bullet+}$ ) is well studied in the literature [84–94]. The  $D_{6h}$  equilibrium point group symmetry of benzene breaks to  $C_{2v}$  in the phenide anion and phenylacetylene. As a result, the lowest degenerate molecular orbitals (MOs) of benzene split into a set of nondegenerate MOs in phenide anion and phenylacetylene. The highest occupied molecular orbital (HOMO), and three lower ones viz., HOMO-1, HOMO-2 and HOMO-3 are plotted in Fig. 3 in order to understand how the canonical MOs of benzene, phenide anion and phenylacetylene correlate with each other. It can be seen from Fig. 3 that the HOMO and HOMO-1 form the degenerate electronic ground JT state of benzene. These correlates to the HOMO-1 and HOMO-2 of phenide anion and HOMO and HOMO-1 of phenylacetylene, respectively. The HOMO-2 and HOMO-3 form the first excited JT state of benzene and the second correlates to the HOMO-3 of phenide anion. However, these two MOs do not correlate to the HOMO-2 and HOMO-3 of

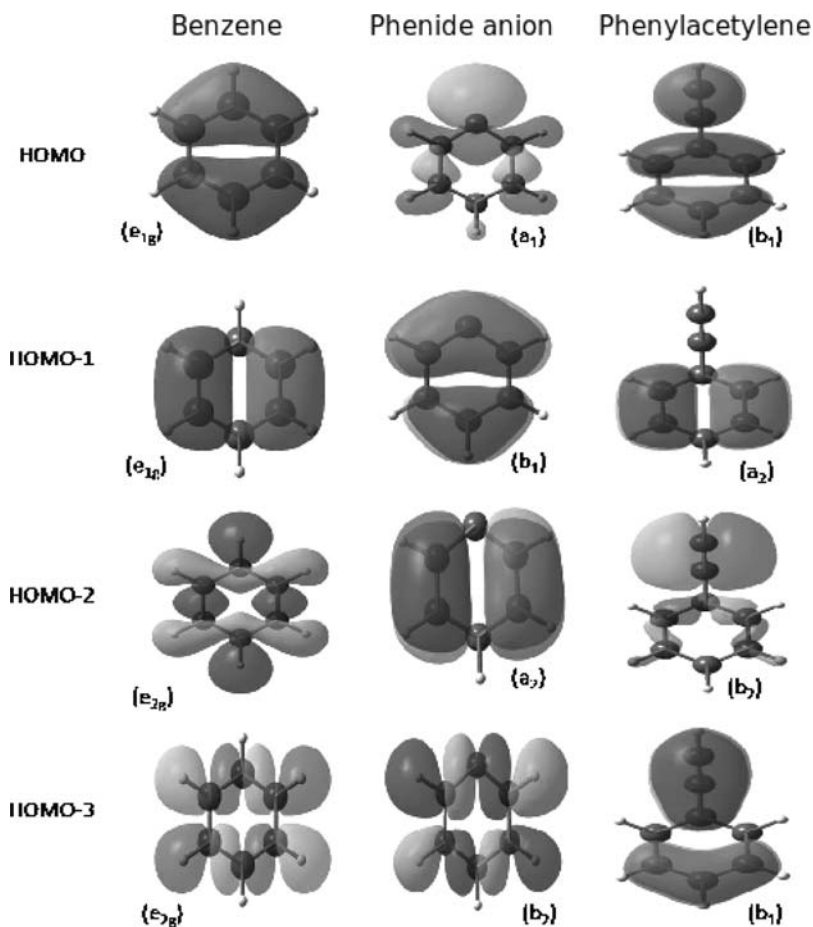


**Fig. 3** Schematic diagram of the canonical MOs of benzene, phenide anion and phenylacetylene. The highest occupied molecular orbital (HOMO) and three lower ones HOMO-1, HOMO-2 and HOMO-3 are shown along with their symmetry representations

phenylacetylene. The latter MOs are predominantly acetylenic  $\pi$ -orbitals parallel and perpendicular to the phenyl ring in phenylacetylene. The HOMO of phenide anion describes a nonbonding type of orbital in which the negative charge is localized. Within Koopman's theorem in the MO picture, ionization from the above MOs would result the MOs of the ionized molecules keeping their nature same. The components of the ground JT state ( $\tilde{X}^2 E_{1g}$ ) of  $BZ^{\bullet+}$  would therefore correlate with the  $\tilde{A}^2 B_1$  and  $\tilde{B}^2 A_2$  electronic states of  $Ph^{\bullet}$  and  $\tilde{X}^2 B_1$  and  $\tilde{A}^2 A_2$  electronic states of  $PA^{\bullet+}$ . These describe situations where the JT degeneracy is lifted by perturbations caused by the deprotonation of and substitution to the benzene ring, respectively.

Phenyl radical ( $\text{Ph}^\bullet$ ) is a prototype reactive intermediate in the chemistry of aromatic hydrocarbons. It plays an important role in combustion chemistry and also in the formation of PAHs [95, 96]. The spectroscopy of the low-lying electronic states of  $\text{Ph}^\bullet$  was studied experimentally. Gunion et al. [9] recorded 351 nm photodetachment spectrum of phenide anion (conjugate base of benzene). The spectrum revealed a well resolved vibronic structure of the electronic ground ( $\tilde{X}^2A_1$ ) state of  $\text{Ph}^\bullet$  and a broad (unresolved) and diffuse hump at high energies. The electronic absorption spectrum recorded by Radziszewski [97] revealed the vibronic structure of the  $\tilde{A}^2B_1$  and higher excited electronic states ( $^2A_1$  and  $^2B_2$ ) of  $\text{Ph}^\bullet$ . Subsequent theoretical calculations by Kim et al. [98] did not reproduce the rich vibronic structure observed in the experiment, and possible  $^2B_1$ – $^2A_2$  vibronic coupling was speculated to be the reason behind the disagreement between the theory and experiment [98]. Furthermore, the well resolved detachment spectrum of the  $\tilde{X}^2A_1$  state of  $\text{Ph}^\bullet$  revealed an anomalous intensity distribution, and the assignment of the progression due to the  $\sim 968\text{ cm}^{-1}$  vibrational mode was ambiguous as there are three vibrational modes of approximately the same frequency in the phenide anion [9].

As shown in Fig. 3, the negative charge in the HOMO of phenide anion is localized in a nonbonding type of orbital, where as it is delocalized over the  $\pi$  type of bonding in HOMO-1 and HOMO-2. The  $\tilde{X}^2A_1$  electronic ground state of  $\text{Ph}^\bullet$  results from the detachment of an electron from the HOMO, where as  $\tilde{A}^2B_1$  and  $\tilde{B}^2A_2$  excited electronic states result from HOMO-1 and HOMO-2. The 27 vibrational modes of phenide anion decompose into  $10 a_1 (\nu_1 - \nu_{10}) \oplus 5 b_1 (\nu_{11} - \nu_{15}) \oplus 9 b_2 (\nu_{16} - \nu_{24}) \oplus 3 a_2 (\nu_{25} - \nu_{27})$  IREPs of the  $C_{2v}$  point group [19]. Symmetry selection rule allows a coupling of the  $\tilde{X}$ – $\tilde{A}$ ,  $\tilde{X}$ – $\tilde{B}$  and  $\tilde{A}$ – $\tilde{B}$  electronic states (in first-order) of  $\text{Ph}^\bullet$  through the vibrational modes of  $b_1$ ,  $a_2$  and  $b_2$  symmetry, respectively.

The  $\tilde{X}$  state of  $\text{Ph}^\bullet$  is well separated from its  $\tilde{A}$  and  $\tilde{B}$  states. The vertical ionization energies  $\sim 1.007$ ,  $\sim 2.862$  and  $\sim 3.433$  eV, respectively, are estimated for these three states [19]. Furthermore, the coupling of the  $\tilde{X}$  state with the  $\tilde{A}$  and  $\tilde{B}$  states occurs at much higher energies and is found to be irrelevant for the photodetachment spectrum. The  $\tilde{A}$  and  $\tilde{B}$  states on the other hand are energetically close and the coupling between them is found to have considerable impact on their vibronic spectrum [19].

To analyze the vibronic structures of the  $\tilde{X}$ ,  $\tilde{A}$  and  $\tilde{B}$  electronic states  $\text{Ph}^\bullet$  we constructed a vibronic Hamiltonian in a diabatic electronic basis which treats the nuclear motion in the  $\tilde{X}$  state adiabatically, and includes the nonadiabatic coupling between the  $\tilde{A}$  and  $\tilde{B}$  electronic states. The Hamiltonian in terms of the dimensionless normal coordinates of the electronic ground state ( $\tilde{X}^1A_1$ ) of phenide anion is given by [19]

$$\mathcal{H} = (\mathcal{T}_N + \mathcal{V}_0)\mathbf{1}_3 + \Delta\mathcal{H} \quad (33)$$

where,

$$\Delta\mathcal{H} = \begin{pmatrix} U^{\tilde{X}} & 0 & 0 \\ & U^{\tilde{A}} & U^{\tilde{A}-\tilde{B}} \\ h.c. & & U^{\tilde{B}} \end{pmatrix} \quad (34)$$

Here  $\mathbf{1}_3$  represents a  $3 \times 3$  unit matrix.  $(\mathcal{T}_N + \mathcal{V}_0)$  represents the zeroth-order Hamiltonian of unperturbed electronic ground state of phenide anion given by (21–22). The elements of the electronic Hamiltonian  $\Delta\mathcal{H}$  are expanded in a Taylor series as follows

$$U^k = E_0^{(k)} + \sum_{i=1}^{10} \kappa_i^{(k)} Q_i + \frac{1}{2} \sum_{i=1}^{27} \gamma_i^{(k)} Q_i^2 + \frac{1}{2} \sum_{i=1}^{10} \sum_{i \neq j, j=1}^{10} \gamma_{ij}^{(k)} Q_i Q_j; k \in \tilde{X}, \tilde{A}, \tilde{B} \quad (35)$$

$$U^{\tilde{A}-\tilde{B}} = \sum_i \lambda_i^{(\tilde{A}-\tilde{B})} Q_i, \quad (36)$$

where  $E_0^k$  represents the vertical ionization energy of the  $k$ th electronic state of the phenyl radical,  $k \in \tilde{X}/\tilde{A}/\tilde{B}$ , measured from the reference equilibrium geometry ( $\mathbf{Q} = \mathbf{0}$ ) of the ground electronic state of phenide anion.  $\kappa_i^{(k)}$ ,  $\gamma_i^{(k)}$  and  $\gamma_{ij}^{(k)}$  defines the linear and diagonal second-order coupling parameters for the  $i$ th vibrational mode in the  $k$ th electronic state. The intermode ( $i$ th and  $j$ th) bilinear coupling parameters are denoted by  $\gamma_{ij}^{(k)}$ . The interstate linear coupling parameters are denoted by  $\lambda_i$  for the  $i$ th vibrational mode. These parameters are calculated by performing ab initio calculations of vertical ionization energies by the OVGf method and utilizing the strategy described in Sect. 3. The bilinear coupling parameters were found to be very small ( $\sim 10^{-3}$  or less) and are excluded from the dynamical simulations.

One dimensional potential energy cuts of the  $\tilde{X}$ ,  $\tilde{A}$  and  $\tilde{B}$  electronic states along the coordinates of most relevant totally symmetric ( $a_1$ ) vibrational modes  $\nu_1$ ,  $\nu_2$ ,  $\nu_5$ ,  $\nu_6$  and  $\nu_7$  are shown in Fig. 4. It can be seen and as pointed out above that the  $\tilde{X}$  state does not undergo low-energy crossings with either  $\tilde{A}$  or  $\tilde{B}$  state. Whereas, the latter two exhibit such crossings particularly along  $\nu_1$  and  $\nu_5$ – $\nu_7$  vibrational modes. These crossings transform to CIs in multidimensions. Within a linear coupling scheme the global minimum of the seam of  $\tilde{A}$ – $\tilde{B}$  CIs is estimated to occur at  $\sim 3.28$  eV. This intersection minimum is found to be only  $\sim 0.01$  eV above the  $\tilde{B}$  state equilibrium minimum. Therefore, the vibrational structure of the  $\tilde{B}$  state is expected to be strongly perturbed by the associated nonadiabatic coupling.

The vibronic structure of the  $\tilde{X}$  state of  $\text{Ph}^\bullet$  is shown in Fig. 5. Both the experimental results of Gunion et al. [9] and our theoretical results [19] are shown in

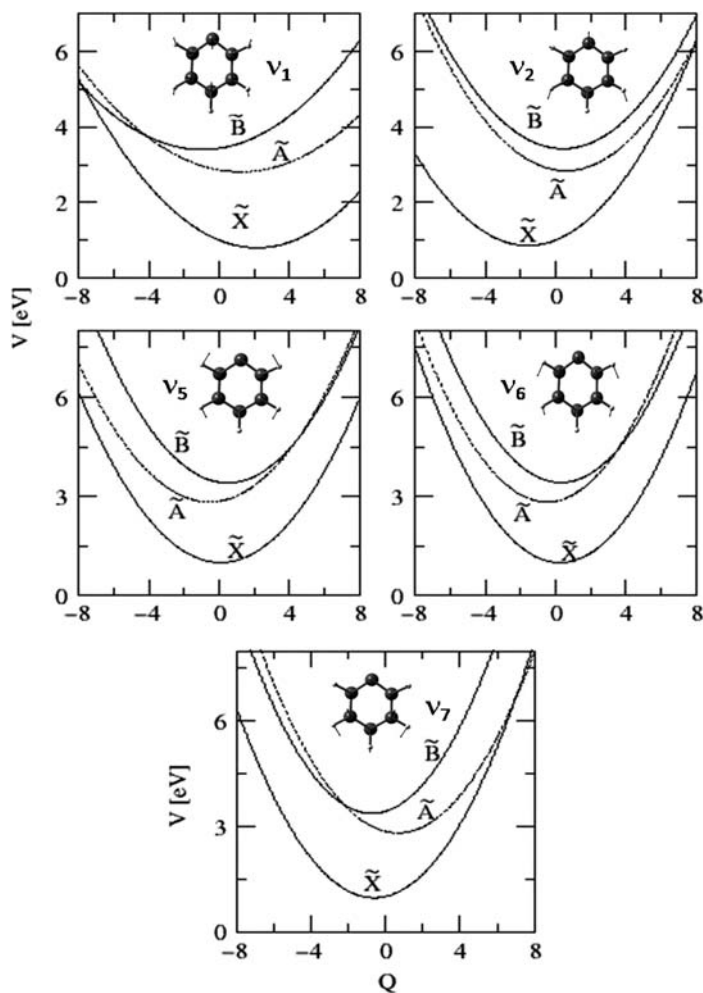


**Fig. 4** Adiabatic potential energies of the  $\tilde{X}$ ,  $\tilde{A}$  and  $\tilde{B}$  electronic states of  $\text{Ph}^\bullet$  along the coordinates of the most relevant  $a_1$  vibrational modes:  $\nu_1$  ( $586\text{ cm}^{-1}$ ),  $\nu_2$  ( $964\text{ cm}^{-1}$ ),  $\nu_5$  ( $1,192\text{ cm}^{-1}$ ),  $\nu_6$  ( $1,453\text{ cm}^{-1}$ ) and  $\nu_7$  ( $1,584\text{ cm}^{-1}$ ). A sketch of the vibrational modes is also shown

the diagram. The theoretical stick spectrum is obtained by including four  $a_1$ , five  $b_1$  and three  $a_2$  vibrational modes employing the matrix diagonalization approach. The resulting stick vibrational spectrum is convoluted with a Lorentzian function of 20 meV FWHM to obtain the spectral envelope. It can be seen that the theoretical results are in fair accord with the experimental data. Somewhat anomalous intensity distribution in the two is attributed to the possible contamination of the benzyne anion spectrum in the experimental data [9]. The dominant progressions in the theoretical band are confirmed to be formed by the  $\nu_1$  and  $\nu_2$  vibrational modes [19]. These modes describe deformation of the benzene ring and are shown at the

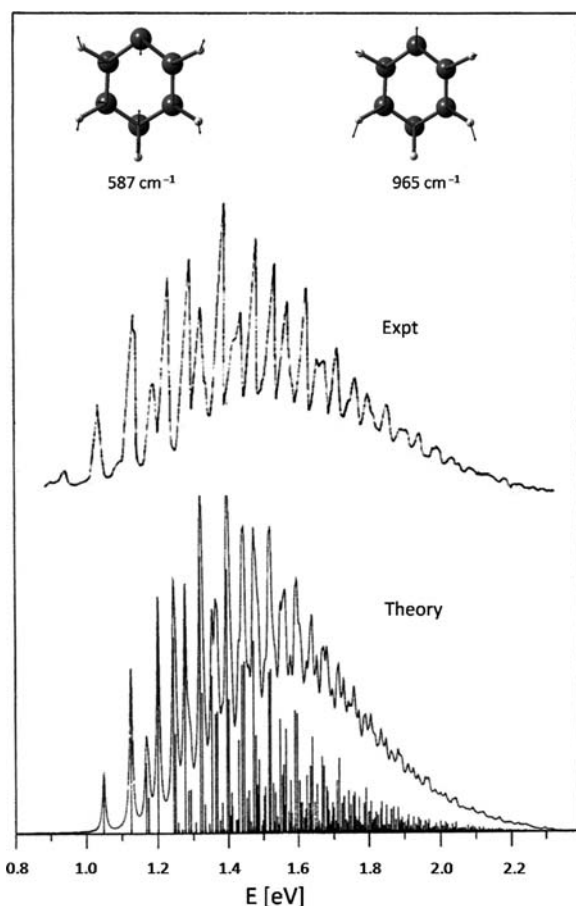


**Fig. 5** The  $\tilde{X}^2A_1$  vibronic spectrum of  $\text{Ph}^\bullet$ . The experimental [9] and present theoretical results are shown (see the text for details). The two  $a_1$  vibrational modes which form the dominant progression in the spectrum are also shown at the top of the figure

top of Fig. 5. Peak spacings of  $\sim 0.0727$  eV and  $\sim 0.1196$  eV corresponding to the frequency of these modes, respectively, are estimated from the theoretical data [19].

The  $\tilde{A}$  and  $\tilde{B}$  electronic states are vertically  $\sim 0.57$  eV spaced. Coupling between these states are primarily caused by the  $b_2$  vibrational modes of viz., ring deformation, C=C stretching and C-H bending type. The vibrational bands for the  $\tilde{A}$ – $\tilde{B}$  coupled electronic states are calculated by including 21 relevant vibrational modes ( $6a_1 + 4b_1 + 9b_2 + 2a_2$ ) [19]. The diagonalization approach was found to be computationally impracticable for a matrix involving two electronic states and 21 vibrational modes in each. The task is accomplished by propagating WPs using the MCTDH algorithm [83]. The calculated theoretical results are shown in Fig. 6a. While the vibronic structure of the  $\tilde{A}$  state is recorded in an electronic absorption measurement [97] (which is shown at the top of Fig. 6a), the  $\tilde{B}$  state is optically dark

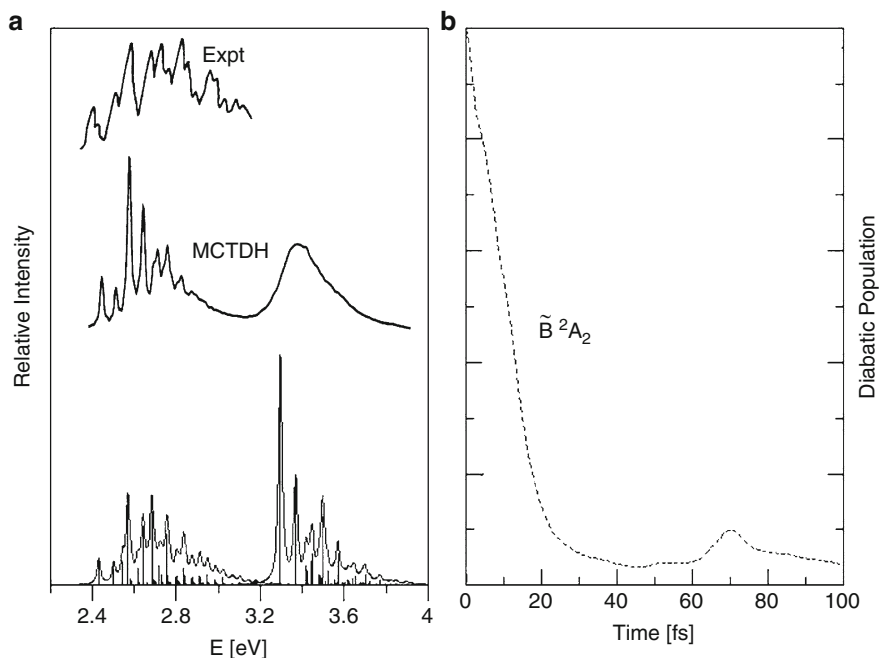


**Fig. 6** The  $\tilde{A}^2B_1-\tilde{B}^2A_2$  vibronic bands of  $\text{Ph}^\bullet$ . The present theoretical results without (uncoupled) and with (coupled) the  $\tilde{A}-\tilde{B}$  coupling are shown in the bottom and middle of the panel (a), respectively. The experimental UV absorption spectrum of [97] is also shown at the top of the panel (a). In the panel (b), the time dependence of  $\tilde{B}$  state population (diabatic) in the  $\tilde{A}-\tilde{B}$  coupled state dynamics is shown

and could not be probed in such measurements. Very sketchy information about the  $\tilde{B}$  state spectrum is perhaps obtained from the broad and extremely poor signal observed in the photodetachment spectrum [9]. The difference in the theoretical and experimental spectral intensity of the  $\tilde{A}$  band results from the fact that experimental absorption band is recorded from the neutral ground electronic state, whereas, the theoretical photodetachment spectrum is calculated from the ground electronic state of the anion. Therefore, only the position of the vibronic energy levels can be compared to the experiment. Comparison calculations were carried out for the uncoupled  $\tilde{A}$  and  $\tilde{B}$  states individually to assess the impact of the nonadiabatic coupling on the vibrational structures of these bands. The uncoupled state spectra are obtained by the matrix diagonalization method and including the relevant vibrational modes (see, [19] for details). These results are shown at the bottom of Fig. 6a. It can be seen that the nonadiabatic coupling causes only a partial demolition of the vibronic structures in the high energy wing of the  $\tilde{A}$  band, whereas, it has huge impact on the vibronic structures of the entire  $\tilde{B}$  band. The dominant progressions in the  $\tilde{A}$  band are formed by the symmetric  $\nu_1$ ,  $\nu_2$ ,  $\nu_3$ , and  $\nu_5$  vibrational modes, the peaks are  $\sim 0.072$ ,  $\sim 0.113$ ,  $\sim 0.12$  and  $\sim 0.14$  eV spaced corresponding to the frequency of



these modes, respectively. Progressions due to  $\nu_1$ ,  $\nu_2$ ,  $\nu_3$ , and  $\nu_6$  vibrational modes are obtained from the uncoupled  $\tilde{B}$  band.

To this end we mention that the JT active  $\tilde{X}^2E_{1g}$  state of  $BZ^{\bullet+}$  correlates to the  $\tilde{A}-\tilde{B}$  coupled states of  $Ph^{\bullet}$ . The JT effect in the  $\tilde{X}$  state of  $BZ^{\bullet+}$  is very weak [93, 94] and therefore, resolved vibronic structures of this state was observed in the experiment [99]. The JT activity in the  $\tilde{X}$  state of  $BZ^{\bullet+}$  is mostly caused by the  $e_{2g}$  vibrational modes  $\nu_6$  (skeletal deformation) and  $\nu_8$  (C=C stretching). Each of these modes splits into  $a_1$  and  $b_2$  components in  $Ph^{\bullet}$ . The  $b_2$  components cause a coupling of the  $\tilde{A}$  and  $\tilde{B}$  states while the  $a_1$  components act as Condon active tuning modes. The  $b_2$  components have coupling constants  $\sim 0.074$  and  $\sim 0.147$  eV similar in magnitude to the JT coupling constants  $\sim 0.077$  and  $\sim 0.152$  eV in  $BZ^{\bullet+}$  for  $\nu_6$  and  $\nu_8$ , respectively [19, 100]. However, the coupling constants of the corresponding  $a_1$  components in  $Ph^{\bullet}$  are  $\sim -0.081$  and  $\sim -0.128$  eV in  $\tilde{A}$  and  $\sim 0.069$  and  $\sim 0.160$  eV in the  $\tilde{B}$  states which cause a larger tuning activity. In addition, the vertical energy gap of the  $\tilde{A}$  and  $\tilde{B}$  states of  $Ph^{\bullet}$  is  $\sim 0.57$  eV and the energetic minimum of the  $\tilde{A}-\tilde{B}$  CIs occurs below the zero-point energy level of the  $\tilde{B}$  state [19]. This causes a considerable mixing of the vibrational continua of the  $\tilde{A}$  state with the low-lying vibrational levels of the  $\tilde{B}$  state and results in the observed blurring (cf., Fig. 6) of the vibrational structure of the latter state.

The time-dependence of the electronic (diabatic) populations of the  $\tilde{B}$  state in the  $\tilde{A}-\tilde{B}$  coupled state dynamics is shown in Fig. 6b. The WP is initially ( $t = 0$ ) located on the  $\tilde{B}$  state and therefore, its population starts from 1.0. Since the equilibrium minimum of the  $\tilde{B}$  state nearly coincides with the minimum of the  $\tilde{A}-\tilde{B}$  CIs, the population of this state decays (nonradiatively) rapidly to the  $\tilde{A}$  state through the CIs, and reaches to a value of  $\sim 0.05$  at longer times. The initial fast decay of the population relates to a decay rate of  $\sim 30$  fs for the  $\tilde{B}$  state.

The vibronic coupling in the  $PA^{\bullet+}$  is bit more involved than in  $Ph^{\bullet}$  [21]. The  $D_{6h}$  equilibrium symmetry of benzene breaks to  $C_{2v}$  upon acetylene substitution. The degenerate  $\tilde{X}^2E_{1g}$  JT state of  $BZ^{\bullet+}$  splits into  $\tilde{X}^2B_1$  and  $\tilde{A}^2A_2$  electronic states in  $PA^{\bullet+}$  as revealed by Fig. 3. Contrary to the phenide anion, where removal of a proton splits the JT degeneracy of benzene, in phenylacetylene (PA), perturbation caused by substitution breaks the JT symmetry.

The 36 vibrational modes of PA decompose into  $13a_1 \oplus 3a_2 \oplus 8b_1 \oplus 12b_2$  IREPs of the  $C_{2v}$  point group. The  $\tilde{X}^2B_1$ ,  $\tilde{A}^2A_2$ ,  $\tilde{B}^2B_2$  and  $\tilde{C}^2B_1$  electronic states of  $PA^{\bullet+}$  are found to be energetically close lying. The vertical ionization energies of these states relative to the electronic ground state of PA are estimated to be  $\sim 8.5$ ,  $\sim 9.15$ ,  $\sim 9.98$  and  $\sim 10.75$  eV, respectively [21]. Symmetry rule allows a coupling in first-order of the  $\tilde{X}-\tilde{A}$ ,  $\tilde{X}-\tilde{B}$ ,  $\tilde{A}-\tilde{B}$ ,  $\tilde{A}-\tilde{C}$  and  $\tilde{B}-\tilde{C}$  electronic states of  $PA^{\bullet+}$  through the vibrational modes of  $b_2$ ,  $a_2$ ,  $b_1$ ,  $b_2$  and  $a_2$  symmetry, respectively. To investigate the detailed vibronic dynamics in the  $\tilde{X}-\tilde{A}-\tilde{B}-\tilde{C}$  coupled electronic states of  $PA^{\bullet+}$  we constructed the following diabatic Hamiltonian in terms of dimensionless normal coordinates of 36 vibrational modes of the electronic ground state of PA [21].

$$\mathcal{H} = (T_N + \mathcal{V}_0)\mathbf{1}_4 + \begin{pmatrix} U^{\tilde{X}} & U^{\tilde{X}-\tilde{A}} & U^{\tilde{X}-\tilde{B}} & U^{\tilde{X}-\tilde{C}} \\ & U^{\tilde{A}} & U^{\tilde{A}-\tilde{B}} & U^{\tilde{A}-\tilde{C}} \\ h.c. & & U^{\tilde{B}} & U^{\tilde{B}-\tilde{C}} \\ & & & U^{\tilde{C}} \end{pmatrix}. \quad (37)$$

In the above  $\mathbf{1}_4$  represents a  $4 \times 4$  unit matrix. As before, the kinetic and potential energy operators of the zeroth-order Hamiltonian are denoted by  $T_N$  and  $\mathcal{V}_0$ , respectively. The non-diagonal matrix Hamiltonian in (37) describes the diabatic electronic PESs (diagonal elements) of the  $\tilde{X}$ ,  $\tilde{A}$ ,  $\tilde{B}$  and  $\tilde{C}$  electronic states of  $\text{PA}^{\bullet+}$  and their coupling potentials (off-diagonal elements). These elements are expanded in a Taylor series around the equilibrium geometry of the reference state at ( $\mathbf{Q} = 0$ ) as [7]

$$U^j = E_0^{(j)} + \sum_{i=1}^{13} \kappa_i^{(j)} Q_i + \frac{1}{2} \sum_{i=1}^{36} \gamma_i^{(j)} Q_i^2 ; \quad j \in \tilde{X}, \tilde{A}, \tilde{B}, \tilde{C} \quad (38)$$

$$U^{j-k} = \sum_i \lambda_i^{(j-k)} Q_i. \quad (39)$$

The parameters of the electronic Hamiltonian are calculated by performing extensive ab initio calculations [21]. Results of calculations of static aspects of the electronic PESs, viz, the equilibrium minimum of the states and energetic minimum of the seam of the CIs within a LVC model are summarized in Table 1. It can be seen from the data that the minimum of the  $\tilde{X}-\tilde{A}$  CIs occurs  $\sim 0.02$  eV above the equilibrium minimum of the  $\tilde{A}$  state. The same for the  $\tilde{A}-\tilde{B}$  CIs occurs at  $\sim 0.84$  eV and  $\sim 0.06$  eV above the equilibrium minimum of the  $\tilde{A}$  and  $\tilde{B}$  states, respectively. The minimum of  $\tilde{B}-\tilde{C}$  CIs occurs  $\sim 1.10$  eV above the equilibrium minimum of the  $\tilde{C}$  state. The minimum of the  $\tilde{X}-\tilde{B}$  CIs occurs  $\sim 2.5$  eV above the equilibrium minimum of  $\tilde{B}$  state. The  $\tilde{X}$  and  $\tilde{C}$  CIs occur at much higher energy and are not considered here. Analysis of the coupling parameters of all 36 vibrational modes revealed the importance of 9  $a_1$  ( $\nu_{13} - \nu_5$ ), 9  $b_2$  ( $\nu_{36} - \nu_{27}$ ), 2  $a_2$  ( $\nu_{16}$  and  $\nu_{14}$ ) and 4  $b_1$  ( $\nu_{20} - \nu_{17}$ ) vibrational modes in the nuclear dynamics in the  $\tilde{X}-\tilde{A}-\tilde{B}-\tilde{C}$  electronic states of  $\text{PA}^{\bullet+}$  [21].

The adiabatic potential energy cuts of the  $\tilde{X}-\tilde{A}-\tilde{B}-\tilde{C}$  electronic states of  $\text{PA}^{\bullet+}$  are plotted along two representative symmetric vibrational modes  $\nu_5$  (acetylenic  $\text{C}\equiv\text{C}$  stretching) and  $\nu_6$  ( $\text{C}=\text{C}$  stretching of the phenyl ring) in Fig. 7, to reveal various low-energy curve crossings. These curve crossings lead to CIs when distorted along the nontotally symmetric vibrational modes. From the energetic locations of  $\tilde{X}-\tilde{A}$  and  $\tilde{A}-\tilde{B}$  intersections, the vibronic structure of the  $\tilde{A}$  state is expected to be severely affected by the associated nonadiabatic coupling.

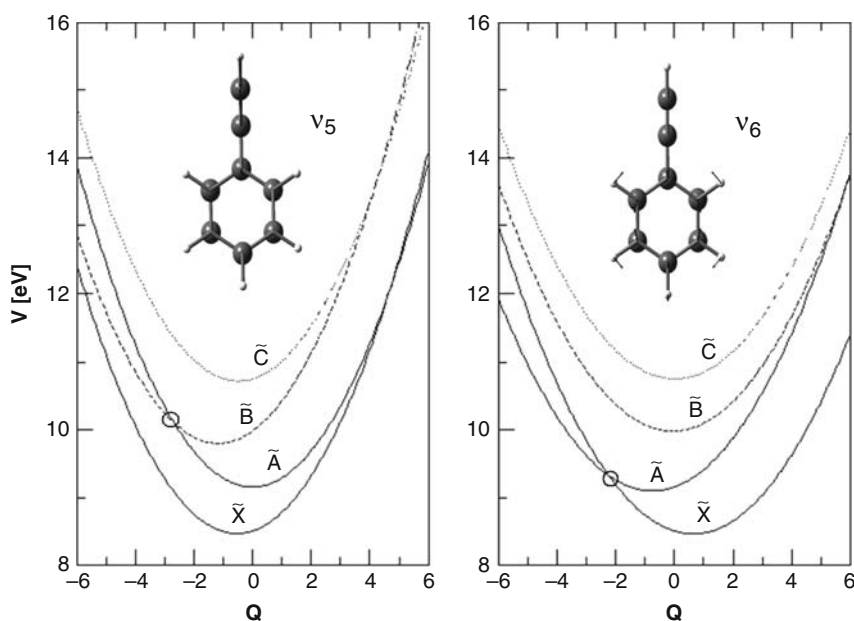
The  $\tilde{X}-\tilde{A}-\tilde{B}-\tilde{C}$  coupled state vibronic spectra are calculated by including the 24 vibrational modes mentioned above, by propagating WPs employing the MCTDH scheme. The theoretical results obtained are plotted in Fig. 8 along with the experimental photoelectron spectroscopy results of [101]. It can be seen that theoretical results are in excellent accord with the experimental findings.

**Table 1** Energetic equilibrium minima (diagonal entries) and minima of the seam of various CIs (off-diagonal entries) of the PESs of  $\text{PA}^{\bullet+}$ ,  $\text{N}^{\bullet+}$  ( $\text{AN}^{\bullet+}$ ). All quantities are given in eV

For $\text{PA}^{\bullet+}$	$\tilde{X}$	$\tilde{A}$	$\tilde{B}$	$\tilde{C}$
	$\tilde{X}$	—	9.01	12.23
	$\tilde{A}$	8.99	—	9.83
	$\tilde{B}$		9.77	—
	$\tilde{C}$			10.59

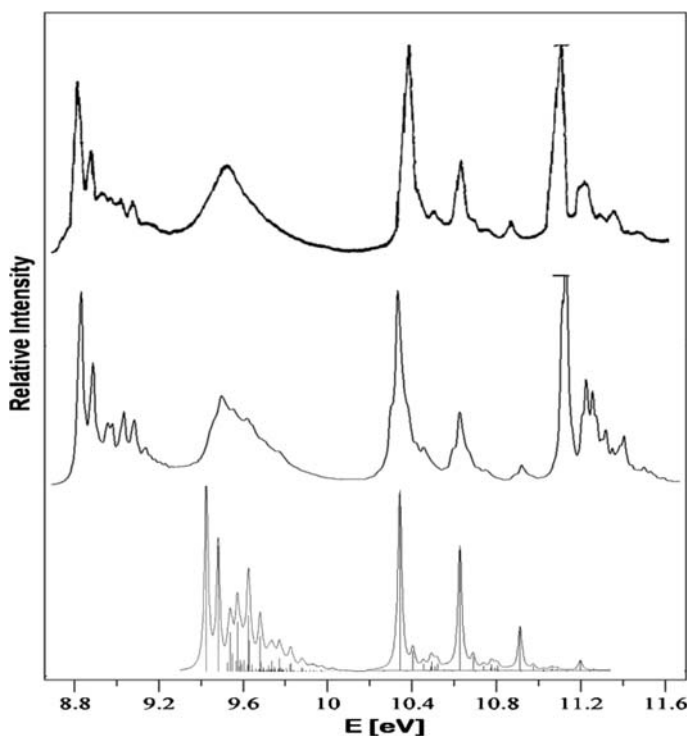
  

For $\text{N}^{\bullet+}$ ( $\text{AN}^{\bullet+}$ )	$D_0$	$D_1$	$D_2$
	$D_0$	—	8.47(8.82)
	$D_1$	8.39(8.10)	—
	$D_2$		9.63(8.76)



**Fig. 7** The  $\tilde{X}$ ,  $\tilde{A}$ ,  $\tilde{B}$  and  $\tilde{C}$  adiabatic potential energy surfaces of  $\text{PA}^{\bullet+}$  along the  $\nu_5$  ( $\text{C}\equiv\text{C}$  stretching) and  $\nu_6$  ( $\text{C}=\text{C}$  stretching) vibrational modes

Nonadiabatic coupling among the four electronic states results the complex vibrational structures of the bands in Fig. 8. In particular, the  $\tilde{X}$  and  $\tilde{A}$  states are strongly coupled through the  $b_2$  vibrational mode  $\nu_{36}$  [21]. Furthermore, since the minimum of the  $\tilde{A}$  state occurs only  $\sim 0.02$  eV above the minimum of the  $\tilde{A}-\tilde{B}$  CIs, the low-lying vibrational levels of the  $\tilde{A}$  state strongly mix with the quasi continuum levels of the  $\tilde{X}$  state. As a result, although low-lying vibronic structures of the  $\tilde{X}$  state are not much affected by this coupling, the entire  $\tilde{A}$  band is strongly perturbed starting



**Fig. 8** The vibronic spectrum of the coupled  $\tilde{X}-\tilde{A}-\tilde{B}-\tilde{C}$  states of  $\text{PA}^{\bullet+}$ . The experimental (from [101]) and present theoretical results are shown. The coupled state spectra calculated by the MCTDH wave packet propagation method is shown at the middle of the panel. The uncoupled  $\tilde{A}$  and  $\tilde{B}$  spectrum of  $\text{PA}^{\bullet+}$  are also shown at the bottom

from its origin. In addition, the  $\tilde{A}$  state is also moderately and weakly coupled with the  $\tilde{B}$  and  $\tilde{C}$  state, respectively, which also cause a clustering of the higher vibrational levels of the  $\tilde{A}$  state. The impact of the latter couplings is however, less than compared to the  $\tilde{X}-\tilde{A}$  coupling. The low-lying vibrational structures of the  $\tilde{B}$  band are also affected by  $\tilde{X}-\tilde{B}$  and  $\tilde{A}-\tilde{B}$  CIs. However, the nonadiabatic coupling due to these CIs is weaker compared to the same due to  $\tilde{X}-\tilde{A}$  CIs. Therefore, the vibrational structure of the  $\tilde{B}$  state is not perturbed as much as that of the  $\tilde{A}$  state. The  $\tilde{C}$  state is very weakly coupled with the  $\tilde{A}$  state through the  $b_2$  vibrational mode  $\nu_{29}$  and this coupling does not have any noticeable impact on its vibronic structure [21]. The uncoupled  $\tilde{A}$  and  $\tilde{B}$  bands obtained by the matrix diagonalization approach in reduced dimensions are also shown at the bottom of Fig. 8 to clearly reveal the impact of nonadiabatic coupling on them.

A detailed analysis of the vibrational progressions in the  $\tilde{X}$ ,  $\tilde{A}$ ,  $\tilde{B}$  and  $\tilde{C}$  states is reported in [21]. Such a discussion is out of the scope and we therefore highlight the main findings here. Extended progressions due to the  $a_1$  vibrational mode  $\nu_{13}$  (6a in Wilson's notation) have been observed in the  $\tilde{X}$ ,  $\tilde{A}$  and  $\tilde{B}$  states. Peak spacings of

$\sim 429\text{ cm}^{-1}$ ,  $\sim 467\text{ cm}^{-1}$  and  $\sim 484\text{ cm}^{-1}$  have been attributed to this mode in these electronic states, respectively. Apart from this, short progressions due to  $\nu_8$  (13) and  $\nu_9$  (9a) in the  $\tilde{X}$  state,  $\nu_8$  and  $\nu_6$  (8a) in the  $\tilde{A}$  state and  $\nu_5$  ( $\nu_{CC}$ ) and  $\nu_8$  in the  $\tilde{B}$  state are also observed. The strong excitation of the  $\sim 2,050\text{ cm}^{-1}$   $\nu_5$  vibration (acetylenic  $\text{C}\equiv\text{C}$  stretching) in the  $\tilde{B}$  state reveals that this state originates from a MO mainly localized on the acetylenic moiety on par with the nature of the HOMO-2 plotted in Fig. 3. In contrast to above,  $\nu_{13}$  is weakly excited in the  $\tilde{C}$  state. We find that among the symmetric vibrational modes  $\nu_{12}$ ,  $\nu_{11}$ ,  $\nu_{10}$ ,  $\nu_7$  and  $\nu_5$  are excited in the  $\tilde{C}$  state spectrum. The stronger JT active  $e_{2g}$  vibrational modes  $\nu_6$  and  $\nu_8$  of  $\text{BZ}^{\bullet+}$  transform to  $\nu_{6a}$  ( $a_1$ ),  $\nu_{6b}$  ( $b_2$ ) and  $\nu_{8a}$  ( $a_1$ ),  $\nu_{8b}$  ( $b_2$ ) modes in  $\text{PA}^{\bullet+}$ . The  $\nu_{6b}$  and  $\nu_{8b}$  modes in  $\text{PA}^{\bullet+}$  have similar coupling constants  $\sim 0.050$  and  $\sim 0.158\text{ eV}$ , respectively, as  $\nu_6$  and  $\nu_8$  (as mentioned above) in  $\text{BZ}^{\bullet+}$  [100]. However, what seems to be more novel in  $\text{PA}^{\bullet+}$  is strong coupling due to the bending  $b_2$  vibrational modes  $\nu_{36}$  and  $\nu_{33}$ . These modes involve the acetylenic moiety and are absent in  $\text{BZ}^{\bullet+}$ , as well as in  $\text{Ph}^{\bullet}$ .

Apart from the photoelectron spectrum, the vibronic structures of the  $\tilde{X}$  and  $\tilde{C}$  state were also compared with the mass analyzed threshold ionization (MATI) [12] and photoinduced Rydberg ionization (PIRI) [13] spectrum recorded for these two states, respectively. For this purpose precise locations of the vibronic lines are calculated by the matrix diagonalization approach including the relevant vibrational modes and interstate coupling. Comparison calculations were also carried out to reveal the excitation of the nontotally symmetric modes in the spectrum. The foregoing discussions on the photoelectron spectrum reveal that  $\tilde{X}-\tilde{A}$  CIs play some role in the high energy tail of the  $\tilde{X}$  band. The experimental MATI spectrum of the  $\tilde{X}$  state is recorded up to an energy  $\sim 2,100\text{ cm}^{-1}$  below the minimum of the  $\tilde{X}-\tilde{A}$  CIs. In the final theoretical simulations of this spectrum, we considered 7  $a_1$  and 4  $b_2$  vibrational modes selected based on their dominant linear coupling strength and obtained the best match with the experiment [21]. A careful examination of the vibronic lines reveals very weak excitation of the  $b_2$  vibrational modes. The fundamental of the  $b_2$  mode  $\nu_{36}$  appears at  $\sim 115\text{ cm}^{-1}$ . This line is observed at  $\sim 110\text{ cm}^{-1}$  in the experiment and attributed to a vibrational mode of  $b_1$  symmetry. Apart from this, the fundamentals of other  $b_2$  modes  $\nu_{34}$ ,  $\nu_{33}$  and  $\nu_{27}$  are found at  $\sim 602$ ,  $\sim 658$  and  $\sim 1,624\text{ cm}^{-1}$  in accordance with their experimental locations at  $\sim 561$ ,  $\sim 658$  and  $\sim 1,505\text{ cm}^{-1}$ , respectively. Very weak excitations of the overtones and combinations of  $\nu_{13}$  and  $\nu_{36}$  are also observed from the theoretical data. We, however did not discover any excitation of the  $b_1$  vibrational modes in the  $\tilde{X}$  state spectrum as noted in the MATI results [12].

Xu et al. have reported the PIRI spectrum of the  $\tilde{C}$  state up to an energy  $\sim 2,200\text{ cm}^{-1}$  above its origin at  $\sim 17,834\text{ cm}^{-1}$  [13]. The dominant progression in the spectrum is reported to be formed by the totally symmetric modes. In order to corroborate to these experimental results, we performed reduced dimensional calculations of the vibrational energy levels of the  $\tilde{C}$  state. The present electronic structure data reveal a weak coupling of the  $\tilde{C}$  with the  $\tilde{A}$  state via  $b_1$  vibrational mode  $\nu_{32}$  [21]. In the dynamical simulations we considered 6  $a_1$ , 3  $b_1$  and 3  $b_2$  vibrational modes and calculated the spectrum of the  $\tilde{C}$  state both by including as

well as excluding the  $\tilde{A}-\tilde{C}$  coupling [21]. An analysis of all these results reveal the following. The  $a_1$  mode  $\nu_{13}$  is reported to be strongly excited at  $\sim 448\text{ cm}^{-1}$  in the experiment [13]. Transitions up to its third overtone level have been reported. In contrast, we find only weak excitation of its fundamental at  $\sim 456\text{ cm}^{-1}$  and its first overtone is hardly found at  $\sim 913\text{ cm}^{-1}$ . Our observation is in accordance with the laser photodissociation spectroscopy results of Pino et al. [102]. We find a strong excitation of the  $a_1$  vibrational mode  $\nu_{12}$  at  $\sim 751\text{ cm}^{-1}$  [21]. Lines up to its second overtone level are found. Apart from these, the fundamentals of  $a_1$  vibrational modes  $\nu_{11}$  at  $\sim 1,028\text{ cm}^{-1}$ ,  $\nu_{10}$  at  $\sim 1,046\text{ cm}^{-1}$ ,  $\nu_8$  at  $\sim 1,232\text{ cm}^{-1}$ ,  $\nu_7$  at  $\sim 1,528\text{ cm}^{-1}$  and  $\nu_5$  at  $\sim 2,280\text{ cm}^{-1}$  are found from the theoretical data. The fundamentals of  $\nu_{10}$ ,  $\nu_8$  and  $\nu_7$  are observed at  $\sim 996\text{ cm}^{-1}$ ,  $\sim 1,147\text{ cm}^{-1}$  and  $\sim 1,467\text{ cm}^{-1}$ , respectively, in the experiment. The weak  $\tilde{A}-\tilde{C}$  vibronic coupling however does not induce any excitation of the nontotally symmetric modes in the lower part of the  $\tilde{C}$  state spectrum [21].

It is clear from the broad and structureless vibronic band of the  $\tilde{A}$  state shown in Fig. 8 that the nonradiative decay of this state occurs through the CIs in an ultrafast time scale. The diabatic population of this state is recorded in Fig. 9a, and a decay rate of  $\sim 20\text{ fs}$  is estimated from the rapid initial decay of the population. The  $\tilde{B}$  state has been generally predicted to be long lived in the experimental studies of monosubstituted benzene cations [14]. A long lived state should devoid of any efficient nonradiative decay channel. But as discussed above, this state is moderately coupled with the  $\tilde{A}$  state in  $\text{PA}^{\bullet+}$  and  $\tilde{A}-\tilde{B}$  coupling has significant effect on the  $\tilde{B}$  band starting from its origin. The decay of the  $\tilde{B}$  state population is shown in Fig. 9b. The initial decay of population relates to a nonradiative decay rate of  $\sim 88\text{ fs}$  of this state. It therefore, emerges from the present analysis that the  $\tilde{B}^2B_2$  state of  $\text{PA}^{\bullet+}$  is not a very long lived state which deviates from the experimental prediction [14]. A sub-picosecond lifetime is also predicted for the  $\tilde{B}^2B_2$  state of  $\text{C}_6\text{H}_5\text{F}^+$  [18]. The  $\tilde{C}$  state of  $\text{PA}^{\bullet+}$  seems to be a long-lived state.

## 4.2 Vibronic Coupling in Naphthalene and Anthracene Radical Cations: Implications in the Interstellar Chemistry

Naphthalene and anthracene radical cations are the two simplest members in the family of the PAH radical cations. Investigation of the photophysics and photochemistry of the latter are of major concern in contemporary chemical dynamics. The radical cations of PAHs are of fundamental importance in the chemistry of the interstellar space, environmental, biological processes and combustion [103–106]. Radical cations of PAHs are most abundant in the interstellar and extragalactic environments [41]. They absorb strong UV radiation emitted by the young stars and get electronically excited. Examination of the fate of electronically excited PAH radical cations invited critical measurements of their optical spectroscopy in the laboratory in recent years [42–44]. Attempt is made to understand the important issues like, (1) photostability and lack of fluorescence emission and (2) the origin of the enigmatic

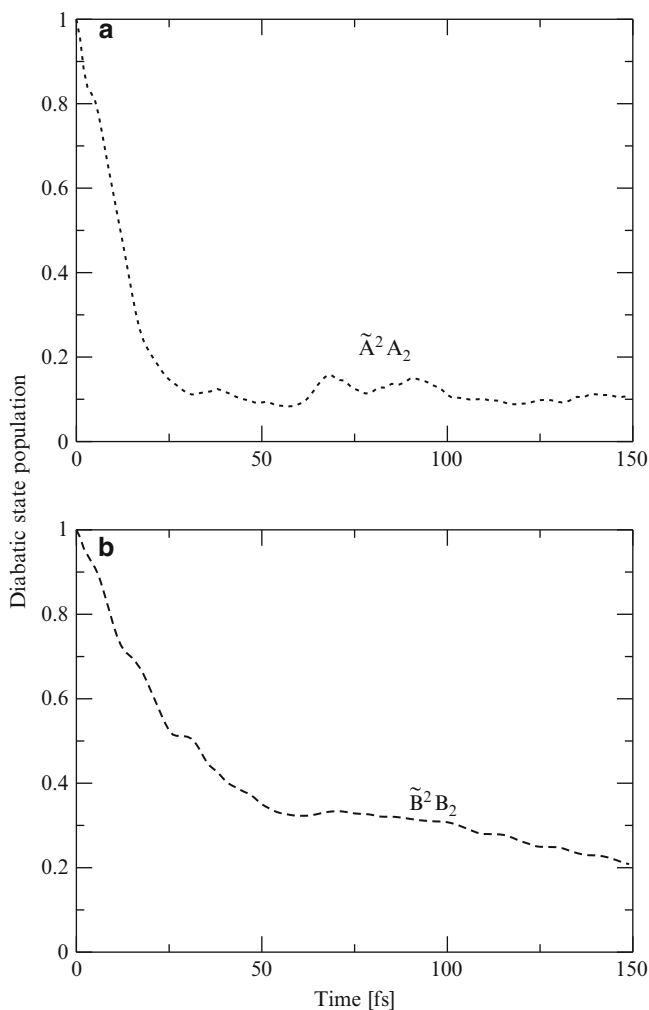


**Fig. 9** Decay of the electronic (diabatic) populations of the  $\tilde{A}$  (panel a) and  $\tilde{B}$  (panel b) electronic states in the coupled  $\tilde{X}-\tilde{A}-\tilde{B}-\tilde{C}$  states dynamics of  $\text{PA}^{\bullet+}$

DIBs. Both these issues seem to be intertwined and originate from the same fundamental aspects of ultrafast nonradiative decay of electronically excited states as discussed above in the case of aromatic biomolecules.

Motivated by these and facilitated by the availability of ample amount of experimental data [16, 42–47], we attempted to investigate the electronic structure and nuclear dynamics of  $\text{N}^{\bullet+}$  and  $\text{AN}^{\bullet+}$  by ab initio based quantum dynamical methods. The main thrust in these studies was to uncover the complex vibronic coupling

mechanism in the low-lying electronic states of these “large” molecular systems and to examine the mechanistic details of their ultrafast nonradiative decay.

The electronic ground  $D_0$  ( $\tilde{X}^2A_u$ ) and excited  $D_1$  ( $\tilde{A}^2B_{3u}$ ) and  $D_2$  ( $\tilde{B}^2B_{2g}$ ) electronic states of  $N^{\bullet+}$  results from ionizations from the valance  $\pi$ -type  $a_u$ ,  $b_{3u}$  and  $b_{2g}$  MOs of the equilibrium ground electronic configuration of neutral naphthalene (N) of  $D_{2h}$  symmetry. The latter possesses 48 vibrational modes which decomposes into  $9 a_g$  ( $\nu_1 - \nu_9$ )  $\oplus$   $4 a_u$  ( $\nu_{10} - \nu_{13}$ )  $\oplus$   $3 b_{1g}$  ( $\nu_{14} - \nu_{16}$ )  $\oplus$   $8 b_{1u}$  ( $\nu_{17} - \nu_{24}$ )  $\oplus$   $4 b_{2g}$  ( $\nu_{25} - \nu_{28}$ )  $\oplus$   $8 b_{2u}$  ( $\nu_{29} - \nu_{36}$ )  $\oplus$   $8 b_{3g}$  ( $\nu_{37} - \nu_{44}$ )  $\oplus$   $4 b_{3u}$  ( $\nu_{45} - \nu_{48}$ ) IREPs of the  $D_{2h}$  symmetry point group. Symmetry allowed coupling between the  $D_0 - D_1$ ,  $D_0 - D_2$  and  $D_1 - D_2$  electronic states of  $N^{\bullet+}$  can be caused by the vibrational modes of  $b_{3g}$ ,  $b_{2u}$  and  $b_{1u}$  symmetry, respectively.

The vibronic spectra of  $D_0 - D_1 - D_2$  electronic states recoded by da Silva Filho et al. [45] revealed resolved vibrational structures of the  $D_0$  and  $D_2$  electronic states and a broad and structureless band for the  $D_1$  state. A slow ( $\approx 3$ –20 ps) and fast ( $\approx 200$  fs) relaxation components are estimated for the  $D_0 \leftarrow D_2$  transition in a (femto)picosecond transient grating spectroscopy measurements [16]. The fast component is attributed to the  $D_0 \leftarrow D_2$  transition and a nonradiative relaxation time of  $\approx 212$  fs is also estimated from the cavity ringdown (CRD) spectroscopy data [42]. Electronic structure results of Hall et al. [107] suggest that the nonradiative  $D_0 \leftarrow D_2$  relaxation occurs via two consecutive sloped type CIs [66, 108]. We developed a global model PESs for the  $D_0 - D_1 - D_2$  electronic states and devised a vibronic coupling model to study the nuclear dynamics underlying the complex vibronic spectrum and ultrafast excited state decay of  $N^{\bullet+}$  [20].

The model diabatic vibronic Hamiltonian of the  $D_0 - D_1 - D_2$  electronic manifold can be expressed in terms of dimensionless normal coordinates of N as [20]

$$\mathcal{H} = (\mathcal{T}_N + \mathcal{V}_0)\mathbf{1}_3 + \begin{pmatrix} U^{D_0} & U^{D_0-D_1} & U^{D_0-D_2} \\ & U^{D_1} & U^{D_1-D_2} \\ h.c. & & U^{D_2} \end{pmatrix}. \quad (40)$$

As before  $\mathcal{T}_N$  and  $\mathcal{V}_0$  refers to the kinetic and potential energy operators of the unperturbed electronic ground state of N and the elements  $U$  are expanded in a Taylor series as

$$U^j = E_0^{(j)} + \sum_{i=1}^9 \kappa_i^{(j)} Q_i + \frac{1}{2} \sum_{i=1}^{48} \gamma_i^{(j)} Q_i^2; j \in D_0, D_1, D_2, \quad (41)$$

$$U^{j-k} = \sum_i \lambda_i^{(j-k)} Q_i; j-k \in D_0 - D_1; D_0 - D_2; D_1 - D_2, i \in b_{3g}; b_{2u}; b_{1u}. \quad (42)$$

Again the parameters are derived by fitting the adiabatic form of the electronic part of the above Hamiltonian to the ab initio calculated energies of the three electronic states. Analysis of various coupling parameters revealed the importance of only 29



vibrational modes in the coupled state dynamics of the  $D_0 - D_1 - D_2$  electronic states [20].

The  $D_0$ ,  $D_1$  and  $D_1$ ,  $D_2$  states are vertically  $\sim 0.70$  and  $\sim 1.27$  eV apart, respectively. The stationary points of the  $D_0 - D_1 - D_2$  PESs are given in Table 1. The data reveal that the minimum of the  $D_0 - D_1$  CIs occurs only  $\sim 0.1$  eV above the minimum of the  $D_1$  state. The minimum of the  $D_1 - D_2$  CIs on the other hand, occurs  $\sim 1.72$  and  $\sim 0.48$  eV above the minimum of the  $D_1$  and  $D_2$  states, respectively. The minimum of the  $D_0 - D_2$  CIs occurs at  $\sim 4.0$  eV above the minimum of the  $D_2$  state and plays no role in the vibronic dynamics studied here [20].

The nuclear dynamics in the  $D_0 - D_1 - D_2$  electronic states are simulated including the 29 relevant vibrational modes and employing the MCTDH WP propagation algorithm [83]. In the following, we only discuss the details of the results relevant for the understanding of photostability of  $\text{N}^{\bullet+}$  and its possible contribution to the DIBs. It was already mentioned that the experiment reveals a well resolved vibrational structure of the  $D_0$  state, and we find only minor nonadiabatic coupling effects due to the  $D_0 - D_1$  and  $D_0 - D_2$  CIs in the energy range of the  $D_0$  band [20]. The  $D_1$  band on the other hand is severely affected by the  $D_0 - D_1$  and  $D_1 - D_2$  nonadiabatic coupling. We recall that the minimum of the seam of the  $D_0 - D_1$  CIs occurs within the zero-point vibrational level of the  $D_1$  state and hence the vibrational structure of this state is perturbed from its onset. The vibrational structure of the uncoupled  $D_1$  state revealed largest deviation from the experiment and the coupled states results. The  $D_1$  band obtained from the present theoretical simulations is shown in Fig. 10 along with the experimental photoelectron spectroscopy results of [45]. Both the uncoupled and coupled surface results obtained from the theoretical simulations are shown. Note that the uncoupled surface results are obtained by the matrix diagonalization approach while the coupled surface results are derived from the WP propagation method. It can be seen that the coupled surface results are in excellent agreement with the experiment [20].

To interpret the observed findings we show the potential energy cuts of the  $D_0$ ,  $D_1$  and  $D_2$  electronic states along the most important symmetric C=C stretching vibrational mode  $\nu_7$ . It can be seen clearly that the  $D_1$  state exhibits very low-energy crossing along this mode. The decay of the  $D_1$  electronic population is also shown in Fig. 10. A nonradiative decay rate of  $\sim 29$  fs is derived from the time dependence of the  $D_1$  electronic populations. The  $D_1$  state is optically dark and could not be probed in the electronic absorption experiment of  $\text{N}^{\bullet+}$ . The  $D_2$  state on the other hand, is optically bright and have been investigated by the CRD experiment [42]. Examination of the  $D_2$  electronic population in the present theoretical treatment reveals a decay rate of  $\sim 217$  fs which agrees very well with the experimental data [20]. The time dependence of the  $D_2$  electronic population is also shown in Fig. 10 and the vibrational spectrum of this state is also shown along with the experimental results.

We now briefly compare the above findings with an analogous study carried out for  $\text{AN}^{\bullet+}$  [22]. Three lowest doublet electronic states of  $\text{AN}^{\bullet+}$  belong to the  $\tilde{X}^2B_{2g}$  ( $D_0$ ),  $\tilde{A}^2B_{1g}$  ( $D_1$ ) and  $\tilde{B}^2A_u$  ( $D_2$ ) symmetry species. These result from ionization from the  $b_{2g}$  (HOMO),  $b_{1g}$  (HOMO-1) and  $a_u$  (HOMO-2)  $\pi$ -type orbital

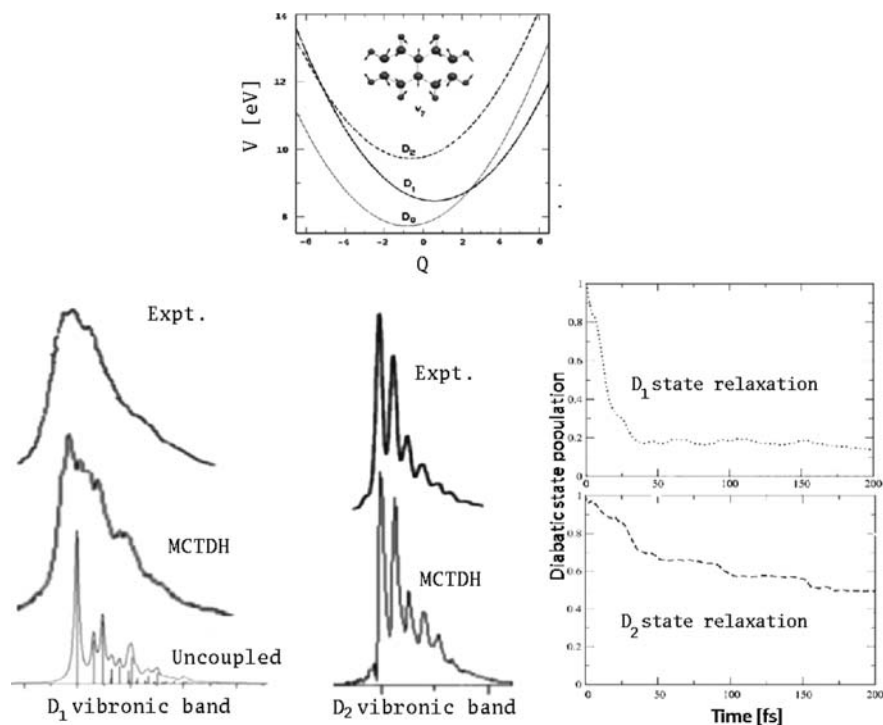


**Fig. 10** The vibronic bands of the  $D_1$  and  $D_2$  states of  $N^{\bullet+}$  are shown in the left and middle of the figure, respectively. The present theoretical results are compared to the available experimental results of [45]. The decay of the diabatic population of the  $D_1$  and the  $D_2$  electronic states in the  $D_0 - D_1 - D_2$  coupled states dynamics is shown in the right side of the figure. The  $D_0$ ,  $D_1$  and  $D_2$  adiabatic potential energy surfaces of  $N^{\bullet+}$  along the  $\nu_7$  (symmetric C=C stretching) vibrational mode is also shown at top of the diagram

of neutral anthracene (AN). The coupling of the  $D_0 - D_1$ ,  $D_0 - D_2$  and  $D_1 - D_2$  electronic states of  $AN^{\bullet+}$  is caused by the vibrational modes of  $b_{3g}$ ,  $b_{2u}$  and  $b_{1u}$  symmetry, respectively. Low-energy curve crossings are established along the totally symmetric C=C stretching vibration ( $\sim 1,601 \text{ cm}^{-1}$ ) in case of  $AN^{\bullet+}$  also. It can be seen from Table 1 that in this case the equilibrium minimum of the  $D_2$  state occurs only  $\sim 0.1 \text{ eV}$  below the minimum of the  $D_1 - D_2$  CIs. The minimum of the  $D_0 - D_1$  and  $D_0 - D_2$  CIs occurs  $\sim 0.72$  and  $\sim 6.6 \text{ eV}$  above the equilibrium minimum of the  $D_1$  and  $D_2$  state, respectively. Examination of the vibronic structure of the coupled  $D_0 - D_1 - D_2$  electronic states reveals that the  $D_2$  band is strongly perturbed by the nonadiabatic coupling in this case [22]. Nonradiative relaxation times of  $\sim 185$  and  $\sim 29 \text{ fs}$  have been estimated for the  $D_1$  and  $D_2$  states of  $AN^{\bullet+}$  in good accord with the available experimental data [16, 22, 47, 109].

To conclude, we have established the role of intricate nonadiabatic coupling in the dynamics of electronically excited radical cations of PAH. The theoretical results presented above support the experimental data on ultrafast nonradiative decay and

provide a general understanding of the lack of fluorescence emission and photostability of these species. The mechanism of photostability is also on par with that discussed for aromatic biomolecules [23]. Observation of the broad and diffuse vibronic bands caused by the strong nonadiabatic coupling effects also adds to the understanding of the DIBs in the interstellar environments. Finally, we mention that one requires to go beyond the LVC coupling approach for these complex molecular systems to interpret the modern experimental data. Although the intermode and further higher order coupling terms are found to be insignificant for the above four systems, importance of such terms is increasingly realized recently for other polyatomic molecular systems (see for example, [110–116]).

## 5 Summarizing Remarks

A brief overview on the recent developments in the photoinduced dynamics of the low-lying electronic states of organic hydrocarbon radical and radical cations is presented in this article. The complex vibronic coupling phenomena are discussed in particular, and their consequence in spectroscopy and nonradiative decay of electronically excited molecular systems are delineated. The basic concept of vibronic coupling leading to the conical intersections of electronic states is reviewed. The theoretical treatment of vibronic coupling employing state-of-the art quantum chemistry and first principles quantum dynamical methods is discussed at length.

The complexity in the assignment of molecular spectra is addressed by showing recent results on four representative examples viz.,  $\text{Ph}^\bullet$ ,  $\text{PA}^{\bullet+}$ ,  $\text{N}^{\bullet+}$  and  $\text{AN}^{\bullet+}$ . The first two are directly derived from the JT active benzene system. Manifestation of the JT activity in these substituted benzenoid systems is also discussed. The mechanistic details of the observed photostability in the PAH radical cations,  $\text{N}^{\bullet+}$  and  $\text{AN}^{\bullet+}$  are examined. The discussions in this article reveal the need of understanding the complex vibronic coupling mechanisms while dealing with the electronically excited molecules in particular, and the recent advancements in the experimental and theoretical techniques to observe and treat them.

**Acknowledgements** This study is supported, in part, by a grant from the DST, New Delhi (Grant No. DST/SF-04/2006). The authors thank CMSD, University of Hyderabad for the computational facilities. VSR thanks CSIR, New Delhi for a senior research fellowship. The authors thank S. Ghanta for his help in obtaining the results on the anthracene radical cation.

## References

1. L. von Neumann, E. Wigner, *Phys. Z.* **30**, 467–470 (1929)
2. W. Domcke, D.R. Yarkony, H. Köppel (eds.), *Conical Intersections: Electronic Structure, Dynamics and Spectroscopy* (World Scientific, Singapore, 2004)
3. M. Born, R. Oppenheimer, *Ann. Phys.* **84**, 457–484 (1927)
4. H.A. Jahn, E. Teller, *Proc. R. Soc. London A*, **161**, 220–235 (1937)

5. G. Herzberg, H.C. Longuet-Higgins, *Discuss. Faraday Soc.* **35**, 77–82 (1963)
6. T. Carrington, *Acc. Chem. Res.* **7**, 20–25 (1974)
7. H. Köppel, W. Domcke, L.S. Cederbaum, *Adv. Chem. Phys.* **57**, 59–246 (1984)
8. D.R. Yarkony, *Acc. Chem. Res.* **31**, 511–518 (1998)
9. R.F. Gunion, M.K. Gills, M.L. Polak, W.C. Lineberger, *Int. J. Mass Spectrom. Ion Process* **117**, 601–620 (1992)
10. C.H. Kwon, H.L. Kim, M.S. Kim, *J. Chem. Phys.* **116**, 10361–10371 (2002)
11. C.H. Kwon, H.L. Kim, M.S. Kim, *J. Chem. Phys.* **119**, 215–223 (2003)
12. C.H. Kwon, H.L. Kim, M.S. Kim, *J. Phys. Chem. A* **107**, 10969–10975 (2003)
13. H. Xu, P.M. Johnson, T.J. Sears, *J. Phys. Chem. A* **110**, 7822–7825 (2006)
14. Y.Y. Youn, C.H. Kwon, J.C. Choe, M.S. Kim, *J. Chem. Phys.* **117**, 2538–2545 (2002)
15. M.S. Kim, C.H. Kwon, J.C. Choe, *J. Chem. Phys.* **113**, 9532–9539 (2000)
16. L. Zhao, R. Lian, I.A. Shkrob, R.A. Crowell, S. Pommeret, E.L. Chronister, A.D. Liu, A.D. Trifunac, *J. Phys. Chem. A* **108**, 25–31 (2004)
17. M. Döscher, H. Köppel, P.G. Szalay, *J. Chem. Phys.* **117**, 2645–2656 (2002)
18. E. Gindensperger, I. Bâldea, J. Franz, H. Köppel, *Chem. Phys.* **338**, 207–219 (2007)
19. V. Sivaranjana Reddy, T.S. Venkatesan, S. Mahapatra, *J. Chem. Phys.* **126**, 074306(1–14) (2007)
20. V. Sivaranjana Reddy, S. Mahapatra, *J. Chem. Phys.* **128**, 091104(1–4) (2008)
21. V. Sivaranjana Reddy, S. Mahapatra, *J. Chem. Phys.* **130**, 124303(1–14) (2009)
22. S. Ghanta, S. Mahapatra, (unpublished data)
23. C.E. Crespo-Hernández, B. Cohen, P.M. Hare, B. Kohler, *Chem. Rev.* **104**, 1977–2019 (2004)
24. A.J.-E. Otterstedt, *J. Chem. Phys.* **58**, 5716–5725 (1973)
25. A.L. Sobolewski, W. Domcke, *Eur. Phys. J. D* **20**, 369–374 (2002)
26. A.L. Sobolewski, W. Domcke, *Europhys. News* **37**, 20–23 (2006)
27. Z. Lan, V. Vallet, A.L. Sobolewski, S. Mahapatra, W. Domcke, *J. Chem. Phys.* **122**, 224315(1–13) (2005)
28. S. Perun, A.L. Sobolewski, W. Domcke, *J. Phys. Chem. A* **110**, 13238–13244 (2006)
29. S. Perun, A.L. Sobolewski, W. Domcke, *Mol. Phys.* **104**, 1113–1122 (2006)
30. V. Vallet, Z. Lan, S. Mahapatra, A.L. Sobolewski, W. Domcke, *Faraday. Discuss.* **127**, 283–293 (2004)
31. F. Bernardi, M. Olivucci, M.A. Robb, *Isr. J. Chem.* **33**, 265–276 (1993)
32. F. Bernardi, M. Olivucci, M.A. Robb, *Chem. Soc. Rev.* **25**, 321–328 (1996)
33. A.L. Sobolewski, W. Domcke, *Phys. Chem. Chem. Phys.* **6**, 2763–2771 (2004)
34. A.L. Sobolewski, W. Domcke, *Chem. Phys.* **294**, 73–83 (2003)
35. J. Jagger, in *Photochemistry and Photobiology of Nucleic Acids*, ed. by S.Y. Wang (Academic, New York 1976), pp. 147–186
36. S. Perun, A.L. Sobolewski, W. Domcke, *J. Phys. Chem. A* **110**, 9031–9038 (2006)
37. T. Schultz, E. Samoylova, W. Radloff, I.V. Hertel, A.L. Sobolewski, W. Domcke *Science* **306**, 1765–1768 (2004)
38. A.L. Sobolewski, W. Domcke, C. Hättig, *Proc. Natl. Acad. Sci. USA* **102**, 17903–17906 (2005)
39. F. Salama, G.A. Galazutdinov, J. Krelowski, L.J. Allamandola, F.A. Musaev, *Astrophys. J.* **526**, 265–273 (1999)
40. T. Henning, F. Salama, *Science* **282**, 2204–2210 (1998)
41. A.G.G.M. Tielens, *Annu. Rev. Astron. Astrophys.* **46**, 289–337 (2008)
42. L. Biennier, F. Salama, L.J. Allamandola, J.J. Scherer, *J. Chem. Phys.* **118**, 7863–7872 (2003)
43. P. Bréchignac, T. Pino, *Astron. Astrophys.* **343**, 49–52 (1999)
44. P. Bréchignac, T. Pino, N. Boudin, *Spectrochim. Acta. Part A* **57**, 745–756 (2001)
45. D.A. da Silva Filho, R. Friedlein, V. Coropceanu, G. Öhrwall, W. Osikowicz, C. Suess, S.L. Sorensen, S. Svensson, W.R. Salaneck, J. Brédas, *Chem. Commun.* 1702–1703 (2004)
46. R.S. Sánchez-Carrera, V. Coropceanu, D. da Silva Filho, R. Friedlein, W. Osikowicz, R. Murdey, C. Suess, W.R. Salaneck, J.-L. Brédas, *J. Phys. Chem. B* **110**, 18904–18911 (2006)

47. O. Sukhorukov, A. Staicu, E. Diegel, G. Roullié, T. Henning, F. Huisken, *Chem. Phys. Lett.* **386**, 259–264 (2004)
48. M. Born, K. Haug, *Dynamical Theory of Crystal Lattices* (Oxford University Press, New York, 1954)
49. B.H. Lengsfeld, D.R. Yarkony, *Adv. Chem. Phys.* **82**, 1–71 (1992)
50. W. Lichten, *Phys. Rev.* **131**, 229–238 (1963)
51. F.T. Smith, *Phys. Rev.* **179**, 111–123 (1969)
52. T.F. O'Malley, *Adv. At. Mol. Phys.* **7**, 223–249 (1971)
53. W. Domcke, G. Stock, *Adv. Chem. Phys.* **100**, 1–169 (1997)
54. H. Köppel, W. Domcke, in *Encyclopedia of Computational Chemistry*, ed. by P.v.R. Schleyer (Wiley, New York, 1998)
55. M. Baer, *Chem. Phys. Lett.* **35**, 112–118 (1975)
56. C.A. Mead, D.G. Truhlar, *J. Chem. Phys.* **77**, 6090–6098 (1982)
57. M. Baer, *Chem. Phys.* **15**, 49–57 (1976)
58. V. Sidis, *Adv. Chem. Phys.* **82**, 73–134 (1992)
59. T. Pacher, L.S. Cederbaum, H. Köppel, *Adv. Chem. Phys.* **84**, 293–391 (1993)
60. A. Thiel, H. Köppel, *J. Chem. Phys.* **110**, 9371–9383 (1999)
61. T. Carrington, *Discuss. Faraday Soc.* **53**, 27–34 (1972)
62. E.R. Davidson, *J. Am. Chem. Soc.* **99**, 397–402 (1977)
63. E. Teller, *J. Phys. Chem.* **41**, 109–116 (1937)
64. D.R. Yarkony, *Rev. Mod. Phys.* **68**, 985–1013 (1996)
65. D.R. Yarkony, *J. Phys. Chem. A* **105**, 6277–6293 (2001)
66. G.J. Atchity, S.S. Xantheas, K. Ruedenberg, *J. Chem. Phys.* **95**, 1862–1876 (1991)
67. I.B. Bersuker, *Chem. Rev.* **101**, 1067–1114 (2001)
68. E.B. Wilson Jr., J.C. Decius, P.C. Cross, *Molecular Vibrations* (McGraw-Hill, New York, 1955)
69. W. Eisfeld, *Phys. Chem. Chem. Phys.* **7**, 832–839 (2005)
70. T. Ichino, A.J. Gianola, W.C. Lineberger, J.F. Stanton, *J. Chem. Phys.* **125**, 084312(1–22) (2006)
71. T. Ichino, S.W. Wren, K.M. Vogelhuber, A.J. Gianola, W.C. Lineberger, J.F. Stanton, *J. Chem. Phys.* **129**, 084310(1–28) (2008)
72. M. Nooijen, *Int. J. Quantum Chem.* **95**, 768–783 (2003)
73. J. Neugebauer, E.J. Baerends, M. Nooijen, *J. Phys. Chem. A* **109**, 1168–1179 (2005)
74. D.R. Yarkony, *J. Phys. Chem. A* **102**, 8073–8077 (1998)
75. D.R. Yarkony, *J. Chem. Phys.* **112**, 2111–2120 (2000)
76. L.S. Cederbaum, W. Domcke, *Adv. Chem. Phys.* **36**, 205–344 (1977)
77. L.S. Cederbaum, *J. Phys. B* **8**, 290–303 (1975)
78. W. Domcke, H. Köppel, L.S. Cederbaum, *Mol. Phys.* **43**, 851–875 (1981)
79. J. Cullum, R. Willoughby, *Lanczos Algorithms for Large Symmetric Eigenvalue Problems*, Vols. I and II (Birkhäuser, Boston, 1985)
80. H.-D. Meyer, U. Manthe, L.S. Cederbaum, *Chem. Phys. Lett.* **165**, 73–78 (1990)
81. U. Manthe, H.-D. Meyer, L.S. Cederbaum, *J. Chem. Phys.* **97**, 3199–3213 (1992)
82. M.H. Beck, A. Jäckle, G.A. Worth, H.-D. Meyer, *Phys. Rep.* **324**, 1–105 (2000)
83. G.A. Worth, M.H. Beck, A. Jäckle, H.-D. Meyer, The MCTDH Package, Version 8.2, (2000), University of Heidelberg, Heidelberg, Germany. Meyer, H.-D.: Version 8.3, (2002). <http://www.pci.uni-heidelberg.de/tc/usr/mctdh/>
84. S.R. Long, J.T. Meel, J.P. Reilly, *J. Chem. Phys.* **79**, 3206–3219 (1983)
85. K. Raghavachari, R.C. Haddon, T.A. Miller, V.E. Bondybey, *J. Chem. Phys.* **79**, 1387–1395 (1983)
86. L.A. Chewter, M. Sander, K. Müller-Dethlefs, E.W. Schlag, *J. Chem. Phys.* **86**, 4737–4744 (1987)
87. J. Eiding, R. Schneider, W. Domcke, H. Köppel, W. von Niessen, *Chem. Phys. Lett.* **177**, 345–351 (1991)
88. H. Krause, H.J. Neusser, *J. Chem. Phys.* **97**, 5923–5926 (1992)

89. R. Linder, K. Müller-Dethlefs, E. Wedum, K. Haber, E.R. Grant, *Science* **271**, 1698–1702 (1996)
90. J.G. Goode, J.D. Hofstein, P.M. Johnson, *J. Chem. Phys.* **107**, 1703–1716 (1997)
91. K. Müller-Dethlefs, J.B. Peel, *J. Chem. Phys.* **111**, 10550–10554 (1999)
92. K. Siglow, H.J. Neusser, *J. Electron Spectrosc. Relat. Phenom.* **112**, 199–207 (2000)
93. B.E. Applegate, T.A. Miller, *J. Chem. Phys.* **117**, 10654–10674 (2002)
94. H. Köppel, M. Döschner, I. Bâldea, H.-D. Meyer, P.G. Szalay, *J. Chem. Phys.* **117**, 2657–2671 (2002)
95. X. Gu, R.I. Kaiser, *Acc. Chem. Res.* **42**, 290–302 (2009)
96. B.S. Haynes, in *Fossil Fuel Combustion*, ed. by A.F. Sarofim, W. Bartok (Wiley Interscience, New York, 1991), pp. 261–326
97. J.G. Radziszewski, *Chem. Phys. Lett.* **301**, 565–570 (1999)
98. G.-S. Kim, A.M. Mebel, S.H. Lin, *Chem. Phys. Lett.* **361**, 421–431 (2002)
99. L. Karlsson, L. Mattsson, R. Jadrny, T. Bergmark, K. Siegbahn, *Phys. Scr.* **14**, 230–241 (1976)
100. I. Bâldea, J. Franz, H. Köppel, *J. Mol. Struct.* **838**, 94–99 (2007)
101. J.W. Rabalais, R.J. Colton, *J. Electron Spectrosc. Relat. Phenom.* **1**, 83–99 (1972)
102. T. Pino, S. Douin, N. Boudin, P. Bréchnignac, *J. Phys. Chem. A* **111**, 13358–13364 (2007)
103. E. Cavalieri, E. Rogan, *Environ. Health. Perspect.* **64**, 69–84 (1985)
104. P. Ehrenfreund, M.A. Sephton, *Faraday Discuss* **133**, 277–288 (2006)
105. A.B. Fialkov, J. Dennebaum, K.H. Homann, *Combust. Flame* **125**, 763–777 (2001)
106. L.H. Keith, W.A. Telliard, *Environ. Sci. Technol.* **13**, 416–423 (1979)
107. K.F. Hall, M. Boggio-Pasqua, M.J. Bearpark, M.A. Robb, *J. Phys. Chem. A* **110**, 13591–13599 (2006)
108. L. Blancafort, F. Jolibois, M. Olivucci, M.A. Robb, *J. Am. Chem. Soc.* **123**, 722–732 (2001)
109. D. Rolland, A.A. Specht, M.W. Blades, J.W. Hepburn, *Chem. Phys. Lett.* **373**, 292–298 (2003)
110. S. Faraji, H. Köppel, W. Eisfeld, S. Mahapatra, *Chem. Phys.* **347**, 110–119 (2008)
111. S. Ghanta, S. Mahapatra, *Chem. Phys.* **347**, 97–109 (2008)
112. U. Höper, P. Botschwina, H. Köppel, *J. Chem. Phys.* **112**, 4132–4142 (2000)
113. S. Mahapatra, V. Vallet, C. Woywod, H. Köppel, W. Domcke, *J. Chem. Phys.* **123**, 231103(1–5) (2005)
114. S. Mahapatra, G.A. Worth, H.-D. Meyer, L.S. Cederbaum, H. Köppel, *J. Phys. Chem. A* **105**, 5567–5576 (2001)
115. T.S. Venkatesan, S. Mahapatra, H. Köppel, L.S. Cederbaum, *J. Mol. Struct.* **838**, 100–106 (2007)
116. T. Mondal, S. Mahapatra, *J. Phys. Chem. A* **112**, 8215–8225 (2008)

# The Jahn–Teller Effect in Binary Transition Metal Carbonyl Complexes

Russell G. McKinlay and Martin J. Paterson

**Abstract** Transition metal carbonyl complexes exhibit a wide-range of vibronic coupling induced phenomena, some of which have only recently begun to be understood via state-of-the-art spectroscopic, as well as theoretical and computational investigations. Historically the Jahn–Teller effect has been used to explain structural information such as ground-state geometries and the lowest energy spin-state. We will review important early work on understanding structural aspects of binary transition metal carbonyl complexes, and then move on to discuss the most recent time-resolved work, and computational studies aimed at explaining these results. The recent time-resolved experiments of have shown that a variety of unexpected features arise from photodissociation of metal carbonyls of the first, second and third rows of the periodic table, and also multiply metal–metal bonded carbonyls. These experiments show that an unsaturated metal carbonyl is produced in the singlet spin-state; the radiationless relaxation being so fast as to preclude a spin–orbit induced change to the high-spin manifold. Such unsaturated metal carbonyls may have accessible geometries that are Jahn–Teller degenerate, and these conical intersections are believed to be the key to ultrafast radiationless decay. This is an exciting development as these systems naturally bring together aspects of the Jahn–Teller effect with photochemistry. Such low-spin degeneracies are not normally found in classical inorganic chemistry; here they are reached photochemically, the exact mechanism from excitation to photoproduct still not fully understood. In relation to modern computational work we discuss current state-of-the-art computational methodologies required to correctly describe metal–carbonyl bonding in the ground and excited states, the resulting potential energy surfaces, and mechanisms of ultrafast photodissociation and subsequent radiationless decay (including conical intersections). We discuss in detail the Jahn–Teller effect in relation to the photochemistry of  $\text{Cr}(\text{CO})_6$ , and  $\text{Fe}(\text{CO})_5$ . Throughout these examples useful group theoretical tools such as the epikernel principle will be exemplified. Several new results will be included at various appropriate points throughout this tutorial review.

## 1 Introduction

The purpose of this tutorial review is to introduce the reader to an important class of transition metal complexes, namely binary metal carbonyls, and aspects of their structure, spectroscopy and photochemistry that necessitate the consideration of vibronic coupling and Jahn–Teller effects. This will include historical justification of geometrical structure, through to modern time-resolved spectroscopy and photochemistry in which Jahn–Teller conical intersections play vital roles and provide wonderful links between theory and experiment in these areas. Important experimental results will be highlighted along with some of the first theoretical studies of the spectroscopy and excited states of these carbonyls. Modern time-resolved studies on their photochemistry will then be summarised. Finally as well as modern experimental work, we will focus extensively on state-of-the-art computational methodologies which are needed to correctly describe metal–carbonyl bonding in the ground and excited states, electronic spectroscopy, the resulting potential energy surfaces, and mechanisms of ultrafast photodissociation, and subsequent radiationless decay (including Jahn–Teller conical intersections). We hope that case studies of  $\text{Cr}(\text{CO})_6$  and  $\text{Fe}(\text{CO})_5$  will highlight the scope and power of modern computational methods applied to inorganic photochemistry in general, and stimulate further work in this area where there is a fascinating and diverse range of vibronically induced chemistry and photochemistry.

### 1.1 Some Fundamentals of M–CO Bonding

To begin a brief overview of the qualitative factors that govern the reactive chemistry of metal carbonyls will be given. In the so-called covalent model, transition metal complexes are considered as metals, bonded to a number of ligands, in their neutral state. Ligands are considered as *x*- or *l*-type according to their electronic structure, or can be a mixture of the two types. An *x*-type ligand coordinates to a metal through a covalent bond, donating one electron, and accepting one electron from the metal in order to complete the octet on the bonding atom of the ligand. An *l*-type ligand normally has eight electrons in its valence shell, and so coordinates to the metal by donating a lone pair of electrons. There are other *l*-type ligands that coordinate in different ways than through a lone pair, such as ethylene ligands, which can donate two electrons to a metal through a  $\pi$ -bond. It should be noted also that *x*-type ligands may also possess a lone pair of electrons but coordinate as an *x*-type ligand since that is energetically favourable. The ligand we shall be focussing exclusively on in this review is the carbonyl ligand, CO. Carbonyl is an *l*-type ligand that bonds via the lone-pair on the carbon. This mode of bonding introduces some complications for multi-configurational wavefunction approaches (*vide infra*).

Transition metal bonding to ligands is primarily governed by their valence electrons in the respective *d*-shell and neighbouring *s*-shell orbitals (to a lesser extent



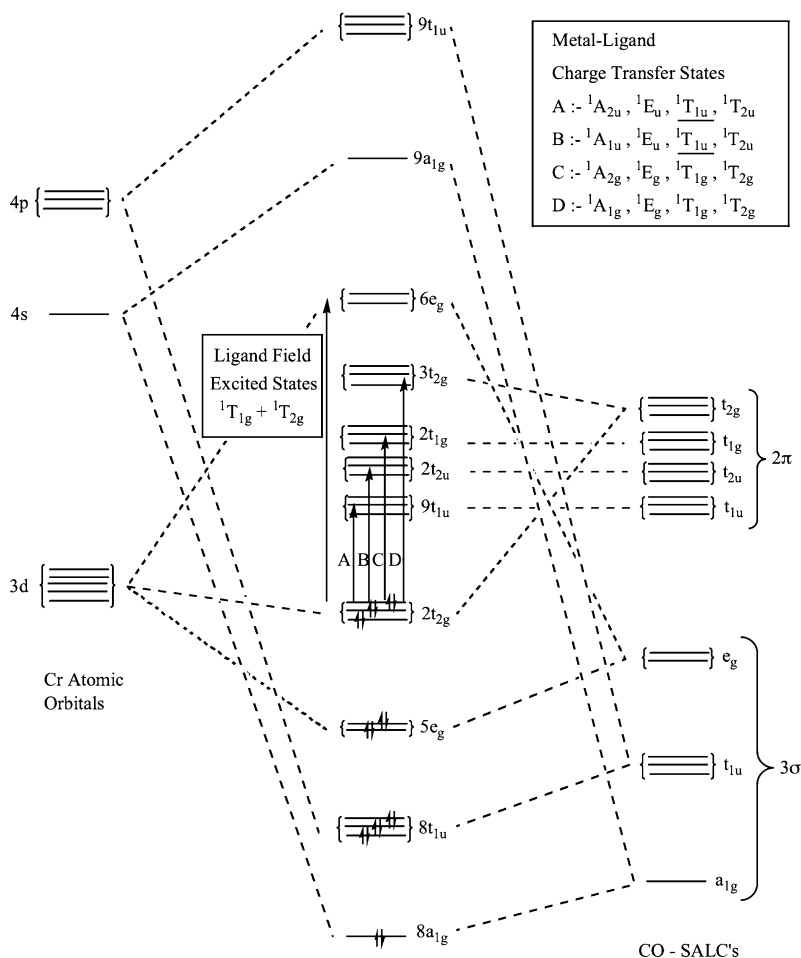


**Fig. 1** Qualitative MO diagram for  $\text{Cr(CO)}_6$ . There are two forbidden ligand-field (LF) excited states ( $a^1T_{1g}$  and  $a^1T_{2g}$ ) arising from  $(2t_{2g})^6 \rightarrow (2t_{2g})^5(6e_g)^1$ , and a manifold of metal–ligand charge-transfer (MLCT) states (A – D), which give rise to two one-photon dipole allowed transitions to  $a$ ,  $b^1T_{1u}$

$p$ -orbitals). See for example the qualitative MO diagrams for  $\text{Cr(CO)}_6$  and  $\text{Fe(CO)}_5$  in Figs. 1 and 2. When ligands bond to a metal to form a complex,  $\text{ML}_n$ , the total number of electrons around the metal centre in the valence shell are then counted. Electron contributions are added to the metal  $d$ -orbital count with each  $x$ -ligand adding one electron, and each  $l$ -ligand adding two electrons, and the overall charge of the complex ( $q$ ) taken into account, according to the formula:

$$N_e = N_m + 2N_l + N_x - q,$$

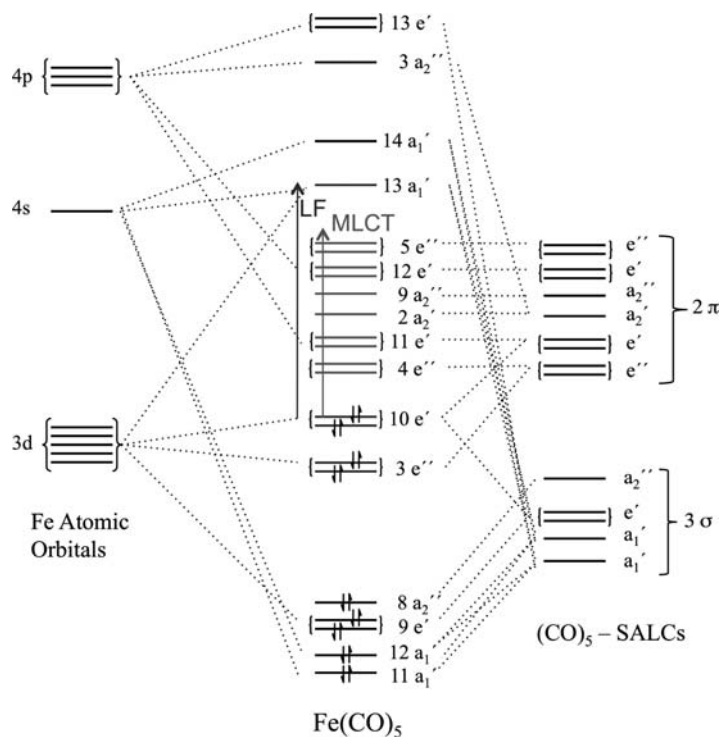


**Fig. 2** Qualitative MO diagram for  $\text{Fe(CO)}_5$ . There are many allowed ligand-field (LF) and metal–ligand charge-transfer (MLCT) transitions that can occur. Selection rules mean that one-photon population of  $^1A_2'$  states is allowed, two-photon population of  $^1A_1'$  and  $^1E'$  states is allowed, while both one- and two-photon population of  $^1E'$  states is allowed and the spectra may overlap

**Table 1** Examples of covalent electron counting in a selection of saturated and unsaturated binary transition metal carbonyls

Binary complex	$N_m$	$2N_l$	$N_{m-m}$	$q$	$N_e$
$\text{Cr(CO)}_6$	6	12	0	0	18
$\text{Cr(CO)}_5$	6	10	0	0	16
$\text{Mn}_2(\text{CO})_{10}$	7	10	1	0	18
$\text{Mn(CO)}_5$	7	10	0	0	17
$\text{Fe(CO)}_5$	8	10	0	0	18
$\text{Fe(CO)}_4$	8	8	0	0	16
$\text{Ni(CO)}_4$	10	8	0	0	18
$\text{Ni(CO)}_3$	10	6	0	0	16

where  $N_e$  is the number of electrons around the metal, and  $N_m$  the electron count from the metal. Stable transition metal complexes generally have  $N_e = 18$ : the famous 18-electron rule. Examples of the electron counts of some binary metal carbonyl complexes are given in Table 1. From a simple ligand-field perspective

the structure of stable 18 electron saturated metal carbonyls is relatively straightforward to deduce (see for example [1]). If the metal carbonyl is co-ordinately unsaturated and the 18-electron rule is not obeyed the species tend to be very reactive, for example the unsaturated species in Table 1, which as we discuss below are the species formed in the ultrafast photodissociation of the parent binary metal carbonyl. It should also be noted that some transition metal carbonyls are most stable in their dimeric form, such as  $\text{Mn}_2(\text{CO})_{10}$ . This is due to having an odd number of electrons in the valence shell of the metal, e.g., for manganese it is seven. Therefore in order to achieve  $N_e = 18$ , an extra electron is gained through metal–metal bond formation ( $N_{\text{m-m}}$ ). Such systems provide examples of metal carbonyl complexes where the photochemistry gains an extra layer of complexity and may proceed through several channels, including metal–ligand dissociation, and metal–metal bond dissociation [2, 3].

Unsaturated metal carbonyls provide excellent examples of Jahn–Teller related phenomena. The position of the coordinate “hole” (determined by the leaving ligand) subsequently gives several possible structural models. As we discuss in detail below it is frequently found that some structures give rise to degenerate electronic states and are therefore Jahn–Teller active. For example in the vertically excited region most metal carbonyls have allowed transitions to degenerate and/or quasi-degenerate states. This means that they tend to have complex initial dynamics, for example in octahedral  $\text{Cr}(\text{CO})_6$  the initially populated MLCT state is Jahn–Teller degenerate and undergoes antisymmetric M–L stretching to remove the degeneracy, and eventually ends up on a dissociative ligand field surface. Also of particular prominence in the low-spin manifold generated in modern femtosecond spectroscopy are Jahn–Teller degeneracies caused by non-filled degenerate *d*-orbitals, often giving rise to multiple possible electronic states (see the discussion on  $\text{Cr}(\text{CO})_5$  and  $\text{Fe}(\text{CO})_4$  below). These Jahn–Teller regions are not often encountered in classical inorganic chemistry as they involve higher energy low-spin states (e.g., open-shell singlets). In the examples we discuss in the latter part of this review it is due to the ultrafast nature of the dissociation that the system is able to reach these Jahn–Teller geometries and undergo radiationless decay to the ground electronic state (also on an ultrafast timescale).

## 2 Early Spectroscopy

Binary transition metal complexes have been the subject of a wide range of studies regarding their structure and spectroscopy for many years beginning with Mond et al. [4] who first reported  $\text{Ni}(\text{CO})_4$  whilst investigating the “Action of Carbon Monoxide on Nickel” in 1890. A wide range of spectroscopic methods and techniques has subsequently been utilised, including X-ray and electron diffraction, IR, and UV/Vis spectroscopy. In almost all cases the Jahn–Teller effect has been invoked to explain certain spectroscopic features. Due to a wide breadth of studies reported in the literature, this review will not be comprehensive. Instead it is

designed to give the reader a flavour of what has been done in this area, where before the advent of computational studies there were often several competing geometrical interpretations possible. Most work covered is concerned with the metals of groups 6 and 8.

## 2.1 Diffraction Studies

Early investigations into the structure of binary group 6 metal carbonyls were conducted by Rüdalt and Hofmann in 1935 [5] who studied the structures of chromium, molybdenum and tungsten hexacarbonyls by X-ray diffraction, and by Brockoway, Ewens and Lister in 1938 [6], who studied the structures of the same species, but by electron diffraction from a vapour. The investigation by X-ray diffraction was not overly successful in reporting an accurate structure, so the study using electron diffraction looked to improve the accuracy of the bond length values. These early studies were fundamental in the understanding of these paradigm complexes in organometallic chemistry, and they concluded that the structure of all three carbonyls is a rectangular octahedron. The crystal structure of  $\text{Cr}(\text{CO})_6$  was reported by Whitaker and Jeffery in 1967 [7]. They also concluded that the monomer was of octahedral symmetry with mean Cr–C bond distances of 1.916 Å.

The structures of iron pentacarbonyl ( $\text{Fe}(\text{CO})_5$ ) was investigated by electron diffraction of a vapour by Ewens and Lister [8]. Photographs of  $\text{Fe}(\text{CO})_5$  were collected at  $-10^\circ\text{C}$ , and from these it was concluded that the structure of the  $\text{Fe}(\text{CO})_5$  was a trigonal bipyramid (TBP). Hanson further analysed the X-ray data in detail and concurred that the structure was indeed TBP [9]. Around the same time, Dahl and Rundle [10] reported the structure of the unsaturated (i.e., less than 18 electron) iron tetracarbonyl ( $\text{Fe}(\text{CO})_4$ ) by X-ray diffraction, and on the basis of their results considered previous works on the structure  $\text{Fe}(\text{CO})_4$  incorrect. They discuss a trimetric structure of  $\text{Fe}(\text{CO})_4$  whose unit cell is *B*-centred with space group  $P2_1/n$ , which is consistent with several possible molecular point groups including  $C_{3v}$  and  $C_{2v}$  (see for example [11] for discussion on the somewhat complicated procedure for determining whether a given molecular point group is compatible with a space group). A refinement of the crystal structure of  $\text{Fe}(\text{CO})_5$  was carried out by Donohue and Caron [12] in order to correctly assign the space group as  $C2/c$ , and to confirm definitively whether the carbon or oxygen was bonded to the metal. They concluded that  $\text{Fe}(\text{CO})_5$  conforms to a TBP structure. Braga et al. [13] also looked again at  $\text{Fe}(\text{CO})_5$  since the older data was by then considered rather imprecise, and highly accurate structural data was needed in order to calibrate with quantum mechanical electronic structure methods which had been carried by then (*vide infra*).

## 2.2 IR Spectroscopy

Infrared spectroscopy has been used for many years in order to investigate metal carbonyl structure, and more importantly for this review, photochemical intermediates. For a description of the typical apparatus used for the study of photo-intermediates of transition metal carbonyls using time-resolved IR spectroscopy, see the paper by Dixon et al. [14] and the recent review by Leadbeater [15].

It was suggested by Garrat and Thomson [16] as far back as 1934 that the initial step in the photochemistry of a metal carbonyl is the loss of a CO ligand. They measured the rate of the photodecomposition of  $\text{Ni(CO)}_4$  in both gas and solution phases, together with the thermal recombination of  $\text{Ni(CO)}_3$  with CO. These suggestions were initially thought of as radical when they were first published, but are now cornerstone features of this field and are today taken for granted.

In 1950 Sheline and Pitzer [17] reported the infrared spectra of  $\text{Fe(CO)}_5$  and  $\text{Fe}_2(\text{CO})_9$ , starting the paper with the phrase “The metal carbonyls are a class of compounds which are by no means fully understood”, a phrase which is very much true today, as we discuss in detail in relation to their time-resolved spectroscopy and photochemistry later. This report showed that the IR bands recorded for  $\text{Fe(CO)}_5$  are consistent with the  $D_{3h}$  structure of  $\text{Fe(CO)}_5$ . A triple carbonyl bridged structure of  $\text{Fe}_2(\text{CO})_9$  is supported by the strong carbonyl band at  $1828\text{ cm}^{-1}$  along with the band for the other carbonyl groups around  $2000\text{ cm}^{-1}$ . The IR spectrum of  $\text{Fe}_3(\text{CO})_{12}$  has also been reported by Cotton and Wilkinson [18]. The IR spectrum of  $\text{Fe(CO)}_5$  was reported in matrices of xenon and argon at 20 K by Swanson and co-workers [19] in which the spectra they obtain have five carbonyl stretching peaks, and three decrease upon annealing. They assign the two bands that persist to  $E'$  and  $A_2'$  CO stretching modes from the  $D_{3h}$  symmetry of the complex.

There have also been a number of IR spectra of metal carbonyls using flash photolysis to investigate unsaturated intermediates. Three such papers are mentioned here. A paper by Church et al [20] looked at flash photolysis of  $\text{Cr(CO)}_6$  in a solution of cyclohexane, showing proof of a  $C_{4v}$   $\text{Cr(CO)}_5$  photoproduct, another [21] looked at flash photolysis in cyclohexane solution saturated with  $\text{H}_2$ , showing production of  $\text{Cr(CO)}_5(\text{H}_2)$ , and a third looking at flash photolysis of  $\text{Fe(CO)}_5$  in a solution of benzene [22].

In 1962 and 1963 a pair of papers by Stolz, Dobson and Sheline [23, 24] looked at the IR spectra of the then suspected pentacarbonyl intermediates of the group 6 metals chromium, molybdenum and tungsten. These papers provided early support for the idea that one CO ligand is initially lost in the first step of the photoreactions of these carbonyls. Analysis of the CO stretching vibrations managed to rule out other possible species such as the  $\text{W}_2(\text{CO})_{10}$  anion and the  $\text{W(CO)}_5$  anion. Analogous results were found for the pentacarbonyls of chromium and molybdenum. The chromium result is particularly relevant for the photochemistry discussed later.

The photochemistry of chromium carbonyl intermediates was also investigated by Graham and co-workers via IR spectroscopy [24, 25] and looked to disprove the possibility that  $\text{Cr(CO)}_5$  forms a structure of  $D_{3h}$  symmetry that is more stable than one of  $C_{4v}$  symmetry, but they make mention that there could be a “rapid

$C_{4v} \rightarrow D_{3h}$  equilibrium lying towards  $C_{4v}$ ” in their suggested photochemical reaction schematic. These conclusions are in agreement with the arguments of Black and Brateman [26] which sought to disprove that a stable  $D_{3h}$  structure is possible for  $\text{Cr}(\text{CO})_5$ .

The mid 1970s saw a brace of investigations into the photochemistry of the group 6 carbonyls via spectroscopic investigation in low temperature matrices by Turner and co-workers [25, 27–29]. One paper looked at the hexa- and pentacarbonyls of Cr, Mo and V at 20K in matrices of argon and methane. These papers were some of the first to try to understand the nature of the initial photoproducts of these three carbonyls, and the procedure of analysing these species in a low temperature matrix produces very sharp bands in the spectra, making it easier to analyse fine structure. They found that all three pentacarbonyls had a  $C_{4v}$  ground state structure, ruling out a possible  $D_{3h}$  TBP geometry. A later paper looked at the interaction of these pentacarbonyls with a variety of matrices. It was shown that these species are very matrix sensitive, and that changes in the visible band of the spectra are due to interaction between the matrix and the sixth empty coordination site of the pentacarbonyl. They go on to discuss from these results the implications of using low temperature matrices to study the photochemistry of unstable intermediates. They advised caution but believed more in-depth studies would reveal new properties of these species, and that the  $C_{4v}$  structure may not be the only possible or most stable geometry of these carbonyls. The last of these papers looked at the possible routes to chromium pentacarbonyl from the hexacarbonyl in a variety of matrices. Using UV photolysis in CO doped argon matrices, the UV and IR spectra collected show evidence of the formation two weak adducts, that of  $\text{Cr}(\text{CO})_5 \bullet \text{CO}$  and  $\text{Cr}(\text{CO})_5 \bullet \text{Ar}$ . The authors looked at altering the concentration of the matrices and of reacting Cr and CO in the argon matrices. All matrices were considered mixed due to the high concentration of CO, and broad bands in the spectra and CO blocking in the high frequency region made interpretation of these spectra very difficult. Wavelength dependent IR studies of the photoproducts of  $\text{Cr}(\text{CO})_6$  [30] and  $\text{Fe}(\text{CO})_5$  [31] have also been reported by the Seder et al. and show the appearance of unsaturated carbonyls missing one CO ligand on a short timescale.

### 2.3 UV and Electronic Spectroscopy

Early work on the electronic spectra and structure of binary metal carbonyls was fundamental in discovering the nature of electronic transitions that govern the photochemistry of these species. Some of the most well known work in this area is that carried out by Gray and co-workers, in the 1960's. A seminal paper from 1963 by Beach and Gray [32] studied the bonding of octahedral metal carbonyls and made the first qualitative attempt to explain the spectroscopic results in terms molecular orbital theory. It was the first discussion of the molecular orbital structure of  $d^6$  octahedral metal hexacarbonyls in an attempt to generalise isoelectronic species in this regard. They suggested a molecular orbital energy level scheme for such

species (see Fig. 1 for a modern representation of the qualitative MO diagram for  $\text{Cr}(\text{CO})_6$ ). They also provided the first discussion of the competition between electronic states of widely different character such as ligand-field (LF) excited states and metal–ligand-charge-transfer (MLCT) states. Beach and Gray correctly assigned the dominant MLCT bands and also rationalized that the observed photodissociation probably took place on a LF state since the  $6e_g$  orbital is primarily anti-bonding in character between the metal and the ligand. Therefore they assigned a shoulder on the MLCT band to this state and verified that irradiation on the shoulder did indeed result in CO loss. As discussed below we now understand that the initial excitation is much more complicated, and indeed is still not fully understood. The UV/Vis absorption spectra of  $\text{W}(\text{CO})_5$  has been reported by Graham and co-workers [33]. The spectra were obtained in an inert matrix and included bands at 44700 and  $34900\text{ cm}^{-1}$  that were assigned to  $^1A_{1g} \rightarrow ^1T_{1u}$  MLCT states, assuming an octahedral geometry. This result agrees with the earlier ones of Beach and Gray that the most intense transition is of MLCT type.

These ideas were further extended in a subsequent paper by Beach and Gray from 1968 [34]. Here electronic spectra of hexacarbonyls of chromium, molybdenum and tungsten were recorded in both vapour and solution phases at 77 and 300 K. The spectral findings were again discussed in terms of transitions between qualitative molecular orbitals. Amongst their assignments were that in the first charge transfer band the shoulder of highest intensity on the low energy side in the neutral group 6 species is  $^1A_{1g} \rightarrow ^1T_{1g}$  (a LF state, Fig. 1). They also discussed the importance of  $\pi$  back-donation in describing the bonding in all the hexacarbonyls. Gray and co-workers then looked at the electronic and vibrational spectra of binuclear metal carbonyls, of which an example is  $\text{Mn}_2(\text{CO})_{10}$  [35]. Similar LF vs MLCT issues arise in the assignment of bands here as well, an issue again at the forefront of current research. For the binuclear carbonyls an extra metal–metal dissociation channel becomes available which further complicates things.

Two papers looking at the photochemistry of iron carbonyls touching upon aspects of their photochemistry that are central to the work below are discussed now. The paper of Hubbard and Lichtenberger [36] from 1981 examined the photoelectron spectrum of  $\text{Fe}(\text{CO})_5$  in the gas phase. This paper is of relevance as they claimed to have evidence of Jahn–Teller distortions in the  $\text{Fe}(\text{CO})_5^+$  cation. Here for the first time it is explicitly mentioned that highly symmetrical transition metal complexes in general have good potential for observable Jahn–Teller activity with regards to their photochemistry after ionization and/or dissociation. They found that ionization into the  $^2E'$  state showed Jahn–Teller activity and discussed this in terms of non-Berry pseudo-rotation.

$\text{Fe}(\text{CO})_5$  state-resolved photofragmentation dynamics have been reported by Waller and Hepburn [37] at a range of wavelengths. They used  $\text{Fe}(\text{CO})_5$  in a supersonic molecular beam, and the photofragments were detected using vacuum ultraviolet laser-induced fluorescence. By using this method properties such as rotational and vibrational distributions of the photoproducts were found. They proposed a reaction that involves sequential loss of all CO ligands, and noted that after irradiation at a wavelength of 193 nm a minor channel opens which produces  $\text{Fe}(\text{CO})_4$

on a very fast timescale. This links in with the earlier mentioned paper by Seder and co-workers [31] which suggests the role of  $\text{Fe}(\text{CO})_4$  involved in the photodissociation process. This is an important initial finding as it relates to results that will be discussed later regarding the use of modern time-resolved spectroscopic and computational techniques relating to how the unsaturated carbonyl with a single ligand coordination hole can channel the system back to the ground electronic state.

### 3 Early Computational Studies

Examples of early computational work [38, 39] involved the use of semi-empirical molecular orbital methods, based on extended Hückel type molecular orbital calculations. The study by Schreiner and Brown [38] used this method to study the qualitative molecular orbitals of  $\text{Cr}(\text{CO})_6$ ,  $\text{Fe}(\text{CO})_5$  and  $\text{Ni}(\text{CO})_4$ . They reported the importance of the  $3d$  and  $4s$  orbitals in both  $\sigma$ - and  $\pi$ -bonding for the three species. They also proposed partial molecular orbital energy level diagrams for each metal carbonyl. Their results differ from the earlier experimental study by Beach and Gray [32] with regards to the spectroscopic assignment in the electronic spectrum of  $\text{Cr}(\text{CO})_6$ , in which a  $t_{2g} \rightarrow e_g$  transition is assigned to a low-intensity, low-energy shoulder in the spectrum.

A method to assign bond enthalpies ( $E$ ) to metal–metal and metal–ligand bonds in various clusters of binary metal carbonyls was proposed by Housecroft and co-workers in 1978 [40], which involves using as a basis the known lengths ( $d$ ), and forming the relationship:  $E = Ad^{-k}$ , where  $A$  and  $k$  are molecule dependent constants. This method was used to conclude that metal–metal bonds are weaker than metal–ligand bonds, and that the metal–ligand bond strength increases with increasing number of metal atoms in the cluster. This method was used again [41] for study of  $\text{Fe}_2(\text{CO})_9$ , specifically to look at the energies of terminal and bridging M–C and C–O bonds, and of the axial and equatorial bond energies of  $\text{Fe}(\text{CO})_5$  which afforded Fe–C bond energies of  $230 \pm 10$  and  $220 \pm 10 \text{ kJ mol}^{-1}$  for axial and equatorial bonds respectively. These results were at odds with the earlier spectroscopic work. Note how close these values are, indeed it is still an open-question which ligand is primarily lost in the initial stages of photodissociation.

With regards to structures of metal carbonyls it has been established that hybrid density functional approaches are generally accurate to within  $0.03 \text{ \AA}$ . Although it has been noted that relativistic effects are important for M–L bondlengths in the second and third rows. This is also the accuracy obtained from the more computationally expensive MP2 and CCSD(T) methods [42]. Of course all of these methods rely on a single-reference framework, which thus limits their use in studies on the reactive chemistry of co-ordinately unsaturated species, due to the preponderance of near and actual degeneracies. The main use of single-reference methods is in benchmarking certain appropriate features of the Jahn–Teller surface such as barrier heights between closed-shell unsaturated photoproducts [43].



In the 1980's more sophisticated computational methodologies could be applied to first row metal carbonyls. Early examples include the work of Veillard and co-workers that utilise multi-configurational methods, applied to such systems for the first time, to study the excited states of  $\text{Fe}(\text{CO})_5$  [44]. They used truncated configuration interaction (CCI) methods to analyse the excited electronic states and photodissociation. Two CI spaces were investigated, one with 15 active orbitals to construct potential energy curves (the orbitals  $3e' - 13a'_1$  shown in Fig. 2), and a larger one with 47 active orbitals to study the energetics of the photoreaction; both CI spaces contain the eight  $3d$  electrons from iron, and include all single and double excitations relative to reference states. They calculated that the ground state of  $\text{Fe}(\text{CO})_5$  is  $^1A'_1$ , with the first excited state a  $^3E''$  ligand field (LF) state at  $33,850\text{ cm}^{-1}$ . They proposed a reaction mechanism for photodissociation which includes intersystem crossing from a initially excited singlet state to the  $^3E''$  state followed by dissociation of a CO ligand along the potential energy surface to the  $^3B_2$  ground state of  $\text{Fe}(\text{CO})_4$ . As will be discussed below this assignment has proven inconsistent with ultrafast spectroscopic work of the last decade. This procedure was reinvestigated 3 years later in 1987 [45], again using CCI calculations, but using CASSCF reference states rather than SCF reference states as in the previous study. They did this to attempt to justify the findings of a photolysis study of  $\text{Fe}(\text{CO})_5$  using transient IR spectroscopy by Seder et al. [31]. For  $\text{Fe}(\text{CO})_5$  an (8,9) active space was used for the  $^1A'_1$  ground state. The resulting orbitals generated were then used to perform CI calculations for the lowest excited states. It was concluded that the values for the excitation energies were overestimated by  $5000\text{ cm}^{-1}$  due to the use of CASSCF orbitals optimised for the ground state. It was also estimated that the  $^1E''$  LF state lies between  $28000$  and  $29000\text{ cm}^{-1}$ , which differs significantly from the value assigned in the previous study.

CASSCF CCI methods (combined with experimental investigations) were once again used to study the spectroscopy of  $\text{Fe}(\text{CO})_5$ , this time focusing on Rydberg states in the vacuum far-UV ( $47000\text{--}90900\text{ cm}^{-1}$ ) [46]. A mixture of (8,9) and (8,10) active spaces were used to provide reference wavefunctions for the CI calculations. It was concluded that the first Rydberg series is within the range of  $49600\text{--}61800\text{ cm}^{-1}$ , and relates to a  $3d_\sigma$  electron excited to  $4s$ ,  $4p$ , and  $4d$  orbitals, with the second Rydberg series within the range of  $64100\text{--}71800\text{ cm}^{-1}$  describing  $3d_\pi$  excitations.

Studies of the M–CO bond energies for a range of carbonyls using more modern computational methodologies have also been reported. Examples of such work include the report by Ziegler and co-workers [47] in which the mean bond energies, and the first dissociation energies of the CO ligand were calculated for group 6, 8 and 10 metal carbonyls of the first three rows. The method used was relativistic  $X\alpha$  density functional theory, with correction terms for electron correlation between electrons of different spins, and non-local corrections to the exchange energy. It was found that the order of the bond strength decreased with increasing  $d$ -orbital shell number  $3d > 4d > 5d$  without the inclusion of relativistic effects, while with the inclusion of relativistic effects the order changed to  $3d > 5d > 4d$  as these effects are most important in the  $5d$  metal carbonyls.

A study by Barnes et al. [48] used *ab initio* methods to look  $\text{Fe}(\text{CO})_n$  ( $n = 1-5$ ) carbonyl dissociation energies for multiple ligands. This is quite important in relation to the photochemistry discussed below, as it is now believed that only a single ligand is lost by photolysis, and the remainder are lost on a longer timescale by thermal processes. They used a modified coupled-pair functional, and basis sets larger than double-zeta size. In particular they found dissociation energies of 39, 31, 25, 22 and  $>5 \text{ kcal mol}^{-1}$  for the iron series, and note that the first dissociation energy relates to both the singlet states of  $\text{Fe}(\text{CO})_5$  and  $\text{Fe}(\text{CO})_4$ , while the second dissociation energy is relative to the accepted triplet ground state of  $\text{Fe}(\text{CO})_4$ , and subsequent dissociations are relative to the lowest energy spin state of the unsaturated species.

A further study looking at the bond-lengths and first dissociation energies of the group 6 hexacarbonyls was carried out by Ehlers and Frenking [49] using high level *ab initio* calculations. For this study MP2 was used to optimise the geometries, followed by coupled-cluster theory with singles, doubles and perturbative triples (CCSD(T)) used to calculate the energetics. The calculated dissociation energies were found to be agreement with experimental values [50]. Similar studies have also been carried out for  $\text{Ni}(\text{CO})_4$ , [51] and again show that correlated electronic structure methods are required for accurate geometry optimisation, and even higher order correlated methods needed for quantitative energetics.

It is fair to say that transition metal carbonyl complexes have been some of the most extensively researched species by computational methods due to their importance in organometallic chemistry. We have attempted here to give a flavour of previous computational work on structural aspects, though the reader is directed to [52–55] for more comprehensive accounts. The most recent computational studies aimed at accurate spectroscopy and photochemical reaction dynamics are discussed in the final section below.

## 4 Modern Time-Resolved Studies: Photodissociation and Ultrafast Relaxation

As hopefully will be evident by now much work has been carried out on the structure and photochemistry particularly over the latter half of the last century, up to the present day, with ever more sophisticated methods being used, from early spectroscopic detection using various matrices, to pure gas and liquid-phase work, to modern time-resolved spectroscopy and state-of-the-art theoretical studies. Here we concentrate on the spectroscopic work that has revived interest in these paradigm systems over the last few years. This will then link up with theoretical studies, including our own continuing work, in the final section.

Matrix isolation experiments (*vide supra*) can provide information on metal carbonyl fragments where absorption data are well defined, and they can resolve structural features due to the long timescale of the experiments and the sensitivity of the spectroscopic methods. In order to remove matrix or solvent effects when

probing the excited states of saturated metal carbonyls, and subsequent photochemistry of the evolving unsaturated photoproducts (which are extremely reactive even with the most inert matrix compound), much effort has been expended to study the gas-phase spectroscopy and dynamics of these systems.

Near UV and Vacuum UV spectra have been reported for  $\text{Fe}(\text{CO})_5$  [46, 56]. The gas phase near-UV optical spectrum of  $\text{Fe}(\text{CO})_5$  was reported by Kotzian et al. [56], while Marquez and co-workers reported the vacuum UV spectrum of  $\text{Fe}(\text{CO})_5$ , supported by a CASSCF/CI theoretical study of the Rydberg states [46]. Semi-quantitative agreement between experiment and theory has been reached although the precise details of the photoexcitation process are still not completely settled.

Initial work with respect to  $\text{Fe}(\text{CO})_5$  photodissociation includes the work mentioned previously by Waller [37] and Seder [31] who studied the state-resolved photochemical breakdown. A number of studies have been reported which looked at the ultrafast (i.e., sub-picosecond) photodissociation dynamics of  $\text{Fe}(\text{CO})_5$ . Examples of such studies include that of Bañares et al. [57], which looked at the photodissociation dynamics of  $\text{Fe}(\text{CO})_5$  in a molecular beam using femtosecond laser pulses via two-photon pumping at 400 nm followed by non-resonant ionisation at 800 nm. Detection of the photoproducts was by means of a time-of-flight mass-spectrometer. The timescale for the dissociation of the CO ligands was measured, and it was found that  $\text{Fe}(\text{CO})_4$  was formed after  $20 \pm 5$  fs,  $\text{Fe}(\text{CO})$  formed after 100 fs, and complete dissociation of the metal and all ligands sometime after 230 fs.

Two papers by Rubner and co-workers [58, 59] also look at the fragmentation dynamics of  $\text{Fe}(\text{CO})_5$ . In the first they propose a simple time-dependent statistical model for CO loss following femtosecond excitation, looking to see if the dissociation mechanism is either concerted or sequential, i.e., whether or not each subsequent CO ligand is lost from an electronically excited species, or whether the first is lost from an electronically excited state and all subsequent ligands thermally lost from the electronic ground state. They applied the model to results given by Zewail and co-workers [60], which are themselves discussed below. The model supports a sequential CO loss mechanism. In a second study [59] they used an experimental setup similar to that of Bañares [57] along with a more detailed time-dependent theoretical model, concluding that there are both sequential and concerted dissociation pathways that can compete with each other.

Work by Zewail and co-workers [60, 61] used ultrafast electron diffraction methods to study in detail the transient  $\text{Fe}(\text{CO})_4$  system formed by photodissociation. This study indicates that in less than 10 ps the dissociation of all ligands is complete. The major conclusion of the Zewail study is that after UV irradiation of  $\text{Fe}(\text{CO})_5$  the major product formed within 200 fs is  $\text{Fe}(\text{CO})_4$  in its ground singlet state. This is based on the structural information in the diffraction data that indicated more open pair-wise L–M–L angles (*vide infra*). For this data to be consistent with high-level quantum chemical calculations the transient had to be in the singlet state, the most obtuse angle being  $169 \pm 2^\circ$ , and the other  $125 \pm 3^\circ$  (see below for our own electronic structure results on this system). This work is an important paper in the field of ultrafast electron diffraction as the resolution of the structural information is great enough to distinguish between two states of a molecule, each with similar

geometries in the same molecular point group ( $C_{2v}$ ). Clearly then the system is able to relax from an upper excited state manifold on an ultrafast timescale and does not undergo an intersystem crossing to the more stable triplet state. By analogy to the multitude of examples in ultrafast organic chemistry (for example see [62–64]) this is highly indicative of a conical intersection connecting the excited products with the ground electronic state. Given the wealth of Jahn–Teller phenomena in structural transition metal carbonyl chemistry this then became the focal point for further research into the nature of the ultrafast relaxation and subsequent events.

Some of the first work that discusses Jahn–Teller activity in  $\text{Fe}(\text{CO})_4$  came in the form of two reports from Poliakoff and co-workers [65, 66]. They reported the first experimental observation of a non-Berry pseudo-rotation in  $\text{Fe}(\text{CO})_4$  at a  $C_{2v}$  geometry [65]. The experiments combined Ar matrix isolation with IR lasers to look at the mechanism of laser induced ligand exchange after enrichment of the species with  $^{13}\text{CO}$ . The results were compared to the  $C_{2v}$  structure of  $\text{SF}_4$  whose ligands can thermally exchange via a Berry pseudo-rotation. The fundamental difference between a Berry and a non-Berry process is intimately related to whether the maximal symmetry (central) point about which the pseudo-rotation takes place is a maximum on the potential surface, or is a conical intersection. This result is further explained by the same authors [66] whereby they reassess the pseudo-rotation using a distorted octahedron topological model which they describe as a qualitative application of the Jahn–Teller theorem. This rationalises the non-Berry pseudo-rotation previously observed by proposing axial-axial, and equatorial-equatorial ligand exchange to axial-equatorial, or equatorial-axial, but crucially not direct exchange between axial-axial and equatorial-equatorial. This model is discussed in more detail in the next section in relation to our own *ab initio* data.  $\text{Fe}(\text{CO})_4$  was the first system where this effect could be observed spectroscopically via time-solved IR studies as other systems underwent either rapid ligand interconversion to all distorted structures, or all interchange was frozen out at the lower temperature of the experiments.

The use of femtosecond lasers (broad in the frequency domain) can be used to “pump” the system under study and create a non-stationary excited state vibrational wavepackets by simultaneously and coherently exciting several vibrational levels on the upper excited surface. This can then be probed by further time-delayed laser pulses (e.g., multi-photon ionisation), which can give detailed information on the evolving excited state dynamics (i.e., time-constants for each sequential process) and on the nature of the ultimate photoproducts. Further work continued in this vein to study the Jahn–Teller distortion in  $\text{Fe}(\text{CO})_4$  by Fuß and co-workers [67] in 2000 who utilised time-resolved ultrafast methods to look at the photolysis of gas-phase  $\text{Fe}(\text{CO})_5$  at 267 nm using femtosecond UV laser excitation. A time-of-flight mass spectrometer was used to monitor the resulting ion signals generated. They concluded that near the Franck–Condon region the dissociation proceeds via a series of Jahn–Teller induced conical intersections due to the very small time-constants for several sequential processes, and a rationalization that the initially populated state is probably MLCT and must somehow reach a LF state before full dissociation occurs. Also, given that there is a manifold of degenerate states that can be populated (Fig. 3(a)) Jahn–Teller conical intersections in this region are almost guaranteed.

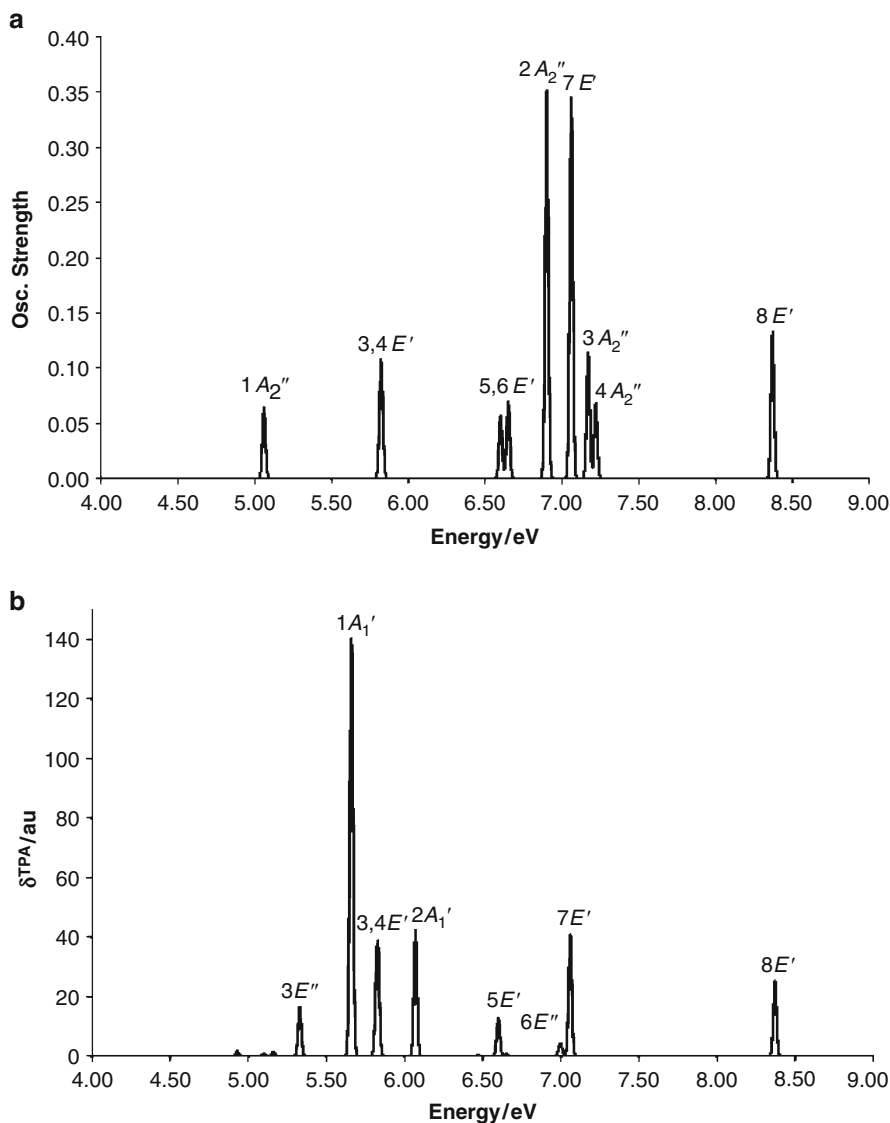


**Fig. 3** Trigonal bipyramid ( $D_{3h}$ )  $\text{Fe}(\text{CO})_5$  (a) simulated pure electronic one-photon absorption spectrum; CCR(3) excitation energy, CCSD oscillator strength, ANO-3 basis. (b) Simulated pure electronic two-photon absorption spectrum; CCR(3) excitation energy, CCSD two-photon cross-section, ANO-3 basis

They proposed a Jahn Teller conical intersection in  $\text{Fe}(\text{CO})_5$  of  $E \otimes e$  nature due to population of the  $2E'$  electronic state coupled to  $e'$  symmetry vibrational coordinates, corresponding to stretching of the equatorial Fe–C and C–O bonds reached within 21 fs. This is followed by relaxation to the  $1A_2'$  state, then again proceeding

back to the path of the  $2E'$  state components by distorting along an  $e''$  coordinate. They also predicted a further conical intersection related to the  $1E'$  state which paves the way to change to a LF state leading to ligand dissociation. Obviously the experimental data fits to kinetic models is less reliable over such small time periods as  $<20$  fs, but this work has shown the complex nature of the initial photochemical dynamics. The previously mentioned work by Poliakoff and co-workers [65, 66] is referenced here to explain a time constant of 47 fs which is attributed to the internal conversion from the  $^1B_2$  first excited state to the  $^1A_1$  ground state of  $C_{2v}$   $Fe(CO)_4$  via a Jahn–Teller induced conical intersection at a tetrahedral geometry. The authors assumed a triply-degenerate state at the Jahn–Teller geometry, and therefore a possible  $T \otimes (t \oplus e)$  intersection; giving several candidate vibrational modes responsible for the vibrational coherence observed in the  $Fe(CO)_4$  photoproduct.

There has been a large body of work carried out over the years on the  $Fe(CO)_5$  system (for a concise highlight of work carried out until 2001 see [68]). The advent of modern ultrafast experimental techniques has shown that this important system is far from simple and displays a complex variety of phenomena, the majority of which highlight the importance of strong vibronic coupling effects.

The Fuß group has pioneered the ultrafast time-resolved study of metal carbonyls. They have studied a wide variety in addition to  $Fe(CO)_5$  discussed above. [67, 69–72] We will discuss further both  $Fe(CO)_5$  and  $Cr(CO)_6$  in the next section in relation to our own theoretical results. Here we note that all the systems studied by the Fuß group show a general trend, the initial excited state populated is a charge-transfer state, and ultrafast vibronic interactions cause the system to relax to a dissociative state. A CO ligand is then lost on the order of a few hundred femtoseconds. If a metal carbonyl can obtain a structure which is Jahn–Teller degenerate in the singlet-spin manifold it will relax to the ground electronic state in less than 100 fs. The unsaturated photoproduct then displays coherent ion signals after being probed by time-resolved ionisation and mass-spectrometry (see the group 6 data in Fig. 4 taken from [72]). In less than a picosecond the ground electronic state of the single-ligand dissociated photoproduct is formed, which undergoes thermal ligand loss on a much longer timescale. This has been experimentally observed in the photodissociation of  $Cr(CO)_6$ ,  $Mo(CO)_6$ ,  $W(CO)_6$ ,  $Fe(CO)_5$ , and  $Mn_2(CO)_{12}$  [67, 69–72]. An interesting exception is the case of  $Ni(CO)_4$  which has a long lived intermediate excited state and undergoes radiative (fluorescence) decay. This has been explained by noting that the  $Ni(CO)_3$  photoproduct does not have any Jahn–Teller geometry, since it has a full  $d^{10}$  configuration.

## 5 Modern Computational Studies: Electronic Structure Aspects, Conical Intersections, and Photochemical Reaction Dynamics

A great deal of work in recent years has been carried out with the goal of gaining a better understanding of the electronic absorption spectra in metal carbonyl complexes. A plethora of methods have been calibrated and applied to these systems

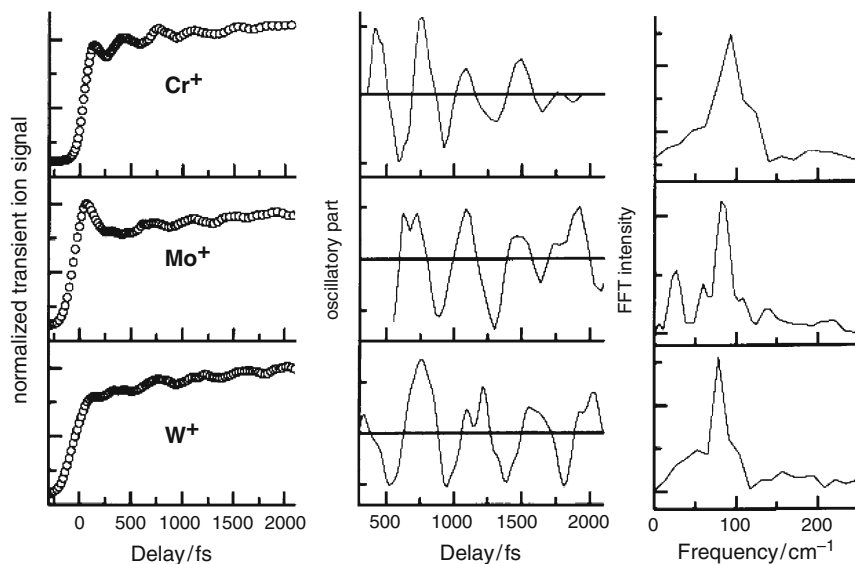


**Fig. 4** Coherent oscillations observed by Fuß and co-workers after ultrafast photodissociation of group 6 metal carbonyls. The Fourier transform of the oscillatory part shows a peak at  $96\text{ cm}^{-1}$ , which compares to  $98\text{ cm}^{-1}$  found for equatorial L–M–L bending in Jahn–Teller “moat” using semi-classical direct dynamics [43] (reused from [70] with permission)

[42, 54, 73–82]. For  $\text{Cr}(\text{CO})_6$  one major achievement has been that it is now established that the initially populated state in the ultrafast photodissociation is not a ligand-field state as was initially believed [34, 73, 77]. Even this paradigm system is not completely understood however, and questions remain regarding the vibronic interactions at very short timescales in the vertically excited region, and exactly how the system evolves onto the ultimate dissociative potential surface. The experimental spectrum is very dense (Fig. 5 from [72]) due to the very high density of (coupled) vibronic states and accurate quantum dynamical modelling of the vibronic excitation in the UV remains a challenging problem. For other carbonyls such as  $\text{Fe}(\text{CO})_5$  similar problems exist at present. Below we present our own recent coupled cluster response calculations for one- and two-photon absorption in  $\text{Fe}(\text{CO})_5$ . Multi-nuclear systems are even more challenging due to the system size, and the most accurate results to date push the boundaries of the current applicability of the CASPT2 method [75].

Following the time-resolved results of Fuß et al in the previous section, we shall presently describe computational efforts to describe and explain the ultrafast relaxation phenomena and dynamics inferred by experimental study. We shall focus on two paradigm systems of chemical importance, namely  $\text{Cr}(\text{CO})_6$  and  $\text{Fe}(\text{CO})_5$  (both 18 electron complexes). The photodissociation, and subsequent ultrafast relaxation to the singlet electronic ground state surface are fundamental to the photochemistry of these species.

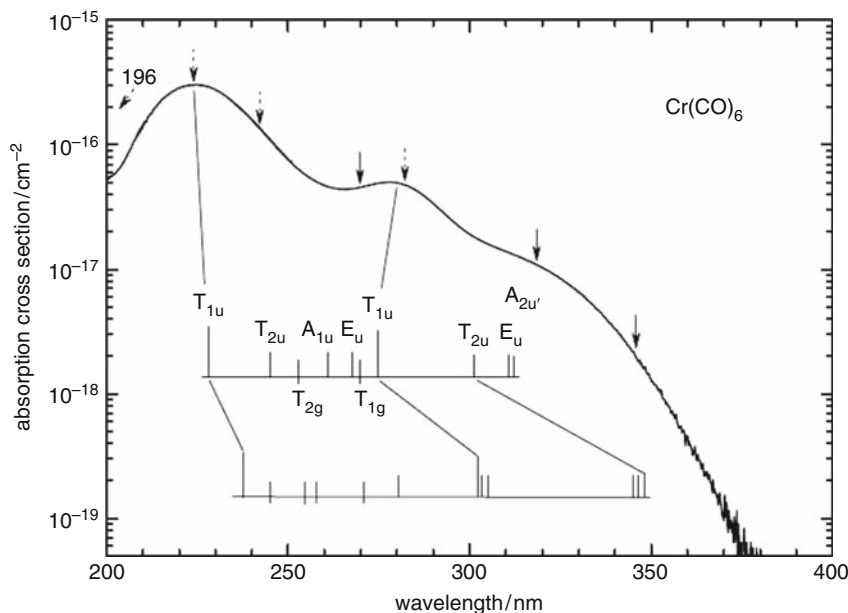


**Fig. 5**  $\text{Cr}(\text{CO})_6$  electronic absorption spectrum as recorded by Fuß et al (reproduced from [72] with permission). Also shown are theoretical results for one-photon electronic transitions; middle panel – Daniel et al, MS-CASPT2 results, [73] lower panel – Pierloot et al, CASPT2 results [76].

As discussed above the  $\text{Cr}(\text{CO})_6$  system has received a great deal of attention. In particular the electronic spectroscopy has undergone considerable attention in recent years [73, 76, 77, 82, 83] and the spectrum is still not completely assigned. In Fig. 5 we show the experimental UV/vis spectrum taken from [72] which includes recent theoretical results at the CASPT2 and MS-CASPT2 levels [73, 76]. Note that there is a very large density of states contributing to each band, and that the results are very sensitive to the theoretical method and basis set used. For example in multi-reference methods like CASPT2 the size of the zero-order reference space, and the degree of state-averaging can affect the accuracy of the band origins by over 1 eV.

Recently it has become possible to apply coupled-cluster methods to the excited states of such relatively large molecules [82]. This is encouraging as such methods treat all excited states on an equal footing, allow excited state mixing, and treat multi-configurational excited states. Coupled-cluster (CC) methodology can be applied to excited states via equation of motion CC (EOM-CC), or the related CC response theory (e.g., linear response CC (LR-CC)). Note that these two methods give exactly the same excitation energies for the “pure” methods like CCSD and CCSDT, although different excitation energies may result using different approximate CC models, such as CC2 or CC3. In general the transition moments from EOM-CC and LR-CC may differ, but usually only by a very small amount [84]. Coupled-cluster response theory is probably the most accurate method available



today to study the electronic absorption spectra of first row binary mono-metallic carbonyls, and can set benchmarks to calibrate other methods, in addition to aiding spectral assignment [73]. In the case of  $\text{Cr}(\text{CO})_6$  EOM-CC (including approximate triple excitations) has proven to be the most accurate and consistent computational method across the entire spectral range [82].

One particular advantage of the CC response methodology is that both single- and multi-photon transitions can be considered [85]. For example the two-photon absorption transition strength is obtained as the first residue of the quadratic response function, while the one-photon absorption transition strength (i.e., oscillator strength) is the residue of the linear response function. Note that the linear and higher-order response functions all give the same excitation energies, as they have the same pole structures.

In Fig. 3 we have shown the pure electronic one- and two-photon absorption spectra obtained from CC theory for  $\text{Fe}(\text{CO})_5$ . The excitation energies were obtained with the non-iterative triples model CCR(3) [86], while the transition strengths were obtained at the CCSD level. An all electron basis set was used [87]. As discussed in detail in [15, 57] dissociative photochemistry of  $\text{Fe}(\text{CO})_5$  is possible by two-photon excitation at 400 nm. Our results clearly show that the one- and two-photon absorption spectra do not strongly overlap, and that there are some strongly allowed low-energy MLCT transitions in the two-photon absorption spectra, not present in the one-photon spectra. It is important to note that when the molecule is non-centrosymmetric, the one- and two-photon absorption spectra may or may not overlap, and that different photochemistry can subsequently result [88–90]. For the gas-phase photochemistry of transition metal carbonyls we expect two-photon (or in generally multi-photon) techniques to be used more frequently as experimental techniques advance. Also note the number of degenerate states that will undergo Jahn–Teller interactions in the vertically excited region for  $\text{Fe}(\text{CO})_5$ . Similarly to  $\text{Cr}(\text{CO})_6$  quantum dynamical simulation of the molecule in this region is an extremely challenging problem and will require coupled multi-state, multi-mode dynamical treatments.

In considering the reactive photochemistry of metal carbonyl species one needs to use multi-configurational methods in order to obtain a balanced description of the potential energy surfaces over a range of geometries, including seams of degeneracy. We shall discuss in detail chromium and iron carbonyls in this section as these systems have seen the most sophisticated computational and theoretical approaches aimed at them. We have previously shown that CASSCF can give reliable potential energy surfaces [43, 91]. Naively one may imagine that ground state structural information can be obtained by using an active space consisting of the metal *d*-orbitals and the appropriate number of metal-based *d*-electrons. Therefore for chromium 6 electrons in 5 orbitals, and for iron 8 electrons in 5 orbitals. However such an active space gives rather poor M–L bond lengths and more worryingly such wavefunctions can display spurious symmetry breaking. To understand why this active space gives poor results we have to remember that CO is a *l*-type ligand, primarily a lone pair donation from the carbon to the metal. Since these bonds are dative, intra-orbital dynamic correlation will be important, and must be included for even qualitative

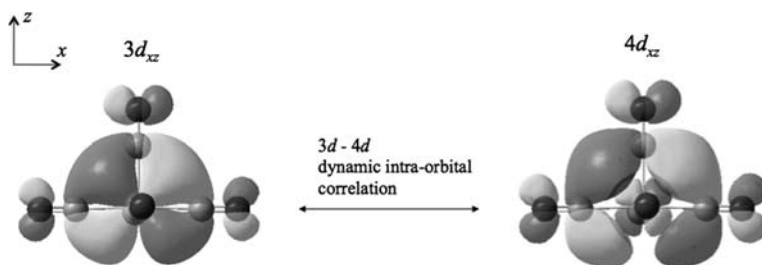


**Fig. 6** Schematic of “orbital doubling” procedure for multi-configurational wavefunctions as applied to transition metal photochemistry. On the left a predominately  $3d_{xz}$  orbital is shown (in phase combination of smaller and larger exponent metal centred basis functions). To account for the dative nature of the M–CO bond any active space needs to be augmented with further orbitals containing extra nodes in the M–L region, here a  $4d_{xz}$  orbital is shown (out of phase combination of smaller and larger exponent metal centred basis functions). In the subsequent configuration interaction this  $3d$ - $4d$  dynamic correlation generates qualitatively reliable wavefunctions

results. This is relatively simple to include in CASSCF: one expands the active space to include higher lying orbitals with nodes in the internuclear M–L regions. This method was introduced by Persson et al. [92] and was shown to give an accurate and robust description of metal carbonyl bonding. As introduced by Persson [92], and subsequently used by Pierloot et al. [76] using CASSCF and CASPT2 to study the optical spectra of  $\text{Cr}(\text{CO})_6$ , the orbitals for a minimal active space for  $\text{Cr}(\text{CO})_6$  are the 2, 3  $t_{2g}$  and 5, 6  $e_g$  in Fig. 1. In our previous studies we altered this approach slightly: we used the 2  $t_{2g}$  and 6  $e_g$  orbitals (i.e., those primarily metal “ $3d$ ” atomic orbitals), and we doubled the active space by including a higher lying set of primarily “ $4d$ ” atomic orbitals. The extra “ $4d$ ” orbitals are the out of phase combinations of the smaller and larger exponent basis functions in (at least) a double-zeta sized basis set, while the “ $3d$ ” orbitals are the in phase combinations. In Fig. 6 we show a pair of such orbitals. When the CASSCF wavefunction is optimised one finds that in the electronic ground state the occupation number (as given by the diagonal elements of the one electron density matrix) of the formally doubly occupied “ $3d$ ” orbitals is  $\sim 1.8$ , while that of the corresponding “ $4d$ ” orbital is  $\sim 0.2$ . Thus inclusion of the extra orbital in the active space introduces an amount of dynamic electron correlation into the wavefunction. This approach to constructing active spaces appears to be very promising, and in general very good energetics and barrier heights can be obtained. For example, for the barrier to pseudo-rotation between square planar  $C_{4v}$  minima, via a  $C_{2v}$  transition state, one can use accurate single reference methods like CCSD since these structures are closed-shell, and one finds that this barrier height is within 2 kcal mol $^{-1}$  for CASSCF with the enhanced active space. Therefore, one can be confident that energy differences between Jahn–Teller degenerate points, minima, and saddle-points are also well represented.

The ultrafast spectroscopic results of Fuß et al. [2, 70–72] for  $\text{Cr}(\text{CO})_6$  indicated that a conical intersection between the ground and first excited singlet state may be responsible for the femtosecond quenching of the electronically excited  $\text{Cr}(\text{CO})_5$

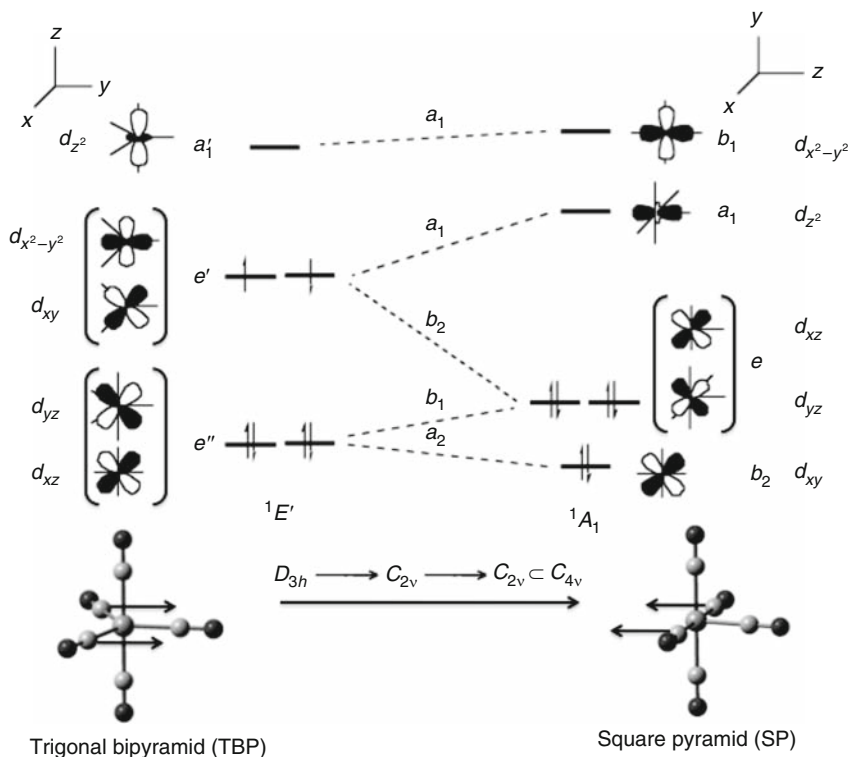


**Fig. 7** Orbital correlation diagram for singlet  $\text{Cr}(\text{CO})_5$  between trigonal bipyramid (TBP),  $D_{3h}$ , and square planar (SP),  $C_{4v}$ , geometries. All intermediate geometries have  $C_{2v}$  symmetry.  $D_{3h}$  and  $C_{4v}$ , are both supergroups of  $C_{2v}$

photoproduct. A change in spin state (i.e., from singlet to triplet) was discounted due to the longer timescales involved in spin-crossover. It is relatively straightforward to see from a simple ligand-field splitting diagram for the unsaturated  $\text{Cr}(\text{CO})_5$  where such conical intersections must exist from symmetry arguments. Thus, whenever we can generate an electronically degenerate state, we know that this molecular structure is but one point on a seam on conical intersections [93, 94], and further we know from the Jahn–Teller theorem [95] the symmetries of the vibrational modes which will couple the component states. Of course identification of molecular structures with degenerate states does not necessarily mean that such geometries can be dynamically reached, and further, several different seams of intersection may exist.

To use  $\text{Cr}(\text{CO})_5$  as a concrete example: it is clear that trigonal bipyramid (TBP) geometries can give rise to degenerate open-shell states (see left side of Fig. 7). Occupying the degenerate  $e'$  orbitals with two electrons gives rise to the following possible electronic states:  $e' \otimes e' = {}^1E' \oplus {}^1A'_1 \oplus {}^3A'_2$  [96], and we would expect the triplet state to be a stable TBP structure. Note that the triplet spin state will always be given by the antisymmetrized direct product since the spin function is symmetric.

However, since we are in the singlet manifold we are interested in the  $^1E'$  and  $^1A'_1$  states and the only way to determine the lowest one is via computation. We indeed find that the lowest singlet state at TBP geometries is  $^1E'$ .

Therefore TBP  $D_{3h}$  geometries are on a seam of intersection between the components of the  $^1E'$  state, i.e., the  $^1A_1$  and  $^1B_2$  states in the largest Abelian subgroup of  $D_{3h} \supset C_{2v}$ . An excellent tool for detailing the Jahn–Teller surface is the epikernel principle of Ceulemans and Vanquickenborne [97]. Here one evaluates the kernels ( $K_i$ ) and epikernels ( $E_i$ ) for a given irreducible representation in a point group, where the nomenclature  $K_i(G, \Lambda)$  and  $E_i(G, \Lambda)$  stands for the  $i$ -th kernel/epikernel of the irreducible representation  $\Lambda$  in the group  $G$ . The kernels are groups of symmetry elements preserved by distortion along a vector spanning the irreducible representation  $\Lambda$ , while the epikernels are selected preserved groups of higher symmetry that are only preserved in part of the (degenerate) distortion space. The seminal theorem of Ceulemans and Vanquickenborne [97] is that given a linear Jahn–Teller distortion the highest ranking epikernels will correspond to the point groups of minima, while lower ranking epikernels and kernels will correspond to saddle-points. For example in  $\text{Cr}(\text{CO})_5$ , one finds that the largest epikernel of  $e'$  in  $D_{3h}$  is  $E(D_{3h}, e') = C_{2v}$ . The number of equivalent epikernel distortion directions is given by the quotient between the orders of the non-Abelian Jahn–Teller point group, and the epikernel sub-group. Thus,  $n_{E(D_{3h}, e')} = \frac{|n_{D_{3h}}|}{|n_{C_{2v}}|} = \frac{12}{4} = 3$ .

In Fig. 8 we have labelled the 3 equivalent  $C_{2v}$  epikernel distortion directions as  $E^1(D_{3h}, e')$ ,  $E^2(D_{3h}, e')$  and  $E^3(D_{3h}, e')$ , with the direction of distortion (forward or reverse) given by the sign, i.e.,  $E^1(D_{3h}, e')$  labels a distortion along the forward direction of epikernel 1, while  $-E^1(D_{3h}, e')$  labels the same epikernel but with the distortion in the reverse direction. In this particular case (an  $E \otimes e$  Jahn–Teller), forward epikernels lead to minima, while reverse epikernels lead to saddle-points of the same symmetry (or *vice-versa*). The three equivalent epikernels are the three independent ways of distorting the TBP L–M–L angles from  $120^\circ$  by keeping two angles the same and allowing the third to differ (the total summing to  $360^\circ$  - see Fig. 7). Thus forward motion corresponds to two angles closing from  $120^\circ$ , while the third opens up; and reverse motion corresponds to two angles opening up from  $120^\circ$ , while the third closes. One interesting thing to occur in  $\text{Cr}(\text{CO})_5$  is that although the entire Jahn–Teller “trough” in Fig. 8 maintains  $C_{2v}$  symmetry, there are points of higher (accidental symmetry). Thus, if two TBP angles are closed to be  $90^\circ$  (the remaining one becomes  $180^\circ$ ), then we accidentally have a structure of  $C_{4v}$  symmetry (i.e., a square planar geometry). Thus  $C_{4v}$  is a supergroup of  $C_{2v}$  and we have to be mindful of accidentally reaching isolated points of a supergroup symmetry since the epikernel principle cannot predict the presence of these. The Jahn–Teller surface for singlet  $\text{Cr}(\text{CO})_5$  is therefore as shown in Fig. 8 with three equivalent SP minima of  $C_{4v}$  symmetry, connected by 3 equivalent saddle-points of  $C_{2v}$  symmetry.

For  $\text{Cr}(\text{CO})_5$  it is interesting to consider the epikernel extrema of  $C_{2v}$  symmetry which correspond to saddle-points for pseudo-rotation (Fig. 8). Generally one imagines such features to be associated with second-order coupling terms in the degenerate intersection space of the conical intersection [94, 98]. However this is by

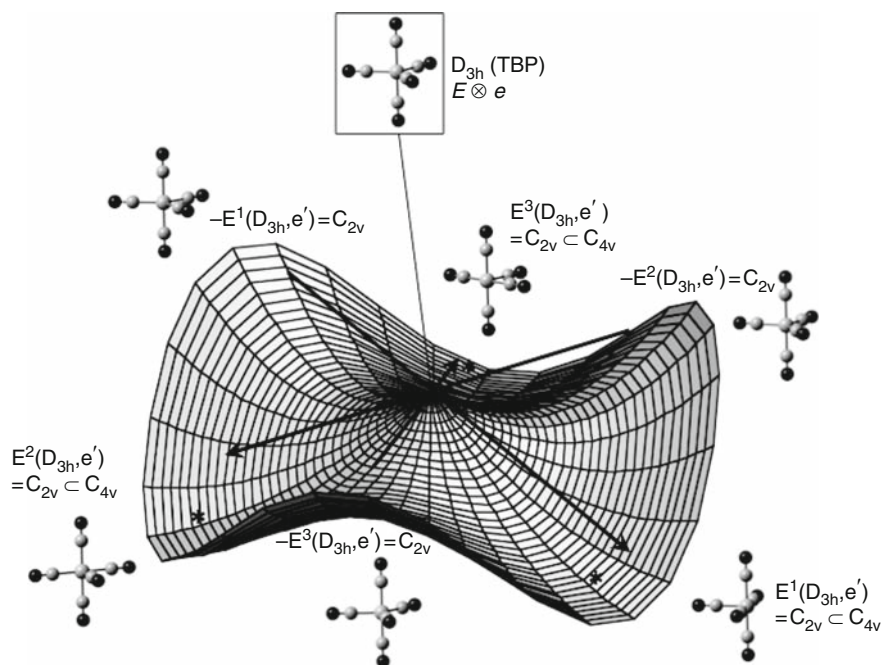


**Fig. 8**  $\text{Cr}(\text{CO})_5$  lowest adiabatic potential around  $E \otimes e$  Jahn–Teller conical intersection at trigonal bipyramid (TBP)  $D_{3h}$  geometry. There are three equivalent epikernel distortion directions for a vibrational coordinate pair spanning  $e'$ ,  $E^i(D_{3h}, e')$ . Motion in the forward direction leads to one of three equivalent square planar (SP)  $C_{4v}$  minima, indicated by \*; while motion in the reverse direction leads to  $C_{2v}$  saddle-points (transition states for the interconversion of SP structures via non-Berry pseudo-rotation). The barrier is around  $12 \text{ kcal mol}^{-1}$

no means the only mechanism for the “Mexican hat” to become a “tricorn”. A diabatic vibronic coupling Hamiltonian constructed to study the quantum dynamics of  $\text{Cr}(\text{CO})_5$  radiationless relaxation (*vide infra*) indicated that strong pseudo-Jahn–Teller coupling between a component of the degenerate  $E'$  state and a higher non-degenerate state was operative [91, 99]. A very useful tool to assign and rationalise the pseudo-Jahn–Teller effect has emerged in recent years based in symmetry restrictions to CASSCF Hessians [100]. Briefly the pseudo-Jahn–Teller effect is a lowering of the symmetry of a non-degenerate state, via a non-degenerate vibrational mode, to stabilise an adiabatic electronic state by mixing with an excited state of the appropriate symmetry [94, 98, 100–102]. In state-specific CASSCF obviously the gradient vector is totally symmetric in an Abelian sub-group. For the Hessian however, non-totally symmetric contributions are important. Such CI vector rotation contributions are obtained from solution of the coupled-perturbed MCSCF (CP-MCSCF) equations, and one can exclude certain symmetry classes by only using configuration state functions (CSFs) of a given symmetry in the Hessian evaluation. Thus one can in affect “switch off” the contribution of non-totally symmetric (derivative) couplings. If one obtains a different Hessian with

those couplings included then one can deduce that a pseudo-Jahn–Teller interaction is present [100]. As an example for  $\text{Cr}(\text{CO})_5$  we have performed this analysis at the  $C_{2v}$  saddle-points using CAS(6,8)/cc-pVDZ (all electron basis for chromium from [103]). Using only CSFs of  $A_1$  symmetry all vibrational frequencies are real, and the lowest frequency mode has  $b_2$  symmetry, and  $\nu = 51.1 \text{ cm}^{-1}$ . If all CSFs of all irreducible representations are included then the lowest mode again has  $b_2$  symmetry, but now  $\nu = 95.6 \text{ cm}^{-1}$ . Therefore the pseudo-Jahn–Teller coupling causes a mixing of the closed-shell non-degenerate ground-state (Fig. 7) with an excited state causing the adiabatic potential energy surface to have negative curvature along this mode. The coupling is between the  $\dots (d_{xy})^2 (d_{yz})^2 (d_{xy})^2 - {}^1A_1$ , and the  $\dots (d_{xy})^2 (d_{yz})^2 (d_{xy})^1 (d_{x^2-y^2})^1 - {}^1B_2$  adiabatic states. In  $C_{2v}$  symmetry a mode of  $b_2$  symmetry can couple these states since  $A_1 \otimes B_2 \otimes B_2 = A_1$ . Thus this method is very insightful and clearly shows the origin of a pseudo-Jahn–Teller effect. Such analytical CASSCF Hessian computation is unfortunately rather expensive, and is currently only possible for active spaces up to around (8,8) due to the fact that the complete CP-MCSCF equations need to be solved. Never the less this indeed a promising tool to differentiate between real second-order Jahn–Teller effects, and pseudo-Jahn–Teller effects and will surely be used a great deal in future studies.

Having an understanding of the potential energy surfaces is of course only half the story regarding photochemical modelling. One must also try to model dynamics via either a classical or quantum description of the nuclei. Molecular dynamics in coupled electronic states is currently a subject of much current research [99, 104–106]. Metal carbonyl complexes are large and challenging targets for such simulations although direct comparison with the most recent experimental results makes them very promising systems. We note that Daniel et al have performed a wide variety of 2D quantum wavepacket calculations on inorganic systems ([54, 74] and references therein). However for the relaxation of metal carbonyl complexes multi-mode effects are prominent, and dynamics of much higher dimensionality are required. Recently the MCTDH methodology [107] has been applied to such a problem, and such software advances (with concomitant hardware advances) mean that first principles dynamical simulation of such systems is within reach as exemplified by two recent studies on  $\text{Cr}(\text{CO})_5$  relaxation.

In [43] a semi-classical surface hopping study was performed using on the fly CASSCF potentials. Here the purpose of the dynamics was not to provide any statistical convergence of some observable, but rather to give mechanistic insight, and determine if the system can dynamically reach a conical intersection, and subsequently decay to the ground state on a sub-picosecond timescale. Note that the active space was reduced slightly in that one “3d” and “4d” orbital pair was not included in the standard (6,10) active space discussed above. By inspecting Fig. 7 it can be seen that across all geometries of interest one  $d$ -orbital remains unoccupied ( $d_{z^2}$  at TBP, and  $d_{x^2-y^2}$  at SP). The virtue of the orbital optimization in CASSCF is that a balanced set of orbitals connecting these two extremes is generated by allowing the  $d_{z^2}$  and  $d_{x^2-y^2}$  to mix at intermediate geometries. Thus, the active space was reduced to (6,8) generating 1176 singlet configuration state functions, meaning

that the computation of analytical gradients, Hessians, and derivative-couplings was possible.

Initially a dissociation trajectory for  $\text{Cr}(\text{CO})_6$  was run on the first excited singlet ligand field (LF) state ( $S_1$ ). This showed that a CO ligand was ejected in around 90 fs (the absolute value here should be treated with caution as the initially populated state is undoubtedly not a LF state [77, 82]). The ejected CO leaves in a rotationally excited state consistent with observations on  $\text{W}(\text{CO})_6$  (a similar group 6 carbonyl) by Holland [108]. A subtle effect is that the remaining ligands in the same plane as the leaving ligand slowly start to bend inwards to fill coordination hole left by the ejected CO. After 100 fs the positions and momenta for the remaining  $\text{Cr}(\text{CO})_5$  were used to study this fragment alone.

The non-adiabatic event was treated using a surface-hopping algorithm. It was noted that within 80 fs a pair of remaining ligands “fold” in so that the geometry becomes TBP, each of the in-plane L–M–L angles is  $120^\circ$  (see Fig. 9). Thus the system quickly reaches the Jahn–Teller geometry. The trajectory study shows a downward crossing and fast recrossing to the upper state before ultimate decay to the ground state. Here the molecular motion in the branching space of the Jahn–Teller intersection begins to change from symmetric bending to antisymmetric bending, and the molecule begins to vibrate along the pseudo-rotational coordinate. This is another example of a non-Berry pseudo-rotation and should be contrasted with the well-known Berry pseudo-rotation in for example  $\text{PF}_5$ . In the trajectory study the molecule remains trapped in the well of a square planar minimum (Fig. 9). The Fourier transform of the angular variation of the pairwise equivalent equatorial L–M–L angle discussed above gives a vibrational frequency of  $98\text{ cm}^{-1}$ , while the experimental coherent oscillation observed by Fuß et al. [2, 70–72] was  $96\text{ cm}^{-1}$  (see Fig. 4). Care should be taken not to read too much into this result other than to show that the mechanistic details of this photo-relaxation can be modelled using a surface-hopping approach. It should also be noted that surface hopping approaches are still rather non-standard, and for the  $\text{Cr}(\text{CO})_5$  system were very time-consuming (several CPU months per trajectory). Recent advances in surface hopping technology (see for example [109]) however mean that this approach should be investigated for other metal carbonyl systems in the future as the semi-classical methods in the full space of coordinates give tremendous mechanistic insight into the photodissociation and relaxation processes, and serve as a prelude to wavepacket computation by highlighting the essential vibrational modes needed to construct model Hamiltonians.

Given the encouraging results of the surface-hopping study on  $\text{Cr}(\text{CO})_5$  a wavepacket dynamics study was undertaken in [91]. The same level of electronic structure theory was used as in the surface-hopping study to generate adiabatic potentials, which were used to fit the parameters of a linear vibronic coupling model Hamiltonian. In fitting to the linear vibronic coupling model it was found that an  $E \otimes e$  model was inadequate to fit to the adiabatic surfaces. It was only when a third (non-degenerate) diabatic state was included, via a pseudo-Jahn–Teller coupling to the degenerate  $E$  state could a reasonable fit be made (the validity of this coupling was discussed in an adiabatic basis above). This highlights the utility of such



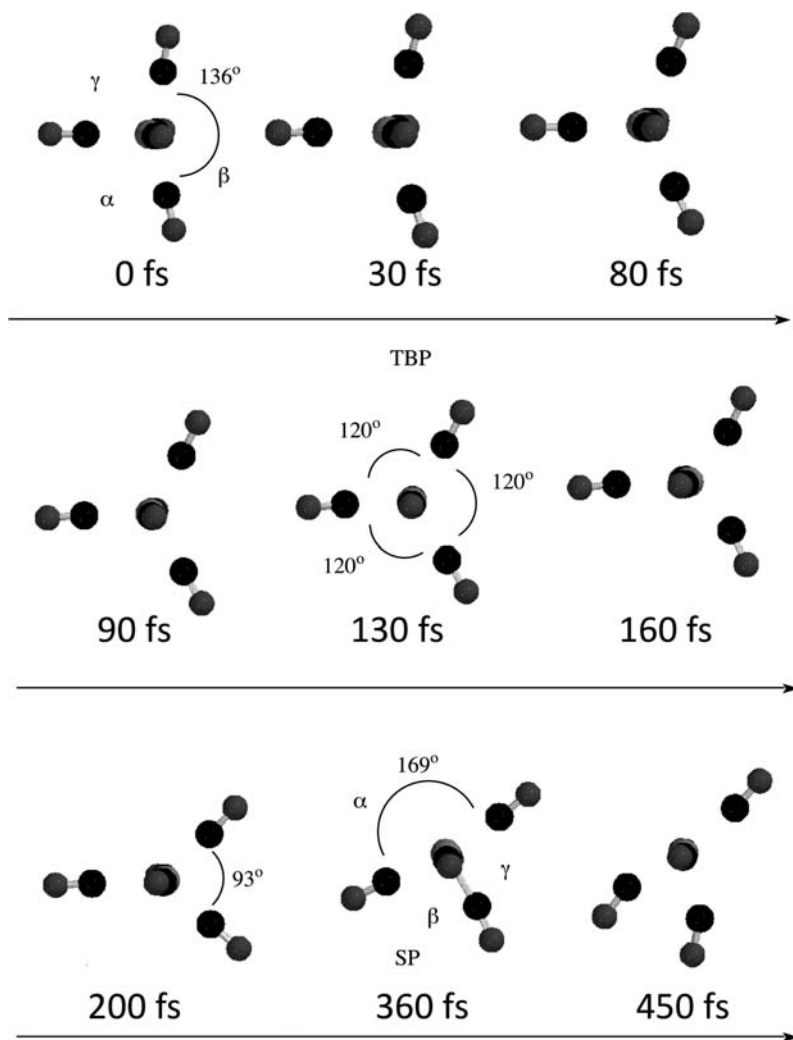


**Fig. 9** Snapshots of sample  $\text{Cr(CO)}_5$  trajectory (viewed down axial ligand axis) through trigonal bipyramidal Jahn–Teller intersection (reached in 130 fs), followed by oscillation in square planar (SP) like structure in Jahn–Teller “trough”. Saddle-point like structure is shown after 200 fs, followed by SP like structure after 360 fs

a model Hamiltonian approach to understand complicated potential energy surface topology in addition to obtaining suitable potentials for dynamics. By fitting adiabatic cuts to suitable models one can readily gain an idea of the various couplings involved as one moves away from the conical intersection. In the case of  $\text{Cr(CO)}_5$ , as discussed above, we checked the  $C_{2v}$  barrier to pseudo-rotation in terms of a pseudo-Jahn–Teller effect, and indeed found that this is the dominant mechanism for warping of the “trough”, rather than pure second order Jahn–Teller effects



as were initially supposed. Indeed the pure second-order Jahn–Teller couplings are almost negligible in this system.

From the surface-hopping study clearly symmetric and anti-symmetric bending of the equatorial ligands are dominant modes in the relaxation dynamics. In [91] a model diabatic vibronic coupling Hamiltonian was set-up and it was determined that the fundamental features of the lowest adiabatic Jahn–Teller surfaces could be obtained from a 3 state, 5 mode vibronic coupling Hamiltonian to first-order. The vibrational modes are shown fully in Fig. 2 of [91]. The doubly-degenerate pairs  $(Q_1, Q_2)$  and  $(Q_{16}, Q_{17})$  transform as  $e'$ , and therefore give rise to a linear Jahn–Teller coupling within each mode. These modes are qualitatively the symmetric and antisymmetric bending of each ligand atom (C or O) in the L-M-L angle. The fifth mode is the totally symmetric breathing mode  $(Q_8)$ , which is usually important in such simulation as this coordinate allows relaxation along the intersection seam itself. In the  $C_{2v}$  Abelian subgroup of  $D_{3h}$  the degenerate  $e$  modes split ( $e \rightarrow a_1 \oplus b_2$ ). The pseudo-Jahn–Teller coupling can then be seen to arise from the off-diagonal coupling to the upper diabatic state ( $^1B_2$ ) via the component modes of  $b_2$  symmetry (modes  $Q_1$  and  $Q_{17}$ ). This vibronic coupling model Hamiltonian contains 9 parameters and seems to capture the essential features of the Jahn–Teller surfaces, therefore it is hoped that such model Hamiltonians can be similarly constructed for other metal carbonyl systems in the future. In the wavepacket simulation there is a fast transfer of population out of the initially excited state resulting in 90% population loss within 90 fs. The motion of the adiabatic wavepacket is shown in the  $(Q_1, Q_2)$  space for both the ground and first excited singlet electronic states in Fig. 10. Population transfer to the ground state takes place after 80 fs and the wavepacket bifurcates symmetrically at the Jahn–Teller point ( $D_{3h}$  symmetry). Note that the wavepacket motion is primarily radial, reaching the outer Jahn–Teller wall after 150 fs, returning to the conical intersection after 240 fs, and crosses through to other side of the potential wall after 340 fs. Also notice that some population returns to the excited states after this passage across the intersection region. A time of 340 fs corresponding to radial motion back and forth across the Jahn–Teller intersection matches well the experimental timescale for the coherent vibration observed [69–72]. This motion should be contrasted with the circular motion observed in the semi-classical dynamics (Fig. 9).

It is interesting that both dynamical methods give the same gross mechanistic explanation (with very good matches for the coherent vibrational timescale), but crucially they differ in the precise nature of the coherent vibration observed. Both dynamics methods have their own deficiencies, and further quantum dynamical simulation with better potentials, more coupled vibrational modes, and longer simulation times are therefore desirable for this important system. Another possible fruitful method is using time-independent vibrational structure approaches, with similar potentials expanded around the unsaturated minima in the Jahn–Teller “moat”. Recent advances in such methodology should see this approach utilized in the near future [110, 111].

The photodissociation of  $\text{Fe}(\text{CO})_5$  to produce  $\text{Fe}(\text{CO})_4$  is a much more challenging system than the chromium carbonyl system discussed above. The manifold

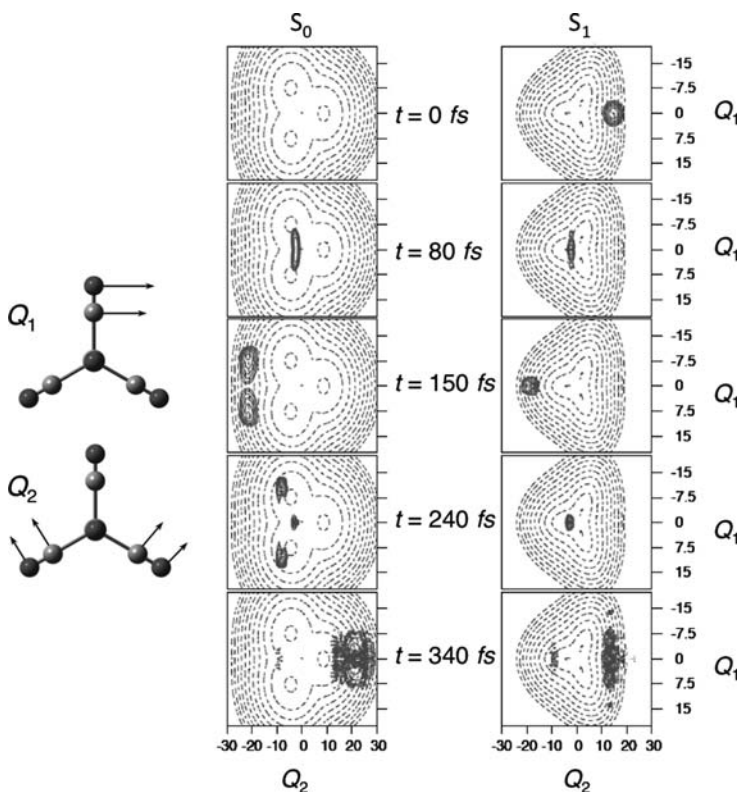


**Fig. 10** Snapshots of  $\text{Cr}(\text{CO})_5$  wavepacket dynamics on the lowest and first excited adiabatic potential surfaces (left and right panels). The contours show the two-dimensional Jahn–Teller surface in the space of the  $(Q_1, Q_2)$  pair of Jahn–Teller active coordinates, shown to the left

of states that can be populated (Figs. 2 and 3) is such that it is still not clear which states are initially populated, nor whether an axial or equatorial CO ligand is ejected. We have recently been studying the potential energy surfaces of  $\text{Fe}(\text{CO})_4$ . Several possible degenerate states can arise at a tetrahedral geometry with a  $d^8$  ( $e^4 t_2^4$ ) configuration:  $t_2 \otimes t_2 = {}^1A_1 \oplus {}^1E \oplus {}^1T_2 \oplus {}^3T_1$ . Multi-configurational wavefunctions are necessary to describe all of these spin-adapted states [112]. Degenerate Jahn–Teller active states exist in both the singlet and triplet spin manifolds, and electronic structure computation is in general required to determine the correct (energetic) ordering of these states. Simple inorganic chemistry models are unable to predict correctly the lowest energy state, including for example the method of Tanabe–Sugano [113]. Here the energies of the various metal atomic terms are correlated with molecular terms in the correct ligand-field split molecular point group, across the domain of ligand-field  $d$ -orbital splitting energies; the energies are always relative to the lowest energy term, which may change at different ligand-field strengths. For  $\text{Fe}(\text{CO})_4$  this method predicts that the first singlet state above the triply-degenerate triplet

ground state is a triply-degenerate singlet state. It should not be surprising that in low-spin manifolds such empirically-derived methods can sometimes fail (another point here is that Tanabe-Sugano diagrams for non-octahedral complexes are generally very hard to find). In their experiments on this system Fuß et al. [67] assumed a triply-degenerate state at  $T_d$  geometries. Our CASSCF results show however that in fact the  $^1E$  state is  $5 \text{ kcal mol}^{-1}$  lower than the  $^1T_2$  state.

The canonical vibrational coordinates for  $\text{Fe}(\text{CO})_4$  ( $T_d$ ) are  $Q_{3N-6} \in 2A_1 \oplus 2E \oplus T_1 \oplus 4T_2$ , and clearly there are many possible Jahn–Teller models including  $E \otimes e$ ,  $T \otimes t$ ,  $(T \oplus E) \otimes t$ ,  $(T \oplus E) \otimes (t \oplus e)$ . We have investigated in detail the  $T \otimes t$  Jahn–Teller intersection in the singlet manifold, in addition to the triplet manifold (i.e., for both the  $^1T_2$  and  $^3T_1$  states). This is because in the triplet manifold there exists a substantial amount of experimental work. However, bearing in mind that quantum chemistry predicts a lower  $^1E$  state the more complex Jahn–Teller models will also have to be investigated in detail as well.

Similarly to the  $\text{Cr}(\text{CO})_5$  case it is changes in the L-M-L angles that differentiate the geometrical structures. For tetrahedral  $\text{Fe}(\text{CO})_4$  the main distinguishing geometrical feature is choosing two pairs of ligands such that each pair changes L-M-L angle from  $109.5^\circ$ . Thus there are three distinct ligand pair choices and the Jahn–Teller distortion corresponds primarily to L-M-L bending for one of the pairs. In analysing the  $T \otimes t_2$  Jahn–Teller effect we can again use the epikernel principle. There are various possible epikernels:  $E_i(T_d, t_2) = C_{3v}, C_{2v}, C_s$  and in this case both the positive and negative distortion directions give rise to equivalent geometrical critical points; compare with  $\text{Cr}(\text{CO})_5$  where the positive epikernel distortion leads to minima, while the negative epikernel distortion leads to the saddle-point. This is a main difference in epikernels when applied to orbitally doubly-degenerate versus triply-degenerate states. We find  $C_{2v}$  minima separated by  $C_s$  saddle-points. The barrier height found is  $5.3 \text{ kcal mol}^{-1}$  using B3LYP/SDD(cc-pVDZ); we could not optimise the  $C_s$  structure with CASSCF as analytical Hessians were required, and these are not currently available for the (8,10) active space needed to describe the  $\text{Fe}(\text{CO})_4$  ground and ligand field excited states. The number of equivalent epikernels are:  $n_{E_1(T_d, t_2)} = \frac{|n_{T_d}|}{|n_{C_{2v}}|} = \frac{24}{4} = 6$  for  $C_{2v}$ , and

$n_{E_2(T_d, t_2)} = \frac{|n_{T_d}|}{|n_{C_s}|} = \frac{24}{2} = 12$  for  $C_s$ . Thus there are 6 equivalent  $C_{2v}$  minima, separated by 12  $C_s$  saddle-points. The three dimensional potential energy surface is shown schematically in Figs. 11 and 12. In Fig. 11 the 2D distortion space for four equivalent  $C_{2v}$  epikernels (type 1) is shown:  $E_1^1(T_d, t_2) = C_{2v}$ ,  $-E_1^1(T_d, t_2) = C_{2v}$ ,  $E_2^1(T_d, t_2) = C_{2v}$ ,  $-E_2^1(T_d, t_2) = C_{2v}$  where the forward and reverse epikernels are distinguished by opening up one of the pair of angles, forward opens one of the pair up, and reverse opens the other up. Orthogonal to this space is another equivalent epikernel distortion, forward and back, to give a total of 6 equivalent  $C_{2v}$  minima as required (denoted by a \* in Figs. 11 and 12). An alternative representation is shown in Fig. 12 (the so-called octahedron model developed originally by Poliakoff and Ceulemans [66]). Here the  $T_d$  structure sits at the centre of an octahedron and the vertices represent the minima (the 6 equivalent epikernel type-1 distortions).

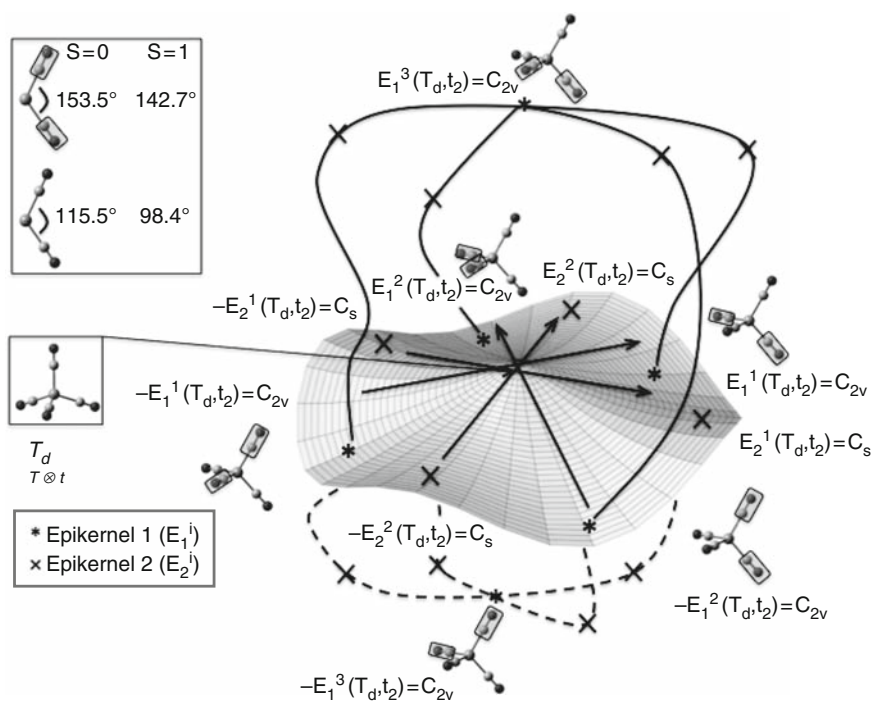


**Fig. 11** Representation of lowest adiabatic potential of singlet ( $S = 0$ ) and triplet ( $S = 1$ )  $\text{Fe}(\text{CO})_4$  around  $T \otimes t$  Jahn–Teller conical intersection at tetrahedral ( $T_d$ ) geometry. There are three equivalent two-dimensional “troughs” in the space spanned by each pair-wise selection of equal L–M–L angles (boxed vs unboxed). The topological connectivity where the “troughs” intersect is indicated. There are two non-equivalent epikernel distortion directions  $E_{1,2}^i(T_d, t_2)$  leading to 6 equivalent  $C_{2v}$  minima (\*), and 12 equivalent  $C_s$ (×) saddle-points respectively. The non-Berry pseudo-rotation barrier is very small ( $\sim 5 \text{ kcal mol}^{-1}$ ). CASSCF optimised geometrical parameters for singlet and triplet states are shown at the top left

The midpoints of the 12 edges are the type-2  $C_s$  epikernels which are saddle-points connecting the minima. Thus, the three loops around the  $T_d$  intersection in Fig. 11 correspond to three equivalent paths from each vertex to its opposite vertex, and back, on the octahedron in Fig. 12. The geometrical parameters from CASSCF for each of the  $C_{2v}$  minima is shown in the upper left of Fig. 12 for the both the singlet and triplet spin states. It should be clear that a very similar mechanism operates in both spin manifolds.

Our work on this very interesting system is still in progress, and we hope to include more electronic states; it is clear that the  $E$  and  $T$  states can pseudo-Jahn–Teller couple to each other via  $t$  vibrations. Given the Jahn–Teller active  $t_2$  vibrations discussed above and the fact that the  $E$  and  $T$  states are very close in energy one would expect these states to strongly pseudo-Jahn–Teller couple. The Jahn–Teller effects in singlet tetrahedral  $\text{Fe}(\text{CO})_4$  are probably similar to those in the  $\text{P}_4^+$  cation (combined Jahn–Teller and pseudo-Jahn–Teller action

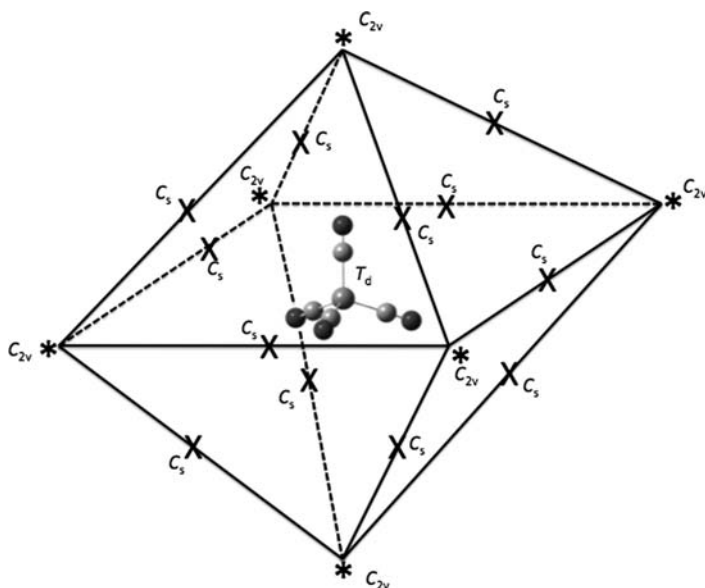


**Fig. 12** Octahedral representation of  $\text{Fe}(\text{CO})_4$   $T \otimes t$  Jahn–Teller surface (originally devised by Poliakoff and Ceulemans in [66]). The non-Berry pseudo-rotation paths shown in Fig. 11 are the paths between opposite vertexes on the octahedron, which are  $C_{2v}$  minima (\*) reached by following the forward and reverse directions of epikernel  $E_1$ . The  $C_s$  saddle-points (x) lie at the centre of each edge

at a tetrahedral geometry [114]). We are currently constructing a vibronic coupling model Hamiltonian for this system in order to subsequently perform quantum wavepacket dynamics in a similar vein to those for  $\text{Cr}(\text{CO})_5$ .

## 6 Conclusions and Outlook for Future Work

We hope that this review has shown that ever more elaborate experimental and computational techniques continue to be applied to elucidate the structure, assign spectra, and rationalize photochemical reaction mechanisms in transition metal carbonyl complexes. These systems provide a wealth of fascinating vibronically induced chemistry that we are only beginning to understand, and it is expected that as experimental and computational techniques further evolve many more studies of these systems will take place. Transition metal carbonyl systems are of primary importance in organometallic chemistry and unsaturated complexes are of key importance in industrial synthesis. Their photochemistry has many aspects that require a true multi-disciplinary approach, requiring knowledge and expertise in the fields of transition metal chemistry, ultrafast spectroscopy, computational spectroscopy, computational photochemistry and conical intersection theory, Jahn–Teller

theory, semi-classical dynamics, and quantum wavepacket dynamics. They further provide an on-going link between the Jahn–Teller and photochemical communities since from simple symmetry arguments we can be sure that conical intersections must be present and accessible in such systems, and therefore provide direct experimental probes of ultrafast conical intersection induced photochemistry.

**Acknowledgements** We thank the EPSRC for funding through grant EP/F01709X. We also thank Dr. Graham Worth for providing us an original version of Fig. 10.

## References

1. T.A. Albright, J.K. Burdett, M.H. Whangbo, *Orbital Interactions in Chemistry* (Wiley, New York, 1985)
2. W. Fuss, S.A. Trushin, W.E. Schmid, *Res. Chem. Int.* **27**, 447 (2001)
3. S.K. Kim, S. Pedersen, A.H. Zewail, *Chem. Phys. Lett.* **233**, 500 (1995)
4. L. Mond, C. Langer, F. Quincke, *J. Chem. Soc.* **57**, 749 (1890)
5. W. Rudalt, U. Hofmann, *Z. Phys. Chem.* **28**, 351 (1935)
6. L.O. Brockway, R.V.G. Ewens, M.W. Lister, *Trans. Faraday Soc.* **34**, 1350 (1938)
7. A. Whitaker, J.W. Jeffery, *Acta Cryst.* **23**, 977 (1967)
8. R.V.G. Ewens, M.W. Lister, *Trans. Faraday Soc.* **35**, 681 (1939)
9. A.W. Hanson, *Acta Cryst.* **15**, 930 (1962)
10. L.F. Dahl, R.E. Rundle, *J. Chem. Phys.* **26**, 1751 (1957)
11. S.F.A. Kettle, *Symmetry and Structure: Readable Group Theory for Chemists*, 3rd edn. (Wiley, New York, 2007)
12. J. Donohue, A. Caron, *Acta Cryst.* **17**, 6 (1964)
13. D. Braga, F. Grepioni, A.G. Orpen, *Organometallics* **12**, 1481 (1993)
14. A.J. Dixon, M.A. Healy, P.M. Hodges, B.D. Moore, M. Poliakoff, M.B. Simpson, J.J. Turner, M.A. West, *J. Chem. Soc. - Faraday Trans.* **82**, 2083 (1986)
15. N. Leadbeater, *Coord. Chem. Rev.* **188**, 35 (1999)
16. A.P. Garrat, H.W. Thompson, *J. Chem. Soc.*, 1817 (1934)
17. R.K. Sheline, K.S. Pitzer, *J. Am. Chem. Soc.* **72**, 1107 (1950)
18. F.A. Cotton, G. Wilkinson, *J. Am. Chem. Soc.* **79**, 752 (1957)
19. B.I. Swanson, L.H. Jones, R.R. Ryan, *J. Mol. Spec.* **45**, 324 (1973)
20. S.P. Church, F.W. Grevels, H. Hermann, K. Schaffner, *Inorg. Chem.* **24**, 418 (1985)
21. S.P. Church, F.W. Grevels, H. Hermann, K. Schaffner, *J. Chem. Soc. - Chem. Comm.*, 30 (1985)
22. S.P. Church, F.W. Grevels, H. Hermann, J.M. Kelly, W.E. Klotzbucher, K. Schaffner, *J. Chem. Soc. - Chem. Comm.*, 594 (1985)
23. I.W. Stolz, G.R. Dobson, R.K. Sheline, *J. Am. Chem. Soc.* **84**, 3589 (1962)
24. I.W. Stolz, G.R. Dobson, R.K. Sheline, *Inorg. Chem.* **2**, 1264 (1963)
25. M.A. Graham, M. Poliakoff, J.J. Turner, *J. Chem. Soc. A - Inorg. Phys. Theo.* 2939 (1971)
26. J.D. Black, P.S. Braterman, *J. Am. Chem. Soc.* **97**, 2908 (1975)
27. R.N. Perutz, J.J. Turner, *J. Am. Chem. Soc.* **97**, 4791 (1975)
28. R.N. Perutz, J.J. Turner, *Inorg. Chem.* **14**, 262 (1975)
29. J.K. Burdett, M.A. Graham, R.N. Perutz, M. Poliakoff, A.J. Rest, J.J. Turner, R.F. Turner, *J. Am. Chem. Soc.* **97**, 4805 (1975)
30. T.A. Seder, S.P. Church, E. Weitz, *J. Am. Chem. Soc.* **108**, 4721 (1986)
31. T.A. Seder, A.J. Ouderkerk, E. Weitz, *J. Chem. Phys.* **85**, 1977 (1986)
32. H.B. Gray, N.A. Beach, *J. Am. Chem. Soc.* **85**, 2922 (1963)
33. M.A. Graham, A.J. Rest, J.J. Turner, *J. Organomet. Chem.* **24**, C54 (1970)

34. N.A. Beach, H.B. Gray, *J. Am. Chem. Soc.* **90**, 5713 (1968)
35. R.A. Levenson, H.B. Gray, G.P. Ceasar, *J. Am. Chem. Soc.* **92**, 3653 (1970)
36. J.L. Hubbard, D.L. Lichtenberger, *J. Chem. Phys.* **75**, 2560 (1981)
37. I.M. Waller, J.W. Hepburn, *J. Chem. Phys.* **88**, 6658 (1988)
38. A.F. Schreiner, T.L. Brown, *J. Am. Chem. Soc.* **90**, 3366 (1968)
39. R.A. Levenson, H.B. Gray, *J. Am. Chem. Soc.* **97**, 6042 (1975)
40. C.E. Housecroft, K. Wade, B.C. Smith, *Chem. Comm.*, 765 (1978)
41. C.E. Housecroft, K. Wade, B.C. Smith, *J. Organomet. Chem.* **170**, C1 (1979)
42. T. Ziegler, J. Autschbach, *Chem. Rev.* **105** (2005)
43. M.J. Paterson, P.A. Hunt, M.A. Robb, O. Takahashi, *J. Phys. Chem. A* **106**, 10494 (2002)
44. C. Daniel, M. Benard, A. Dedieu, R. Wiest, A. Veillard, *J. Phys. Chem.* **88**, 4805 (1984)
45. A. Veillard, A. Strich, C. Daniel, P.E.M. Siegbahn, *Chem. Phys. Lett.* **141**, 329 (1987)
46. A. Marquez, C. Daniel, J.F. Sanz, *J. Phys. Chem.* **96**, 121 (1992)
47. T. Ziegler, V. Tschinke, C. Ursenbach, *J. Am. Chem. Soc.* **109**, 4825 (1987)
48. L.A. Barnes, M. Rosi, C.W. Bauschlicher, *J. Chem. Phys.* **94**, 2031 (1991)
49. A.W. Ehlers, G. Frenking, *J. Chem. Soc. - Chem. Comm.*, 1709 (1993)
50. K.E. Lewis, D.M. Golden, G.P. Smith, *J. Am. Chem. Soc.* **106**, 3905 (1984)
51. N. Rosch, M. Kotzian, H. Jorg, H. Schroder, B. Rager, S. Metev, *J. Am. Chem. Soc.* **108**, 4238 (1986)
52. M.F. Zhou, L. Andrews, C.W. Bauschlicher, *Chem. Rev.* **101**, 1931 (2001)
53. E. Weitz, *J. Phys. Chem.* **91**, 3945 (1987)
54. C. Daniel, *Coord. Chem. Rev.* **238**, 143 (2003)
55. M. Poliakoff, E. Weitz, *Acc. Chem. Res.* **20**, 408 (1987)
56. M. Kotzian, N. Rosch, H. Schroder, M.C. Zerner, *J. Am. Chem. Soc.* **111**, 7687 (1989)
57. L. Bñaires, T. Baumert, M. Bergt, B. Kiefer, G. Gerber, *Chem. Phys. Lett.* **267**, 141 (1997)
58. O. Rubner, V. Engel, *Chem. Phys. Lett.* **293**, 485 (1998)
59. O. Rubner, T. Baumert, M. Bergt, B. Kiefer, G. Gerber, V. Engel, *Chem. Phys. Lett.* **316**, 585 (2000)
60. H. Ihee, J. Cao, A.H. Zewail, *Chem. Phys. Lett.* **281**, 10 (1997)
61. H. Ihee, J.M. Cao, A.H. Zewail, *Angew. Chem. Int. Ed.* **40**, 1532 (2001)
62. M.J. Paterson, L. Blancafort, S. Wilsey, M.A. Robb, *J. Phys. Chem. A* **106**, 11431 (2002)
63. M.J. Paterson, M.A. Robb, L. Blancafort, A.D. DeBellis, *J. Am. Chem. Soc.* **126**, 2912 (2004)
64. M.J. Paterson, M.A. Robb, L. Blancafort, A.D. DeBellis, *J. Phys. Chem. A* **109**, 7527 (2005)
65. B. Davies, A. McNeish, M. Poliakoff, J.J. Turner, *J. Am. Chem. Soc.* **99**, 7573 (1977)
66. M. Poliakoff, A. Ceulemans, *J. Am. Chem. Soc.* **106**, 50 (1984)
67. S.A. Trushin, W. Fuß, K.L. Kompa, W.E. Schmid, *J. Phys. Chem. A* **104**, 1997 (2000)
68. M. Poliakoff, J.J. Turner, *Angew. Chem. Int. Ed.* **40**, 2809 (2001)
69. W. Fuß, S.A. Trushin, W.E. Schmid, *Res. Chem. Int.* **27**, 447 (2001)
70. S.A. Trushin, W. Fuß, W.E. Schmid, *Chem. Phys.* **259**, 313 (2000)
71. S.A. Trushin, W. Fuß, W.E. Schmid, K.L. Kompa, *J. Phys. Chem. A* **102**, 4129 (1998)
72. S.A. Trushin, K. Kosma, W. Fuß, W.E. Schmid, *Chem. Phys.* **347**, 309 (2008)
73. N. Ben Amor, S. Villaume, D. Maynau, C. Daniel, *Chem. Phys. Lett.* **421**, 378 (2006)
74. C. Daniel, *Curr. Chem.* **241**, 119 (2004)
75. O. Kuhn, M.R.D. Hachey, M.M. Rohmer, C. Daniel, *Chem. Phys. Lett.* **322**, 199 (2000)
76. K. Pierloot, E. Tsokos, L.G. Vanquickenborne, *J. Phys. Chem.* **100**, 16545 (1996)
77. A. Rosa, E.J. Baerends, S.J.A. van Gisbergen, E. van Lenthe, J.A. Groeneveld, J.G. Snijders, *J. Am. Chem. Soc.* **121**, 10356 (1999)
78. A. Rosa, G. Ricciardi, E.J. Baerends, D.J. Stufkens, *Inorg. Chem.* **34**, 3425 (1995)
79. A. Rosa, G. Ricciardi, E.J. Baerends, D.J. Stufkens, *Inorg. Chem.* **35**, 2886 (1996)
80. O. Rubner, V. Engel, M.R. Hachey, C. Daniel, *Chem. Phys. Lett.* **302**, 489 (1999)
81. S.J.A. van Gisbergen, J.A. Groeneveld, A. Rosa, J.G. Snijders, E.J. Baerends, *J. Phys. Chem. A* **103**, 6835 (1999)
82. S. Villaume, A. Strich, C. Daniel, S.A. Perera, R.J. Bartlett, *Phys. Chem. Chem. Phys.* **9**, 6115 (2007)
83. C. Pollak, A. Rosa, E.J. Baerends, *J. Am. Chem. Soc.* **119**, 7324 (1997)



84. O. Christiansen, *Theor. Chem. Acc.* **116**, 106 (2006)
85. M.J. Paterson, O. Christiansen, F. Pawłowski, P. Jørgensen, C. Hättig, T. Helgaker, P. Salek, *J. Chem. Phys.* **124** (2006)
86. O. Christiansen, H. Koch, F. Jørgensen, *J. Chem. Phys.* **105**, 1451 (1996)
87. The atomic natural orbital basis (ANO-3: R. Pou-Américo, M. Merchán, I. Nebot-Gil, P.-O., Widmark, B.O. Roos, *Theor. Chem. Acc.* **92**, 149 (1995)) for iron (6 contracted sets of s functions, 4 contracted sets of p functions, 3 contracted sets of d functions, 1 contracted set of f functions, and the cc-pVDZ basis on carbon and oxygen.
88. M. Johnsen, M.J. Paterson, J. Arnberg, O. Christiansen, C.B. Nielsen, M. Jørgensen, P.R. Ogilby, *Phys. Chem. Chem. Phys.* **10**, 1177 (2008)
89. J. Arnberg, M.J. Paterson, M. Jørgensen, O. Christiansen, P.R. Ogilby, *J. Phys. Chem. A* **111**, 5756 (2007)
90. J. Arnberg, A. Jiménez-Banzo, M.J. Paterson, S. Nonell, J. Borrell, O. Christiansen, P.R. Ogilby, *J. Am. Chem. Soc.* **129**, 5188 (2007)
91. G.A. Worth, G. Welch, M.J. Paterson, *Mol. Phys.* **104**, 1095 (2006)
92. B.J. Persson, B.O. Roos, K. Pierloot, *J. Chem. Phys.* **101**, 6810 (1994)
93. M.J. Paterson, M.J. Bearpark, M.A. Robb, L. Blancafort, *Journal of Chemical Physics* **121**, 11562 (2004)
94. M.J. Paterson, M.J. Bearpark, M.A. Robb, L. Blancafort, G.A. Worth, *Phys. Chem. Chem. Phys.* **7**, 2100 (2005)
95. H.A. Jahn, E. Teller, *Proc. Roy. Soc. A* **161**, 220 (1937)
96. P.W. Atkins, M.S. Child, C.S.G. Phillips, *Tables for Group Theory* (Oxford University Press, Oxford, 1970)
97. A. Ceulemans, L.G. Vanquickenborne, *Struct. Bond.* **71**, 125 (1989)
98. I.B. Bersuker, *Chem. Rev.* **101**, 1067 (2001)
99. G.A. Worth, H.D. Meyer, L.S. Cederbaum, in *Conical Intersections*, ed. by W. Domcke, D.R. Yarkony, H. Koppel (World Scientific, Singapore, 2004), p. 573.
100. M.J. Bearpark, L. Blancafort, M.A. Robb, *Mol. Phys.* **100**, 1735 (2002)
101. I.B. Bersuker, *The Jahn–Teller Effect* (Cambridge University Press, Cambridge, 2006)
102. M.J. Paterson, N.P. Chatterton, G.S. McGrady, *New. J. Chem.* **28**, 1434 (2004)
103. N.B. Balabanov, K.A. Peterson, *J. Chem. Phys.* **123**, 064107 (2005)
104. G.A. Worth, L.S. Cederbaum, *Ann. Rev. Phys. Chem.* **55**, 127 (2004)
105. G.A. Worth, H.D. Meyer, H. Koppel, L.S. Cederbaum, I. Burghardt, *Int. Rev. Phys. Chem.* **27**, 569 (2008)
106. G.A. Worth, M.A. Robb, B. Lasorne, *Mol. Phys.* **106**, 2077 (2008)
107. M.H. Beck, A. Jackle, G.A. Worth, H.D. Meyer, *Phys. Rep.* **324**, 1 (2000)
108. J.P. Holland, R.N. Rosenfeld, *J. Chem. Phys.* **89**, 7217 (1988)
109. M. Barbatti, G. Granucci, M. Persico, M. Ruckebauer, M. Vazdar, M. Eckert-Maksic, H. Lischka, *J. Photochem. Photobiol. A: Chem.* **190**, 228 (2007)
110. O. Christiansen, *J. Chem. Phys.* **120**, 2140 (2004)
111. O. Christiansen, J. Kongsted, M.J. Paterson, J.M. Luis, *J. Chem. Phys.* **125**, 214309 (2006)
112. M.J. Paterson, O. Christiansen, F. Jensen, P.R. Ogilby, *Photochem. Photobiol.* **82**, 1136 (2006)
113. Y. Tanabe, S. Sugano, *J. Phys. Soc. Jpn.* **9**, 753 (1954)
114. R. Meiswinkel, H. Köppel, *Chem. Phys. Lett.* **201**, 449 (1993)



**Part III**  
**Impurities; Spectroscopy of Transition**  
**Metal Complexes**

# Jahn–Teller Effect for the 3d Ions (Orbital Triplets in a Cubic Crystal Field)

M.G. Brik, N.M. Avram, and C.N. Avram

**Abstract** Jahn–Teller effect and related phenomena attract considerable attention of researchers during last several decades. In the present chapter aimed at the students and postgraduates first of all, as well as at the beginners in this field, we review thoroughly the main mechanisms underlying the Ham effect (which means quenching of the spin–orbit interaction due to the interaction of the electronic energy levels with the crystal lattice vibrations). To make the chapter complete from the educational and pedagogical points of view, all necessary mathematical equations needed for calculations are derived and explained. It is shown how the effective second-order spin-Hamiltonian can be used for a description of the Ham effect and estimation of the Jahn–Teller stabilization energy. In addition, an alternative method of determining the Jahn–Teller stabilization energy based on the harmonic approximation and geometrical consideration of the adiabatic surfaces of the potential energy of the ground and excited electronic states is described. The chapter is followed by an attachment with the derivation of the Ham reduction factor.

## 1 Introduction

As Jahn and Teller showed [1, 2], an electronically degenerate state of a nonlinear molecule or complex is unstable (except for the case of simple Kramers degeneracy) with respect to some asymmetric nuclear displacements, which lift the degeneracy. If the coupling between the electrons and such displacements (which best of all can be represented as a linear combination of normal modes) is sufficiently strong relative to the zero-point energy of the associated vibrational modes, the complex undergoes a static distortion to a new configuration of minimum energy [3–5]. If the coupling is less strong, or if the zero-point vibrational energy is comparable with the energy barrier separating equivalent configurations, no static distortion occurs, but a complicated interaction between the electrons of the central ion and the vibrational modes takes place [6–8]. All phenomena related to a further splitting of the degenerate electronic states and symmetry lowering around a central ion as a result of vibrations of surrounding atoms are referred to as the Jahn–Teller (JT) effect.

Two different kinds of JT effect are distinguished in the literature: the static and dynamic JT effects. In the static JT effect the molecule or complex remains distorted in a particular way long enough for the distortion to be detected experimentally. In the dynamic JT effect, the molecule or complex resonates between two or more equivalent modes of distortion, and the distortion is not directly observable [9].

Although the JT effect has been discovered in 1937 as a very general phenomenon, it had to wait until 1952 for its first evidence by EPR (electron-paramagnetic resonance) [10]. In the first period, soon after this experiment, the phenomenon was detected in only a very limited class of systems and the main effort in this field has been theoretical. This has led to mainly mathematical developments and sophistications rather than to the analysis of the experimental results. In last 40 years the situation has been completely changed and the JT effect is being investigated both experimentally and theoretically [11].

In the present chapter we focus on the optical spectra of the transitional metal ion impurities, as the point defects in insulating crystals. The reasons are because the JT effect is most often encountered in the transitional metal complexes, and very common in the octahedral complexes. We shall make use of the configuration coordinate approach [12], which enables one to apply much of the theory developed for molecules to the case of an isolated impurity in a crystal.

In the next sections we describe briefly the main interactions, which are in charge of splitting of the 3d ions energy levels in crystals. These interactions include the Coulomb interaction, the crystal field interaction, the spin–orbit interaction and the JT interaction. As it was pointed out by Ham [13], the observed spin–orbit and trigonal field splittings of the orbital triplet states are significantly affected by the dynamic JT effect.

We shall make use of the “effective Hamiltonian” formalism [14] that enables us to isolate effects of interest from irrelevant complications. We divide the electronic Hamiltonian into a “strong” part  $H^0$  and a “weak” part  $H'$ , and we shall suppose that  $H^0$  is simple enough to be solved exactly. The Hamiltonian including the cubic field and interelectronic repulsion only is the usual choice for  $H^0$  in the case of the 3d group ions. Then  $H'$  should include all other interactions (spin–orbit coupling, lower symmetry fields, electron–phonon interaction, external fields, strain etc). The most important assumption is that the perturbations, described by the  $H'$  Hamiltonian (in particular the JT interaction) must be smaller relative to the initial splitting due to  $H^0$ . In the case of the 3d metal ions the assumption is usually well justified.

In the present chapter aimed at the students and postgraduates first of all, as well as at the beginners in this field, we consider thoroughly the dynamic Jahn–Teller effect for the  $3d^3$  ( $3d^7$ ) ions in the octahedral (tetrahedral) impurity centers. Energy level structure of the orbital triplet  $^4T_2$  and interaction of its states with the  $\alpha_{1g}$ ,  $\varepsilon_g$ ,  $\tau_{2g}$  normal modes of the octahedral center ( $\alpha_1$ ,  $\varepsilon$ ,  $\tau_2$  normal modes of the tetrahedral center) form the main subject of the chapter.

Another orbital triplet  $^4T_1$ , which appears in the energy level schemes of the chosen ions, represents somewhat more sophisticated case. The matter is that there are two  $^4T_1$  states arising from two different LS terms ( $^4F$  and  $^4P$ ) of the  $d^3$  ( $d^7$ ) electron configurations. These states are mixed up by both crystal field Hamiltonian

and spin–orbit interaction, which makes the whole story more complicated. However, if such a mixture of both triplets can be neglected (as a first approximation or, which is more realistic, when the crystal field splitting is small and the  ${}^4P$  term is positioned energetically much higher than the  ${}^4F$  term), there will be no difference in a way of considering the JT effect in the  ${}^4T_1$  state too.

The chapter contains a detailed description of two methods of determining the JT energy: (1) the spin–orbit splitting quenching (the Ham effect) and (2) analysis of the potential energy surfaces in the excited electronic state.

## 2 A General Picture of the Energy Levels of 3d Ions in a Cubic Crystal Field Without and with Interaction with Normal Vibrational Modes

The energy levels of a 3d ion in a crystal field are generally described by the following Hamiltonian (we assume that no external fields act upon a considered crystal):

$$H = H_{\text{FI}} + H_{\text{CF}} + H_{\text{SO}} + H_{\text{JT}}, \quad (1)$$

where  $H_{\text{FI}}$  is a free ion Hamiltonian (which describes electrostatic interaction between electrons of the unfilled electron shell giving rise to different LS terms),  $H_{\text{CF}}$  is a crystal field Hamiltonian (which splits the LS terms into a definite number of sublevels, with the overall pattern of splitting being determined by the symmetry of crystal field and interactions between a 3d ion and its environment),  $H_{\text{SO}}$  is a spin–orbit (SO) interaction Hamiltonian (which produces a further splitting of the crystal field terms), and  $H_{\text{JT}}$  is a JT Hamiltonian (which characterizes interaction of the 3d ion electronic states with crystal lattice vibrations).

The magnitude of these terms is approximately as follows:  $\sim 10^4 \text{ cm}^{-1}$  for  $H_{\text{FI}}$ ,  $10^4 \text{ cm}^{-1}$  for  $H_{\text{CF}}$ ,  $10^2\text{--}10^3 \text{ cm}^{-1}$  for both  $H_{\text{SO}}$  and  $H_{\text{JT}}$ . The  $H_{\text{FI}}$ ,  $H_{\text{CF}}$ ,  $H_{\text{JT}}$  operators mix only the terms with the same spin, whereas the  $H_{\text{SO}}$  operator can have nonzero matrix elements between the states with different spin.

It is not a problem to diagonalize the Hamiltonian (1) with the first two or three terms (neglecting the JT interaction would correspond to the so called rigid lattice approximation). All necessary matrix elements required for these calculations can be readily found in the literature [15–20].

In a cubic crystal field neglecting the SO interaction would yield the set of the orbitally degenerated energy levels, with the degeneracy not greater than three (which is the maximum dimension of irreducible representations in the  $O_h$  point group); the states with different multiplicity can be mixed up only by the SO interaction. Since some states with different spins can be rather close to each other, these “nondiagonal” matrix elements of SO interaction can be quite important. The SO splitting can be analyzed by employing the  $O_h$  double group; an immediate conclusion is that only states transforming as the  $\Gamma_6$ ,  $\Gamma_7$ ,  $\Gamma_8$  irreducible representations

**Table 1** Splitting of the LS terms of the  $d^3$  ( $d^7$ ) electron configuration in a cubic crystal field without (the third column) and with (the fourth column) spin–orbit interaction

LS term	Degree of degeneracy of LS term	Splitting of LS terms in a cubic crystal field	Splitting of the crystal field terms by spin–orbit interaction
$^4F$	28	$^4A_{2g}$	$\Gamma_8$
		$^4T_{1g}$	$\Gamma_6 + \Gamma_7 + 2\Gamma_8$
		$^4T_{2g}$	$\Gamma_6 + \Gamma_7 + 2\Gamma_8$
$^4P$	12	$^4T_{1g}$	$\Gamma_6 + \Gamma_7 + 2\Gamma_8$
$^2P$	6	$^2T_{1g}$	$\Gamma_6 + \Gamma_8$
		$^2E_g$	$\Gamma_8$
$^2D_1$	10	$^2T_{2g}$	$\Gamma_7 + \Gamma_8$
		$^2E_g$	$\Gamma_8$
$^2D_2$	10	$^2T_{2g}$	$\Gamma_7 + \Gamma_8$
		$^2A_{2g}$	$\Gamma_7$
$^2F$	14	$^2T_{1g}$	$\Gamma_6 + \Gamma_8$
		$^2T_{2g}$	$\Gamma_7 + \Gamma_8$
		$^2A_{1g}$	$\Gamma_6$
		$^2E_g$	$\Gamma_8$
$^2G$	18	$^2T_{1g}$	$\Gamma_6 + \Gamma_8$
		$^2T_{2g}$	$\Gamma_7 + \Gamma_8$
		$^2E_g$	$\Gamma_8$
$^2H$	22	$^2T_{1g}$ (two states)	$\Gamma_6 + \Gamma_8$ (twice)
		$^2T_{2g}$	$\Gamma_7 + \Gamma_8$
Total number of states: 120			

(the first two are two-dimensional, whereas the third one is four-dimensional) will appear in a general scheme of energy levels.

Table 1 shows how the LS terms of a free  $d^3$  ( $d^7$ ) ion split in a cubic crystal field and how these crystal field states are split by the SO interaction.

The mixture of states with the same symmetry implies that in this case the Hamiltonian matrix can be transformed into a three sub-blocks’ matrix, corresponding to the  $\Gamma_6$ ,  $\Gamma_7$ ,  $\Gamma_8$  irreducible representations. In the case of a  $3d^3$  ( $3d^7$ ) ion the total number of states for such an electronic configuration is 120, and the sizes of the sub-blocks are 9 for both  $\Gamma_6$ ,  $\Gamma_7$  and 21 for  $\Gamma_8$  (which gives 120 in total, if the twofold degeneracy for the  $\Gamma_6$ ,  $\Gamma_7$  and fourfold degeneracy for the  $\Gamma_8$  is taken into account).

The orbital triplet states (transforming as the  $T_1$  or  $T_2$  irreducible representations) interact with crystal lattice vibrations, and this interaction affects also the SO splitting of these states. From the computational point of view, the effects of interaction between the electronic levels arising from the orbital triplet and surrounding ions can be modeled easier if each orbital triplet would be considered individually, without explicit treatment of mixture with electronic states from other

triplets. Also from the computational point of view, this means that the SO splitting of the 12-fold degenerated  ${}^4T_{2g}$  state can be successfully modeled by considering its own  $12 \times 12$  matrix only. However, even in this case of a smaller matrix there is an elegant way of taking into account the mixture of *all* other states from *all* other multiplets. This method is based on the concept of an effective first- and second-order SO Hamiltonian [21–23] and the quantum-mechanical theory of the orbital momentum, which allows to consider three orbital states of the orbital triplet as three components of a state with an effective (“effective” means that not all properties of the quantum mechanical operator of orbital momentum are hold true for this operator; see below) orbital momentum  $L = 1$ . The set of three real functions  $\xi, \eta, \zeta$  transforming according to the  $T_2$  irreducible representation of the  $O_h$  group can be obtained from five  $d$ -orbital  $|22\rangle, |21\rangle, |20\rangle, |2-1\rangle, |2-2\rangle$  as follows [24]:

$$\begin{aligned}\xi &= \frac{i}{\sqrt{2}} (|21\rangle + |2-1\rangle) \sim yz, \quad \eta = -\frac{1}{\sqrt{2}} (|21\rangle - |2-1\rangle) \sim xz, \\ \zeta &= \frac{1}{i\sqrt{2}} (|22\rangle - |2-2\rangle) \sim xy\end{aligned}\quad (2)$$

It is convenient to introduce another three functions  $|11\rangle, |10\rangle, |1-1\rangle$  (which correspond to the above mentioned effective orbital momentum  $L = 1$  and its three projections; these should be distinguished from the  $|22\rangle, |21\rangle, |20\rangle, |2-1\rangle, |2-2\rangle$  functions, which are related to the real orbital momentum of the  $d$  electrons). These functions are as follows:  $|11\rangle = |2-1\rangle, |10\rangle = \frac{1}{\sqrt{2}} (|22\rangle - |2-2\rangle), |1-1\rangle = -|21\rangle$ . In terms of these functions of effective orbital momentum the  $\xi, \eta, \zeta$  functions can be written as follows:

$$\xi = \frac{i}{\sqrt{2}} (|11\rangle - |1-1\rangle), \quad \eta = \frac{1}{\sqrt{2}} (|1-1\rangle + |11\rangle), \quad \zeta = -i |10\rangle. \quad (3)$$

The effective second-order SO Hamiltonian

$$H_{\text{eff}} = \lambda \vec{L} \cdot \vec{S} + \kappa (\vec{L} \cdot \vec{S})^2 + \rho (L_x^2 S_x^2 + L_y^2 S_y^2 + L_z^2 S_z^2), \quad (4)$$

is defined in the space of all 12 wave functions of the  ${}^4T_{2g}$  state with  $L = 1$  and  $S = \frac{3}{2}$ . The parameters  $\lambda, \kappa, \rho$  have dimension of energy,  $\vec{L}, \vec{S}$  are the operators of the orbital and spin momenta, respectively, with their components  $L_j, S_j (j = x, y, z)$ . Namely the second and the third terms in the last equation take into account the influence of other states on the overall SO splitting of the  ${}^4T_{2g}$  state. The matrix elements of the above Hamiltonian can be easily calculated using the raising and lowering operators  $L_+, L_-, S_+, S_-$ . In terms of these operators:  $L_x = \frac{L_+ + L_-}{2}, L_y = \frac{L_+ - L_-}{2i}$  (similar expressions – with changing  $L$  into  $S$  – can be written for the  $S_x, S_y$  operators). The action of these raising/lowering operators upon the  $|lm\rangle$  wave functions is given by the following

expression:

$$L_{\pm} |lm\rangle = \sqrt{l(l+1) - m(m \pm 1)} |lm \pm 1\rangle, \quad L_z |lm\rangle = m |lm\rangle. \quad (5)$$

The matrices of the  $L_j, S_j (j = x, y, z)$  operators in the basis set defined by the functions from (3) are then as follows (for the spin operators the set of the four spin functions  $|\frac{3}{2} \frac{3}{2}\rangle, |\frac{3}{2} \frac{1}{2}\rangle, |\frac{3}{2} - \frac{1}{2}\rangle, |\frac{3}{2} - \frac{3}{2}\rangle$  was used):

$$L_x = \begin{pmatrix} 0 & 0 & 0 \\ 0 & 0 & i \\ 0 & -i & 0 \end{pmatrix}, \quad L_y = \begin{pmatrix} 0 & 0 & -i \\ 0 & 0 & 0 \\ i & 0 & 0 \end{pmatrix}, \quad L_z = \begin{pmatrix} 0 & i & 0 \\ -i & 0 & 0 \\ 0 & 0 & 0 \end{pmatrix},$$

(they coincide with the matrices given by (7.3)–(7.5) in the book by Sugano, Tanabe, and Kamimura [17]. It is worthwhile to note here that the matrices of the orbital momentum  $L_j (j = x, y, z)$  operators in the basis set spanned by the  $p$ -wave functions will have an opposite sign [17]. Therefore, the  $L_j$  matrices as defined above do not satisfy the commutation relation for the components of the orbital momentum, and this emphasizes that in this chapter we speak about an “effective” operator  $L$ , which turns out to be very efficient for a solution of the considered problem. However, the sign of the matrix elements in the above-given matrices is consistent with the chosen basis set in (3)).

$$\begin{aligned} S_x &= \begin{pmatrix} 0 & \frac{\sqrt{3}}{2} & 0 & 0 \\ \frac{\sqrt{3}}{2} & 0 & 1 & 0 \\ 0 & 1 & 0 & \frac{\sqrt{3}}{2} \\ 0 & 0 & \frac{\sqrt{3}}{2} & 0 \end{pmatrix}, \\ S_y &= \begin{pmatrix} 0 & -i\frac{\sqrt{3}}{2} & 0 & 0 \\ i\frac{\sqrt{3}}{2} & 0 & -i & 0 \\ 0 & i & 0 & -i\frac{\sqrt{3}}{2} \\ 0 & 0 & i\frac{\sqrt{3}}{2} & 0 \end{pmatrix}, \\ S_z &= \begin{pmatrix} \frac{3}{2} & 0 & 0 & 0 \\ 0 & \frac{1}{2} & 0 & 0 \\ 0 & 0 & -\frac{1}{2} & 0 \\ 0 & 0 & 0 & -\frac{3}{2} \end{pmatrix}. \end{aligned} \quad (6)$$

The general expressions of the 12 wave functions of the  ${}^4T_{2g}$  (represented as the product of the orbital and spin parts are listed below (only the projection of the spin momentum is shown after the orbital part):  $|\xi \frac{3}{2}\rangle, |\xi \frac{1}{2}\rangle, |\xi - \frac{1}{2}\rangle, |\xi - \frac{3}{2}\rangle, |\eta \frac{3}{2}\rangle, |\eta \frac{1}{2}\rangle, |\eta - \frac{1}{2}\rangle, |\eta - \frac{3}{2}\rangle, |\zeta \frac{3}{2}\rangle, |\zeta \frac{1}{2}\rangle, |\zeta - \frac{1}{2}\rangle, |\zeta - \frac{3}{2}\rangle$ . The matrix elements of the Hamiltonian (4), in this basis, are given in Appendix A. However, it is possible to simplify significantly the calculations of the eigenvalues of this matrix by using the symmetry adapted wave functions:

$$|\Gamma\gamma'\rangle = \sum_{i,M_S} C(i, M_S) |iM\rangle, \quad (7)$$

where the wave functions of the “old” basis are denoted by  $|iM\rangle$ , the wave functions of the new symmetrized basis transforming in accordance with the  $\gamma'$ th line of the irreducible representation  $\Gamma$  ( $\Gamma = \Gamma_6, \Gamma_7, \Gamma_8$ ) are denoted by  $|\Gamma\gamma'\rangle$ , and the coefficients  $C(i, M_S)$  were taken from [25] (they are given in Table 2 below). In this new basis the Hamiltonian matrix has the block-diagonal form. There are four two by two blocks

$$\left( \begin{array}{cc} \frac{17}{10}\rho - \lambda + \kappa & \frac{3}{5}\rho \\ \frac{3}{5}\rho & \frac{33}{10}\rho + \frac{3}{2}\lambda + \frac{9}{4}\kappa \end{array} \right), \text{ two diagonal matrix elements} \\ \frac{25}{4}\kappa + \frac{7}{2}\rho - \frac{5}{2}\lambda \text{ and two diagonal matrix elements} \\ \frac{9}{4}\kappa + \frac{3}{2}\rho + \frac{3}{2}\lambda, \text{ which yields the following eigenvalues:} \\ \left. \begin{array}{l} E(\Gamma_6) = \frac{3}{2}\lambda + \frac{9}{4}\kappa + \frac{3}{2}\rho \\ E(\Gamma_7) = -\frac{5}{2}\lambda + \frac{25}{4}\kappa + \frac{7}{2}\rho \\ E(\Gamma_8)_{1,2} = \frac{A+B}{2} \pm \sqrt{\frac{1}{4}(A-B)^2 + \frac{9}{25}\rho^2} \end{array} \right\}, \quad (8)$$

with  $A = -\lambda + \kappa + \frac{17}{10}\rho$ ,  $B = \frac{3}{2}\lambda + \frac{9}{4}\kappa + \frac{33}{10}\rho$ .

To determine the numerical values of the effective Hamiltonian parameters  $\lambda, \kappa, \rho$ , the least-square fitting of the energy levels from (8) to the calculated values of the SO splitting should be performed (using the complete Tanabe-Sugano, Eisenstein or Runciman's matrices [17–19]).

To take now into account the JT interaction, a phenomenological approach [9,26] should be followed. It is based on substituting the crystal by an imaginary molecule consisting of an impurity ion and its six nearest neighbors. Thus, for the 3d<sup>3</sup> ions (usually occupying the octahedral positions in crystals) the considered cluster is an octahedron with one  $\varepsilon_g$  and one  $\tau_{2g}$  JT active modes. The linear JT Hamiltonian corresponding to the interaction of the electronic  ${}^4T_{2g}$  state with the  $\varepsilon_g$  vibration is [9]:

$$H_{JT} = \frac{P^2}{2\mu} + \frac{KQ^2}{2} - V \begin{bmatrix} -\frac{1}{2}Q_\theta + \frac{\sqrt{3}}{2}Q_\varepsilon & 0 & 0 \\ 0 & -\frac{1}{2}Q_\theta - \frac{\sqrt{3}}{2}Q_\varepsilon & 0 \\ 0 & 0 & Q_\theta \end{bmatrix}, \quad (9)$$

where  $P, Q$  are the momentum and coordinate corresponding to the  $\varepsilon_g$  normal mode,  $K$  is the force constant,  $V$  is the coupling constant and  $Q_\theta \sim x^2 - y^2$ ,  $Q_\varepsilon \sim 3z^2 - r^2$  are two different collective coordinates of the  $\varepsilon_g$  normal mode. It should be pointed out that interaction of the orbital triplet states with the triply degenerated normal modes is much smaller [9], and this will be supported below by the numerical estimations. However, the situation is not always that simple; for example, in



**Table 2** Coefficients  $C(i, M_S)$  used for diagonalization of the Hamiltonian from (4) in a symmetry adapted basis (7). Adopted from [25]

	$\xi$				$\eta$				$\zeta$			
	3/2	1/2	-1/2	-3/2	3/2	1/2	-1/2	-3/2	3/2	1/2	-1/2	-3/2
$\Gamma_8$	$\frac{i}{\sqrt{5}}$ 0 0 0	0 $-\frac{i}{\sqrt{5}}$ 0 $\frac{2i}{\sqrt{15}}$	$\frac{2i}{\sqrt{15}}$ 0 $-\frac{i}{\sqrt{5}}$ 0	0 0 0 $\frac{i}{\sqrt{5}}$	$\frac{1}{\sqrt{5}}$ 0 0 0	0 $\frac{1}{\sqrt{5}}$ 0 $\frac{2}{\sqrt{15}}$	$-\frac{2}{\sqrt{15}}$ 0 $-\frac{1}{\sqrt{5}}$ 0	0 0 0 $-\frac{1}{\sqrt{5}}$	0 $-i\sqrt{\frac{3}{5}}$ 0 0	$\frac{i}{\sqrt{15}}$ 0 0 0	0 0 0 $-\frac{i}{\sqrt{15}}$	0 0 $i\sqrt{\frac{3}{5}}$ 0
$\Gamma_8'$	$\frac{i}{\sqrt{20}}$ 0 $i\sqrt{\frac{5}{12}}$ 0	0 $-\frac{i}{\sqrt{20}}$ 0 $-i\sqrt{\frac{3}{20}}$	$-i\sqrt{\frac{3}{20}}$ 0 $-\frac{i}{\sqrt{20}}$ 0	0 $i\sqrt{\frac{5}{12}}$ 0 $\frac{i}{\sqrt{20}}$	$\frac{i}{\sqrt{20}}$ 0 $-\sqrt{\frac{5}{12}}$ 0	0 $\frac{1}{\sqrt{20}}$ 0 $-\sqrt{\frac{3}{20}}$	$\sqrt{\frac{3}{20}}$ 0 $-\frac{1}{\sqrt{20}}$ 0	0 $\sqrt{\frac{5}{12}}$ 0 $-\frac{1}{\sqrt{20}}$	0 $\frac{i}{\sqrt{15}}$ 0 0	$i\sqrt{\frac{3}{5}}$ 0 0 0	0 0 0 0	0 0 0 $-\frac{i}{\sqrt{15}}$
$\Gamma_7$	0 $\frac{i}{2}$ 0	$\frac{i}{\sqrt{12}}$ 0 0	0 $-\frac{i}{\sqrt{12}}$ 0	$-\frac{i}{2}$ 0 $\frac{i}{2}$	0 $\frac{i}{2}$ 0	$\frac{1}{\sqrt{12}}$ 0 0	0 $\frac{1}{\sqrt{12}}$ 0	$\frac{1}{2}$ 0 0	0 0 0	0 0 $-\frac{i}{\sqrt{3}}$	$-\frac{i}{\sqrt{3}}$ 0 0	0 0 0
$\Gamma_6$	0 $-\frac{i}{\sqrt{12}}$	$\frac{i}{2}$ 0	0 $-\frac{i}{2}$	$\frac{i}{\sqrt{12}}$ 0	0 $\frac{1}{\sqrt{12}}$	$-\frac{1}{2}$ 0	0 $-\frac{1}{2}$	$\frac{1}{\sqrt{12}}$ 0	$-\frac{i}{\sqrt{3}}$ 0	0 0	0 0	0 $-\frac{i}{\sqrt{3}}$

some cyanide complexes with very stiff chemical bonds between 3d metals and CN ligands, interaction with the  $\tau_2$  mode was shown to be dominating [27]. Considering only the ground vibrational state (which, actually, corresponds to the case when absolute temperature is zero), Sturge [22] demonstrated that the matrix elements of the second order effective spin Hamiltonian in the first order of the perturbation theory (interaction with the normal modes (9) is treated as a small perturbation to the Hamiltonian (4)) can be written as:

$$\left\langle Mi00 \left| H_{\text{eff}}^{(I)} \right| M'j00 \right\rangle = [\delta_{ij} + \gamma (1 - \delta_{ij})] \langle Mi | H_{\text{eff}} | M'j \rangle, \quad (10)$$

where  $M, M'$  are magnetic spin quantum numbers,  $i, j = \xi, \eta, \zeta$  and  $\gamma = \exp\left(-\frac{3E_{\text{JT}}}{2\hbar\omega}\right)$  is expressed in terms of the ratio of the JT energy  $E_{\text{JT}}$  and the energy  $\hbar\omega$  of the Jahn–Teller active normal mode. Derivation of the reduction factor  $\gamma$  is given in Appendix B. In the new symmetry-adapted basis, defined by (7), (10) will look like

$$\begin{aligned} \langle \Gamma\gamma | H_{\text{eff}}^{(I)} | \Gamma'\gamma' \rangle &= \sum_{i,M} \sum_{j,M'} C^*(i, M) C(j, M') [\delta_{ij} + \gamma (1 - \delta_{ij})] \\ &\times \langle Mi | H_{\text{eff}} | M'j \rangle. \end{aligned} \quad (11)$$

This transformation reduces the Hamiltonian  $H_{\text{eff}}$  to the block diagonal form with the following sub-blocks:

$$\begin{pmatrix} \frac{17}{10}\rho + \frac{17}{10}\kappa - \gamma\lambda - \frac{7}{10}\gamma\kappa & \frac{3}{5}\rho + \frac{3}{5}\kappa - \frac{3}{5}\gamma\kappa \\ \frac{3}{5}\rho + \frac{3}{5}\kappa - \frac{3}{5}\gamma\kappa & \frac{33}{10}\rho + \frac{33}{10}\kappa + \frac{3}{2}\gamma\lambda - \frac{21}{20}\gamma\kappa \end{pmatrix} \text{ (two blocks),}$$

$\frac{7}{2}\rho + \frac{7}{2}\kappa - \frac{5}{2}\gamma\lambda + \frac{11}{4}\gamma\kappa$  (two blocks) and  $\frac{3}{2}\kappa + \frac{3}{2}\rho + \frac{3}{2}\gamma\lambda + \frac{3}{4}\gamma\kappa$  (two blocks). The eigenvalues of these blocks are again given by (8) but the following substitution:  $\lambda \rightarrow \gamma\lambda$ ,  $\kappa \rightarrow \gamma\kappa$ ,  $\rho \rightarrow \kappa + \rho - \gamma\kappa$  should be made in this case (this can be easily checked out: substitution of these modified  $\lambda, \kappa, \rho$  into the matrix blocks given before (8) immediately transforms them to the above given ones). Thus, the matrix elements are decreased exponentially, resulting in an exponential decrease of the relative separation between the  $\Gamma_6, \Gamma_7, \Gamma_8, \Gamma_8'$  states (which is also known as quenching of the SO splitting [13], as schematically shown in Fig. 1). It is also possible to proceed with the second order of the perturbation theory. In the second order, according to [22], we have

$$\begin{aligned} \left\langle Mi00 \left| H_{\text{eff}}^{(II)} \right| M'j00 \right\rangle &= -\frac{[f_b\delta_{ij} + (1 - \delta_{ij})f_a]}{\hbar\omega} \\ &\sum_{l, M'' (l \neq i, j)} \langle Mi | H_{\text{eff}} | M''l \rangle \langle M''l | H_{\text{eff}} | M'j \rangle, \end{aligned} \quad (12)$$

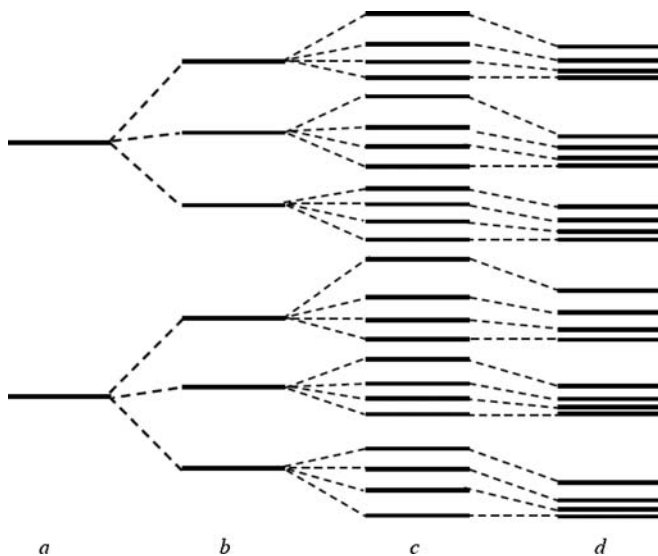


**Fig. 1** General scheme of the origin of the 3d ion energy levels with different interactions considered. From the *left* to the *right*: (a) the LS terms (Coulomb interaction between the 3d electrons); (b) crystal field splitting of the LS terms; (c) SO splitting of the crystal field energy levels; (d) Ham quenching of the SO splitting (effect of the crystal lattice vibrations)

where

$$f_a = \exp(-x) G\left(\frac{x}{2}\right), \quad f_b = \exp(-x) G(x),$$

$$G(x) = \int_0^x \frac{1}{u} (\exp(u) - 1) du, \quad x = \frac{3E_{JT}}{\hbar\omega}, \quad (13)$$

and  $\hbar\omega$  was defined after (10). Again, (12) should be modified, if the symmetrized basis functions from (7) are used. It will transform to the following form:

$$\begin{aligned} \langle Mi00 | H_{\text{eff}}^{(II)} | M'j00 \rangle = & - \sum_{i,M} \sum_{j,M'} C^*(i, M) C(j, M') \frac{[f_b \delta_{ij} + (1 - \delta_{ij}) f_a]}{\hbar\omega} \\ & \times \sum_{l, M'' (l \neq i, j)} \langle Mi | H_{\text{eff}} | M''l \rangle \langle M''l | H_{\text{eff}} | M'j \rangle. \end{aligned} \quad (14)$$

The second order correction is, as a rule, much smaller then the first order one and can be safely neglected in a vast majority of cases. If the second order correction is considered, no analytical solution can be obtained, and the matrix diagonalization should be performed numerically.

Equations (8), (12), and (14) can be used to calculate the eigenvalues of the effective Hamiltonian for values of  $\gamma$  varying from 0 (extremely strong JT interaction;  $E_{JT} \rightarrow \infty$ ) to 1 (complete absence of the JT interaction;  $E_{JT} = 0$ ).

### 3 Geometry of the Orbital Triplet States: Shift of the Potential Surfaces Minima and Chemical Bonds Changes

As a result of different bonding properties (which arise from different interionic separations in these electronic states) in the ground and excited states of an impurity ion in a crystal, they may have different geometries, what is revealed in the shift of the potential energy surfaces of the considered electron states and their different curvature. The latter is defined by the differences of the vibrational frequencies in these states, and, since this difference rarely exceeds few percents, can be readily neglected. In order to perform a qualitative analysis of this phenomenon, we use the effective Hamiltonian  $H_{VIB}$ , which describes the interaction of the electron states with the lattice normal modes in the form

$$H_{VIB} = \sum_i \left[ \frac{P_i^2}{2\mu_i} + \frac{1}{2} K_i Q_i^2 + \left( \frac{\partial V}{\partial Q_i} \right)_0 Q_i \right]. \quad (15)$$

Here  $\mu_i$  is the effective mass of the  $i$ th vibration and  $P_i$  is the momentum conjugate to the corresponding normal vibrational coordinate  $Q_i$ . The first two terms transform the electronic levels into potential energy manifolds in the coordinates of the octahedral normal modes  $Q_i$  with vibrational frequencies  $\omega_i = \sqrt{K_i/\mu_i}$ , and the complete wave functions in the Born–Oppenheimer approximation can be written as a product of the electronic and vibrational parts. The third term describes the distortions produced by the vibrations and can be interpreted in terms of a force  $F_i$ , which acts along the vibrational mode  $Q_i$  associated with the electronic state  $\Gamma$ :

$$F_i = - \left\langle \Gamma \left| \frac{\partial V}{\partial Q_i} \right|_0 \Gamma \right\rangle, \quad (16)$$

where the subscript means that the derivative is to be found at the equilibrium configuration. The third term lowers the symmetry of the octahedral complex and leads to a new equilibrium position, which can be estimated from the condition that this distorting force is balanced by the harmonic restoring force  $K_i \Delta Q_i$  at the distorted geometry

$$\Delta Q_i = - \frac{F_i}{K_i}. \quad (17)$$

This distortion lowers the energy of the electronic state by an amount

$$E_i = \frac{1}{2} K_i (\Delta Q_i)^2 \quad (18)$$

comparing to the equilibrium position. Group theory predicts that only distortions along the  $\alpha_{1g}$ ,  $\varepsilon_g$ ,  $\tau_{2g}$  octahedral modes are important for the  $^4T_{2g}$  electron state. The Hamiltonian (15) can be rewritten in the basis consisting of the above-defined  $\xi$ ,  $\eta$ ,  $\zeta$  real orbitals:

$$\begin{aligned}
 H_{\text{VIB}} = & \sum_i \left( \frac{P_i^2}{2\mu_i} + \frac{1}{2} K_i Q_i^2 \right) + \left\langle ^4T_{2g} \left\| \frac{\partial V}{\partial Q_{\alpha_{1g}}} \right\| ^4T_{2g} \right\rangle \begin{pmatrix} Q_{\alpha_{1g}} & 0 & 0 \\ 0 & Q_{\alpha_{1g}} & 0 \\ 0 & 0 & Q_{\alpha_{1g}} \end{pmatrix} \\
 & + \left\langle ^4T_{2g} \left\| \frac{\partial V}{\partial Q_{\varepsilon_g}} \right\| ^4T_{2g} \right\rangle \begin{pmatrix} \frac{1}{2} Q_{\varepsilon_g\theta} - \frac{\sqrt{3}}{2} Q_{\varepsilon_g\varepsilon} & 0 & 0 \\ 0 & \frac{1}{2} Q_{\varepsilon_g\theta} + \frac{\sqrt{3}}{2} Q_{\varepsilon_g\varepsilon} & 0 \\ 0 & 0 & -Q_{\varepsilon_g\theta} \end{pmatrix} \\
 & + \left\langle ^4T_{2g} \left\| \frac{\partial V}{\partial Q_{\tau_{2g}}} \right\| ^4T_{2g} \right\rangle \begin{pmatrix} 0 & Q_{\tau_{2g}\zeta} & Q_{\tau_{2g}\eta} \\ Q_{\tau_{2g}\zeta} & 0 & Q_{\tau_{2g}\xi} \\ Q_{\tau_{2g}\eta} & Q_{\tau_{2g}\xi} & 0 \end{pmatrix}.
 \end{aligned} \tag{19}$$

In this equation the reduced matrix elements in the front of the matrices represent the vibronic coupling constants between the triple degenerate electronic state  $^4T_{2g}$  and the normal vibration modes  $\alpha_{1g}$ ,  $\varepsilon_g$ ,  $\tau_{2g}$ , respectively. They can be evaluated using explicit expressions obtained in [28]:

$$\left\langle ^4T_{2g} \left\| \frac{\partial V}{\partial Q_{\alpha_{1g}}} \right\| ^4T_{2g} \right\rangle = -\frac{50}{\sqrt{6}R_0}Dq, \tag{20}$$

$$\left\langle ^4T_{2g} \left\| \frac{\partial V}{\partial Q_{\varepsilon_g}} \right\| ^4T_{2g} \right\rangle = -\frac{25}{R_0\sqrt{3}}Dq, \tag{21}$$

$$\left\langle ^4T_{2g} \left\| \frac{\partial V}{\partial Q_{\tau_{2g}}} \right\| ^4T_{2g} \right\rangle = -\frac{12\sqrt{3}}{7R_0}Dq \left( \frac{1}{\eta} - \frac{5}{9} \right), \tag{22}$$

where  $Dq$  is the crystal field strength, and  $R_0$  is the equilibrium distance between the impurity ion and nearest ligands, and [28]

$$\eta = \left( \frac{\langle r^2 \rangle R_0^2}{\langle r^4 \rangle} \right)^{-1} = \frac{3}{5} \times \frac{3 - 4e_\pi/e_\sigma}{1 + e_\pi/e_\sigma}, \tag{23}$$

with the angular overlap model parameters  $e_\pi$  and  $e_\sigma$  defined in [29]. The  $e_\pi/e_\sigma$  ratios are different for different complexes and can be found in the literature [29].

It also should be mentioned here that there are another ways to treat the vibronic coupling constants in the frameworks of the crystal field theory [30, 31] and DFT [27]. We shall not go into further details here, but advise a reader to go through these references.

As can be seen from the structure of (19), the coupling with the fully symmetric  $\alpha_{1g}$  mode is diagonal, producing an overall shift of all three electron states in the  $Q_{\alpha_{1g}}$  space. The coupling with the  $\varepsilon_g$  normal mode is also diagonal, but it results in

splitting of the three electron states (since the diagonal elements of this matrix are different) and displacements of all its components along different directions in the  $Q_{\varepsilon_g\theta}$ ,  $Q_{\varepsilon_g\varepsilon}$  space. The direct comparison of the electron–phonon coupling constants shows that, indeed, the coupling with the  $\tau_{2g}$  normal mode is the weakest among all the modes, and can be safely neglected, as it was done in the previous section.

The equilibrium magnitude  $|\Delta Q_i|_{eq}$  of the  $i$ th normal mode with energy  $\hbar\omega_i$  is related to the Huang-Rhys factor  $S_i$  and force constant  $K_i$  by the following equation [32]:

$$|\Delta Q_i|_{eq} = \left[ \frac{2S_i \hbar\omega_i}{K_i} \right]^{1/2}. \quad (24)$$

The force constants  $K_i$  were calculated using the FG matrix method for an octahedral  $MX_6$  molecule [33]:

$$K_{\alpha_{1g}} = \frac{4\pi^2 c^2 \sigma_{\alpha_{1g}}^2}{\mu_X + \mu_Y}, \quad K_{\varepsilon_g} = \frac{4\pi^2 c^2 \sigma_{\varepsilon_g}^2}{\mu_X + \mu_Y}, \quad (25)$$

where  $\mu_X$ ,  $\mu_Y$  are reciprocal masses of an impurity ion and a single ligand,  $\sigma_{\alpha_{1g}}$  and  $\sigma_{\varepsilon_g}$  are the frequencies (in  $\text{cm}^{-1}$ ) of the corresponding normal vibrations. Different units can be used for calculations of the force constants. If the SI system is used – they are expressed in  $\text{N m}^{-1}$ . It is also possible to measure the force constants in  $\text{mdyn } \text{\AA}^{-1}$  or  $\text{cm}^{-1} \text{\AA}^{-2}$  ( $K$  (in  $\text{mdyn } \text{\AA}^{-1}$ ) =  $K(\text{cm}^{-1} \text{\AA}^{-2})/50,350$ ). The values of the Huang-Rhys factor can be easily estimated from the experimental absorption and emission spectra.

It is more convenient to express the character of the ligands displacements in terms of the interatomic bonds changes, since such a representation allows for a visualization of the total distortion. In the  $T_{2g} \otimes \varepsilon_g$  case the three potential wells of the  ${}^4T_{2g}$  components  $\xi$ ,  $\eta$ ,  $\zeta$  are spatially separated, i.e., each of these three components distorts along a different direction in the  $Q_{\varepsilon_g\theta}$ ,  $Q_{\varepsilon_g\varepsilon}$  space [11]. All these components are related by symmetry (in fact, they are rotated by  $120^\circ$  with respect to each other) and, therefore, it is sufficient to consider just one single component. The coordinate system in the  $Q_{\varepsilon_g\theta}$ ,  $Q_{\varepsilon_g\varepsilon}$  space can always be chosen in such a special way, that the potential minimum of the considered  ${}^4T_{2g}$  component (anyone from  $\xi$ ,  $\eta$ ,  $\zeta$ ) lies on the  $Q_\theta$  axis (this means, no distortion takes place along the  $Q_\varepsilon$  axis). Then it is possible to consider the  $|\Delta Q_{\varepsilon_g}|_{eq}$  values as corresponding to  $|\Delta Q_{\varepsilon_g\theta}|_{eq}$ , whereas the  $|\Delta Q_{\varepsilon_g\varepsilon}|_{eq}$  values are zero. Using the transformation matrix, which can be easily obtained from the explicit expressions for the normal vibrations of the octahedral complex [34] (the equilibrium subscript “eq” is suppressed in this equation)

$$\begin{pmatrix} \Delta x \\ \Delta y \\ \Delta z \end{pmatrix} = \frac{1}{2} \begin{pmatrix} \sqrt{\frac{2}{3}} - \sqrt{\frac{1}{3}} & -1 \\ \sqrt{\frac{2}{3}} - \sqrt{\frac{1}{3}} & 1 \\ \sqrt{\frac{2}{3}} & \sqrt{\frac{4}{3}} & 0 \end{pmatrix} \begin{pmatrix} \Delta Q_{\alpha_{1g}} \\ \Delta Q_{\varepsilon_g\theta} \\ \Delta Q_{\varepsilon_g\varepsilon} \end{pmatrix}, \quad (26)$$

the values of the  $|\Delta Q_{\alpha_{1g}}|_{eq}$  and  $|\Delta Q_{\varepsilon_g \theta}|_{eq}$  can be converted into the changes in the metal–ligand bond lengths  $\Delta x$ ,  $\Delta y$ ,  $\Delta z$ .

After the force constants and amplitudes of the ionic displacements are found, it is possible to draw the potential energy surface of the  ${}^4T_{2g}$  excited electronic state. In the harmonic approximation, this energy is described by the following expression:

$$V = \frac{1}{2} K_{\alpha_{1g}} (\Delta Q_{\alpha_{1g}} - \Delta Q_{\alpha_{1g},eq})^2 + \frac{1}{2} K_{\varepsilon_g} (\Delta Q_{\varepsilon_g} - \Delta Q_{\varepsilon_g,eq})^2. \quad (27)$$

An inverse to the (26) transformation should be used to analyze dependence of the potential energy on the changes of the interionic distances. The contour plot of the potential energy surface in the  ${}^4T_{2g}$  state can be also used to estimate from it the value of the Jahn–Teller stabilization energy, as will be shown below.

## 4 Example of Estimations of the Jahn–Teller Energy from the Second Order Ham Effect

We shall consider in details how the above described approach can be applied to  $Cr^{3+}$  ion doped in  $KMgF_3$  crystal, at perfect octahedral site symmetry [35]. After doping,  $Cr^{3+}$  substitutes for  $Mg^{2+}$  ions at the center of an octahedron formed by six fluorine ions. The  $Cr^{3+} - F^-$  distance is 1.995 Å [36]. We do not discuss here the charge compensating mechanisms required to maintain electrical neutrality of the samples, but, instead, focus on the electronic and optical properties of the  $[CrF_6]^{3-}$  units. The DFT-based treatment of the defects related to the doping and their impact on the JT effects was given in [37].

Detailed optical studies [38] allowed to determine reliably the fine structure of the  $Cr^{3+} {}^4T_{2g}$  state (see column 3 in Table 3), which is crucial for a correct estimation of the JT stabilization energy.

The second column (labeled as “a” in Table 3) contains the calculated positions of the four levels arising from the  ${}^4T_{2g}$  state after it is split by SO interaction. These energy levels were obtained by diagonalizing complete matrices of the  $3d^3$  configuration with the following values of the crystal field strength  $Dq$ , Racah parameters  $B$ ,  $C$  and the SO interaction constant (all in  $cm^{-1}$ ): 1,450; 760; 3,426; 226 [38]. The  ${}^4T_{2g}$  state splitting can be also obtained using the second-order effective SO Hamiltonian with the parameters (all in  $cm^{-1}$ ):  $\lambda = 29.8$ ,  $\kappa = 9.7$ ,  $\rho = -29.2$  (4). After the following substitution:  $\lambda \rightarrow \gamma\lambda$ ,  $\kappa \rightarrow \gamma\kappa$ ,  $\rho \rightarrow \kappa + \rho - \gamma\kappa$ , the best fit to the experimental energy levels is obtained if  $\gamma = 0.31$  (column “c” in the Table). Since  $\gamma = \exp\left(-\frac{3E_{JT}}{2\hbar\omega}\right)$  and the energy of the Jahn–Teller active  $\varepsilon_g$  mode is  $457\text{ cm}^{-1}$  [38], the JT stabilization energy is  $E_{JT} = 356.7\text{ cm}^{-1}$ .

In this case the second-order correction (14) was not greater than few tenths of  $cm^{-1}$  and was neglected.

**Table 3** Fine structure of the  $^4T_{2g}$  state in  $KMgF_3$

$O_h$ double group irreducible representation	a	b	c
$\Gamma_7$	0	0	0
$\Gamma_8$	40	21	19.8
$\Gamma_8'$	93	48.5	48.5
$\Gamma_6$	139	69.5	70.1

(a) Calculation using the full  $d^3$  matrix [19] with the following experimental parameters [38] (all in  $\text{cm}^{-1}$ ):  $Dq = 1,450$ ,  $B = 760$ ,  $C = 3,426$ ,  $\xi_{SO} = 226$ . This last value is different from that given by formal relation  $\xi_{SO} = 3 \lambda$  for  $^4T_{2g}$  term of  $\text{Cr}^{3+}$   
(b) Experimentally observed relative energies [38]  
(c) Calculation including the Jahn–Teller effect with the Ham parameter  $\gamma = 0.31$ . The experimental  $^4T_{2g}$  spinor splitting in column b is well reproduced by the dashed line with filled circles in Fig. 2

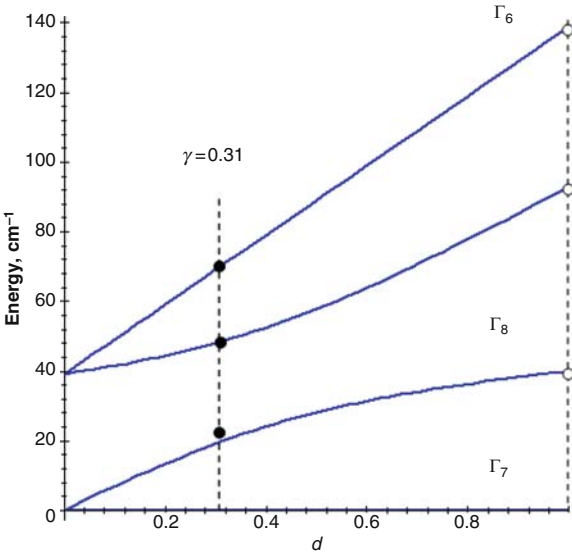


**Fig. 2** Dependence of the  $^4T_{2g}$  term fine structure for the  $\text{Cr}^{3+}$  ion in  $KMgF_3$ . The curves are the splitting as the functions of the Ham reduction factor  $\gamma$  calculated from the first and second order Ham theory. The *open circles* correspond to the energy of spinors in a static crystal field ( $\gamma = 1.0$ ), and the *filled circles* are observed experimental energies. The best fit is obtained for  $\gamma = 0.31$ . All four curves are merged into two (if  $\gamma = 0$ ; extremely strong Jahn–Teller interaction) with the separation of  $2(k + \rho)$

Figure 2 shows how the relative energies of the four sublevels of the  $^4T_{2g}$  state depend on the “strength” of the JT interaction.

Since the value of the JT energy is greater than the SO constant and the second order SO effective Hamiltonian parameters, the weak (in comparison with the JT



effect) SO interaction approximation is readily justified. One final point, which will be used in the next section, is worthwhile to be mentioned. Having found the value of the JT energy  $E_{JT}$ , the value of the Stokes shift  $S_{\varepsilon_g}$  corresponding to the  $\varepsilon_g$  normal mode can be immediately evaluated as  $S_{\varepsilon_g} = \frac{E_{JT}}{\hbar\omega}$ . The numerical estimations return the value of  $S_{\varepsilon_g} = 0.78$ .

## 5 Example of Estimations of the Jahn–Teller Stabilization Energy Using the Excited State Geometry Analysis

Here we show how the same problem can be analyzed by using the second approach described above. Using (20)–(22) and the experimental crystal field strength value  $Dq = 1,450 \text{ cm}^{-1}$ , it is possible to estimate the constants of the electron-vibrational interaction in Hamiltonian (19). Using the ratio  $e_\pi/e_\sigma = 0.31$  for the  $[\text{CrF}_6]^{3-}$  cluster [29], we got for these constants the following numerical values:

$$\begin{aligned} \left\langle {}^4T_{2g} \left\| \frac{\partial V}{\partial Q_{\alpha_{1g}}} \right\| {}^4T_{2g} \right\rangle &= -0.29 \text{ mdyn}, \\ \left\langle {}^4T_{2g} \left\| \frac{\partial V}{\partial Q_{\varepsilon_g}} \right\| {}^4T_{2g} \right\rangle &= -0.21 \text{ mdyn}, \\ \left\langle {}^4T_{2g} \left\| \frac{\partial V}{\partial Q_{\tau_{2g}}} \right\| {}^4T_{2g} \right\rangle &= -0.051 \text{ mdyn}. \end{aligned}$$

The constant of interaction with the  $\tau_{2g}$  mode is the smallest among these three, which allows to neglect the interaction with this mode and restrict our consideration by the  $\varepsilon_g$  mode only.

With  $\hbar\omega_{\alpha_{1g}} = 562 \text{ cm}^{-1}$  and  $\hbar\omega_{\varepsilon_g} = 457 \text{ cm}^{-1}$  the corresponding force constants are  $K_{\alpha_{1g}} = 2.589 \text{ mdyn } \text{\AA}^{-1}$  and  $K_{\varepsilon_g} = 1.712 \text{ mdyn } \text{\AA}^{-1}$ . The Huang-Rhys factor  $S_{\varepsilon_g} = 0.78$  has been estimated above, and neglecting the vibronic coupling with the  $\tau_{2g}$  normal mode, the Huang-Rhys factor  $S_{\alpha_{1g}}$  for the fully symmetric mode can be estimated as  $S_{\alpha_{1g}} = S - S_{\varepsilon_g} = 2.13 - 0.78 = 1.35$  (where the value of the total Huang-Rhys factor  $S = 2.13$  was determined in [35]). Using this data and (24), the magnitudes of the normal modes displacements are  $|\Delta Q_{\alpha_{1g}}|_{eq} = 0.108 \text{ \AA}$  and  $|\Delta Q_{\varepsilon_g}|_{eq} = 0.091 \text{ \AA}$ . As previously demonstrated, the sign of the  $|\Delta Q_{\alpha_{1g}}|_{eq}$  should be positive, whereas the sign of the  $|\Delta Q_{\varepsilon_g}|_{eq}$  is negative [34, 39]. These values can be easily converted into the changes of the chemical bonds lengths in an octahedral complex (using (26)), which are  $\Delta x_{eq}, \Delta y_{eq} = 0.070 \text{ \AA}$ , and  $\Delta z_{eq} = -0.008 \text{ \AA}$ .

Figure 3 visualizes the last result. As seen from this figure, the  $[\text{CrF}_6]^{3-}$  complex in  $\text{KMgF}_3$  undergoes an equatorial expansion and a slight axial compression.

These distortions should not be simply understood as a static lowering of the point symmetry from the  $O_h$  in the ground  ${}^4A_{2g}$  state to  $D_{4h}$  in the

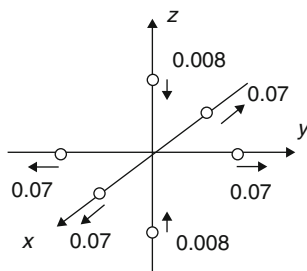


**Fig. 3** Distortion of the  $[\text{CrF}_6]^{3-}$  complex in the  ${}^4\text{T}_{2g}$  excited state with respect to the ground state (directions of the displacements and their magnitudes in angstroms are shown by *arrows* and *numbers*, respectively)

excited  ${}^4\text{T}_{2g}$  state along a given  $z$ -axis in the crystal. This is dynamical distortion, which takes place along each of the three axes of the octahedral cluster  $[\text{CrF}_6]^{3-}$ . Similar analysis which was performed for the  $\text{Cr}^{3+}$  ion in the  $\text{Cs}_2\text{NaInCl}_6$ ,  $\text{Cs}_2\text{NaYCl}_6$ ,  $\text{Cs}_2\text{NaYBr}_6$ ,  $\text{K}_2\text{NaScF}_6$  [40–43] and  $\text{V}^{2+}$  ion in  $\text{CsCaF}_3$  [44], resulted in analogous character of the dynamical deformations of the octahedral cluster formed around the  $\text{Cr}^{3+}$  ion.

After the force constants and amplitudes of the ionic displacements are found, it is possible to draw the potential energy surface of the  ${}^4\text{T}_{2g}$  excited electronic state. In the harmonic approximation, this energy is described by (27). An inverse transformation should be used to get the dependence of the potential energy on the changes of the interionic distances. The contour plot of the potential energy surface in the  ${}^4\text{T}_{2g}$  state is shown in Fig. 4.

In Fig. 4 the equilibrium position of the ground state is indicated by the open circle, the equilibrium position of the excited state is shown by the black square. Neglecting the interaction with the  $\varepsilon_g$  normal mode (this means that  $S_{\varepsilon_g} = 0$ ), we found the values of the  $\Delta x$ ,  $\Delta y$ ,  $\Delta z$  displacements produced by the full-symmetric vibration  $\alpha_{1g}$  to be  $\Delta x = \Delta y = \Delta z = 0.044 \text{ \AA}$ . This position is shown in Fig. 4 by the black circle. Using these coordinates, the JT stabilization energy can be readily estimated to be  $356.64 \text{ cm}^{-1}$ .

## 6 Summary of Results for the Octahedrally Coordinated $3d^3$ Ions

Table 4 collects all characteristic results of analysis of the JT interaction in a number of crystals doped with several  $3d^3$ -ions like  $\text{V}^{2+}$ ,  $\text{Cr}^{3+}$ ,  $\text{Mn}^{4+}$ . As seen from the table, the JT stabilization energy is always of the order of several hundred wave numbers, varying from  $257 \text{ cm}^{-1}$  for  $\text{Cs}_2\text{NaYF}_6:\text{Cr}^{3+}$  to  $584 \text{ cm}^{-1}$   $\text{K}_2\text{NaScF}_6:\text{Cr}^{3+}$ .

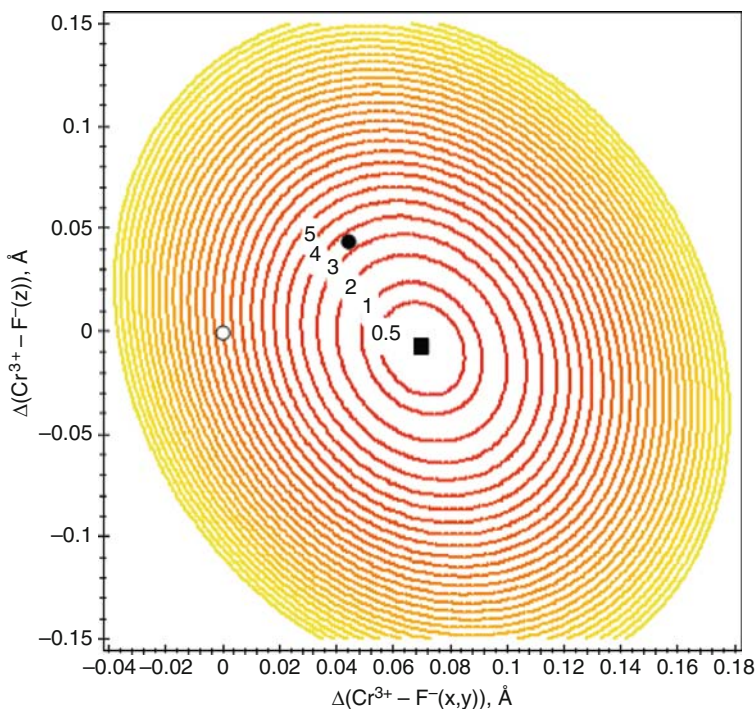


**Fig. 4** Contour plot of the  ${}^4T_{2g}$  potential energy surface for the  $\text{KMgF}_3 : \text{Cr}^{3+}$  system as a function of changes in  $\text{Cr}^{3+} - \text{F}^-(x, y)$  and  $\text{Cr}^{3+} - \text{F}^-(z)$  distances. The energies of individual contours are given in hundreds of wave numbers. The *open circle* at the origin corresponds to the equilibrium position of the ground  ${}^4A_{2g}$  potential energy surface; the *black square* indicates the equilibrium position of the  ${}^4T_{2g}$  potential energy surface shifted with respect to the ground state as a combined result of the  $\alpha_{1g}$  and  $\varepsilon_g$  normal vibrations. The *black circle* shows the hypothetical position of  ${}^4T_{2g}$  potential energy surface minimum if there were no  $\varepsilon_g$  normal vibration (i.e., in the absence of the Jahn–Teller distortion). The value on the potential energy surface of the  ${}^4T_{2g}$  state at this point (between 300 and 400  $\text{cm}^{-1}$  from the figure) corresponds to the Jahn–Teller stabilization energy for the considered complex (adopted from [35])

One more common feature is that in all cases the considered octahedral unit expands in the equatorial plane, as a result of the combined effect of the  $\alpha_{1g}$  and  $\varepsilon_g$  normal modes. Regarding the axial (along the  $z$ -axis) deformation, it should be noted that it can be of two types: either expansion ( $\text{Cs}_2\text{NaYF}_6:\text{Cr}^{3+}$ ,  $\text{CsCaF}_3:\text{V}^{2+}$ ,  $\text{Cs}_2\text{GeF}_6:\text{Mn}^{4+}$ ) or compression ( $\text{Cs}_2\text{NaInCl}_6:\text{Cr}^{3+}$ ,  $\text{Cs}_2\text{NaScCl}_6:\text{Cr}^{3+}$ ,  $\text{K}_2\text{NaScF}_6:\text{Cr}^{3+}$ ,  $\text{Cs}_2\text{NaYCl}_6:\text{Cr}^{3+}$ ,  $\text{Cs}_2\text{NaYBr}_6:\text{Cr}^{3+}$ ,  $\text{K}_2\text{LiAlF}_6:\text{Cr}^{3+}$ ,  $\text{KMgF}_3:\text{Cr}^{3+}$ ). A simple criterion which defines the contraction along the  $z$ -axis, is:  $|\Delta Q_{\alpha_{1g}}| < |\Delta Q_{\varepsilon_g}| \sqrt{2}$  [45].

**Table 4** Frequencies of the  $\alpha_{1g}$  and  $\varepsilon_g$  normal modes, Huang-Rhys parameters, force constants, magnitudes of the normal coordinates displacements, corresponding chemical bonds lengths and the Jahn–Teller stabilization energies for some 3d<sup>3</sup>-ions in cubic crystals

Ref.	$\alpha_{1g}$ mode		$\varepsilon_g$ mode		$\Delta Q_{\alpha_{1g}}$ , Å	$\Delta Q_{\varepsilon_g}$ , Å	Combined result of both $\alpha_{1g}$ and $\varepsilon_g$ modes		Result of $\alpha_{1g}$ mode only	$E_{JT}$ , cm <sup>−1</sup>				
	$\hbar\omega$ , cm <sup>−1</sup>	$10^2 K$ , mdyn Å <sup>−1</sup>	$S$	$\hbar\omega$ , Cm <sup>−1</sup>			$10^2 K$ , mdyn Å <sup>−1</sup>	$S$			$\Delta x$ , Å	$\Delta z$ , Å		
	Cs <sub>2</sub> NaInCl <sub>6</sub> : Cr <sup>3+</sup>	[43]	298	110	1.6	240	72	1.3	0.13	−0.13	0.09	−0.02	0.053	312
	Cs <sub>2</sub> NaSeCl <sub>6</sub> : Cr <sup>3+</sup>	[43]	298	110	1.4	236	69	1.3	0.12	−0.13	0.09	−0.03	0.050	307
	K <sub>2</sub> NaScF <sub>6</sub> : Cr <sup>3+</sup>	[43]	542	241	0.9	449	165	1.3	0.09	−0.11	0.07	−0.03	0.037	584
	Cs <sub>2</sub> NaYF <sub>6</sub> : Cr <sup>3+</sup>	[43]	501	206	3.2	402	133	0.64	0.18	−0.09	0.09	0.02	0.072	257
	Cs <sub>2</sub> NaYCl <sub>6</sub> : Cr <sup>3+</sup>	[43]	291	105	1.6	227	64	1.5	0.13	−0.15	0.10	−0.03	0.054	340
	Cs <sub>2</sub> NaYBr <sub>6</sub> : Cr <sup>3+</sup>	[43]	183	62	3.7	144	39	3.0	0.21	−0.21	0.15	−0.04	0.085	432
	K <sub>2</sub> LiAlF <sub>6</sub> : Cr <sup>3+</sup>	[46]	558	255	1.3	469	180	1.0	0.11	−0.10	0.073	−0.015	0.043	469
	KMgF <sub>3</sub> : Cr <sup>3+</sup>	[35]	562	259	1.35	457	171	0.78	0.11	−0.09	0.07	−0.008	0.044	357
	CsCaF <sub>3</sub> : V <sup>2+</sup>	[44]	460	173	4.05	388	123	0.95	0.21	−0.11	0.12	0.02	0.086	369
	Cs <sub>2</sub> GeF <sub>6</sub> : Mn <sup>4+</sup>	[45]	512	218	2.75	494	203	0.89	0.16	−0.09	0.09	0.01	0.065	440

## 7 Some Results for the Tetrahedrally Coordinated 3d Ions

The above described formalism can be readily applied to the analysis of the orbital triplets splitting and interaction of their electronic states with the local vibrations in the case of the tetrahedrally coordinated 3d ions. However, the number of publications devoted to these systems is not that large, and partly it is because the results can not be visualized so easily. The matter is that if in an octahedral center all normal modes are defined in one system of reference centered at the center of an octahedron, in a tetrahedral complex all normal modes are usually expressed in the local system of coordinates centered at each of the four ligands. Of course, conversion of these modes into one system of reference is possible, but it makes the final expressions to be quite lengthy.

One of the results obtained for tetrahedral centers formed by 3d ions is that one for  $\text{Mn}^{2+}$  ( $3d^5$ -configuration) in ZnS [47]. The splitting of the  $^4T_1$  orbital triplet of  $\text{Mn}^{2+}$  ion was analyzed using the second-order effective spin-Hamiltonian and comparing the calculated splittings with the observed ones. The lowest estimate for the JT energy in  $\text{ZnS:Mn}^{2+}$  was obtained to be  $750\text{ cm}^{-1}$  [47].

Recently several papers on JT effect in the  $\text{Co}^{2+}$ -bearing crystals were published [48–50]. In particular, the authors of [48] estimate the JT energy for  $\text{Co}^{2+}$  in  $\text{ZrO}_2$  to be  $1,200 \pm 250\text{ cm}^{-1}$  (significantly higher than for the octahedral centers), which is quite close to analogous values for  $\text{Co}^{2+}$  in  $\text{CaF}_2$  and  $\text{CdF}_2$  (about  $1,900\text{ cm}^{-1}$ ) [49]. One of the possible reasons for higher JT energy in tetrahedral complexes can be considerably shorter metal-ligand distance, which, obviously, leads to an overall enhancement of the vibronic interaction and increase of the vibronic coupling constants.

Another example of  $\text{Co}^{2+}$  was described in [50, 51]. Octahedrally coordinated  $\text{Co}^{2+}$  in the  $\text{Sr}^{2+}$  position in  $\text{SrLaGa}_3\text{O}_7$  strongly interacts with the local modes. The important difference of this case from the previously described is that the ground states for the octahedrally coordinated  $\text{Co}^{2+}$  is not an orbital singlet (like for octahedrally coordinated  $3d^3$  ions), but the orbital triplet  $^4T_1$ . The JT stabilization energy for the ground state in  $\text{SrLaGa}_3\text{O}_7 : \text{Co}^{2+}$  was estimated to be  $502\text{ cm}^{-1}$  for coupling with the  $\varepsilon_g$  mode and  $507\text{ cm}^{-1}$  for coupling with the  $\tau_{2g}$  mode. The JT stabilization energies in the excited state  $^4T_2$  was estimated to be much less – about  $1.2\text{--}1.3\text{ cm}^{-1}$  for both normal modes.

## 8 Conclusions

The present chapter was devoted to the detailed consideration of the dynamic JT effect in the orbital triplet states for the 3d ions in a cubic crystal field, which included analysis of the spin–orbit splitting quenching (Ham effect) and geometry of the excited states (deformation of the equilibrium ligands configuration and cross-section of the potential energy surfaces). All necessary equations involved into such an analysis were given and explained. Theoretical description has been supported by

several examples for real physical systems: detailed analysis of the structure of the linear vibronic Hamiltonian, including numerical estimations of the constants of the electron–phonon coupling, was performed. This analysis supplied with estimation of the force constants for the Jahn–Teller active modes, gave a possibility to estimate the equilibrium displacements of the ligands due to the combined result of the  $\alpha_{1g}$  and  $\varepsilon_g$  normal modes. It was shown that the net result of both vibrations can be an equatorial expansion and either an axial compression or an axial expansion.

Following the literature data, for the tetrahedral centers the JT energy in the excited state is several times higher than for the octahedral.

It is also worthwhile to note that it is also possible to establish a close relation between the crystal field effects, covalent effects (overlap between the wave functions of an impurity ion and ligands) and electron–phonon interaction and JT effects [52–54]. It was shown in these works that it is possible to distinguish and analyze separately different contributions (arising from the point charge and exchange interactions) to the vibronic effects.

## Appendix A Matrix Elements of Heff

	$ \xi, 3/2\rangle$	$ \xi, 1/2\rangle$	$ \xi, -1/2\rangle$	$ \xi, -3/2\rangle$
$\langle\xi, 3/2 $	$3\rho + 3\kappa$	0	$-\frac{\sqrt{3}}{2}\rho - \frac{\sqrt{3}}{2}\kappa$	0
$\langle\xi, 1/2 $	0	$2\rho + 2\kappa$	0	$-\frac{\sqrt{3}}{2}\rho - \frac{\sqrt{3}}{2}\kappa$
$\langle\xi, -1/2 $	$-\frac{\sqrt{3}}{2}\rho - \frac{\sqrt{3}}{2}\kappa$	0	$2\rho + 2\kappa$	0
$\langle\xi, -3/2 $	0	$-\frac{\sqrt{3}}{2}\rho - \frac{\sqrt{3}}{2}\kappa$	0	$3\rho + 3\kappa$
$\langle\eta, 3/2 $	$(\frac{3i}{2}\lambda - \frac{3i}{4}\kappa)\gamma$	0	$i\frac{\sqrt{3}}{2}\kappa\gamma$	0
$\langle\eta, 1/2 $	0	$(\frac{i}{2}\lambda - \frac{i}{4}\kappa)\gamma$	0	$i\frac{\sqrt{3}}{2}\kappa\gamma$
$\langle\eta, -1/2 $	$-i\frac{\sqrt{3}}{2}\kappa\gamma$	0	$(-\frac{i}{2}\lambda + \frac{i}{4}\kappa)\gamma$	0
$\langle\eta, -3/2 $	0	$-i\frac{\sqrt{3}}{2}\kappa\gamma$	0	$(-\frac{3i}{2}\lambda + \frac{3i}{4}\kappa)\gamma$
$\langle\zeta, 3/2 $	0	$(-\frac{\sqrt{3}}{2}\lambda - \frac{\sqrt{3}}{4}\kappa)\gamma$	0	0
$\langle\zeta, 1/2 $	$(\frac{\sqrt{3}}{2}\lambda - \frac{3\sqrt{3}}{4}\kappa)\gamma$	0	$(-\lambda + \frac{1}{2}\kappa)\gamma$	0
$\langle\zeta, -1/2 $	0	$(\lambda - \frac{1}{2}\kappa)\gamma$	0	$(-\frac{\sqrt{3}}{2}\lambda + \frac{3\sqrt{3}}{4}\kappa)\gamma$
$\langle\zeta, -3/2 $	0	0	$(\frac{\sqrt{3}}{2}\lambda + \frac{\sqrt{3}}{4}\kappa)\gamma$	0

$ \eta, 3/2\rangle$	$ \eta, 1/2\rangle$	$ \eta, -1/2\rangle$	$ \eta, -3/2\rangle$
$\langle\xi, 3/2 $	$(-\frac{3i}{2}\lambda + \frac{3i}{4}\kappa)\gamma$	0	$i\frac{\sqrt{3}}{2}\kappa\gamma$
$\langle\xi, 1/2 $	0	$(-\frac{i}{2}\lambda + \frac{i}{4}\kappa)\gamma$	0
$\langle\xi, -1/2 $	$-i\frac{\sqrt{3}}{2}\kappa\gamma$	0	$(\frac{i}{2}\lambda - \frac{i}{4}\kappa)\gamma$
$\langle\xi, -3/2 $	0	$-i\frac{\sqrt{3}}{2}\kappa\gamma$	0

(continued)

	$ \eta, 3/2\rangle$	$ \eta, 1/2\rangle$	$ \eta, -1/2\rangle$	$ \eta, -3/2\rangle$
$\langle\eta, 3/2 $	$3\rho + 3\kappa$	0	$\frac{\sqrt{3}}{2}\rho + \frac{\sqrt{3}}{2}\kappa$	0
$\langle\eta, 1/2 $	0	$2\rho + 2\kappa$	0	$\frac{\sqrt{3}}{2}\rho + \frac{\sqrt{3}}{2}\kappa$
$\langle\eta, -1/2 $	$\frac{\sqrt{3}}{2}\rho + \frac{\sqrt{3}}{2}\kappa$	0	$2\rho + 2\kappa$	0
$\langle\eta, -3/2 $	0	$\frac{\sqrt{3}}{2}\rho + \frac{\sqrt{3}}{2}\kappa$	0	$3\rho + 3\kappa$
$\langle\zeta, 3/2 $	0	$\left(i\frac{\sqrt{3}}{2}\lambda + i\frac{3\sqrt{3}}{4}\kappa\right)\gamma$	0	0
$\langle\zeta, 1/2 $	$\left(i\frac{\sqrt{3}}{2}\lambda - i\frac{3\sqrt{3}}{4}\kappa\right)\gamma$	0	$(i\lambda - \frac{i}{2}\kappa)\gamma$	0
$\langle\zeta, -1/2 $	0	$(i\lambda - \frac{i}{2}\kappa)\gamma$	0	$\left(i\frac{\sqrt{3}}{2}\lambda - i\frac{3\sqrt{3}}{4}\kappa\right)\gamma$
$\langle\zeta, -3/2 $	0	0	$\left(i\frac{\sqrt{3}}{2}\lambda + i\frac{3\sqrt{3}}{4}\kappa\right)\gamma$	0
	$ \xi, 3/2\rangle$	$ \xi, 1/2\rangle$	$ \xi, -1/2\rangle$	$ \xi, -3/2\rangle$
$\langle\xi, 3/2 $	0	$\left(\frac{\sqrt{3}}{2}\lambda - \frac{3\sqrt{3}}{4}\kappa\right)\gamma$	0	0
$\langle\xi, 1/2 $	$\left(-\frac{\sqrt{3}}{2}\lambda - \frac{\sqrt{3}}{4}\kappa\right)\gamma$	0	$(\lambda - \frac{1}{2}\kappa)\gamma$	0
$\langle\xi, -1/2 $	0	$(-\lambda + \frac{1}{2}\kappa)\gamma$	0	$\left(\frac{\sqrt{3}}{2}\lambda + \frac{\sqrt{3}}{4}\kappa\right)\gamma$
$\langle\xi, -3/2 $	0	0	$\left(-\frac{\sqrt{3}}{2}\lambda + \frac{3\sqrt{3}}{4}\kappa\right)\gamma$	0
$\langle\eta, 3/2 $	0	$\left(-i\frac{\sqrt{3}}{2}\lambda + i\frac{3\sqrt{3}}{4}\kappa\right)\gamma$	0	0
$\langle\eta, 1/2 $	$\left(-i\frac{\sqrt{3}}{2}\lambda - i\frac{\sqrt{3}}{4}\kappa\right)\gamma$	0	$(-i\lambda + \frac{i}{2}\kappa)\gamma$	0
$\langle\eta, -1/2 $	0	$(-i\lambda + \frac{i}{2}\kappa)\gamma$	0	$\left(-i\frac{\sqrt{3}}{2}\lambda - i\frac{\sqrt{3}}{4}\kappa\right)\gamma$
$\langle\eta, -3/2 $	0	0	$\left(-i\frac{\sqrt{3}}{2}\lambda + i\frac{3\sqrt{3}}{4}\kappa\right)\gamma$	0
$\langle\zeta, 3/2 $	$\frac{3}{2}\rho + \frac{3}{2}\kappa$	0	0	0
$\langle\zeta, 1/2 $	0	$\frac{7}{2}\rho + \frac{7}{2}\kappa$	0	0
$\langle\zeta, -1/2 $	0	0	$\frac{7}{2}\rho + \frac{7}{2}\kappa$	0
$\langle\zeta, -3/2 $	0	0	0	$\frac{3}{2}\rho + \frac{3}{2}\kappa$

## Appendix B Derivation of the Ham Reduction Factor

The coordinates of the potential energy surfaces minima (with respect to the ground state) are as follows (19):

$$\begin{aligned}
 Q_{\theta}^{(1)} &= Q_{\theta} - \Delta Q_i, & Q_{\theta}^{(2)} &= Q_{\theta} + \frac{1}{2}\Delta Q_i, & Q_{\theta}^{(3)} &= Q_{\theta} + \frac{1}{2}\Delta Q_i, \\
 Q_{\varepsilon}^{(1)} &= Q_{\varepsilon}, & Q_{\varepsilon}^{(2)} &= Q_{\varepsilon} + \frac{\sqrt{3}}{2}\Delta Q_i, & Q_{\varepsilon}^{(3)} &= Q_{\varepsilon} - \frac{\sqrt{3}}{2}\Delta Q_i,
 \end{aligned} \quad (\text{B.28})$$

where  $\Delta Q_i$  is given by (17). Assuming that only the ground vibrational state is occupied (the wave function of the harmonic oscillator for  $n = 0$  is  $\Psi_0 = \left(\frac{\alpha}{\pi}\right)^{1/4} \exp\left(-\frac{\alpha Q^2}{2}\right)$ ,  $\alpha = \frac{m\omega}{\hbar}$ ), the vibration overlap  $S$  for the harmonic oscillator wave functions centered at  $\left(Q_{\theta}^{(2)}, Q_{\varepsilon}^{(2)}\right)$  and  $\left(Q_{\theta}^{(3)}, Q_{\varepsilon}^{(3)}\right)$  is:

$$S = \int_{-\infty}^{\infty} \Psi_0(Q_{\theta}^{(2)}) \Psi_0(Q_{\theta}^{(3)}) dQ_{\theta} \int_{-\infty}^{\infty} \Psi_0(Q_{\varepsilon}^{(2)}) \Psi_0(Q_{\varepsilon}^{(3)}) dQ_{\varepsilon}. \quad (\text{B.29})$$

Since, as seen from (B.28), there is no overlap between  $Q_{\theta}^{(2)}$  and  $Q_{\theta}^{(3)}$ , the first integral immediately yields unity, and the second integral can be rewritten as

$$S = \left(\frac{\alpha}{\pi}\right)^{1/2} \int_{-\infty}^{\infty} \exp\left(-\frac{\alpha}{2}\left(Q_{\varepsilon} - \frac{\sqrt{3}}{2}\Delta Q_i\right)^2\right) \exp\left(-\frac{\alpha}{2}\left(Q_{\varepsilon} + \frac{\sqrt{3}}{2}\Delta Q_i\right)^2\right) dQ_{\varepsilon} = \left(\frac{\alpha}{\pi}\right)^{1/2} \int_{-\infty}^{\infty} \exp(-\alpha Q_{\varepsilon}^2) \exp\left(-\frac{3\alpha}{4}\Delta Q_i^2\right) dQ_{\varepsilon} = \exp\left(-\frac{3\alpha}{4}\Delta Q_i^2\right). \quad (\text{B.30})$$

Since  $\Delta Q_i = -\frac{F_i}{K_i}$  and, on the other hand, the force constant and frequency of vibrations are related through the mass of the oscillator  $K_i = m\omega^2$  we get from (B.30) that

$$S = \exp\left(-\frac{3}{4} \frac{m\omega}{\hbar} \frac{F_i^2}{K_i^2}\right) = \exp\left(-\frac{3}{2} \frac{E_{\text{JT}}}{\hbar\omega}\right), \quad (\text{B.31})$$

where  $E_{\text{JT}} = \frac{F_i^2}{2K_i} = \frac{K_i \Delta Q_i^2}{2}$ , and S is just the reduction factor (noted in the text, after (10), with  $\gamma$ ).

## References

1. H. A. Jahn, E. Teller, Proc. Roy. Soc. (London) **A161**, 220 (1937)
2. H. A. Jahn, Proc. Roy. Soc. (London) **A164**, 117 (1938)
3. J. H. Van Vleck, J. Chem. Phys. **7**, 72 (1939)
4. U. Opik, M. H. L. Pryce, Proc. Roy. Soc. (London) **A138**, 425 (1957)
5. A. D. Liehr, J. Phys. Chem. **67**, 389 (1963)
6. W. Mofitt, D. H. Liehr, Phys. Rev. **106**, 1195 (1957)
7. W. Mofitt, W. Thorson, Phys. Rev. **108**, 1251 (1957)
8. H. C. Longuet-Higgins, U. Opik, M. H. L. Pryce, R. A. Sack, Proc. Roy. Soc. (London) **A244**, 1 (1958)
9. M. D. Sturge, in *Advanced in Solid State Physics*, vol. 20, ed. by F. Seitz, D. Turnbull, H. Ehrenreich (Academic, New York, 1967), p. 91
10. B. Bleaney, K. D. Bowers, Proc. Roy. Soc. (London) **A65**, 667 (1952)
11. I. B. Bersuker, *The Jahn–Teller Effect* (Cambridge University Press, Cambridge, 2006)
12. B. Henderson, G. F. Imbush, *Optical Spectroscopy of Inorganic Solids* (Clarendon Press, Oxford, 1989/2006)
13. F. S. Ham, Phys. Rev. A **138**, 1727 (1965)
14. Y. Tanabe, H. Kamimura, J. Phys. Soc. Japan **13**, 394 (1958)
15. Y. Tanabe, S. Sugano, J. Phys. Soc. Japan **9** 753 (1954)
16. Y. Tanabe, S. Sugano, J. Phys. Soc. Japan **9** 766 (1954)
17. S. Sugano, Y. Tanabe, H. Kamimura, *Multiplets of Transition-Metal Ions in Crystals* (Academic, New York, 1970)



18. J.C. Eisenstein, J. Chem. Phys. **34**, 1628 (1961)
19. W.A. Runciman, K.A. Schroeder, Proc. Roy. Soc. (London) **A265**, 489 (1962)
20. C.W. Nielsen, G.F. Koster, *Spectroscopic Coefficients for the  $pn$ ,  $dn$ , and  $fn$  Configurations*, (MIT Press, Cambridge, Massachusetts, 1963)
21. J. Kanamori, Progr. Theor. Phys. (Kyoto) **17**, 177 (1957)
22. M.D. Sturge, Phys. Rev. B **1**, 1005 (1970)
23. M.D. Sturge, H.J. Guggenheim, Phys. Rev. B **4**, 2092 (1971)
24. J.S. Griffith, *The Theory of Transition Metal Ions* (Cambridge University Press, Cambridge, 1961)
25. G.F. Koster, J.O. Dimmock, R.G. Wheeler, H. Statz, *Properties of the Thirty-Two Point Groups*, Table 83 (The M.I.T. Press, Cambridge, Massachusetts, 1963)
26. F.S. Ham, in (Ed.), *Electron Paramagnetic Resonance*, ed. by S. Geschwind (Plenum Press, New York – London, 1972), p. 1
27. M. Atanasov, P. Comba, C.A. Daul, A. Hauser, J. Phys. Chem. A **111**, 9145 (2007)
28. K. Wissing, J. Degen, Mol. Phys. **95**, 51 (1998)
29. T. Schönherr, Topics Current Chem. **191**, 87 (1997)
30. M. Bacci, Chem. Phys. Lett. **58**, 537 (1978)
31. M. Bacci, Chem. Phys. **40**, 237 (1979)
32. T.C. Brunold, H.U. Güdel, in *Inorganic Electronic Structure and Spectroscopy*, vol. I: *Methodology*, ed. by E.I. Solomon, A.B.P. Lever (John Wiley & Sons, Inc, New York, 1999)
33. K. Venkateswarlu, S. Sundaram, Phys. Chem. Neue Folge **9**, 174 (1956)
34. E.I. Solomon, D.S. McClure, Phys. Rev. B **9**, 4690 (1974)
35. M.G. Brik, N.M. Avram, I. Tanaka, Phys. Stat. Solidi **B 241**, 2982 (2004)
36. L.A. Muradyan, V.E. Zavodnik, I.P. Makarova, K.S. Aleksandrov, V. I. Simonov, Kristallografiya **29**, 392 (1984)
37. F. Gilardoni, J. Weber, K. Bellafrrouh, C. Daul, H.U. Güdel, J. Chem. Phys. **104**, 7624 (1996)
38. M. Mortier, Q. Wang, J. Y. Buzare, M. Rousseau, B. Piriou, Phys. Rev. B **56**, 3022 (1997)
39. R.B. Wilson, E.I. Solomon, Inorg. Chem. **17**, 1729 (1978)
40. R. Knochenmuss, C. Reber, M.V. Rajasekharan, H.U. Güdel, J. Chem. Phys. **85** 4280 (1986)
41. H.U. Güdel, T.R. Snellgrove, Inorg. Chem. **17**, 1617 (1977)
42. O.S. Wenger, H.U. Güdel, J. Chem. Phys. **114**, 5832 (2001)
43. N.M. Avram, M.G. Brik, J. Mol. Struct. **838**, 198 (2007)
44. C.N. Avram, N.G. Brik, I. Tanaka, N.M. Avram, Physica B **355**, 164 (2005)
45. N.M. Avram, M.G. Brik, Z. Naturforsch. **60a**, 54 (2005)
46. N.M. Avram, M.G. Brik, C.N. Avram, I. Sildos, A. Reisz, XIX International Symposium on the Jahn–Teller Effect: Vibronic Interaction and Orbital Physics in Molecules and in Condensed Phase, Heidelberg, 25th–29th August 2008; Solid State Communications, doi:10.1016/j.ssc.2009.08.020
47. P. Koidl, Physica Status Solidi B **74**, 477 (1976)
48. V.M. Orera, R. Merino, R. Cases, R. Alcalá, J. Phys.: Condens. Matter **5**, 3717 (1993)
49. W. Ulrici, *The Dynamic Jahn–Teller Effect in Localized Systems. Modern Problems in Condensed Matter Sciences*, ed. by V.M. Agranovich, A.A. Maradudin (North Holland: Amsterdam, 1984)
50. M. Grinberg, S.M. Kaczmarek, M. Berkowski, T. Tsuboi, J. Phys.: Condens. Matter **13**, 743 (2001)
51. M. Grinberg, T. Tsuboi, M. Berkowski, S.M. Kaczmarek, J. Alloys Compds. **341**, 170 (2002)
52. M.G. Brik, C.N. Avram, J. Lumin. **102–103**, 283 (2003)
53. S.I. Klokishner, B.S. Tsukerblat, O.S. Reu, A.V. Palii, S.M. Ostrovsky, Chem. Phys. **316**, 83 (2005)
54. S.I. Klokishner, O.S. Reu, S.M. Ostrovsky, A.V. Palii, L.L. Kulyuk, B.S. Tsukerblat, E. Towe, J. Mol. Struct. **838**, 133 (2007)

# Constructing, Solving and Applying the Vibronic Hamiltonian

Philip L.W. Tregenna-Piggott and Mark J. Riley

**Abstract** The Jahn–Teller effect is shrouded in mysticism and cynicism. To paraphrase a remark that a colleague recently relayed, “For every anomalous spectrum, structural distortion or novel physical property, there is a vibronic Hamiltonian and ensuing explanation that few can appreciate or comprehend.” The aim of this article is to provide a basic introduction to the Jahn–Teller effect, pitched at a level that undergraduates in chemistry can understand, with an emphasis on how to calculate a given experimental quantity. We show that armed with just a little group theory and matrix mechanics, vibronic Hamiltonians can be readily constructed, solved, and the molecular property of interest extracted from the eigenvalues and eigenfunctions. The manifestation of the Jahn–Teller effect does indeed come in many shapes and forms, three signatures of which are briefly discussed. (1) The vibronic energy spectrum is best revealed by spectroscopy and two examples are taken from the literature that elucidate the intricate energy-level pattern of the  $E \otimes e$  vibronic interaction. (2) ‘The Ham effect’, ‘Ham factors’ and ‘Ham quenching’ are now common parlance in spectroscopy and the phenomenon is aptly illustrated by the magnetic and spectroscopic data of the titanium(III) and vanadium(III) aqua ions. (3) The plasticity of the co-ordination sphere is the quintessential feature of transition metals exhibiting strong Jahn–Teller coupling. We show how a concomitant description of structural and spectroscopic data can be obtained employing a model in which the potential energy surface resulting from the cubic Jahn–Teller Hamiltonian is perturbed by anisotropic strain.

## 1 Setting Up and Solving the $E \otimes e$ Vibronic Hamiltonian

### 1.1 Vector Coupling Coefficients

Consider the direct product of two irreducible representations within the O point group,

$$E \otimes E \rightarrow A_1 \oplus [A_2] \oplus E. \quad (1)$$

Following Sugano, Tanabe and Kamimura [1] the vector coupling coefficients (otherwise known as Clebsch–Gordan coefficients) shown in Table 1 inform us how the decomposition products are constructed from the initial functions.

Reading down the columns, we obtain,

$$\begin{aligned} A_1 &= \frac{1}{\sqrt{2}} (\theta_1 \theta_2 + \varepsilon_1 \varepsilon_2), \\ A_2 &= \frac{1}{\sqrt{2}} (\theta_1 \varepsilon_2 - \varepsilon_1 \theta_2), \\ E_\theta &= \frac{1}{\sqrt{2}} (-\theta_1 \theta_2 + \varepsilon_1 \varepsilon_2), \\ E_\varepsilon &= \frac{1}{\sqrt{2}} (\theta_1 \varepsilon_2 + \varepsilon_1 \theta_2). \end{aligned} \quad (2)$$

Where  $\theta$  and  $\varepsilon$  denote the two components of the  $E$  irreducible representation of the O point group with transformation properties,

$$\begin{aligned} \theta &\sim 2z^2 - x^2 - y^2, \\ \varepsilon &\sim x^2 - y^2. \end{aligned} \quad (3)$$

The irreducible representations on the right hand side of (1) are divided into those which are symmetric (unbracketed) and anti-symmetric (bracketed) with respect to the interchange of indices as can be seen explicitly in (2).

## 1.2 The Wigner Eckart Theorem

An important use of vector coupling coefficients lies in the calculation of matrix elements of the operators in the vibronic Hamiltonian. Knowing the symmetry properties of the basis functions and of the operators, the ratio of the matrix elements can be deduced by inspection of the vector coupling coefficients. Without resorting to complicated formulae, a restricted use of the Wigner Eckart theorem may be illustrated as follows. First let us reduce Table 1 to those columns involving only the decomposition products of  $E$  symmetry (Table 2).

Under the column labelled  $\gamma_1$  are listed the symmetries of the operators, in this case  $E_\theta$  and  $E_\varepsilon$ . Under the column  $\gamma_2$  are listed the symmetries of the kets and under the columns of the decomposition products  $E_\theta$  and  $E_\varepsilon$ , the symmetries of the bras. The numbers in the cells reveal the ratios of the matrix elements. In matrix form we may write down:

$$\begin{array}{cc} \hat{\theta} & \begin{array}{cc} |\theta\rangle & |\varepsilon\rangle \end{array} \\ \begin{array}{c} \langle\theta| \\ \langle\varepsilon| \end{array} & \begin{pmatrix} -c_E & 0 \\ 0 & c_E \end{pmatrix} \end{array} \quad \begin{array}{cc} \hat{\varepsilon} & \begin{array}{cc} |\theta\rangle & |\varepsilon\rangle \end{array} \\ \begin{array}{c} \langle\theta| \\ \langle\varepsilon| \end{array} & \begin{pmatrix} 0 & c_E \\ c_E & 0 \end{pmatrix} \end{array}. \quad (4)$$

The constant  $c_E$  is commonly referred to as a reduced matrix element.

**Table 1**  $E \otimes E$  vector-coupling coefficients with cubic bases. The symmetry labels  $\theta$  and  $\varepsilon$  are equivalent to  $\mu$  and  $\nu$  used by Sugano, Tanabe and Kamimura

$E \otimes E$		$\Gamma$	$A_1$	$A_2$	$E$	
		$\gamma$	$E_I$	$E_2$	$\theta$	$\varepsilon$
$\gamma_1$	$\gamma_2$					
$\theta$	$\theta$		$1/\sqrt{2}$	0	$-1/\sqrt{2}$	0
	$\varepsilon$		0	$1/\sqrt{2}$	0	$1/\sqrt{2}$
$\varepsilon$	$\theta$		0	$-1/\sqrt{2}$	0	$1/\sqrt{2}$
	$\varepsilon$		$1/\sqrt{2}$	0	$1/\sqrt{2}$	0

**Table 2**  $E \otimes E$  vector-coupling coefficients with cubic bases, showing only the E decomposition products

		$\Gamma$	$E$	
		$\gamma$	$\theta$	$\varepsilon$
$\gamma_1$	$\gamma_2$			
$\theta$	$\theta$		$-1/\sqrt{2}$	0
	$\varepsilon$		0	$1/\sqrt{2}$
$\varepsilon$	$\theta$		0	$1/\sqrt{2}$
	$\varepsilon$		$1/\sqrt{2}$	0

### 1.3 Construction of the Vibronic Hamiltonian from Group Theoretical Principles

Let us express the potential energy of a molecule as a Taylor expansion in its normal co-ordinates about the origin:

$$V = V_0 + \sum_i \left( \frac{\partial V}{\partial Q_i} \right)_0 Q_i + \frac{1}{2} \sum_{i,j} \left( \frac{\partial^2 V}{\partial Q_i \partial Q_j} \right)_0 Q_i Q_j + \dots \quad (5)$$

Consider the form of the operator  $\left( \frac{\partial V}{\partial Q_i} \right)_0$  for a molecule with an orbitally degenerate ground term, forming a basis for the  $E$  irreducible representation within the  $O$  point group. This operator has matrix elements within the  $E$  term only if it transforms as one of the decomposition products in Table 1, i.e. we need only consider  $\left( \frac{\partial V}{\partial Q_{A_1}} \right)_0$ ,  $\left( \frac{\partial V}{\partial Q_{A_2}} \right)_0$ ,  $\left( \frac{\partial V}{\partial Q_\theta} \right)_0$ ,  $\left( \frac{\partial V}{\partial Q_\varepsilon} \right)_0$ . When the molecule is displaced along the normal co-ordinate transforming as  $A_1$ , the energy of the  $E$  term is shifted, without being split by the distortion. Terms containing  $\left( \frac{\partial V}{\partial Q_{A_1}} \right)_0$  may be eliminated by setting  $V_0$  appropriately. The operator  $\left( \frac{\partial V}{\partial Q_{A_2}} \right)_0$  naturally transforms as  $A_2$ . From inspection of the  $A_2 \otimes E$  vector-coupling coefficients, any operator of  $A_2$  symmetry has the following form in the cubic  $E$  basis,

$$\hat{A}_2 \begin{array}{cc} |\theta\rangle & |\varepsilon\rangle \\ \langle\theta| & \begin{pmatrix} 0 & c_{A_2} \\ -c_{A_2} & 0 \end{pmatrix} \\ \langle\varepsilon| & \end{array} \quad (6)$$

In order for the operator to be Hermitian, the constant  $c_{A_2}$  must be imaginary. However, the operators in the expansion (5) are a result of the movement of atoms, and can be expressed as real numbers. For this reason, the matrix representation of  $\left(\frac{\partial V}{\partial Q_{A_2}}\right)_0$  must be real in a real basis. Both these considerations are satisfied only when  $c_{A_2}$  is set to zero. Coupling terms of  $A_2$  symmetry can only occur within an  $E$  electronic state when the coupling is to the conjugate momentum, rather than to the coordinate operator [2].

The terms  $\left(\frac{\partial V}{\partial Q_\theta}\right)_0$  and  $\left(\frac{\partial V}{\partial Q_\varepsilon}\right)_0$  give rise to a linear splitting of the  $E$  electronic state, as may be deduced from inspection of the matrices in (4). The extent to which the minimum will be displaced along these co-ordinates will then depend on the magnitudes of these terms relative to the harmonic restoring force. In 1936, Jahn and Teller formulated their famous theorem by considering whether an asymmetric normal mode  $Q_i$  exists such that  $\left(\frac{\partial V}{\partial Q_i}\right)_0$  is non-zero for molecules of all the molecular point groups. “A group-theoretical investigation shows that except for molecules in which all atoms lie on a straight line only undegenerate states or the doubly degenerate states of molecules with an odd number of electrons can correspond to stable configurations” [3]. Modern day formulations of the theorem invoke ideas of “symmetry breaking” and the “lifting of degeneracy” that are as ubiquitous as they are misleading. Returning to (5) we see that the electronic operator  $\left(\frac{\partial V}{\partial Q_i}\right)_0$  is multiplied by  $Q_i$ , a position operator of the same symmetry. The first order term thus becomes,

$$\sum_{\theta,\varepsilon} \left(\frac{\partial V}{\partial Q_{\theta,\varepsilon}}\right)_0 Q_{\theta,\varepsilon} = A_1 (U_\theta Q_\theta + U_\varepsilon Q_\varepsilon), \quad (7)$$

where  $A_1$  is a constant in the context, not a symmetry label.  $Q_\theta$  and  $Q_\varepsilon$  are dimensionless co-ordinates of the  $E$  vibration.  $U_\theta$  and  $U_\varepsilon$  are the electronic operators,

$$U_\theta = \begin{pmatrix} -1 & 0 \\ 0 & 1 \end{pmatrix}, \quad U_\varepsilon = \begin{pmatrix} 0 & 1 \\ 1 & 0 \end{pmatrix}. \quad (8)$$

From inspection of (2) we note that the operator in (7) transforms totally symmetric in the parent point group, which means that regardless of the strength of this vibronic interaction, all the functions still transform as irreducible representations of the octahedral point group; i.e. the Jahn–Teller effect alone does not give rise to a lowering of symmetry; it can only facilitate the lowering of symmetry. Consider this formulation of the Jahn–Teller effect by the late great Mary O’Brien [4], which is as precise as it is opaque to the inorganic chemist: “For any set of orbitally degenerate electronic energy levels, a term in the Hamiltonian can be found that is linear in the

normal co-ordinates of some vibration and operates within the degenerate states, the exception being linear molecules”.

Turning now to the higher-order terms, the readers should convince themselves from inspection of (2) that the products  $Q_\theta^2 + Q_\varepsilon^2$ ,  $-Q_\theta^2 + Q_\varepsilon^2$ ,  $2Q_\theta Q_\varepsilon$ ,  $Q_\theta(-Q_\theta^2 + Q_\varepsilon^2) + Q_\varepsilon(2Q_\theta Q_\varepsilon)$  transform as  $A_1$ ,  $E_\theta$ ,  $E_\varepsilon$  and  $A_1$  respectively. Each must be combined with an electronic operator  $\sum_{i,j} \left( \frac{\partial^2 V}{\partial Q_i \partial Q_j} \right)_0$ , of the same symmetry. The potential energy may then be expressed as,

$$V = A_1 (Q_\theta U_\theta + Q_\varepsilon U_\varepsilon) + \frac{1}{2} \hbar \omega (Q_\theta^2 + Q_\varepsilon^2) U_\tau + A_2 ((-Q_\theta^2 + Q_\varepsilon^2) U_\theta + 2Q_\theta Q_\varepsilon U_\varepsilon) + A_3 ((3Q_\theta Q_\varepsilon^2 - Q_\theta^3) U_\tau). \quad (9)$$

In (9),  $A_1$  and  $A_2$  are the linear and quadratic coupling constants;  $\hbar \omega$  and  $A_3$  represent the vibrational frequency and the anharmonic coupling constant respectively, and  $U_\tau$  denotes the  $(2 \times 2)$  unit matrix.

## 1.4 Potential Energy Surfaces

The potential energy surface can be readily constructed by repeated diagonalisations of the 2 by 2 matrix in (9) for different values of  $Q_\theta$  and  $Q_\varepsilon$ . With the quadratic and anharmonic terms ( $A_2$ ,  $A_3$ ) set to zero, the surface takes the form of the well-known Mexican hat, shown in Fig. 1.

The distortion in the  $\{Q_\theta Q_\varepsilon\}$  co-ordinate space is conveniently expressed in polar co-ordinates,

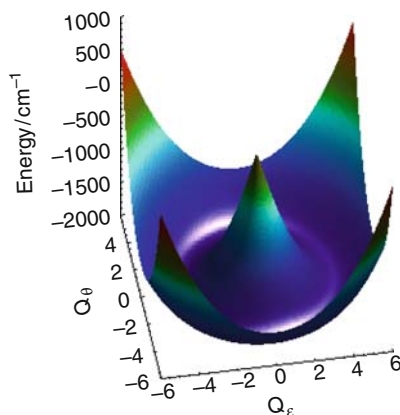


**Fig. 1** The  $E \otimes e$  potential energy surface calculated from (9) with  $\hbar \omega = 250 \text{ cm}^{-1}$ ,  $A_1 = -1,000 \text{ cm}^{-1}$  and  $A_2 = A_3 = 0$

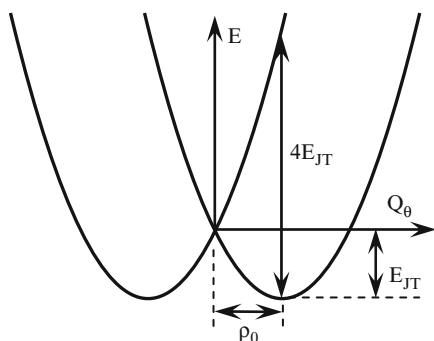


Fig. 2 Cross-section through the  $E \otimes e$  potential energy surface shown in Fig. 1

$$\begin{aligned} Q_\theta &= \rho \cos \phi_\rho, \\ Q_\varepsilon &= \rho \sin \phi_\rho. \end{aligned} \quad (10)$$

The Jahn–Teller radius,  $\rho_0$ , is given by,

$$\rho_0 = \frac{A_1}{\hbar\omega}. \quad (11)$$

A cross section through the surface is shown in Fig. 2 above. As a consequence of the Jahn–Teller interaction, the minimum of the potential energy surface is lowered by,

$$E_{JT} = \frac{A_1^2}{2\hbar\omega}. \quad (12)$$

The energy difference between the upper and lower sheets is  $4E_{JT}$  at the position of the minimum  $\rho_0$ . For copper(II) [5], chromium(II) [6] and manganese(III) [7] complexes, the transition can be readily observed by optical spectroscopy, falling in the near infrared/visible region of the electromagnetic spectrum.

The inclusion of either the second order or anharmonic term leads to minima in the directions of  $\pm Q_\theta, \mp \frac{1}{2}Q_\theta \pm \frac{\sqrt{3}}{2}Q_\varepsilon, \pm \frac{1}{2}Q_\theta \mp \frac{\sqrt{3}}{2}Q_\varepsilon$ , corresponding to elongations/compressions, as shown in the contour plot of Fig. 3. These are co-kernel (or epikernel) points of  $D_{4h}$  symmetry. All other linear combinations of the distortion co-ordinates give rise to configurations of  $D_{2h}$  symmetry. This result is in accordance with the epikernel principle of Arnout Ceulemans [8], which states that the minima in the Jahn–Teller potential energy surface will generally occur at the points of co-kernel symmetry when these are present. A useful table detailing the symmetries obtained when a molecule is displaced along a given displacement co-ordinate is to be found in [9].

As both second-order and anharmonic effects give rise to a warping of the Mexican hat surface, it is common practice to drop the anharmonic term, absorbing its effect in the second-order Jahn–Teller coupling term.

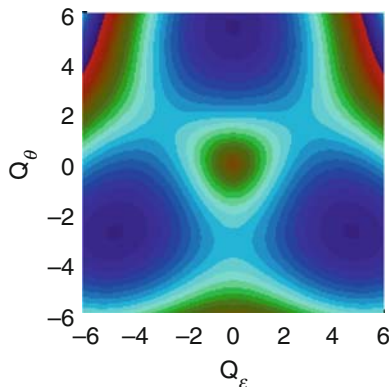


**Fig. 3** The  $E \otimes e$  potential energy surface including linear and quadratic coupling. The contour plot was calculated from (9) with  $\hbar\omega = 250 \text{ cm}^{-1}$ ,  $A_1 = -1,000 \text{ cm}^{-1}$ ,  $A_2 = 30 \text{ cm}^{-1}$  and  $A_3 = 0$

The degeneracy of the three potential minima is lifted by including additional terms in the Hamiltonian:

$$H_{st} = -e_\theta U_\theta - e_\varepsilon U_\varepsilon. \quad (13)$$

$e_\theta$  and  $e_\varepsilon$  are the two components of the strain tensor of  $E$  symmetry. Note that (13) has a similar form to the linear Jahn–Teller coupling in (7) except that the position operators are absent. The inclusion of the terms  $-e_\theta U_\theta$  and  $-e_\varepsilon U_\varepsilon$  describe low-symmetry structural distortions, transforming as totally symmetric in the  $D_{4h}$  and  $D_{2h}$  point groups respectively; and can be defined in terms of a displacement along the  $Q_\theta$ ,  $Q_\varepsilon$  modes [10]. It should be noted that the low symmetry terms in (13) are strictly speaking not part of the  $E \otimes e$  vibronic Hamiltonian. However, it is important to consider such terms in the context of the Jahn–Teller effect as we will show in Sect. 3 that even small low symmetry terms can have a large effect on Jahn–Teller potential surfaces and the spectroscopic observables. By analogy with (10) the strain may be described in polar co-ordinates,

$$\begin{aligned} e_\theta &= \delta \cos \phi_\delta, \\ e_\varepsilon &= \delta \sin \phi_\delta. \end{aligned} \quad (14)$$

The sign of the parameters comprising the Hamiltonian are defined such that the effect of strain alone is to localise the minimum at the value  $\phi_\rho = \phi_\delta$ , whereas the higher order terms (without strain) give rise to minima at points of co-kernel symmetry. The form of the potential energy surface is then largely governed by the magnitude  $\delta$  relative to the barrier height, given by  $2\beta = 2|A_2|A_1^2 / (\hbar\omega^2 - 4|A_2|^2)$ . The interplay between the parameters  $\delta$  and  $2\beta$  is illustrated in plots shown in Fig. 4, where the path of the minimum energy is plotted as a function of  $\phi_\rho$ .



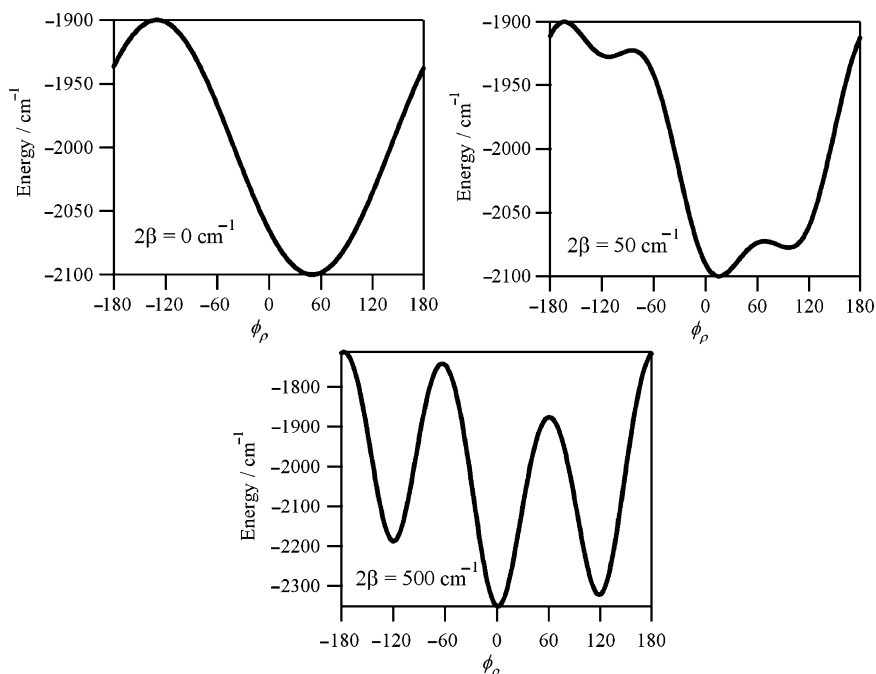


**Fig. 4** Path of Minimum energy on the  $E \otimes e$  potential energy surface for values of  $2\beta$  indicated. For all plots,  $A_I = -1,000 \text{ cm}^{-1}$ ,  $h\omega = 250 \text{ cm}^{-1}$ ,  $\delta = 100 \text{ cm}^{-1}$ ,  $\phi_\delta = 50^\circ$

The surfaces in Fig. 4 were calculated with parameters corresponding to  $E_{JT}$  equal to  $2,000 \text{ cm}^{-1}$ , which is in the strong coupling limit typical of copper(II) complexes [11].  $E \otimes e$  coupling is also realised when the orbital degeneracy lies in the  $\pi$ -antibonding  $t_{2g}$  orbitals and the molecules are axially distorted. In this instance the coupling is much weaker and is comparable to the first-order splitting of the states by spin-orbit coupling. This pseudo-Jahn–Teller coupling may then only soften the potential without giving rise to minima at distorted configurations [12].

Analytical expressions for the first-order coupling coefficients can be readily obtained within the framework of the Angular Overlap Model (AOM) [13–15]. Numerical estimates that are in impressive agreement with experiment have been obtained by calculating points on the potential energy surface using density functional theory [16–18].

### 1.5 Numerical Solution of the Vibronic Hamiltonian

When the kinetic energy operators are added to (9), the Hamiltonian for the system becomes,

$$\begin{aligned} \hat{H} = & \frac{1}{2}\hbar\omega (P_\theta^2 + P_\varepsilon^2 + Q_\theta^2 + Q_\varepsilon^2) U_\tau + A_1 (Q_\theta U_\theta + Q_\varepsilon U_\varepsilon) \\ & + A_2 ((-Q_\theta^2 + Q_\varepsilon^2) U_\theta + 2Q_\theta Q_\varepsilon U_\varepsilon) + A_3 ((3Q_\theta Q_\varepsilon^2 - Q_\theta^3) U_\tau) - e_\theta U_\theta - e_\varepsilon U_\varepsilon. \end{aligned} \quad (15)$$

The dimensionless  $P$  and  $Q$  are related to the observables for momentum ( $\hat{p}$ ) and position ( $\hat{q}$ ) by the relations [19],

$$Q = \sqrt{\frac{\mu\omega}{\hbar}} \hat{q}; \quad P = \frac{1}{\sqrt{\mu\hbar\omega}} \hat{p}. \quad (16)$$

Their matrix elements are expressed as,

$$\begin{aligned} Q &= \frac{1}{\sqrt{2}} (a^\dagger + a), \quad P = \frac{i}{\sqrt{2}} (a^\dagger - a), \\ a | \varphi_n \rangle &= \sqrt{n} | \varphi_{n-1} \rangle, \quad a^\dagger | \varphi_n \rangle = \sqrt{n+1} | \varphi_{n+1} \rangle, \end{aligned} \quad (17)$$

where  $n$  is the quantum number of the one-dimensional harmonic oscillator. The Hamiltonian in (15) is most easily solved by first constructing it as a matrix in a basis of products of the electronic states and the uncoupled states of the two dimensional  $\{n_\theta n_\varepsilon\}$  harmonic oscillator of dimension  $N = \frac{1}{2} (n_v + 1) (n_v + 2)$ , up to the level  $n_v$ . The levels up to  $n_v = 5$  are shown in Fig. 5 below.

A worthwhile exercise is to convince oneself using (17) that the harmonic term is diagonal within the basis  $|n_\theta, n_\varepsilon\rangle$  with elements  $(n_\theta + n_\varepsilon + 1) \hbar\omega$ .

Including terms up to second-order in the distortion co-ordinates leads to a large sparse real symmetric matrix. The eigenvalues and eigenfunctions in the energy range of interest can be readily obtained by numerical diagonalisation and the Lanczos algorithm is well suited to these types of problems. The eigenfunctions are then expressed as,

$$\Psi = \sum_i \sum_{j+k=0}^{n_v} a_{ijk} | \psi_i, n_{\theta j}, n_{\varepsilon k} \rangle, \quad (18)$$

where  $\psi_i$  spans the electronic functions and  $n_\theta$  and  $n_\varepsilon$  are the quantum numbers of the harmonic oscillators. The total size of the  $N \times N$  matrix for a vibronic basis is

5	{5,0}	{4,1}	{3,2}	{2,3}	{1,4}	{0,5}
4	{4,0}	{3,1}	{2,2}	{1,3}	{0,4}	
3		{3,0}	{2,1}	{1,2}	{0,3}	
2			{2,0}	{1,1}	{0,2}	
1				{1,0}	{0,1}	
$n_\theta+n_\varepsilon=0$					{0,0}	

**Fig. 5** Levels of the two-dimensional harmonic oscillator up to  $n_v = n_\theta + n_\varepsilon = 5$ , expressed in terms of  $\{n_\theta, n_\varepsilon\}$ , the quantum numbers of the components  $Q_\theta$  and  $Q_\varepsilon$

given by  $N = 2 \times \frac{1}{2} \times (n_v + 1)(n_v + 2)$  and depends on the number of vibrational basis levels ( $n_v$ ) required to converge the problem to the desired accuracy.

## 1.6 The Vibronic Energy Levels

The vibronic energy levels obtained from the matrix diagonalisation described above are shown in Fig. 6 as a function of the coupling constants  $A_1$  and  $A_2$ . It can be seen that quite a complex pattern of energy levels are generated and these can be rationalised by examining the limiting cases in each figure. In Fig. 6a the energy levels are for linear coupling only ( $A_2, A_3 = 0$ ) which gives rise to the “Mexican hat” potential surface with cylindrical symmetry as shown in Fig. 1. On the Y axis ( $A_1 = 0$ ) one finds the energy levels of a two dimensional harmonic oscillator as shown in Fig. 5. The levels are equally spaced and have a  $2(n_\theta + n_\varepsilon + 1)$  degeneracy. As the first order coupling constant is increased, the levels are seen to oscillate about a mean value before decreasing and approaching a limiting value for large coupling on the right hand side. In the large coupling limit the levels can be described as combinations of a radial vibration ( $n_\rho$ ) and a pseudo-rotation with an odd-half integer quantum number taking the values  $j = 1/2, 3/2, 5/2 \dots$ . All levels are doubly degenerate, although some are actually composed of two one-dimensional states that are “accidentally” degenerate. As well as these accidental degeneracies, the fact that the levels cross rather than showing avoided crossings, in

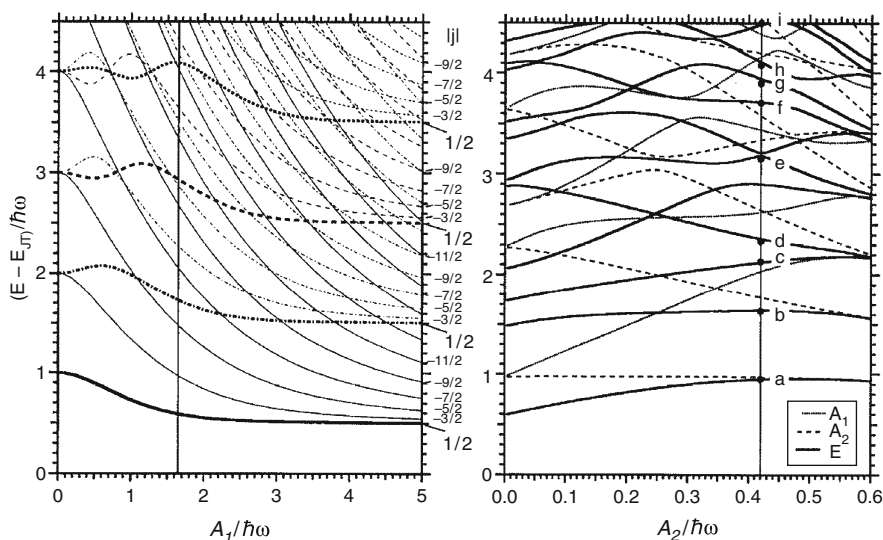


**Fig. 6** The  $E \otimes e$  vibronic energy levels as a function of (a) the first-order coupling with ( $A_2 = 0$ ), and (b) the second-order coupling constant for a fixed value of  $A_1/\hbar\omega = 1.65$

Fig. 6a shows that there are additional symmetries at work. The vibronic matrix can be made block diagonal using the quantum number  $j$  and thereby reducing the size of the computational problem [20].

The accidental degeneracies are removed when the second order coupling ( $A_2$ ) is made non-zero as shown in Fig. 6b. Now only levels of different symmetries cross, although some points where the avoided crossings are close give the appearance of crossing. The left hand side of Fig. 6b ( $A_2 = 0$ ) gives energy levels that are the same as those of the vertical line at  $A_1/\hbar\omega \sim 1.65$  in Fig. 6a. As the second-order coupling is increased the  $A_1/A_2$  vibronic states split, as shown by the dotted and dashed lines respectively in Fig. 6b. As discussed in Sect. 1.4, the second order coupling results in three equivalent minima separated by barriers, and in the limit of large second-order coupling, the doubly degenerate and singly degenerate vibronic levels “pair up” to approach a three fold degeneracy. This approach to three-fold degeneracy occurs for the lower vibronic levels before the higher levels, as the energy separations represent a “tunnelling splitting” and it takes a higher barrier to localise the higher vibronic levels within the minima. It should be noted that for all values of the coupling constants, the lowest vibronic level is required to be of  $E$  symmetry [21]. The first excited singlet is a vibronic state of  $A_2(A_1)$  symmetry for minima at the positions  $\phi = 0^\circ, 120^\circ, 240^\circ$  ( $60^\circ, 180^\circ, 300^\circ$ ) on the potential surface and this is determined by whether the product of the first and second order coupling constants is negative (positive). For an six-coordinate Cu(II) complex, the first excited singlet is of  $A_2(A_1)$  symmetry when each of the three minima corresponds to equivalent tetragonally elongated (compressed) geometries.

## 2 Calculation of the Experimental Quantities

### 2.1 Structural Data

The structure of a molecule that one observes will depend on the timescale of the experiment relative to the dynamics of the molecule. Crystallography yields the space-averaged structure. One obtains information regarding the average position of the atoms, the dynamics are swallowed up in the temperature factors. The calculation proceeds by first identifying the dominant vibrational mode(s) involved in the coupling. For  $d^9$  and high-spin  $d^4$  complexes, this is the  $\nu_2(\text{ML}_6)$  asymmetric skeletal stretch depicted in Fig 7 below:

Displacements along these co-ordinates may be expressed in a basis of increments in the metal-ligand (M-L) bond lengths:

$$Q_\theta = \frac{1}{\sqrt{12}}(2r_1 + 2r_4 - r_2 - r_5 - r_3 - r_6),$$

$$Q_\varepsilon = \frac{1}{2}(r_2 + r_5 - r_3 - r_6),$$
(19)

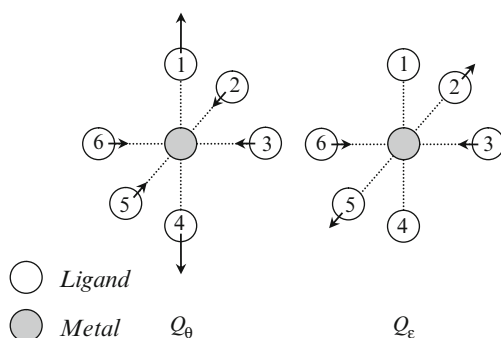


**Fig. 7** The two components of the  $\nu_2(\text{ML}_6)$  vibration. Arrows indicate the directions and relative magnitudes of the displacements

where  $r_i$  is a unit displacement along the  $\text{M-L}_i$  bond vector, and the ligands are numbered according to the scheme used in Fig. 7. The unit displacements,  $r_i$  are related to  $\langle \hat{q}_\theta \rangle_T$  and  $\langle \hat{q}_\varepsilon \rangle_T$  by,

$$\begin{aligned} r_1 = r_4 &= \frac{1}{\sqrt{12}} 2 \langle \hat{q}_\theta \rangle_T ; r_2 = r_5 = \frac{(-\langle \hat{q}_\theta \rangle_T + \sqrt{3} \langle \hat{q}_\varepsilon \rangle_T)}{\sqrt{12}} ; \\ r_3 = r_6 &= \frac{(-\langle \hat{q}_\theta \rangle_T - \sqrt{3} \langle \hat{q}_\varepsilon \rangle_T)}{\sqrt{12}} \end{aligned} \quad (20)$$

where it is understood that  $\langle \hat{q}_\theta \rangle_T$  and  $\langle \hat{q}_\varepsilon \rangle_T$  are the Boltzmann average of the expectation values over the thermally populated vibronic energy levels. From (16) to (18) the expectation value for a given level,  $\Psi$ , is calculated according to:

$$\begin{aligned} \langle \hat{q}_\theta \rangle &= \sqrt{\frac{\hbar}{\mu\omega}} \langle \Psi | \hat{Q}_\theta | \Psi \rangle = \sqrt{\frac{\hbar}{\mu\omega}} \sum_i \sum_{i'} \sum_{j+k=0}^{n_v} \sum_{j'+k'=0}^{n_v} \\ &\times a_{ijk}^* a'_{i'j'k'} \langle n_{\theta j} | \hat{Q}_\theta | n_{\theta j'} \rangle \delta_{ii'} \delta_{kk'} \\ &= \sqrt{\frac{\hbar}{\mu\omega}} \sum_i \sum_{j+k=0}^{n_v} \left( a_{i(j+1)k}^* a_{ijk} \sqrt{\frac{j+1}{2}} + a_{i(j-1)k}^* a_{ijk} \sqrt{\frac{j}{2}} \right) \end{aligned} \quad (21)$$

and analogously for  $\langle \hat{q}_\varepsilon \rangle$ .

The literature is replete with examples of crystallographic studies of copper(II) and manganese(III) complexes where the  $\text{ML}_6$  skeletal framework is reported to be regular. In these instances it is not uncommon to read of the Jahn–Teller effect being “suppressed”. The use of such language could be taken to mean that the potential

energy minimum falls at the undistorted, high symmetry, configuration. Since the linear Jahn–Teller coupling is pronounced for  $d^9$  and high-spin  $d^4$  complexes, a Jahn–Teller radius so small as to render a Jahn–Teller distortion undetectable would imply a force constant of heroic proportions. No structural distortion is observed because the complexes exhibit either a dynamic Jahn–Teller effect, in which the complexes oscillate between the tetragonal distortions depicted in Fig. 3, or a disordered static Jahn–Teller effect, in which the complexes are randomly localised in one of the three potential minima. In a seminal paper by Bürgi et al. describing an EPR and crystallographic study of the  $\text{Cu}(\text{tach})_2$  complex ( $\text{tach} \equiv \text{cis}, \text{cis-1,3,5-triaminocyclohexane}$ ) it was shown how the Jahn–Teller radius may be extracted from the temperature factors of complexes with seemingly regular octahedra [22]. We illustrate the method by its application to the caesium manganese alum  $\text{Cs}[\text{Mn}(\text{OH}_2)_6](\text{SO}_4)_2 \cdot 6\text{H}_2\text{O}$ , which undergoes a cubic ( $Pa\bar{3}$ ) to orthorhombic ( $Pbca$ ) phase transition at temperatures below 156 K due to co-operative Jahn–Teller interactions [23]. In the high temperature phase the hexa-aqua ion lies on a site of  $S_6$  symmetry; all the Mn–O bond lengths are therefore equivalent by symmetry. Below the transition temperature the  $[\text{Mn}(\text{OH}_2)_6]^{3+}$  lies on a site of  $C_i$  symmetry and exhibits the quintessential Jahn–Teller tetragonal elongation; at 5 K the Mn–O bond lengths are 1.929(1), 1.924(1) and 2.129(2) Å. The Jahn–Teller radius,  $\rho_0$ , may be estimated from the deviation of the bond lengths from the mean value,  $(r - r_{\text{mean}})$ , using the formula,

$$\rho_0 = \left( \sum_{i=1}^6 (r_i - r_{\text{mean}})^2 \right)^{1/2}, \quad (22)$$

from which  $\rho_0 = 0.234(2)$  Å. Now consider the fractional co-ordinates and thermal parameters for the manganese and oxygen atoms obtained in the cubic phase at 170 K, tabulated in Table 3.

The Mn–O bond vector is closely aligned with the crystal  $X$  axis and the anisotropic thermal parameters  $B_{13}$  and  $B_{12}$  are close to zero. The mean-square amplitude of the oxygen atom along the Mn–O bond vector is then given directly by the parameter  $B_{11}$ , without the need for a co-ordinate transformation.

It follows that the mean-square displacement pertaining to the metal(III)-oxygen stretching motion is,

**Table 3** Fractional coordinates (X,Y,Z) and isotropic ( $B_{\text{iso}}$ ) and anisotropic ( $B_{11}$ ,  $B_{22}$ ,  $B_{33}$ ,  $B_{23}$ ,  $B_{13}$ ,  $B_{12}$ ) thermal parameters ( $\text{\AA}^2$ ) for the manganese and oxygen atoms constituting the Mn–O bond, obtained by single-crystal neutron diffraction for  $\text{Cs}[\text{Mn}(\text{OH}_2)_6](\text{SO}_4)_2 \cdot 6\text{H}_2\text{O}$  at 170 K ( $Pa\bar{3}$ ) [23]

	X	Y	Z	Biso	B11	B22	B33	B23	B13	B12
Mn	0	0	0	0.98(6)	–	–	–	–	–	–
O	0.16007(10)	–0.00228(13)	–0.00051(13)	–	1.62(5)	1.59(5)	2.58(6)	0.67(5)	0.02(5)	0.11(5)

$$\langle \Delta d^2 \rangle = \frac{B_{11}(O) - B_{iso}(\text{metal(III)})}{8\pi^2} \text{ \AA}^2, \quad (23)$$

where the quantity  $\langle \Delta d^2 \rangle$  is composed of contributions from all the metal-oxygen stretching vibrations. For isostructural alums formed with Ti(III), Ga(III) and V(III),  $\langle \Delta d^2 \rangle \approx 0$  [23], whereas for  $\text{Cs}[\text{Mn}(\text{OH}_2)_6](\text{SO}_4)_2 \cdot 6\text{H}_2\text{O}$  at 170K,  $\langle \Delta d^2 \rangle = 0.0081(10) \text{ \AA}^2$ . A rough estimate of  $\rho_0$  can be obtained by setting  $\langle \Delta d^2 \rangle$  to the quantity  $(r_i - r_{av})^2$  in (22), in which case  $\rho_0 \sim 0.22 \text{ \AA}$ , in good agreement with the value estimated from the 5 K structural data.

The  $\Delta d$  values can be calculated explicitly using the vibronic wavefunctions given in (18) that result from the numerical diagonalisation and the analytic equations of the one dimensional vibrational wavefunctions [19]. It is best to consider plots of the square of the vibronic wavefunctions as one otherwise encounters difficulties with the sign change associated with the geometric (or Berry's) phase [24]. Such a plot is given in Fig. 8, as a function of the  $Q_\theta$ ,  $Q_\epsilon$  coordinates (upper) and the bond length displacements (lower). The latter are calculated from the expressions given in (20) appropriate for an  $\text{ML}_6$  complex. For both first order only and for first and second order coupling, the mean geometry is the high symmetry or undistorted octahedral configuration. For first-order coupling ( $A_2 = 0$ ), the probability function on the top left of Fig. 8 has a cylindrical symmetry corresponding to the localisation about the bottom of the lower Jahn–Teller surface. The probability function in terms of the  $\Delta d(\text{M-L})$  shows equal positive and negative displacements. If one were able to determine the higher moments for the thermal parameters of such a system one would find, for all six ligands, a symmetrical dumb-bell shape.

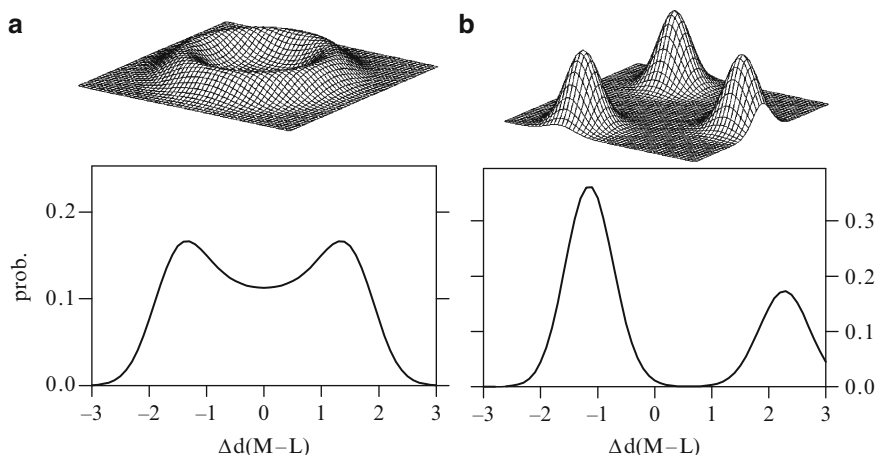


**Fig. 8** Probability functions for lowest vibronic level of an  $\text{E} \otimes \text{e}$  system. (a)  $A_1/\hbar\omega = 3.0$ ,  $A_2/\hbar\omega = 0$ ; (b)  $A_1/\hbar\omega = 3.0$ ,  $A_2/\hbar\omega = 0.125$ . The  $\Delta d(\text{M-L})$  functions are identical for all ligands

For the case of a warped Jahn–Teller surface the probability functions, as shown in Fig. 8b, are localised at the positions of the Jahn–Teller minima and now the  $\Delta d(\text{M-L})$  values show a 2/3 and 1/3 probabilities at displacements of  $-1/3x$  and  $+2/3x$  respectively. This structure reflects the underlying tetragonal elongation at the minima of the potential surface. Again, for these dynamic Jahn–Teller effects all six ligands would show the same probability distribution centred at equal bond lengths, but now with asymmetric dumb-bell shaped thermal ellipsoids.

As discussed in Sect. 3.3 below, if the structure of the above types of systems were determined by XAFS spectroscopy, then one would observe the “instantaneous” molecular structure rather than the time-, space-averaged bond lengths given by crystallography.

## 2.2 Magnetic Data

The magnetic moment per ion is defined as,

$$M_{ion} = \frac{\sum_n \left( -\frac{dE_n}{dB} \right) \exp(-E_n / kT)}{\sum_n \exp(-E_n / kT)}. \quad (24)$$

The derivative is found most elegantly by application of the Hellman–Feynman theorem,

$$\frac{dE_n}{dB} = \langle \Psi_n | \frac{d\hat{H}}{dB} | \Psi_n \rangle = \sum_i \sum_{i'} \sum_{j+k=0}^{n_v} a_{ijk}^* a_{i'jk} \langle \psi_i | \frac{d\hat{H}}{dB} | \psi_{i'} \rangle. \quad (25)$$

This method allows the magnetic moment at a given field to be calculated exactly from one numerical diagonalisation of the vibronic Hamiltonian [25].

## 2.3 Spectroscopic Data

When the timescale of the experiment is fast compared to the internal dynamics of the molecule, spectroscopic transitions may be calculated by assuming that during the electronic transition the nuclei remain fixed at their positions in the initial state, in accordance with the Frank–Condon principle.

The intensity of a transition between states  $\Psi$  and  $\Psi'$  of energy  $E_i$  and  $E_f$ , is calculated according to:

$$I \propto \exp\left(\frac{-E_i}{kT}\right) \langle \Psi | \hat{O} | \Psi' \rangle \langle \Psi' | \hat{O} | \Psi \rangle \delta(E_f - E_i). \quad (26)$$



where  $\hat{O}$  is the transition moment operator. From (18) we obtain:

$$\langle \Psi | \hat{O} | \Psi' \rangle = \sum_i \sum_{i'} \sum_{j+k=0}^{n_v} \sum_{j'+k'=0}^{n'_v} a_{ijk}^* a'_{i'j'k'} \langle \psi_i | \hat{O} | \psi_{i'} \rangle \delta_{jj'} \delta_{kk'}. \quad (27)$$

The electronic absorption, emission and Raman spectra presented in this chapter were all computed from this expression.

When the timescale of the experiment is slow compared to the internal dynamics of the molecule, the spectrum should be calculated as the thermal average over all populated levels [6, 11].

### 3 Examples of the Manifestation of the Jahn–Teller Effect

#### 3.1 The $E \otimes e$ Vibronic Energy Levels

##### 3.1.1 Electronic Raman Spectrum of Copper(II) Doped CaO

Experimental investigations into the vibronic structure of copper(II) doped CaO (CaO : Cu<sup>2+</sup>) and MgO (MgO : Cu<sup>2+</sup>), constitute some of the most rigorous and instructive studies of Jahn–Teller active systems [26]. Foremost among these is the Raman study on CaO : Cu<sup>2+</sup> by Guha and Chase [27]. The spectrum, shown in Fig. 9 below, displays a plethora of bands in the  $\sim 3\text{--}250\text{ cm}^{-1}$  region that were assigned by the authors to transitions within hindered rotational levels, characteristic of the  $E \otimes e$  vibronic problem, depicted in Fig. 10.

The experimental spectrum is characteristic of the  $\{A_1, A_2\}$  first excited states ( $j = 3/2$ ) being  $\sim 10\text{ cm}^{-1}$  wavenumbers above the  $E$  ( $j = 1/2$ ) ground state, split to appear at  $\sim 4$  and  $26\text{ cm}^{-1}$  by a small warping term.

The zeroth-order electronic Raman cross section,  $I$ , for a transition from state  $i$  to state  $f$ , is calculated according to [28],

$$I \propto E_s^4 \exp\left(\frac{-E_i}{kT}\right) \langle \Psi | \hat{\alpha}_{\Gamma\gamma} | \Psi' \rangle \langle \Psi' | \hat{\alpha}_{\Gamma\gamma} | \Psi \rangle \delta(E_f - E_i - E_0 + E_s), \quad (28)$$

where  $E_0$  and  $E_s$  are the energies of the incident and scattered radiation,  $E_i$ ,  $E_f$  the energies of the states  $\Psi$  and  $\Psi'$ , and  $\hat{\alpha}_{\Gamma\gamma}$  is the component of the Raman polarisability tensor, transforming as the  $\gamma$ th component of the  $\Gamma$ th irreducible representation of the  $O_h$  point group.

Guha and Chase reported that an electronic Raman spectrum could be observed only in experiments that select a component of the polarisability tensor transforming as  $E_\theta$  or  $E_\varepsilon$ . The electronic matrix elements in these polarisation geometries are,

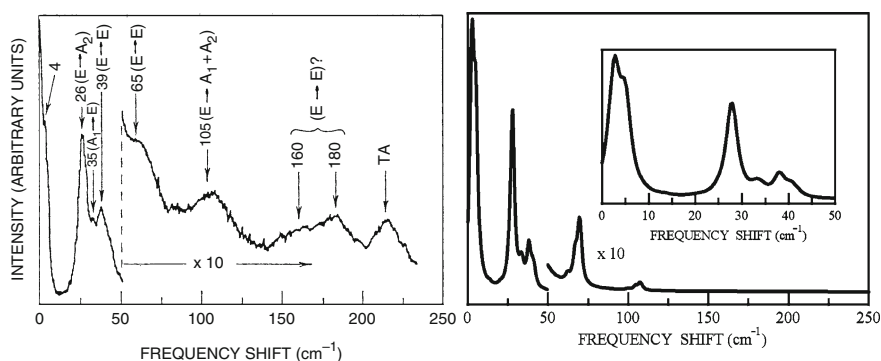


**Fig. 9** Experimental and theoretical electronic Raman spectra of  $\text{CaO} : \text{Cu}^{2+}$ . The experimental spectrum, (a), is reproduced from the work by S. Guha and L.L. Chase [27] and was collected at  $\sim 4.2$  K in a polarisation geometry which facilitates the observation of transitions of  $E_g$  symmetry only. The theoretical spectrum was calculated using (28) employing the following parameters:  $\hbar\omega = 216 \text{ cm}^{-1}$ ,  $A_1 = -1,030 \text{ cm}^{-1}$ ,  $A_2 = -1.0 \text{ cm}^{-1}$ ,  $e_\theta = 3 \text{ cm}^{-1}$ ,  $e_\varepsilon = 3 \text{ cm}^{-1}$ ,  $n_v = 30$ ,  $T = 7$  K

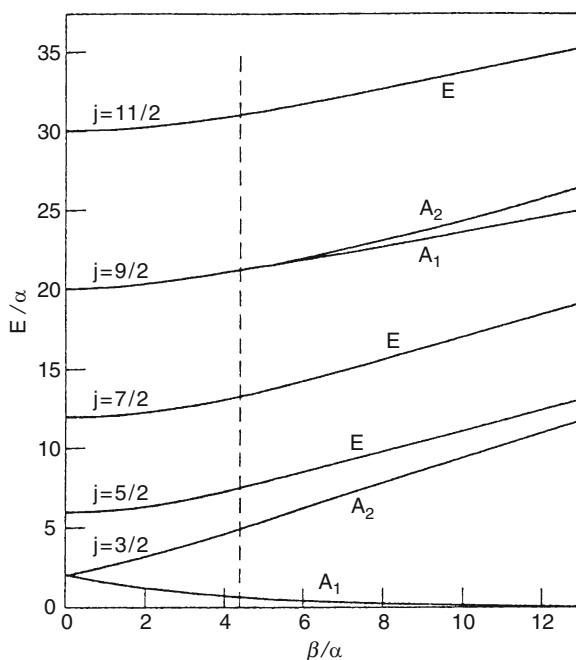


**Fig. 10** Eigenvalues of the hindered-rotational levels of the  $E \otimes e$  vibronic problem, reproduced from the work of Guha and Chase [27]. The parameters  $\alpha$  and  $\beta$  relate to the linear and quadratic coupling respectively, as defined by O'Brien [29]. The broken line corresponds to the value of  $\beta/\alpha$ , which best fits the  $\text{CaO} : \text{Cu}^{2+}$  data

$$\begin{aligned}
\langle \Psi | \hat{\alpha}_{E_\theta} | \Psi' \rangle &\propto \langle U_\theta \rangle = \sum_{j+k=0}^{n_v} \sum_{j'+k'=0}^{n'_v} \left( -a_{\theta jk}^* a'_{\theta j'k'} + a_{\varepsilon jk}^* a'_{\varepsilon j'k'} \right) \delta_{jj'} \delta_{kk'} \\
\langle \Psi | \hat{\alpha}_{E_\varepsilon} | \Psi' \rangle &\propto \langle U_\varepsilon \rangle = \sum_{j+k=0}^{n_v} \sum_{j'+k'=0}^{n'_v} \left( a_{\theta jk}^* a'_{\varepsilon j'k'} + a_{\varepsilon jk}^* a'_{\theta j'k'} \right) \delta_{jj'} \delta_{kk'}.
\end{aligned} \tag{29}$$

The calculated electronic Raman transitions were folded with a Lorentzian bandwidth, with constant width across the whole spectrum.

With  $\hbar\omega = 216 \text{ cm}^{-1}$ , as deduced by O'Brien from the broad band Raman spectrum [30], good agreement with experiment can be obtained with  $A_1 = -1,030 \text{ cm}^{-1}$ ,  $A_2 = -1.0 \text{ cm}^{-1}$ . The best reproduction of the energies and intensities was found with a small directional strain corresponding to  $\delta = 4.25 \text{ cm}^{-1}$ ,  $\phi_\delta = 45^\circ$ , which could arise from different thermal expansion coefficients of the crystal and the glue used to affix the crystal to the goniometer head. Agreement was further improved [28] by performing the calculation at 7 K, rather than at the reported temperature of 4.2 K. The data may also be reproduced with alternative choices for the effective phonon frequency, as the energy spacing is an approximate function of  $\hbar\omega^3/A_1^2$ .

### 3.1.2 The EPR Spectrum of Copper(II) Doped MgO

The EPR spectra of Cu(II) doped MgO single crystals have recently been re-examined in detail within the framework of a dynamic Jahn–Teller effect [31]. The experimental 1.8 K X-band spectra is shown in Fig. 11a as a function of the magnetic field direction for a rotation from  $H||\langle 001 \rangle$  to  $H||\langle 110 \rangle$ . This spectrum has a number of unusual and intriguing features.

- The spectrum has strain broadening reminiscent of a powder spectrum, The low (high) field resonances having positive (negative) distortions of the derivative lineshape.
- The two sets of four hyperfine lines have a complicated pattern of avoid crossings at the  $H||\langle 111 \rangle$  direction.
- There is clearly more than the expected 4 hyperfine lines in the high field set at  $\theta \sim 10\text{--}30^\circ$  from  $\langle 001 \rangle$ .

The spectrum can be modelled as shown in Fig. 11b, in terms of a cubic spin Hamiltonian operating within the set of four Kramers doublets corresponding to the four lowest vibronic energy levels of a  $E \otimes e$  Jahn–Teller problem. This “four state” model must also include vibronic (Ham) reduction factors (see Sect. 3.2.1 following) and a random distribution of the crystal strain. It has found to be important to treat the Zeeman, hyperfine, tunnelling and strain terms without recourse to perturbation theory as these terms are of a similar magnitude. However, most spectral features could be reproduced with a spin Hamiltonian for an isolated  $^2E_g(\Gamma_8)$  ground state, of the form given by (36) in Sect. 3.2 below. The relevant operators transforming as the  $A_1$ ,  $E_\theta$  and  $E_\varepsilon$  irreducible representations used to fit the spectrum are given in Table 4.

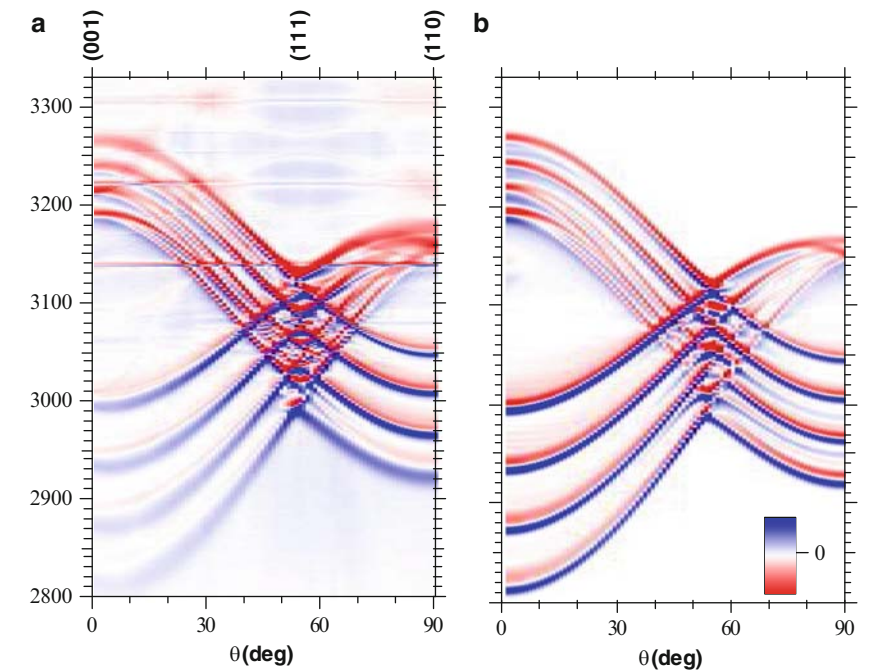


**Fig. 11** Image plot of the experimental (a) and calculated (b) X-band EPR spectrum at 1.8 K as a function of the magnetic field direction rotated from the (001) by  $\theta$  to the (110) direction

**Table 4** The spin Hamiltonian terms for Cu(II)/MgO

	Electronic Zeeman	Hyperfine	Strain	Nuclear quadrupole
$G_{A1}$	$g_1 \mu_B H.S$	$A_{h1} I.S$	—	—
$G_\theta$	$\frac{1}{2} g_2 \mu_B (3H_z S_z - H.S)$	$\frac{1}{2} A_{h2} (3I_z S_z - I.S)$	$\delta_s \cos \phi_s$	$\frac{1}{2} P_2 (3I_z I_z - I.I)$
$G_\epsilon$	$\frac{1}{2} \sqrt{3} g_2 \mu_B (H_x S_x - H_y S_y)$	$\frac{1}{2} \sqrt{3} A_{h2} (I_x S_x - I_y S_y)$	$\delta_s \sin \phi_s$	$\frac{1}{2} \sqrt{3} P_2 (I_x I_x - I_y I_y)$

As discussed by Ham [32], for each interaction two parameters are required, the isotropic terms  $g_1$ ,  $A_{h1}$  and a “cubic anisotropy”  $g_2$ ,  $A_{h2}$ . The angular dependent spectrum in Fig. 11 disappears above the relatively low temperatures of 6 K, being replaced by an isotropic spectrum characterised by the  $g_1$ ,  $A_{h1}$  values alone which are the same as the low temperature  $g_1$ ,  $A_{h1}$  values. The parameters used to reproduce the spectra in Fig. 11 are given in Table 5 together with those found for Cu(II)/CaO.

While the main features of the Cu(II)/MgO spectrum can be reproduced using an isolated  ${}^2E_g$  state, details such as the relative strain broadening between the hyperfine lines, requires the inclusion of the excited vibronic singlets. For Cu(II)/MgO it is found that the first excited singlet is of  $A_2$  symmetry, indicating that the  $\text{CuO}_6$  centre has the expected  $E \otimes e$  Jahn–Teller potential energy surface with three equivalent minima at tetragonally elongated octahedral geometries. Surprisingly, the opposite occurs for Cu(II)/CaO, and this appears to be a rare example of the three equivalent

**Table 5** Values of the spin Hamiltonian parameters for Cu(II)/MgO [31] and Ca(II)/CaO [33]

host	T/K	Strain	$\Delta/\text{cm}^{-1}$	$g_1$	$qg_2$	$A_{h1}$ ( $\times 10^{-4} \text{ cm}^{-1}$ )	$qA_{h2}$ ( $\times 10^{-4} \text{ cm}^{-1}$ )	$qP_2$ ( $\times 10^{-4} \text{ cm}^{-1}$ )
MgO	6.0	–	–	2.193	–	$\pm 18.5$	–	–
	1.8	$\bar{\delta} = 0$	$\Delta_2 = 4$	2.190	0.110	$-19.0$	$-42.0$	$+5.5$
		$\delta_\Delta = 2 \text{ cm}^{-1}$	$\Delta_1 = 150$					
CaO	77	–	–	2.2205	–	$\pm 21.8$	–	–
	1.8	$\bar{\delta}/\Delta_1 = 0.67$	$\Delta_1 = 3$	2.2211	0.122	$\pm 31.2$	$\pm 24.2$	–

minima at a compressed octahedral geometry. The energy of the  $A_1$  and  $A_2$  vibronic states above the ground  $E$  vibronic state are given by  $\Delta_1$  and  $\Delta_2$  respectively in Table 5.

The small random crystal strains can be quantified and this is also given in Table 5. It was found that the strain can be described by a Gaussian distribution characterised by a mean value,  $\bar{\delta}$ , of zero and a half width of  $\delta_\Delta = 2 \text{ cm}^{-1}$ . The analysis also differed from that of previous workers in both the hyperfine values and the requirement of a nuclear quadrupole term. The transitions within the lowest excited singlet could also be observed directly [31]. It can be concluded that the Cu(II)/MgO system can be described as an almost pure dynamic Jahn–Teller case.

### 3.1.3 The $S_1 \leftarrow S_0$ Resonant Two-Photon Ionisation Spectrum of Supersonically Cooled Triptycene

The molecule triptycene provides an example where the vibronic transitions to and from a Jahn–Teller active  $E$  state can be reproduced quantitatively using the techniques described in Sect. 2.3 [34]. Figure 12 shows the experimental spectrum measured via two-colour resonant two photon ionisation (2C-R2PI). The high resolution is due to triptycene being cooled by the super-sonic expansion of an Argon carrier gas. A tuneable dye-laser is scanned across the absorption spectrum, when the molecules absorbs this first photon a second laser ( $\bar{\nu} < 35,000 \text{ cm}^{-1}$ ) ionises the molecule which is then detected by a mass spectrometer. No ion signal is detected with either laser (colour) used alone. The rejection of  $^{13}\text{C}$  isomers further narrows the spectral bands, the remaining  $1\text{--}1.4 \text{ cm}^{-1}$  vibronic line-width is due to the blue shaded rotational envelope. In what follows we will simply call the 2C-R2PI spectrum in Fig. 12 the absorption spectrum.

Figure 13 shows the dispersed fluorescence spectra for laser excitation directly into the different vibronic lines labelled **a–h** in Fig. 12. Under the experimental conditions there is no relaxation from these excited vibronic levels within the 20 ns fluorescence lifetime. Figure 12 thus contains the  $A \rightarrow E$  transitions from the lowest vibrational level of the ground electronic state, and Fig. 13 contains the  $A \leftarrow E$  transitions for a number of initial vibronic  $E$  levels to the numerous vibrational levels of the ground electronic state.

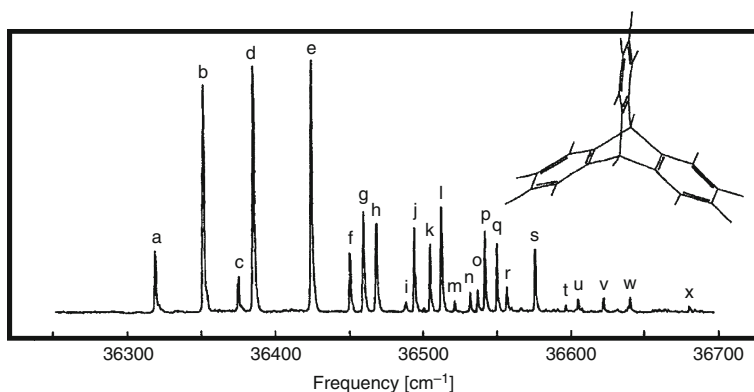


Fig. 12 The 2C-R2PI “absorption” spectrum of triptycene

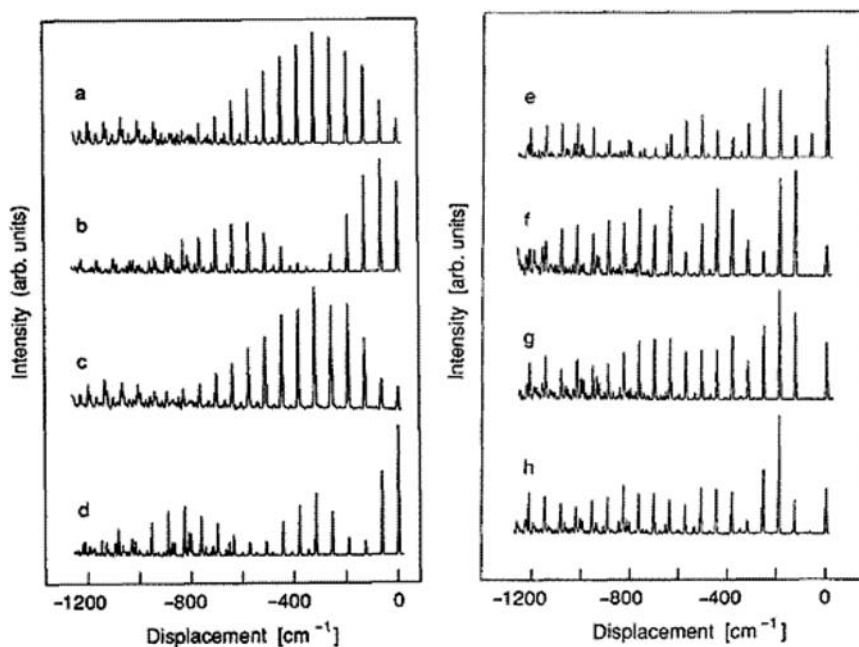


Fig. 13 The unrelaxed fluorescence from the vibronic levels labelled a–h in Fig. 12

A cursory examination of these spectra immediately reveals:

- (a) There is no mirror image symmetry of the absorption/emission spectra. The  $A \rightarrow E$  spectra (Fig. 12) are distributed over  $\sim 350 \text{ cm}^{-1}$ , while the  $A \leftarrow E$  fluorescence from the electronic origin (Fig. 13a) is distributed over  $\sim 800 \text{ cm}^{-1}$ .

- (b) The ground state is very harmonic showing progressions with an energy separation of  $64.2\text{ cm}^{-1}$  extending out to  $n > 30$  for the fluorescence from the highly excited  $E$  levels. The energy separation of the last pair is  $<0.5\text{ cm}^{-1}$  different from the separation of the first pair.
- (c) The excited state is extremely “anharmonic”, no single line of the spectrum can be interpreted as a combination of any two other lines. The energy separation of the four most intense lines **a**, **b**, **d**, **e** are irregularly spaced (32.8, 33.5, 39.0) with an average separation of  $\sim 35\text{ cm}^{-1}$ .

The fact that a progression in the same  $64\text{ cm}^{-1}$  vibrational mode is seen in the fluorescence from all levels shows that the irregularly spaced vibronic lines in the absorption spectrum must belong to the same  $64\text{ cm}^{-1}$  vibrational mode that is harmonic in the ground state. This mode can be described as a wagging of rigid benzene rings [35]. These observations are typical of an  $A \rightarrow E$  transition where the irregularly spaced levels corresponds to the transitions to the coupled  $E \otimes e$  vibronic levels. The parameters required to simulate the spectra are the first and second order coupling constants ( $A_1$ ,  $A_2$ ) and the harmonic vibrational energy ( $\hbar\omega$ ) that would occur in the absence of the Jahn–Teller effect. The particular values that reproduce experiment are given in Table 6 and a comparison between experimental and calculated spectra shown in Fig. 14.

Remarkably, most of the complex structure observed experimentally is given by the simple Jahn–Teller model. At first it may seem an easy matter to arrive at these values but in practice it is very difficult unless one is quite close to the correct ones. Figure 6b shows the calculated  $E \otimes e$  energy levels as a function of the second-order coupling constant  $A_2$ . Since only the lowest vibrational level of the  $A$  ground electronic state is populated, only transitions to the vibronic levels of  $E$  symmetry have intensity. The experimental energies are marked with **a–i** in Fig. 6b. It can be seen that the energy levels vary in a complicated manner as a function of  $A_2$  with many avoid crossings. Even in this one dimensional slice with all other parameters fixed to they “best fit” values, it would be difficult to match the calculated levels with experiment using a least square fitting procedure.

The key to arriving at the correct fit is to understand the intensity patterns in the fluorescence spectra. In Fig. 13 the fluorescence from level **a** has the usual Franck-Condon pattern with the intensity increasing with  $n$  to a maximum ( $n = 5$ ) and then decreasing. The fluorescence from level **b** goes through a maximum ( $n = 1$ )

**Table 6** Potential Parameters and Derived Properties of the  $E \otimes e$  surface of triptycene

Potential Parameters	Derived Properties	
$\hbar\omega_g = 64.2\text{ cm}^{-1}$	$E_{\text{JT}} = 113.4\text{ cm}^{-1}$	Jahn–Teller stabilisation energy
$\hbar\omega_e = 47.8\text{ cm}^{-1}$	$E_{\text{barr}} = 67.8\text{ cm}^{-1}$	Barrier height
$A_1 = 78.9\text{ cm}^{-1}$	$\rho_0 = 2.87$	Radial position of the minima
$A_2 = 20.4\text{ cm}^{-1}$	$\rho_s = 1.16$	Radial position of the saddle points
	$3\Gamma = 0.93\text{ cm}^{-1}$	tunnelling splitting

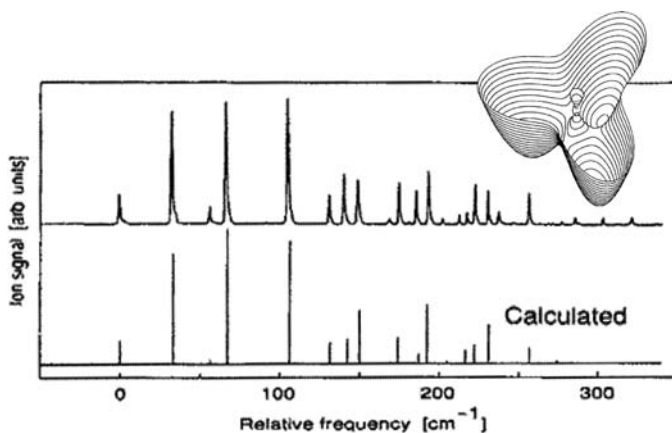


**Fig. 14** The comparison of experimental with the  $A \rightarrow E$  spectrum calculated with the parameters in Table 6. A plot of the  $E \otimes e$  potential energy surface is shown

and minimum ( $n = 5$ ) and a second maximum ( $n = 9$ ) before decreasing for higher  $n$ . The fluorescence from level **d** oscillates further, having 2 minima while the fluorescence from level **e** has 3 minima.

The 0, 1, 2, 3 minima in the fluorescence intensities from levels **a**, **c**, **d**, **e** respectively reflects the nodal structure of the initial state vibronic wavefunctions in the radial direction. The paraboloid of the ground state potential energy surface does not vary in the angular direction which results in it not being possible to observe the angular nodal structure of the vibronic wavefunctions. As the Jahn–Teller minima of the excited state are displaced with respect to the ground state in the radial direction, the radial distribution of the vibronic wavefunctions is reflected in the fluorescence intensity patterns. Thus the fluorescence intensity patterns in Fig. 13 are the projection of the excited state vibronic probability functions onto the ground state surface. This is analogous to the semi-classical description of the Franck–Condon intensity patterns observed in vibronically resolved electronic spectra between non-degenerate states. The semi-classical the Franck–Condon envelope is a projection of the initial state probability function projected onto the final state potential surface, which will be close to linear at large displacements, resulting in a Gaussian like intensity distribution.

We can associate the lowest levels with the approximate quantisation in radial and angular directions, characterised by the local mode quantum numbers  $n_\rho$  and  $n_\phi$ . The levels **a**, **b**, **d**, **e** then correspond to approximate radial excitations  $n_\rho = 0, 1, 2, 3$  with the approximate energy separation of  $\sim 35 \text{ cm}^{-1}$ . The fluorescence from the vibronic level **c** has a similar zero node pattern as that from level **a**, indicating that it too has a  $n_\rho = 0$ , but is the first excited angular state  $n_\phi = 1$ . The approximate energy of this angular mode is  $\sim 56 \text{ cm}^{-1}$ . This immediately indicates that the second-order coupling is relatively large. The  $E \otimes e$  surface



is warped to such an extent that, within the minima below the barriers, the curvature in the angular direction is larger than in the radial direction. This situation can be contrasted with the parameters typical for alkali trimers such as  $\text{Na}_3$  where the second-order coupling and thus barrier heights are small and the angular vibration is better described as a hindered internal rotation [36].

As the potential energy surfaces are known to high precision, one may turn to some of the more subtle details of the spectroscopy of this system. This includes the coupling to a vibration of  $a_2$  symmetry peak by momentum coupling [37] and the perturbation of the spectrum by complexation with noble gas atoms [38].

## 3.2 The Ham Effect

### 3.2.1 Theoretical Concept

In the mid- to late 1960s, Frank Ham produced two papers [10,39] and a review article [32] on the Jahn–Teller effect that have had a profound influence on the way in which experimentalists view the phenomena. Ham showed that the dynamical Jahn–Teller effect, whilst not giving rise to a static distortion, can give rise to a substantial “quenching” of the effect of certain orbital operators. “The Ham effect”, “Ham-quenching” and “Ham-factors” are now common parlance amongst spectroscopists, being used to describe the reduction of the orbital Zeeman effect and spin-orbit coupling beyond that expected from covalent bonding. We introduce the theoretical concept by first considering a simple, hypothetical example [40], before considering the application of the theory to the  $E \otimes e$  problem. Spectroscopic and magnetic data from salts containing the titanium(III) and vanadium(III) hexaaqua cations serve to demonstrate the experimental manifestation of the Ham-effect.

Our hypothetical molecule possesses  $D_{4h}$  symmetry and has a valence electron in the  $\{p_x, p_y\}$  set of orbitals. The ground term is therefore  ${}^2E_g$  and we assume that all other terms are too high in energy to mix with it significantly. The  $\{p_x, p_y\}$  orbitals may interact with the non-degenerate mode  $b_1$ , depicted below (Fig. 15).

The coupling of a doubly degenerate electronic state with a single non-degenerate vibrational mode is the simplest possible example of the Jahn–Teller effect, for which the  $E \otimes b_1$  Hamiltonian is,

$$\hat{H} = \frac{1}{2}\hbar\omega (P^2 + Q^2) U_\tau + A_1 \begin{bmatrix} -Q & 0 \\ 0 & Q \end{bmatrix}, \quad (30)$$

where the matrix operates within the  $\{p_x, p_y\}$  orbital state basis. This Hamiltonian can be rewritten as a pair of Hamiltonians:

$$\begin{aligned} \hat{H} &= \frac{1}{2}\hbar\omega (P^2 + Q^2) U_\tau \pm A_1 Q \\ &= \frac{1}{2}\hbar\omega \left( P^2 + \left( Q \pm \frac{A_1}{\hbar\omega} \right)^2 \right) U_\tau - \frac{A_1^2}{2\hbar\omega}. \end{aligned} \quad (31)$$

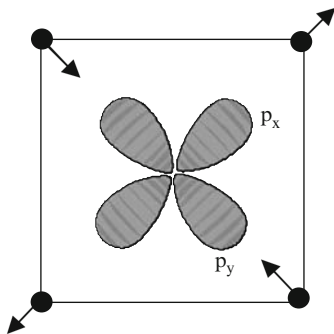


**Fig. 15** The p orbitals  $\{p_x, p_y\}$  in a square of neighbours interacting with a single asymmetric mode

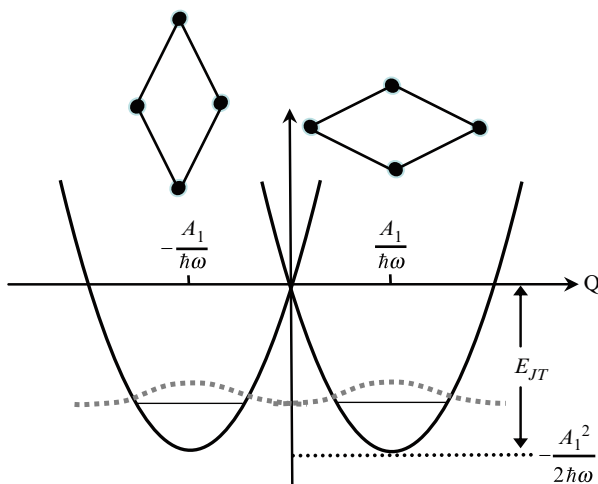


**Fig. 16** The potential  $\frac{1}{2}\hbar\omega Q^2 \pm A_1 Q$  of (31). Also shown is the form of the ground state vibrational wavefunctions localised in the potential energy minima

These represent a pair of harmonic oscillators with their minima displaced by  $\pm \frac{A_1}{\hbar\omega}$  and reduced in energy by  $E_{JT} = \frac{A_1^2}{2\hbar\omega}$ , as depicted in Fig. 16.

The point to emphasise concerning this example is the reduced overlap between the ground vibronic wavefunctions associated with the two electronic states, on account of the displacement of the potential energy minima. The expectation value of any electronic operator connecting the two orbital electronic states will be similarly affected. Consider the orbital Zeeman interaction about the  $z$  axis, given by

$$\hat{H} = B_z \beta k \hat{L}_z = B_z \beta k U_{A_2}, \quad (32)$$

where  $B_z$  is the magnetic field,  $\beta$  the Bohr magneton and  $k$  the orbital reduction factor. In the  $\{p_x, p_y\}$  orbital basis, the electronic operator  $U_{A_2}$  is off-diagonal and

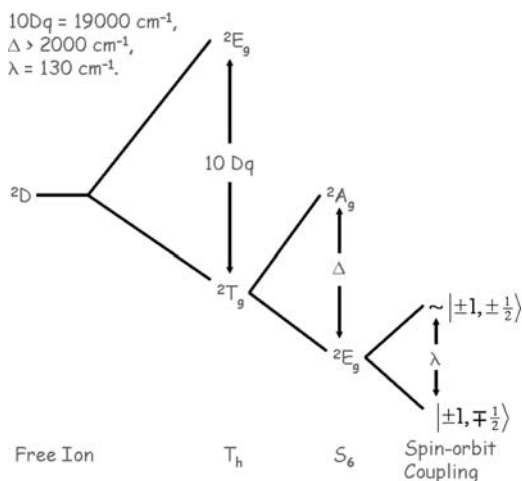


**Fig. 17** Energy Level diagram pertaining to the  $[\text{Ti}(\text{OH}_2)_6]^{3+}$  cation, following the one-electron orbital energy level scheme postulated by Best [47]. The wavefunctions of the  ${}^2E_g$  ground term are defined in terms of the quantum numbers  $|M_L, M_S\rangle$

imaginary,

$$U_{A_2} = \begin{pmatrix} 0 & -i \\ i & 0 \end{pmatrix}. \quad (33)$$

In the basis of the ground vibronic wavefunctions  $\psi_{i=x,y}\phi_0$ , localised at positions along  $Q$  of  $\pm \frac{A_1}{\hbar\omega}$  in Fig. 16, an additional reduction factor is required to account for the reduced overlap between the vibrational wavefunctions:

$$\hat{H} = B_z \beta k \, p_{E \otimes b_1} U_{A_2}, \quad (34)$$

where,

$$\begin{aligned} p_{E \otimes b_1} &= \frac{\langle \psi_y(Q = \frac{A_1}{\hbar\omega})\phi_0 | \hat{L}_z | \psi_x(Q = -\frac{A_1}{\hbar\omega})\phi_0 \rangle}{\langle \psi_y(Q=0)\phi_0 | \hat{L}_z | \psi_x(Q=0)\phi_0 \rangle} = \frac{\langle \psi_x(Q = -\frac{A_1}{\hbar\omega})\phi_0 | \hat{L}_z | \psi_y(Q = \frac{A_1}{\hbar\omega})\phi_0 \rangle}{\langle \psi_x(Q=0)\phi_0 | \hat{L}_z | \psi_y(Q=0)\phi_0 \rangle} \\ &= \exp\left(-\frac{E_{JT}}{\hbar\omega}\right) \end{aligned} \quad (35)$$

The reduction in the orbital Zeeman interaction approaches zero exponentially as  $E_{JT}$  increases and  $\hbar\omega$  decreases. Note that the quantity  $E_{JT}$  depends solely on the potential energy.

The beauty of Ham's theory is its simplicity. The Ham factors for any particular problem can be classified by symmetry. This means that any other operator which is a function of the  $U_{A_2}$  will be reduced by the same factor. Note that Ham's treatment implies that the linear coupling is large compared to the additional terms in the Hamiltonian that are subsequently evaluated as perturbations of the ground vibronic energy levels.

For the  $^{2S+1}E \otimes e$  problem, the Hamiltonian describing the perturbation of the isolated  $^{2S+1}E$  ground term has the form [10],

$$\hat{H} = G_{A_1} U_\tau + p G_{A_2} U_{A_2} + q (G_\theta U_\theta + G_\varepsilon U_\varepsilon), \quad (36)$$

where  $G_{A_1}$ ,  $G_{A_2}$ ,  $G_\theta$  and  $G_\varepsilon$  are functions of the spin operators transforming as the  $A_1$ ,  $A_2$ ,  $E_\theta$  and  $E_\varepsilon$  irreducible representations respectively of the octahedral point group and  $p$  and  $q$  are the Ham factors for the  $E \otimes e$  problem.

The Hamiltonian in (36) operates on the ground state vibronic wavefunctions  $\Psi_\theta$  and  $\Psi_\varepsilon$  which can be expressed as products of electronic functions and an expansion of the two dimensional vibrational states  $\varphi_i$  of appropriate symmetry [41]. The linear combinations are found using the  $E \otimes e$  and  $A_2 \otimes e$  vector coupling coefficients (the  $A_1 \otimes e$  coefficients are of course trivial) following the same procedure as used to construct the vibronic Hamiltonian in (15). It may then be readily shown that for strong linear coupling,  $p \rightarrow 0$  and  $q \rightarrow 1/2$  [10, 41]. Note however, for second order coupling  $q$  can take values less than  $1/2$  [42].

### 3.2.2 Paramagnetism of Caesium Titanium Alum

The way in which to calculate the paramagnetic susceptibility was first set out by Van Vleck in 1932 [43], who then set about applying the theory to explain the magnetic data from a number of inorganic salts [44]. Among these was the alum  $\text{Cs}[\text{Ti}(\text{OH}_2)_6](\text{SO}_4)_2 \cdot 6\text{H}_2\text{O}$ , in which the titanium(III) cations are on sites of trigonal symmetry and are well-separated by two water molecules and a sulphate anion [45]. With but one unpaired electron, the  $[\text{Ti}(\text{OH}_2)_6]^{3+}$  complex was thought to be ideally suited for the application of the crystal field theory that had recently been developed. A satisfactory description of this ostensibly simple system proved elusive however. The breakthrough came over half a century later from the insight of the inorganic chemist Stephen Best. From arguments based upon AOM calculations of Daul and Goursot [46], complemented by structural and spectroscopic studies of a host of isostructural  $\beta$ -alums, the trigonal field was shown to be large with the  $e_g$  component lower lying [47]. On this basis, the following energy level diagram shown in Fig. 17 for the  $[\text{Ti}(\text{OH}_2)_6]^{3+}$  cation follows from elementary ligand field theory.

The key point of this energy-level diagram is that the trigonal field is large with the orbital doublet term lower lying. The wavefunctions of the lower lying Kramers doublet are then of the form  $|M_L, M_S\rangle = |\pm 1, \mp \frac{1}{2}\rangle$ , with corresponding  $g$  values:

$$\begin{aligned} g_{||} &= 2(1 - kp_\lambda), \\ g_{\perp} &= 0, \end{aligned} \quad (37)$$

where  $k$  is the orbital reduction factor and  $p_\lambda$  is the Ham reduction factor. The theoretical  $g$  values are seemingly in contradiction with the experimental ground state  $g$  values of  $g_{||} = 1.25$ ,  $g_{\perp} = 1.14$ , determined below 4.2 K [48]. However, the

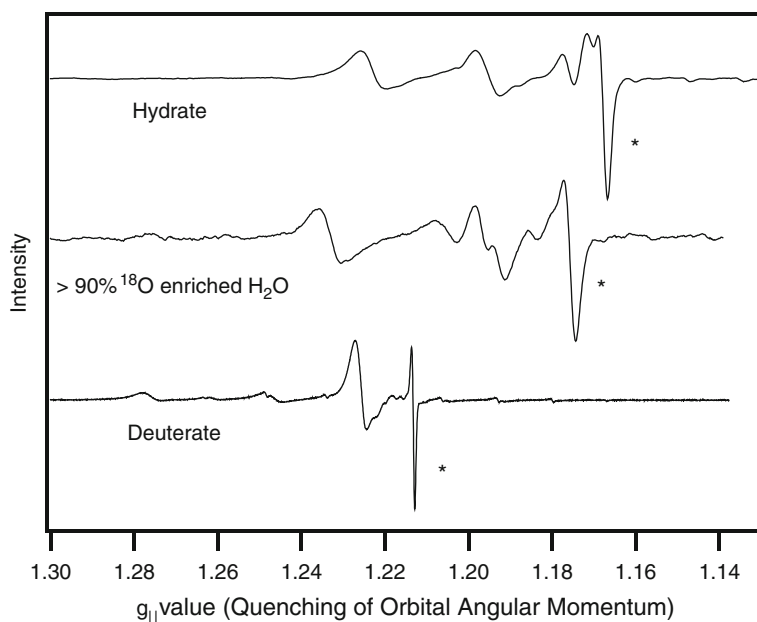


**Fig. 18** EPR spectra of  $< 1\%[Ti(OH_2)_6]^{3+}$  cation doped into  $Cs[Al(OH_2)_6](SO_4)_2 \cdot 6H_2O$  with the trigonal axis aligned parallel to the external magnetic field after [50]

$g$  values in (37) are valid only for strict axial symmetry. The subsequent discovery of the 13 K phase transition [49] has led to a satisfactory explanation of all the experimental data within the framework of the energy level diagram given above. Experiments on the  $[Ti(OH_2)_6]^{3+}$  cation doped into diamagnetic alums isostructural to  $Cs[Ti(OH_2)_6](SO_4)_2 \cdot 6H_2O$  aptly demonstrate the manifestation of the Ham effect and are the focus of this discussion. Let us first consider single crystal EPR spectra of the  $[Ti(OH_2)_6]^{3+}$  cation doped into  $Cs[Al(OH_2)_6](SO_4)_2 \cdot 6H_2O$  [50] (Fig. 18).

The spectra shown above were recorded with the crystal oriented such as to yield  $g_{||}$ . The spectra are complicated, consisting of many EPR lines that can be attributed to chemically distinct  $[Ti(OH_2)_6]^{3+}$  cations subject to different degrees of low-symmetry strain [51, 52]. The transition in the spectrum of the hydrate marked with an asterisk corresponds to  $[Ti(OH_2)_6]^{3+}$  cations in a near trigonal environment with  $g_{\perp} \sim 0$ . The important point to note is the dependence of the spectrum upon isotopic substitution. As the reduced mass of the ligand increases,  $g_{||}$  increases, corresponding to a greater quenching of orbital angular momentum. This is a direct result of the factor  $p_{\lambda}$  decreasing with values of decreasing  $\hbar\omega$ , in this parameter range. Note that the change in the ground state  $g$  value is far more pronounced for deuteration than for substitution of  $^{16}O$  by  $^{18}O$ . To understand this result let us consider  $e_g$  asymmetric distortions of the  $[Ti(OH_2)_6]^{3+}$  cation, components for which are shown below.

Modes (a) and (b) involve the rigid motion of the water molecules; the increase in the reduced mass of the vibrations upon deuteration and  $^{18}O$  for  $^{16}O$  substitution

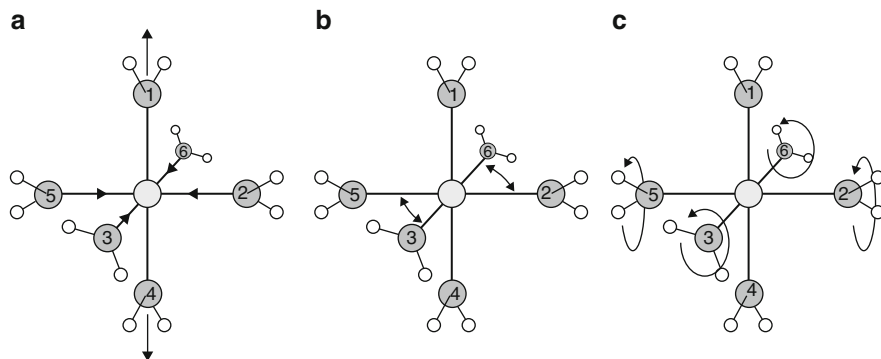


**Fig. 19** Examples of symmetrised distortions of a hexa-aqua complex: **(a)** the  $Q_\theta$  component of the  $\nu_2(\text{MO}_6)$ ,  $e_g(\text{T}_h)$  stretching vibration; **(b)** The  $Q_\zeta$  component of the  $\nu_5(\text{MO}_6)$ ,  $t_g(\text{T}_h)$  bending vibration; **(c)** the  $Q_\zeta$  component of the  $\tau[\text{M}(\text{OH}_2)_6]$ ,  $t_g(\text{T}_h)$  twisting libration

is the same. This means that if the Jahn–Teller coupling was dominated by coupling to these modes, the change in the value of  $g_{||}$  would also be expected to be the same, which is clearly not the case. The librational mode of water depicted in Fig. 19c corresponds to a rotation of the hydrogen atoms about the metal–oxygen bond vector. The reduced mass of the twisting libration is more or less independent of the mass of the oxygen atom but doubles upon deuteration. If the coupling was dominated by this mode,  $g_{||}$  would be independent of the oxygen isotope but would increase significantly upon deuteration. This scenario is more or less reflected in the experimental data, though we have simplified the argument for the purpose of this discussion. The energies of the  $t_{2g}$  orbitals are indeed very sensitive to a displacement along the twisting libration of water, a result predicted by AOM calculations [15, 53] and borne out by the structural characterisation of the 13 K phase transition [23].

Now let us consider the next highest state. According to the ligand field scheme in Fig. 17, the spin-orbit splitting of the  $^2E_g$  ground term should be of the order  $\sim 130 \text{ cm}^{-1}$ . However, Raman data of 1% titanium(III) doped  $\text{Cs}[\text{Ga}(\text{OH}_2)_6](\text{SO}_4)_2 \cdot 6\text{H}_2\text{O}$  clearly identify an electronic transition at  $\sim 18 \text{ cm}^{-1}$ , attributable to the  $[\text{Ti}(\text{OH}_2)_6]^{3+}$  impurity [54]. The origin of the  $18 \text{ cm}^{-1}$  peak can be understood with reference to the energy-level scheme shown in Fig. 20 below, which begins where the scheme in Fig. 17 ends. As a result of the Jahn–Teller interaction, some of the electronic properties of the upper Kramers doublet are transferred to the first vibrational excitation, and the energy gap relative to the ground state is diminished. This is the basis for the effective quenching of the spin-orbit coupling interaction.

Since the ground state second order Zeeman coefficient is proportional to  $-1/\lambda$ , this vibronic interaction has a profound influence on the magnetic properties of the  $[\text{Ti}(\text{OH}_2)_6]^{3+}$  cation [50, 54, 55]. With just the ground state populated, the susceptibility and effective magnetic moment have the form:

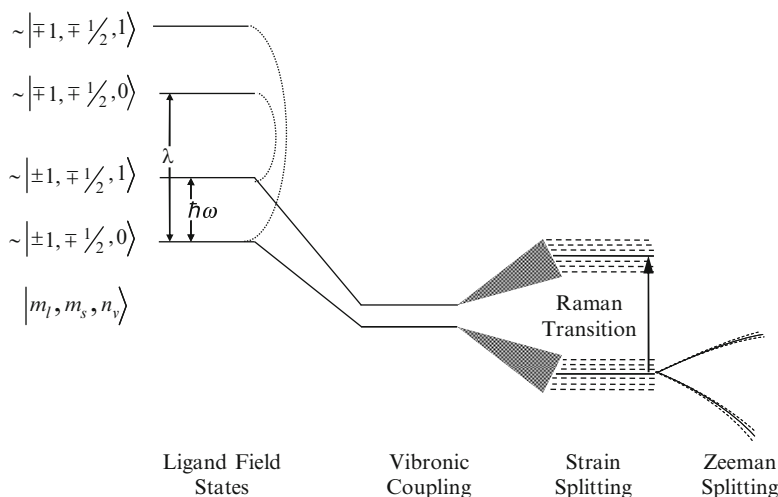


**Fig. 20** Schematic diagram showing the effects of the Jahn–Teller, strain, and Zeeman interactions on the states of the  ${}^2E_g$  ground term. The diagram starts where Fig. 17 finishes. The states are specified as  $|M_l, M_s, n_v\rangle$  and the figure depicts the Jahn–Teller matrix elements between the ground and first vibrational excitations by means of curved broken lines

$$\chi = \frac{(W_0^{(1)})^2}{T} - 2 \sum_{i \neq 0} W_i^{(2)}, \quad (38)$$

$$\mu_{eff} \propto \left( (W_0^{(1)})^2 - 2T \sum_{i \neq 0} W_i^{(2)} \right)^{1/2}.$$

Quenching of the orbital Zeeman effect and spin-orbit coupling results in an enhancement of both  $W_0^{(1)}$  and  $\sum_{i \neq 0} W_i^{(2)}$ . This in turn yields a larger ground-state effective magnetic moment and a steeper increase in its value with increasing temperature, than would otherwise be expected from a ligand field model. The experimental  $\mu_{eff}$  data are shown in Fig. 21 as function of temperature, along with theoretical curves calculated with and without the dynamical Jahn–Teller interaction [50]. There are two important points to note. The first is that it is essential to include the dynamical Jahn–Teller effect to obtain a satisfactory reproduction of the experimental data. The second point to emphasise is that the two theoretical curves converge to the same asymptotic value at high temperatures. This is because the effect of the orbital operators that we have discussed, are not lost but are redistributed to other states and are recovered when these states become thermally populated.

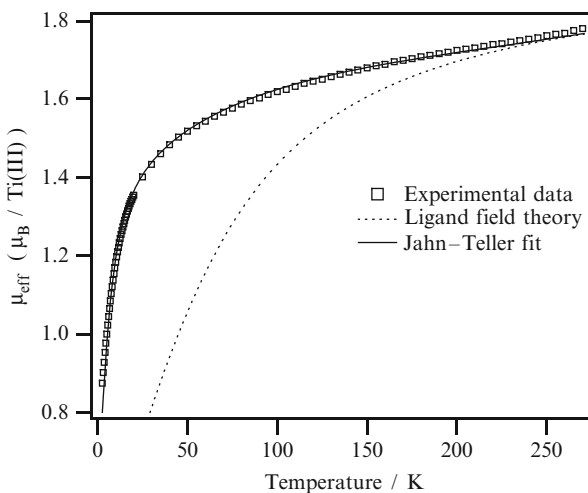


**Fig. 21** Variation of the effective magnetic moment with temperature for 8.4%  $[\text{Ti}(\text{OH}_2)_6]^{3+}$  cation doped into  $\text{Cs}[\text{Ga}(\text{OH}_2)_6](\text{SO}_4)_2 \cdot 6\text{H}_2\text{O}$ . The curve labelled “ligand field theory” was calculated from the basis states of the  ${}^2E_g(S_6)$  term only with  $\lambda = 130\text{ cm}^{-1}$  and  $k = 0.88$ . The curve labelled Jahn–Teller fit was calculated with the same electronic parameters but allowing for Jahn–Teller coupling to two modes with energies of 53 and  $894\text{ cm}^{-1}$  [50]

### 3.2.3 Electronic Raman Spectrum of Guanidinium Vanadium Sulphate

The vanadium(III) cation possesses one more valence electron than titanium(III). This means that the alum trigonal field that led to an orbitally degenerate ground term for titanium(III), splits the vanadium(III)  ${}^3T_{1g}(\text{O}_h)$  ground term into  ${}^3A$  and  ${}^3E(C_3)$  components with the non-degenerate term lower lying, as depicted in Fig. 22. The Jahn–Teller effect is now manifested in the excited state as shown most beautifully by electronic Raman spectra of  $[\text{C}(\text{NH}_2)_3][\text{V}(\text{OH}_2)_6](\text{SO}_4)_2$  [56, 57], presented in Fig. 23. The three prominent transitions in the Raman spectrum, centred at ca.  $2,720\text{ cm}^{-1}$ , separated by ca.  $70\text{ cm}^{-1}$ , are assigned to the transitions depicted in Fig. 22, between the spinor levels of the  ${}^3A(C_3)$  and  ${}^3E(C_3)$  terms, as confirmed by the temperature dependence of the spectrum. The zero-field-splitting parameter of the ground term,  $D$ , has been determined independently by EPR to be  $3.73(5)\text{ cm}^{-1}$  [58].

If the spectroscopic data are interpreted within the confines of ligand field theory [25], values for  $D$ ,  $\Delta$  and  $A\lambda$  of  $3.73(5)$ ,  $\sim 2,720$  and  $\sim 70\text{ cm}^{-1}$  are respectively obtained, where  $A$  is a ligand-field parameter reflecting the  ${}^3T_{1g}(\text{F})$ ,  ${}^3T_{1g}(\text{P})$  mixing. These values are, however, mutually incompatible. In the limit where  $\Delta \gg A\lambda$ , the parameter,  $D$ , is of the order  $\sim (A\lambda)^2/\Delta$  from ligand field theory; with  $\Delta$  and  $A\lambda$  set to  $2,720$  and  $70\text{ cm}^{-1}$ , a value for  $D$  of  $\sim 1.8\text{ cm}^{-1}$  is then obtained, which is less than half that determined from EPR studies. On the other hand, values for  $D$  and  $\Delta$  of  $3.73$  and  $2,720\text{ cm}^{-1}$  yield a value for  $A\lambda$  of  $\sim 100\text{ cm}^{-1}$  which is considerably larger than that suggested by the spacing of the



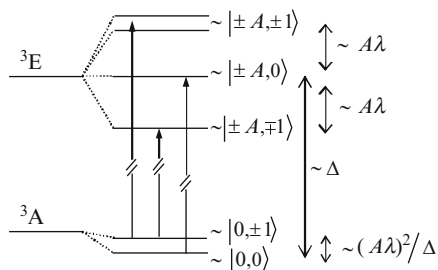


**Fig. 22** Ligand-field energy level diagram showing the spinor levels and energies of the  ${}^3T_{1g}(O_h)$  ground term in the limit where  $\Delta \gg A\lambda$ . The solid arrows designate the allowed  ${}^3A \rightarrow {}^3E(C_3)$  electronic Raman transitions, based on the  $\Delta M_s = 0$  selection rule. The states are labelled according to the zeroth-order ligand-field wavefunctions, where  $A$  is a ligand-field parameter reflecting the  ${}^3T_{1g}(F)$ ,  ${}^3T_{1g}(P)$  mixing

three prominent electronic Raman bands. The poor agreement is not improved when the ligand field basis is expanded to include all 45 states arising from the  $d^2$  electron configuration. The discrepancy between experiment and ligand field theory is a result of a pronounced excited state Jahn–Teller effect that reduces the energy gap between the low-lying states of the  ${}^3E$  term, i.e. the quantity  $A\lambda$  cannot simply be extracted from the electronic Raman spectrum.

In Fig. 23 are shown theoretical electronic Raman profiles [56]. The spectra were calculated from the eigenvalues and eigenfunctions of  $({}^3A \oplus {}^3E) \otimes e$  vibronic interaction [25], constructed in trigonal symmetry using the group theoretical principles outlined in Sect. 1. The calculated spectra take no account of the additional splitting caused by the two crystallographically distinct  $[V(OH_2)_6]^{3+}$  species, and the width of the Lorentzian bands is set to a constant value across the spectrum. With  $E_{JT}$  set to zero, three bands are expected, with an energy separation of  $\sim A\lambda$ . The relative intensities of the bands reflect the thermal populations of the states of the  ${}^3A(C_3)$  ground term. The two higher lying spinor levels of the  ${}^3E(C_3)$  term are split to second-order by spin-orbit coupling, as depicted in Fig. 22. The splitting is not resolved in the calculated spectrum, though the higher energy band is visibly broader than the other two. The curve calculated with  $E_{JT} = 300 \text{ cm}^{-1}$ , is seen to provide a much better reproduction of the energies of the observed electronic Raman bands, as well as the intensity distribution across the spectrum, with the presence of a weak vibronic sideband emerging naturally from the  $({}^3A \oplus {}^3E) \otimes e$  vibronic calculations. The zero-field-splitting of the  ${}^3A$  term is reduced slightly, the reduction being facilitated by the high energy of the Jahn–Teller active vibration. With  $A\lambda$  set to  $107 \text{ cm}^{-1}$ , a satisfactory account of both the Raman data and the parameter,  $D$  is obtained.

The magnitude of the Jahn–Teller coupling in the  $[Ti(OH_2)_6]^{3+}$  and  $[V(OH_2)_6]^{3+}$  cations is weak compared to the  $[Cu(OH_2)_6]^{2+}$  and  $[Cr(OH_2)_6]^{2+}$  cations that we will consider in Sect. 3.3. Nevertheless, the effect on the electronic coordinates are no less profound since spin-orbit coupling acts to first order in orbital triplet ground terms and is greatly affected by the Jahn–Teller interaction. The Ham effect

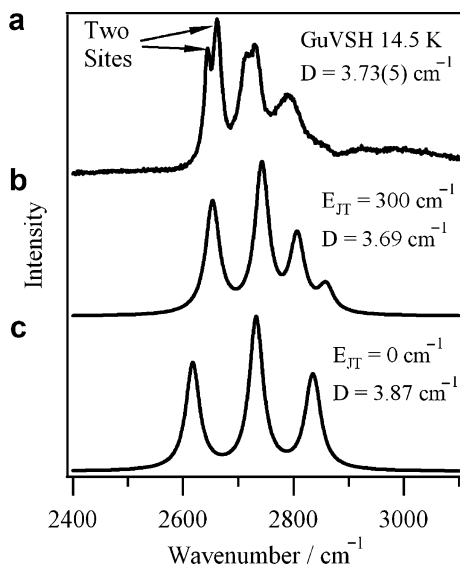


**Fig. 23** Experimental (a) and calculated (b) electronic Raman profiles, corresponding to the  ${}^3A \rightarrow {}^3E(C_3)$  transition depicted in Fig. 22. The theoretical profiles were calculated with  $A\lambda = 107\text{ cm}^{-1}$ ,  $\Delta = 2720\text{ cm}^{-1}$ ,  $\hbar\omega = 800\text{ cm}^{-1}$  and  $T = 14.5\text{ K}$ . The value of  $E_{JT}$  used to calculate each profile is given in the figure, along with calculated (b) and experimental (a) values of the zero-field-splitting parameter,  $D$ . The electronic Raman transitions were folded with a Lorentzian bandshape, with constant width of  $15\text{ cm}^{-1}$  across the spectrum after [56]

will be apparent for transition metal ions with orbital triplet terms whenever certain conditions are met. First, spin-orbit coupling should be comparable or less than the strength of the Jahn–Teller interaction. Secondly, orbitals on the ligands should be available for  $\pi$ -bonding and the metal–ligand  $\pi$ -interaction should be highly anisotropic, as is the case for the water ligand [59]. Only in this instance will the energies of the  $t_{2g}$  orbitals exhibit sufficient sensitivity to a given vibration of the complex. Great attention should be paid to magnetic data from high-symmetry complexes of the 3d transition metals formed with ligands such as water, hydroxide, imidazole, pyridine, imidazolate, thiophene, amides, carboxylates, oxalate, acetylacetonate, and porphyrins where significant Jahn–Teller coupling, involving the librational modes of these ligands, can be expected.

### 3.3 Plasticity of the Coordination Sphere

#### 3.3.1 The Copper(II) and Chromium(II) Tutton's Salts

Tutton's salts with the general formula  $M^I M^{II}(\text{H}_2\text{O})_6(\text{SO}_4)_2$  offer many isomorphous structures of both pure copper(II) compounds and hosts for doping  $\text{Cu}(\text{H}_2\text{O})_6^{2+}$  impurities. These compounds show temperature dependent EPR

spectra which can be understood in terms of the warped  $E \otimes e$  Jahn–Teller potential surface as shown in Fig. 3, together with a low symmetry rhombic field due to the  $C_i$  site symmetry [60]. This rhombic field has a large component which corresponds to a tetragonal compression and the three Jahn–Teller minima become inequivalent, but with two minima lower than the third, as shown in Fig. 4c. This gives rise to a temperature dependent EPR spectrum as each vibronic level will have different electronic properties. If the transitions between the Boltzmann populated vibronic levels are fast on the EPR time scale, an averaged EPR spectrum is observed rather than the superimposed spectra of the individually populated vibronic levels. This averaging occurs for copper(II) systems where the symmetry is low enough that the vibronic levels are separated by  $>50\text{ cm}^{-1}$ . Exceptions occur where the transition rate between close lying levels is slow. The Cu(II) doped MgO system discussed above is an example where an anisotropic to isotropic spectrum transition occurs at  $\sim 6\text{ K}$ . This temperature dependence results from a temperature dependent exchange rate between the strain split ground vibronic E state and an excited vibronic singlet state.

The  $g$  values as a function of temperature are shown in Fig. 24 for the copper(II) ion doped into  $M^I\text{Zn}(\text{H}_2\text{O})_6(\text{SO}_4)_2$ ,  $M^I = \text{K}^+, \text{Rb}^+, \text{Cs}^+$ . The interpretation is as follows. The  $\text{Cu}(\text{H}_2\text{O})_6^{2+}$  ion will attempt to adopt the  $E \otimes e$  Jahn–Teller potential energy surface with three equivalent minima at the preferred tetragonally elongated geometry. However, the orthorhombic site symmetry of the host crystal results in a large low symmetry perturbation of the  $E \otimes e$  Jahn–Teller surface with  $\phi_\delta$ ,  $\sim 180^\circ$  in (14) which stabilises two minima below a third as shown on the right hand side of Fig. 24. The rhombic nature of the low symmetry field means that  $\phi_\delta$  is not directed exactly at  $180^\circ$  resulting in the strain discriminating between the two lower minima.

At low temperature the molecules are in their lowest vibronic level, which is localised in the lowest energy minimum. This minimum is shifted from the  $\phi_\delta = 120^\circ$  exact tetragonal geometry so the resulting  $g$  values are slightly orthorhombic at low temperature, but approximate the  $g$  values of a tetragonally elongated complex ( $\sim g_\perp < \sim g_\parallel$ ). As the temperature is increased, the population of a higher vibronic level localised in the other minimum ( $\phi_\delta \sim 240^\circ$ ) occurs. Whereas the first minimum corresponds to an approximate geometry with an elongation along the  $x$  molecular axis, the higher energy minimum corresponds to a geometry with an elongation along  $y$ . This approximates the swapping of  $x$  and  $y$  axes, and results in the lowest  $g$  value oriented along the  $z$  axis being temperature independent and the two higher  $g$  values being averaged.

There is much information that can be gained from the temperature dependent  $g$  values. The experimental data can be fitted to the vibronic energies and wavefunctions obtained from a parameterised Jahn–Teller surface with the low symmetry strain terms. The vibronic wavefunctions can then be used to calculate the  $g$  values and the energy levels can be used to determine the Boltzmann average. Implicit in this approach are the assumptions:

- (a) That each vibronic level can be treated as an isolated Kramers' doublet (the applied magnetic field does not mix the levels)
- (b) There is fast averaging between vibronic levels.

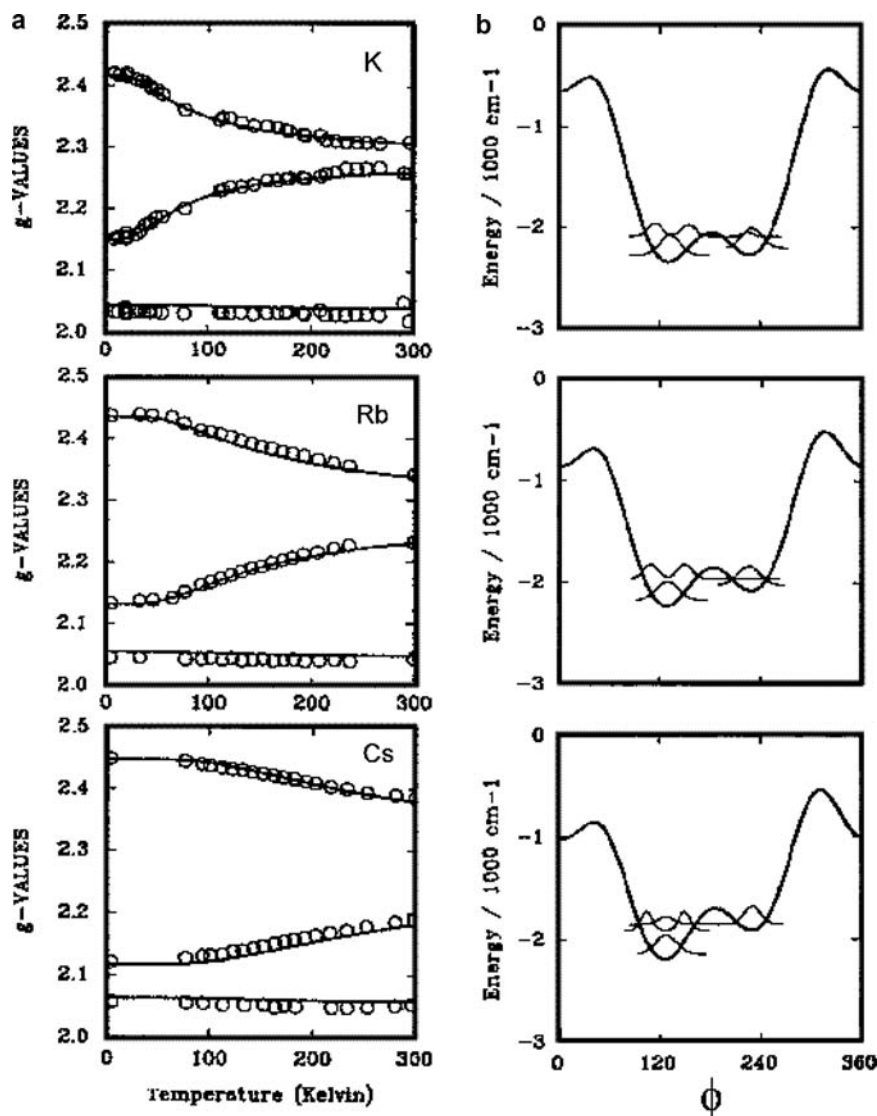


Fig. 24 The variation of the g-values for a number of Cu(II) doped Tutton's salts, after [60].

These conditions are fulfilled for these low symmetry hosts with large strain. It should be noted that these strain terms are much larger than those that were originally introduced for Jahn–Teller systems [32]. Strictly, such a large strain should reduce the problem to a pseudo Jahn–Teller effect and results in many of the symmetry related vibronic coupling constants contained in (15) not being constrained to be equal. However, the resulting large number of coupling constants would greatly over parameterise the problem, and it has been found that a meaningful picture can be obtained by retaining the high symmetry coupling constants. The model works

because the cubic Hamiltonian + low symmetry strain still captures the physics of the problem. Parameters which are now not required to be equal, will still have similar values as they originate from the same electronic driving forces. It is preferable to continue with what are now effective first and second order coupling constants rather than introducing the 3 and 9 independent parameters respectively that the low symmetry problem formally requires.

The trends in the experimental data that can be directly related to the fitted potentials shown in Fig. 24 are as follows. At low temperature the  $g$  values become increasingly close to tetragonal, going down the series  $K^+$ ,  $Rb^+$ ,  $Cs^+$ . This is because the magnitude of the strain,  $\delta$ , is also decreasing down the series. As  $\delta$  increases the two minima at  $\phi_s = 120^\circ, 240^\circ$  are gradually shifted to a single minimum at  $\phi_s = 180^\circ$ . Therefore the  $K^+$  host, with the largest  $\delta$ , will have the largest shift from  $\phi_s = 120^\circ$  and the most orthorhombic  $g$  values at low temperature. The temperature dependence of the  $g$  values decreases down the series  $K^+$ ,  $Rb^+$ ,  $Cs^+$ . This is due to an increase in the energy difference between the two lowest minima, which in turn is determined by the orthorhombic component of the strain or the deviation of  $\phi_s$  from  $180^\circ$ . The strain obtained from such an analysis can be related to the geometry of the host lattice, the copper(II) ion acts as a probe to determine the host geometry [61].

The deuterated Tutton's salt  $(ND_4)_2Cu(D_2O)_6.(SO_4)_2$  has been studied by a number of groups and the structural data are collected in Fig. 25. At low temperature the three independent bond lengths of the  $C_i$  site corresponds to a tetragonally elongated octahedron with a small rhombic distortion. The bonds remain temperature independent until  $\sim 150$  K, above which the long and medium bonds approach each other so that, at face value, the 320 K geometry would be better described as a tetragonally compressed octahedron. However, rather than the bond lengths changing from elongated along Cu-O(8) to compressed along Cu-O(9), the diffraction data are actually the result of an average of two structural isomers. The situation corresponds to a ground state potential energy surface similar to that given in Fig. 4c and Fig. 24, with two minima lower than the third. At low temperature the  $Cu(D_2O)_6^{2+}$  complex is localised in the lowest minimum, and an elongated geometry is observed. At temperatures above 150 K, the population of the 2nd minima become appreciable. The geometry at this second minimum is elongated along an axis different to that of the lowest minimum. The diffraction experiments average Cu-O(7) and Cu-O(8), while that of Cu-O(9) remains temperature independent.

One way to verify this is to measure X-ray absorption fine structure (XAFS) spectra as a function of temperature [62]. Here the X-ray absorption spectrum is essentially instantaneous from the equilibrium ground state geometry. The fine structure appearing in the spectrum due to the scattering of the photoelectron ejected from the Cu centre with nearest neighbouring atoms can be modelled in terms of the distances between the atoms. The XAFS derived bond lengths are given by the lines in Fig. 25 show no temperature dependence. Both structural isomers shown on the right hand side of Fig. 25 look the same to the XAFS experiment.

It was pointed out by Ham [32] that one of the interesting features of the Jahn–Teller effect in the solid state is that the high symmetry  $E \otimes e$  potential energy

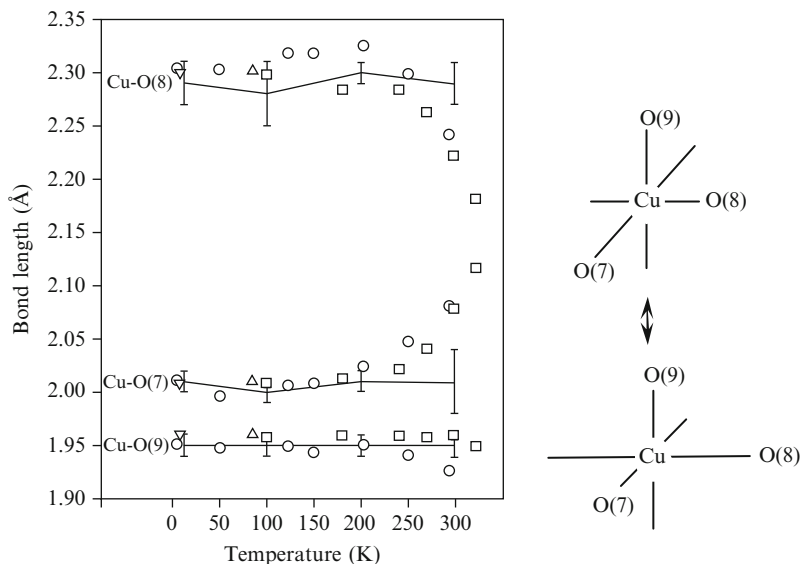


**Fig. 25** The Cu–O bond lengths of  $(\text{ND}_4)_2\text{Cu}(\text{D}_2\text{O})_6 \cdot (\text{SO}_4)_2$  as a function of temperature. X-ray and Neutron diffraction symbols, error bars and lines from the analysis of XAFS data

surface is very susceptible to low symmetry perturbations. This has been realised in the lower symmetry environment of the  $(\text{ND}_4)_2\text{Cu}(\text{D}_2\text{O})_6(\text{SO}_4)_2$  Tutton's salt [63]. The energy difference in the two lowest minima is quite small ( $\sim 100 \text{ cm}^{-1}$ ) and a relatively small value of orthorhombic strain (change in  $\phi_8$ ) can reverse the energy order. The crystal packing, when the  $\text{Cu}(\text{D}_2\text{O})_6^{2+}$  ion has the geometry of the higher energy minimum, results in a slightly smaller cell volume. This means that an application of external hydrostatic pressure effectively changes  $\phi_8$  and reverses the energies of the lowest two minima. A much larger geometry change is observed than one would see in applying pressure to a non-Jahn–Teller system and is an example of the amplification of a small perturbation that Ham has discussed [32].

The  $[\text{Cr}(\text{OH}_2)_6]^{2+}$  ion possesses the high-spin  $d^4$  electronic configuration and is also subject to strong  $E \otimes e$  coupling. By analogy with the ammonium copper Tutton's salts, the electronic and molecular structure of the complex in  $(\text{ND}_4)_2\text{Cr}(\text{D}_2\text{O})_6(\text{SO}_4)_2$  exhibits an intriguing temperature dependence that requires the explicit consideration of the vibronic interaction [6, 64, 65]. The primary difficulty in undertaking Jahn–Teller coupling calculations for high-spin  $d^4$  complexes is the size of the electronic basis. Recent work by Graham Carver and co-workers has demonstrated the limitations of Ham's perturbative model on account of the close proximity of the  ${}^3\text{T}_{1g}$  term to the ground  ${}^5\text{E}_g$  term [66]. The problem was solved by constructing an effective  ${}^3\text{T}_1 + (E \otimes e)$  Hamiltonian in the trigonal point group of the molecule using the AOM. Carver showed how the model could in principle be applied to any high-spin  $d^4$  complex where the ligand-field parameters in the undistorted trigonal or octahedral configuration can be reliably estimated.

### 3.3.2 Sterically Strained Manganese(III) Complexes

The biological activity of manganese(III) complexes is rendered by their redox-activity and the lability of the first-order co-ordination sphere [67]. Biochemists often depict manganese(III) enzymes as little factories with molecules approaching the active site in one direction and being ejected out in another. This plasticity of the co-ordination sphere may be appreciated by considering the effect of steric strain on the  $E \otimes e$  potential energy surface. Consider the  $[\text{Mn}(\text{bpia})(\text{OAc})(\text{OCH}_3)]^-$  complex, the structure for which is shown below [68] (Fig. 26).

Crystallographic [68] and spectroscopic [69] measurements are consistent with the classification of the complex as a rare example of a compressed Jahn–Teller octahedron. The additional stabilisation of the  $3d_{z^2}$  orbital via interaction with the  $4s$  orbital and anharmonic contributions to the vibrational potential contribute to the stabilisation of axially elongated octahedra in manganese(III) co-ordination compounds [11, 70–74]. Therefore, a compression can result only if  $\phi_\delta$  has a value close to  $\sim 60^\circ$ ,  $180^\circ$  or  $300^\circ$  and  $\delta$  is large compared to  $2\beta$ , as illustrated by the plots in Fig. 4. In heteroleptic complexes of manganese(III), the ligands tend to arrange themselves so as to provide a tetragonal strain of the same sign, as this is energetically more favourable. For example in manganese(III) complexes formed with terminal and bridging fluoride ligands, the overwhelming tendency is for a tetragonally elongated geometry with the bridging ligands in the axial positions [75]. The result has been rationalised in terms of the force constant for the Mn(III)–F bond being stronger when the fluoride ligand is terminal rather than bridging. When the co-ordination positions are largely dictated by polydentate ligands, a compression may become competitive. The strain may be regarded as having two principal

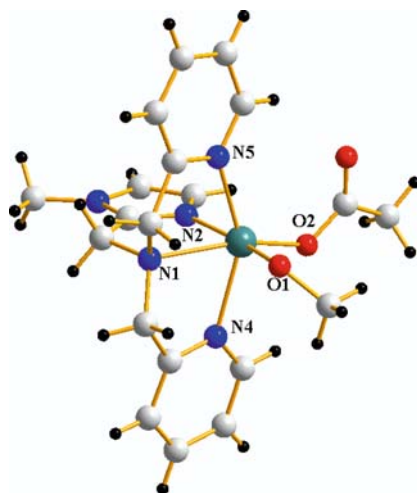


**Fig. 26** Structure of  $[\text{Mn}(\text{bpia})(\text{OAc})(\text{OCH}_3)](\text{PF}_6)$ . The unique short axes are indicated by means of arrows

contributions. The first is the geometrical distortion arising primarily from the steric constraints imposed by the polydentate ligand. The second is an electronic factor arising from the differing  $\sigma$ -bonding capabilities of the ligands. In the framework of the AOM, the strain may be written down in terms of the angular co-ordinates and  $\sigma$ -bonding strengths of the ligands. Neglecting  $\pi$ -bonding,  $\hat{H}_{st}$  in (13) has the explicit form,

$$\hat{H}_{st} = \begin{pmatrix} \sum_i e_\sigma^i [F_\sigma^i(d_{x^2-y^2})]^2 & \sum_i e_\sigma^i [F_\sigma^i(d_{x^2-y^2})][F_\sigma^i(d_{z^2})] \\ \sum_i e_\sigma^i [F_\sigma^i(d_{x^2-y^2})][F_\sigma^i(d_{z^2})] & \sum_i e_\sigma^i [F_\sigma^i(d_{z^2})]^2 \end{pmatrix}, \quad (39)$$

where the sum is over all the ligands of the complex, whose positions are described by the polar angles  $\theta$  and  $\phi$ . The angular overlap factors for the one-electron orbitals are [71],

$$\begin{aligned} F_\sigma(d_{x^2-y^2}) &= (\sqrt{3}/4) \cos 2\phi (1 - \cos 2\theta), \\ F_\sigma(d_{z^2}) &= (1 + 3 \cos 2\theta)/4. \end{aligned} \quad (40)$$

In order to gain an appreciation of the influence of the changing ligand field environment on the geometric structure, it is useful to break the Hamiltonian up into its cubic and anisotropic parts. In Fig. 27 is shown the variation of the strain vector as a function of  $e_\sigma$  for the monodentate ligands, while the  $e_\sigma$  values for the polydentate ligand are fixed at  $7,000 \text{ cm}^{-1}$ . It is seen from Fig. 27 that a strain vector in which the  $e_\sigma$  values for the oxygen-binding ligands are  $\sim 7,000 \text{ cm}^{-1}$  bisects the cubic minima that correspond to elongated octahedra, in a direction that equates to a compression along the N2–Mn and Mn–O1 bond vectors, with  $\delta = 1,752 \text{ cm}^{-1}$  and  $\phi_\delta = 55^\circ$ . In fact, varying the  $e_\sigma$  values of all ligands between  $6,500$  and  $7,500 \text{ cm}^{-1}$  always results in a strain vector that tends to stabilise a compression along these bond axes. It is reasonable to expect that the  $e_\sigma$  values of the ligands fall within this range. We conclude, therefore, that as a consequence of the combined effects of the pronounced geometrical angular distortion and the similar  $\sigma$ -donor capacities of the ligands, the low-symmetry strain calculated for the  $[\text{Mn}(\text{bpia})(\text{OAc})(\text{OCH}_3)]^+$  complex favours a compression along the N2–Mn and Mn–O1 bond vectors, in accordance with the observed structure. With the geometric constraints held constant, the effect of substituting oxygen for a weaker  $\sigma$ -donor is a shift in the angular direction of the vector towards  $\phi_\rho = 0^\circ$  and a decrease in the magnitude. This prediction is also consistent with experiment since substitution of the monodentate ligands by chloride leads to a tetragonally elongated octahedron, with the minimum close to  $\phi_\rho = 0^\circ$ . The potential energy surfaces resulting from the diagonalisation of all terms in the Hamiltonian are shown in Fig. 28, showing clearly the shift in the potential energy minimum on account of the identity of the monodentate ligands. Note that the sensitivity of  $\phi_\delta$  to the sigma-donor strength of the ligands is apparent only on account of the pronounced geometrical angular distortion imposed by the polydentate ligand, which goes some way to explaining the plasticity of the co-ordination sphere in bio-inorganic manganese(III) complexes.



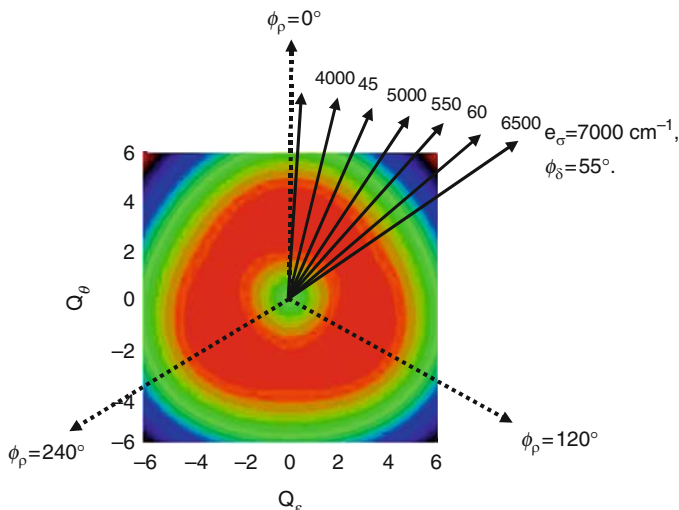


**Fig. 27** Cubic  $E \otimes e$  Jahn–Teller Potential Energy Surface calculated with the parameters  $\hbar\omega = 450 \text{ cm}^{-1}$ ,  $A_1 = -1,400 \text{ cm}^{-1}$ ,  $A_2 = 10 \text{ cm}^{-1}$  in the  $\{Q_\theta, Q_\epsilon\}$  co-ordinate frame. The barrier height is  $\sim 193 \text{ cm}^{-1}$  with the minima at angular positions of  $\phi_p = 0^\circ$ ,  $120^\circ$  and  $240^\circ$ . Overlaid are vectors representative of the magnitude and angular direction of the strain interaction obtained from AOM calculations. The length of the arrows is proportional to  $\delta$ , and the  $\{e_\theta, e_\epsilon\}$  co-ordinate frame is coincident with that of  $\{Q_\theta, Q_\epsilon\}$  such that  $\phi_\delta$  varies from  $3^\circ$  to  $55^\circ$ . The AOM calculations (39 and 40) are for a complex based upon  $[\text{Mn}(\text{bpia})(\text{OAc})(\text{OCH}_3)]^+$ . The AOM angles are derived from the atomic positions of the complex and the  $e_\sigma$  values for the nitrogen ligators of the tripodal ligand fixed at  $7,000 \text{ cm}^{-1}$ . The  $e_\sigma$  values for the remaining two ligators are varied between  $4,000$  and  $7,000 \text{ cm}^{-1}$ , as indicated in the figure. When  $\delta$  is large compared to the barrier height ( $2\beta \sim 2A_2(A_1/\hbar\omega)^2$ ), the potential energy minimum is dictated largely by the value of  $\phi_\delta$ , after [76]

## 4 Concluding Remarks

In this chapter we have endeavoured to make the vibronic calculation of observables accessible to the reader who is not well acquainted with the Jahn–Teller effect. We trust that by introducing simple systems studied using a wide range of experimental techniques, the reader will gain an appreciation of the underlying physics and will be encouraged to become engaged in this field of research. Just as a little group theory goes a long way, the computer too can be a surprisingly good teacher. There is no substitute for hands on calculations to explore numerically the various vibronic Hamiltonians and their consequences for the electronic and molecular structures of Jahn–Teller active systems. Finally there is no greater satisfaction in seeing a signature that one recognises woven into nature’s rich tapestry.

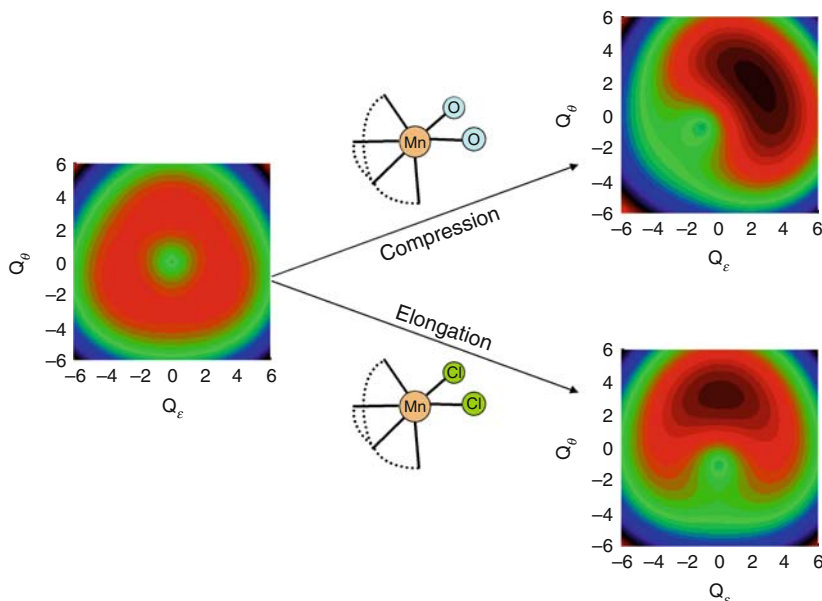


**Fig. 28**  $E \otimes e$  Jahn–Teller potential energy surfaces of complexes resembling  $[\text{Mn}(\text{bpia})(\text{OAc})(\text{OCH}_3)]^+$  and  $[\text{Mn}(\text{bpia})\text{Cl}_2]^+$ . The parameters defining the cubic part of the Hamiltonian are  $\hbar\omega = 450\text{ cm}^{-1}$ ,  $A_1 = -1,400\text{ cm}^{-1}$ ,  $A_2 = 10\text{ cm}^{-1}$ . The low-symmetry crystal field was calculated using the AOM, as described in the text. The polar angles were generated from the atomic co-ordinates and  $e_\sigma$  values of  $7,000\text{ cm}^{-1}$  were used to model the bonding interaction with both the nitrogen and oxygen ligators. The  $e_\sigma$  values of the chloride ligands were reduced to  $4,000\text{ cm}^{-1}$ , all other parameters remaining unchanged, after [76]

## References

1. S. Sugano, Y. Tanabe, H. Kamimura, *Multiplets of Transition Metal Ions In Crystals* (Academic, New York, 1970)
2. M.J. Riley, A. Furlan, *Chem. Phys.* **210**, 389 (1996)
3. H.A. Jahn, E. Teller, *Proc. Roy. Soc. London, A* **161**, 220 (1937)
4. M.C.M. O'Brien, From her lecture on "The Paramagnetism of Caesium Titanium Alum", given at the Department of Chemistry, University of Bern in 1997, shortly before her untimely death.
5. M.A. Hitchman, T.D. Waite, *Inorg. Chem.* **15**(9), 2150 (1976)
6. C. Dobe, C. Noble, G. Carver, P.L.W. Tregenna-Piggott, G. McIntyre, A.L. Barra, A. Neels, S. Janssen, F. Juranyi, *J. Am. Chem. Soc.* **127**(10), 3642 (2005)
7. P.L.W. Tregenna-Piggott, H. Weihe, A.-L. Barra, *Inorg. Chem.* **42**, 8504–8508 (2003)
8. A. Ceulemans, D. Beyens, L.G. Vanquickenborne, *J. Am. Chem. Soc.* **106**, 5824 (1984)
9. P. Murray-Rust, H.-B. Bürgi, J.D. Dunitz, *Acta. Cryst.* **A35**, 703–713 (1979)
10. F.S. Ham, *Phys. Rev.* **166**, 307 (1968)
11. M.J. Riley, *Top. Curr. Chem.* **214**, 5 (2001)
12. I.B. Bersuker, *The Jahn–Teller Effect* (Cambridge University Press, Cambridge, 2006)
13. M. Bacci, *Chem. Phys. Lett.* **58**, 537 (1978)
14. M. Bacci, *Chem. Phys.* **40**, 237 (1979)
15. G. Carver, J. Bendix, P.L.W. Tregenna-Piggott, *Chem. Phys.* **282**, 245–263 (2002)
16. R. Bruyndonckx, C. Daul, P.T. Manoharan, E. Deiss, *Inorg. Chem.* **36**, 4251 (1997)

17. T.K. Kundu, R. Bruyndonckx, C. Daul, P.T. Manoharan, *Inorg. Chem.* **38**, 3931 (1999)
18. M. Atanasov, P. Comba, C.A. Daul, A. Hauser, *J. Phys. Chem. A* **111**, 9145–9163 (2007)
19. C. Cohen-Tannoudji, B. Diu, F. Laloe, *Quantum Mechanics*, Vol. 1, Chapter V (1977)
20. H.C. Longuet-Higgins, U. Opik, M.H.L. Pryce, R.A. Sack, *Proc. Roy. Soc. Lond.* **A244**, 1 (1958).
21. F.S. Ham, *Phys. Rev. Lett.* **58**, 725 (1987)
22. J. Ammeter, H.B. Buergi, E. Gamp, V. Meyer-Sandrin, W.P. Jensen, *Inorg. Chem.* **18**(3), 733–750 (1979)
23. P.L.W. Tregenna-Piggott, H.P. Andres, G.J. McIntyre, S.P. Best, C.C. Wilson, J.A. Cowan, *Inorg. Chem.* **42**, 1350 (2003)
24. D.R. Yarkony, *Acc. Chem. Res.* **31**, 511 (1998)
25. P.L.W. Tregenna-Piggott, G. Carver, *Inorg. Chem.* **43**, 8061 (2004)
26. A. Dick, E.R. Krausz, K.S. Hadler, C.J. Noble, P.L.W. Tregenna-Piggott, M.J. Riley, *J. Phys. Chem. C* **112**(37), 14555–14562 (2008).
27. S. Guha, L.L. Chase, *Phys. Rev. B* **12**, 1658 (1975)
28. P.L.W. Tregenna-Piggott, *Adv. Quantum Chem.* **44**, 461 (2003)
29. M.C.M. O'Brien, *Proc. R. Soc., A* **281**, 323 (1964)
30. M.C.M. O'Brien, *J. Phys. C. Solid State Phys.* **16**, 85 (1983)
31. M.J. Riley, C.J. Noble, P.L.W. Tregenna-Piggott, *J. Chem. Phys.*, **130**, 104708, (2009); *J. Chem. Phys.*, **130**, 199901, (2009).
32. F.S. Ham, in *Electron Paramagnetic Resonance*, ed. by S. Geshwind (Plenum Press: New York, 1972)
33. R.W. Reynolds, L.A. Boatner, M.M. Abraham, Y. Chen, *Phys. Rev. B*, **10**, 3802 (1974)
34. A. Furlan, M.J. Riley, S. Leutwyler, *J. Chem. Phys.* **96**, 7306–7320 (1992)
35. A. Furlan, T. Fischer, P. Fluekiger, H.U. Guedel, S. Leutwyler, H.P. Luethi, M.J. Riley, J. Weber, *J. Phys. Chem.* **96**, 10713–10719 (1992)
36. G. Delacrétaz, E.R. Grant, R.L. Whetten, L. Wöste, J.W. Zwanziger, *Phys. Rev. Lett.* **56**, 2598 (1986)
37. M.J. Riley, A. Furlan, H.U. Guedel, S. Leutwyler, *J. Chem. Phys.* **98**, 3803–3815 (1993)
38. A. Furlan, S. Leutwyler, M.J. Riley, *J. Chem. Phys.* **100**, 840–855 (1994)
39. F.S. Ham, *Phys. Rev.* **138**, A1727 (1965)
40. M.C.M. O'Brien, C.C. Chancey, *Am. J. Phys.* **61**, 688–697 (1993)
41. A. Abragam, B. Bleaney, *Electron Paramagnetic Resonance of Transition Metal Ions* (Oxford University Press, Oxford, 1970), p. 815
42. F.I.B. Williams, D.C. Krupa, D.P. Breen, *Phys. Rev.* **179**, 255 (1969)
43. J.H. Van Vleck, *Electric and Magnetic Susceptibilities* (Oxford University Press, New York, 1932)
44. J.H. Van Vleck, *J. Chem. Phys.* **7**, 61–71 (1939)
45. J.K. Beattie, S.P. Best, B.W. Skelton, A.H. White, *J. Chem. Soc., Dalton Trans.* 2105 (1981)
46. C. Daul, A. Goursot, *Inorg. Chem.* **24**, 3554–3558 (1985)
47. S.P. Best, J.B. Forsyth, *J. Chem. Soc., Dalton Trans.* 1721 (1991)
48. B. Bleaney, G.S. Bogle, A.H. Cooke, R.J. Duffus, M.C.M. O'Brien, K.W.H. Stevens, *Proc. Phys. Soc. London, Ser. A* **68**, 57 (1955)
49. P.L.W. Tregenna-Piggott, S.P. Best, M.C.M. O'Brien, K.S. Knight, J.B. Forsyth, J.R. Pilbrow, *J. Am. Chem. Soc.* **119**, 3324–3332 (1997)
50. P.L.W. Tregenna-Piggott, M.C.M. O'Brien, J.R. Pilbrow, H.U. Güdel, S.P. Best, C. Noble, *J. Chem. Phys.* **107**, 8275 (1997)
51. L. Dubicki, M.J. Riley, *J. Chem. Phys.* **106**, (1997) 1669
52. P.L.W. Tregenna-Piggott, C.J. Noble, J.R. Pilbrow, *J. Chem. Phys.* **113**, 3289–3301 (2000)
53. G. Carver, C. Dobe, T.B. Jensen, P.L.W. Tregenna-Piggott, S. Janssen, E. Bill, G.J. McIntyre, A.L. Barra, *Inorg. Chem.* **45**, 4695 (2006)
54. P.L.W. Tregenna-Piggott, H.U. Güdel, *Inorg. Chem.* **40**, 5497–5506 (2001)
55. P.L.W. Tregenna-Piggott, M.C.M. O'Brien, H. Weihe, H.U. Güdel, *J. Chem. Phys.* **109**, 2967 (1998)
56. G. Carver, S. Spichiger, P.L.W. Tregenna-Piggott, *J. Chem. Phys.* **122**, 124511 (2005)

57. D. Spichiger, G. Carver, C. Dobe, J. Bendix, P.L.W. Tregenna-Piggott, R. Meier, G. Zahn, *Chem. Phys. Lett.* **337**, 391 (2001)
58. P.L.W. Tregenna-Piggott, D. Spichiger, G. Carver, B. Frey, R. Meier, H. Weihe, J. Cowan, G. McIntyre, G. Zahn, A.-L. Barra, *Inorg. Chem.* **43**, 8049–8060 (2004)
59. S.P. Best, B.N. Figgis, J.B. Forsyth, P.A. Reynolds, P.L.W. Tregenna-Piggott, *Inorg. Chem.* **34**, 4605–4610 (1995)
60. M.J. Riley, M.A. Hitchman, A.W. Mohammed, *J. Chem. Phys.* **87**, 3766 (1987)
61. K.S. Hadler, J.R. Kilmartin, G.R. Hanson M.A. Hitchman, C.J. Simmons, M.J. Riley, *Inorg. Chem.* **47**, 8188 (2008)
62. V.M. Masters, M.J. Riley, M.A. Hitchman, *Inorg. Chem.* **40**(5), 843–849 (2001)
63. C.J. Simmons, M.A. Hitchman, H. Stratemeier, A.J. Schultz, *J. Am. Chem. Soc.* **115**, 11304 (1993)
64. C. Dobe, H.P. Andres, P.L.W. Tregenna-Piggott, S. Mossin, H. Weihe, S. Janssen, *Chem. Phys. Lett.* **362**, 387 (2002)
65. C. Dobe, T. Straessle, F. Juranyi, P.L.W. Tregenna-Piggott, *Inorg. Chem.* **45**, 5066 (2006)
66. G. Carver, M. Thut, C. Noble, P.L.W. Tregenna-Piggott, *J. Chem. Theory Comput.* **4**, 603–613 (2008)
67. Weatherburn D.C., in *Handbook on Metalloproteins*, ed. by I. Bertini, A. Sigel, H. Sigel (Marcel Dekker, New York, 2001), pp. 193–268. P.E.M. Siegbahn, *Curr. Opin. Chem. Biol.* **6**, 227 (2002)
68. M.U. Triller, D. Pursche, W. Hsieh, V.L. Pecoraro, A. Rempel, B. Krebs, *Inorg. Chem.* **42**, 6274 (2003).
69. Q. Scheifele, C. Riplinger, F. Neese, H. Weihe, A.L. Barra, F. Juranyi, A. Podlesnyak, P.L.W. Tregenna-Piggott, *Inorg. Chem.* **47**, 439–447 (2008)
70. R.J. Deeth, M.A. Hitchman, *Inorg. Chem.* **25**, 1225 (1986)
71. B.N. Figgis, M.A. Hitchman, *Ligand-Field Theory and Its Applications* (Wiley-VCH, New York, 2000)
72. M.J. Riley, *Inorg. Chim. Acta* **268**, 55 (1998)
73. I. Krivokapic, C. Noble S. Klitgaard, P.L.W. Tregenna-Piggott, H. Weihe, A.L. Barra, *Angew. Chem. Int. Ed.* **44**, 3613 (2005)
74. Q. Scheifele, T. Birk, J. Bendix, P.L.W. Tregenna-Piggott H. Weihe, *Angew. Chem. Int. Ed.* **47**, 148 (2007)
75. D. Reinen, M. Atanasov, W. Massa, Z. Anorg. Allg. Chem. **632**, 1375 (2006)
76. P.L.W. Tregenna-Piggott, *Inorg. Chem.* **47**, 448 (2008)

# Instabilities in Doped Materials Driven by Pseudo Jahn–Teller Mechanisms

P. García-Fernández, A. Trueba, J.M. García-Lastra, M.T. Barriuso, M. Moreno, and J.A. Aramburu

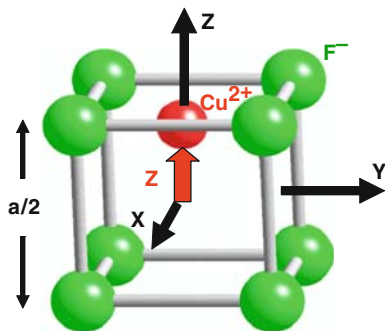
**Abstract** Substitution of a host lattice ion by an impurity can produce a spontaneous instability lowering the initial local symmetry of the site. In some cases the impurity remains *on-centre* and the distortion only involves the motion of the nearest ions while in other cases the impurity moves *off-centre* along particular directions of the lattice. In this article experimental and theoretical work on spontaneous instabilities of impurities in ionic solids driven by pseudo Jahn–Teller vibronic coupling mechanisms is reviewed. Particular attention is paid to the results of density functional theory calculations addressed to understand the microscopic origin of the instability and also to quantify the involved distortion. Particularly, we aim to help to overcome a paradigm taken root among many researchers of physics and chemistry of solids: that the instabilities of atoms and ions in pure and doped solids are due to difference of atomic sizes. On the contrary, we present a great quantity of experimental evidences and theoretical results showing that it is an effect of the vibronic coupling.

## 1 Introduction

Doped insulating and semiconductor materials are widely investigated due to the new optical, magnetic and electrical properties introduced by a given impurity in a crystal lattice [1–11]. Knowledge of the geometrical and electronic relaxations produced in the stabilization of the impurity into the host crystal is certainly a prerequisite for understanding all the associated physico-chemical properties due to the impurity centres. Nowadays relevant information on this issue can be obtained by means of several experimental techniques, but all of them have important limitations [12–18]. The huge development of *ab initio* calculations during last years has greatly contributed to quantify the relaxations, understand its microscopic origin and to have some predictive control [19, 20].

Very different situations are experimentally found when truly diluted impurities in insulators are considered. Sometimes, the impurity replaces a host lattice ion producing a totally *symmetric* distortion of neighbour ions that keeps the local symmetry, at least in the electronic ground state [21–32]. However, there are other cases

**Fig. 1** Picture of the off-centre  $\langle 001 \rangle$  motion of  $\text{Cu}^{2+}$  in the  $\text{SrF}_2$  lattice



where the substitutional impurity gives also rise to a *spontaneous* instability, that is, not due to the presence of *close* defects such as vacancies, interstitials or even foreign ions, producing a symmetry lowering from the initial high local symmetry of the site [20]. In many cases the substitutional impurity remains *on-centre* in the electronic ground state but there is a non-symmetric distortion of neighbour ions (ligands) leading to a reduction of the local symmetry. It is well-known that this behaviour often (but not always) appears for all systems with orbital degeneracy (Jahn–Teller effect) [20, 33–37]. However, it is worth nothing that on-centre instabilities with lowering of local symmetry can also happen for ions *without* orbital degeneracy. A good example of this possibility concerns the  $\text{Mn}^{2+}$  impurity in  $\text{BaF}_2$  [38–42] where the local symmetry is  $T_d$  and not  $O_h$  as is found for isomorphous lattices like  $\text{CaF}_2$  or  $\text{SrF}_2$  [43–46]. On the contrary, in other cases the impurity does not remain at the substituted ion position but undergoes an *off-centre* displacement along a certain direction of the lattice. This phenomenon, responsible for drastic changes of the coordination number and associated properties of the impurity, seems to be very subtle. For example, it is observed for  $\text{SrF}_2 : \text{Cu}^{2+}$  [47] (Fig. 1) but not for  $\text{Cu}^{2+}$ -doped  $\text{CaF}_2$  [48]. Off-centre motions are also observed in cases like  $\text{KCl} : \text{Li}^+$  [49–56] and  $\text{KBr} : \text{Cu}^+$  [57–62] involving closed shell impurities.

To understand the microscopic origin of high-symmetry instabilities is an issue of interest shared by many areas of physics, chemistry and materials science. Particularly, in molecular sciences it has been subject of multiple investigations during decades beginning from the concepts of directed valences, localized electron pairs, and valence shell electron pair repulsion (VSEPR), to the most recent vibronic interaction theory [20]. A fundamental step in the development of this theory was the Bersuker's works [20, 63, 64] proving that any instability of a high-symmetry structure in any polyatomic system (molecular and condensed matter) is related to the coupling between electronic and nuclear motions (vibronic coupling). In systems with an orbital degenerate state this coupling often (but not always) gives rise to a Jahn–Teller (JT) instability (Renner–Teller in the case of linear systems) which is necessarily driven by an even mode when there is an inversion symmetry. In the case of systems with a non-degenerate state the instability is due to what is called a pseudo Jahn–Teller (PJT) effect [20] which can involve odd distortion modes. It should be remarked here that  $d^9$  ions like  $\text{Cu}^{2+}$  or  $\text{Ag}^{2+}$  replacing  $\text{Sr}^{2+}$  in the cubic

SrCl<sub>2</sub> lattice do not exhibit a linear JT effect but undergo an *off-centre* motion along a C<sub>4</sub> axis driven by a  $t_{1u}$  mode [48, 65–68] (Fig. 1).

While the JT effect is today very popular among researchers working on instabilities in pure and doped solids, the PJT effect is much less known. The PJT origin of distortions in fluxional molecules that present stereochemical non-rigidity has been subject of many studies [20, 69–72]. However, many solid state researchers ignore or misunderstand the PJT effect as the origin of spontaneous instabilities in non-degenerate systems. The PJT problem was formulated by first time in 1957 by Öpik and Pryce [73] extending the JT theorem to consider instabilities associated with almost degenerate states. This fact has led many researchers to the erroneous conception that PJT instabilities are limited to coupling between quasi-degenerate states [74–77]. On the contrary, the modern developments of the PJT vibronic theory and many numerical calculations have clearly established that there are not a priori limits for instabilities and so, if the coupling constant between two states is large, excited states at considerable energies (several eV) can produce the instability [20]. A text-book example of it is the out-of-plane displacement of the nitrogen atom of the ammonia molecule where the principal excited state lies 6–7 eV above the ground state [20].

A representative example of that confusion is the study of the nature of the ferroelectric phase transitions in oxides with perovskite structure, as BaTiO<sub>3</sub> or PbTiO<sub>3</sub>, a subject intensely debated during last six decades. In 1966 Bersuker suggested [78] that the spontaneous polarization has a vibronic origin and so the PJT distortion may lead to dipole-moment formation and hence cooperative effects between centres result in spontaneous polarization of the crystal. He also proposed what is, in fact, the first order-disorder model for ferroelectrics based on an eight-well potential [78]. This was later confirmed by the diffuse X-ray experiments of Comes et al. [79, 80]. Nowadays, the dominant theory to explain ferroelectric transition is Cochran's soft-mode model [81–83] in which the Ti ion actually changes position from the  $\langle 111 \rangle$  direction, to  $\langle 110 \rangle$ ,  $\langle 100 \rangle$  or to the octahedral position as temperature rises. Even though it has experimental support there are other recent experiments that indicate that even at high temperature the Ti ions are placed on the  $\langle 111 \rangle$  directions [84–86] similarly to what is predicted by the eight-site or PJT models. Also DFT calculations indicate [87–89] that the origin of the distortion is based on bond changes as predicted by the PJT model.

In the realm of impurities in solids the first system where the existence of an *off-centre* displacement was well established corresponds to Li<sup>+</sup>-doped KCl. After the initial work by Lombardo and Pohl [49], additional experiments [50–56] lead to the conclusion that Li<sup>+</sup> in KCl moves in a  $\langle 111 \rangle$  direction. Therefore, as there are eight equivalent equilibrium positions for the Li<sup>+</sup> ion, the dipole moment formed by this ion and the associated vacancy can change its orientation by tunneling among equivalent minima. During the following years, the possibility of inducing some new phase transitions in the matrix by means of off-centre impurities gave rise to a great number of experimental and theoretical studies. In addition, diluted impurities with off-centre instabilities were used as model objects for the investigation of ferroelectric instabilities and tunnel movement of atomic particles and quantum

diffusion mechanisms in solid state which were pressing problems in solid state physics and chemistry [90–93]. Concerning the microscopic origin of the off-centre instabilities produced by impurities in solids, it is also a controversial issue. Already in 1965 Matthew indicated [94] that off-centre instabilities are related to the substitution of a lattice ion by a smaller impurity, the classical attraction forces producing a decrease in the ion core repulsive potential. However, in 1969 Quigley and Das [95] noted that this explanation based on *size effects* was not satisfactory because there are some exceptions to this rule along the series of known off-centre impurities. Despite this experimental evidence, that will be widely discussed along the article, this simplistic explanation has prevailed [96–109], although some authors have noted the PJT origin of these dipolar (off-centre) distortions in a similar way to other systems [20, 69, 70, 110–119].

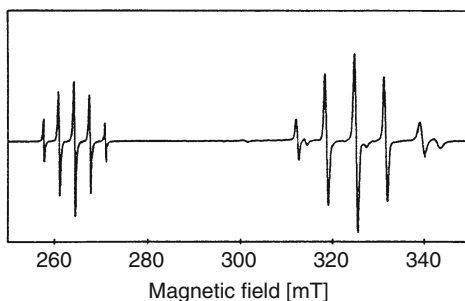
In this article spontaneous instabilities in the ground state of monoatomic impurities in ionic solids driven by PJT vibronic coupling mechanisms are reviewed. Particular attention is paid to the results of recent calculations addressed to understand the microscopic origin of the instability and also to quantify the involved distortion. Although many other interesting impurities can be found in covalent solids the number of works in this field is too large to be covered here. This article is arranged as follow. Section 2 provides a short description of main experimental techniques used in the characterization and analysis of PJT instabilities present in impurities in solids. A brief review of the principal monoatomic impurity centres in which ground state PJT instabilities have been detected is given in Sect. 3. Some specific off-centre and on-centre instabilities are analyzed in detail in the following sections combining DFT calculations with PJT models. Basic aspects of the PJT theory are summarized in Sect. 4, while Sect. 5 provides with main details of the DFT calculations. A wide study into the off-centre displacement sometimes observed for  $d^9$  ( $\text{Ni}^+$ ,  $\text{Cu}^{2+}$  and  $\text{Ag}^{2+}$ ) [19, 48, 65–68, 120–122] and  $d^7$  ( $\text{Fe}^+$ ) [123–125] impurities in crystals with fluorite structure (Fig. 1) is provided in Sect. 5. Section 6 deals with the controversial case of  $\text{Fe}^+$  in the incipient ferroelectric  $\text{KTaO}_3$ , a conspicuous example showing the limitations of magnetic resonance tools in oxides [126–129]. Section 7 is devoted to understand the microscopic origin of the reversible tetrahedral-octahedral transition experimentally observed more than 30 years ago for  $\text{BaF}_2 : \text{Mn}^{2+}$  at  $T \sim 50$  K, not observed for other  $\text{MF}_2$  ( $\text{M} = \text{Ca}, \text{Sr}, \text{Cd}$ ) lattices or in any fluoroperovskite [38–42]. Finally, the main conclusions of the present work are gathered in Sect. 9.

## 2 Experimental Techniques for Observation and Characterization of Instabilities

A key issue in the realm of impurities experiencing off-centre displacements is the availability of experimental data which prove unambiguously the existence of such a distortion. To achieve this goal a good advance comes out when *selective* tools (silent for the pure host lattice) can be used a fact which allows one to explore



**Fig. 2** EPR spectrum measured for  $\text{CaF}_2 : \text{Ni}^{2+}$  at  $T = 20 \text{ K}$  with the magnetic field parallel to  $\langle 100 \rangle$  [121]. The five superhyperfine lines seen on the right correspond to centres whose principal axis is either  $\langle 010 \rangle$  or  $\langle 001 \rangle$ , while those corresponding to the left packet correspond to “parallel” centres where the principal axis is  $\langle 100 \rangle$



in some detail the local geometry related to a *particular* impurity. In the case of transition-metal impurities in insulators good information on the local structure around the impurity is provided by magnetic resonance techniques thanks to the observation of hyperfine interaction from unpaired electrons with nearest nuclei, shortly called superhyperfine [130].

The power of the electron paramagnetic resonance (EPR) technique for proving that the  $\text{Ni}^{2+}$  ion in the  $\text{CaF}_2$  lattice is not placed at the centre of the cube but moves off-centre (Fig. 1) [120, 121] is well illustrated in Fig. 2. Let us assume that the  $\text{Ni}^{2+}$  impurity is surrounded by a number,  $N_L$ , of chemically equivalent  $\text{F}^-$  ions (nuclear spin for  $^{19}\text{F}$  is  $I = 1/2$ ) which are also magnetically equivalent for a given orientation of the magnetic field,  $\mathbf{H}$ . The number of superhyperfine lines is just equal to  $2IN_L + 1$ , thus reflecting *directly* the number of ligands [120, 121, 130]. According to this simple reasoning, if  $\text{Ni}^{2+}$  is placed at the centre of the cube and  $\mathbf{H}$  is parallel to one of the three  $C_4$  axes, then  $N_L = 8$  and thus nine superhyperfine lines should be observed. As shown in Fig. 2 the number of superhyperfine lines detected experimentally for  $\text{CaF}_2 : \text{Ni}^{2+}$  is however equal only to five, a fact consistent with a number of equivalent ligands equal to four. This key experimental result thus supports the off-centre motion of  $\text{Ni}^{2+}$  along  $\langle 001 \rangle$  type directions (Fig. 1). Aside from reaching this relevant conclusion a detailed analysis of the experimental superhyperfine tensor allows one to get a reasonable estimation of the distance between the final position and the centre of the cube [121]. Similarly to the results displayed in Fig. 2, the off-centre motion undergone by  $\text{Cu}^{2+}$ ,  $\text{Ag}^{2+}$  or  $\text{Fe}^{3+}$  impurities in  $\text{SrCl}_2$  has been supported by the observation of 13 superhyperfine lines consistent with a nuclear spin  $I = 3/2$  for the two isotopes of chlorine [65–68, 120–125]. In the domain of off-centre displacements it is crucial to be sure that the instability has a spontaneous character and thus it is not driven by the presence of another defect close to the impurity. Relevant information on this issue can be derived through the electron nuclear double resonance (ENDOR) technique which is able to explore *beyond* the first neighbours shell [130]. In the ENDOR study carried out on  $\text{CaF}_2 : \text{Ni}^{2+}$  [121] and  $\text{SrCl}_2 : \text{Fe}^{3+}$  [124] no evidence of a close defect has been encountered. The power of magnetic resonance techniques is reduced when ligands have zero nuclear spin such as it happens for  $^{16}\text{O}$ . However, in these cases an

anisotropic  $\mathbf{g}$  tensor and the existence of a zero field splitting (for ions with  $S > 1/2$ ) point out that the local symmetry around the impurity is not cubic [126–128]. On these basis, a recent study carried out on  $\text{KTaO}_3 : \text{Fe}^+$  put forward that  $\text{Fe}^+$  is not at the  $\text{K}^+$  site but experiences an off-centre motion along  $\langle 001 \rangle$  directions [129].

The existence of an off-centre motion for  $nd^{10}$  ions like  $\text{Cu}^+ (n = 3)$  [57–62, 131–137] or  $\text{Ag}^+ (n = 4)$  [138–148] in alkali halides and  $\text{CaF}_2$  has also been widely investigated. Although these ions are not paramagnetic in the ground state they exhibit some optical absorption bands in the near UV where the host lattice is transparent [57–60, 133, 137, 138]. Thus absorption in the optical domain is a selective tool for exploring  $nd^{10}$  ions. Despite this fact, the optical absorption technique provides with less detailed information on the local geometry around the impurity. In particular the interaction of electronic excited states with local and lattice vibrations gives rise to bandwidths of about  $1,000 \text{ cm}^{-1}$  at room temperature which precludes the observation of any hyperfine splitting. For this reason in the case of  $nd^{10}$  ions placed in cubic lattices an evidence, though indirect, on the off-centre motion can be reached from the integrated intensity of broad bands associated with a  $nd^{10} \rightarrow nd^9(n+1)s$  transition [57–60, 133, 137, 138]. If the local symmetry is cubic that transition is parity forbidden while such a selection rule is broken when the ion moves off centre and thus the local symmetry is reduced. In the latter case the  $nd^{10} \rightarrow nd^9(n+1)s$  transition becomes allowed for the electric dipole selection rules and the oscillator strength, directly related to the integrated intensity, is essentially independent on the temperature. By contrast, if the  $nd^{10}$  ion remains on-centre the oscillator strength is borrowed from the vibronic coupling involving both odd excited states and odd vibrational modes. Calling  $Q_u$  and  $\nu_u$  the normal coordinate and frequency of such a mode the oscillator strength depends on the thermal average  $\langle Q_u^2 \rangle$  and thus grows linearly with the temperature provided  $k_B T \gg h\nu_u$ . According to this reasoning, if the experimental integrated intensity is temperature independent it can be concluded that ions have moved off-centre but it is hard to know the actual magnitude of the motion [137].

A selective tool to study the local structure around an impurity is the Extended X-ray Absorption Fine Structure (EXAFS) spectroscopy. Despite this fact, only the work of Emura et al. on  $\text{Cu}^+$ -doped  $\text{NaCl}$  [149] and  $\text{NaBr}$  [150] has, to our knowledge, employed this technique in the field of off-centre impurities in insulating materials. In contrast with magnetic resonance techniques, EXAFS can also be used to explore non-paramagnetic impurities provided they can absorb X-rays, a fact that excludes light elements like Li or C. By contrast, EPR is better to work with low impurity concentrations below about 50 ppm and also when different oxidation states of the same element (for instance,  $\text{Fe}^{3+}$  and  $\text{Fe}^+$  [151]) are simultaneously present in a given sample.

Let us say a few words on non-selective techniques which have been employed in the study of  $\text{Li}^+$  systems [93, 152]. If this impurity moves off-centre in an alkali halide lattice the pair formed by the positive vacancy and the  $\text{Li}^+$  ion gives rise to an electric dipole,  $\mathbf{p}$ . It is well known that *free* dipoles under an applied electric field,  $\mathbf{E}$ , tend to place  $\mathbf{p}$  parallel to  $\mathbf{E}$  while thermal disorder is opposed to this effect. For this reason, if the average value of  $\mathbf{p}$  at a given temperature is designated by

$\langle \mathbf{p} \rangle$ , the  $|\langle \mathbf{p} \rangle|$  value increases when temperature is reduced following a Curie-Debye law. Thus, the existence of free dipoles gives a supplementary contribution to the dielectric constant which is temperature dependent. It is worth noting that this situation can not always be applied to the case of dipoles in insulating lattices where they are *not necessarily free* for reorienting following the applied external field,  $\mathbf{E}$ . In other words when the dipoles are trapped in a deep well and thus they are not able to jump to equivalent positions they can not be detected through dielectric constant or ionic thermocurrent measurements. Even in the case when reorientation takes place, one should not forget that these techniques give information on *all* formed dipoles. In particular, the presence in the samples of unwanted impurities requiring charge compensation leads to the formation of dipoles with the associated vacancy. More details on non-selective techniques can be found for instance in the works by Deigen and Glinchuk [152] and Bridges [93].

### 3 PJT Instabilities of Monoatomic Impurities in Solids: Survey of Experimental Results

Dipolar instabilities of impurities in solids were discovered in 1965 by Lombardo and Pohl in  $\text{Li}^+$ -doped KCl [49]. Since then, a large amount of off-centre and on-centre instabilities of monoatomic impurities in insulator and semiconductor materials have been reported. In many cases the impurity centres are not well characterized and the observed instabilities could be due to close defects. In this article we only consider centres with spontaneous instabilities driven by PJT mechanisms. An exhaustive review of all these centres is beyond the scope of this report and we have selected representative examples based on the authors' interest. Some early reviews can be found in [93, 152, 153].

#### 3.1 Off-Centre $\text{Li}^+$ Ions in Alkali Halides

In 1965 Lombardo and Pohl observed an electrocaloric effect in  $\text{Li}^+$ -doped KCl [49] suggesting that the small  $\text{Li}^+$  ion might not be stable at the normal lattice site but they would be sit off-centre in the cage of the nearest neighbours, thus leading to a dipole moment of about  $1.14 \text{ eÅ}$  which can change its orientation. Further determinations of the dipole moment were obtained from electric-field changes of the specific-heat anomaly [50], far-infrared absorption [51, 52] and from paraelectric resonance [53, 54]. The dipole moment of the  $\text{Li}^+$  ion is equal to zero for the stationary tunneling states, the impurity being equally distributed between the potential wells. The orientation of the dipoles was investigated by measurements of the sound velocity [55] and nuclear magnetic resonance (NMR) [56] showing that  $\text{Li}^+$  in KCl is displaced in a  $\langle 111 \rangle$  direction and thus eight equilibrium positions exist.

A great number of experiments have been carried on  $\text{Li}^+$  impurities in different alkali halide lattices. However, only three other systems have shown any indication of off-centre behaviour,  $\text{Li}^+$ -doped NaCl, RbCl and KBr lattices (Table 1). Considering the case of  $\text{KBr}:\text{Li}^+$ , early paraelectric cooling [154], infrared (IR) absorption [155] and specific heat [156] measurements did not indicate off-centre behaviour. However, later IR measurements in  $\text{KBr}:\text{LiBr}$  alloys observed a 100% shift of the Li-activated KBr resonant mode, coherent with an incipient instability associated with low-lying modes [157]. New IR measurements under electric field and stress [51] were interpreted as due to an off-centre  $\langle 111 \rangle$  instability with a low-barrier-potential well. Similar conclusions were obtained by Narayanamurti and Pohl [91] from paraelectric resonance spectra, but the orientation of the dipole appeared more consistent with a  $\langle 110 \rangle$  model. Also IR measurements under stress by Zoller et al. [158] and sensitive paraelectric resonance measurements by Russel and Bridges [159] and Ready et al. [160] indicate a  $\langle 110 \rangle$  model although it could not explain all data. Finally Greene and Sievers [161] performed a systematic study of the paraelectric modes with far-IR Fourier transform technique, showing that the spurious satellite modes reported by Bridges et al. [158, 159] are due to  $\text{Li}^+$  pairs. In the case of  $\text{NaCl}:\text{Li}^+$ , Estle and Carnes [162] reported the observation of paraelectric resonance, but no electrocaloric effect has been observed in this system [163]. Moreover, IR absorption under an external electric-field by Russell and Bridges [164] show strong paraelectric character inconsistent with a  $\langle 111 \rangle$  model, similar a  $\text{KBr}:\text{Li}^+$ . In  $\text{RbCl}:\text{Li}^+$ , experiments with electrocaloric techniques [163, 165] detected no paraelectric behaviour. However, from dielectric measurements at low temperatures under hydrostatic pressure up to a 7 kbar Thormer and Lüty suggested

**Table 1** Summary of experimental information for  $\text{Li}^+$ ,  $\text{Cu}^+$  and  $\text{Ag}^+$  impurities in alkali halide lattices. All lattices present rock salt structure except CsCl and CsBr that have CsCl-type structure. *Italic letters* indicate a doubtful assignment

Lattice	$\text{Li}^+$	$\text{Cu}^+$	$\text{Ag}^+$
NaF	–	On-centre	–
KF	–	<i>On-centre</i>	–
LiCl	–	On-centre	–
NaCl	<i>Off-centre <math>\langle 110 \rangle</math></i>	<i>On-centre</i>	On-centre
KCl	Off-centre $\langle 111 \rangle$	Deep off-centre $\langle 111 \rangle$	On-centre
RbCl	<i>Deep off-centre <math>\langle 111 \rangle</math></i>	Off-centre	Shallow off-centre $\langle 110 \rangle$
LiBr	–	–	–
NaBr	–	Shallow off-centre $\langle 111 \rangle$	–
KBr	<i>Off-centre <math>\langle 111 \rangle</math></i>	Deep off-centre $\langle 111 \rangle$	On-centre
RbBr	–	Off-centre	Shallow off-centre $\langle 110 \rangle$
NaI	–	Deep off-centre	–
KI	–	Off-centre	On-centre+off-centre
RbI	–	Off-centre	Deep off-centre $\langle 111 \rangle$
CsCl	–	–	Off-centre $\langle 110 \rangle$
CsBr	–	–	Deep off-centre $\langle 111 \rangle$

[166] that an enhanced off-centre displacement can lead to drastic decreases in the dipole mobility so that reorientation rates may freeze in at rather high temperatures like classical dipoles.

Computations of minimum-energy configurations for some off-centre systems were first carried out on the basis of polarizable rigid-ion models, mainly devoted to  $\text{KCl}:\text{Li}^+$  [95, 167–169]. Van Winsum et al. [170] computed potential wells using a polarizable point-ion model and a simple shell model. Catlow et al. used a shell model with newly derived interionic potentials [171–174]. Hess used a deformation-dipole model with single-ion parameters [175]. At the best of our knowledge, only very limited ab initio calculations (mainly Hartree-Fock or pair potential) have been performed on these systems [176, 177].

Concerning the microscopic origin of the local off-centre instabilities, most common explanations are based on steric effects (differences of ionic radii and/or electrostatic effects) [94, 100, 110, 112, 178] but it is not satisfactory because there are many exceptions to this rule. For example, it can be observed in Table 1 that  $\text{Li}^+$  remains on-centre in  $\text{NaCl}$ ,  $\text{NaBr}$ ,  $\text{KBr}$  and  $\text{RbCl}$  lattices despite the smaller size of the impurity with respect to the substituted cation. Qualitative PJT models have been proposed by several authors [20, 110–113] considering the admixture of the ground state with different excited states. It should also be noted that a model based exclusively on size properties would always provide the same kind of distortion, i.e. in the  $\langle 111 \rangle$  direction and could not be able to explain that  $\text{Li}^+$  goes in  $\langle 111 \rangle$  or  $\langle 110 \rangle$  directions. We believe that this can only be explained taking into account the chemical bond like in PJT models.

### 3.2 Off-Centre $\text{Cu}^+$ and $\text{Ag}^+$ Impurities in Alkali Halides

A second group of off-centre cation systems is formed by  $\text{Cu}^+$  and  $\text{Ag}^+$  ions ( $d^{10}$  configuration) in alkali halides. On the basis of the ensemble of experimental results (Table 1)  $\text{Cu}^+$  ion is not at the on-centre position at low temperatures (Table 1) in  $\text{NaCl}$ ,  $\text{KCl}$ ,  $\text{RbCl}$ ,  $\text{NaBr}$ ,  $\text{RbBr}$ ,  $\text{KBr}$ ,  $\text{NaI}$ ,  $\text{KI}$  and  $\text{RbI}$  lattices. The best understood system is  $\text{KCl}:\text{Cu}^+$ , where optical absorption [131–133], ionic thermocurrent (ITC) [134], magnetic circular dichroism (MCD) [135], lifetime [136] and two photon spectroscopy [134, 137] measurements have shown the characteristics of  $\langle 111 \rangle$ -oriented  $\text{Cu}^+$  dipoles at higher temperatures. This effect, however, was found [133] to “freeze-in” at about 65 K, yielding an Arrhenius-type expression for the dipole relaxation time with activation energy of 0.155 eV. This is in agreement with the negative electrocaloric measurements at 4 K [165]. Haneda et al. [135] found that diffusion coefficients of the  $\text{Cu}^+$  cation in  $\text{NaCl}$  and  $\text{KCl}$  lattices exceed by three or four orders of magnitude the corresponding self-diffusion coefficients in the intrinsic temperature regions. This fast diffusion has been explained as due to the noncentral position of the impurities [136].

In the case of  $\text{Ag}^+$  ions, a  $\langle 111 \rangle$  off-centre distortion was considered in  $\text{Ag}^+$ -doped  $\text{RbCl}$  from the temperature dependence of the UV absorption spectrum [138] and later confirmed by electrocaloric [139] and paraelectric cooling [53] measurements as well as calculations by means of a polarizable-ion model [140]. However, IR results were not compatible with a  $\langle 111 \rangle$  model but could be explained by a  $\langle 110 \rangle$  displacement [141]. This model was confirmed by measurements of the electrocaloricism of UV absorption [142] and UV absorption under stress [143]. Dielectric constant [132], optical absorption [132] and paraelectric resonance [144] measurements under hydrostatic pressure have allowed observing a rapid transition from off- to on-centre near 1.35 kbar, a “localized analog” to pressure-induced displacive phase transition in ferroelectrics. From optical absorption measurements it has also been concluded that  $\text{Ag}^+$  presents a shallow off-centre distortion for  $\text{NaBr}$  [132] while the displacements are along  $\langle 110 \rangle$  in  $\text{RbBr}$  with reorientation by  $90^\circ$  tunneling processes at  $T < 5$  K and classical thermally activated reorientation at higher temperatures [139]. However, an on-centre position was suggested for  $\text{KBr:Ag}^+$  [138].

The anomalous temperature dependence of the far IR spectrum and dielectric constant of  $\text{KI:Ag}^+$  has been interpreted considering two inequivalent elastic configurations simultaneously available to the defect-lattice system [145–147]. At low temperatures the  $\text{Ag}^+$  ion is on-centre and resonant mode absorption is observed in the far IR [145–147]. When the temperature is increased a second elastic configuration which has an energy about 24 K above the ground state becomes populated [145–147]. The large increase in the defect contribution to the dielectric constant indicates that the  $\text{Ag}^+$  ion is off-centre in this second elastic state. An  $\langle 111 \rangle$  off-centre configuration has also been suggested for  $\text{RbI:Ag}^+$  from the behaviour of the UV absorption under stress [148]. The observed freezing-in of dipole reorientation around 27 K indicated deep off-centre wells (barrier height about 50 meV) with small mobility of  $\text{Ag}^+$  ions. It is worth noting (Table 1) the increasing off-centre displacements (and decreasing mobility of dipoles) of  $\text{Ag}^+$  and  $\text{Cu}^+$  ions along  $\text{RbCl} \rightarrow \text{RbBr} \rightarrow \text{RbI}$  series, while  $\text{Li}^+$  ions presents the opposite trend in the same series. It has been suggested [148] that the sizeable quadrupole deformability of  $\text{Ag}^+$  and  $\text{Cu}^+$  ions might be responsible of this behaviour.

### 3.3 Other Off-Centre Impurities in Alkali Halides

$\text{NaBr:F}^-$  is the only system where a monoatomic anion has been found to have off-centre distortions. From paraelectric cooling [154, 165], dielectric susceptibility [165], specific heat [165], NMR [179, 180] and nuclear magnetic double resonance (DNMR) [112] measurements it has been well established that  $\text{F}^-$  experiences a  $\langle 110 \rangle$  distortion with tunneling at  $T < 15$  K and thermal activation above.

The existence of some off-centre neutral atoms in alkali halides has been suggested in connection with singularities of the EPR spectra. EPR spectra of  $\text{Cu}^0$  ( $4s^1$ ) atoms entering cationic sites of  $\text{KCl}$  and  $\text{RbCl}$  lattices show pronounced temperature

dependence indicating an  $\langle 111 \rangle$  off-centre position of the Cu atom at low temperatures [181, 182]. The observed linewidth and hyperfine constant increase with temperature of  $\text{Ag}^0$  ( $5s^1$ ) atoms in anionic sites of KCl, at  $T < 100$  K, has also been explained by a  $\langle 111 \rangle$  distortion [183, 184]. A similar model has been suggested for  $\text{Mn}^0$  ( $3d^5 4s^2$ ) in NaCl [185, 186]. However, the off-centre movement of the  $\text{Cu}^0$  atom in KCl at lower temperatures has been later reanalyzed as a local second-order phase transition, indicating that  $\text{Cu}^0$  is shifted about  $0.69 \text{ \AA}$  toward one of the  $\text{Cl}^-$  ions in the  $\langle 100 \rangle$  direction [187].

Of the various  $s^2$  ions (e.g.  $\text{Ga}^+$ ,  $\text{In}^+$ ,  $\text{Tl}^+$ ,  $\text{Sn}^{2+}$ ,  $\text{Pb}^{2+}$ ,  $\text{Ge}^{2+}$ ) which have used for doping potassium halide crystals, the  $\text{Ge}^{2+}$  ion presents unique properties. The off-centrality of the  $\text{Ge}^{2+}$  ions in KCl, KBr and KI lattices has been suggested from optically detected magnetic resonance (ODMR) data and the temperature dependence of the optical absorption and luminescence spectra [188–190]. It is worth nothing that a lot of work is being performed on  $s^2$ -based ferroelectric materials in order to get coexistence of magnetism and ferroelectricity (multiferroic). Examples include  $\text{BiFeO}_3$ ,  $\text{BiMnO}_3$  and  $\text{PbVO}_3$  materials, where the A-site cation ( $\text{Bi}^{3+}$ ,  $\text{Pb}^{2+}$ ) has a stereochemically active  $6s^2$  lone-pair which causes the Bi  $6p$  (empty) orbital to come closer in energy to the  $2p(\text{O})$  orbitals. This leads to hybridization between the  $6p(\text{Bi})$  and  $2p(\text{O})$  orbitals and drives the off-centering of the cation towards the neighboring anion resulting in ferroelectricity [191–195].

In 1985 Badalyan et al. [196] reported the first-ever observation of the temperature dependence of the configuration of energy minima of a local centre. EPR measurements performed on  $\text{Mn}^+$  ( $3d^5 4s$ ) centres in KCl in the 300–4 K temperature range revealed a sequence of two local first-order phase transitions, not appearing in the pure KCl lattice, lowering the local symmetry from  $O_h \rightarrow C_{4h} \rightarrow C_{3v}$  in the course of the cooling. Near the transitions between phases, the EPR spectra corresponding to different phases coexist. The microscopic origin of these local phase transitions has recently been explained assuming a PJT effect involving a soft quasi-local vibration [41].

### 3.4 Off-Centre Impurities in Alkali-Earth Oxides

Alkaline-earth oxide host lattices are isostructural with the alkali halides, and so similar off-centre displacements might be expected to occur in suitably doped crystals. However, an important difference is that the alkaline earth oxides generally accommodate divalent rather than monovalent impurities, with the advantage for studies of off-centre effects that divalent transition-metal cations can be studied by spectroscopic techniques. The earliest identification of an off-centre displacement in the alkaline earth oxides is for the case of  $\text{BaO}:\text{Mn}^{2+}$ , for which Sochava et al. [197] found an EPR spectrum of trigonal symmetry about a  $\langle 111 \rangle$  axis below  $\sim 140$  K, but a motionally averaged, isotropic spectrum above 250 K. The authors explained these results by postulating off-centre potential minima along  $\langle 111 \rangle$  directions, with adjacent minima being separated by a potential barrier of  $\sim 0.04$  eV. A similar



situation to  $\text{BaO:Mn}^{2+}$  was found by Krylov and Sochava for  $\text{Ni}^{2+}$ -doped SrO [198]. In the cases of  $d^9$  ions  $\text{Cu}^{2+}$ - and  $\text{Ni}^{2+}$ -doped SrO Sochava et al. have found [199, 200] that the impurities are also shifted along  $\langle 111 \rangle$  directions but the symmetry of separate minimum is lower than  $C_{3v}$  ( $C_s$  and  $C_1$ , respectively) due to the additional tetragonal deformation of the off-centre ion closest environment caused by static JT effect in the  $^2E$  ground state. Also Sochava et al. [201, 202] reported that the EPR spectrum of  $\text{SrO} : \text{Co}^{2+}$  shows the presence of a  $C_{2v}$  centre, tentatively identified as arising from an off-centre motion of  $\text{Co}^{2+}$  along a  $\langle 110 \rangle$  direction. However, later optical absorption, EPR, MCD [203] and visible and IR absorption [204] measurements showed that the dominant EPR spectrum in these samples displayed trigonal symmetry about a  $\langle 111 \rangle$  axis. EPR spectra of  $\text{Fe}^{2+}$  and  $\text{Fe}^{3+}$  ions in single crystals of SrO have been reported by several authors [205, 206], leading to off-centre displacements in  $\langle 110 \rangle$  and  $\langle 111 \rangle$  directions, respectively. Edgar and Haider [205] indicated that these experimental observations are in general agreement with the intuitive notion that the instability of a substitutional transition metal ion in the alkaline earth oxides with respect to off-centre motion depends upon the difference of host and impurity cation radii. Thus the larger ions,  $\text{V}^{2+}$  and  $\text{Mn}^{2+}$ , are stable at on-centre positions in SrO, whereas the smaller ions,  $\text{Co}^{2+}$  and  $\text{Cu}^{2+}$ , undergo off-centre displacements.

All investigated off-centre ions in alkali-earth oxide lattices are in states localized in separate wells of the multiwell potential, the situation being fundamentally different from the tunneling states of  $\text{Li}^+$  in KCl. Hopping motion of off-centre ions in multiwell potential reveals itself in two kinds of experiments [199]: (1) arising of preferential orientation of off-centre displacements under the action of external electric field; (2) motional narrowing of the EPR spectrum, i.e., transformation of initial spectrum into a new one, exhibiting higher symmetry. It is worth noting that the *localization* of the ion in separate wells essentially arises from *random strains* induced by defects which are *inevitably* present in any real crystal. The low symmetry detected by EPR spectra at low temperatures is thus related to the form displayed by the random strains at a given lattice point. The key role played by random strains in JT and PJT phenomena was firstly emphasized by Ham [207].

### 3.5 Off-Centre Impurities in Fluorites

Fluorite crystals  $\text{MF}_2$  ( $M = \text{Ca, Ba, Sr, Cd, Pb}$ ) have a simple cubic structure in which the divalent cation  $M$  is surrounded by eight fluorine anions located at the corners of the unit cell. Therefore, these materials provide the possibility of investigating impurity ions in eightfold coordination, when the ions are substituted on cation sites. Moreover, the fluorine nucleus has relatively large nuclear magnetic moment and  $I = 1/2$ . This circumstance makes easy the observation of the superhyperfine interaction in EPR spectra of transition-metal impurities in fluorides, a fact which allows to get a good knowledge on the local geometry. Various divalent and trivalent ions of iron group elements and rare-earth elements have been introduced



into fluorite lattices to study the local structure of the host lattice and the associated dynamics.

Properties of hydrogen impurities in fluorite crystals have been extensively studied from the 1960s. Interstitial hydrogen centres  $H_i^0$  were formed in hydrolysed  $SrF_2$  and  $BaF_2$  crystals by X-irradiation [208–211]. These defects are paramagnetic and can be studied by EPR. In order to explain the anomalous temperature dependence of the hyperfine splitting parameters [208, 209] Hodby [209] suggested that charge transfer  $2p(F)$  orbitals are mixed in the ground state. Latter, from electron spin echo decay results it was suggested [210, 211] that the  $H_i^0(I)$  centre consists in a H atom in a  $\langle 100 \rangle$  off-centre position which reorients among the six equivalent minima by  $\langle 100 \rangle$  and  $\langle 110 \rangle$  jumps. Interestingly, although the lattice parameter is smaller in  $SrF_2$  than in  $BaF_2$ , it follows from the experimental data that the displacements are larger in  $SrF_2$  than in  $BaF_2$ , about 0.1 and 0.05 Å, respectively [211].

Big off-centre motions ( $\approx 1$  Å) have been reported from EPR measurements performed on JT  $d^9$  ( $Ni^{2+}$ ,  $Cu^{2+}$  or  $Ag^{2+}$ ) [47, 65–67, 120, 121] and  $d^4$  ( $Cr^{2+}$ ) [212–214] impurities in some fluorite type crystals (Table 2). Experimental results collected in Table 2 again indicated that off-centre instabilities are not due to size effects. In fact,  $Ni^{2+}$  moves off-centre in the three  $CaF_2$ ,  $SrF_2$  and  $SrCl_2$  lattices [68, 120, 121], while the smaller isoelectronic  $Cu^{2+}$  ion remains on-centre in  $CaF_2$ , the fluorine ligands suffering an orthorhombic  $T_{2g} \otimes (t_{2g} + e_g)$  JT distortion [47, 48, 68].

A relatively great number of papers have been reported for on  $Mn^{2+}$  and  $Fe^{3+}$  centres ( $d^5$  ions with  $^6S$  ground state) on fluorite crystals. With the possible exception of  $Fe^{3+}$  in  $BaF_2$  [151], the two  $d^5$  impurities remain on-centre. Nevertheless, Roelfsema and den Hartog [215, 216] have investigated the effect of an applied

**Table 2** Summary of experimental information and DFT calculations on the on-centre/off-centre character for several impurities in fluorite type lattices [19, 41, 48, 122]. The ground state of cations in hexahedral geometry is shown. When available the experimental or DFT-calculated value of the equilibrium coordinate,  $Z_0$ , is also given in parenthesis. Experimental values of  $a/4$  ( $a$  is the lattice parameter) are also given under each host lattice. All distances are given in pm units

Impurity	Ground state	$CaF_2$	$SrF_2$	$BaF_2$	$SrCl_2$
$Ni^{2+}$	$^2T_{2g}(3d^9)$	118 Off-centre (107)	126 Off-centre (121)	155 Off-centre –	151 Off-centre (157)
$Cu^{2+}$	$^2T_{2g}(3d^9)$	On-centre (0)	Off-centre (33)	Off-centre –	Off-centre (106)
$Ag^{2+}$	$^2T_{2g}(3d^9)$	On-centre (0)	On-centre (0)	Off-centre –	Off-centre (158)
$Fe^{2+}$	$^4A_{2g}(3d^7)$	– –	– –	– (122)	Off-centre (131)
$Cu^{+}$	$^1A_{1g}(3d^{10})$	Off-centre	–	–	–
$Cr^{2+}$	$^5X(3d^4)$	On-centre	On-centre	Off-centre	Off-centre
$H_i^0$	$^2A_{1g}(1s^1)$	On-centre	Off-centre (10)	Off-centre (5)	–

electric field on the EPR signal of the cubic  $\text{Mn}^{2+}$  centre in  $\text{SrCl}_2$ . Using the polarizable point-ion model they have shown that the potential energy curves for displacements of the  $\text{Mn}^{2+}$  impurity along the  $\langle 100 \rangle$ ,  $\langle 111 \rangle$  and  $\langle 110 \rangle$  directions are flat within 0.01 eV over distances of 0.3, 0.5 and 0.4 Å, respectively. However, electric field effect experiments on  $\text{BaF}_2 : \text{Mn}^{2+}$  gave the result that in this system the  $\text{Mn}^{2+}$  ion cannot be shifted by the external electric field [216]. This fact represents a new argument against the idea that the difference of the ionic radii between the impurity ion and the replaced host ion is not the only criterion for the possibility of an off-centre movement. From the experimental evidence that the non-JT  $\text{Mn}^{2+}$  ( $d^5$ ) ion remains on-centre in the same lattices [215,216] some authors [217] have tried to relate the off-centre motion with the JT effect. Nevertheless, recent experiments [123,124] carried out on  $\text{SrCl}_2$  containing the monovalent  $\text{Fe}^+$  ( $d^7$ ) ion strongly suggest that the impurity undergoes a big off-centre motion along  $\langle 001 \rangle$  type directions, with no evidence of any close defect to  $\text{Fe}^+$  impurity [124]. As  $\text{Fe}^+$  in  $\text{SrCl}_2$  exhibits a high spin value  $S = 3/2$  its ground state in a perfect cubal symmetry would be  $^4A_2(e_g^4 t_{2g}^3)$  with *no orbital degeneracy*, a situation which is thus different to that of  $d^9$  ions in fluorite type lattices [125].

### 3.6 Off-Centre Impurities in Oxoperovskites

As it was pointed out in the Introduction, the problem of the coexistence of displacive and order-disorder phenomena at the ferroelectric phase transitions of  $\text{BaTiO}_3$  has met growing interest in recent time. Strong support of the order-disorder model comes 30 years ago from EPR measurements performed on  $\text{Mn}^{4+}$ -,  $\text{Cr}^{3+}$ -, and  $\text{Fe}^{3+}$ -doped  $\text{BaTiO}_3$  [218–222] because in the low-temperature rhombohedral phase it was observed that  $\text{Mn}^{4+}$ , which substitutes isovalent  $\text{Ti}^{4+}$  sites, is displaced off-centre by 0.14 Å along  $\langle 111 \rangle$  directions with a reorientational hopping with correlation times  $10^{-9}$ – $10^{-10}$  s.

In recent years, strong attention has been paid to the investigation of the behavior of microscopic dipole impurities in incipient ferroelectrics, also called quantum paraelectric, materials (as  $\text{SrTiO}_3$  or  $\text{KTaO}_3$ ) searching to induce phase transitions and other interesting properties. A lot of experimental and theoretical work has been performed on  $\text{Li}^+$ -doped  $\text{KTaO}_3$ . In 1974 Yacobi and Linz [223] carried out Raman and fluorescence measurements ion finding that substitutional  $\text{Li}^+$  ions gets spontaneously displaced along  $\langle 100 \rangle$  directions from the K site. The off-centre character of Li ions has also been indicated by electric susceptibility [224], NMR [225], dielectric relaxation, pyroelectricity, ultrasound and birefringence [224, 226] and photoconductivity [227] studies. Many shell models, semiempirical and *ab initio* calculations have also been performed on this system [228–231]. It is worth noting that impurity induced ferroelectricity has also observed in systems as  $\text{KTaO}_3 : \text{Nb}^{5+}$  [232] or  $\text{SrTiO}_3 : \text{Ba}^{2+}$  [233] where impurity ions are larger than the substituted host ions or nearly the same.

An important experimental problem studying paramagnetic impurity centres in oxide lattices is that magnetic resonance techniques do not always provide with a definite characterization of paramagnetic impurity centres partially due to the lack of superhyperfine structure coming from  $^{16}\text{O}$  nuclei. A conspicuous example showing the limitations of EPR technique in oxides concerns the axial iron centre observed in  $\text{KTaO}_3$ , where models of  $\langle 100 \rangle$  off-centre distortions of  $\text{Fe}^{+} (3d^7)$  ion replacing  $\text{K}^{+}$  [126, 127] and  $\text{Fe}^{5+} (3d^3)$  ion located at  $\text{Ta}^{5+}$  site [128] have been suggested. This puzzling problem will be considered in Sect. 7, showing the usefulness of *ab initio* calculations for clarifying this situation.

### 3.7 Off-Centre Impurities in Other Ionic Lattices

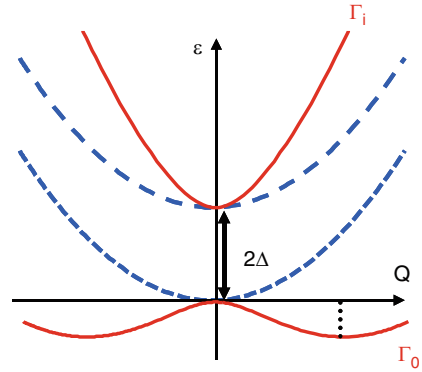
Many studies have been performed on optical properties of doped fluoroperovskite lattices searching for new tunable lasers. Dielectric-loss and ultrasonic measurements on  $\text{KZnF}_3 : \text{Li}$  have revealed that the  $\text{Li}^{+}$  impurity sits in a  $\langle 100 \rangle$  off-centre position approximately  $0.15 \text{ \AA}$  from a normal  $\text{K}^{+}$  site [234]. In the case of  $\text{Cu}^{+}$  in the cubic  $\text{KMgF}_3$  lattice, from the temperature dependence of the absorption spectra and from MCD measurements a clear indication of the off-centre configuration of  $\text{Cu}^{+}$  ion replacing a  $\text{K}^{+}$  ion was obtained [235].

Absorption, emission and polarized excitation spectra, as well as lifetimes, were measured for  $\text{Cu}^{+}$  ions in the hexagonal  $\text{RbMgF}_3$  lattice [236]. From these measurements it was concluded that  $\text{Cu}^{+}$  enters in two different  $\text{Rb}^{+}$  sites of the hexagonal lattice, site I with  $D_{3h}$  symmetry (two equivalent  $\text{Mg}^{2+}$  ions at equidistant positions along the  $c$  axis) and site II with  $C_{3v}$  symmetry (a  $\text{Mg}^{2+}$  and a  $\text{Rb}^{+}$  as neighbours along the  $c$  axis). Moreover, it was suggested that  $\text{Cu}^{+}$  ion at site I is most likely in an off-centre configuration lowering the local symmetry from  $D_{3h}$  to  $C_{3v}$ . For  $\text{Li}^{+}$ -doped cubic  $\text{KZnF}_3$  fluoroperovskite dielectric-loss measurements have revealed [236] that the  $\text{Li}^{+}$  defect possesses an electric dipole moment and, therefore, it sits in an off-centre position approximately  $0.15 \text{ \AA}$  from a normal  $\text{K}^{+}$  site. Complementary ultrasonic measurements indicate [236] that  $\text{Li}^{+}$  constitutes a  $\langle 100 \rangle$  orthorhombic defect.

## 4 Pseudo Jahn–Teller Effect

Following the vibronic coupling theory [20] it has been proved that, for any molecule or solid which in principle possesses a centre of symmetry, the origin of the off-centre instability is always a PJT coupling of the ground state  $\Gamma_0$  (of energy  $E_0$ ) with excited states  $\Gamma_1$  (energy  $E_1$ ) of appropriate symmetry when the system is distorted along the normal mode represented by  $Q$  (Fig. 3). For simplicity we will consider here that all  $\Gamma_0$ ,  $\Gamma_1$  and  $Q$  are singlets, but the formulation is completely general. This mixing can easily be formulated using second-order perturbation

**Fig. 3** Schematic view of the PJT coupling between two singlet states separated by a gap  $2\Delta$  giving rise to an off-centre instability. *Dashed* and *solid lines* represent adiabatic surfaces before and after coupling, respectively, by a mode  $Q$



theory, where the energy is expanded around the (reference) equilibrium high symmetry configuration ( $Q = 0$ ) as

$$E(Q) = E_0 + \frac{1}{2}KQ^2 + \dots \quad (1)$$

Here,  $K$  is the force constant associated to the vibration represented by  $Q$ .  $K$  can be expressed as the sum of two terms

$$K = K_0 + K_v. \quad (2)$$

If we define  $W$  as the sum of the nuclear-electronic and nuclear-nuclear interactions of the potential energy operator, then the primary force constant,  $K_0$ , is

$$K_0 = \left\langle \Gamma_0 \left| \frac{\partial^2 W}{\partial Q^2} \right| \Gamma_0 \right\rangle \quad (3)$$

and  $K_v$  is the vibronic coupling contribution

$$K_v = 2 \sum_I \frac{|F_I|^2}{E_0 - E_I}, \quad (4)$$

where  $F_I = \left\langle \Gamma_0 \left| \frac{\partial W}{\partial Q} \right| \Gamma_I \right\rangle$  is the PJT coupling constant and the sum extends over all excited states,  $I$ .  $K_0$  is equal to the force constant that a system would have if the electron density was frozen to its value when  $Q = 0$ . According to Bersuker [20],  $K_0$  is always positive and represents the force opposing the distortion due to all electrons.  $K_v$  represents the contribution to the force constant partially reflecting the actual change of the electron density to adapt to the distorted geometry. For the ground state  $E_0 - E_1$  is always negative so  $K_v$  is negative. Since  $K_0 > 0$ , a necessary condition of instability is that the curvature of  $E(Q)$  at  $Q = 0$  is negative (Fig. 3), then  $K_0 < |K_v|$ .

Direct calculation of the vibronic coupling matrix elements involved in PJT models is mathematically not easy and requires explicit knowledge of the many excited states, which is difficult to obtain. The calculation can be greatly simplified assuming that the excited state wavefunction  $|\Gamma_I\rangle$  differs from the ground state one  $|\Gamma_0\rangle$  by just a one-electron excitation,  $\varphi_i \rightarrow \varphi_j$  [20]. In this case, we can approximate the force constant in state I by

$$K_I \approx K_0 + \sum_{i,j} (n_i^{(I)} - n_j^{(I)}) \frac{|\langle \varphi_i | dv/dQ | \varphi_j \rangle|^2}{\Delta_{ij}^{(I)}} = K_0 + \sum_{i,j} (n_i^{(I)} - n_j^{(I)}) K_v^{ij}, \quad (5)$$

where  $n_i^{(I)}$  is the population of orbital  $\varphi_i$  in state I,  $v$  is the interaction potential between one electron and the nuclei,  $\Delta_{ij}^{(I)}$  is the transition energy when one electron is taken from  $\varphi_i$  and placed in  $\varphi_j$ , and  $K_v^{ij}$  is the vibronic contribution to the force constant due to the coupling of orbitals  $i$  and  $j$ . What this formula tells us is that if one electron is excited from orbital  $a$  to  $b$ , which is vibronically coupled to the first, we would find that the force constant of the excited state has *increased* by  $2K_v^{ab}$ . This way, using (5) and calculating the force constants of the ground and excited electronic configurations we can find which orbitals are more involved in the distortion by checking when the force constant varies more strongly. Thus, using (5) we can consider approximately the influence of each electron independently on the nuclear framework and its dynamics, providing a more intuitive picture of the electronic processes involved in the distortion compared to the case when full multielectronic states are used. Moreover, an interpretation in terms of orbitals means that the results are transferable to systems with similar orbital schemes, something not easily done through full multistate calculations. A more detailed analysis of (5) and its consequences is given in [20, 237].

Vibronic interactions are *also* responsible for the JT effect which *may appear* when the ground state is orbitally degenerate. If the ground state wavefunctions are simply designated by  $|\Gamma_0, \mu\rangle$  (where the index  $\mu$  reflects the degeneracy) the JT effect is controlled to a good extent only by the  $\left\langle \Gamma_0, \mu \left| \frac{\partial W}{\partial Q} \right| \Gamma_0, \nu \right\rangle$  matrix elements related to the *linear* vibronic term  $Q \frac{\partial W}{\partial Q}$  in the Hamiltonian. For this reason when the JT effect takes place in a system with cubic symmetry the involved mode is *always* even, thus triggering an *on-centre* distortion of the system. Furthermore, in most cases, JT distortions involve changes in distance which are much smaller than interatomic ones [238]. For example, in the case of  $d^9$  impurities ( $\text{Cu}^{2+}$ ,  $\text{Ag}^{2+}$ ,  $\text{Ni}^{+}$ ) in sites with octahedral symmetry the distortion along the JT active  $e_g$  mode usually involves displacements not higher than 0.4 Å from the initial position [33, 35, 68, 70, 238]. It is worth noting here that displacements higher than 1 Å can happen for distortions driven by a PJT mechanism [65–68, 122, 125, 129].

It should be remarked here that the presence of a  $d^9$  ion at a cubic site does *not necessarily* mean that the observed distortion must be related to the JT effect. In fact, we can not forget that this possibility is always *in competition* with other distortions driven by a PJT effect involving an odd mode. For instance all  $d^9$  impurities in

SrCl<sub>2</sub> do not exhibit a JT distortion but exhibit an off-centre distortion driven by an odd  $t_{1u}$  mode [65–68, 122, 125]. Obviously this fact requires that: (1) The inequality  $|F_I|^2/(E_0 - E_I) > K_0$  is fulfilled; (2) The energy gain due to the off-centre distortion is higher than that for a JT involving an even mode. One realizes the importance of the first condition looking at experimental data of Cu<sup>2+</sup> and Ag<sup>2+</sup> impurities in CaF<sub>2</sub> where such a condition is not verified, a fact which thus allows developing a JT distortion. Additional discussion on this important issue is given in Sect. 6.

Although in the previous modelization of the PJT effect we have only considered one active vibrational coordinate  $Q$ , it is important to note that in most cases there are many normal modes that can couple the relevant electronic states. This is called the *multimode* problem. Nevertheless, in most of the problems described here a good approximation to the complete problem can be reached using the *interaction* mode [20], where the mode  $Q$  is written using a linear combination of all the active vibrations and takes the system from the high-symmetry configuration to the stable low-symmetry one. It must be noted that this approximation is only useful to describe equilibrium geometries and have some basic notions of the dynamics of the system. When other subtler properties are to be understood (see, for example, the BaF<sub>2</sub> : Mn<sup>2+</sup> problem, Sect. 7) models where individual modes and the intermode coupling is fully accounted for have to be used.

Finally, it is worth noting that the term “second-order JT effect” sometimes used [108, 195, 239, 240] instead of PJT effect may be misleading [20]: there are no first-order (JT) and second-order (PJT) effects, the two effects are described by two different and independent vibronic coupling constants, and the PJT effect may be very strong when the proper JT effect is zero.

## 5 Quantum Mechanical Calculations

The computational modelling of instabilities in doped materials is a very demanding field. On one hand, high precision calculations are needed for obtaining the small barriers and wells usually involved in these problems. On the other hand, calculations are expensive because it is necessary to simulate an impurity in a nearly infinite solid. In the case of diluted impurities in solids one could obtain all the band structure of the doped solid by means of periodic supercell calculations. However, this procedure is computationally very expensive because very large supercells have to be considered in order to avoid interaction between impurities. Moreover, many impurities are *charged* with respect to the ion they substitute producing strong long range interactions between supercells that in practice makes impossible the SCF convergence. So, most of the calculations of diluted impurities in insulators are performed using the cluster approximation, that is, dividing the system in two parts: (a) A quantum-mechanical cluster including the impurity and some shells of atoms of the lattice, that have to contain most of the active electrons of the impurity; (b) The perturbation from the rest of the lattice ions (embedding).

In the case of transition metal impurities  $M$  in ionic crystals electrons of the impurity are usually *localized* in the  $ML_n$  complex formed with the nearest neighbours or ligands. For this reason a calculation of the  $ML_n$  complex in vacuo at the experimental equilibrium geometry offers a reasonable first approximation for understanding electronic properties such as the spin-Hamiltonian parameters or the absorption maxima. However, for calculating the equilibrium geometry itself and all vibrational properties it is necessary to use greater clusters, including more atomic shells. Ideally the cluster size has to be increased until good convergence of properties is reached. With respect to the embedding, two different approximations have been used in the calculations performed in this work.

All systems analysed in Sects. 6, 7 and 8 have been explored by means of Density Functional Theory (DFT) calculations [241]. As it is well known, in this type of calculations accuracy is combined with relatively low computational cost when compared with highly correlated wavefunction-based calculations. All DFT calculations have been performed in its standard spin unrestricted and non-relativistic Kohn-Sham formalism [241]. Most calculations have been carried out using the Local Density Approximation (LDA) [242] or the Generalized Gradient Approximation (GGA) for the exchange-correlation functional [243,244] as implemented in the Amsterdam Density Functional (ADF) code [245]. Basis sets of the best quality in the ADF code have been employed. The cluster was embedded in a infinite array of point charges. Although this embedding procedure is only able to reproduce long-range interactions it is the main contribution to the embedding of clusters in the case of ionic solids.

Due to the shallow wells involved in some off-centre instabilities, the three parameter hybrid semiempirical B3LYP functional [246] implemented in Gaussian 98 [247] has also been used in shallow well cases. These calculations use the double zeta LANL2DZ basis, which employ Gaussian type orbitals and pseudopotentials to simulate the core electrons. Some semiempirical Self Consistent Charge Extended Hückel (SCCEH) calculations have also been performed in order to study the effect of the removal of some orbitals from the basis set on the off-center instabilities. More details about this method can be found in [248].

## 6 Off-Centre Impurities in Fluorite-Type Crystals: Microscopic Origin

EPR measurements performed on transition metal impurities in fluorite lattices indicate a very puzzling situation (Table 2). So, a  $3d^9$  cation as  $\text{Cu}^{2+}$  remains on-centre in the  $\text{CaF}_2$  lattice [249,250], while undergoes a small off-centre  $\langle 100 \rangle$  displacement ( $\sim 0.5 \text{ \AA}$ ) in  $\text{SrF}_2$  [47,249,251], and a huge displacement ( $\sim 1.35 \text{ \AA}$ ) in  $\text{SrCl}_2$  [65]. However, the isoelectronic  $\text{Ni}^+$  cation gives rise to off-centre  $\langle 100 \rangle$  displacements in all these lattices [120–122] (Fig. 1), although this monovalent ion has a *bigger size* than  $\text{Cu}^{2+}$ . Moreover, the  $4d^9$  cation  $\text{Ag}^{2+}$  remains on-centre in the  $\text{CaF}_2$  and  $\text{SrF}_2$  host lattices while only in  $\text{SrCl}_2$  such an impurity experiences

an off-centre  $\langle 111 \rangle$  instability [65–67, 252, 253]. Although some authors have postulated the JT effect as possible origin of the off-centre instability, the recent experimental evidence [123, 124] of off-centre  $\langle 100 \rangle$  distortion in  $\text{SrCl}_2 : \text{Fe}^+$  ( $3d^7$  configuration with *non-degenerate*  $^4A_2$  ground state) discards this hypothesis.

DFT calculations were performed on clusters of different size (from 21, Fig. 4, until 107 atoms) simulating  $\text{Ni}^{+}$ -,  $\text{Cu}^{2+}$ -,  $\text{Ag}^{2+}$ - and  $\text{Fe}^+$ -doped  $\text{MF}_2$  ( $M = \text{Ca}, \text{Sr}, \text{Ba}$ ) and  $\text{SrCl}_2$  lattices in order to reproduce these subtle phenomena and then to explain their microscopic origin. Results of Table 2 corresponds to LDA exchange-correlation functionals (GGA functionals lead to similar results) for  $\text{Ni}^+$  and  $\text{Fe}^+$  impurities, while the hybrid B3LYP functional was used for  $\text{Cu}^{2+}$  and  $\text{Ag}^{2+}$  centres where LDA and GGA functionals lead to poorer results [48].

In Fig. 5 the energy profile for the off-centre movement of the  $\text{Ni}^+$  impurity in  $\text{CaF}_2$  as a function of the displacement  $Z$  along a  $\langle 100 \rangle$  direction is displayed. In this process ligands are kept at the positions corresponding to their final (relaxed) values. It can be appreciated how an off-centre minimum of depth  $\Delta E = 0.19 \text{ eV}$  is predicted at the equilibrium value  $Z_0 = 1.07 \text{ \AA}$ . It can be also noted in this plot that  $(\partial E / \partial Z)_0 = 0$ , so indicating that in systems like  $\text{CaF}_2 : \text{Ni}^+$  the origin of the distortion is *not* the JT effect. From the results of Table 2 we can observe that the off-centre distortion (and also the well depth) increases for the same impurity when the lattice parameter of the host lattice increases. Moreover, distortions and

**Fig. 4** Cluster of 21 ions  $\text{CuL}_8\text{M}_{12}^{16+}$ , used to simulate the  $\text{Cu}^{2+}$ -doped  $\text{ML}_2$  ( $M = \text{Ca}^{2+}, \text{Sr}^{2+}$ ;  $L = \text{F}^-, \text{Cl}^-$ ) lattices

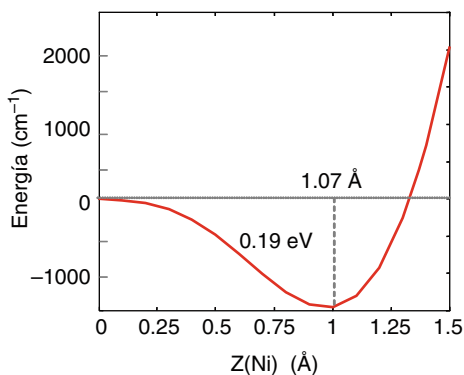
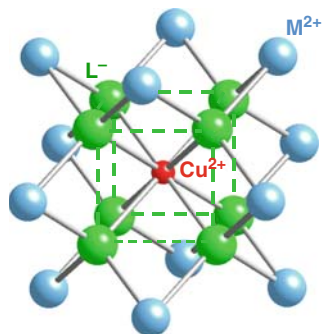


**Fig. 5** DFT-LDA calculated energy profile  $\text{CaF}_2 : \text{Ni}^+$  along the  $Z$  distortion



stabilization energies are in general larger for monovalent impurities like  $\text{Ni}^+$  than for divalent ones like  $\text{Cu}^{2+}$ .

As it was previously indicated, the driving force for all spontaneous off-centre instabilities is the PJT coupling of the ground state with excited states by means of odd vibrational modes. Following the PJT model explained in Sect. 4, the total energy along the distortion can be divided in two parts,  $\Delta E(Z) = \delta_0(Z) - \delta_v(Z)$ , where  $\delta_v(Z)$  and  $\delta_0(Z)$  represent the vibronic or bonding (force constant  $K_v$ , favouring the distortion) and repulsive ( $K_0$ , opposing) contributions, respectively.  $\delta_0(Z)$  term contains the repulsion between electronic cores that only plays a role when the ions are closely packed and, also, the electrostatic interaction between the impurity and the rest of the lattice [48], which is displayed in Fig. 6 for some systems. This potential allows understanding some experimental trends in Table 2. In particular, as the potential due to the lattice on the impurity decreases when the lattice parameter increases, the off-centre motion is favoured in large lattices as  $\text{SrCl}_2$ . On the other hand, increasing the ionic charge of the impurity gives rise to a greater lattice potential opposing the off-centre motion. However, we find that nominal charges seldom resemble real charges. Also, variation of the nominal charge of an ion has an important effect over the electronic structure and PJT coupling and we find that these phenomena are more relevant than the interaction of the ion's charge with the electrostatic potential of the rest of the lattice. In fact, the origin of the distortion is explained by the attractive term  $\delta_v(Z)$  coming from the PJT coupling of the ground state with excited states.

Calculations performed in  $\text{SrCl}_2 : \text{Fe}^+$  confirm that the instability of  $\text{Fe}^+$  is spontaneous despite the ground state  ${}^4\text{A}_2 (e_g^4 t_{2g}^3)$  has *no orbital degeneracy*, a situation which is thus different to that for  $d^9$  and  $d^4$  ions in fluorite type lattices. It is found that  $\text{Fe}^+$  performs a big excursion of 1.3 Å from the centre of the  $\text{FeCl}_8^{7-}$  cube to a position close to the centre of a  $\{001\}$  face. Despite this huge distortion the associated well depth is found to be only 0.28 eV, so

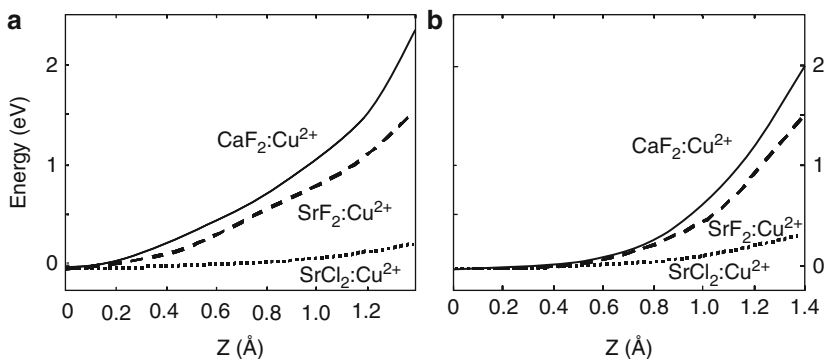


**Fig. 6** (a) Profiles of energy for the different systems for  $(xy)^{5/3}(yz)^{5/3}(zx)^{5/3}$  occupations as calculated in DFT-GGA. The curvature of the different curves represents the opposition that the lattice presents to the off-centre movement of the impurity. (b) Simple model representing the barrier through the potential generated by point charges located at lattice sites

indicating the subtle origin of the instability. The ground state corresponds to a  $a_1(3z^2 - r^2)^2 b_1(x^2 - y^2)^2 e(xz, yz)^2 b_2(xy)^1$  configuration, the  $b_2(xy)$  level lying  $\sim 1$  eV above  $e(xz, yz)$ , which is very close to  $b_1(x^2 - y^2)$  and  $a_1(3z^2 - r^2)$  orbitals. It is worth noting that in the  $^4A_{2g}$  ground state only the unpaired electron residing on the  $b_2(xy)$  orbital is responsible for the isotropic superhyperfine constant well detected experimentally [123, 124]. Indeed the overlap of a  $xz$  wavefunction of free  $\text{Fe}^+$  with  $3s$  wavefunctions of four top  $\text{Cl}^-$  ligands is rigorously zero when  $Z = a/4$ . By contrast, the  $b_2(xy)$  level would be empty if the ground state has  $S = 1/2$ .

At variance with what happens for JT distortions, off-centre displacements cannot be understood looking only to the half filled  $t_{2g}$  antibonding orbitals, being related *from the beginning* to modifications of involved wavefunctions as described by the PJT theory. The polarization of the electronic cloud through admixtures of  $3d(\text{Fe}^+)$  orbitals with deep fully occupied  $3p(\text{Cl}^-)$  as well as unoccupied  $4p(\text{Fe}^+)$  orbitals is found to play a key role, while the electrostatic field of the rest of the lattice  $V_C$  acts against the distortion. Searching to gain a better insight on this issue the orbital energy is portrayed (Fig. 7) as a function of  $Z$  for some relevant valence levels of the  $\text{FeCl}_8^{7-}$  complex. In addition to ligand levels, the evolution of antibonding  $t_{2g}$  levels which are partly filled is also depicted in Fig. 7. Under a  $C_{4v}$  symmetry there is a splitting between  $e(xz, yz)$  and  $b_2(xy)$  levels emerging from the antibonding  $t_{2g}$  in  $O_h$ . In Fig. 7 is also plotted the  $Z$ -dependence of unoccupied  $e(4p_x, 4p_y)$  orbitals arising from the  $4p$  shell of free  $\text{Fe}^+$ . It can be expected that when  $\text{Fe}^+$  moves significantly upwards bonding is established mainly with  $e$  and  $b_2$  orbitals of top ligands while the ionic negative charge of bottom ligands increases

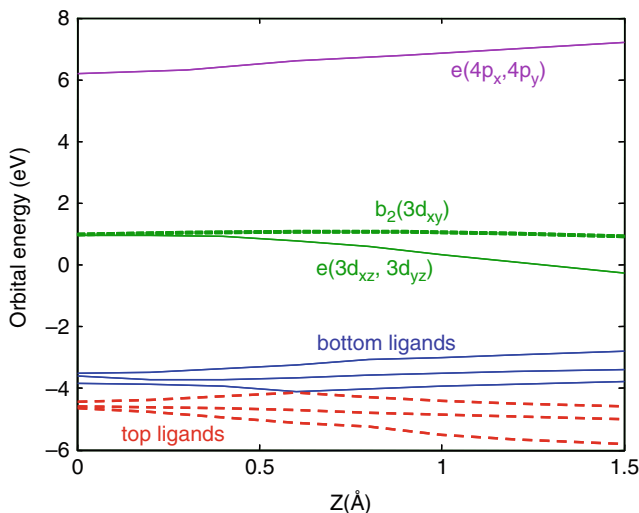


**Fig. 7** Energy profiles obtained from DFT calculations as a function of the distortion coordinate,  $Z$ , for the relevant orbitals of  $\text{SrCl}_2 : \text{Fe}^+$

by  $0.02e$ , as it is well reflected in the orbital energies variation of Fig. 7. It can be noticed in Fig. 7 that for  $Z > 0.5 \text{ \AA}$  the mainly top and bottom orbitals are separated. The former orbitals have a smaller energy than the latter ones as a result of being in the neighbourhood of the positive  $\text{Fe}^+$  ion. Moreover, as it could be anticipated, bonding effects appear to be more important on the top ligands than on the bottom ones. The energy variation of antibonding  $e(xz, yz)$  and  $b_2(xy)$  levels along the  $Z$  coordinate (Fig. 7) also reflects the influence of  $V_C(Z)$  upon the energy of such levels. It should be remarked that  $V_C(Z)$  acts against the motion of the positive iron ion as a whole but favours an energy decrease of mainly  $3d$  levels.

Together with the bonding-antibonding mechanism of occupied  $e$  and  $b_2$  levels, attention should be paid to the behaviour displayed by the *unoccupied*  $e(4p_x, 4p_y)$  orbitals in Fig. 7. It can firstly be noticed that the energy of such unoccupied orbitals increases following the distortion parameter  $Z$ . Moreover, this fact is accompanied by the energy decrease of other partly or fully occupied  $e$  levels lying below. To explore the importance of unoccupied  $4p$  orbitals in the off-centre motion of  $\text{Fe}^+$  in  $\text{SrCl}_2$  SCCEH calculations have also been performed. In addition to normal SCCEH calculations, results have also been derived *removing* the  $4p$  orbitals from the basis set [125]. It was noted [125] that normal SCCEH calculations are able to reproduce (albeit qualitatively) the main features of the off-centre instability observed for  $\text{SrCl}_2 : \text{Fe}^+$ . By contrast, when the  $4p$  orbitals are removed from the basis set  $(\partial^2 E(Z)/\partial Z^2)_{Z=0}$  is found to be positive and the on-centre position to be stable. We have verified that if the  $4s$  orbital of  $\text{Fe}^+$  is suppressed from the basis set the off-centre instability is still encountered in SCCEH calculations. This result is not surprising because linear vibronic coupling between  $3d$  and  $4s$  levels of  $\text{Fe}^+$  via the  $t_{1u}$  mode is forbidden due to parity restrictions. This simple reasoning can shed light on the different role played by the  $4s$  and  $4p$  orbitals of  $\text{Fe}^+$  with regard to the off-centre instability.

The present results emphasize the important role played by the  $4p$  orbitals of monovalent  $3d$  ions as regards the off-centre instabilities in fluorite type lattices. It is worth noting that the importance of this mechanism likely decreases on passing from monovalent to divalent ions. In fact, in the latter cases the separation between  $3d$  and  $4p$  levels lies above  $10 \text{ eV}$ , being equal to  $15 \text{ eV}$  for free  $\text{Cu}^{2+}$  [48]. The hybridization between  $3d_{yz}$  and  $4p_y$  orbitals produces a shift of electronic density from the lower part to the upper one of the orbitals. Through this mechanism the bonding with top ligands is favoured while bottom ligands are progressively disconnected.

Relevant information on the two rebonding (or PJT) mechanisms contributing to the off-centre distortion of  $\text{Fe}^+$  in  $\text{SrCl}_2$  can be obtained by means of DFT calculations performed for *different* electronic configurations (Table 3). Following previous works on  $d^9$  impurities [48, 128], in a first step calculations have been made for the artificial  $(3z^2 - r^2)^{7/5}(x^2 - y^2)^{7/5}xz^{7/5}yz^{7/5}xy^{7/5}$  configuration with the seven electrons equally distributed into the five  $3d$  orbitals. It can be observed in Table 3 that, in contrast to results for  $d^9$  impurities, the off-centre distortion is not quenched for this average configuration, although the well depth is smaller than for the actual ground state. In a second step the influence of the  $xy$  occupation, but keeping the

**Table 3** Depth of the energy well and equilibrium value of the off-centre distortion,  $Z_0$ , obtained from DFT calculations for different  $C_{4v}$  electronic configurations of  $\text{SrCl}_2 : \text{Fe}^+$ , including the ground state (GS). The corresponding cubal ( $O_h$ ) configurations are also shown

$C_{4v}$ electronic configuration	$O_h$ configuration	Energy (eV)	$Z_0$ (Å)
$a_1(z^2)^2b_1(x^2 - y^2)^2e(xz, yz)^2b_2(xy)^1$ (GS)	$e_g^4t_{2g}^3$	0.28	1.31
$a_1(z^2)^{7/5}b_1(x^2 - y^2)^{7/5}e(xz, yz)^{14/5}b_2(xy)^{7/5}$	$e_g^{14/5}t_{2g}^{21/5}$	0.16	1.13
$a_1(z^2)^2b_1(x^2 - y^2)^2e(xz, yz)^1b_2(xy)^2$	$e_g^4t_{2g}^3$	0	0
$a_1(z^2)^1b_1(x^2 - y^2)^0e(xz, yz)^4b_2(xy)^2$	$e_g^1t_{2g}^6$	0.07	0.97
$a_1(z^2)^2b_1(x^2 - y^2)^2e(xz, yz)^3b_2(xy)^0$	$e_g^4t_{2g}^3$	1.30	1.59
$a_1(z^2)^2b_1(x^2 - y^2)^1e(xz, yz)^4b_2(xy)^0$	$e_g^3t_{2g}^4$	1.73	1.56
$a_1(z^2)^2b_1(x^2 - y^2)^0e(xz, yz)^4b_2(xy)^1$	$e_g^2t_{2g}^5$	1.01	1.57
$a_1(z^2)^2b_1(x^2 - y^2)^1e(xz, yz)^3b_2(xy)^1$	$e_g^3t_{2g}^4$	0.62	1.48

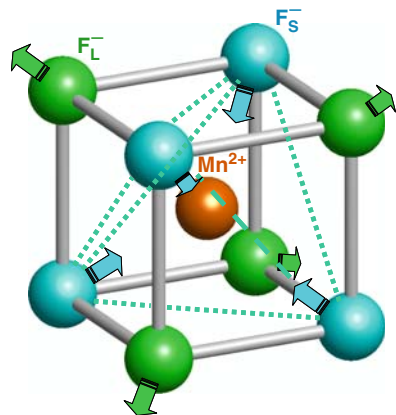
$e_g^4t_{2g}^3$  ground state configuration (in cubal symmetry), has been explored. As it is shown in Table 1, the  $\text{Fe}^+$  impurity remains *on-centre* when the  $xy$  orbital is fully occupied  $(3z^2 - r^2)^2(x^2 - y^2)^2xz^{0.5}yz^{0.5}xy^2$  configuration), while the off-centre excursion is very reinforced when the  $xy$  level is empty. These results already evidence the crucial role of the  $xy$  orbital in the off-centre motion of  $\text{Fe}^+$ . It is worth noting that on passing from the  $(3z^2 - r^2)^2(x^2 - y^2)^2xz^{0.5}yz^{0.5}xy^2$  to the  $(3z^2 - r^2)^1(x^2 - y^2)^0xz^2yz^2xy^2$  configuration (where both  $xy$  and  $e(xz, yz)$  levels are fully occupied) a small off-centre instability is recovered. This result thus shows that an increase of the population of  $e(xz, yz)$  levels favours the off-centre motion indeed. Calculations carried out for other electronic configurations in Table 3 do support that the off-centre instability is favoured by decreasing the  $xy$  population and increasing that of  $e(xz, yz)$  levels. In particular the biggest effect is found for the  $(3z^2 - r^2)^2(x^2 - y^2)^1xz^2yz^2xy^0$  configuration such as it is displayed in Table 3.

## 7 On-Centre Instability in $\text{BaF}_2 : \text{Mn}^{2+}$ at $T \sim 50$ K: Origin of the Phenomenon

Seeking to clarify the microscopic origin of the  $O_h - T_d$  reversible instability experimentally observed by EPR in  $\text{Mn}^{2+}$ -doped  $\text{BaF}_2$  at  $T > T_c \approx 50$  K [38, 39, 42], DFT calculations on three  $\text{Mn}^{2+}$ -doped  $\text{MF}_2$  ( $M = \text{Ba}, \text{Ca}$  and  $\text{Sr}$ ) fluorites lattices have been carried out using clusters involving up to 51 atoms. As a salient feature it is found that while the local symmetry is cubic for  $\text{CaF}_2 : \text{Mn}^{2+}$  and  $\text{SrF}_2 : \text{Mn}^{2+}$ , for  $\text{BaF}_2 : \text{Mn}^{2+}$  there are two equivalent tetrahedral configurations which are more stable than the cubic one by about  $50 \text{ cm}^{-1}$ . For the  $\text{MnF}_8^{6-}$  complex with eighth  $\text{F}^-$  ligands (Fig. 8), the calculated  $R_S = 2.33 \text{ Å}$  and  $R_L = 2.62 \text{ Å}$  values for the  $T_d$  geometry are consistent with  $R_L - R_S = 0.25 \text{ Å}$  derived from the analysis of the two isotropic superhyperfine constants [40].

In order to understand the microscopic origin of the instability we have performed a study based in the PJT model explained in Sect. 4. In our system the

**Fig. 8** Illustration of the distortions (arrows) corresponding to the normal coordinates of the  $a_{2u}$  vibrational mode of the  $\text{MnF}_8^{6-}$  complex in  $\text{BaF}_2 : \text{Mn}^{2+}$ . The “short” tetrahedron of  $\text{F}_S^-$  ligands (blue atoms) moves inwards while the “long” tetrahedron (green atoms) moves outwards. The  $z$  component of the  $t_{1u}$  mode is depicted in Fig. 1



ground state,  $\Gamma_0$ , belongs to the totally symmetric representation and the distortion mode has  $A_{2u}$  symmetry so only coupling to  $A_{2u}$  states make  $F_I \neq 0$  and contribute to the instability. Let us consider the valence orbitals of the cubal  $\text{MnF}_8^{6-}$  complex. When the  $a_{2u}$  mode is switched-on symmetry is reduced and new orbital mixings are allowed, giving rise to the energy lowering. In particular, the  $a_{2u}$  mode destroys the inversion symmetry existing in the  $O_h$  group allowing some even and odd parity orbitals of the same multiplicity to mix and form bonding-antibonding pairs. Using (5) we can write a model expression for the force constant  $K_I$  in an electronic state  $\Gamma_I$  along the distortion as a function of the allowed orbital contributions  $K_{ij}^{(v)}$  and the number of electrons occupying orbital  $i$ ,  $n_i$ , in the  $\Gamma_I$  state:

$$\begin{aligned}
 K \approx K_0 - K_{4t_{2g}-4t_{1u}}^{(v)} (n_{4t_{2g}} - n_{4t_{1u}}) - K_{3t_{2g}-4t_{1u}}^{(v)} (n_{3t_{2g}} - n_{4t_{1u}}) - \\
 - K_{2t_{2g}-4t_{1u}}^{(v)} (n_{2t_{2g}} - n_{4t_{1u}}) - K_{3t_{1u}-4t_{2g}}^{(v)} (n_{3t_{1u}} - n_{4t_{2g}}) - \\
 - K_{2t_{1u}-4t_{2g}}^{(v)} (n_{2t_{1u}} - n_{4t_{2g}}) - K_{1e_u-2e_g}^{(v)} (n_{1e_u} - n_{2e_g})
 \end{aligned} \quad (6)$$

Then, we have explored through DFT calculations which electronic configurations favour the distortion and which ones are against it. In Table 4 we present the results of B3LYP calculations for the position of the energy minimum, the energy stabilization, and force constant for several electronic configurations involving the orbitals of interest in this problem. The main conclusion that can be extracted is that the redistribution of the  $\text{Mn}(3d)$  electrons between the  $e_g$  and  $t_{2g}$  orbitals favour larger distortions when the latter is depopulated and destroy it when electrons are poured into it, indicating that the  $t_{2g}$  orbitals play a very important role in the creation of the new bonds. This idea is reinforced by the fact that excitation of electrons from  $t_{1u}$  orbitals (coupled to  $t_{2g}$ ) produce the largest force constants. Fitting through a means square procedure the  $K_I$  values calculated for the electronic configurations shown in Table 4 with the model expression (6) the following values of  $K_0$  and  $K_{ij}^{(v)}$  were obtained:  $K_0 = 17.33$ ,  $K_{4t_{2g}-4t_{1u}}^{(v)} = -1.82$ ,  $K_{3t_{2g}-4t_{1u}}^{(v)} = -0.20$ ,  $K_{2t_{2g}-4t_{1u}}^{(v)} = -0.86$ ,  $K_{3t_{1u}-4t_{2g}}^{(v)} = -1.15$ ,  $K_{2t_{1u}-4t_{2g}}^{(v)} = -1.24$  and  $K_{1e_u-2e_g}^{(v)} = -0.44$  in

**Table 4** Results of B3LYP calculations for the position of energy minima,  $Q_{\min}$  (in Å), stabilization energies,  $\Delta E$  (in  $\text{cm}^{-1}$ ), and force constants,  $K_I$  (in  $\text{eV}/\text{\AA}^2$ ), for several electronic configurations involving the orbitals of interest in  $\text{BaF}_2 : \text{Mn}^{2+}$

Configuration	$Q_{\min}$	$\Delta E$	$K_I$
$2t_{1u}^6 2t_{2g}^6 3t_{1u}^6 3t_{2g}^6 1e_u^4 2e_g^2 4t_{2g}^3$	-0.42	-52	-0.24
$2t_{1u}^6 2t_{2g}^6 3t_{1u}^6 3t_{2g}^6 1e_u^4 2e_g^4 4t_{2g}^1$	-0.76	-593	-0.45
$2t_{1u}^6 2t_{2g}^6 3t_{1u}^6 3t_{2g}^6 1e_u^4 2e_g^0 4t_{2g}^5$	0	0	0.17
$2t_{1u}^6 2t_{2g}^6 3t_{1u}^6 3t_{2g}^6 1e_u^3 2e_g^3 4t_{2g}^3$	0	0	0.74
$2t_{1u}^6 2t_{2g}^6 3t_{1u}^6 3t_{2g}^6 1e_u^3 2e_g^2 4t_{2g}^4$	0	0	0.79
$2t_{1u}^6 2t_{2g}^6 3t_{1u}^6 3t_{2g}^5 1e_u^4 2e_g^2 4t_{2g}^4$	0	0	0.16
$2t_{1u}^6 2t_{2g}^6 3t_{1u}^6 3t_{2g}^5 1e_u^4 2e_g^3 4t_{2g}^3$	0	0	0.11
$2t_{1u}^6 2t_{2g}^6 3t_{1u}^5 3t_{2g}^6 1e_u^4 2e_g^2 4t_{2g}^4$	0	0	1.55
$2t_{1u}^6 2t_{2g}^6 3t_{1u}^5 3t_{2g}^6 1e_u^4 2e_g^3 4t_{2g}^3$	0	0	1.57
$2t_{1u}^6 2t_{2g}^5 3t_{1u}^6 3t_{2g}^6 1e_u^4 2e_g^2 4t_{2g}^4$	0	0	1.20
$2t_{1u}^6 2t_{2g}^5 3t_{1u}^6 3t_{2g}^6 1e_u^4 2e_g^2 4t_{2g}^3$	0	0	1.19
$2t_{1u}^5 2t_{2g}^6 3t_{1u}^6 3t_{2g}^6 1e_u^4 2e_g^2 4t_{2g}^4$	0	0	1.64
$2t_{1u}^5 2t_{2g}^6 3t_{1u}^6 3t_{2g}^6 1e_u^4 2e_g^3 4t_{2g}^3$	0	0	1.33

$\text{eV } \text{\AA}^{-2}$ . It can be observed in Table 4 that our model fits reasonably well the DFT results. From these  $K_{ij}^{(v)}$  values it can be concluded that there are two dominant distortion mechanisms. The first one is the previously mentioned coupling between the  $\text{Mn}(3d) 4t_{2g}$  orbitals and  $2t_{1u}$  and  $3t_{1u}$  orbitals with  $2p(\text{F})$  character. This admixture displaces the electronic density so that it is reinforced on the lines connecting the metal with four fluorine neighbours forming a tetrahedron while it is weakened on the other four, as illustrate in Fig. 8. The second mechanism induces the polarization of the electronic cloud around the manganese ion through the mixing between  $4t_{2g}$  and  $4t_{1u}$  orbitals with  $3d(\text{Mn})$  and  $4p(\text{Mn})$  character, respectively, in a similar way to that found in the off-centre displacement of  $\text{SrCl} : \text{Fe}^+$ . The hybrid  $3d-4p$  orbital of manganese due to vibronic coupling is better adapted to form sigma bonds in tetrahedral symmetry, giving rise a larger overlap with  $2p$  ligand orbitals, and favouring a diminution of energy along the distortion.

Another important feature of this system is the local symmetry change at  $T \sim 55 \text{ K}$ . DFT calculations indicate that the energy barrier is about  $50 \text{ cm}^{-1}$  which seems consistent with the transition temperature. However, a detailed study [41] has shown that it is necessary to take into account the anharmonic coupling between several vibrational modes not directly involved in the distortion to obtain a reasonable transition temperature.

Finally, we would like to discuss why the tetrahedral distortion occurs in  $\text{BaF}_2 : \text{Mn}^{2+}$  but is not present in other cubic or octahedral centres. It should be noted here that while in octahedral centres the force constant is dominated by the metal-ligand contribution, this appears to be not longer true when dealing with systems like  $\text{MF}_2 : \text{Mn}^{2+}$  ( $\text{M} = \text{Ca}, \text{Sr}, \text{Ba}$ ) with hexahedral coordination. In these cases the force constant of the symmetric  $a_{1g}$  mode has been found [41] to be dominated by the ligand-ligand contribution. As the force constant for the  $a_{2u}$  mode is independent on this contribution this leads to  $\omega(a_{2u})$  values which are clearly

smaller than the corresponding  $\omega(a_{1g})$ . In addition to the independence of  $\omega(a_{2u})$  on the ligand–ligand interaction, there are two relevant facts favouring the  $a_{2u}$  instability observed [38, 39, 42] below 50 K in  $\text{BaF}_2 : \text{Mn}^{2+}$ : an unusually big  $\text{Mn}^{2+}\text{-F}^-$  distance and the pseudo Jahn–Teller coupling of the  ${}^6A_{1g}$  ground state with excited states allowed by an  $a_{2u}$  distortion. According to ionic radii of  $\text{Mn}^{2+}$  and  $\text{F}^-$  and Pauling’s rule a  $\text{Mn}^{2+}\text{-F}^-$  distance of 2.22 Å is expected for  $\text{Mn}^{2+}$  ions surrounded by a cube of eight  $\text{F}^-$  ions. While the measured  $\text{Mn}^{2+}\text{-F}^-$  distance [40] for  $\text{CaF}_2 : \text{Mn}^{2+}$  is only 3% higher than this quantity such a difference is calculated to be *four times* bigger for  $\text{BaF}_2 : \text{Mn}^{2+}$  and thus helps to reduce the force constant of a  $\text{Mn}^{2+}\text{-F}^-$  bond. It is worth noting that for  $\text{Mn}^{2+}$  impurities in octahedral coordination [40] the measured  $\text{Mn}^{2+}\text{-F}^-$  distance always coincides with 2.13 Å within 3%.

## 8 The Axial Centre in Fe-doped $\text{KTaO}_3$ : Results from Calculations

The limitations of the EPR technique for characterizing paramagnetic impurities in oxides are well exemplified by the axial iron centre observed in  $\text{KTaO}_3$  [126–128]. This centre is described by  $S_{\text{eff}} = 1/2$ ,  $g_{\perp}^{\text{eff}} = 4.33$  and  $g_{\parallel}^{\text{eff}} = 2.02$  and the principal direction associated with  $g_{\parallel}^{\text{eff}}$  is a  $\langle 001 \rangle$  type direction of the host lattice. Two  $\langle 100 \rangle$  off-centre models have been proposed in the literature: a  $\text{Fe}^+$  ( $3d^7$ ) ion replacing a  $\text{K}^+$  ion (shortly referred to as  $\text{Fe}^+_{\text{K}}$ ) [126, 127] or a  $\text{Fe}^{5+}$  ( $3d^3$ ) ion located at  $\text{Ta}^{5+}$  site ( $\text{Fe}^{5+}_{\text{Ta}}$ ) (Fig. 9) [128]. Furthermore, it has been proposed [128] that the off-centre motion would arise from the smaller ionic radius of  $\text{Fe}^{5+}$  (estimated in the 40–50 pm range) when compared to that of  $\text{Ta}^{5+}$  (64 pm).

Looking for the equilibrium geometry of the  $\text{Fe}^{5+}_{\text{Ta}}$  centre in  $\text{KTaO}_3$  optimizations on the 21 ion  $\text{FeO}_6\text{K}_8\text{Ta}_6^{27+}$  cluster at the  ${}^3A_{1g}(t_{2g}^3)$  ground state have been carried out. Using LDA and GGA functionals the  $\text{Fe}^{5+}$  impurity remains on-centre

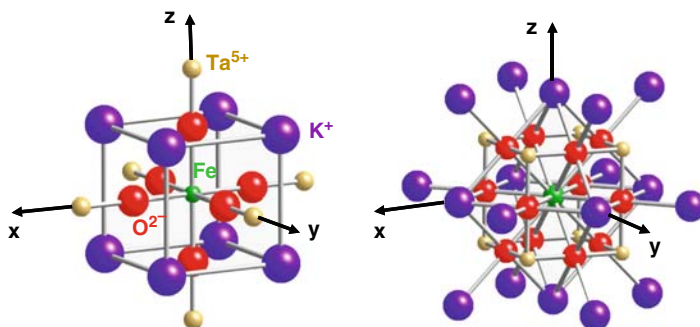


**Fig. 9** *Left*: 21 atom cluster used in the calculations of the  $\text{Fe}^{5+}_{\text{Ta}}$  centre in  $\text{KTaO}_3$ . *Right*: 39 atom cluster used for the  $\text{Fe}^+_{\text{K}}$  centre



in the  $\text{Ta}^{5+}$  position. The  $E(Z_{\text{Fe}})$  profile obtained for this ground state has a single minimum at  $Z_{\text{Fe}} = 0$  and exhibits a huge barrier which precludes the existence of any off-centre displacement along  $\langle 001 \rangle$  directions. This big barrier comes from the overlapping of electronic clouds of the impurity and the closest ligand (placed at a distance equal to  $R_{\text{ML}} - Z_{\text{Fe}}$ ) which increases substantially when  $Z_{\text{Fe}}$  does. This phenomenon is described, in a phenomenological way, by the Born-Mayer repulsion term and acts against the decrease of electrostatic energy obtained considering all ions as point charges. The calculated equilibrium value of the Fe-O distance,  $R_{\text{ML}}$ , was found to be equal to 206.3 pm. It is worth noting that these values are a bit higher than the experimental Ta-O distance in the host lattice, equal to  $a/2 = 199.4$  pm ( $a$  is the cubic lattice parameter). This  $\sim 3.5\%$  outwards relaxation produced under the  $\text{Ta}^{5+} \rightarrow \text{Fe}^{5+}$  substitution thus stresses that the size of  $\text{Fe}^{5+}$  is certainly not significantly smaller than that of  $\text{Ta}^{5+}$ . This fact is partially related to covalent effects present in every transition-metal complex with closed shell ligands, leading to a net transfer of electronic charge from them to the central cation. In the present case the Mulliken charge on iron for the  $\text{Fe}^{5+}_{\text{Ta}}$  centre is found to be equal to  $+1.1e$  ( $e$  denotes the proton charge), which is substantially smaller than the nominal value of  $+5e$ . Interestingly, the value at equilibrium of the energy separation, 10Dq, between  $e_g$  ( $\sim x^2 - y^2$ ,  $3z^2 - r^2$ ) and  $t_{2g}$  ( $\sim xy$ ,  $xz$ ,  $yz$ ) levels of the  $O_h$   $\text{FeO}_6^{7-}$  complex is calculated to be equal to 1.0 eV. This figure is much bigger than the corresponding value computed for  $\text{Fe}^{+}$  in dodecahedral coordination, a matter discussed below.

Then we have explored the  $\text{FeK}^{+}$  ( $3d^7$ ) model for the axial centre (Fig. 9). Under a  $\langle 001 \rangle$  displacement of the  $\text{Fe}^{+}$  cation,  $t_{2g}$  and  $e_g$  levels of the  $O_h$   $\text{FeO}_{12}^{23-}$  complex split, respectively, in  $b_2$  ( $\sim xy$ ),  $e$  ( $\sim xz$ ,  $yz$ ) and  $b_1$  ( $\sim x^2 - y^2$ ),  $a_1$  ( $\sim 3z^2 - r^2$ ) levels of the distorted  $C_{4v}$   $\text{FeO}_4\text{O}_4\text{O}_4^{23-}$  complex, which has three inequivalent groups of ligands. Total energy DFT calculations have been carried out on the 39 atom  $\text{FeO}_{12}\text{Ta}_8\text{K}_{18}^{47+}$  cluster (Fig. 9) for all possible configurations with  $S = 3/2$  corresponding to different occupations of mainly  $3d(\text{Fe})$  levels with seven electrons. In the on-centre geometry ( $Z_{\text{Fe}} = 0$ ) the minimum energy configuration is  $b_1(x^2 - y^2)^2 a_1(3z^2 - r^2)^2 b_2(xy)^1 e(xz, yz)^2$ , using the  $C_{4v}$  group notation, with  $\Delta E_0 = -0.71$  eV and  $Z_{\text{Fe}}^0 = 93$  pm. This fact thus supports that a  $\text{Fe}^{+}$  impurity at a  $\text{K}^{+}$  site moves spontaneously off-centre. Calculated  $E(Z_{\text{Fe}})$  profiles of the total energy for four electronic configurations with  $S = 3/2$  is displayed in Fig. 10. As a salient feature it can be seen in Fig. 10 that  $b_1^1 a_1^2 b_2^2 e^2$  becomes the ground state after a relatively small off-centre displacement of the  $\text{Fe}^{+}$  impurity ( $Z_{\text{Fe}} = 20$  pm). This change in the ground state is helped by the crossing of  $b_1$  ( $\sim xy$ ) and  $b_2$  ( $\sim x^2 - y^2$ ) levels which takes place during the off-centre displacement and the small energy difference (0.06 eV) between  $b_1^1 a_1^2 b_2^2 e^2$  and  $b_1^2 a_1^2 b_2^1 e^2$  states obtained for  $Z_{\text{Fe}} = 0$ .

In a spontaneous off-centre excursion of a given impurity there is always a change of covalency with near ions which is behind the required diminution of total energy. Despite this fact some insight can be obtained looking at the electrostatic potential,  $V_{\text{M}}$ , created by the rest of *point* ions on a rigid impurity. It can be noticed that  $V_{\text{M}}(0, 0, Z_{\text{Fe}})$  is essentially flat in the  $0 \text{ pm} < Z_{\text{Fe}} < 100 \text{ pm}$  region, while it behaves as a barrier for  $Z_{\text{Fe}} \geq 120 \text{ pm}$  [129]. It is worth noting that the results of present



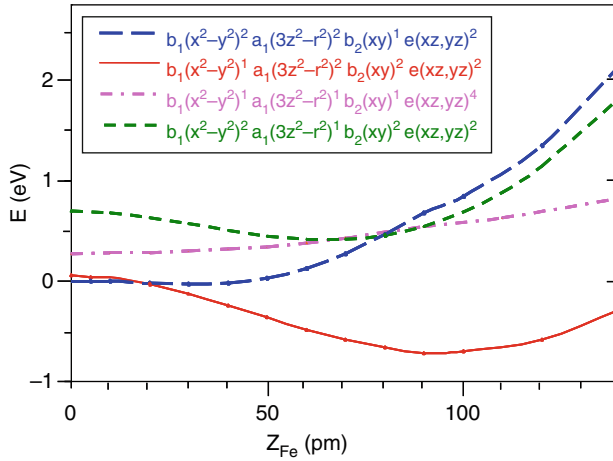


**Fig. 10** Profiles of the DFT total energy of the  $\text{Fe}_K^+$  centre in  $\text{KTaO}_3 : \text{Fe}^+$  as a function of the  $Z_{\text{Fe}}$  coordinate calculated for four  $S = 3/2$  electronic configurations. Results correspond to GGA-BP calculations for the 39 atom cluster

calculations are consistent with the form of  $V_M(0, 0, Z_{\text{Fe}})$ . Indeed the obtained equilibrium coordinate  $Z_{\text{Fe}}^0 = 93 \text{ pm}$  places the  $\text{Fe}^+$  impurity in the zone where  $V_M(0, 0, Z_{\text{Fe}})$  is still flat [129].

The axial Fe centre is characterized by an axial g-tensor whose components for  $S_{\text{eff}} = 1/2$  are  $g_{\perp}^{\text{eff}} = 4.33$  and  $g_{\parallel}^{\text{eff}} = 2.02$  [126–128]. If the spin of the ground state is  $S = 3/2$  the true values  $g_{\parallel} = 2.02$  and  $g_{\perp} = 2.16$  are thus derived. Therefore, it turns out that  $g_{\perp} - g_0$  is significantly higher than  $g_{\parallel} - g_0$  a fact which is a fingerprint of the axial centre [126–128]. In the present study this tensor has been calculated by means of the ADF package at the equilibrium geometry corresponding to the  $\text{Fe}_K^+$  centre. The obtained values,  $g_{\parallel} = 2.08$  and  $g_{\perp} = 2.18$ , are not unreasonable.

## 9 Summary

In this article experimental and theoretical work on spontaneous instabilities of impurities in solids driven by PJT vibronic coupling mechanisms is reviewed. Particular attention is paid to the results of calculations addressed to understand the microscopic origin of off-centre and on-centre instabilities and also to quantify the involved distortions. Especially, we aim to help to overcome a paradigm taken root among many researchers of physics and chemistry of solids: that the instabilities of atoms and ions in pure and doped solids are due to difference of atomic sizes. On the contrary, we have presented a great quantity of experimental evidences and theoretical results showing that it is an effect of the vibronic coupling.

**Acknowledgements** Partial support by the Spanish Ministerio de Ciencia y Tecnología under Project No. FIS2006–02261 is acknowledged.

## References

1. G. Blasse, B.C. Grabmaier, *Luminescent Materials* (Springer, Berlin, 1994)
2. R.C. Powell, *Physics of Solid-State Laser Materials* (Springer, New York, 1997)
3. M. Nikl, Phys. Status Solidi A **178**, 595 (2000)
4. V. Babin, A. Krasnikov, M. Nikl, Nitsch K, A. Stolovits, S. Zazubovich, J. Lumin. **101**, 219 (2003)
5. P. Dorenbos, Phys. Status Solidi A **202**, 195 (2005)
6. M. Secu, S. Schweizer, U. Rogulis, J.-M. Spaeth, J. Phys.: Condens. Matter **15**, 2061 (1993)
7. G. Corradi, M. Secu, S. Schweizer, J.-M. Spaeth, J. Phys.: Condens. Matter **16**, 1489 (2004)
8. N. Kodama, N. Sasaki, M. Yamaga, Y. Masui, J. Lumin. **19**, 94 (2001)
9. K. Nassau, *The Physics and Chemistry of Colour* (Wiley, New York, 1983)
10. R.G. Burns, *Mineralogical Applications of Crystal Field Theory* (Cambridge University Press, Cambridge, 1993)
11. K. Nassau, *The Science of Color*, ed. by S.K. Shevell (Elsevier, Amsterdam, 2003)
12. J.H. Barkyoub, A.N. Mansour, Phys. Rev. B **46**, 8768 (1992)
13. L. Cheng, N.C. Sturchio, M.J. Bedzyk, Phys. Rev. Lett. **63**, 144104 (2001)
14. G. Dalba, P. Fornasini, R. Grisenti, J. Purans, Phys. Rev. Lett. **82**, 4240 (1999)
15. M.T. Barriuso, J.A. Aramburu, M. Moreno, J. Phys.: Cond. Matter **11**, L525 (1999)
16. B. Villacampa, R. Cases, V.M. Orera, R. Alcalá, J. Phys. Chem. Solids **55**, 263 (1994)
17. M.T. Barriuso, M. Moreno, J.A. Aramburu, Phys. Rev. B **65**, 064441 (2002)
18. M. Moreno, J.A. Aramburu, M.T. Barriuso, J. Phys. C: Sol. State Phys., **19**, L315 (1986)
19. M. Moreno, M.T. Barriuso, J.A. Aramburu, P. García-Fernández, J.M. García-Lastra, J. Phys.: Cond. Matter **18**, R315 (2006)
20. I.B. Bersuker, *The Jahn–Teller Effect* (Cambridge University Press, Cambridge, 2006)
21. K. Knox, R.G. Shulman, S. Sugano, Phys. Rev. **130**, 512 (1963)
22. T.P.P. Hall, W. Hayes, R.W.H. Stevenson, J. Wilkens, J. Chem. Phys. **38**, 1977 (1963)
23. J.J. Rousseau, A. Leble, J.C. Fayet, J. Phys **39**, 1215 (1978)
24. F. Rodríguez, M. Moreno, J. Chem. Phys. **84**, 692 (1986)
25. M.T. Barriuso, J.A. Aramburu, M. Moreno, J. Phys.: Condens. Matter **11**, L525 (1999)
26. Villacampa B, Cases R, Orera V M, Alcalá R J. Phys. Chem. Solids **55**, 263 (1994)
27. R. Knochenmuss, C. Reber, M.V. Rajasekharan, H.U. Gudel, J. Chem. Phys. **85**, 4280 (1986)
28. C. Marco de Lucas, F. Rodríguez, J.M. Dance, M. Moreno, A. Tressaud, J. Lumin. **48–49**, 553 (1991)
29. P.A. Tanner, Chem. Phys. Lett. **388**, 488 (2004)
30. J.A. Aramburu, M. Moreno, K. Doclo, C. Daul, M.T. Barriuso, J. Chem. Phys. **110**, 1497 (1999)
31. J.M. Dance, J. Grannec, A. Tressaud, M. Moreno, Phys. Status Solidi B **173**, 579 (1992)
32. J.A. Aramburu, J.I. Paredes, M.T. Barriuso, M. Moreno, Phys. Rev. B **61**, 6525 (2000)
33. H. Bill, *The Dynamical Jahn–Teller Effect in Localized Systems*, ed. by Yu.E. Perlin, M. Wagner (Elsevier, Amsterdam, 1983)
34. H. Vercammen, D. Schoemaker, B. Briat, F. Ramaz, F. Callens, Phys. Rev. B **59**, 11286 (1999)
35. M.T. Barriuso, P. García-Fernández, J.A. Aramburu, M. Moreno, Solid State Commun. **120**, 1 (2001)
36. E. Minner, D. Lovy, H. Bill, J. Chem. Phys. **99**, 6378 (1993)
37. L.A. Boatner, R.W. Reynolds, M.M. Abraham, Y. Chen, Phys. Rev. Lett. **31**, 7 (1973)
38. A.G. Badalyan, P.G. Baranov, V.S. Vikhnin, V.A. Khramtson, JETP Lett. **44**, 110 (1986)

39. H. Soethe, V.A. Vetrov, J.M. Spaeth, J. Phys.: Condens. Matter **4**, 7927 (1992)
40. M.T. Barriuso, P.G. Baranov, M. Moreno, Radiat. Eff. Defects Solids **119–121**, 177 (1991)
41. P. García-Fernández, J.A. Aramburu, M.T. Barriuso, M. Moreno, J. Chem. Phys. **128**, 124513 (2008)
42. S. Lijewski, S.K. Hoffmann, J. Goslar, M. Wencka, V.A. Ulanov, J. Phys.: Condens. Matter **20**, 385208 (2008)
43. R.J. Richardson, S. Lee, T.J. Menne, Phys. Rev. B **6**, 1065 (1972)
44. F. Rodriguez, I. Hernandez, M. Moreno, R. Alcalá, J. Chem. Phys. **119**, 8686 (2003)
45. J.H. Barkyoumb, A.N. Mansour, Phys. Rev. B **46**, 8768 (1992)
46. J.L. Pascual, L. Seijo, J. Chem. Phys. **102**, 5368 (1995)
47. V.A. Ulanov, M. Krupski, S.K. Hoffmann, M.M. Zaripov, J. Phys.: Condens. Matter **15**, 1081 (2003)
48. P. García-Fernández, J.A. Aramburu, M.T. Barriuso, M. Moreno, Phys. Rev. B **69**, 174110 (2004)
49. G. Lombardo, R.O. Pohl, Phys. Rev. Lett. **15**, 291 (1965)
50. J.P. Harrison, P.P. Peressini, R.O. Pohl, Phys. Rev. **171**, 1037 (1968)
51. R.D. Kirby, A.E. Hughes, A.J. Sievers, Phys. Rev. B **2**, 481 (1970)
52. A.M. Kahan, M. Patterson, A.J. Sievers, Phys. Rev. B **14**, 5422 (1976)
53. R.A. Herendeen, R.H. Silsbee, Phys. Rev. **188**, 645 (1969)
54. X. Wang, F. Bridges, Phys. Rev. B **46**, 5122 (1992)
55. N.E. Byer, H.S. Sack, Phys. Rev. Lett. **17**, 72 (1966)
56. D.W. Alderman, R.M. Cotts, Phys. Rev. B **1**, 2870 (1970)
57. E. Krätzig, T. Timusk, W. Martienssen, Phys. Stat. Sol. B **10**, 709 (1965)
58. M. Piccirilly, G. Spinolo, Phys. Rev. B **4**, 1339 (1971)
59. T. Tsuboi, Phys. Rev. B **22**, 1871 (1980)
60. M. Siu-Li, M. de Souza, Phys. Rev. B **7**, 4677 (1973)
61. S. Emura, M. Ishiguro, Phys. Stat. Sol. B **153**, 863 (1989)
62. L. Oliveira, M. Siu-Li, Thin Solid Films **268**, 30 (1995)
63. I.B. Bersuker, Nouv. J. Chim. **4**, 139 (1980)
64. I.B. Bersuker, N.N. Gorinchoi, V.Z. Polinger, Theor. Chim. Acta **66**, 161 (1984)
65. H. Bill, Phys. Lett. A **44**, 101 (1973)
66. H. Bill, C. Milleret, R. Lacroix, *Proc. XVII Congress Ampere*, ed. by V. Hovi (North-Holland, Amsterdam, 1973), p. 233
67. M. Moreno, Anales Física (Spain) **70**, 261 (1974)
68. P. García-Fernández, J.A. Aramburu, M. Moreno, M.T. Barriuso, J. Chem. Phys. **129**, 187101 (2008)
69. I.B. Bersuker, *Electronic Structure and Properties of Transition Metal Compounds. Introduction to Theory* (Wiley, New York, 1996)
70. I.B. Bersuker, Chem. Rev. **101**, 1067 (2001)
71. P. García-Fernández, I.B. Bersuker, J.E. Boggs, Phys. Rev. Lett. **96**, 16305 (2006)
72. P. García-Fernández, I.B. Bersuker, J.E. Boggs, J. Chem. Phys. **111**, 10409 (2007)
73. U. Öpik, M.H.L. Pryce, Proc. R. Soc. London A **238**, 425 (1957)
74. A.M. Stoneham, M. Lannoo, J. Phys. Chem. Solids **30**, 1769 (1969)
75. S.T. Pantelides, W.A. Harrison, F. Yndurain, Phys. Rev. B **37**, 1016 (1988)
76. S. Mishra, Ph.D. Thesis, Technischen Universität München (2006)
77. J. Andriesen, E. van der Kolk, P. Dorenbos, Phys. Rev. B **76**, 075124 (2007)
78. I.B. Bersuker, Phys. Lett. **20**, 589 (1966)
79. R. Comes, M. Lambert, A. Guinier, Solid State Commun. **6**, 715 (1968)
80. R. Comes, M. Lambert, A. Guinier, Acta Crystallogr A **26**, 244 (1970)
81. W. Cochran, Phys. Rev. Lett. **3**, 412 (1959)
82. W. Cochran, Adv. Phys. **9**, 387 (1960)
83. W. Cochran, Phys. Status Solidi **30**, K157 (1968)
84. B. Zalar, V.V. Laguta, R. Blinc, Phys. Rev. Lett. **90**, 037601 (2003)
85. R. Pirc, R. Blinc, Phys. Rev. B **70**, 134107 (2004)
86. B. Zalar, A. Lebar, J. Seliger, R. Blinc, V.V. Laguta, M. Itoh, Phys. Rev. B **71**, 0064107 (2005)

87. R.E. Cohen, H. Krakauer, *Phys. Rev. B* **42**:6416 (1990)
88. R.E. Cohen, *Nature* **358**, 136 (1992)
89. W. Zhong, D. Vanderbilt, K.M. Rabe, *Phys. Rev. B* **52**, 6301 (1995)
90. V.S. Vikhnin, L.S. Sochava, Y.N. Tolparov, *Defects in Insulating Crystals*, ed. by K.K. Shvarts (Springer, Berlin, 1982)
91. V. Narayanamurti, R.O. Pohl, *Rev. Mod. Phys.* **42**, 201 (1970)
92. A.S. Barker, A.J. Sievers, *Rev. Mod. Phys.* **47**, S122 (1975)
93. F. Bridges, *CRC Critical Rev. Sol. Stat. Sci.* **5**, 1 (1975)
94. J.A.D. Matthew, *Solid State Commun.* **3**, 365 (1965)
95. R.J. Quigley, T.P. Das, *Phys. Rev. B* **177**, 1340 (1969)
96. G.J. Dienes, *Comm. Solid State Phys.* **1**, 81 (1968)
97. M.S. Li, M. de Souza, *Phys. Rev. B* **7**, 4677 (1973)
98. J.A.D. Matthew, *Solid State Commun.* **3**, 365 (1965)
99. A.M. Stoneham, *Theory of Defects in Solids* (Clarendon, Oxford, 1975)
100. A. Logachev, B. Ya. Moizhes, *Sov. Phys. Sol. State* **19**, 1635 (1977)
101. P.I. Reisberg, J.S. Olson, *J. Biol. Chem.* **255**, 4144 (1980)
102. Q.T. Islam, B.A. Bunker, *Phys. Rev. Lett.* **59**, 2701 (1987)
103. N.W. Thomas, *Acta Cryst. B* **45**, 337 (1989)
104. I.D. Brown, *Acta Cryst.* **B48**, 553 (1992)
105. Z. Wang, B.A. Bunker, *Phys. Rev. B* **46**, 11277 (1992)
106. R.I. Eglitis, A.V. Postnikov, G. Borstel, *Phys. Rev. B* **55**, 12976 (1997)
107. I.A. Kornev, L. Bellaiche, *Phys. Rev. Lett.* **91**, 116103 (2003)
108. C. Ederer, N.A. Spaldin, *Phys. Rev. B* **74**, 024102 (2006)
109. J. Trajic, A. Golubovic, M. Romcevic, N. Romcevic, S. Nikolic, V.N. Nikiforov, *J. Serb. Chem. Soc.* **72**, 55 (2007)
110. M.D. Glinchuk, M.F. Eigen, A.A. Karmazin, *Sov. Phys. Solid State* **15**, 1365 (1974)
111. N.N. Kristofel, *Sov. Phys. Sol. State* **21**, 523 (1979)
112. S. Nagasaka, T. Kamikawa, *J. Phys (Paris)* **C6**, 412 (1981)
113. I.B. Bersuker, V.Z. Polinger, *Phys. Stat. Sol. B* **125**, 401 (1984)
114. G.G. DeLeo, W.B. Fowler, G.D. Watkins, *Phys. Rev. B* **29**, 3193 (1984)
115. S. Canuto, A. Fazzio, *Phys. Rev. B* **33**, 4432 (1986)
116. O.A. Valle do Amaral, A. Antonelli, A. Fazzio, *Phys. Rev. B* **35**, 6450 (1987)
117. A. Mauger, H.J. von Berdeleben, J.C. Bourgoin, F. Lannoo, M. Lannoo, *Europhys. Lett.* **4**, 1151 (1987)
118. G.G. DeLeo, G.D. Watkins, W.B. Fowler, *Phys. Rev. B* **37**, 1013 (1988)
119. F.G. Andersson, *Phys. Rev. B* **39**, 5392 (1989)
120. J. Casas Gonzalez, H.W. den Hartog, R. Alcalá, *Phys. Rev. B* **21**, 3826 (1980)
121. P. Studzinski, J. Casas González, J.-M. Spaeth, *J. Phys. C* **17**, 5411 (1984)
122. J.A. Aramburu, P. García-Fernández, M.T. Barriuso, M. Moreno, *Phys. Rev. B* **67**, 020101 (2003)
123. S.V. Nistor, M. Stefan, D. Schoemaker, *Phys. Stat. Sol. B* **214**, 229 (1999)
124. D. Ghica, S.V. Nistor, H. Vrielinck, F. Callens, D. Schoemaker, *Phys. Rev. B* **70**, 024105 (2004)
125. P. García-Fernández, J.A. Aramburu, M.T. Barriuso, M. Moreno, *Phys. Rev. B* **73**, 184122 (2006)
126. M.D. Glinchuk, V.V. Laguta, I.P. Bykov, J. Rosa, L. Jastrabik, *Chem. Phys. Lett.* **232**, 232 (1995)
127. M.D. Glinchuk, V.V. Laguta, I.P. Bykov, J. Rosa, L. Jastrabik, *J. Phys.: Cond. Matter* **7**, 2605 (1995)
128. P.G. Baranov, A.G. Badalyan, D.V. Azamat, V.A. Trepakov, A.P. Bundakova, E.A. Ruzanova, V.S. Vikhnin, H. Hesse, S. Kapphan, *Phys. Rev. B* **74**, 054111 (2006)
129. A. Trueba, P. García-Fernández, J.M. García-Lastra, M.T. Barriuso, J.A. Aramburu, M. Moreno, *Phys. Rev. B* **78**, 085122 (2008)
130. J.-M. Spaeth, H. Overhof, *Point Defects in Semiconductors and Insulators* (Springer, Berlin, 2003)

131. G.J. Dienes, *Comm. Solid St. Phys.* **1**, 81 (1968)
132. U. Holland, F. Lüty, *Phys. Rev. B* **19**, 4298 (1979)
133. R. Sittig, *Phys. Stat. Sol. B* **34**, K189 (1969)
134. S.A. Payne, A.B. Goldberg, D.S. McClure, *J. Chem. Phys.* **81**, 1529 (1984)
135. K. Haneda, T. Ikeda, S. Yoshida, *J. Phys. Soc. Japan* **25**, 643 (1988)
136. F. Despa, V. Topa, *Rad. Eff. Def. Solids* **137**, 299 (1995)
137. D.S. McClure, S. Weaves, *J. Phys. Chem. Solids* **52**, 81 (1991)
138. W. Dreybrodt, K. Fussgaenger, *Phys. Stat. Sol.* **18**, 133 (1966)
139. S. Kapphan, F. Lüty, *Solid State Comm.* **6**, 907 (1968)
140. W.D. Wilson, R.D. Hatcher, F. Smoluchowski, G.J. Dienes, *Phys. Rev.* **184**, 844 (1969)
141. R.D. Kirby, A.E. Hughes, A.J. Sievers, *Phys. Rev. B* **2**, 481 (1970)
142. S. Kapphan, F. Lüty, *Phys. Rev. B* **6**, 1537 (1972)
143. R.V. Jimenez, F. Lüty, *Phys. Rev. B* **12**, 1531 (1975)
144. F. Bridges, *J. Phys. C* **16**, L777 (1983)
145. A.J. Sievers, L.H. Greene, *Phys. Rev. Lett.* **52**, 1234 (1984)
146. S.B. Hearom, A.J. Sievers, *Phys. Rev. B* **30**, 4853 (1984)
147. A.J. Sievers, R. Lai, *Physica D* **119**, 205 (1998)
148. R.V. Jimenez, F. Lüty, M. Siu Li, M. de Souza, *Phys. Stat. Sol. B* **106**, 683 (1981)
149. T. Murata, S. Emura, *J. Phys* **C8**, 795 (1986)
150. T. Murata, S. Emura, H. Ito, H. Maeda, *Physica B* **158**, 613 (1989)
151. E. Zhiteitsev, V. Ulanov, M. Zarirov, E. Zheglov, *Phys. Solid State* **48**, 1887 (2006)
152. M.F. Deigen, M.D. Glinchuk, *Sov. Phys. Usp.* **17**, 691 (1975)
153. W. Gehlhoff, W. Ulrici, *Phys. Status Solidi B* **102**, 11 (1980)
154. G. Lombardo, R.O. Pohl, *Bull. Am. Phys. Soc.* **11**, 212 (1966)
155. I.G. Nolt, A.J. Sievers, *Phys. Rev. Lett.* **16**, 1103 (1966)
156. J.P. Harrison, P.P. Peresini, R.O. Pohl, *Phys. Rev. B* **171**, 1037 (1968)
157. B.P. Clayman, I.G. Nolt, A.J. Sievers, *Phys. Rev. Lett.* **19**, 111 (1967)
158. W. Zoller, F. Bridges, *Phys. Rev. B* **24**, 4796 (1981)
159. R.J. Russel, F. Bridges, *Phys. Rev. B* **26**, 3386 (1982)
160. S. Ready, J. Bulman, F. Bridges, *Solid State Commun.* **51**, 685 (1984)
161. L.H. Green, A.J. Sievers, *Phys. Rev. B* **31**, 3948 (1985)
162. T.L. Estle, J.G. Carnes Jr., *Bull. Am. Phys. Soc.* **14**, 346 (1969)
163. S. Kapphan, Ph. D. thesis (Cornell University, 1965) (unpublished)
164. R.J. Russell, F. Bridges, *Bull. Am. Phys. Soc.* **23**, 18 (1978)
165. R.J. Rollefson, *Phys. Rev. B* **5**, 3235 (1972)
166. K. Thörmer, F. Lüty, *Phys. Stat. Sol. B* **90**, 277 (1978)
167. G.J. Dienes, R.D. Hatcher, R. Smoluchowski, W. Wilson, *Phys. Rev. Lett.* **16**, 25 (1966)
168. W.D. Wilson, R.D. Hatcher, G.J. Dienes, R. Smoluchowski, *Phys. Rev.* **161**, 888 (1967)
169. R.J. Quigley, T.P. Das, *Phys. Rev.* **164**, 1185 (1967)
170. J.A. van Winsum, H.W. den Hartog, T. Lee, *Phys. Rev. B* **18**, 178 (1978)
171. C.R.A. Catlow, J. Corish, P.W.M. Jacobs, M.J. Norgett, *J. Phys. (Paris) Colloq.* **37**, C7–253 (1976)
172. C.R.A. Catlow, K.M. Diller, M.J. Norgett, J. Corish, B.M.C. Parker, P.W.M. Jacobs, *Phys. Rev. B* **18**, 2739 (1978)
173. P.B. Fitzsimmons, J. Corish, P.W.M. Jacobs, *Cryst. Latt. Def. Amorp. Mat.* **15**, 7 (1987)
174. P.W.M. Jacobs, *J. Chem. Soc. Faraday Trans.* **2**, 85 (1989)
175. F. Hess, *J. Phys. Chem. Solids* **46**, 1463 (1985)
176. H. Yamada, T. Kojima, *J. Phys. C* **18**, 731 (1985)
177. J.M. Recio, E. Francisco, M. Flórez, A. Martín Pendás, *J. Phys.: Condens. Matter* **5**, 4975 (1993)
178. C. Ederer, N.A. Spaldin, *Phys. Rev. B* **74**, 024102 (2006)
179. O. Kanert, R. Küchler, W. Küchler, *Solid State Commun.* **54**, 999 (1985)
180. Y. Manmoto, M. Tei, J. Nogami, M. Furuyama, *Int. J. Quantum Chem.* **75**, 961 (1999)
181. H. Wegerle, *Phys. Lett. A* **27**, 87 (1968)
182. P.G. Baranov, R.A. Zhitnikov, N.G. Romanov, *Sov. Phys. Solid St.* **18**, 1013 (1976)

183. N.I. Melnikov, P.G. Baranov, R.A. Zhitnikov, *Phys. Stat. Sol. B* **46**, K73 (1971)
184. P.G. Baranov, R.A. Zhitnikov, N.I. Melnikov, *Sov. Phys. Sol. Stat.* **14**, 1876 (1972)
185. M. Ikeya, N. Itoh, *J. Phys. Soc. Jpn.* **29**, 1295 (1970)
186. G.J. Dienes, R.D. Hatcher, O.W. Lazareth, B.S.H. Royce, F. Smoluchowski, *Phys. Rev. B* **7**, 5332 (1973)
187. A.G. Badalyan, P.G. Baranov, V.S. Vikhnin, M.M. Petrosyan, V.A. Khramtsov, *Sov. Phys. Sol. Stat.* **29**, 268 (1987)
188. P.G. Baranov, V.A. Vetrov, N.G. Romanov, V. Topa, *Phys. Status Solidi B* **136**, 699 (1986)
189. S. Zazubovich 1994, *Int. J. Mod. Phys. B* **8**, 985 (1994)
190. T. Tsuboi, T. Kamewari, *J. Phys.: Condens. Matter* **6**, 8613 (1994)
191. H. Schmidt, *Ferroelectrics* **162**, 317 (1994)
192. R. Seshadri, N.A. Hill, *Chem. Mater.* **13**, 2892 (2001)
193. N.A. Hill, A. Filippetti, *J. Magn. Magn. Mater.* **242–245**, 976 (2002)
194. T. Shishidou, N. Mikamo, Y. Uratani, F. Ishii, T. Oguchi, *J. Phys.: Condens. Matter* **16**, S5677 (2004)
195. R. Ramesh, N.A. Spaldin, *Nature Mat.* **6**, 21 (2007)
196. A.G. Badalyan, P.G. Baranov, S.V. Vikhnin, M.M. Petrosyan, V.A. Khramtsov, *Sov. Phys. JETP* **61**, 808 (1985)
197. L.S. Sochava, N. Yu. Tolparov, N.N. Kovalev, *Sov. Phys. Sol. State* **13**, 1219 (1971)
198. V.A. Krylov, L.S. Sochava, *Sov. Phys. Sol. State* **21**, 1586 (1979)
199. L.S. Sochava, Yu. N. Tolparov, N.N. Kovalev, *Sov. Phys. Sol. State* **17**, 127 (1975)
200. V.S. Vikhnin, L.S. Sochava, *Sov. Phys. Sol. State* **21**, 1193 (1979)
201. N. Yu. Tolparov, V.A. Krylov, L.S. Sochava, *Sov. Phys. Sol. State* **21**, 1778 (1979)
202. L.S. Sochava, N. Yu. Tolparov, N.N. Kovalev, *Sov. Phys. Sol. State* **13**, 1219 (1971)
203. N.B. Manson, A. Edgar, *Semicond. Insulat.* **3**, 209 (1978)
204. V.A. Krylov, L.S. Sochava, *Sov. Phys. Sol. State* **22**, 1389 (1980)
205. A. Edgar, Y. Haider, *J. Phys. C* **11**, 2595 (1978)
206. S.N. Arutyunov, N.N. Kovalev, L.S. Sochava, *Sov. Phys. Sol. State* **27**, 327 (1985)
207. F.S. Ham, *Phys. Rev.* **138**, A1727 (1965)
208. B. Welber, *Phys. Rev. B* **136**, A1408 (1964)
209. J.W. Hodby, *J. Phys. C* **2**, 404 (1969)
210. A.B. Arauzo, V.M. Orera, P.J. Alonso, *J. Phys. Chem. Solids* **57**, 1861 (1996)
211. P.J. Alonso, A.B. Arauzo, *J. Phys. Chem. Solids* **59**, 921 (1998)
212. P.B. Oliete, V.M. Orera, P.J. Alonso, *Phys. Rev. B* **53**, 3047 (1996)
213. P.B. Oliete, V.M. Orera, P.J. Alonso, *Phys. Rev. B* **54**, 12099 (1996)
214. P.B. Oliete, V.M. Orera, P.J. Alonso, *Appl. Magn. Reson.* **15**, 155 (1998)
215. K.E. Roelfsema, H.W. den Hartog, *Phys. Rev. B* **13**, 2723 (1976)
216. K.E. Roelfsema, H.W. den Hartog, *J. Magn. Reson.* **29**, 255 (1978)
217. S.K. Hoffmann, J. Goslar, S. Lijewski, V.A. Ulanov, *J. Chem. Phys.* **127**, **124705** (2007)
218. E. Siegel, K.A. Muller, *Phys. Rev. B* **20**, 3587 (1979)
219. K.A. Muller, W. Berlinger, J. Albers, *Phys. Rev. B* **32**, 5837 (1985)
220. K.A. Muller, W. Berlinger, J. Albers, *Phys. Rev. B* **34**, 5136 (1986)
221. K.A. Muller, W. Berlinger, K.W. Blazey, J. Albers, *Sol. St. Comm.* **61**, 21 (1987)
222. G. Völkel, K.A. Müller, *Phys. Rev. B* **76**, 094105 (2007)
223. Y. Yacobi, A. Linz, *Phys. Rev. B* **9**, 2723 (1974)
224. U.T. Höchli, H.E. Weibel, L.A. Boatner, *Phys. Rev. Lett.* **41**, 1410 (1978)
225. F. Borsa, U.T. Höchli, J.J. van der Klink, D. Rytz, *Phys. Rev. Lett.* **45**, 1884 (1980)
226. J.J. van der Klink, D. Rytz, F. Borsa, U.T. Höchli, *Phys. Rev. B* **27**, 89 (1983)
227. R.S. Klein, G.E. Kugel, M.D. Glinchuk, R.O. Kuzian, I.V. Kondakova, *Phys. Rev. B* **50**, 9721 (1994)
228. J.J. van der Klink, S.N. Khanna, *Phys. Rev. B* **29**, 2415 (1984)
229. M. Exner, H. Donnerberg, C.R.A. Catlow, O. Schirmer, *Phys. Rev. B* **52**, 3930 (1995)
230. I.I. Tupitsyn, A.A. Deineka, V.A. Trepakov, L. Jastrabik, S.E. Kapphan, *Phys. Rev. B* **64**, **195111** (2001)
231. S.A. Prosandeev, E. Cockayne, B.P. Burton, *Phys. Rev. B* **68**, 014120 (2003)

- 232. O. Hanske Petitpierre, Y. Yacoby, J. Mustre deLeon, E.A. Stern, J.J. Rehr, *Phys. Rev. B* **44**, 6700 (1991)
- 233. A.V. Sotonikov, V.V. Lemanov, E.P. Smirnova, M. Weihnacht, R. Kunze, *Ferroelectrics* **223**, 113 (1999)
- 234. J. Toulouse, X.Q. Wang, M. Rousseau, *Phys. Rev. B* **44**, 6635 (1991)
- 235. T. Tsuboi, A. Scacco, *J. Phys.: Condens. Matter* **10**, 7259 (1998)
- 236. K. Tanimura, W.A. Sibley, L.G. DeShazer, *Phys. Rev. B* **31**, 3980 (1985)
- 237. P. García-Fernández, L. García-Canales, J.M. García-Lastra, J. Junquera, M. Moreno, J.A. Aramburu, *J. Chem. Phys.* **129**, 124313 (2008)
- 238. A. Trueba, J.M. García-Lastra, C. de Graaf, P. García-Fernández, M.T. Barriuso, J.A. Aramburu, M. Moreno, *Chem. Phys. Lett.* **430**, 51 (2006)
- 239. R.G. Pearson, *Proc. Nat. Acad. Sci. USA* **72**, 2104 (1975)
- 240. M. Gerloch, M.C. Constable, *Transition metal chemistry* (VCH, New York, 1994)
- 241. R.G. Parr, W. Yang, *Density Functional Theory of Atoms and Molecules* (Oxford University Press, New York, 1989)
- 242. S.H. Vosko, L. Wild, M. Nusair, *Can. J. Phys.* **58**, 1200 (1980)
- 243. A.D. Becke, *Phys. Rev. A* **38**, 3098 (1988)
- 244. C. Lee, W. Yang, R.G. Parr, *Phys. Rev. B* **37**, 785 (1988)
- 245. G. te Velde, F.M. Bickelhaupt, E.J. Baerends, C. Fonseca Guerra, S.J.A. van Gisbergen, J.G. Snijders, T. Ziegler, *J. Comp. Chem.* **22**, 931 (2001)
- 246. A.D. Becke, *J. Chem. Phys.* **98**, 5648 (1993)
- 247. M. J. Frisch et al., *Gaussian 98* (Gaussian Inc., Pittsburgh PA, 1998)
- 248. J.H. Ammeter, A.B. Burgi, J.C. Thibeault, R. Hoffman, *J. Am. Chem. Soc.* **100**, 3686 (1978)
- 249. M.M. Zaripov, V.A. Ulanov, *Sov. Phys. Solid State* **30**, 896 (1988)
- 250. V.A. Ulanov, M.M. Zaripov, V.A. Shustov, I.I. Fazlizhanov, *Phys. Solid State* **40**, 408 (2001)
- 251. S.K. Hoffmann, V.A. Ulanov, *J. Phys.: Condens. Matter* **12**, 1855 (2000)
- 252. M.M. Zaripov, V.A. Ulanov, M.L. Falin, *Sov. Phys. Solid State* **29**, 1264 (1987)
- 253. M.M. Zaripov, V.A. Ulanov, M.L. Falin, *Sov. Phys. Solid State* **29**, 1264 (1989)



# The Influence of Jahn–Teller Coupling on the High-Spin/Low-Spin Equilibria of Octahedral $M^{III}L_6$ Polyhedra ( $M^{III}$ : Mn – Cu), with $NiF_6^{3-}$ as the Model Example

D. Reinen and M. Atanasov

The appearance of  $d^4$ –to– $d^8$  cations in their respective high- or low-spin ground states is not solely a matter of the interplay between the ligand field strength  $\Delta$  and the Racah parameters of interelectronic repulsion  $B$  and  $C$ , but can be steered by additional Jahn–Teller (JT) coupling – as in the  $d^4$  and  $d^7$  cases, where vibronic  $E_g \otimes \varepsilon_g$  interactions strongly stabilise a high- and low-spin ground state, respectively. Also in octahedral complexes with  $d^5$  and  $d^6$  cations JT interactions come into play, though only via the much weaker  $T_{2g} \otimes \varepsilon_g$  coupling – here contributing to the stabilisation of the low spin  $^2T_{2g}$  and the high spin  $^5T_{2g}$  state, respectively. Ni(III) occurs, with so far only one exception, as a low spin-species – in the fluoride case exclusively due to the large energy increment stemming from the tetragonal ground state JT splitting. It is further shown for  $NiF_6^{3-}$ , adopting additionally to spectroscopic, magnetic and structural results, reliable data from DFT, that the minimum positions of the alternative  $^2_aA_{1g}$  ( $^2_aE_g$ ) and  $^2_aA_{2g}$  ( $^2_aT_{1g}$ ) ground state potential curves differ by only  $\Delta_{2,4} \cong 130\text{ cm}^{-1}$ . The energy barrier, on the other hand, which steers the transformation of low into high spin species with increasing temperature, amounts to about  $400\text{ cm}^{-1}$ . O- and N-ligand atoms, which induce larger  $\Delta$  and smaller  $B$  and  $C$  values, considerably enhance the mentioned critical quantity  $\Delta_{2,4}$ . Interestingly enough, the distinct tetragonal polyhedron distortion, which accompanies the low spin ground state, vanishes in oxidic host lattices, as soon as oxygen serves as a bridging ligand in the respective structure. Band broadening, which suppresses JT coupling, and distinctly enhanced Ni – O bond covalency characterise the bonding in such phases – for example in the  $K_2NiF_4$ -type compound  $Nd_{0.8}Sr_{1.2}Ni^{III}O_{3.9}$  and in the perovskite  $LaNiO_3$ , where even metallic conductivity is observed.  $Co^{III}$  possesses a high- to low-spin energy barrier to overcome interelectronic repulsion, which is similar to that for  $Ni^{III}$  – but without the strong support by  $E_g \otimes \varepsilon_g$  JT coupling. Thus,  $CoF_6^{3-}$  is high-spin, while oxygen-ligand atoms induce challenging high-spin/low-spin equilibria, which are discussed and analysed. The high-spin ( $^5E_g$ )/low-spin ( $^3T_{1g}$ ) separation energy for  $Mn^{III}$  bears a different sign in comparison to  $Ni^{III}$ , due to a larger spin-pairing energy and a pronounced JT coupling, which both favour the high spin ground state in this case. Accordingly, more covalent ligands, positioned higher in the spectrochemical series than fluoride and oxygen, are needed for the high- to-low-spin flip. The  $d^8$  configuration of  $Cu^{III}$ , finally, represents a unique case in so far, as here the singlet-triplet separation energy



can only be overcome via excessively tetragonally elongated octahedra. The effect behind is formally described as a pseudo-JT coupling in  $O_h$  between the lowest energy excited  ${}^1_a E_g$  and  ${}^1_a A_{1g}$  states, launching considerable lowering in energy of the  ${}^1_a A_{1g}$  ( ${}^1_a E_g$ ) split state – the new ground state in  $D_{4h}$ . Indeed, while the  $\text{CuF}_6^{3-}$  octahedron is high-spin, the less ionic oxygen ligand usually induces a (nearly) square-planar  $\text{Cu}^{\text{III}}\text{O}_4$  coordination. The  $\text{Cu}^{\text{III}}\text{-O}$  binding properties in various host lattices are characterised, and discussed in respect to the oxidic mixed-valence copper superconductors. Basis for the discussion in all cases are available structural, magnetic and spectroscopic (ligand field, EPR, XANES) data besides results from theory.

## 1 Introduction and Outline

$d^n$  cations with  $n = 4\text{--}7$  in octahedral ligand fields may occur alternatively in low- and high-spin ground state configurations. The critical energy conditions at the cross-over points, if only the diagonal energies in the ligand field matrices [1] are considered, are listed in Table 1. It is frequently forgotten, however, that in cases of orbital degeneracy additional energy increments due to vibronic coupling come into play, which considerably alter these conditions. In particular, the interaction between electronic  $E_g$  ground states and the  $\varepsilon_g$  vibrations (a  $\sigma$ -antibonding effect) is generally very pronounced and much larger than the  $T_g \otimes \varepsilon_g$  coupling of only  $\pi$ -antibonding nature (Fig. 1). Both interactions induce tetragonal polyhedron distortions. A coupling to  $\tau_{2g}$  modes, possible in the case of  $T_g$  ground states, leads to trigonal ( $D_{3d}$ ) and – for  $T_g \otimes (\varepsilon_g + \tau_{2g})$  vibronic interactions – to orthorhombic  $D_{2h}$  polyhedron distortions [3]. They will not be considered here, because they are usually significantly smaller than those aiming at a  $D_{4h}$  symmetry – at least in the here treated cases [2] (see the  $\text{CN}^-$  ligand, however [4]). The energy conditions for the appearance of a high- or low-spin ground state, if the stabilisation induced by tetragonal polyhedron distortions is taken into account, are also given in Table 1.

The following equations for the  $E_g \otimes \varepsilon_g$  and  $T_{2g} \otimes \varepsilon_g$  vibronic interaction of a  $d^1$  cation and some definitions supply the necessary background from theory:

$$\begin{aligned} E_{\text{JT}}^{\text{e(c)}} &= \frac{1}{2} A_1 \rho_{\varepsilon}^{\text{e(c)}}; \rho_{\varepsilon}^{\text{e(c)}} = A_1 / (K_{\varepsilon} - (+)2A_2) \equiv 2\Delta a / \sqrt{3} \\ E_{\text{FC}}^{\text{e(c)}} &= 2 \left( A_1 \rho_{\varepsilon}^{\text{e(c)}} + (-)A_2 \rho_{\varepsilon}^{\text{e(c)2}} \right) \equiv 4\delta_1 (\delta_1') \end{aligned} \quad (1)$$

(the upper index e and c stands for  $D_{4h}$ , elongation and compression, respectively;  $A_1$  ( $\text{eV} \cdot \text{\AA}$ ) and  $A_2$  ( $\text{eV} \cdot \text{\AA}^{-2}$ ): first and second order JT coupling constants, respectively;  $K_{\varepsilon}$  ( $\text{eV} \cdot \text{\AA}^{-2}$ ): force constant;  $\rho_{\varepsilon}$  ( $\text{\AA}$ ): radial distortion parameter;  $\Delta a$  ( $\text{\AA}$ ): difference between long and short bond lengths),

$$\begin{aligned} E_{\text{JT}}^{\text{c(e)}} &= \frac{1}{2} (1/4) V_{\varepsilon} \rho_{\varepsilon}^{\text{c(e)}}; \rho_{\varepsilon}^{\text{c(e)}} = V_{\varepsilon} / (2)K_{\varepsilon} \\ E_{\text{FC}}^{\text{c(e)}} &= \frac{3}{2} V_{\varepsilon} \rho_{\varepsilon}^{\text{c(e)}} \equiv 3\delta_2^{\text{c(e)}} \end{aligned} \quad (2)$$

**Table 1** The alternative high-spin and low-spin ground states of six-coordinated  $d^n$  cations ( $n = 4-8$ ) in  $O_h$ , and the energy criteria at the spin-crossover (only the diagonal energies in the octahedral ligand field matrices [1] are listed). Furthermore, the energy criteria for the stabilisation of the high-spin ground state and of the low-spin alternative, are given, together with the expected distortion symmetries (5/6. and 7/8. column, respectively), if vibronic coupling (see (1, 2), Fig. 2) is additionally taken into account. The latter expressions refer to the vertical energy differences left and right from the spin-crossover, alternatively viewed from the high- and from the low-spin ground state, respectively. In the  $d^8$  case a spin change is not feasible in  $O_h$ , but may occur via a pronounced distortion according to a tetragonal elongation (pseudo-JT effect in excited spin-singlet states; see text)

n	High spin	Low spin	Cross-over ( $O_h$ ) at
4	$^5E_g(t_{2g}^3e_g^1)$	$^3T_{1g}(t_{2g}^4)$	$\Delta = 6B + 5C$
5	$^6A_{1g}(t_{2g}^3e_g^2)$	$^2T_{2g}(t_{2g}^5)$	$\Delta = 7.5B + 5C$
6	$^5T_{2g}(t_{2g}^4e_g^2)$	$^1A_{1g}(t_{2g}^6)$	$\Delta = 2.5B + 4C$
7	$^4T_{1g}(t_{2g}^5e_g^2)$	$^2E_g(t_{2g}^6e_g^1)$	$\Delta = 4B + 4C$
8	$^3A_{2g}(t_{2g}^6e_g^2)$	$^1E_g(t_{2g}^6e_g^2)$	$0 = 8B + 2C$

H- Spin ground state in	LF ( $< I_{rep}$ ) <sup>1,2</sup>	L- Spin ground state in	LF ( $> I_{rep}$ ) <sup>1,2</sup>
$^5B_{1g}(e_g^2b_{2g}^1a_{1g}^1)$	$D_{4h}^e$	$^3A_{2g}(b_{2g}^2e_g^2)$	$D_{4h}^c$
$^6A_{1g}(t_{2g}^3e_g^2)$	$O_h$	$^2B_{2g}(e_g^4b_{2g}^1)$	$D_{4h}^e$
$^5B_{2g}(b_{2g}^2e_g^2b_{1g}^1a_{1g}^1)$	$D_{4h}^c$	$^1A_{1g}(t_{2g}^6)$	$O_h$
$^4A_{2g}(e_g^4b_{2g}^1a_{1g}^1b_{1g}^1)$	$D_{4h}^e$	$^2A_{1g}(e_g^4b_{2g}^2a_{1g}^1)$	$D_{4h}^e$
$^3A_{2g}(t_{2g}^6e_g^2)$	$O_h$	$^1A_{1g}(e_g^4b_{2g}^2a_{1g}^2)$	$D_{4h}^e$

<sup>1</sup>ligand field energy in terms of the cubic ligand field strength and the tetragonal splitting parameters, with respect to interelectronic repulsion in terms of the Racah parameters B, C, as given in the 4. column (I<sub>rep</sub>).

<sup>2</sup>The  $\delta_1$ ,  $\delta_1'$ ,  $\delta_2$  splitting parameter are defined in (1 and 2) and in Fig. 2. The upper index (\*) indicates, that the splittings refer to excited states – with the optimised radial distortion parameters in the respective *ground states*, in difference to (1, 2).

( $V_\varepsilon$  (eV · Å<sup>-1</sup>): first order coupling constant; higher order coupling is usually not significant).

We refer to [2] concerning the derivation of these relations. The Franck-Condon transition energies within an  $E_g$  and  $T_g$  state ( $E_{FC}$ ) define splitting parameters  $\delta_1$  ( $\delta_1'$ ) and  $\delta_2$ , as illustrated in Fig. 2; here, *only the electronic* energy changes with respect to the  $O_h - t_{2g}$  and  $e_g$  MOs are depicted, which obey the centre-of-gravity rule in the case of small state splittings  $E_{FC}$  in comparison to the ligand field strength  $\Delta$ . If the potential energy contributions due to the restoring force ( $1/2 K_\varepsilon \rho_\varepsilon^2$ ) are included, the relevant stabilisations are the Jahn–Teller energies  $E_{JT}$ , as given in (1 and 2). The higher-order  $A_2$  coupling constant in (1) is mainly due to the configuration interaction between the  $nd_z^2$ -electron ( $a_{1g}$  in  $D_{4h}$ ) and the totally symmetric  $(n + 1)$  s-electron cloud, and mostly a numerically significant quantity [5]. It depresses the  $a_{1g}$  ( $d_z^2$ ) MO and accordingly favours the tetragonal elongation to the compression ( $\delta_1 > \delta_1'$ ). For a closer ligand-field energy analysis, we refer to the matrices for 6-coordinated  $d^n$  cations with  $n = 4, 6, 7$ , based on this approach ( $\Delta$ ,  $B$ ,  $C$ ,  $\delta_1$ ,  $\delta_2$ ) [2].

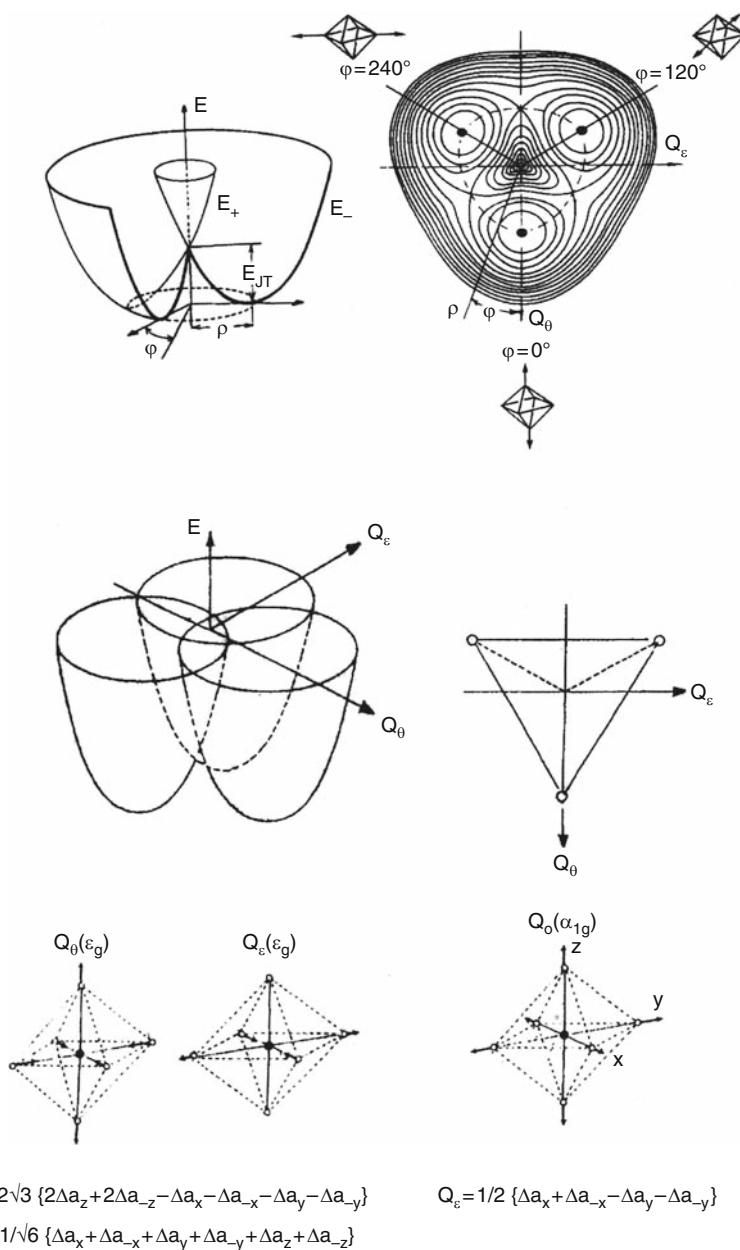


**Fig. 1** The adiabatic potential surface of an electronic  $E_g$  state due to the linear vibronic interaction with a vibrational  $\epsilon_g$  mode (top); the mexican hat-shaped curve on the left is modified by higher order coupling terms, yielding a three minima-refinement, which is shown in a cross section perpendicular to the energy axes on the right. The potential surface, resulting from  $T_g \otimes \epsilon_g$  coupling (amidst), leads to an analogous three-well-structure already in first order – each of these corresponding to a tetragonal polyhedron distortion along one of the three molecular axes. The vibrational  $\alpha_{1g}$  and  $\epsilon_g$  modes are shown on the bottom (adopted from [2])

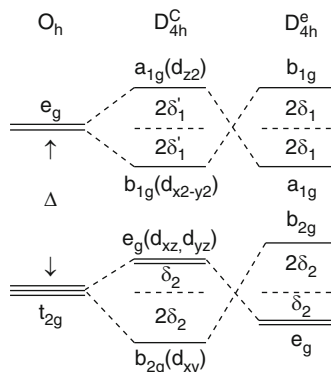


**Fig. 2** Schematic energy diagrams, depicting the Jahn–Teller splittings of the antibonding  $t_{2g}$ - and  $e_g$ -MOs according to  $D_{4h}$ , elongated and compressed (formal assumption:  $\delta_l = \delta_l'$ ;  $\delta_2^c = \delta_2^e$ )

In this contribution we will consider  $3d^n$  cations in their (+III) oxidation states, which are comparatively stable up to  $n = 6$ , but easily reduced for  $n > 6$  by ligands, positioned high in the nephelauxetic series [6], i.e. which induce rather small Racah parameters of interelectronic repulsion  $B$ ,  $C$  in respect to the free-ion values. Indicating such reducing properties, low-lying ligand-to-metal charge transfer bands sometimes appear already in the near-UV, even in the crystal field of the fluoride ligand with the highest electronegativity – as in the case of  $Ni^{III}$ , and in particular,  $Cu^{III}$ . The  $d^8$  configuration of the latter cation is furthermore interesting, because – though a triplet-to singlet spin-flip is not possible in  $O_h$  – a low-spin  $^1A_{1g} (e_g^4 b_{2g}^2 a_{1g}^2)$  ground state is eventually stabilised (and indeed observed) in  $D_{4h}^e$ , with a near-to-square planar coordination. Here, invoked by a pseudo-JT coupling in the lowest excited spin-singlet state, a strong tetragonal field can outweigh the energy barrier due to interelectronic repulsion in favourable cases (Table 1). We will consider this effect in a separate section. Already a short glance into Table 1, comparing the spin-flip criteria for the  $d^4$  and  $d^7$  configuration, substantiates the distinct influence of  $E_g \otimes e_g$  JT coupling. Though interelectron repulsion favours the high-spin in respect to the low-spin state for  $d^4$  more than for  $d^7$ , it is clearly the pronounced JT effect according to a tetragonal elongation, which creates the extreme situation, that  $Ni^{III}$  is generally low-spin, while  $Mn^{III}$  is nearly always high-spin configured.

We will now treat the various  $d^n$  cases individually in greater detail.

## 2 The $NiF_6^{3-}$ Polyhedron: High-Spin or Low-Spin?

(+III) is a rather unstable oxidation state for nickel and only well defined, if counteranions with pronounced electronegativity, such as fluoride or oxygen and nitrogen ligand atoms, constitute the ligand field. It is similar in this respect to  $Cu^{III}$ , whose

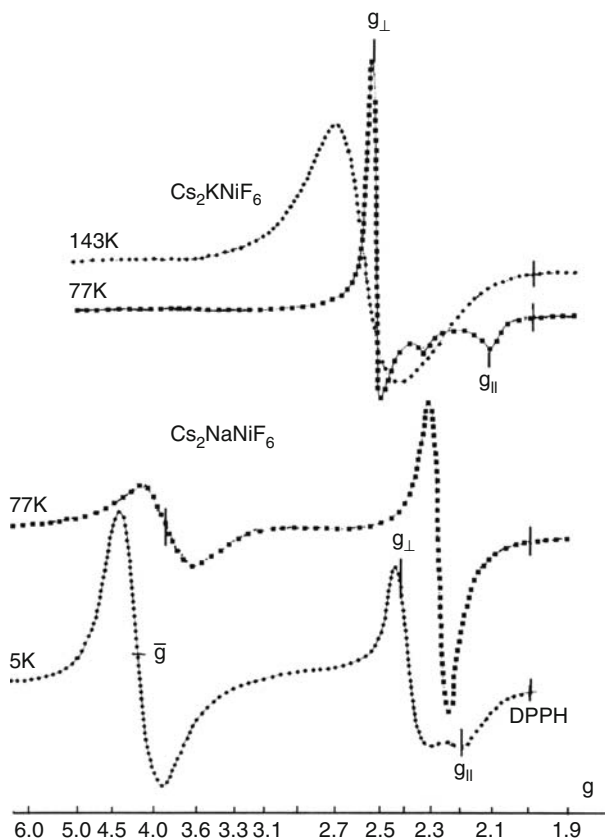


**Fig. 3** EPR spectra of the elpasolite  $\text{Cs}_2\text{KNiF}_6$  and of the hexagonal variant  $\text{Cs}_2\text{NaNiF}_6$  (see Fig. 5), the latter displaying signals of low-spin and high-spin  $\text{Ni}^{\text{III}}$  side by side

optical electronegativity is even larger – easily oxidising even chloride, if combined with this anion. In difference, the  $\text{Co}^{\text{III}}$  cation can be also stabilised by less electronegative ligands. The spin state of the hexafluoro- $\text{Ni}^{\text{III}}$  complex has long been subject of diverging discussions. Unambiguous proof came from the EPR investigation [7], performed on various elpasolites, prepared by Alter and Hoppe [8]; the low-temperature spectra showed the typical anisotropic signal near to  $g = 2.0$ , characteristic of a cation with an octahedral  ${}^2E_g$  ( $e_g^1$  or  $e_g^3$ ) ground state in the presence of strong  $E_g \otimes \varepsilon_g$  Jahn–Teller coupling [9] (Fig. 3).

A low-spin ground state had been suggested already earlier by Allen and Warren, who assigned the weak, lowest-energy band around  $6,500\text{ cm}^{-1}$  in the d–d spectra to a Jahn–Teller-split  $E_g$  ground state as the apparently only reasonable explanation [10]. The ligand field calculation on the basis of the available spectral data yields a vertical doublet-quartet separation energy of  $\delta_{2,4}^{\text{eff}} = 770\text{ cm}^{-1}$  – enhanced to about  $900\text{ cm}^{-1}$ , when including LS-coupling [7] (Fig. 4). The upper

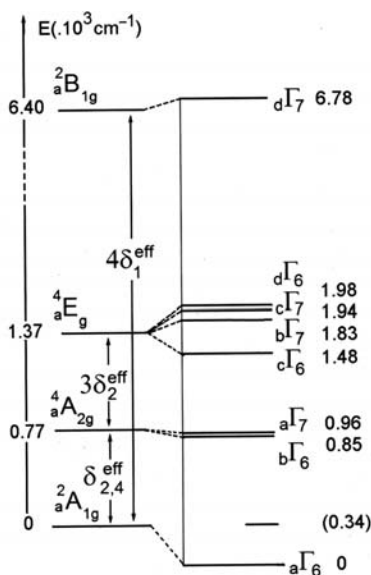


**Fig. 4** Energy diagram (adopted from [7]) of the  $\text{NiF}_6^{3-}$  polyhedron in the elpasolite  $\text{Cs}_2\text{KNiF}_6$  in the region of the octahedral lowest-energy  ${}^2E_g(\rightarrow {}^2A_{1g}, {}^2B_{1g})$  and  ${}^4T_{1g}(\rightarrow {}^4A_{2g}, {}^4E_g)$  states; the relevant parameters are listed in Table 2, the LS coupling parameter is chosen as  $\xi = 500 \text{ cm}^{-1}$ . The lower, left index at the term symbols indicates, that configuration interaction has been accounted for, and counts the energetic sequence of terms with the same symmetry

index (eff) indicates that configuration interaction via interelectronic repulsion has been taken into account. The expression for the diagonal  $\delta_{2,4}$  energy is readily taken from Table 1:

$$\delta_{2,4} = \Delta - 4(B + C) + 2(\delta_1 - \delta_2^*) \quad (3)$$

and is of the magnitude  $100 \text{ cm}^{-1}$ .

The low-temperature structure of the considered elpasolites is shown in Fig. 5; the polyhedron axes of tetragonal elongation are oriented parallel, exhibiting an elastic order pattern of the *ferrodistortive* type. According to the  $(d_z^2)^1$  electronic configuration the magnetic order is hence *antiferromagnetic*, leading to EPR silence at low temperatures. At higher temperatures the solids undergo second-order tetragonal-to-cubic phase transitions, induced by the transformation of low-spin into high-spin  $\text{Ni}^{\text{III}}$ , on the one hand, and by the static local JT distortion becoming dynamic at elevated temperatures, on the other hand; here, as common among chemists, the terminology *dynamic* characterises a situation, in which a thermal equilibration of the bond lengths leads to an  $O_h$  symmetry in the time average (Fig. 1). The thermal averaging is nicely seen by physical methods with larger time frames, as EPR for example, where the anisotropic transforms into an isotropic signal when increasing the temperature (Fig. 3, top). The experimental data, derived

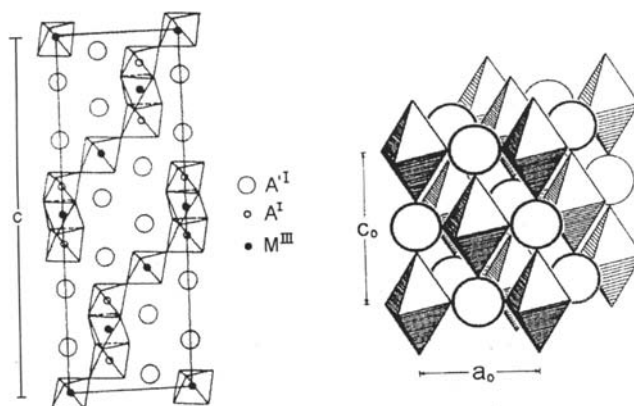


**Fig. 5** The ferrodistorive order of  $D_{4h}$ -elongated  $\text{NiF}_6^{3-}$  polyhedra in elpasolites  $A_2'\text{AMF}_6$  (right) – the circles standing for the intervening  $A^1$  cations – and the hexagonal  $\text{Cs}_2\text{NaNiF}_6$  structure [63] (left); in  $\text{Cs}_2\text{NaNiF}_6$ , with the latter structure,  $\text{Ni}^{\text{III}}$  is low-spin and high-spin, depending on whether it occupies octahedra, corner-connected with its neighbour-polyhedra, or octahedral sites, possessing common faces with two  $\text{Na}^+$  polyhedra, respectively

**Table 2** Ligand field parameters (in  $10^3 \text{ cm}^{-1}$ ) and vibronic coupling constants ( $A_1$ ,  $V_\varepsilon$ : in  $\text{eV} \cdot \text{\AA}^{-1}$ ;  $A_2$  in  $\text{eV} \cdot \text{\AA}^{-2}$ ) for the  $\text{NiF}_6^{3-}$  polyhedron (top). Structural data (in  $\text{\AA}^{-1}$ ), energy quantities (in  $10^3 \text{ cm}^{-1}$ ) and force constants (in  $\text{eV} \cdot \text{\AA}^{-2}$ ) for low-spin (amidst) and high-spin  $\text{Ni}^{\text{III}}$  (bottom) are also given. The data in brackets refer to effective values, with configuration interaction being accounted for. Listed results are from experiment and DFT (see text)

$\Delta$	B	C/B	$A_1$	$A_2$	$V_\varepsilon$
13.1(1) <sup>a</sup>	0.78 <sup>a</sup>	4.0 <sup>a</sup>	2.05	$\cong 0.9$	0.5 <sub>5</sub> (1) <sup>b</sup>

$\rho_\varepsilon$	$a_{av}$	$E_{JT}$	$\delta_I$	$\delta_2^*$	$\delta_{2,4}$	$K_\varepsilon$	$\Delta E_{2,4}$
0.189	1.881	1.60	1.70	0.4(1)	0.26	12.7	—
[0.183] <sup>c</sup>	—	[1.48]	[1.60]	[0.3(1)]	[0.77]	—	[0.4(1)] <sup>d</sup>

$\rho_\varepsilon$	$a_{av}$	$E_{JT} = \delta_2$	$\delta_I^*$	$\delta_{4,2}$	$K_\varepsilon$
0.07	1.915	0.16(3)	0.57	1.70	8.6
[0.06]	—	[ $\cong 0.1$ ]	[0.42]	[0.9 <sub>5</sub> ]	—

<sup>a</sup>from EPR and d–d spectra

<sup>b</sup>with a larger uncertainty, discussed elsewhere [2].

<sup>c</sup>estimation from experiment:  $\geq 0.14 \text{ \AA}$  [11].

<sup>d</sup>energy barrier for the spin-flip, from magnetic measurements and potential curves (Fig. 6).

from the d–d spectra [7, 10], the EPR results [7], the structure [11] and the magnetic susceptibility measurements [2, 8] are collected in Table 2.

The diagram in Fig. 4 demonstrates, that it is the large vertical  $E_g \otimes \varepsilon_g$  Jahn–Teller splitting  $4 \delta_1^{\text{eff}}$  of low-spin  $\text{Ni}^{\text{III}}$ , which actually stabilises the doublet ground

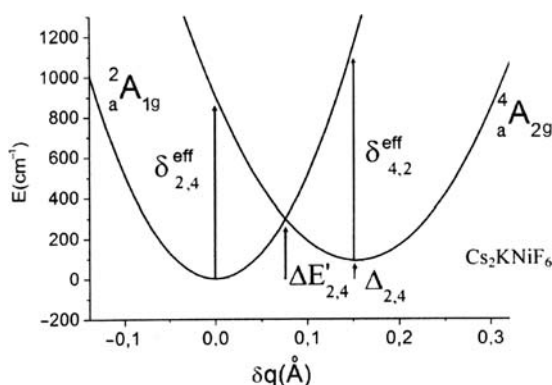
state. In order to obtain knowledge about the potential energy curves for the alternative spin states and hence about the respective *non-adiabatic* energy difference between the two minimum positions, help by reliable calculations was needed. DFT was our method of choice; here [2, 12], our experience is, that one may confidently use DFT results, if only Franck-Condon transitions from the ground state to lower excited states and polyhedron structures at or near to those for the ground state are utilised – and also, that the calculations are performed in the presence of a charge-compensating solvent medium. One has further to note, that the Racah parameters of interelectronic repulsion cannot be reproduced by DFT sufficiently well – they usually come out too small in comparison to the experimental values.

Table 2 gives a survey of the DFT results supplying available experimental data. With these additional informations from DFT, we can now sketch the ground state potential diagrams for low- and high-spin  $\text{Ni}^{\text{III}}$ . In particular, we use the force constants and distortion parameters for low- and high-spin  $\text{Ni}^{\text{III}}$ , as well as the force constant  $K_\alpha$  for the totally symmetric  $\alpha_{1g}$  mode, because there is a small but distinct average bond length difference between dublet and quartet  $\text{Ni}^{\text{III}}$ , which has to be accounted for. For this purpose, we define a displacement coordinate  $\delta q$ , comprising motions according to both, the  $\varepsilon_g$  and the totally symmetric  $\alpha_{1g}$  vibration, when moving from the minimum of the low-spin to the minimum of the high-spin potential curve (Fig. 6) – following Bersukers concept [13] of a single interacting mode:

$$\frac{1}{2} K_\varepsilon^{\text{hsp}} (\delta q')^2 \equiv \frac{1}{2} K_\varepsilon^{\text{hsp}} (\delta \rho_\varepsilon^{\text{eff}})^2 + \frac{1}{2} K_\alpha (\sqrt{6} \delta a_{\text{av}})^2 \quad (4a)$$

$$\delta q' \equiv \left\{ (\delta \rho_\varepsilon^{\text{eff}})^2 + 6 (K_\alpha / K_\varepsilon^{\text{hsp}}) (\delta a_{\text{av}})^2 \right\}^{1/2}$$

$$\delta \rho_\varepsilon^{\text{eff}} = 0.183 - 0.060 = 0.123 \text{ \AA}; \delta a_{\text{av}} = 0.034 \text{ \AA} \quad (4b)$$



**Fig. 6** Adiabatic potential energy surfaces for the low-spin ground state and the high-spin excited state of lowest energy, for the  $\text{NiF}_6^{3-}$  polyhedron in the elpasolite  $\text{Cs}_2\text{KNiF}_6$ , along the  $q$  coordinate (5);  $\Delta E'_{2,4}$  is related to the thermal spin-flip barrier and  $\Delta_{2,4}$  is the non-adiabatic high-spin/low-spin separation



(with  $K_\alpha/K_\epsilon^{\text{hsp}} \cong 1.2$ , from IR data and DFT)  $\Rightarrow \delta q' = 0.153 \text{ \AA}$

Utilising the data from Table 2, we have estimated  $\delta q'$  (4a) and can now construct the adiabatic potential curves for the low-spin and the hypothetical high-spin ground state via the equations:

$$E^{\text{lsp}} = \left\{ \frac{1}{2} K_\epsilon^{\text{lsp}} - A_2 \right\} (\delta q)^2; \quad E^{\text{hsp}} = \frac{1}{2} K_\epsilon^{\text{hsp}} (0.153 - \delta q)^2 \quad (5)$$

and at  $\delta q' = 0.153$  and 0, respectively:

$$\frac{1}{2} K_\epsilon^{\text{lsp}} (0.153)^2 = \delta_{4,2}^{\text{eff}} + \Delta_{2,4}; \quad \frac{1}{2} K_\epsilon^{\text{hsp}} (0.153)^2 = \delta_{2,4}^{\text{eff}} - \Delta_{2,4}$$

With the precisely known doublet-quartet separation energy  $\delta_{2,4}^{\text{eff}}$  from experiment (Fig. 4) we can now evaluate the stabilisation energy of the low-spin with respect to the high-spin  $\text{Ni}^{\text{III}}$  polyhedron; it comes out to be very small:  $\Delta_{2,4} \cong 130 \text{ cm}^{-1}$ . With this value at hand, one can also – within the limit of about  $250 \text{ cm}^{-1}$  – reproduce the quartet-doublet separation energy  $\delta_{4,2}^{\text{eff}}$ , which results from a ligand field calculation, if *the same  $\Delta$  and Racah parameters are employed as for low-spin  $\text{Ni}^{\text{III}}$* . Finally, we have determined the energy  $\Delta E'_{2,4} (\cong 300 \text{ cm}^{-1})$  at the point of intersection, which should be loosely correlated with the barrier height, steering the transformation of low-spin in to high-spin  $\text{Ni}^{\text{III}}$  with increasing temperature (Table 2). Magnetic data provide more precise information with respect to this critical energy separation ( $\Delta E_{2,4} = 500 \text{ cm}^{-1}$ ) [2, 8].

The presence of an only very small nonadiabatic energy barrier between high- and low-spin  $\text{NiF}_6^{3-}$  is further confirmed by the EPR spectrum of the solid  $\text{Cs}_2\text{NaNiF}_6$  (Fig. 3), which crystallises in a hexagonal variant of the elpasolite structure (Fig. 5). The spectrum shows low-spin and high-spin  $\text{Ni}^{\text{III}}$  side-by-side, according to the two crystallographic sites in the mentioned hexagonal structure. One may readily assume, that the central  $\text{Ni}^{\text{III}}\text{F}_6^{3-}$  polyhedron within the face-connected group of three is somewhat geometrically restricted in its tendency towards an  $E_g \otimes \epsilon_g$ -type Jahn–Teller distortion, as compared to the normal elpasolitic site with corner-connections to its neighbours. Apparently, the mentioned small structural strain is significant enough to prevent spin-pairing in this site. EPR signals can here be observed down to 4 K, because the low-spin  $\text{Ni}^{\text{III}}$  centres are too far apart from each other in the structure to induce antiferromagnetic interactions of noticeable strength.

The  $\text{NiF}_6^{3-}$  polyhedron is a beautiful example for a low-spin/high-spin equilibrium, with an only very small preference for the former spin-state. The structural data, energy quantities and vibronic coupling parameters, listed in Table 2, originate from the experiment, supplemented by carefully selected DFT results. They are rather precisely characterising the energetic situation near to the spin-crossover for the  $\text{NiF}_6^{3-}$  polyhedron. Interesting for the Jahn–Teller community is, that this preference is the consequence of the stabilisation of the low-spin state by  $E_g \otimes \epsilon_g$  vibronic coupling; high-spin  $\text{Ni}^{\text{III}}$  is only stabilised via a by a factor of 10 smaller  $T_{2g} \otimes \epsilon_g$ -type coupling energy.

### 3 Ni<sup>III</sup> with Oxygen and Nitrogen Ligator Atoms

Solids of the constitution  $\text{La}_2^{\text{III}}\text{M}^{\text{III}}_{1/2}\text{Li}_{1/2}\text{O}_4$  were first described by Blasse [14] and later characterised by Demazeau et al. [15–17]. They crystallise in the  $\text{K}_2\text{NiF}_4$  lattice with an ordered distribution of the  $\text{Li}^{\text{I}}$  and  $\text{M}^{\text{III}}$  cations on the octahedral sites (Fig. 7). A single crystal study of the  $\text{Ni}^{\text{III}}$  compound reveals a very pronounced distortion of the  $\text{Ni}^{\text{III}}\text{O}_6$  polyhedron ( $\rho_e = 0.39 \text{ \AA}$ ; Table 3) according to a tetragonal elongation [18]. In rating the extent of the distortion, one has to consider, that a structural strain is present in the lattice in such a way, that the contrapolarising power of  $\text{La}^{3+}$ , parallel to  $c$ , is larger than that by  $\text{Li}^+$ , perpendicular to  $c$  (Fig. 7), and is present already in the absence of any electronic instability. It is of considerable magnitude and can be estimated, for the solid with the non-JT cation  $\text{M}^{\text{III}} = \text{Al}$  and with a similar ionic radius as (low-spin)  $\text{Ni}^{\text{III}}$ , to cause a distortion of the  $\text{AlO}_6$ -polyhedron according to  $\rho_e \cong 0.19 \text{ \AA}$ . The strain influence is even more pronounced for the larger and more polarisable  $3d^{10}$  cation  $\text{Ga}^{\text{III}}$  ( $\rho_e \cong 0.34 \text{ \AA}$ ), but without coming up with the value for  $\text{Ni}^{\text{III}}$ . Hence, there is no doubt, that the enhancement of  $\rho_e$  toward  $0.43 \text{ \AA}$  is due to the  $E_g \otimes \varepsilon_g$  JT instability of  $\text{Ni}^{\text{III}}$  in the low-spin state. Spectral energy effects, originating from the modification of the binding properties of oxygen ligator atoms toward a  $3d^n$  cation by the second-sphere environment of the ligand, has been studied elsewhere [21, 22].

The EPR spectrum [17] confirms this conclusion – showing the anisotropic low-spin signal exclusively ( $g_{\parallel} = 2.014$ ,  $g_{\perp} = 2.256$ ; see the 77 K-spectrum of  $\text{Cs}_2\text{KNiF}_6$  in Fig. 3 for comparison), even up to 298 K. The deviation of  $g_{\parallel}$  from the spin-only value ( $\delta g_{\parallel} = 0.012$ ) allows an estimation of the quartet-doublet separation energy; for large  $\delta_{2,4}^{\text{eff}}$  values the following equation is valid:

$$\delta g_{\parallel} \cong 2 \left( \xi / \delta_{2,4}^{\text{eff}} \right)^2 \quad (6)$$

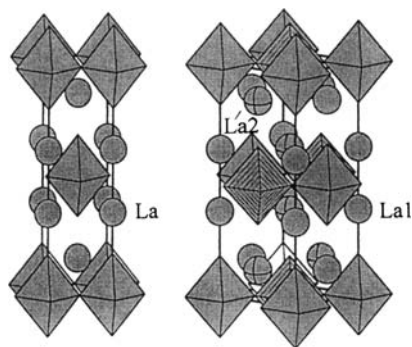


**Fig. 7** The  $\text{K}_2\text{NiF}_4$ -type unit cell of  $\text{La}_2^{\text{III}}\text{Ni}^{\text{II}}\text{O}_4$  (*left*) and the superstructure, induced by cation ordering on the octahedral sites, of solids  $\text{La}_2^{\text{III}}\text{Li}_{1/2}^{\text{I}}\text{M}_{1/2}^{\text{III}}\text{O}_4$  (*right*; hatched polyhedra predominantly, occupied by  $\text{M}^{\text{III}} = \text{Ni, Co}$  cations) – adopted from [18]

**Table 3** Solids crystallizing in an ordered  $K_2NiF_4$ -type lattice –  $La_2^{III}M_{0.5}^{III}Li_{0.5}^IO_4$ , top part – and compounds with a regular  $K_2NiF_4$  structure –  $LaSrM^{III}O_4$ , bottom part: equatorial ( $a_{\perp}$ ) and averaged bond lengths ( $a_{av}$ ) in  $MO_6$  polyhedra, radial distortion parameters (in Å) and information from ionic radii tables

$M^{III}$	$a_{\perp} (4x)^a$		$a_{av}^b$	$\rho_{\epsilon}$	ref.
Mn	1.87	–	(2.01 <sub>5</sub> )	0.50 <sup>c</sup>	–
Co	1.86	1.91	(1.91 <sub>5</sub> )	0.18	[18]
Ni	1.83	1.94	(1.93)	0.39	[18]
Cu	1.80	–	–	– <sup>d</sup>	[18]
Al	1.85	–	(1.90 <sub>5</sub> )	0.19 <sup>c</sup>	[19]
Ga	1.89	–	(1.99)	0.34 <sup>c</sup>	[18]

<sup>a</sup>when utilising  $a_{\perp} (Li-O) = 1.92 \text{ Å}$ , as found for  $Ni^{III}$ ,  $Co^{III}$  [18];  $Mn^{III}$  is high-spin,  $Co^{III}$  and  $Ni^{III}$  are low-spin.

<sup>b</sup>values from ionic radii (with  $r(O^{2-}) = 1.37 \text{ Å}$ ) [20] in parenthesis.

<sup>c</sup>using the experimental  $a_{\perp}$  bond lengths and  $a_{av}$  from ionic radii.

<sup>d</sup> $\rho_{\epsilon}$  loses its meaning in the case of a near-to-square-planar coordination.

M	$c/a^a$	$a_{\perp} (4x)$		$a_{av}$	$\rho_{\epsilon}$	Ref.
Mn	3.43	1.88 <sub>5</sub>	–	(2.01 <sub>5</sub> )	0.45 <sup>b</sup>	[24]
Co	3.28	1.90	1.94 <sub>5</sub>	(1.91 <sub>5</sub> )	0.16	[38] <sup>d</sup>
	3.31	1.91	1.97	(1.98) <sup>c</sup>	0.21	[38] <sup>e</sup>
Ni	3.25	1.91 <sub>3</sub>	1.93	(1.93)	0.06	[31] <sup>f</sup>
Cu	3.52	1.88	$\approx 2.00^g$	–	$\approx 0.4$	[52] <sup>f</sup>
Ga	3.30	1.92 <sub>5</sub>	–	(1.99)	0.22 <sup>b</sup>	[24]

<sup>a</sup>ratios from the tetragonal structure, roughly reflecting the extent of the polyhedron distortion.

<sup>b</sup>using the experimental  $a_{\perp}$  bond lengths and  $a_{av}$  from ionic radii [20].

<sup>c</sup>high-spin value.

<sup>d</sup>results for 100 k and

<sup>e</sup>for 673 K, respectively.

<sup>f</sup>stoichiometric solid without oxygen deficiency, prepared under oxygen pressure.

<sup>g</sup>the bond length, expected from ionic radii [20], is  $\approx 1.91 \text{ Å}$  for  $Cu^{III}$  and (see text) 2.10 for  $Cu^{II}$ .

yielding – with an LS coupling strength according to  $\xi = 400 \text{ cm}^{-1}$  – a vertical separation of  $\approx 5,000 \text{ cm}^{-1}$ . The optical spectrum of the greyish-brown solid [18] is obscured by broad low-energy charge transfer bands, and accordingly one has to estimate the ligand field parameters by other means, in order to obtain approximate information about the energy status with respect to the spin-crossover. In Table 4, the cubic ligand field parameters of  $M^{III}$  cations in an octahedral fluoride coordination are listed, together with those for the  $Cr^{III}O_6$  polyhedron, as found in various oxidic solids [21, 23]. On that basis one can roughly evaluate the ligand field strength  $\Delta$  and the Racah parameter  $B$  also for the cations from  $Mn^{III}$  to  $Cu^{III}$  in oxide matrices. Oxygen is in many ways a chameleon in its binding properties. If combined with a high-charged and small contrapolarising cationic species ( $O-P^V$ , for example; see Sect. 5), its apparent electronegativity is large and gives rise to comparatively small  $\Delta$ -values and rather large Racah parameters. On the other hand, comparatively large  $\Delta$ - and small  $B$ -parameters result, if oxygen is bonded to further cations of larger size and comparable or even smaller charge [21, 22] than  $M^{III}$  – as in the here con-

**Table 4** Ligand field parameters (in  $10^3 \text{ cm}^{-1}$ ) for  $M^{\text{III}}\text{F}_6^{3-}$  complexes with various 3d- $M^{\text{III}}$  cations ( $\text{Mn}^{\text{III}}$ ,  $\text{Co}^{\text{III}}$  high-spin;  $\text{Ni}^{\text{III}}$  low-spin) [2], 2. to 5.column – and for  $M^{\text{III}}\text{O}_6$  polyhedra in perovskite and  $\text{K}_2\text{NiF}_4$ -type host lattices – 6., 7. and 4., 5.column; the magnitudes of the parameters for  $\text{Mn}^{\text{III}}$  to  $\text{Cu}^{\text{III}}$  in the latter case are estimated on the basis of those, found for  $\text{Cr}^{\text{III}}$  [23]

$M^{\text{III}}$	$\Delta$	$\beta^a$	$B_0$	$C/B$	$\Delta$	$\beta^a$
Cr	16.2	0.74 <sub>5</sub>	0.92	–	16.5(5)	0.65(5)
Mn	14.4	0.80	0.97	4.6	14. <sub>6</sub>	0.7 <sub>0</sub>
Co	12.7	0.77	1.07	4.3	12. <sub>9</sub>	0.6 <sub>7</sub>
Ni	13.1	0.70	1.12	4.0	13. <sub>3</sub>	0.6 <sub>1</sub>
Cu	14.5	0.62 <sup>b</sup>	1.2	4.2	14. <sub>8</sub>	0.54 <sup>b</sup>

<sup>a</sup>nephelauxetic ratios  $B/B_0$ , where  $B_0$  is the free cation value (from [10]); the  $\beta$ -ratios for  $\text{Mn}^{\text{III}}$  to  $\text{Ni}^{\text{III}}$  refer to global  $B$  parameters, those listed for  $\text{Cr}^{\text{III}}$  and  $\text{Cu}^{\text{III}}$  are  $B_{\text{te}}$  (for the nomenclature see Sect. 3)

<sup>b</sup>the  $\beta_{ee}$  ratio for  $\text{F}^-$  as the ligand is 0.51 (Fig. 15) and for oxygen ligator atoms accordingly 0.4<sub>5</sub> (see text)

sidered cases. The data, collected in Table 4, are meant for compounds of the latter category. We further mention, that  $B$  and  $C$  are not global parameters – which was assumed here in a coarse approach (Table 4) – but depend on whether only weakly  $\pi$ -antibonding  $t_{2g}$ - or moderately strong  $\sigma$ -antibonding  $e_g$ -electrons are involved within an interelectronic pair-interaction. C.K. Jorgensen has analysed this differential binding effect and distinguishes between  $B_{\text{tt}}$ ,  $B_{\text{te}}$  and  $B_{\text{ee}}$  (and similarly for  $C$ ) [6]. The energetic differences are small or even vanishing in the case of weak covalency, as for  $M^{\text{II}}$  ( $3d^n$ ) –  $\text{F}(\text{O})$ -bonds, but already considerable for the considered  $M^{\text{III}}(3d^n)$  cations.

We deduce from the magnitudes of the estimated ligand field parameters for the  $\text{Ni}^{\text{III}}\text{O}_6$  polyhedra in  $\text{La}_2\text{Ni}_{0.5}\text{Li}_{0.5}\text{O}_4$ , that– due to the more pronounced nephelauxetic effect of oxygen as compared to fluoride – *the system stays rather near to the spin-crossover already in the absence of vibronic coupling*. With  $\Delta$ ,  $B$  and  $C/B$  from Table 4 one derives  $\delta_{2,4} \cong -300 \text{ cm}^{-1}$  in  $O_h$  (see Table 1, 4.column), and, with configuration interaction accounted for,  $\delta_{2,4}^{\text{eff}} \cong +100 \text{ cm}^{-1}$ . A huge JT splitting energy of  $\delta_1 (= 3 \delta_2^*) \approx 3.5 \cdot 10^3 \text{ cm}^{-1}$  has to be presupposed, in order to reproduce in a ligand field calculation the  $\delta_{2,4}^{\text{eff}}$  value from EPR (6). It originates from a very pronounced  $E_g \otimes \varepsilon_g$  coupling, but also from the considerable lattice strain.

In host solids such as  $\text{LaSrGaO}_4$ , with the regular  $\text{K}_2\text{NiF}_4$  structure (Fig. 7), the strain, imposed on the  $M^{\text{III}}\text{O}_6$  polyhedra via the presence of contrapolarising cations with different charge and size in the oxygen coordination sphere, is smaller than in the previously considered ordered lattice type. It is further striking, that the JT coupling of  $\text{Ni}^{\text{III}}$  is obviously completely suppressed (Table 3). If one analyses the lattice parameters of mixed crystals  $\text{LaSrGa}_{1-x}\text{Ni}_x\text{O}_{4-8}$  (with oxygen deficiency), one finds however [24], that tetragonally elongated  $\text{Ni}^{\text{III}}\text{O}_6$  polyhedra in the low-spin state are still partly present up to  $x \cong 0.6$ , which vanish only at higher concentrations. The EPR spectra of  $\text{Ni}^{\text{III}}$ -doped  $\text{LaSrGaO}_4$  [24] and  $\text{LaSrAlO}_4$  [25]

show indeed the same anisotropic low-spin signal as  $\text{La}_2\text{Ni}_{0.5}\text{Li}_{0.5}\text{O}_4$ , with somewhat differing  $g$ -values ( $g_{\parallel} = 2.044$ ;  $g_{\perp} = 2.250$ ); in addition a rather sharp isotropic signal appears ( $g_{\text{iso}} \cong 2.205$ ), which we tentatively assign to  $\text{Ni}^{\text{III}}$  centres with suppressed JT distortion. We follow here the arguments of Angelov, Friebel et al. [26], who detect similar intermediate resonances in a high-resolution EPR spectrum of  $\text{Ni}^{\text{III}}$  doped (low-spin)  $\text{LiCo}^{\text{III}}\text{O}_2$ . The assignment to two kinds of centres is straightforward: One, appearing at lower doping levels, is low-spin and originates from isolated  $\text{Ni}^{\text{III}}\text{O}_6$  polyhedra; the second is ascribed to  $\text{Ni}^{\text{III}}\text{O}_6$  octahedra, interconnected with neighboured  $\text{Ni}^{\text{III}}$  cations via common oxygen bridges, thus forming pairs and small clusters in advance to the final cooperative bulk properties. The  $\text{K}_2\text{NiF}_4$  lattice (Fig. 7), and the  $\text{LiM}^{\text{III}}\text{O}_2$  structure-types as well, offer this geometric possibility – in contrast to compounds  $\text{La}_2\text{M}_{0.5}^{\text{III}}\text{Li}_{0.5}^{\text{III}}\text{O}_4$ , where the cation order in the octahedral sites impedes such an effect. The electron delocalisation exceeds the one due to the anyhow pronounced local metal-to-oxygen covalency within the  $\text{Ni}^{\text{III}}\text{O}_6$  polyhedra [27], considerably. As the consequence of this cooperativity, particularly the  $\sigma$ -antibonding  $e_g$  MOs broaden into a band. For such a case, Thomas and Höck [28] predict a suppression of vibronic coupling, if the band width distinctly exceeds the potential JT splitting energy (here  $4\delta_1$ ). The enhanced  $\text{Ni}^{\text{III}}\text{-O}$  bond covalency in  $\text{LaSrNiO}_{4-8}$ , with respect to that in  $\text{La}_2\text{Ni}_{0.5}\text{Li}_{0.5}\text{O}_4$ , is beautifully reflected by the lower-energy shift of the pre-edge peak in the X-ray absorption spectrum (XAS) at the oxygen K-edge (Fig. 8, left); the increased peak-width mirrors the cooperative electron delocalisation within the equatorial planes of the structure (Fig. 7) [29, 30]. Furthermore, *the appearance of only one absorption also for the  $\text{K}_2\text{NiF}_4$ -type solid indicates low-spin  $\text{Ni}^{\text{III}}$  in both cases.* A high-spin configuration would demand two excitations – into the  $e_g$ - but also into the open  $t_{2g}$ -subshell. The XA spectra at the Ni –  $\text{L}_{2,3}$  near-edge (Fig. 8, right) of the two solids are nearly identical; only the fine structure is distinctly broadened in the case of  $\text{Ni}^{\text{III}}\text{-O} - \text{Ni}^{\text{III}}$  electron delocalisation.

From the fit to the experimental  $\text{Ni}^{\text{III}}\text{-XA}$  spectra one can derive in-formations about the  $\text{Ni}^{\text{III}}\text{-O}$  bond covalency. The wave-function for the considered  $\text{M}^{\text{III}}$  polyhedron, if an electron is excited from a low-lying ligand-centred band into the open 3d-shell, is usually given as:

$$\phi = \alpha_o | \underline{3d^n} > + \beta_o | \underline{3d^{n-1}} \underline{\text{L}} > \quad (\alpha_o^2 + \beta_o^2 = 1) \quad (7)$$

where the underlined electron states refer to hole configurations at the metallic centre and the ligand. The mixing coefficients measure the extent of delocalisation in the metal-ligand bond. For  $\text{Nd}_2\text{Ni}_{0.5}\text{Li}_{0.5}\text{O}_4$  and  $\text{Nd}_{0.9}\text{Sr}_{1.1}\text{NiO}_{3.95}$   $\beta_o^2$  amounts to 49% and 58%, respectively [29]. The doublet-quartet separation energy of the isolated  $\text{Ni}^{\text{III}}\text{O}_6$  polyhedra in the  $\text{LaSrGaO}_4$ - host is estimated from  $\delta g_{\parallel} = 0.042$  [24, 25] via (6) to be of the magnitude  $\delta_{2,4}^{\text{eff}} \cong 3,000 \text{ cm}^{-1}$ ; it is hence smaller than in the case of the  $\text{La}_2\text{M}_{0.5}^{\text{III}}\text{Li}_{0.5}\text{O}_4$ -matrix, because of a reduced lattice strain, though opposed by the more pronounced nephelauxetic effect. Due to its large electronegativity and a pronounced bond covalency even in combination with strongly electronegative ligator atoms, the (+III) oxidation state of nickel becomes rather

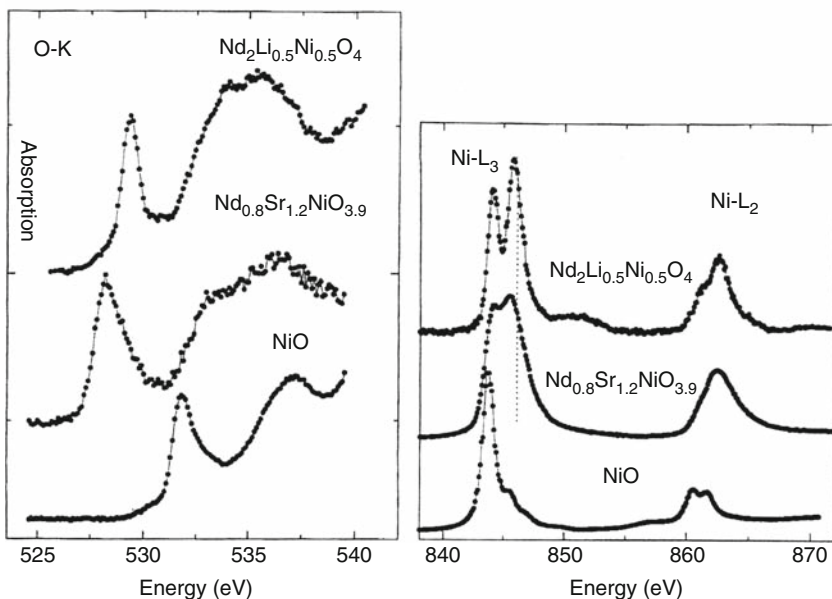


**Fig. 8** O–K- (left) and Ni –  $L_{2,3}$ - (right) XA spectra of two solids with isolated (top) and cooperatively embedded (amidst)  $\text{Ni}^{\text{III}}\text{O}_6$  polyhedra, respectively, in comparison with  $\text{Ni}^{\text{II}}\text{O}$  ( $\text{Nd}^{\text{III}}$  was chosen in order to obtain Ni –  $L_3$  data, which are free of overlap with spectral structures from  $\text{La}^{\text{III}}$  [29])

unstable, if the host structure allows electron delocalisation via Ni–L–Ni bridgings between neighboured polyhedra. A tendency towards itinary electrons and band formation, as well as toward mixed-valence  $\text{Ni}^{\text{III}}/\text{Ni}^{\text{II}}$  properties, develops, which lastly leads to a suppression of Jahn–Teller coupling (see Sect. 7). In accordance, solids  $\text{La}(\text{Nd})\text{SrNiO}_{4-\delta}$  with  $\delta = 0$  can only be prepared under oxygen pressure [31]. If one recalls the decreased Racah-parameters  $B$  and  $C$  with respect to those given in Table 4 and the results of the ligand field calculation for  $\text{La}_2\text{Ni}_{0.5}\text{Li}_{0.5}\text{O}_4$ , reported above, a low-spin ground state is in fact expected even in the absence of JT coupling ( $\delta_1, \delta_2^* = 0$ ).

$\text{Ni}^{\text{III}}$  can also be stabilised in isolated complexes with nitrogen ligator atoms. Due to the enhanced ligand field strength and a slightly decreased nephelauxetic ratio in respect to oxygen as the ligand [32], one can with certainty predict a low-spin ground state even for vanishing vibronic coupling (Tables 1 and 4). This is indeed the case for the two reported examples with the tridentate tri-azacyclononane (TACN) [33] and the bidentate bipyridyl [34] as the ligand, where structural, EPR and ligand field data are available. The  $g$ -tensor components of the ( $e_g^1$ )-type EPR spectra are nearly identical, with  $g_{\parallel} = 2.030(4)$  and  $g_{\perp} = 2.132(5)$ ; they indicate the expected tetragonal elongation.  $\delta_{2,4}^{\text{eff}}$  amounts to  $2.4(2) \cdot 10^3 \text{ cm}^{-1}$  (see (6), with  $\xi = 400 \text{ cm}^{-1}$ ). The radial distortion parameter is  $\rho_e = 0.16 \text{ \AA}$  ( $a_{\text{av}} = 2.017 \text{ \AA}$ ) in the former and  $\approx 0.10 \text{ \AA}$  ( $a_{\text{av}} = 1.982$ ) in the latter case (see here the discussion in [33]), considerably smaller than in (isolated) polyhedra with oxygen ligator atoms.

The d–d spectrum of the brown compound  $[\text{Ni}(\text{TACN})_2](\text{S}_2\text{O}_6)_3 \cdot 7\text{H}_2\text{O}$  is only partly resolved; the lowest-energy absorption, which very probably corresponds to the  ${}^2E_g$  ground state splitting  $4\delta_1^{\text{eff}}$ , appears at  $6,500\text{ cm}^{-1}$ .

After all, solids and complexes with  $\text{Ni}^{\text{III}}\text{L}_6$  polyhedra can be prepared with  $\text{L} = \text{F}, \text{O}$  and  $\text{N}$  ligator atoms – but in the case of oxidic hosts as stable, stoichiometric compounds in general only, if the polyhedra occur isolated in the lattice. While the low-spin state is very slightly preferred with respect to the high-spin state for fluoride as the ligand, the quartet-doublet separation becomes large, if ligator atoms, located higher in the spectrochemical and lower in the nephelauxetic series, constitute the ligand sphere.

## 4 $\text{Co}^{\text{III}}$ in Fluorides and Oxidic Solids: High-Spin and Low-Spin, Respectively?

The d–d spectrum of a fluoridic elpasolite, with constituting colour centres  $\text{Co}^{\text{III}}\text{F}_6^{3-}$ , in Fig. 9, can only be understood on the basis of a high-spin  ${}^5T_{2g}(t_{2g}^4e_g^2)$ -ground state (octahedral parent symmetry) and a – distinctly JT-split –  ${}^5E_g(t_{2g}^3e_g^3)$  – excited state [10, 36].  $T_{2g} \otimes \varepsilon_g$  vibronic coupling demands a distortion according to a tetragonal compression ( $D_{4h}^c$ ; Fig. 2) and hence a  ${}^5B_{2g}(b_{2g}^2e_g^2b_{1g}^1a_{1g}^1)$  ground state (Table 1). The additional features, in particular in the spectrum of the – elsewhere considered [2] – solids  $\text{A}^1\text{CoF}_4$ , are due to spin-forbidden quintet-triplet transitions, mainly occurring within the octahedral  $t_{2g}^4e_g^2$ -configuration. The ligand field parameters, obtained by a best fit to the spectra, but using the ground state splitting  $3\delta_2$  as calculated by DFT, are listed in Table 5. With furthermore the polyhedron distortion derived from DFT at hand, also the vibronic coupling parameters can be deduced via (1 and 2). For further details we refer to [2].

The alternatively possible  ${}^1A_{1g}(t_{2g}^6)$  low-spin ground state is here calculated to appear as an excited state at  $7.5 \cdot 10^3\text{ cm}^{-1}$  (diagonal energy), according to (Table 1):

$$\delta_{5,1} = 5B + 8C - 2\Delta + 2\delta_2 \quad (8)$$

It undergoes considerable configuration interaction, however, reducing the singlet-quintet separation in a very pronounced way (see  $\delta_{5,1}^{\text{eff}}$  in Table 5). It is also interesting to analyse more closely the *intermediate-spin state*, i.e. the lowest-energy many-electron split state in  $D_{4h}^c$ , originating from the excited octahedral  $t_{2g}^5e_g^1$  parent configuration. It turns out to be:  ${}^3A_{2g}(b_{2g}^1e_g^4b_{1g}^1)$  from the lowest  ${}^3T_{1g}$  state (see the section of the  $d^6$ -Tanabe Sugano diagram in Fig. 11 [1]). The corresponding vertical triplet-quintet separation energy – deduced from the respective diagonal energies of the ligand field matrices in  $D_{4h}$ , compressed [2] – is:

$$\delta_{5,3} = 5B + 5C - \Delta - 2\delta_1^{/*} + 4\delta_2 \quad (9)$$

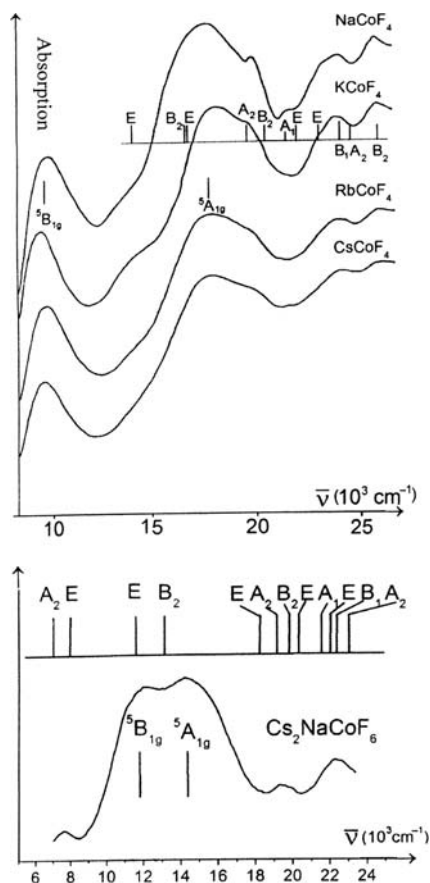


**Fig. 9** The d–d spectra of the rhombohedral elpasolite  $\text{Cs}_2\text{NaCo}^{\text{III}}\text{F}_6$  and of compounds  $\text{ACo}^{\text{III}}\text{F}_4$  (adopted from [2, 35]). The assignment and fitting of the quintet–quintet and of the spin-forbidden quintet–triplet (top-listing) transitions – better resolved in the case of the  $\text{ACoF}_4$ -solids – is according to tetragonally compressed  $\text{Co}^{\text{III}}\text{F}_6$ -octahedra; the ligand field parameters  $\Delta$ ,  $B$ ,  $C$  and  $\delta_I^*$  ( $\delta_2$  was taken from DFT), derived for the elpasolite-type solids, are listed in Table 5

and – with the parameter values in Table 5 and configuration interaction included – of the magnitude  $\delta_{5,3}^{\text{eff}} = 7.0 \cdot 10^3 \text{ cm}^{-1}$ .  ${}^3_aA_{2g}$  is hence located about  $2,000 \text{ cm}^{-1}$  above the  ${}^1_aA_{1g}$  state. We will come back to the problem, whether an intermediate spin-state might eventually appear as the ground state, when discussing oxygen as the ligator atom. While this is strictly excluded in  $O_h$  symmetry (Fig. 11), the strong vibronic coupling in the  $e_g^1$  subshell possibly supplies a large enough JT stabilisation in  $D_{4h}$  symmetry.

We now turn to oxygen as the ligand. In Fig. 10 we display the O–K–XA spectrum of  $\text{La}_2\text{Co}_{0.5}^{\text{III}}\text{Li}_{0.5}\text{O}_4$  [30, 37]; one narrow pre-edge feature is observed, which is compatible only with just one open d-subshell and hence a low-spin  ${}^1A_{1g}$  ( $t_{2g}^6$ ) ground state. The same conclusion holds for the perovskite  $\text{LaCoO}_3$ , where the



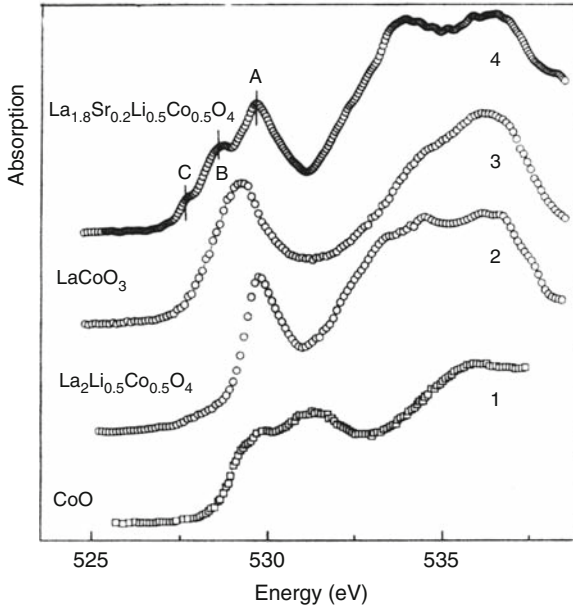


**Fig. 10** O–K–XA spectra of oxide ceramics with  $\text{Co}^{\text{II}}$  (1),  $\text{Co}^{\text{III}}$  (2, 3) and of a solid with 60 and 40 mole %  $\text{Co}^{\text{III}}$  and  $\text{Co}^{\text{IV}}$ , respectively (4); adopted from [30]

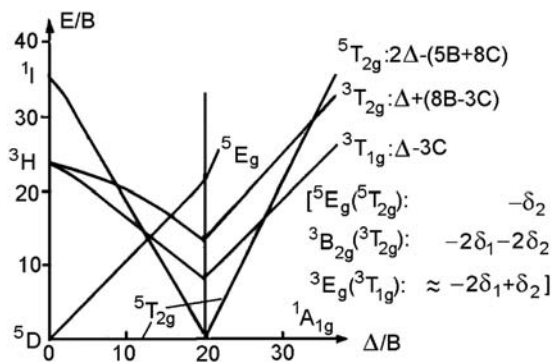
**Table 5** Ligand field energy parameters (in  $10^3 \text{ cm}^{-1}$ ), vibronic coupling constants ( $A_1$ ,  $V_\epsilon$ : in  $\text{eV} \cdot \text{\AA}^{-1}$ ;  $A_2$ ,  $K_\epsilon$ : in  $\text{eV} \cdot \text{\AA}^{-2}$ ) and structural data from DFT (in  $\text{\AA}$ ) for the tetragonally compressed  $\text{Co}^{\text{III}}\text{F}_6^{3-}$  polyhedron.  $\delta_{5,1}^{\text{eff}}$ ,  $\delta_{5,3}^{\text{eff}}$  are the separation energies between  $^5B_{2g}(b_{2g}^2 e_g^2 b_{1g}^1 a_{1g}^1)$  and  $^1A_{1g}(\approx b_{2g}^2 e_g^4)$ ,  $^3A_{2g}(\approx b_{2g}^1 e_g^4 b_{1g}^1 a_{1g}^0)$  (in  $10^3 \text{ cm}^{-1}$ ), respectively

$\Delta$	B	C/B	$A_1$	$A_2$	$V_\epsilon$	$K_\epsilon$
12.7	0.82 <sub>5</sub>	4.3	2.00	0.8	0.65	8.1

$\rho_\epsilon$	$a_{\text{av}}$	$\delta_2 = E_{JT}$	$\delta_I^*$	$\delta_{5,1}^{\text{eff}}$	$\delta_{5,3}^{\text{eff}}$
0.081	1.927	0.21	0.62 <sub>5</sub>	4.8	7.0

$\text{Co}^{\text{III}}\text{O}_6$  centres are corner-connected with each other in a 3-dimensional network, and we may confidently anticipate, that this should be also true for the compound  $\text{LaSrCoO}_4$ , where the bridging-network is 2-dimensional (Fig. 7). Reported structural data (Table 3) are in line with polyhedron distortions, which are not supported by vibronic coupling. It is possible to partly transform  $\text{Co}^{\text{III}}$  into  $\text{Co}^{\text{IV}}$  by increasing the Sr/La-ratio in the ordered  $\text{K}_2\text{NiF}_4$ -type compound beyond unity. EPR and O–K–XAS evidences the expected  $t_{2g}^5$  configuration for  $\text{Co}^{\text{IV}}$  (see [37] and Fig. 10 for details). Single crystal X-ray data for the mixed-valence compound  $\text{Sr}_{1.2}\text{La}_{0.8}\text{Co}_{0.5}\text{Li}_{0.5}\text{O}_4$  with 40 mole%  $\text{Co}^{\text{IV}}$  indicate a slightly enhanced ( $\rho_\epsilon = 0.21 \text{ \AA}$ ;  $a_{\text{av}} = 1.93 \text{ \AA}$ ) polyhedron distortion with respect to the parent  $\text{Co}^{\text{III}}$  solid, possibly caused by  $T_{2g} \otimes \epsilon_g$  JT-coupling of low-spin  $\text{Co}^{\text{IV}}$ .



**Fig. 11** Section from the Tanabe-Sugano diagram for an octahedral  $d^6$  configuration (with  $C/B = 4.8$ ) [1]. The *diagonal energies* for the  $^5T_{2g}$ ,  $^3T_{1g}$ ,  $^3T_{2g}$  states in respect to the  $^1A_{1g}$  ground state are specified – as well as the energy additions for the lower energy split terms of these, in  $D_{4h}^e$  (in brackets; see Table 6)

The magnetic  $\chi_M^{-1}$ -versus- $T$  measurements of Demazeau et al. [16] are in accord with a  $^1A_{1g}$  ground state as well. The authors deduce from the distinct temperature dependence with a maximum at about 200 K, that admixtures not only due to spin-quintet, but also according to spin-triplet states occur via Boltzmann population, involving energy barriers of about  $1,500\text{ cm}^{-1}$ . In order to get some understanding for such a possible energetic situation, we have, to begin with, estimated the Franck-Condon energy separations  $\delta_{1,5}^{\text{eff}}$  and  $\delta_{1,3}^{\text{eff}}$  via a ligand field calculation, where we used the parameters for oxygen ligands in Table 4; however, a slightly enhanced ligand field strength was chosen, because a two-electron jump is involved when switching from the high-spin configuration in fluorides to  $t_{2g}^6$  in oxide coordination (Table 6). In a second step we attempted to fix the approximate position of the *potential energy minimum* of the lowest intermediate-spin  $t_{2g}^5 e_g^1$  state. It is expected to undergo a distinct shift along the  $q(\approx \rho_e)$  coordinate in respect to the  $^1A_{1g}$  minimum (see the discussion in Sect. 2), because a pronounced  $e_g \otimes e_g$ -type vibronic stabilisation via the singly occupied  $e_g$  MO is involved; hence, the non-adiabatic  $\Delta_{1,3}^{\text{eff}}$  energy separation (see Table 6) might be considerably smaller than  $\delta_{1,3}^{\text{eff}}$ , and provide a more appropriate magnitude for the energy barrier, steering the thermal equilibrium. From model ligand field calculations in  $O_h$  and  $D_{4h}$ , with tentatively chosen  $\delta_1$ - and  $\delta_2$ -energies – but adjusted to the energetic landscape as occurring for oxygen as the ligand – one obtains the triplet-singlet and quintet-singlet separation energies, listed in Table 6. Explicitly,  $\Delta_{1,3}^{\text{eff}}$  is the (estimated) non-adiabatic separation energy between the minimum of the  $^3A_{2g}$  or  $^3E_g$  potential curve at  $q^{\min} \approx \rho_e^{\min}(\text{tripl})$  and the minimum of the  $^1A_{1g}$  potential curve at  $q^{\min}(\text{singl}) = 0$ , where we have approximately made allowance for the involved change of the restoring energy.  $\Delta_{1,5}^{\text{eff}}$  was coarsely assumed to also refer to the  $\rho_e^{\min}(\text{tripl})$  coordinate. The result for  $O_h$  indicates close neighbourhood to the spin-singlet/spin-quintet cross-over (Fig. 11), but also signalizes a rather large *vertical*  $\delta_{1,3}^{\text{eff}}$  separation energy. However, if one looks at the *minimum posi-*

**Table 6** Adiabatic (in  $O_h$ ) and non-adiabatic (in  $D_{4h}$ ) quintet-singlet- ( $\delta_{1,5}^{\text{eff}}$ ,  $\Delta_{1,5}^{\text{eff}}$ ) and triplet-singlet- ( $\delta_{1,3}^{\text{eff}}$ ,  $\Delta_{1,3}^{\text{eff}}$ ) separation energies for low-spin  $\text{Co}^{\text{III}}\text{O}_6$  polyhedra, with  $\Delta = 13.6$ ,  $B = 0.725 \cdot 10^3 \text{ cm}^{-1}$  and  $C/B = 4.3$ , as for  $\text{La}_2\text{Co}_{0.5}\text{Li}_{0.5}\text{O}_4$  (Table 4 and text) – from model ligand and field calculations, in  $O_h$  and  $D_{4h}$ , compressed and elongated (in  $10^3 \text{ cm}^{-1}$ ). In  $D_{4h}$ ,  $\Delta_{1,3}^{\text{eff}}$  is defined as the energy difference between the minimum position of the lowest spin-triplet (at  $\rho_e^{\text{min}}(\text{trip})$ ) and the minimum of the  ${}^1A_{1g}$  potential curve; for  $\Delta_{1,5}^{\text{eff}}$ ,  $\rho_e^{\text{min}}(\text{trip})$  is also the (here coarsely supposed) point of reference (on the lowest spin-quintet potential curve)

	$\Delta_{1,5}^{\text{eff } a}$	$\Delta_{1,3}^{\text{eff } a}$	Involved states
$O_h$	0.85	5.0 <sub>5</sub>	${}^1A_{1g}, {}^5T_{2g}, {}^3T_{1g}$
$D_{4h}^c$	0.2 <sub>5</sub> <sup>b</sup>	4.0 <sup>bd</sup>	${}^1A_{1g}, {}^5B_{2g}, {}^3A_{2g}$
	−0.1 <sup>b</sup>	3.5 <sup>bd</sup>	
$D_{4h}^e$	0.5 <sub>5</sub> <sup>c</sup>	3.8 <sup>ce</sup>	${}^1A_{1g}, {}^5E_g ({}^5T_{2g}),$
	0.4 <sup>c</sup>	3.0 <sup>ce</sup>	${}^3E_g ({}^3T_{1g})$

<sup>a</sup>in  $O_h$ :  $\delta_{1,5}^{\text{eff}}$  and  $\delta_{1,3}^{\text{eff}}$

<sup>b</sup>with  $\delta_1' = 2.5$   $\delta_2 = 1.6$  and  $2.5$ , respectively

<sup>c</sup>with  $\delta_1 = 3$   $\delta_2 = 2.0$  and  $3.0$ , respectively

<sup>d</sup>the triplet-term, next in energy to  ${}^3A_{2g}$ , is  ${}^3E_g ({}^3T_{2g})$ , at by 0.9 (top) and 0.3 (bottom) higher energies

<sup>e</sup>the triplet-term, next in energy to  ${}^3E_g ({}^3T_{1g})$ , is  ${}^3B_{2g} ({}^3T_{2g})$ , at by 2.0 (top) and 1.2 (bottom) higher energies

tion of the lowest-energy potential curve, originating from the intermediate  $t_{2g}^5 e_g^1$  configuration, the (non-adiabatic) triplet-singlet energy difference is much smaller, particularly in  $D_{4h}^e$ . With  $\delta_1 = 3,000 \text{ cm}^{-1}$ , magnitudes of  $\Delta_{1,3}^{\text{eff}}$  and  $\Delta_{1,5}^{\text{eff}}$  are estimated, which are coarsely in the range of the energy barriers, suggested by the magnetic measurements. The splitting parameters of the model calculations were chosen in the limits of those found for  $\text{Ni}^{\text{III}}$ , neighboured in the number of d-electrons to  $\text{Co}^{\text{III}}$ . A significant conclusion from the calculations is, that a cross-over between the lowest singlet  ${}^1A_{1g}$  and the lowest triplet  ${}^3A_{2g}$  or  ${}^3E_g ({}^3T_{1g})$  term in  $D_{4h}$  is not within reach, even if unrealistically large  $\delta_1$  or  $\delta_1'$  parameters are chosen.

The magnetic  $\chi_m^{-1}/T$ -data for  $\text{LaSrCoO}_4$  [38] show only a weak deviation from linearity above 600 K, and thus indicate rather a large high-spin/low-spin separation energy in respect to  $\text{La}_2\text{Co}_{0.5}\text{Li}_{0.5}\text{O}_4$  with isolated  $\text{CoO}_6$  octahedra. In analogy to  $\text{Ni}^{\text{III}}$ , this can be traced back to a larger overlap covalence in the case of  $\text{Co}^{\text{III}} - \text{O} - \text{Co}^{\text{III}}$  bridges in the structure; the correspondingly reduced Racah parameters enhance  $\delta_{1,5}^{\text{eff}}$  and  $\delta_{1,3}^{\text{eff}}$  (Table 6, Fig. 11). The respective delocalisation phenomena are nicely documented by a red-shift and an increase of the half-width of the pre-edge peak in the O-K-XA spectra of the perovskite  $\text{LaCoO}_3$ , where all oxygen-ligand atoms of the  $\text{CoO}_6$  octahedra are in bridging functions (Fig. 10; spectra 2, 3). The mentioned effects are less pronounced than for  $\text{Ni}^{\text{III}}$  (Fig. 8), however, due to the larger ionicity of  $\text{Co}^{\text{III}}$ . Referring to (7), a delocalisation according to  $\beta_o^2 = 0.28$  is reported for  $\text{La}_2\text{Co}_{0.5}\text{Li}_{0.5}\text{O}_4$  [39], considerably less than for  $\text{Ni}^{\text{III}}$  in the same host. If the  $\text{Co}^{\text{III}}\text{O}_6$  octahedra are embedded in a 3-dimensional bridging  $\text{O} - \text{Co}^{\text{III}} - \text{O}$  network,  $\beta_o^2$  increases to 0.38 [40]. In ligand fields of more covalent ligand atoms the  ${}^1A_{1g}$  ground state is progressively further stabilised; the same effect is observed, if  $\Delta$  becomes larger. We keep in mind, that

isolated  $\text{Co}^{\text{III}}\text{O}_6$ -polyhedra, as occurring in  $\text{La}_2(\text{Nd}_2)\text{Co}^{\text{III}}_{0.5}\text{Li}_{0.5}\text{O}_4$  for example, represent cases not too far from the singlet–quintet spin-crossover.

## 5 Remarks on $\text{Mn}^{\text{III}}$ and $\text{Fe}^{\text{III}}$

$\text{Fe}(\text{III})$  is usually found to be high-spin in octahedral complexes. According to the large interelectronic repulsion energy increments and the small electronic stabilisation by  $T_{2g} \otimes \varepsilon_g$  coupling (Table 1), a low-spin  $^2T_{2g}$  ground state is only found with ligands, positioned high in the spectrochemical series; one prominent example is the ferricyanide anion  $\text{Fe}(\text{CN})_6^{3-}$ , where the  $T_{2g} \otimes \varepsilon_g$  Jahn–Teller interaction has recently been analysed [4]. Prussian Blue,  $\text{Fe}^{\text{III}}_4 [\text{Fe}^{\text{II}}(\text{CN})_6]_3 \cdot n\text{H}_2\text{O} \equiv (\text{H}_2\text{O})_{2-8} [\text{Fe}^{\text{III}}(\text{Fe}_{0.75}^{\text{II}})] (\text{CN})_{4.5}(\text{OH}_2)_{1.5}$ , a mixed valence compound with an elpasolite-type structure, is a beautiful model example, where the analysis of the structural, of various spectroscopic and of the magnetic properties has lead to a rather complete understanding of the binding situation within this fascinating pigment [41]. However,  $\text{Fe}^{\text{III}}$  is high-spin here, because it is ligated to the nitrogen-atoms of the bridging  $\text{CN}^-$  anions, which exert an even weaker ligand field on the central cation than  $\text{NH}_3$ , for example; carbon, is bonded to  $\text{Fe}^{\text{II}}$ .

Figure 12 displays the optical spectra of  $\text{Fe}^{\text{III}}$  in the octahedral position of the spinel  $\text{ZnGa}_2\text{O}_4$ , where the weak, spin-forbidden sextet-to-quartet d–d transitions appear in the low-energy range. The ligand-to-metal electron transfer region starts at about  $25,000\text{ cm}^{-1}$  for small doping levels, i.e. where the  $\text{Fe}^{\text{III}}\text{O}_6$  octahedra occur isolated in the lattice. They extend into the visible spectral region down to  $\approx 15,000\text{ cm}^{-1}$  in the case of  $\text{ZnFe}_2\text{O}_4$ , caused by electron-delocalisation along the  $\text{Fe}^{\text{III}} - \text{O} - \text{Fe}^{\text{III}}$ -bridges. As expected, the d–d band positions change only slightly with  $x$ ; the increase of the  $\text{Fe}^{\text{III}} - \text{O}$  bond covalence by electron delocalisation is hence small. The shift of the charge-transfer bands into the higher-energy visible region with increasing  $x$  – causing striking colour-changes from yellowish to ochre and finally to brown – exemplarily illustrates the palette of hues, with brownish red, yellow and even black, which is found in iron-bearing rocks in nature and in industrial pigments on iron-oxide basis. The derived ligand field parameters fit well into the sequence of those, estimated for oxygen ligated to  $3d^n \text{M}^{\text{III}}$  cations with  $n$  near to 5 (Table 4). The d–d transitions in the spectrum of  $\text{NH}_4\text{FeP}_2\text{O}_7$  show a distinct blue-shift in respect to those, just discussed; the accordingly very different  $\Delta$  and  $B$  parameters are the result of the strongly contrapolarising  $P^{\text{V}}$  centres, which enhance the apparent electronegativity of the oxygen ligator atoms and hence the ionicity of the  $\text{Fe}^{\text{III}}\text{-O}$  bond. We refer here to the discussion in Sect. 3 in connection with the data in Table 4.

Proceeding to nitrogen as the ligator atom, one usually observes a spin-flip from  $t_{2g}^3 e_g^2$  to  $t_{2g}^5$ ; though thorough studies are scarce [42], small spin sextet-to-doublet separation energies can be suggested (vide infra). We refrain to go into details, because the  $d^5$  cross-over is only weakly influenced by JT forces.

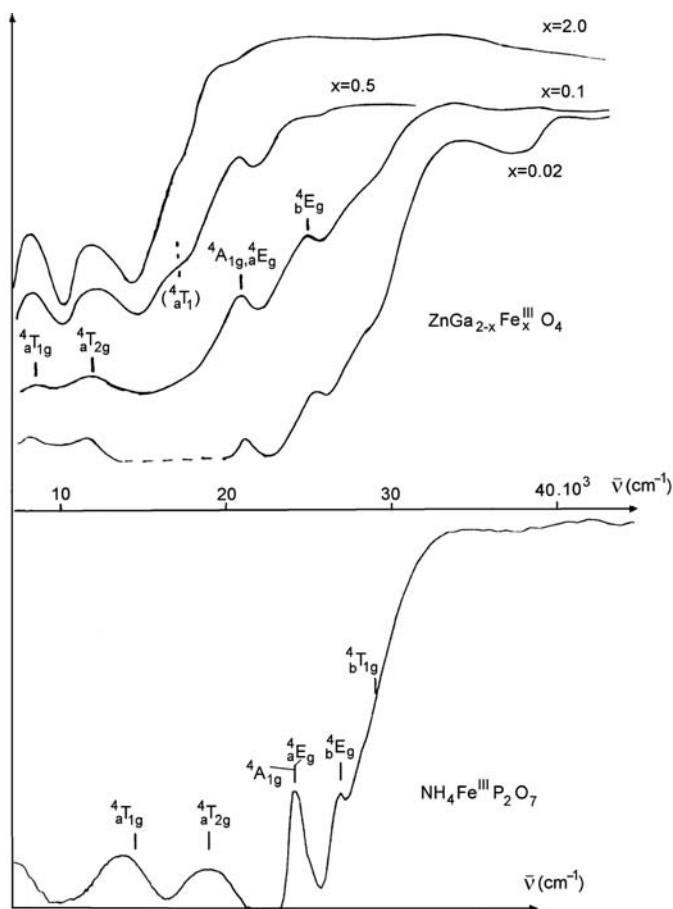


**Fig. 12** Absorption spectra of  $\text{Fe}^{\text{III}}\text{O}_6$  octahedra in spinel mixed crystals  $\text{ZnGa}_{2-x}\text{Fe}_x^{\text{III}}\text{O}_4$  (top) and in the solid  $\text{NH}_4\text{Fe}^{\text{III}}\text{P}_2\text{O}_7$  (bottom); the best-fit band positions with respect to the  ${}^6A_{1g}(t_{2g}^3e_g^2)$  ground state are obtained with the parameters  $\Delta \cong 15.8$ ,  $B \cong 0.625$  (for  $x = 0.1$ ) and  $\Delta = 12.35$ ,  $B = 0.70 \cdot 10^3 \text{ cm}^{-1}$  – nephelauxetic ratios: 0.61 and 0.69 – respectively ( $C/B = 4.9$ ). The shoulder at  $\approx 17,000 \text{ cm}^{-1}$  in the spinel spectra is presumably due to tetrahedral  $\text{Fe}^{\text{III}}$  on the  $\text{Zn}^{2+}$ -site

d–d spectral and magnetic data for various solids with  $\text{Mn}^{\text{III}}\text{F}_6$  polyhedra have been reported [43], and were recently supplemented by DFT results [12]. The derived ligand field and Racah parameters, the structural distortion and the vibronic coupling constants are collected in Table 7. It is clear from these findings, that  $\text{Mn}^{\text{III}}$  occurs in the high-spin state, with a pronounced stabilisation of the  ${}^5E_g(t_{2g}^3e_g^1)$  ground state by a tetragonal elongation of the  $\text{Mn}^{\text{III}}\text{F}_6^{3-}$ -polyhedron, initiated by  $E_g \otimes e_g$  vibronic interactions; the ground state splitting is considerable, with  $4\delta_1 \cong 9,000 \text{ cm}^{-1}$ . Recently, the first hyperfine-EPR spectrum of an  $\text{MnF}_6^{3-}$  complex was reported [44], which nicely mirrors the ( $S = 2$ )-ground state.

**Table 7** Ligand field parameters (in  $10^3\text{ cm}^{-1}$ ), vibronic coupling constants ( $A_I$ ,  $V_e$ : in  $\text{eV} \cdot \text{\AA}^{-1}$ ;  $A_2$ ,  $K_e$ : in  $\text{eV} \cdot \text{\AA}^{-2}$ ) and structural data (in  $\text{\AA}$ ) for the  $\text{Mn}^{\text{III}}\text{F}_6^{3-}$  polyhedron from experiment and DFT, after [35,43]

$\Delta$	B	C/B	$A_1$	$A_2$	$V_e$	$K_e$
14.4	0.78	4.6	2.00	0.70	0.6(1)	9.1
$\rho_\varepsilon$	$a_{av.}$	$E_{JT}$	$\delta_I$	$\delta_2^*$		
0.26(2)	1.93	0.26	2.3	0.65(1)		

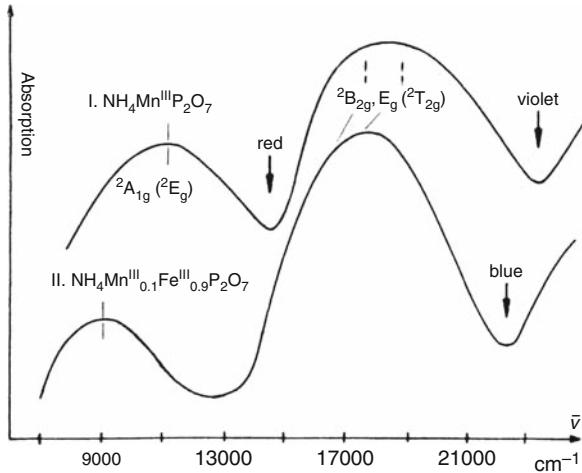


**Fig. 13** The d–d spectra of the  $\text{Mn}^{\text{III}}\text{O}_6$  colour centres in the  $\text{NH}_4\text{Fe}^{\text{III}}\text{P}_2\text{O}_7$  host-structure, indicating a distinct polyhedron distortion according to a tetragonal elongation ( $4\delta_I \cong 9.0$  and  $11.0$ , respectively, with  $\Delta \approx 12.5 \cdot 10^3\text{ cm}^{-1}$ ); the excited state’s splitting ( $3\delta_2^*$ ) is not or only faintly visible. The solids are transparent in the spectral ranges of the minima

Figure 13 displays the d–d spectra of  $\text{Mn}^{\text{III}}$  in the  $\text{NH}_4\text{Fe}^{\text{III}}\text{P}_2\text{O}_7$  host structure; the spin-forbidden transitions due to  $\text{Fe}^{\text{III}}$  (Fig. 12, bottom), which lend only a faint pinkish colour to the  $\text{Fe}^{\text{III}}$  compound, are dominated by the  $\text{Mn}^{\text{III}}$  absorption. The ground state JT-splitting of the doped solid is about equal to that of the  $\text{Mn}^{\text{III}}\text{F}_6^{3-}$  polyhedron, but – due to cooperative-elastic JT forces – considerably enhanced in  $\text{NH}_4\text{Mn}^{\text{III}}\text{P}_2\text{O}_7$ . Interestingly enough, one can control the colour of the solids by varying the polyhedron distortion, which is sensitively mirrored by the energy of, in particular, the lowest-energy absorption band. The hues are, depending on the positions of the minima in the spectra, violet-blue in the doped case and red-violet for the  $\text{Fe}^{\text{III}}$ -free solid. The  $\Delta$ -value – which can be only estimated, because the splitting of the  ${}^5T_{2g}$ -excited state is not resolved – amounts to  $\approx 12,500\text{ cm}^{-1}$ , similar to the ligand field strength of  $\text{Fe}^{\text{III}}$  in the same host lattice.

Structural data for various other oxide host compounds confirm, that  $\text{Mn}^{\text{III}}$  always induces pronounced polyhedron distortions according to a tetragonal elongation, as in  $\text{La}_2\text{Mn}_{0.5}\text{Li}_{0.5}\text{O}_4$ , but in  $\text{LaSrMn}^{\text{III}}\text{O}_4$  as well (Table 3). The,

in comparison to the  $\text{Ni}^{\text{III}} - \text{O} -$  bond, much less covalent  $\text{Mn}^{\text{III}} - \text{O}$ -bond impedes extended electron delocalisation via  $\text{Mn}^{\text{III}} - \text{O} - \text{Mn}^{\text{III}}$  bridges in the latter solid and thus suppression of the JT-coupling. Interesting results are reported for the solid-solution compounds  $\text{Sr}_2^{\text{III}} (\text{Zn}_{1-x}^{\text{II}} \text{Mn}_x^{\text{III}}) (\text{Te}_{1-x}^{\text{VI}} \text{Sb}_x^{\text{V}}) \text{O}_4$  [24], which crystallise in the elpasolite lattice, with an order on the octahedral sites between the di- and trivalent cations, on the one hand, and the Te- and Sb-atoms with the oxidation states six and five, on the other hand. While the solids are (pseudo-) cubic up to  $x = 0.5$ , they undergo a first-order phase transition into a structural modification with tetragonally elongated  $\text{Mn}^{\text{III}}\text{O}_6$  octahedra in ferrodistoritive order (Fig. 5, right) above this critical concentration. At  $x < 0.5$  the polyhedra are dynamically distorted – where we use this terminology for a thermally induced oscillation between the three minima of the ground state potential surface (Fig. 1, top to the right), which leads to an apparent  $O_h$  symmetry, if observed via physical methods with larger time frames. At  $x \geq 0.9$  the cation order on the octahedral sites breaks down and reduces the magnitude of the polyhedron distortion due to intra-lattice strain effects.

Many further  $\text{Mn}^{\text{III}}$  compounds and complexes with oxygen and nitrogen ligator atoms have been studied, all of them characterised by distinct JT-distortions [42]. Also octahedral complexes with the more covalent chloride anion have been prepared and optically investigated; in spite of the pronounced nephelauxetic effect with estimated  $B$  parameters of about  $500 \text{ cm}^{-1}$  ( $\Delta \cong 13,000 \text{ cm}^{-1}$ ), the optical spectra still indicate a high-spin  ${}^5B_{1g}({}^5E_g)$  ground state. There is a tendency, to repel one axial ligand, leaving an  $\text{MnCl}_5^{2-}$  polyhedron with a strongly elongated (approximate)  $C_{4v}$  structure; the formation of the 5-coordinated species – spectroscopically and structurally well characterised [45, 46] – is evident, if the additional JT stabilisation caused by the loss of one axial ligand is considered [2].

To our knowledge, the only low-spin complex, for which spectral data are reported, is the  $\text{Mn}(\text{CN})_6^{3-}$  anion [42]. A rough estimate of the ligand field parameters for the latter polyhedron yields, if one utilises the factorisations according to the nephelauxetic and spectrochemical series of ligands [6] in relation to the known  $\Delta$  and  $B$  parameters for fluoride (Table 4):

$$\Delta \approx 27.0, B \approx 0.46 \cdot 10^3 \text{ cm}^{-1} (C/B = 4.6) \quad (7a)$$

With these data at hand, a (diagonal)  ${}^3T_{2g} \leftarrow {}^5E_g$ -separation energy in  $O_h$  of the magnitude  $\delta_{5,3} \approx 13.500 \text{ cm}^{-1}$  is obtained, which cannot be overcome by any realistic value for the JT energy increment  $2\delta_1 - \delta_2^*$  due to vibronic coupling (see Table 1). Applying an analogous consideration to  $\text{NH}_3$  as the ligand, however:

$$\Delta \approx 20.0, B \approx 0.63 \cdot 10^3 \text{ cm}^{-1} (C/B = 4.6) \quad (7b)$$

one calculates an energy separation of  $\delta_{5,3}(O_h) \approx 1,700 \text{ cm}^{-1}$ , which is easily overcompensated by the vibronic coupling contribution.

The cross-over condition for  $\text{Fe}^{\text{III}}$  in  $O_h$  is close to that for  $\text{Mn}^{\text{III}}$  (Table 1), but lacks the additional stabilisation of the high-spin state by JT coupling. This energetic situation causes (usually) low-spin properties of  $\text{Fe}^{\text{III}}\text{N}_6$  polyhedra, but renders

a  ${}^3T_{1g}$  ground state exceptional in the  $d^4$  case. After all, the best chance for the preparation of a six-coordinate  $\text{Mn}^{\text{III}}$ -complex with a  ${}^5B_{1g}$  ground state in  $D_{4h}^e$  and a nearby  ${}^3A_{2g}$  potential energy minimum is probably to select nitrogen-bearing ligands with donor properties. Polydentate ligands offer the additional possibility to steer the magnitude of  $2\delta_I - \delta_2^*$  via steric ligand strains.

## 6 The Jahn–Teller-Introduced High-Spin-to-Low-Spin Transition of $\text{Cu}^{\text{III}}$

The oxidation state (+III) is rather unstable for copper and can only be stabilised in an environment of highly electronegative ligands.  $\text{Cu}^{\text{III}}\text{F}_6^{3-}$  occurs in the elpasolite matrix, a structure-type with a large lattice energy, and the d–d spectrum has been analysed [10]. Its appearance is cubic, according to a  ${}^3A_{2g}$  ground state. Table 8 summarises the derived magnitudes of the ligand field parameters as well as the vibronic coupling constants, estimated by DFT – here utilising excited states’ optimisations [2].

At the first sight surprisingly, the  $\text{Cu}^{\text{III}}$  centres in  $\text{La}_2\text{Cu}_{0.5}\text{Li}_{0.5}\text{O}_4$  are low-spin, as the diamagnetism caused by spin-pairing of the two  $e_g$ -electrons in the  $t_{2g}^6e_g^2$  ground state configuration indicates [15]. Single crystal X-ray studies further show, that the structure is the same as for the solids with  $\text{Co}^{\text{III}}$  and  $\text{Ni}^{\text{III}}$  (Fig. 5, right) – but that the polyhedron distortion is very pronounced, near to square-planar [18] (Table 3, top). Analogously, in  $\text{KNa}_4[\text{Cu}^{\text{III}}(\text{HIO}_6)_2] \cdot 12\text{H}_2\text{O}$  [47], the underlying  $\text{Cu}^{\text{III}}\text{O}_4(\text{OH}_2)_2$  polyhedron has a similar square-planar structure with equatorial Cu–O bond lengths of 1.838(4) Å and axial Cu–OH<sub>2</sub> distances at >2.7 Å.

We proceed to present a model, appropriate to understand the conditions, which steer the alternative appearance of  $\text{Cu}^{\text{III}}$  in the cubic high-spin  ${}^3A_{2g}$  ( $t_{2g}^6e_g^2$ ) ground state, and in the diamagnetic  ${}^1A_{1g}$  ( $e_g^4b_{2g}^2a_{1g}^2$ ) electronic configuration. The d–d spectra of the  $\text{Cu}^{\text{III}}\text{F}_6^{3-}$  polyhedron in an elpasolite matrix, and of an hexacoordinated complex with the isoelectronic  $\text{Ni}^{2+}$  cation in a fluoridic host solid, are displayed in Fig. 14. The lowest-energy ( ${}^3A_{2g} \rightarrow {}^1A_{1g}$ ) triplet-singlet transition occurs at  $\approx 1.9$  eV for  $\text{Ni}^{2+}$ , but this energy is substantially lowered to about 1.25 eV in the case of  $\text{Cu}^{\text{III}}$  – due to an enhanced nephelauxetic effect by the pronounced  $\text{Cu}^{\text{III}} - \text{O}$  bond covalence.

**Table 8** Ligand field parameters (in  $10^3 \text{ cm}^{-1}$ ) for the  $\text{Cu}^{\text{III}}\text{F}_6^{3-}$  polyhedron in elpasolites  $\text{A}_2'\text{ACuF}_6$  ( $\text{A}'$ , A: alkaline ions), as well as the  $\text{Cu}^{\text{III}}\text{–F}$  bond length (in Å) and the vibronic coupling parameters ( $A_1$ ,  $V_\epsilon$  : in  $\text{eV} \cdot \text{\AA}^{-1}$ ;  $A_2$ ,  $K_\epsilon$  :  $\text{eV} \cdot \text{\AA}^{-2}$ ), derived by DFT from excited electronic states [2]

$\Delta$	B	C/B	$A_1$	$A_2$	$V_\epsilon$	$K_\epsilon$	a
14.5	0.7 <sub>5</sub>	4.2	1.1 <sub>5</sub>	0.7	0.2	5.3	1.91



Basically, the  ${}^1A_{1g}$  split term of  ${}^1E_g(t_{2g}^6e_g^2)$  can be stabilised as the new ground state in a ligand field with a strong tetragonal  $D_{4h}^e$  component. However, inspecting the orbital compositions of the states originating from  $e_g^2$  in  $O_h(\rightarrow {}^3A_{2g}, {}^1E_g, {}^1A_{1g}$ ; see Table A24 in [1], for example), one immediately recognises, that the degeneracy of  ${}^1E_g$  in  $O_h$  can only be lifted via a pseudo-JT interaction, which encloses the  ${}^1A_{1g}$  state as well. Fernandez, Bersuker and Boggs [48] have worked out the  $({}^1E_g + {}^1A_{1g}) \otimes \varepsilon_g$  coupling model for  $d^8$ , and we follow their basic arguments – though in the diction of ligand field theory. The optical transition to the before-mentioned  ${}^1_aA_{1g}(\approx t_{2g}^6e_g^2)$  state is usually not resolved in the d–d spectra, but is calculated to occur at a by  $\approx 1$  eV higher energy than  ${}^1_aE_g$  (see caption of Fig. 14).

The ligand field matrix for  $d^8$  in  $D_{4h}^e$ , which includes the two  ${}^1A_1$  states, originating from  $e_g^2$ , and the two further  ${}^1A_{1g}$  states, stemming from  ${}^1A_{1g}$  and  ${}^1E_g(t_{2g}^4e_g^4)$  in  $O_h$  and connected with the former two via non-diagonal  $B$ - and  $C$ -terms, is listed in Table 9a. The energies are in respect to a  ${}^3B_{1g}({}^3A_{2g})$  ground state in  $D_{4h}^e$ ; the additionally listed energy increment has to be added to each diagonal element. The significant (non-diagonal) vibronic coupling term is  $4\delta_I$  between  ${}^1E_g$  and  ${}^1A_{1g}$ , both from  $t_{2g}^6e_g^2$ . The small  $\delta_2$  energy, originating from  $t_{2g}^4e_g^2$ , is only significant in higher order. Neglecting in a first step the latter interactions, one obtains for the energy of the lowest energy spin-singlet term:

$$E({}^1_aA_{1g}) \cong 12B + 3C - 4\delta_I\{1 + ((4B + C)/4\delta_I)^2\}^{1/2} \quad (8a)$$

The critical condition for stabilising a spin-singlet ground state ( $E({}^1_aA_{1g}) < E({}^3B_{1g})$ ; see Table 1) is, accordingly:

$$4\delta_I \geq 2\sqrt{2(4B + C)} \quad (8b)$$

The energy of the  ${}^1B_{1g}$  split state of  ${}^1E_g(t_{2g}^6e_g^2)$  is not affected perceptibly by the vibronic interaction (see the respective matrix in Table 9b). The Franck-Condon

**Table 9** The energy matrices for  ${}^1A_{1g}$  and  ${}^1B_{1g}$ , restricting from the octahedrae  ${}^1A_{1g}$   ${}^1E_{1g}$  parent terms in  $D_{4h}^e$

a:				
${}^1A_{1g}$ matrix	${}^1E_g(t_{2g}^6e_g^2)$	${}^1A_{1g}(t_{2g}^6e_g^2)$	${}^1E_g(t_{2g}^4e_g^4)$	${}^1A_{1g}(t_{2g}^4e_g^4)$
(8B + 2C)	0	$-4\delta_I$	$2B\sqrt{3}$	0
+	$-4\delta_I$	8B + 2C	0	$(2B + C)\sqrt{6}$
	$2B\sqrt{3}$	0	$B + 2\Delta - 2\delta_2$	$2\sqrt{2}\delta_2$
	0	$(2B + C)\sqrt{6}$	$2\sqrt{2}\delta_2$	$10B + 3C + 2\Delta$
b:				
${}^1B_{1g}$ Matrix	${}^1E_g(t_{2g}^6e_g^2)$	${}^1E_g(t_{2g}^4e_g^4)$		
(8B + 2C)	0	$-2\sqrt{3}B$		
+	$-2\sqrt{3}B$	$B + 2\Delta + 2\delta_2$		

energy within  ${}^1A_g$  is, after (8), of the approximate magnitude:

$$E({}^1A_{1g} \rightarrow {}^1B_{1g}) \cong 4\delta_I \{1 + ((4B + C)/4\delta_I)^2\}^{1/2} - (4B + C) \quad (8c)$$

In order to complete the vibronic treatment, we have to supplement the electronic energies by the restoring energy increment. This is coarsely done by replacing  $4\delta_I$  in (8b) by half of this value – see  $E_{JT}$  in (1) and the electronic ground state stabilisation of the  $e_g$ -MO in Fig. 2 – which stiffens the condition for the high-to-low-spin cross-over. With the parameter set for  $\text{Cu}^{\text{III}}\text{O}_6$ -polyhedra from Table 4 – but utilising the smaller  $B_{ee} = 540 \text{ cm}^{-1}$ , valid for the here involved singlet-states – one estimates  $\delta_I \approx 6,300 \text{ cm}^{-1}$ ; if the non-diagonal matrix elements are additionally taken into account, this value is lowered to  $\delta_I^{\text{eff}} \approx 5,800 \text{ cm}^{-1}$ .

More information were deduced from a DFT calculation for the charge-compensated  $\text{Cu}(\text{OH})_6^{3-}$  polyhedron in  $D_{4h}$  (Table 10). The complex is clearly low-spin, with a huge tetragonal elongation and a bond length  $a_{\perp}$ , which is near to that, reported for  $\text{La}_2\text{Cu}_{0.5}\text{Li}_{0.5}\text{O}_4$  (Table 3). The splitting parameter  $\delta_I$  is close to the one estimated for an energetic landscape, where the  ${}^1A_{1g}$  ( ${}^1E_g$ ) – in  $D_{4h}^e$  – and  ${}^3A_{2g}$  – in  $O_h$  – potential curves possess nearly identical energetic minimum positions. The minima are separated, however, by a very pronounced shift along the displacement coordinate  $q$  (see Sect. 2 and Fig. 6 for definitions). The Franck-Condon excitation energy  $\delta_{I,3}^{\text{eff}}$  between the two states, at the  $D_{4h}^e$  minimum, is accordingly very large, with about  $12,000 \text{ cm}^{-1}$  (Table 10).

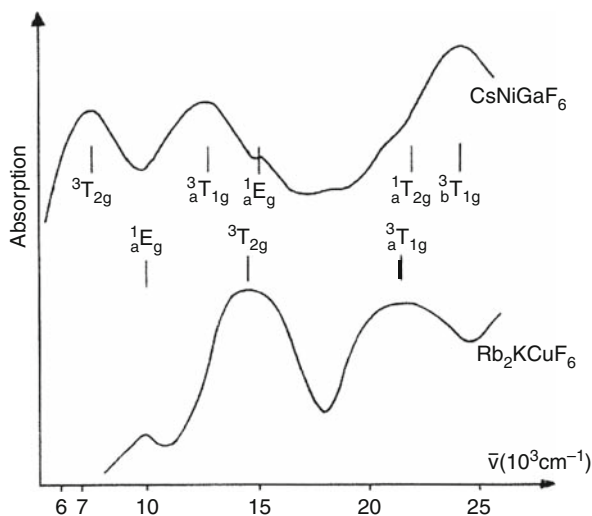


**Fig. 14** The d–d spectra of  $\text{Ni}^{\text{II}}$  and  $\text{Cu}^{\text{III}}$  in octahedral fluoride coordination. The spectra are fitted with:  $\Delta = 7,500$ ,  $B = 950 \text{ cm}^{-1}$ ,  $C/B = 4.2$  ( $\text{CsNiGaF}_6$ , pyrochlor type) and  $\Delta = 14,500$ ,  $B_{et} \approx 750$ ,  $B_{ee} = 610 \text{ cm}^{-1}$ ,  $C/B = 4.2$  ( $\text{Cu}^{\text{III}}$ -elpasolite) – after [2]. The calculated positions of the usually not resolved  ${}^3A_{2g} \rightarrow {}^1A_{1g}$  transition are  $\cong 23,700 \text{ cm}^{-1}$  for the  $\text{Ni}^{\text{II}}\text{F}_6$  and  $\cong 17,500 \text{ cm}^{-1}$  for the  $\text{Cu}^{\text{III}}\text{F}_6$  polyhedron

**Table 10** Results from a DFT calculation for a  $\text{Cu}(\text{OH})_6^{3-}$  polyhedron (charge compensated by a polarisable solvent medium, as described elsewhere [35]), within the electronic  $t_{2g}^6 e_g^2$  ground state manifold ( $\rightarrow {}^1A_{1g}(2x), {}^1B_{1g}, {}^3A_{2g}$  in  $D_{4h}$ ) – energies in  $10^3 \text{ cm}^{-1}$  ( $C/B = 4.2$ ), bond lengths in Å; the listed state energies ( $D_{4h}$  nomenclature) are in respect to the  ${}^1A_{1g}({}^1E_g)$  ground state

$\delta_I$	$\delta_2$	B	$a_{\perp}$	$a_{\parallel}$
5.8	$\approx 0$	0.51	1.77	2.78
$E({}^3B_{1g})$		$E({}_a{}^1B_{1g})$		$E({}_b{}^1A_{1g})$
12.3		21.0		49.8

The lowest-energy spin-allowed transition is that within the octahedral  ${}^1E_g(t_{2g}^6 e_g^2)$  state and predicted to occur at  $\approx 21,000 \text{ cm}^{-1}$ . This is well in line with the optical spectrum of  $\text{La}_2\text{Cu}_{0.5}\text{Li}_{0.5}\text{O}_4$ , which is – in accord with the red colour of the compound – empty up to  $17,000 \text{ cm}^{-1}$  [18], the onset of the charge-transfer region. Figure 15 surveys the *electronic* effects of the pseudo-JT ( $E_g + A_{1g}$ )  $\otimes \varepsilon_g$  interaction for an octahedrally coordinated  $d^8$  cation, with the eventual stabilisation of a  ${}^1A_{1g} \left[ \left( d_z^2 \right)^2 \right]$  ground state. The results of the respective ligand field calculations on the basis of the matrices in Table 9 are depicted in dependence on the splitting parameter  $\delta_I$ , and using the parameter set for the  $\text{Cu}^{\text{III}}\text{O}_6$  polyhedron in Table 3. The spin-flip occurs at  $\delta_I \approx 3,000 \text{ cm}^{-1}$ , as presumed half in magnitude of the critical value, if the restoring force is accounted for.

The ligand field matrices, applied in the context of this contribution, are constructed on the basis of the validity of the centre-of-gravity rule for the tetragonal splitting. In view of the, for  $\text{Cu}^{\text{III}}$ , very large deviation from octahedral, the ligand field strength  $\Delta$  largely loses its meaning; however, because this parameter is only involved in the energies displayed in Fig. 15 and in Table 10 in higher order, one may confidently use the results in good approximation.

Instead of making use of a  $(E_g + A_{1g}) \otimes \varepsilon_g$  pseudo-JT interaction in  $O_h$  one may alternatively start from an  $\text{ML}_4$  tetrahedron [49] and follow the distortion pathway toward a square-planar coordination. The advantage of an alternative  $T \otimes \varepsilon$  and/or  $(E + A_1) \otimes \varepsilon$  coupling model in  $T_d$  is, that the bond length (nearly) and the coordination number remain unchanged and that the active mode is of pure bending type. We have to remark here, that a square-planar coordination of a  $d^8$  cation is not necessarily connected with diamagnetism, as found for the  $\text{Ni}^{\text{II}}\text{O}_4$ -slice in  $\text{Li}_2\text{NiO}_2$ , for example [50].

The decrease of the nephelauxetic ratio, when proceeding from the  $\text{Co}^{\text{III}}\text{O}_6$  and  $\text{Ni}^{\text{III}}\text{O}_6$  to the  $\text{Cu}^{\text{III}}\text{O}_6$  polyhedra in solids  $\text{La}_2\text{M}_{0.5}^{\text{III}}\text{Li}_{0.5}\text{O}_4$ , amounts to 20% (Table 4). The correspondingly enhanced bond covalence is also seen by XAS [39] via a dramatic percentage increase of  $\beta_o^2$  (7) from 28% to 70%. The latter value matches with the one for  $\text{Cu}(\text{OH})_6^{3-}$ , derived from DFT. The dominating participation of ligand electrons in the ground state wave-function has consequences for the relative energetic positions of the metal-3d and ligand-2p parent wave-functions in the respective MO-schemes (Fig. 16). Even for the (high-spin)  $\text{CuF}_6^{3-}$  polyhe-

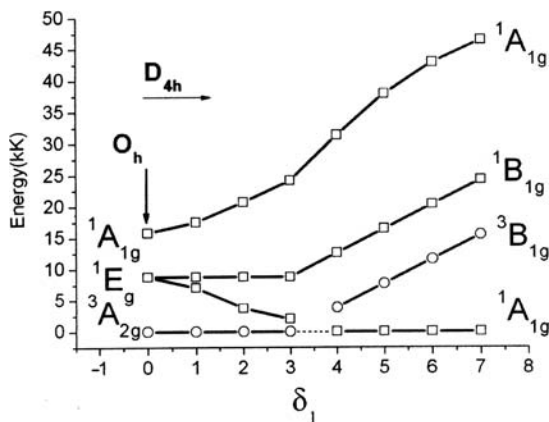


**Fig. 15** Energy diagram of the electronic states, originating from the electronic  $t_{2g}^6 e_g^2$  configuration of a  $\text{Cu}^{\text{III}}\text{O}_6$  polyhedron in  $D_{4h}^e$  symmetry, in dependence on the splitting parameter  $\delta_1$  – results of a ligand field calculation (matrices in Table 9) with:  $\Delta = 14.8$ ,  $B = 0.54 \cdot 10^3 \text{ cm}^{-1}$  and  $C/B = 4.2$  (Table 3), with respect to a (high-spin)  ${}^3B_{1g}$  ( ${}^3A_{2g}$ ) and a (low-spin)  ${}^1A_{1g}$  ( ${}^1E_g$ ) ground state, respectively. The energy sketch has no mirror symmetry when extending toward negative values of the splitting parameter, because  $\delta_1'$  (in  $D_{4h}^c$ ) is distinctly smaller due to the higher-order  $A_2$  parameter (1)

dron  $\beta_o^2 (\cong 0.6)$  is already larger than the metalc–3d participation  $\alpha_o^2$  [51]. In the following section we will discuss the binding properties of  $\text{Cu}^{\text{III}}\text{O}_6$  polyhedra in oxide solids, where these entities don't occur isolated in the lattice anymore. We expect here an even more pronounced  $\text{Cu}^{\text{III}} - \text{O}$  bond-covalence, which further stabilises a spin-singlet ground state.

## 7 The $\text{Cu}^{\text{III}}/\text{Cu}^{\text{II}}$ Ambivalence in Oxidic Host Solids: A Preposition for Superconductivity?

$\text{LaSrCu}^{\text{III}}\text{O}_4$  can be prepared as a pure compound under oxygen pressure, and approximate bond-length data have been reported ( $a_{\perp} = 1.88$ ,  $a_{\parallel} \approx 2.23 \text{ \AA}$ ) [52]. The large  $c/a$  ratio – even in comparison to  $\text{Mn}^{\text{III}}$  – and the coarsely estimated radial distortion parameter indicate a pronounced polyhedron distortion (Table 3). This is not necessarily expected, because the analogous change from the  $\text{La}_2\text{M}_{0.5}^{\text{III}}\text{Li}_{0.5}\text{O}_4$ - to the  $\text{LaSrM}^{\text{III}}\text{O}_4$ - host leads to a complete suppression of the JT coupling in the case of  $\text{Ni}^{\text{III}}$ . The obvious reason is, that the splitting of the  ${}^1A_{1g}$  ( ${}^1E_g$ ) state is by a factor of about 1.8 larger than for  $\text{Ni}^{\text{III}}$ . Thus, for a quenching of vibronic coupling, a further increase of the  $b_{1g}$  ( $d_{x^2-y^2}$ )-band width is needed, in order to meet the critical condition of having a  $({}^1A_{1g} - {}^1A_{1g})$  splitting, which is less than the mentioned band width. In the rhombohedral perovskite  $\text{LaCuO}_3$ , where electron delocalisation along  $\text{Cu}^{\text{III}} - \text{O} - \text{Cu}^{\text{III}}$  bridges occurs along *each* octahedral bond direction, the electron

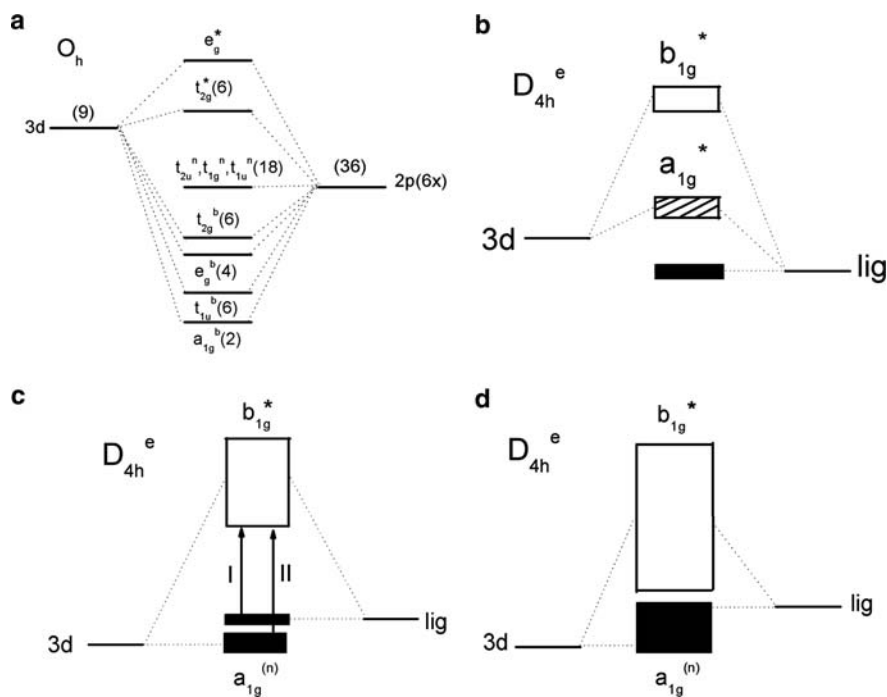


**Fig. 16** Schematic MO diagrams for six-coordinate  $M^{III}O_6$  polyhedra (indices  $*$ ,  $n$ : antibonding and nonbonding; hatched and uniform black: half-filled and fully occupied, respectively): (a) local, predominantly ionic binding scheme in  $O_h$  symmetry ( $M^{III}$ : low-spin  $d^6$  cation); (b) section, displaying only the non-bonding ligand-centred (lig) and the  $\sigma$ -antibonding  $e_g^*$ -split MOs in  $D_{4h}^e$  – as for the JT distorted  $Mn^{III}O_6$  polyhedron in  $La_2Mn_{0.5}^{III}Li_{0.5}O_4$  ( $e_g^{*2}b_{2g}^{*1}a_{1g}^{*1}b_{1g}^{*0}$ ); (c) and (d) sections illustrating the binding situation in low-spin  $Cu^{III}O_6$  polyhedra of  $D_{4h}^e$  symmetry, with a near-to square planar coordination and a filled narrow  $a_{1g}^*$  band, which is nearly non-bonding with respect to  $3d$ ; (c) approximately valid for  $La_2Cu_{0.5}^{III}Li_{0.5}O_4$  and (d) for  $LaSrCu^{III}O_4$ , but here with very probably an overlap between the filled ligand and the empty  $b_{1g}^*$  ( $d_{x^2-y^2}$ ) band (see text)

delocalisation is apparently enhanced to such an extent, that the  $CuO_6$  polyhedra are forced into a regular structure, with bond length of 1.95 Å [15]. Figure 16 illustrates the energetic situation in the region of the JT-split  $\sigma$ -antibonding  $e_g$ -level via sections of MO-diagrams. The sketch (b) refers to approximately the bonding situation in  $La_2Mn_{0.5}Li_{0.5}O_4$  (Tables 3 and 4), where the metal-to-oxygen bonds possess a high degree of ionicity and the electron-transfer from the non-bonding ligand to the predominantly metal centred  $e_g$  MOs lies in the UV.

Figure 16c sketches the relative locations of the involved MOs for the  $Cu^{III}O_6$  polyhedra in  $La_2Cu_{0.5}^{III}Li_{0.5}O_4$ . In the case of a (near-to) square-planar coordination the energies of the  $\sigma$ -antibonding  $b_{1g}$  and  $a_{1g}$  levels are, in the diction of the angular overlap model (AOM):

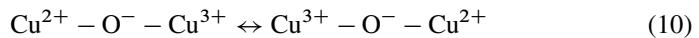
$$E(b_{1g}) = 3e_{\sigma}^{\perp} E(a_{1g}) = e_{\sigma}^{\perp} - E_{ds} \quad (9a)$$

Here,  $3e_{\sigma}^{\perp}$  and  $e_{\sigma}^{\perp}$  are the metal-oxygen overlap energies (3d contributions) for  $d_{x^2-y^2}$  and  $d_z^2$ , respectively, in the  $x$ – $y$  plane.  $E_{ds}$  stands for the, already discussed, repulsive energy reduction of  $a_{1g}(3d_z^2)$  by  $a_{1g}(4s)$ , and can be shown to render a nearly non-bonding character to the  $d_z^2$ -MO, at least in the case of extreme tetragonal distortions [5]. We adopt this finding here, and give the splitting energy  $\Delta E$  under this assumption:

$$\Delta E = E(b_{1g}) - E(a_{1g}) \approx 3e_{\sigma}^{\perp} \quad (9b)$$

Having further in mind, that the ligand orbitals are positioned higher in energy than the metal 3d-orbitals, the ligand-to-metal charge transfer  $E(I)$  is expected at lower energy than the  $a_{1g} \rightarrow b_{1g}^*$  transition  $E(II)$ , which reflects exactly the experimental observation (vide supra).

Figure 16d depicts an MO-scheme, which approximately refers to the binding properties of the  $\text{CuO}_6$  polyhedra in the deep reddish-brown coloured  $\text{LaSrCu}^{\text{III}}\text{O}_4$ . Electron delocalisation via the  $\text{Cu}^{\text{III}}\text{—O—Cu}^{\text{III}}$  bridges in the equatorial plane further broadens particularly the empty  $b_{1g}(d_{x^2-y^2})$  band in respect to  $\text{La}_2\text{Cu}_{0.5}^{\text{III}}\text{Li}_{0.5}\text{O}_4$ . One may even suggest an overlap of the empty antibonding  $b_{1g}$ - with the non-bonding oxygen band, located at the upper edge of the lower-energy filled band. This would allow a ligand-to-metal charge flow or, in a single-bond terminology, the partial formation of  $\text{Cu}^{\text{II}}$ , with an electron hole at the ligand. Such a supposition is supported by some bond-length considerations.  $\text{Cu}^{2+}$  possesses a by about 0.2 Å larger ionic radius than  $\text{Cu}^{3+}$  in octahedral coordination [20]; in fact, a distinct increase of the average bond length is indeed indicated for the  $\text{CuO}_6$  polyhedron in  $\text{LaSrCuO}_4$  (Table 3 bottom, footnote g). Apparently, the suggested overlap of the (non-bonding) ligand by the  $\sigma$ -antibonding, partly metal-centred  $b_{1g}^*$  band has enhanced the mobility of electrons within the equatorial plane of the  $\text{K}_2\text{NiF}_4$ -type lattice of  $\text{LaSrCuO}_4$ , thereby initiating the partial formation of  $\text{Cu}^{\text{II}}$ , according to:



Electron delocalisation of such a type is a necessary qualitative condition for the observation of superconductivity in oxidic mixed valence copper compounds [53]. A further mandatory presupposition is, however, that the  $\text{Cu}^{\text{III}} \rightarrow \text{Cu}^{\text{II}}$  transformation can occur *without an essential change of the polyhedron structure*. This is granted, because octahedrally coordinated  $\text{Cu}^{\text{II}}$  also undergoes a strong  $E_g \otimes \varepsilon_g$  vibronic coupling, leading to a large tetragonal elongation or frequently even to a square-planar ligand environment [9] – similar to  $\text{Cu}^{\text{III}}$ . Thus, for example in  $\text{La}_2\text{CuO}_4$  with the  $\text{K}_2\text{NiF}_4$ -structure,  $\text{Cu}^{\text{II}}\text{—O}$  bond lengths of  $a_{\perp} = 1.905$  and  $a_{\parallel} = 2.46$  Å ( $\rho_e \cong 0.65$  Å) are observed [54], and the  $c/a$  ratio (3.46) is similar to that for  $\text{LaSrCu}^{\text{III}}\text{O}_4$  (Table 3). More specifically, the subsequent survey illustrates by X-ray data of well defined mixed crystals the nearly equal increase of the  $c/a$ -ratio – by 0.18(2) – for an

intervalence  $\text{Cu}^{\text{II}}/\text{Cu}^{\text{III}}$  and a pure  $\text{Cu}^{\text{II}}$  phase (with the same total copper content) in comparison to the host solid [53]:

solid ( $\text{K}_2\text{NiF}_4$ structure)	$a$ (Å)	$c/a$
$\text{La}_{1.8}^{\text{III}}\text{Sr}_{0.2}^{\text{II}}[\text{Ga}_{0.04}^{\text{III}}\text{Cu}_{0.8}^{\text{II}}\text{Cu}_{0.16}^{\text{III}}]\text{O}_4$	3.782	3.505
$\text{La}_{1.96}^{\text{III}}\text{Sr}_{0.04}^{\text{II}}[\text{Ga}_{0.04}^{\text{III}}\text{Cu}_{0.96}^{\text{II}}]\text{O}_4$	3.804	3.460
$\text{La}^{\text{III}}\text{Sr}^{\text{II}}\text{Ga}^{\text{III}}\text{O}_4$	3.848	3.305

For a further discussion of also symmetry aspects, possibly involved in the mechanism of superconductivity in oxide  $\text{Cu}^{\text{II}}/\text{Cu}^{\text{III}}$ -solids, we refer to the literature [21, 53, 55].

We conclude by stating, that the spin cross-over in the case of hexa-coordinated  $\text{Cu}^{\text{III}}$  – which is accompanied by a drastic structural change from octahedral to nearly square-planar – occurs at ligand field parameters in the range of those valid for oxygen as the ligand (Table 4). The employed considerations indicate, that high-spin  $\text{Cu}^{\text{III}}\text{O}_6$  polyhedra might eventually be stabilised in host structures, which impose a strain on the guest-octahedron, opposing its tendency toward square-planar. Besides the here discussed oxide compounds with  $\text{Cu}^{\text{III}}$ , we mention  $\text{KCuO}_2$  with a chain structure of side-connected square-planar  $\text{Cu}^{\text{III}}\text{O}_4$  entities and  $\text{Cu}^{\text{III}} - \text{O}$  bond lengths of 1.84 Å [56], and furthermore refer to a review by Müller-Buschbaum, surveying the structures of copper, specifically in a planar four-coordinate oxide environment [57].

## 8 Final Remarks

Usually the spin cross-over of six-coordinated transition metal complexes is grossly discussed in  $O_h$  symmetry, without referring to the significant energy modifications by vibronic coupling, particularly if  $\sigma$ -antibonding  $E_g$  ground states are involved. Thus, in the  $d^7$  case, the  $E_g \otimes \varepsilon_g$  Jahn–Teller interaction is large enough to stabilise a spin-doublet ground state even for fluoride as the ligand; only by structural strains in the host lattice, opposing the tendency towards a tetragonal distortion of the  $\text{NiF}_6^{3-}$  polyhedron, one succeeds to create a high-spin  $t_{2g}^5 e_g^2$  configuration of lowest energy – as for one  $\text{Ni}^{\text{III}}$  site in  $\text{Cs}_2\text{NaNiF}_6$ . In difference, for the  $d^6$ -configured  $\text{Co}^{\text{III}}$  centre, lacking a vibronic support by JT coupling, the quintet-to-singlet spin-flip occurs only, if one proceeds from fluoride to the less electronegative oxygen ligand. Here, as analysed, interesting high-spin/low-spin correlations are frequently observed.

Though vibronic effects may play an important role in high-spin/low-spin equilibria, another determinant exerts also significant influence, specifically in the here considered series of  $\text{M}^{\text{III}} (3d^n)$  cations: the considerable increase of the electronegativity from  $\text{Mn}^{\text{III}}$  toward  $\text{Cu}^{\text{III}}$  (Table 11). It parallels the nephelauxetic effect of decreasing  $\beta$ -ratios and is a significant particular in the understanding of high-to-low spin interrelations. Thus, it is the low value of the relevant Racah parameter

**Table 11** Electronegativity ( $\chi$ ) data for  $M^{III}(3d^n)$  cations [2] and for fluoride and oxygen [58]; global nephelauxetic ratios  $\beta$  for  $M^{III}O_6$  polyhedra are also given, for the case that if the oxygen ligator atoms possess approximately  $\chi$  values around 3.0 (as in Table 3)

$M^{III}$	$\chi$	$\beta$	Ligator	$\chi$
Mn	2.5	0.7 <sub>0</sub>	F <sup>−</sup>	3.9
Fe	2.6	(0.6 <sub>1</sub> ) <sup>c</sup>	P <sup>V</sup> ...O <sup>2−</sup>	3.5
Co	(2.8) <sup>a</sup>	0.6 <sub>7</sub>	Ca <sup>II</sup> ...O <sup>2−</sup>	3.0
Ni <sup>b</sup>	2.9 <sub>5</sub>	0.6 <sub>1</sub>	Cs <sup>I</sup> ...O <sup>2−</sup>	2.2
Cu	3.5	0.5 <sub>4</sub> <sup>d</sup>		

<sup>a</sup>Estimated value<sup>b</sup>The corresponding values for the isoelectronic Co<sup>2+</sup> ion are:  $\chi = 2.0$ ;  $\beta = 0.86$  ( $B_0 = 970\text{ cm}^{-1}$ ) and (in comparison to 13.3, Table 3)  $\Delta \cong 9.2 \cdot 10^3\text{ cm}^{-1}$ <sup>c</sup>Coarse value from spin-forbidden bands<sup>d</sup> $\beta_{ee}$  is 0.45

$B_{ee}(C_{ee} = 4.2 B_{ee})$  of about  $540\text{ cm}^{-1}$  for  $\text{Cu}^{III}$  (Table 3) when proceeding from fluoride to oxygen as the ligand, which – though with the very large JT splitting parameter  $\delta_J \approx 6,000\text{ cm}^{-1}$  as the predominant energy contribution – finally stabilises a singlet  $^1A_{1g}$  ( $e_g^4 b_{2g}^2 a_{1g}^2$ ) ground state. The respective expansion of the 3d-electron cloud toward the ligands may be taken from the MO diagrams in Fig. 16c, d. The 3d-AOs are located below the ligand 2p atomic orbitals and give rise to a pronounced shift of ligand electron density toward the metal ion. The change from the octahedral high- to the near-to-square planar low-spin configuration is quite spectacular and occurs in the case of oxygen ligator atoms at  $B_{ee}$  and  $\Delta$  parameters of 0.58(3) and  $\approx 14.7 \cdot 10^3\text{ cm}^{-1}$ , respectively. The underlying vibronic phenomenon is elegantly analysed by utilising a pseudo-JT-type symmetry concept. Oxygen is, due to its formal (2-) charge, a very versatile ligator toward  $M^{II}$  and  $M^{III}$  transition metal ions, because its electronegativity can be steered via a widely varying cationic higher-sphere environment [21]. Highly charged and small cations, such as  $P^V$ , induce large-electronegativity properties, while voluminous cations of low charge lend soft properties to the binding toward a considered probe M-cation (Table 11) – see the discussion in [58], Chapt. 6. The covalence within the M–O bond is small in the former, but pronounced in the latter case, reflected by the respective nephelauxetic and spectrochemical effects in the case of 3d–M cations, for example. An illustrating example offers Fig. 12, where the  $\text{Fe}^{III} - \text{O}$  bond is rather ionic in  $\text{NH}_4\text{FePO}_4$  and more covalent in the case of a second-sphere coordination constituted by the larger and less-charged  $\text{Ga}^{3+}$ ,  $\text{Fe}^{3+}$ ,  $\text{Zn}^{2+}$  cations; here the  $\Delta$ -value is enhanced and the  $B$ -parameter reduced – by about 25% and 15%, respectively. We learn, that the covalence effects offer a further steering instrument to the experimental inorganic chemist, interested in the synthesis of complexes, which are innocent in respect to the adoption of a high-, low- or even intermediate-spin ground state at first sight. Higher-sphere environmental effects are equally of importance in the case of nitrogen ligators ( $\text{N}^{3-}$ ), where a rich complex chemistry, involving 3d–M cations is well established.



We supplement our survey with a side-glance into the complex chemistry of  $\text{Co}^{\text{II}}$ , iso-electronic with  $\text{Ni}^{\text{III}}$ . Mainly due to the much larger Racah parameter and a distinctly reduced ligand field strength (Table 11) in comparison to the latter cation, the  ${}^4T_{1g}(O_h) \rightarrow {}^2A_{1g}(D_{4h})$  spin-flip occurs in the wide range of nitrogen as the ligator atom, positioned higher in the spectrochemical and lower in the nephelauxetic series than oxygen. Complexes with these ligands are usually high-spin; however, the tridentate ligands 1, 4, 7-triazacyclononane (TACN) and terpyridine, for example, generate high-spin [32] and low-spin ground states [59, 60], respectively – apparently caused by a small increase of  $\Delta$  by  $\approx 10\%$  and a slight decrease of  $\beta$  by about 5% in the latter case. Interesting is, that in the terpyridine case the high-spin/low-spin separation energy can be varied by changing the counteranions, the water content and, via these parameters, also details of the crystal structure – thereby even obtaining compounds, where high percentages of high-spin coexist besides low-spin  $\text{Co}^{\text{II}}$  at ambient temperatures. The interplay between the imposed steric strain of the tridentate ligand and the JT coupling, as well as the disturbances introduced by the partial presence of high-spin species, have been analysed in comparison with corresponding  $\text{Ni}^{\text{II}}$  complexes, where only the strain-influence, and with  $\text{Cu}^{\text{II}}$  compounds, where the spin-state is definite and hence exclusively the vibronic coupling/strain interference could be studied [61]. A binding strain (vide infra) – if chosen correctly for supporting the JT distortion – may also eventually stabilise a low-spin ground state via an enhancement of the splitting parameter  $\delta_I$ ; for example, the substitution of the axial ligator atoms in TACN by oxygen in the above mentioned  $\text{Co}^{\text{II}}$  complex straight-forwardly transforms the spin-quartet into a spin-doublet ground state [32].

The side-leap was meant to demonstrate, that basic and semi-empirical theory has the potential to provide means and rules, how to prepare high- or low-spin complexes in an aimed way; we again emphasize, that – if orbitally degenerate, in particular  $E_g$ , ground states are involved – Jahn–Teller coupling and (eventually) energetic strain contributions come into play, in addition to the ligand field parameters  $\Delta$  and  $B$ ,  $C$ .

We are still left to define precisely, what we understand by *strain*. The strain concept was introduced into vibronic theory by Ham [62], as a quantity, closely related to the first order vibronic coupling constant; this is termed *binding strain* in our diction [2]. It can be of significant influence, if complexes with slightly or even distinctly differing ligator atoms are considered. There is, however, a second strain increment, not considered in the concept of Ham, which models the force constant in a similarly symmetry-dependent way. This component is related to the elastic properties of a polyhedron, embedded into a specific host lattice, and designated *structural* or *steric strain* in our notion [2]; it mirrors distortion effects imposed on the guest polyhedron by the low symmetry of the host structure or of rigid polydentate ligands, for example. *Structural* and *binding strain* components [2] are of perceptible energetic influence on the spin-cross over only in the case of orbitally degenerate ground states, and may enhance or reduce the ground state JT splitting in a coarsely predictive way. In particular,  $\text{Co}^{\text{II}}$  and  $\text{Ni}^{\text{III}}$  with the  $d^7$  configuration, in oxygen and nitrogen ligand fields, are fascinating in this respect, because the

quartet-doublet spin-flip can be induced here via a great manifold of chemical parameters, such as the choice of various macrocyclic ligands of biochemical interest or of ligator atoms with different binding properties, as discussed.

We finally note, that the preference of the tetragonal elongation in respect to the compression is only a second order energy effect in the  $E_g \otimes \varepsilon_g$  coupling case (1), though very significant for large polyhedron distortions. The respective energy barrier can be overcome by an appropriately chosen strain – as has been shown by a few model examples [9].

**Acknowledgements** The authors are indebted to thanks to Prof. Dr. Horst Köppel, Heidelberg, for his generous help in the technical handling of this contribution.

## References

1. J.S. Griffith, *The Theory of Transition-Metal Ions* (Cambridge University Press, Cambridge, 1971)
2. D. Reinen, M. Atanasov, P. Köhler, D. Babel, *Coord. Chem. Reviews*, to be published (2010)
3. U. Öpik, M.H.L. Pryce, *Proc. R. Soc. London, Ser. A*, **238**, 425 (1957)
4. M. Atanasov, P. Comba, C.A. Daul, A. Hauser, *J. Phys. Chem.* **111**, 9145 (2007)
5. B.N. Figgis, M.A. Hitchman, *Ligand Field Theory and its Applications* (Wiley, New York, 2000)
6. C.K. Jorgensen, *Struct. Bonding* **1**, 3 (1966) and in: *Oxidation Numbers and Oxidation States*, Springer 1969
7. D. Reinen, C. Friebe, V. Propach, *Z. Anorg. Allg. Chem.* **408**, 187 (1974)
8. E. Alter, R. Hoppe, *Z. Anorg. Allg. Chem.* **405**, 167 (1974)
9. D. Reinen, C. Friebe, *Struct. Bonding* **37**, 1 (1979)
10. G.C. Allen, K.D. Warren, *Struc. Bonding* **9**, 67 (1971)
11. J. Grannec, Ph. Sorbe, B. Chevalier, J. Etourneau, J. Portier, *C. R. Acad. Sci., Paris* **282C**, 815 (1976)
12. D. Reinen, M. Atanasov, W. Massa, *Z. Anorg. Allg. Chem.* **632**, 1375 (2006)
13. I.B. Bersuker, *The Jahn–Teller Effect and Vibronic Interactions in Modern Chemistry* (Plenum, New York, 1984) (with supplementing reference volume: *The Jahn–Teller Effect – A Bibliographic Review*)
14. G. Blasse, *J. Inorg. Nucl. Chem.* **27**, 2683 (1965)
15. G. Demazeau, C. Parent, M. Pouchard, P. Hagenmüller, *Mater. Res. Bull.* **7**, 913 (1972)
16. G. Demazeau, M. Pouchard, M. Thomas, J.F. Colombet, J.C. Grenier, L. Fournès, J.L. Soubeyroux, P. Hagenmüller, *Mater. Res. Bull.* **15**, 451 (1980)
17. G. Demazeau, J.L. Marty, M. Pouchard, T. Rojo, J.M. Dance, P. Hagenmüller, *Mater. Res. Bull.* **16**, 47 (1981)
18. S. Abou-Warda, W. Pietzuch, G. Berghöfer, U. Kesper, W. Massa, D. Reinen, *J. Solid State Chem.* **138**, 18 (1998)
19. F. Abbatista, M. Vallino, *Atti Acad. Sci. Torino* **116**, 89 (1982)
20. R.D. Shannon, C.T. Prewitt, *Acta Cryst.* **B35**, 925 (1969)
21. D. Reinen, M. Atanasov, S.-L. Lee, *Coord. Chem. Reviews* **175**, 91 (1998)
22. M. Atanasov, D. Reinen, *Comprehensive Coord.Chem. II, Vol. I. Fundamentals*, Chapter 1.36 (2003) 669, Elsevier, Ed. A.B.P. Lever
23. D. Reinen, *Struct. Bonding* **6**, 30 (1969)
24. D. Reinen, U. Kesper, D. Belder, *J. Solid State Chem.* **116**, 355 (1995)
25. Yu.V. Yablokov, T.A. Ivanova, S.Yu. Shipunova, N.V. Chezina, I.A. Zvereva, N.P. Bobrysheva, *Appl. Magn. Reson.* **2**, 547 (1991)

26. S. Angelov, C. Friebel, E. Zhechewa, R. Stoyanova, J. Phys. Chem. Solids **53**, 443 (1992)
27. M. Atanasov, D. Reinen, J. Electron Spectr. **86**, 185 (1997)
28. K.H. Höck, H. Nickisch, H. Thomas, Helv. Phys. Acta **56**, 237 (1983)
29. Z. Hu, M.S. Golden, J. Fink, G. Kaindl, S.A. Warda, D. Reinen, P. Mahavedan, D.D. Sarma, Phys. Rev.B **61**, 3739 (2000)
30. Z. Hu, G. Kaindl, A. Heyer, D. Reinen, Z. Anorg. Allg. Chem. **627**, 2647 (2001)
31. G. Demazeau, M. Pouchard, P. Hagenmüller, J. Solid State Chem. **18**, 159 (1976)
32. D. Reinen, A. Ozarowski, B. Jakob, J. Pebler, H. Stratemeier, K. Wieghardt, I. Tolksdorf, Inorg. Chem. **26**, 1010 (1987)
33. K. Wieghardt, W. Walz, B. Nuber, J. Weiss, A. Ozarowski, H. Stratemeier, D. Reinen, Inorg. Chem. **25**, 1650 (1986)
34. J.C. Brodovitch, R.I. Haines, A. McAuley, *Can. J. Chem.* **59** 1610 (1981); D.H. Szalda, D.H. Macartney, N. Sutin, Inorg. Chem. **23**, 3473 (1984)
35. D. Reinen, M. Atanasov, P. Köhler, J.Molec.Struct. **838**, 151 (2007)
36. F.A. Cotton, M.D. Meyers, J. Am. Chem. Soc. **82**, 5023 (1960)
37. S.A. Warda, W. Massa, D. Reinen, Z. Hu, G. Kaindl, F.M.F. de Groot, J. Solid State Chem. **146**, 79 (1999)
38. G. Demazeau, Ph. Courbin, G. Le Flem, M. Pouchard, P. Hagenmüller, J.L. Soubeyroux, J.G. Main, G.A. Robins, Nouveau J. Chimie **3** 171 (1979)
39. Z. Hu, Ch. Mazumdar, G. Kaindl, F.M.F. de Groot, S.A. Warda, D. Reinen, Chem. Phys. Letters **297**, 321 (1998)
40. M. Abbate, R.H. Potze, G.A. Sawatzky, A. Fujimuri, Phys. Rev. **B49**, 7210 (1994)
41. H.J. Buser, D. Schwarzenbach, W. Petter, A. Ludi, Inorg. Chem. **16**, 1704 (1977)
42. A.P.P. Lever, *Inorganic Electronic Spectroscopy* (Elsevier, Amsterdam, 1984) and cited references
43. P. Köhler, W. Massa, D. Reinen, B. Hofman, R. Hoppe, Z. Anorg. Allg. Chem. **446**, 131 (1978)
44. Qu. Scheifele, T. Birk, J. Bendix, Ph. Tregenna-Piggott, H. Weihe, Angew. Chem. Int. Ed. **47**, 148 (2008)
45. C. Bellitto; A.A. Tomlinson, C. Furlani, J. Chem. Soc. (A) 3267 (1971)
46. I. Bernal, N. Elliot, R. Lalancette, Chem. Commun. 803 (1971)
47. Y. Adelsköld, L. Eriksson, P.L. Wang, P.E. Werner, Acta Crystallogr., Sect.C **44**, 597 (1988)
48. P. Garcia-Fernandez, I.B. Bersuker, J.E. Boggs, J. Chem. Phys. **125**, 104102 (2006)
49. D. Reinen, M. Atanasov, G.St. Nikolov, F. Steffens, Inorg. Chem. **27**, 1678 (1988)
50. H. Rieck, R. Hoppe, Z. Anorg. Allg. Chem. **392**, 193 (1972)
51. Z. Hu, G. Kaindl, S.A. Warda, D. Reinen, F.M.F. de Groot, B.G. Müller, Chem. Phys. **232**, 63 (1998)
52. J.B. Goodenough, G. Demazeau, M. Pouchard, P. Hagenmüller, J. Solid State Chem. **325**, 8 (1973)
53. D. Reinen, J. Wegwerth, Physica C **183**, 261 (1991)
54. B. Grande, Hk. Müller-Buschbaum, M. Schweizer, Z. Anorg. Allg. Chem. **428**, 120 (1977)
55. M.D. Kaplan, Physica C, **180**, 351 (1991)
56. K. Hestermann, R. Hoppe, Z. Anorg. Allg. Chem. **367**, 249 and 261 (1969)
57. Hk. Müller-Buschbaum, Angew. Chem. **89**, 704 (1977)
58. J.A. Duffy, *Bonding, Energy Levels and Bands in Inorganic Solids* (Longman, 1990), Chapter 5
59. St. Kremer, W. Henke, D. Reinen, Inorg. Chem. **21**, 3013 (1982)
60. W. Henke, St. Kremer, Inorg. Chimica Acta **65**, L115 (1982)
61. J.V. Folgado, W. Henke, R. Allmann, H. Stratemeier, D. Beltran-Porter, T. Rojo, D. Reinen, Inorg. Chem. **29**, 29 (1990)
62. F.S. Ham, in *Electron Paramagnetic Resonance*, ed. by S. Geshwind (Plenum, New York, 1972)
63. D. Babel, R. Haegele, J. Solid State Chem. **18**, 36 (1976)

## **Part IV**

# **Fullerenes and Fullerides**

# Following Jahn–Teller Distortions in Fulleride Salts by Optical Spectroscopy

G. Klupp and K. Kamarás

**Abstract**  $C_{60}$  salts represent perfect model systems for the Jahn–Teller effect, in particular for the interplay between the molecular dynamics and the distorting crystal field. In this paper, after a brief introduction to the theoretical background, we review experimental results on salts with fulleride anions containing different charge states in the solid state. Mid-infrared (MIR) and near infrared (NIR) spectroscopic measurements and their conclusions are reported in detail, while the results obtained by nuclear magnetic resonance (NMR), electron spin resonance (ESR) and X-ray diffraction are briefly summarized. The following questions are addressed: Are fulleride ions distorted in various solids? Is the distortion dominated by the molecular Jahn–Teller effect or by the potential field of the environment? What is the shape of the distortion? Is the distortion static or dynamic, is there a pseudorotation, are there transitions between static and dynamic JT states? How do these effects manifest themselves in vibrational and electronic excitations? The experimental difficulties one has to face when studying Jahn–Teller distortions in solids are also discussed. These limitations originate not only in the performance of the spectroscopic methods used, but also in the chemistry of some of the compounds, which can lead to segregation and polymerization.

## 1 Introduction to the Theory of the Jahn–Teller Effect in Fulleride Ions

The neutral  $C_{60}$  molecule possesses the highest symmetry point group found in nature, the icosahedral  $I_h$  group (see Fig. 1). This high symmetry leads to degeneracies of both the electronic and vibrational energy levels. Its HOMO (highest occupied molecular orbital), LUMO (lowest unoccupied molecular orbital) and LUMO+1 (next lowest unoccupied molecular orbital) belong to the  $h_u$ ,  $t_{1u}$  and  $t_{1g}$  representation, respectively [1]. The LUMO can be partially or completely filled with electrons upon reacting  $C_{60}$  with suitable electron donors, e.g. alkali metals. This way a  $C_{60}^{n-}$  ( $n < 6$ ) molecular ion with degenerate electronic states is formed, which is subject to Jahn–Teller distortion. The  $t$  orbital can couple to vibrational



**Fig. 1** The icosahedral symmetry of the  $C_{60}$  molecule. The atoms above the plane of the paper are marked black, those under it grey. In the left figure one of the  $C_5$  and  $S_{10}$  axes is perpendicular to the plane of the paper. This is the axis along which the  $C_{60}^-$ , the  $C_{60}^{2-}$  and the  $C_{60}^{4-}$  molecules are elongated or compressed by a  $D_{5d}$  distortion. In the figure in the middle, one of the  $C_3$  and  $S_6$  axes is perpendicular to the plane of the paper. This is the axis along which the above molecules are distorted in a  $D_{3d}$  symmetry. In the right figure a  $C_2$  axis is perpendicular to the plane of the paper, another  $C_2$  axis is horizontal, and the third one is vertical. In this figure one of the mirror planes of the molecule coincides with the plane of the paper, the other two are perpendicular to it and to each other. [4] Copyright (2006) by the American Physical Society

modes of  $H_g$  and  $A_g$  symmetry [2]. Since the  $A_g$  vibrations do not change the symmetry of the molecule, we will only consider  $H_g$  vibrations in the following. As we will see below, the fulleride ions have a spherical APES (adiabatic potential energy surface) in the first approximation. Thus the notation commonly used for the fulleride ions as Jahn–Teller systems is  $p^n \otimes H$  in analogy with the  $p^n$  electron configuration of atoms [3].

The Hamiltonian of the  $p^n \otimes H$  system for linear coupling can be written as [3]:

$$\hat{\mathcal{H}} = -\frac{1}{2} \sum_{i=1}^5 \frac{\partial^2}{\partial Q_i^2} + \frac{1}{2} \sum_{i=1}^5 Q_i^2 + \hat{M}(Q_i), \quad (1)$$

where  $\hat{M}(Q_i)$  is the vibronic interaction energy and  $Q_i$  are the five normal coordinates spanning a five dimensional space containing the APES. The different energy terms are in  $\hbar\omega$  units, where  $\omega$  is the frequency of the coupled vibration.

After a change of variables in the potential energy  $\hat{V}$ , it becomes apparent that the APES has a minimum not only at a single point, but in a three dimensional spherical subspace of the five dimensional  $Q$  space [3, 5]. The smallest eigenvalue of the M matrix is  $-\eta k Q$ , where  $k$  is the vibronic coupling constant and  $\eta$  is a constant depending on the charge state of the fulleride ion [5]. Substituting this into  $\hat{V}$  we get

$$\hat{V} = \frac{1}{2} Q^2 - \eta k Q; \quad (2)$$

and a minimum at  $Q = \eta k$ . The result is the same if we take into account all of the 8  $H_g$  modes of  $C_{60}^{n-}$  [6]. Thus the minimum of the APES is a three dimensional spherical surface with a radius of  $\eta k$  [3, 7].

If a molecule with  $I_h$  symmetry is distorted by the JT effect in the direction of an  $H_g$  vibration, its point group will become  $D_{2h}$ ,  $D_{3d}$  or  $D_{5d}$  [5, 8]. The distortion corresponding to the minimum of the APES is a prolate in the  $p \otimes H$  and the  $p^2 \otimes H$  system and an oblate in the  $p^4 \otimes H$  and the  $p^5 \otimes H$  system [7]. The different points of the APES correspond to different directions of the main axis of these spheroids. As all points corresponding to the minimum of the APES are equivalent, all distortions corresponding to these points are equally probable. This leads to a continuously wandering main distortion axis: the molecule performs pseudorotation [3, 7]. In the course of the pseudorotation the point group of the molecule changes, but it remains icosahedral on the average.

For the  $p^3 \otimes H$  system one possible shape of the distortion is depicted in Fig. 2b. It can be seen that the distortion is not symmetric about any axis in this case [7]. Although the shape is not the same as in the other anions, this molecule will also perform pseudorotation.

If nonlinear terms of the vibronic coupling are also taken into account or we allow for anharmonic interatomic forces, the spherical symmetry of the minima of the APES will be lost [5, 9]. The distortions corresponding to the new minima on the APES have to bear the highest possible symmetry [9]. Depending on the parameters, this scenario can be achieved if the lowest energy configurations belong to the  $D_{3d}$ ,  $D_{5d}$ , or  $D_{2h}$  configurations [5, 6, 10].

The isolated  $C_{60}^{n-}$  molecule can be distorted into six different directions with  $D_{5d}$  symmetry and ten directions with  $D_{3d}$  symmetry. In the isolated molecule the distortions belonging to the same point group but pointing in different directions have the same energy [6]. The barrier between these distortions is small, so the molecule can move from one distortion to the other via pseudorotation [11, 12].

Relatively few theoretical works have attempted to determine the exact distortion where the APES of the isolated molecule has minima. An early Hartree–Fock calculation by Koga and Morokuma on  $C_{60}^-$  found no significant energy difference

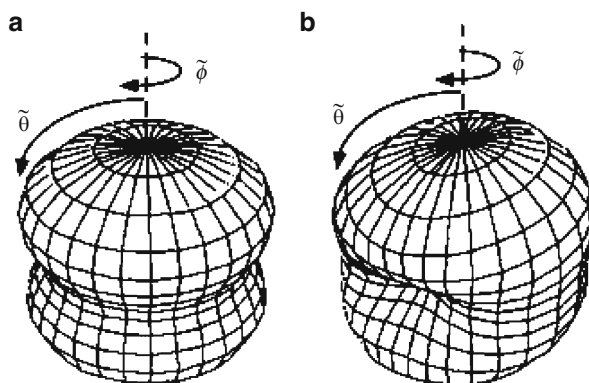


**Fig. 2** One possible shape of the Jahn–Teller distortion of  $C_{60}^{n-}$  (a) for  $n = 1, 2, 4, 5$  and (b) for  $n = 3$ . [7] Copyright (1994) by the American Physical Society

between  $D_{2h}$ ,  $D_{3d}$  and  $D_{5d}$  geometries [13], but resulted in the correct prolate shape. Green et al. performed DFT (density functional theory) calculations on isolated  $C_{60}^{n-}$  anions [14]. They also found very small energy differences between different distortions in most of the anions. The lowest energy configuration was  $D_{3d}$  in the case of  $C_{60}^-$ . The triplet and singlet state of  $C_{60}^{2-}$  were also very close in energy, with  $D_{3d}$  and  $D_{2h}$  geometry, respectively. The  $C_{60}^{3-}$  had an icosahedral quartet ground state. The  $C_{60}^{4-}$  ion and the  $C_{60}^{5-}$  ion are the electron-hole analogues of the  $C_{60}^{2-}$  and the  $C_{60}^-$  ions concerning their frontier MOs. Despite this fact, the calculation led to a  $D_{5d}$  configuration of the triplet  $C_{60}^{4-}$ .

In real fulleride salts we also have to consider the potential field generated by the environment in a solid. In alkali fullerides containing cations larger than  $Na^+$ , the dominating interaction is the repulsion between the cation and the anion arising from wave function overlap, i.e. the steric crowding [15]. This potential field generated by the alkali metal ions is the crystal field (a strain) which can lower the potential energy of a specific distortion. If the barrier to other minima on the APES of the molecule is high, a static distortion appears [3]. If the barrier is lower than the thermal energy, the distortion is still dynamic.

Going from the molecular picture to that of collective properties in a solid means adding translational symmetry to the point group symmetry. The theoretical description does this by introducing a phase of the distortion throughout the material, which is determined by the spatial variation of the variously distorted molecules. If, as is usual in a classical crystal, the phase of the distortion shows the translational symmetry of the solid, the so-called cooperative Jahn–Teller effect appears where the shape of one molecule and the space group determines the shape of all the others. If the distortions are not correlated, however, the phase is random and the situation is not different from that of isolated molecules. This is the dynamic Jahn–Teller effect where the distortions cannot be detected but the solid-state consequences still appear in the electronic structure [16].

Thus in fulleride solids, depending on the interplay of several parameters, multiple phases are possible and phase transitions can occur when varying the cation size or the temperature or pressure. Dunn [11] has investigated these effects in detail for the cooperative Jahn–Teller effect in solids and gave a general description for icosahedral systems.

Fabrizio and Tosatti introduced the idea of the Mott-Jahn-Teller insulator and performed a model calculation for an  $E \otimes e$  system. Dunn [11, 17] extended this model to the  $p^n \otimes h$  system for fullerenes and determined the properties of various cooperative JT distorted phases.

## 2 Experimental Methods Used in the Detection of Jahn–Teller Distortions

In this section, we briefly summarize the principles of the measurements which can be applied to detect the consequences of the JT effect on physical properties. We will start with a short summary of the most widely applied methods, and then give



a detailed description on vibrational and optical spectroscopy of fullerene solids, where to our knowledge no comprehensive review exists. On other topics, excellent overviews have been written, e.g. by Reed and Bolskar [18] on structural and spectroscopic (near infrared, nuclear magnetic resonance and electron spin resonance) investigations on discrete fulleride anions, by Brouet et al. [19] on collective magnetic properties detected by nuclear magnetic resonance spectroscopy, and by Arcon and Blinc [20] on the detection of pseudorotational dynamics by nuclear resonance.

We have to state right away that the experimentalist trying to determine the consequences of the JT effect in fullerides has no easy task. Part of the difficulties stem from the material and part from the complicated and intertwined phenomena which occur in most systems containing fullerene balls. The first step is to prepare the appropriate materials in homogeneous and stable form; the second, once the measurements are done, to isolate the effects of Jahn–Teller origin from the vast amount of exotic phenomena caused by the environment or physical conditions as temperature and pressure. The complexity of the problem is matched by the array of sophisticated state-of-the-art techniques which have been applied recently (e.g. free-electron laser [21], scanning tunneling microscopy (STM) [22], and storage ring spectroscopy [12]).

## 2.1 General Description of Applied Methods

To investigate the Jahn–Teller effect appearing in isolated fulleride ions experimentally, the most straightforward method would be spectroscopy in the gas phase. However, according to calculations, only  $C_{60}^-$  and  $C_{60}^{2-}$  ions exist in the gas phase, the other ions emit electrons spontaneously [14].  $C_{60}^-$  [12,21] and  $C_{60}^{2-}$  [23,24] have indeed been prepared in an electron storage ring with long enough lifetime to study their spectroscopic properties.

In solution, all six possible fulleride anions can be prepared and have been studied by various methods. The results are summarized in the review by Reed and Bolskar [18]. The most common reduction methods are the reaction with alkali metals or electrochemistry. In these cases, marked solvent dependence is observed indicating that the effect of the environment is not negligible even in dilute solutions.

In solids, the situation is further complicated by external strain originating from both steric crowding and Coulomb interactions. Roughly two types of fulleride salts can be distinguished: the ones containing bulky organic cations where the ions can be regarded as isolated, but the geometry of the counterions results in a low-symmetry environment which coexists with the Jahn–Teller type symmetry lowering; and the ones with simple cations (the prime examples being the alkali salts) where the principal interaction is steric crowding when the ions get close.

Since Jahn–Teller distortions involve the deformation of the molecules, structural studies are expected to provide the most straightforward results. These include X-ray and neutron diffraction and tunneling microscopy. Diffraction studies are hindered by the scarcity of suitable single crystals, which would give exact atomic

coordinates. On powder samples, Rietveld refinements indicate the deviation from the symmetric shape in one or the other direction, but these results have to be treated with caution because the static or dynamic nature cannot be distinguished. With exceptional care and experimental effort, fulleride monolayers can also be prepared and studied with STM at low temperature where the motion of the fullerene balls is stopped [22].

Inelastic neutron scattering (INS) is suitable to detect librations, low-energy rotational motions in solids. It was used to follow molecular reorientations as a function of temperature [25]. These reorientations should not be confused with pseudorotation as they involve actual displacements of atoms in the crystal; they correspond to an abrupt change in the crystal field [4] and their intensity scales with the crystal field strength.

Vibrational spectra are very sensitive to symmetry changes in a molecule. The splitting of bands in infrared (IR) and Raman spectra correlates with the point group of the molecule which changes when distortions appear. The nature of the splitting, i.e. the number of resulting bands in the distorted state, can be predicted from simple group theory considerations.

Likewise, the electronic transitions between frontier orbitals show characteristic splitting when the symmetry is lowered. These transitions fall into the near infrared (NIR) range in fulleride ions, and are therefore studied by NIR spectroscopy [4, 18].

A special type of measurement is that of ions in the gas phase by intense radiation which causes electron detachment and the absorption spectrum is detected through the deionized molecules it produces. Such radiation sources are either a high-intensity near-infrared laser [12] or infrared radiation from a free-electron laser [21].

High-resolution electron-energy loss spectroscopy (EELS) yields similar information as optical spectroscopy but extends to a much wider frequency range (albeit with lower resolution). Transmission EELS spectra have contributed significantly to our knowledge of fulleride salts [26, 27]. EELS spectra have the advantage with respect to optical spectroscopy that the momentum of the particles and thereby momentum transfer can be controlled; however, since the momentum transfer is always finite, in principle the results cannot be directly compared with those of optical spectroscopy. In practice low-momentum transfer results yield the dielectric loss function with high enough accuracy that it can be subjected to Kramers–Kronig transformation and the complex dielectric function can be derived.

Nuclear magnetic resonance (NMR) spectra can yield information on magnetic properties, rotational states and of the symmetry of both the molecules and their environment. Mostly,  $^{13}\text{C}$  is used as a probe, but in alkali salts, alkali atoms as Na or Li have also been applied. The effect of molecular dynamics, including pseudorotations, on the NMR line shape is thoroughly discussed in [20, 28].

Electron spin resonance (ESR) is extensively used in the study of fulleride ions, as the magnetic characterization of these molecular ions yields fundamental information on the electronic structure. An ESR signal can in principle appear in any system containing fulleride ions, as the configuration can involve unpaired spins even in systems with an even number of electrons. In solids, the Pauli susceptibility indicates a metallic state.

Indirect but important data on molecular symmetry are provided by transport and magnetic measurements in solids. These properties reflect the collective behavior of electrons in the system, and are indicative of the band structure.

The dynamic nature of the distortion is not always detected by spectroscopy [3]. If the lifetime of the excited state generated during the measurement is shorter than the time it takes the molecule to transform from one distortion to the other, then the molecule can be excited several times while in a single potential minimum. Thus we will measure the spectrum of a distorted molecule. If, on the other hand, the molecule adopts a different distortion faster than the time scale of the measurement, the molecule will take up different distortions during a single excitation event. In this case the spectrum will show the time average of the distortions. As a consequence, it can happen that the molecule is found to be distorted by one measurement and undistorted or even spherical by another; in the solids, where the spatial average is measured as well, different methods can come to different conclusions regarding whether the material consists of identically distorted molecules (cooperative Jahn–Teller effect) or whether the spatial average is symmetric while the individual molecules perform random motions (dynamic Jahn–Teller effect) [16].

Despite the difficulties mentioned above, by now a critical mass of data has been compiled enabling us to formulate a concise picture of the nature of the JT effect in these fascinating materials. In the rest of this paper we would like to summarize such experimental data with respect to the following questions: Are the fulleride ions found in various compounds distorted? Is the distortion dominated by the molecular Jahn–Teller effect or by the potential field of the environment? In which direction is the molecule distorted and what is the shape of the distortion? Is the distortion static or dynamic? The way we approach these questions is the study of symmetry change through vibrational and electronic transitions. The fundamental concepts of these methods will be summarized in the next section.

## 2.2 *Vibrational and Electronic Spectra of Fulleride Solids*

$C_{60}$  has four infrared allowed vibrations, all of which belong to the  $T_{1u}$  representation. The correlation table (Table 1) lists the possible splitting in various point groups describing the molecule when the icosahedral symmetry is lost. Since the LUMO of the molecule which accommodates the extra electrons in the anions, is also a  $t_{1u}$  orbital, the same correlations hold for the electrons as well. The resulting schemes are shown in Fig. 3 for different occupation numbers 0–6 [29]. These schemes are based on the calculations of Auerbach et al. [7] for isolated anions with correlations between electrons neglected. This calculation resulted in low-spin states for all ions which, because of the full occupation of the lowest levels, are not subject to further JT activity.

It is apparent from Table 1 that while  $D_{3d}$  and  $D_{5d}$  symmetries retain a double degeneracy, in  $D_{2h}$  all representations are one-dimensional, thus the entire degeneracy is lifted. In practical terms, this means that in an infrared spectrum the four

**Table 1** Correlation table for the  $T_{1u}$  representation. The correlation table for the  $T_{1g}$  representation is identical, with the indexes  $u$  changed to  $g$

$I_h$	$D_{5d}$	$D_{3d}$	$D_{2h}$
$T_{1u}$	$A_{2u} + E_{1u}$	$A_{2u} + E_u$	$B_{1u} + B_{2u} + B_{3u}$

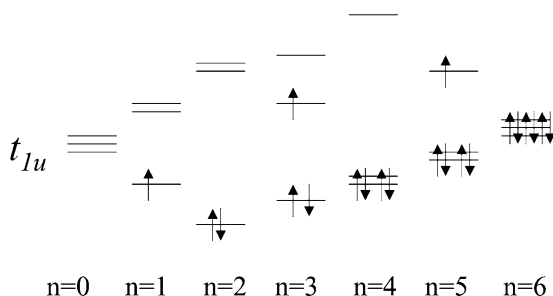


**Fig. 3** Jahn–Teller splitting of the  $t_{1u}$  orbitals of  $C_{60}^{n-}$  [29]. Copyright (2002) by the American Physical Society

allowed modes would show two- or threefold splitting depending on the symmetry resulting from the distortion. Because of the usually small structural changes, the split infrared bands are expected in the immediate vicinity of the original  $T_{1u}$  frequencies. Upon symmetry lowering, silent modes also become activated, but for the purpose of identification the splitting pattern of the  $T_{1u}$  modes is the least ambiguous. Among these, the highest-frequency  $T_{1u}(4)$  mode is the most characteristic; this mode is not only sensitive to symmetry through splitting, but also to the charge of the anion through its downshift in frequency from the  $1429\text{ cm}^{-1}$  position in neutral  $C_{60}$  [30].

Further symmetry reduction can happen as a result of strain from the crystal field of the cations in crystals. If the site symmetry of the fulleride ion is a subgroup of the  $I_h$  icosahedral point group, with lower symmetry than the JT distorted shape (e.g.  $C_{2h}$ ), a simple symmetry lowering occurs to the shape dictated by the site symmetry. If the site symmetry is not a subgroup, the distortion happens into the highest common subgroup of the site symmetry and the icosahedral group. Examples of such distortions will be given when discussing the specific materials.

It is worth mentioning that although the  $I_h$  point group shows a very high symmetry, it lacks a fourfold axis. The structure of many fulleride salts, though, which contain the ions in a tetragonal cation environment, can be described as tetragonal based on diffraction data. This can only happen when the fullerene cages are disordered with respect to the  $C_2$  axis which is parallel to the principal axis of the crystal. Formally, the picture is often described as the sum of two perpendicular orientations (the so-called “standard orientations”), but from structural data it cannot be decided what exactly the shapes are, or even whether the disorder is static or dynamic. We will show examples of mono- and tetravalent salts where this orientational disorder

occurs. It is expected that in such cases vibrational spectroscopy yields more precise information on the shape of the molecular ion and thus the type of the disorder.

The splitting of the electronic orbitals (Fig. 3) also gives rise to additional structure in the electronic spectra. The transitions between levels in the figure are dipole-forbidden and thus cannot be detected by optical methods; however, excitations to the LUMO + 1  $t_{1g}$  level, which will also split in a lower symmetry environment, will show characteristic structure depending on the shape of the fullerene cage. We will give an example of such analysis in Sect. 3.2.1.

### 3 Results on Fulleride Salts

In this section we present the results on fulleride salts in various charge states. The grouping is not strictly in the order of increasing charge, for both fundamental and practical reasons. The main practical reason is the scarce availability of some groups of the fulleride family. Of the alkali salts,  $A_2C_{60}$  (except for  $Na_2C_{60}$ ) and  $A_5C_{60}$  were found to phase separate, and could not be prepared even in a segregated form.  $Na_2C_{60}$  is a nanosegregated mixture at room temperature and the JT features can only be studied in its high-temperature phase [31].

We will not cover the optical properties of superconducting  $A_3C_{60}$  salts, either, both because the theoretical implications of the Jahn–Teller effect on superconductivity has been extensively discussed [32] and because experimental spectra in these compounds concentrate on electronic effects [33] and vibrational spectra have not been discussed in detail, partly because of the interference with the background of free electrons.

We will concentrate on the monovalent and tetravalent systems where enough data exist to present a consistent picture based on optical spectra but in accordance with other experimental results.

#### 3.1 $C_{60}^-$

In the  $C_{60}^-$  anion in the gas phase the presence of the dynamic Jahn–Teller effect has been shown by sophisticated measurements in both the NIR [12] and the MIR [21] spectral range. In both cases, it was found that the pseudorotation of the molecules is fast enough to yield the spectrum of an undistorted ion. The multiple pattern found in the NIR spectra [12] was attributed to transitions between pseudorotational levels.

In solutions or in frozen matrices the effect of the environment is not negligible any more. The NIR spectra of  $C_{60}^-$  were measured in various frozen noble gas matrices [34] and  $D_{3d}$  or  $D_{5d}$  distortions were found. The result was the same in the apolar methylcyclohexane matrix, while the distortion was  $D_{2h}$  in the polar 2-methyltetrahydrofuran (2-MeTHF) matrix [35]. One might expect the same polarity dependence in solutions, but electrochemically generated  $C_{60}^-$  ions showed a

NIR spectrum consistent with  $D_{5d}$  and  $D_{3d}$  symmetry both in benzonitrile and in dichloromethane [36]. These findings indicate that the symmetry of the environment has to be taken into account besides simple polarity considerations in frozen matrices [37] and in solutions.

A static-to-dynamic transition was also observed in Na(dibenzo-18-crown-6) $C_{60}$  in frozen 2-MeTHF solution [37]. The ESR spectrum showed an ellipsoidal distortion of the  $C_{60}^-$  ion at low temperature, and heating lead to an isotropic signal.

Another possibility to measure nearly isolated fulleride ions is the investigation of solid fulleride salts with bulky cations. The large cations separate the fulleride ions but in many cases they are capable of lowering their symmetry at the same time. In  $Ni(C_5Me_5)_2C_{60}$  the  $C_{60}^-$  ion was found by X-ray diffraction to be oblate shaped and to have roughly  $D_{2h}$  symmetry [38]. This results probably from the enhanced  $\pi - \pi$  interaction between the  $C_5Me_5$  and the fullerene units.

In (TDAE) $C_{60}$  (TDAE=tetrakis-dimethylaminoethylene) the Jahn–Teller effect has an intriguing consequence [20]: it results in a ferromagnetic ground state with a Curie temperature  $T_c = 16$  K [39]. The temperature dependence of the correlation time of pseudorotation from 5–20 K was obtained from  $^{13}C$  NMR measurements [28] and was found to decrease from  $10^{-6}$  s to  $10^{-7}$  s.

Salts formed with the metalloorganic cations tetraphenylphosphonium and tetraphenylarsonium can be prepared as relatively large crystals by electrochemical methods and are not air sensitive, contrary to the other monoanionic fullerides mentioned above; as a consequence, they have been extensively studied by several methods [40–44]. The composition of the crystals is always two counterions to one fulleride monoanion, and charge neutrality is preserved by one halide ion ( $Cl^-$ ,  $Br^-$  or  $I^-$ ) per fulleride ion. The type of the halide ion depends on preparation conditions and can be homogeneous or a mixture of two kinds of halides. This fact introduces an additional disorder into the structure, but as we will see, its impact is relatively weak.

The most thorough structural study has been performed by Launois et al.[40] by single-crystal X-ray diffuse scattering and diffraction. Above 130 K, the structure was identified as tetragonal ( $I4/m$ ), arising from a superposition of two orientations of the fulleride anion. (As the icosahedral  $C_{60}$  molecule has no fourfold axis, this is the way to explain its presence in a tetragonal environment.) Below 120 K, the model which could explain diffuse scattering was that of separate domains of  $I2/m$  symmetry, which is consistent with a  $C_{2h}$  distortion of the fulleride anion. This is another example of Jahn–Teller distortion complemented by external strain: interaction of the electrons with vibrations of  $h$  symmetry should result in no lower than the  $D_{2h}$  point group [3], but since the  $C_{60}^-$  ions occupy sites of  $2/m$  ( $C_{2h}$ ) symmetry, their point group has to be lowered accordingly.

The situation is illustrated in Fig. 4. In part (a), the structure is the dynamic average of two standard orientations, differing in the direction of one of the fullerene axes (it is easiest to associate this direction with that of the bond separating two hexagons, intersected by a  $C_2$  axis, depicted on the right of Fig. 1). In part (b) the structure is envisaged to consist of independent domains, including fulleride ions of  $C_{2h}$  symmetry but of different orientations. Within the domains, the

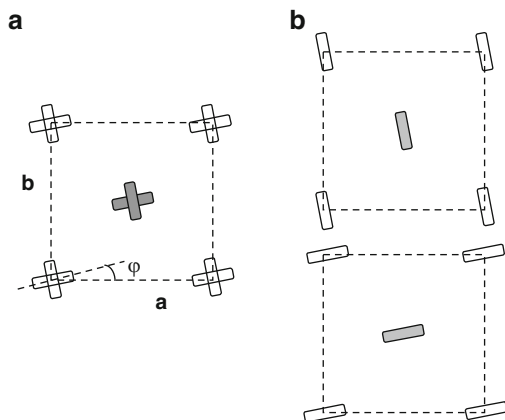


**Fig. 4** Schematic models of  $(\text{Ph}_4)_2\text{PBrC}_{60}$  at **(a)** high temperature and **(b)** low temperature. Reprinted from [40]. With kind permission of The European Physical Journal (EPJ)

cooperative Jahn–Teller effect is realized; however, the whole crystal is not uniform but disordered.

Bietsch et al. [43] determined the  $g$ -factor anisotropy of  $(\text{Ph}_4\text{P})_2\text{P}(\text{As})\text{C}_{60}(\text{I},\text{Cl})$  as a function of temperature. Their results complement perfectly the structural data: the  $g$ -factor is isotropic above a specific temperature (As: 125 K, P: 142 K) where it becomes anisotropic and the principal axes of the  $g$ -tensor do not coincide with the crystal axes.

Infrared spectra also show line splittings indicating a deformation in both tetraphenylphosphonium [42] and tetraphenylarsonium [44] salts. The main conclusion of the first paper is that in contrast to ESR spectra, infrared lines still show a splitting due to deformation at room temperature, indicating a dynamic JT state; nevertheless, some of the lines, including counterion modes, exhibit anomalies in their temperature dependence around the ordering transition temperature (Fig. 5). A thorough combined experimental and theoretical study has been performed in the second paper, concluding that the most probable deformation of the  $\text{C}_{60}^-$  anion is either  $\text{C}_{2h}$  with the principal axis connecting the centers of two opposite pentagons ( $\text{C}_{2h,5}$ ) (according to the  $\text{D}_{5d}$  symmetry undergoing further distortion to  $\text{C}_{2h}$ ) or  $\text{C}_i$ .  $\text{C}_{2h}$  symmetry is compatible with both the site symmetry  $2/m$  and the result from the  $g$ -factor anisotropy [43], but the calculated vibrational fine structure assuming  $\text{C}_i$  symmetry agrees more with the experiment. A further reduction in symmetry can of course easily happen in such a complicated crystal and since both point groups contain one-dimensional representations, more subtle effects have to be taken into account in both theory and experiment.

Likewise, room-temperature Raman spectra of single crystals of tetraphenylphosphonium salts with all three halide ions [45] showed a broadening of  $\text{H}_g$  lines which can be fitted with five oscillators. This indicates the lifting of the fivefold degeneracy, which is the case in  $\text{C}_{2h}$  (or lower) symmetry.

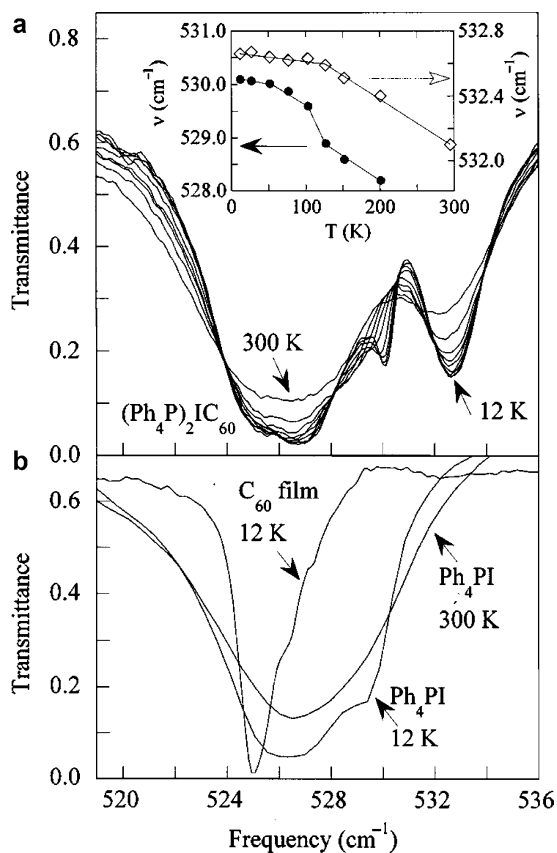


**Fig. 5** Temperature dependence of (a) the  $(\text{Ph}_4\text{P})_2\text{IC}_{60}$  multiplet and (b) the pristine  $\text{C}_{60}$  and  $\text{Ph}_4\text{PI}$  absorbances which contribute to it. The inset in (a) shows frequency versus temperature for the high  $\nu$  side of the  $T_{1u}(1)$ -derived doublet (*open diamonds*) and the 530  $\text{cm}^{-1}$  counterion feature (*solid circles*), with *solid lines* to guide the eye. Reprinted from [42]. Copyright (1998) by the American Physical Society

The exact temperature of the phase transition in the experiments above is subject to some uncertainty, which we attribute to the stoichiometric variations in both the central atom of the counterion (P,As) and the type of the halide. The picture that emerges, however, is compatible with the full scope of experimental results: a dynamic Jahn–Teller effect at high temperature, a structural phase transition in the 120–150 K range, and a distortion of the molecular ion in the low-temperature phase, arising from the positive synergy of the cooperative Jahn–Teller effect and the low symmetry of the environment. The static-to-dynamic transition does not coincide with the structural transition and its temperature depends on the detection method: whereas ESR spectra are isotropic at room temperature, infrared lines are still split, indicating a distorted state on the time scale of the measurement. This



phenomenon puts the time scale of the pseudorotation between  $10^{-9}$  and  $10^{-13}$  s, respectively.

We can compare the above results to those of TDAE- $C_{60}$  investigated by nuclear magnetic resonance [20, 28]. In these studies, based on NMR line shape analysis, a static-to-dynamic transition has been found in the ferromagnetic phase, below 10 K. The time scale at this temperature of the pseudorotation was estimated as 3 ns, somewhat higher than the higher limit of the room-temperature range mentioned above. Even though the systems are not identical, the qualitative picture that emerges is in accordance with the transition occurring in the order of characteristic frequencies (NMR  $\rightarrow$  ESR  $\rightarrow$  IR). An attractive model has been proposed for the magnetic ordering of fulleride monoanions in this salt, based on Jahn–Teller distorted states [20]: according to the calculations of Kawamoto [46], ferromagnetic order develops if the principal axes of neighboring  $C_{60}^-$  ions are perpendicular, whereas antiferromagnetic order results from parallel ordering of the principal axes. A cooperative but complex Jahn–Teller state consisting of molecular ions ordered perpendicularly thus could show ferromagnetism which would disappear at the temperature where the system becomes dynamic due to increased pseudorotation frequency.

Unfortunately, the simplest fulleride salts, the monovalent  $AC_{60}$  ( $A = K, Rb, Cs$ ) alkali fullerides, exist in a polymerized phase at room temperature (see Sect. 4.2) and depolymerize only above 400 K where the rotation of the balls averages out any distortion. Infrared spectra of monoanions at this high temperature show unperturbed icosahedral symmetry [47, 48].

### 3.2 $C_{60}^{4-}$ and $C_{60}^{2-}$

We begin this section with the discussion of  $C_{60}^{4-}$  systems, because these are the ones where experimental results are abundant. Among the non-superconducting systems, the tetravalent salts were studied most thoroughly both experimentally and theoretically. Several factors contributed to this fortunate situation. On the materials side, the full series of  $A_4C_{60}$  ( $A = Na, K, Rb, Cs$ ) could be prepared as single-phase powders, and except for  $Na_4C_{60}$  which is a polymer at room temperature, proved to be similar in structure and properties. On the theory side, the controversy between band structure calculations predicting metallic behavior [49] and the insulating character found experimentally has been noticed early on and has led to extensive effort to resolve it.

$C_{60}^{2-}$  was thought to be the electron-hole analogue to  $C_{60}^{4-}$  and studies on these materials could have complemented the  $C_{60}^{4-}$  results with valuable information. Unfortunately, only  $Na_2C_{60}$  could be prepared so far and that material is not single phase at all temperatures, either. We will report our results regarding the JT effect and the other intriguing properties of this system after discussing the tetravalent alkali salts, which are the most complete series for conclusions about the JT effect to be drawn.

### 3.2.1 $C_{60}^{4-}$

Both in solutions [36] and in a solid with large organic cations [50] the  $C_{60}^{4-}$  ions were shown to be distorted. A low temperature STM study on  $K_4C_{60}$  monolayers also showed distorted fulleride ions. The ground state of both  $[Na(crypt)]_4C_{60}$  [50],  $K_4C_{60}$  [51] and  $Rb_4C_{60}$  [52] was shown to be singlet (Fig. 3), with a close-lying triplet excitation, in accordance with the distortion.

The molecular Jahn–Teller effect plays an important role in determining the electrical and magnetic properties of solid  $A_4C_{60}$  and  $A_2C_{60}$  salts. This is because electron correlation localizes the electrons on the fulleride ions; these solids can be described as nonmagnetic Mott–Jahn–Teller insulators [16]. Intersite electron repulsion ( $U$ ) localizes the electrons and leads to the observed insulating behavior [53–55], while the Jahn–Teller splitting leads to a nonmagnetic ground state [51] pairing the electrons in contempt of Hund’s rule.

In contrast to the  $A_4C_{60}$  salts, monomeric  $Na_4C_{60}$  – stable above about 500 K – is a metal. The reason is that the shorter interfullerene distances of this compound reduce the Hubbard  $U$  and increase the bandwidth  $W$ , leading to an  $U/W$  value lying in the metallic domain [56].  $Li_4C_{60}$  also has a metallic monomer phase above 470 K [57, 58]. The presence of distorted fulleride ions has not been investigated in these phases yet.

$K^+$ ,  $Rb^+$  and  $Cs^+$  form salts with  $C_{60}^{4-}$  which contain monomeric fulleride ions at all temperatures. The structure of these salts is  $I4/mmm$  body centered tetragonal (bct) structure at all temperatures [4, 59, 60], except  $Cs_4C_{60}$  at room temperature and below, which is  $Immm$  orthorhombic (bco) [61]. According to our present knowledge, the fulleride ions in these phases are not rotating [4, 60]. Thus the effect of the crystal field must be taken into account.

In the bct phase the nearest cations surrounding a  $C_{60}^{4-}$  ion form a  $D_{4h}$  structure (see Fig. 6). As the fulleride ion does not have a fourfold rotation axis, it cannot distort into this point group (see Sect. 2.2). In this case the molecule has to distort into the largest common subgroup of  $D_{4h}$  and  $I_h$ , which is  $D_{2h}$ . The three twofold rotation axes of the  $D_{2h}$  distorted molecule can then coincide with those of the crystal. The overall tetragonal structure is realized in a way similar to  $(Ph_4P)_2C_{60}$ , with two standard orientations (Fig. 4a), but in this case the angle  $\phi$  is zero.

In the bco phase of  $Cs_4C_{60}$  the cations show a similar arrangement as in the bct  $A_4C_{60}$  phases, but they form a  $D_{2h}$  structure, i.e. they allow only one orientation of the fulleride ions. Thus the *molecular* point group caused by the crystal field is  $D_{2h}$  in both the bct and the bco structure and we would expect identical molecular spectra.

As we have seen in Sect. 2. the molecular Jahn–Teller effect distorts the molecule into either  $D_{3d}$  or  $D_{5d}$  symmetry. It is not impossible to place such distorted anions in a lattice so that the overall symmetry remains tetragonal, but the main axis of these distortions cannot coincide with the principal crystallographic axis of the  $A_4C_{60}$  crystals. In line with the suggestions by Fabrizio and Tosatti [16], the main distortion axis of the molecule could be disordered or ordered in some way, but the average structure has to be that found by diffraction.

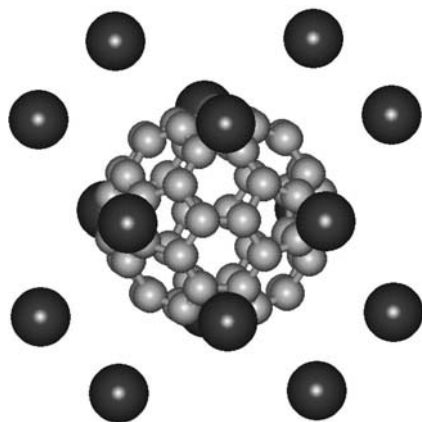


**Fig. 6** A  $\text{C}_{60}^{4-}$  ion (in light grey) and its nearest neighbor  $\text{K}^+$  ions (in black) in the bct  $\text{A}_4\text{C}_{60}$  salts (based on [59]). The fourfold  $c$  axis of the crystal is perpendicular to the plane of the paper, whereas the  $a$  axis is horizontal and the  $b$  axis vertical. The size of the spheres denoting the atoms is not to scale

The competition between the strain caused by the crystal and the molecular degrees of freedom producing the JT distortion results in several phases in  $\text{A}_4\text{C}_{60}$  salts. In the following sections we will discuss these different phases and their phase transitions.

### Orthorhombic $\text{A}_4\text{C}_{60}$ Phases

No single crystals were grown from these materials, and only powder diffraction experiments could be performed. From these measurements the distortion of the  $\text{C}_{60}^{4-}$  ion could only be determined in bco  $\text{Cs}_4\text{C}_{60}$  [60]. The point group of the fulleride ion was found to be  $\text{D}_{2h}$  in accordance with the symmetry of the crystal field. Nevertheless, the C atoms which were the most further apart from the icosahedral geometry were not found in the direction of the longest crystallographic axis. Thus the distortion is dominated by the crystal field, but the role of the Jahn–Teller effect is also significant [60].

The MIR spectrum of  $\text{Cs}_4\text{C}_{60}$  contains a threefold split  $\text{T}_{1u}(4)$  peak below 400 K (Fig. 7c) [4]. This also corresponds to a  $\text{D}_{2h}$  distortion (see Table 1.). Magic angle spinning (MAS) NMR experiments could also detect the distorted geometry of the  $\text{C}_{60}^{4-}$  ion in  $\text{Cs}_4\text{C}_{60}$  at room temperature [62]. In the NIR spectrum of the fulleride ions we find peaks corresponding to transitions between the split  $t_{1g} \leftarrow t_{1u}$  orbitals [27]. The number of detected transitions correlates with the point group of the molecule (see Fig. 8). As the NIR spectrum of the bco phase of  $\text{Cs}_4\text{C}_{60}$  contains four peaks (Fig. 9b), the point group of the  $\text{C}_{60}^{4-}$  ion cannot be higher than  $\text{D}_{2h}$  [4], in agreement with the above explained measurements.

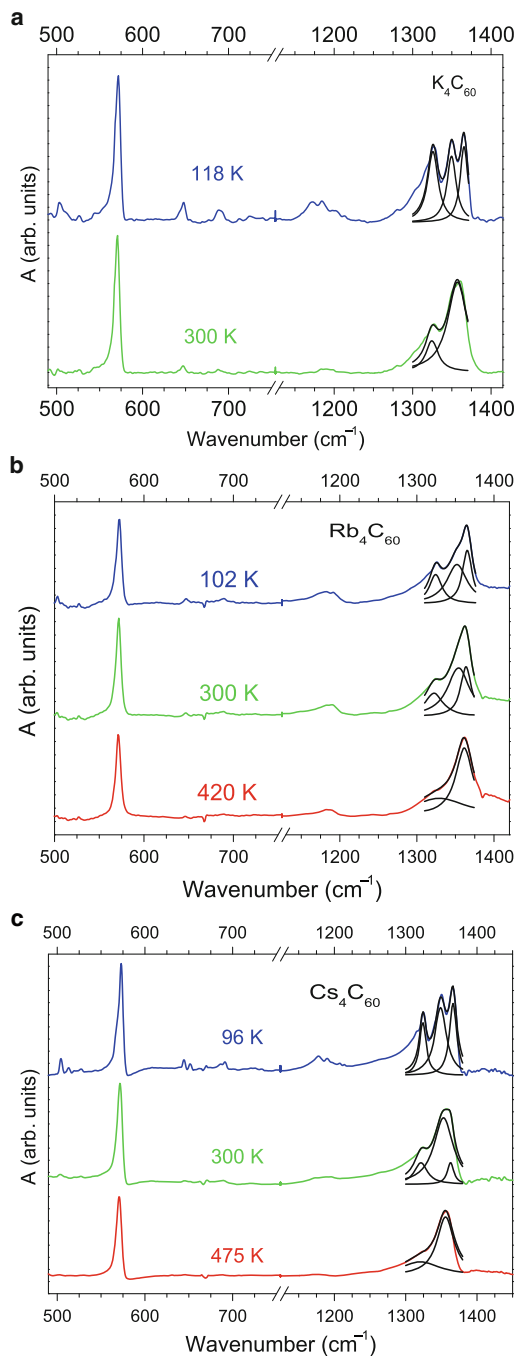


**Fig. 7** MIR spectrum of (a)  $K_4C_{60}$ , (b)  $Rb_4C_{60}$ , and (c)  $Cs_4C_{60}$  at selected temperatures. The  $T_{1u}(4)$  mode can be fitted with three Lorentzians at low temperature and two Lorentzians at high temperature (*black lines*). These splittings indicate a molecular symmetry change with temperature [4]. Copyright (2006) by the American Physical Society

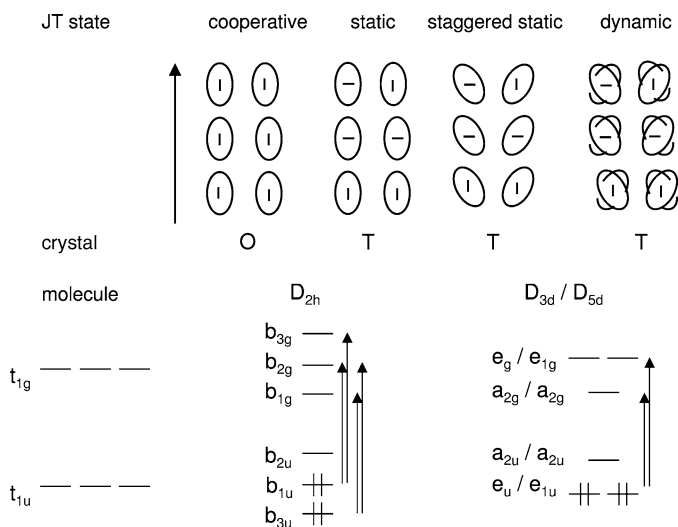


**Fig. 8** *Upper panel*: schematic representation of fulleride ion orientation in various Jahn–Teller states. The *arrow* indicates the crystallographic *c*-axis, the bars in the ovals the orientation of a hexagon-hexagon double bond. *Lower panel*: The split frontier MOs of the  $C_{60}^{4-}$  ions and the dipole allowed transitions indicated by *arrows*. For comparison we depicted these MOs for the  $I_h C_{60}$ , as well. The ordering of the  $b_{1-3u}$  and of the  $b_{1-3g}$  orbitals is arbitrary. [4] Copyright (2006) by the American Physical Society

Under pressure  $Rb_4C_{60}$  undergoes a phase transition to an orthorhombic phase similar to that of  $Cs_4C_{60}$  [63]. Previously it was believed that  $Rb_4C_{60}$  transforms into a metallic phase under pressure [64]. In a recent thorough study, though, no such transition has been found up to 2 GPa [65]. The nature of the fulleride ion distortion in the orthorhombic  $Rb_4C_{60}$  is as yet unknown.

#### $K_4C_{60}$ and $Rb_4C_{60}$ at Low Temperature

In the static  $^{13}C$  NMR spectrum of  $K_4C_{60}$  and  $Rb_4C_{60}$  a continuous broadening from about 15 ppm to about 200 ppm was found on cooling [51, 64]. According to Kerkoud et al. the low temperature broad peak arises from the superposition of the 9 inequivalent C atoms of a  $D_{2h}$  distorted molecule [64].

The  $D_{2h}$  distortion of the fulleride ions was also confirmed by MIR and NIR spectroscopy in  $K_4C_{60}$  below about 270 K and in  $Rb_4C_{60}$  below about 330 K [4]. Both the MIR and NIR spectra show similar splittings as in  $Cs_4C_{60}$ , although the crystal structure is different (see Figs. 7 and 9) [4]. As we have seen above, this symmetry can be regarded as proof for crystal-field dominated distortion.

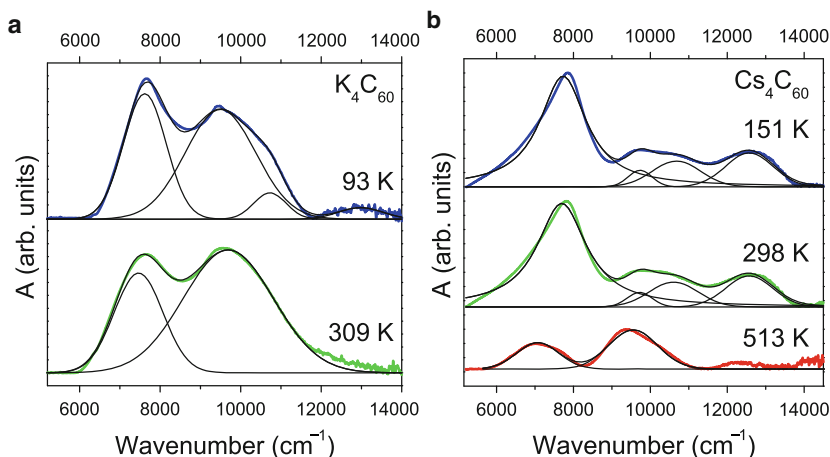


**Fig. 9** Baseline-corrected NIR spectrum of (a)  $\text{K}_4\text{C}_{60}$ , and (b)  $\text{Cs}_4\text{C}_{60}$  at selected temperatures. The spectra were fitted with Gaussians, with the exception of the lowest frequency peak of  $\text{Cs}_4\text{C}_{60}$  at 151 K and 298 K where a Lorentzian produced a better fit. These fits are shown with black lines. [4] Copyright (2006) by the American Physical Society

#### $\text{A}_4\text{C}_{60}$ at High Temperature

In  $\text{K}_4\text{C}_{60}$  at room temperature the positions of the C atoms could not be derived from diffraction measurements, but it was shown that the distortion is quite small: the difference between the axial and the equatorial axis of the molecule is smaller than 0.04 Å [66].

The detection of a dynamic distortion is complicated by the fact that measurements with a short characteristic time scale will detect the molecule to be symmetric, therefore they will not prove the presence of the distortion. This can be the situation of NMR at room temperature. Both in  $\text{K}_4\text{C}_{60}$  and in  $\text{Rb}_4\text{C}_{60}$  all C atoms of the  $\text{C}_{60}^{4-}$  molecule were found to be identical by  $^{13}\text{C}$  MAS NMR, i.e. the molecule was detected to be icosahedral [67]. Above 350 K MAS NMR also detected a single C line in  $\text{Cs}_4\text{C}_{60}$ , although this was explained by the starting of the rotation of the fulleride ion [62].

The Raman spectrum of the  $\text{A}_4\text{C}_{60}$  materials did not show a splitting, which would have shown the symmetry lowering of the fulleride ion [61,68], although the lines were found to broaden.

The timescale of infrared spectroscopy is such that it is capable of detecting dynamic distortions. This method is sensitive to the local structure, so that it detects the distortions of the single molecules and not their average. The MIR spectra of the  $\text{A}_4\text{C}_{60}$  compounds at high temperatures show a twofold split  $\text{T}_{1u}(4)$  mode (Fig. 7) corresponding to either a  $\text{D}_{3d}$  or a  $\text{D}_{5d}$  distortion (see Table 1.) [4, 69]. The NIR spectra contain two peaks (Fig. 7), which also correspond to  $\text{D}_{3d}$  or  $\text{D}_{5d}$  structures (see Fig. 8) [4]. These are the distortions favored by the molecular Jahn–Teller effect. It has been shown that at high temperatures these distortions are dynamic [4].

### Static-to-Dynamic Transition

We propose the following explanation for the transition between the static and dynamic state [4, 70]: At low temperature the distorting potential field of the cations is strong, leading to an APES where the lowest minimum has  $D_{2h}$  symmetry. As at low temperature only the lowest energy states are occupied, no transition can take place to other higher lying minima. On heating two processes have to be taken into account. The first is caused by the thermal expansion: the steric crowding decreases and the potential energy minimum created by the crystal field will become more shallow. The other effect is that more higher lying states will become thermally accessible. These two factors lead to the gradual appearing of  $D_{3d}/D_{5d}$  distortions and disappearing of the  $D_{2h}$  distortions, until only the former will be present. Of course if there is a phase transition, like in  $Cs_4C_{60}$  on heating, that overrides the gradual nature of this scenario.

$D_{3d}/D_{5d}$  distortions in different directions have different energy in the solid, due to an additional anisotropic term from the crystal field. The appearance of the  $D_{3d}/D_{5d}$  distortions starts with the lower energy ones, connected by possible pseudorotation. On heating the confinement of the pseudorotation relaxes as more and more  $D_{3d}/D_{5d}$  distortions become accessible, until at high temperatures the pseudorotation will become free.

The main process which emerges is that the fulleride ion can be thought of as an independent entity, which undergoes a distortion even in the absence of external strain. If we put this ion into a crystal with a given symmetry, a competition between the molecular degrees of freedom and the constraints of the environment will result. The molecular degrees of freedom will gain in importance when the kinetic energy is higher (at higher temperature) or when the constraint is lower (the lattice is less crowded). The increase of the transition temperature with cation size is in agreement with this picture.

#### 3.2.2 $C_{60}^{2-}$

The geometry of the  $C_{60}^{2-}$  ion in its benzonitrile and dichloromethane solution was found by NIR spectroscopy to be  $D_{3d}$  or  $D_{5d}$  [36]. A  $D_{3d}$  distortion was also found in  $(ND_3)_8Na_2C_{60}$  by diffraction measurements [71]. This latter distortion must be static, since diffraction can only detect such distortions.

In contrast to these findings probably the symmetry lowering effect of the counterions is reflected in the  $C_i$  distortion found in  $(PPN)_2C_{60}$  ( $PPN^+$  = bis-(triphenylphosphine)iminium ion) by X-ray diffraction. The shape of the deformation is an axial elongation with a rhombic squash [72].

To study the Jahn–Teller effect of fulleride ions in the condensed phase a symmetric environment would be ideal.  $Na_2C_{60}$  was reported to be cubic: simple cubic below 319 K and face centered cubic (fcc) above [73, 74]. In the fcc phase the  $C_{60}^{2-}$  ions are rapidly rotating [73, 74], thus the crystal field acting on the fulleride ion is

spherical. Unfortunately, though,  $\text{Na}_2\text{C}_{60}$  shows nanosegregation below 460 K and the phase containing  $\text{C}_{60}^{2-}$  ions appears only at high temperature [31].

The Jahn–Teller effect overrides Hund’s rule and the ground state of the  $\text{C}_{60}^{2-}$  molecules is a singlet with a low lying excited triplet state [18, 51] (Fig. 3). Thus  $\text{Na}_2\text{C}_{60}$  is nonmagnetic [51].

We have studied the Jahn–Teller effect in this phase by MIR spectroscopy [31, 70]. The  $T_{1u}(4)$  mode shows a twofold splitting and modes that are silent in  $\text{C}_{60}$  appear, indicating a  $D_{3d}$  or  $D_{5d}$  distortion of the molecule (Fig. 10). As the  $\text{C}_{60}^{2-}$  ions are rotating in this phase [73, 74], the distortion cannot be caused by the crystal field but must be due to the molecular Jahn–Teller effect. As there is no crystal field to lock the  $\text{C}_{60}^{2-}$  into a single potential well, the distortion is dynamic, with the rate of pseudorotation smaller than that of the infrared measurement.

This latter result proves beyond doubt that fulleride anions can be regarded as preserving their molecular identity. To show lower symmetry without a constraining crystal field cannot be explained by any other mechanism.

From the data on divalent and tetravalent salts, a consistent picture emerges which is in perfect agreement with the Mott–Jahn–Teller insulator model of Fabrizio and Tosatti [16]. The Jahn–Teller distortion, even if dynamic, can be unambiguously detected from vibrational and low-energy electronic spectra and proves that the molecular JT effect causes the nonmagnetic insulating behavior in these materials. Systems with smaller cations are on the metallic side of the U/W diagram; it would be of interest to study these systems by vibrational spectroscopy as well.

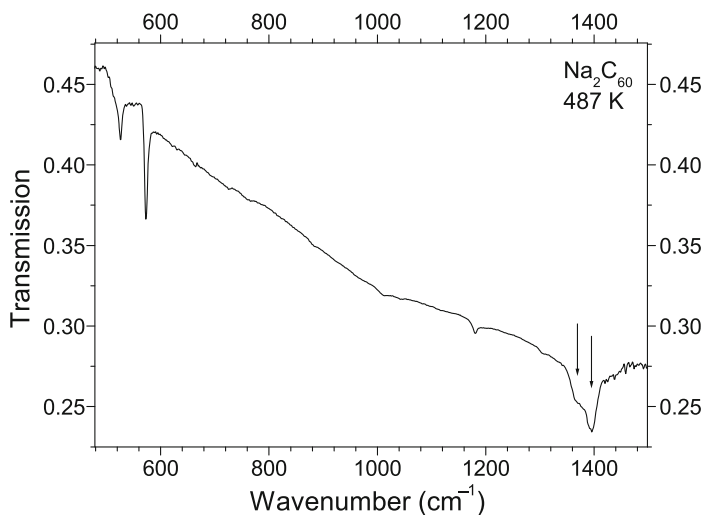


**Fig. 10** MIR spectrum of  $\text{Na}_2\text{C}_{60}$  at 487 K. The twofold splitting of the  $T_{1u}(4)$  mode due to the Jahn–Teller effect is shown by arrows. Reprinted from [70]. Copyright (2007) Elsevier Science



### 3.3 $C_{60}^{3-}$

In the work of Lawson et al. a NIR spectroscopic evidence was found for the distortion of  $C_{60}^{3-}$  ions in benzonitrile and in dichloromethane solution [36]. The point group of the molecule is not known, but it is such that its irreducible representations are all nondegenerate. The ground state of the  $C_{60}^{3-}$  molecule is  $S = 1/2$  [18] also indicating the splitting of the  $t_{1u}$  orbitals (Fig. 3.) This low-spin state was found in  $Li_3(NH_3)_6C_{60}$  [75] as well, despite the fact that the fulleride ions are surrounded by a bcc lattice, where no crystal field splitting of the  $t_{1u}$  orbitals is expected. This shows the Jahn–Teller origin of the splitting in  $C_{60}^{3-}$ .

In contrast to the above results, no Jahn–Teller distortion was found in metallic  $A_3C_{60}$  compounds. The geometry of the fulleride ion was measured in  $K_3C_{60}$  by neutron powder diffraction at room temperature, and it was found to belong to the  $T_h$  point group [76]. The low-temperature STM study on monolayers of  $K_3C_{60}$  by Wachowiak et al. [22] found undistorted molecules in the topographic image and a metallic band structure by tunneling spectroscopy. No splitting was found in the MIR and NIR spectra of these compounds, either [30, 69]. Careful comparison of several  $C_{60}^{3-}$ -containing salts by Iwasa and Takenobu [77] led to the conclusion that high-spin orbital degeneracy can prevail in these systems, provided the anions are sufficiently close and the environment is symmetric enough. The degeneracy breaks down when ammonia molecules are inserted into the structure and either increase the distance or lower the symmetry; in this case, the metallic behavior is also lost and the system becomes an insulator without a superconducting transition.

To understand the coexistence of metallicity and symmetry, we can look at the Mott–Jahn–Teller picture starting from a collective electron system, instead of building up the solid from individual JT distorted molecular ions. (Such a reasoning is given very clearly by Dahlke et al. [60].) If we imagine a metallic solid where the atomic cores are replaced by  $C_{60}$  molecules and all extra electrons are delocalized, the closed-shell cores will not be subject to distortion. As soon as localization occurs, the  $t_{1u}$  LUMO's will be occupied and the usual JT effect takes place. The borderline between the two scenarios is the critical  $U/W$  value between the metallic and Mott–Hubbard insulating state. It seems that in fullerides this critical value depends on both the charge of the anion and the cation-anion distance and  $A_3C_{60}$  salts with  $A = K$  and  $Rb$  are already on the metallic side, whereas even-charged systems are on the insulating side; however, the boundary seems to be very close as the example of  $Na_4C_{60}$  and  $Li_4C_{60}$  shows. Further details could be provided by combined spectroscopic and theoretical efforts.

Since there is near consensus about the mechanism of superconductivity in these compounds being related to electron–phonon coupling, there were many attempts to relate this mechanism to the Jahn–Teller effect. The topic is summarized extensively in the work of Gunnarson [32]. Han, Gunnarson and Crespi [78] presented a particularly appealing model of the connecting superconducting pairing with the Jahn–Teller effect. In their picture, the electron pairs formed by the JT effect in  $C_{60}^{3-}$  are mobile and constitute the pairing mechanism required by superconductivity. Since the JT stabilization energy for anions with even-numbered electrons is

much larger, the pairs there will be localized and superconductivity will not occur. A further advantage of the model is that it is also in accordance with other special properties of fulleride superconductors as, e.g. the short coherence length.

## 4 Unusual Phases: Why do we Not See Isolated Fulleride Ions in Alkali Salts?

We have seen above that close-lying thermally accessible orbitals can give rise to many unusual phenomena in fulleride solids. We now briefly discuss two further consequences of the presence of such states: possible chemical reactions (as, e.g. polymerization) and the coexistence of several phases in a solid at the same temperature (segregation). Both are a source of new information but unfortunately they also prohibit a full systematic investigation of the monomeric alkali fulleride salts series.

### 4.1 Segregation

The first example of segregation in fullerenes was the so called intermediate phase of  $\text{KC}_{60}$  [79]. In this material the  $\text{K}^+$  ions are not homogeneously distributed in the  $\text{C}_{60}$  lattice: there are regions of pure neutral  $\text{C}_{60}$  and regions with a composition of  $\text{K}_3\text{C}_{60}$ . Synchrotron X-ray diffraction measurements showed the different lattice constant of the regions with different compositions [79]. It was found that the lattice of the  $\text{C}_{60}$  region, which has smaller lattice parameter, expands ( $a = 14.18 \text{ \AA}$  instead of  $14.14 \text{ \AA}$ ) and the lattice of  $\text{K}_3\text{C}_{60}$  contracts ( $a = 14.22 \text{ \AA}$  instead of  $14.25 \text{ \AA}$ ). The MIR spectrum shows vibrational lines characteristic of  $\text{C}_{60}$  and of  $\text{C}_{60}^{3-}$  (Fig. 11). On heating the material above  $460 \text{ K}$ , the segregation disappears and a  $\text{KC}_{60}$  phase with  $\text{C}_{60}^-$  ions appears [79].

A similar segregated structure is present in  $\text{Na}_2\text{C}_{60}$  at room temperature [31]. This structure consists of  $\text{C}_{60}$  and the  $\text{Na}_3\text{C}_{60}$  regions with the size of about  $3\text{--}10 \text{ nm}$ . X-ray diffraction could not distinguish the two lattice constants in this case, probably because of the closeness of the two lattice parameter values of the parent lattices ( $a(\text{C}_{60}) = 14.15 \text{ \AA}$  and  $a(\text{Na}_3\text{C}_{60}) = 14.19 \text{ \AA}$ ). The presence of  $\text{C}_{60}$  and  $\text{Na}_3\text{C}_{60}$  was proven by a combined effort using  $^{13}\text{C}$  NMR, ESR and MIR spectroscopy and neutron scattering (Fig. 11). On heating the  $\text{Na}^+$  ions start to diffuse and the composition of the whole material becomes homogeneous. This is the phase where Jahn–Teller distorted  $\text{C}_{60}^{2-}$  ions were found [31].

Segregation was also proposed in  $\text{Na}_3\text{C}_{60}$  based on the presence of  $\text{C}_{60}$  seen by  $^{13}\text{C}$  NMR. This material was also detected to be single phase by x-ray diffraction [80].

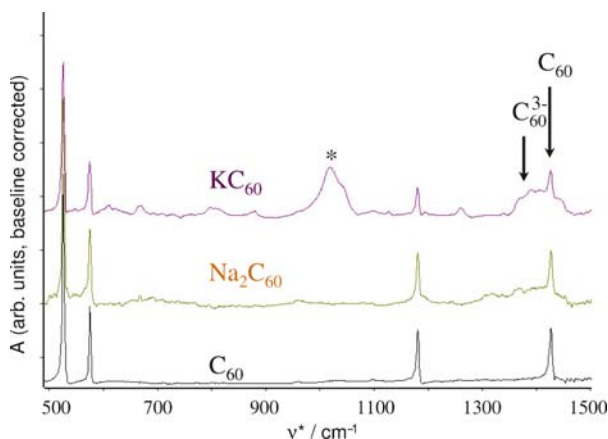


**Fig. 11** Baseline-corrected MIR spectrum of  $\text{KC}_{60}$  and  $\text{Na}_2\text{C}_{60}$  compared to the spectrum of  $\text{C}_{60}$ . The line positions characteristic of neutral  $\text{C}_{60}$  and of  $\text{C}_{60}^{3-}$  molecules are shown. Amorphous carbon impurity in the  $\text{KC}_{60}$  sample is denoted by an *asterisk*

## 4.2 Polymerization

For the fulleride ions to polymerize two conditions have to be met: the molecules have to be close enough to each other, and they have to be in adequate orientation. The type of bonding depends on the charge of the fulleride ion [81]. Neutral  $\text{C}_{60}$  and  $\text{C}_{60}^-$  favor chains with [2+2] cycloadditional bonds. The former can be found in the  $\text{C}_{60}$  photopolymer [82], and the latter in  $\text{AC}_{60}$  polymers [83].  $\text{AC}_{60}$  (Fig. 12a) were the first ionic polymers discovered and were extensively studied due to their stability in air. They undergo reversible depolymerization between 450 and 480 K and can be quenched into a metastable dimer phase [84] with bonds similar to those in Fig. 12b [85].

The most stable bonding pattern of  $(\text{C}_{60}^{3-})_n$  is a linear chain with single interfullerene bonds (Fig. 12b) [81], which can be found in  $\text{Na}_2\text{AC}_{60}$  salts [86]. The affinity of these compounds to polymerize depends on the interfullerene distance, which can be controlled by choosing metal A.  $\text{Na}_2\text{KC}_{60}$  polymerizes already below 310 K [87], while  $\text{Na}_2\text{RbC}_{60}$  only below around 230 K [86], and  $\text{Na}_2\text{CsC}_{60}$  does not polymerize on cooling [88]. Both the  $\text{Na}_2\text{RbC}_{60}$  and the  $\text{Na}_2\text{CsC}_{60}$  polymer can be prepared on applying pressure [88, 89]. Polymeric  $\text{Na}_2\text{KC}_{60}$  and  $\text{Na}_2\text{RbC}_{60}$  were shown to be metallic [90, 91].

$\text{Na}_4\text{C}_{60}$  was the first fulleride polymer containing single bonds and the first one which is two dimensional and can be synthesized at ambient pressure [92]. The structure agrees with the one calculated to be the most stable for polymers, which are built from  $\text{C}_{60}^{4-}$  ions (Fig. 12c) [81]. Polymeric  $\text{Na}_4\text{C}_{60}$  was found to be metallic [92], and transforms to an also metallic monomer phase around 500 K [56].

$\text{Li}_4\text{C}_{60}$  is also a two dimensional polymer, but it has a bonding pattern containing both cycloadditional and single interfullerene bonds (see Fig. 12d) [93]. This

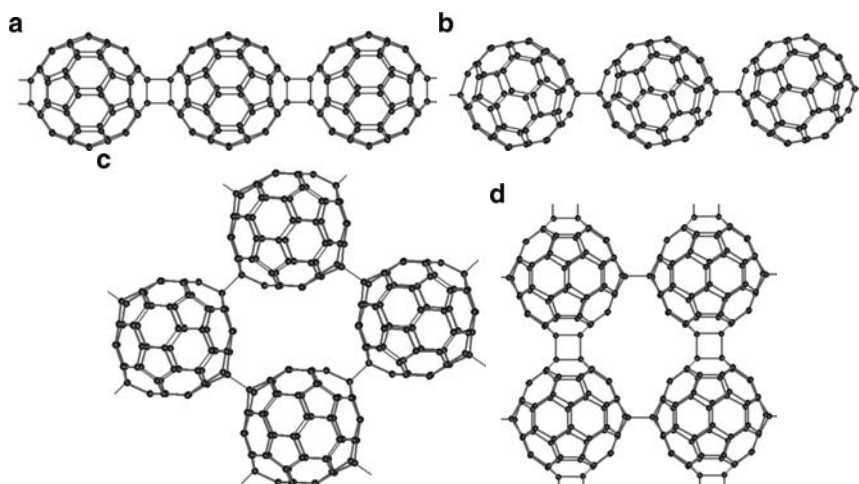


**Fig. 12** Bonding of fulleride ions in various polymers. a:  $\text{AC}_{60}$ , b:  $\text{Na}_2\text{AC}_{60}$ , c:  $\text{Na}_4\text{C}_{60}$ , d:  $\text{Li}_4\text{C}_{60}$

material has an insulating ground state, but is an ionic conductor due to the high mobility of the  $\text{Li}^+$  ions above 200 K [58].

## 5 Conclusions

In the present paper, we have tried to show how the Jahn–Teller effect, an inherently molecular property, influences exotic solid-state phenomena as superconductivity and magnetism in fulleride salts; and how spectroscopy can amplify the effect of distortions which are minuscule at the structural level. Vibrational and electronic spectra in the solid state can unambiguously prove the dynamic character of the Mott–Jahn–Teller insulating phase, as predicted by Fabrizio and Tosatti [16]. The characteristic time scale of optical spectroscopy being much shorter than that of magnetic resonance methods, it has the advantage of detecting dynamic distortions even at room temperature. Despite the existing experimental difficulties, it would be worthwhile extending the scope of measurements to more fulleride salts.

**Acknowledgements** Financial support was provided by the Hungarian National Research Fund and the National Office for Research and Technology under grant no. NI 67842 and T 049338.

## References

1. R.C. Haddon, L.E. Brus, K. Ragavachari, *Chem. Phys. Lett.* **125** 459 (1986)
2. H.A. Jahn, E. Teller, *Proc. R. Lond. Soc. Ser. A* **191** 220 (1937)

3. C.C. Chancey, M.C.M. O'Brien, *The Jahn-Teller Effect in C<sub>60</sub> and Other Icosahedral Complexes* (Princeton University Press, Princeton, 1997)
4. G. Klupp, K. Kamarás, N.M. Nemes, C.M. Brown, J. Leao, *Phys. Rev. B* **73** 085415 (2006)
5. M.C.M. O'Brien, *Phys. Rev. B* **53** 3775 (1996)
6. J.L. Dunn, C.A. Bates, *Phys. Rev. B* **52** 5996 (1995)
7. A. Auerbach, N. Manini, T. E, *Phys. Rev. B* **49** 12998 (1994)
8. A. Ceulemans, D. Beyens, L.G. Vanquickerborne, *J. Am. Chem. Soc.* **106** 5824 (1984)
9. A. Ceulemans, *J. Chem. Phys.* **87** 5374 (1987)
10. J.L. Dunn, unpublished
11. J.L. Dunn, *Phys. Rev. B* **69** 064303 (2004)
12. S. Tomita, J.U. Andersen, E. Bonderup, P. Hvelplund, B. Liu, S.B. Nielsen, U.V. Pedersen, J. Rangama, K. Hansen, O. Echt, *Phys. Rev. Lett.* **94** 053002 (2005)
13. N. Koga, K. Morokuma, *Chem. Phys. Lett.* **196** 191 (1992)
14. W.H. Green, Jr., S.M. Gorun, G. Fitzgerald, P.W. Fowler, A. Ceulemans, B.C. Titeca, *J. Phys. Chem.* **100** 14892 (1996)
15. J.E. Fischer, P.A. Heiney, *J. Phys. Chem. Solids* **54** 1725 (1993)
16. M. Fabrizio, E. Tosatti, *Phys. Rev. B* **55** 13465 (1997)
17. J.L. Dunn, *J. Phys.: Condens. Matter* **17** 5499 (2005)
18. C.A. Reed, R.D. Bolskar, *Chem. Rev.* **100** 1075 (2000)
19. V. Brouet, H. Alloul, S. Garaj, L. Forró, *Struct. Bonding* **109** 165 (2004)
20. D. Arcon, R. Blinc, *Struct. Bonding* **109** 231 (2004)
21. P. Kupser, J.D. Steill, J. Oomens, G. Meijer, G. von Helden, *Phys. Chem. Chem. Phys.* **10** 6862 (2008)
22. A. Wachowiak, R. Yamachika, K.H. Khoo, Y. Wang, M. Grobis, D.H. Lee, S.G. Louie, M.F. Crommie, *Science* **310** 468 (2005)
23. B. Liu, P. Hvelplund, S.B. Nielsen, S. Tomita, *Phys. Rev. Lett.* **92** 168301 (2004)
24. S. Tomita, J.U. Andersen, H. Cederquist, B. Concina, O. Echt, J.S. Forster, K. Hansen, B.A. Huber, P. Hvelplund, J. Jensen, B. Liu, B. Manil, L. Maunory, S.B. Nielsen, J. Rangama, H.T. Schmidt, H. Zettergren, *J. Chem. Phys.* **124** 024310 (2006)
25. D.A. Neumann, J.R.D. Copley, D. Reznik, W.A. Kamitakahara, J.J. Rush, R.L. Paul, R.M. Lindstrom, *J. Phys. Chem. Solids* **54** 1699 (1993)
26. M. Knupfer, J. Fink, J.F. Armbuster, *Z. Phys. B* **101** 57 (1996)
27. M. Knupfer, J. Fink, *Phys. Rev. Lett.* **79** 2714 (1997)
28. P. Jeglic, R. Blinc, T. Apih, A. Omerzu, D. Arcon, *Phys. Rev. B* **68** 184422 (2003)
29. V. Brouet, H. Alloul, S. Garaj, L. Forró, *Phys. Rev. B* **66** 155124 (2002)
30. T. Pichler, R. Winkler, H. Kuzmany, *Phys. Rev. B* **49** 15879 (1994)
31. G. Klupp, P. Matus, D. Quintavalle, L.F. Kiss, E. Kováts, N.M. Nemes, K. Kamarás, S. Pekker, A. Jánossy, *Phys. Rev. B* **74** 195402 (2006)
32. O. Gunnarson, *Rev. Mod. Phys.* **69** 575 (1997)
33. L. Degiorgi, E.J. Nicol, O. Klein, G. Grüner, P. Wachter, S.M. Huang, J. Wiley, R.B. Kaner, *Phys. Rev. B* **49** 7012 (1994)
34. J. Fulara, M. Jakobi, J.P. Maier, *Chem. Phys. Lett.* **211** 227 (1993)
35. H. Kondo, T. Momose, T. Shida, *Chem. Phys. Lett.* **237** 111 (1995)
36. D.R. Lawson, D.L. Feldheim, C.A. Foss, P.K. Dorhout, C.M. Elliott, C.R. Martin, B. Parkinson, *J. Electrochem. Soc.* **139** L68 (1992)
37. J. Stinchcombe, A. Pnicaud, P. Bhayrappa, P.D.W. Boyd, C.A. Reed, *J. Am. Chem. Soc.* **115** 5212 (1993)
38. W.C. Wan, X. Liu, G.M. Sweeney, W.E. Broderick, *J. Am. Chem. Soc.* **117** 9580 (1995)
39. P.M. Allemand, K.C. Khemani, A. Koch, F. Wudl, K. Holczer, S. Donovan, G. Gruner, J.D. Thompson, *Science* **253** 301 (1991)
40. P. Launois, R. Moret, N.R. de Souza, J.A. Azamar-Barrios, A. Pénicaud, *Eur. Phys. J. B* **15** 445 (2000)
41. B. Gotschy, M. Keil, H. Klos, I. Rystau, *Solid State Commun.* **113** 8266 (1994)
42. V.C. Long, J.L. Musfeldt, K. Kamarás, A. Schilder, W. Schütz, *Phys. Rev. B* **58** 14338 (1998)
43. W. Bietsch, J. Bao, J. Lüdecke, S. van Smaalen, *Chem. Phys. Lett.* **324** 37 (2000)

44. V.C. Long, E.C. Schundler, G. B.Adams, J. B.Page, W. Bietsch, I. Bauer, *Phys. Rev. B* **75** 125402 (2007)
45. M. Polomska, J.L. Sauvajol, A. Graja, A. Girard, *Solid State Commun.* **111** 107 (1999)
46. T. Kawamoto, *Solid State Commun.* **101** 231 (1997)
47. K. Kamarás, L. Gránásy, D.B. Tanner, L. Forró, *Phys. Rev. B* **52** 11488 (1995)
48. K. Kamarás, D.B. Tanner, L. Forró, *Fullerene Sci. Technol.* **5** 465 (1997)
49. S.C. Erwin, in *Buckminsterfullerenes*, ed. by w. A. Billups, M. Ciufolini (VCH, New York, 1992), p. 217
50. Y. Sun, C.A. Reed, *Chem. Commun.* p. 747 (1997)
51. V. Brouet, H. Alloul, S. Garaj, L. Forró, *Phys. Rev. B* **66** 155122 (2002)
52. I. Lukyanchuk, N. Kirova, F. Rachdi, C. Goze, P. Molinie, M. Mehring, *Phys. Rev. B* **51** 3978 (1995)
53. R.F. Kiefl, T.L. Duty, J.W. Schneider, A. Macfarlane, K. Chow, J.W. Elzey, P. Mendels, G.D. Morris, J.H. Brewer, E.J. Ansaldo, C. Niedermayer, D.R. Noakes, C.E. Stronach, B. Hitti, J.E. Fischer, *Phys. Rev. Lett.* **69** 2005 (1992)
54. P.J. Benning, F. Stepniak, J.H. Weaver, *Phys. Rev. B* **48** 9086 (1993)
55. Y. Iwasa, S. Watanabe, T. Kaneyasu, T. Yasuda, T. Koda, M. Nagata, N. Mizutani, *J. Phys. Chem. Solids* **54** 1795 (1993)
56. G. Oszlányi, G. Baumgartner, G. Faigel, L. Gránásy, L. Forró, *Phys. Rev. B* **58** 5 (1998)
57. M. Ricco, M. Belli, D. Pontiroli, M. Mazzani, T. Shiroka, D. Arcon, A. Zorko, S. Margadonna, G. Ruani, *Phys. Rev. B* **75** 081401(R) (2007)
58. D. Arcon, A. Zorko, M. Mazzani, M. Belli, D. Pontiroli, M. Ricco, S. Margadonna, *New Journal of Physics* **10** 033021 (2008)
59. R.M. Fleming, M. J.Rosseinsky, A.P. Ramirez, D.W. Murphy, J.C. Tully, R.C. Haddon, T. Siegrist, R. Tycko, S.H. Glarum, P. Marsh, G. Dabbagh, S.M. Zahurak, A.V. Makhija, C. Hampton, *Nature* **352** 701 (1991)
60. P. Dahlke, M.J. Rosseinsky, *Chem. Mater.* **14** 1285 (2002)
61. P. Dahlke, P.F. Henry, M.J. Rosseinsky, *J. Mater. Chem.* **8** 1571 (1998)
62. C. Goze, F. Rachdi, M. Mehring, *Phys. Rev. B* **54** 5164 (1996)
63. A. Huq, P.W. Stephens, *Phys. Rev. B* **74** 075424 (2006)
64. R. Kerkoud, P. Auban-Senzier, D. Jérôme, S. Brazovskii, I. Luk'yanchuk, N. Kirova, F. Rachdi, C. Goze, *J. Phys. Chem. Solids* **57** 143 (1996)
65. A. Iwasiewicz-Wabnig, T. Wagberg, T.L. Makarova, B. Sundqvist, *Phys. Rev. B* **77** 085434 (2008)
66. C.A. Kuntscher, G.M. Bendele, P.W. Stephens, *Phys. Rev. B* **55** R3366 (1997)
67. J. Reichenbach, F. Rachdi, I. Luk'yanchuk, M. Ribet, G. Zimmer, M. Mehring, *J. Chem. Phys.* **101** 4585 (1994)
68. M.G. Mitch, J.S. Lannin, *Phys. Rev. B* **51** 6784 (1995)
69. Y. Iwasa, T. Kaneyasu, *Phys. Rev. B* **51** 3678 (1995)
70. G. Klupp, K. Kamarás, *J. Mol. Struct.* **838** 74 (2007)
71. A.J. Fowkes, J.M. Fox, P.F. Henry, S.J. Heyes, M.J. Rosseinsky, *J. Am. Chem. Soc.* **119** 10413 (1997)
72. P. Paul, Z. Xie, R. Bau, P.D.W. Boyd, C.A. Reed, *J. Am. Chem. Soc.* **116** 4145 (1994)
73. T. Yildirim, J.E. Fischer, P.W. Stephens, A.R. McGhie, in *Progress in Fullerene Research*, ed. by H. Kuzmany, J. Fink, M. Mehring, S. Roth (World Scientific, Singapore, 1994), p. 235
74. T. Yildirim, J.E. Fischer, A.B. Harris, P.W. Stephens, D. Liu, L. Brard, M. Strongin, A.B.S. III, *Phys. Rev. Lett.* **71**, 1383 (1993)
75. P. Durand, G.R. Darling, Y. Dubitsky, A. Zaopo, M.J. Rosseinsky, *Nat. Mater.* **2** 605 (2003)
76. K.M. Allen, W.I.F. David, J.M. Fox, R.M. Ibberson, M.J. Rosseinsky, *Chem. Mater.* **7** 764 (1995)
77. Y. Iwasa, T. Takenobu, *J. Phys.: Condens. Matter* **15** R495 (2003)
78. J.E. Han, O. Gunnarsson, V.H. Crespi, *Phys. Rev. Lett.* **90** 167006 (2003)
79. G. Faigel, G. Bortel, M. Tegze, L. Gránásy, S. Pekker, G. Oszlányi, O. Chauvet, G. Baumgartner, L. Forró, P.W. Stephens, G. Mihály, A. Jánosy, *Phys. Rev. B* **52** 3199 (1995)

80. R.W. Schurko, M.J. Willans, B. Skadtchenko, D.M. Antonelli, J. Solid State Chem. **177** 2255 (2004)
81. S. Pekker, G. Oszlányi, G. Faigel, Chem. Phys. Lett. **282** 435 (1998)
82. E. Kováts, G. Oszlányi, S. Pekker, J. Phys. Chem. B **109** 11913 (2005)
83. P.W. Stephens, G. Bortel, G. Faigel, M. Tegze, A. Jánossy, S. Pekker, G. Oszlányi, L. Forró, Nature **370** 636 (1994)
84. M.C. Martin, D. Koller, X. Du, P.W. Stephens, L. Mihaly, Phys. Rev. B **49** 10818 (1994)
85. G. Oszlányi, G. Bortel, G. Faigel, L. Gránásy, G.M. Bendele, P.W. Stephens, L. Forró, Phys. Rev. B **54** 11849 (1996)
86. G.M. Bendele, P.W. Stephens, K. Prassides, K. Vavekis, K. Kodatos, K. Tanigaki, Phys. Rev. Letters **80** 736 (1998)
87. T. Saito, V. Brouet, H. Alloul, L. Forró, in *Electronic Properties of Novel Materials Molecular Nanostructures*, AIP Conference Proceedings vol. 544, ed. by H. Kuzmany, S. Roth, M. Mehring, J. Fink (2000), p. 120
88. S. Margadonna, C.M. Brown, A. Lappas, K. Prassides, K. Tanigaki, K.D. Knudsen, T.L. Bihan, M. Mézouar, J. Solid State Chem. **145** 471 (1999)
89. Q. Zhu, Phys. Rev. B **52** R723 (1995)
90. D. Arcon, K. Prassides, S. Margadonna, A.L. Maniero, L.C. Brunel, K. Tanigaki, Phys. Rev. B **60** 3856 (1999)
91. N. Cegar, F. Simon, G. Baumgartner, A. Sienkiewicz, L. Forró, B. Ruziska, L. Degiorgi, L. Mihály, in *Electronic Properties of Novel Materials Science and Technology of Molecular Nanostructures*, AIP Conference Proceedings vol. 486, ed. by H. Kuzmany, S. Roth, M. Mehring (1999), p. 64
92. G. Oszlányi, G. Baumgartner, G. Faigel, L. Forró, Phys. Rev. Lett. **78**, 4438 (1997)
93. S. Margadonna, D. Pontiroli, M. Belli, T. Shiroka, M. Ricco, M. Brunelli, J. Am. Chem. Soc. **126**, 15032 (2004)

# Jahn–Teller Effects in Molecules on Surfaces with Specific Application to C<sub>60</sub>

Ian D. Hands and Janette L. Dunn, Catherine S.A. Rawlinson,  
and Colin A. Bates

**Abstract** Scanning tunnelling microscopy (STM) is capable of imaging molecules adsorbed onto surfaces with sufficient resolution as to permit intra-molecular features to be discerned. Therefore, imaging molecules subject to the Jahn–Teller (JT) effect could, in principle, yield valuable information about the vibronic coupling responsible for the JT effect. However, such an application is not without its complications. For example, the JT effect causes subtle, dynamic distortions of the molecule; but how will this dynamic picture be affected by the host surface? And what will actually be imaged by the rather slow STM technique? Our aim here is to present a systematic investigation of the complications inherent in JT-related STM studies, to seek out possible JT signatures in such images and to guide further imaging towards identification and quantification of JT effects in molecules on surfaces. In particular, we consider the case of surface-adsorbed C<sub>60</sub> ions because of their propensity to exhibit JT effects, their STM-friendly size and because a better understanding of the vibronic effects within these ions may be important for realisation of their potential application as superconductors.

## 1 Introduction

The scanning tunnelling microscope (STM), invented by Binnig and Rohrer in the early 1980s [1, 2], has developed into a powerful tool for probing surfaces at atomic resolution. The construction and principles of operation of STMs have been amply described in the literature, and for a full account the reader is referred to any one of several texts on the subject (see, e.g. [3, 4]). There are three main components to these devices: the surface under investigation, the probe ‘tip’, which is placed in close proximity to the surface, and the positioning and control mechanism, which acts as a means of measuring and regulating the tunnelling current between the tip and surface as their relative positions are altered. Tunnelling across the tip-surface gap occurs when a potential difference is applied. Using positive sample bias, electrons tunnel from the tip into unfilled surface states or, for molecular species, the lowest unoccupied molecular orbitals (LUMOs). Conversely, negative sample bias reverses the direction of the flow, from occupied surface states to the tip, and so an image builds up of the surface’s highest occupied molecular orbitals (HOMOs).



Data is usually collected in one of two modes. In constant-height mode, the tip-surface distance is fixed and the tip moved parallel to the surface. By recording the tunnelling current as this scan proceeds, an image of the surface is generated. The other mode uses a feedback mechanism to adjust the tip-surface distance to maintain a fixed tunnelling current. In this constant-current mode, an image is produced from the height adjustments measured as the surface is scanned. In both modes, the STM can respond to molecules adsorbed onto the surface, and this produces an image of the adsorbate itself.

In 2005, Wachowiak et al. [5] used the technique to obtain remarkable images of  $C_{60}$  molecules co-deposited onto a gold surface with potassium. They found that K doping produced discrete domains corresponding to monolayers with stoichiometries  $K_3C_{60}$  and  $K_4C_{60}$ . Furthermore, the latter were electrically insulating whilst the former were conducting in nature. This behaviour was attributed to the Jahn–Teller (JT) effect. Wachowiak et al. went even further and suggested that their images could be explained by assuming the  $C_{60}^{4-}$  ions in the insulating phase had been distorted by the JT effect into species of  $D_{2h}$  symmetry. The  $C_{60}^{3-}$  ions in the conducting phase, however, were not showing signs of a JT effect of any kind, according to their interpretation.

These results are extremely interesting in light of the discovery made in 1991 that alkali-doped  $A_3C_{60}$  compounds exhibit superconductivity with transition temperatures  $T_c \sim 18\text{--}28\text{ K}$  [6, 7]. Since then, these fullerides have been the subject of great interest and other compounds with even higher  $T_c$  values have been synthesized [8]. Superconductivity in fullerides [9] may, in part, be due to vibronic coupling and so observation of the JT effect in fulleride ions in various charge states using STM is particularly attractive. If correctly interpreted, the STM results should permit quantitative data on the degree of coupling in these ions to be ascertained. This, in turn, should allow an assessment to be made of the contribution vibronic coupling makes to superconductivity in these compounds.

It is apparent, therefore, that methods of interpreting the ways in which the JT effect affects the images produced using tunnelling microscopy need to be developed. Currently, it would seem, experiment outstrips theoretical work as little appears to have been written about the JT effect in a specifically surface-adsorbed environment. There may be good reasons for this. The JT effect is a rather subtle effect. At its core, is a spontaneous loss of symmetry driven by the ensuing lowering of the energy of the system. However, there is always more than one way in which this JT distortion can be achieved. Subsequently, quantum mechanical tunnelling between these differently distorted forms restores the original symmetry provided we consider a sufficiently long period of time. How will this dynamic picture be affected by the presence of a surface? Are there other complications that need to be considered? One of our aims here is to give recognition to some of the problems that may complicate observation of the JT effect via STM.

In Sect. 2, we give a general discussion of some of the problems that need to be considered when a JT-active molecule is adsorbed onto a surface, with specific application to  $C_{60}$ . Then, in Sect. 3 we give an overview of the  $C_{60}$ -related STM images that have been published in the literature. Some of these images can be

readily accounted for without invoking a JT effect; this is the main thrust of Sect. 4. In Sect. 5, we try to concentrate on what features could be produced in an STM image by the JT effect. Finally, in Sect. 6 we draw our considerations to an end with a summary of our most important findings.

## 2 General Considerations

For an isolated system, treatment of the intramolecular Jahn–Teller effect is relatively simple. As the system is isolated, we may ignore molecular rotation and consider a molecule-fixed coordinate system. Within this frame of reference, the electronic and vibrational states can be formulated in terms of the irreducible representations (irreps) of the reference configuration. Overall, the system Hamiltonian is generally written in the form

$$\mathcal{H} = \mathcal{H}_0 + \mathcal{H}_{\text{JT}}, \quad (1)$$

where  $\mathcal{H}_{\text{JT}}$  constitutes the JT interaction Hamiltonian and  $\mathcal{H}_0$  is the vibrational Hamiltonian.

Now consider a system that is not isolated but interacts with a surface. We now need to add an additional term  $\mathcal{H}_S$  to (1) that represents the interaction with the surface. In general, the surface interaction will lead to distortion of the system and so  $\mathcal{H}_S$  could be written as an expansion in terms of the normal modes  $Q^\Gamma$  of the system, such that

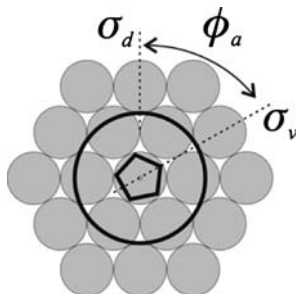
$$\mathcal{H}_S = \mathcal{H}_S^{(0)} + \sum_{\Gamma, \gamma} W_\gamma^\Gamma Q_\gamma^\Gamma. \quad (2)$$

In this expression,  $\mathcal{H}_S^{(0)}$  represents a purely electronic interaction between an undistorted system and the surface, and  $W^\Gamma$  are electronic operators determining the interaction between a vibration (irrep  $\Gamma$ , component  $\gamma$ ) and the surface. These latter operators must therefore have transformation properties dictated by the symmetry of both the adsorbed molecule and the surface. The form of (2) is suggestive of the standard method by which JT theory is developed, and this may be a desirable approach for future work. As a first approximation, however, we ignore the additional complication of surface-induced distortion and concentrate on the zeroth order term  $\mathcal{H}_S^{(0)}$ .

Unlike the isolated molecule case, the presence of a surface defines a reference set of coordinates so that molecular orientation cannot be ignored. In other words, the interaction between the molecule and the surface depends on the orientation of the molecule with respect to the surface so that

$$\mathcal{H}_S^{(0)} = \mathcal{H}_S^{(0)}(\mathbf{R}, \boldsymbol{\Omega}), \quad (3)$$

**Fig. 1** Plan view of a  $C_{60}$  molecule (*black ring*) on a hexagonal surface. In this figure, the  $C_{60}$  is chosen to be on top of a surface atom with a five-membered ring (*black pentagon*) directed towards that atom. The PES depends on their relative orientations as given by the azimuthal angle  $\phi_a$



with  $\mathbf{R}$  a vector specifying the location of the molecule with respect to a surface-fixed frame and  $\mathbf{\Omega} = (\phi, \theta, \psi)$  a set of Euler angles specifying its orientation. For  $C_{60}$ , the interaction will therefore depend on whether a pentagonal, hexagonal, or other characteristic site (e.g. a double or single bond, or even a single atom) is oriented towards the surface *and* the symmetry of the surface involved. For example, consider a scenario in which a pentagonal face of the  $C_{60}$  molecule binds preferentially to a surface of  $C_{6v}$  symmetry, as in Fig. 1. The interaction energy in this case will clearly depend on the separation between the  $C_{60}$  and the surface and an azimuthal angle  $\phi_a$  defined as the angle between a surface-fixed ( $\sigma_d$ ) and molecule-fixed ( $\sigma_v$ ) mirror plane. In this case, the surface interaction is subject to the condition  $\mathcal{H}_S^{(0)}(Z, \phi_a + \pi/3) = \mathcal{H}_S^{(0)}(Z, \phi_a)$  and six local minima in the potential energy surface (PES) are to be expected.

For a very strong interaction, the freedom of the molecule to rotate around the surface normal will be diminished, perhaps to the point where the molecule will be ‘locked’ into a particular potential well. For weaker interactions, the system can tunnel from one well to another making the system dynamic and restoring a higher degree of symmetry to the system. These possibilities are analogous to the concept of static vs. dynamic JT effects but they will be present even if the adsorbed molecule is not JT-active. Note that if this system happened to be in a dynamic state, and was subsequently observed via STM, then the molecule’s fivefold symmetry would not be apparent, even though it must still be present as the molecule is rigid.

The foregoing discussion raises the question of temperature. At low temperatures, the  $C_{60}$ -surface interaction has a greater ability to lock the adsorbed molecule into a fixed orientation. Therefore, intramolecular detail is most likely to be apparent in STM images at low temperatures. Raising the temperature will give greater freedom for the molecule to rotate about the surface  $Z$ -axis and therefore the STM image will be more likely to show features indicative of the substrate symmetry. For example, in Fig. 1 the STM image of the molecule would be expected to have sixfold symmetry. Adsorption at an interstitial site could similarly result in STM images having threefold symmetry if the rotational freedom is great enough. At even higher temperatures, full rotational freedom could result in spherically symmetric STM images. In this respect, what constitutes a ‘high’ or ‘low’ temperature will depend on the strength of interaction with the surface. Therefore, it is possible that

for a given temperature and surface, STM images of individual  $C_{60}$  molecules could appear different simply because they are adsorbed at sites with different degrees of  $C_{60}$ -surface interaction. We shall look more closely at the effect of temperature later in Sect. 2.1.

Another problem encountered due to the presence of the surface is that of charge transfer (CT). This is especially so in light of the fact that  $C_{60}$  is a good electron acceptor with an electron affinity of 2.689 eV [10]. Thus, CT is likely to occur whenever  $C_{60}$  is adsorbed onto a metallic surface. The donated electrons will be accommodated in the  $T_{1u}$  orbitals of  $C_{60}$ , and this will render them susceptible to a JT effect. In Sect. 2.2, we tabulate some values for the CT found or calculated for some surfaces commonly used in STM.

Whenever CT occurs, we can expect it to engender a strong interaction with the surface as the ions will interact strongly with their cationic counter-images induced within the metal. Subsequently, the LUMO could be strongly split due to the presence of a metallic surface alone. Of course, any such splitting will be governed by the symmetry of the interaction as well. Multiple occupancy of the  $T_{1u}$  orbitals also brings with it the problem of electron–electron interactions. These issues are dealt with more thoroughly in Sect. 2.3. Finally, we shall also give a brief discussion in Sect. 2.4 of another surface related problem, viz. the formation of monolayers.

## 2.1 Time-Scales and Temperature

Existing STM techniques are undoubtedly slow, with the fastest machines having a millisecond time resolution. This has led to attempts to develop techniques of improving temporal resolution 100-fold [11]. However, even with the limited time resolution currently available there have been some useful time-dependent STM studies. For example, compilation of several series of static images into video clips has provided valuable insight into catalytic activity and diffusion of molecules on surfaces [12]. A typical, nominally ‘fast’, scan rate used in the latter work suggests that an area  $140 \times 140 \text{ \AA}^2$  can be imaged in  $\sim 13$  s.  $C_{60}$  has a diameter of  $\sim 7 \text{ \AA}$ , which gives a dwell time per  $C_{60}$  of roughly 33 ms. This limitation arises from the electronics used and not the tunnelling process [11]. We can therefore safely assume that any motion faster than this is not currently detected in STM experiments. In fact, as electrons injected or removed by the STM tip will create excitations in the vibronic states, tunnelling could be induced by the STM tip itself. Hence JT tunnelling is likely to remain fast compared to STM measurements, even with potential future improvements in electronics. Nevertheless, we can proceed to estimate upper limits on survival times of static distortions by ignoring the effect of the STM measurement process itself.

Many of the STM images involving  $C_{60}$  are obtained at low temperatures ( $\sim 5$  K). It is pertinent to consider what the time-scales are for typical molecular motions at these low temperatures. Repp et al. [13] recorded STM images of copper clusters, comprising 1–3 atoms on a Cu(111) surface, at a variety of temperatures. The

copper dimer appears as a circular object via STM, even at 5–7 K. The dimer is so imaged because the copper atoms have enough energy to diffuse locally between face-centred cubic (fcc) and hexagonal close-packed (hcp) sites. The authors measured the rate at which fcc–fcc dimers converted to fcc–hcp dimers as a function of temperature. Above  $\sim 6$  K, the measured conversion rate  $r$  conforms to the classical Arrhenius equation,

$$r = r_{\infty} \exp(-E_b/kT) \quad (4)$$

where  $E_b$  is the barrier to conversion and  $r_{\infty}$  is the ‘attempt frequency’. From the experiments, it was found that  $r_{\infty} = 8 \times 10^{11 \pm 0.5} \text{ s}^{-1}$  and the barrier to diffusion was  $E_b = 18 \pm 3 \text{ meV}$ . At 6 K, this implies a conversion rate of  $6.1 \times 10^{-4} \text{ s}^{-1}$ . Therefore, the time taken to jump from one configuration to another is  $\sim 10^3 \text{ s}$ . This slow process would obviously be easy to measure using STM.

At 7 K, the conversion rate has increased 100-fold to  $\sim 0.1 \text{ s}^{-1}$ , so that it takes about 10 s to hop between configurations. Even the fastest scanners take about this time to capture their data and so slower systems could be expected to see the dimer as a circular blur. It is interesting that a relatively modest change in temperature of 1 K should make the difference between observation of  $\text{Cu}_2$  as a ‘dumb-bell’ or something more isotropic. Clearly, for ‘small’ barriers, even a small temperature change can have a significant effect on the STM image.

Treating the  $\text{Cu}_2$  dimer as a rigid rotor (bond length  $\sim 2.6 \text{ \AA}$ ), results in a moment of inertia of  $I_{\text{Cu}_2} = 3.6 \times 10^{-45} \text{ kg m}^2$ , corresponding to a rotational constant of  $B_{\text{Cu}_2} = 1.0 \times 10^{-2} \text{ meV}$ . A direct calculation of the rotational energy gives a mean value of  $\langle E_J \rangle = 0.52 \text{ meV}$  at 6 K. If we equate this with the kinetic energy for a classical rotor ( $\frac{1}{2} I \omega^2$ ), we get a measure of the mean angular velocity  $\omega$ . We suppose that an attempt to cross the barrier has occurred if the dimer rotates by the angle sufficient to take the dimer from a fcc–fcc well minimum to a barrier maximum. Simple geometry shows the angle to be  $16.1^\circ$ , which combines with the rotation speed to yield  $r_{\infty}(\text{Cu}_2) = 7.8 \times 10^{11} \text{ s}^{-1}$ . This is in very good agreement with the observed rate.

We can repeat this rough calculation for  $\text{C}_{60}$  which has a much larger moment of inertia than the dimer ( $1.0 \times 10^{-43} \text{ kg m}^2$ ). At 6 K, we estimate the angular velocity to be  $\omega_{\text{C}_{60}} = 4.1 \times 10^{10} \text{ rad s}^{-1}$ , leading to an estimated attempt frequency of  $r_{\infty}(\text{C}_{60}) = 7.8 \times 10^{10} \text{ s}^{-1}$ . This is ten times smaller than in the copper dimer case. At this stage, we can use (4) to calculate a critical barrier height  $E_{\text{crit}}$  for low temperature STM. For  $r \sim 10^{-3} \text{ s}^{-1}$  and  $kT = 0.52 \text{ meV}$  (6 K), we find

$$E_{\text{crit}} \sim 17 \text{ meV}. \quad (5)$$

If the barrier energy is lower than this critical value, rotational motion will be fast at 6 K and the STM image will be smeared out and STM simulations will need to include time averaging. If the barrier is larger, then the image may have threefold or sixfold symmetry depending on the energies of the local minima.

Repeating the above steps for a general temperature yields

$$E_{\text{crit}} \sim \frac{1}{2}kT (\ln kT + 64.6) \quad (E_{\text{crit}}, kT \text{ in meV}) . \quad (6)$$

(This assumes the attempt frequency has a temperature dependence. If instead we assume that  $r_{\infty} = 7.8 \times 10^{10} \text{ s}^{-1}$  irrespective of temperature, then (6) becomes  $E_{\text{crit}} \sim 32.0 kT$ .)

A recent density functional theory (DFT) study [14] of  $\text{C}_{60}$  on Cu(111) indicates that the adsorbate is most energetically stable when localized over a hcp site (although the fcc site is only 20 meV higher in energy). A barrier to rotation of 300 meV is predicted. According to (5), this barrier would be sufficient to prevent rotation on an STM time-scale at 6 K. However, at room temperature (6) suggests that the critical barrier should be nearer to 855 meV, and so rotation may not be suppressed.

The overall conclusion is that provided  $T \sim 7\text{--}10 \text{ K}$  we should be fairly confident that  $\text{C}_{60}$  adsorbs onto metallic substrates with a fixed orientation, with little rotational freedom. Of course, the observation of intramolecular detail in STM is a reliable indicator that rotation has been suppressed to some degree. However, as we have tried to emphasise, even this observation may not mean that motion has been completely stifled.

## 2.2 Charge Transfer

As  $\text{C}_{60}$  has a high electron affinity (2.689 eV [10]), charge transfer will be a distinct possibility whenever  $\text{C}_{60}$  is adsorbed onto a metallic surface. The  $T_{1u}$  LUMO of  $\text{C}_{60}$  can accept up to six electrons, but there is no reason to believe, a priori, that such a large CT should be sustainable on a metallic surface. In fact, a calculation by Burstein et al. [15] suggests that a maximum CT of two electrons to each  $\text{C}_{60}$  is to be expected, regardless of the work function of the metal.

The problem of charge transfer from metals to  $\text{C}_{60}$  molecules adsorbed on their surfaces has been addressed by several authors using both experimental [16–19] and theoretical approaches [15, 20, 21]. A (non-exhaustive) summary of their results is given in Table 1, which also lists the work functions of the substrates involved. As can be seen from the table, a larger CT generally correlates with a smaller work function, as might be expected. It is also interesting that even relatively inert metals such as gold are thought to transfer  $\sim 1$  electron to the  $\text{C}_{60}$ . Also note that the tabulated CT values appear to support Burstein's calculation of a maximum CT of  $2e/\text{C}_{60}$  [15].

Charge transfer to the  $\text{C}_{60}$  molecule will lead to occupation of the  $T_{1u}$  LUMO of the neutral molecule and this should be sufficient to render the molecule liable to distortion via the JT effect. Therefore, if it is possible to observe signatures of the JT effect using STM, then these signatures should be apparent in even the simplest experiments involving  $\text{C}_{60}$  on metal surfaces, provided CT occurs.

**Table 1** A selection of substrate work functions and the charge transfer that occurs from them to adsorbed  $C_{60}$  molecules. Numbers in italic font are calculated values and references are in square brackets

Surface	Work function <sup>a</sup> (eV)	Charge transfer <sup>b</sup> ( $e/C_{60}$ )
Ag(polycr.)	$4.3 \pm 0.1$ [18]	$1.7 \pm 0.2$ [18]
Ag(001)	4.64	$1.7 \pm 0.08$ [19]
Ag(110)	4.52	
Ag(111)	4.74	0.75 [17]
Au(polycr.)	$5.2 \pm 0.1$ [18]	$1.0 \pm 0.2$ [18]
Au(110)	5.37	$1 \pm 1$ [16]
Au(111)	5.31	
Cu(polycr.)	$4.5 \pm 0.1$ [18]	$1.8 \pm 0.2$ [18]
Cu(111)	4.94	0.8 [14], 1.6 [22]
Pt(110)	5.84	$-0.07$ [21]
Rh(111)	5.4 [23]	$\ll 1$ [24]
Si(100)–(2×1)	4.91	0 [25]
Si(111)–(7×7)	4.60	$(0.7 \text{ to } 3)^c \pm 1$ [25]

<sup>a</sup> From [26], unless otherwise referenced.<sup>b</sup> Mean number of electrons transferred from the surface to each  $C_{60}$ .<sup>c</sup> Dependent on coverage.

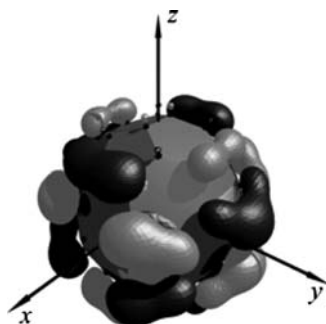
In a certain sense, the simple  $C_{60}$ –metal system provides the ‘purest’ test cases in which to seek the JT effect. Additional doping by co-deposition of, say, potassium has the benefit of creating more highly charged ions, e.g.  $C_{60}^{3-}$ , which may be subject to stronger vibronic coupling. This could increase the likelihood of observing the JT effect via STM, but there is also the possibility that the dopant may have other hidden effects that could unwittingly affect the image and lead to erroneous conclusions being drawn.

As a final comment on this aspect of the problem, it is worth mentioning that even in situations where  $C_{60}$  can be effectively decoupled from the surface, JT effects may still be apparent. This is because of the tunnelling nature of STM which necessarily involves electron transportation through the molecule. Thus, vibronic signatures have been recently recorded in differential tunnelling-current vs. bias ( $dI/dV$ ) spectra in single  $C_{60}$  molecules supported upon 1,3,5,7-tetraphenyladamantane nanostructures on a gold substrate [27].

### 2.3 Surface Interactions and Symmetry

There are 17 two-dimensional space groups arising from five Bravais nets associated with translation over a surface [28]. A  $C_{60}$  molecule adsorbed onto a surface will therefore be subject to a local symmetry belonging to one of ten possible site symmetries:  $C_{6v}$ ,  $C_6$ ,  $C_{4v}$ ,  $C_4$ ,  $C_{3v}$ ,  $C_3$ ,  $C_{2v}$ ,  $C_2$ ,  $C_s$ , and  $C_1$ . None of these site groups support triply degenerate irreps and so the  $T_{1u}$  LUMO will be split whenever  $C_{60}$

**Fig. 2** Electron distribution associated with the  $T_{1uz}$  orbital. The lighter lobes correspond to wave functions with a positive sign. The other orbitals are identical apart from their orientation (obtained by cyclic permutation of the axes)



is adsorbed onto a surface. If the symmetry is  $C_3$  or higher (i.e. one of the first six symmetries in the list above), the LUMO will split into a doublet and a singlet. If the symmetry is  $C_{2v}$  or lower, it will split into three singlets.  $C_{60}$  on a surface will therefore be subject to a Jahn–Teller effect involving one of these states, or to a pseudo-JT effect involving more than one of these states.

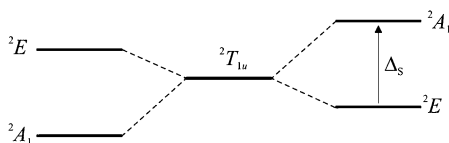
Consider the case of  $C_{60}$  adsorbed onto the (111) surface of a fcc lattice as exemplified by Au(111), Ag(111) and Cu(111), surfaces that are commonly used in STM studies. These surfaces belong to the  $C_{3v}$  factor group, which has irreps  $A_1$ ,  $A_2$  and  $E$ . When the  $C_{60}$  molecule is oriented so that it is subject to this  $C_{3v}$  environment, the correlations  $\{T_{1u}, T_{2u}\} \rightarrow \{A_1 + E\}$  and  $\{H_u\} \rightarrow \{A_2 + 2E\}$  apply. Therefore, the  $T_{1u}$  LUMO will be split into two sets of molecular orbitals. Examination of the distributions associated with the  $T_{1u}$  orbitals shows that the electrons occupy an ‘equatorial’ belt around the molecule with respect to the associated axis. For example, Fig. 2 shows the  $T_{1uz}$  orbital in a frame in which the Cartesian axes pass through carbon–carbon double bonds. This suggests that upon adsorption in a  $C_{3v}$  environment, the  $A_1$  orbital should be associated with the direction normal to the surface and the degenerate  $E$  orbitals should be associated with two orthogonal directions parallel to the surface.

The energy difference  $\Delta_S = E_{A_1} - E_E$  between the  $(A_1, E)$  pair is determined by the interaction with the surface, and the sign of  $\Delta_S$  could be positive or negative. In general, we need to consider three cases, referred to as  $p^1 (\equiv p^5)$ ,  $p^2 (\equiv p^4)$ , and  $p^3$ , corresponding to the number of electrons which would occupy the unsplit  $p$ -like  $T_{1u}$  orbitals in the absence of surface interaction. However, we must include electrons transferred as a result of charge transfer to reflect the  $C_{60}$  species that is present on the substrate. Thus, the  $p^1$  case accounts for a nominally  $C_{60}^-$  ion (or  $C_{60}^{5-}$  ion using electron-hole symmetry). This situation could arise if  $C_{60}$  is adsorbed onto a metal which subsequently donates one electron to it, or if an adsorbed but still neutral  $C_{60}$  molecule is chemically doped using an adsorbate such as an alkali metal.

Like the JT effect, the surface interaction will tend to favour low spin configurations. On the other hand, electron–electron Coulombic repulsion will favour high spin arrangements. Therefore, we need to derive correlation diagrams for the electronic interactions that will arise in each of the three  $p^n$  cases. In Fig. 3, we show the simple term splitting diagram for the  $p^1$  case with  $C_{3v}$  surface splitting.



**Fig. 3** Correlation diagram for  $p^1$  ( $C_{60}^-$ ) or  $p^5$  ( $C_{60}^{5-}$ ). The central term is that appropriate to free icosahedral ions, the right hand side for positive  $C_{3v}$  surface splitting  $\Delta_S > 0$ , and the left hand side for equivalent negative splitting



The central part of the diagram represents the case of a free  $C_{60}^-$  ion and the right hand side shows the behaviour to be expected if a positive surface splitting occurs. Conversely, the left hand side applies to negative splitting. The same diagram applies to the  $p^5$  case provided we reflect the diagram horizontally (or change the sign of  $\Delta_S$ ) because of electron-hole symmetry. Thus, a  $p^5$  configuration with positive splitting gives rise to a  $^2A_1$  ground state.

The same format used in Fig. 3 is adopted in the multielectron cases shown in Figs. 4 and 5. In the absence of surface interaction (centre of each diagram), electron–electron repulsion gives rise to three possible electronic terms, whose separations are determined by an exchange parameter  $J$  [29]. For  $p^2$ , the terms are  $\{^3T_{1g}, ^1H_g, ^1A_g\}$  with energies  $\{-J, J, 4J\}$ , and for  $p^3$  the terms are  $\{^4A_u, ^2H_u, ^2T_{1u}\}$  with energies  $\{-3J, 0, 2J\}$ . Calculated values of  $J$  vary considerably, with the actual value likely to be somewhere in the range 30–110 meV (see [29] and references therein). These terms will be split if the surface interaction is included as a perturbation, producing (in  $C_{3v}$  surface symmetry) singly and doubly degenerate orbitals as shown to the left and right of the centre of the diagrams. Note that the splitting shown here has only qualitative significance. On the extreme left and right of Figs. 4 and 5, the configurations that exist in the case of infinitely strong surface interaction are shown. For a strong but finite interaction, these configurations will be split by the electron–electron interaction which is now considered to be a weak perturbation.

The term diagrams in Figs. 3–5 allow the expected pattern of electronic excitation to be predicted for a surface splitting of  $C_{3v}$  symmetry, provided the strength of the interaction with the surface is known. Conversely, we might hope to deduce the magnitude of the surface interaction from knowledge of excitation spectra, if these can be obtained from adsorbates.

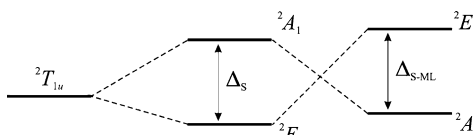
In this section, we have considered the specific example of a  $C_{60}$  ion subject to a  $C_{3v}$  surface splitting. Analysis for lower symmetries can be performed in a similar way, where for all symmetries  $C_3$  or higher there is still a doublet and a singlet, and for symmetries of  $C_{2v}$  or lower there will be three singlets.

## 2.4 $C_{60}$ Monolayers

A further complication to the picture already presented arises when the concentration of  $C_{60}$  molecules on the surface increases. Clearly, the greater the surface



**Fig. 6** Net splitting  $\Delta_{S-ML}$  of the  $T_{1u}$  LUMO in  $C_{60}$  due to a  $C_{3v}$  interaction with a surface and subsequent monolayer formation



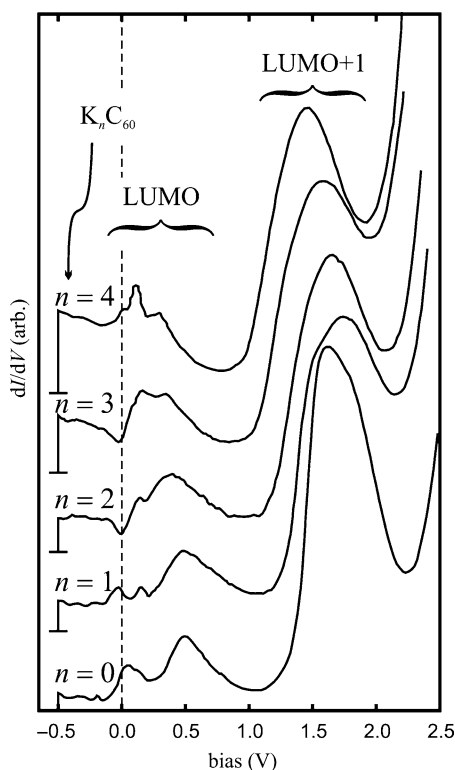
belts that point toward the surface. These, therefore, are expected to interact more strongly with the surface but be less inclined to interact with neighbours. In some respects, then, ML formation negates the surface interaction, as shown in Fig. 6. Even a very strong surface interaction could be cancelled by strong interactions within the monolayer. There may be evidence in the literature for this splitting cancellation. Photoemission spectra obtained from an increasingly K-doped monolayer of  $C_{60}$  on Ag(111) shows a triply degenerate LUMO progressively filling with electrons, but no splitting [17]. In contrast, a study [30] using STM techniques to sequentially K-dope an *individual*  $C_{60}$  molecule on a Ag(001) surface showed a clear splitting in the  $dI/dV$  spectrum of the undoped  $C_{60}$ , as shown in Fig. 7. This splitting could be an indication that the interaction of a single  $C_{60}$  molecule with the silver surface is non-zero, i.e.  $\Delta_S \neq 0$ .

Provided the monolayer interaction splits the LUMO into a singlet and a doublet, and the surface does the same, then there will be an effective, overall splitting which we call  $\Delta_{S-ML}$ . The correlation diagrams in Figs. 3–5, therefore, will still be applicable. On the other hand, it is clearly conceivable that the combination of all the interactions affecting any particular  $C_{60}$  may completely lift the degeneracy of the LUMO. In this case, STM images matching individual components of the LUMO may be obtainable depending on the bias used. Thus, STM should provide an ideal technique for experimentally determining the order and energy of any splitting present. This, in turn, should provide evidence for the local symmetry experienced by the molecule on the surface.

### 3 STM Imaging of Fullerenes: An Overview

The first paper to report an STM image of  $C_{60}$  molecules on a surface [of Au(111)] was published in 1990 [31], where the tendency of  $C_{60}$  to form hexagonally close-packed monolayers is apparent. In this early work, the fullerene molecules look little more than spherical blobs. Since then refinements to the STM technique, including the ability to record images at liquid helium temperatures, have greatly increased the quality of the images and the data therein. Subsequently, a large body of knowledge has been accumulated. It is not our purpose to give a thorough review of this body here. Instead, we will pick out a limited number of the most relevant papers in order to illustrate the most important features that have been observed. Subsequently, we will attempt to rationalise these features using theoretical simulations. A more general review of STM imaging as applied to fullerenes up to 1996 can be found in [32].

**Fig. 7** Tunnelling spectra from a single  $C_{60}$  molecule on Ag(001) subject to progressive K-doping. The spectra have been off-set to improve clarity. The LUMO appears to be split differently in each trace; possibly due to the influence of  $K^+$  ions. Note, however, that the undoped trace also shows signs of splitting, implying  $\Delta_S \neq 0$ . Reprinted figure with permission from R Yamachika, M Grobis, A Wachowiak and MF Crommie, *Science* **304**, 281 (2004) [30]. Copyright (2004) by The American Association for the Advancement of Science



One of the earliest works showing clear evidence of intramolecular detail within individual  $C_{60}$  units is that of Motai et al. [33], as shown in Fig. 8. These images are striking because it strongly suggests that the  $C_{60}$  adsorbs to the copper surface with a hexagonal face pointing downwards and that each  $C_{60}$  cooperatively aligns itself with its neighbours. It also exemplifies the tendency of  $C_{60}$  to form close-packed monolayers. These bias-dependent images can be explained in terms of the electron distributions associated with the LUMO and HOMO of  $C_{60}$  [34], as we illustrate in Sect. 4.2.

Further internal electronic structure arising from the HOMO orbitals was observed by Tsuchie et al. [35], who studied  $C_{60}$  monolayers on a  $Si(111)-\sqrt{3} \times \sqrt{3}$ -Ag surface at room temperature and at 60 K using a fixed sample bias of  $-2$  V. Figure 9 shows the images obtained from a plain  $C_{60}$  monolayer and one that has been doped with potassium. It is readily seen that doping has a significant effect on the resulting images. The reason why doping has such a marked effect on the image does not seem to have been explained or thoroughly investigated. One would expect K-doping to alter the energies of the imaged orbitals as a result of charge transfer to the fullerene cage. This would bring different orbitals ‘into view’ at the fixed bias used. Another possibility is that doping affects the molecule’s electronic structure to such an extent that the molecule rotates into a different orientation upon doping.

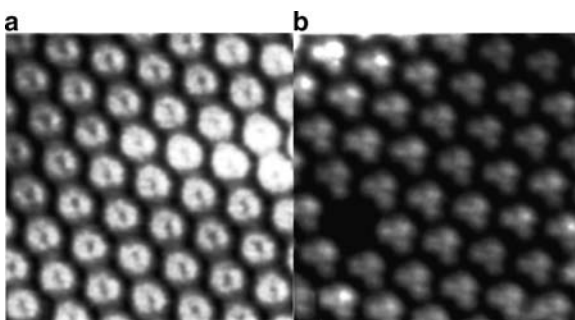


**Fig. 8** STM images of a  $C_{60}$  monolayer on Cu(111) showing intramolecular detail. (a) images the HOMO (sample bias  $-2$  V) and (b), the LUMO (at  $+2$  V). Reprinted figure with permission from K Motai, T Hashizume, H Shinohara, Y Saito, HW Pickering, Y Nishina and T Sakurai, *Jpn. J. Appl. Phys.* **32**(3B), L450 (1993) [33]. Copyright (1993) by the Japan Society of Applied Physics

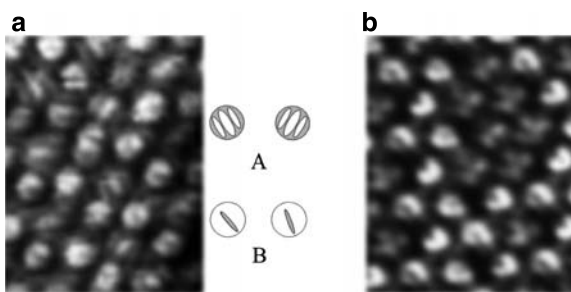


**Fig. 9** STM images of  $C_{60}$  on a  $Si(111)-\sqrt{3} \times \sqrt{3}-Ag$  surface at 60 K and sample bias  $-2$  V. (a) Shows the undoped monolayer which consists of molecules presenting two different kinds of striped image, labelled A and B. In (b), a K-doped monolayer is imaged, which results in a completely different set of images; bright 'U' and dim 'X' shaped molecules now dominate. Reprinted figure with permission K Tsuchie, T Nago and S Hasegawa, *Phys. Rev. B* **60**, 11131 (1999) [35]. Copyright (1999) by the American Physical Society

This could, in fact, be evidenced by Fig. 9 as the structures shown in Fig. 9a are consistent with molecules oriented with a  $C_2$  rotational axis perpendicular to the surface, whereas this does not appear to be the case in Fig. 9b. Of course, the presence of additional atoms on the surface could also affect orientation due to simple steric effects.

Hou et al. [36] observed similar striped HOMO-derived images at a sample bias of  $-1.8$  V on a  $Si(111)-(7 \times 7)$  surface (at 78 K). These workers, however, also captured other images at a variety of biases, obtaining different images at each bias used. To explain the observed images, the authors used DFT and found that, depending on adsorption site, the  $C_{60}$  molecules adsorb onto the surface with either a single bond or individual atom pointing downwards towards the surface.

Further proof that orientation can be unequivocally assigned on the basis of high-resolution STM images has been provided by Schull et al. [37]. This work shows



**Fig. 10** Low temperature STM image of  $C_{60}$  on Au(111) recorded using a bias of 1.5 V. This excerpt, from the original image of a  $(7\times 7)$  superstructure, shows a strip of eight molecules in which the orientation changes progressively from left to right. Reprinted figure with permission from G Schull and R Berndt, *Phys. Rev. Lett.* **99**, 226105 (2007) [37]. Copyright (2007) by the American Physical Society

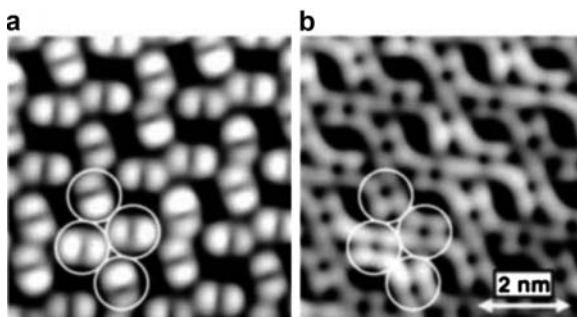


**Fig. 11** STM images of  $K_4C_{60}$  on Au(111) at small biases: (a)  $-0.1$  V and (b)  $+0.1$  V. Reprinted figure with permission from A Wachiwiak, R Yamachika, KH Khoo, Y Wang, M Grobis, DH Lee, SG Louie and MF Crommie, *Science* **310**, 468 (2005) [5]. Copyright (2005) by The American Association for the Advancement of Science

that long-range orientational ordering of  $C_{60}$  molecules adsorbed onto a Au(111) substrate can produce a  $(7\times 7)$  superstructure of adsorbates in which each  $C_{60}$  has a slightly different orientation, as shown in Fig. 10. This image, recorded at a sample bias of 1.5 V, corresponds to visualising LUMO orbitals and can be reproduced quite easily by imaging the  $T_{1u}$  orbitals of  $C_{60}$ .

Other workers have realised that the charge state of a  $C_{60}$  molecule has important implications with regards electron-vibration interactions and have actively sought to use STM to study the effects of doping. Of particular merit is the work of Crommie and co-workers who, in a series of papers [5, 30, 38, 39], have recorded some very intriguing images and spectra of a series of doped  $C_{60}$  molecules. In one experiment [on Ag(111)], these workers were able to use the STM tip to progressively attach/detach potassium atoms to individual  $C_{60}$  molecules and subsequently record the scanning tunnelling spectroscopy data shown in Fig. 7. In a later work [5], they studied an insulating phase  $K_4C_{60}$  and compared it to a conducting layer  $K_3C_{60}$ . For small biases, the images of the former are shown in Fig. 11. The authors argue that as the images shown in Fig. 11 are different from each other, there must be a JT effect present in the doped layer. However, as doping fills the LUMO of  $C_{60}$ , we would expect the images to derive from the  $T_{1u}$  orbitals, and, as we show later, it is possible to obtain identical images to those shown provided we take certain combinations of the molecular orbitals. The reasons why those particular combinations must be made could be due to the JT effect. However, it could also be due to a

surface and/or monolayer interaction or, indeed, some other perturbation. We do not believe that the experiments made to date provide concrete proof that it is possible to directly observe the JT effect in STM images. This is a subject we will return to later. First, though, we will look at a simple way of modelling STM images using molecular orbitals.

## 4 STM Simulations and Comparison with Experiment

We will base our simulations on a simple Hückel molecular orbital (HMO) picture of  $C_{60}$ . This approach may not embody the rigour inherent in more sophisticated methods of calculation, such as DFT, but is capable of demonstrating the underlying physical principles without incurring the additional computational cost of methods such as DFT. Where appropriate, we will make comparisons with other theoretical results in the literature, most notably DFT, in order to note similarities or discrepancies.

### 4.1 Hückel Molecular Orbital Theory for $C_{60}$

The starting point for our simulations is the analytical treatment of the HMO problem for  $C_{60}$  as given by Deng and Yang [40]. These workers used group-theoretic techniques to reduce the  $60 \times 60$  Hückel Hamiltonian for  $C_{60}$  to ten  $6 \times 6$  sub-matrices, each describable in terms of their parity,  $p$  ( $= \pm 1$ ), and an angular momentum-type quantum number,  $m$  ( $= 0, \pm 1, \pm 2$ ). The net result is that the form of the HMOs belonging to any particular irrep can be found in terms of 6 constants.

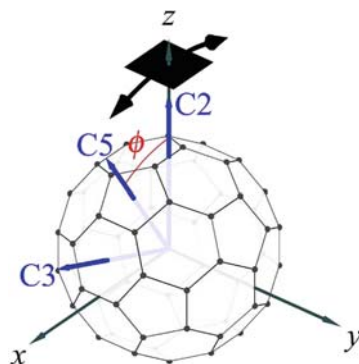
Deng and Yang [40] tabulate expressions for the HMOs that are appropriate to the case where single and double carbon-carbon bonds are equivalent (in the sense that their respective resonance integrals  $\beta_s$  and  $\beta_d$  are equal). However, the theory is sufficient to allow easy extension to a picture in which  $\beta_s \neq \beta_d$ . To this end, the authors introduce a parameter  $\alpha = -\beta_s$  which requires that  $\beta_d = \alpha - 2$ . In an earlier work [41], we introduced a similar parameter to account for this bond ‘alternation’, as it is often termed,  $\tau = \beta_d/\beta_s$ . Thus, the two treatments are related by

$$\alpha = 2(1 + \tau)^{-1}, \quad (7)$$

with the simple, equal-bond picture corresponding to  $\alpha = \tau = 1$ . In [41], the value  $\tau = 1.433$  was derived in order to explain the experimentally observed bond alternation of  $r(C = C) = 1.391 \text{ \AA}$  and  $r(C - C) = 1.455 \text{ \AA}$ . This implies  $\alpha = 0.8220$ , which is the value of  $\alpha$  that we will use when generating our images.

We are interested in generating simple pictures of the molecular orbitals. To do this, we form the required combinations of the sixty radially disposed  $2p$  orbitals localized at the carbon nuclei in  $C_{60}$ . We assume that the wave functions drop off as

**Fig. 12** Definition of the molecular axes and angle  $\phi$  needed to orient the molecule towards the viewing plane (black square)



$e^{-kr}$ , where, for hydrogen-like atoms,  $k = Z_{\text{eff}}/2a_0$ , with  $Z_{\text{eff}}$  the effective nuclear charge and  $a_0$  the Bohr radius. In keeping with our simple approach, we take the effective nuclear charge to be 3.14, as determined by Clementi and Raimondi [42], corresponding to  $k \approx 3.0$ .

We take our standard molecular axes to pass through the centres of a set of orthogonal carbon–carbon double bonds in the manner shown in Fig. 12. We then set up a fixed ‘viewing plane’ at a given distance away from the centre of the molecule, as shown Fig. 12. Rotation of the molecule around the  $y$ -axis by the correct amount then presents the desired face to the STM tip. Alternatively, we could consider moving the viewing plane in the opposite direction by an equivalent amount. Three important axes are highlighted, each labelled according to the symmetry type: C2 images the molecule when a double bond is pointing downwards towards the surface, whilst C5 ( $\phi = 31.72^\circ$ ) and C3 ( $\phi = 69.09^\circ$ ) present pentagonal and hexagonal faces for viewing. Note, however, that we can also view in this way the two other important orientations, namely over a single bond and an individual atom.

If the orbitals within each irrep are degenerate, then the sums of the squares of the electron densities for the LUMO ( $T_{1u}$ ) and HOMO ( $H_u$ ) have the appearances given in Fig. 13 (also see Fig. 2 for the shape of one of the components of the  $T_{1u}$  irrep). For neutral  $C_{60}$  this means that the filled orbitals are characterised by electrons being localised near the C=C bonds and so these bonds should be prominent at negative STM biases. On the other hand, at positive bias electrons should, at least initially, tunnel into the regions of space associated with the LUMO. In such images, the pentagonal faces (i.e. the C–C single bonds) will appear ‘bright’.

## 4.2 Simulating STM Images

In common with most workers, we use the simple tunnelling theory developed by Tersoff and Hamann [43] to provide the final link between the available orbitals and predicted STM image. Their work, which by their own admission contains many



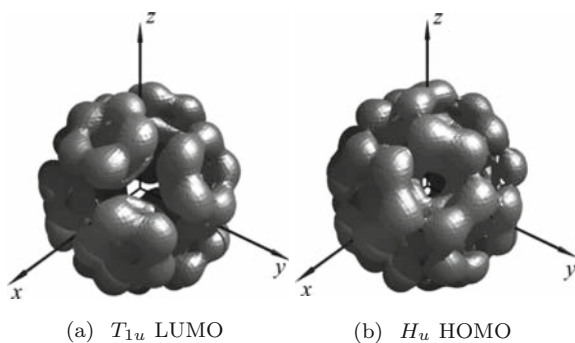


**Fig. 13** Isoelectronic density surfaces for (a), the LUMO ( $\rho = 0.0050 e \text{ \AA}^{-3}$ ) and (b), the HOMO ( $\rho = 0.0083 e \text{ \AA}^{-3}$ ) in the case when orbital degeneracy is present

approximations, suggests that the tunnelling current  $I$  measured during STM is such that

$$I \propto \sum_v |\psi_v(\mathbf{r}_0)|^2 \delta(E_v - E_F), \quad (8)$$

where  $\psi_v$  is the wave function of a surface state of energy  $E_v$ ,  $\mathbf{r}_0$  determines the position of the STM tip,  $E_F$  is the Fermi energy and  $v$  runs over all the available surface states. In imaging the LUMO, therefore, we assume that sufficient positive bias is applied to the surface so that

$$I_{\text{LUMO}}(\mathbf{r}_0) \propto \rho_{\text{LUMO}}(\mathbf{r}_0) = \sum_{\alpha=x,y,z} |T_{1u\alpha}(\mathbf{r}_0)|^2, \quad (9)$$

where  $\rho_{\text{LUMO}}(\mathbf{r}_0)$  is the electron density evaluated at  $\mathbf{r}_0$ , which is some position vector located within the viewing plane shown in Fig. 12. It is a simple matter to evaluate this expression in a given plane and hence generate a ‘constant height’ STM image. It is also relatively easy to extend the calculations to create plots which show the tip height required to maintain a constant tunnelling current, i.e. to produce ‘constant current’ simulations.

Of course, (9), and its obvious extension to the negative bias case involving  $\sum_{\alpha} |H_{u\alpha}(\mathbf{r}_0)|^2$ , would only be appropriate if all the orbitals involved are degenerate. Thus, we can use the density functions shown in Figs. 13b and 13c to simulate simple constant height STM images for this degenerate case. Some specific results are shown in Fig. 14.

Although simple, some of these simulations bear a strong resemblance to real STM images observed experimentally. Thus, the LUMO and HOMO pictures obtained by viewing along the C3 axis are very similar to those shown in Fig. 8. The LUMO picture viewed along the C2 axis also gives a good match to Fig. 11a. Figure 14b also shows that we can account for the long-range ordering observed by Schull et al. depicted in Fig. 10. However, it is clear that the six images shown in Fig. 14a do not account for all the different STM features that have been observed.

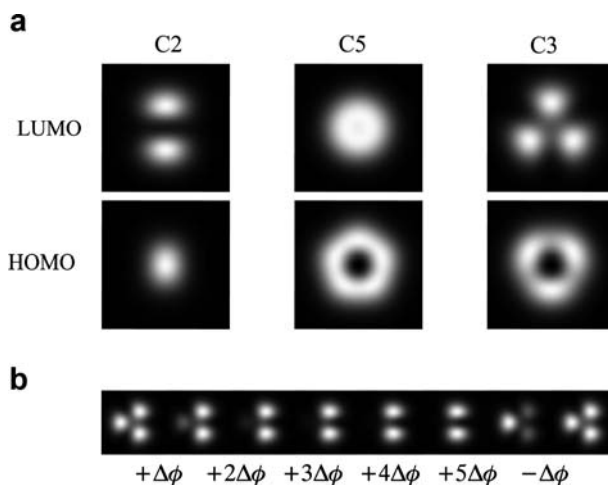


**Fig. 14** Simulated, constant-height STM images of  $C_{60}$ . In (a), we show the expected appearance of the LUMO and HOMO orbitals when viewed along specific axes (each image is  $10 \times 10 \text{ \AA}^2$ ). (b) Shows a simulation of the orientational effect shown in Fig. 10. The starting orientation corresponds to  $\phi = 69.09^\circ$ . Additional rotation of  $\Delta\phi \simeq 2.6^\circ$  is subsequently added up to a critical rotation after which the subsequent molecules return to orientations close to the original one

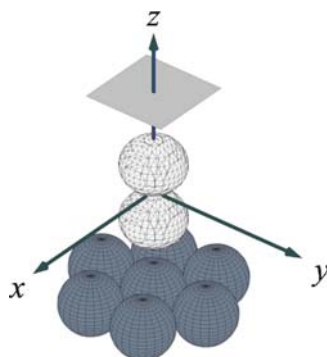
One simple extension would be to vary the orientation to cover the possibility that adsorption occurs with a low-symmetry axis pointing towards the surface, e.g. a C–C single bond or individual C atom could be prone to the surface. However, the most serious omission is, perhaps, the treatment of the LUMO and HOMO as if they retain their three- and five-fold degeneracies in the adsorbed environment. This is certainly not something that would be expected for  $C_{60}$  molecules adsorbed onto a surface.

### 4.3 Effects of Surface Interaction on STM Images

Let us suppose that the interaction with the surface is sufficiently strong to cause a loss of degeneracy in the frontier orbitals. Furthermore, assume that the split combinations require different biases for imaging by STM. It is possible that the degeneracy could be lifted completely depending on the symmetry of the surface. Hence, we need a general method of finding which orbitals remain degenerate when exposed to the influence of a surface interaction of a given symmetry.

Here, we describe a simple method of probing degeneracy involving the characters of the orbitals under the group operations associated with the surface symmetry. As (111) surfaces are commonly used in these studies, we shall use as an example a surface symmetry of  $C_{6v}$ , as depicted in Fig. 15. We consider the molecule to have a C=C bond pointing towards the surface so that the LUMO basis functions

**Fig. 15** Diagrammatic representation of the  $C_{60}$ -surface system. The surface (dark-grey, close-packed spheres) imposes  $C_{6v}$  symmetry on the adsorbed molecule's orbitals (white lobes). Here, a  $p_z$  orbital represents the  $T_{1uz}$  orbital of  $C_{60}$  and the light-grey square is the viewing plane for STM



$\{T_{1ux}, T_{1uy}, T_{1uz}\}$  transform as the  $(x, y, z)$ -axes themselves or, for illustration purposes, a set  $(p_x, p_y, p_z)$  of  $p$ -orbitals. Actually, as the  $T_{1u}$  orbitals form a basis for the spherical harmonics with angular momentum  $L = 1$ , this basis can be used whatever orientation is chosen. However, the same cannot be said for the HOMO orbitals as the  $L = 5$  harmonics decompose as  $T_{1u} \oplus T_{2u} \oplus H_u$  in icosahedral symmetry.

In Fig. 15, we can see that when exposed to an environment of  $C_{6v}$  symmetry, the  $p_z$  orbital, and hence equivalently the  $T_{1uz}$  orbital, will have a character of 1 under any of the group operations of the  $C_{6v}$  group and so it transforms as the totally symmetric  $A_1$  irrep. Similarly, we can show that the  $p_x$  and  $p_y$  orbitals have the same characters and form a basis for the doubly degenerate  $E_1$  irrep. Therefore, this surface interaction will split the LUMO into two parts: a doubly degenerate pair ( $T_{1ux}, T_{1uy}$ ) and a singly degenerate  $T_{1uz}$  orbital. These two sets of orbitals would be expected to produce two distinct STM images (at different biases).

We can repeat the above process for the HOMO orbitals by considering the transformation properties of a set of  $H_u$  orbitals. However, as already mentioned, this is more difficult than for the LUMO as these orbitals derive from spherical harmonics with  $L = 5$ . For any given orientation, an orthogonal basis must be found and then the transformation properties examined. Finally, combinations of orbitals must be constructed which have the same transformation characteristics. The overall result is that the fivefold degenerate HOMO splits into three parts: one singly- and two doubly-degenerate combinations. Details of these calculations will be left for a subsequent publication. We do, however, present the resulting STM images to be expected for the configuration currently being considered (i.e. C=C prone to the surface), in Fig. 16.

The simulated STM images in Fig. 16 have been generated in constant current mode using a large tunnelling current in order to give a clear view of the electron densities associated with the images. Note that these 'enhanced' pictures are not realistic simulations of what might be observed in practice. However, they still allow the regions of electron density 'nearest' to the observer to be determined and so it is easy to imagine what the corresponding real STM image might look like. Thus, for the HOMO, two of the combinations (one  $A$ , one  $E$ ) will produce STM images having a striped appearance. These bear a strong resemblance to the

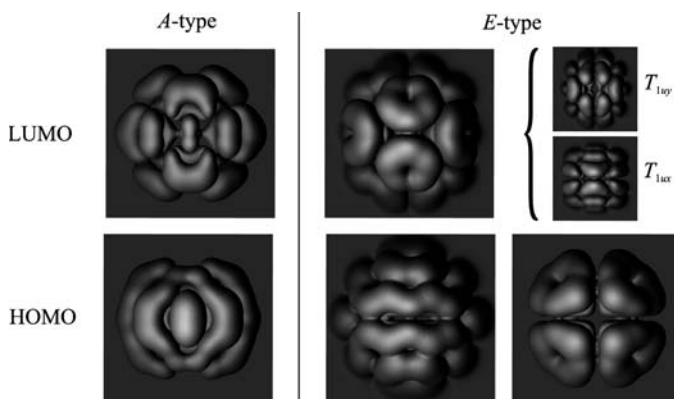


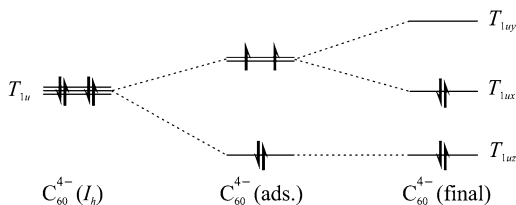
**Fig. 16** High-resolution, constant-current simulated STM images for a surface-adsorbed  $C_{60}$  molecule. The distribution of the orbitals into doublets and singlets has been induced by a surface with  $C_{6v}$  site symmetry

experimentally-obtained STM images for ‘A’ and ‘B’ species shown in Fig. 9a, although a direct correspondence is unlikely as our simulated images would be expected to require two different biases for visualisation. The image of the *A*-type HOMO orbital in Fig. 16 is also interesting because it is *identical* to a simulation made using DFT by Pascual et al. [44]. In fact, the simple methods used here are able to reproduce all the images obtained using sophisticated DFT calculations in [44] and this fact gives us confidence in the procedures we have used.

The LUMO-derived images in Fig. 16 should also be compared with the picture of the  $T_{1uz}$  orbital shown in Fig. 2. This orbital becomes the *A*-type orbital in the presence of the surface (in the  $-z$  direction) and as the electron density is held in an equatorial belt lying in the  $(x, y)$  plane, the corresponding STM image would be weak. On the other hand, the *E*-type combination is strong and produces an image very similar to that shown in Fig. 11a. In Fig. 2, this image corresponds to the sum of the images obtained looking down the  $x$ - and  $y$ -axes, as highlighted in the upper right part of Fig. 16. In fact, the strong, two-lobed STM image in Fig. 11a can be accounted for using the  $T_{1ux}$  orbital *alone*. The  $T_{1uy}$  orbital, in isolation, produces a weak STM image that matches very closely those seen in Fig. 11b. The implication of this observation is that the STM images are consistent with a complete loss of degeneracy in the  $T_{1u}$  orbitals in the  $K_4C_{60}$  monolayer – in other words, the symmetry must be  $C_{2v}$  or lower. A schematic representation of the overall energy level scheme is shown in Fig. 17.

If the  $C_{60}$  is positioned at a substrate site of  $C_{6v}$  symmetry, then the additional lowering of symmetry must be due to an interaction that has been so far neglected. One possibility is that the  $K^+$  counter ions, whose whereabouts are unknown, could reduce the site symmetry beyond that considered. With 4 counter ions to accommodate per  $C_{60}$ , it is not difficult to imagine a configuration in which the assumed  $C_{6v}$  symmetry could be reduced to  $C_{2v}$ , in which degeneracy must be absent. Another

**Fig. 17** Illustration of the envisaged energy changes occurring in the LUMO orbitals of K-doped  $C_{60}$  (not to scale). The final order is consistent with the STM images of Wachowiak et al. [5]



possible mechanism, as can be inferred from Fig. 17, is that the doubly occupied  $E$ -type orbitals could be responding to a JT interaction of the kind  $E \otimes e$ . If this were the case, then a strong JT interaction could result in distortion of the molecular cage. However, even though the STM images show remarkable detail, it is very doubtful that the technique is sufficiently detailed enough to resolve the small changes in the shape of the very rigid  $C_{60}$  molecule that would accompany JT interaction. The interesting question, considering that STM responds to electronic information and the JT effect affects both vibrational and electronic wave functions, is whether the JT effect can manifest itself in an STM image purely electronically. This is an issue we seek to address in Sect. 5.

In summary, we have seen that using quite primitive methods of visualising molecular orbitals, we can reproduce most of the STM images of  $C_{60}$  presented in Sect. 3 without necessarily invoking the JT effect. The images that have eluded reproduction, interestingly enough, are the ones from  $C_{60}$  molecules that have been K-doped. The lack of an ability to describe these images could be due to the JT effect, although the anticipated electron transfer that occurs even in the absence of doping would preclude reservation of the K-doped derivatives for special treatment. It is fairly likely that the added  $K^+$  ions influence the STM image through steric effects and, if these ions are located preferentially on the surface itself, it would be easy to envisage that doping could cause a change in the orientation of the adsorbed  $C_{60}$  molecules, as appears to be the case in Fig. 9.

Overall, the evidence to support suggestions that JT effects have been unequivocally observed in STM images [5] seems very thin. One problem with a JT interpretation of these images is that real STM images are influenced by many factors, some of which may be considerably more significant than the rather subtle JT interaction. In contrast, theoretical simulations can be specifically tailored to consider only the effects of a JT interaction, the results of which can be used as a guide to what may appear in actual experiments.

## 5 Jahn–Teller Effects in Surface-Adsorbed Molecules

In this section we shall consider some general aspects of the central problem of interest here. Let us suppose that a JT-active molecule is adsorbed onto a surface in preparation for imaging via STM. In as simple a way as possible, we want to discover what JT-related effects might appear in the captured image under ideal

conditions. By ‘ideal’, we mean ignoring all complications that are present in real images, such as the effect of finite tip size, low resolution, molecule-tip interactions, and even the surface interaction itself. The intention is to concentrate on what arises purely on the basis of the JT effect. Even here, it must again be noted that the very act of performing STM will excite molecules into vibronically-coupled electronic states which may promote dynamical tunneling processes which, in turn, could influence the recorded STM image. Such complications are also ignored here.

### 5.1 A hypothetical $E \otimes e$ Example: $X_3$

We shall initially dispense with the fullerene molecule itself because of the complicated nature of the JT effects that are possible in this large and highly symmetric molecule (see Sect. 5.2.1). Instead, we consider a simple  $E \otimes e$  JT system exemplified by a hypothetical triatomic molecule of the form  $X_3$  of the kind exemplified by  $\text{Na}_3$ , i.e. one constructed from atoms whose valence electrons reside in  $s$ -type atomic orbitals. The molecule is adsorbed onto a similarly hypothetical, atomically flat surface so that each atom is equidistant from the surface. The surface, therefore, is merely a platform to support the molecule so that it can be imaged via STM. In this way, we attempt to isolate, using simple STM simulations, the features of the image that can be attributed solely to the JT nature of the molecule.

The  $X_3$  molecule constitutes an example of the well-known  $E \otimes e$  JT problem, a textbook vibronic coupling problem [45] whose low dimensionality permits the consequences of vibronic interaction to be appreciated using simple pictorial methods. The coupling occurs between doubly degenerate orbitals  $\{E_x, E_y\}$  which are occupied by a single electron and have the form

$$\begin{aligned} E_x &= (\psi_b - \psi_c)/\sqrt{2}, \\ E_y &= (2\psi_a - \psi_b - \psi_c)/\sqrt{6}, \end{aligned} \quad (10)$$

where  $\psi_a$  is the  $s$ -orbital centred at atom ‘a’, etc.

In the absence of a JT effect, the atoms will be arranged in the high-symmetry  $D_{3h}$  configuration and the electron density sampled will correspond to  $|E_x|^2 + |E_y|^2$  for some particular bias. A simulation of the STM image produced by this electron density is shown in Fig. 18, which also shows the doubly-degenerate, in-plane normal modes of vibration of interest

$$\begin{aligned} Q_x &= (2x_a - x_b - \sqrt{3}y_b - x_c + \sqrt{3}y_c)/\sqrt{12}, \\ Q_y &= (2y_a + \sqrt{3}x_b - y_b - \sqrt{3}x_c - y_c)/\sqrt{12}, \end{aligned} \quad (11)$$

where  $x_a$  is the displacement from equilibrium of atom ‘a’ in the  $x$  direction, etc.

The simulation in Fig. 18a shows the characteristics that might be expected from this symmetrical arrangement of anti-bonding orbitals, namely, threefold symmetry

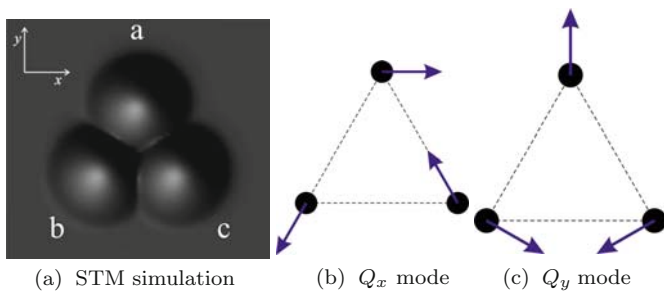
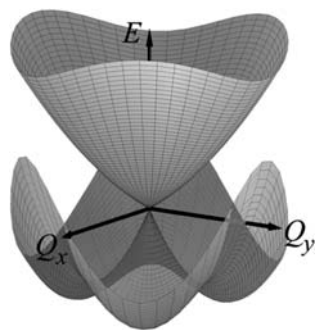


**Fig. 18** A simulated, constant-current STM image of a hypothetical  $X_3$  molecule in its high-symmetry  $D_{3h}$  configuration is shown in (a). The  $(x, y)$ -axes are arranged so that atom ‘a’ lies on the  $y$ -axis and the centre of mass is at the origin. The corresponding degenerate normal modes of vibration are shown in (b) and (c)

**Fig. 19** A graphical depiction of the variation in the energies of the upper (excited) and lower (ground) potential energy surfaces in normal-mode or  $Q$ -space for the quadratic  $E \otimes e$  JT problem. The origin corresponds to the system in its degenerate, high-symmetry  $D_{3h}$  configuration shown in Fig. 18



and nodes between atoms. The next step is to add in a JT effect. In general, the system Hamiltonian can be expressed in the form

$$\mathcal{H} = \mathcal{H}_0 + V'_1 \mathcal{H}_1 + V'_2 \mathcal{H}_2, \quad (12)$$

where  $\mathcal{H}_1$  is the linear JT interaction Hamiltonian involving terms linearly dependent on the normal mode coordinates  $Q_i$ ,  $\mathcal{H}_2$  is the quadratic interaction Hamiltonian dependent on products of the form  $Q_i Q_j$ ,  $\mathcal{H}_0$  is the Hamiltonian in the absence of coupling and  $V'_i$  ( $i = 1$  or  $2$ ) are dimensionless coupling constants. The explicit form of this Hamiltonian and its solutions are well known [45].

The most obvious effect of the JT interaction is that the electronic orbitals are no longer degenerate, as shown in  $Q$ -space in Fig. 19. This implies that we will observe two different STM images at different biases; one from the ground PES and another from the excited PES. Therefore, for imaging purposes, we shall assume that the two biases required are sufficiently large that each electron density can be imaged with negligible interference from the other. Note that this splitting also suggests that STM, if properly calibrated, should be capable of directly measuring energies related to the JT stabilisation energy which, in turn, can be related to coupling strengths.

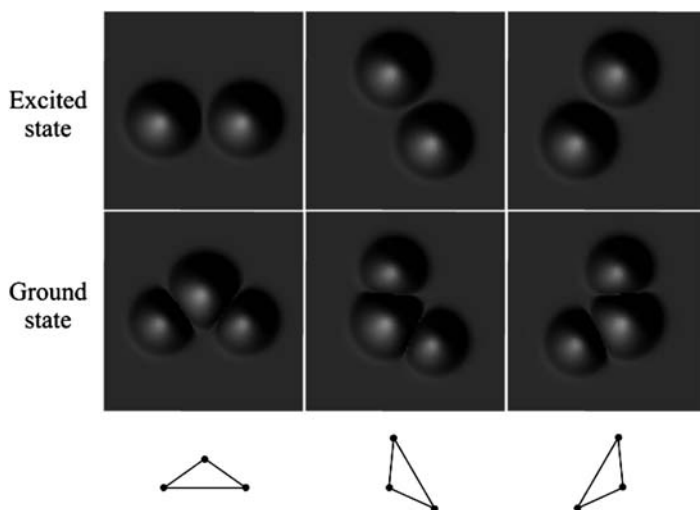


**Fig. 20** STM simulation of an  $X_3$  molecule subject to a strong JT effect (to the extent that each configuration has an internal angle of  $110^\circ$ )

In Fig. 19, we have illustrated the consequences of a general quadratic JT interaction, viz. the ground PES possesses 3 discrete, isoenergetic minima symmetrically placed around the origin. If the vibronic coupling is very strong, then the system will become trapped in one of these potential minima or ‘wells’ – i.e. there is a static JT effect. The probability of finding the system in each well will be the same and so 3 equivalent images would be expected to be observed using STM, as indicated in Fig. 20, in which the minima have been arbitrarily associated with an obtuse geometry. Of course, each pair of images are identical but for orientation, and conversion between them corresponds to the unique dynamical motion referred to as pseudorotation [46].

It is clear from Fig. 20 that the presence of a strong JT effect has had a significant effect on the original, unperturbed image shown in Fig. 18a. The ground state image clearly shows a reduction in symmetry from  $D_{3h}$  to  $C_{2v}$  and the excited state appears to have an atom missing. This latter facet arises as the ‘missing’ atom lies on a nodal plane. Figure 20 also allows us to visualise the effects of accounting for the corrugation of the surface, which has so far been assumed to be flat. Depending on the symmetry of the corrugation (and we notably except  $C_{6v}$  and  $C_{3v}$  here) the energies of the three configurations shown will become different. Thus, the surface interaction, in the first instance, will have the effect of favouring a subset of the available wells; in other words, the molecule may become locked into one particular well. Or, if two or more wells remain isoenergetic, it may jump between the remaining equivalent configurations. In fact, this is actually the behaviour that we would expect to occur in reality in the ‘static’ case itself shown in Fig. 20. It is only because we have chosen to consider the vibronic interaction to be arbitrarily large that we have assumed the rate of pseudorotation to be so slow as to be negligible



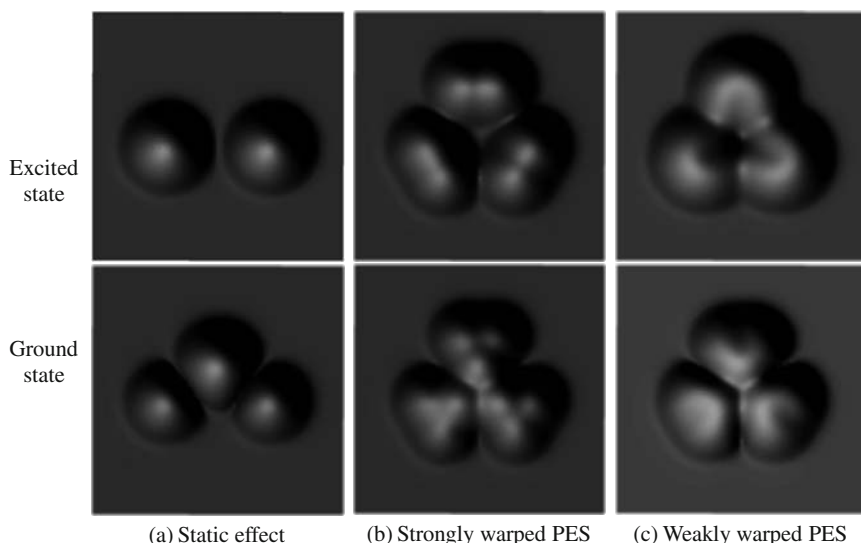


**Fig. 21** STM simulations for systems subject to a static vs. dynamic JT effect. The top row corresponds to the excited state and the bottom to the ground state. In (a), infinitely strong coupling locks the molecule into one particular well. Finite but strong coupling (so that the system jumps between three wells) is shown in (b). Further reduction in localisation leads to essentially free pseudorotation, producing the time-averaged images in (c)

on the time-scale used to capture the STM images. As this time-scale itself is very slow, this suggests that an extremely large vibronic coupling would be required to produce the results shown in Fig. 20.

If we now allow the system to jump between wells, what effect would this have on the image? We can do this by simulating STM images at particular points in  $Q$ -space and then taking weighted averages. As we are only interested in first approximations, we can consider two types of behaviour. If the PES is strongly warped (large but finite coupling), then we can expect the system to spend most of its time localised in the wells. Taking the average of the three images in Fig. 20, we arrive at the image shown in Fig. 21b. If the warping is further reduced, so that the PES becomes essentially a flat trough in  $Q$ -space, then the system can freely pseudorotate around the trough. Thus, we take an average over 100 equally-spaced points in the trough to obtain the time-average shown in Fig. 21c.

We can see from Fig. 21 that if the JT effect is dynamic on the time-scale associated with STM capture, then the recorded image takes on a much more symmetrical ( $D_{3h}$ ) appearance than when the effect was considered static. However, even if the pseudorotation rate is very fast compared to the response rate of the STM imaging apparatus, there will still be residual effects due to the JT interaction. The most apparent effect is that the circular orbits traced out by the nuclei are imaged by STM in both the ground and excited states. It is interesting that in the image shown in Fig. 21c, the ground state electron density appears to be preferentially localised

inside the equilateral triangle formed by the average nuclear positions, whereas the converse is true for the excited state.

The occurrence of blurred ‘rings of motion’ like those shown in Fig. 21c in real STM images would provide novel confirmation that pseudorotation is occurring and that the system is actively avoiding the high symmetry configuration. However, this would only be observed if a strong enough JT interaction was present because the diameter of the blurred ring depends on the JT coupling strength; too small a diameter and the vestiges of the JT effect in the image will vanish. This is particularly true for  $C_{60}$ , where the molecular bonds are very strong and so the expected displacement of the atoms from their high-symmetry position is very small.

## 5.2 *Jahn–Teller Effects in Surface-Adsorbed Fullerenes*

The simple  $E \otimes e$  JT system discussed in the previous section is useful as it allows one to explore the sort of features that may occur in STM images of JT-active molecules. The same general arguments developed there can also be applied to more complicated systems, such as surface-adsorbed  $C_{60}$ . The high symmetry of  $C_{60}$  means that a multitude of interesting electron-vibration coupling systems can be formed when the molecule is doped. A brief review of these systems follows in Sect. 5.2.1. When  $C_{60}$  is adsorbed onto a metallic substrate, the most likely doping event to occur will be transferral of electron density into the  $T_{1u}$  LUMO. This will be further enhanced if additional doping is carried out using electropositive metals such as potassium. Therefore, we concentrate for the rest of this section on images derived from the LUMO.

We have seen in Sect. 3 that the resolution of the STM images of fullerenes is sufficient to show up some intramolecular detail. However, as the bonding in the fullerene cage is strong, the resolution will not be great enough to show up small changes in shape due to the JT effect. Therefore, we shall ignore the small distortions in our simulations and look for purely electronic effects.

### 5.2.1 A review of Jahn–Teller effects in discrete fullerene systems

A comprehensive assessment of the JT effect in icosahedral systems may be found in the book by Chancey and O’Brien [47]. Together with the references therein, this book gives a good introduction to the possible JT effects expected in  $C_{60}$ . Therefore, only a brief discussion of these systems is given here.

Hückel theory, as we have seen, indicates that the neutral molecule has a fully-filled, fivefold degenerate HOMO of  $H_u$  symmetry. The JT effect is therefore absent in the neutral molecule itself. The LUMO, with  $T_{1u}$  symmetry, lies about 2 eV higher in energy and is readily available to the molecule leading to a high electron affinity of  $\sim 2.7$  eV [10].

Reduction of  $C_{60}$ , most commonly achieved by reaction with highly electropositive Group 1A metals, will thus produce several JT-active species of the form  $C_{60}^{n-}$  ( $1 \leq n \leq 5$ ) possessing a set of partially filled  $T_{1u}$  orbitals. The latter can couple to vibrations with  $h_g$  symmetry. Single occupation of the LUMO leads to the well-studied  $T_{1u} \otimes h_g$  JT system. Higher LUMO occupancies are written in the form  $p^n \otimes h$ . It is also possible, but more difficult, to oxidise  $C_{60}$ . Removal of a single electron (or, equivalently, addition of a single ‘hole’) produces the  $C_{60}^+$  ion which is subject to a  $H_u \otimes (g \oplus h)$  JT effect. Once again, further doping is possible leading to the general coupling problem  $h_u^n \otimes (g \oplus h)$ , but the corresponding ions are less likely to be of practical importance due to their difficult preparation and high reactivity.

It quickly becomes clear that there is a rich variety of vibronically coupled systems that may be present in compounds containing doped  $C_{60}$ . There are other complications that arise that further complicate the theoretical description of these problems. One such complication is that each of these coupling problems is actually a multimode problem. That is, there are several modes of vibration of  $C_{60}$  that can simultaneously couple to the aforementioned electronic states ( $6g_g$  and  $8h_g$ , to be precise). Although this complication can be dealt with (see, e.g. [48]), it is often easier to work in terms of a single, effective mode as this is far simpler and reproduces most of the important aspects of the problem. In fact, in the current context, even the details of some effective mode of vibration are effectively irrelevant as we are ignoring the distortion of the  $C_{60}$  cage.

Another complication that warrants mention here is that multiply-doped molecules will be susceptible to electron–electron interactions in addition to vibronic coupling. Once again, this complication can be dealt with, especially if we are interested in numerical results only (see, e.g. [49, 50]). Unsurprisingly, in light of the coarseness of our method of simulation, this is another aspect of the problem that will be neglected here. Similarly, we will neglect any intermolecular charge transfer processes and effectively treat the ions as individual entities, with a fixed position on the surface and a fixed charge state.

### 5.2.2 The LUMO-Surface Interaction

Let us now concentrate on the  $T_{1u}$  LUMO of  $C_{60}$ . Referring to Fig. 12, we want to let the molecule have an orientation  $\phi$  with respect to the surface-tip arrangement. Thus, we make new combinations of the basis functions to be associated with laboratory axes ( $X, Y, Z$ ). The  $Z$ -axis will be taken as the normal to the surface, i.e. along the orientation axis and so we take

$$T_{1uZ} = \cos \phi T_{1uz} + \sin \phi T_{1ux}, \quad (13)$$

to be the molecular orbital associated with the  $Z$ -axis. For different values of  $\phi$ , the  $y$ -axis remains static and so we take the  $Y$ -axis to be coincident with its molecular counterpart, so that:

$$\begin{aligned} T_{1uY} &= T_{1uy} , \\ T_{1uX} &= -\sin \phi \, T_{1uz} + \cos \phi \, T_{1ux} . \end{aligned} \quad (14)$$

If the effect of adsorption is to split the triply degenerate  $T_{1u}$  level into a singlet  $A$  and doublet  $E$ , then we can write the effect of the surface interaction Hamiltonian  $\mathcal{H}_S$  as

$$\begin{aligned} \mathcal{H}_S T_{1uX} &= \frac{1}{2} \delta \, T_{1uX} \\ \mathcal{H}_S T_{1uY} &= \frac{1}{2} \delta \, T_{1uY} \\ \mathcal{H}_S T_{1uZ} &= -\delta \, T_{1uZ} \end{aligned} \quad (15)$$

so that the magnitude of the surface splitting is  $|\Delta_S| = \frac{3}{2}|\delta|$ . We also allow  $\delta$  to be positive or negative to give the required splitting order. Combining (13)–(15), the expression for the interaction Hamiltonian in this case, written in the usual  $\{T_{1ux}, T_{1uy}, T_{1uz}\}$  electronic basis, is

$$\mathcal{H}_S = -\frac{\delta}{4} \begin{pmatrix} 1 - 3 \cos 2\phi & 0 & 3 \sin 2\phi \\ 0 & -2 & 0 \\ 3 \sin 2\phi & 0 & 1 + 3 \cos 2\phi \end{pmatrix}. \quad (16)$$

It should be noted that this form of  $\mathcal{H}_S$  will only be true for specific orientations  $\phi$  which result in a symmetry of  $C_3$  or higher, which we expect to correspond to alignment of the  $Z$  axis with a  $C_2$ ,  $C_5$  or  $C_3$  axis. For more general orientations, corresponding to lower symmetries, the  $T_{1u}$  level will be split into three singlets and a modified form of  $\mathcal{H}_S$  will be required involving an additional parameter.

If we treat  $\mathcal{H}_S$  in (16) as an additional perturbation to the dynamic JT system, we can find first order corrections to the energies of the wells involved. For orientations away from those which split the LUMO into a doublet and a singlet, this is an approximation. However, we proceed this way to avoid introducing an additional parameter. The results are shown in Fig. 22. In  $D_{5d}$  symmetry, for example, the contribution to the energy of well C [which is in the  $(x, z)$ -plane] is,

$$\langle E_C \rangle = \frac{(1, 0, \varphi) \mathcal{H}_S (1, 0, \varphi)^T}{(1, 0, \varphi) (1, 0, \varphi)^T} = -\frac{\delta}{4} \left[ 1 + \frac{3}{\sqrt{5}} (\cos 2\phi + 2 \sin 2\phi) \right],$$

where the label used and its definition follow those used previously<sup>1</sup> [51, 52] and  $\varphi = \frac{1}{2}(\sqrt{5} + 1)$  is the golden mean.

As we might have expected, the energy of well C is a minimum when the angle  $\phi$  is such that the well is oriented towards the surface. Naturally, the other 5 wells are isoenergetic for this arrangement. The inference is that, if the molecule

<sup>1</sup> The electronic states for the  $D_{2h}$  wells in [52] apply to the  $(h_u)^2 \otimes h_g$  JT system, as is appropriate for  $C_{60}^{2+}$  ions. Hence, they involve a 10-dimensional electronic basis  $\{T_{1g}, T_{2g}, G_g\}$ . For use here, only the  $T_1$  part is required.

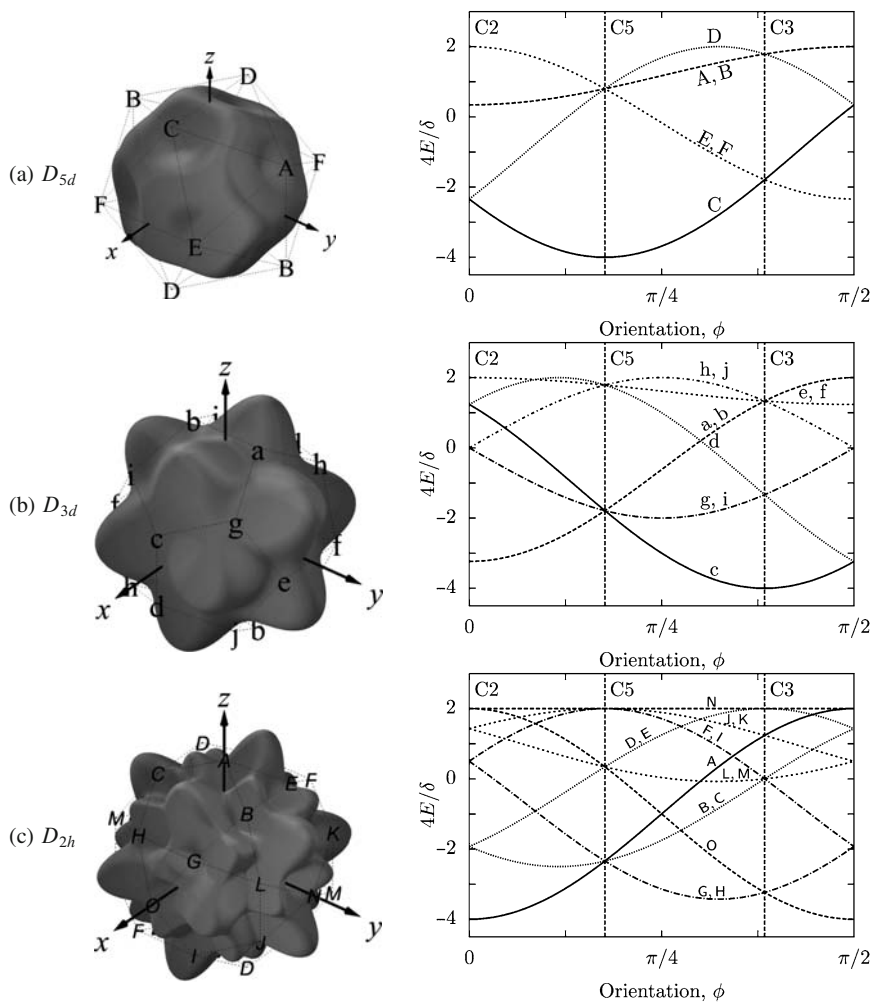


**Fig. 22** Pictorial representations of some of the potential wells of various symmetry appropriate to molecules with  $I_h$  symmetry. The labels used to identify the potential minima match those used in earlier work [51, 52]. The graphs on the right show the corresponding surface-induced splitting of the wells. As used in Fig. 12,  $\phi$  specifies the angle at which the surface is oriented with respect to the wells

is experiencing a  $D_{5d}$  distortion due to the JT effect and subsequently becomes adsorbed onto a surface with a pentagonal face prone to the surface, then the molecule could become locked into the particular well associated with that face. Or, if  $\delta < 0$ , the molecule could become preferentially locked in one of the other 5 wells, but pseudorotation between all 5 may also occur. We could use this information to predict what might be seen via STM. However, the resulting images would exhibit fivefold symmetry.

With Fig. 11 in mind, in which twofold symmetry is apparent, we consider instead the case when  $\phi = 0$  and the molecule is adsorbed with a C=C bond prone to the surface. The combinations of the wells that need to be considered are apparent from Fig. 22. For example, for a  $D_{2h}$ -distorted molecule, there are two preferred configurations. One possibility is that when  $\delta > 0$ , well A, with electronic state  $T_{1uz}$ , has the lowest energy; the other is that wells N ( $\sim T_{1uy}$ ) and O ( $\sim T_{1ux}$ ) form a degenerate pair (i.e. when  $\delta < 0$ ). We do not need to simulate pictures for these cases as they would be virtually indistinguishable from those in the upper part of Fig. 16. The latter scenario is the most interesting: if the system was pseudorotating between wells N and O, then we could generate a ground state image to match the negative bias result in Fig. 11. The positive bias image requires knowledge of the excited electronic states, which requires further work that will be left for another publication.

Now consider a  $D_{5d}$ -distorted system. We can see from Fig. 22a that wells C and D are related to each other by a  $C_2$  rotation about the  $z$ -axis. As we are viewing the molecule along this axis, these two wells will appear identical to each other but inverted. The same applies to the other pairs (A, B) and (E, F). Therefore, we only need to simulate one of each degenerate pair, plus the time-average that would result if the system hopped from one of the wells to its 'twin'. For brevity, let us denote pseudorotation or hopping between two or more wells using the notation  $A \leftrightarrow B$ . We collect the resulting images in Fig. 23, together with a picture of the electron distribution associated with a single well (well C). Comparing these simulations with Fig. 16, we see that two of the pseudorotating pairs,  $C \leftrightarrow D$  and  $E \leftrightarrow F$ , produce images that match the double-lobe negative-bias image shown in Fig. 11. Interestingly, the other pair,  $A \leftrightarrow B$ , produces an image very similar to the fourfold symmetric positive-bias image in Fig. 11.

However, the (A, B) pair cannot be directly responsible for producing this image in the real STM data. This is because the states derived from combinations of the wells are all part of the ground electronic state and, as Fig. 11 images  $C_{60}^{4-}$  ions, these combinations must correspond to filled states. As already mentioned, further consideration of the excited state manifold is required in order to explain the positive bias images.

Finally we consider the case of  $D_{3d}$ -distorted ions. Using Fig. 22 as a guide, we consider the well pairs (a, b) and (e, f) and make comparable simulations, as shown in Fig. 24. These pairs were chosen because they correspond to the lowest and highest energies (depending on  $\delta$ ). The simulated images in this case very closely match those in Fig. 16 and, therefore, the images obtained assuming the presence of  $D_{2h}$  wells.

The overall conclusion is that it is possible to generate STM simulations of features that have been found in real images starting from molecules that are  $D_{2h}$ ,  $D_{5d}$  or  $D_{3d}$  distorted. If a particular type of distortion is chosen, then there are always several ways in which that distortion can be applied to  $C_{60}$ . One cannot simply pick one particular distorted form; rather, it is necessary to look for other forms that are equal in energy (even if adsorbed onto a surface) and to then account for interconversion by hopping or pseudorotation, as this is likely to be fast on the STM time-scale.

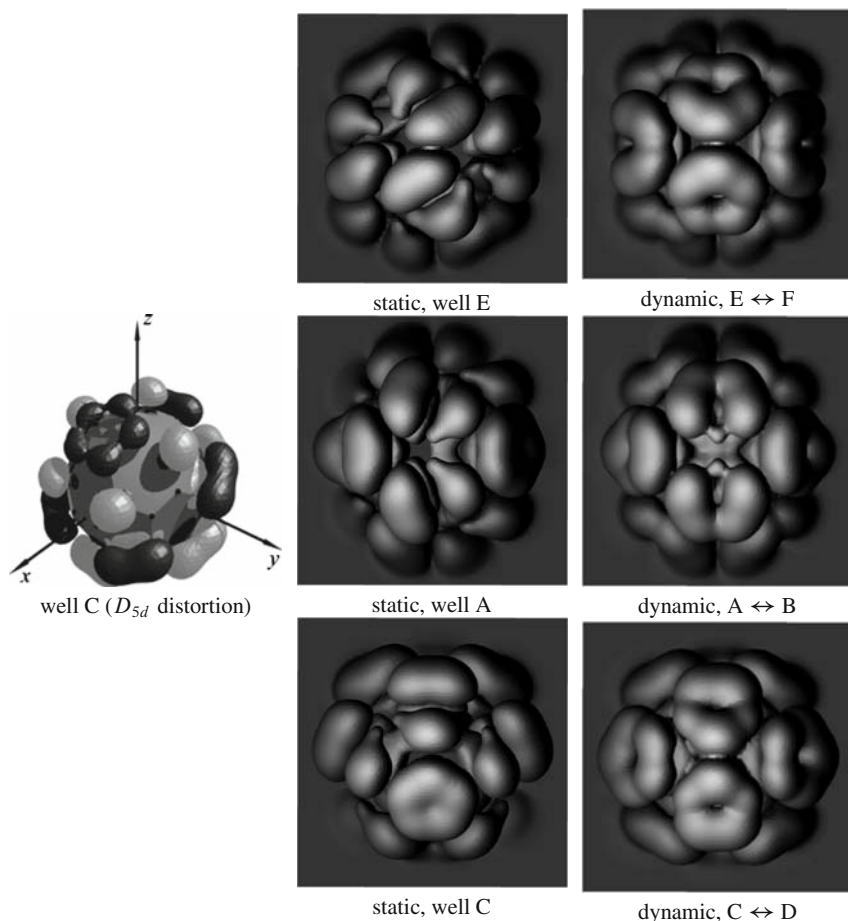


**Fig. 23** Plot to show the electronic orbital associated with a  $D_{5d}$  minimum (well C). *Light-grey* lobes represent wave functions with a positive polarity. The adjacent STM simulations show the images expected for the different cases discussed in the text, as viewed along the  $z$ -axis

## 6 Summary and Conclusions

It is undoubtedly an exciting proposition to study vibronically coupled molecules at the molecular level using tunnelling microscopy. In this article, we have attempted to draw attention to the many complications that may influence the appearance and interpretation of the images obtained via STM. We have used a simple  $E \otimes e$  system to illustrate what might be visible in ideal circumstances, but our main goal has been to simulate what might be observed when  $C_{60}$  molecules are imaged.  $C_{60}$  molecules are an especially exciting choice of JT system to study using STM because they are relatively large and highly symmetric. Thus, the doped molecules can display a

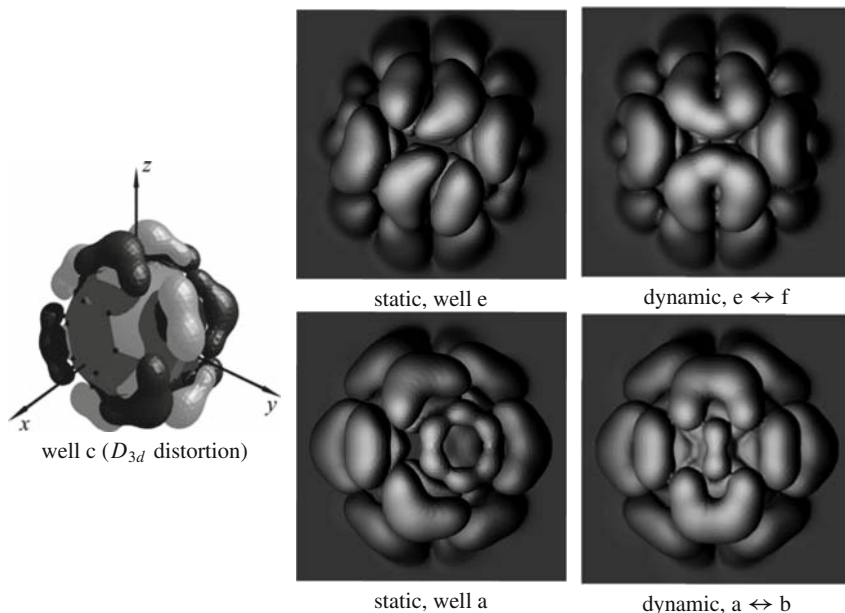


**Fig. 24** As for Fig. 23, but illustrating the images produced by  $D_{3d}$ -distorted molecules

diverse and rich variety of JT effects and the resulting distortion has a reasonable chance of making itself apparent in the STM image.

We have tried to distinguish between static and dynamic JT effects. However, the difference between these two regimes is really the time-scale with which the molecule is observed. Data capture in STM is undoubtedly ‘slow’ and this must be seen as one drawback of this method of study. For a JT-active molecule, there is usually a set of distorted configurations that are isoenergetic (or, perhaps, nearly isoenergetic if the host surface has a weak effect on them) and interconversion between them is to be expected. The interconversion rate is expected to be rapid on the STM time-scale and so its effect on the recorded STM image needs to be addressed.

In  $C_{60}$ , the intramolecular bonds are strong and it is thought that the distortion caused by the JT effect will be small. If this is the case, then current STM equipment may not have the resolution required to directly detect the change in shape that results. In any case, as outlined above, the dynamic nature of the JT effect may produce a time-averaged shape that is essentially icosahedral. Our best hope seems to be that the electronic components of the vibronic states alone will provide sufficient evidence for unequivocal identification of the JT effect present.

To this end, we have used the electronic states associated with the ground state wells of  $D_{5d}$ ,  $D_{3d}$  and  $D_{2h}$  symmetry to provide a first attempt at simulating what might be observed via STM. In each case, we can produce images to match those observed by Wachowiak et al. [5]. We can also do this without invoking a JT effect,



provided we assume that the surface or some other interaction (e.g. neighbouring  $C_{60}$  molecules) splits the  $T_{1u}$  orbitals. Therefore, we do not think that the STM results currently available in the public domain constitute conclusive evidence to justify claims that the JT effect has been observed using this technique. However, this does not preclude the possibility that features have been observed which are, in fact, due to the JT effect – simply that the case is not proven. A more thorough investigation is called for which examines both ground and excited states and takes into account coupling strengths and the corresponding time-scales.

There is still much work to be done if we are to fully understand the complicated interplay between the JT effect, surface interaction and the dynamic processes that are inevitably present. Further experimental work will doubtless follow, and has the potential to reveal much. Consequently, it is essential that theoretical work keeps apace so that the information revealed is correctly interpreted.

**Acknowledgements** IDH and JLD gratefully acknowledge funding for this work from EPSRC (UK) [Grant number EP/E030106/1].

## References

1. G. Binnig, H. Rohrer, *Helv. Phys. Acta* **55**(6), 726 (1982)
2. G.K. Binnig, H. Rohrer, *IBM Journal of Research and Development* **30**(4), 355 (1986). [Reprinted, *ibid.* **44**(1), 279 (2000)]
3. C. Bai, *Scanning Tunneling Microscopy and Its Application*, 2nd edn. (Springer, 2000)
4. C.J. Chen, *Introduction to Scanning Tunneling Microscopy*, 2nd edn. (Oxford University Press, New York, 2008)
5. A. Wachowiak, R. Yamachika, K.H. Khoo, Y. Wang, M. Grobis, D.H. Lee, S.G. Louie, M.F. Crommie, *Science* **310**(5747), 468 (2005)
6. A.F. Hebard, M.J. Rosseinsky, R.C. Haddon, D.W. Murphy, S.H. Glarum, T.T.M. Palstra, A.P. Ramirez, A.R. Kortan, *Nature* **350**, 600 (1991)
7. M.J. Rosseinsky, A.P. Ramirez, S.H. Glarum, D.W. Murphy, R.C. Haddon, A.F. Hebard, T.T.M. Palstra, A.R. Kortan, S.M. Zahurak, A.V. Makhija, *Phys. Rev. Lett.* **66**, 2830 (1991)
8. O. Gunnarsson, *Alkali-Doped Fullerenes: Narrow-Band Solids with Unusual Properties* (World Scientific, Singapore, 2004)
9. O. Gunnarsson, *Rev. Mod. Phys.* **69**, 575 (1997)
10. X.B. Wang, C.F. Ding, L.S. Wang, *J. Chem. Phys.* **110**(17), 8217 (1999)
11. U. Kemiktarak, T. Ndikum, K.C. Schwab, K.L. Ekinci, *Nature* **450**(7166), 85 (2007)
12. F. Besenbacher, E. Lægsgaard, I. Stensgaard, *Mater. Today* **8**(5), 26 (2005)
13. J. Repp, G. Meyer, K.H. Rieder, P. Hyldgaard, *Phys. Rev. Lett.* **91**(20), 206102 (2003)
14. L.L. Wang, H.P. Cheng, *Phys. Rev. B* **69**, 045404 (2004)
15. E. Burstein, S.C. Erwin, M.Y. Jiang, R.P. Messmer, *Phys. Scr.* **T42**, 207 (1992)
16. S. Modesti, S. Cerasari, P. Rudolf, *Phys. Rev. Lett.* **71**, 2469 (1993)
17. L.H. Tjeng, R. Hesper, A.C.L. Heessels, A. Heeres, H.T. Jonkman, G.A. Sawatzky, *Solid State Commun.* **103**, 31 (1997)
18. B.W. Hoogenboom, R. Hesper, L.H. Tjeng, G.A. Sawatzky, *Phys. Rev. B* **57**, 11939 (1998)
19. C. Cepek, M. Sancrotti, T. Greber, J. Osterwalder, *Surf. Sci.* **454**, 467 (2000)
20. R. Nouchi, I. Kanno, *J. Appl. Phys.* **97**, 103716 (2005)
21. M. Casarin, D. Forrer, T. Orzali, M. Petukhov, M. Sami, E. Tondello, A. Vittadini, *J. Phys. Chem. C* **111**, 9365 (2007)

22. T. Kobayashi, C. Tindall, O. Takaoka, Y. Hasegawa, T. Sakurai, J. Korean Phys. Soc. **31**, S5 S8 (1997)
23. E. Bertel, G. Rosina, F.P. Netzer, Surf. Sci. **172**, L515 (1986)
24. A. Sellidj, B.E. Koel, J. Phys. Chem. **97**, 10076 (1993)
25. S. Suto, K. Sakamoto, T. Wakita, C.W. Hu, A. Kasuya, Phys. Rev. B **56**, 7439 (1997)
26. D.R. Lide. CRC Handbook of Chemistry and Physics, 88th Edition online. Table 12-114 (2008). URL <http://www.hbcpnetbase.com/>. Accessed 18 December 2008
27. T. Frederiksen, K.J. Franke, A. Arnau, G. Schulze, J.I. Pascual, N. Lorente, Phys. Rev. B **78**, 233401 (2008)
28. A.M. Bradshaw, N.V. Richardson, Pure & Appl. Chem. **68**, 457 (1996)
29. M. Wierzbowska, M. Luders, E. Tosatti, J. Phys. B-At. Mol. Opt. Phys. **37**, 2685 (2004)
30. R. Yamachika, M. Grobis, A. Wachowiak, M.F. Crommie, Science **304**, 281 (2004)
31. R.J. Wilson, G. Meijer, D.S. Bethune, R.D. Johnson, D.D. Chambliss, M.S. de Vries, H.E. Hunziker, H.R. Wendt, Nature **348**, 621 (1990)
32. T. Sakurai, X. Wang, Q.K. Xue, Y. Hasegawa, T. Hashizume, H. Shinohara, Prog. Surf. Sci. **51**, 263 (1996)
33. K. Motai, T. Hashizume, H. Shinohara, Y. Saito, H.W. Pickering, Y. Nishina, T. Sakurai, Jpn. J. Appl. Phys. **32**, L450 (1993)
34. Y. Maruyama, K. Ohno, Y. Kawazoe, Phys. Rev. B **52**, 2070 (1995)
35. K. Tsuchie, T. Nagao, S. Hasegawa, Phys. Rev. B **60**, 11131 (1999)
36. J.G. Hou, Y. Jinlong, W. Haiqian, L. Qunxiang, Z. Changgan, L. Hai, B. Wang, D.M. Chen, Q. Zhu, Phys. Rev. Lett. **83**, 3001 (1999)
37. G. Schull, R. Berndt, Phys. Rev. Lett. **99**(22), 226105 (2007)
38. Y. Wang, R. Yamachika, A. Wachowiak, M. Grobis, K. Khoo, D.H. Lee, S.G. Louie, M.F. Crommie, Phys. Rev. Lett. **99**(8), 086402 (2007)
39. Y. Wang, R. Yamachika, A. Wachowiak, M. Grobis, M.F. Crommie, Nature Mater. **7**, 194 (2008)
40. Y. Deng, C.N. Yang, Phys. Lett. A **170**(2), 116 (1992)
41. I.D. Hands, J.L. Dunn, C.A. Bates, V.Z. Polinger, Chem. Phys. **278**(1), 41 (2002)
42. E. Clementi, D.L. Raimondi, J. Chem. Phys. **38**(11), 2686 (1963)
43. J. Tersoff, D.R. Hamann, Phys. Rev. B **31**, 805 (1985)
44. J.I. Pascual, J. Gómez-Herrero, C. Rogero, A.M. Baró, D. Sánchez-Portal, E. Artacho, P. Ordejón, J.M. Soler, Chem. Phys. Lett. **321**, 78 (2000)
45. I.B. Bersuker, V.Z. Polinger, *Vibronic Interactions in Molecules and Crystals* (Springer-Verlag, Heidleberg, 1989)
46. I.B. Bersuker, *The Jahn-Teller Effect* (Cambridge UP, 2006)
47. C.C. Chancey, M.C.M. O'Brien, *The Jahn-Teller Effect in  $C_{60}$  and other Icosahedral Complexes* (Princeton University Press, Princeton, 1997)
48. I.D. Hands, J.L. Dunn, W.A. Diery, C.A. Bates, Phys. Rev. B **73**, 115435 (2006)
49. I.D. Hands, W.A. Diery, J.L. Dunn, C.A. Bates, Phys. Rev. B **76**, 085426 (2007)
50. L.M. Sindi, I.D. Hands, J.L. Dunn, C.A. Bates, J. Mol. Struct. **838**, 78 (2007)
51. J.L. Dunn, C.A. Bates, Phys. Rev. B **52**, 5996 (1995)
52. I.D. Hands, W.A. Diery, J.L. Dunn, C.A. Bates, J. Mol. Struct. **838**, 66 (2007)

**Part V**  
**Jahn-Teller Effect and Molecular**  
**Magnetism**

# Jahn–Teller Effect in Molecular Magnetism: An Overview

Boris Tsukerblat, Sophia Klokishner, and Andrew Palii

**Abstract** In this article we review applications of the concepts of the Jahn–Teller effect in molecular magnetism. The scope of the contemporary field of molecular magnetism and its fascinating applications are shortly described. The theoretical background of molecular magnetism as well as the applications of molecular magnets are closely related to the basic concepts of the Jahn–Teller effect through their structural properties affecting magnetic anisotropy, interaction with light, photo-induced magnetism, co-operative behavior of molecule-based magnetic systems, and dynamical properties affected by relaxation processes and spin coherence times.

We show that a wide class of symmetric spin-frustrated systems are orbitally degenerate, and the Jahn–Teller effect plays an important role in the description of their properties. In high-nuclearity magnetic clusters (single molecule magnets) the Jahn–Teller coupling stabilizes a specific alignment of the local magnetic axes, giving rise to a global anisotropy and consequently to a spin reorientation barrier. The problem of the double exchange in mixed-valence systems is considered, with the emphasis on the underlying role of the pseudo Jahn–Teller coupling in localization/delocalization of the mobile electron. Under certain conditions the latter gives rise to a reduction of the double exchange and, in particular, reduces the magnetic anisotropy in the presence of orbital degeneracy. The properties of mixed-valence systems are closely related to a complicated interplay between the pseudo Jahn–Teller interaction, isotropic exchange and double exchange. Manifestations of the Jahn–Teller effect are discussed for a wide class of photoactive (photo-switchable) systems. Pseudo Jahn–Teller models are employed for the description of the tautomeric transformations and extremely long living metastable states in photochromic compounds. Finally, we review the problem of co-operative phenomena in molecule-based extended mixed-valence systems, for which the Jahn–Teller mechanism is shown to result in the charge and structural ordering. The concept of the Jahn–Teller effect combined with the so-called quasidynamical approach allows to describe the intervalence optical bands and to reveal the underlying physical mechanism (quantum resonances of the vibronic levels) of the intricate quantum phenomena of the coexistence of localized and delocalized states in crystals based on interacting mixed-valence units.

## Abbreviations

JTE	Jahn–Teller effect
JT coupling	Jahn–Teller coupling
SMM	Single molecule magnets
MV	Mixed-valency
AS exchange	Antisymmetric exchange
HDVV model	Heisenberg–Dirac–Van Vleck model
ITO	Irreducible tensor operator
PKS model	Piepho–Krausz–Schatz model
P-model	Piepho model
SNP	Sodium nitroprusside

## 1 Molecular Magnetism: Diversity of the Field

Contemporary molecular magnetism originates from classical magnetochemistry and represents an interdisciplinary field of science that incorporates basic concepts of physics, chemistry and material sciences. The objects of molecular magnetism are molecular metal clusters and/or organic molecules, i.e., molecular assemblies consisting of a finite number of exchange-coupled ions (spins), which represent the so-called class of zero-dimensional magnets [1–21]. These systems are of current interest in many areas of research and applications, like material science, biophysics, biochemistry and have prospective applications as single molecule magnets (SMM) [1, 2, 8–10] and multifunctional nanomaterials. As was recently demonstrated, coexistence of ferromagnetism and metallic conductivity can be reached in one molecular material [22, 23]. Organic molecules of increasing sizes and large numbers of unpaired electrons are also being explored as building blocks for molecular-based magnets [24, 25]. The modern trend in molecular magnetism is focused on the possibility to use molecular clusters as magnets of nanometer size, which exhibit magnetic bistability and quantum tunneling of magnetization at low temperatures. This kind of molecular nanomagnets, so-called SMMs can be placed on the border line between quantum and classical physics. Indeed, on one side they show slow relaxation of magnetization and magnetic hysteresis as a bulk magnet, and on the other side they are still small enough to exhibit important quantum effects.

The first ten years of activity summarized in [3] showed that the fundamentals of molecular magnetism are well established (at least the main concepts), and molecular magnets are expected to provide many important nano-technological applications. SMMs based on large metal clusters with significant magnetic anisotropy resulting in a barrier for spin reorientation are promising in the design of the new memory storages at the molecular level, and at the same time open a new interesting area of physics within the nanoscopic scale [1, 2]. In this regard, special attention has been paid to *molecular magnets* [4–7] that have been proposed as the leading

candidates for use as carriers of quantum information, *nanoscale qubits*, due to a number of vitally important advantages. This opens a novel route to a spin-based implementation of quantum information processing [26–41]. The first observation of Rabi oscillations in a molecular nanomagnet has now been reported [33] (see also detailed discussion in [34, 35]); this is expected to make an impact on the development of this area of research and applications. An attractive class of materials is represented by the photoswitchable compounds that are suggested to have promising applications in the hot area of energy and information storage [42–44]. The theoretical backgrounds of molecular magnetism, as well as the applications of molecular magnets, are closely related to the basic concepts of the Jahn–Teller effect (JTE) [45–47] through the structural properties affecting magnetic anisotropy, interaction with light, photo-induced magnetism, co-operative behavior and dynamical properties affected by the relaxation processes and spin coherence times.

In this review article we will summarize the application of the JT concepts to the field of molecular magnetism. The article is organized as follows. In Sect. 2 we consider metal clusters based on the orbitally non-degenerate ions excluding the on-site JTE. Nevertheless, if the overall symmetry is high enough, the collective spin-frustrated states prove to be degenerate, and therefore exhibit JT coupling that affects magnetic properties and spectroscopic phenomena. Section 3 is devoted to the double exchange in the so-called mixed valence (MV) systems, in which the “extra” electron can move among spin cores. Description of the vibronic models are given with the emphasis on the problem of localization that is closely related to the magnetism and spectroscopy of MV systems. Section 4 is devoted to mixed-valency and double exchange in isolated systems, with the emphasis on the magnetic properties and localization through the vibronic mechanisms. In Sect. 5 we shortly review a wide area of co-operative phenomena in extended MV systems comprising dimeric and trimeric MV subunits, like charge and structural ordering, coexistence of localized and delocalized states and their spectroscopic manifestations. These interesting phenomena have JTE at the heart of the basis. A wide class of photo-switchable coordination compounds exhibiting light-induced long-living metastable states, like in the case of the photochromic effect, which is closely related to the JT structural transformations, are considered in Sect. 5. Finally, in Sect. 6 the pseudo JT mechanism of valence tautomeric transformation in cobalt compounds is briefly considered in connection with their magnetic properties and charge transfer optical absorption bands.

## 2 Jahn–Teller Instability in Spin-Frustrated Metal Clusters

### 2.1 Introductory Remarks

In this Section we focus on the manifestations of pseudo JT coupling in the magnetic anisotropy of exchange-coupled frustrated systems, in which the antisymmetric (AS) exchange is the main source of the magnetic anisotropy. We will demonstrate

the role of AS exchange [48,49] in the magnetic anisotropy of spin-frustrated system and reveal how the vibronic JT interaction affects the magnetic anisotropy caused by the AS exchange. Spin frustration in highly symmetric systems with triangular faces is shown to be closely related to the orbital degeneracy in the total spin states. Understanding of the special role of the AS exchange in spin frustrated systems, particularly in trinuclear transition metal clusters, dates back to the seventies (see [13, 14] and references therein). AS exchange was shown to result in a zero-field splitting of the frustrated ground state of the half-integer triangular spin systems, magnetic anisotropy, essential peculiarities of the EPR spectra and wide range of phenomena related to hyperfine interactions [50–55] closely related to JTE. We shortly summarize the manifestations of the AS exchange in the cluster anion present in  $K_6[V^{IV}_{15}As_6O_{42}(H_2O)] \cdot 8H_2O$  (hereafter  $V_{15}$  cluster) containing a spin-frustrated trinuclear unit, in which the role of the JTE [45–47] becomes crucially important.

## 2.2 Exchange Interactions, Analysis of the Degeneracy

The  $V_{15}$  cluster was discovered more than 15 years ago [56], and has since attracted continuous and increasing attention as a unique molecular magnet based on a unique structure exhibiting layers of different magnetization [57–59]. Studies of the adiabatic magnetization and quantum dynamics of the  $V_{15}$  cluster with an  $S = 1/2$  ground state proved that this system exhibits the hysteresis loop of magnetization of molecular origin and can be referred to as a mesoscopic system [60–65]. Recently, the long living coherent quantum oscillations have been discovered in the molecular magnet  $V_{15}$  [33]. This finding creates a strong hope to employ nanomagnets in a spin-based quantum information processing (*spin-based qubits*) that is expected to provide a revolutionary development in the implementation of quantum computing [34, 35]. The magnetic properties of the  $V_{15}$  cluster are inherently related to spin frustration effect in the layered quasispherical arrangement of vanadium ions, and from this point of view  $V_{15}$  represents a system for which the manifestations of the AS exchange are especially interesting, and the vast amount of available experimental data does allow to find out precisely the key parameters.

The molecular cluster  $V_{15}$  has a distinctly layered quasispherical structure within which fifteen  $V^{IV}$  ions ( $s_i = 1/2$ ) are placed in a central triangle sandwiched by two hexagons [56]. At low temperatures two hexanuclear  $V^{IV}_6$  are spin-paired, so that only the excitations within the frustrated antiferromagnetic  $V^{IV}_3$  triangle affect the magnetic properties [57, 58, 66–69]. The isotropic superexchange can be described by the Heisenberg-Dirac-Van Vleck (HDVV) Hamiltonian:

$$H_0 = 2J (S_1 S_2 + S_2 S_3 + S_3 S_1), \quad (1)$$

where  $S_1$ ,  $S_2$  and  $S_3$  denote the spin operators on the sites 1, 2 and 3,  $S_i = 1/2$ , and for the antiferromagnetic case the exchange parameter  $J > 0$ . As usually the

following spin coupling scheme  $S_1 S_2(S_{12}) S_3 S \equiv (S_{12}) S$  is assumed, with  $S_{12}$  being the intermediate spin, so that in our case  $(S_{12})S = (0)1/2$ ,  $(1)1/2$  and  $(1)3/2$ . The energy levels  $\varepsilon_0(S) = J [S(S + 1) - 9/4]$  are independent of  $S_{12}$ . An equilateral spin triangle with the antiferromagnetic exchange represents an example in which exchange coupling in the ground state forces spins to be aligned antiparallel in each pair while this condition can not be satisfied. This situation is usually referred to as spin frustration. The analysis of the HDVV Hamiltonian revealed that the degeneracy with respect to the intermediate spin within the spin coupling scheme in the ground manifold  $(S_{12})S = (0)1/2$ ,  $(1)1/2$  is associated with the exact orbital degeneracy in the triangular system, so that the ground term is the orbital doublet  ${}^2E$  of the trigonal point group, while the excited one is the orbital singlet  ${}^4A_2$  [14]. The orbital doublet  ${}^2E$  proves to be the ground term for all symmetric triangular systems which are composed of half-integer spins [14]. One can see that spin-frustration in general is inherently related to the orbital degeneracy and therefore leads to the JT instabilities. At the same time the ground state is split by a spin-orbital interaction that appears as AS exchange term in the spin-Hamiltonian.

The AS exchange is responsible for the magnetic anisotropy of the system [14] (see full discussion in [13, 14, 66–69]). The main results of the study of the AS exchange are the following: (1) a zero-field splitting of two spin doublets  $(S_{12})S = (0)1/2$ ,  $(1)1/2$ . This splitting is the first order effect with respect to the “normal” component of AS exchange (parameter  $D_n$ ) and contains second order corrections arising from the mixing of different spin states through an “in-plane” contribution, parameter  $D_I$ ; (2) a zero field splitting of the  $S = 3/2$  state that is a second order effect arising from the mixing of different spin states through “in-plane” contributions; (3) a magnetic anisotropy resulting in a strong reduction of the magnetic moments in a weak perpendicular field due to a reduction of the Zeeman interaction by the AS exchange; (4) a restoration of the pure spin magnetic moments in a strong field due to the reduction of the AS exchange under strong field conditions; (5) special rules for the crossing/anticrossing Zeeman levels based on the pseudoangular momentum representation, resulting in the special shape of magnetization vs. field; (6) special selection rules in EPR, including specific rules for the line intensities.

Three peculiarities of the energy pattern that are closely related to the magnetic behavior should be noticed: 1) the ground state involving two degenerate  $S = 1/2$  levels shows zero-field splitting into two Kramers doublets separated by the gap  $\Delta = \sqrt{3}D_n$ ; 2) at low fields  $g\beta H \leq \Delta$  the Zeeman energies are doubly degenerate and show a quadratic dependence on the field, like in a van Vleck paramagnet. This behavior is drastically different from that in the isotropic model and from the linear magnetic dependence in parallel field and can be considered as a breaking of the normal AS exchange by the perpendicular field (see [5, 8] and literature cited therein). It is evident that the magnetic moments associated with the ground state are strongly reduced at low fields; 3) the magnetic sublevels arising from  $S = 3/2$  ( $M = -1/2$  and  $M = -3/2$ ) cross the sublevels belonging to  $S = 1/2$  spin levels; no avoided crossing points are observed. At high perpendicular field the levels exhibit again linear magnetic dependence [69].



In the framework of the isotropic model, the magnetization exhibits two sharp non-broadened steps, one at zero field and the second one at the field  $H = 3J/g\beta$  when the level with  $S = 3/2$ ,  $M = -3/2$  crosses the degenerate pair of the levels ( $S_{12} = 0$  and  $S_{12} = 1$ )  $S = 1/2$ ,  $M = -1/2$ , so that the  $S = 3/2$  level becomes favorable against  $S = 1/2$ . As one can see, the normal part of the AS exchange results in the broadening of the low field step in  $\mu(H)$ ; meanwhile, the high field step remains non-broadened. The broadening of the first step is closely related to the magnetic anisotropy of the AS exchange that gives rise to a quadratic Zeeman effect in the low perpendicular field. It can be said that the normal part of AS exchange reduces perpendicular magnetization at low field and allows only second order magnetic splitting and van Vleck paramagnetism. The model that includes AS exchange interaction gives a perfect fit of the field dependence of magnetization in the whole range of fields for all temperatures, including extremely low temperature [69].

### 2.3 Vibronic Interaction in a Spin-Frustrated Triangular System

The symmetry-adapted vibrations  $A_1(Q_{A_1} \equiv Q_1)$  and doubly degenerate  $E$  type ( $Q_{Ex} \equiv Q_x$ ,  $Q_{Ey} \equiv Q_y$ ) of an equilateral triangular unit are shown in Fig. 1 along with the molecular coordinate system. The vibronic interaction arises mainly from the modulation of the isotropic exchange interactions by the molecular displacements and can be expressed as:

$$H_{ev} = \lambda (\hat{V}_1 Q_1 + \hat{V}_x Q_x + \hat{V}_y Q_y), \quad (2)$$

where  $\lambda \equiv \sqrt{6}(\partial J_{ij}(R_{ij})/\partial R_{ij})_0$  is the vibronic coupling parameter associated with the modulation of HDVV exchange, and the expressions for the operators  $\hat{V}_\alpha$  are the following:

$$\begin{aligned} \hat{V}_1 &= \sqrt{\frac{2}{3}}(\mathbf{S}_1\mathbf{S}_2 + \mathbf{S}_2\mathbf{S}_3 + \mathbf{S}_3\mathbf{S}_1), \\ \hat{V}_y &= \frac{1}{\sqrt{6}}(\mathbf{S}_2\mathbf{S}_3 + \mathbf{S}_3\mathbf{S}_1 - \mathbf{S}_1\mathbf{S}_2), \quad \hat{V}_x = \frac{1}{\sqrt{2}}(\mathbf{S}_2\mathbf{S}_3 - \mathbf{S}_3\mathbf{S}_1). \end{aligned} \quad (3)$$

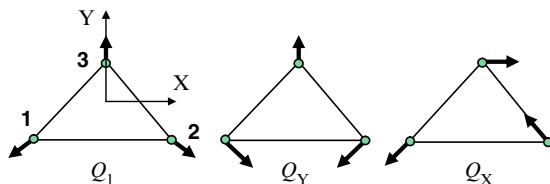


Fig. 1 Full symmetric ( $A_1$ ) and double degenerate ( $E$ ) modes of a triangular unit

Evaluation of the vibronic matrices can be performed with the aid of the irreducible tensor operators (ITO) approach [4, 16]; the results are given in [70].

## 2.4 Ground State and Adiabatic Surfaces

It is reasonable to assume that the gap  $3J$  exceeds considerably the vibronic coupling and AS exchange, and therefore the basis set comprises only four low lying spin  $1/2$  states. Since the system has axial magnetic anisotropy one can assume that the field is applied in a ZX plane ( $H_y = 0$ ). The vibronic interaction leads to a complicated combined JT and pseudo JT problem. The following dimensionless parameters are introduced: vibronic coupling parameter  $\nu = (\lambda/\hbar\omega)(\hbar/M\omega)^{1/2}$ , zero-field splitting of the ground state  $\delta = \sqrt{3}D_n/\hbar\omega \equiv \Delta/\hbar\omega$ , applied field  $\xi = g\beta H/\hbar\omega$  and coordinates  $q_\alpha = (M\omega/\hbar)^{1/2}Q_\alpha$ ,  $H_z = H \cos \theta$ . Finally,  $\rho$  is the radial component in the plane  $q_x q_y$  defined as  $q_x = \rho \cos \varphi$ ,  $q_y = \rho \sin \varphi$ .

The mixing of  $S = 1/2$  and  $S = 3/2$  levels through “in-plane” AS exchange results in a small warping of the low-lying surface that is neglected here. In the case of  $\delta = 0$  and  $\xi = 0$  one faces a two-mode pseudo JT problem ( $Q_1$  mode is excluded), and one obtains simple expressions for a pair of doubly degenerate surfaces that are quite similar to those in the pseudo JT  ${}^2E \otimes e$  problem taking the spin-orbital interaction into account (here the signs “+” and “−” are related to the upper and lower surfaces, respectively):

$$U_{\pm}(\rho)/\hbar\omega = \rho^2/2 \pm \sqrt{\delta^2 + 3\nu^2\rho^2}/2. \quad (4)$$

One can see that in the limit of the isotropic exchange model the surface represents a “Mexican hat”, with a conical intersection at  $\rho = 0$  that corresponds to the basic JT  $E \otimes e$  problem [45–47]:  $U_{\pm}(\rho)/\hbar\omega = \rho^2/2 \pm (\sqrt{3}/2\sqrt{2})|\nu|\rho$ . In general, the shape of the surfaces depends on the interrelation between the AS exchange and vibronic coupling that proved to be competitive. In the case of weak vibronic coupling and/or strong AS exchange  $\nu^2 < 4|\delta|/3$ , the lower surface possesses its only minimum at  $q_x = q_y = 0$  ( $\rho = 0$ ), so that the symmetric (trigonal) configuration of the system proves to be stable. In the opposite case of strong vibronic interaction and/or weak AS exchange,  $\nu^2 > 4|\delta|/3$ , the symmetric configuration of the cluster is unstable, and the minima are arranged at the ring of a trough of radius  $\rho_0 = (1/2)\sqrt{3\nu^2/2 - 8\delta^2/3\nu^2}$ . The radius  $\rho_0$  decreases with the increase of AS exchange and vanishes at  $|\delta| = 3\nu^2/4$ . These two types of pseudo JT surfaces are shown in Fig. 2a, b. The depth of the minima ring in the second type (respectively to the top in the low surface) depends on the interrelation between the JT constant and AS exchange and is found to be  $\varepsilon_0 = (3\nu^2 - 4\delta^2)^2/48\nu^2$ , while the gap between the surfaces in the minima points  $3\nu^2/4$  is independent of the AS exchange.

The nuclear motion in the bottom of the trough for the JT  $E \otimes e$  problem is described in [46, 47]. The metal sites of a distorted triangle move along circles, so that the phases of the ions 2 and 3 are shifted by the angles  $2\pi/3$  and  $4\pi/3$ ,

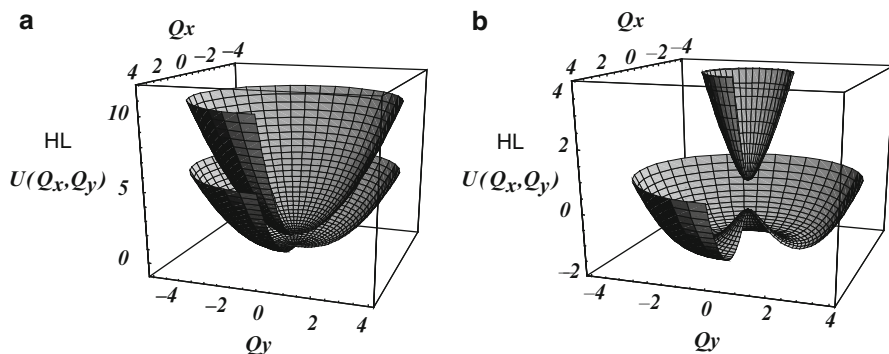
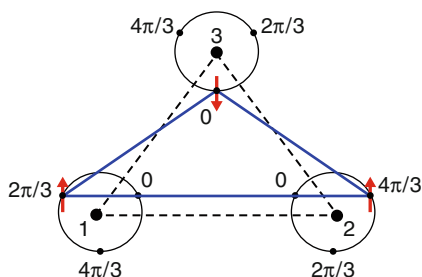


**Fig. 2** Adiabatic potentials for the ground state of a triangular exchange system in the space of the double degenerate vibrations: (a) weak vibronic interaction and/or strong AS exchange ( $\delta = 1.0$ ,  $\nu = 1.0$ ); (b) weak AS exchange and/or strong vibronic interaction ( $\delta = 1.0$ ,  $\nu = 3.0$ )

**Fig. 3** Rotation of the distorted configurations (solid triangle) in the bottom of the trough - illustration for the elimination of spin frustration through the JT instability. Symmetric configuration is shown by the dashed line

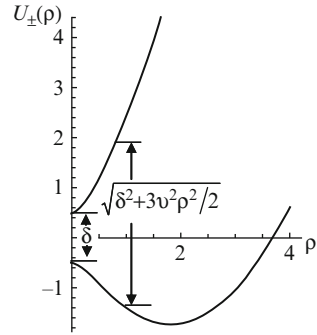


respectively, to the phase of ion 1. Figure 3 shows an instant nuclear configuration in the course of this motion in which the side 12 is elongated, while the sides 13 and 23 are compressed, taking advantage from the new exchange network. In this geometry of the system two antiferromagnetic pathways 13 and 23 are energetically favorable, while the connection 12 is ferromagnetic. One can see that the system possesses a definite spin alignment, so that spin frustration is eliminated by the JT distortion with the instant isosceles configuration corresponding to  $S_{12} = 1$  in the ground state.

## 2.5 Influence of the Jahn–Teller Interaction on the Magnetization

In order to reveal the effects of the JT vibronic interaction [74]–[76] one can employ the adiabatic approximation that was proved to provide a quite good accuracy in the description of the magnetic properties of MV clusters [77] and allowed to avoid numerical solutions of the dynamic problem. According to the adiabatic approach the magnetization can be obtained by averaging the derivatives  $-\partial U_i(\rho, H)/\partial H_\alpha$  over the vibrational coordinates. In the case of an arbitrary  $\rho \neq 0$  the gap between

**Fig. 4** Section of the adiabatic potentials in the case of JT instability, illustration for the zero-field splitting of the ground state in the vibronically distorted configurations



spin  $1/2$  levels is increased, and at  $H = 0$  the zero-field is  $\delta(\rho) = \sqrt{3v^2\rho^2/2 + \delta^2}$ , as illustrated in Fig. 4. The Zeeman sublevels in an arbitrary configuration  $\rho$  in a weak field range up to the second order terms with respect to the field  $\xi$  defined by the angle  $\theta$  can be found as:

$$\begin{aligned}\varepsilon_{1,3}(\rho, \xi)/\hbar\omega &= -\delta(\rho)/2 \pm \kappa_1(\theta) \xi/2 - \kappa_2(\theta) \xi^2, \\ \varepsilon_{2,4}(\rho, \xi)/\hbar\omega &= +\delta(\rho)/2 \pm \kappa_1(\theta) \xi/2 + \kappa_2(\theta) \xi^2,\end{aligned}\quad (5)$$

where  $g_{||} = g_{\perp} = g$  and the first and second order van Vleck coefficients [78]  $\kappa_1(\theta)$  and  $\kappa_2(\theta)$  in the Zeeman energies are the functions of the angle  $\theta$  and the JT coupling parameter. They can be directly related to the JT splitting and AS exchange:

$$\begin{aligned}\kappa_1(\theta) &= \sqrt{(E_{JT}^2 + \delta^2 \cos^2 \theta)/(E_{JT}^2 + \delta^2)}, \\ \kappa_2(\theta) &= \delta^2 \sin^2 \theta / 4(E_{JT}^2 + \delta^2)^{3/2}.\end{aligned}$$

One can see that with the increase of the JT interaction the coefficient  $\kappa_1(\theta)$  becomes independent of the angle  $\theta$  ( $\kappa_1(\theta) \approx 1 - \delta^2 \sin^2 \theta / (2E_{JT}^2)$ ) and tends to unity, while  $\kappa_2(\theta)$  disappears ( $\kappa_2(\theta) = \delta^2 \sin^2 \theta / (4E_{JT}^3)$ ), so that in the limit of strong vibronic coupling we arrive at the isotropic linear Zeeman splitting that is obtained within the HDVV model. The suppression of the magnetic anisotropy [14] is a quite general conclusion that is closely related to the reduction of the physical quantities of the orbital nature by the JT interaction (Ham effect) [45–47]. In the case of a parallel field ( $\mathbf{H}||C_3$ ) one finds  $\kappa_1(0) = 1$  and  $\kappa_2(0) = 0$ , so we have the following Zeeman pattern:

$$\begin{aligned}\varepsilon_{1,3}(\xi)/\hbar\omega &= -\sqrt{E_{JT}^2 + \delta^2}/2 \pm \xi/2, \\ \varepsilon_{2,4}(\xi)/\hbar\omega &= +\sqrt{E_{JT}^2 + \delta^2}/2 \pm \xi/2.\end{aligned}\quad (6)$$

Equation (13) exhibits linear Zeeman splitting in a pair of spin doublets in the parallel field, but the zero-field splitting is now represented by a combined effective gap

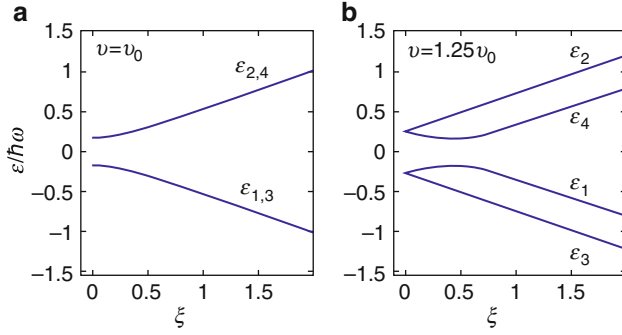


**Fig. 5** Influence of the JT interaction (defined by the vibronic coupling parameter  $\nu$ ) on the Zeeman energy pattern in a perpendicular magnetic field ( $\mathbf{H}||C_3$ )

$\sqrt{E_{JT}^2 + \delta^2}$  instead of the initial one  $|\delta|$  related solely to the AS exchange. This does not affect the magnetic moments of the ground manifold, so that neither the JT interaction nor the AS exchange do manifest themselves in the magnetic characteristics in the case of  $\mathbf{H}||C_3$ .

In the case of a perpendicular field  $\mathbf{H} \perp C_3$  one obtains that  $\kappa_1(\pi/2) = E_{JT}/\sqrt{E_{JT}^2 + \delta^2}$ ,  $\kappa_2(\pi/2) = \delta^2/4(E_{JT}^2 + \delta^2)^{3/2}$ , and therefore the Zeeman energy in this case is given by:

$$\begin{aligned} \varepsilon_{1,3}(\xi)/\hbar\omega &= -\sqrt{E_{JT}^2 + \delta^2}/2 \pm \xi E_{JT}/2\sqrt{E_{JT}^2 + \delta^2} - \xi^2\delta^2/4(E_{JT}^2 + \delta^2)^{3/2}, \\ \varepsilon_{2,4}(\xi)/\hbar\omega &= +\sqrt{E_{JT}^2 + \delta^2}/2 \pm \xi E_{JT}/2\sqrt{E_{JT}^2 + \delta^2} + \xi^2\delta^2/4(E_{JT}^2 + \delta^2)^{3/2}, \end{aligned} \quad (7)$$

where the eigenvalues are denoted as  $\varepsilon_i(\xi) \equiv \varepsilon_i(\rho'_0, \xi)$ . Equation (7) shows that the Zeeman pattern contains both linear and quadratic contributions. The role of the JT coupling can be understood by comparing the Zeeman picture so far obtained with that provided by  $\nu = 0$ . In the absence of the JT coupling the linear Zeeman terms disappear, and the Zeeman energies contain only quadratic terms. Thus Fig. 5a illustrates two degenerate pairs of Zeeman levels in a perpendicular field in the symmetric nuclear configuration. In a weak-field range they are given by:

$$\begin{aligned} \varepsilon_1(\xi)/\hbar\omega = \varepsilon_3(\xi)/\hbar\omega &= -|\delta|/2 - \xi^2/4|\delta|, \\ \varepsilon_2(\xi)/\hbar\omega = \varepsilon_4(\xi)/\hbar\omega &= +|\delta|/2 + \xi^2/4|\delta|. \end{aligned} \quad (8)$$

This can be referred to as the effect of the reduction of the magnetization in a low magnetic field that is perpendicular to the axis of AS exchange. A reduction of the Zeeman energy by the AS exchange gives rise to a small van Vleck-type contribution to the magnetic susceptibility at low field  $g\beta H \ll D_n$ . An essential effect is that the JT interaction leads to the occurrence of linear terms for the Zeeman energies at low field. This is shown in Fig. 5b that illustrate the transformation of the Zeeman levels

under the influence of vibronic coupling. As a result, the JT coupling essentially increases the magnetic moments of the system at low perpendicular fields when magnetization in the symmetric configuration is reduced by the AS exchange. The range of the linear Zeeman splitting increases with the increase of the JT coupling, and the crossing point moves into the high field region. This can be considered as the effect of the reduction of the AS exchange by the JT distortions accompanied by the restoration of the magnetic moments.

Figure 6 illustrates the influence of the JTE on the field dependence of the magnetization. The magnetization vs. perpendicular field at  $T = 0$  is presented as a function of the vibronic coupling parameter  $\nu$  that is assumed to satisfy the condition of instability  $\nu^2 > \nu_0^2 \equiv 4|\delta|/3$ . One can see that provided that  $\nu = \nu_0$  (and of course  $\nu < \nu_0$ , which corresponds to a symmetric stable configuration) the magnetization slowly increases with the increase of the field (due to reduction of the Zeeman interaction in the low field), then reaches saturation when the magnetic field is strong enough to break the AS exchange. Increase of the JT coupling leads to the fast increase of the magnetic moments in the region of low field and formation of the step in magnetization caused by the reduction of the magnetic anisotropy (appearance of the linear terms in the Zeeman levels). The height of the step  $M(H = 0) = g\beta E_{JT}/2\sqrt{E_{JT}^2 + \delta^2}$  increases with the increase of the vibronic coupling. Finally, when the JT coupling is strong enough one can observe staircase like behavior of magnetization, with a sharp step in which  $M(H)$  jumps from zero to  $M(H = 0) = g\beta/2$  at zero field (and  $T = 0$ ) that is expected for a magnetically isotropic system.

### 3 Vibronic Interaction in Mixed-Valence Clusters

#### 3.1 Overview of the Vibronic Models of Mixed Valency

Mixed-valence (MV) clusters contain ions in different oxidation states. The delocalization of the extra electron gives rise to the so-called *double exchange* that couples the localized magnetic moments through an itinerant electron that can travel between the magnetic centers. Since the itinerant electron keeps the orientation of its spin in course of transfer, double exchange results in a strong spin polarization effect, which favors a ferromagnetic spin alignment in the system. This mechanism of electron-spin interaction was suggested [79–81] to explain the ferromagnetism observed in the mixed-valence (MV) manganites of perovskite structure, such as  $(\text{La}_x\text{Ca}_{1-x})(\text{Mn}^{\text{III}}\text{Mn}^{\text{IV}}_{1-x})\text{O}_3$ . MV oxides are a focus of solid state chemistry, as they exhibit colossal magnetoresistance, a property that has been attributed to double exchange.

Along with the electronic interactions (double exchange, HDVV exchange, etc.) the coupling of electronic and vibrational motions (*vibronic coupling*) plays a crucial role in MV systems. One of the main characteristics of MV compounds is the

presence of the intense (in most cases, featureless) intervalence absorption bands in the near-infrared or visible regions, which result from the transitions within a ground vibronic manifold of the MV system. Earlier simplified vibronic models of MV systems [82,83] were aimed to provide an explanation of the main aspects of the intervalence absorption bands (energy and width), and they were quite successful in explaining the features of MV dimers in which the ions are very weakly coupled electronically. Although in such compounds there is some delocalization, different distinct oxidation states are still identifiable on the two centers. Robin and Day [82] term these class II MV compounds.

Piepho, Krausz and Schatz (PKS) formulated a vibronic model [84] that includes pseudo JT coupling to the vibrations localized on the constituent metal centers and proposed a classification of MV compounds according to the degree of localization (classes I, II and III) [82, 84]. This PKS model has been used to analyze MV dimeric [85–87], trinuclear [88–90, 92], tetranuclear [93, 94] and higher nuclearity [95–98] MV compounds. Later on, Piepho [99] demonstrated that, along with the PKS modes, the multi-center vibrations are also important participants in the vibronic coupling. Within the model including both these types of vibronic modes (we will refer to this model as the Piepho model) it was possible to describe in more detail the features of intervalence absorption bands for MV dimers. In the subsequent studies [100–103] the model was extended to the analysis of many-electron MV clusters of higher nuclearity.

### 3.2 Double Exchange in Mixed-Valence Clusters

Let us consider a MV dimer  $d^{n+1} - d^n$  in which for the sake of definiteness we assume that  $n \leq 4$  (less than half-filled d-shells). The main features of the phenomenon can be understood in the framework of the classical spin model [77]. As distinguished from a quantum spin, a classical spin represents the infinite spin limit for which all the directions in the space are allowed. From the classical point of view, for Hund's configuration of the  $d^{n+1}$  ion the extra electron lines up its spin,  $s_e$ , parallel to the spin  $s_0$  of the  $d^n$  ion (spin core). In the classical limit,  $s_0 \gg 1/2$ , so that  $S_{\max} \approx 2s_0$  and  $S_{\min} \approx 0$ . These two extremes correspond to parallel and antiparallel orientations of the core's spins (Fig. 6), while the intermediate spin values are to be correlated with the intermediate angles between the core's spins. One can see that the transfer is most efficient when both core's spins are parallel ( $\theta = 0$ ). The corresponding maximum value of the transfer integral will be denoted by  $t$ . On the other hand, the transfer is suppressed when the core's spins are antiparallel ( $\theta = \pi$ ). Considering the spins of the metal ions ( $s_1$  and  $s_2$ ) as classical vectors, one can express the total spin as  $S = s_1 + s_2$ , where  $s_1 = s_2 = s_0$ . Now one can express  $t$  in terms of  $s_0$  and  $S$  as  $t(S) = t S / (2s_0)$ . This expression confirms that the rate of transfer is spin-dependent and increases with the increase of the total spin  $S$ . Thus, for parallel  $s_1$  and  $s_2$  we have  $S = S_{\max} = 2s_0$ , and the rate of transfer achieves its maximum value  $t$ ; meanwhile, in the antiparallel case ( $S = S_{\min} = 0$ ) the transfer rate

**Fig. 6** Influence of the JT interaction on dependence magnetization vs. perpendicular field ( $\mathbf{H}||C_3$ )

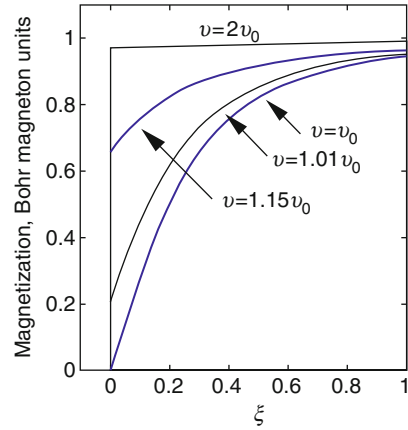
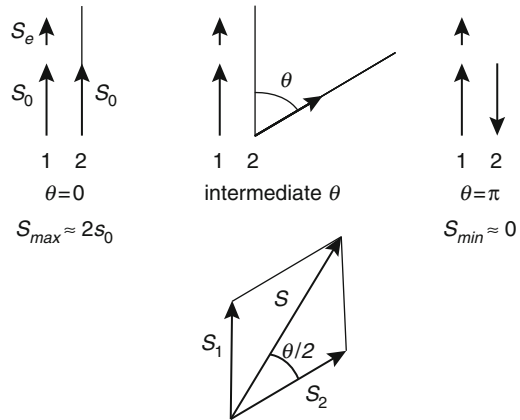


**Fig. 7** Spin dependence of the double exchange in a classical spin model



vanishes. One can see that the energy levels of a MV dimer form a continuous band of width  $2t$ , in which each sublevel corresponds to a definite angle between classical spins  $s_1$  and  $s_2$ , and the double exchange gives rise to a strong ferromagnetic effect. The quantum-mechanical expression for  $E_{\pm}(S)$  can be obtained from the classical one with the aid of substitutions  $S \rightarrow S + 1/2$ ,  $s_0 \rightarrow s_0 + 1/2$  [77]:

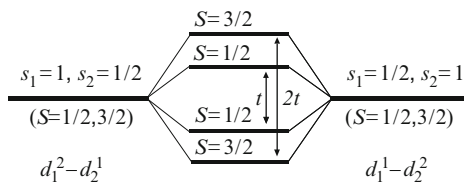
$$E_{\pm}(S) = \pm tS = \pm t(S + 1/2)/(2s_0 + 1),$$

This result proves to be valid for all MV  $d^{n+1} - d^n$  pairs with  $n \leq 4$ , provided that the spin core is defined as an ion without extra electron. It is also valid for  $n > 4$  but in such case the spin core must be defined as an ion without extra hole. The ferromagnetic effect of the double exchange is illustrated by Fig. 7. Along with the double exchange, the isotropic exchange interaction plays an important role in MV clusters. This interaction is described by the HDVV spin Hamiltonian:

$$H_{ex} = -2J s_1 s_2 \quad (9)$$



**Fig. 8** Effect of the double exchange on the energy pattern of mixed valence  $d^2 - d^1$  dimer



that is operative within each configuration, so that one can find the energies:

$$E_{\pm}(S) = -J S(S+1) \pm t(S+1/2)/(2s_0+1). \quad (10)$$

Providing  $J > 0$  both interactions produce a ferromagnetic effect, and a ground state of an MV dimer will always possess a maximal  $S$  value. In the presence of an antiferromagnetic exchange the ground spin state will be the result of the competition between the exchange and double exchange interactions, as illustrated by Fig. 9 for the  $d^4 - d^3$  dimer. When double exchange is weak enough, the HDVV exchange dominates, and the  $S = 1/2$  state is the ground one. When the ratio  $t/|J|$  increases, the ground state becomes successively  $S = 3/2$ ,  $5/2$  and, finally,  $7/2$  in the strong double exchange limit. Consequently, the magnetic properties are the result of the interplay of the HDVV exchange and double exchange.

### 3.3 Piepho-Krausz-Schatz Model and Robin and Day Classification of Mixed-Valence Compounds

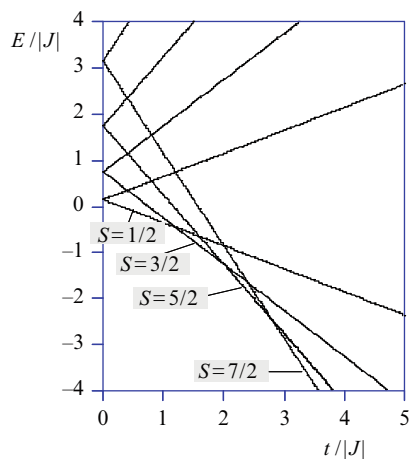
Let us denote the coordinates of the *full-symmetric* displacements of ligand surroundings as  $Q_1$  and  $Q_2$  (*breathing* modes); then two new collective coordinates can be constructed, which refer to the *in-phase* ( $Q_+$ ) and *out-of-phase* ( $Q_-$ ) vibrations of the two moieties 1 and 2:

$$Q_+ = (1/\sqrt{2}) (Q_1 + Q_2), \quad Q_- = (1/\sqrt{2}) (Q_1 - Q_2). \quad (11)$$

Nuclear displacements corresponding to the  $Q_+$  vibration (both coordination spheres are expanded or compressed simultaneously) decrease or increase the potential energy of the system independently of the site of localization. Interaction of the moving electron with the in-phase vibration can be eliminated. On the contrary, the out-of-phase vibration,  $Q_-$ , is relevant to the electron transfer. When  $Q_- < 0$  the coordination sphere of moiety “1” is compressed, while that of “2” is expanded. This nuclear movement increases the energy of the electron located on 1, promoting thus the electron transfer  $1 \rightarrow 2$ . In the opposite phase ( $Q_- > 0$ ) the extra electron jumps back. The adiabatic potential comprises two branches  $U_+$  and  $U_-$  (Fig. 10):

$$U_{\pm}(q) = (\omega/2) q^2 \pm \sqrt{t^2 + v^2 q^2}. \quad (12)$$

**Fig. 9** Correlation diagram for a  $d^4 - d^3$  dimer showing the combined effect of double exchange and antiferromagnetic HDVV exchange interactions



where  $\nu$  is the PKS vibronic coupling parameter,  $\hbar = 1$ ,  $\omega$  is the vibrational frequency for the out-of-phase mode, and  $q = Q_- / \sqrt{\hbar / (M_{\text{PKS}} \omega^2)}$  is the corresponding dimensionless normal coordinate ( $M_{\text{PKS}}$  is the effective mass). In absence of electronic interaction between the sites ( $t = 0$ ), one obtains two independent potentials associated with the  $1^* 2$  and  $1 2^*$  configurations (Fig. 10a). In this case the system is fully localized (Class I in Robin and Day classification). When the vibronic interaction is strong compared with transfer ( $\nu^2/\omega > |t|$ ), we obtain a double well potential curve  $U_-(q)$  (Fig. 10b) so that the transfer requires activation energy (Class II). Finally, in the case of weak vibronic interaction ( $\nu^2/\omega < |t|$ ) both branches have a minimum at  $q = 0$  (Fig. 10c), and the electron is fully delocalized (Class III).

The main spectroscopic consequence of the combined action of electron transfer and vibronic interaction is the occurrence of the so-called electron transfer optical absorption (intervalence band), which is shown by the arrows in Fig. 10. The shape and intensity of the intervalence band in the PKS model is defined by the ratio  $|t|/(\nu^2/\omega)$ . In the case of weak transfer the Franck-Condon transitions are almost forbidden, and at the same time, the Stokes shift can be significant. Therefore the MV dimers of Class I are expected to exhibit weak and wide intervalence bands. On the contrary, in the Class III compounds the Franck-Condon transition is allowed, and the Stokes shift is zero. For this reason, intervalence optical bands in delocalized MV dimers are strong and narrow. When the extra electron jumps over the spin cores in a multielectron MV dimer  $d^n - d^{n+1}$  ( $n \geq 1$ ) [85–87] we are dealing with independent vibronic problems for each total spin value, so the two branches of the adiabatic potential corresponding to the total spin  $S$  are given by:

$$U_{\pm}^S(q) = (\omega/2) q^2 \pm \sqrt{t_S^2 + \nu^2 q^2}, \quad (13)$$

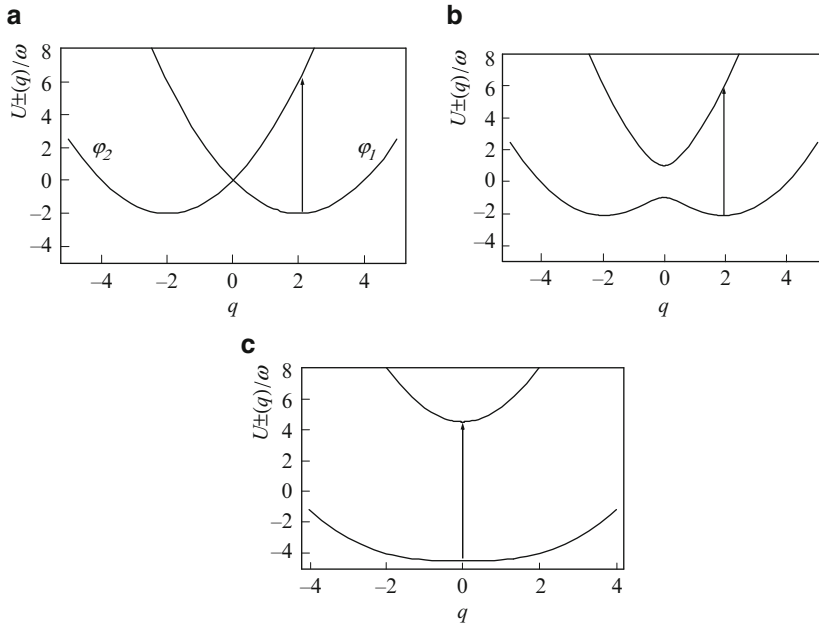


**Fig. 10** The adiabatic potential calculated for MV  $d^1 - d^0$  dimer in PKS-model: (a)  $t = 0$ ,  $v = 2\omega$ , (b)  $t = \omega$ ,  $v = 2\omega$ , (c)  $t = 4.5\omega$ ,  $v = 2\omega$ . Franck-Condon transitions are indicated by the arrows

where  $t_S$  is the effective (many-electron) spin-dependent double exchange parameter. Since  $t_S$  increases with the increase of  $S$ , the condition for localization will be more favorable for the states with smaller spin values, whereas delocalization will be favored for the larger  $S$ . Figure 11 illustrates the effect of the vibronic interaction on the magnetic properties of a MV dimer  $d^2 - d^1$  in the case when the HDVV exchange can be neglected. The vibronic interaction gives an antiferromagnetic contribution to the adiabatic energy pattern, because the states with  $S = 1/2$  undergo stronger vibronic stabilization than those with  $S = 3/2$ . In the limit of strong vibronic coupling the electron proves to be fully trapped in one of the two wells, and the  $S = 1/2$  and  $S = 3/2$  energies coincide, giving thus a paramagnetic mixture of the initial  $s_1 = 1/2$ ,  $s_2 = 1$  and  $s_1 = 1$ ,  $s_2 = 1/2$  states. Therefore, in this limit the ferromagnetic effect of the double exchange is suppressed in the ground manifold, whereas the excited states are very high in energy and cannot be populated at reasonable temperatures. For this reason, the system will exhibit the magnetic behavior specific for the valence-localized  $d^2 - d^1$  system. The HDVV exchange is the only interaction effectively operating in the strong vibronic coupling limit. In this case the HDVV scheme of levels proves to be restored in the minima of the lower sheets of the adiabatic potential. The semiclassical approximation (that allows to avoid diagonalization of the vibronic matrix [84–87]) was shown to describe the temperature-dependence of the magnetic moment with very high

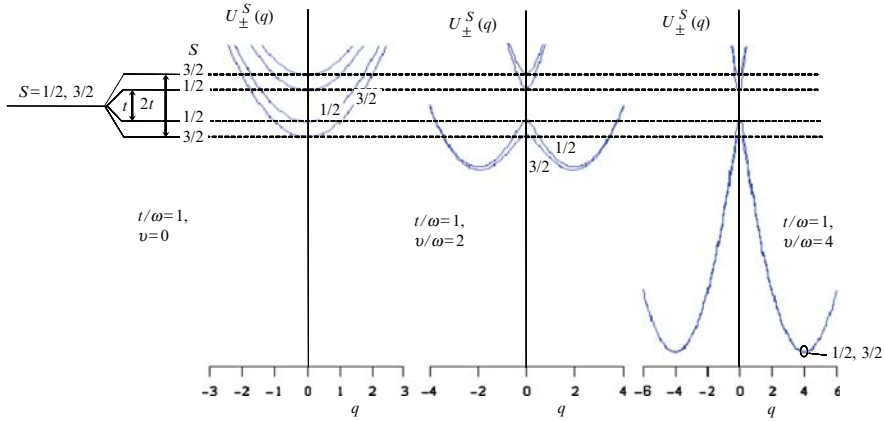


**Fig. 11** Vibronic reduction of the double exchange splitting for the  $d^2 - d^1$  dimer

accuracy [77]. Figure 12 shows the effect of suppression of the double exchange by the PKS vibronic coupling for a MV  $d^4 - d^3$  dimer. For a relatively weak coupling ( $\nu = 2\omega$  and  $2.6\omega$ ) the system is ferromagnetic, since double exchange dominates over HDVV exchange and vibronic coupling; meanwhile, for  $\nu = 3\omega$  the system is antiferromagnetic, because the double exchange is strongly reduced. This example shows that the reduction of the double exchange due to the pseudo JT coupling cannot be simply represented as an effective decrease of the transfer parameter. In terms of the correlation diagram (Fig. 9) one can imagine that, passing from the right side (strong double exchange) to the left side (weak double exchange), the domain of  $S_{gr} = 5/2$  and  $3/2$  is missed.

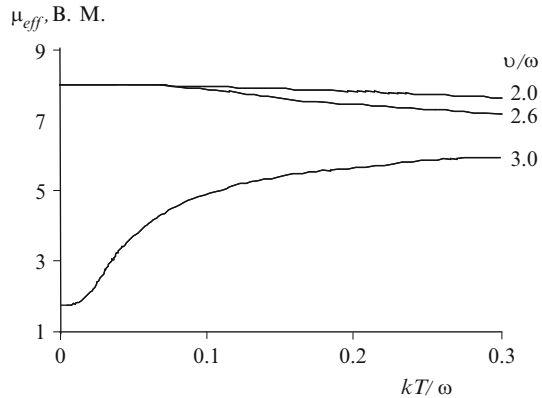
### 3.4 Effect of Multicenter Vibrations

The vibronic coupling of this type appears as a result of modulation of the transfer integral by the changes in the intermetallic distances  $R \equiv R_{12}$ . The value  $Q = R - R_0$  ( $R_0$  is the equilibrium intermetallic distance) plays the role of a vibrational coordinate. The transfer integral can be expanded in the series:  $t(R) = t(R_0) - \lambda(R - R_0) + \dots$ , where  $\lambda = -(\partial t / \partial R)_{R=R_0}$  is the vibronic interaction parameter, and  $t(R_0)$  is the transfer parameter. The adiabatic potential (Fig. 13) has two branches, corresponding to two delocalized states  $\psi_+$  and  $\psi_-$ :

$$U_{\pm} = (\Omega/2) (Q \mp Q_0)^2 \pm t - \lambda^2/(2\Omega), \quad (14)$$

where  $Q_0 = \lambda/\Omega$ ,  $\Omega$  is the vibrational frequency, and  $Q = (R - R_0)/\sqrt{\hbar/(M_P\Omega^2)}$  ( $M_P$  is the effective mass). Both states are stabilized by the value  $-\lambda^2/(2\Omega)$ , and the branches  $U_{\pm}$  possess minima at  $\pm Q_0$ . In the bonding state,

**Fig. 12** Effect of the PKS vibronic coupling on the effective magnetic moment of  $d^4 - d^3$  MV dimer:  $t/\omega = 3.5$ ,  $J/\omega = -0.2$



$\psi_-$ , the transfer is effectively increased ( $t(-Q_0) = t + \lambda^2/\Omega$ ); meanwhile, in the antibonding state,  $\psi_+$ , the transfer is decreased ( $|t(+Q_0)| = t - \lambda^2/\Omega$ ). One can see that the  $P$ -vibration produces a strong detrapping effect, *i.e.* stabilizes delocalized states.

### 3.5 Robin and Day Classification in Generalized Vibronic Model: Localization-Delocalization, Hyperfine Constants

The adiabatic surface of a MV dimer has two sheets in the  $q$   $Q$ -space [100, 101]:

$$U_{\pm}^S(q, Q) = -J S(S+1) + (1/2) (\omega q^2 + \Omega Q^2) \pm \sqrt{(t_S - \lambda_S Q)^2 + v^2 q^2}. \quad (15)$$

For the sake of simplicity we assume that  $t$ ,  $v$  and  $\lambda$  are positive. Depending on the relative values of the key parameters, several qualitatively different cases should be distinguished.

*Case 1.* PKS-coupling exceeds P-coupling, that is  $v^2/\omega > \lambda_S^2/\Omega$ . Within case 1 there are two different situations: comparatively weak transfer (*Case 1a*), defined by the inequality  $t_S < v^2/\omega - \lambda_S^2/\Omega$ , and comparatively strong transfer (*Case 1b*), for which  $t_S \geq v^2/\omega - \lambda_S^2/\Omega$ .

*Case 2.* P-coupling exceeds the PKS-coupling ( $v^2/\omega \leq \lambda_S^2/\Omega$ ). Two different situations should be considered: comparatively weak transfer (*Case 2a*), defined by  $t_S < \lambda_S^2/\Omega - v^2/\omega$ , and the case of comparatively strong transfer (*Case 2b*), for which  $t_S \geq \lambda_S^2/\Omega - v^2/\omega$ .

In *Case 1a*, the lower sheet,  $U_-^S(q, Q)$ , possesses two equivalent minima (Fig. 14a, b) at the points  $\{\pm q_0(S), Q_0(S)\}$ , where  $q_0(S) = (v/\omega)\sqrt{1 - \gamma_S^2}$ ,  $Q_0(S) = -(\lambda_S/\Omega)\gamma_S$ , and  $\gamma_S = t_S/(v^2/\omega - \lambda_S^2/\Omega)$ . These two minima are separated by one or two saddles located at the points  $\{0, Q_-(S)\}$  (lower saddle)

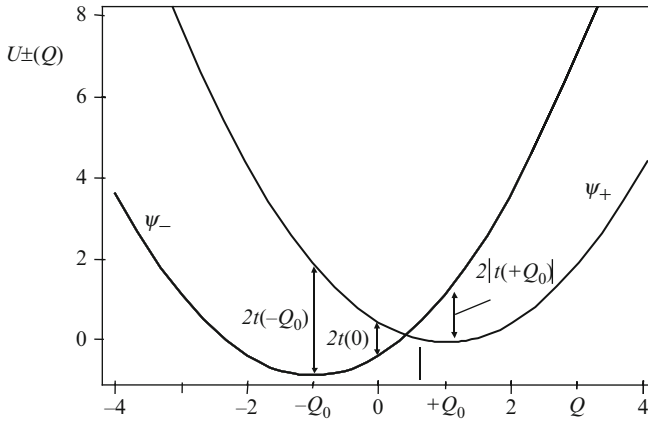


**Fig. 13** Adiabatic potential of the  $d^1 - d^0$  system as a function of the coordinate of P-vibration calculated with  $t/\Omega = 0.4$  and  $\lambda/\Omega = 1$

and  $\{0, Q_+(S)\}$  (upper saddle), with  $Q_{(+)}^-(S) = \bar{c}_{(+)}\lambda_S/\Omega$ . Under the condition  $t_S > \lambda_S^2/\Omega$  the upper saddle point disappears. One obtains the following expressions for the electronic densities on the sites 1 and 2 in the minima points of  $U_-^S(q, Q)$ :

$$\begin{aligned} \rho_1 [-q_0(S), Q_0(S)] &= \rho_2 [+q_0(S), Q_0(S)] = \rho_S, \\ \rho_1 [+q_0(S), Q_0(S)] &= \rho_2 [-q_0(S), Q_0(S)] = 1 - \rho_S, \end{aligned} \quad (16)$$

where  $\rho_S = (1/2)(1 + \sqrt{1 - \gamma_S^2})$ . Providing  $\gamma_S = 0$ , the system is fully localized ( $\rho_S = 1$ ). With the increase of  $\gamma_S$ , the two minima  $\{\pm q_0, Q_0\}$  move toward the deeper saddle point  $\{0, Q_-(S)\}$ , and the system in these minima becomes more and more delocalized. The discussed localized minima can be detected experimentally from the analysis of the hyperfine structure of Mössbauer, EPR, ENDOR and NMR spectra of MV clusters, which provide direct information about the degree of localization of the moving electron [102, 105–108]. This analysis is performed with the aid of the following expressions for the effective “vibronic” hyperfine constants related to the minima [102]:

$$\begin{aligned} A_S [-q_0(S), Q_0(S)] &= B_S [q_0(S), Q_0(S)] = \frac{1}{2} [\rho_S(a^* - a) + a] \\ &\quad \pm \frac{s_0 + 3/4}{2S(S+1)} [\rho_S(a^* + a) - a], \\ A_S [q_0(S), Q_0(S)] &= B_S [-q_0(S), Q_0(S)] = \frac{1}{2} [\rho_S(a - a^*) + a^*] \\ &\quad \mp \frac{s_0 + 3/4}{2S(S+1)} [\rho_S(a + a^*) - a^*]. \end{aligned} \quad (17)$$

Here, the effective hyperfine constants  $A_S$  and  $B_S$  describe the interaction of the total spin  $\hat{S}$  of the dimer with the nuclear spins  $\hat{I}_1$  and  $\hat{I}$ , respectively.  $a^*$  and  $a$  are

the hyperfine constants for  $d^{n+1}$  and  $d^n$  ions; the upper (lower) sign relates to the case  $n \leq 4$  ( $n > 4$ ).

At the limit  $\gamma_S = 1$  the two minima are merged, and instead of a deeper saddle point the surface  $U_-^S(q, Q)$  possesses a single delocalized minimum in the  $\{0, Q_-(S)\}$  position ( $\rho_S = 1/2$ ), Fig. 13c. Further increase of  $\gamma_S$  leads to the stabilization of the minimum located at the point  $\{0, Q_-(S)\}$ . In *Case 1b* the system is fully delocalized, irrespectively of the relative values of the transfer integral and the vibronic parameters, and the hyperfine constants are averaged:

$$A_S[0, Q_-(S)] = B_S[0, Q_-(S)] = \frac{1}{4} (a^* + a) \pm \frac{s_0 + 3/4}{4 S (S + 1)} (a^* - a). \quad (18)$$

Providing weak transfer (*Case 2a*), the adiabatic surface  $U_-^S(q, Q)$  possesses two minima with different energies shown in Fig. 13d. These minima are located in the same positions  $\{0, Q_-(S)\}$  and  $\{0, Q_+(S)\}$  in which the saddle points are located in the *Case 1a*. At the same time now  $\{\pm q_0(S), Q_0(S)\}$  are the coordinates of two energetically equivalent saddles. The adiabatic wave-functions in the minima points are  $\psi_+(S)$  (deep minimum) and  $\psi_-(S)$  (shallow minimum) so that in the *Case 2a* the system proves to be fully delocalized. The localized states correspond to the saddle points, and hence they are unstable. Increase of  $t$  leads to the transformation of the adiabatic surface in such a way that the saddle points move toward the shallow minimum  $\{0, Q_+(S)\}$ , until it disappears when the transfer is strong enough (*Case 2b*). Independently of the key parameters defining the position of the minima and that of the saddle points (as well as the heights of the barriers), the system remains fully delocalized in the *Case 2*, and the hyperfine interaction is described by the averaged hyperfine constants.

The results obtained shows that only one kind of minima can exist in each particular case: these can be either the minima in which the system is partially or fully localized (delocalized states are unstable) or the minima in which the system is delocalized (localized states are unstable). The coexistence of the localized and delocalized minima proves to be impossible. This is similar to the well-known situation in the classical Jahn–Teller  $T_2 \otimes (e + t_2)$  problem, for which either tetragonal or trigonal minima can exist but never both of them simultaneously [46, 47].

Let us discuss the Robin and Day classification scheme from the point of view of the generalized vibronic model. In the case of strong PKS - coupling (*Case 1*), depending on the magnitude of the electron transfer parameter, MV compounds can belong to Classes I, II or III. So, when  $t_S \ll v^2/\omega - \lambda_S^2/\Omega$  the system is strongly localized and belongs to Class I. Providing  $t_S < v^2/\omega - \lambda_S^2/\Omega$  the system can be assigned to Class II. Finally, for  $t_S \geq v^2/\omega - \lambda_S^2/\Omega$  we arrive at the fully delocalized system (Class III). These conditions are formally similar to those used in the PKS-model for the classification of the MV compounds. However, there is an essential difference between these two kinds of criteria: in the Piepho model, instead of pure PKS vibronic contribution  $v^2/\omega$ , we are dealing with the combined parameter  $v^2/\omega - \lambda_S^2/\Omega$ . This leads to the suppression of the vibronic trapping effect. In fact, the tunneling of the system between the two minima is expected to

occur through the saddle point (that is shifted along  $Q$ ) rather than along the  $q$ -axis, where the barrier is higher. As a result the MV system can belong to Classes II or III, even providing weak electron transfer (or strong PKS- coupling). On the other hand, strong localization (Class I) is achieved only for weak transfer and/or weak P-coupling.

If  $P$ -coupling dominates (*Case 2*) the system is fully delocalized independently of the relative values of  $t$  and  $v^2/\omega$ . This means that in the *Case 2* the system always belongs to Class III, even providing small  $t$ . This result is in striking contradiction with the prediction of the PKS model in which the degree of the delocalization in the symmetric MV dimers is determined only by the interplay between the electron transfer and the PKS - vibronic coupling. Figure 15 illustrates two vertical sections of the adiabatic potential shown for the *Case 2a*. One can see that within the PKS model the system could be assigned to Classes I or II, because  $U_-^S(q, Q_0)$  possesses two minima. However, as a matter of fact, these minima prove to be the saddle points in the two-dimensional  $Q$ - $q$  space, and the minima correspond to the fully delocalized states (Class III).

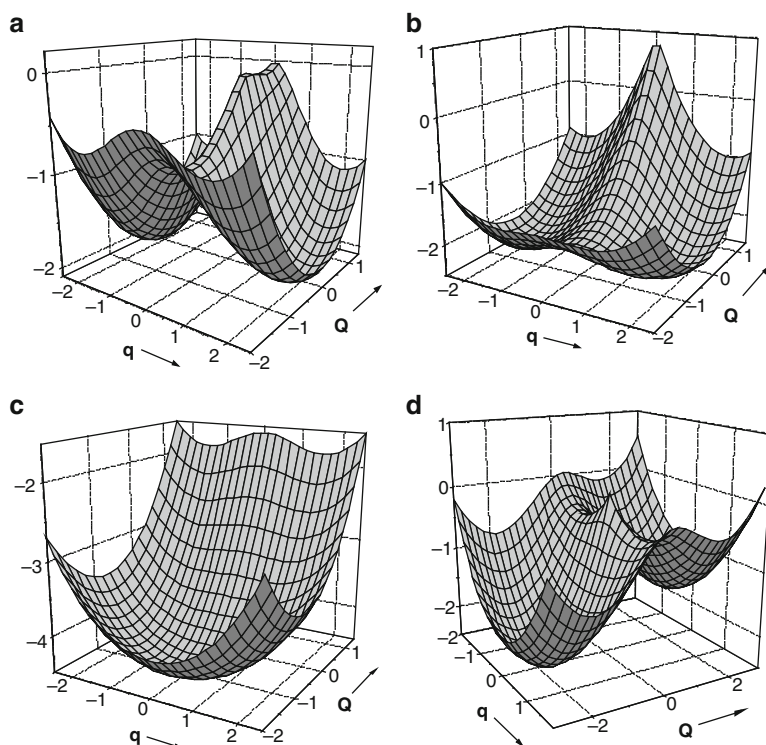


**Fig. 14** The lower sheet  $U_-^S(q, Q)$  of the adiabatic potential for MV dimer ( $\omega = \Omega$ ): (a)  $t_S = 0.4$ ,  $v = 2\omega$ ,  $\lambda_S = \omega$ ; (b)  $t_S = 1.5\omega$ ,  $v = 2\omega$ ,  $\lambda_S = \omega$ ; (c)  $t_S = 4\omega$ ,  $v = 2\omega$ ; (d)  $t_S = 0.4\omega$ ,  $v = \omega$ ,  $\lambda_S = 2\omega$



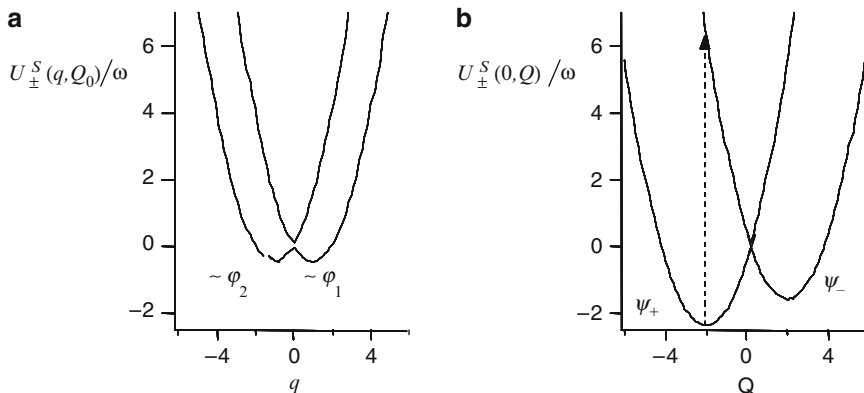


**Fig. 15** Sections of the surfaces  $U_{\pm}^S(q, Q)$  calculated with  $t_S = 0.4\omega$ ,  $v = \omega$ ,  $\lambda_S = 2\omega$ ,  $\Omega = \omega$ , (Case 2a): (a)  $U_{\pm}^S(q, Q_0)$ -section, (b)  $U_{\pm}^S(0, Q)$ -section (arrow-Frank-Condon transition)

In view of these results, the correlation between the degree of localization and the parameters of the intervalence bands (width, position and intensity) established in the PKS model is to be reconsidered. Particularly, in the contrast to the conclusion based on the PKS model, a fully delocalized system (Class III) can now exhibit a strong and broad (instead of narrow) intervalence band, if the P-coupling is dominant. In fact, the Frank-Condon transition in the Case 2a is intense (allowed  $\psi_+ \rightarrow \psi_-$  transition), and a large Stokes shift,  $2Q_0$  gives rise to a broad band. In the description of the magnetic properties of MV clusters one can use the semiclassical approximation that assures a very good accuracy [86]. Figure 16 illustrates the combined effect of two types of vibrations in the case when the PKS - coupling is strong as compared to the double exchange. At the same time the double exchange is much stronger than the Heisenberg exchange ( $t = 10 |J|$ ). In this case in the absence of the P-coupling ( $\lambda = 0$ ) the double exchange is strongly reduced by the PKS-interaction, and hence even weak antiferromagnetic exchange proves to be able to stabilize the state with  $S = 1/2$ . When  $\lambda \neq 0$  the P-coupling competes with the PKS-coupling and for  $\lambda/v \geq 1$  the ferromagnetic  $S = 3/2$  state becomes the ground one. One can see that the case of strong P-coupling in the generalized vibronic model is equivalent to the case of strong double exchange (or/and weak PKS - interaction) in the PKS model. This conclusion is also in agreement with the fact that a delocalization of the extra electron produces a ferromagnetic effect, and in this sense, double exchange and vibronic P - coupling act similarly.

### 3.6 Vibronic Effects in Mixed-Valence Dimers Containing Orbitally Degenerate Ions

The extension of the theory of the double exchange to systems containing orbitally degenerate metal ions with unquenched orbital angular momenta is given in [109–111]. As an example we will consider the corner-shared bioctahedral dimer

**Fig. 16** Combined effect of the two types of vibrations on the effective magnetic moment of  $d^2 - d^1$  MV dimer:  $t/\omega = 1$ ,  $J/\omega = -0.1$ ,  $v/\omega = 2$ ,  $\Omega = \omega$

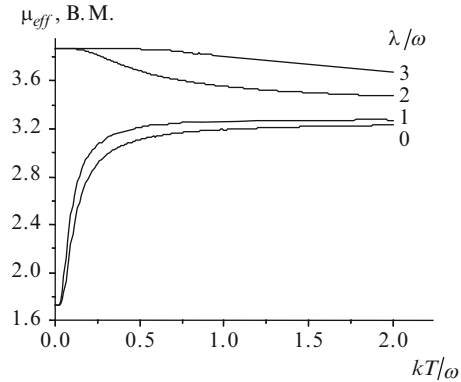
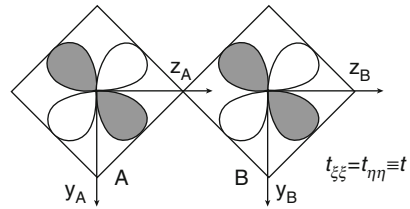


**Fig. 17** Illustration for the transfer pathways in a MV dimer involving orbitally degenerate ions



${}^3T_1(t_2^2) - {}^4A_2(t_2^3)$  (overall  $D_{4h}$ -symmetry). In this case all transfer integrals except  $t_{\xi\xi} = t_{\eta\eta} \equiv t$  (Fig. 17) vanish. The total spin of the dimer takes on the values  $S = 1/2, 3/2, 5/2$ . Besides that the  ${}^3T_1(t_2^2)$ -ion (orbital triplet state) possesses an unquenched orbital angular momentum  $l = 1$ ; meanwhile, for the  ${}^4A_2(t_2^3)$ -ion  $l_* = 0$ , so the total orbital angular momentum of the dimer is  $L = 1$ . It is important that the orbitally-dependent double exchange produces a strong magnetic anisotropy of the system [110]. The energy pattern is shown in Fig. 18, in which the corresponding wave-functions

$$|\pm, SM_S, LM_L\rangle = \left( \frac{1}{\sqrt{2}} \right) (|[s_*l_*]_1 [s]_2 SM_S LM_L\rangle \pm |[s]_1 [s_*l_*]_2 SM_S LM_L\rangle) \quad (19)$$

are also displayed in order to explicitly indicate the orbital contribution. The central level with  $E = 0$  involves all  $S$  values and corresponds to  $M_L = 0$ , while all the states with the energies  $\pm(1/3)t(S + 1/2)$  possess  $M_L = \pm 1$ . All energy levels depend on  $|M_L|$  (axial magnetic symmetry).

Let us analyze the principal components of the magnetic susceptibility tensor ( $\chi_{||}$  and  $\chi_{\perp}$ ). The spin part of the magnetic susceptibility is isotropic, so the anisotropy arises from the orbital part  $\Delta\chi = \chi_{||}^{\text{orb}} - \chi_{\perp}^{\text{orb}}$ . At low temperatures  $\chi_{||}^{\text{orb}}$  is evidently large because it appears as a first-order Zeeman splitting of the ground state with  $M_L = \pm 1$ . On the contrary  $\chi_{\perp}^{\text{orb}}$  is relatively small and arises from the Zeeman mixing (second-order effect) of the ground  $|-, 5/2, \pm 1\rangle$  and excited  $|-, 5/2, 0\rangle$  states. Therefore the magnetic anisotropy is expected to be strong, with  $\Delta\chi$  being

positive. The influence of the vibronic coupling on the magnetic anisotropy caused by the orbitally dependent double exchange was discussed in the framework of the Piepho model [110]. This model can be applied when the vibronic coupling with the PKS and P modes exceeds the interaction with the local JT vibrations. The interaction with the PKS – type vibration  $q$  mixes the states with the same quantum numbers  $S$ ,  $M_S$ ,  $M_L$  and opposite parity, thus leading to the pseudo-Jahn–Teller effect. On the other hand, the interaction with the  $P$ - type  $Q$  mode is diagonal in the  $|\pm, S, M_L\rangle$  basis. In fact, this interaction leads to a modulation of the transfer integral due to the changes of the metal-metal distances. In the case when only the interaction with the PKS - vibrations is nonvanishing ( $\nu \neq 0$ ,  $\lambda = 0$ ) the central electronic level ( $E = 0$ ) comprising all  $S$  states with  $M_L = 0$  gives rise to two intersected paraboloids shifted along the  $q$  axis toward the points  $\pm \nu/(\omega\sqrt{2})$ . The remaining surfaces belong to definite  $S$  values, and their shapes are quite similar to those found for spin-clusters. Figure 19 represents the adiabatic potentials corresponding to  $S = 5/2$  (these levels are extracted from the full set of the levels depicted in Fig. 18). Due to the preference of the JT stabilization of the  $M_L = 0$  central level with respect to those with  $M_L = \pm 1$ , the initial (at  $q = 0$ ) gap  $t$  between the ground level with  $|-; 5/2; \pm 1\rangle$  and the first excited  $|\pm, 5/2, 0\rangle$ -level proved to be compressed in the deep minima. The resulting state in each minimum comprises all  $M_L$  values belonging to  $L = 1$  ( $M_L = 0, \pm 1$ ), and hence it can be regarded as  ${}^6P$  atomic level that is fully magnetically isotropic. We thus arrive at the conclusion that the vibronic PKS-coupling reduces the magnetic anisotropy of the system. This conclusion can be illustrated by plotting  $\chi_{||} - \chi_{\perp}$  as a function of the vibronic parameter and temperature. The dependence of the magnetic anisotropy on the strength of the PKS vibronic coupling calculated at different temperatures with the aid of a semiclassical approach [111] are shown in Fig. 19. At a given temperature  $\chi_{||} - \chi_{\perp}$

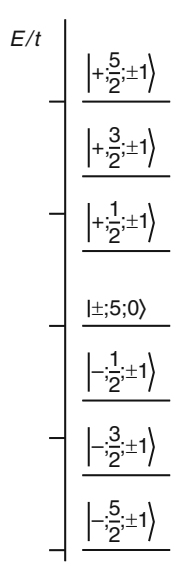
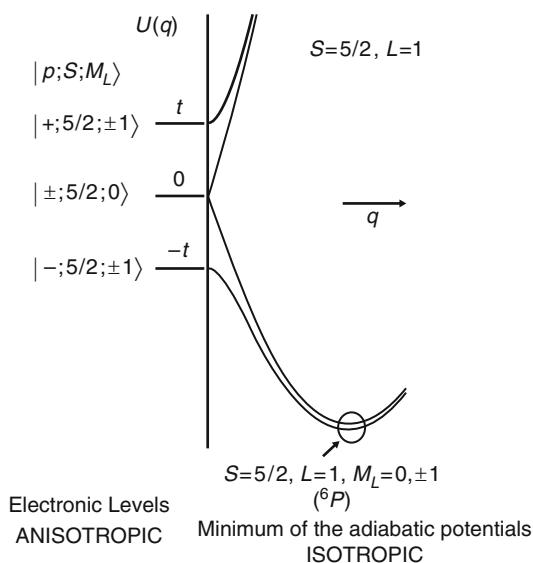


**Fig. 18** Energy diagram for  ${}^3T_1(t_2^2) - {}^4A_2(t_2^3)$  MV dimer of  $D_{4h}$  symmetry. A short notation  $|\pm; S, M_S; L = 1; M_L\rangle \equiv |\pm; S; M_L\rangle$  is used

**Fig. 19** Suppression of the magnetic anisotropy by PKS - vibrations



decreases with the increase of the vibronic parameter, in accordance with the above qualitative arguments. The anisotropy is more pronounced at low temperatures when the population of the ground level with  $M_L = \pm 1$  significantly exceeds the population of the first excited level with  $M_L = 0$ . At high temperatures when these two levels are almost equally populated, the anisotropy disappears (Fig. 20).

In general, the interactions with both PKS- and P-vibrations are nonvanishing ( $\nu \neq 0$ ,  $\lambda \neq 0$ ). Depending on the relative values of the vibronic constants and the double exchange parameter we can have either partially localized minima (*case 1a*) or fully delocalized ones (*cases 1b, 2a, 2b*). Let us assume for the sake of definiteness that we are dealing with the fully delocalized situation (the only minimum, *cases 1b, 2a and 2b*) for the ground spin state with  $S = 5/2$  and consider the section  $q = 0$  of this adiabatic surface (Fig. 21). One can see that the intercenter vibration stabilizes the ground state with  $M_L = \pm 1$  with respect to the state with  $M_L = 0$ . In fact, in the deep minimum associated with  $M_L = \pm 1$  the corresponding gap  $\Delta E_{\min}$  is strongly increased with respect to the initial (at  $Q = 0$ ) gap  $t$  produced by the double exchange. This can be regarded as an increase of the effective anisotropic double exchange by the intercenter vibrations. As a result, the magnetic anisotropy of the system is strongly increased. Note that this conclusion is valid not only in the delocalized case but also providing double-well surface (*case 1*) that is, the enhancement of the anisotropy due to the intercenter vibration is a rather general phenomenon. This effect is illustrated by Fig. 22 showing  $\chi_{\parallel} - \chi_{\perp}$  at different temperatures as a function of the strength of the vibronic coupling, with the intercenter vibration calculated at fixed values of  $t$  and  $\nu$ , which correspond to the vertical section (dashed line) in Fig. 19.

**Fig. 20**  $\chi_{||} - \chi_{\perp}$  vs.  $\nu/t$  curves calculated at different temperatures,  $t = 500 \text{ cm}^{-1}$  and  $\lambda = 0$

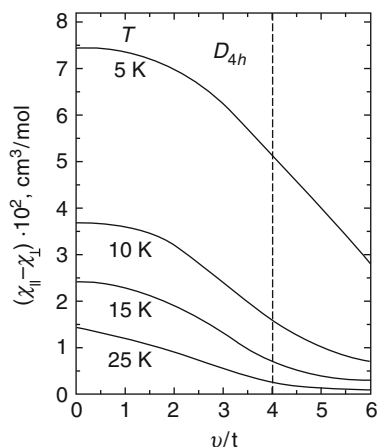
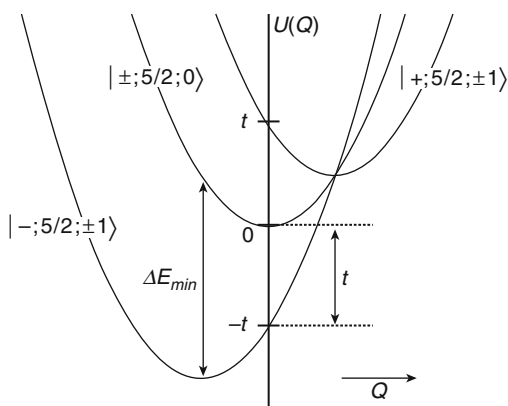


**Fig. 21** Enhancement of the magnetic anisotropy by the intercenter vibration  $Q$



### 3.7 Multimode Jahn–Teller Problem in Mixed-Valence Trimers: Vibronic Localization-Delocalization

In the one-electron triangular cluster of  $C_{3v}$  symmetry the one-electron transfer results in the energy pattern consisting of two levels  $A_1$  and  $E$  separated by the gap  $3|t|$ , with the orbital doublet (singlet) being the ground state, provided that  $t > 0$  ( $t < 0$ ). Both PKS and P-vibrations are operative within the  $E$ -term and also mix  $A_1$  and  $E$ . The PKS and P-vibrations  $a_1$  and  $e$  for the triangular cluster are schematically shown in Figs. 23 and 1, respectively. The interaction with the full-symmetric PKS mode can be eliminated by shifting of  $q_{a_1}$ . On the contrary, the interaction with the full-symmetric P-vibration modulates the gap between the electronic  $A_1$  and  $E$  levels, thus affecting the shape of the potential surface. For this reason the multicenter  $a_1$ -vibration cannot be eliminated, and in general we are dealing with the vibronic  $(A_1 + E) \otimes (a_1 + 2e)$ -problem. Since the study of the surface in the five-dimensional vibrational space is rather complicated, we will

**Fig. 22**  $\chi_{||} - \chi_{\perp}$  vs.  $\lambda/\nu$  curves for singlet-triplet  $D_{4h}$  pair at different  $T$ ,  $t = 500 \text{ cm}^{-1}$  and  $\nu/t = 4$

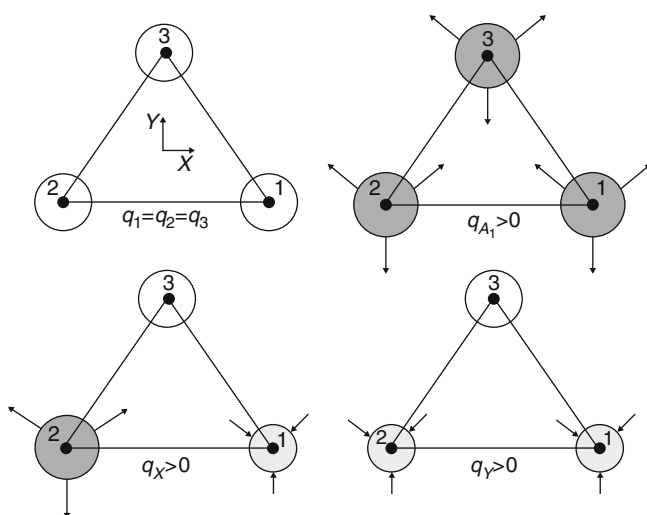
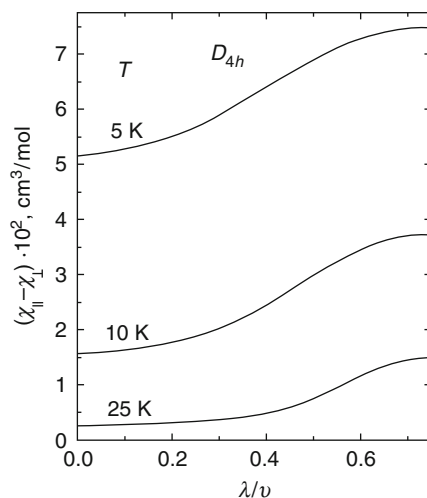


**Fig. 23** PKs-vibrations of a triangular cluster

only discuss two limiting cases  $\nu \gg \lambda$  (strong PKS-coupling) and  $\nu \ll \lambda$  (strong  $P$ -coupling), which provide clear insight into the physical role of these two types of vibrations.

1. Case of  $\nu \gg \lambda$ : vibronic ( $A_1 + E$ )  $\otimes e$  -problem. Providing  $t > 0$  (ground state  $E$ ) and strong transfer, the lower sheet of the adiabatic surface represents the so-called “Mexican hat” characteristic of the  $E \otimes e$ -JT problem [46, 47]. In this case the electronic distribution is dynamically averaged, and the system behaves as fully delocalized. The decrease of the electron transfer and/or the increase of the vibronic coupling results in the appearance of three minima (pseudo-JTE),

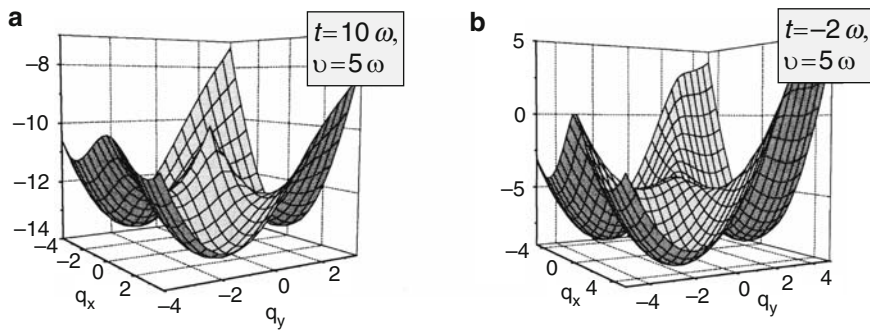


**Fig. 24** Lower sheet of the potential surface for  $d^1-2d^0$ -cluster in the strong *PKS*-coupling limit ( $\lambda = 0$ ): (a)  $t > 0$ , (b)  $t < 0$

in which the extra electron is mainly localized on the sites 1, 2 and 3 (Fig. 24a). In the strong *PKS* coupling limit (accidental  $A_1 + E$ -degeneracy), the system becomes fully localized, so that the electronic densities ( $\rho_1, \rho_2, \rho_3$ ) in the three minima are (1,0,0), (0,1,0) and (0,0,1).

In the case of negative  $t$  (ground state  $A_1$ ) and strong transfer the system is fully delocalized in the only minimum at  $q_X = q_Y = 0$ . On the contrary, providing weak transfer and/or strong *PKS*-coupling, the pseudo JTE leads to an adiabatic surface with three minima (Fig. 24b), in which the extra electron is mainly localized on the sites 1, 2 and 3. Finally, providing intermediate vibronic coupling one can find four minima in the lower sheet. The shallow central minimum corresponds to a fully delocalized state, while the other three minima correspond to the localized states. The above consideration shows that, for a trigonal trimeric cluster containing the extra electron, one can have either a fully delocalized state or a state in which the extra electron is localized (fully or partially) on one site.

2. Case of  $v \ll \lambda$ : vibronic  $(A_1 + E) \otimes (a_1 + e)$ -problem. The adiabatic problem for a trigonal  $d^1-2d^0$  cluster in the strong *P*-coupling limit has been considered in [103]. Providing positive  $t$  (ground doublet) and strong transfer we arrive at the dynamically averaged electronic distribution that is peculiar to the  $E \otimes e$ -JT problem. An increase of *P*-coupling shifts  $Q_{A_1}$  so that the triangle is compressed absorbing the energy of transfer, and in addition three minima appear at the bottom of the ring in  $Q_X Q_Y$ -space. In the minimum on the  $Q_Y$  axis the side 1–2 is elongated; meanwhile, the sides 1–3 and 2–3 are compressed. The maximum localization degree corresponds to the following electronic wave-functions:

$$\begin{aligned}
 \Phi_1 &= \left(1/\sqrt{6}\right) (2\psi_1 - \psi_2 - \psi_3), \\
 \Phi_2 &= \left(1/\sqrt{6}\right) (2\psi_2 - \psi_1 - \psi_3), \\
 \Phi_3 &= \left(1/\sqrt{6}\right) (2\psi_3 - \psi_1 - \psi_2).
 \end{aligned} \tag{20}$$

In this case the degree of localization in the minima can be represented (approximately) by the vector  $(\rho_1, \rho_2, \rho_3) = (4, 1, 1), (1, 4, 1), (1, 1, 4)$ . An increase of  $P$ -coupling and/or decrease of  $t$  leads to a more uniform distribution of the electronic densities in the minima. If the electron transfer is small enough, the lower sheet of the adiabatic potential contains also an excited minimum, for which  $Q_{a_1} \neq 0$ ,  $Q_X = Q_Y = 0$ . For the electronic wave-function in this minimum we find the following full-symmetric superposition of the localized states:

$$\Phi_0 = \left(1/\sqrt{3}\right) (\psi_1 + \psi_2 + \psi_3), \quad (21)$$

which corresponds to the full delocalization of the extra electron. Finally, in the limit of strong  $P$ -coupling and/or weak transfer the electronic wave-functions in the three minima arranged at the bottom of the ring become the following:

$$\begin{aligned} \Phi_1 &= \left(1/\sqrt{6}\right) (\psi_1 - \psi_2 - \psi_3), \\ \Phi_2 &= \left(1/\sqrt{6}\right) (\psi_2 - \psi_1 - \psi_3), \\ \Phi_3 &= \left(1/\sqrt{6}\right) (\psi_3 - \psi_1 - \psi_2). \end{aligned} \quad (22)$$

In this limit four minima (three minima at the bottom of the ring and the “central” minimum) possess the same energy. Although in each minimum located at the bottom of the ring the triangle is distorted, the electronic density is uniformly distributed. This unusual type of the electronic density distribution in the distorted system is reached providing an accidental  $A_1 + E$ -degeneracy. Providing  $t = 0$  the adiabatic potentials calculated within the model of multicenter vibrations are shown in Fig. 25. Both minima are equivalent and correspond to the delocalized states  $\psi_-$  and  $\psi_+$  of the distorted system (compressed and elongated). In the case of negative  $t$  (ground state  $A_1$ ) the lower sheet of the adiabatic potential shows the only “central” minimum in which the system is fully delocalized.

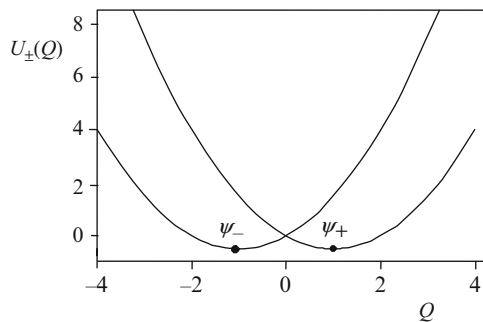


**Fig. 25** Adiabatic potential of the  $d^1 - d^0$  system in strong  $P$ -coupling limit:  $t = 0$ ,  $\lambda/\Omega = 1$



### 3.8 High-Nuclearity Mixed-Valence Clusters: Localization vs. Delocalization of the Electronic Pair in the Double Reduced Polyoxometallates with Keggin Structure

In recent years large MV systems containing many electrons shared over a network metal ions have been in the focus of research. In this view an important class of so-called polyoxometallates should be mentioned. These compounds present discrete structures of definite sizes with highly symmetric networks of metal ions in octahedral and tetrahedral surroundings. The structure of a representative example, namely, the Keggin structure is shown in Fig. 26 (see [15] for the details). It was found that the reduced polyoxometallates containing a delocalized electronic pair are strongly antiferromagnetic, and this phenomenon cannot be explained with a model assuming coupling of electrons via multi-route superexchange. An explanation based on the concept of delocalization that can stabilize the spin-paired ground state without implying a direct exchange interaction was worked out in [96,98]. The vibronic problem in the high-nuclearity systems is very complicated due to the large number of the active vibrations.

Here, we will briefly discuss the results of the adiabatic vibronic approach developed for the bielectronic problem in the twelve-site Keggin structure [15, 97]. This provides a basic picture of the different ways of electron delocalization in this kind of clusters. The vibronic problem involves a considerable number of electronic states and twelve vibrational PKS coordinates. This problem can be simplified if the electronic basis set is restricted to the wavefunctions of the most distant electron pairs (when the Coulomb repulsion in the electronic pairs is minimized), neglecting the mixing of these low-lying groups of levels with those belonging to other kinds of configurations. Accordingly, the electronic structure of the system consists of two spin triplets  $^3T_1$  and  $^3T_2$ , and three spin singlets  $^1A_1$ ,  $^1E$  and  $^1T_2$ , which are split by the effect of the double transfer processes (see detail in [96,97]). As distinguished from the case of one itinerant electron, only the *in phase* (symmetric)

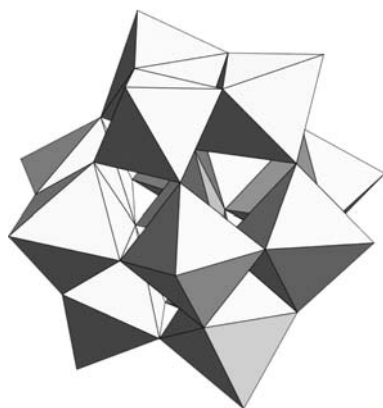


**Fig. 26** Keggin structure of a  $[XM_{12}O_{40}]$  cluster ( $M = Mo, W$ ;  $X = B^{III}, Si^{IV}, P^V, Co^{II}, Co^{III}, Fe^{III}, Cu^{II}$ , etc.) with delocalized electronic pair

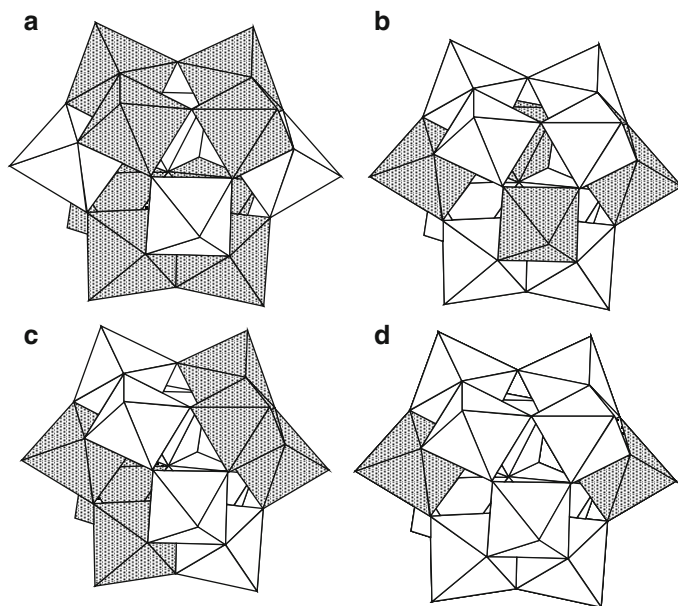


**Fig. 27** Possible types of the delocalization of the electronic pair in the Keggin structure

PKS mode changes simultaneously the potential energy of both electrons. In turn, the antisymmetric (out-of-phase) displacement does not change the common potential energy of the electron pair, since it has the effect of increasing the energy of one electron (compressed site), while the energy of the second electron decreases (expanded site). For this reason only the six symmetric vibrational coordinates are involved in the transfer processes. These are of the type  $a$ ,  $e$  and  $t_2$ , but only the  $e$  and  $t_2$  vibrational modes have been proved to be relevant in the vibronic problem under consideration. Therefore, this vibronic problem will finally involve the coupling of these two modes with the two electronic spin subsets: i.e., the JT and pseudo JT problems, and  $(^3T_1 + ^3T_2) \otimes (e + t_2)$  and  $(^1A_1 + ^1A_2 + ^1T_2) \otimes (e + t_2)$ . Several kinds of spatial electronic distributions have been found to correspond to stable points of the energy surfaces. Thus, for spin-triplet states, weak vibronic coupling in the space of  $e$ -modes restricts electron delocalization to two of the three metal sites of each  $M_3O_{12}$  triad in such a way that each electron moves over a tetrameric unit in which the metal sites are alternatively sharing edges and corners (shaded octahedra in Fig. 27a); in the limit of strong coupling, the electron delocalization is restricted to one of the three metal octahedra (Fig. 27b), but since these four sites are not connected through oxygen bridges the system is expected to be fully localized. In the space of  $t_2$ -modes the electronic pair can be either delocalized over two opposite  $M_3O_{12}$  triads (case of weak vibronic coupling; Fig. 27c), or be completely localized (case of strong vibronic coupling, Fig. 27d). In all these cases the JT coupling leads always to a partial delocalization, or even to a full localization of the

electron pair. By no means one can obtain from the coupling with the spin-triplet states a full delocalization of the electronic pair over twelve sites. This is possible only when the vibronic coupling with the spin-singlet states is considered. Thus, it has been found that, for both positive and negative values of the transfer parameter and weak enough vibronic coupling, the system possesses a stable point in the high-symmetrical nuclear configuration, corresponding to a uniform electronic distribution of the electron pair in the Keggin cluster.

## 4 Vibronic Problem of Cooperative Phenomena in Mixed-Valence Crystals

### 4.1 Introductory Remarks

The phenomena of charge and structural ordering in crystals based on the JT ions have been discovered long time ago [107–109] and became an important part of solid state physics. Studies of electron transfer in solid-phase coordination compounds have led to the discovery of the effect of charge ordering in crystals comprising MV clusters as structural units [110–127]. This discovery made this field of research an inherent part of molecular magnetism. A number of spectroscopic and thermodynamic measurements revealed charge ordering in a series of biferrocenium derivatives (Fig. 28), e.g. dialkylbiferrocenium triiodide crystals with substituent ions  $X = \text{H}, \text{CH}_2\text{CH}_3, (\text{CH}_2)_2\text{CH}_3, (\text{CH}_2)_3\text{CH}_3$ , dihalobiferrocenium triiodide, and dibromiodide crystals with substitute ions  $X = \text{Br}, \text{I}$  [120–124]. The phase transition in biferrocene triiodide crystals has been proved experimentally by Mössbauer spectroscopy and variable temperature heat capacity. Charge ordering has also been revealed in crystals containing trinuclear metal acetate compounds  $[\text{M}_3\text{O}(\text{O}_2\text{CCH}_3)_6(\text{L}_3)\text{S}]$ , where M is a transition metal element such as iron or manganese, L is a ligand and S is a solvate molecule [120–124]. Vast experimental material gave rise to a new trend within the theory of mixed valency, namely the

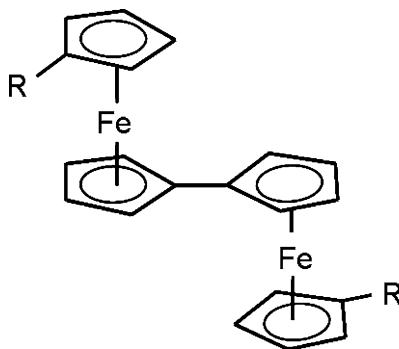


**Fig. 28** Structural unit of MV Fe(II)-Fe(III) biferrocen crystals

study of cooperative phenomena in extended MV systems. In the first papers dealing with the phase transitions in binuclear and trinuclear MV systems [130–132] a phenomenological description has been done.

A qualitative consideration behind the concept of charge ordering [133–171] is the following. In states with fixed valence clusters possess significant dipole moments exceeding those for ordinary ferroelectrics. Tunneling leads to the stationary states in which the dipole moment vanishes. A sufficiently strong inter-cluster dipole-dipole interaction can stabilize the charge-ordered phase of a crystal. On the other hand, the deformation of the lattice by the migrating electron stabilizes the state of the cluster with fixed oxidation degrees and simultaneously leads to intercluster coupling via the phonon field. The competition between these two mechanisms of intercluster interaction leads to different types of structural and charge ordering. Since the magnetic properties of the cluster are dependent on the migration rate of “extra” electrons such type of phase transitions are accompanied by a modification of magnetic properties. Hereunder we summarize the main results obtained in the field of phase transitions in systems of interacting MV clusters.

## 4.2 Charge and Structural Ordering in Crystals Comprising Mixed-Valence Clusters

The electronic spectrum of an isolated binuclear MV  $d^n - d^{n+1}$  cluster consists of pairs of levels belonging to the same spin value and possessing different parity:

$$\varepsilon(2S+1 A_{1g(2u)}) = -J(S(S+1) - S_a(S_a+1) - S_b(S_b+1)) \pm (-1)^{S+1} (S+1/2)t(2S_0+1). \quad (23)$$

Here,  $S$  is the total spin of the cluster,  $J$  is the parameter of the HDVV exchange interaction,  $t$  is the parameter of double exchange,  $S_a$  and  $S_b$  are the spins of the cluster ions, and  $S_0$  is the minimal of these spins. For the sake of definiteness the orbitals are assumed to be spherical, and the symmetry labels of  $D_{4h}$  point group are employed. The presence of these levels in the electronic spectrum of MV dimers and their mixing by the out-of-phase mode  $q$  ( $q = (Q_a - Q_b)/\sqrt{2}$ ;  $Q_a$  and  $Q_b$  are the full symmetric vibrational modes of the cluster fragments (Fig. 29a))

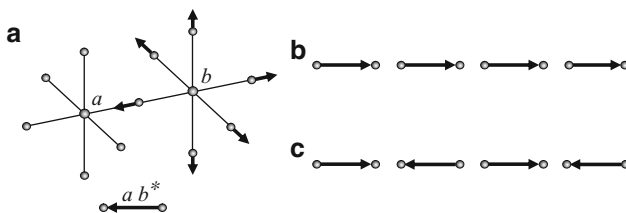


**Fig. 29** Charge and structural ordering in dimeric mixed-valence systems: a) structural unit in the  $ab^*$  state; b) ferro-distortional ordering; c) antiferro-distortional ordering

produces a JT situation [143]. Due to the dispersion of crystal modes, the interaction of the clusters via the phonon field appears, and this interaction induces structural phase transitions, which will be first shortly described for the  $d^1 - d^2$  systems. The consideration is based on the Hamiltonian

$$H = \sum_l H_l - \frac{1}{2} \sum_{l,l'} K(l-l') d_0^2 \tau_l^z \tau_{l'}^z + H_L + \sum_{kl} v_k \tau_l^z \exp(-ikl) (a_k^+ + a_{-k}), \quad (24)$$

where the first term describes the system of non-interacting clusters, the second term is the dipole-dipole interaction, the third term describes the free phonons, and finally, the fourth term represents the electron-phonon coupling.  $d_0$  is the dipole of a  $d^n - d^{n+1}$  cluster with a fully localized electron,  $l$  numbers the clusters in crystal,  $K(l-l') = (3 \cos^2 \theta_{ll'} - 1) R_{ll'}^{-3} a_k^+$  and  $a_k$  are the phonon operators,  $\kappa \equiv \kappa v$  numbers the wave vectors and branches of the vibrations,  $\omega_{\kappa v}$  is the frequency of the vibration  $\kappa$ . In the basis of the isolated cluster states  $^{2S+1}A_{1g(2u)}$  the matrix  $\tau_l^z$  has the form:

$$\tau_l^z = \begin{pmatrix} 0 & \sigma_x^l \\ \sigma_x^l & 0 \end{pmatrix} \quad (25)$$

A canonical shift transformation  $\tilde{H} = \exp(R) H \exp(-R)$  where  $R$  is a matrix operator of the form

$$R = \sum_{k,l} (\hbar\omega)^{-1} \tau_l^z [\exp(ikl) v_k^* a_k - \exp(-ikl) v_k a_k^+], \quad (26)$$

is proposed in theory of structural ordering in solids [107]. This transformation diagonalizes the phonon part of the Hamiltonian. The transformed Hamiltonian takes on the form:

$$\tilde{H} = \sum_l \tilde{H}_l + H_L - \Delta E - \frac{d_0^2}{2} \sum_{l,l'} K(l-l') \tau_l^z \tau_{l'}^z - \frac{1}{2} \sum_{l,l'} \Lambda(l-l') \tau_l^z \tau_{l'}^z, \quad (27)$$

$$\Lambda(\mathbf{l}-\mathbf{l}') = 2 \sum_k \frac{|v_k|^2}{\hbar\omega_k} \exp[i\mathbf{k}(\mathbf{l}-\mathbf{l}')] ]$$

Here,  $\Delta E$  is the energy of JT stabilization connected with odd cluster vibrations  $q$ ; the fifth term in the Hamiltonian, (27), describes the intercluster interaction through the phonon field. The Hamiltonian of an isolated cluster  $\tilde{H}_C$  ( $C = A, B$ ) after transformation contains phonon variables, because the odd coordinate  $q$  mixes the exchange-resonance multiplets with the same spin. Then, the crystal is subdivided into two equivalent sublattices  $A$  and  $B$ ; the clusters of these sublattices are numbered by letters  $n$  and  $m$ . The interaction between the nearest neighbors is only taken into account; the interaction Hamiltonian is the following:

$$H_{\text{int}} = -\frac{d_0^2}{2} \sum_{n,m} K^{AB}(n-m) \tau_n^z \tau_m^z - \frac{1}{2} \sum_{n,m} \Lambda^{AB}(n-m) \tau_n^z \tau_m^z. \quad (28)$$

Then, the mean field approximation is to be applied. The thermal averages  $\overline{\tau^A} = \langle \tau_n^A \rangle$  and  $\overline{\tau^B} = \langle \tau_n^B \rangle$  describing simultaneously the dipole moments and the distortions in sublattices *A* and *B* serve as the order parameters. For the low temperature range  $\hbar\omega_k > kT$  the problem reduces to the static one. The magnitude

$$D_{AB} = \sum_m (d_0^2 K^{AB}(\mathbf{n} - \mathbf{m}) + \Lambda^{AB}(\mathbf{n} - \mathbf{m})) + \begin{cases} \mu \\ 0 \end{cases} \quad (29)$$

plays the role of a molecular field parameter; in the case of structural phase transitions accompanied by a homogeneous crystal deformation  $D_{AB}$  includes the parameter  $\mu$  of intercluster electron-deformational coupling [114]. The transfer parameter  $t$  in this case is substituted for the reduced one,  $\tilde{p} = t \exp(-2 \sum_k |\nu_k|^2 / (\hbar\omega_k)^2)$ .

The parameter  $\tilde{p}$  represents the tunnel splitting of the ground vibrational level. For  $D_{AB} > 0$  both the dipole moments and the structural distortions have parallel alignment, i.e. charge and structural ordering of the ferro-distortional type occurs (Fig. 29b). A structural phase transition for  $D_{AB} > 0$  leads to a homogeneous deformation of the crystal, as well as to the reduction of the crystal symmetry. In the opposite situation,  $D_{AB} < 0$ , the antiparallel arrangement of the structural distortions and dipole momenta of the *A* and *B* sublattices takes place. In this case, the macroscopic deformation of the crystal does not arise; but the symmetry of the crystal, as for  $D_{AB} > 0$ , becomes lower. The antiferro-distortional structural ordering is accompanied only by doubling of the unit cell of the crystal and the appearance of antiferroelectricity (Fig. 29c). If the contributions from the intercluster dipole-dipole interaction and interaction of the clusters through the phonon field to the parameter  $D_{AB}$  are of the same sign, then the electron-phonon coupling promotes stabilization of a charge-ordered phase. For different signs of these contributions, the charge and structural ordering destabilize one another. From physical considerations, it is clear that delocalization of the electron leads to a gain in the energy of the cluster by  $\tilde{p}/2$  or  $\tilde{p}$  for states with  $S = 1/2$  and  $S = 3/2$ , respectively. In a charge and structurally ordered crystal, the states of a single cluster should stabilize with the loss of the corresponding energies. If in this case the energy gain due to intercluster interaction exceeds the destabilization energy, the ordering proves to be energetically favorable. Thus, the distribution of the electron density in the ground state of the crystal is determined by the competition between the double exchange leading to the delocalization of the extra electron, intercluster dipole-dipole interaction and interaction of the clusters via the phonon field. The system behavior is described by two dimensionless parameters  $x = J/|\tilde{p}|$ ,  $y = |\tilde{p}|/D_{AB}$ .

Figure 30a shows three qualitatively different types of the temperature dependences of the order parameter  $|\bar{\tau}| = |\bar{\tau}^A| = |\bar{\tau}^B|$  in the case of antiferromagnetic intracluster exchange [133–135]: a) the monotonic decrease of the order parameter (Fig. 30a, curves 1, 2 and 4); b) the nonmonotonic temperature dependence of  $|\bar{\tau}|$  when it initially increases and then decreases with temperature increase (Fig. 30a, curve 3); c) the case of the two phase transitions, when the order parameter is non-zero in the limited temperature ranges (Fig. 30a, curves 5 and 6). In this way the

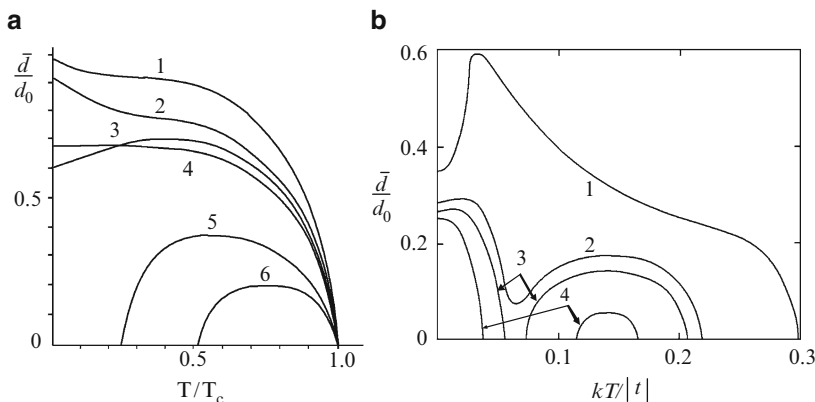


**Fig. 30** Temperature dependence of the order parameter for  $J < 0$ : (a) the case of  $d^1 - d^2$  system: 1)  $y = 0.5$ ,  $|x| = 0.3$ ; 2)  $y = 0.8$ ,  $|x| = 0.3$ ; 3)  $y = 0.8$ ,  $|x| = 0.05$ ; 4)  $y = 0.9$ ,  $|x| = 0.25$ ; 5)  $y = 1.1$ ,  $|x| = 0.2$ ; 6)  $y = 1.1$ ,  $|x| = 0.1$ . (b) The case of  $d^2 - d^3$  system,  $x = 0.08$ : 1)  $y = 1.4$ ; 2)  $y = 1.444$ ; 3)  $y = 1.448$ ; 4)  $y = 1.458$

system is disordered not only at high temperatures  $T \geq T_{c2}$  but also at low temperatures  $T \leq T_{c1}$ . This unusual phenomenon can be explained as follows. At low temperatures, when only the ground level  $^4A_{1g}$  ( $\tilde{p} > 0$ ,  $|x| < 1/6$ ) is populated for  $1 < y < 4/3$ , the electron localization in the system with the tunnel parameter  $2\tilde{p}$  is impossible, the population of the  $^2A_{2u}$  softens the conditions of charge-ordered phase stabilization. Further rise of temperature leads to the population of the  $^2A_{1g}$  level, and the thermal fluctuations destroy the molecular field; as a result the crystal again becomes disordered. The theory of charge and structural ordering was generalized to the case of crystals consisting of many-electron dimeric clusters  $d^2 - d^3$ ,  $d^5 - d^6$  [141, 142]. It was shown that in crystals comprising these clusters (high-spin ions) the case of three phase transitions can be put into effect as well. In such a way the system can be ordered at low  $0 < T < T_{c1}$  and high  $T_{c2} < T < T_{c3}$  temperatures, while disordered in the range of intermediate  $T_{c1} \leq T \leq T_{c2}$  and high  $T \geq T_{c3}$  temperatures (Fig. 30b).

A remarkable manifestation of charge and structural ordering in crystals comprising interacting MV clusters is the anomalous behavior of the magnetic moment caused by the crossover of levels and change of the ground state spin in the molecular field [133–135] (Fig. 31). Curve 3 in Fig. 32 describes the magnetic moment  $\mu(T)$  for the system of interacting binuclear  $d^1 - d^2$  clusters. The low-temperature limit of the magnetic moment is  $\mu(0) = 1.73\mu_B$ ; meanwhile, for the system of non-interacting clusters  $\mu(0) = 3.87\mu_B$ . This behavior of the magnetic moment arises from the dipole-dipole interaction and interaction of clusters via the phonon field. The phase transition from the disordered to the structurally and charge-ordered state of the crystal is accompanied by a transition between two paramagnetic states of the crystal.

**Fig. 31** Temperature behavior of the energy levels of the cluster in the molecular field approximation for  $J < 0$ ,  $\tilde{p} > 0$ ,  $y = 0.2$ ,  $|x| = 0.2$

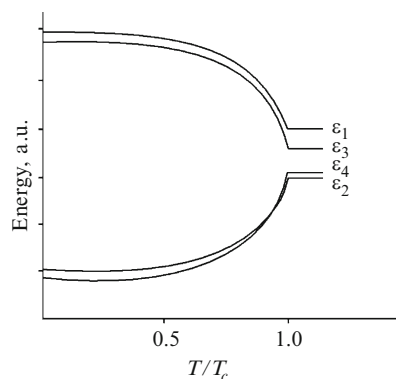
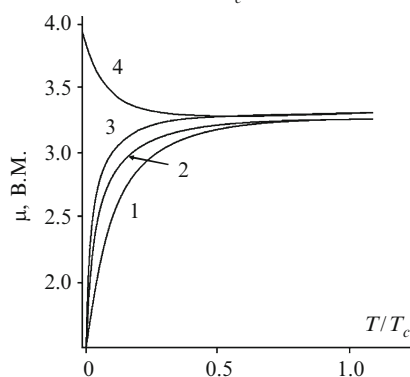


**Fig. 32** Temperature-dependence of the effective magnetic moment for  $J < 0$ :

- 1)  $y = 0.2$ ,  $|x| = 0.6$ ;
- 2)  $y \rightarrow \infty$ ,  $|x| = 0.6$ ;
- 3)  $y = 0.2$ ,  $|x| = 0.2$ ;
- 4)  $y \rightarrow \infty$ ,  $|x| = 0.2$



The spectrum of elementary excitations of molecular crystals comprising MV  $d^1 - d^2$  clusters has been studied in [159]. In these crystals the phase transitions are associated with the condensation of the soft (or low frequency) mode in the spectrum of elementary excitations as well as by the softening of the elastic modulus. At the same time MV systems reveal peculiarities distinct from those of ferroelectrics with perovskite structure and rare-earth zircons. In ferroelectrics and rare-earth compounds the softening of the collective mode frequency usually takes place for a single temperature, while in MV crystals in the case of two phase transitions a branch of elementary excitations may exist, the frequency of which proves to be zero in the finite temperature range  $T < T_{c1}$ . Moreover, for the same range of intra- and intercluster parameters, the elastic modulus falls to zero at two points. Charge and structural ordering in crystals based on trimeric MV clusters, as well as the related phenomena, have been discussed in detail in [120–134, 153–167].

### 4.3 Quasidynamical Model for the Cooperative Jahn–Teller Effect. Vibronic Intervalence Optical Bands

MV clusters usually exhibit characteristic absorption bands within the infrared or visible spectral ranges. These bands are related to light-induced transfer of the “extra” electron between metal ions. This absorption is called intervalence,



while the corresponding bands are denoted as electron transfer bands. Since a mononuclear complex cluster moiety does not exhibit intervalence absorption, the latter is one of the most important features of the phenomenon of mixed valency. A classical example is represented by the so-called Creutz-Taube ion  $[(\text{NH}_3)_5\text{Ru}-\text{N}-\text{N}-(\text{NH}_3)_5]^{5+}$ .

The “extra” electron creates a deformation of the crystal surroundings, and therefore gives rise to the vibronically assisted charge transfer bands that have an appreciable width and a characteristic shape. The quantum-mechanical approach to band shape calculations based on the numerical solution of the pseudo JT problem in a finite molecular system cannot be applied to the description of many-particle system of interacting clusters. To overcome this fundamental difficulty, an approximate quasidynamical approach was proposed [131, 138, 144, 146] to describe electron transfer bands in MV charge-ordered systems. The idea of this approach lies in the use of the adiabatic approximation in the calculation of the order parameter of a charge-ordered crystal. The second stage within the framework of the molecular field approximation method consists in solving the dynamical (quantum-mechanical) vibronic problem for a single cluster affected by the molecular field produced by the charge-ordered crystal. Then the vibronic wavefunctions are utilized for electron transfer band shape calculation.

Let us consider a crystal, whose structural units are MV  $d^0-d^1$  dimeric clusters. The Hamiltonian of the crystal can be presented as:

$$H = H_0 + \hbar\omega v \sum_l q_l \sigma_x^l + \sum_l H_L^l, \\ H_L^l = \sum_l \frac{\hbar\omega}{2} \left( q_l^2 - \frac{\partial^2}{\partial q_l^2} \right) \quad (30)$$

where the Hamiltonian  $H_0$  includes the Hamiltonian of isolated non-interacting clusters and the intercluster dipole-dipole interactions; the second term describes the interaction of each cluster with the out-of-phase mode  $q_l$ ,  $v$  is the dimensionless (in units of  $\hbar\omega$ ) vibronic coupling constant, the third term describes the free vibrations of the clusters. The mode  $q_l$  is assumed to be local, and the dispersion of the vibrations is not taken into account. In the molecular field approximation, the total Hamiltonian of the crystal can be expanded as a sum of single-cluster Hamiltonians  $\tilde{H}_l$

$$\tilde{H}_l = H_L^l + \hbar\omega t \sigma_z^l + \hbar\omega v q_l \sigma_x^l - L d_0^2 \bar{\sigma} \sigma_x^l \quad (31)$$

where  $t$  is the dimensionless transfer parameter,  $\bar{\sigma} = \bar{d}/d_0$ . Within the framework of the quasidynamical approach, at the first stage the kinetic energy of the nuclei is neglected, and one obtains a self-consistent equation for the order parameter in the adiabatic approximation. A family of curves  $\bar{\sigma} = \bar{d}/d_0$  is presented in Fig. 33 in order to illustrate the effect of the vibronic interaction on the temperature-dependence of the order parameter. Calculations of the temperature-dependence of the mean dipole moment performed in the semiclassical approximation have shown that: (1) for weak vibronic coupling the temperature behavior of the order parameter does not differ from that in the rigid lattice. The phase

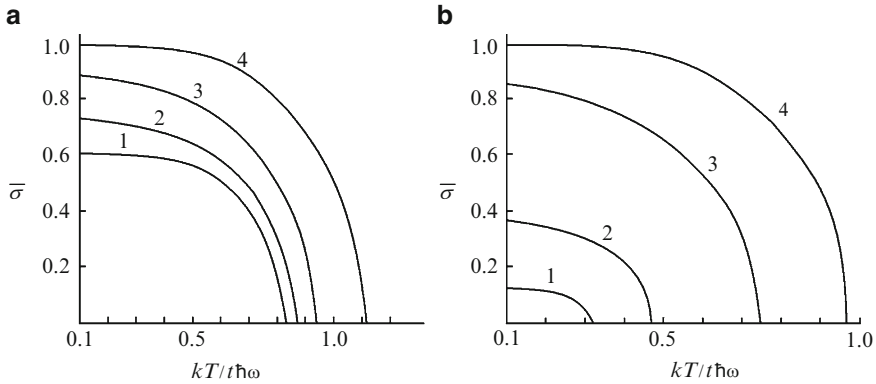


**Fig. 33** Temperature-dependence of the order parameter a)  $t = 1.0$ ,  $t/\zeta = 0.8$ : 1)  $\nu = 0.1$ ; 2)  $\nu = 0.5$ ; 3)  $\nu = 1.0$ ; 4)  $\nu = 3.0$ ; b)  $t = 1.0$ ,  $t/\zeta = 1.0$ : 1)  $\nu = 0.1$ ; 2)  $\nu = 0.3$ ; 3)  $\nu = 1.0$ ; 4)  $\nu = 3.0$

transition temperature is determined by the competition between the stabilizing effect of intercluster interaction and tunnel intracluster interaction; (2) with increase of the vibronic coupling the phase transition temperature  $T_c$  and the maximum value of the mean dipole moment increase. The vibronic interaction leads to an additional localization of the extra electron, as well as to the expansion of the range of parameters for which charge ordering can be observed; (3) for strong vibronic coupling the electron transfer is suppressed, and the phase transition temperature is only determined by the intercluster interaction energy. Thus, from the physical point of view, the order parameter determined in the semiclassical approximation reveals physically correct peculiarities of the temperature behavior in the cases of strong, intermediate and weak vibronic coupling. At the following stage, the single cluster vibronic problem with the Hamiltonian (31), wherein the order parameter is determined semiclassically, is solved. The vibronic wave functions of the crystal are written as the expansions over unperturbed electronic and vibrational states:

$$\Phi_v(r, q) = \sum_{n=0}^{\infty} (u_{vn}\varphi_b(r)\chi_n(q) + a_{vn}\varphi_a(r)\chi_n(q)) \quad (32)$$

Here,  $\chi_n(q)$  denotes the harmonic oscillator wave-functions,  $\varphi_a(r)$  and  $\varphi_b(r)$  correspond to the states of electrons localized on  $a$  and  $b$  ions, the index  $\nu$  numbers the hybrid cluster states in the molecular field. It should be noted that, within the scope of the adopted approach, the quantum properties of the vibronic states in a self-consistent field are taken into account. Therefore, it is reasonable to call the proposed approximation quasidynamical. The vibronic states obtained within the scope of the quasidynamical approach are hybrid, i.e. retaining the quantum properties of both electronic and vibrational states. In the case of strong vibronic coupling, i.e. in the case of adiabatic potentials possessing deep minima both the

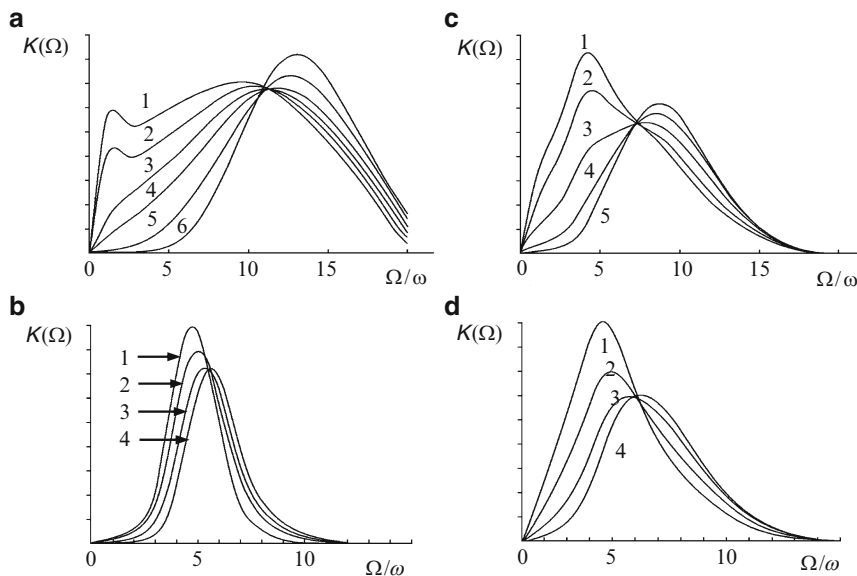


**Fig. 34** Temperature-dependence of the absorption coefficient (in arbitrary units)

- a)  $\zeta = 1$ ,  $t = 0.5$ ,  $\nu = 2.5$ : 1)  $T/T_c = 1.0$ ; 2) 0.9; 3) 0.8; 4) 0.7; 5) 0.5; 6) 0.1;  
 b)  $\zeta = 1$ ,  $t = 2.0$ ,  $\nu = 1.0$ : 1)  $T/T_c = 1.0$ ; 2) 0.8; 3) 0.5; 4) 0.1;  
 c)  $\zeta = 1$ ,  $t = 1.0$ ,  $\nu = 2.0$ : 1)  $T/T_c = 1.0$ ; 2) 0.8; 3) 0.6; 4) 0.4; 5) 0.2;  
 d)  $\zeta = 1$ ,  $t = 1.0$ ,  $\nu = 1.5$ : 1)  $T/T_c = 1.0$ ; 2) 0.8; 3) 0.5; 4) 0.2

ordered and disordered states, the band has two maxima (Fig. 34a) at high temperatures  $T \sim T_c$ . The high-frequency maximum is related to the Franck-Condon transition. This transition can be associated with the vertical transition from the minimum of the adiabatic potential lower sheet to the upper sheet. The temperature-dependence of this band maximum is related to two physical factors: (1) explicit temperature-dependence of the cluster band shape that takes place in the case of the fixed shape of the adiabatic potential sheets; (2) temperature-dependence of the order parameter, which determines the temperature-dependent shape of the cluster adiabatic potentials. When temperature decreases, the band narrows and shifts to the high-frequency range. When the vibronic coupling parameter decreases, the low-frequency maximum of the optical curves (in the vicinity of  $T_c$ ) disappears and turns into a shoulder (Fig. 34e). If the coupling is further reduced, this maximum is absent at any temperature. For all parameters and temperatures the charge transfer bands remain essentially asymmetric and possess a long tail in the high-frequency range. It is to be noted that in the intermediate and weak coupling range the semiclassical approach does not describe adequately the contour of absorption band, both in the cases of low and high temperatures. In this case the quasidynamical curves are bell-shaped, and significant absorption takes place in the classically forbidden region  $\hbar\Omega < 2t$ . At high temperatures the semiclassical approximation

can hardly be applied to the case of moderate vibronic coupling. The elucidated intervalence band features corroborate the existence of the charge-ordered state and provide unique information about the key parameters of interacting clusters in crystal charge-ordered state and phase transitions.

#### ***4.4 Pseudo Jahn–Teller Problem of Mössbauer Spectra of Charge-Ordered Biferrocenium Crystals: Coexistence of Localized and Delocalized States***

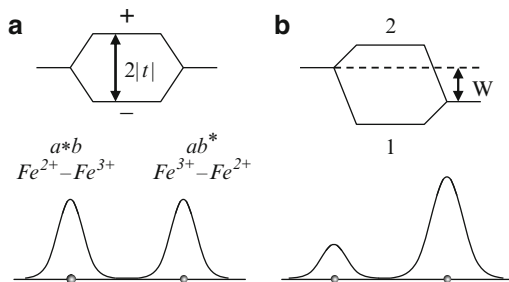
The charge-ordering characteristics and attributes are exhibited most of all in Mössbauer spectra of biferrocenium derivatives crystals containing interacting dimeric MV iron clusters. It will be shown that an intricate feature of the Mössbauer spectra of these compounds can be attributed to a pseudo JTE in the quantum regime. Reviewing briefly the experimental results [117, 119–123, 173–176] at least three types (I,II,III) of Mössbauer spectra can be distinguished: (a) in type I Mössbauer spectra at low temperatures there are two doublets with isomeric shifts and quadrupole splittings that are typical for  $\text{Fe}^{2+}$  and  $\text{Fe}^{3+}$  ions. When the temperature is raised, the lines corresponding to the two doublets draw together, and eventually, at high temperatures beginning with a certain critical value, there is only one Mössbauer doublet with averaged parameters; (b) The low-temperature type II spectrum is composed of two doublets, corresponding to  $\text{Fe}^{2+}$  and  $\text{Fe}^{3+}$  ions. In the intermediate temperature range simultaneously with the two doublets of localized  $\text{Fe}^{2+}$  and  $\text{Fe}^{3+}$  ions there is also observed the averaged spectrum. The overall spectrum in this intermediate temperature range contains three doublets. When temperature rises, the intensity of the central doublet lines increases. At the same time the two  $\text{Fe}^{2+}$  and  $\text{Fe}^{3+}$  doublets draw together and eventually, at high temperatures, the overall spectrum is transformed into the averaged spectrum. This was observed in 1'6'-dibromobiferrocenium dibromiodate [121], biferrocenium triiodate [117]. (c) Type III spectra contain over two doublets within a wide temperature range [119, 120].

The qualitative explanation [153, 155] of the Mössbauer spectra is the following. Under the assumption that the orbitals  $\varphi_a(r)$  and  $\varphi_b(r)$  overlap relatively weak, the spatial distribution of the electronic density, both for the ground and excited states of the binuclear cluster of low-spin iron in biferrocenium derivative crystals case, is given in the static ( $\nu = 0$ ) case by the function:

$$\rho_{\text{sym}}(r) = (|\phi_a(r)|^2 + |\phi_b(r)|^2)/2 \quad (33)$$

One can see that the electronic density at ions  $a$  and  $b$  is the same (Fig. 35a), not only in the isolated cluster, but also in the symmetric cluster in the charge-ordered crystal when  $T \geq T_c$ . In the charge-ordered state each cluster is under action of an averaged molecular field produced by the adjacent clusters; therefore, the localized

**Fig. 35** Schematic picture of the distribution of the electronic density in a MVcluster: *a*-disordered phase, *b*-ordered phase



states  $\varphi_a(r)$  and  $\varphi_b(r)$  energies are not identical (Fig. 35b). The cluster energy in a molecular field is the following:

$$\varepsilon_{1,2} = \pm(p^2(\hbar\omega)^2 + (Ld_0^2\bar{\sigma})^2)^{1/2} \quad (34)$$

The electronic density distribution for the ground state with the energy  $\varepsilon_2$  is found as:

$$\rho_{\text{asym}}(r) = (1/2) (1 + Ld_0^2\bar{\sigma}/\varepsilon_1) |\phi_a(r)|^2 + (1/2) (1 - Ld_0^2\bar{\sigma}/\varepsilon_1) |\phi_b(r)|^2 \quad (35)$$

The molecular field causes an asymmetric distribution of the electronic density, both in the ground and excited states (Fig. 35b). This distribution results in two doublets in Mössbauer spectrum. When the temperature rises, the molecular field  $Ld_0^2\bar{\sigma}$  tends to zero, and the Mössbauer spectrum amounts to a single averaged doublet (delocalized spectrum). The static model explains thus only type I spectra and cannot explain in principle the coexistence of localized and delocalized spectra.

If one refers to the vibronic *PKS* model and introduces the cluster adiabatic potential in the molecular field, it becomes asymmetric and looks like:

$$U_{1,2} = (\hbar\omega/2) q^2 \pm \hbar\omega \left( p^2 + (vq - Ld_0^2\bar{\sigma}/\hbar\omega)^2 \right)^{1/2} \quad (36)$$

Consequently, the distribution of the electronic density in the inequivalent minima becomes asymmetric (Fig. 36b, c). When vibronic coupling is strong ( $v^2 > p$ ) and the intercluster interaction  $L\bar{d}d_0$  is appreciable, the upper and lower adiabatic potential branches have minima at

$$q_{1(2)} \approx \pm v, \quad q_3 = -Ld_0^2\bar{\sigma}/\hbar\omega v. \quad (37)$$

The corresponding values of  $U_2(q_{1(2)})$  and  $U_3(q_3)$  are approximately the following:

$$U_2(q_{1(2)}) \approx \hbar\omega \left( -v^2/2 \pm Ld_0^2\bar{\sigma}/\hbar\omega \right), \quad U_3(q_3) \approx \hbar\omega \left( Ld_0^2\bar{\sigma} \right)^2 / 2v^2 (\hbar\omega)^2. \quad (38)$$

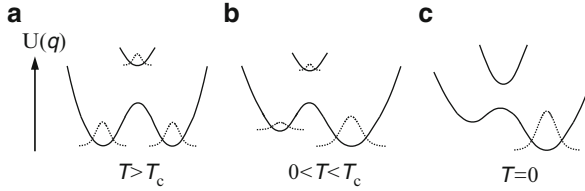


**Fig. 36** Cluster adiabatic potential in disordered (a) and charge-ordered (b,c) crystal states

In the case under consideration, i.e. when the vibronic coupling is strong, at  $T = 0$  only the deepest minimum of the lower adiabatic potential sheet is populated (see Fig. 36c). In this case the system state is well localized ( $\psi_2(q_1) \approx \varphi_a(r)$ ,  $\psi_2(q_2) \approx \varphi_b(r)$ ), which gives rise to two doublets in the Mössbauer spectrum. As the temperature is increased, the energies of the minima draw together. At the same time the higher minimum of the lower sheet is being populated, as well as the minimum of the upper sheet (Fig. 36b). Both lower sheet minima correspond to the asymmetric distribution of the electronic density, i.e. they yield two doublets (originating from  $\text{Fe}^{2+}$  and  $\text{Fe}^{3+}$ ) in the spectrum. The upper sheet corresponds to the symmetric distribution of the electronic density ( $\psi_1(q_3) \approx (\varphi_a + \varphi_b)/\sqrt{2}$ ), and its population produces a delocalized component of the spectrum. This physical picture provides a qualitative condition for coexistence of localized and delocalized spectra. For the observation of a delocalized spectrum there must take place an appreciable population of the upper adiabatic potential sheet. This can occur if the vibronic interaction is not too strong. Otherwise, the gap between the upper and lower sheets is large, even for small values of  $Ld_0^2\bar{\sigma}$ . On the other side, an increase of  $Ld_0^2\bar{\sigma}$  is accompanied by the growth of the temperature allowing the population of the symmetric minimum. In [153, 155] the quantitative explanation of different types of Mössbauer spectra (especially those of type III) was given in the framework of the quasidynamical model. In this model the quadrupole splitting on the ion  $a$  and the nuclear isomer shift  $\delta_a^{(\nu)}$  for a cluster in the  $\nu$  th vibronic state looks as follows

$$\Delta E_a^{(\nu)} = \frac{1}{2}e^2 Q_n \left( q(\text{Fe}^{3+}) \sum_{n=0}^{\infty} u_{\nu n}^2 + q(\text{Fe}^{2+}) \sum_{n=0}^{\infty} a_{\nu n}^2 \right),$$

$$\delta_a^{(\nu)} = \delta(\text{Fe}^{3+}) \sum_{n=0}^{\infty} u_{\nu n}^2 + \delta(\text{Fe}^{2+}) \sum_{n=0}^{\infty} a_{\nu n}^2, \quad (39)$$

Here,  $Q_n$  is the nuclear quadrupole moment;  $q(\text{Fe}^{3+})$ ,  $\delta(\text{Fe}^{3+})$  and  $q(\text{Fe}^{2+})$ ,  $\delta(\text{Fe}^{2+})$  are the mean values of the electric field gradients and isomeric shifts for  $\text{Fe}^{3+}$  and  $\text{Fe}^{2+}$  ions. The coefficients  $u_{\nu n}$  and  $a_{\nu n}$  are found from the solution of the dynamic vibronic problem for the arbitrary values of  $\bar{\sigma}(T)$ . The expressions for  $\Delta E_b^{(\nu)}$  and  $\delta_b^{(\nu)}$  can be obtained by means of the substitution  $u_{\nu n} \leftrightarrow a_{\nu n}$ . The total Mössbauer spectrum  $F(\Omega)$  was obtained summing the spectra yielded by different cluster vibronic states in the molecular field, taking into account their equilibrium

populations and  $F(\Omega) = F_a(\Omega) + F_b(\Omega)$ . The form-function of the Mössbauer doublet produced by each cluster nucleus is described by the superposition of the Lorentz curves:

$$F_c(\Omega) = \frac{1}{Z} \sum_{\pm} \sum_v \exp(-E_v/kT) \frac{\Gamma}{\Gamma^2 + (\Omega - \delta_c^{(v)} \pm (\Delta E_c^{(v)}/2))^2}. \quad (40)$$

The spectra are calculated (Fig. 37) using the following parameters characteristic of low- spin  $Fe^{2+}$ ,  $Fe^{3+}$  ions  $e^2 Q_n q(Fe^{2+})/2 = 2 \text{ mm s}^{-1}$ ,  $e^2 Q_n q(Fe^{3+})/2$

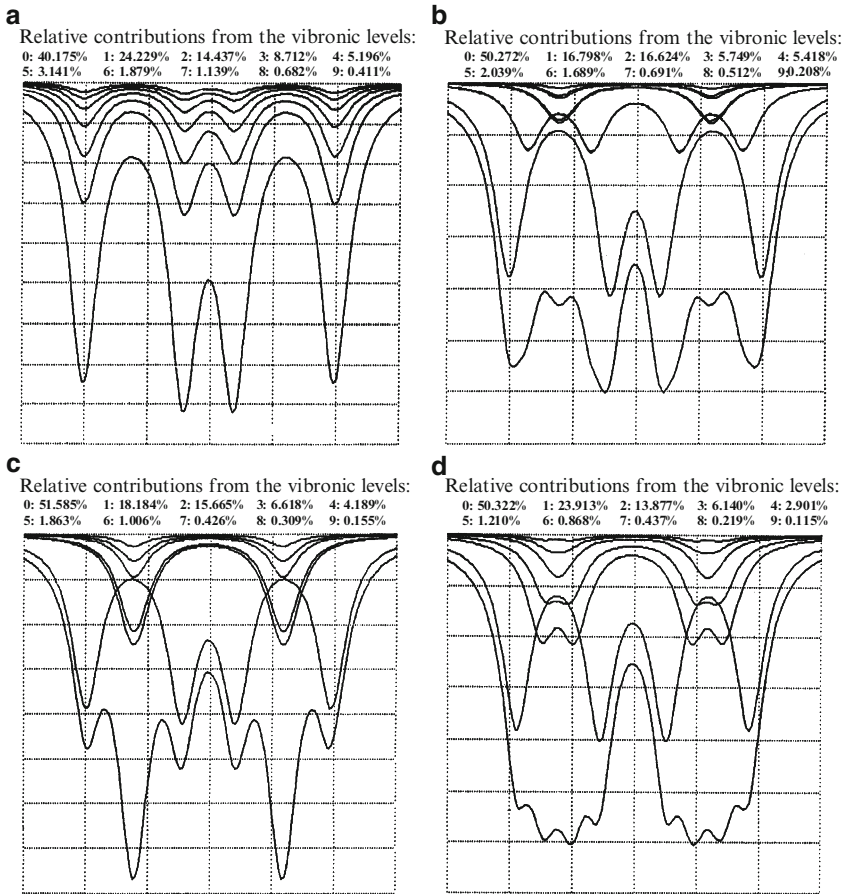


**Fig. 37** Mossbauer spectra of charge-ordered MV dimers of low-spin iron in the case of a)  $v = 3.0$ ,  $p = 0.5$ ,  $\zeta = 1$ ,  $T = 0.9750T_c$ ; b)  $v = 2.5$ ,  $p = 0.5$ ,  $\zeta = 1$ ,  $T = 0.9000T_c$ ; c)  $v = 2.0$ ,  $p = 1.0$ ,  $\zeta = 1$ ,  $T = 0.9005T_c$ ; d)  $v = 1.5$ ,  $p = 1.0$ ,  $\zeta = 1$ ,  $T = 0.9348T_c$ . The low curve is the full spectrum obtained by the summation of partial spectra. The numbering of the partial spectra from separate vibronic levels  $v = 0, 1, \dots$  from the *bottom* to *up* is accepted in Figures *a, b, c, d*. The relative contributions from the vibronic levels are indicated in each case

$= 0.4 \text{ mm s}^{-1}$ ,  $\Gamma(\text{Fe}^{2+}) = \Gamma(\text{Fe}^{3+}) = 0.14 \text{ mm s}^{-1}$ ,  $\delta(\text{Fe}^{2+}) = \delta(\text{Fe}^{3+}) = 0.486 \text{ mm s}^{-1}$  [112]. These spectra are conventionally referred to as the cases of strong, moderate and weak vibronic coupling. In the case of strong vibronic coupling ( $\nu = 3$ ) and a relatively weak transfer ( $t = 0.5$ ) even at temperatures close to the transition temperature  $T_c$ , the spectrum consists of two doublets, and all significantly populated vibronic levels give rise to the same quadrupole splitting peculiar to  $\text{Fe}^{2+}$  and  $\text{Fe}^{3+}$  ions (Fig. 37a). At the phase transition temperature the spectrum is completely averaged; all vibronic levels provide delocalized contributions to the summary spectrum. In such a way in the case of strong vibronic coupling the model reproduces type I spectra. For lower value of the vibronic coupling constant ( $\nu = 2.5$ ) and  $t = 0.5$  the spectrum at low temperatures consists, as in the previous case, of two doublets. At  $T = 0.9000 T_c$  (Fig. 36b) only the ground vibronic level provides two doublets corresponding to a localized spectrum. The Mössbauer spectrum lines originating from the first and second excited vibronic levels have quadrupole splittings different from  $\Delta E_Q(\text{Fe}^{2+})$  and  $\Delta E_Q(\text{Fe}^{3+})$ . Finally, the partial spectra originating from excited states ( $\nu \geq 3$ ) belong to the delocalized spectrum type, i.e. they have averaged parameters. The delocalized spectrum component has an appreciable intensity and is clearly visible in the total spectrum. The spectrum consists of three doublets, two of them localized and one delocalized. At  $T = T_c$  the spectrum is averaged. Thus, the Mössbauer spectrum of type II is feasible under intermediate vibronic coupling. In the case of weaker coupling ( $\nu = 2$ ) and a not too large electron transfer parameter ( $t = 1$ ) and intercluster interaction ( $Ld_0^2/\hbar\omega = 1$ ), the total spectrum at relatively low temperatures approximates a superposition of  $\text{Fe}^{2+}$  and  $\text{Fe}^{3+}$  spectra, because the contribution of delocalized states is small. When the temperature rises, the contribution of delocalized states significantly increases. When summing up all delocalized partial spectra along with the two doublets originating from the ground vibrational state, beginning with certain temperatures at which the excited vibrational levels are effectively populated, there obviously appears also an averaged spectrum of a delocalized type. This effect of coexistence of localized and delocalized spectra is very clearly seen in Fig. 37c. At  $T = 0.9005 T_c$  the delocalized component becomes more intensive, its intensity making up about a half of the whole spectrum intensity. Since the localized spectrum portion is concentrated in two doublets, the delocalized portion seems visually much more intensive, this effect becomes more pronounced due to the fact that the delocalized component is slightly broadened and is distinctly resolved against the background of two doublets. Therefore, the vibronic theory of phase transitions provides a precise physical explanation of the coexistence of localized and delocalized spectra discovered in experiments of Hendrickson's group. We can also see that there is a full theoretical confirmation of the possibility to observe a strong delocalized spectrum component, which is resolved as it is stated in [112, 115, 116]. The vibronic coupling constant, for which the Mössbauer spectrum contains three doublets, is close to that  $\nu = 1.8$  determined from the JT energy and the energy of the vibrational quantum characteristic for biferrocenium derivatives. At  $T = T_c$  and higher temperatures the calculations lead to the delocalized spectrum experimentally observed. In the case of intermediate coupling  $\nu = 1.5$ ,  $t = 1$  (Fig. 37d)



the partial spectra with  $\nu \geq 2$  become delocalized at relatively low temperatures. However, their contribution to the total spectra is small, and, therefore, at low temperatures the total spectrum is split into two doublets. With the temperature rise two additional doublets appear in the spectrum; their intensity is comparable with the localized spectra intensity. The spectrum of a localized type is mainly due to the contribution of the ground vibronic level ( $\nu = 0$ ). The first vibronic state with  $\nu = 1$  gives two doublets with close quadrupole parameters, which differ essentially from those of  $Fe^{2+}$  and  $Fe^{3+}$ . Therefore, the partial spectrum lines belonging to  $\nu = 1$  can be resolved against the background of two spectrum doublets with  $\nu = 0$ . On the other hand, the delocalized spectrum originating from excited levels with  $\nu \geq 2$  is not intensive enough to prevent the resolution of doublets arising from the state with  $\nu = 1$ . Thus, in the total spectrum there are observed not three but four doublets. This treatment explains the spectra of the compounds biferrocenium hexafluorophosphate [119, 120] and exo,exo-1.12-dimethyl 1.1-ferrocenophanium triiodide [119], for which the best fit procedure gives not two or three but four doublets (spectra of type III). The results obtained within the scope of quantum theory can be qualitatively explained in terms of adiabatic potentials. In the case of strong vibronic coupling under consideration, the lower sheet of the adiabatic potential has two deep minima at all temperatures. The system states near these minima may be regarded with a good accuracy as localized, and close to the levels of a harmonic oscillator. When the temperature changes in the range  $T < T_c$  the levels in two potential wells shift relative to each other, and at  $T = 0.9 T_c$  the 0-th vibrational level of the shallow well resonates with the first vibrational level of the deeper minimum (Fig. 38). The spectrum of localized states of the shallower well may be visualized as being shifted towards higher energies relative to the deep well spectrum. Thus, the excited vibronic states come to resonance. However, due to a large barrier width, tunneling is suppressed, and the partial Mössbauer spectra possess a localized character. When the vibronic coupling constant decreases, the width and height of the barrier between the potential wells diminishes, and for excited states localized in different wells, the tunnel effect becomes possible. The magnitude of

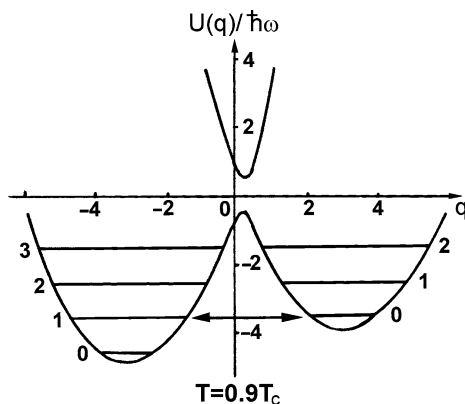


**Fig. 38** Adiabatic potentials in the molecular field approximation:  $\nu = 3$ ,  $t = 0.5$ ,  $\zeta = 1$ ,  $T = 0.9000T_c$

the tunnel splitting increases with the increase of the quantum number of the localized state. Correspondingly, the excited vibronic states become partially or totally delocalized. Depending on the degree of delocalization of the excited vibronic state, the partial spectrum will contain two doublets with quadrupole splittings which differ from  $\Delta E_Q(\text{Fe}^{2+})$  and  $\Delta E_Q(\text{Fe}^{3+})$ , or one doublet with averaged parameters. It should be emphasized that the coexistence of localized and delocalized spectra is essentially a quantum phenomenon closely related to the resonances of the vibronic levels that cannot be explained in the framework of a semiclassical approach.

## 5 Pseudo -Jahn–Teller Problem of the Photochromic Compounds

### 5.1 Photochromic Effect

During last decade the fascinating phenomenon of the photochromic effect, closely related to JTE, became a hot problem of molecular magnetism and spectroscopy, due to its promising application in the design of new memory storage systems at the molecular level. This phenomenon has been discovered and studied in several nitrosyl complexes of transition metal ions [177–182]. At low temperatures, the most extensively studied sodium nitroprusside  $\text{Na}_2[\text{Fe}(\text{CN})_5(\text{NO})] \cdot 2\text{H}_2\text{O}$  (SNP) demonstrates two excited metastable states (MS1 and MS2), induced by visible light in the region 350–600 nm. At temperatures below 150 K, the metastable states are extremely long-living and do not show any indications of spontaneous and thermal decay. Both metastable states can be depopulated by temperature rise, or reversibly converted back to the ground state (GS) by red light irradiation. During the thermal decay of the metastable states, no emission of radiation could be observed in the energy range 0.3–5 eV. Calorimetry experiments [183] show that the MS1 state is higher in energy than the MS2 state. Above 160 K, the decay of the metastable states in SNP obey the Arrhenius law, with the activation energies 0.7 and 0.5 eV for MS1 and MS2, respectively [184]. The change in color exhibited with the generation of the excited MS1 and MS2 states has been proposed as the basis for an information storage system, since information can be written and erased reversibly using light of two different wavelengths [184]. An essential advance in the study of the photochromic effect came from X-ray diffraction experiments [185, 186], with the aid of which the geometries of the ground and the two excited metastable states have been determined. The atomic rearrangements were proved to be far from those that usually accompany optical excitation in molecules. The Fe-(NO) group was found to be linear in the GS. The diffraction evidences a bent geometry of the system in the MS2 state in which NO is sideways bound, while in the MS1 state an interchange of N and O takes place so that the NO group is connected with Fe through oxygen. Mössbauer [187] and electron-spin resonance measurements [188] proved that the GS and both metastable states are diamagnetic. The downshift of the NO stretch

and Fe-(NO) stretch frequencies suggests weaker bonds for MS1 and MS2 [191]. The metastable states with similar properties have been found in several nitrosyl-ruthenium and nitrosyl-osmium complexes so that, in fact, the phenomenon is quite general.

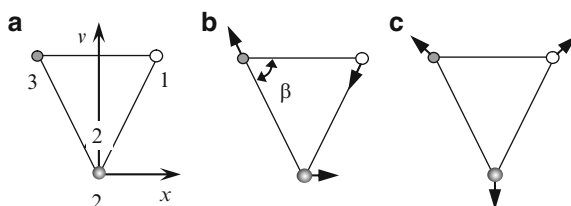
Earlier theoretical studies were focused on the origin of the metastable states. DFT calculations of the energy of the SNP [192–194] as a function of the angle  $\angle\text{FeNO}$  revealed that three minima of the ground term correspond to three possible configurations of the Fe-NO fragment: linear, bent and inverted. At the same time DFT calculations gave a correct order of the energies of the GS, MS1 and MS2 states. In detailed *ab initio* calculations [195] the number of variable structural parameters was extended, and along with the consideration of the ground potential surface of the SNP, the consideration in [195] takes into account the transition states connecting the states GS with MS2 and MS2 with MS1, which elucidates the effect of the transition states on the photo-isomerisation. The JT coupling mechanism is discussed as an origin of the structural rearrangement.

A model of the photochromic effect based on the concept of the pseudo JTE was suggested in [196–197]. This vibronic model allows us to examine the microscopic physical origin of the nuclear rearrangement and the underlying mechanism of the photochromic effect at the electronic level. At the same time the pseudo JTE approach can be considered as a background for the dynamical (quantum-mechanical solution) of the problem of light absorption and emission including the crucial question of interpretation of the anomalous lifetimes for the excited states and shape-functions of the optical bands.

## 5.2 Pseudo Jahn–Teller Vibronic Model for Sodium Nitroprusside

At the first step we consider the FeNO fragment of the whole SNP that is really involved in the photochromic reorganization. Following the idea of the PJT effect we start with the triangular “reference” configuration of the FeNO fragment. For the sake of simplicity the differences in the masses of N and O is neglected, so the symmetry is supposed to be  $C_{2v}$  (Fig. 39). Although the atomic displacements in the photochromic reorganization cannot be considered small, we will exploit a consideration based on normal coordinates. This difficult problem is common for

**Fig. 39** Vibrations of the Fe-(NO) fragment:  
1 – O, 2 – Fe, 3 – N,  
*a* – “reference” configuration,  
*b* – non-symmetric  
 $B_1$  – vibration,  
*c* – full-symmetric  
 $A_1$  – vibration



JT systems with strong coupling, and some efficient approaches have been formulated in the theory of so-called non-rigid molecules. The triangular molecule has two normal vibrational coordinates that span two irreducible representations,  $A_1$  and  $B_1$ . The normal vibrational modes  $Q_{B_1}$  and  $q_{A_1}^{(1)} \equiv q_{A_1}$  of the FeNO fragment are shown in Fig. 39. Further on, the second fully symmetric vibration  $q_{A_1}^{(2)}$  of the triangular moiety will not be taken into account insofar as its effect is similar to that of  $q_{A_1}$ . Starting from the accepted idealized  $C_{2v}$  symmetry of the FeNO fragment of the nitroprusside ion, one can assume that the metastable states are formed upon a light-induced charge transfer from the highest occupied molecular orbital (Fe, mainly  $a_2$ ) to the lowest unoccupied orbitals  $a_1$  and  $b_1$  of mostly  $\pi^*$  NO character [195]. Hereunder, small letters are used for labeling the symmetry of single orbitals, while capital letters denote the states of the whole FeNO moiety. The basis includes the states of the system with the following fixed oxidation degrees of the fragments:

$${}^1A_1(\text{Fe}^{2+}(a_1^2 b_1^2 a_2^2)), \quad {}^1B_2(\text{Fe}^{3+}(a_1^2 b_1^2 a_2) b_1(\pi_x^* \text{NO})), \\ {}^1A_2(\text{Fe}^{3+}(a_1^2 b_1^2 a_2) a_1(\pi_y \text{NO})).$$

These states (Fig. 40) are coupled by the electron transfer from the  $\text{Fe}^{2+}$ -ion to the  $\pi^*$  level of the NO ligand. The PJT problem arises from the mixing of the  ${}^1A_2$  and  ${}^1B_2$  states by the  $B_1$  – vibration of the triangle. The coupling of the states  ${}^1A_1$ ,  ${}^1A_2$ ,  ${}^1B_2$  with the fully symmetric vibration of the FeNO fragment is taken into account as well. In such a way we face a two-mode-three level pseudo JT problem of the type:  $(A_1 + A_2 + B_2) \otimes (A_1 + B_1)$ . The non-diagonal matrix elements  $\langle {}^1A_2 | H_e | {}^1A_1 \rangle$  and  $\langle {}^1B_2 | H_e | {}^1A_1 \rangle$  of the electronic Hamiltonian

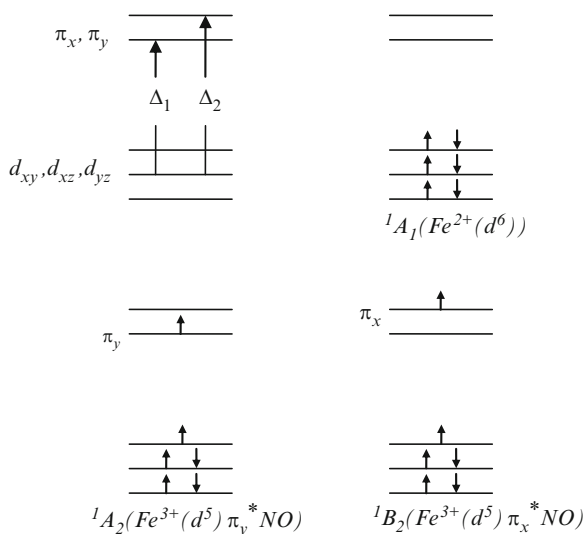


**Fig. 40** Scheme of the electronic states of the Fe-(NO) fragment

$H_e$  represent parameters describing the electron transfer from the  $\text{Fe}^{2+}$ -ion to the  $\pi^*$  level of the NO ligand. At the first step these parameters were put equal to  $\langle {}^1A_2 | H_e | {}^1A_1 \rangle = \langle {}^1B_2 | H_e | {}^1A_1 \rangle = t$ . In the model under consideration three vibronic parameters are involved. The parameter  $V = \langle {}^1A_2 | V_{B_1} | {}^1B_2 \rangle$  characterizes the coupling of the states  ${}^1B_2(\text{Fe}^{3+}(\text{d}^5)\pi_x^*\text{NO})$  and  ${}^1A_2(\text{Fe}^{3+}(\text{d}^5)\pi_y^*\text{NO})$  by the  $B_1$ -mode. The parameters  $\nu_1 = \langle {}^1A_2 | \nu_{A_1} | {}^1A_2 \rangle - \nu$  and  $\nu_2 = \langle {}^1B_2 | \nu_{A_1} | {}^1B_2 \rangle - \nu$ ,  $\nu = \langle {}^1A_1 | \nu_{A_1} | {}^1A_1 \rangle$  describe the interaction of the states  ${}^1A_2$  and  ${}^1B_2$  with the fully-symmetric ( $A_1$ ) mode. The vibronic matrix in the basis of the states  ${}^1A_2$ ,  ${}^1B_2$ ,  ${}^1A_1$  can be represented in the following form:

$$H = \begin{pmatrix} \Delta_2 + \nu_2 q & VQ & t \\ VQ & \Delta_1 + \nu_1 q & t \\ t & t & 0 \end{pmatrix}. \quad (41)$$

To reveal the nature of the strongly localized states it is worthwhile to employ the adiabatic approximation, neglecting thus the nuclear kinetic energy.

### 5.3 Adiabatic Potentials: Formation of Metastable States Through the Pseudo Jahn–Teller Mechanism

The shapes of the adiabatic potential sheets are governed by eight parameters:  $V$ ,  $\nu_1$ ,  $\nu_2$ ,  $\Delta_1$ ,  $\Delta_2$ ,  $t$ ,  $\omega_{B_1}$ ,  $\omega_{A_1}$ . In order to elucidate the conditions which favor the photochromic effect, the values of the above-mentioned parameters are to be discussed. For a reasonable value of  $k \approx 10^5$  dyn/cm the frequencies  $\omega_{B_1}$  and  $\omega_{A_1}$  are estimated as 340 and 400  $\text{cm}^{-1}$ , respectively. The energy gaps  $\Delta_2$  and  $\Delta_1$  can be approximately identified with those between the HOMO and the split components of LUMO in the MS2 state. These values are calculated in [195] by the DFT method and prove to be equal to  $\Delta_2 = 21,185 \text{ cm}^{-1}$  and  $\Delta_1 = 15,850 \text{ cm}^{-1}$ . The vibronic coupling parameter  $V$  was roughly evaluated under the assumption that  $\nu_1 = \nu_2 = 0$ ,  $t = 0$ . If the energy

$$E_a = \hbar\omega_{B_1}(\Delta_1 + \Delta_2)^2/8V^2 + V^2/2\hbar\omega_{B_1} - (\Delta_1 + \Delta_2)/2 \quad (42)$$

of the thermally activated transition from the sheet  $u_2(q = 0, Q)$  to the sheet  $u_1(q = 0, Q)$  is set to be equal to the value of 0.5 eV estimated by the calorimetry methods [183] for the MS2 state, one can estimate the parameter  $V$  as  $V = 9.65\omega_{B_1}$ . The parameter  $t$  was taken in the range  $0 \leq t \leq 10\omega_{B_1}$ . Insofar as the energy gap  $\Delta_2$  exceeds significantly the gap  $\Delta_1$ , the parameter  $\nu_2$  was taken bigger than  $\nu_1$ . In Fig. 41 the ground adiabatic potential sheet is shown for an appropriate set of parameters. One can see that the lower adiabatic potential branch has three minima; the energies of these minima are successively increased, so that the energy of the ground minimum is  $-1.93 \hbar\omega_{B_1}$ , whereas the energies of the excited minima are equal to  $-1.15 \hbar\omega_{B_1}$  and  $-0.84 \hbar\omega_{B_1}$ . In such a way, at temperatures below

**Fig. 41** The lower adiabatic potential sheet  $U_1(q, Q)$ ,  
 $V = 9.8\hbar\omega_{B_1}$ ,  $t = 5.5\hbar\omega_{B_1}$ ,  
 $\nu_2 = 6.2\hbar\omega_{B_1}$ ,  $\nu_1 = 1.5\hbar\omega_{B_1}$ ,  
 $\Delta_1 = 15850\text{ cm}^{-1}$ ,  
 $\Delta_2 = 21185\text{ cm}^{-1}$ ,  
 $\omega_{B_1} = 340\text{ cm}^{-1}$ ,  
 $\omega_{A_1} = 400\text{ cm}^{-1}$

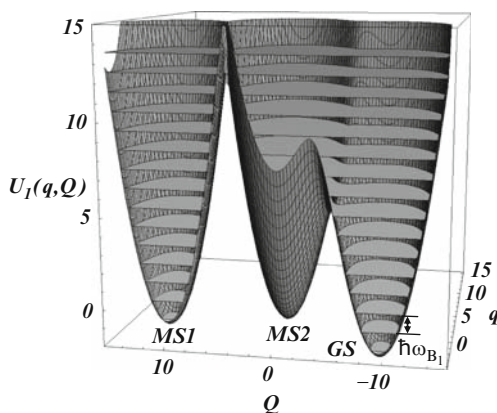


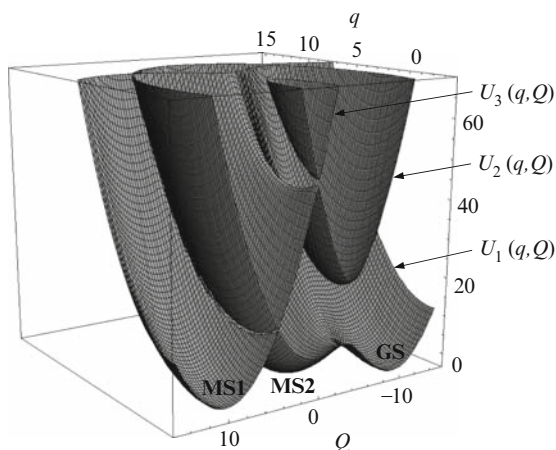
**Table 1** Angles (degrees) for the ground, first and second excited minima of the lower adiabatic potential sheet (the parameters are the same as in Fig. 41)

Minimum	$Q_i$	$q_i$	Angle $\beta$ (theor.)	Angle $\beta$ (exp.[9])
Ground	-9.63	-3.21	146	176
First excited	-0.21	-0.06	74.8	82
Second excited	9.83	-3.28	0.1	3

180K the thermal population of both excited minima is negligible. At the same time Fig. 41 demonstrates that the potential barrier separating the ground and first excited minima is lower than that separating the excited minima. A quantitative estimation of the barrier heights can be made with the aid of Fig. 41, wherein the adiabatic potential wells are cut by horizontal planes separated by the gaps  $\hbar\omega_{B_1}$ . The height of the barrier between the ground and the first excited minima is about  $7.3\hbar\omega_{B_1} \approx 0.3\text{ eV}$ . The barrier between the first and the second excited minima attains the value  $13.7\hbar\omega_{B_1} \approx 0.6\text{ eV}$ . At the next stage the geometrical structure of the Fe-(NO) cluster corresponding to the minima of the ground adiabatic potential surface is determined. In the Table the calculated values of the angle  $\beta_i$  corresponding to the lowest ( $\beta_1$ ) and the excited minima ( $\beta_2$ ,  $\beta_3$ ) of the ground adiabatic potential sheet are given, together with the experimental values of these angles determined by X-ray diffraction studies. In Table 1 the dimensionless coordinates  $Q_i$  and  $q_i$  of the adiabatic potential minima are also listed. For the set of parameters so far defined, the obtained values of the angles  $\beta_i$  are in quite good agreement with experimental data [186]. So, the lowest minimum corresponds to the usual bonding of the Fe- ion with NO-group and can be identified with the ground state. The first excited minimum describes the bent geometry and can be assigned to the MS2 state. The highest minimum relates to a linear configuration in which the NO-ligand has rotated by  $\sim 180^\circ$  compared to the GS. Such an arrangement of the NO-group is characteristic of the MS1-state.

Finally, let us briefly discuss the heights of the barriers separating GS, MS1, MS2 states and the mechanism of population of the metastable states by photoexcitation.

**Fig. 42** The adiabatic potentials  $U_1(q, Q)$ ,  $U_2(q, Q)$ ,  $U_3(q, Q)$  (the parameters are the same as in Fig. 41)



The first excited adiabatic potential sheet  $U_2(q, Q)$  has two minima; the highest sheet  $U_3(q, Q)$  is cone-shaped and possesses one minimum. The light-induced Franck-Condon transition from the lowest minimum (GS) of the ground adiabatic potential sheet  $U_1(q, Q)$  to the sheet  $U_3(q, Q)$  leads to the population of the single minimum of this sheet; then the relaxation can be followed by a radiative (or non-radiative) de-excitation onto the ground adiabatic potential surface, populating thus with a significant probability the local minimum MS2. Another way of depopulation of the minimum of the branch  $U_3(q, Q)$  passes through two minima of the middle adiabatic potential sheet  $U_2(q, Q)$ . In this case GS, MS2 and MS1 may be populated. The light-induced transition of the system from GS to the  $U_2(q, Q)$  surface results in the population of the highest minimum of this surface. The decay of this excitation may lead to the population of GS and MS2. The optical transitions from MS1 and MS2 to  $U_2(q, Q)$  have lower energies than that from GS to  $U_3(q, Q)$ . However, the transition  $MS1 \rightarrow U_2(q, Q)$  populates MS2, whereas the transition  $MS2 \rightarrow U_2(q, Q)$ , in its turn, transfers the system to MS1. In such a way, the consideration carried out shows that, in the framework of the adiabatic potential scheme, it is possible to pass from GS into MS1 and MS2, from MS1 into MS2, and vice versa, in qualitative agreement with experiment.

The calculated barrier heights are of the same order of magnitude as the experimental values of the activation energies for the metastable states MS1 and MS2 [184]. The obtained relation between the barrier heights (Fig. 41) separating the GS-state and the metastable states seems to be also correct. At the same time the order of the minima of the ground potential sheet, the higher barrier between the MS1 and MS2 states along with the absence of a direct contact between the potential wells corresponding to GS and MS1 leads to the conclusion that the model gives a decay temperature for the MS2-state lower than that of the MS1-state, and this is in agreement with experimental data [183, 184]. In spite of the fact that the calculated barriers are smaller than the experimental values of the activation energies these barriers are sufficiently large to explain the long lifetimes of the MS1 and MS2 states (Fig. 42).

## 6 Dynamic Vibronic Problem of the Valence-Tautomeric Interconversion in Cobalt Compounds

### 6.1 Tautomeric Compounds [Low-Spin



The concept of valence tautomerism was introduced to define the properties of a molecular adduct  $\text{A} - \text{D}^+$  ( $\text{A}$  = acceptor,  $\text{D}$  = donor) whose electronic ground state is described by two or more isomers with different charge distributions. The interconversion between different valence tautomers is accomplished by an intramolecular electron transfer according to the following equation  $\text{A} - (\text{D}^+) \leftrightarrow (\text{A}^+) - \text{D}$ . To obtain molecular adducts characterized as valence tautomers, two conditions must be simultaneously satisfied: the degree of covalency in the interaction between  $\text{A}$  and  $\text{D}$  must be low, and the energy of the frontier orbitals of the two counterparts must be similar. The transition metal complexes of Co, Mn, Fe, Rh, Ir and Cu with ligands derived from substituted *o*-benzoquinones show valence tautomerism [191–211]. Large changes in optical and magnetic properties are found to associate with valence tautomeric transformation. The most pronounced effects in spectroscopic and thermodynamic properties have been identified for Co complexes with two *o*-quinone derived ligands, for which the interconversion can be described by the equation:  $[\text{low-spin}(\text{ls})\text{-Co}^{3+}(\text{N}^{\wedge}\text{N})\text{sq}^1\text{-cat}^{2-}] \leftrightarrow [\text{high-spin}(\text{hs})\text{-Co}^{2+}(\text{N}^{\wedge}\text{N})(\text{sq}^{-1})_2]$ , where  $\text{N}^{\wedge}\text{N}$  is a chelating diiminium ligand; the ligands semiquinone (sq) and catecholate (cat) can be obtained from *o*-quinone by an addition of one and two electrons to the empty  $\pi^*$  molecular orbital [218]. The dynamical processes in a valence tautomeric cobalt complex are schematically shown in Fig. 43.

For a complex in solution the valence tautomeric interconversion occurs gradually over a large temperature range of about 100K, and the magnetic moment increases from  $1.73 \mu_{\text{B}}$  at low temperatures to  $4\text{--}4.4 \mu_{\text{B}}$  at higher temperatures. With temperature growth, the visible absorption spectrum characteristic of the ls-Co(III)-tautomer completely converts to that belonging to the hs-Co(II)-tautomer [214]. At low temperatures in the near infrared region of spectrum of complexes in solution a band appears at 2,500 nm [214]. The intensity of this band decreases significantly as the temperature is increased from 15 to 295 K. In the present section we discuss the magnetic properties of the valence tautomeric Co-complex, the role of JTE in the formation of the optical band in the near infrared range, the nature of this band, and the reasons of its temperature transformation. The dynamic vibronic JT problem appears in the description of the magnetic and optical properties of the Co valence tautomeric complex due to the coupling through electron transfer of the localized molecular states arising from configurations  $[\text{ls-Co(III),cat,sq}]$  and  $[\text{ls-Co(II),sq,sq}]$  of the complex. The description of the magnetic properties of valence tautomeric systems based on the adiabatic approximation has been carried out in [212]. The model developed in [212] involved electron transfer processes, magnetic exchange, vibronic and cooperative interactions. The validity of the adiabatic approximation



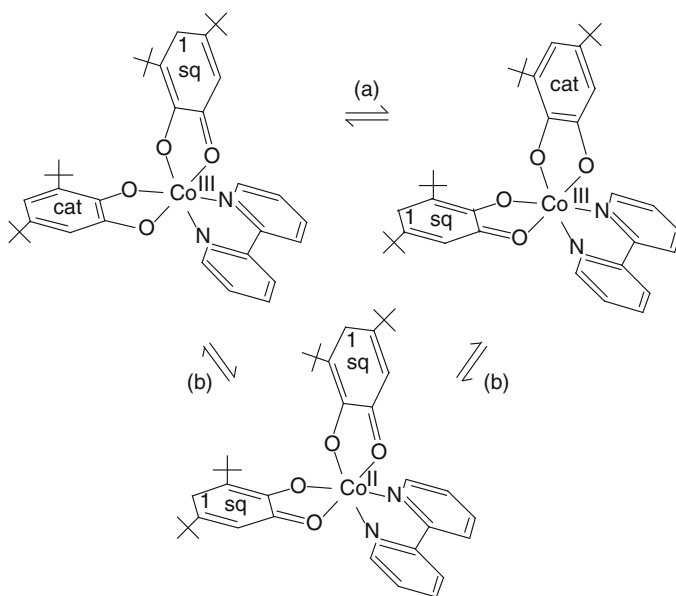


**Fig. 43** Possible intramolecular electron transfer processes present in a cobalt complex with two semiquinone anion ligands

for the evaluation of the optical JT band is restricted to the case of strong vibronic coupling and/or high temperatures. Detailed studies also show that in JT systems some regions of the absorption spectrum for visible light for whose calculation the non-adiabatic effects are important cannot be described, even in the favorable case of high temperatures and strong vibronic coupling [225]. Similar problems also appear in the description of optical bands of tautomeric systems arising in the infrared region and are related to light-induced electron transfer within a single valence tautomeric molecule, so far as in this case the mixing of the tunnel states of the molecule by molecular vibrations results in the pseudo JTE. An adequate description requires quantum-mechanical consideration that takes also the kinetic energy of the nuclei into consideration.

## 6.2 Dynamic Vibronic Problem for a Valence Tautomeric System

A vibronic dynamic problem of valence tautomerism in a single molecule was discussed in [221, 222]. As a basis set we take the following states of the molecule with localized electrons arising from its four configurations:

- I.  $1s\text{-Co(III)}(a), \text{cat}(b), \text{sq}(c)$ ;
- II.  $1s\text{-Co(III)}(a), \text{sq}(b), \text{cat}(c)$ ;
- III.  $1s\text{-Co(II)}(a), \text{sq}(b), \text{sq}(c)$ ;

IV.  $hs\text{-Co(II)}(a),sq(b),sq(c)$ ;

In the molecular states arising from configurations I and II the total spin of the molecule is  $1/2$ . For states arising from configuration III the spin values are  $1/2, 1/2$  and  $3/2$ . Configuration IV gives rise to spin states  $1/2, 3/2, 3/2, 5/2$ . States of configurations I, II possessing the spin  $1/2$  are connected by electron transfer with same spin state of configuration III. The electron transfer between states I and II is also included in the model owing to the mixed-valence structure of ligands. The key parameters of the problem are the multielectronic exchange parameters  $J_3$  and  $J_4$  for states of configurations III and IV, the parameters  $t_1$  and  $t_2$  that describe the electron transfer from the  $cat^{2-}$  ligand to the  $ls\text{-Co(II)}$ -ion and from the  $cat^{2-}$  to  $sq^{1-}$  ligand. The interaction of the Co-ion with the breathing  $A_1$  mode is taken into account. Correspondingly, two vibronic parameters  $\nu_3$  and  $\nu_4$  which describe the interaction of the Co-ion in the states  $ls\text{-Co}^{2+}$  and  $hs\text{-Co}^{2+}$  with the  $A_1$  mode appear in the problem. For numerical calculations of the eigenvalues and eigenvectors of the vibronic dynamic problem 60 unperturbed oscillator states were taken into account (general dimension of the vibronic matrix  $360 \times 360$ ).

### 6.3 Magnetic Moments and Absorption Bands

The Van-Vleck equation [78] and the vibronic levels are used for the calculation of the magnetic moment of the valence tautomeric molecule. The following values of the key parameters were utilized in calculations:  $\nu_3 = 1,050\text{ cm}^{-1}$ ,  $\nu_4 = 1,575\text{ cm}^{-1}$ ,  $J_3 = 40\text{ cm}^{-1}$ ,  $J_4 = 30\text{ cm}^{-1}$ ,  $\Delta_3 = 1,145\text{ cm}^{-1}$ ,  $\Delta_4 = 2,018\text{ cm}^{-1}$ ,

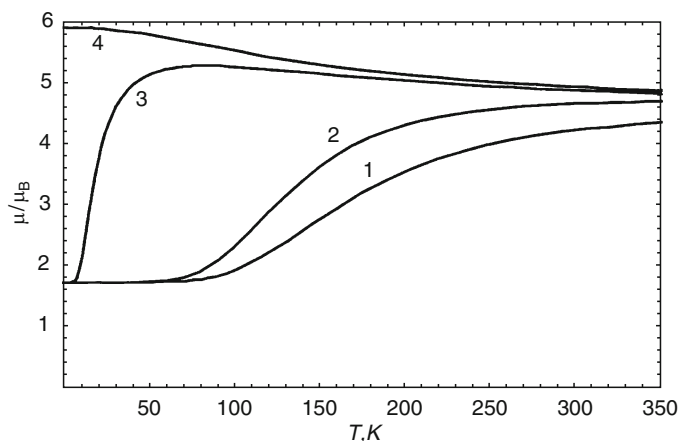


**Fig. 44** Plot of the magnetic moment versus temperature for the parameters:  $\Delta_3 = 1,145\text{ cm}^{-1}$ ,  $\Delta_4 = 2,018\text{ cm}^{-1}$ ,  $\nu_3 = 1,050\text{ cm}^{-1}$ ,  $\nu_4 = 1,575\text{ cm}^{-1}$ ,  $J_3 = 40\text{ cm}^{-1}$ ,  $J_4 = 30\text{ cm}^{-1}$ ,  $\hbar\omega = 390\text{ cm}^{-1}$ ,  $t_2 = 73\text{ cm}^{-1}$ ; (1), (2)  $t_1 = 1,075\text{ cm}^{-1}$ ; (3)  $t_1 = 850\text{ cm}^{-1}$ ; (4)  $t_1 = 800\text{ cm}^{-1}$ . The curves 1 and 2 were calculated in the dynamic and semiclassical models, respectively

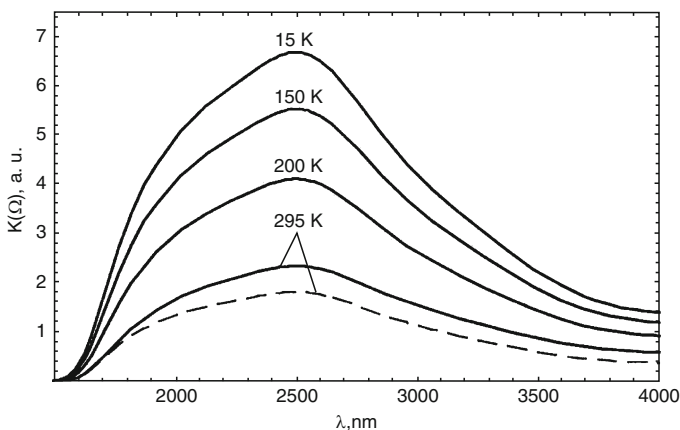


**Fig. 45** Temperature-dependence of the absorption coefficient for the parameters:  $\Delta_3 = 1,145 \text{ cm}^{-1}$ ,  $\Delta_4 = 2,018 \text{ cm}^{-1}$ ,  $t_1 = 1,075 \text{ cm}^{-1}$ ,  $t_2 = 73 \text{ cm}^{-1}$ ,  $J_3 = 40 \text{ cm}^{-1}$ ,  $J_4 = 30 \text{ cm}^{-1}$ ,  $\nu_3 = 1,050 \text{ cm}^{-1}$ ,  $\nu_4 = 1,575 \text{ cm}^{-1}$ ,  $\varphi = 130^\circ$ ,  $\hbar\omega = 390 \text{ cm}^{-1}$ ,  $T = 295 \text{ K}$ : dashed line - contribution to the band shape of the optical transitions between the ground vibronic state and excited ones.

$t_1 = 1,075 \text{ cm}^{-1}$ ,  $t_2 = 73 \text{ cm}^{-1}$ ,  $\hbar\omega = 390 \text{ cm}^{-1}$  (Fig. 44, curves 1, 2), where  $\Delta_3$  and  $\Delta_4$  are the energies of the states arising from configurations III and IV with allowance only for crystal-field splitting and intra- and intercenter Coulomb interactions, these energies are counted off from the energy of the configurations I and II. The values of the parameters  $\nu_j$ ,  $J_j$ ,  $\Delta_j$ , ( $j = 3, 4$ ),  $t_1$ ,  $t_2$  are close to those estimated in [212] from the crystal field model and experimental data. The magnetic moment (Fig. 44) increases gradually from  $1.73 \mu_B$  to  $4.34 \mu_B$  with the increase of temperature. The valence tautomeric interconversion takes place in the temperature range of about 100 K. The obtained values of the magnetic moment at low and high temperatures, as well as the width of the temperature range wherein the transformation occurs, are close to experimental ones. Curves 3 and 4 in Fig. 44 are calculated with the same parameters  $\Delta_j$ ,  $\nu_j$ ,  $J_j$ ,  $t_2$  as curves 1 and 2, but smaller values for  $t_1$  are taken. For  $t_1 = 850 \text{ cm}^{-1}$  the magnetic moment increases abruptly (Fig. 44, curve 3). For the parameter  $t_1 = 800 \text{ cm}^{-1}$  (Fig. 44, curve 4) the low-temperature limit of the magnetic moment corresponds to the total spin  $S = 5/2$ . For all temperatures the band  $K(\Omega) \sim \Omega F(\Omega)$  (Fig. 45) remains essentially asymmetric and possesses a shoulder in the high-frequency range ( $\lambda = 2,000 \text{ nm}$ ) and a long tail in the low-frequency range. The position of the band at  $\lambda_m = 2,500 \text{ nm}$  remains unchanged with temperature rise. The intensity of the charge transfer band diminishes with temperature rise. The peculiarities of the temperature behavior of the charge-transfer band can be explained as follows. In the temperature range 15–70 K the lowest two vibronic levels with  $\nu = 0$  and  $\nu = 1$  corresponding to  $S = 1/2$  are mainly populated. Therefore, at these temperatures the charge-transfer band has its maximum intensity, while the magnetic moment acquires its minimum value  $1.73 \mu_B$ . The obtained temperature-dependence of the charge transfer band is in

accordance with that of the magnetic moment and qualitatively agrees with the experimental data [214].

## 7 Final Remarks

In this review we have presented a brief outline of the applications of the JT concepts in molecular magnetism. A general conclusion that can be derived from this review is that the JTE is one of the most general concepts that allows to comprehend a wide class of phenomena closely related to the main trends in molecular magnetism. Essential results were elucidated in the study of so-called spin-frustrated metal clusters possessing orbitally degenerate states. In these systems JT coupling produces a dynamical symmetry lowering and thus reduces the anisotropy caused by AS exchange, giving rise to a specific field and temperature dependence of magnetization. The problem of spin-frustration and consequences of orbital degeneracy are shown to have deep consequences in the topical areas of solid state physics [223]. It was shown that all aspects of the problem of mixed valency are closely related to the JTE. JT coupling was shown to determine the degree of localization of the mobile electron in MV clusters, and it thus directly affects all spectroscopic and magnetic properties of MV compounds. It is also demonstrated that the concept of pseudo JTE lies in the background of the cooperative phenomena, like charge and structural ordering in extended systems comprising MV units as building blocks. It is remarkable that the quantum properties of the JT vibrations in extended systems, like quantum resonances, have a clear signature in the experimental observation (Mössbauer spectra) and can be described within the so-called quasidynamical approximation. It was demonstrated that a JT-based approach allows one to understand the microscopic origin of the photochromic transformation and formation of the extremely long-living metastable states in photochromic systems. Finally, a crucial role of the pseudo JT coupling mixing metal-ligand orbitals is indicated as a microscopic origin of tautomeric transformations and the origin of the magnetic properties and intervalence absorption in this class of optically active compounds.

In this article we have not discussed an important problem of exchange interactions in magnetic clusters based on orbitally degenerate metal ions inherently related to the magnetic manifestations of JTE. This issue (which is a key issue for the problem of structural and charge ordering in crystals [112, 113]) deserves a special review, which is why here we give only some general comments and references. If the constituent ions are placed in a high-symmetric (octahedral) surrounding, their ground states can be orbitally degenerate, so that the electronic shells carry not only spin but also orbital angular momentum contributions. Under this condition the conventionally accepted HDVV Hamiltonian is inapplicable even as a rough approximation. A general form of the effective Hamiltonian for the systems containing ions with the unquenched orbital angular momenta has been proposed in [113] and deduced in the general form in [224–230]. The exchange interaction in clusters comprising orbitally degenerate ions can not be expressed in terms of

spin operators only, like for the HDVV Hamiltonian supplemented by relatively small anisotropic contributions. The Hamiltonian in the case of degeneracy becomes orbitally dependent, which means that it includes along with the HDVV contribution also orbitally-dependent terms that are, in general, of the same significance as spin-spin coupling. The main magnetic manifestations of these new kinds of interaction is a strong magnetic anisotropy of orbital nature. Since the electronic shells are orbitally degenerate, the JT coupling should be taken into account along with the orbitally dependent terms in the effective Hamiltonian. Since the JTE can be considered (in terms of the adiabatic approach) as a symmetry lowering, a significant reduction of the magnetic anisotropy by the JTE is expected, like it was observed in the degenerate spin-frustrated systems so far discussed. Quantum-mechanical *ab initio* calculations of orbitally dependent exchange interactions in a series of cyanide bridged systems, as well as the microscopic approach to the evaluation of the JT coupling parameters, are given in [231–236].

In the limit of strong JTE the distortions become stable so that the degeneracy is removed. In the adiabatic limit the ground states are orbital singlets so the magnetic interactions can be treated within the HDVV Hamiltonian. This case of strong JT coupling is observed in the so-called *Mn*12-acetate that was the first SMM discovered [1, 2]. The system is composed of a tetrahedral core of oxygen-coordinated  $Mn^{4+}$  ions, which are surrounded by a ring of eight  $Mn^{3+}$  ions with oxo and acetate coordination. Antiferromagnetic interactions between the  $Mn^{4+}$  and  $Mn^{3+}$  ions lead to an  $S = 10$  ground state. The  $Mn^{3+}$  coordination environment is JT distorted [71–73] and the distortions are correlated within the molecule to give a structure with the specific axes of local anisotropic contributions. The concerted action of the resulting  $Mn^{3+}$  single-ion anisotropies leads to an overall easy-axis-type anisotropy of the  $S = 10$  cluster ground state. It is just this anisotropy that creates a barrier for the reversal of magnetization in SMM *Mn*12-acetate. As was demonstrated in [91], the situation of a strong JTE resulting in static distortion occurs in a ferromagnetically coupled *Mn*<sub>19</sub> aggregate with a record  $S = 83/2$  ground spin state. This shows that the JT based “cooperativity” at the molecular level is a quite common (at least for Mn compounds) phenomenon for high-nuclearity magnetic clusters that is closely related to a general problem of interplay between orbital ordering and cooperative JTE [104, 112–114].

Finally, an interesting area of magnetoelastic instability resulting in field-induced cooperative phenomena in molecule-based magnets has recently been opened [189, 190]. This area is expected to be promising in the control of the properties of molecular magnetic materials by means of external fields.

**Acknowledgements** This review article is partially based on our papers published in coauthorship with M. Belinsky, J.J. Borrás-Almenar, J.M. Clemente-Juan, E. Coronado, A. Müller, S. Ostrovsky, O. Reu, A. Tarantul. B.T. thanks Israel Science Foundation for the financial support (grant no. 168/09). We thank our colleagues for the long-term collaboration and many fruitful discussions. Financial support from the German-Israeli Foundation for Scientific Research and Development (grant G-775–19.10/2003) and USA-Israel Binational Science Foundation (Grant No. 2006498) is gratefully acknowledged. Financial support from the Supreme Council for Science and Technological Development of Moldova is also appreciated.

## References

1. D. Gatteschi, R. Sessoli, *Angew. Chem. Int. Ed.*, **42**, 268 (2003)
2. D. Gatteschi, R. Sessoli, R.J. Villain, *Molecular Nanomagnets* (Oxford University Press, Oxford, 2006)
3. D. Gatteschi, R. Sessoli, *J. Mag. Mag. Mat.* **272–276**, 1030 (2004)
4. A. Bencini, D. Gatteschi, *Electron Paramagnetic Resonance of Exchange Coupled Systems* (Springer, Berlin, 1990)
5. O. Kahn, *Molecular Magnetism* (VCH, New York, 1993)
6. R. Willett, D. Gatteschi, O. Kahn (eds.), *Magneto-structural Correlation in Exchange Coupled Systems*, NATO ASI Series C140 (Dordrecht, Kluwer, 1985)
7. J. Miller, A. Epstein, *MRS Bull.* **21** (2000)
8. G. Christou, D. Gatteschi, D.N. Hendrickson, R. Sessoli, *MRS Bull.* **25**, 66 (2000)
9. R. Sessoli, H.-L. Tsai, A.R. Schake, S. Wang, J.B. Vincent, K. Folting, D. Gatteschi, G. Christou, D.N. Hendrickson, *J. Am. Chem. Soc.* **115**, 1804 (1993)
10. R. Sessoli, D. Gatteschi, A. Caneschi, M.A. Novak, *Nature* **365**, 141 (1993)
11. J.M. Clemente-Juan, E. Coronado, *Coord. Chem. Rev.* **193–195**, 361 (1999)
12. M. Verdaguer, A. Bleuzen, J. Vaissermann, M. Seuleiman, C. Desplanches, A. Scuiller, C. Train, G. Gelly, C. Lomench, I.V.P. Rosenman, C. Cartier, F. Villian, *Coord. Chem. Rev.* **190–192**, 1023 (1999)
13. B.S. Tsukerblat, M.I. Belinsky, *Magnetochemistry and Radiospectroscopy of Exchange Clusters*; Pub. Stiintsa (Acad. Sci. Moldova), Kishinev, 1983 (Rus)
14. B.S. Tsukerblat, M.I. Belinskii, V.E. Fainzilberg, *Magnetochemistry and Spectroscopy of Transition Metal Exchange Clusters*, in *Soviet Sci. Rev. B*, vol. 9, ed. by M.E. Vol'pin (Harwood Academic, New York, 1987), pp. 337–481
15. J.J. Borrás-Almenar, J.M. Clemente-Juan, E. Coronado, A.V. Palii, B.S. Tsukerblat, in *Magnetoscience-From Molecules to Materials*, ed. by J. Miller, M. Drillon (Wiley, New York, 2001), pp. 155–210
16. B.S. Tsukerblat, *Group Theory in Chemistry and Spectroscopy* (Dover, Mineola, New York, 2006)
17. V.Ya. Mitrofanov, A.E. Nikiforov, V.I. Cherepanov, *Spectroscopy of Exchange-Coupled Complexes in Ionic Crystals* (Nauka, Moscow, 1985) (Rus)
18. E. Coronado, R. Georges, B.S. Tsukerblat, in *Localized and Itinerant Molecular Magnetism: From Molecular Assemblies to the Devices*, NATO ASI Series, ed. by E. Coronado, P. Delhaes, D. Gatteschi, J. Miller (Kluwer, Dordrecht, 1996), pp. 65–84
19. J.M. Clemente, R. Georges, A.V. Palii, B.S. Tsukerblat, *Exchange Interactions: Spin Hamiltonians*, *ibid.*, pp. 85–104
20. R. Böca, *Theoretical Foundations of Molecular Magnetism* (Elsevier, Amsterdam, 1999)
21. B. Tsukerblat, *Inorg. Chim. Acta*, **361**, 3746 (2008)
22. E. Coronado, J.R. Galán-Mascarós, C.J. Gómez-García, V. Laukhin, *Nature*, **408**, 447 (2000)
23. F. Palacio, J.S. Miller, *Nature*, **408**, 421 (2000)
24. M. Tamura, Y. Nakagawa, D. Shiomi, Y. Nozawa, M. Hosokoshi, M. Ishikawa, M. Takahashi, M. Kinoshita, *Chem. Phys. Lett.* **186**, 401 (1991)
25. F. Palacio, G. Antorrena, M. Castro, M. Brunel, J.M. Rawson, J.M. Smith, J.N.B.N. Bricklebank, J. Novoa, C. Ritter, *Phys. Rev. Lett.* **79**, 2336 (1997)
26. M. Leuenberger, D. Loss, *Nature* **410**, 789 (2001)
27. D.P. DiVincenzo, *Fortschr. Phys.* **48**, 771 (2000)
28. W. Wersndorfer, *Nat. Mater.* **6**, 174 (2007)
29. J. Lehmann, A. Gaita-Arino, E. Coronado, D. Loss, *Nature Nanotechnology*, **2**, 312 (2007)
30. F. Troiani, A. Ghirri, M. Affronte, S. Carretta, P. Santini, G. Amoretti, S. Piligkos, G. Timco, R.E.P. Winpenny, *Phys. Rev. Lett.* **94**, 207208–1 (2005)
31. M. Affronte, F. Troiani, A. Ghirri, S. Carretta, P. Santini, V. Corradini, R. Schuecker, C. Muryn, G. Timco and R.E. Winpenny, *Dalton Trans.* 2810 (2006)

32. M. Affronte, F. Troiani, A. Ghirri, A. Candini, M. Evangelisti, V. Corradini, S. Carretta, P. Santini, G. Amoretti, F. Tuna, G. Timco and R.E. Winpenny, *J. Phys. D: Appl. Phys.* **40**, 2999 (2007)
33. S. Bertaina, S. Gambarelli, T. Mitra, B. Tsukerblat, A. Müller, B. Barbara, *Nature* **453**, 20 (2008)
34. P.C.E. Stamp, *Nature* **453**, 167 (2008)
35. R.E.P. Winpenny, *Angew. Chem. Int. Ed.* **47**, 2 (2008)
36. D. Stepanenko, M. Trif, D. Loss, *Inorg.Chim.Acta.* **361**, 3740 (2008)
37. A. Ardavan, O. Rival, J.J.L. Morton, S. Blundell, A.M. Tyryshkin, G.A. Timco, E.P. Winpenny, *Phys. Rev. Lett.* **98**, 057201 (2007)
38. F.K. Larsen, E.J.L. McInnes, H. El Mkami, J. Overgaard, S. Piligkos, G. Rajaraman, E. Rentschler, A.A. Smith, G.M. Smith, V. Boote, M. Jennings, G.A. Timco, R.E.P. Winpenny, *Angew. Chem. Int. Ed.* **42**, 101–105 (2003)
39. A. Morello, P.C.E. Stamp and I.S. Tupitsyn, *Phys. Rev. Lett.*, **97**, 207206 (2006)
40. S.B. Braun-Sand, O. Wiest, *J. Phys. Chem. A*, **107**, 285–291 (2003)
41. V.V. Dobrovitski, M.I. Katsnelson, B.N. Harmon, *Phys. Rev. Lett.* **84**, 3458 (2000)
42. P. Gütllich, Y. Garcia, T. Woike, *Coordination Chemistry Reviews* **219–221**, 839 (2001)
43. A.B. Gaspar, V. Ksenofontov, M. Sereidyuk, P. Gütllich, *Coord. Chem. Rev.* **249**, 2661 (2005)
44. P. Gütllich, Y. Garcia, *The Encyclopedia of Materials: Science and Technology* (Elsevier Science, Amsterdam, 2001), pp. 6951–6955
45. R. Englman, *The Jahn–Teller Effect in Molecules and Crystals* (Wiley, London, 1972)
46. I.B. Bersuker, V.Z. Polinger, *Vibronic Interactions in Molecules and Crystals* (Springer-Verlag, Berlin, 1989)
47. I.B. Bersuker, *The Jahn–Teller Effect* (Cambridge University Press, Cambridge, 2006)
48. I.E. Dzyaloshinsky, *Zh. Exp. Teor. Fiz.* **32**, 1547 (1957) [*Sov. Phys. JETP.*, **5**, 1259 (1957)]
49. T. Moria, *Phys. Rev.* **120**, 91 (1960)
50. B.S. Tsukerblat, M.I. Belinsky, A.V. Ablov, *Phys. Stat. Solidi (b)* **51**, K71 (1972)
51. M.I. Belinskii, B.S. Tsukerblat, *Fizika. Tverdogo Tela (Russian)* **15**, 29 (1973)
52. B.S. Tsukerblat, M.I. Belinskii, A.V. Ablov, *Fiz.. Tverd. Tela (Rus)* **16**, 989 (1974)
53. B.S. Tsukerblat, B. Ya. Kuavskaya, M.I. Belinskii, A.V. Ablov, V.M. Novotortsev, V.T. Kalinnikov, *Theor. Chim. Acta.* **38**, 131 (1975)
54. V.E. Fainzilberg, M.I. Belinskii and B.S. Tsukerblat, *Mol. Phys.* **44**, 1177 (1981); **44**, 1195 (1981); **45**, 807 (1982)
55. J. Yoon, L.M. Mirica, T.D.P. Stack, E.I. Solomon, *J. Am. Chem. Soc.* **126**, 12586 (2004)
56. A. Müller, J. Döring, *Angew. Chem. Int. Ed. Engl.* **27**, 1721 (1988)
57. D. Gatteschi, L. Pardi, A.-L. Barra, A. Müller, J. Döring, *Nature* **354**, 465 (1991)
58. A.-L. Barra, D. Gatteschi, L. Pardi, A. Müller, J. Döring, *J. Am. Chem. Soc.* **114**, 8509 (1992)
59. D. Gatteschi, L. Pardi, A.-L. Barra, A. Müller, *Mol. Eng.* **3**, 157 (1993)
60. B.J. Barbara, *J. Mol. Struct.* **656**, 135 (2003)
61. I. Chiorescu, W. Wernsdorfer, A. Müller, H. Bögge, B. Barbara, *Phys. Rev. Lett.* **84**, 3454 (2000)
62. I. Chiorescu, W. Wernsdorfer, A. Müller; S. Miyashita, B. Barbara, *Phys. Rev.B.* **67**, 020402(R) (2003)
63. S. Miyashita, *J. Phys. Soc. Japan.* **65**, 2734 (1996)
64. H. Nojiria, T. Taniguchia, Y. Ajiro, A. Müller, B. Barbara, *Physica B.* **346–347**, 216 (2004)
65. S. Miyashita, *J. Phys. Soc. Japan* **64**, 3207 (1995)
66. B. Tsukerblat, A. Tarantul, A. Müller, *Phys. Lett. A.* **353**, 48 (2006)
67. A. Tarantul, B. Tsukerblat, A. Müller, *Chem. Phys. Lett.* **428**, 361 (2006)
68. B. Tsukerblat, A. Tarantul, A. Müller, *J. Chem. Phys.* **125**, 054714 (2006)
69. A. Tarantul, B. Tsukerblat, A. Müller, *Inorganic Chemistry* **46**, 161 (2007)
70. B. Tsukerblat, A. Tarantul, A. Müller, *J. Mol. Structure*, **838**, 124 (2007)
71. A. Tarantul, B. Tsukerblat, A. Müller, *Solid State Sciences*, **10**, 1814 (2008)
72. A. Tarantul, B. Tsukerblat, A. Müller, *J. Mol. Structure*, **890**, 170 (2008)
73. C.A. Bates and R.F. Jasper, *J. Phys. C: Sol. State Phys.* **4**, 2341 (1971)

74. J.J. Borrás-Almenar, E. Coronado, H.M. Kishinevsky, B.S. Tsukerblat, *Chem. Phys. Lett.* **217**, 525 (1994)
75. O. Kahn, *Molecular Magnetism* (VCH, New York, 1993)
76. C. Zener, *Phys. Rev.* **82**, 403 (1951)
77. P.W. Anderson, H. Hasegawa, *Phys. Rev.* **100**, 675 (1955)
78. P.-G. De Gennes, *Phys. Rev.* **118**, 141 (1960)
79. M.B. Robin, P. Day, *Adv. Inorg. Chem. Radiochem.* **102**, 47 (1967)
80. N.S. Hush, *Prog. Inorg. Chem.* **8**, 391 (1967)
81. S.B. Piepho, E.R. Krausz, P.N. Schatz, *J. Am. Chem. Soc.* **100**, 10, 2996 (1978)
82. B.S. Tsukerblat, A.V. Palii, V.Ya. Gamurar, A.S. Berengolts, H.M. Kishinevsky, *Phys. Lett. A*, **158**, 341 (1991)
83. B.S. Tsukerblat, A.V. Palii, H.M. Kishinevsky, V.Ya. Gamurar, A.S. Berengolts, *Mol. Phys.*, **76**, 1103 (1992)
84. K.Y. Wong, P.N. Schatz, *Prog. Inorg. Chem.* **28**, 369 (1981)
85. J.P. Launay, F. Babonneau, *Chem. Phys.* **67**, 295 (1982)
86. S.A. Borshch, I.N. Kotov, I.B. Bersuker, *Chem. Phys. Lett.* **89**, 381 (1982)
87. R.D. Cannon, L. Montri, D.B. Brown, K.M. Marshall, C.M. Elliott, *J. Am. Chem. Soc.* **106**, 2591 (1984)
88. A.J. Marks, K. Prassides, *New. J. Chem.* **17**, 59 (1993)
89. A.J. Marks, K. Prassides, *J. Chem. Phys.*, **98**, 4805 (1993)
90. J.J. Borrás-Almenar, J.M. Clemente, E. Coronado, B.S. Tsukerblat, A.V. Palii, *Zeitschrift für Physikalische Chemie*, **201**, 189 (1997)
91. S.I. Boldirev, V.Ya. Gamurar, B.S. Tsukerblat, A.V. Palii, *Mol. Phys.* **81**, 621 (1994)
92. J.J. Borrás-Almenar, J.M. Clemente-Juan, E. Coronado, B.S. Tsukerblat, *Chem. Phys.* **195**, 1 (1995)
93. J.J. Borrás-Almenar, J.M. Clemente-Juan, E. Coronado, B.S. Tsukerblat, *Chem. Phys.* **195**, 17 (1995)
94. J.J. Borrás-Almenar, J.M. Clemente-Juan, E. Coronado, B.S. Tsukerblat, *Chem. Phys.* **195**, 29 (1995)
95. S.B. Piepho, *J. Am. Chem. Soc.* **110**, 6319 (1988)
96. J.J. Borrás-Almenar, E. Coronado, S.M. Ostrovsky, A.V. Palii, B.S. Tsukerblat, *Chem. Phys.* **240**, 149 (1999)
97. J.J. Borrás-Almenar, E. Coronado, S.M. Ostrovsky, A.V. Palii, B.S. Tsukerblat, in *Proceedings of XIV International Symposium on Electron-Phonon Dynamics and Jahn–Teller Effect*, ed. by G. Bevilacqua, L. Martinelli, N. Terzi (World Scientific Publishing, Singapore, 1999), p. 293–301
98. A.V. Palii, M.I. Belinsky, B.S. Tsukerblat, *Chem. Phys.* **255**, 51 (2000)
99. J.J. Borrás-Almenar, J.M. Clemente, E. Coronado, S.M. Ostrovsky, A.V. Palii, B.S. Tsukerblat, in *Proceedings of XIV International Symposium on Electron-Phonon Dynamics and Jahn–Teller Effect*, ed. by G. Bevilacqua, L. Martinelli, N. Terzi (World Scientific Publishing, Singapore, 1999), p. 302–310
100. A.X. Trautwein, E. Bill, E.L. Bominaar, H. Winkler, *Struct. Bonding* **78**, 1 (1991)
101. I. Bertini, S. Ciulri, C. Luchinat, *Struct. Bonding* **83**, 1 (1995)
102. X.-Q. Ding, E.L. Bominaar, E. Bill, H. Winkler, A.X. Trautwein, S. Drücke, P. Chaudhuri, K. Wieghardt, *J. Chem. Phys.* **92**, 178 (1990)
103. D.R. Gamelin, E.L. Bominaar, M.L. Kirk, K. Wieghardt, E.I. Solomon, *J. Am. Chem. Soc.* **118**, 8085 (1996)
104. J.J. Borrás-Almenar, J.M. Clemente-Juan, E. Coronado, A.V. Palii, B.S. Tsukerblat, *Chem. Phys.* **254**, 275 (2000)
105. J.J. Borrás-Almenar, J.M. Clemente-Juan, E. Coronado, V. Yu. Mirovitskii, A.V. Palii, B.S. Tsukerblat, in *Vibronic Interactions: Jahn–Teller Effect in Crystals and Molecules*, vol. 19, ed. by M.D. Kaplan, G.O. Zimmerman; NATO Science Series (Kluwer, Dordrecht, 2001), p. 111–122
106. A.V. Palii, *Phys. Lett. A*, **295**, 147 (2002)



107. M.D. Kaplan, B.G. Vekhter, *Cooperative Phenomena in Jahn–Teller Systems* (Plenum, New York, 1995)
108. K.I. Kugel, D.I. Khomskii, *Sov. Phys. Usp.* **136**, 231 (1982)
109. G.A. Gering, K.A. Gering, *Rep. Prog. Phys.* **38**, 1 (1975)
110. T.-X. Dong, M.J. Cohn, D.N. Hendrickson, G.G. Pierpoint, *J. Am. Chem. Soc.* **107**, 4777 (1985)
111. M.J. Cohn, T.-Y. Dong, D.N. Hendrickson, S.J. Geib, A.L. Rheingold, *J. Chem. Soc. Commun* **16**, 1095 (1985)
112. T.-Y. Dong, D.N. Hendrickson, K. Iwai, M.J. Cohn, A.L. Rheingold, H. Sano, I. Motoyama, S.J. Makashima, *J. Am. Chem. Soc.* **107**, 7996 (1985)
113. T.-Y. Dong, D.N. Hendrickson, G.G. Pierpoint, M.F. Moore, *J. Am. Chem. Soc.* **108**, 963 (1986)
114. M.F. Moore, S.R. Wilson, M.J. Cohn, T.-Y. Dong, U.T. Mueller-Westerhoff, D.N. Hendrickson, *Inorg. Chem.* **24**, 4559 (1985)
115. T.-Y. Dong, T. Kambara, D.N. Hendrickson, *J. Am. Chem. Soc.* **108**, 4423 (1986)
116. T.-Y. Dong, T. Kambara, D.N. Hendrickson, *J. Am. Chem. Soc.* **108**, 5857 (1986)
117. M. Sorai, A. Nishimori, D.N. Hendrickson, T.-Y. Dong, M.J. Cohn, *J. Am. Chem. Soc.*, **109**, 4266 (1987)
118. T. Kambara, D.N. Hendrickson, T.-Y. Dong, M.J. Cohn, *Chem. Phys.* **86**, 2362 (1987)
119. J. Webb, P.M. Hagen, R.J. Witterbort, M. Sorai, D.N. Hendrickson, *Inorg. Chem.* **31**, 1791 (1992)
120. S.M. Oh, T. Kambara, D.N. Hendrickson, M. Sorai, K. Kaji, S.E. Woehler, R.J. Witterbort, *J. Am. Chem. Soc.* **107**, 5540 (1985)
121. M. Sorai, K. Kaji, D.N. Hendrickson, S.M. Oh, *J. Am. Chem. Soc.* **108**, 702 (1986)
122. Y. Kaneko, M. Nakano, Sorai M., Jang H.G., Hendrickson D.N., *Inorg. Chem.* **28**, 1067 (1989)
123. M. Nakano, M. Sorai, J.B. Vincent, G. Christou, H.G. Jang, D.N. Hendrickson, *Inorg. Chem.* **26**, 4608 (1989)
124. H.G. Jang, J.B. Vincent, M. Nakano, J.C. Huffman, G. Christou, M. Sorai, R.J. Witterbort, D.N. Hendrickson, *J. Am. Chem. Soc.*, **111**, 7778 (1989)
125. T. Kambara, D.N. Hendrickson, M. Sorai, S.M. Oh, *J. Chem. Phys.* **85**, 2895 (1986)
126. R.M. Stratt, S.H. Adachi, *J. Chem. Phys.* **86**, 7156 (1987)
127. S.H. Adachi, A.E. Panson, R.M. Stratt, *J. Chem. Phys.* **88**, 1134 (1988)
128. S.I. Klokishner, B.S. Tsukerblat, *Pisma Zh. Exp. Teor. Fiz. (Rus)* **45**, 25 (1987)
129. S.I. Klokishner, B.S. Tsukerblat, *Fiz. Tverd. Tela (Rus)*, **29**, 2679 (1987)
130. S.I. Klokishner, B.S. Tsukerblat, *Chem. Phys.* **125**, 11 (1988)
131. S.I. Klokishner, B.S. Tsukerblat, *Fiz. Tverd. Tela (Rus)*, **31**, 85 (1989)
132. B.S. Tsukerblat, Klokishner S.I., *Dokl. Akad. Nauk SSSR (Rus)*, **305**, 144 (1989)
133. S.I. Klokishner, A.V. Pali, B.S. Tsukerblat, *Solid State Communications* **71** (1989) 879
134. B.S. Tsukerblat, Klokishner S.I., in *Electron Magnetic Resonance of Disordered Systems*, ed. by N.D. Iordanov (World Scientific, Singapore, 1989), p. 319–337
135. S.I. Klokishner, B.S. Tsukerblat, *Fiz. Tverd. Tela, (Rus)* **32**, 642 (1990)
136. S.I. Klokishner, A.V. Koryachenko, B.S. Tsukerblat, *Fiz. Tverd. Tela (Rus)* **32**, 311 (1990)
137. S.I. Klokishner, A.V. Koryachenko, B.S. Tsukerblat, *Phys. Stat. Sol. (b)* **160**, 641 (1990)
138. S.I. Klokishner, B.S. Tsukerblat, *Spectroscopy Letters* **23**, 637 (1990)
139. S.I. Klokishner, B.S. Tsukerblat, *Chem. Phys. Lett.* **177**, 543 (1991)
140. A.V. Koryachenko, S.I. Klokishner, B.S. Tsukerblat, *Chem. Phys.* **150**, 295 (1991)
141. A.V. Koryachenko, S.I. Klokishner, B.S. Tsukerblat, *Fiz. Tverd. Tela (Rus)* **33**, 2176 (1991)
142. B.S. Tsukerblat, M.I. Belinskii, S.I. Klokishner *Materials Science*, **17**, 69 (1991)
143. B.S. Tsukerblat, M.I. Belinskii, S.I. Klokishner, *Zh. Strukt. Khim. (Rus)* **31**, 137 (1990)
144. B.S. Tsukerblat, S.I. Klokishner, B.L. Kushkuley, *Chem. Phys.* **166**, 97 (1992)
145. A.V. Koryachenko, S.I. Klokishner, B.S. Tsukerblat, *Chem. Phys.* **161**, 141 (1992)
146. S.I. Klokishner, B.L. Kushkuley, B.S. Tsukerblat, *Fiz. Tverd. Tela (Rus)*, **34**, 832 (1992)
147. B.S. Tsukerblat, S.I. Klokishner, *Chem Phys. Lett.* **203**, 55 (1993)
148. S.I. Klokishner, B.S. Tsukerblat, B.L. Kushkuley, *New Journal of Chemistry*, **17**, 43 (1993)
149. S.I. Klokishner, B.D. Geikhman, *Fiz. Tverd. Tela (Rus)*, **35**, 2239 (1993)

150. S.I. Klokishner, B.S. Tsukerblat, B.L. Kushkuley, *Phys. Lett. A* **179**, 429 (1993)
151. S.I. Klokishner, A.V. Koryachenko, *Fiz. Tverd. Tela (Rus)*, **37**, 422 (1995)
152. S.I. Klokishner, B.D. Geikhsman, *Phys. Stat. Sol.(b)*, **188**, 623 (1995)
153. S.I. Klokishner, I.V. Rementova, *Fiz. Tverd. Tela (Rus)*, **37**, 1342 (1995)
154. S.I. Klokishner, *Phys. Stat. Sol.(b)* **200**, 405 (1997)
155. S.I. Klokishner, A.I. Hincu, *Mol. Cryst. Liq. Cryst.* **305**, 341 (1997)
156. S.I. Klokishner, J. Linares, F. Varret, *Chem. Phys.* **226**, 171 (1998)
157. F. Varret, S. Klokishner, K. Boukheddaden, *Phys. Rev. B*, **60**, 150 (1999)
158. S. Klokishner, F. Varret, K. Boukheddaden, in *Proceedings of the XIY International Symposium on Electron-Phonon Dynamics and Jahn–Teller Effect* (World Scientific Publishing, Singapore, 1999)
159. S. Klokishner, J. Linares, F. Varret, in *Proceedings of the XIY International Symposium on Electron-Phonon Dynamics and Jahn–Teller Effect* (World Scientific Publishing, Singapore, 1999)
160. S.I. Klokishner, L.L. Gorceac, *Chem. Phys. Lett.* **300**, 613 (1999)
161. S.I. Klokishner, O.S. Reu, *Fiz. Tverd. Tela (Rus)* **44**, 779 (2002)
162. S.I. Klokishner, O.S. Reu, *Phys. Stat. Sol. B*, **234**, 611 (2002)
163. K. Boukheddaden, J. Linares, F. Varret, *Chem. Phys.* **172**, 239 (1993)
164. K. Boukheddaden, J. Linares, F. Varret, *Chem. Phys.* **182**, 225 (1994)
165. J. Linares, K. Boukheddaden, F. Varret, *Phys. Rev. B* **49**, 15659 (1994)
166. K. Boukheddaden, J. Linares, S. Galam, F. Varret, *J. Phys. Cond. Matter* **5**, 469 (1993)
167. T.-Y. Dong, M.J. Cohn, D.N. Hendrickson, G.G. Pierpoint, *J. Am. Chem. Soc.* **108**, 963 (1993)
168. T.-Y. Dong, M.J. Cohn, D.N. Hendrickson, G.G. Pierpoint, *J. Am. Chem. Soc.* **107**, 4777 (1985)
169. M.J. Cohn, T.-Y. Dong, D.N. Hendrickson, S.J. Geib, A.L. Rheingold, *J. Chem. Soc. Chem. Commun.* **16**, 1095 (1985)
170. M.D. Lowery, W.S. Hammack, H.G. Drickamer, D.N. Hendrickson, *J. Am. Chem. Soc.* **109**, 8019 (1987)
171. R.J. Webb, S.J. Geib, D.L. Staley, A.L. Rheingold, D.N. Hendrickson *J. Am. Chem. Soc.* **112**, 5031 (1990)
172. U. Hauser, V. Oestreich, H.D. Rohrweck, *Z. Phys.* **A280**, 17 (1977)
173. U. Hauser, V. Oestreich, H.D. Rohrweck, *Z. Phys.* **A284**, 9 (1978)
174. Th. Woike, H. Zöllner, W. Krasser, S. Haussühl, *Solid State Commun.* **73**, 149 (1990)
175. Th. Woike, S. Haussühl, *Solid State Commun.* **86**, 333 (1993)
176. J.A. Güida, O.E. Piro, P.J. Aymonino, *Inorg. Chem.* **34**, 4113 (1995)
177. K. Ookubo, Y. Morioka, H. Tomizawa, E. Miki, *J. Mol. Struct.* **379**, 241 (1996)
178. H. Zöllner, Th. Woike, W. Krasser, S. Haussühl, *Z. Kristallogr.* **188**, 139 (1989)
179. T. Woike, W. Kirchner, G. Schetter, T. Barthel, K. Hyung-Sang, S.S. Haussühl, *Opt. Commun.* **106**, 6 (1994)
180. M.R. Pressprich, M.A. White, Y. Vekhter, P. Coppens, *J. Am. Chem. Soc.* **116**, 5233 (1994)
181. M.D. Carducci, M.R. Pressprich, P. Coppens, *J. Am. Chem. Soc.* **119**, 2669 (1997)
182. H. Zöllner, W. Krasser, T. Woike, S. Haussühl, *Hyperfine Interactions*, **7**, 265 (1993)
183. C. Terrile, O.R. Nascimento, I.J. Moraes, E.E. Castellano, O.E. Piro, J.A. Guida, P.J. Aymonino, *Solid State Commun.* **73**, 481 (1990)
184. J.A. Guida, O.E. Piro, P.J. Aymonino, *Solid State Commun.* **57**, 175 (1986)
185. B. Delley, J. Scheffer, Th. Woike, *J. Chem. Phys.* **107**, 10067 (1997)
186. P. Boulet, M. Buchs, H. Chermette, C. Daul, F. Gilardoni, F. Rougemond, C.W. Schläpfer, J. Weber, *J. Phys. Chem.* **A105**, 8991 (2001)
187. P. Boulet, M. Buchs, H. Chermette, C. Daul, F. Gilardoni, F. Rougemond, C.W. Schläpfer, J. Weber, *J. Phys. Chem.* **A105**, 8999 (2001)
188. M. Atanasov, T. Schönherr, *J. Mol. Structure (TheoChem)* **592**, 79 (2002)
189. E. Coronado, S. Klokishner, O. Reu, B. Tsukerblat, *Polyhedron* **22**, 2527 (2003)
190. E. Coronado, S. Klokishner, O. Reu, B. Tsukerblat, *Adv. Quant. Chem.* **44**, 429 (2003)
191. R.M. Buchanan, C.G. Pierpont, *J. Am. Chem. Soc.* **102**, 4951 (1980)
192. D.M. Adams, A. Dei, A.L. Rheingold, D.N. Hendrickson, *Angew. Chem. Int. Ed. Engl.* **32**, 880 (1993)

193. D.M. Adams, A. Dei, A.L. Rheingold, D.N. Hendrickson, *J. Am. Chem. Soc.* **115**, 8221 (1993)
194. G.A. Abakumov, V.K. Chercasov, M.P. Bubnov, O.G. Ellert, Z.B. Dobrokhotova, L.N. Zakharov, Y.T. Struchkov, *Dokl. Akad. Nauk (Rus)*, **328**, 12 (1993)
195. J.K. McCusker, H.G. Jang, S. Wang, G. Christou, D.N. Hendrickson, *Inorg. Chem.* **31**, 1874 (1992)
196. O.S. Jung, C.G. Pierpont, *Inorg. Chem.* **33**, 2227 (1994)
197. M.W. Lynch, D.N. Hendrickson, B.J. Fitzgerald, C.G. Pierpont, *J. Am. Chem. Soc.* **106**, 2041 (1984)
198. S.A. Attia, C.G. Pierpont, *Inorg. Chem.* **34**, 1172 (1995)
199. M.W. Lynch, M. Valentine, D.N. Hendrickson, *J. Am. Chem. Soc.* **104**, 6982 (1982)
200. S.A. Attia, S. Bhattacharya, C.G. Pierpont, *Inorg. Chem.* **34**, 4427 (1995)
201. S.A. Attia, O.S. Jung, C.G. Pierpont, *Inorg. Chim. Acta* **226**, 91 (1994)
202. G.A. Abakumov, V.A. Garnov, V.I. Nevodchikov, V.K. Cherkasov, *Dokl. Akad. Nauk USSR* **304**, 107 (1989)
203. G.A. Abakumov, G.A. Razuvaev, V.I. Nevodchikov, V.K. Cherkasov, *J. Organomet.Chem.* **341**, 485 (1988)
204. C. Roux, D. Adams, J.P. Itié, A. Polian, D.N. Hendrickson, M. Verdaguer, *Inorg. Chem.* **35**, 2846 (1996)
205. C.G. Piepont, C.W. Lange, *Progr. Coord. Chem.* **41**, 381 (1993)
206. D.M. Adams, B. Li, J.D. Simon, D.N. Hendrickson *Angew. Chem. Int. Ed. Engl.* **34**, 1481 (1995)
207. D.M. Adams, D.N. Hendrickson, *J. Am. Chem. Soc.* **118**, 11515 (1996)
208. P. Guetlich, A. Dei, *Angew. Chem. Int. Ed. Engl.* **36**, 2734 (1997)
209. C.G. Pierpont, R.M. Buchanan, *Coord. Chem. Rev.* **38**, 45 (1981)
210. D.N. Hendrickson, D.M. Adams, in *Magnetism: A. Supramolecular Function*, ed. by O. Kahn (Kluwer, Dordrecht, 1996), p. 357
211. D.M. Adams, L. Noodleman, D.N. Hendrickson, *Inorg. Chem.*, **36**, 3966 (1997)
212. S. Klokishner, *Chem. Phys.* **269**, 411 (2001)
213. Yu.E. Perlin, B.S. Tsukerblat, in *The Dynamical Jahn–Teller Effect in Localized Systems*, ed. by Yu.E. Perlin, M. Wagner (North-Holland, Amsterdam, 1984), p. 251
214. S.I. Klokishner, O.S. Reu, *Chem. Phys.* **286**, 115 (2003)
215. S.I. Klokishner, O.S. Reu, *Polyhedron*, **22**, 2401 (2003)
216. L.N. Bulaevskii, C.D. Batista, M.V. Mostovoy, D.I. Khomskii, *Phys. Rev. B*, **78**, 024402 (2008)
217. J.J. Borrás-Almenar, J.M. Clemente-Juan, E. Coronado, A.V. Palií, B.S. Tsukerblat, *J. Phys. Chem.* **102**, 200 (1998)
218. J.J. Borrás-Almenar, J.M. Clemente-Juan, E. Coronado, A.V. Palií, B.S. Tsukerblat, *J. Chem. Phys.* **114**, 1148 (2001)
219. J.J. Borrás-Almenar, J.M. Clemente-Juan, E. Coronado, A.V. Palií, B.S. Tsukerblat, *Chem. Phys.* **274**, 131 (2001)
220. J.J. Borrás-Almenar, J.M. Clemente-Juan, E. Coronado, A.V. Palií, B.S. Tsukerblat, *Chem. Phys.* **274**, 145 (2001)
221. V. Palií, A.B.S. Tsukerblat, E. Coronado, J.M. Clemente-Juan, J.J. Borrás-Almenar, *J. Chem. Phys.* **118**, 5566 (2003)
222. A.V. Palií, S.M. Ostrovsky, S.I. Klokishner, B.S. Tsukerblat, J.R. Galán-Mascarós, C.P. Berlinguette, K.R. Dunbar, *J. Am. Chem. Soc.*, **126**, 16860 (2004)
223. B.S. Tsukerblat, A.V. Palií, S.M. Ostrovsky, S.V. Kunitsky, S.I. Klokishner, K.R. Dunbar, *J. Chem. Theory & Computation* **1** (2005)
224. D. Reinen, M. Atanasov, P. Kohler, *J. Mol. Str.* **838**, 151 (2007)
225. M. Atanasov, P. Comba, C.A. Daul, *J. Phys. Chem. A*, **110**, 13332 (2006)
226. M. Atanasov, C. Busche, P. Comba, F. El Hallak, B. Martin, G. Rajaraman, G. Rajaraman, J. van Slageren, H. Wadeh, *Inorg. Chem.* **47**, 8112 (2008)
227. M. Atanasov, P. Comba, C.A. Daul, *Inorg. Chem.* **47**, 2449 (2008)

- 228. M. Atanasov, P. Comba, C.A. Daul, A. Hauser, J. Phys. Chem. A **111**, 9145 (2007)
- 229. M. Atanasov, P. Comba, *this volume*, p. . .(to be inserted)
- 230. A. Sieber, R. Bircher, O. Waldmann, G. Carver, G. Chaboussant, H. Mutka, H.-U. Güdel, Angew. Chem. Int. Ed. **44**, 4239 (2005)
- 231. J. van Slageren, S. Dengler, J. Gómez-Segura, D. Ruiz-Molina, M. Dressel, Inorg. Chim. Acta **361**, 3714 (2008)
- 232. M. Soler, W. Wernsdorfer, Z. Sun, D. Ruiz, J.C. Huffman, D.N. Hendrickson, G. Christou, Polyhedron, **22**, 1783 (2003)
- 233. A.M. Ako, I.J. Hewitt, V. Mereacre, R. Clérac, W. Wernsdorfer, C.E. Anson, A.K. Powell, Angew. Chem. Int. Ed. **45**, 4926 (2006)
- 234. V.Z. Polinger, this issue, pp. . .
- 235. O. Waldmann, C. Dobe, S.T. Ochsenbein, H.-U. Güdel, I. Sheikin, Phys. Rev. Lett. **96**, 027206 (2006).
- 236. O. Waldmann, Phys. Rev.B **75**, 174440 (2007)

# The Effect of Jahn–Teller Coupling in Hexacyanometalates on the Magnetic Anisotropy in Cyanide-Bridged Single-Molecule Magnets

Mihail Atanasov and Peter Comba

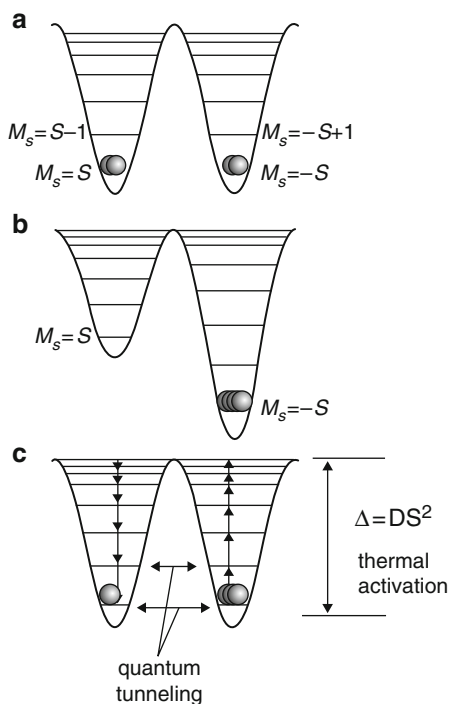
**Abstract** The factors that govern the nature of the lowest spin-states and the magnetic anisotropy in mono- and oligonuclear cyanide complexes of 3d-metal ions are analyzed on the basis of a combination of density functional theory (DFT) and ligand field theory (LFT), the ligand field density functional theory approach (LFDFT). In this chapter we analyze first the factors that govern the magnetic anisotropy in the low-spin  $[\text{Fe}(\text{CN})_6]^{3-}$  ( $^2T_{2g}$ ) complexes - the Jahn–Teller activity (vibronic coupling) within the triply degenerate ground states as well as unquenched orbital momenta which influence the spin subsystem via spin–orbit coupling. In a second step we derive the parameters of the spin-Hamiltonian in a general form of a binuclear  $\{(\text{L})\text{Cu}^{\text{II}}-\text{NC}-\text{Fe}^{\text{III}}(\text{CN})_5\}$  unit and discuss on this basis the factors that govern its magnetic anisotropy. The nature of the lowest spin multiplet and the spin anisotropy gap are analyzed for this system using first principles.

## 1 Single-Molecule Magnetism

Much effort has been directed to the synthesis and characterization of oligonuclear transition metal complexes with single-molecule magnetic behavior (SMM) [1–22]. These are *high-spin* molecules with two-fold degenerate states (implying axial three- or fourfold symmetries) with maximum spin  $\pm S$ , separated in energy from the states of lower spin by an energy gap, quantified by the zero-field splitting parameter  $D$ . With an applied magnetic field oriented along the easy axis of the magnetization, one of the two  $M_s$  components becomes stabilized with respect to the other (Fig. 1). An induced magnetic moment is created, and, if temperature is below the blocking temperature ( $T < T_B$ ), relaxation is slow and the moment persists when removing the field. This can be used to record and read information at a molecular level. It follows that in order to increase the thermal activation energy ( $U = D \cdot S^2$ ), the anisotropy  $D$  and/or the total spin  $S$  need to be increased. However, quantum tunneling leads to effective energy barriers  $U_{\text{eff}}$  which are usually smaller than  $U$  [23].

Prominent examples with SMM properties are cyanide complexes of the 3d-transition metals [18]. Due to the occupied  $\sigma$  and empty or occupied  $\pi$ -orbitals

**Fig. 1** Energy levels for a spin state  $S$  with easy axis magnetic anisotropy. (a) Zero magnetic field, the  $+M$  levels (left) and  $-M$  levels (right) are equally populated; (b) application of a magnetic field (bias) leads to a selective population of the right well; (c) equilibration after removing the magnetic field by quantum tunneling or thermal activation (adopted from [23])

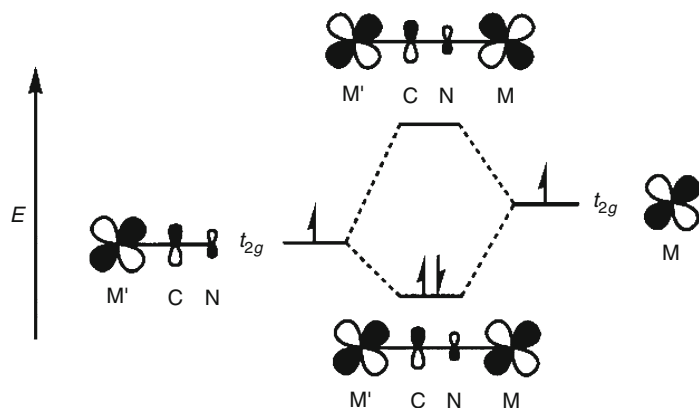


the cyanide ligand provides particularly efficient pathways for magnetic exchange (Fig. 2). Prussian blue type solids ( $M[M'(CN)_6] \cdot zH_2O$ ) with the properties of bulk magnets up to room temperature have been reported [24, 25].

Based on the experience with Prussian-blue-compounds, oligonuclear complexes with CN- bridged subunits and various nuclearity have been prepared [14, 22]. It is remarkable that even for the small trinuclear complexes  $Mn^{III}-NC-M-CN-Mn^{III}$  ( $M = Cr^{3+}, Fe^{3+}$ ) significant effective energy barriers  $U_{eff}$  of 16 and  $9\text{ cm}^{-1}$ , leading to slow magnetic relaxation, as shown by the out-of-phase component of the AC susceptibility, have been observed (Fig. 3). Focusing on  $[Fe(CN)_6]^{3-}$ , we have analyzed the effect of spin-orbit and Jahn-Teller coupling (first order effects within the  $^2T_{2g}$  ground state of  $Fe^{III}$ ) on the magnetic anisotropy, in the mononuclear  $[Fe(CN)_6]^{3-}$  subunit alone [26] and in exchange coupled complexes of various nuclearity [27, 28].

Experimental [1–22] and theoretical [29–39] work in this field is quite extensive, and several review articles with experimental [32] and theoretical data [40] have been published. The aim of the present account is to summarize our own experimental and theoretical activities in the field [28, 41–44] with special emphasis on our theoretical studies. First, using a DFT computational scheme, we will discuss the Jahn-Teller activity in the triply degenerate ground states of cyanide complexes of the 3d-metals, specifically  $[Fe(CN)_6]^{3-}$  [26]. Second, based on the known Jahn-Teller distortions and geometrical or bonding strain, we will discuss in a simple

Antiferromagnetic Exchange Coupling:



Ferromagnetic Exchange Coupling:

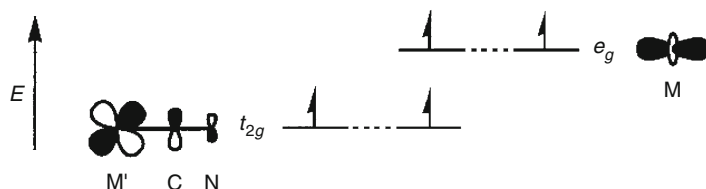


**Fig. 2** Orbital interaction diagrams for a dinuclear  $M'-CN-M$  unit with octahedral coordination at the metal centers (adopted from [18])

dinuclear  $Cu^{II}-NC-Fe^{III}$  unit their effects on the magnetic anisotropy [27]. Special emphasis will be placed on detailed derivations of most expressions in order to make the approach described here generally accessible.

## 2 Electronic Structure of 3d Transition Metal Complexes with Triply Degenerate Ground States

### 2.1 Jahn–Teller Coupling

The Hamiltonian matrix of the  $T_g \otimes (\varepsilon_g + \tau_{2g})$  vibronic coupling problem up to first order vibronic coupling terms set up within the  $\xi(\alpha)$ ,  $\eta(\beta)$  and  $\zeta(\gamma)$  basis functions of the  $T_g = T_{2g}(T_{1g})$  electronic state is given in (1) [45, 46].  $Q_\theta$ ,  $Q_\varepsilon$

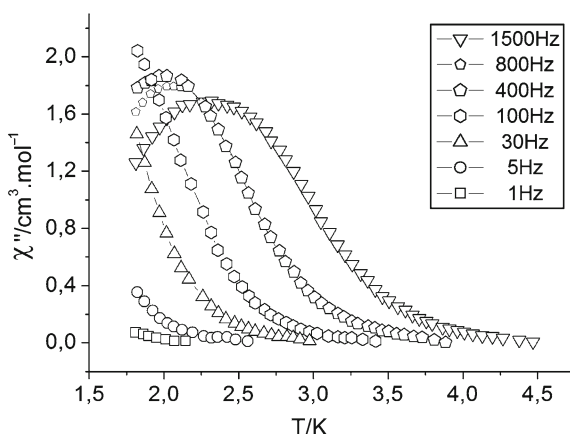
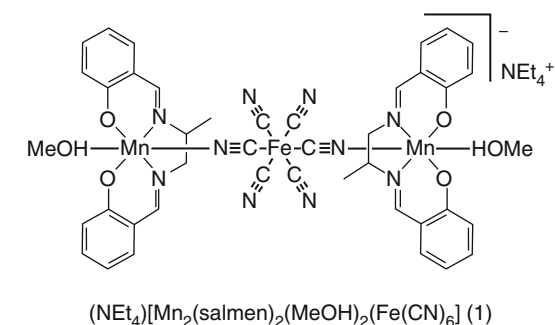
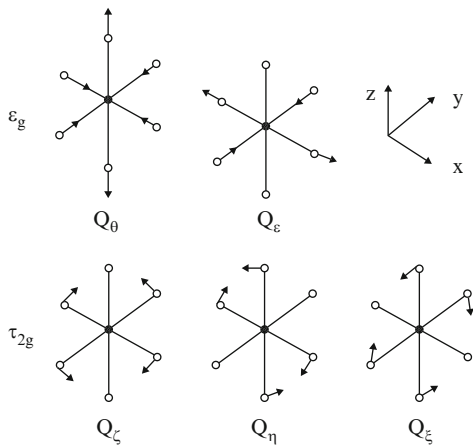


**Fig. 3** Temperature dependence of the imaginary part ( $\chi''$ ) of the alternating current (ac) susceptibility of (Net<sub>4</sub>)[Mn<sub>2</sub>(salmen)<sub>2</sub>(MeOH)<sub>2</sub>Fe(CN)<sub>6</sub>] (salmen: rac-N,N'-(1-methylethylene)bis(salicylideneiminato)), measured under various oscillating frequencies (1–1500 Hz). Solid lines are a guide for the eyes (adopted from [22]);  $S = 9/2$  spin-ground state with relaxation time following an Arrhenius law  $\ln \tau = \ln \tau_0 + \Delta_{\text{eff}}/(k_B T)$  with  $\tau_0 = 2.5 \cdot 10^{-7}$  s and  $\Delta_{\text{eff}} = 9.3 \text{ cm}^{-1}$ ;  $\tau_0$  saturates at  $T < 0.3$  K to a value around 470 s, i.e. quantum tunneling becomes the dominant process of relaxation; further parameters:  $J(\text{Mn-Fe}) = 3.5 \text{ cm}^{-1}$  and  $D = -0.86 \text{ cm}^{-1}$  (from field dependence of the magnetization for  $0.04 \text{ K} < T < 1.1 \text{ K}$ ; with  $J = 3.5 \text{ cm}^{-1}$ , an  $S = 9/2$  ground state and  $S = 7/2$  and  $S = 5/2$  excited levels at  $J/2 = 1.75$  and  $J = 3.5 \text{ cm}^{-1}$  are deduced; with  $D \sim 1 \text{ cm}^{-1}$  strong mixing of corresponding  $S$  levels is calculated. An analogous compound with Cr<sup>III</sup> – K[(5-Brsalen)<sub>2</sub>(H<sub>2</sub>O)<sub>2</sub>Mn<sup>III</sup><sub>2</sub>Cr<sup>III</sup>(CN)<sub>6</sub>].2H<sub>2</sub>O [5-Brsalen = N,N'-ethylene bis(5-bromosalicylidene) aminato dianion] behaves as an  $S = 5/2$  ground state magnetic cluster with  $J = -12.6 \text{ cm}^{-1}$  (antiferromagnetic Mn–NC–Cr coupling,  $\Delta_{\text{eff}} = 16 \text{ cm}^{-1}$ ,  $\tau_0 = 610 \cdot 10^{-10}$  s,  $D = -2.67 \text{ cm}^{-1}$ ), reported in [14] (adopted from [22])

and  $Q_\xi$ ,  $Q_\eta$ ,  $Q_\zeta$  are the  $\varepsilon_g$  and  $\tau_{2g}$  vibrations visualized in Fig. 4.  $V_\varepsilon$  and  $V_\tau$  are the linear JT coupling constants for the  $T_g \otimes \varepsilon_g$  and  $T_g \otimes \tau_{2g}$  problems and  $K_\varepsilon$  and  $K_\tau$  are the harmonic force constants for the  $\varepsilon_g$  and  $\tau_{2g}$  vibrational modes; **I** is the 3×3 identity matrix



**Fig. 4** The  $\varepsilon_g$  and  $\tau_{2g}$  vibrational modes and their components and shapes (adopted from [26])



$$\mathbf{H}_1 = \begin{bmatrix} V_\varepsilon \cdot \left( \frac{1}{2} Q_\theta - \frac{\sqrt{3}}{2} Q_\varepsilon \right) & -V_\tau Q_\zeta & -V_\tau Q_\eta \\ -V_\tau Q_\zeta & V_\varepsilon \cdot \left( \frac{1}{2} Q_\theta + \frac{\sqrt{3}}{2} Q_\varepsilon \right) & -V_\tau Q_\xi \\ -V_\tau Q_\eta & -V_\tau Q_\xi & -V_\varepsilon Q_\theta \end{bmatrix} + \left[ \frac{1}{2} K_\varepsilon (Q_\theta^2 + Q_\varepsilon^2) + \frac{1}{2} K_\tau (Q_\zeta^2 + Q_\eta^2 + Q_\xi^2) \right] \mathbf{I} \quad (1)$$

Coordinates of the stationary points on the ground state potential energy surface can be derived with the method of Öpic and Price [47]. Instead of diagonalizing the Hamiltonian matrix of (1) directly, this method makes use of paths of high-symmetry on the ground state potential energy surface. There are three, four and six symmetry-equivalent stationary points of  $D_{4h}$ ,  $D_{3d}$  and  $D_{2h}$  symmetry, which can be visualized as the axes, corners and edges of a cube, respectively. Restricting, in accordance with the Jahn–Teller theorem, to the non-degenerate ground states in these high symmetry configurations, the electronic eigenfunctions with  $D_{4h}$ ,  $D_{3d}$  and  $D_{2h}$  geometries are given by:

$$\mathbf{c}_{D4h} = \begin{pmatrix} 0 \\ 0 \\ 1 \end{pmatrix}; \mathbf{c}_{D3d} = \begin{pmatrix} \frac{1}{\sqrt{3}} \\ \frac{1}{\sqrt{3}} \\ \frac{1}{\sqrt{3}} \end{pmatrix}; \mathbf{c}_{D2h} = \begin{pmatrix} \frac{1}{\sqrt{2}} \\ \pm \frac{1}{\sqrt{2}} \\ 0 \end{pmatrix} \quad (2)$$

Using these eigenvectors, energy expressions for the ground state for the geometries of  $D_{4h}$ ,  $D_{3d}$  and  $D_{2h}$  symmetry are obtained according to (3), (4), and (5), respectively.

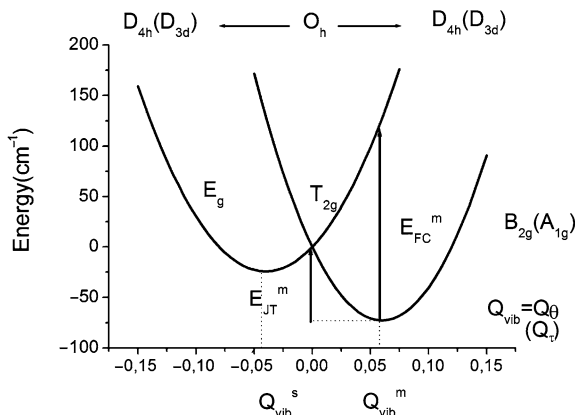


**Fig. 5** Energy profile for the components split from the  $T_g = T_{2g}$  ground states for  $d^{1.5}$  (and similarly for  $d^{2.4}$ ) transition metal ions due to  $T_g \times \varepsilon_g$  ( $T_g \times \tau_{2g}$ ) JT coupling along a distortion pathway which preserves the highest possible symmetry (epikernel symmetry)  $D_{4h}$  ( $D_{3d}$ ) and lifts the orbital degeneracy. The basic model parameters, i.e. the JT stabilization energy,  $E_{JT}^m$ , the energy of the vertical (Franck-Condon) transition at the  $D_{4h}$  ( $D_{3d}$ ) minimum  $E_{FC}^m$ , and the distortions of the active mode  $Q_{vib}^m$ ,  $Q_{vib}^s$  (vib =  $\varepsilon_g$ ,  $\tau_{2g}$ ) for the minima ( $m$ ) and saddle points ( $s$ ) are illustrated (adopted from [26])

$$E(D_{4h}) = \tilde{\mathbf{c}}_{D4h} \cdot \mathbf{H}_1 \cdot \mathbf{c}_{D4h} = \frac{1}{2} K_\varepsilon (Q_\theta^2 + Q_\varepsilon^2) + \frac{1}{2} K_\tau (Q_\xi^2 + Q_\eta^2 + Q_\zeta^2) - V_\varepsilon Q_\theta \quad (3)$$

$$E(D_{3d}) = \tilde{\mathbf{c}}_{D3d} \cdot \mathbf{H}_1 \cdot \mathbf{c}_{D3d} = \frac{1}{2} K_\varepsilon (Q_\theta^2 + Q_\varepsilon^2) + \frac{1}{2} K_\tau (Q_\xi^2 + Q_\eta^2 + Q_\zeta^2) - \frac{2}{3} V_\tau (Q_\xi + Q_\eta + Q_\zeta) \quad (4)$$

$$E(D_{2h}) = \tilde{\mathbf{c}}_{D2h} \cdot \mathbf{H}_1 \cdot \mathbf{c}_{D2h} = \frac{1}{2} K_\varepsilon (Q_\theta^2 + Q_\varepsilon^2) + \frac{1}{2} K_\tau (Q_\xi^2 + Q_\eta^2 + Q_\zeta^2) + \frac{1}{2} V_\varepsilon Q_\theta \pm V_\tau Q_\xi \quad (5)$$

These represent electronic states of  $B_{2g}(A_{2g})$ ,  $A_{1g}(A_{2g})$  and  $B_{2g}(B_{3g})$  symmetry in the case of the low spin  $t_{2g}^{1.5}$  ( $t_{2g}^{2.4}$ ) electronic configurations, respectively. In a similar way, excited state geometries are also obtained. An energy diagram with a single configurational coordinate (Fig. 5) illustrates the basic geometric and energetic parameters of the model. These are the tetragonal ( $D_{4h}$ ) or trigonal ( $D_{3d}$ ) elongations or compressions of an octahedron [tetragonal:  $Q_\theta > 0$  (elongation),  $Q_\theta < 0$  (compression); trigonal:  $Q_\tau = Q_\xi = Q_\eta = Q_\zeta$ ;  $Q_\tau < 0$  (elongation),  $Q_\tau > 0$  (compression)] with the Jahn–Teller stabilization energy ( $E_{JT}^m$ ) and the energy of the vertical electronic transition from the minimum of the non-degenerate

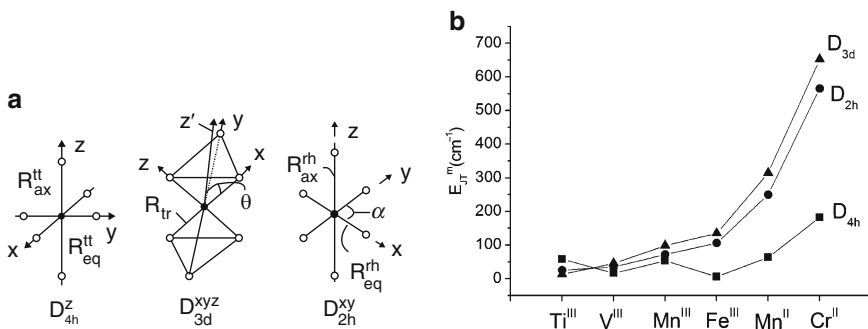


**Fig. 6** (a) Geometric parameters to describe the JT distortions of  $T_g \times \varepsilon_g (D_{4h}^z)$ ,  $T_g \times \tau_{2g} (D_{3d}^{xyz})$  and  $T_g \times (\varepsilon_g + \tau_{2g}) (D_{2h}^{xy})$  type, and deduced from DFT geometry optimizations with electronic configurations with correct spin and space symmetries in  $D_{4h}$  [ $^2 B_{2g} (d^1, \text{low-spin } d^5), ^3 A_{2g} (d^2, \text{low-spin } d^4)$ ],  $D_{3d}$  [ $^2 A_{1g} (d^1, \text{low-spin } d^5), ^3 A_{2g} (d^2, \text{low-spin } d^4)$ ] and  $D_{2h}$  [ $^2 B_{2g} (d^1, d^5), ^3 B_{2g} (d^2, d^4)$ ]; (b) JT stabilization energies in hexacyanometalates of the 3d series in orbitally degenerate octahedral ground states in their  $D_{4h}$ ,  $D_{3d}$  and  $D_{2h}$  minima of the ground state potential energy surface (adopted from [26])

ground state to the doubly degenerate excited state ( $E_{FC}^m$ ; Franck-Condon, FC). A procedure to obtain these parameters from DFT has been developed [26]:

1. A geometry optimization in  $D_{4h}$  is performed by using the orbital occupations appropriate for the non-degenerate ground state of interest [ $^2 B_{2g} (d^1, \text{low-spin } d^5), ^3 A_{2g} (d^2, \text{low-spin } d^4)$ ]; these are the configurations  $b_{2g}^1 (Ti^{III}), e_g^2 (V^{III}), b_{2g}^2 e_g^2 (Mn^{III}, Cr^{II}), e_g^4 b_{2g}^1 (Fe^{III}, Mn^{II})$ . As a result, the metal-ligand bond distances for the axial and equatorial bonds ( $R_{ax}^t, R_{eq}^t$ , Fig. 6a) are obtained and used to calculate  $Q_0^m$ .
2. Based on the geometry obtained in step 1, one calculates  $E_{FC}^m (D_{4h})$  as the difference between the energy of the excited state ( $^2 E_g$  or  $^3 E_g$ ) and the ground state ( $^2 B_{2g}$  or  $^3 A_{2g}$ ) for  $d^{1,5}$  or  $d^{2,4}$ .
3. A geometry optimization in  $D_{3d}$  is then performed to yield the geometry of the non-degenerate ground states of interest [ $^2 A_{1g} (d^1, \text{low-spin } d^5), ^3 A_{2g} (d^2, \text{low-spin } d^4)$ ]; more explicitly, these are the configurations  $a_{1g}^1 (Ti^{III}), e_g^2 (V^{III}), a_{1g}^2 e_g^2 (Mn^{III}, Cr^{II}), e_g^4 a_{1g}^1 (Fe^{III}, Mn^{II})$ . The distance  $R_{tr}$  and the angle  $\theta$  (Fig. 6a) quantify the trigonal distortion and are used to calculate  $Q_\tau^m$ .
4. Based on the geometry of step 3, one calculates  $E_{FC}^m (D_{3d})$  as the difference between the energy of the excited state ( $^2 E_g$  or  $^3 E_g$ ) and the ground state ( $^2 A_{1g}$  or  $^3 A_{2g}$ ) for  $d^{1,5}$  or  $d^{2,4}$ .

From these data one can deduce  $V_\varepsilon$ ,  $K_\varepsilon$ ,  $V_\tau$ ,  $K_\tau$  (6, 7). In terms of these parameters the JT stabilization energies  $E_{JT}^m (D_{4h})$  and  $E_{JT}^m (D_{3d})$  and  $E_{JT}^m (D_{2h})$  are obtained by the expressions given in (8–10). A more elaborate treatment, which includes

**Table 1** Linear ( $V_\varepsilon$  and  $V_\tau$ , in  $\text{cm}^{-1}/\text{\AA}$ ) and quadratic ( $L_\varepsilon$  and  $L_\tau$  in  $\text{cm}^{-1}/\text{\AA}^2$ ) vibronic coupling parameters, Jahn–Teller stabilization energies [ $E_{\text{JT}}(D_{4h})$  and  $E_{\text{JT}}(D_{3d})$  in  $\text{cm}^{-1}$ ] and vibronic coupling strengths [ $\lambda_\varepsilon = E_{\text{JT}}(D_{4h})/\hbar\omega_\varepsilon$ ,  $\lambda_\tau = E_{\text{JT}}(D_{3d})/\hbar\omega_\tau$ ]<sup>b</sup> of the  ${}^2T_{2g} \otimes \varepsilon_g$  and  ${}^2T_{2g} \otimes \tau_{2g}$  Jahn–Teller problems in  $[\text{Fe}(\text{CN})_6]^{3-}$  as deduced from DFT calculations<sup>a</sup> on a charge-compensated model complex, using water as a solvent and a LDA(VWN) functional as well as a triple zeta basis set<sup>c</sup>

${}^2T_{2g} \otimes \varepsilon_g$				${}^2T_{2g} \otimes \tau_{2g}$			
$V_\varepsilon = -855$	$L_\varepsilon = 8235$	$K_\varepsilon = 65882$	$V_\tau = 1052$	$L_\tau = 1584$	$X_\tau = 449$	$K_\varepsilon = 6069$	
$E_{\text{JT}}(D_{4h}) = 5$	$\hbar\omega_\varepsilon = 292$	$\lambda_\varepsilon = 0.017$	$E_{\text{JT}}(D_{3d}) = 135$	$\hbar\omega_\tau = 93$	$\lambda_\tau = 0.965$		

<sup>a</sup>see [26] for the recipe of deducing vibronic coupling constants from DFT calculations and about the computational procedure

<sup>b</sup>vibrational frequencies due to the  $\varepsilon_g$  and  $\tau_{2g}$  vibrational modes  $\hbar\omega_\varepsilon$  and  $\hbar\omega_\tau$ , respectively, have been computed from the corresponding harmonic force constants  $K_\varepsilon$  and  $K_\tau$  (in  $\text{cm}^{-1}/\text{\AA}^2$ ) and their effective masses

<sup>c</sup>The vibronic coupling constant due to simultaneous activation of the  $\varepsilon_g$  and  $\tau_{2g}$  vibrations, i.e.  $W$  of the combined  ${}^2T_{2g} \otimes (\varepsilon_g + \tau_{2g})$  coupling problem is zero

second order vibronic terms ( $L_\varepsilon$ ,  $L_\tau$ ,  $X_\tau$ ,  $W$ ) and technical details on the DFT procedure is given elsewhere [26]. Table 1 shows the values of the parameters for  $[\text{Fe}(\text{CN})_6]^{3-}$ . From these, we conclude that, with the exception of  $[\text{Ti}(\text{CN})_6]^{3-} D_{3d}$  stationary points are stable minima of the ground state potential surface (Fig. 6b).

$$V_\varepsilon = \frac{2}{3} \frac{E_{\text{FC}}^{\text{m}}(D_{4h})}{Q_\theta^{\text{m}}}; \quad K_\varepsilon = \frac{2}{3} \frac{E_{\text{FC}}^{\text{m}}(D_{4h})}{(Q_\theta^{\text{m}})^2} \quad (6)$$

$$V_\tau = \frac{1}{3} \frac{E_{\text{FC}}^{\text{m}}(D_{3d})}{Q_\tau^{\text{m}}}; \quad K_\tau = \frac{2}{9} \frac{E_{\text{FC}}^{\text{m}}(D_{3d})}{(Q_\theta^{\text{m}})^2} \quad (7)$$

$$E_{\text{JT}}^{\text{m}}(D_{4h}) = \frac{1}{2} \frac{V_\varepsilon^2}{K_\varepsilon} \quad (8)$$

$$E_{\text{JT}}^{\text{m}}(D_{3d}) = \frac{2}{3} \frac{V_\tau^2}{K_\tau} \quad (9)$$

$$E_{\text{JT}}^{\text{m}}(D_{2h}) = \frac{1}{4} E_{\text{JT}}^{\text{m}}(D_{4h}) + \frac{3}{4} E_{\text{JT}}^{\text{m}}(D_{3d}) \quad (10)$$

## 2.2 Spin–orbit Coupling

The  ${}^2T_2$  ground state of  $[\text{Fe}(\text{CN})_6]^{3-}$  is split by spin–orbit coupling into an  $E''$  ground state and an  $U'$  excited state at  $(3/2)\zeta$ .  $\mathbf{g}$ -tensor value expressions show significant orbital contribution to the low-temperature magnetic behavior (Table 2). Similarly, the  ${}^3T_1$  ground state of  $[\text{M}(\text{CN})_6]$  ( $\text{M} = \text{Mn}^{\text{III}}$ ,  $\text{Cr}^{\text{II}}$ ) splits into an  $A_1$

**Table 2** Effect of spin–orbit coupling on the splitting of the  $^2T_{2g}$  and  $^3T_{1g}$  ground states of octahedral  $[\text{Fe}(\text{CN})_6]^{3-}$  and  $[\text{Mn}(\text{CN})_6]^{3-}$  complexes, with expressions for the  $\mathbf{g}$ -tensors and values of the spin–orbit coupling constants from relativistic zero-order regular approximation DFT calculations<sup>a</sup>

$\text{Fe}^{\text{III}}(t_{2g}^5) -^2 T_2 \rightarrow E''(-\zeta) \quad U'(\zeta/2)$		
$g = (-1/3)(2 + 4k) \quad (1/3)(2 - 2k)$		
$\zeta[\text{Fe}(\text{CN})_6^{3-}] = 347 \text{ cm}^{-1}$		
$\text{Mn}^{\text{III}}, \text{Cr}^{\text{II}}(t_{2g}^4) -^3 T_1 \rightarrow A_1(-\zeta)$		
$J' = 0$	$T_1(-\zeta/2)$	$T_2, E(\zeta/2)$
$g = 0$	1	2
	$1 - (3/4)k$	$1 - (3/4)k$
$\zeta[\text{Mn}(\text{CN})_6^{3-}] = 243 \text{ cm}^{-1}$		

<sup>a</sup>k- orbital reduction factor**Table 3** Effects of configuration interaction on the Jahn–Teller coupling energies  $E_{\text{JT}}(D_{3d})$  (in  $\text{cm}^{-1}$ ) in the  $^3T_{1g}$  and  $^2T_{2g}$  ground states of  $[\text{M}(\text{CN})_6]^{3-}\text{M}^{\text{III}} = \text{V}^{\text{III}}(t_{2g}^2)$ , low-spin  $\text{Mn}^{\text{III}}(t_{2g}^4)$  and  $\text{Fe}^{\text{III}}$ ,  $\text{Mn}^{\text{II}}$  (both in a  $t_{2g}^5$  configuration), respectively<sup>a</sup>

$[\text{M}(\text{CN})_6]^{3-}\text{V}^{\text{III}}$		$\text{Mn}^{\text{III}}$	$\text{Fe}^{\text{III}}$	$\text{Mn}^{\text{II}}$
M =	$(t_{2g}^2)$	$(t_{2g}^4)$	$(t_{2g}^5)$	$(t_{2g}^5)$
$E_{\text{JT}}(D_{3d})$				
No CI	46	98	135	314
With CI	74	147	262	387
$\Delta E(\text{SOC})$	$95(T_2, E)$	$284(A_1)$	$347(E'')$	$243(E'')$

<sup>a</sup>stabilization of the lowest split components (specified in parenthesis) of the triply degenerate ground terms due to spin–orbit coupling only is shown for the sake of comparison

ground state and  $T_1$  and  $T_2, E$  excited states with energies of  $(1/2)\zeta$  and  $(3/2)\zeta$ . Spin–orbit coupling energies deduced from relativistic DFT calculations are collected and compared with Jahn–Teller stabilization energies in Table 3. It emerges that spin–orbit and Jahn–Teller coupling for this ion are comparable in magnitude and should therefore be accounted for on the same footing.

The operator  $\hat{H}_{\text{SO}} = \zeta_1 \hat{\mathbf{l}}_1 \hat{\mathbf{s}}_1$  of the spin–orbit coupling interaction of  $[\text{Fe}(\text{CN})_6]^{3-}$  is represented within the  $t_{2g}$   $(\xi, \eta, \zeta)\alpha$  and  $(\xi, \eta, \zeta)\beta$  spin–orbital basis in (11) (the spin–orbit coupling constant  $\zeta$  is defined as positive for  $\text{Fe}^{\text{III}}$ ); see Sect. 3.1 for its further use.

$$\mathbf{H}_{\text{SO}} = \begin{matrix} \xi\alpha_1 & \eta\alpha_1 & \zeta\alpha_1 & \xi\beta_1 & \eta\beta_1 & \zeta\beta_1 \\ \begin{bmatrix} 0 & -\frac{i}{2}\zeta & 0 & 0 & 0 & \frac{1}{2}\zeta \\ \frac{i}{2}\zeta & 0 & 0 & 0 & 0 & -\frac{i}{2}\zeta \\ 0 & 0 & 0 & -\frac{1}{2}\zeta & \frac{i}{2}\zeta & 0 \\ 0 & 0 & -\frac{1}{2}\zeta & 0 & \frac{i}{2}\zeta & 0 \\ 0 & 0 & -\frac{i}{2}\zeta & -\frac{1}{2}\zeta & 0 & 0 \\ \frac{1}{2}\zeta & \frac{i}{2}\zeta & 0 & 0 & 0 & 0 \end{bmatrix} \end{matrix} \quad (11)$$

## 2.3 Configuration Interaction

We have considered the  $^2T_{2g}$  and  $^3T_{1g}$  ground states and focus here on a single  $t_{2g}^n$  configuration. Strictly, this is only valid for  $t_{2g}^1(\text{Ti}^{\text{III}})$ , and it is an approximation for the  $d^5$  and  $d^{2,4}$  electronic configurations. The  $^2T_{2g}$  and  $^3T_{1g}$  ground states of  $[\text{Fe}(\text{CN})_6]^{3-}$  and  $[\text{Mn}(\text{CN})_6]^{3-}$  are mixtures of as much as ten ( $T_{2g}$ ) and seven ( $T_{1g}$ ) species of the same symmetry, which differ in their electron configurations of the MOs of d-character. These terms mix with each other via interelectronic repulsion (CI) and are split because of excited state JT coupling, due to  $\pi$ -type vibronic mixing (via the  $\tau_{2g}$  mode, splitting of the  $t_{2g}$  orbitals). For  $[\text{Fe}(\text{CN})_6]^{3-}$  and  $[\text{Mn}(\text{CN})_6]^{3-}$  (strong ligand field), the  $t_{2g}^5$  and  $t_{2g}^4$  configurations are expected to dominate the ground state wave function but the excited state configurations might still be important for the ground state vibronic coupling. Unfortunately, there are no DFT methods for the explicit geometry optimization of electronic states of multiconfigurational character. In DFT, one assumes that a single configuration dominates the electronic and geometric structure. To trace the effect of CI on the ground state JT effect of these ions, we resort to ligand field theory (LFT) and focus on the  $D_{3d}$  minima of the ground state potential energy surface. For some of the complexes studied here, approximate values of 10Dq, B and C are known [48]. They have been used in a CI calculation of the ground state  $^2T_{2g}(\text{Fe}^{\text{III}}, \text{Mn}^{\text{II}})$  and  $^3T_{1g}(\text{V}^{\text{III}}, \text{Mn}^{\text{III}})$  terms. From the known values of the trigonal distortion angle  $\theta$ , the energy  $E_{\text{FC}}^{\text{m}}$  and the value of 10Dq, we deduce the angular overlap parameters from one electron calculations and then switch to a many-electron CI treatment. The ground state splitting, which results from such a calculation is  $E_{\text{FC}}^{\text{CI}}$ . Since the energies  $E_{\text{FC}}$  and  $E_{\text{JT}}$  are interrelated, we can use (12) to obtain the approximate JT stabilization energy.

$$E_{\text{JT}}^{\text{CI}} = E_{\text{JT}}^{\text{m}}(E_{\text{FC}}^{\text{CI}}/E_{\text{FC}}^{\text{m}}) \quad (12)$$

The results in Table 3 show that CI mixing is essential and leads to an enhancement of the ground state splitting and an increase of the magnitude of  $E_{\text{FC}}$  by about a factor of 2 for  $[\text{Fe}(\text{CN})_6]^{3-}$  and  $[\text{V}(\text{CN})_6]^{3-}$ . For hexacyanovanadate the effect of CI is opposite to complexes with  $\pi$ -donor ligands ( $\text{VF}_6^{3-}$ ), where, on the basis of structural and spectroscopic data, it was found that CI reduces the  $^3T_1$  ground state JT coupling [49].

## 2.4 Interpretation of Magnetic and EPR Data of Low-Spin $[\text{Fe}(\text{CN})_6]^{3-}$

$[\text{Fe}(\text{CN})_6]^{3-}$  has been studied by single crystal EPR and susceptibility measurements and these data have been interpreted by a ligand field model, assuming tetragonal distortions within a  $D_{4h}$  symmetry description [50–57]. We have shown

that another interpretation, based on a  $D_{3d}$  distortion, is possible. With this concept and the known extent of the geometrical distortions from the reported crystal structure of  $K_3[Fe(CN)_6]^{3-}$  we have reproduced the single crystal  $g$ - and susceptibility  $\chi$ -tensors [26]. The impressive result from this interpretation is that the magnetic anisotropy of  $[Fe(CN)_6]^{3-}$  in both crystallographic forms of  $K_3[Fe(CN)_6]$  (the monoclinic and the orthorhombic structure) are very similar and only compatible with a trigonally compressed geometry, as indicated by the vibronic Jahn–Teller coupling model. A change of the octahedral angle  $\theta = 54.735^\circ$  (i.e. the angle between the Fe–C bond direction and the  $C_3$  axis) by only  $1^\circ$  is large enough to account for the observed anisotropy of the  $g$ - and the  $\chi$ -tensors.

### 3 Analysis of the Magnetic Anisotropy in the $Fe^{III}$ –CN– $Cu^{II}$ Pair

#### 3.1 Theory

Exchange coupling in oligonuclear cyanide-bridged complexes  $L^1M^1-NC-M^2L^2$  depends on the geometry and the electronic ground state of the  $L^1M^1(NC)$  and  $(NC)M^2L^2$  paramagnetic subunits, the electronic structure of the cyanide bridging ligand and the geometry of the  $M^1-NC-M^2$  bridge. An analysis of the dependence of the magnetic exchange across the cyanide bridge on the nature of the metal ions and, in particular, of its electronic configuration in  $Cu^{II}-NC-M^{III}$  ( $M = Cr, Fe, Mn$ , see Fig. 7) metal pairs based on spin-polarized DFT calculations has been reported and a study of the same effects within the Valence Bond CI model [58–62] allows to link the DFT data with meaningful chemical concepts [63–66]. We now consider a dinuclear  $Cu^{II}-Fe^{III}$  complex with  $[Fe(CN)_6]^{3-}$  subunits, and analyze the exchange as a function of the multiplet structure and Jahn–Teller coupling of the  $Fe^{III}$  unit. Due to the closely spaced energy levels (Jahn–Teller splitting

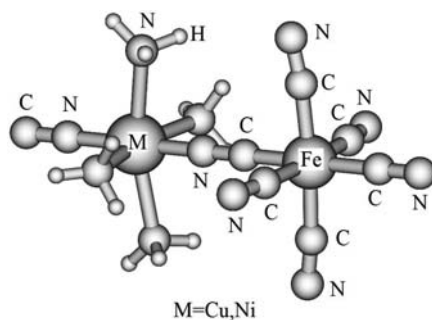


**Fig. 7** Dinuclear model complex of  $C_{4v}$  symmetry, used for the calculation of the anisotropic exchange coupling (adopted from [27])

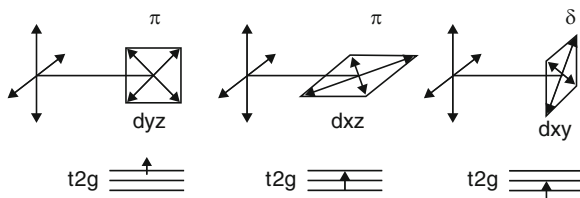


**Fig. 8** Pathways for the exchange between  $\text{Cu}^{\text{II}}$  and  $\text{Ni}^{\text{II}}$  with fully occupied  $t_{2g}$   $\pi$ -orbitals and  $\text{Fe}^{\text{III}}$  in dependence of the symmetry of the singly-occupied  $t_{2g}$  orbital of  $\text{Fe}^{\text{III}}$

and distortions observed in the crystal lattices included), no SCF convergence was achieved on this model complex with programs such as ADF [67] and ORCA, [68] which have been found to be very efficient in other examples. Therefore, an approximation based on first using high-symmetry ( $D_{4h}$ ) and then accounting for symmetry lowering by virtue of a vibronic coupling approach, turned out to be necessary for the analysis. With published results on  $[\text{Fe}(\text{CN})_6]^{3-}$ , the magnetic anisotropy in M–NC–Fe exchange pairs with  $\text{M} = \text{Cu}^{\text{II}}$  and  $\text{Ni}^{\text{II}}$  ( $S = 1/2$  and  $S = 1$ , respectively, with  $\sigma$ -antibonding ground states in both cases) could be analyzed (Fig. 8). The lowest four and six spin states of the Fe–CN–Cu ( $2 \times 2$ ) and Fe–CN–Ni ( $2 \times 3$ ) pairs, respectively, were calculated independently, with all orbital effects of  $\text{Cu}^{\text{II}}$  and  $\text{Ni}^{\text{II}}$  included in the effective  $\mathbf{g}$ -tensors. Two different forms of the Hamiltonian were used, the effective spin-Hamiltonian of (13–15), and the real ligand field plus exchange model Hamiltonian of (16). In (13)  $J$  is the isotropic exchange coupling constant,  $\mathbf{D}_{12}$  (14) and  $\mathbf{A}_{12}$  (15) are the traceless tensors for symmetric and antisymmetric exchange, respectively,  $\mathbf{D}_2$  is the single center zero-field splitting tensor (e.g. for  $\text{Ni}^{\text{II}}$ ,  $S = 1$ ) and  $\mathbf{g}_1$  and  $\mathbf{g}_2$  are the effective  $\mathbf{g}$ -tensors for the  $[\text{Fe}(\text{CN})_6]^{3-}$  and  $\text{Cu}^{\text{II}}$  or  $\text{Ni}^{\text{II}}$  sites, respectively.

$$\begin{aligned} \mathbf{H}_{\text{sph}} = & -J\mathbf{s}'_1\mathbf{s}_2 + \mathbf{s}'_1\mathbf{D}_{12}\mathbf{s}_2 + \mathbf{s}_2\mathbf{D}_2\mathbf{s}_2 + \mathbf{s}'_1\mathbf{A}_{12}\mathbf{s}_2 \\ & + \mu_B\mathbf{s}'_1\mathbf{g}_1\mathbf{B} + \mu_B\mathbf{s}_2\mathbf{g}_2\mathbf{B} \end{aligned} \quad (13)$$

$$\mathbf{D}_{12} = \begin{bmatrix} D_{xx} & D_{xy} & D_{xz} \\ D_{xy} & D_{yy} & D_{yz} \\ D_{xz} & D_{yz} & -D_{xx} - D_{yy} \end{bmatrix} = \begin{bmatrix} -\frac{2}{3}D + 2E & D_{xy} & D_{xz} \\ D_{xy} & -\frac{2}{3}D - 2E & D_{yz} \\ D_{xz} & D_{yz} & \frac{4}{3}D \end{bmatrix} \quad (14)$$

$$\mathbf{A}_{12} = \begin{bmatrix} 0 & A_z & -A_y \\ -A_z & 0 & A_x \\ A_y & -A_x & 0 \end{bmatrix} \quad (15)$$



$$\hat{\mathbf{H}} = -\hat{\mathbf{O}}_{\mathbf{S}} \cdot \mathbf{s}_{\text{Fe}} + \zeta_{Fe} \hat{\mathbf{l}}_{\text{Fe}} \cdot \hat{\mathbf{s}}_{\text{Fe}} + \hat{\mathbf{H}}_{JT}^{Fe} \quad (16)$$

$$\begin{aligned} \hat{\mathbf{O}} = \begin{bmatrix} J_{\xi\xi} & J_{\xi\eta} & J_{\xi\zeta} \\ J_{\xi\eta} & J_{\eta\eta} & J_{\eta\zeta} \\ J_{\xi\zeta} & J_{\eta\zeta} & J_{\zeta\zeta} \end{bmatrix} &= J_{a1} \hat{\mathbf{T}}_{a1} + J_{e\theta} \hat{\mathbf{T}}_{e\theta} + J_{e\varepsilon} \hat{\mathbf{T}}_{e\varepsilon} + J_{t2\xi} \hat{\mathbf{T}}_{t2\xi} \\ &+ J_{t2\eta} \hat{\mathbf{T}}_{t2\eta} + J_{t2\zeta} \hat{\mathbf{T}}_{t2\zeta} \end{aligned} \quad (17)$$

$$\hat{\mathbf{T}}_{a1} = \hat{\mathbf{1}} = \frac{1}{2} \hat{\mathbf{L}}^2 \quad J_{a1} = \frac{1}{3} (J_{\xi\xi} + J_{\eta\eta} + J_{\zeta\zeta}) \quad (18)$$

$$\hat{\mathbf{T}}_{e\theta} = (\hat{\mathbf{L}}_z^2 - \frac{2}{3} \hat{\mathbf{1}}) = (\hat{\mathbf{L}}_x^2 - \frac{1}{3} \hat{\mathbf{L}}^2) \quad J_{e\theta} = \frac{1}{2} (J_{\xi\xi} + J_{\eta\eta}) - J_{\zeta\zeta} \quad (19)$$

$$\hat{\mathbf{T}}_{e\varepsilon} = \hat{\mathbf{L}}_x^2 - \hat{\mathbf{L}}_y^2 \quad J_{e\varepsilon} = \frac{1}{2} (J_{\eta\eta} - J_{\xi\xi}) \quad (20)$$

$$\hat{\mathbf{T}}_{t2\xi} = \hat{\mathbf{L}}_y \hat{\mathbf{L}}_z + \hat{\mathbf{L}}_z \hat{\mathbf{L}}_y \quad J_{t2\xi} = -J_{\eta\zeta} \quad (21)$$

$$\hat{\mathbf{T}}_{t2\eta} = \hat{\mathbf{L}}_x \hat{\mathbf{L}}_z + \hat{\mathbf{L}}_z \hat{\mathbf{L}}_x \quad J_{t2\eta} = -J_{\xi\zeta} \quad (22)$$

$$\hat{\mathbf{T}}_{t2\zeta} = \hat{\mathbf{L}}_x \hat{\mathbf{L}}_y + \hat{\mathbf{L}}_y \hat{\mathbf{L}}_x \quad J_{t2\zeta} = -J_{\xi\eta} \quad (23)$$

Equation (16) includes an orbital-dependent exchange operator (first term), spin-orbit coupling (second term) and Jahn–Teller coupling (third term). A restriction to the  $^2T_{2g}$  ground state of  $[\text{Fe}(\text{CN})_6]^{3-}$  allows to factorize the orbital-dependent exchange operator into irreducible tensors which are based on products of orbital momentum operators and symmetry-related coefficients. Based on (17) we can deduce the symmetry-independent coupling constants, which emerge when lowering the symmetry from  $O_h$  to its subgroups. Only terms which are totally symmetric in a given point group are non-zero. Therefore, in  $O_h$  (i.e. when the  $\text{Fe}^{3+}$  and  $\text{Cu}^{2+}$  centers collapse) only one parameter ( $J_{a1} \equiv J$ ) is allowed by symmetry. Upon lowering the symmetry towards an axial Cu–NC–Fe pair ( $D_{4h}$ ) there are two parameters,  $J_{a1}$  and  $J_{e\theta}$  (in  $D_{4h}$  the term with  $J_{e\theta}$  is totally symmetric). One more term, i.e.  $J_{e\varepsilon}$  emerges for Cu–NC–Fe with orthorhombic geometry ( $D_{2h}$ ). A deviation of the Cu–NC–Fe fragment from linearity ( $C_s$  or  $C_1$  symmetry) would induce five or six parameters. From a comparison of the lowest four and six eigenvalues and eigenfunctions of the Hamiltonian of (16) and that of the spin Hamiltonian of (13) (see below for a detailed description of this procedure), the isotropic exchange energy  $J$  and the symmetric ( $\mathbf{D}_{12}$ ) and antisymmetric ( $\mathbf{A}_{12}$ ) exchange tensors can be obtained (see Table 5, columns 5–7). The zero-field splitting tensor for the single centre anisotropy parameter of Ni ( $\mathbf{D}_2$ ) can also be taken into account. An essential point here is the use of DFT to approximate the diagonal terms of the orbital-dependent exchange operator  $\hat{\mathbf{O}} \cdot \hat{\mathbf{s}}_1 \cdot \hat{\mathbf{s}}_2$  (Table 4) [27]. There is strong ferromagnetic coupling between the singly occupied orbitals of  $\text{Fe}^{\text{III}}$ ,  $d_{xz}$  or  $d_{yz}$ , and  $\text{Cu}^{\text{II}}$  (or  $\text{Ni}^{\text{II}}$ ),  $d_{z2}$ ; the interaction energy with the  $d_{xy}$  orbital is much smaller.

**Table 4** Values of the exchange coupling energies of the  $\text{Fe}^{\text{III}}\text{-CN-Ni}^{\text{II}}(d_{x^2-y^2}^1, d_{z^2}^1)$  exchange pair, using the B1LYP functional with spin projection, in comparison with the corresponding energy obtained for the  $\text{Fe}^{\text{III}}\text{-CN-Cu}^{\text{II}}(d_{z^2})$  exchange pair

	$\text{Fe}(^2\text{E})$ $J_{\xi\xi} = J_{\eta\eta} = J_{\text{E}}$	$\text{Fe}(^2\text{B}_2)$ $J_{\xi\xi} = J_{\text{B}_2}$
$\text{Cu}(d_{z^2}^1)$	19.4	1.6
$\text{Ni}(d_{z^2}^1 d_{x^2-y^2}^1)$	12.9	0.0

**Table 5** Spin levels ( $E_i, i = 1-4$ ),  $\chi T$  (in  $\text{cm}^3 \cdot \text{K/mol}$ ) values at  $T_{\text{max}}$  (in  $^\circ\text{K}$ ) corresponding to maximum anisotropy of the main values of the susceptibility  $\chi_{ii}$  ( $i = \text{xx}, \text{yy}, \text{zz}$ ) tensor,  $\chi_{\text{av}} T[\chi_{\text{av}} = (1/3)(\chi_{\text{xx}} + \chi_{\text{yy}} + \chi_{\text{zz}})]$  and anisotropic  $\mathbf{D}_{12}$  and  $\mathbf{A}_{12}$  tensor parameters of a  $\text{Fe}^{\text{III}}\text{-CN-Cu}^{\text{II}}$  model complex with and without trigonal Jahn–Teller distortions from model calculations accounting for the difference of  $J_{\text{E}}$  and  $J_{\text{B}_2}$  exchange coupling parameters (exchange anisotropy) or alternatively, assuming an isotropic Heisenberg exchange ( $J = J_{\text{E}} = J_{\text{B}_2}$ )

Parameter set <sup>a</sup>	$E_1$	$(\chi_{zz} T)_{\text{max}}^b$		$J$	$D_{xz}$	$A_x$
	$E_2$	$[T_{\text{max}}]$	$(\chi_{\text{av}} T)_{\text{max}}$	$D$	$D_{yz}$	$A_y$
	$E_3$	$(\chi_{\text{xx}} T_{\text{max}})^b$	$[T_{\text{max}}]$	$E$	$D_{xy}$	$A_z$
	$E_4$	$(\chi_{yy} T_{\text{max}})^b$				
$J_{\text{E}} = 19.4$	0.00	1.199 <sup>b</sup>	0.801	−4.13	0.00	0.00
$J_{\text{B}_2} = 1.6$	0.52	[3]	[8]	6.20	0.00	0.00
$Q_{\tau} = 0$	6.34	0.495 <sup>b</sup>		0.00	0.00	0.53
	6.34	0.495 <sup>b</sup>				
$J_{\text{E}} = 19.4$	0.00	1.485 <sup>b</sup>	0.999	−4.02	0.83	0.40
$J_{\text{B}_2} = 1.6$	0.29	[3]	[5]	6.10	−0.40	−1.63
$Q_{\tau} = 0.128$	2.56	1.054 <sup>b</sup>		−2.93	−5.87	−0.04
	10.46	0.355 <sup>b</sup>				
$J_{\text{E}} = 13.5$	0.00	0.87 <sup>b</sup>	0.87	−1.50	0.00	0.00
$J_{\text{B}_2} = 13.5$	4.42	[4]	[4]	2.25 <sup>c</sup>	0.00	0.00
$Q_{\tau} = 0$	4.42	0.87 <sup>b</sup>		0.00	0.00	4.50 <sup>c</sup>
	4.42	0.87 <sup>b</sup>				
$J_{\text{E}} = 13.5$	0.00	1.35 <sup>b</sup>	1.05	−3.78	−2.95	1.74
$J_{\text{B}_2} = 13.5$	1.79	[3]	[4]	3.53	−1.74	−0.53
$Q_{\tau} = 0.128$	1.79	0.36 <sup>b</sup>		−2.78	−5.55	1.42
	9.80	1.40 <sup>b</sup>				

<sup>a</sup> $J$  parameters (in  $\text{cm}^{-1}$ ) and trigonal (Jahn–Teller distortions,  $Q_{\tau}$  in  $\text{\AA}$ ) are listed, other parameters adopted in these calculations are as follows: vibronic coupling parameters from Table 1 (second column),  $\zeta_{\text{Fe}} = 345 \text{ cm}^{-1}$ ,  $k_{\text{Fe}} = 0.79$ ,  $g$ -tensor values for Cu:  $g_{\text{xx}} = g_{\text{yy}} = 2.18$ ,  $g_{\text{zz}} = 2.00$

<sup>b</sup>Directions corresponding to the main-values of the susceptibility tensor have been taken to coincide with those of the  $g$ -tensor (see Table 6)

<sup>c</sup>Due to the threefold degeneracy of the  $T_2$  spin state these values are not be taken literally

The matrix of the exchange Hamiltonian  $-J_{ij}\hat{s}_i\hat{s}_j$  ( $i$  and  $j$  are the magnetic orbitals on center 1 and 2) within the spin only basis  $\alpha_i\alpha_j, \beta_i\alpha_j, \alpha_i\beta_j$  and  $\beta_i\beta_j$  is given by (24). The combination of (11) and (24) with the Jahn–Teller Hamiltonian of (1) leads to the total Hamiltonian (25), represented by the product of the spin–orbit basis of  $\text{Fe}^{\text{III}}$  and the spin-only basis functions of  $\text{Cu}^{\text{II}}$   $\alpha', \beta'$ :  $[(\xi, \eta, \zeta)\alpha_1; (\xi, \eta, \zeta)\beta_1]\alpha'$  and  $[(\xi, \eta, \zeta)\alpha_1 (\xi, \eta, \zeta)\beta_1]\beta'$ .

$$\mathbf{H}_{\text{exc}}(i, j) = \begin{matrix} & \alpha_i\alpha_j & \beta_i\alpha_j & \alpha_i\beta_j & \beta_i\beta_j \\ \begin{bmatrix} -\frac{1}{4}J_{ij} & 0 & 0 & 0 \\ 0 & \frac{1}{4}J_{ij} & -\frac{1}{2}J_{ij} & 0 \\ 0 & -\frac{1}{2}J_{ij} & \frac{1}{4}J_{ij} & 0 \\ 0 & 0 & 0 & -\frac{1}{4}J_{ij} \end{bmatrix} & \end{matrix} \quad (24)$$

We now focus on the specific case of a  $\text{Fe}^{\text{III}}\text{--CN--Cu}^{\text{II}}$  pair with  $C_{4v}$  symmetry (no Jahn–Teller distortion at the  $[\text{Fe}(\text{CN})_6]^{3-}$  center). We use the eigenfunctions of  $\mathbf{H}_{\text{SO}}$  in as given in [69], which transform as  $E''(\alpha'', \beta'')$  and  $U'(\mu, \nu, \kappa, \lambda)$  in the octahedral double group, defined by the column vectors  $\mathbf{c}(i)$  ( $i = \alpha'', \beta'', \mu, \nu, \kappa, \lambda$ ), given in (26). The transformed matrix  $\mathbf{T}'\mathbf{H}_{\text{SO}}\mathbf{T}$  is diagonal with eigenvalues  $-\zeta[E''(\alpha'', \beta'')]$  and  $\zeta/2[U'(\mu, \nu, \kappa, \lambda)]$ , and with a Zeeman Hamiltonian in  $z$  direction [i.e.  $\hat{H}_{Z2} = \mu_B(\mathbf{s}_{z1} + k\mathbf{l}_{z1})B_z$ ], given by (27), and with an effective  $M_s'$  value of each of the components of  $E''(\alpha'', \beta'')$  and  $U'(\mu, \nu, \kappa, \lambda)$  as indicated.

The  $\text{Fe}^{\text{III}}[E''(\alpha'', \beta''), M_s' = \pm 1/2, U'(\mu, \nu, \kappa, \lambda); M_s' = \pm 3/2, \pm 1/2,] - \text{Cu}^{\text{II}}[\alpha', \beta'(m_s = \pm 1/2)]$  pair states, can be classified according to the total  $M_s = M_s' \pm m_s$  value. Using (26),  $\mathbf{H}$  of (25) can be reduced to a block diagonal form, and in  $C_{4v}$  symmetry we obtain the symmetry-adapted functions of the Fe–Cu pair states and the corresponding energy expressions (28–31). As follows from these expressions, there is configurational mixing between the pair of states of lowest energy  $B_1(E'')$ ,  $B_2(E'')$  and  $B_1(U')$ ,  $B_2(U')$ . With perturbation theory we obtain (32, 33) for the second order energy change, where exchange terms in the denominator have been neglected. With the values of  $J(^2E) = 19.4$ ,  $J(^2B_2) = 1.6$  and  $\zeta = 345$  (all in  $\text{cm}^{-1}$ ) we obtain  $\Delta E[B_1(E'')] = -0.008 \text{ cm}^{-1}$  and  $\Delta E[B_2(E'')] = -0.106 \text{ cm}^{-1}$ , i.e. a negligible influence on the ground state spin levels from the  $\text{Fe}^{\text{III}}(U') - \text{Cu}^{\text{II}}$  excited spin states. The energies of the lowest four spin states, which arise from  $\text{Fe}^{\text{III}}(E'') - \text{Cu}^{\text{II}}$  exchange coupling, are given by (34), with  $\delta J(^2E)$  to account for the possible decrease of symmetry,  $C_{4v} \rightarrow C_{2v}$  (35).

$$\mathbf{H} = \begin{bmatrix} (\xi, \alpha_1)\alpha' & (n\alpha_1)\alpha' & (\zeta\alpha_1)\alpha' & (\xi, \beta_1)\alpha' & (n\beta_1)\alpha' & (\zeta\beta_1)\alpha' & (\xi, \alpha_1)\beta' & (n\alpha_1)\beta' & (\zeta\alpha_1)\beta' & (\xi, \beta_1)\beta' & (n\beta_1)\beta' & (\zeta\beta_1)\beta' \\ -\frac{J^{(2E)}}{4} & -\frac{i}{2}S - V_\tau Q_\zeta & -V_\tau Q_\eta & 0 & 0 & \frac{1}{2}S & 0 & 0 & 0 & 0 & 0 & 0 \\ \frac{i}{2}S - V_\tau Q_\zeta & -\frac{J^{(2E)}}{4} & -V_\tau Q_\xi & 0 & 0 & -\frac{i}{2}S & 0 & 0 & 0 & 0 & 0 & 0 \\ -V_\tau Q_\eta & -V_\tau Q_\xi & -\frac{J^{(2B_2)}}{4} & -\frac{1}{2}S & \frac{i}{2}S & 0 & 0 & 0 & 0 & 0 & 0 & 0 \\ 0 & 0 & -\frac{1}{2}S & \frac{J^{(2E)}}{4} & \frac{i}{2}S - V_\tau Q_\zeta & -V_\tau Q_\eta & -\frac{J^{(2E)}}{2} & 0 & 0 & 0 & 0 & 0 \\ 0 & 0 & -\frac{i}{2}S & -\frac{i}{2}S - V_\tau Q_\eta & \frac{J^{(2E)}}{4} & -V_\tau Q_\xi & 0 & -\frac{J^{(2E)}}{2} & 0 & 0 & 0 & 0 \\ \frac{1}{2}S & \frac{i}{2}S & 0 & -V_\tau Q_\eta & -V_\tau Q_\xi & \frac{J^{(2B_2)}}{4} & 0 & 0 & -\frac{J^{(2B_2)}}{2} & 0 & 0 & 0 \\ 0 & 0 & 0 & 0 & 0 & 0 & \frac{J^{(2E)}}{4} & -\frac{i}{2}S - V_\tau Q_\zeta & -V_\tau Q_\eta & 0 & 0 & \frac{1}{2}S \\ 0 & 0 & 0 & 0 & -\frac{J^{(2E)}}{2} & 0 & 0 & \frac{J^{(2E)}}{4} & -V_\tau Q_\xi & 0 & 0 & -\frac{i}{2}S \\ 0 & 0 & 0 & 0 & 0 & 0 & -V_\tau Q_\eta & -V_\tau Q_\xi & \frac{J^{(2B_2)}}{4} & -\frac{1}{2}S & \frac{i}{2}S & 0 \\ 0 & 0 & 0 & 0 & 0 & 0 & 0 & -V_\tau Q_\xi & -\frac{J^{(2B_2)}}{4} & -\frac{1}{2}S & -\frac{i}{2}S & 0 \\ 0 & 0 & 0 & 0 & 0 & 0 & 0 & 0 & -\frac{1}{2}S & -\frac{J^{(2E)}}{4} & \frac{i}{2}S - V_\tau Q_\zeta & -V_\tau Q_\eta \\ 0 & 0 & 0 & 0 & 0 & 0 & 0 & 0 & -\frac{i}{2}S - V_\tau Q_\zeta & -\frac{J^{(2E)}}{4} & -\frac{i}{2}S & -V_\tau Q_\xi \\ 0 & 0 & 0 & 0 & 0 & 0 & \frac{1}{2}S & \frac{i}{2}S & 0 & -V_\tau Q_\eta & -V_\tau Q_\xi & -\frac{J^{(2B_2)}}{4} \end{bmatrix} \quad (25)$$

$$\begin{aligned}
& [\mathbf{c}(\alpha'') \quad \mathbf{c}(\beta'') \quad \mathbf{c}(\mu) \quad \mathbf{c}(\nu) \quad \mathbf{c}(\kappa) \quad \mathbf{c}(\lambda)] = \\
& = \mathbf{T} = \begin{bmatrix} 0 & \frac{i}{\sqrt{3}} & -\frac{i}{\sqrt{2}} & 0 & -\frac{i}{\sqrt{6}} & 0 \\ 0 & \frac{1}{\sqrt{3}} & \frac{1}{\sqrt{2}} & 0 & -\frac{1}{\sqrt{6}} & 0 \\ \frac{i}{\sqrt{3}} & 0 & 0 & -i\sqrt{\frac{2}{3}} & 0 & 0 \\ \frac{i}{\sqrt{3}} & 0 & 0 & \frac{i}{\sqrt{6}} & 0 & \frac{i}{\sqrt{2}} \\ -\frac{1}{\sqrt{3}} & 0 & 0 & -\frac{1}{\sqrt{6}} & 0 & \frac{1}{\sqrt{2}} \\ 0 & -\frac{i}{\sqrt{3}} & 0 & 0 & -i\sqrt{\frac{2}{3}} & 0 \end{bmatrix} \quad (26)
\end{aligned}$$

$$\begin{aligned}
& \begin{array}{cccccc} \alpha'' & \beta'' & \mu & \nu & \kappa & \lambda \\ M'_s = 1/2 & -1/2 & 3/2 & 1/2 & -1/2 & -3/2 \end{array} \\
& \mathbf{H}_{Z1}^z = \mu_B B_z \begin{bmatrix} -\frac{1}{3} - \frac{2}{3}k & 0 & 0 & -\frac{\sqrt{2}}{3}(2+k) & 0 & 0 \\ 0 & \frac{1}{3} + \frac{2}{3}k & 0 & 0 & 0 & 0 \\ 0 & 0 & 1-k & 0 & 0 & 0 \\ -\frac{\sqrt{2}}{3}(2+k) & 0 & 0 & \frac{1}{3} - \frac{1}{3}k & 0 & 0 \\ 0 & 0 & 0 & 0 & -\frac{1}{3} + \frac{1}{3}k & 0 \\ 0 & 0 & 0 & 0 & 0 & -1+k \end{bmatrix} \quad (27)
\end{aligned}$$

$$\begin{aligned}
& M_s = \pm 2 : E \quad U' \\
& \quad \quad \quad M_s = +2 \quad \mu, \alpha' \\
& \quad \quad \quad M_s = -2 \quad \lambda, \beta' \\
& \mathbf{H}(E) = \frac{1}{2}\zeta - \frac{1}{4}J(^2E) \quad (28) \\
& M_s = \pm 1 : E : \quad \begin{array}{ccc} E'' & U' & U' \\ +1 & \alpha''\alpha' & \nu\alpha' & \mu\beta' \\ -1 & \beta''\beta' & \kappa\beta' & \lambda\alpha' \end{array}
\end{aligned}$$

$$\mathbf{H}(E) = \begin{bmatrix} -\zeta + \frac{1}{6}J(^2E) - \frac{1}{12}J(^2B_2) & \pm \frac{1}{6\sqrt{2}}[J(^2E) + J(^2B_2)] & \pm \frac{1}{\sqrt{6}}J(^2E) \\ \pm \frac{1}{6\sqrt{2}}[J(^2E) + J(^2B_2)] & \frac{1}{2}\zeta + \frac{1}{12}J(^2E) - \frac{1}{6}J(^2B_2) & \frac{1}{2\sqrt{3}}J(^2E) \\ \pm \frac{1}{\sqrt{6}}J(^2E) & \frac{1}{2\sqrt{3}}J(^2E) & \frac{1}{2}\zeta + \frac{1}{4}J(^2E) \end{bmatrix} \quad (29)$$

$$M_s = 0 : B_1(E'') = \frac{1}{\sqrt{2}}(-\beta''\alpha' + \alpha''\beta') \quad B_1(U') = \frac{1}{\sqrt{2}}(\kappa\alpha' + \nu\beta')$$

$$\mathbf{H}(B_1) = \begin{bmatrix} -\zeta - \frac{1}{8}J(^2E) - \frac{1}{12}J(^2B_2) & \frac{1}{6\sqrt{2}}[-J(^2E) + J(^2B_2)] \\ \frac{1}{6\sqrt{2}}[-J(^2E) + J(^2B_2)] & \frac{1}{2}\zeta - \frac{1}{12}J(^2E) - \frac{1}{6}J(^2B_2) \end{bmatrix} \quad (30)$$

$$B_2(E'') = \frac{1}{\sqrt{2}}(\beta''\alpha' + \alpha''\beta') \quad B_2(U') = \frac{1}{\sqrt{2}}(\kappa\alpha' - \nu\beta')$$

$$\mathbf{H}(B_2) = \begin{bmatrix} -\zeta - \frac{1}{8}J(^2E) + \frac{1}{4}J(^2B_2) & \frac{1}{2\sqrt{2}}[J(^2E) + J(^2B_2)] \\ \frac{1}{2\sqrt{2}}[J(^2E) + J(^2B_2)] & \frac{1}{2}\zeta - \frac{1}{12}J(^2E) + \frac{1}{2}J(^2B_2) \end{bmatrix} \quad (31)$$

$$\Delta E[B_1(E'')] = \Delta E[E(E'')] = -\frac{1}{108} \frac{[J(^2B_2) - J(^2E)]^2}{\zeta} \quad (32)$$

$$\Delta E[B_2(E'')] = -\frac{1}{12} \frac{[J(^2B_2) + J(^2E)]^2}{\zeta} \quad (33)$$

$$\mathbf{H}_{Fe(\Gamma_7)Cu} =$$

$\alpha''\alpha'$	$\beta''\alpha'$	$\alpha''\beta'$	$\beta''\beta'$
$\left[ \begin{array}{cccc} \frac{1}{6}J(^2E) - \frac{1}{12}J(^2B_2) & 0 & 0 & -\frac{1}{3}\delta J(^2E) \\ 0 & -\frac{1}{6}J(^2E) + \frac{1}{12}J(^2B_2) & \frac{1}{6}J(^2B_2) & 0 \\ 0 & \frac{1}{6}J(^2B_2) & -\frac{1}{6}J(^2E) + \frac{1}{12}J(^2B_2) & 0 \\ -\frac{1}{3}\delta J(^2E) & 0 & 0 & \frac{1}{6}J(^2E) - \frac{1}{12}J(^2B_2) \end{array} \right]$			

(34)

$$\delta J(^2E) = \frac{J_{\xi\xi} - J_{\eta\eta}}{2} \quad (35)$$

$$J(^2E) = \frac{J_{\xi\xi} + J_{\eta\eta}}{2} \quad (36)$$

The parameters J, D and E of the spin Hamiltonian  $\hat{H}_{\text{sph}}$  (37), i.e. a simplified form of (13) are derived by comparison of (34) with the representation of  $\hat{H}_{\text{sph}}$  in the basis  $\alpha''\alpha'$ ,  $\beta''\alpha'$ ,  $\alpha''\beta'$ ,  $\beta''\beta'$  (38). From (37) to (38), the substitutions described in [32, 39, 40] were made, and these are derived, using the direct products  $\mathbf{s}_i \otimes \mathbf{s}_j$  ( $i, j = x, y, z$ ) of the spin matrices for  $\frac{1}{2}$  (42).

$$\hat{H}_{\text{sph}} = -J\mathbf{s}'_1\mathbf{s}_2 + \frac{2D}{3}(2\mathbf{s}'_{1z}\mathbf{s}_{2z} - \mathbf{s}'_{1x}\mathbf{s}_{2x} - \mathbf{s}'_{1y}\mathbf{s}_{2y}) + 2E(\mathbf{s}'_{1x}\mathbf{s}_{2x} - \mathbf{s}'_{1y}\mathbf{s}_{2y}) \quad (37)$$

$$\mathbf{H}_{\text{sph}} = \begin{bmatrix} -\frac{1}{4}J + \frac{1}{3}D & 0 & 0 & E \\ 0 & \frac{1}{4}J - \frac{1}{3}D & -\frac{1}{2}J - \frac{1}{3}D & 0 \\ 0 & -\frac{1}{2}J - \frac{1}{3}D & \frac{1}{4}J - \frac{1}{3}D & 0 \\ E & 0 & 0 & -\frac{1}{4}J + \frac{1}{3}D \end{bmatrix} \quad (38)$$

$$-s'_1 s_2 \Rightarrow \begin{bmatrix} -\frac{1}{4} & 0 & 0 & 0 \\ 0 & \frac{1}{4} & -\frac{1}{2} & 0 \\ 0 & -\frac{1}{2} & \frac{1}{4} & 0 \\ 0 & 0 & 0 & -\frac{1}{4} \end{bmatrix}; \quad (39)$$

$$2s'_{1z}s_{2z} - s'_{1x}s_{2x} - s'_{1y}s_{2y} \Rightarrow \begin{bmatrix} \frac{1}{2} & 0 & 0 & 0 \\ 0 & -\frac{1}{2} & -\frac{1}{2} & 0 \\ 0 & -\frac{1}{2} & -\frac{1}{2} & 0 \\ 0 & 0 & 0 & \frac{1}{2} \end{bmatrix} \quad (40)$$

$$s'_{1x}s_{2x} - s'_{1y}s_{2y} \Rightarrow \begin{bmatrix} 0 & 0 & 0 & \frac{1}{2} \\ 0 & 0 & 0 & 0 \\ 0 & 0 & 0 & 0 \\ \frac{1}{2} & 0 & 0 & 0 \end{bmatrix} \quad (41)$$

$$\begin{matrix} \alpha\beta & \alpha\beta & \alpha\beta \\ s_x = \frac{1}{2} \begin{bmatrix} 0 & 1 \\ 1 & 0 \end{bmatrix}; s_y = \frac{i}{2} \begin{bmatrix} 0 & -1 \\ 1 & 0 \end{bmatrix}; s_z = \frac{1}{2} \begin{bmatrix} 1 & 0 \\ 0 & -1 \end{bmatrix}; \end{matrix} \quad (42)$$

From a comparison between (34) and (38) we get expressions (43–45), which relate the parameters of the spin-Hamiltonian  $-J$ ,  $D$  and  $J_E$ ,  $J_{B2}$  (DFT).

$$-\frac{1}{4}J + \frac{1}{3}D = \frac{1}{6}J(^2E) - \frac{1}{12}J(^2B_2) \quad (43)$$

$$-\frac{1}{2}J - \frac{1}{3}D = \frac{1}{6}J(^2B_2) \quad (44)$$

$$E = -\frac{1}{3}\delta J(^2E) \quad (45)$$

It is not always possible to directly derive the parameters of the spin Hamiltonian from first principle calculations. As seen from (29) to (31), there is a configuration mixing between the spin multiplets due to the  $E''$ – $\text{Cu}^{\text{II}}$  and the multiplets due to the  $U'$ – $\text{Cu}^{\text{II}}$  interaction via exchange coupling terms. In the example discussed above,  $\zeta \gg J(^2E)$ ,  $J(^2B_2)$  and the parameters  $J$ ,  $D$  and  $E$  (43–45) are unique and can easily be determined. However, starting from the  $\text{Fe}^{\text{III}}$ – $\text{CN}$ – $\text{Cu}^{\text{II}}$  pair in  $C_{4v}$  symmetry (octahedral  $[\text{Fe}(\text{CN})_6]^{3-}$  fragment), and introducing a  $D_{3d}$  Jahn–Teller distortion,  $U'$  splits into  $E''$  and  $E'$ , and the later start mix with  $E'$  (originating from  $E''$  in  $O_h$ ). In Fig. 9, we plot the electronic energy levels of  $[\text{Fe}(\text{CN})_6]^{3-}$  in dependence of the ratio  $V_\tau Q_\tau / \zeta$  [this is obtained by diagonalization of the Hamiltonian of (25), with setting  $J(^2E) = J(^2B_2) = 0$ ]. It follows, that the electronic ground state is well separated from the excited states, both in  $O_h$  and in distorted  $D_{3d}$  geometries. One can understand this result if one transforms the spin–orbit coupling matrix into the trigonal basis given by (46). Here,  $\mathbf{H}_{\text{JT}}$  is diagonal with the energies of  $^2A_1$  and  $^2E$ , given by  $-2V_\tau Q_\tau$  and  $V_\tau Q_\tau$ , respectively.

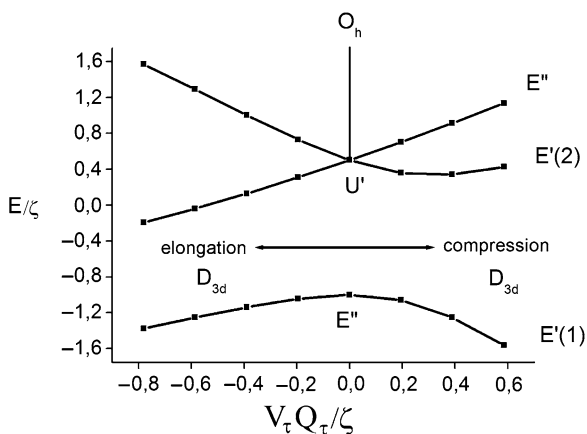


**Fig. 9** Electronic levels of  $[\text{Fe}(\text{CN})_6]^{3-}$  in dependence of the vibronic coupling energy in units of  $\zeta$

$$\begin{aligned}
 \varphi(A_1) &= \frac{1}{\sqrt{3}}(\xi + \eta + \zeta) \\
 \varphi(E_y) &= \frac{1}{\sqrt{2}}(\xi - \eta) \\
 \varphi(E_x) &= \frac{1}{\sqrt{6}}(-\xi - \eta + 2\zeta)
 \end{aligned} \tag{46}$$

While  ${}^2A_1$  is the ground state for trigonally compressed geometries, it is of  ${}^2E$  symmetry in elongated geometries. However, the  ${}^2E$  term splits to first order by spin–orbit coupling with an energy difference between the  $E'(1)$  ground state and the  $E''$  lowest excited state, given by  $\zeta$ . The splitting is again much larger than  $J({}^2E)$  and  $J({}^2B_2)$ . Therefore, one can apply the spin-Hamiltonian (13) and deduce its parameters by comparison with the eigenvalues of (25) in the whole range of Jahn–Teller-distorted geometries between  $Q_\tau = -0.256$  and  $-0.256\text{Å}$ . In the given example (Table 5, second row, columns 5 to 7,  $Q_\tau = 0.128\text{Å}$ ) one first diagonalizes  $\mathbf{H}_{\text{SO}} + \mathbf{H}_{\text{JT}}$ , including the Zeeman matrix with a small magnetic field ( $B_z = 0.0001\text{ T}$ ), to obtain the proper components  $\alpha''$  and  $\beta''$  of the ground state Kramers doublet  $E'(1)$  (Fig. 9). With the resulting eigenvectors, one transforms the Hamiltonian (25) to yield the following traceless matrix (with energies in  $\text{cm}^{-1}$ ) of the ground state spin levels:

$$\mathbf{H}_{\text{sph}} = \begin{bmatrix} \alpha''\alpha' & \beta''\alpha' & \alpha''\beta' & \beta''\beta' \\ 3.038 & 0.615 & 0.200(-1+i) & -2.933(1-i) \\ 0.615 & -3.038 & 0.020(-1+i) & 0.200(1-i) \\ 0.200(-1-i) & 0.020(-1-i) & -3.038 & -0.615 \\ -2.933(1+i) & 0.200(1+i) & -0.615 & 3.038 \end{bmatrix} \tag{47}$$



Simple manipulations, described by (37–42) show that within the  $\alpha''\alpha'$ ,  $\beta''\alpha'$ ,  $\alpha''\beta'$  and  $\beta''\beta'$  basis, the spin-Hamiltonian of (13) leads to the matrix representation given by (48).

$$\mathbf{H}_{\text{sph}} = \begin{matrix} & \alpha''\alpha' & \beta''\alpha' & \alpha''\beta' & \beta''\beta' \end{matrix} \begin{bmatrix} \frac{1}{3}D - \frac{1}{4}J & \frac{1}{4}(D_{xz} - iD_{yz} - iA_x - A_y) & \frac{1}{4}(D_{xz} - iD_{yz} + iA_x + A_y) & E - \frac{1}{2}iD_{xy} \\ \frac{1}{4}(D_{xz} + iD_{yz} + iA_x - A_y) & -\frac{1}{3}D + \frac{1}{4}J & -\frac{1}{3}D - \frac{1}{2}J - \frac{1}{2}A_z & \frac{1}{4}(-D_{xz} + iD_{yz} - iA_x - A_y) \\ \frac{1}{4}(D_{xz} + iD_{yz} - iA_x + A_y) & -\frac{1}{3}D - \frac{1}{2}J + \frac{1}{2}A_z & -\frac{1}{3}D + \frac{1}{4}J & \frac{1}{4}(-D_{xz} + iD_{yz} + iA_x + A_y) \\ E + \frac{1}{2}iD_{xy} & \frac{1}{4}(-D_{xz} - iD_{yz} + iA_x - A_y) & \frac{1}{4}(-D_{xz} - iD_{yz} - iA_x + A_y) & \frac{1}{3}D - \frac{1}{4}J \end{bmatrix} \quad (48)$$

From the comparison of the matrix of (47), obtained by a numerical calculation and (48), the following general equations for the spin-Hamiltonian parameters (13) of the  $\text{Cu}^{\text{II}}\text{--Fe}^{\text{III}}$  pair result:

$$\begin{aligned} J &= -(4/3)[H_{\text{sph}}(1, 1) + \text{real}(H_{\text{sph}}(2, 3))] \\ D &= 2[H_{\text{sph}}(1, 1)] - \text{real}(H_{\text{sph}}(2, 3)) \\ E &= \text{real}(H_{\text{sph}}(1, 4)) \\ D_{xy} &= -2\text{imag}(H_{\text{sph}}(1, 4)) \\ D_{xz} &= 2[\text{real}(H_{\text{sph}}(1, 2)) + \text{real}(H_{\text{sph}}(1, 3))] \\ D_{yz} &= -2[\text{imag}(H_{\text{sph}}(1, 3)) + \text{imag}(H_{\text{sph}}(1, 2))] \\ A_x &= 2[\text{imag}(H_{\text{sph}}(1, 3)) - \text{imag}(H_{\text{sph}}(1, 2))] \\ A_y &= 2[\text{real}(H_{\text{sph}}(1, 3)) - \text{real}(H_{\text{sph}}(1, 2))] \\ A_z &= -2\text{imag}(H_{\text{sph}}(2, 3)) \end{aligned}$$

Within the spin-only basis and without distortions on  $[\text{Fe}(\text{CN})_6]^{3-}$ , the Zeeman operator  $\hat{H}_{Z1}$  is represented by the matrices given in (50–52), which directly show the coupling of the local g-tensors of  $\text{Fe}^{\text{III}}$  and  $\text{Cu}^{\text{II}}$ .

$$\mathbf{H}_{Z1}^x = \mu_B B_x \begin{matrix} & \alpha''\alpha' & \beta''\alpha' & \alpha''\beta' & \beta''\beta' \end{matrix} \begin{bmatrix} 0 & -\frac{1}{3} - \frac{2}{3}k & \frac{1}{2}g_{2x} & 0 \\ -\frac{1}{3} - \frac{2}{3}k & 0 & 0 & \frac{1}{2}g_{2x} \\ \frac{1}{2}g_{2x} & 0 & 0 & -\frac{1}{3} - \frac{2}{3}k \\ 0 & \frac{1}{2}g_{2x} & -\frac{1}{3} - \frac{2}{3}k & 0 \end{bmatrix} \quad (49)$$

$$\mathbf{H}_{Z1}^y = \mu_B B_y \begin{matrix} & \alpha''\alpha' & \beta''\alpha' & \alpha''\beta' & \beta''\beta' \end{matrix} \begin{bmatrix} 0 & \frac{i}{3} + \frac{2i}{3}k & -\frac{i}{2}g_{2y} & 0 \\ -\frac{i}{3} - \frac{2i}{3}k & 0 & 0 & -\frac{i}{2}g_{2y} \\ \frac{i}{2}g_{2y} & 0 & 0 & \frac{i}{3} + \frac{2i}{3}k \\ 0 & \frac{i}{2}g_{2y} & -\frac{i}{3} - \frac{2i}{3}k & 0 \end{bmatrix} \quad (50)$$

$$\mathbf{H}_{Z1}^z = \mu_B B_z$$

$$\begin{array}{cccc} & \alpha''\alpha' & \beta''\alpha' & \alpha''\beta' & \beta''\beta' \\ \left[ \begin{array}{ccccc} -\frac{1}{3} - \frac{2}{3}k + \frac{1}{2}g_{2z} & 0 & 0 & 0 \\ 0 & \frac{1}{3} + \frac{2}{3}k + \frac{1}{2}g_{2z} & 0 & 0 \\ 0 & 0 & -\frac{1}{3} - \frac{2}{3}k - \frac{1}{2}g_{2z} & 0 \\ 0 & 0 & 0 & \frac{1}{3} + \frac{2}{3}k - \frac{1}{2}g_{2z} \end{array} \right] & (51) \end{array}$$

### 3.2 Effect of Spin–Orbit Coupling at the Regular Octahedral Subunits

As has been shown in Sect. 2.2, the  $^2T_{2g}$  ground state of  $[\text{Fe}(\text{CN})_6]^{3-}$  splits by spin–orbit coupling into a ground state doublet  $E''(\alpha'', \beta'')$  and an excited  $U'(\kappa, \lambda, \mu, \nu)$  Kramers quartet, separated by  $(3/2)\zeta$ . In the  $C_{4v}$  symmetry of the linear Fe–CN–Cu unit, the  $E''(\alpha'', \beta'')$  state couples via spin-exchange with the  $E'(\alpha', \beta')$  spin state of  $\text{Cu}^{\text{II}}$  to give rise to a  $B_1$  ground state and to  $B_2$  and E excited spin states (52), which are visualized in Fig. 10, where spin eigenfunctions are also included. The spin ground state ( $B_1$ ) is non-magnetic. However, the  $B_2 - B_1$  energy separation  $[1/3J(^2B_2)]$  is small, the singly occupied  $a_1$  orbital ( $d_{z^2}$ ) of Cu interacts weakly with the  $b_2(d_{xy})$  magnetic orbital of  $\delta$ -type of Fe, resulting in a very small exchange energy  $J(^2B_2)$  of  $1.6 \text{ cm}^{-1}$ . This can be compared with the much larger energy of the  $a_1(d_{z^2})$  Cu e ( $d_{xz}, d_{yz}$ ) Fe  $\pi$ -interaction  $J(^2E)$  of  $19.4 \text{ cm}^{-1}$ . The latter places the E spin state at  $6.47 \text{ cm}^{-1}$  above the ground state. Analytical expressions and numerical values of the parameters of the spin-Hamiltonian J, D and  $\mathbf{g}_1(\text{Fe})$  and  $\mathbf{g}_2(\text{Cu})$  have been derived (53). It is remarkable that in the dinuclear complex, the  $\mathbf{g}_1(\text{Fe})$  and  $\mathbf{g}_2(\text{Cu})$  local tensors couple with a different sign. This leads to the interesting and unexpected result that the E-term, which usually is assigned to the magnetic  $M_s = \pm 1$  pair in a ferromagnetically coupled complex with two  $s = 1/2$  ions and with a negative zero-field splitting D, is now highest in energy with small (for  $g_z(E)$ ) or vanishing (for  $g_{x,y}(E)$ )  $\mathbf{g}$ -tensor components.

$$\begin{aligned} E(B_1) &= -\frac{1}{6}J(^2E) - \frac{1}{12}J(^2B_2) \\ E(B_2) &= -\frac{1}{6}J(^2E) + \frac{1}{4}J(^2B_2) \end{aligned} \quad (52)$$

$$\begin{aligned} E(E) &= \frac{1}{6}J(^2E) - \frac{1}{12}J(^2B_2) \\ J &= -\frac{2}{9}J(^2E) - \frac{1}{9}J(^2B_2) = -4.49 \text{ cm}^{-1} \\ D &= \frac{1}{3}J(^2E) - \frac{1}{3}J(^2B_2) = 5.94 \text{ cm}^{-1} \end{aligned} \quad (53)$$

$$g_{1x} = g_{1y} = g_{1z} = -\frac{2}{3} - \frac{4}{3}k = -1.72 \quad g_{2x} = g_{2y} = 2.18; g_{2z} = 2.00$$

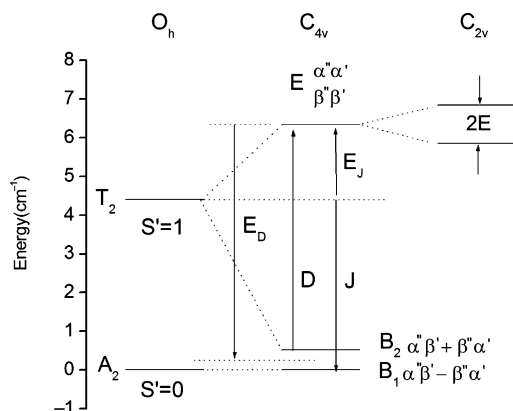


**Fig. 10** Spin energy levels and spin functions for the  $\text{Fe}^{\text{III}}\text{--CN--Cu}^{\text{II}}$  exchange pair of  $C_{4v}$  symmetry;  $\alpha', \beta'$  ( $\alpha'', \beta''$ ) are the spins (effective spins) of  $\text{Cu}^{\text{II}}$  ( $\text{Fe}^{\text{III}}$ ); parameters used for the  $C_{4v}$  energy levels:  $J(^2E) = 19.4 \text{ cm}^{-1}$ ;  $J(^2B_2) = 1.6 \text{ cm}^{-1}$ ;  $\zeta(\text{Fe}) = 345 \text{ cm}^{-1}$ ; energy levels of the pair in  $O_h$  symmetry (collapsing  $\text{Cu}^{\text{II}}$  and  $\text{Fe}^{\text{III}}$  nuclei) and the effect of an additional  $C_{2v}$  orthorhombicity are shown schematically (adopted from [27])

In contrast, the  $B_1$  and  $B_2$  states are composed of an equal admixture of  $M_s = +1$  and  $M_s = -1$  functions and are non-magnetic. However, an external magnetic field ( $\mathbf{B}||z$ ) leads to mixing of these states and thus tends to induce  $M_s = 1$  (or  $M_s = -1$ ) magnetic moments.

$$g_z(E) = g_{2z} + g_{1z} = 0.28; g_{xy}(E) = 0 \quad (54)$$

Because the  $B_2 - B_1$  energy separation is small and the local  $\mathbf{g}_1(\text{Fe})$  and  $\mathbf{g}_2(\text{Cu})$  tensors couple with the same sign in the off-diagonal Zeeman term ((55), weak magnetic fields can already induce magnetic behavior as shown by the dependence of the energies of these states on the magnetic field parallel and perpendicular to the  $z$ -axis of the dinuclear model (Fig. 11). A strong anisotropy is predicted with an easy axis along the  $z$ -direction. Therefore, if the rate of magnetic relaxation is small [i.e. when mediated by phonons (phonon bottleneck)] a single-molecule magnetic behavior in a given time frame and in an applied external magnetic field may result.

$$\hat{H}(B_1, B_2) = \begin{bmatrix} 0 & \mu_B(-g_{1z} + g_{2z})B \\ \mu_B(-g_{1z} + g_{2z})B & \frac{1}{3}J(^2B_2) \end{bmatrix} \quad (55)$$

Due to the unusual coupling of the  $\mathbf{g}_1(\text{Fe})$  and  $\mathbf{g}_2(\text{Cu})$  tensors, the calculated values of  $J$  and  $D$  are opposite in sign compared to those conventionally assumed ( $J > 0, D < 0$ ).

The zero-field splitting energy of  $D = 6 \text{ cm}^{-1}$  exceeds the value of the isotropic coupling parameter  $J$ . As follows from the expression for  $D$  this arises from the high difference between the exchange coupling parameters  $J(^2E)$  and  $J(^2B_2)$ , and

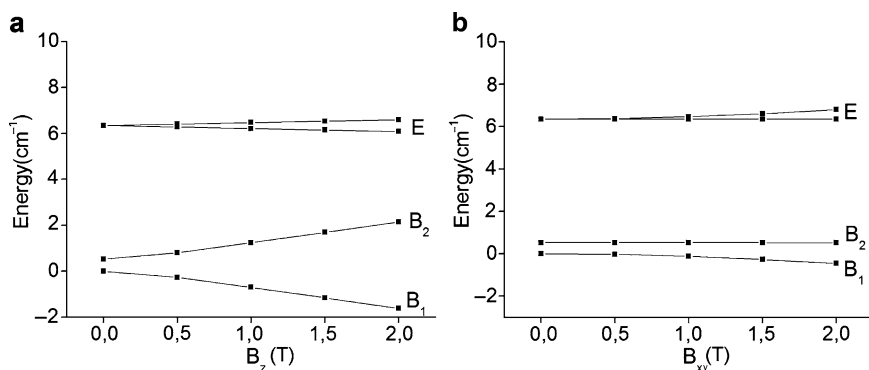


**Fig. 11** Energies of the spin states of the  $\text{Fe}^{\text{III}}\text{-CN-Cu}^{\text{II}}$  pair in a magnetic field parallel (a) and perpendicular (b) to the bridging z axis; parameters:  $k(\text{Fe}) = 0.79$ ;  $g_{xy}(\text{Cu}) = 2.18$ ;  $g_z(\text{Cu}) = 2.000$  (other parameters as in Fig. 10, adopted from [27])

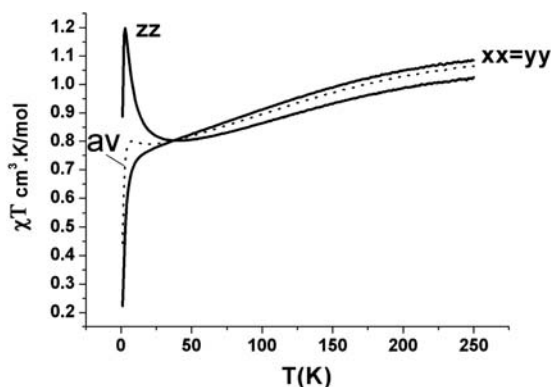


**Fig. 12** The  $\chi T$  vs  $T$  ( $H = 0.5 \text{ T}$ ) dependence for a  $\text{Fe}^{\text{III}}\text{-CN-Cu}^{\text{II}}$  model complex with  $[\text{Fe}(\text{CN})_6]^{3-}$  in an octahedral field without distortions.  $\chi T$  vs  $T$  curves are plotted along directions coinciding with the large ( $g_{zz} = 3.745$ ) and small (approximately zero) components of the  $\mathbf{g}$ -tensor. The  $\chi T$  curve, after averaging along all directions, is also shown. Calculations have been done with the following set of parameters:  $J_E = 19.4 \text{ cm}^{-1}$ ,  $J_{B2} = 1.6 \text{ cm}^{-1}$ ,  $\zeta = 345 \text{ cm}^{-1}$ ,  $k = 0.79$ ,  $g_{xy}(\text{Cu}) = 2.18$ ,  $g_z(\text{Cu}) = 2.00$  ( $z$  along the  $\text{Cu-NC-Fe}$  tetragonal axis)

therefore represents an anisotropy of the exchange type (two-center or exchange anisotropy). We can conclude that the rather large  $D$  in the given model examples is due to the unquenched orbital momenta on  $\text{Fe}^{\text{III}}$ , resulting from the lowest spin multiplet by an orbital dependent exchange mechanism. The rather large zero-field splitting  $D$  leads to the anisotropy of the  $\mathbf{g}$ -tensor shown in Fig. 11 and is found to be exclusively of the Ising type. The rather large magnetic anisotropy manifests itself in the susceptibility tensor (Fig. 12  $(\chi T)_{xx,yy,zz}$ ).

### 3.3 Effect of Combined Spin–Orbit and Static Jahn–Teller Coupling Along Trigonal Modes

We now discuss the added effect of Jahn–Teller distortions at the  $\text{Fe}^{\text{III}}$  center of the  $\text{Fe}^{\text{III}}\text{–CN–Cu}^{\text{II}}$  pair. As has been shown in Sect. 2.1, distortions along the angles ( $T \otimes \tau_2$  coupling) rather than along the bonds ( $T \otimes \varepsilon$  coupling) are those energetically preferred in the systems discussed here. A plot of the dependence of the spin-energy levels on the angle  $\theta$  of trigonal distortion is given in Fig. 13. As expected, the lowering of symmetry leads to a quenching of the orbital momenta, and this leads to a strong decrease (increase) of the anisotropic (isotropic) exchange energies  $D$  and  $J$ , which are quantified in Fig. 13 by the energies  $E_D$  and  $E_J$ , respectively. Therefore, a trigonal compression of an octahedral  $[\text{Fe}(\text{CN})_6]^{3-}$  complex with changes of  $\theta$  by 2 to  $3^\circ$  is calculated to lead to a reduction of  $D$  by one order of magnitude. Such a structural pattern is frequently found in structural data on exchange coupled cyanide complexes. The lowering of the magnetic anisotropy leads to specific changes in the main values of the susceptibility tensor (Fig. 14), which becomes off-axial with a large splitting between the components along the  $x$  and  $y$  directions, perpendicular to the easy axis and therefore creates a transversal anisotropy.

We now discuss these results in the context of an approximation adopted in some theoretical studies [70–74], which only assumes isotropic exchange (i.e. the first term in (17),  $J = (2J_E + J_{B2})/3$ ; see however [75, 76] as exceptions to this approximation). As follows from a symmetry analysis (see (17–23)) and the related discussion in Sect. 3.2), this is strictly valid in  $O_h$  symmetry with collapsing Cu and Fe centers. A calculation for such a hypothetical case (Table 5, fourth row; the Cu–Fe coupling is ferromagnetic but the  $\alpha''$  pseudo-spins of Fe behave as real spins  $\beta$ , resulting in a negative  $g$ -value of Fe) yields the result that the spin ground state is non-degenerate ( $A_1$ ) and is separated by a gap of  $4.42 \text{ cm}^{-1}$  from the excited  $T_2$  state. It follows, that for a linear Fe–CN–Cu fragment with an undistorted octahedral  $[\text{Fe}(\text{CN})_6]^{3-}$  subunit, the exchange anisotropy (i.e. the difference between  $J_E$  and  $J_{B2}$ ) is the only source of the magnetic anisotropy. Therefore, not one ( $J$ ) but

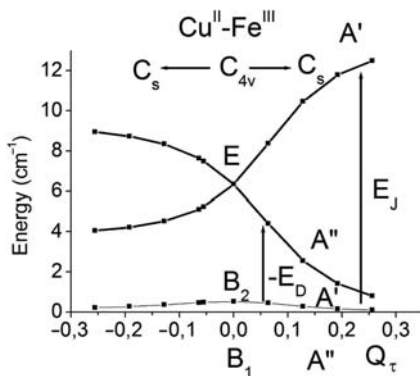


**Fig. 13** Effect of the trigonal ( $\tau_{2g}$ ) Jahn–Teller distortions along (1,1,1) ( $Q_\tau > 0$ , trigonal compression) and (−1, −1, −1) ( $Q_\tau < 0$ , trigonal elongation) on the spin energy levels of  $\text{Fe}^{\text{III}}\text{–Cu}^{\text{II}}$  (adopted from [27])

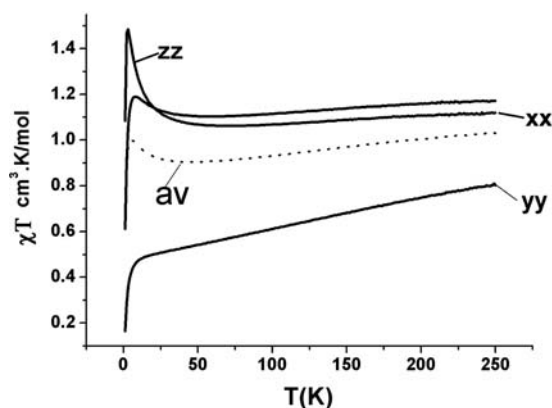


**Fig. 14** The  $\chi T$  vs  $T$  ( $H = 0.5 T$ ) dependence for a  $\text{Fe}^{\text{III}}\text{--CN--Cu}^{\text{II}}$  model complex with a JT-distorted  $[\text{Fe}(\text{CN})_6]^{3-}$  site (trigonal distortions corresponding to the minimum of the ground state potential energy surface,  $Q_\tau = 0.128 \text{ \AA}$ ).  $\chi T$  vs  $T$  curves are plotted along directions coinciding with the large ( $zz$ ) and small (approximately zero) components of the  $g$ -tensor. The  $\chi T$  curve after averaging along all directions is also shown. Calculations have been done with all other parameters specified in Fig. 12

two parameters ( $J_{a1}$  and  $J_{e\theta}$ ) need to be used. Both low-temperature maxima of the magnetic susceptibility and exchange tensor parameters are calculated to be essentially different under the assumption of a single  $J$ , compared to the case, where, in addition to  $J$ ,  $D$  is also accounted for (Table 5, compare second and fourth rows). The lowering of symmetry due to Jahn–Teller distortions leads to essentially off-diagonal  $\mathbf{D}_{12}$  and  $\mathbf{A}_{12}$  tensors. Owing to the difficulty to approximate all parameters, they have been neglected in the interpretations of the magnetic data in many experimental [1–22] and theoretical [70–74] studies on systems with degenerate ground states (see however a recent study with inelastic neutron scattering and a theoretical analysis [77]). The lowering of symmetry due to Jahn–Teller activity and/or geometrical or bonding strain in solids also leads to the fact that in oligonuclear complexes, the zero-field and  $\mathbf{g}$  tensors are generally *not collinear*. To illustrate this point, in Table 6 we include the main (diagonal) values of the  $\mathbf{D}_{12}$ ,  $\mathbf{D}_{12} + \mathbf{A}_{12}$  and  $\mathbf{g}$  tensors and their eigenvalues (cosine functions of the angles between the easy and hard axes, and the cartesian X,Y,Z axes of the molecules), based on a trigonal distortion of  $Q_\tau = 0.128 \text{ \AA}$  (see Sect. 2.1). While the main values of  $\mathbf{D}_{12}$  and  $\mathbf{D}_{12} + \mathbf{A}_{12}$  are found in a good approximation to be mutually collinear and oriented parallel to the directions X, Y and Z of the molecule (i.e. along the initial  $D_{4h}$  axes coinciding with the Fe–CN directions), the molecular  $\mathbf{g}$ -tensor is not, taking in this case the orientation due to the anisotropy of the  $[\text{Fe}(\text{CN})_6]^{3-}$  itself, with an easy axis along the  $(-1, -1, 2)$  direction, i.e. perpendicular to the  $C_3$  axis of the Jahn–Teller distorted  $[\text{Fe}(\text{CN})_6]^{3-}$  subunit (Table 6, second row, with  $J_E = 19.4$  and  $J_{B2} = 1.6 \text{ cm}^{-1}$ ). As in Table 5, a large difference between  $\mathbf{D}_{12}$  and  $\mathbf{D}_{12} + \mathbf{A}_{12}$ , obtained in the two treatments is found. We conclude that an elaborate model which takes the anisotropic and off-diagonal character of the exchange coupling tensors

**Table 6** Main (diagonal) components of the symmetric ( $\mathbf{D}_{12}$ ) and the total ( $\mathbf{D}_{12} + \mathbf{A}_{12}$ ) exchange anisotropy tensors and the  $\mathbf{g}$  tensor<sup>a</sup>, corresponding to the lowest two pair states of a  $\text{Cu}^{\text{II}}\text{–NC–Fe}^{\text{III}}$  complex and their orientations in the adopted molecular coordinate system (X,Y,Z) with the Z axis coinciding with the Cu–NC–Fe bridge, assumed to be linear and with a Jahn–Teller distorted geometry ( $Q_{\text{T}} = 0.128 \text{ \AA}$ ), corresponding to the trigonal minimum of the ground state potential energy surface of  $[\text{Fe}(\text{CN})_6]^{3-}$  with ( $J_{\text{E}} = 19.4 \text{ cm}^{-1}$ ,  $J_{\text{B2}} = 1.6 \text{ cm}^{-1}$ , second row) and without ( $J_{\text{E}} = J_{\text{B2}} = 13.5 \text{ cm}^{-1}$ , third row), taking anisotropic exchange coupling into account

$\mathbf{D}_{12}$ -tensor			$(\mathbf{D}_{12} + \mathbf{A}_{12})$ -tensor			$\mathbf{g}$		
–12.38	4.12	8.26	–12.28	4.30	7.98	0.00	0.00	4.35 <sup>b</sup>
0.92	–0.37	0.09	0.92	–0.37	0.23	0.71	0.61	–0.36
0.38	0.91	–0.14	0.40	0.93	–0.32	–0.71	0.61	–0.36
–0.03	0.17	0.98	0.04	–0.04	0.92	0.00	0.51	0.86
–10.94	5.00	5.94	–10.70	5.35	5.35			
0.90	–0.41	–0.15	0.86	0.26 <sup>d</sup>	0.26 <sup>d</sup>			– <sup>c</sup>
0.38	0.57	0.73	0.48	0.79 <sup>d</sup>	0.79 <sup>d</sup>			
0.21	0.71	–0.67	0.17	0.55 <sup>d</sup>	0.55 <sup>d</sup>			

<sup>a</sup>diagonal g-tensor values are given for pseudo-spin  $1/2$

<sup>b</sup>non-degenerate ground state with an excited spin-state only  $0.29 \text{ cm}^{-1}$  apart, which can mix in a magnetic field

<sup>c</sup>non-degenerate ground state separated by a larger gap ( $1.79 \text{ cm}^{-1}$ ) from the excited, accidentally degenerate spin state

<sup>d</sup>with eigenvectors components, being complex numbers only absolute values are given

$\mathbf{D}_{12}$  and  $\mathbf{A}_{12}$  into account, is mandatory to correctly interpret magnetic data from experiment.

In our studies thus far we have assumed a  $C_{4v}$  pseudo-symmetry for a given  $\text{Fe}^{\text{III}}\text{–CN–M}^{\text{II}}$  ( $\text{M} = \text{Cu}^{\text{II}}, \text{Ni}^{\text{II}}$ ) pair along the  $\text{Fe}^{\text{III}}\text{–CN–M}^{\text{II}}$  bridge to define two exchange parameters  $J_{\text{E}} = J_{\xi\xi} = J_{\eta\eta}$  and  $J_{\text{B2}} = J_{\zeta\zeta}$ . This allowed us to use DFT and the broken symmetry approach to calculate these parameters from first principles. In the general case of a low-symmetric bridge with violated linearity, all six independent parameters of (17) have to be taken into account. In such a situation and in the presence of closely spaced orbitals (near degeneracy) SCF procedures in DFT and ab-initio calculations usually break down. A new and user oriented ab-initio based method to allow the calculation of all symmetry-independent exchange coupling energies for a coupled pair of transition metal ions as well as other examples of exchange coupled pairs containing ions in orbitally degenerate ground states will be published separately [66].

## 4 Conclusions

With a combined DFT and ligand field approach we have analyzed the magnetic anisotropy in  $[\text{Fe}(\text{CN})_6]^{3-}$  and we have shown that, due to symmetry lowering, very small distortions are able to induce magnetic anisotropy. The analysis of this

symmetry-induced increase of the magnetic anisotropy shows that the combination of Jahn–Teller coupling and spin–orbit coupling, which are otherwise competitive and lead to a stabilization of an orbitally non-degenerate ground state in regular and distorted octahedral geometries, respectively, contribute to an increase of the magnetic anisotropy of a single center  $[\text{Fe}(\text{CN})_6]^{3-}$  complex. Trigonal compressions induce an orbitally non-degenerate ground state and lead to an anisotropy of the  $g_z < g_{x,y}$  type (i.e. to an anisotropy with an easy plane), while trigonal elongation, with an orbitally degenerate  ${}^2E_g$  ground state, leads to an anisotropy of the type  $g_z > g_{x,y}$  (i.e. to an anisotropy with an easy axis). The situation changes completely when  $[\text{Fe}(\text{CN})_6]^{3-}$  is part of a dinuclear complex with a common CN bridge in a  $\text{M}^{\text{II}}\text{--NC--Fe}^{\text{III}}$  unit ( $\text{M} = \text{Cu}^{\text{II}}, \text{Ni}^{\text{II}}$ ). Here, with a regular  $[\text{Fe}(\text{CN})_6]^{3-}$  complex with a four fold symmetry ( $C_{4v}$ ) with respect to the Cu–NC–Fe bridge, a large anisotropy of the exchange-type emerges. Orbital contributions, which affect the spin-subsystem via the mechanism of spin–orbit coupling (orbital dependent exchange), results in an anisotropy of the Ising type. Geometrical distortions, leading to a quenching of spin–orbit coupling, lead to a reduction of the magnetic anisotropy. Therefore, trigonal distortions of only 1–2° are able to completely destroy the magnetic anisotropy. A similar anisotropy of the Ising-type has been reported in theoretical studies of  $\text{Mn}^{\text{II}}\text{--NC--Mo}^{\text{V}}$  [30, 78] and  $\text{M--NC--Os}^{\text{III}}$  ( $\text{M} = \text{Cr}^{\text{III}}, \text{Mn}^{\text{II}}, \text{Ni}^{\text{II}}$ ) [79] exchange-coupled pairs.

**Acknowledgements** Our own contributions are generously supported by the University of Heidelberg and the German Science Foundation (DFG, SPP1137 “Molecular Magnetism”). We are grateful for this invaluable help and the contributions of our co-workers and collaboration partners, whose names appear in the references.

## References

1. D. Li, R. Clérac, S. Parkin, G. Wang, G.T. Yee, S.M. Holmes, *Inorg. Chem.* **45**, 5251 (2006)
2. B.M. Bartlett, D.T. Harris, M.W. DeGroot, J.R. Long, *Z. Anorg. Allg. Chem.* **633**, 2380 (2007)
3. Z.-G. Gu, Q.-F. Yang, W. Liu, Y. Song, Y.-Z. Li, J.-L. Zuo, X.-Z. You, *Inorg. Chem.* **45**, 8895 (2006)
4. D. Li, S. Parkin, G. Wang, G.T. Yee, R. Clérac, W. Wernsdorfer, S.M. Holmes, *J. Am. Chem. Soc.* **128**, 4214 (2006)
5. H. Oshio, O. Tamada, H. Onodera, T. Ito, T. Ikoma, S. Tero-Kubota, *Inorg. Chem.* **38**, 5686 (1999)
6. H. Oshio, M. Yamamoto, T. Ito, *Inorg. Chem.* **41**, 5817 (2002)
7. D. Li, S. Parkin, G. Wang, G.T. Yee, A.V. Prosvirin, S.M. Holmes, *Inorg. Chem.* **44**, 4903 (2005)
8. W. Liu, C.-F. Wang, Y.-Z. Li, J.-L. Zuo, X.-Z. You, *Inorg. Chem.* **45**, 10058 (2006)
9. C.-F. Wang, J.-L. Zuo, B.M. Bartlett, Y. Song, J.R. Long, X.-Z. You, *J. Am. Chem. Soc.* **128**, 7162 (2006)
10. Z.-G. Gu, W. Liu, Q.-F. Yang, X.-H. Zhou, J.-L. Zuo, X.-Z. You, *Inorg. Chem.* **46**, 3236 (2007)
11. K. van Langenberg, S.R. Batten, K.J. Berry, D.C.R. Hockless, B. Moubaraki, K.S. Murray, *Inorg. Chem.* **36**, 5006 (1997)
12. C.P. Berlinguette, J.R. Galán-Mascarós, K.R. Dunbar, *Inorg. Chem.* **42**, 3416 (2003)
13. S. Wang, J.-L. Zuo, H.-C. Zhou, H.J. Choi, Y. Ke, J.R. Long, X.-Z. You, *Angew. Chem. Int. Ed.* **43**, 5940 (2004)



14. H.J. Choi, J.J. Sokol, J.R. Long, *Inorg. Chem.* **43**, 1606 (2004)
15. W.-W. Ni, Z.-H. Ni, A.-L. Cui, X. Liang, H.-Z. Kou, *Inorg. Chem.* **46**, 22 (2007)
16. Z.-H. Ni, H.-Z. Kou, L.-F. Zhang, W.-W. Ni, Y.-B. Jiang, A.-L. Cui, J. Ribas, O. Sato, *Inorg. Chem.* **44**, 9631 (2005)
17. C.P. Berlinguette, D. Vaughn, C. Cañada-Vilalta, J.R. Galán-Mascarós, K.R. Dunbar, *Angew. Chem.* **115**, 1561 (2003)
18. L.M.C. Beltran, J.R. Long, *Acc. Chem. Res.* **38**, 325 (2005)
19. A. Rodríguez-Diéguez, R. Kivekäs, R. Sillanpää, J. Cano, F. Lloret, V. McKee, H. Stoeckli-Evans, E. Colacio, *Inorg. Chem.* **45**, 10537 (2006)
20. L.M. Toma, R. Lescouëzec, J. Pasán, C. Ruiz-Pérez, J. Vaissermann, J. Cano, R. Carrasco, W. Wernsdorfer, F. Lloret, M. Julve, *J. Am. Chem. Soc.* **128**, 4842 (2006)
21. L.M. Toma, F.S. Delgado, C. Ruiz-Pérez, R. Carrasco, J. Cano, F. Lloret, M. Julve, *J. Chem. Soc., Dalton Trans.* 2836 (2004)
22. M. Ferbinteanu, H. Miyasaka, W. Wernsdorfer, K. Nakata, K. Sugiura, M. Yamashita, C. Coulon, R. Clérac, *J. Am. Chem. Soc.* **127**, 3090 (2005)
23. R. Sessoli, D. Gatteschi, *Angew. Chem. Int. Ed.* **42**, 268 (2003)
24. S. Ferlay, T. Mallah, R. Ouahes, P. Veillet, M. Verdaguer, *Nature* **378**, 701 (1995)
25. D. Gatteschi, R. Sessoli, J. Villain, *Molecular Nanomagnets* (Oxford University Press, Oxford, 2006)
26. M. Atanasov, P. Comba, C.A. Daul, A. Hauser, *J. Phys. Chem. (A)* **111**, 9145 (2007)
27. M. Atanasov, P. Comba, C.A. Daul, *Inorg. Chem.* **47**, 2449 (2008)
28. M. Atanasov, C. Busche, P. Comba, F. El Hallak, B. Martin, G. Rajaraman, J. van Slageren, H. Wadepohl, *Inorg. Chem.* **47**, 8112 (2008)
29. H. Weihe, H.U. Güdel, *Comments Inorg. Chem.* **22**, 75 (2000)
30. V.S. Mironov, L.F. Chibotaru, A. Ceulemans, *J. Am. Chem. Soc.* **125**, 9750 (2003)
31. M. Verdaguer, A. Bleuzen, C. Train, R. Garde, F. Fabrizi de Biani, C. Desplanches, *Philos. Trans. R. Soc. London, Ser. A* **357**, 2959 (1999)
32. M. Verdaguer, A. Bleuzen, V. Marvaud, J. Vaissermann, M. Seuleiman, C. Desplanches, A. Scullier, C. Train, R. Grade, G. Gelly, C. Lomenech, I. Rosenman, P. Veillet, C. Cartier, F. Villain, *Coord. Chem. Rev.* **190–192**, 1023 (1999)
33. O. Kahn, B. Briat, *J. Chem. Soc. Faraday Trans. 1* **72**, 268 (1976)
34. O. Kahn, B. Briat, *J. Chem. Soc. Faraday Trans. 1* **72**, 1441 (1976)
35. V. Eyert, B. Siberchicot, M. Verdaguer, *Phys. Rev. B* **56**, 8959 (1997)
36. N.M. Harrison, B.G. Searle, E.A. Seddon, *Chem. Phys. Lett.* **266**, 507 (1997)
37. M. Nishino, S. Takeda, W. Mori, A. Nakamura, K. Yamaguchi, *Synth. Met.* **85**, 1763 (1997)
38. M. Nishino, Y. Yoshioka, K. Yamaguchi, *Chem. Phys. Lett.* **297**, 51 (1998)
39. E. Ruiz, A. Rodríguez-Forteza, S. Alvarez, M. Verdaguer, *Chem. Eur. J.* **11**, 2135 (2005)
40. B. Tsukerblat, *Inorg. Chim. Acta.* **361** 3746 (2008)
41. M. Atanasov, P. Comba, Y.D. Lampeka, G. Linti, T. Malcherek, R. Miletich, A.I. Prikhod'ko, H. Pritzkow, *Chem. Eur. J.* **12**, 737 (2006)
42. M. Atanasov, P. Comba, S. Förster, G. Linti, T. Malcherek, R. Miletich, A. Prikhod'ko, H. Wadepohl, *Inorg. Chem.* **45**, 7722 (2006)
43. P. Comba, M. Kerscher, *Coord. Chem. Rev.* **253**, 564 (2009)
44. M. Atanasov, P. Comba, S. Hausberg, B. Martin, *Coord. Chem. Rev.* **253**, 2306 (2009), in press; doi: 10.1016/j.ccr.2009.01.033
45. I.B. Bersuker, *The Jahn–Teller Effect and Vibronic Interactions in Modern Chemistry* (Plenum Press, New York, 1984)
46. I.B. Bersuker, *The Jahn–Teller Effect* (Cambridge University Press, Cambridge, 2006)
47. U. Öpik, M.H.L. Pryce, *Proc. Roy. Soc. London, Ser. A* **238**, 425 (1957)
48. J.J. Alexander, H.B. Gray, *J. Am. Chem. Soc.* **90**, 4260 (1968)
49. D. Reinen, M. Atanasov, P. Köhler, *J. Mol. Struct.* **838**, 151 (2007)
50. J.M. Baker, B. Bleaney, K.D. Bowers, *Proc. Phys. Soc. London, Sect. B* **69**, 1205 (1956)
51. B. Bleaney, M.C.M. O'Brien, *Proc. Phys. Soc. London, Sect. B* **69**, 1216 (1956)
52. B.N. Figgis, *Trans. Faraday Soc.* **57**, 204 (1961)
53. J. Baker, B.N. Figgis, *Aust. J. Chem.* **35**, 265 (1982)

54. R.M. Golding, *Mol. Phys.* **12**, 13 (1967)
55. W.T. Oosterhuis, G. Lang, *Phys. Rev.* **178**, 439 (1969)
56. P.B. Merrithew, A.J. Modestino, *J. Am. Chem. Soc.* **94**, 3361 (1972)
57. B.N. Figgis, B.W. Skelton, A.H. White, *Aust. J. Chem.* **31**, 1195 (1978)
58. J. Zaanen, G.A. Sawatzky, *Can. J. Phys.* **65**, 1262 (1987)
59. S.V. Didziulis, S.L. Cohen, A.A. Gewirth, E.I. Solomon, *J. Am. Chem. Soc.* **110**, 250 (1988)
60. F. Tuczek, E.I. Solomon, *Inorg. Chem.* **32**, 2850 (1993)
61. C.A. Brown, G.J. Remar, R.L. Musselmann, E.I. Solomon, *Inorg. Chem.* **34**, 688 (1995)
62. F. Tuczek, E.I. Solomon, *Coord. Chem. Rev.* **219–221**, 1075 (2001)
63. H. Weihe, H.U. Güdel, H. Toftlund, *Inorg. Chem.* **39**, 1351 (2000)
64. H.M. McConnell, *J. Chem. Phys.* **39**, 1910 (1963)
65. M. Atanasov, P. Comba, C.A. Daul, *J. Phys. Chem. A*, **110**, 13332 (2006)
66. M. Atanasov, P. Comba, in *Structure and Function*, ed. by P. Comba (Springer, Berlin, 2009), in press
67. A. Bérces, C. Bo, P.M. Boerrigter, L. Cavallo, D.P. Chong, L. Deng, R.M. Dickson, D.E. Ellis, L. Fan, T.H. Fischer, C. Fonseca Guerra, S.J.A. van Gisbergen, J.A. Groeneveld, O.V. Gritsenko, M. Grüning, F.E. Harris, P. van den Hoek, H. Jacobsen, G. van Kessel, F. Kootstra, E. van Lenthe, D.A. McCormack, V.P. Osinga, S. Patchkovskii, P.H.T. Philipsen, D. Post, C.C. Pye, W. Ravenek, P. Ros, P.R.T. Schipper, G. Schreckenbach, J.G. Snijders, M. Sola, M. Swart, D. Swerhone, G. te Velde, P. Vernooijs, L. Versluis, O. Visser, E. van Wezenbeek, G. Wiesenekker, S.K. Wolff, T.K. Woo, E.J. Baerends, J. Autschbach, T. Ziegler, *ADF2006.01 SCM, Theoretical Chemistry* (Vrije Universiteit, Amsterdam, The Netherlands, 2006)
68. F. Neese, ORCA, version 2.4, an ab initio, density functional and semiempirical program package, version 2.4; Max-Planck-Institut für Bioanorganische Chemie: Mülheim an der Ruhr, Germany, 2005
69. J.S. Griffith, *The Theory of Transition Metal Ions* (Cambridge University Press, London, 1971)
70. A.V. Palii, S.M. Ostrovsky, S.I. Klokishner, B.S. Tsukerblat, C.P. Berlinguette, K.R. Dunbar, J.R. Galán-Mascarós, *J. Am. Chem. Soc.* **126**, 16860 (2004)
71. S.M. Ostrovsky, K. Falk, J. Pelikan, D.A. Brown, Z. Tomkowicz, W. Haase, *Inorg. Chem.* **45**, 688 (2006)
72. A.V. Palii, S.M. Ostrovsky, S.I. Klokishner, O.S. Reu, Z.-M. Sun, A.V. Prosvirin, H.-H. Zhao, J.-G. Mao, K.R. Dunbar, *J. Phys. Chem. A* **110**, 14003 (2006)
73. B.S. Tsukerblat, A.V. Palii, V.Yu. Mirovitskii, S.M. Ostrovsky, K. Turta, T. Jovmir, S. Shova, J. Bartolome, M. Evangelisti, G. Filoti, *J. Chem. Phys.* **115**, 9528 (2001)
74. S.M. Ostrovsky, R. Werner, D.A. Brown, W. Haase, *Chem. Phys. Lett.* **353**, 290 (2002)
75. A.V. Palii, S.M. Ostrovsky, S.I. Klokishner, B.S. Tsukerblat, K.R. Dunbar, *ChemPhysChem* **7**, 871 (2006).
76. A.V. Palii, S.M. Ostrovsky, S.I. Klokishner, B.S. Tsukerblat, E.J. Schelter, A.V. Prosvirin, K.R. Dunbar, *Inorg. Chim. Acta*, **360**, 3915 (2007)
77. P.L.W. Tregenna-Piggott, D. Sheptyakov, L. Keller, S.I. Klokishner, S.M. Ostrovsky, A.V. Palii, O.S. Reu, J. Bendix, T. Brock-Nannestad, K. Pedersen, H. Weihe, H. Mutka, *Inorg. Chem.* **48**, 128 (2008)
78. V.S. Mironov, *Dokl. Phys. Chem.* **397**, 350 (2004)
79. V.S. Mironov, *Dokl. Phys. Chem.* **415**, 199 (2007)

**Part VI**  
**The Cooperative Jahn-Teller Effect and**  
**Orbital Ordering**

# Cooperative Jahn–Teller Effect: Fundamentals, Applications, Prospects

Michael Kaplan

**Abstract** Keeping in mind the pedagogical goal of the presentation the first third of the review is devoted to the basic definitions and to the description of the cooperative Jahn-Teller effect. Among different approaches to the intersite electron correlation in crystals the preference is with the most fundamental and systematic Hamiltonian shift transformation method. Order parameter equations and their connection to the crystal elastic properties and to the orbital ordering are considered. An especial attention is paid to the dynamics of Jahn-Teller crystals based on the coupled electronic, vibrational, and magnetic excitations which are of big interest nowadays in orbital physics.

In the next part of the review some of the most important applications of cooperative Jahn-Teller effect and related new phenomena in materials are under discussion. Ferro- and antiferroelectricity are considered using a dielectric zircon structure antiferroelectric as an example. The relative roles of different phonon modes are analyzed. Giant dynamic and static magnetostriction and electrostriction as typical properties of Jahn-Teller crystals are discussed. Qualitative analysis of these properties and the results of numerical calculations and experimental data for different materials are presented. The new phenomena of metaelasticity and metamagnetoelasticity and their experimental observation and theoretical description are demonstrated. These phenomena are discussed in connection with the giant magnetoelectricity found in Jahn-Teller crystals and the relation of these phenomena to the magnetoelectricity of modern multiferroics. The review is ending with some suggestions on possible development in the field.

## 1 Introduction

The cooperative Jahn–Teller effect (CJTE) as a viable mechanism of structural transformations in solids was mentioned for the first time in 1957 by Dunitz and Orgel [1] and McClure [2]. Relatively soon after that Kanamori [3] published a fundamental paper defining the basic approach to the problem. In 1966 Bersuker [4] suggested a Jahn–Teller model for formation an electric dipole moment of a molecule

(structural unit). Simultaneously he made the next step offering a mechanism of ferroelectricity – ordering of the electric dipole moments in a crystal.

Despite these early landmark efforts, the systematic study of cooperative vibronic systems began much later. Not until early 70s, prompted by studies at Oxford involving scientists from various countries (see [5]; [6]) did comprehensive experimental and theoretical research begin on compounds with CJTE. The first most impressive experimental and theoretical results were obtained for rare-earth oxides with zircon structure. Vanadates, phosphates, and arsenates of this class of materials became model systems in the field. Later inspired by these results scientists returned back to the transition metal compounds with which the studies in the field started and are continuing nowadays. Several very interesting and important reviews on the subject were written. Among them we have to mention first of all excellent articles by Gehring and Gehring [7] and Reinen and Friebe [8]. While the books by Engman [9] and Bersuker and Polinger [4] contained chapters on cooperative phenomena, the first book by Kaplan and Vekhter [10] devoted entirely to the analysis of properties of crystals with CJTE appeared in 1995.

The physics of CJTE looks very simple and clear. Because of the vibronic (electron-vibrational) interaction each Jahn–Teller (JT) molecule (center) is characterized with several energetically equivalent minima corresponding to a possible distortion of the initial (at the absence of the vibronic interaction) symmetry. In case of many JT centers in a crystal matrix an effective interaction caused by lattice strains around the centers takes place. This interaction breaks the equivalence of the minima. The preference of the specific distortions around each of the JT centers leads to the ordering of the local distortions – structural phase transitions. As each distortion is related to a specific electronic state (orbital) the JT structural transition is at the same time an ordering of orbitals. The last is a central question of the modern orbital physics.

As the quantum mechanics language is more general and as a rule more appropriate in discussions of the JT effect, the interaction between JT centers should be considered as a virtual phonon exchange between the electrons in orbitally degenerate states.

It is worthy to give a direct definition of CJTE. CJTE is virtual phonon exchange at electron orbital degeneracy, leading to the correlation of local distortions and selfconsistent correlation of electrons. The virtual phonon exchange is the result of electron-phonon (vibronic) interaction and of phonon dispersion.

On the Fig. 1 different “packing” possibilities for two JT squared molecules with orthorhombic distortion are shown. Depending upon the sign of the interaction between the molecules the  $(++)$  or  $(--)$  and  $(+-)$  or  $(-+)$  combinations are possible. The adiabatic potential  $U(Q)$  of one JT center in the presence of a JT molecular field is shown on Fig. 1 below the squared molecules. This molecular field is the reason of the non-equivalence of the minima and the possibility (at low enough temperatures, as it will be discussed below) of the structural phase transition.

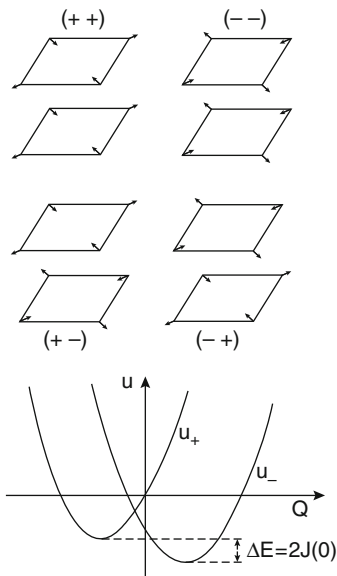


**Fig. 1** Packaging of local distortions for a pair of JT centers and their adiabatic potential [10]

## 2 Hamiltonians

The CJTE system will be considered as a crystal containing a lattice (or one of the sublattices) of JT ions (structural units). A typical Hamiltonian should describe the JT effect at each of the corresponding centers plus the elastic energy related to the appearance of the homogeneous strain as a result of the structural phase transition.

Such a Hamiltonian could be written like that

$$\begin{aligned}
 H &= H_{ph} + H_{el-ph} + H_{str} + H_{el-str} + H_{cryst} + H_{magn} \\
 H_{ph} &= \sum_{\kappa} \hbar \omega_{\kappa} \left( b_{\kappa}^{+} b_{\kappa} + \frac{1}{2} \right) \\
 H_{el-ph} &= - \sum_{m\kappa\gamma} \left( V_{m\kappa}^{\gamma} b_{\kappa} + V_{m-\kappa}^{\gamma*} b_{-\kappa}^{+} \right) O_m^{\gamma} \\
 H_{el-str} &= -g_0 \sqrt{\frac{C_0 \Omega}{N}} \sum_{m\gamma} U^{\gamma} O_m^{\gamma} \\
 H_{str} &= \frac{1}{2} C_0 \Omega \sum_{\gamma} U^{\gamma 2}
 \end{aligned} \tag{1}$$

where the first two terms describe the free phonon energy and the electron-phonon interaction, next two are the elastic energy of the strained crystal and the electron-strain interaction, and, finally, the last two terms are related to the crystal field

electron energy splitting and the magnetic interactions (external magnetic fields, exchange interactions and so on).

In this Hamiltonian  $k$  is the wave vector of the phonons,  $\gamma$  is the phonon mode branch,  $g_0$  and  $V_{mk}$  are the electron-strain and the electron-phonon interaction constants. It is important to remind that as it was noted for the first time by Kanamori [3], the electron interaction with the homogeneous strain  $U$  should be considered separately from the electron-phonon interaction as that type of strain can not be represented by phonons. The introduction of the last ones depends upon the Born-Karman conditions that are changing at the structural phase transition.

As it was mentioned in the Introduction, the central part of the CJTE is the virtual phonon exchange interaction. There are different methods to get this effective interaction starting with the Hamiltonian (1). Sugihara [11] was first (1959) to show that this interaction could be obtained considering the vibronic interaction as a perturbation (weak JT effect).

In the second order of perturbation theory the effective intercenter interaction has a form of

$$H_{eff} = - \sum_{\substack{mnk\gamma\gamma^1 \\ m \neq n}} \frac{V_{m-k}^{\gamma*} V_{n\kappa}^{\gamma^1}}{\hbar\omega_\kappa} O_m^\gamma O_n^{\gamma^1} \quad (2)$$

$$V_{m\kappa}^\gamma = \xi^\gamma(\kappa) \exp(i\kappa R_m)$$

where  $O_m^\gamma$  are the electron operators and  $R_m$  is the radius-vector of the  $m$  site of the crystal lattice.

Kanamori in his seminal work [3] suggested a more general approach called the displacement operator method. According to this method the initial  $b_\kappa$  phonon operators are replaced in the Hamiltonian (1) with the  $a_\kappa$  new ones like that

$$\begin{aligned} a_\kappa^+ &= b_\kappa^+ + \sum_m \frac{V_{m-\kappa}^*}{\hbar\omega_\kappa} O_m \\ a_\kappa &= b_\kappa + \sum_m \frac{V_{m\kappa}}{\hbar\omega_\kappa} O_m \end{aligned} \quad (3)$$

As a result of this replacement the linear vibronic interaction in Hamiltonian (1) is cancelled, and the effective virtual phonon interaction operator appears. However the use of this method that formally could be applied to any Hamiltonian is related to some practical difficulties. These difficulties take place in case of the presence of some non-commuting electron operators in the initial Hamiltonian. They are especially serious when the dynamics of the JT system is under discussion.

Slightly a different method to analyze the intersite electron correlation was suggested by Thomas [6] (in more detail it was discussed by Bersuker and Polinger [4]). In their works the lattice Hamiltonian is described as a bilinear distortion interaction. Together with the regular vibronic interaction it leads to the electron-electron

correlation. When this Hamiltonian is treated exactly the corresponding results are not different from the approach by Kanamori [3]. However in most of the articles where the last method was employed, several approximations (simplifications of the lattice Hamiltonian) had been used leading to less general results. Nevertheless in case the local vibronic dynamics is of primary interest this method has its advantages.

The most general approach to the formation of the effective operator of the intersite virtual phonon exchange interaction is based on the canonical shift transformation of the Hamiltonian

$$\begin{aligned} H_{eff} &= (\exp iR) H (\exp(-iR)) \\ R &= \sum_m g_m O_m \\ g_m &= i \sum_{\kappa} (V_{m-\kappa}^* b_{-\kappa}^+ - V_{m\kappa} b_{\kappa}) (\hbar\omega_{\kappa}^{-1}) \end{aligned} \quad (4)$$

As a result of this type of Hamiltonian transformation the linear electron-phonon interaction disappears, an effective interaction between the JT centers is created, but the Hamiltonian may become very complicated. The transfer of the mixing of the phonon and electron operators to the other Hamiltonian terms is the price for the accuracy of the canonical transformation. Of course, in this case also the problem can not be solved exactly and some approximations should be applied.

While the transformed Hamiltonians with the intercentral interactions as it was mentioned above, are complicated, an especially difficult situation takes place in the case of a double degenerate vibrational e-mode active in the JT effect. Here different approximations could be involved depending upon relationship between parameters characterizing the JT effect.

If the vibronic coupling is weak (in comparison with the phonon energy) the second order perturbation theory for the local Exe problem will give

$$\begin{aligned} H_{int} = - \sum_{\substack{mn\kappa \\ m \neq n}} \left[ \frac{(V_{m\kappa}^{\theta})^* V_{n\kappa}^{\theta}}{\hbar\omega_{\kappa}} \sigma_{\theta}^m \sigma_{\theta}^n + \frac{(V_{m\kappa}^{\varepsilon})^* V_{n\kappa}^{\varepsilon}}{\hbar\omega_{\kappa}} \sigma_{\varepsilon}^m \sigma_{\varepsilon}^n + 2 \frac{(V_{m\kappa}^{\theta})^* V_{n\kappa}^{\varepsilon}}{\hbar\omega_{\kappa}} \sigma_{\theta}^m \sigma_{\varepsilon}^n \right] \\ + H_{dyn} \end{aligned} \quad (5)$$

where the last term describes the mixing of the electrons and vibrations in the higher (than second) order in V coupling. The  $\theta$ - and  $\varepsilon$ -components of the pseudospin operator  $\sigma$  (correspondingly to the components of the double degenerate E-mode) often are represented by  $\sigma_z$  and  $\sigma_x$  operators.

However, if, just oppositely, the vibronic interaction is strong (much stronger than phonon quantum), the lowest adiabatic potential only could be taken in consideration.

The lowest state of the local electrons could be represented as a combination of two degenerate states

$$\Psi = \frac{\cos \theta_m}{2} \varphi_u + \sin \frac{\theta_m}{2} \varphi_v \quad (6)$$



where  $\theta_m$  is the angle in the plane of the local coordinates of the e-mode. At  $T = 0$  it could be shown that

$$\bar{\sigma}_{zm} = \cos \theta_m \quad \bar{\sigma}_{xm} = \sin \theta_m \quad (7)$$

and the energy of the interaction between the JT centers can be written like

$$E = - \sum_{\substack{mn\kappa \\ m \neq n}} \left[ \frac{(V_{m\kappa}^z)^* (V_{n\kappa}^z)}{\hbar \omega_\kappa} \cos \theta_m \cos \theta_n + \dots \sin \theta_m \sin \theta_n + \dots \right] \quad (8)$$

In case of the quadratic vibronic interactions are taken into account three minima appear on the lowest sheet of the adiabatic potential. The tunneling between them leads to a complicated local dynamics that in its turn significantly influences the cooperative problem interaction. If the lowest ground state is a vibronic doublet and the first excited state is a vibronic singlet well separated from the higher energy levels, Thomas and Muller [12] had shown that the Hamiltonian of the CJTE system can be described as

$$H_{\text{int}} = -\frac{1}{2} \Omega \sum_m (\sqrt{2} S_x^m - E_2^m) - \sum_{\substack{mn \\ m \neq n}} A_{mn} E_1^m E_1^n \quad (9)$$

where the pseudospin operator  $S = 1$  corresponds to three vibronic states, and  $\Omega$  is the gap separating the ground doublet from the excited singlet.

### 3 Structural Phase Transitions and Orbital Ordering

The correlation of the electrons at different JT centers caused by the virtual phonon exchange leads at some temperatures to the ordering of the local distortions and of the self consistently coupled to them electronic states (orbitals). This happens when the loss in the elastic energy and entropy at the ordering is compensated by the gain in the energy of the crystal electronic subsystem. At this case the electronic order parameter (an average of a pseudospin operator) of the phase transition becomes different from zero and because of that the spontaneous lattice (sublattice) strain is also not zero.

In case of the ferroelastic ordering in the crystal (for example, for a ground doublet state of the JT center)

$$\begin{aligned} \bar{\sigma}_z^m &= \bar{\sigma}_z \\ U &= (C_0 \Omega)^{-1} [P + g_0 (C_0 \Omega N)^{1/2} \bar{\sigma}_z] \\ \bar{\sigma}_z &= Tr \exp(-\beta H \sigma_z) / Tr \exp(-\beta H) \end{aligned} \quad (10)$$

where the spontaneous crystal strain  $U$  at the external pressure  $P = 0$  is proportional to the electronic order parameter – the difference in the populations of the electronic doublet components). The order parameter  $\sigma_z$  could be calculated in the molecular field approximation, random phase approximation, or any higher level of approximation.

If the structural ordering is of the antiferrodistortive type, the crystal lattice could be divided in two sublattices (with different principal axes of the sublattice strains).

Correspondingly two order parameters are characterizing the system, and the total crystal strain is zero

$$\begin{aligned}\bar{\sigma}_{zI} &= -\bar{\sigma}_{zII} \\ U &= \bar{U}_I + \bar{U}_{II} = 0\end{aligned}\quad (11)$$

Similarly to the situation in magnetism CJTE can lead to ferrielasticity with

$$\begin{aligned}\bar{\sigma}_{zI} &\neq \bar{\sigma}_{zII} \\ \bar{U}_I &\neq \bar{U}_{II} \\ \bar{U} &\neq 0\end{aligned}\quad (12)$$

or to even more complicated helicoidal structure, glass, or incommensurate phase transitions.

The preferred type of ordering in the JT crystal depends upon the interaction between the centers that has the form (2) where, in general,  $k$  is the phonon wave vector and the branch of the phonon mode. The crystal ordering occurs correspondingly to the wave vector  $k$  for which the Fourier transform of the interaction constant is a maximum. It leads to the occupation by the electrons of the certain preferred components of the electron degenerate term at different crystal sites and correspondingly to the preferred orientation of local JT distortions.

The interaction Hamiltonian and the Fourier transform of the interaction constant can be written as [7]

$$\begin{aligned}H_{\text{int}} &= - \sum_{\substack{mn\kappa \\ m \neq n}} \frac{2V^2(\kappa)}{\hbar \omega_\kappa} \exp[i\kappa(R_m - R_n)] O_m^\gamma O_n^\gamma \\ J(\kappa) &= \frac{2V^2(\kappa)}{\hbar \omega_\kappa} - \frac{1}{N} \sum_{\kappa} \frac{2V^2(\kappa)}{\hbar \omega_\kappa} \\ J(\kappa) &= \frac{2V^2}{(\hbar \omega_\kappa)^2} - \frac{1}{N} \sum_{\kappa} \frac{2V^2}{(\hbar \omega_\kappa)^2}\end{aligned}\quad (13)$$

where the last expression for the Fourier transform in (13) is correct for some specific crystal forms only. The last formula in (13) is conclusively showing that in the absence of the phonon dispersion the virtual phonon exchange is zero and there is no any CJTE in the system.

As it is seen from (13), all crystal phonon modes contribute to the interaction between JT centers. However analysis of the concrete crystal structure and of the

specific experimental data allows for the differentiation of the different phonon modes contribution.

Rewriting the vibronic interaction operator in the form

$$H_{vib} = \sum_m \sum_{\kappa \neq 0} V(\kappa) \exp(i\kappa R_m) O_m^\gamma (b_\kappa + b_{-\kappa}^+) \quad (14)$$

that is correct for the acoustic modes (for the optical modes it would include  $k = 0$  term in the sum), the vibronic constant expression can be used as

$$V(\kappa) = V_s \frac{i}{2} \left( \frac{\hbar}{2MN\omega_\kappa} \right)^{1/2} [\kappa_i e_j(\kappa) + \kappa_j e_i(\kappa)] \quad (15)$$

Then the Fourier transform takes the form of

$$\begin{aligned} J(\kappa) &= \frac{V_s^2}{2MN} \left[ \left( \frac{\kappa_i e_j(\kappa) + \kappa_j e_i(\kappa)}{\omega_\kappa} \right)^2 - \frac{1}{N} \sum_{\kappa \neq 0} \left( \frac{\kappa_i e_j(\kappa) + \kappa_j e_i(\kappa)}{\omega_\kappa} \right)^2 \right] \\ &\equiv K(\kappa) - \nu \end{aligned} \quad (16)$$

The last term in (16) is the self energy term corresponding to the sum of the local JT stabilization energies. It can be shown that the limit of the first term taken in a specific space direction that corresponds to the contribution in the interaction of the homogeneous spontaneous strain at  $k = 0$  is

$$\lim K(\kappa) = g_0^2 \quad (17)$$

It is easy to see from formula (16) that the interaction constant can be of any sign depending upon concrete situation. If the interaction with strain is very big the constant at  $k = 0$  is positive and the ferrodistorptive ordering is favorable.

For the optical modes as it was mentioned above in the operator (16)  $k = 0$  is included.

However if the JT ion is located in the center of inversion, only odd optical modes are active in the JT effect (in case of pseudodegeneracy this could be not true). For the odd optical modes  $V(k = 0) = 0$  and

$$J(0) = \sum_{n \neq m} J(m - n) = -\frac{1}{N} \sum_{\kappa} \frac{2V^2(\kappa)}{\hbar\omega_\kappa} < 0 \quad (18)$$

In this case the interaction constant at  $k = 0$  is negative, i.e. the phonons tend to establish the antiferrodistorptive ordering.

## 4 Elastic Properties of Jahn–Teller Crystals

While the elastic properties of JT crystals could be an example of possible applications of the CJTE theory for microscopic description of the materials properties, these properties are analyzed in advance and separated from others. It is related to the fact that strain and elastic susceptibility are the principal characteristics of structural phase transitions.

Here the elastic properties are briefly considered for several concrete crystals.

The  $\text{TmVO}_4$  crystal undergoes a structural  $D_{4h}^{19} \rightarrow D_{2h}^{24}$  phase transition at around 2.1 K. The spontaneous orthorhombic strain symmetry is  $B_{2g}(D_{4h})$  and the local  $\text{Tm}^{3+}$  ion symmetry in the paraphrase is  $D_{2d}$ . The ground state of the JT ion is a spin-orbital doublet well separated from higher lying levels.

In this case the spontaneous strain  $U$ , the order parameter  $\overline{\sigma_z}$ , and the elasticity constant  $C = C_{66}$  are described by the following formulae and the graph presented in the Fig. 2.

As we see from these formulae the elasticity constant  $C_{66}$  (the reciprocal of elastic susceptibility) tends to zero at  $T = T_c$ . The experimental dependence of the modulus of elasticity upon temperature is measured at  $T > T_c$  only because of the strong domain wall related ultrasound attenuation. The agreement between the MFA theory (the continuous line in the Fig. 2) and experiment is very good.

Another good example of successful acoustic properties description based on CJTE is  $\text{DyVO}_4$  – a crystal from the same zircon structure family. While this crystal has the same structure that  $\text{TmVO}_4$  and undergoes a similar tetragonal-orthorhombic structural phase transition, the symmetry of the ordered phase is different and correspondingly different are the acoustic properties. All this is well understood in the framework of CJTE taking into account the difference in the electronic structures for the JT ion  $\text{Tm}^{3+}$ . On the Fig. 3 the order parameter temperature dependence as it was found from the Raman light scattering [5] and the temperature dependence of the soft modulus of elasticity  $C_1 = 1/2(C_{11} - C_{12})$  (ultrasonic measurements [14]) are shown.

The anomalous temperature dependence of elastic constants found from the CJTE calculations is shown for transition metal compounds of the  $\text{NiCr}_2\text{O}_4$  and  $\text{CuCr}_2\text{O}_4$  type crystals on the Fig. 4. As in this case the soft acoustic mode is double degenerate there is a splitting of the high symmetry modulus of elasticity  $C_1$  of the cubic crystal phase in  $C_2$  and  $C_3$  constants of the tetragonal phase.

## 5 Dynamics of JT Crystals

The coupling of the electron and vibrational variables is a characteristic property of JT systems. Nevertheless in analysis of thermodynamics of the JT crystals every effort was made to develop an approximation separating the variables and simplifying the calculations. However the situation is fundamentally different in the dynamics of the CJTE. The dynamic spectrum of CJTE crystals is represented by

**TmVO<sub>4</sub>: tetragonal  $\leftrightarrow$  orthorhombic transition**

$$U = (C_0 \Omega)^{-1} [P + g_0 (C_0 \Omega N)^{1/2} \bar{\sigma}_z] \quad C_0 = C_{66}; \quad \bar{\kappa} \parallel [110], e \parallel [\bar{1}\bar{1}0]$$

$$\text{At } P = 0, T < T_c \quad U \neq 0, \text{ if } \bar{\sigma}_z \neq 0$$

$$\bar{\sigma}_z = \tanh \frac{A \bar{\sigma}_z + g_0 P / (C_0 \Omega N)^{1/2}}{kT}; \quad 1/C = \left( \frac{\partial U}{\partial P} \right)_{P=0, T}$$

$$C(T) = C_0 \frac{1 - \frac{A}{kT} \sec^2 h^2 \frac{A \bar{\sigma}_z}{kT}}{1 - \frac{A - g_0^2}{kT} \sec^2 h^2 \frac{A \bar{\sigma}_z}{kT}} \quad \begin{array}{c} T < T_c \\ \downarrow \\ 2.15K \\ \downarrow \\ T > T_c \end{array}$$

$$A = g_0^2 + \lambda, \quad \lambda = 2 \sum_{\substack{nk \\ m \neq n}} \frac{V_{nk} V_{mk}^*}{\hbar \omega_k}; \quad \text{At } T > T_c:$$

$$C(T) = \frac{1 - (\lambda + g_0^2) / kT}{1 - \lambda / kT}$$

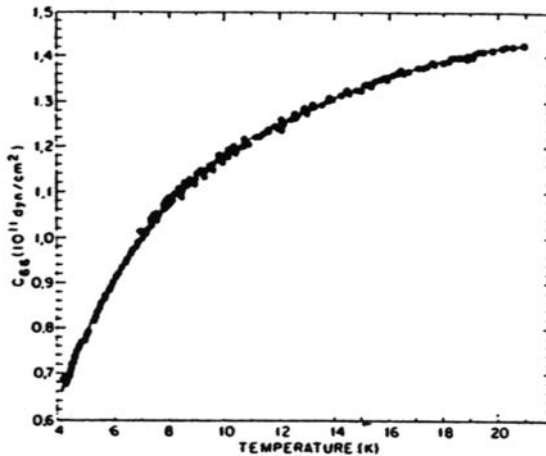


**Fig. 2** Experimentally found temperature dependence of  $C_{66}$  (T) for the TmVO<sub>4</sub> crystal (ultrasound measurements) [13]

the elementary excitations that are dynamically coupled vibron-phonon (or even vibron-phonon-magnon) modes. The importance of the elementary excitation spectrum of the JT crystals is related to the fact that only analysis of the temperature dependence of the elementary crystal excitations answers the question about the soft mode responsible for the phase instability in the system and the order-disorder transformation.

Let's consider as an example the elementary excitations of the TmVO<sub>4</sub> crystal in the external magnetic field  $H$  parallel to the crystal tetragonal (at  $T > T_c$ )  $c$ -axis.

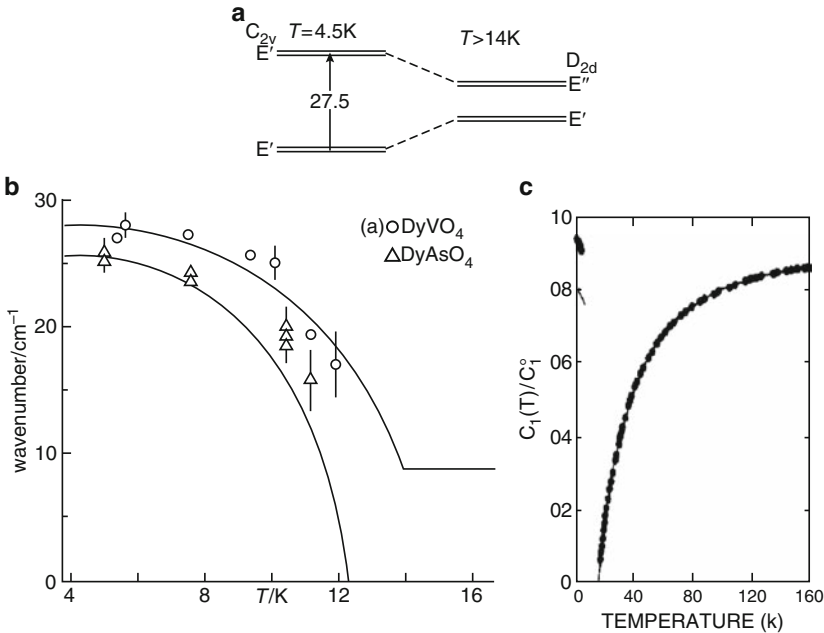


**Fig. 3** Lowest electronic states (a) for DyVO<sub>4</sub> crystal, temperature dependence of the energy gap between ground and excited doublets (b) (for comparison Raman scattering results are shown for the DyAsO<sub>4</sub> crystal with similar electronic and crystal structures), and the ultrasonic measurements (c) of the elastic constant  $C_1 = 1/2(C_{11}-C_{12})$  for DyVO<sub>4</sub> crystal

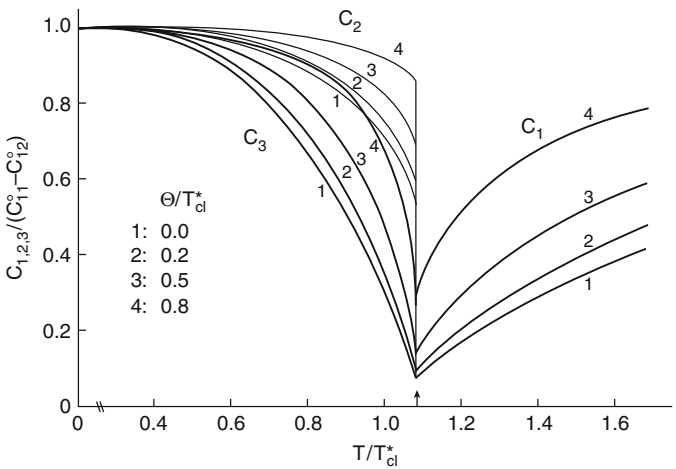


**Fig. 4** Temperature dependence of the elastic constants  $C_1$ ,  $C_2$ , and  $C_3$  in crystals with the cubic to tetragonal phase transition ( $\Theta = g_0^2$ ,  $T_{cl}^* = A$  [15])

The convenience of this example consideration is related to the possibility to control the dynamic vibron-phonon coupling by the external  $H$  parameter.

The Hamiltonian of the crystal after the shift canonical transformation is [10]

$$\begin{aligned} \tilde{H} = & \frac{1}{2}C_0\Omega U^2 - g_0\sqrt{\frac{C_0\Omega}{N}}U \sum_m \sigma_z^m + \sum_{\kappa} \hbar\omega_{\kappa} \left( b_{\kappa}^+ b_{\kappa} + \frac{1}{2} \right) - \sum_{\substack{m n \kappa \\ m \neq n}} \frac{V_{m\kappa}^* V_{n\kappa}}{\hbar\omega_{\kappa}} \\ & \times \sigma_z^m \sigma_z^n - g\beta H \sum_m (\sigma_y^m \cos 2g_m + \sigma_x^m \sin 2g_m) \end{aligned} \quad (19)$$

The last term describes the coupling of the electron and phonon variables. Its complication is the price for the accuracy of the intersite interaction operator and the crystal Hamiltonian overall.

Using the Green function method and some decoupling approximations corresponding to the RPA and the Zeeman reduced splitting smaller than Debye phonon quantum, it is possible to get the dispersion equation

$$D \equiv \hbar^3 \omega^3 [\hbar^2 \omega^2 - \hbar^2 \omega_{el}^2 (1 + \alpha)] = 0 \quad (20)$$

where

$$\alpha = \frac{8 \sum_j \frac{V_{jq}^2}{\hbar\omega_{jq}} g\beta\gamma^2 H (\hbar^2 \omega^2 - \hbar^2 \omega_{jq}^2)}{1 - 8 \sum_j \frac{V_{jq}^2}{\hbar\omega_{jq}} g\beta\gamma H \bar{\sigma}_y (\hbar^2 \omega^2 - \hbar^2 \omega_{jq}^2)^{-1}} \quad (21)$$

$$\hbar^2 \omega_{el}^2(q) = 4A^2 (\bar{\sigma}_z)^2 + 2g\beta\gamma H (2g\beta\gamma H - A(q) \bar{\sigma}_y) \quad (22)$$

$$A \equiv g_0^2 + 2 \sum_{\substack{n \kappa \\ m \neq n}} V_{m\kappa} V_{n\kappa}^* (\hbar\omega_{\kappa})^{-1} \quad (23)$$

$\gamma$  is the vibronic reduction factor.

This spectrum of elementary excitation in case of the weak vibronic coupling was obtained first by Elliott, Harley, Hayes, and Smith [5] and in case of the arbitrary vibronic interaction (including the strong one) by Kaplan and Vekhter [16].

Analysis of the (20) shows, in part, that the electron and vibrational modes are coupled and in some parts of the Brillouin zone that lead to dramatic changes in the excitation energies. These results schematically are shown on Fig. 5.

In  $\text{TmVO}_4$  crystal the external magnetic field can be of order of the JT molecular field and significantly influence the structural phase transition. As a result of that at low enough temperatures the structural phase transition can be induced by magnetic field.

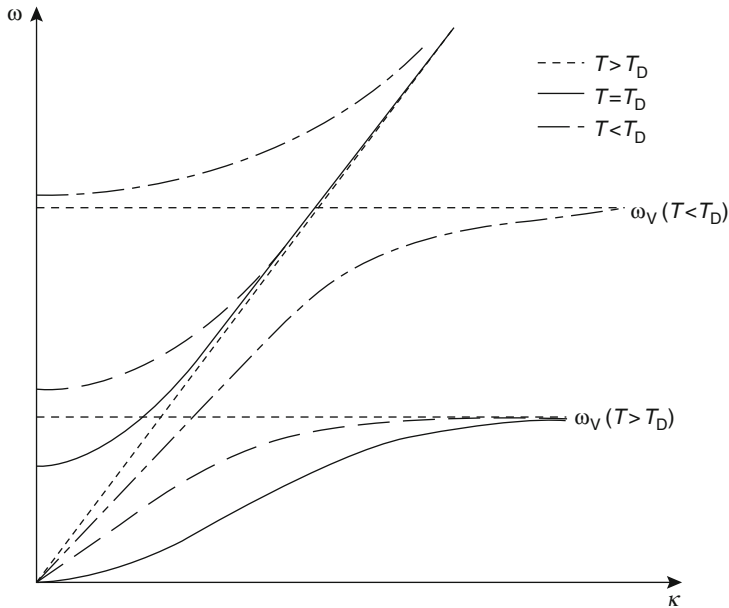


**Fig. 5** Schematic presentation of the electron-phonon excitations in the Jahn–Teller crystals at different temperatures [7]

Figure 6 demonstrates the results of the neutron scattering measurements by Kjems, Hayes, and Smith [17] that clearly show the coupled electron-vibrational modes in  $\text{TmVO}_4$ .

As it follows from the (26) and Fig. 6, at the absence of the magnetic field ( $H = 0$ ) the dynamic coupling does not exist and the unrenormalized acoustic phonon mode active in the CJTE linearly depends upon the wave vector. However when  $H$  is not zero the dynamic coupling drastically changes both the phonon and the electronic mode.

It is important to note that the electronic mode (see (28)) is not the soft one (it does not go to zero at  $T \rightarrow T_c$ ). However the renormalized phonon mode does. That means that the phonon mode is responsible for the instability in the crystal what should be expected at the structural phase transition caused by the CJTE.

The fundamental role of the dynamic electron-phonon coupling in the Jahn–Teller crystals was clearly demonstrated by the Raman light scattering experiments [18].

Harley, Hayes, and Smith [18] had measured the zone-center vibron energy  $\hbar\omega(0)$  of the  $\text{TmAsO}_4$  crystal under external magnetic field. In that crystal, like in  $\text{TmVO}_4$ , the dynamic coupling is not zero in the presence of the external magnetic field only. As it is shown on the Fig. 7 the electronic excitation is the soft mode at the absence of the electron-strain interaction only ( $g_0^2 = 0$ , dashed line). However when the electron-strain constant is not zero (all other lines on the Fig. 7) the



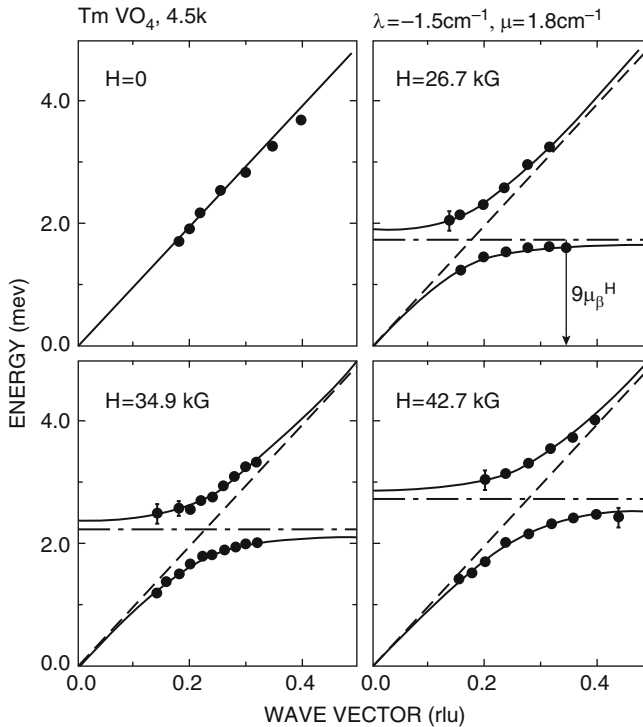


**Fig. 6** Spectrum of coupled electron-phonon modes in the TmVO<sub>4</sub> crystal under external magnetic field  $H_z$  according to neutron scattering data [17]

electronic excitation energy is not zero and the acoustic mode becomes the soft one as it is supposed to be at the structural phase transition.

## 6 Examples of Applications of CJTE Theory

### 6.1 Structural Transitions. Ferro- and Antiferroelectricity

Among different applications of the CJTE structural phase transitions are the most important one. However as they already were briefly discussed above now we will focus the attention on ferroelectricity. The first general ideas in the field belong to Bersuker [4]. The development of these ideas went in two directions: a) systems with local pseudo-JT effect characterized by wide energy gaps and local center of inversion; b) systems with small energy gap between the ground and excited states (JT or pseudo-JT effect) in crystals without local center of inversion.

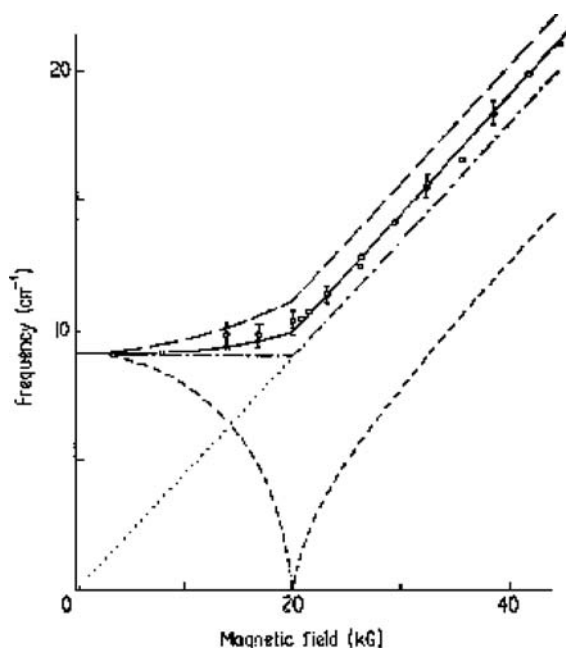


**Fig. 7** The zone-center electronic excitation  $h\omega(0)$  by Raman scattering in  $\text{TmAsO}_4$  at  $T = 2.5\text{K}$  as a function of magnetic field [7]

The first direction was explored in the works of many different research groups [19] (also see [19] for a complete review of these results and their experimental confirmation).

Here the second direction will be considered in more detail for an example.

Experimentally ferro- and antiferroelectricity of this type was discussed for rare earth compounds in [20–22]. Unoki and Sakudo [20] were the first who found the antiferroelectric anomaly in the  $\text{DyVO}_4$  crystal that is simultaneously ferroelastic and antiferroelectric.

Microscopic theory of this phenomenon was suggested by Vekhter and Kaplan [23] and then developed in many studies (see references in [10]).

The coupling between the distortion and electric dipole moment structures is very tight and unusual. Both these orderings are the result of the virtual phonon exchange. The absence of the local center of inversion is the reason why the JT distortion is responsible for the formation of the electric dipole moment (see Fig. 8). At this situation the ordering of the distortions is accompanied by the ordering of the dipole moments.

The Hamiltonian of the crystal with possible ordering of the electric dipole moments [24] additionally to the traditional terms discussed above contains the energy of the polarized crystal, the electron-polarization interaction (similar to the electron-strain interaction), and the interaction with the external electric field. After

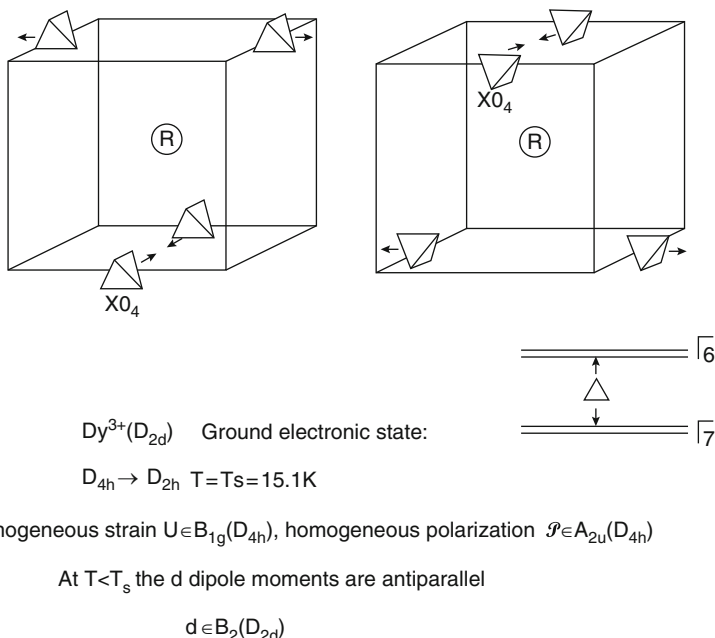


**Fig. 8** Distortion of the non-centrosymmetric component of the nearest surrounding of the two R ions in the unit cell as a result of phase transition

the canonical Hamiltonian transformation the crystal could be divided in two sublattices in which the electric dipole moments are directed oppositely (this is the only ordering possibility for the electric dipole moments as the  $\text{DyVO}_4$  crystal is still keeping its center of symmetry after the structural phase transition).

On the Fig. 9 the results of the theoretical calculations of the dielectric constant without external pressure ( $P = 0$ ) and in its presence are compared with the experimental data for  $\text{DyVO}_4$ .

The calculations are based on the following formulae:

$$\begin{aligned}
 U_{B_{1g}} &= \frac{P}{C_0 \Omega} + g_0 \sqrt{\frac{\Omega}{C_0 N}} \sum_{m\alpha} \bar{\sigma}_z^{m\alpha} \\
 \mathcal{P}_Z &= \chi_0 \mathcal{E}_Z + \frac{4\pi \chi_0^2}{\varepsilon_0} f \sum_m (\bar{\sigma}_z^{ml} - \bar{\sigma}_z^{mll}) \\
 A &= 3.9 \text{ cm}^{-1}, \quad B = 7.2 \text{ cm}^{-1}, \quad f_2 = 2.4 \text{ cm}^{-1}, \\
 \chi_0 &= 1.48, \text{ and } \Delta = 4.5 \text{ cm}^{-1}
 \end{aligned} \tag{24}$$

where A and B are the intra- and intersublattice molecular field constants, f is the electron-polarization interaction constant, and  $\chi_0$  is the initial (unrenormalized) electrical susceptibility,  $\alpha = I, II$  is the index of the sublattices of the  $\text{Dy}^{3+}$  ions.

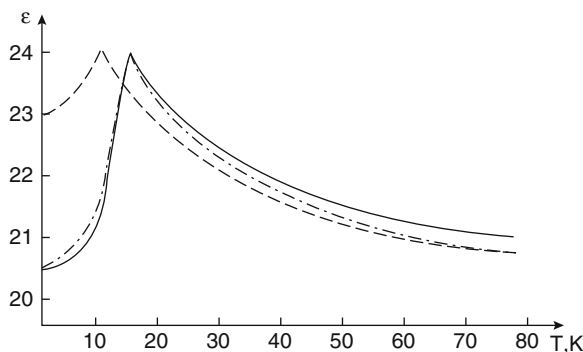


**Fig. 9** “Longitudinal” dielectric constant of  $\text{DyVO}_4$  vs. temperature, experimental (solid curve) and theoretical (dot-dash curve). The influence of the external pressure  $P = 10 \text{ cm}^{-1}$  is shown by the dashed curve

It is important to mention that from the analysis of the elastic and dielectric measurements and of the A and B molecular field constants the relative contribution of the acoustical and optical vibrations to the structural ordering could be estimated.

## 7 Magnetoelasticity and Electroelasticity

Giant static and dynamic magneto- or (and) electrostriction is a characteristic property of crystals with CJTE [25]. It is clear that striction effects are attributable to the mixing of electronic states by the external field (magnetic or electric). The striction coefficients are large in systems with degenerate or pseudo-degenerate electronic states (then their mixing is strong), with big vibronic constants (then the magneto- or electroelastic forces are big), and with small (“soft”) elastic coefficients (so that the strain of the lattice under the field is maximal). The first two conditions point at the JT effect situation, and the third one takes place in crystals with the CJTE.

On the Fig. 10 the experimental and calculation data are presented for different crystals. It is seen that both static ((a), top left corner of the Fig. 10) and dynamic ((b), c), and d) of the Fig. 10) striction in JT crystals are big. The dynamic striction is characterized by a strong maximum near the critical temperature (Fig. 10d) (or critical magnetic field (Fig. 10c)) of the structural phase transition. The dynamic striction coefficient  $D$  is defined as a derivative of the spontaneous strain  $U$  upon the external field (magnetic or electric). As the spontaneous strain in CJTE systems is proportional to the electronic order parameter average,  $D$  is proportional to the derivative of this average upon the field (see Fig. 10c, d).

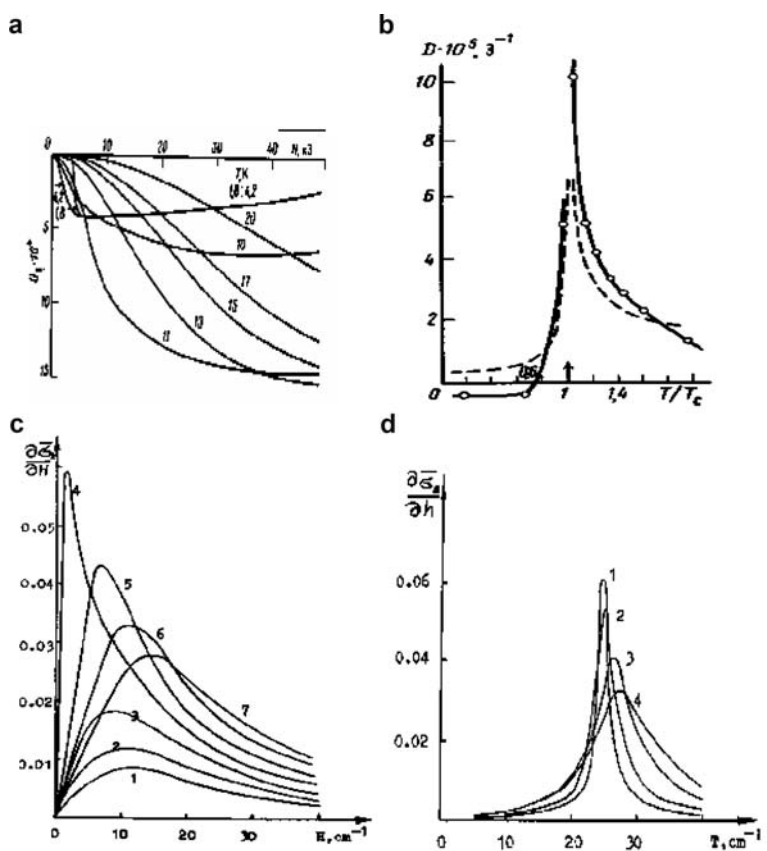


**Fig. 10** Static and dynamic magnetostriction in the  $DyVO_4$  (a,b),  $TbVO_4$  (c), and  $Tb_{1-x}Gd_xVO_4$  (d) Jahn-Teller crystals. (a) and (b) are the experimental results by V. Sokolov, Z. Kazey e.a. (c) and (d) are the theoretical data by M. Kaplan, B. Vekhter e.a. [10]

## 8 Metamagnetism and Metamagnetoelasticity

The strong magnetostriction of the JT crystals is responsible for their unusual metamagnetism and a new phenomenon called metamagnetoelasticity [26].

The metamagnetism of the non-magnetic JT crystals was observed in  $KDy(MoO_4)_2$  crystal by Leask, Tropper, and Wells [27], and Kazey and Sokolov [28]. The detailed discussion of the phenomenon was presented by Kaplan [29]. Approximately at the same time (in 1982) a new phenomenon of metamagnetoelasticity was predicted.

It is convenient to start the explanation of these phenomena with the another property of the CJTE crystals that is called metaelasticity (the term was suggested in [26]). Due to strong anisotropic character of the ordering of the local JT distortions this phenomenon is a direct analogy of the Ising metamagnetism. However in the

ordered JT crystals the external uniaxial pressure leads to the overturn of one of the distortion sublattices in the antiferroelastic system.

The strong electron-phonon coupling causes the dramatic change in the sublattice electronic structure related to the crystal structure change. At the same time the vibronic coupling through the magnetostriction can allow the overturn of the distortion sublattice by the external magnetic field. The result of that is the dramatic increase of the homogeneous crystal strain at the critical magnetic field – metamagnetoelasticity. At the same time the change of the electronic structure supports the dramatic increase of the induced magnetic moment of the total system – metamagnetism (Figs. 11–13).

Similar phenomena of metamagnetoelasticity and metamagnetism were observed in colossal magnetoresistance manganites by Nojiri, Kaneko, Motokawa, Hirota, Endo, and Takahashi [30].

They additionally had (Figs. 12, 13) demonstrated that these phenomena correlate with the anomalies of the magnetoresistance.

In colossal magnetoresistance manganites the metamagnetoelasticity is connected with the XY-ordering of the elongated octahedra surrounding the  $\text{Mn}^{3+}$  cations. As a result of this type of ordering the crystal lattice is increasing the elementary cell size in the *ab*-plane and decreasing along the tetragonal axis *z*-direction. If the magnetic field is applied in the *ab* crystal plane the metamagnetism and metamagnetoelasticity caused by magnetostriction could be expected. The magnetic field that is directing along *z*-axis and supporting the elongation of the crystal cell along *z*-axis could be responsible for a similar phase transition when the Zeeman energy is of the order of the intersublattice JT molecular field. This situation was analyzed by Kaplan and Zimmerman [31]. Some examples of their calculations are shown on the Fig. 14. The Fig. 15 shows that at the magnetic field induced structural transition the magnetic susceptibility has an anomalous behavior while the crystal is paramagnetic at all temperatures.

The lowest curve corresponds to the lowest temperature  $T = 0.1$  (the magnetic field is much smaller than the Jahn–Teller ordering molecular field). If the molecular field is much smaller than Zeeman interaction the metamagnetoelastic jump disappears.

The lowest curve does not show any anomaly in the susceptibility behavior as the temperature ( $T = 4.0$ ) is too high in comparison with the magnetic field.

Similarly there are no susceptibility anomalies for very low temperatures ( $T = 2.2$  and lower; three highest curves at small  $H_z$ ) as at this case the strong molecular field is suppressing the Zeeman interaction.

As it could be seen from the Fig. 14 the anomalous jump of the magnetic moment disappears when the temperature is higher than the critical temperature of the structural XY-ordering in the crystals (for  $T = 0.1$  the magnetic field value is not big enough for the sublattice overturn, *T*-units are dimensionless). Similarly the susceptibility anomaly is maximum at  $T = T_s = 2.6$ .

It is clear that the metaelasticity similar to the observed one in the rare-earth compounds is present in the colossal magnetoresistance systems. The results of the corresponding behavior of the uniaxial spontaneous strain depending upon the uni-

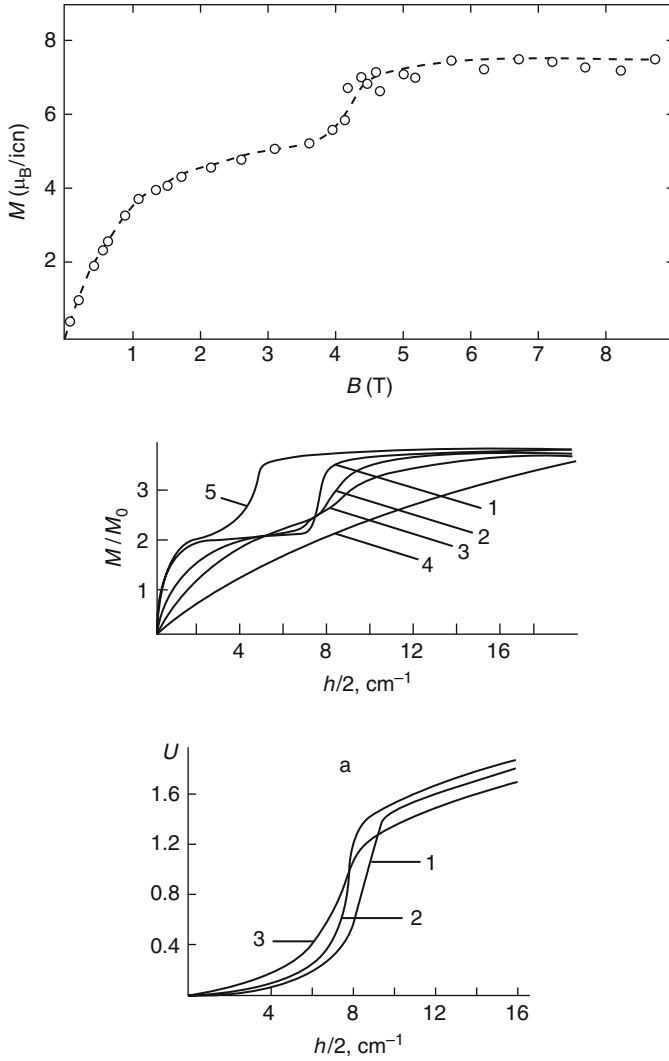


**Fig. 11** Experimental and theoretical data demonstrating the metamagnetism and metamagnetoelasticity of the Jahn–Teller crystals with structural transitions:  $M(B)$  – metamagnetism of  $\text{KDy}(\text{MoO}_4)_2$  [27];  $M/M_0(h/2)$  – theory ( $h = 1/2g\mu_B H$ );  $U(h/2)$  – metamagnetoelasticity of an antiferroelastic (theory) [29]

axial stress as well as of the dynamic magnetostriction calculation are shown on the Figs. 16 and 17.

When the  $P_z$  magnitude is bigger than 3.0 the lowest curve corresponds to  $T = 0.1$  (the sharpest jump of the order parameter) and the highest curve is related to  $T = 4.0$  (there is no phase transition at this case).

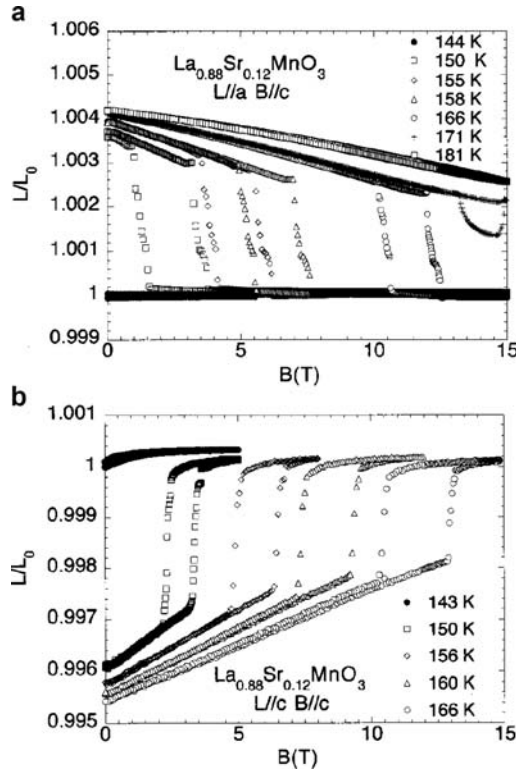


**Fig. 12** Metamagnetoelasticity of the colossal magnetoresistance  $\text{La}_{0.88}\text{Sr}_{0.12}\text{MnO}_3$  manganites (at all temperatures the phase is ferromagnetic) [30]

## 9 Orbital-Magnetic Structure at Orbital Degeneracy

While the virtual phonon exchange as a rule is the major electron correlation mechanism in CJTE crystals, there is no doubts that in different situations other electron interactions could play an important role. In JT compounds the structural phase transitions very often are followed, preceded, or accompanied by magnetic transitions. These magnetic transitions as a rule are due to the superexchange at the orbital degeneracy of the JT centers. The effective Hamiltonian describing this type of interaction was suggested by Kugel and Khomskii [33, 34]. They had demonstrated that the orbital and real spin operators are coupled so that the ordering of spins depends upon the ordering of the orbitals. A typical Hamiltonian of superexchange interaction in the simplest case of the symmetrical model (transfers between similar orbitals only are not zero and all are equal) for orbital doublets on the site looks like

$$H_{se} = \sum_{ij} (J_1 \vec{S}_i \vec{S}_j + J_2 \vec{\tau}_i \vec{\tau}_j + 4J_3 \vec{S}_i \vec{S}_j \vec{\tau}_i \vec{\tau}_j) \quad (25)$$



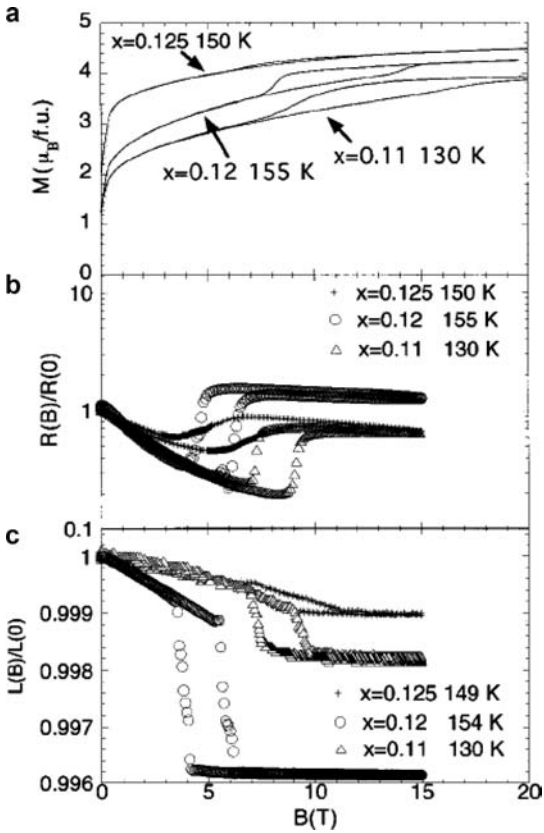


**Fig. 13** Correlation of the metamagnetism, metamagnetoelasticity, and colossal magnetoresistance in manganites. The vertical shifts of the magnetization curves are given for convenience only; the curves of strain  $L$  and resistivity  $R$  are normalized by their values at zero field [30]

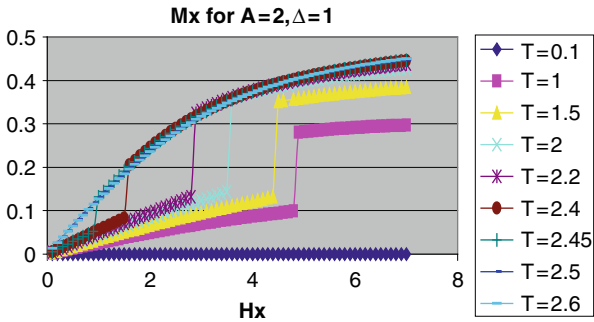


**Fig. 14** Metamagnetism at XY-ordering in Jahn–Teller crystals [31]

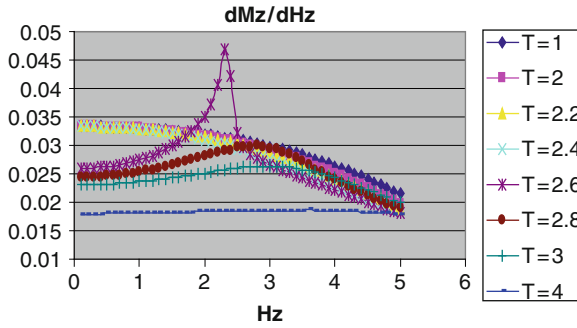


**Fig. 15** Magnetic susceptibility anomalies in paramagnetic XY-ordered JT crystals

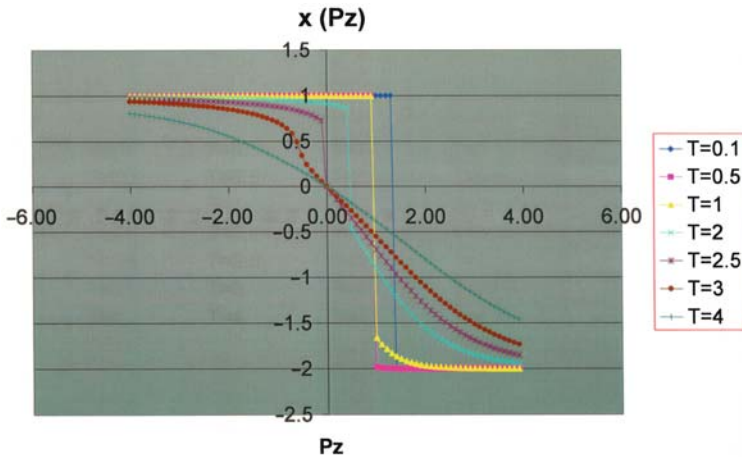


**Fig. 16** Metaelasticity in JT crystals with XY-ordering [32].  $P_z$  is the uniaxial stress along the z-axis of the crystal;  $x$  is the octahedron elongation along the x-axis

where  $\tau$  are orbital operators and  $S$  are real spin operators. Using this approach Kugel and Khomskii were able to explain and predict several very interesting magnetic structures in crystals. An example of these is the  $\text{KCuF}_3$  crystal with ferromagnetic ordering in the plane and antiferromagnetic ordering between the planes. It can be shown that this magnetic ordering is the direct result of the antiferrotype ordering of the d-orbitals of the  $\text{Cu}^{2+}$  ion. That is, of course, simultaneously coupled to the antiferrodistortive ordering of the octahedron distortions around these ions.

The orbital structure of the  $\text{KCuF}_3$  crystal is shown on the Fig. 18.

It should be mentioned that while in the Hamiltonian of the superexchange interaction at orbital degeneracy there are no vibrational operators, the vibronic interaction as a rule plays a decisive role in the ordering of the orbitals in the JT crystals.

As it was discussed above in these systems the virtual phonon exchange is the leading interaction responsible for the structural phase transition and for the cor-

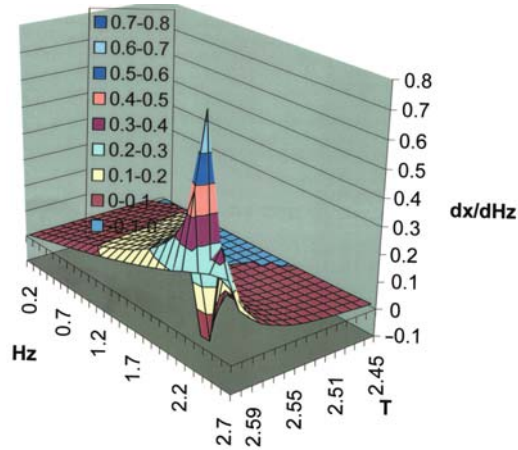


**Fig. 17** Magnetic and temperature dependences of giant dynamic magnetostriction in JT crystals with the structural XY-ordering [32] (x is the octahedron elongation along the x-axis)

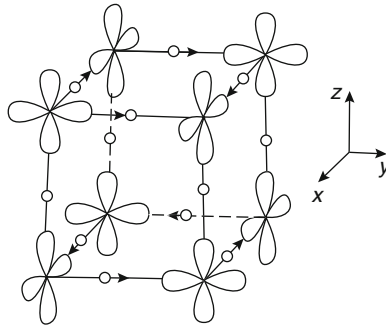


**Fig. 18** Ordering of electronic states in  $\text{KCuF}_3$  crystal [34]

responding ordering of the orbitals. That orbital ordering in its turn influences the magnetic ordering.

Nowadays these questions are in the focus of attention in the studies of the magnetic properties of the transition metal oxides and of the colossal magnetoresistance compounds in part. For the  $\text{LaMnO}_3$  crystals the most consistent approach based on taking into account both the CJTE and the superexchange Hamiltonians was developed by Ishihara, Inoue, and Maekawa [35].

## 10 Magnetolectricity

As it was shown in section VI, as a rule the JT crystals are characterized by combination of big magnetostriction and electrostriction effects. However Mitsek and

Smolenskii [36] were the first who had proved that the combination of such a phenomena will lead to strong magnetoelectricity: the dependences of the polarization and the dielectric crystal constant upon the external magnetic field and of the magnetization and magnetic susceptibility upon the external electric field. Vekhter and Kaplan [10, 26, 37] noted that as the magneto- and electrostriction effects are big in JT crystals and can be successfully understood in the framework of the CJTE theory, it is natural to expect big magnetoelectric effects in the JT systems and their complete microscopic description.

Additionally, as it was predicted in [10], in these types of materials some metamagnetoelectric effects (for example, sharp increase of the polarization with the external magnetic field) should be observed.

The phenomenological and microscopic theory of the JT paramagnetic and paraelectric ferroelastics was discussed in detail in [10]. An example of such a material is the crystal of  $\text{TmAsO}_4$  that is undergoing a ferroelastic transformation from the tetragonal to the orthorhombic phase at 6.1K. Taking into account the lowest electronic states of the  $\text{Tm}^{3+}$  ion – the ground doublet and the excited singlet – it is possible to calculate the magnetoelectric coefficients in this compound using their connection to the electronic structure and concrete phonon spectrum.

As among the JT ferroelastics there are materials with the magnetic and ferro- (or antiferro-) electric orderings, it is interesting to take a look at their magnetoelectricity description. Examples of materials with the coexisting structural, magnetic, and electric dipole moments are  $\text{DyVO}_4$  (ferroelastic, antiferromagnetic, antiferroelectric),  $\text{KDy}(\text{MoO}_4)_2$  (antiferroelastic, antiferroelectric, “tilted” magnetic),  $\text{TbPO}_4$  (ferroelastic, antiferroelectric, “canted” magnetic), and others.

Among these materials the record big magnetoelectric effect is related to  $\text{TbPO}_4$  as it was experimentally discovered by Rado, Ferrari, and Maish [38] and later discussed in more detail by Bluck and Kahle [39]. Theory of this phenomenon was discussed in [10, 26, 37, 39, 40]. The Hamiltonian describing the CJTE in  $\text{TbPO}_4$  crystal with the ferroelastic (simultaneously antiferroelectric) and antiferromagnetic phase transitions is based on the on the lowest three (ground non-Kramers doublet and the first excited singlet) electronic states. The energy gap between the ground and excited states is  $\Delta = 2.2\text{ cm}^{-1}$ . The electron-phonon and electron-strain interactions after standard shift transformation of the Hamiltonian  $H$  described in section II (eqn. (4)) yield an effective intersite interaction (second term of  $H$  in Fig. 19) and causes a structural transition at  $T = T_s = 2.15\text{ K}$ . The orbital (rather spin-orbital due to strong spin-orbital interaction) JT center  $P_m$  operators are describing the mixture of the doublet and singlet ion states and are coupled with the local monoclinic distortions. The third term in  $H$  of the Fig. 19 corresponds to the isotropic in plane magnetic intersite interaction and is responsible for a paramagnetic-antiferromagnetic transition at  $T_N = 2.28\text{ K}$ . The  $A_{1,2}$  and  $J_{1,2}$  constants are the inter- and intrasublattice parameters of the virtual phonon exchange and magnetic exchange correspondingly. As the local symmetry of the  $\text{Tb}^{3+}$  ion is  $D_{2d}$  (has no center of inversion) and the unit cell contains two formula units, the spontaneous monoclinic strain produces local dipole moments (because of local piezoelectric effect).

# FERROELASTIC ANTIFERROELECTRIC AND ANTIFERROMAGNETIC TbPO<sub>4</sub> CRYSTAL

$$T_s \approx T_N \quad T_s = 2.15 \text{ K}, \quad T_N = 2.28 \text{ K}$$

At  $T < T_N$ : paramagnetic  $\square$  antiferromagnetic transition;  $M \parallel c$

At  $T < T_s$ : tetragonal symmetry (zircon structure)  $\square$  monoclinic symmetry

$Tb^{3+}(D_{2d})$ : ground orbital doublet separated by  $\Delta = 2.2 \text{ cm}^{-1}$  from the first excited singlet

$$H = -\Delta \sum_{m\alpha} Q_m^\alpha - \sum_{mn} A_{mn}^{\alpha\alpha'} P_m^\alpha P_n^{\alpha'} + \sum_{mn} J_{mn}^{\alpha\alpha'} (S_x^{m\alpha} S_x^{n\alpha'} + S_y^{m\alpha} S_y^{n\alpha'} + S_z^{m\alpha} S_z^{n\alpha'})$$

$$J_{xx} \approx J_{yy} \approx J_{zz} = J$$

$$Q = \begin{pmatrix} 1 & 0 & 0 \\ 0 & 0 & 0 \\ 0 & 0 & 0 \end{pmatrix} \quad P = \frac{1}{\sqrt{2}} \begin{pmatrix} 0 & 0 & 1 \\ 0 & 0 & -1 \\ 1 & -1 & 0 \end{pmatrix} \quad S_z = \begin{pmatrix} 1 & 0 & 0 \\ 0 & -1 & 0 \\ 0 & 0 & 0 \end{pmatrix} \quad S_x = \frac{1}{\sqrt{2}} \begin{pmatrix} 0 & 0 & 1 \\ 0 & 0 & 1 \\ 1 & 1 & 0 \end{pmatrix}$$

6 order parameters:  $\overline{S_z^\alpha}$ ,  $\overline{S_x^\alpha}$ ,  $\overline{P_\alpha}$ ;  $J = J_1 + J_2 = -1.5 \text{ K}$ ;  $A = A_1 + A_2 = 3.1 \text{ K}$

$$\alpha_{ij} = (\partial M_i / \partial \mathcal{E}_j)$$

At  $T_s < T < T_N$  and  $\mathcal{E}_y \neq 0$ :  $M_x \neq 0$ ,  $M_z = 0 \rightarrow \alpha_{xy} \neq 0$ ,  $\alpha_{zy} = 0$

At  $T < T_s$ :  $\alpha_{xy} \neq 0$ ;  $\alpha_{zy} \neq 0$

Magnetoelectric coefficients vs. temperature. 1)  $\alpha_{xy}$ ; 2)  $\alpha_{zy}$ .

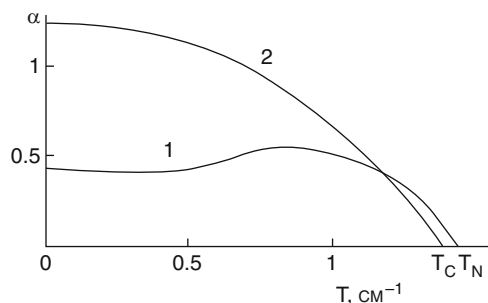


**Fig. 19** Hamiltonian, definition of magnetoelectric coefficients  $\alpha$ , and theoretical calculations of the magnetoelectric coefficients temperature dependences (simplified model) [37]

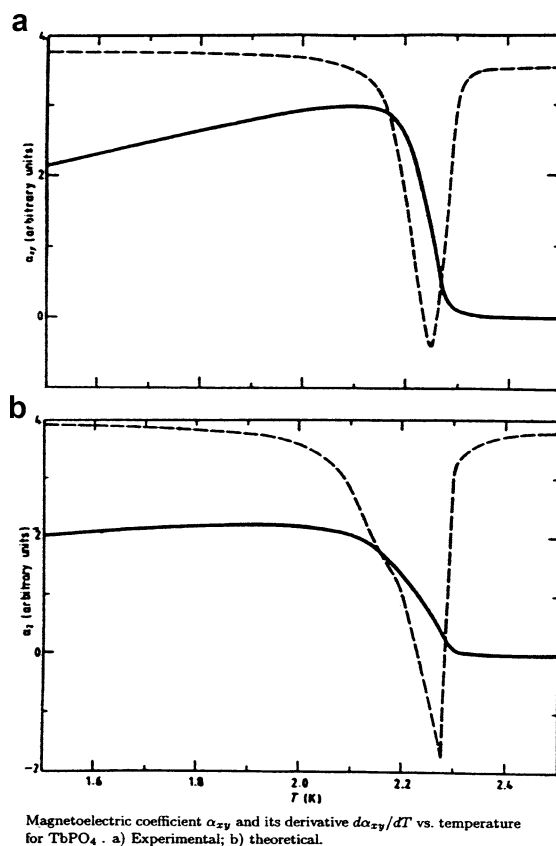


**Fig. 20** The experimental and theoretical data for the magnetolectric coefficients of  $\text{TbPO}_4$  crystal according to [39]

As the crystal cell below the structural transition remains centrosymmetrical one, the dipole moments in the cell are antiparallel. Thus, the magnetostructural phase transition at  $T = T_s$  is simultaneously an antiferroelectric transition (Fig. 20).

Lately the interest to the magnetoelectricity was revived in connection with the discovery [41–44] of new magnetoelectric properties in multiferroics – materials with the magnetic and electric dipole orderings. Among them the probably most “fashionable” material is  $\text{TbMnO}_3$ . This compound has a colossal magnetoresistance, but mostly is known for its magnetoelectricity. Some experimental results for  $\text{TbMnO}_3$  crystal by Kimura, Goto, Shintani, Ishizaka, Arima, and Tokura [41] are presented on the Figs. 21–23.

The crystal has a spiral magnetic ordering and some peculiar ferroelectric ordering. As it could be seen from the Figs. 21–23 this compound is characterized by a tight connection between the magnetic and the lattice subsystems, by a magnetic field induced structural transition, by some metamagnetism and metam-

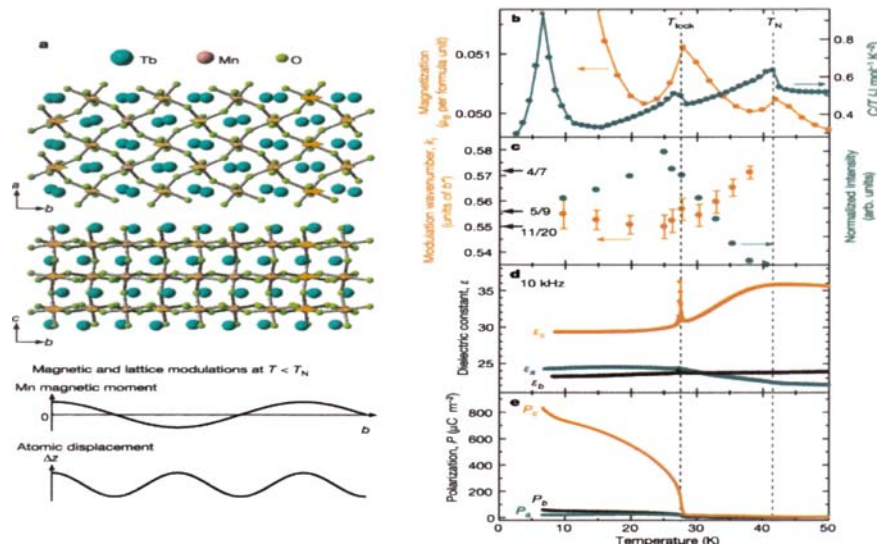


**Fig. 21** Crystal structure (a) and temperature dependences of magnetization (b), modulation wavenumber (c), dielectric constant (d), and polarization (e) in TbMnO<sub>3</sub> crystal [38] (modulations of magnetic moment and lattice displacement are shown at the bottom left)

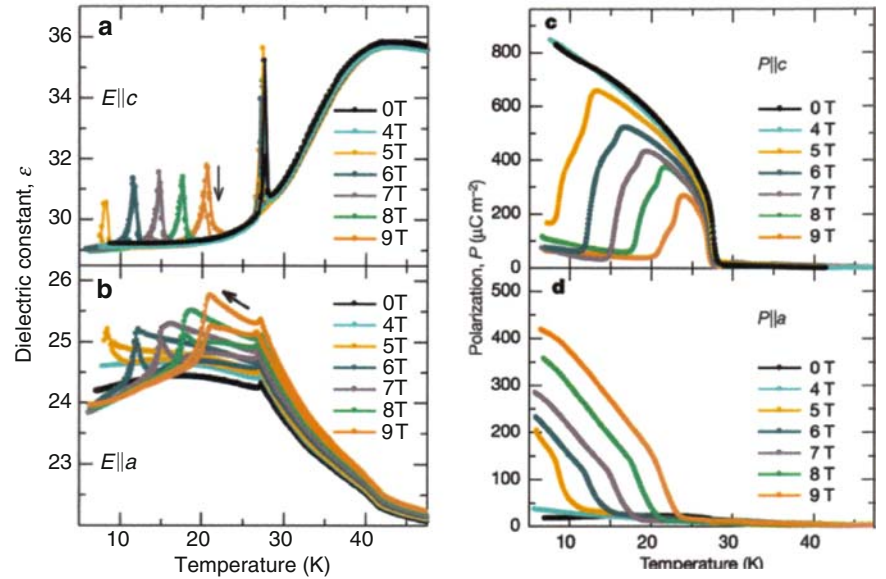


**Fig. 22** Temperature dependences of dielectric constant (a, b) and of polarization (c, d) in TbMnO<sub>3</sub> crystal [38]



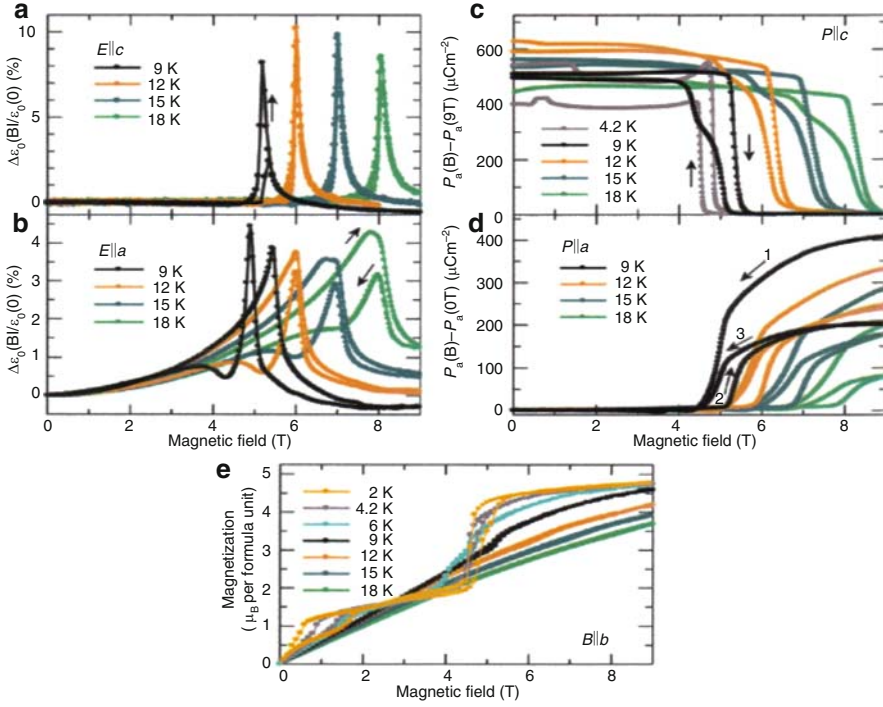


**Fig. 23** Magnetic and magnetoelectric properties of TbMnO<sub>3</sub> crystal [38]

agnetoelectricity, and by the presence of the return phase transition (return to the phase without the polarization at lowering the temperature or external magnetic field).

It should be noted that almost all new multiferroic materials contain a spiral magnetic structure. In connection with that, trying to explain the mechanism of the strong connection between the magnetic and electric dipole moments in them, many new interesting theoretical concepts were developed [41–48 and references therein]. Almost all of them are more or less related to the following ideas: (a) magnetic non-collinearity leads to the loss of the crystals center of inversion; (b) the exchange striction will induce the polarization that could be modified by the external magnetic field – magnetoelectricity.

However it should be mentioned that all peculiarities of the new multiferroic materials are typical for the JT crystals. In each of the multiferroics there is a Mn<sup>3+</sup> or another JT (or pseudo JT) ion with the orbital electronic degeneracy (or pseudo degeneracy). In this situation it is possible to speculate that CJTE is leading in this type of materials to some structural transitions with helicoidal distortional structure (such a transitions were first discussed by Maaskant and Haije [49]). The helicoidal distortional structure is inducing the magnetic helicoidality and the corresponding electric dipole ordering [50].



It is important to note that the exchange striction as a rule is very weak and can not explain the strong magnetoelectric effect. However the JT crystals – materials with significant electron-vibrational interaction – are able to provide strong coupling between magnetic moments and distortions (electric dipole moments). Such an approach to the magnetoelectricity of the multiferroics was discussed in [50, 51].

## 11 Further Development

When talking about the prospects in the CJTE field it should be clearly understood that a lot of work has been started already. With this in mind the first as one of the most important, I think, should be mentioned the problem of *conductivity in JT crystals*. The progress in this direction could lead to the understanding of high T<sub>c</sub> superconductivity, colossal magnetoresistance, properties of buckyballs and other phenomena. Theory of CJTE should be extended to *new types of structural transitions* in transition metal compounds, polymers, metalloorganics, systems with “rotational transitions”. Basing on the complete analysis of both superexchange and virtual phonon exchange interactions *new types of magnetic and orbital orderings* should be discussed. It is very probable that in the future a lot of attention will be paid to the microscopic analysis of *CJTE of materials with new anomalous thermodynamic properties* like crystals with negative Poisson ratio, unusual thermal expansion, new type of adiabatic cooling and others. Nowadays it is already on the way the development of physics of *multiferroics* and connected to it *chirality*. The vibronic interactions based approach could be very fruitful in studies of *self assembly* (stripes are a simple example), *Berry phase in CJTE systems*, *JT clusters*. All these problems are of huge importance for physics, chemistry, and biology. Of course, the semiconductor industry of the future and electronics in general could be very much interested in properties of *JT nanocrystals*.

Overall it should be mentioned that the CJTE field is well developed, but a lot of big problems in the field still need to be resolved.

## References

1. J.D. Dunitz, L.E. Orgel, J. Phys. Chem. Solids. **3**, 20 (1957)
2. D.S. McClure, J. Phys. Chem. Solids. **3**, 311 (1957)
3. J. Kanamori, J. Appl. Phys. **31**, 14S (1960)
4. I.B. Bersuker, Phys. Lett. **A20**, 589 (1966); (see more detail in I.B. Bersuker, V.Z. Polinger, Vibronic Interactions in Molecules and Crystals, New York, Springer, 1989)
5. R.J. Elliott, R.T. Harley, W. Hayes, S.R.P. Smith, Proc. R. Soc. London **A328**, 217 (1972)
6. H. Thomas, in *Electron-Phonon Interactions and Phase Transitions*, ed. by T. Riste (Plenum Press, New York, 1977)
7. G.A. Gehring, K.A. Gehring, Rep. Prog. Phys. **38**, 1 (1975)
8. D. Reinen, C. Friebe, Struct. Bonding. **37**, 1 (1979)

9. R. Englman, *The Jahn–Teller effect in Molecules and Crystals* (Wiley, London, 1972)
10. M.D. Kaplan, B.G. Vekhter, *Cooperative Phenomena in Jahn–Teller Crystals* (Plenum Press, New York and London, 1995)
11. K. Sugihara, J. Phys. Soc. Jpn. **14**, 1231 (1959)
12. H. Thomas, K.A. Muller, Phys. Rev. Lett. **28**, 820 (1972)
13. R.L. Melcher, E. Pytte, B.A. Scott, Phys. Rev. Lett. **31**, 307 (1973)
14. R.L. Melcher in *Physical Acoustics*, vol. **12**, ed. by W.P. Mason, R.N. Thurston (Academic Press, New York, 1976)
15. M. Kataoka, J. Kanamori, J. Phys. Soc. Jpn. **32**, 113 (1972)
16. M.D. Kaplan, B.G. Vekhter, Sov. Phys. Solid State. **17**, 43 (1975)
17. J.K. Kjems, W. Hayes, S.H. Smith, Phys. Rev. Lett. **35**, 1089 (1975); J.K. Kjems, in *Electron-Phonon Interactions and Phase Transitions*, ed. by T. Riste (Plenum Press, New York, 1977)
18. R.T. Harley, W. Hayes, S.R.P. Smith, J. Phys. C: Solid St. Phys. **5**, 1501 (1972)
19. I.B. Bersuker, *The Jahn–Teller Effect*, (University Press, Cambridge, 2006)
20. H. Unoki, T. Sakudo, Phys. Rev. Lett. **38**, 137 (1977)
21. D.R. Taylor, in *Electron-Phonon Interactions and Phase Transitions*, ed. by T. Riste, (Plenum Press, New York, London, 1977)
22. L.N. Pelikh, A.A. Gurskas, Sov. Phys. Solid State. **21**, 1223 (1979)
23. B.G. Vekhter, M.D. Kaplan, Sov. Phys. Solid State. **20**, 824 (1978)
24. B.G. Vekhter, M.D. Kaplan, Sov. Phys. JETP. **51**, 892 (1980)
25. B.G. Vekhter, M.D. Kaplan, Sov. Phys. Solid State. **16**, 1064 (1974)
26. M.D. Kaplan, JETP Lett. **35**, 105 (1982); in *Cooperative Phenomena: Proc. of the Int. Symp. on Synergetics and Cooperative Phenomena in Solids*, 18 (1983)
27. M.J.M. Leask, A.C. Tropper, M.R. Wells, J. Phys. C: Solid State Phys. **14**, 3481 (1981)
28. Z.A. Kazey, V.I. Sokolov.
29. M.D. Kaplan, Sov. Phys. Solid State. **26**, 51 (1984)
30. H. Nojiri, K. Kaneko, M. Motokawa, K. Hirota, Y. Endoh, K. Takahashi, Phys. Rev. B. **60**, 4142 (1999)
31. M.D. Kaplan, G.O. Zimmerman, Phys. Rev. B. **77**, 104426 (2008)
32. M.D. Kaplan, G.O. Zimmerman, Phys. Rev. B. **73**, 064103 (2006)
33. K.I. Kugel, D.I. Khomskii, Sov. Phys. JETP. **37**, 725 (1973)
34. K.I. Kugel, D.I. Khomskii, Sov. Phys. Usp. **136**, 231 (1982)
35. S. Ishihara, J. Inoue, S. Maekawa, Phys. Rev. B. **55**, 8280 (1997)
36. A. I. Mitsek, G.A. Smolenskii, Sov. Phys. Solid State. **4**, 2620 (1963)
37. M. D. Kaplan, B.G. Vekhter, Vth European Meeting on Ferroelectricity, Abstr., Benalmadena-Torremolinos. 21 (1983); B.G. Vekhter, M.D. Kaplan, Sov. Phys. Bull. Acad. Sci. USSR, Phys. **51**, 9 (1987)
38. G.T. Rado, J.M. Ferrari, W.J. Maish, Phys. Rev. B. **29**, 4041 (1984)
39. S. Bluk, H.G. Kahle, J. Phys. C: Solid State Phys. **21**, 5193 (1988)
40. J. Sivardiere, Phys. Rev. B, **8**, 2004 (1973)
41. T. Kimura, T. Goto, H. Shintani, K. Ishizka, T. Arima, Y. Tokura, Nature (London). **426**, 55 (2003)
42. M. Fiebig, J. Phys. D. **38**, R123 (2005)
43. M. Kenzelmann, A.B. Harris, S. Jonas, C. Broholm, J. Schefer, S.B. Kim, C.L. Zhang, S.-W. Cheong, O.P. Vajk, J.W. Lynn, Phys. Rev. Lett. **95**, 087206 (2005)
44. G. Lawes, A.B. Harris, T. Kimura, N. Rodago, R.J. Cava, A. Aharony, O. Entin-Wohlman, T. Yildirim, M. Kenzelmann, C. Broholm, A.P. Ramirez, Phys. Rev.
45. H. Katsura, N. Nagaosa, A.V. Balatsky, Phys. Rev. Lett. **95**, 057205 (2005)
46. I.A. Sergienko, C. Sen, E. Dagotto, Phys. Rev. Lett. **97**, 227204 (2006)
47. M. Mostovoy, Phys. Rev. Lett. **96**, 067601 (2006)
48. A.B. Harris, Phys. Rev. B. **76**, 054447 (2007)
49. J.A. Maaskant, W.G. Haije, J. Phys. C. **19**, 5295 (1986)
50. M. Kaplan, Proc. of Int. Sugano Symposium on Left-Right Symmetry in Physics, Chemistry, and Biology, p.10, Tsukuba (2006)
51. M. Kaplan, XVIII Int. JT Symposium, Abstracts, Trieste (2006)

# Orbital Ordering Versus the Traditional Approach in the Cooperative Jahn–Teller Effect: A Comparative Study

Victor Polinger

**Abstract** In Jahn–Teller crystals, at low temperatures, symmetry-breaking lattice distortion creates an ordering of otherwise degenerate atomic orbitals. In the theory of cooperative Jahn–Teller effect, the traditional approach includes solving the complex problem of coupled dynamics of the respective electron-vibrational system. During last two decades, an alternative way of treating the cooperative Jahn–Teller effect attracts increasing attention. It replaces ligand-mediated intercell coupling by an effective intersite orbital exchange of electron-degenerate atoms. Known as the *orbital ordering approach*, it explores stable ordered patterns due to the exchange coupling of orbital pseudo spins. The respective symmetry break of crystal lattice structure is treated as a secondary effect resulting from the orbital ordering. This paper examines some approximations implicitly included in the orbital ordering approach and compares it to the traditional theory of the Jahn–Teller effect. As the orbital ordering approach replaces ligand-mediated intersite coupling by an orbital exchange, the fundamental effect of dynamic strengthening chemical bonds with low-symmetry lattice distortions is lost. This may bring to a wrong conclusion about possible bond-ordered structures. On the other hand, a number of cases are outlined when both approaches yield close results. Based on these estimates, conclusions regarding applicability of the orbital ordering approach are derived and some general recommendations are given.

## 1 Introduction

Crystal structure is determined by chemical bonds between elementary cells, as well as by the conditions under which the crystal is formed. This paper is focused on bonding-structure relationship in Jahn–Teller (JT) crystals. In simple cases (see below), of several possible crystal structures, the one beneficial for chemical bonding and steric effects actually develops. They determine molecular skeleton of elementary cells, their geometric shape and size. Combined with the requirements of close packing, these are the necessary conditions of growing an ideal crystal with long-range atomic order.

Except some special cases, this way of understanding crystal structures provides reasonable results under condition that each elementary cell is in an orbital singlet (nondegenerate) electron ground state. If the ground state is orbitally degenerate, elementary cells are unstable with respect to low-symmetry nuclear distortions. This degeneracy-driven instability in crystals is known as the JT effect [1–3].

At present, there are two different ways of addressing the problem of cooperative JT instability in crystals. One was introduced in 1970 by Englman and Halperin [4]. Here we call it the *traditional* approach. It is based on the concept of intercell elastic<sup>1</sup> correlation of JT-unstable elementary cells. The JT effect determines symmetry-breaking local (one-site) distortion of each elementary cell. In the case of a structural phase transition of order-disorder type, in the high-temperature phase, the intercell elastic coupling is averaged out. Still, there may be a *disorder* of distorted elementary cells. At lower temperature, due to the intercell elastic coupling, local distortions form an ordered pattern of a low-symmetry crystal lattice [5–7]. In the case of a displacive phase transition, in the high-temperature phase, neither local, nor global lowering symmetry takes place. (Obviously, these are just the two limiting cases. In real crystals, there is a nontrivial combination of both, the order-disorder and the displacive character.) In the traditional theory of the cooperative JT effect, the low-symmetry orbital and magnetic (if any) arrangement is believed to follow the respective low-symmetry crystal structure of ordered elementary cells.

Another way of treating the cooperative JT effect was introduced in 1960 by Kanamori [8]. Extensively developed by the Oxford team (see review by Gehring and Gehring [5]) and in Kishinev (see Kaplan and Vekhter's book [7]), it was successfully applied to rare-earth JT compounds with extremely weak JT and relatively strong magnetic coupling. Adopted by Kugel and Khomskii [9] to explain some cooperative properties of transition metal compounds, today it is known as the Kugel-Khomskii model, and, also, as the *orbital ordering approach* (OOA). It explores rotational degrees of freedom of degenerate one-electron orbitals of undistorted elementary cells [9]. Treated in terms of the respective pseudo spins, they are believed to be oriented by the intersite *orbital exchange* coupling, quite similar to spin ordering due to magnetic exchange coupling in magnetic materials. With an additional effect of real spin ordering, if any, pseudo spin ordering determines a variety of different low-symmetry orbital and magnetic crystal-lattice patterns. The respective low-symmetry crystal (atomic) structure is believed to follow the orbital ordered structure of spin-electron states. As distinguished from the traditional approach, the OOA reduces the manifold of wave functions to a finite (usually, relatively small) number of orbitally degenerate electron states. The OOA looks simpler and, therefore, is more attractive than the traditional cooperative JT effect. In both approaches, the OOA and the traditional theory, the question of which real structure manifests itself is answered in the usual way.

---

<sup>1</sup> In this review, the term “elastic” is applied to inter-atomic forces of chemical bonding treated in harmonic approximation, to be distinguished from bulk elasticity in solids (see Kanamori [27]).

Free energy of the crystal is minimized with respect to the corresponding order parameter.

The key feature distinguishing the OOA from the cooperative JT effect is the way the chemical bonding effects are included. This will be an important part of the present study. In Sect. 2, we present a simple qualitative description of the cooperative JT effect. First, in Sect. 2.1, we demonstrate the chemical nature of the JT instability. In Sect. 2.2, the cooperative JT effect is presented as interplay of short-range chemical bonding effects with the long-range intercell elastic coupling. To reveal the most important differences of the two approaches from one another, in Sect. 3 we present a simplified version of the OOA. In Sect. 4, we discuss some additional effects that are closely related to JT instability in crystals.

In most cases, the OOA is an approximation (see Sect. 5). It has its limits of applicability and, therefore, has to be applied with some caution. As it follows from the seminal review paper on the OOA [9], its originators, Kugel and Khomskii, were well aware of the imminent limitations of this approximation. However, in some papers the important assumptions of the OOA are forgotten or just ignored. Among other goals of this comparative study is underlying cases when the OOA can and when it cannot be applied. Finally, in Sect. 6, we cumulate the concluding remarks and provide some general recommendations.

Both the cooperative JT effect in its traditional form and the OOA has a reach list of applications discussed in many related publications. Numbered in thousands, they all cannot be reviewed in one paper. Therefore, in no way the present work can be considered as a comprehensive review of either one of these two approaches. Fortunately, some JT crystals, mostly perovskites, were considered by different authors in both ways, applying the OOA and the traditional approach. This provides an opportunity to compare their results using as example a relatively short list of JT crystals. Regarding the cooperative JT effect, an updated review is provided by Kaplan in the present book [6]. For the OOA, its most important details can be found in the fundamental review by Kugel and Khomskii [9]. Recent results were reviewed by Khomskii [10] and Khaliullin [11].

## 2 Cooperative Jahn–Teller Effect: The Traditional Approach

The cooperative JT effect is one of multiple manifestations of JT instability in elementary cells with degenerate ground state. In what follows in this section, we provide examples demonstrating chemical nature of JT distortions. When elementary cells undergo a low-symmetry distortion, their potential energy lowers. This is the so-called JT stabilization energy,  $E_{JT}$ . Covalent bond strength is measured by the energy required to break the bond. Therefore, one can interpret  $E_{JT}$  as a cumulative effect of strengthening the respective covalent bonds.

Sometimes, this chemical origin of the JT effect is lost behind complex group-theoretical reasoning usually present in every book or review paper on the JT effect. Compared to standard texts of quantum mechanics [12] or inorganic chemistry [13],

or monographs on the JT effect [1–3], the way we present the JT instability in this paper is somewhat different.

Less general in some respect<sup>2</sup>, it emphasizes the chemical-bonding nature of the JT effect. Most important, in *every* JT case, its chemical nature can be revealed in a similar way. *In any JT molecule, its symmetry-breaking instability is due to an energy stabilization of the respective chemical bonds.*

## 2.1 Chemical Nature of the Jahn–Teller Effect

For symmetry-breaking JT instability, its chemical nature is illustrated below using two simple examples of a transition metal in a sixfold coordinated octahedral surrounding. In this example, we assume a strong tetragonal component of the respective crystal field. The octahedron is elongated or compressed by the tetragonal crystal field, so the local symmetry group is  $D_{4h}$ . Consider the simplest case of orbital electron degeneracy, an electron doublet ( $E$  term) ground state in high-symmetry configuration of each tetragonal elementary cell. For example, it can be a first-row transition metal compound with electron configuration  $3d^1$  [as for Ti(III)] or  $3d^2$  [as for V(III)].

Octahedral component of the crystal field splits fivefold one-electron energy level of  $3d$  orbitals into the ground-state threefold  $t_{2g}$  and the excited twofold  $e_g$ . The tetragonal component of the crystal field lifts the threefold degeneracy of the ground state. The  $t_{2g}$  level splits into a tetragonal singlet  $b_{2g}$ , transforming as  $xy$ , and a tetragonal twofold degenerate energy level  $e_g$ , transforming as  $xz$  and  $yz$ . The sign of tetragonal crystal field is assumed to be such as to make the  $e_g$  orbital to be the ground state.

The  $c$ -axis ( $z$ -axis) view of the tetragonal elementary cell with the respective ground-state orbitals of the central atom is provided in the top part of Fig. 1. Only upper lobes of the  $xz$  and  $yz$  orbitals, above the equatorial plane (above the  $ab$  plane,  $xy$  plane), are shown. The ones beneath the  $ab$  plane have the same shape but opposite sign.

Also, for simplicity, we include just the valence-shell  $2s$  and  $2p$  orbitals of the six ligand atoms. Most interesting are four  $2p_z$  orbitals of equatorial ligands. They combine into symmetry-adapted group orbitals including twofold  $e_g(2p)$  orbital with components  $e_x(2p) = \frac{1}{\sqrt{2}}(p_{1z} - p_{3z})$  and  $e_y(2p) = \frac{1}{\sqrt{2}}(p_{2z} - p_{4z})$ . The respective overlaps are not zero (dashed areas in the upper part of Fig. 1),  $\langle 3d_{xz} | e_x(2p) \rangle = \langle 3d_{yz} | e_y(2p) \rangle \neq 0$ . Therefore,  $e_g(2p)$  orbitals form coordination chemical bonds with the central atom. In high-symmetry nuclear configuration (tetragonal, local group  $D_{4h}$ ), the two overlap integrals are equal. Even with these chemical bonds included, the ground state remains degenerate.

<sup>2</sup> This discussion is based on approximated one-determinant Hartree-Fock presentation of the respective electron configuration. In its general formulation, the JT theorem does not require orbital structure of the electron wave functions. Its only condition is electron degeneracy due to a high symmetry of the molecular frame.

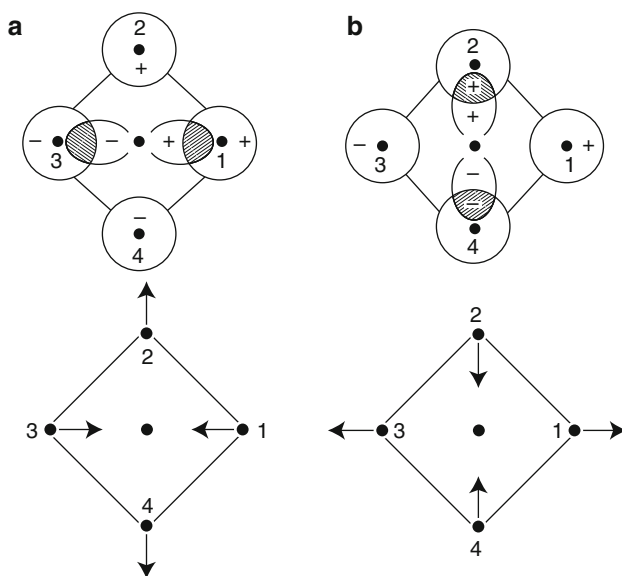


**Fig. 1** Rhombic distortion of a tetrahedral elementary cell increases overlap of highest occupied orbitals,  $3d_{xz}$  (a) and  $3d_{yz}$  (b), of the central atom with respective symmetry-adapted ligand orbitals,  $e_x(2p)$  and  $e_y(2p)$ . The  $c$  axis view. Only upper lobes (above the  $ab$  plane) are shown

As we can see in Fig. 1, rhombic distortion of ligands provides a better overlap and, therefore, a stronger chemical bond with the central atom. Depending on the sign of the respective distortion, positive in Fig. 1a and negative in Fig. 1b, the rhombic distortion lowers energy of one or another component of the  $e_g(2p)$  orbital,  $e_x(2p)$  or  $e_y(2p)$ . Respectively, the rhombic distortion lifts the above-mentioned degeneracy. For one of the orbital states, its energy is lifted up and the other one drops down in energy by exactly the same amount.

If there is just one electron [as, say, in the case of Ti(III)] or one hole [as in the case of V(III)], with this low-symmetry distortion, the elementary cell lowers its total energy (Fig. 2a). This energy benefit for the respective chemical bonds is the chemical origin of the symmetry-breaking JT instability in electron degenerate elementary cells [1, 2]. Essentially, this is what we call the JT effect.

In the symmetry group  $D_{4h}$ , the rhombic distortion transforms as the irreducible representation  $B_{1g}$ . Therefore, for this case, the commonly used notation is  $E \otimes b_1$ . Here  $E$  stands for the ground-state orbital doublet, the  $E$  term. Without the rhombic distortion, at  $Q = 0$ , it is degenerate. We use its energy as the reference energy level (zero energy). At small rhombic distortion,  $Q \neq 0$ , the respective overlap integrals can be expanded in powers of  $Q$ . Keeping just the linear term, we describe the energy splitting by the following JT Hamiltonian:

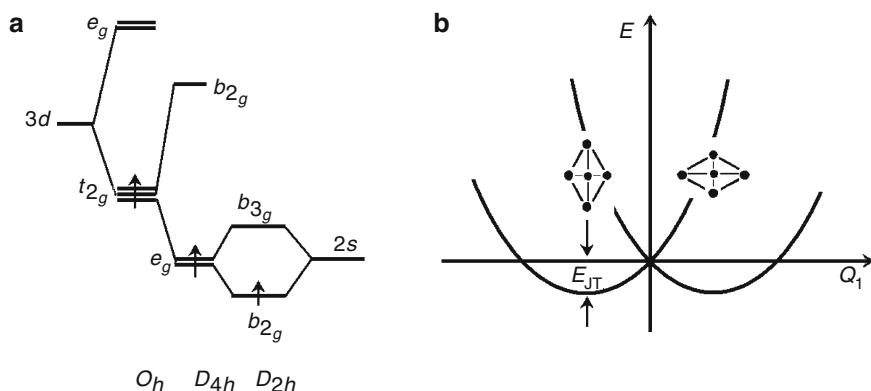


**Fig. 2** Energy stabilization of chemical bonds in a tetragonal elementary cell with rhombic JT instability. **(a)** Ground-state splitting due to symmetry reduction,  $O_h \rightarrow D_{4h} \rightarrow D_{2h}$ , followed by formation of the coordination bond of the central atom with equatorial ligands (cf. Fig. 1). Rhombic distortion splits the ground-state energy level  $e_g$  into  $b_{2g}$  and  $b_{3g}$ . This lowers energy of the populated state and lifts the nonpopulated one resulting in a stabilization of the total energy. **(b)** Adiabatic potential energy versus distortion coordinate  $Q$ . The symmetry-breaking energy gain is  $E_{JT}$

$$H_{JT} = VQ \begin{pmatrix} |Ex\rangle & |Ey\rangle \\ 1 & 0 \\ 0 & -1 \end{pmatrix} = VQ\sigma_z. \quad (1)$$

Here  $\sigma_z$  is one of Pauli matrices operating in the manifold of the two states,  $|Ex\rangle$  and  $|Ey\rangle$ , and

$$V = \frac{d}{dQ} \langle Ex | H | Ex \rangle |_{Q=0} \quad (2)$$

is the so-called vibronic coupling constant. The latter is rate of change of the respective matrix elements with the symmetry-breaking distortion coordinate  $Q$ . Added to one-cell elastic energy,  $\frac{1}{2}KQ^2$ , eigenvalues of the JT matrix (1),  $\pm VQ$ , determine the two branches,  $E(Q) = \frac{1}{2}KQ^2 \pm VQ$ , of the adiabatic potential energy graph shown in Fig. 2b.

Another example is a cubic crystal (local symmetry group  $O_h$ ) with a twofold degenerate ground state, an  $E_g$  or  $E_u$  term, as in octahedral  $[\text{CuO}_6]$  with  $\text{Cu}^{2+}$  at the center (Fig. 3). Its highest occupied orbital is  $e_g$  with components  $\theta = |3z^2 - r^2\rangle$  and  $\varepsilon = |x^2 - y^2\rangle$  populated with three electrons or, in other terms, one hole. Linear coupling to symmetry-adapted tetragonal distortions, local  $E_g$  modes,  $Q_\theta$  and  $Q_\varepsilon$ , lifts the orbital degeneracy (Fig. 3d). Populated with two electrons, one of the component orbitals,  $a_{1g}$ , lowers its energy. The other component,  $b_{1g}$ , populated with one electron lifts its energy up by exactly the same amount. In this way, total energy drops down.

Thus, the resultant energy stabilization is due to a strengthening the respective chemical bond. This is the so-called  $E \otimes e$  case. The respective JT Hamiltonian is [cf. (1)]



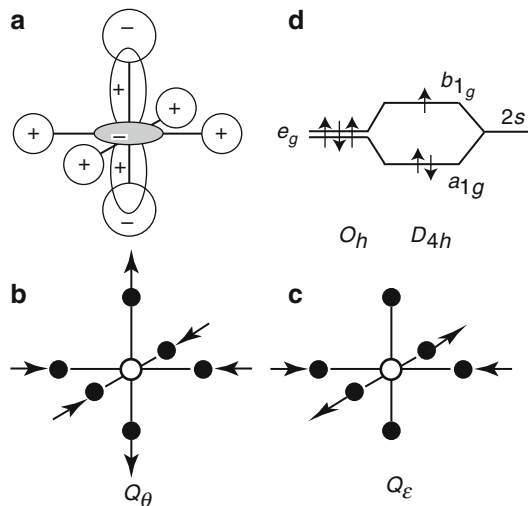


**Fig. 3** The JT instability in octahedral elementary cell  $[\text{CuO}_6]$  with a twofold degenerate ground energy level  ${}^2E_g$ . (a) Nonzero overlap of the central-atom 3d orbital,  $\theta = |3z^2 - r^2\rangle$ , with symmetry-adapted ligand group orbital,  $|\theta(2s)\rangle$ . (b) and (c) Twofold degenerate tetragonal distortion,  $Q_\theta$  and  $Q_\epsilon$ . (d) Tetragonal distortion  $Q_\theta$  lifts the orbital degeneracy. Double populated orbital,  $a_{1g}$ , lowers in energy and single populated orbital,  $b_{1g}$ , goes up in energy lowering the total energy

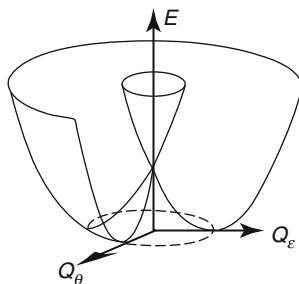


**Fig. 4** Adiabatic potential energy surface of a cubic elementary cell with an orbital  $E$  term linearly coupled to tetragonal distortions,  $Q_\theta$  and  $Q_\epsilon$ . With the circular trough at its bottom, it resembles a Mexican hat (after Longuet-Higgins et al. [14])

$$H_{\text{JT}} = V \begin{pmatrix} |\theta\rangle & |\epsilon\rangle \\ Q_\theta & Q_\epsilon \\ Q_\epsilon & -Q_\theta \end{pmatrix} = V (Q_\theta \sigma_z + Q_\epsilon \sigma_x). \quad (3)$$

Added to one-cell elastic energy,  $\frac{1}{2}K_E(Q_\theta^2 + Q_\epsilon^2)$ , the two eigenvalues of this matrix represent adiabatic potential energy surfaces (APESs) shown in Fig. 4. Its shape resembles the Mexican hat. At the no-distortion point,  $Q_\theta = Q_\epsilon = 0$ , the two sheets coalesce in the electron-degenerate  $E$  term.

Compared to the standard presentation of the JT effect in other books and monographs, this approach is somewhat different. However, it can be transformed into the standard formulation of the JT effect if the above arguments are applied to the  $d$ -shell projected angular-overlap model.

## 2.2 Inter-Cell Coupling in the Cooperative Jahn–Teller Effect

For a crystal with JT instability in its every elementary cell, in the case of coupling  $E \otimes b_1$  as in (1), the JT Hamiltonian is just a sum over different elementary cells:

$$H_{\text{JT}} = V \sum_i Q(i) \sigma_z(i). \quad (4)$$

Here  $Q(i)$  is the rhombic distortion in  $i$ th elementary cell (Fig. 1). In the simple case, when different elementary cells do not share common atoms, without the JT effect, the relevant part of the elastic energy is

$$U_{\text{elast}} = \frac{1}{2} \sum_{i,j} Q(i) K(i-j) Q(j). \quad (5)$$

Here  $K(i-j)$  is the  $ij$  matrix element of the respective dynamical matrix of force constants. Combined with the JT coupling (4), the potential energy is:

$$U = \frac{1}{2} \sum_{i,j} Q(i) K(i-j) Q(j) + V \sum_i Q(i) \sigma_z(i). \quad (6)$$

At relatively high temperature, the elastic intercell coupling is averaged out. Therefore, at different elementary cells, geometric shapes and amplitudes of the JT distortions are independently random. In other words, there is some distortion-magnitude disorder in the crystal lattice. At average, the respective X-ray crystal structure looks perfectly tetragonal.

With kinetic energy of JT active vibrations, the Hamiltonian is:

$$H = \frac{1}{2} \sum_i P^2(i) + \frac{1}{2} \sum_{i,j} Q(i) K(i-j) Q(j) + V \sum_i Q(i) \sigma_z(i) \quad (7)$$

Here  $P(i)$  is linear momentum conjugated to the distortion coordinate  $Q(i)$ .

In the theory of the JT effect, the linear-coupling case  $E \otimes b_1$  described by the Hamiltonian (7) is the easiest one. Its matrix part includes just diagonal matrices,  $\sigma_z(i)$ . As distinguished from this simple case, the general JT case is a tough problem of complex dynamics of electrons coupled to crystal lattice vibrations. The

usual approach is based upon the mean field approximation [4]. In what follows, we illustrate this approximation in a typical sequence of steps applicable to any other JT case as well.

In the low-symmetry phase, every operator can be presented as its temperature average plus a deviation (fluctuation) from the mean:

$$Q(i) = \bar{Q} + q(i), \quad \sigma_z(i) = \bar{\sigma} + s(i). \quad (8)$$

For simplicity, consider the so-called ferrodistoritive ordering pattern. We assume that all elementary cells are distorted in exactly the same way. Therefore, explicitly, the averages,  $\bar{Q}$  and  $\bar{\sigma}$ , do not depend on the elementary cell number,  $i$ . Assuming the fluctuations,  $q(i)$  and  $s(i)$ , much smaller than the respective averages,  $\bar{Q}$  and  $\bar{\sigma}$ , we can neglect terms of second-order in  $q(i)$  and  $s(i)$  and keep just the linear ones. The JT Hamiltonian (7) decouples into the following sum of translationally identical one-cell terms,

$$H = \frac{1}{2}P^2 + \frac{1}{2}KQ^2 + WQ + VQ\sigma_z, \quad (9)$$

with the low-symmetry mean-field,

$$W = \bar{Q} \sum_{m \neq n} K(m - n) = \bar{Q} \sum_{m \neq 0} K(m) \quad (10)$$

Compared to the high-symmetry one-cell JT Hamiltonian,  $\frac{1}{2}(P^2 + KQ^2) + VQ\sigma_z$ , the only difference of (9) is the low-symmetry term with the mean field  $W$ . According to (10), the latter is due to intercell elastic coupling. It is proportional to the average distortion  $\bar{Q}$  of all other elementary cells in the crystal. In general, even without the mean-field term, solving the respective one-center JT problem requires a nontrivial effort [1]. Including the symmetry-lowering term with  $W$  makes it even more difficult. In the cooperative JT effect, eigenstates and eigenvalues of one elementary cell are used to evaluate the respective averages,  $\bar{Q}$  and  $\bar{\sigma}$ .

Self-consistent nature of the mean-field approximation is in averaging  $Q$  and  $\sigma$  simultaneously with solving the eigenvalue problem (9). Moreover, the averaging includes temperature population of excited vibronic states. This gives temperature dependence of  $\bar{Q}$  and  $\bar{\sigma}$ . In particular, it provides an estimate of the temperature of the respective phase transition, an option that goes beyond the imminent limitations of the OOA (see below, Sect. 3.2).

Developed by Englman and Halperin [4], the above steps represent the traditional way in the cooperative JT problem. It's conceptual advantage and important part is solving the respective one-cell JT problem (9) including the low-symmetry mean field (10) of all other distorted cells. In this way, both effects, the dynamic strengthening chemical bonds with low-symmetry lattice distortions and the intercell elastic coupling, are included.

### 3 The Orbital Ordering Approach and its Basic Assumptions

The problem of cooperative JT effect can be reformulated in a slightly different way. So far, for a JT crystal, the general setup *is quite accurate*. Considered above in Sect. 2.2, the particular case of  $E \otimes b_1$  coupling does not represent any significant difficulty. In what follows, we are going to demonstrate an alternative route of getting to this point. In a way, it is misleading (see the respective discussion in Sect. 5.1). However, its attractive simplicity demonstrates the origin and basic approximations of the OOA and explains the popularity of the latter.

Although in their review [9], to derive the OOA, Kugel and Khomskii generalized the original setup suggested by Kanamori [8], in what follows, we use the way suggested by Ghering and Gehring [5]. Formally, it brings us to the same Hamiltonian and, at the same time, clearly demonstrates its relation to the JT effect. As in Sect. 2.2, we limit the consideration with the simple case, when different elementary cells do not share common atoms. This limitation allows a simpler derivation of the symmetry-correct electron Hamiltonian. Below, in Sect. 3.2, we will see that the general form of the electron Hamiltonian is based upon symmetry only and remains true in the most general case when next-neighbor elementary cells share common atoms as well.

#### 3.1 Two Simple Examples of the Orbital Ordering Approach

In the OOA, its general idea is in shifting the vibrational variables,  $Q(n)$ , to new reference position, the minimum point of the potential energy (6). To find the minimum, set the derivatives of  $U$  to zero,  $\partial U / \partial Q(n) = 0$ . This brings us to the following system of linear equations,

$$\sum_j K(i-j) Q(j) = -V\sigma_z(i). \quad (11)$$

Its solution is

$$\overline{Q}(i) = -V \sum_j \langle i | \mathbf{K}^{-1} | j \rangle \sigma_z(j). \quad (12)$$

Here  $\mathbf{K}^{-1}$  is the inverse of the dynamical matrix  $\mathbf{K}$  with elements  $K(i-j)$  introduced in (5). As in (8), we introduce new coordinates,  $q(i)$ , such that

$$Q(i) = \overline{Q}(i) + q(i) \quad (13)$$

with the “equilibrium” coordinates,  $\overline{Q}(i)$ , from (12). Plugging the shifted coordinates (13) into the Hamiltonian (7), we separate the phonon variables from the electron ones,

$$H = H_{\text{ph}} + H_{\text{el}}. \quad (14)$$

Here  $H_{\text{ph}}$  describes free phonons, and  $H_{\text{el}}$  is the Hamiltonian of the orbital–electron part,

$$H_{\text{el}} = - \sum_{\langle i, j \rangle} J(i - j) \sigma_z(i) \sigma_z(j), \quad (15)$$

with

$$J(i - j) = \frac{1}{2} V^2 \langle i | \mathbf{K}^{-1} | j \rangle. \quad (16)$$

In (15), the symbol  $\langle i, j \rangle$  means summation over next neighbors only. In (14), the two terms,  $H_{\text{el}}$  and  $H_{\text{ph}}$ , commute with one another,  $[H_{\text{el}}, H_{\text{ph}}] = 0$ . In other words, the Hamiltonian (14) is a sum of two independent terms. Electron motion is *decoupled* (!) from lattice vibrations.

The electron Hamiltonian (15) describes the so-called orbital exchange coupling in a three-dimensional (3D) crystal lattice. The Pauli matrices,  $\sigma_z(i)$ , have the same properties as the  $z$ -component spin operator with  $S = \frac{1}{2}$ . As  $\sigma_z(i)$  represents not a real spin but orbital motion of electrons, it is called *pseudo spin*. For the respective solid-state 3D-exchange problem, basic concepts and approximations were well developed in physics of magnetic phase transitions. The key approach is the mean-field approximation. Similar to (8), it is based on the assumption that fluctuations,  $s(i) = \sigma(i) - \bar{\sigma}$ , are small enough, so terms quadratic in  $s(i)$  can be neglected. We do not go into details here because the respective solution is well-known and discussed in many basic texts of solid state physics (e.g., see [15]).

At low temperatures, similar to real-spin magnetic exchange, the orbital exchange coupling results in an ordered phase. It corresponds to a minimum of the free energy with respect to an order parameter. Equal for all  $n$  in the case of the so-called *ferro* type ordering, the latter can be the average value of  $\sigma_z(n)$ . Another ordering pattern is alternating-sign values of  $\sigma_z(n)$  for next-neighbor elementary cells in the *antiferro* ordering (Fig. 5). Also, depending on which type of ordering provides the absolute minimum of free energy, there may be even a more complex type of pseudo spin ordering pattern. The determining factor is the parameter,  $J(i - j)$ , its sign and the way it depends on  $i$  and  $j$ .

When averages of  $\sigma_z(i)$  have certain values, pseudo spin ordering corresponds to a particular orientation of the respective orbitals arranged into an ordering pattern. In other words, the pseudo spin ordering is equivalent to an *orbital ordering* [9]. As it follows from (12), average values of  $\sigma_z(i)$  determine respective average values of  $Q(i)$ . So, in other words, the ordering pattern of pseudo spins,  $\sigma_z(i)$ , determines the resultant structure of the crystal lattice.

In the traditional theory of the cooperative JT effect, its significant part is one-center JT problem in a low-symmetry mean field (see the last paragraph of Sect. 2.2). In particular, it includes the eigenvalue problem for the Hamiltonian, similar to (7), operating in an infinite manifold of vibrational one-center states. Compared to this relatively complex step, in the OOA, the mean-field approximation is much simpler. In the OOA, one has to solve just a finite-size matrix ( $2 \times 2$  in this case) or, for other JT cases, a somewhat larger matrix but finite anyway. In the theory of the cooperative JT effect, this important advantage of the OOA allows to proceed farther than

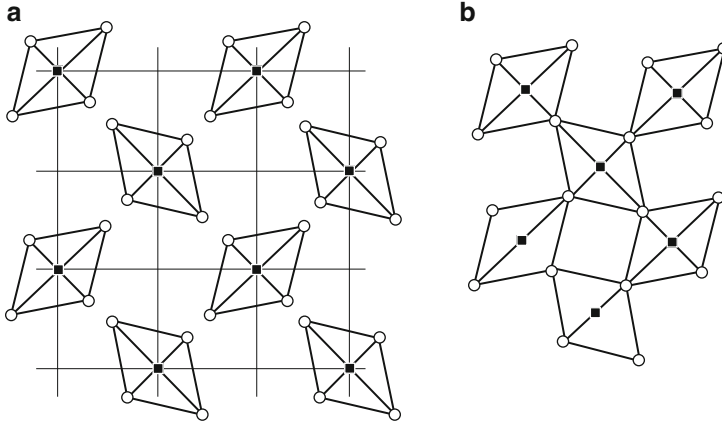


**Fig. 5** Antiferrodistortive ordering of tetragonal elementary cells with rhombic JT instability of  $E \otimes b_{1g}$  type ( $z$  axis view of the  $xy$  plane). **(a)** The case when elementary cells do not share common atoms. **(b)** Same when elementary cells share common vertices. (From [16, 17])

is usually done in the traditional approach. In addition to orbital exchange, it makes possible including the intersite electron hopping (Sect. 4.1), intersite magnetic exchange coupling of real spins (Sect. 4.2), on-site Hund exchange, etc.

The above-listed steps of the OOA represent an approximation and, therefore, in some respect are misleading (see the discussion in Sect. 5.1). However, formally, the same sequence of steps can be applied to any JT case. This is an attractive advantage of the OOA. As another example, consider a cubic crystal with JT instability  $E \otimes e$  described by the JT Hamiltonian (3). Similarly to (11)–(16), we come to the decoupled Hamiltonian (14) with

$$H_{el} = - \sum_{i,j} \sum_{\gamma,\lambda} J_{\gamma\lambda} (i-j) \sigma_{\gamma}(i) \sigma_{\lambda}(j), \quad \gamma, \lambda = x, z \quad (17)$$

and

$$J_{\gamma\lambda} (i-j) = \frac{1}{2} V^2 \langle i, \gamma | \mathbf{K}^{-1} | j, \lambda \rangle. \quad (18)$$

Here  $\mathbf{K}^{-1}$  is inverse of the respective dynamical matrix. In (17) it describes elastic coupling of tetragonal distortions,  $Q_{\theta}(n)$  and  $Q_{\varepsilon}(n)$ , the ones active in the JT case  $E \otimes e$ . Obviously, the only important contribution comes from the orbital exchange of close neighbors. In cubic symmetry, (17) simplifies to

$$H_{el} = -J \sum_{\langle i,j \rangle} [\sigma_x(i) \sigma_x(j) + \sigma_z(i) \sigma_z(j)]. \quad (19)$$

As in (15),  $\langle i, j \rangle$  means summation over next neighbors only.

### 3.2 Basic Assumptions of the Orbital Ordering Approach

The electron Hamiltonian (17) represents the essence of the OOA. Qualitatively, one can interpret it in the following way. Considered separately from other elementary cells, one-cell degenerate electron states have the well-known phase uncertainty. Any orthogonal linear form of degenerate wave functions has the same energy. Therefore, degenerate orbitals are free to rotate about the JT center. Without the exchange coupling (17), there is an *orientation orbital disorder*. If, as in (17), pseudo spins are coupled to one another, they tend to order into a low-symmetry pattern, “ferromagnetic”, “antiferromagnetic”, or a more complex pattern, bringing the free energy of the system to a minimum. This is what we call the *orbital ordering*.

As it follows from (12), ground-state averages of orbital pseudo spin operators determine the numeric values of  $\overline{Q}(i)$  and, thereby, the respective symmetry-adapted distortion of every elementary cell of the crystal. Instead of “ferromagnetic”, “antiferromagnetic”, etc., the appropriate name to use is “ferrodistortive”, “antiferrodistortive”, etc.

Now we can formulate basic assumptions of the OOA. Although in some papers, their authors mean to include underlying effects (JT distortions, temperature sequence of phase transitions, etc.), the following list represents what is actually done in a large number of papers applying the OOA to particular crystals.

1. The Hamiltonian (17) includes order parameters with the position numbers  $i$  and  $j$  of just the JT sites. Considering a transition metal compound, they determine position of transition metal atoms, a regular component of the respective crystal lattice. Ligand sites are missing in (17). Therefore, instead of a real crystal, the OOA considers its simplified version, the sublattice of JT active sites. *Explicitly, ligands are omitted.* (Fig. 6b); implicitly, metal-to-ligand chemical bonding is hidden in the respective parameters,  $J_{ij}$ , of orbital exchange.
2. Usually, in a transition-metal compound, metal atoms are located at sites of the respective primitive lattice. As the basis of all other atoms is omitted, *the only ones left are crystal symmetry axes of the primitive lattice.* They determine directions for possible low-symmetry ordering patterns.
3. Parameters (18) include vibronic coupling constant,  $V$ , and phonon band-structure factors,  $\langle i, \gamma | \mathbf{K}^{-1} | j, \lambda \rangle$ . For a particular crystal, finding these factors is a laborious problem of crystal lattice dynamics. Instead, in the OOA,  $J_{ij}$  are used as free parameters of the theory. Still consistent with the fundamental theory of the JT effect, in this form the OOA is not directly derived from the theory. In other words, in the theory of cooperative JT effect, the OOA is a *phenomenological approach*.
4. The OOA is not designed for and cannot consider temperature dependence of any observable of the bulk crystal. The main goal of the OOA is determining the low-temperature (0 K) symmetry pattern of the orbitally ordered ground state.

The Hamiltonian of orbital exchange, (15), or (17), is invariant of the respective symmetry group of the undistorted crystal in its high-symmetry phase. Similarly to

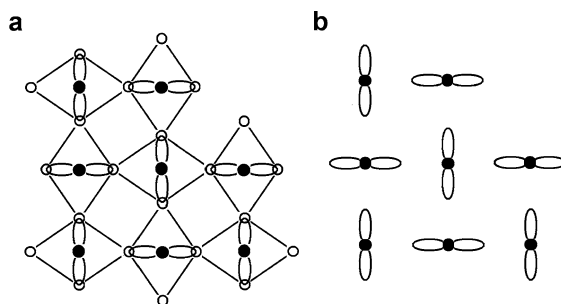


**Fig. 6** Antiferrodistortive order of tetragonal elementary cells with rhombic JT instability of the  $E \otimes b_{1g}$  type (similar to Fig. 3b). **(a)** In the traditional approach, ligands are explicitly included. Orientation of central-atom orbitals is determined by formation of chemical bonds with nearest-neighbor ligands. **(b)** In the OOA ligands are omitted. Central-atom orbitals point toward next-neighbor sites

what we usually do in EPR to derive the effective Hamiltonian, one can present (17) as a finite sum of scalar convolutions of the respective pseudo-spin orbital operators. In the case of a twofold degenerate ground term (the  $E$ -term case), these are Pauli matrices,  $\sigma_x$ ,  $\sigma_y$ , and  $\sigma_z$ . In the case of a threefold degenerate ground term (the  $T$ -term case), they are  $3 \times 3$  orbital matrices,  $L_x$ ,  $L_y$ , and  $L_z$ , or pseudo-spin matrices of higher dimension if local symmetry is icosahedral, as in the case of fullerides. In the OOA, coefficients of different scalar convolutions, the respective reduced matrix elements, are free parameters of the theory. In the form of a trial-and-error numeric experimentation, assuming a particular type of ordering, varying these parameters within a reasonable range of numeric values, and comparing total energy of the crystal, it is possible to derive some conclusions about existence and stability of different orbital-ordered patterns. At the same time, one has to keep in mind that the OOA is an approximation. It has its range of applicability and has to be applied cautiously (Sect. 5).

An interesting example is  $\text{KCuF}_3$ , a pseudo-cubic perovskite crystal. Its parent crystal lattice,  $\text{KZnF}_3$ , is cubic with metal-ligand octahedrons  $[\text{ZnF}_6]^{4-}$  sharing common vertices (Fig. 7). In high-symmetry lattice, local symmetry group is  $O_h$ . In the case of  $[\text{CuF}_6]^{4-}$ , its electron configuration is  $e_g^3(3d^9)$  with the ground-state electron term  ${}^2E_g$ , a JT doublet. Above  $T \approx 800$  K, the crystal lattice of  $\text{KCuF}_3$  is cubic. Due to the JT instability, at  $T \approx 800$  K,  $\text{KCuF}_3$  undergoes a structural phase transition to a low-symmetry phase reducing its local symmetry to  $D_{4h}$ . The cubic degeneracy of the highest occupied electron orbital  $e_g$  is lifted by the spontaneous JT distortions,  $Q_\theta$  and  $Q_\epsilon$ , (Fig. 3b and c). Octahedrons  $[\text{CuF}_6]^{4-}$  elongate along two of the three fourfold symmetry axes. At room temperature, two different polytypes have been identified experimentally, which differ in their atomic-plane stacking along the  $c$  axis, ferro- and antiferrodistortive (Fig. 8).

Assuming different orbital-ordering patterns, varying the parameter  $J$  of the orbital exchange in (17) within a reasonable range of numeric values, and comparing total energy of the crystal, Kugel and Khomskii [19] found two energy-equivalent





**Fig. 7** Cubic perovskite crystal structure of high-symmetry parent compound  $\text{KZnF}_3$ . Large spheres are cations,  $\text{K}^+$ , medium-size dark spheres are anions,  $\text{F}^-$ , and small black spheres are metal ions,  $\text{Zn}^{2+}$ . Metal-ligand octahedra share common vertices. (From [18])

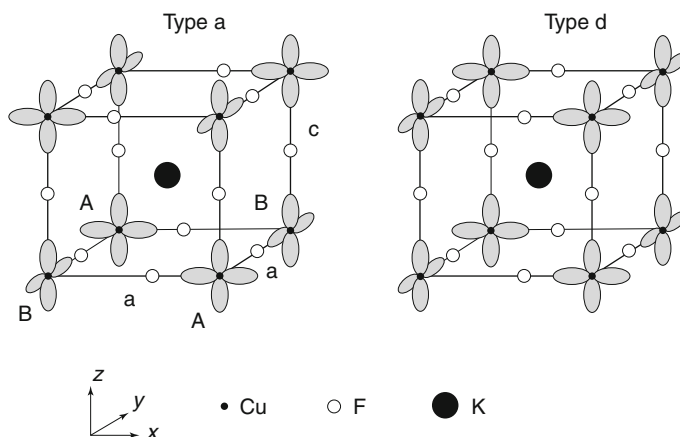


**Fig. 8** Orbital ordering in pseudo-cubic perovskite  $\text{KCuF}_3$  with vertex-sharing octahedrons  $[\text{CuF}_6]^{4-}$ . “Type a” is layer-antiferrodistortive and Type d is layer-ferrodistortive pattern. (After Kugel and Khomskii [19], Reinen and Friebe [16], and Binggeli and Altarelli [20])

types of orbital ordering shown in Fig. 8. Although, in their work, ligands were omitted from consideration, after the electron ordering pattern was established, Kugel and Khomskii [19] determined the respective distortion of the fluorine sublattice. From the two electron ordering patterns, in accordance with (12), they found the two types of crystal lattice distortion, ferro- and antiferrodistortive, same as in Fig. 8. Following the same route of reasoning but in the opposite direction, from distortions to orbital ordering, based on their EPR and X-ray data, Reinen and Friebe [16] deduced the same two ordering patterns in  $\text{KCuF}_3$ . Without separating out the electron orbital system, in the so-called cluster model for the octahedron  $[\text{CuF}_6]^{4-}$ , the

molecular JT instability was considered by Shashkin and Goddard [21]. In its various modifications, the OOA was applied to this case several times (e.g., see [22]). With crystal lattice geometry optimization, based on the *ab initio*  $LDA + U$  electronic structure calculations for  $KCuF_3$ , the cooperative JT effect was considered by Bingeli and Altarelli [20]. In the traditional approach, the cooperative JT effect in  $KCuF_3$ , gives both at once, the two types of distortion of the fluorine sublattice and the accompanying orbital ordering pattern [23].

In the OOA, for the orbital ordering phase transition in  $KCuF_3$ , the highest theoretical temperature is about 350 K [24], more than twice below the measured one of about 800 K. Attempts to bring the OOA-predicted temperature of orbital ordering closer to the experimental value require nonrealistically high values of the parameters of orbital exchange [20, 24, 25]. This is due to the way the OOA is set up. The effective Hamiltonian of the OOA does not include vibrational degrees of freedom. Vibrations of fluorine octahedrons are averaged out with undistorted wave functions. This presumes high symmetry of the fluorine octahedrons and frozen nature of the parameters of orbital exchange coupling.

At the same time, based on simple physical reasons, it is pretty obvious that these parameters are strongly affected by position of bridge ligands. In a better version of the theory, parameters of orbital exchange coupling and, correspondingly, electron wave functions (eigenfunctions of the effective Hamiltonian of the OOA) should depend on nuclear displacements. In the Hamiltonian, one can expand these dependencies up to linear or second-order terms. Then crystal lattice vibrations would not separate from electrons any longer. It would become necessary to solve the vibrational part of the Hamiltonian simultaneously with the orbital electron part. In this way we return back to the traditional approach in the cooperative JT effect and all the advantage of the OOA is lost. Bottom line of this discussion, this is an intrinsic weakness of the OOA. In this respect, there is nothing one can do to improve the OOA to make its predictions more accurate.

Most discouraging is the discrepancy in temperatures of the two phase transitions, structural (JT) and magnetic. According to the OOA, temperature of both transitions should be of the same order, relatively close. However, even in  $KCuF_3$ , a good case for the OOA, experimental Néel temperature, 38 K for polytype *a* and 22 K for the polytype *b*, is more than 20 times lower than the temperature of the structural phase transition, 800 K. In resonant elastic X-ray scattering, the resonant signal is dominated by the JT distortion of fluorine octahedrons. As one should expect, orbital ordering of Cu-3*d* orbitals is saturated already at vanishing JT distortions [20]. At the same time, a change in the magnetic structure has a small influence on the JT distortion. This brings us to conclusion that magnetic properties of  $KCuF_3$  cannot be adequately explained just in the framework of the OOA, without including some other low-symmetry distortions of the crystal lattice frame [24].

The dramatic difference of the experimental temperature gap of structural and magnetic phase transitions as compared to (almost) no-difference OOA-predicted ones is a clear indication of overestimating magnetic coupling in the OOA (Sect. 4.2). Physical reasons of this discrepancy are quite obvious. JT distortion is *not a secondary effect* that follows the orbital ordering. Quite opposite, being an

order of magnitude stronger (Sect. 5.1), the JT coupling determines the symmetry-breaking distortion of the crystal lattice. Therefore, in transition metal compounds, at the temperature of JT (structural) phase transition, effects of magnetic exchange coupling can be simply ignored. Being an order of magnitude weaker than the JT coupling, the respective intersite magnetic coupling has to be included *after* the strong JT coupling lifts the orbital degeneracy in elementary cells. In the low-temperature distorted phase, ground state of elementary cells is an orbital singlet populated by one electron. In this case, as a rule, the magnetic coupling is dominated by simple Heisenberg exchange. The respective magnetic phase transition takes place at a much lower Curie/Néel temperature.

## 4 Extension and Expansion of the Orbital Ordering Approach

Most attractive advantage of the OOA is its relative simplicity and clear physical meaning. As mentioned above, the OOA reduces the manifold of wave functions to a finite number of degenerate electron states. Sometimes, the OOA displays physical content of the theory more explicitly than the first-principle based traditional approach. Thanks to its relative simplicity, the OOA allows to proceed a little farther. It provides an insight into intimate mechanisms of some interesting phenomena closely related to the cooperative JT effect such as electron hopping, magnetic coupling of real spins, phase separation [26–31], charge ordering [29], formation and structure of magnetic polarons [32, 33], formation of superstructures in doped JT crystals [34], to mention just some of them. All these applications can be considered in terms of the traditional theory as well. In what follows, we will briefly consider just two of them, intersite electron hopping (Sect. 4.1) and intersite magnetic exchange coupling of real spins (Sect. 4.2).

### 4.1 *Effects of Intersite Electron Hopping*

In each elementary cell of a JT crystal, ground-state orbital,  $\psi_{\Gamma\gamma}(n)$ , is degenerate. This means it is partly populated by electrons. Therefore, at each metal site, there is room to accept additional electrons, one at least. In other words, in high-symmetry phase, when the intersite electron orbital overlap is included, JT crystals can be treated as conductors. At the same time, most of these crystals (transition metal oxides, fluorides, etc.) are well-known insulators. This dramatic difference in their conductive properties has two reasons related to two determining effects. One is due to relatively low temperatures of observation. In a great majority of these compounds, temperature of the JT structural phase transition is way above room temperature. Therefore, at normal conditions (room temperature), such a JT crystal is in its low-symmetry phase. According to JT theorem, electron degeneracy is

lifted, and the orbital “room” for the traveling electron is reduced to just one singlet state per site.

Still, there is opposite-spin state left at each site. Hopping to one of the next-neighbor sites requires a spin flip. Therefore, metal-insulator transitions involve intersite magnetic exchange coupling. This is the second effect directly or indirectly involved in conductive properties of these crystals. Magnetic effects are briefly discussed in Sect. 4.2.

In this section, following Efremov, Sboychakov, and Khomskii [35], we consider an important example of electron bands in orbitally ordered  $\text{LaMnO}_3$ . It belongs to the family of layered perovskites, interesting from both experimental and theoretical point of view. In this compound, in its high-symmetry phase, the octahedron  $[\text{MnO}_6]^{4-}$  has ground-state high-spin configuration  $t_{2g}^3 e_g$ , and its respective ground-state term is  ${}^5E_g$ , a JT-active orbital doublet.

Let  $c_\gamma(n)$  be the operator that annihilates an electron in the orbital state  $3d_\gamma$  at  $n$ th metal site. The ground-state energy level broadens into an energy band. The bandwidth is proportional to the effective “overlap” integral,

$$t_{mn}(\gamma, \lambda) = \langle d_\gamma(m) | d_\lambda(n) \rangle = t_{mn}(\gamma, \lambda) \langle 0 | c_\gamma^\dagger(m) c_\lambda(n) | 0 \rangle. \quad (20)$$

Actual meaning of the “overlap” parameter (20) is revealed in the first-principles consideration [36] by including hidden effects of metal-to-ligand-to-metal hopping.

Evidently enough, next-site “overlaps” only make sense. The JT-coupling matrices can be presented in terms of  $c_\gamma(n)$  and  $c_\gamma^\dagger(n)$  as well. For example, for the Pauli matrix  $\sigma_z(n)$  we have:  $\sigma_z(n) = c_\theta^\dagger(n) c_\theta(n) - c_\theta^\dagger(n) c_\theta(n)$ . Due to the high symmetry of the layered perovskite  $\text{LaMnO}_3$ , the hopping parameters are interrelated. In this case, next-neighbor overlap only makes sense. Therefore, of the twelve parameters (20), just one parameter,

$$t = [\langle \psi_\theta(m) | \psi_\theta(n) \rangle + \langle \psi_\epsilon(m) | \psi_\epsilon(n) \rangle], \quad (21)$$

is large enough to be included. The respective term in the Hamiltonian, the one describing the intercenter electron hopping, is

$$H_{\text{hopp}} = t \sum_{\langle m, n \rangle} [c_\theta^\dagger(m) c_\theta(n) + c_\epsilon^\dagger(m) c_\epsilon(n)]. \quad (22)$$

Here  $\langle m, n \rangle$  means summation over next neighbors only. Assuming infinite on-site Hund energy, including hopping and intersite double exchange coupling, we come to the following Hamiltonian [35]:

$$H = t \sum_{\langle m, n \rangle} [c_\theta^\dagger(m) c_\theta(n) + c_\epsilon^\dagger(m) c_\epsilon(n)] + J \sum_{\langle m, n \rangle} \mathbf{S}_m \mathbf{S}_n. \quad (23)$$

At this point, considering the  $A$  type structure of  $\text{LaMnO}_3$  (ferromagnetic planes stacked antiferromagnetically), we can limit consideration with just one layer, the square-planar system  $[\text{MnO}_2]$ . In this case, in (23), the summation is in two dimensions.

With the Fourier transforms,

$$\begin{aligned} a_1(\mathbf{p}) &= \sum_m e^{-i\mathbf{p}\mathbf{R}_m} [\alpha_{\mathbf{p}} c_{\epsilon}(m) + \beta_{\mathbf{p}} c_{\theta}(m)], \\ a_2(\mathbf{p}) &= \sum_m e^{-i\mathbf{p}\mathbf{R}_m} [-\beta_{\mathbf{p}} c_{\epsilon}(m) + \alpha_{\mathbf{p}} c_{\theta}(m)], \end{aligned} \quad (24)$$

the Hamiltonian (23) transforms to a diagonal form. Originating from the  $e_g$  orbitals,  $\theta = |3z^2 - r^2\rangle$  and  $\epsilon = |x^2 - y^2\rangle$ , its eigenvalues form the following two electron bands [35]:

$$\epsilon_{1,2}(\mathbf{p}) = -t \left( \cos p_x + \cos p_y \pm \sqrt{\cos^2 p_x + \cos^2 p_y - \cos p_x \cos p_y} \right). \quad (25)$$

For the doped crystal,  $\text{La}_{1-x}\text{Ca}_x\text{MnO}_3$ , the number of electrons,  $n = x - 1$ , in these two bands depends on doping  $x$  and can be gradually changed.

It is interesting to follow evolution of the Fermi surface with doping. Actually, in this two-dimensional case, the Fermi “surface” is just a boundary curve separating electron-populated parts of the energy band from the unpopulated ones (Fig. 9). At small concentration, electrons fill the bottom of the lower energy band,  $\epsilon_1(\mathbf{p})$ , well separated from the upper band,  $\epsilon_2(\mathbf{p})$ . The filling starts at the center of the Brillouin zone, close to its  $\Gamma$  point at the center, where the wave function is dominated by  $|x^2 - y^2\rangle$  states (Fig. 9a). At some points of the Brillouin zone, the two energy bands have equal energy. This is the so-called “nesting”. When the Fermi “surface” reaches the nesting points, at  $n \approx 0.54$ , filling of the second band begins. This creates an island (a pocket) at the center of the Brillouin zone (Fig. 9d).

At complete filling,  $n = 1$ , in the case of undoped  $\text{LaMnO}_3$ , the Fermi “surfaces” become straight lines, “flat”. Also, at  $n = 1$ , there is a perfect nesting. The energies of two bands coincide,  $\epsilon_1(\mathbf{p} + \mathbf{Q}) = \epsilon_2(\mathbf{p})$ , with a shift by the wave vector  $\mathbf{Q} = \langle \pi, \pi \rangle$ . In three dimensions (3D), for the ferromagnetic case, a similar nesting takes place with the 3D-vector,  $\mathbf{Q} = \langle \pi, \pi, \pi \rangle$ .

To explore the possibility of pairing, in particular, forming excitons, Efremov and Khomskii [35] extended the band description of conductive manganites,  $\text{A}_{1-x}\text{B}_x\text{MnO}_3$  with  $\text{A} = \text{La, Pr, Nd, etc.}$  and  $\text{B} = \text{Ca, Sr}$ . Instead of proceeding farther in this interesting direction, we will discuss some concerns regarding the abovementioned energy bands.

The basic assumption of the OOA is limiting the consideration with transition metal sites. Ligands are omitted. In the Hamiltonian (23), the only routs for electron transfer are the ones with direct hopping from one metal site to another, one of the close neighbors in the lattice. In real manganites, this distance is of the order of 2.8 Å. A detailed analysis of the wave functions (24) (by returning back

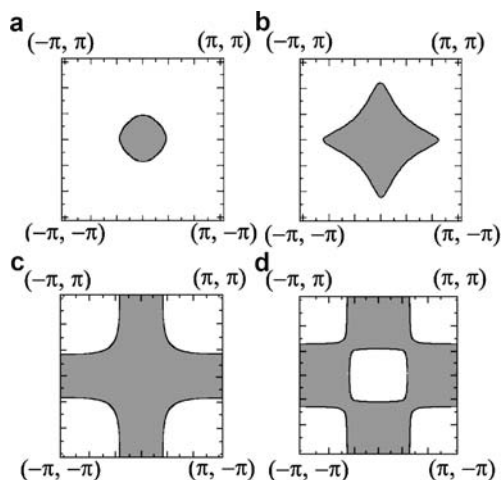


**Fig. 9** Evolution of the Fermi “surface” in the two-dimensional energy band with doping (after (Efremov and Khomskii [35])). (a) At small concentration of electrons, the central part of the lower energy band is filled. (b) At higher concentration of electrons, the filled part of the energy band reflects its tetragonal symmetry. (c) At a higher concentration of dopants, the lower energy band is almost completely filled with an exception of four pockets. (d) At  $x \approx 0.54$ , due to nesting, filling of the upper energy band begins. This creates the fifth pocket at the center of the Brillouin zone

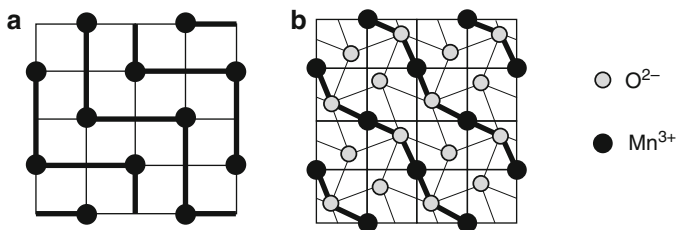


**Fig. 10** Routes of conductivity in  $\text{La}_{1-x}\text{Ca}_x\text{MnO}_3$  (highlighted). (a) In the OOA, ligands are omitted. Electron hopping is in the directions of the primitive lattice, from one metal site to another, about 4 Å away. (b) Same square planar crystal lattice with ligands explicitly shown. Routes of electron transfer include ligands, about 1.5 Å away from metal sites

to coordinate representation) reveals even a longer distance of about 4 Å. In this model, possible routes of electron conductivity are shown in Fig. 10a. For an electron jump, 4-Å distance seems to be too long to be true.

More realistic routes must include participation of ligands, oxygen atoms in this case. They are true mediators in the electron intersite transfer (Fig. 10b). It must follow regions of high electron density determined by metal-ligand chemical bonds. The latter was examined by resonant X-ray diffraction combined with XANES at the Mn K-edge of  $\text{La}_{0.5}\text{Ca}_{0.5}\text{MnO}_3$  and  $\text{Pr}_{0.6}\text{Ca}_{0.4}\text{MnO}_3$  [37]. The observed pattern of atom displacements suggests trapping of electrons between pairs of Mn sites,

involving bridge oxygen atom. Combined with local distortions, it forms a polaron-like vibronic state. Daoud-Aladine interpreted this state as a Zener polaron [37].

Correspondingly, possible routs of electron conductivity must be along bent oxygen bridges. According to the abovementioned results, they are along diagonals in the equatorial plane of manganese-oxygen octahedrons (Fig. 10b). For electron hopping in this case, the respective distance is the length of the metal-ligand bond, about 1.4 Å. This is about three times shorter than the one obtained by Efremov and Khomskii [35].

For the system of pseudo spins, low-lying elementary excitations are described in terms of the so-called *orbitons*, similar to magnons in ferromagnets [38]. Fermions in their nature, at zero temperature orbitons are believed to form the so-called *orbital liquid*. Though this formal analogy is quite obvious, the new term, *orbital*, is misleading. First, the ground state of a JT center is not just an orbital pseudo spin. The electron pseudo spin is coated with phonons [39,40]. The stronger the JT coupling, the thicker is the coat. The respective ground state is essentially vibronic. Therefore, propagating in JT crystal, the elementary excitation is not an “orbital” but a low-symmetry JT *polaron* (Zener polaron) or, shorter, a *vibron*. Also, if and when spin-orbital coupling is active and included, bounded to JT polarons are magnons, the real spin-wave excitations. Participating in coating, they no longer exist as a separate branches of elementary excitations. This may be the reason why no changes due to magnetic ordering were detected in excitation spectra of  $\text{LaMnO}_3$ ,  $\text{KCuF}_3$  and  $\text{YTiO}_3$  [41,42].

With phonon coating, JT polarons are substantially heavier in their effective mass than the orbitons or magnons. All these important details bring new physics in the theory of JT crystals. In particular, trapped as heavy JT polarons, electric charge carriers in JT crystals have low mobility and manifest the tendency for a metal-insulator transition, alternative to the Mott-Hubbard model [43]. In the ferromagnetic phase, the carriers are still mobile, but strongly scattered due to fluctuating JT distortions yielding a poor metal. The transition from a paramagnetic to ferromagnetic phase is believed to be the reason of the “colossal” magneto resistance [44]. (This issue is widely discussed in physics of highly-correlated crystals. It cumulated a broad range of different approaches. There is not enough room here for going into details of this interesting topic.)

Second, without ligands, disregarded in the OOA, for traveling elementary excitations, the only possible routs include direct hopping from one metal site to next neighboring another one. At the same time, quite evidently, the hopping is via ligands. If, as in  $\text{KCuF}_3$ , the participating ligand is collinear with the two metal sites, including ligands does not change the direction of hopping. However, in some cases, as, say, in layered perovskite  $\text{LaMnO}_3$  or in hexagonal perovskite  $\text{CsCuF}_3$ , ligands do not lie on the same line with metal atoms. Compared to predictions of the OOA for the respective traveling pseudo spin waves, actual wave functions are substantially different. With this in mind, the electron density described by wave functions (23) does not seem to be correct. Then the respective eigenvalues, the energy bands (25), are not reliable enough. There is not much reason left to trust the energy spectrum of elementary excitations predicted by the OOA.

In energy spectrum, the strongly damped pseudo orbital excitations (orbitons) merge into a common continuum with vibronic and magnetic excitations [41]. Going up in energy, above the ground-state energy, we find a narrow energy gap,  $\lesssim 20 \text{ cm}^{-1}$ , between one-site ground-state (pseudo spin) energy level and the part of the continuous energy spectrum where excited vibronic states begin to have a significant density. This gap is due to a relatively small contribution of long-wave acoustic phonons and magnons in local JT effect. In the system of pseudo spins, for a realistic representation of elementary excitations, the only part of energy spectrum to get them right is this one, “empty” of other elementary excitations. In particular, in terms of energy, the pseudo spin wave must be way below the tunneling splitting energy gap. At intermediate-to-strong JT coupling, the latter one may be of the order of several wave numbers. In general, excited vibronic states are beyond the general setup of the OOA. At any nonzero temperature, in the OOA, elementary excitations manifest instability of any long-range spin order [45], 46].

Included in the effective Hamiltonian of the OOA, electron-hopping terms (22) provide an additional flexibility for electron wave functions to redistribute along intersite “bonds” (Fig. 11a). Such a “bond-centered” electron distribution can break the inversion symmetry and generates hopes for combining magnetism with ferroelectricity [10, 35, 47–50], an interesting and promising issue. This new class of materials would provide a possible switch of magnetic memory cells with electric field.

Without going into details of different approaches to ferroelectricity, here we highlight the important results. The effect of spontaneous polarization is a structural phase transition when local odd-parity distortions order in a ferroelectric pattern.

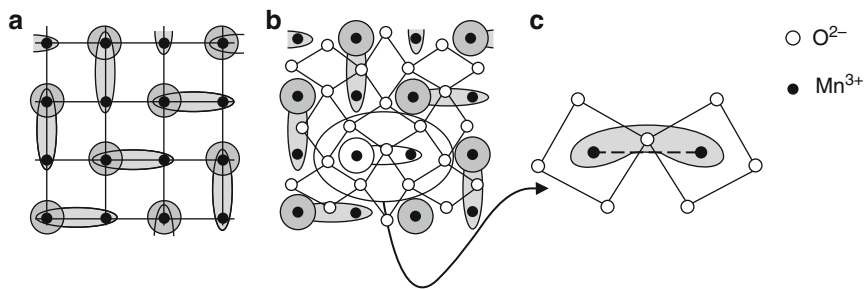


**Fig. 11** “Bond-centered” charge ordering in layered perovskite  $\text{Pr}_{0.60}\text{Ca}_{0.40}\text{MnO}_3$ . One layer,  $\text{MnO}_2$ , is shown. (a) In the OOA, ligands (oxygen atoms) are omitted. Electron density is partly delocalized spreading over “bonds”  $\text{Mn}^{3+} - \text{Mn}^{3+}$  along axes of the primitive lattice (after Efremov et al. [47, 48]). (b) Same with oxygen atoms shown explicitly. The effective bonds  $\text{Mn}^{3+} - \text{Mn}^{3+}$  point slightly off the target. Direction of real chemical bonds  $\text{Mn}^{3+} - \text{O}^{2-}$  is not the same as the directions of the primitive lattice. (c) Actual distribution of electron density includes bridge oxygen atoms (shaded, after Daoud-Aladine et al. [37]). Broken line shows direction of the effective bond metal-to-metal in the OOA



The well-known Landau-Ginsburg-Cochran-Anderson theory is a phenomenological approach. Of the first-principle theories, just one, the vibronic theory of ferroelectricity (e.g., see [1,51]), is consistently based upon electronic structure and chemical nature of the respective compounds.

As in other cases of vibronic coupling, in ferroelectric crystals, the electric polarization is due to a structural instability of elementary cells with respect to dipole-active displacements of the molecular skeleton. Usually, these are off-center displacements of the metal atom from its site. Similar to the JT effect, the driving mechanism is strengthening metal-ligand chemical bonds with the low-symmetry distortions. Admixed with these distortions, the active electron states are not necessarily degenerate. This is the only difference from the cooperative JT effect. The energy gap separating the admixed electron states can be quite large. However, the respective vibronic coupling provides even stronger stabilization energy. Therefore, in the vibronic theory, ferroelectricity is a particular case of the more general cooperative *pseudo* JT effect.

In the OOA, as it was discussed above, ligands are omitted. The vibrational motion of low-symmetry distortions is averaged out. Electron wave functions do not follow nuclear displacements. Therefore, in the OOA, the abovementioned crystal-lattice mechanism of spontaneous polarization is lost. The only possibility left in the OOA is polarization of electron wave functions. Without lattice distortion involved, this pure electron-shell mechanism was discussed in literature long ago, back about 45 years. Lacking supporting evidence from experimental data and electron-structure evaluation, it was rejected. On the contrary, the vibronic theory of ferroelectricity cumulated overwhelming experimental evidence. (For an updated review, see Sect. 8.3 in Bersuker's book [1].)

In its treatment of ferroelectricity, the OOA introduces inaccuracies and may bring to wrong conclusions. One example is shown in Fig. 11. Applied to layered perovskite  $\text{Pr}_{0.60}\text{Ca}_{0.40}\text{MnO}_3$ , the OOA gives a “bond-centered” electron density distribution. The “bonds” are directed along axes of the primitive crystal lattice, from one metal site to another, over the distance of about 4 Å (Fig. 11a). As every chemist knows, there are no true metal-to-metal  $3d - 3d$  bonds that extend over a distance of 4 Å.

One can argue that these are “effective” bonds. Real bonds include mediating participation of ligands implicitly included in the OOA. However, there is an additional difficulty in this picture. The “bond-centered” distribution of electron density points slightly off the target, over the empty space between ligands. This can be seen in Fig. 11b and c, where oxygen bridge atoms are shown explicitly. Evidently, the bond-centered distribution of electron density must point the directions of real chemical bonds, from metal atoms to ligands. This idea is supported by resonant X-ray diffraction combined with XANES at the Mn K-edge of  $\text{La}_{0.5}\text{Ca}_{0.5}\text{MnO}_3$  and  $\text{Pr}_{0.6}\text{Ca}_{0.4}\text{MnO}_3$  [37]. Shown in Fig. 11c, true electron density is distributed over oxygen bridges, covers 2-Å long metal-to ligand chemical bonds, and does not manifest breaking of the inversion symmetry.

## 4.2 Magnetic Exchange of Orbital-Degenerate Centers

The greatest advantage of the OOA is its combined description of orbital and magnetic ordering patterns. In this case, besides orbital pseudo spin system and nuclear distortions (phonons), we include real spins, the third participant in the nontrivial coupling.

In magnetic materials, even without orbital ordering, the problem of magnetic ordering is complex enough and represents a huge trend in solid state physics. In the system of real spins, ordering patterns are determined by different contributions in magnetic exchange coupling, from simple Heisenberg type of coupling to Kramers-Anderson superexchange, double exchange, etc.

For the effects of possible interplay of magnetic exchange with the orbital exchange coupling, the general review is provided by Kugel and Khomskii [9]. In JT crystals, all relevant interactions are pair-wise type. Therefore, the microscopic theory of magnetic anisotropy can be borrowed from the theory of magnetic exchange in binuclear metal clusters. A rigorous theory of magnetic anisotropy for orbitally degenerate binuclear metal clusters can be found in [52–54]. A comprehensive review of the JT effect in molecular magnetism is given by Tsukerblat et al. [55].

Here we just comment on the most important sides of this theory. For the interplay of magnetic and orbital ordering, the key effect is spin-orbital interaction. When it is weak or even zero, the system of real spins orders independently from the orbital system of pseudo spins. Usually, without the spin-orbital coupling, the dominating mechanism of magnetic ordering is the isotropic Heisenberg exchange. With the *intra*-site spin-orbital coupling included, the *intersite* exchange coupling in the two systems, orbital and magnetic, is no longer independent. Coupled to the orbital system, magnetic ordering is no longer isotropic. Energetically favorable direction of ordering, the so-called easy axis, is determined by the relative strength of the two ordering patterns or, in terms of quantum mechanics, by the relative energy gaps in the energy spectrum of the two systems.

If real-spin magnetic gaps are larger (as, say, in rare earth compounds), the real-spin order determines the easy axis and dominates over the orbital ordering pattern. In the opposite case of larger orbital energy gaps (as in transition metal compounds), the easy axis is determined by the pseudo spin system, and magnetic order follows the orbital pattern.

An interesting example of this type is spin-canted zigzag-chain compound  $[\text{Co}(\text{H}_2\text{L})(\text{H}_2\text{O})]_\infty$  with  $\text{L} = 4 - \text{Me} - \text{C}_6\text{H}_4 - \text{CH}_2\text{N}(\text{CH}_2\text{PO}_3\text{H}_2)_2$  (see [56]). It includes Co(II) ions in octahedral coordination with one nitrogen and five oxygen ligands. The respective crystal field includes a strong tetragonal component. Neighboring octahedrons  $[\text{Co}(\text{II})\text{O}_5\text{N}]$  share one oxygen and, also, have a  $\text{CPO}_3$  bridge connecting two other equatorial oxygen atoms. In each Co(II) octahedron, due to a strong spin-orbital coupling, the easy axis is tilted to the common oxygen atom. The tilting of the anisotropy axes gives rise to spin canting and, consequently, to a nonvanishing magnetization for this compound.

One can imagine other cases, when the two kinds of exchange coupling are of the same order of magnitude. Also, sometimes crystal field effect can be of the

same order or even less than the spin-orbital splitting. In these cases, more complex ordering patterns are possible. In particular, one can find canted magnetic orders or even frustrated arrangements of real and pseudo spins.

It is interesting to follow the role of the JT effect in this picture. Dressed with phonons, orbital states transform into the so-called JT polaron states. The orbital pseudo spin becomes vibronic pseudo spin (a detailed discussion of this side of the story is given below in Sects. 5.2 and 5.3). Instead of free rotations of the *orbital* pseudo spin we come to hindered rotations of the *vibronic* pseudo spin. At each metal site, the equipotential continuum of different orientations of the orbital spin is transformed into alternating bumps and wells of the vibronic pseudo spin. The latter ones correspond to favorable directions of the vibronic pseudo spin along metal-ligand chemical bonds.

In the limiting case of very strong JT coupling, the JT polaron becomes so heavy that no orientation dynamics is possible. Instead, we come to static orientation of the vibronic pseudo spin towards one of several equivalent directions to ligands. According to the JT theorem, the respective electron ground state is an orbital singlet. In this case, orbital motion is completely quenched (the respective vibronic reduction factor is zero), and real spins are released from their dependence upon orbital motion. For magnetic ordering with no spin-orbital coupling, in singlet orbital ground state, the dominating mechanism is the abovementioned Heisenberg exchange coupling.

This physical picture brings us to the following two important conclusions. First, with the spin-orbital coupling included, ligands play an important role in establishing the easy axis. In the OOA, ligands are omitted from consideration. However, some crystal symmetry imprint is still there in the effective Hamiltonian of the OOA. It keeps the symmetry of the primitive lattice of metal sites. If the metal-ligand bridges are collinear with the directions of the primitive lattice, the OOA can provide a realistic magnetic ordering pattern. If, however, the metal-ligand bridges are bent (as, say, in the hexagonal perovskite  $\text{CsCuCl}_3$  or in the layered perovskite  $\text{LaMnO}_3$ ), the easy axis may point in a direction different from the directions of the primitive crystal lattice. In these cases, the OOA can result in a wrong ordering pattern.

Second conclusion considers the strength of the JT coupling. To observe the interesting interplay of the orbital ordering pattern with the magnetic ordering, the JT coupling should be of weak-to-intermediate strength. At strong coupling, the orbital motion is diminished by the respective vibronic reduction factor. In this case, there is nothing left but the simple Heisenberg exchange coupling.

## 5 When the Orbital Ordering Approach is Correct and When it Can Go Wrong

In the OOA, one of its basic assumptions is reducing the intercell correlation to symmetry equivalent intersite orbital exchange coupling. This assumption simplifies the physical picture of the cooperative JT effect. Ligands and all the respective

implications of the intra cell metal-ligand chemical bonding are omitted. Most important effect is the directional ordering of the on-site degenerate orbitals. Crystal lattice is believed to adjust to the symmetry-breaking orbital ordered pattern.

For relatively simple crystal structures, as  $\text{KCuF}_3$  (Sect. 3.2), the OOA provides a correct low-symmetry ordering pattern. However, due to short-range nature of chemical bonding, the JT effect is due to strengthening chemical bonds of the central atom, Cu(II), with close-neighbor ligands, not the second- or third-neighbor sites. A simple example of this possible controversy is the hexagonal perovskite crystal  $\text{CsCuCl}_3$ . Its high-symmetry parent structure in  $\text{CsNiCl}_3$  is shown in Fig. 12.

In  $\text{CsNiCl}_3$ , ions of  $\text{Cs}^+$  and  $\text{Cl}^-$  form close-packed layers which are stacked as...ABABAB... Ions of  $\text{Ni}^{2+}$  are in between these layers. They form linear chains of face-sharing octahedrons  $[\text{NiCl}_6]$ . In  $\text{CsCuCl}_3$ , however, each octahedron  $[\text{CuCl}_6]$  is in electron configuration  $3d^9$  with JT-unstable ground state  ${}^2E_g$ , quite similar to the abovementioned example of  $[\text{CuF}_6]$  in  $\text{KCuF}_3$  (Sect. 3.2).

The JT crystal  $\text{CsCuCl}_3$  exhibits a structural phase transition at  $T = 423$  K. Above that temperature, the octahedrons,  $[\text{CuCl}_6]^{4-}$ , are dynamically disordered. The face-sharing arrangement implements a special boundary condition for the JT-distorted next-neighbor octahedrons. The way they can adjust to one another is shown in Fig. 13a. Along linear chains of  $[\text{CuCl}_6]$ , long axes of elongated octahedrons form a helical pattern that triple the lattice period along the  $c$  axis. Relative to each other, directions of elongation are in three vertical (parallel to  $c$  axis) planes turned by about  $120^\circ$  to one another forming a helical pattern. As the JT distortions are adiabatically coupled to the respective electron wave functions, the latter align along the elongated octahedrons as in Fig. 13a ([42, 57].

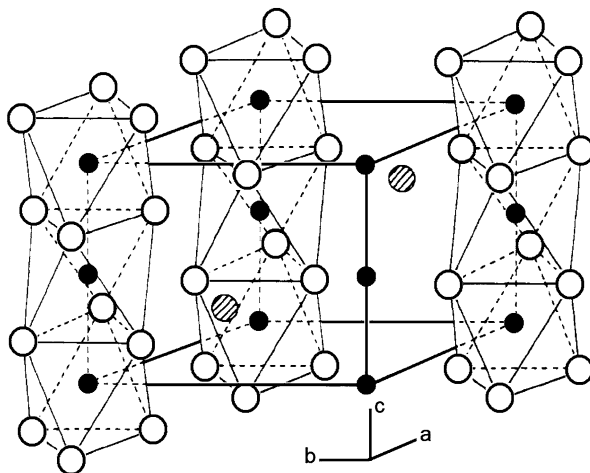


**Fig. 12** Hexagonal perovskite crystal structure of the parent compound  $\text{CsNiCl}_3$ . Black circles represent transition metal atoms,  $\text{Ni}^{2+}$  in this case. White circles are ligands. Shaded circles are atoms of  $\text{Cs}^+$ . Face-sharing octahedrons  $[\text{NiCl}_6]$  are packed in linear chains (From [57])

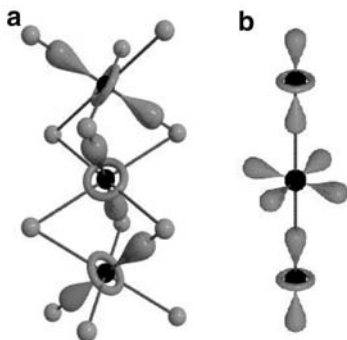


**Fig. 13** A fragment of the crystal lattice  $\text{CsCuCl}_3$  with JT instability  $E \otimes e_g$  in each of its face-sharing octahedrons  $[\text{CuCl}_6]$ . JT-induced elongation of octahedrons forms a helical pattern. (a) In traditional approach,  $3d(\text{Cu})$  orbitals point toward nearest-neighbor ligands. (b) In the OOA, ligands are omitted.  $3d(\text{Cu})$  orbitals point toward  $\text{Cu}^{2+}$  of the next-neighbor sites. A possible orbital ordering can be “antiferro” type with orbitals oriented along symmetry axes of the primitive lattice

Most significant, the OOA cannot explain the ordering shown in Fig. 13a. As ligands are omitted, for possible low-symmetry ordering patterns, the only directions left are the ones of the primitive crystal lattice of the perovskite structure. One can anticipate a “ferro”, or “antiferro”, or some other, more complex type of orbital ordering. In the OOA, no matter what type of ordering will dominate, the ordered orbitals are aligned along one of the crystal symmetry axes of the primitive lattice, as in Fig. 13b. In the OOA, there is no way of getting anything even close to the structure shown in Fig. 13 a.

The failure of the OOA in the case of  $\text{CsCuCl}_3$  reflects limitations and the approximated nature of the OOA. In what follows in this section, we will revise the physical background of the OOA. This will help to decide when the OOA is going to work well or, alternatively, when it can go wrong.

For intersite orbital exchange coupling, there are several competing mechanisms. In addition to the JT effect mediated by intercell elastic coupling, there may be a purely electronic coupling [9, 10, 19], or, even a direct quadrupole–quadrupole intersite interaction, as in rare earths compounds. In any case, according to Khomskii [10], even if the main driving force of an orbital ordering is purely electronic, the lattice would relax to adjust the ordered orbitals with a corresponding lattice (JT) distortion.

This statement includes two inaccuracies. The first one is symmetry related. In the most interesting case of transition metal compounds, the JT-active orbitals cannot participate in any other “purely electronic coupling” but the quadrupole–quadrupole intersite interaction. In the JT-active electron states, the dominant contribution is due to transition-metal  $3d$  orbitals. The latter ones have even parity and do not have dipole properties. In the multipole–multipole expansion of intersite electron coupling, first nonzero contribution comes from the quadrupole–quadrupole term.

Therefore, the only competitor of the cooperative JT coupling is the quadrupole–quadrupole intersite interaction.

Another side of the story is the way this purely electron quadrupole–quadrupole coupling operates. It can be direct or, in most cases, ligand mediated. Proportional to the respective overlap integral, the direct coupling is of several orders of magnitude weaker than any other reasonable type of coupling and, therefore, can be neglected. In what follows (see below) we will provide an estimate of the ligand-mediated quadrupole–quadrupole coupling.

The second inaccuracy is a mix-up between cause and effect. Obviously, the two phenomena, crystal lattice distortion and low-symmetry orbital ordering, are interrelated. However, the JT distortion can take place even without any long-range orbital ordering. Above the temperature of structural (JT) phase transition, in each elementary cell, the JT effect is still active. Considered separately from one another, due to the JT effect, elementary cells can be locally distorted. These local distortions are not ordered, and respective X-ray data provide evidence of time averaged high symmetry lattice. However, above the temperature of structural phase transition, disordered JT distortions manifest themselves in XAFS [58].

From another hand, in transition metal compounds (fluorides, etc.) without JT coupling, driven by pure electron intersite interaction, orbital ordering takes place at very low temperatures, of the order of 10–100 K. At normal conditions (room temperature), orbital ordering can be neglected. In this sense, we can say that orbital ordering does not happen without JT distortions. As the JT distortions can take place without orbital ordering, and orbital ordering cannot take place without the JT distortions, the latter cannot be the effect and the former cannot be the cause. Unfortunately, in most papers on the OOA discussing symmetry-breaking ordering patterns, the cause and the effect are reversed.

At this point, it is important to have a realistic estimate of the three types of coupling. The intra cell JT coupling is known to vary from one compound to another. Speaking of orders of magnitude,  $E_{JT}$  ranges from several  $\text{cm}^{-1}$  in rare-earth compounds to about 0.5 eV ( $4000 \text{ cm}^{-1}$ ) in some transition metal compounds [59]. The intercell elastic coupling is of the order of average optical phonon energy,  $\hbar\omega \approx 500 \text{ cm}^{-1}$ .

For the orbital exchange coupling, the upper limit can occur in metals with chains of transition metal ions bound directly to one another. For transition metal compounds, this situation is relatively seldom. In most cases, transition metal ion is surrounded by a polyhedron of ligands. In the latter case, neighboring-site metal atoms are separated from one another by one or several bridge ligand atoms. The respective polyhedrons can be corner sharing (Figs. 7 and 8), side sharing, face sharing (Figs. 12 and 13), or even more complex, with no common atoms in neighboring elementary cells (Fig. 5a). For the respective parameter of orbital exchange, its magnitude strongly depends on the number of bridge ligand atoms and on the orientation of the neighboring polyhedrons relative to one another.

In the simple case of corner-sharing octahedrons with first-long-period transition metals ( $3d$  elements) bridged by one second- or third-period ligand atom, the orbital exchange coupling can be approximated as a perturbation-theory energy correction.

In second order, its maximum value is

$$E_{\text{orb.exch}} \approx J_{ij} \approx \frac{\langle 3d_i | H | 2p \rangle_{\text{max}} \langle 2p | H | 3d_j \rangle_{\text{max}}}{E_{3d} - E_{2p}} = \frac{|\langle 3d_i | H | 2p \rangle_{\text{max}}|^2}{E_{3d} - E_{2p}}. \quad (26)$$

Here  $|3d\rangle$  and  $|2p\rangle$  are wave functions of the central atom and bridge ligand atoms respectively, whereas  $E_{3d}$  and  $E_{2p}$  are the corresponding energy values. In the numerator of (26), the matrix element,  $\langle 3d_i | H | 2p \rangle_{\text{max}}$ , is of the order of 0.1 eV, and the energy gap in the denominator is of the order of 3 eV. This gives  $J_{ij}$  of the order of 3 meV  $\approx 30 \text{ cm}^{-1}$ . Extremely large values of  $J_{ij}$  of the order of 200  $\text{cm}^{-1}$  can be found in some systems with electron-conjugated bridges as in, say, the binuclear copper(II) acetate hydrate,  $[\text{Cu}(\text{OAc})_2\text{H}_2\text{O}]_2$ . In this compound, a reasonable fitting of magnetic susceptibility data is achieved with the value of  $J_{ij}$  of about 167  $\text{cm}^{-1}$  (Bersuker [59]).

From another hand, in a similar way we can estimate the JT stabilization energy,  $E_{\text{JT}} = V^2 / 2M\omega^2$ . Here  $M$  is mass of one ligand atom,  $\omega$  is frequency of the JT-active vibration, and  $V$  is of the order of the derivative of the matrix element  $\langle 3d | H | 2p \rangle_{\text{max}}$  [c.f. (2)]<sup>3</sup>. Assuming that the matrix element,  $\langle 3d | H | 2p \rangle$  changes from zero to its maximum value at about  $0.1a$ ,  $a$  being interatomic distance, the rough estimate is  $V \approx 10\langle 3d | H | 2p \rangle / a$ . The denominator,  $M\omega^2$ , is related to the elastic energy gain  $M\omega^2 Q^2$ . At the distance of mean vibrational amplitude,  $\sqrt{\langle Q^2 \rangle}$ , it is of the order of  $1/2\hbar\omega$ . Assuming  $Q \approx 0.1a$ , we find  $M\omega^2 \approx 50\hbar\omega/a^2$ . Then the JT stabilization energy is

$$E_{\text{JT}} \approx \frac{V^2}{2M\omega^2} \approx \frac{|\langle 3d_i | H | 2p \rangle_{\text{max}}|^2}{\hbar\omega}. \quad (27)$$

Dividing (27) over (26) we find

$$\frac{E_{\text{JT}}}{E_{\text{orb.exch}}} \approx \frac{|E_{3d} - E_{2p}|}{\hbar\omega}. \quad (28)$$

The energy gap,  $|E_{3d} - E_{2p}|$ , is of the order of 3 eV. The one-phonon energy,  $\hbar\omega$ , is of the order of 500  $\text{cm}^{-1} \approx 60 \text{ meV}$ . Then the ratio (28) is of the order or above 50. Based on these estimates, we can formulate the following rule. In transition-metal compounds we have  $E_{\text{JT}} \gg E_{\text{orb.exch}}$ . The intra-cell JT coupling is much stronger than the intersite orbital exchange interaction. In some cases, one can find extremely large values of the parameter of orbital exchange, of the order of 100  $\text{cm}^{-1}$ . However, in the same compound, the respective JT stabilization energy is expected to

<sup>3</sup> The matrix element (2) includes molecular orbital  $|Ex\rangle$ . The latter is a covalent combination of symmetry-adapted atomic orbitals,  $|Ex\rangle = \alpha|3d_{xz}\rangle + \beta|e_x(2p)\rangle$ . Evidently, the diagonal contributions,  $\langle 3d_{xz} | H | 3d_{xz} \rangle$  and  $\langle e_x(2p) | H | e_x(2p) \rangle$ , do not depend on the distortion coordinate,  $Q$ . Therefore, dominant contribution in the derivative  $V$  comes from the off-diagonal matrix element,  $\langle 3d_{xz} | H | e_x(2p) \rangle$ .

be no less than an order of magnitude stronger,  $5,000\text{ cm}^{-1}$  or above. As pure electronic orbital exchange coupling,  $H_{\text{orb.exch}}$ , is much weaker, it should be included *after* the stronger players on the field,  $H_{\text{JT}}$  and  $H_{\text{elast}}$ , are taken into consideration. Instead, in the OOA, as we could see,  $H_{\text{orb.exch}}$  (together with the respective magnetic exchange and electron hopping terms) is the first and, in most cases, the only intercell coupling included.

This point raises an important question. Why is the OOA so successful in determining low-symmetry ordering patterns in most of transition metal compounds considered so far? One answer is pretty obvious. Taken in the form (15) and/or (17), the so-called “orbital exchange” *is not the pure electronic exchange* coupling. In fact, it is an effective intersite coupling induced by the intra cell JT coupling mediated by the intercell elastic coupling. For transition-metal compounds, from the point of view of real physics, there is another important question: how legitimate is partitioning the pure electronic orbital system out of the coupled electron vibrational system. Evidently, this partitioning is an approximation. It has its limits of applicability which will be discussed in the following two sections.

### 5.1 The “Lucky” Case: Adiabatic Jahn–Teller Coupling

In Sect. 3, the decoupling of electrons from low-symmetry vibrations was achieved by the change of variables (13). Though seeming to be correct, actually, this transformation is an approximation. In quantum theory, only legitimate are transformations that conserve probability expressed by the normalization integral of any wave function,  $\langle\psi|\psi\rangle$ . In other words, it has to be a unitary transformation. To shift a coordinate,  $Q$ , by a *number*  $a$ , the respective unitary transformation is  $S = \exp\left(a\frac{d}{dQ}\right)$ .

Applying  $S$  to an operator,  $U(Q)$ , we get:  $SU(Q)S^{-1} = e^{a\frac{d}{dQ}}U(Q)e^{-a\frac{d}{dQ}} = U(Q + a)$ . Consider a harmonic oscillator with a shifted minimum and zero energy at  $Q = 0$ . Its potential energy is a quadratic form  $U(Q) = AQ^2 + BQ$ . The respective parabola has its vertex at  $\bar{Q} = -B/(2A)$ . The unitary transformation,  $S = \exp\left(a\frac{d}{dQ}\right)$ , with  $a = \bar{Q} = -B/2A$  is a horizontal shift to the vertex of the parabola. It gives  $SU(Q)S^{-1} = AQ^2 - B^2/(4A)$  with no linear term. In other words, by shifting to the minimum point,  $\bar{Q} = -B/(2A)$ , we complete the square and eliminate the linear term,  $BQ$ .

In the simplest adiabatic case with an orbital singlet term, potential energy of the crystal lattice is parabolic with one minimum point. At low temperatures, vibrations of the lattice are localized at the bottom of this well, and as a rule, the so-called harmonic approximation applies. This corresponds to the so-called polaron effect and brings us to the concept of electrons coated with phonons.

In the JT case, electron-phonon coupling is represented by a matrix Hamiltonian, similar to (1), or (3). Diagonalization of  $H_{\text{JT}}$  decouples the matrix of potential energy into a multisheet APES. In addition to their diabatic admixture, another difficult side of the JT effect is strong anharmonicity of the APES. As a rule, it has



not just one but several minimum points, sometimes a continuum of minima as in Fig. 4. Usually, in the JT case, it is impossible to eliminate the linear JT coupling by a coordinate shift transformation to several minimum points at once.

However, this limitation has a couple of exceptions, the “lucky” cases. One is the tetragonal  $E \otimes b_{1g}$  case discussed in Sect. 2.1 with the respective APES shown in Fig. 2b. As the JT Hamiltonian (1) is a diagonal matrix, the distortion coordinate  $Q$  can be shifted to the two minimum points at once. With the diagonal Pauli matrix  $\sigma_z$  in the exponent, the coordinate-shift operator has a simple diagonal form,

$$S = e^{a\sigma_z \frac{d}{dQ}} = \begin{pmatrix} e^{a \frac{d}{dQ}} & 0 \\ 0 & e^{-a \frac{d}{dQ}} \end{pmatrix}. \quad (29)$$

It has simple physical meaning. Each eigenvalue is a linear-term addition to the harmonic potential energy. Resulting from the effect of strengthening the respective chemical bonds, it corresponds to an extra force added to the elastic force. Different for different electron states, it shifts differently the vertex of the respective parabola. Applied to the potential energy (4), the coordinate shift (29) transforms it to the nonshifted form, (3), with an extra term (15). In other words, (29) performs a simultaneous coordinate shift to the two minimum points of the APES (Fig. 2b). This transformation brings us to the orbital exchange Hamiltonian (15), similar to the term  $-B^2/(4A)$  in the above example of  $U(Q) = AQ^2 + BQ$ . Note that behind this “lucky” exception we have one simplifying circumstance. The JT Hamiltonian (1) is a diagonal electron matrix. It corresponds to two different branches of the APES each having just one minimum (Fig. 2b).

As distinguished from this “lucky” case, in the  $E \otimes e_g$  coupling, the APES has a continuum of minimum points, a trough, shown by broken line in Fig. 4. With higher-order terms in the JT coupling, the “Mexican hat” transforms into a “tricorné” with three minimum points at the bottom [1,2]. Still the number of minimum points (three) is larger than the number of states (two). Therefore, there is no such a unitary transformation expressed by a diagonal matrix  $2 \times 2$  that would provide three different coordinate shifts at once. As distinguished from (29) with two shift operators on the main diagonal, no matrix  $2 \times 2$  has enough room for three different shift operators. Formally, for a JT crystal with linear coupling  $E \otimes e_g$ , the respective shift operator could be

$$S = \exp \left\{ -\frac{V}{\omega^2} \sum_n \left[ \sigma_z(n) \frac{\partial}{\partial Q_\theta(n)} + \sigma_x(n) \frac{\partial}{\partial Q_\epsilon(n)} \right] \right\}. \quad (30)$$

However, as distinguished from (29), it cannot be transformed to the simple diagonal form. With noncommutative Pauli matrices  $\sigma_z$  and  $\sigma_x$  in the exponent, the operator  $S$  in (30) cannot be presented in analytic form as a diagonal matrix with shift operators in its main diagonal, though it can be brought to a closed general  $2 \times 2$  matrix form, whose matrix elements contain the above derivatives.

Actually, for most of the well-known JT problems, the JT Hamiltonian includes noncommutative matrices. To my knowledge, there are just three “lucky” exceptions. One, the so-called  $E \otimes b_{1g}$  case, was considered above. Another one is the  $E \otimes b_{2g}$  case for a tetragonal  $E$  term linearly coupled to  $b_{2g}$  mode of vibrations. The respective Hamiltonian is [cf. (1)]:

$$H_{JT} = VQ \begin{array}{c} |Ex\rangle \quad |Ey\rangle \\ \left( \begin{array}{cc} 0 & 1 \\ 1 & 0 \end{array} \right) \end{array} = VQ\sigma_x. \quad (31)$$

It includes Pauli matrix  $\sigma_x$ . Though nondiagonal, it can be transformed to a diagonal form with eigenvalues  $\pm 1$ . Formally, it coincides with (1). The rest of the solution, including separation of the orbital exchange part (15), is the same as in Sect. 3 with no approximations involved.

Most important, transforming (31) to a diagonal form, the unitary shift transformation commutes with the operator of kinetic energy. It remains unchanged and does not include off-diagonal matrix elements, the ones responsible for diabatic admixture of the two branches of the APES. Therefore, similar to the  $E \otimes b_{1g}$  case, the  $E \otimes b_{2g}$  case is the so-called adiabatic JT problem. With no off-diagonal matrix elements in the Hamiltonian, the two-branch Schrödinger equation decouple into two independent equations easy to solve.

The third “lucky” case is the so-called  $T \otimes e_g$  problem in a cubic system. The JT instability of the orbital triplet term (the  $T$  term) is due to its linear coupling to twofold degenerate vibrations,  $Q_\theta$  and  $Q_\varepsilon$ , shown in Fig. 3b and c [1, 2]. As it is similar to the tetragonal  $E \otimes b_{1g}$  case, for this cooperative JT effect we do not go into its details. Just note that there are three minimum points in this case and there are three matrix positions on the main diagonal allowing the respective simultaneous coordinate shift to these three vertices.

## 5.2 *Weak-to-Intermediate Jahn–Teller Coupling. Virtual Phonon Exchange*

The adiabatic JT problems, tetragonal  $E \otimes b_{1g}$  and  $E \otimes b_{2g}$ , and cubic  $T \otimes e_g$ , are just a small minority in the large family of JT cases. If the JT Hamiltonian includes noncommutative matrices, no unitary shift transformation can eliminate the electron-phonon coupling. The nonseparability of electrons from phonons is due to the diabatic nature of JT coupling. Among the diabatic JT cases, the best known is the  $E \otimes e_g$  coupling in cubic systems. The respective shift transformation (30) cannot be transformed to the diagonal form as simple as (29). Instead, at weak coupling, when  $E_{JT} \ll \hbar\omega$ , perturbation theory applies with the JT coupling term,  $H_{JT}$ , being its small parameter. In what follows, we discuss the simpler version of the perturbation theory working with multielectron states. Perturbation theory in the manifold of one-electron orbitals will be briefly discussed at the end of this section.

As  $H_{JT}$  is linear in phonon coordinates  $Q_\theta(i)$  and  $Q_\epsilon(i)$ , its diagonal matrix elements equal zero and, therefore, the first-order perturbation correction equals zero. The Hamiltonian of the second-order,

$$H_2 = H_{JT} \left( \sum_n \frac{|n\rangle \langle n|}{E_0 - E_n} \right) H_{JT}, \quad (32)$$

is bilinear with respect to phonon coordinates. The cumulative index  $n = \{n_\theta(i), n_\epsilon(i)\}$  numbers excited states of the unperturbed Hamiltonian,  $H_0$ , with phonon occupation numbers  $n_\theta(i)$  and  $n_\epsilon(i)$ . Following [36], we will average  $H_2$  with ground-state phonon wave functions (the so-called phonon vacuum),  $|0\rangle$ . In this case, for the JT coupling  $E \otimes e_g$  expressed by (3), the only nonzero contributions are [cf. (17)]:

$$\langle H_2 \rangle = \langle 0 | H_2 | 0 \rangle = - \sum_{i,j} \sum_{\gamma,\lambda} J_{\gamma\lambda} (i - j) \sigma_\gamma (i) \sigma_\lambda (j), \quad \gamma, \lambda = x, z, \quad (33)$$

with

$$J_{\gamma\lambda} (i - j) = V^2 \sum_{n \neq 0} \frac{\langle 0 | Q_\gamma (i) | n \rangle \langle n | Q_\lambda (j) | 0 \rangle}{E_n - E_0}. \quad (34)$$

In (34), the effective Hamiltonian  $\langle H_2 \rangle$  is still a matrix in the orbital space of electron wave functions. Similar to (17), it describes intersite orbital exchange coupling. In (34) and (35), the factor  $J(i - j)$  is the parameter of orbital exchange coupling, same as in (3.7). This time it is supported by the assumption of weak JT coupling. The matrix elements  $\langle 0 | Q_\gamma (i) | n \rangle$  are determined with zero-coupling oscillator wave functions. They take a nonzero value for  $n = 1$  only. In other words, in the effective Hamiltonian  $\langle H_2 \rangle$ , the virtual excited states are one-phonon states. Therefore, the effective Hamiltonian (34) describes phonon-mediated orbital exchange.

Understanding the cooperative JT effect as an orbital ordering due to exchange of virtual phonons is only correct in the limiting case of weak JT coupling. At a stronger JT coupling, phonons cease to exist. They are not independent elementary excitations propagating in the crystal. Instead, one can imagine a JT polaron or, shorter, a traveling “vibron”. In the limit of strong JT coupling, for a finite concentration of JT centers, due to a very strong JT-induced lattice anharmonicity, the concept of phonons does not apply.

The expression (34) for the orbital exchange parameter,  $J(i - j)$ , can be simplified. As the matrix elements  $\langle 0 | Q_\gamma (i) | n \rangle$  are not equal to zero for  $n = 1$  only, we have

$$J_{\gamma\lambda} (i - j) = \frac{1}{2} V^2 \langle i, \gamma | \mathbf{K}^{-1} | j, \lambda \rangle, \quad \gamma, \lambda = \theta, \epsilon, \quad (35)$$

similar to (3.8).

Behind the OOA, the basic concept is the so-called orbital pseudo spin. For one-center JT effect, in general the JT coupling does not change transformation

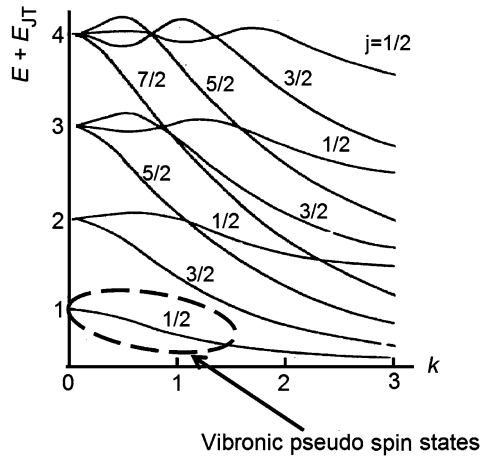


**Fig. 14** Vibronic energy levels in the linear  $E \otimes e$  case (in units of  $\hbar\omega$ ) versus dimensionless coupling constant  $k$  (after Muramatsu and Sakamoto [60]). Encircled is the domain of coupling constants where the vibronic ground state is well energy separated from excited vibronic states and the concept of vibronic pseudo spin applies

properties of ground-state wave functions. They are the same as the original electron-degenerate orbital states with no coupling. This provides a chance to extend the concept of pseudo spin to the case of intermediate coupling (Fig. 14). JT centers at each elementary cell can be treated as an ensemble of *vibronic* pseudo spins with the respective exchange coupling, quite similar to orbital pseudo spins and to real spins in conventional magnetic crystals.

As distinguished from the orbital pseudo spin, for the vibronic pseudo spin, the mechanism of intercell coupling is different. It is dominated by the respective terms of elastic intercell interaction,

$$\frac{1}{2} \sum_{i,j} \sum_{\gamma,\lambda} Q_{\gamma}(i) K_{\gamma\lambda}(i-j) Q_{\lambda}(j). \quad (36)$$

Following the idea of the basis set limited with just ground-state vibronic wave functions, the vibrational operators,  $Q_{\gamma}(i)$  can be replaced by their respective matrix representation,

$$\mathbf{Q}_{\theta}(i) = -\frac{qV}{\omega^2} \sigma_z, \quad \mathbf{Q}_{\epsilon}(i) = -\frac{pV}{\omega^2} \sigma_x. \quad (37)$$

Here  $\omega^2 = K_{\theta\theta}(0)$  is elastic constant of the tetragonal  $E$  vibrations in one octahedron. The coefficients  $q$  and  $p$  are well-known vibronic reduction factors [1, 2, 61]. As the vibronic coupling constant,  $V$ , increases, the reduction factors,  $q$  and  $p$ , approach their limiting values,  $q = \frac{1}{2}$  and  $p = 0$ . Therefore, at strong vibronic coupling, the product  $qV$  in (38) increases linearly with  $V$ . Therefore,  $qV$  is known as the factor of *vibronic amplification* [1, 2, 61]. At the same time, the factor  $pV$

approaches zero. With the replacement (38), neglecting the reduced contribution of  $Q_\varepsilon(j)$ , the intercell interaction (37) takes the form of “orbital exchange” dominated by  $\theta - \theta$  coupling,

$$\frac{E_{JT}}{4\omega^2} \sum_{i,j} K_{\theta\theta} (i - j) \sigma_z(i) \sigma_z(j). \quad (38)$$

Here  $E_{JT} = \frac{1}{2}(V^2/\omega^2)$  is the JT stabilization energy. Compared to the parameters of direct orbital exchange, its magnitude is one or even two orders stronger [cf. (28)]. This explains unusually large values of parameters of “orbital exchange” in perovskites. Also, it is important to note that “ $\theta$  directions” are determined by orientation of the metal-ligand octahedron and may be different from directions of the primitive lattice.

In solid state physics, the OOA is a part of a more general trend well-known and widely used in quantum theory. Its basic idea is partitioning the Hilbert space of crystal wave functions into two subspaces. One (the  $M$  space) includes transition-metal  $d$  orbitals. The other one (the  $L$  space) is the manifold of all ligand orbitals. Matrix Hamiltonian of the system can be presented as a composition of the respective blocks: the *metal* part of the matrix,  $H_{MM}$ , its *ligand* part,  $H_{LL}$ , and its *metal-ligand* blocks,  $H_{ML}$  and  $H_{LM}$ , composed of the respective mixing matrix elements. For partitioning, one can apply the method of projection operator, or the simpler version, perturbation theory with the metal-ligand matrix parts,  $H_{ML}$  and  $H_{LM}$ , as small parameters [36]. In molecular theory of transition metal compounds, averaged over ligand states, the second-order Hamiltonian,  $\langle H_{MM}^{(2)} \rangle_L$ , was used to derive metal-only semi-empiric Hamiltonian of the *angular overlap model* [59].

Expanded up to fourth-order perturbation theory and averaged over ligand states, the Hamiltonian  $\langle H_{MM}^{(4)} \rangle_L$  becomes a fourth-degree form of metal-only  $3d$  orbital operators of creation and annihilation [36]. The advantage of the effective Hamiltonian  $\langle H_{MM}^{(4)} \rangle_L$  is in operating within a relatively small manifold of metal-only  $3d$  states. In the Hamiltonian  $\langle H_{MM}^{(4)} \rangle_L$ , in terms of modern solid state theory, same-site terms represent electron correlation. Thus, we gain in reducing the manifold of relevant states, and, instead, we lose in appearance of the new terms to deal with, the strong on-site correlation. The remaining terms describe intersite pseudo spin exchange coupling. Therefore, the Hamiltonian  $\langle H_{MM}^{(4)} \rangle_L$  is the effective Hamiltonian of the OOA.

Actual derivation of this Hamiltonian is based on perturbation theory which is the only solid background of its applicability. The “small parameter” is the metal-ligand matrix part,  $H_{ML}$  and  $H_{LM}$ . In solid state physics it is attributed to electron hopping. In quantum chemistry, it is responsible for chemical bonding. As we can see, in the OOA, in deriving its effective Hamiltonian, chemical bonding terms are averaged out.

The metal-ligand matrix elements,  $H_{ML}$  and  $H_{LM}$ , are distance dependent and can be expanded in terms of symmetry-adapted nuclear displacements,  $Q_{\Gamma\gamma}(m)$ . For a JT crystal, in this expansion the linear term is similar to the JT Hamiltonian, as (1)

and (3). Being a part of the metal-ligand block,  $H_{ML}$ , in the fourth-order perturbation theory, these “JT terms” generate the same type of intersite correlation as in (23). Therefore, formally, after ligand states are averaged out, the JT contribution in orbital exchange cannot be distinguished from direct orbital exchange [36].

### 5.3 The Strong Coupling Case. Tunneling Splitting and Extended Vibronic Pseudo Spin

In the case of intermediate-to-strong JT coupling, the energy gap separating the vibronic ground state from excited vibronic states decreases with vibronic coupling. For one JT center, this phenomenon is well known. A detailed discussion of its physical origin and different manifestations can be found in [1, 2]. As the JT coupling increases, second- and higher-order vibronic coupling effects become more important. At the bottom of the trough (Fig. 4), bumps and wells grow. Rotation along the circular trough is not free any longer. The rotation becomes hindered and, when the potential wells are deep enough (compared to  $\hbar\omega$ ), the system spends relatively long time in the wells. In the vibronic energy spectrum, this type of motion is expressed by the tunneling splitting [1].

At normal conditions (room temperature), all components of the tunneling-splitting vibronic multiplet are temperature populated. As a good initial approximation, the tunneling splitting can be neglected, and the vibronic states in the potential wells can be considered degenerate.

The number of tunneling ground states equals the number of wells at the lowest sheet of the APES. In the case of quadratic  $E \otimes e$  coupling, there are three wells and, therefore, three tunneling states (Fig. 15).

Correspondingly, vibronic pseudo spin space has to be extended to include all tunneling splitting components. In the case of quadratic  $E \otimes e$  coupling with three wells, it is expressed by the vibronic pseudo spin  $\tau = 1$  matrices  $3 \times 3$ . Similar to the intermediate coupling case, the intersite vibronic exchange is dominated by the elastic intercell interaction (36).

Vibrational operators,  $Q_\theta(i)$  and  $Q_\epsilon(i)$ , can be replaced by their respective matrix representation,

$$\mathbf{Q}_\theta(i) = \rho_0 \mathbf{C}_\theta(i), \quad \mathbf{Q}_\epsilon(i) = \rho_0 \mathbf{C}_\epsilon(i), \quad (39)$$

where  $\rho_0 = V/\omega^2$  is radius of the trough on the lower sheet of the APES (Fig. 4). In (39), the  $3 \times 3$  matrices  $\mathbf{C}_\theta(i)$  and  $\mathbf{C}_\epsilon(i)$  operate in the manifold of the three vibronic states localized at the bottom of the respective potential wells,

$$\mathbf{C}_\theta = \frac{1}{2} \begin{pmatrix} 1 & 0 & 0 \\ 0 & 1 & 0 \\ 0 & 0 & -2 \end{pmatrix}, \quad \mathbf{C}_\epsilon = \frac{\sqrt{3}}{2} \begin{pmatrix} -1 & 0 & 0 \\ 0 & 1 & 0 \\ 0 & 0 & 0 \end{pmatrix}. \quad (40)$$

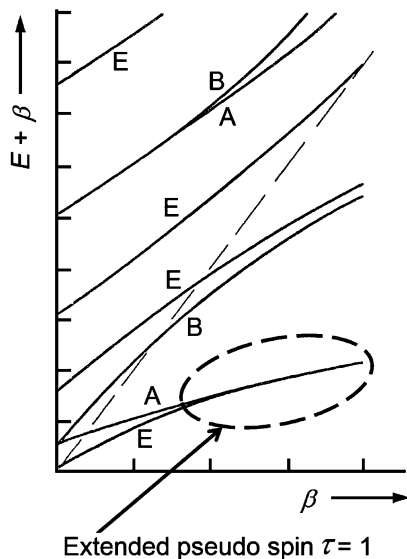


**Fig. 15** Vibronic energy levels versus the warping factor  $\beta$  (both  $E$  and  $\beta$  are in units of  $4\alpha$ , where  $\alpha$  is rotational quantum) in a JT elementary cell with quadratic coupling  $E \otimes e$  [after O'Brien [62]]. Encircled is the domain of a very small tunneling energy gap where the concept of extended vibronic pseudo spin applies

Plugging (39) into (36), we come to the effective Hamiltonian

$$H = \frac{E_{JT}}{2\omega^2} \sum_{i,j} \sum_{\gamma,\lambda} K_{\gamma\lambda} (i - j) C_{\gamma}(i) C_{\lambda}(j), \quad \gamma, \lambda = \theta, \epsilon. \quad (41)$$

Formally, it looks similar to the effective Hamiltonian of the OOA. However, its physical meaning is different. First, it does not describe free rotations of the respective states. There are just three positions around each JT center. Second, these are multielectron vibronic states, not one-electron orbitals. Third, most important, the parameter of this intercell “vibronic exchange” coupling is enhanced by the JT stabilization energy, a factor that can be very strong, up to an order of 0.5 eV.

The three-state extended pseudo spin model is equivalent to the Potts model well-known in solid state physics. Its application to JT structural phase transitions was developed by Höck et al. [63]. Also, as a useful tool, it was mentioned by Kugel and Khomskii [9]. It was applied to hexagonal perovskites by Crama and Maaskant [64]. It has multiple applications to layered manganites (e.g., see [65]).

In the case of  $E \otimes e$  coupling, under some special conditions, including higher orders of JT coupling can result in six wells [1, 2]. Correspondingly, in this case, the extended vibronic pseudo spin is expressed by spin-5/2 matrices  $6 \times 6$ . In the linear  $T \otimes t_2$  case, there are four symmetry equivalent wells [2]. Correspondingly, the matrices of extended vibronic pseudo spin are  $4 \times 4$ , and the respective pseudo spin value is  $\tau = 3/2$ .

## 6 Discussion: Warnings and Recommendations

The OOA, also known as Kugel-Khomskii approach, is based on the partitioning of a coupled electron-phonon system into an electron spin-orbital system and crystal lattice vibrations. Correspondingly, Hilbert space of vibronic wave functions is partitioned into two subspaces, spin-orbital electron states and crystal-lattice phonon states. A similar partitioning procedure has been applied in many areas of atomic, molecular, and nuclear physics with widespread success. It's most important advantage is the limited (finite) manifold of orbital and spin electron states in which the effective Hamiltonian operates. For the complex problem of cooperative JT effect, this partitioning simplifies its solution a lot.

Although the effective Hamiltonian can be justified by orthogonal projection or by the respective perturbation theory; in the OOA it is just postulated. Analysis of the background theory reveals its physical meaning. The OOA is based on a shift transformation to a minimum point of APES for an elementary cell in the respective low-symmetry mean field of all other cells of the crystal. Vibrational motion of ligands is averaged out [36].

In the "orbital" exchange coupling, actual participants are so-called pseudo spins. In real systems, due to the JT effect, they are coated with low-symmetry phonons. The stronger the JT coupling, the thicker the coat is, the more phonons are involved in the formation of the JT polaron. The abovementioned shift transformation strips down the phonon coat leaving the orbital pseudo spin naked. This makes an impression of the "orbital" exchange coupling when in reality it is coupling of vibronic pseudo spins. Therefore, the terms "orbital" ordering and "orbital" exchange coupling are misleading.

In the OOA, ligands are omitted from consideration. For real crystal structures, this eliminates the so-called basis. In other words, crystal lattice with basis is replaced by the respective primitive lattice with transition metal atoms at its sites. Chemical bonding of the transition metal with ligands is included indirectly in parameters of orbital exchange. Correspondingly, in the OOA, possible low-symmetry ordering patterns follow directions of symmetry axes of the primitive lattice. Therefore, the OOA provides reasonable results under condition that ligands are collinear with next-neighbor metal atoms (as in  $\text{KCuF}_3$ , Figs. 21.8 and 9) or, in other words, directions of the primitive lattice coincide with orientation of chemical bonds with ligands.

In real systems, ordering is dominated by metal-ligand chemical bonds. Compared to the primitive lattice, they may point in different directions. If ligand bridges are bent (as in  $\text{CsCuCl}_3$ , Figs. 21.12 and 13a, or in  $\text{LaMnO}_3$ , Figs. 10b and 11c), the OOA fails to provide physically reasonable results. This may bring to wrong conclusions about ordering patterns oriented along axes of the primitive lattice of just metal sites.

Returning back to its real physical meaning, the concept of vibronic pseudo spin has a relatively large area of applicability. It includes the case of intermediate-to-strong JT coupling. However, the character of the intersite coupling is dominated by elastic intercell interaction. The latter is amplified by strong JT coupling (known as



*vibronic amplification* [1, 2, 61]) and has special directions of strong intersite correlation. Compared to directions of the primitive lattice of metal sites, they may be different (as in  $\text{CsCuCl}_3$  or in  $\text{LaMnO}_3$ ). At strong JT coupling, when the tunneling splitting energy gap is small, the multiplicity of the vibronic pseudo spin has to be extended to include all tunneling components of the ground-state energy level.

Parameters of orbital exchange are strongly affected by position of bridge ligands. In the OOA, this dependence is lost. The only degree of freedom left is ability of electron wave functions to turn around the respective metal atom. The wave functions keep their rigid shape. In general, they do not follow nuclear displacements. Contrary to the fundamental idea of adiabatic approximation, this makes a wrong impression that lattice distortions follow electron ordering. From another hand, adiabatic approximation is well known to apply well to strongly coupled JT systems, a large group in the family of JT crystals. Even in the case of intermediate vibronic coupling, it is hard to believe that heavy nuclei follow light electrons. From this point of view, interpreting JT structural changes as dominated by electrons is a mix-up between cause and effect.

The OOA was not designed for and does not apply to temperature dependencies of any kind in JT crystals. In particular, one cannot expect a reasonable estimate of the temperature of phase transitions in crystal lattice (structural), electron orbital, and/or spin system. This follows from the partitioning procedure that includes averaging over vibrational degrees of freedom. One can see the same reason from another perspective. The pseudo spin of a JT site, as the basic concept used in the OOA, operates in the basis of degenerate ground state wave functions. Excited vibronic states are beyond the pseudo spin setup. Therefore, in the OOA, by its very definition, temperature population of excited states does not make sense.

Also, one cannot expect a reliable description of spontaneous polarization of the crystal lattice. This phenomenon substantially involves strengthening chemical bonds of the central atom with ligands. As these chemical bonds are averaged out, ferroelectricity cannot be adequately described in the OOA.

**Acknowledgements** It is a pleasure to thank I.B. Bersuker for suggesting this study and for many stimulating discussions. I would also like to thank K. I. Kugel, D. I. Khomskii, R. Englman, A. E. Nikiforov and B.S. Tsukerblat for reading the manuscript, its thorough critical analysis, helpful discussions, and pointing my attention to different papers directly and indirectly related to the subject of this review.

## References

1. I.B. Bersuker, *The Jahn-Teller Effect*. (Cambridge University Press, Cambridge, 2006)
2. I.B. Bersuker, V.Z. Polinger, *Vibronic Interactions in Molecules and Crystals*. Springer Series in Chemical Physics. vol. 49 (Springer-Verlag, Berlin-Heidelberg-New York, 1989)
3. R. Englman, *The Jahn-Teller Effect in Molecules and Crystals*. (Wiley-Interscience, London, 1972)
4. R. Englman, B. Halperin, Phys. Rev. B. (1970). doi:10.1103/PhysRevB.2.75
5. G.A. Gehring, K.A. Gehring, Rept. Prog. Phys. (1975). doi:10.1088/0034-4885/38/1/001

6. M.D. Kaplan, *The Jahn-Teller-Effect*. (2009)
7. M.D. Kaplan, B.G. Vekhter, (Plenum Press, New York-London, 1995)
8. J. Kanamori, J. Appl. Phys. (Suppl.). **31**, No.5, 14S–23S (1960)
9. K.I. Kugel, D.I. Khomskii, Sov. Phys. – Uspekhi. **25**, 231–256 (1982)
10. D.I. Khomskii, Phys. Scr. **72**, CC8–CC14 (2005)
11. G. Khaliullin, Prog. Theor. Phys. Suppl. (Jpn). **160**, 155–202 (2005)
12. L.D. Landau, E.M. Lifshits, *Quantum Mechanics: Non-Relativistic Theory*. 3rd edn. (Elsevier Science, 2003)
13. R. Janes, E. Moore, *Metal-Ligand Bonding*. (Royal Society of Chemistry/Open University, Great Britain, 2004)
14. H.C. Longuet-Higgins, U. Opik, M.H.L. Pryce, R.A. Sack, Proc. Roy Soc. A. **244**, 1–16 (1958)
15. C. Kittel, *Introduction to Solid State Physics*, 8th edn. (Wiley, New York, 2005)
16. D. Reinen, C. Friebel, in *Structural Problems. Structure and Bonding*, vol. 37, (Springer-Verlag, Berlin-Heidelberg-New York, 1979), pp. 1–160
17. D. Reinen, M. Atanasov, Magn. Resonance Rev. **15**, 167–139 (1991)
18. T.V. Ramakrishnan, 71st Annual Meeting at Tiruchirappalli, Indian Academy of Sciences Web.[http://www.ias.ac.in/meetings/annmeet/71am\\_talks/tvramakrishnan/img0.html](http://www.ias.ac.in/meetings/annmeet/71am_talks/tvramakrishnan/img0.html) (2005). Accessed 23 December 2008
19. K.I. Kugel, D.I. Khomskii, Sov. Phys. – JETP. **37**, 725–730 (1973)
20. N. Binggeli, M. Altarelli, Phys. Rev. B. (2004). doi:10.1103/PhysRevB.70.085117
21. S.Yu. Shashkin, W.A. Goddard III, Phys. Rev. B. (1986). doi:10.1103/PhysRevB.33.1353
22. J.E. Medvedeva, M.A. Korotin, V.I. Anisimov, A.J. Freeman, Phys. Rev. B. (2002). doi:10.1103/PhysRevB.65.172413
23. A.E. Nikiforov, S.Yu. Shashkin, Phys. Solid State. **38**, 1880–1884 (1996)
24. E. Pavarini, E. Koch, A.I. Lichtenstein, Rev. Lett. (2008). doi:10.1103/PhysRevLett.101.266405
25. I. Leonov, N. Binggeli, D.m. Korotin, V.I. Anisimov, N. Stojic, D. Vollhardt, Phys. Rev. Lett. (2008). doi:10.1103/PhysRevLett.101.096405
26. K.I. Kugel, A.L. Rakhmanov, A.O. Sboychakov, N. Poccia, A. Bianconi, Phys. Rev. B. (2008). doi:10.1103/PhysRevB.78.165124
27. K.I. Kugel, A.L. Rakhmanov, A.O. Sboychakov, D.I. Khomskii, Phys. Rev. B. (2008). doi:10.1103/PhysRevB.78.155113
28. M.Yu. Kagan, A.V. Klaptsov, I.V. Brodskii, K.I. Kugel, A.O. Sboichakov, A.L. Rakhmanov, Phys. Usp. (2003). doi:10.1070/PU2003v046n08ABEH001649
29. M.Yu. Kagan, K.I. Kugel, A.L. Rakhmanov, D.I. Khomskii, Low Temp. Phys. (2001). doi:10.1063/1.1399195
30. A.O. Sboychakov, K.I. Kugel, A.L. Rakhmanov, Phys. Rev. B. (2007). doi:10.1103/PhysRevB.76.195113
31. A.O. Sboychakov, K.I. Kugel, A.L. Rakhmanov, Phys. Rev. B. (2006). doi:10.1103/PhysRevB.74.014401
32. M.Yu. Kagan, K.I. Kugel, A.L. Rakhmanov, K.S. Pazhitnykh, J. Phys. Cond. Matter. (2006). doi:10.1088/0953-8984/18/48/018
33. K.I. Kugel, A.L. Rakhmanov, A.O. Sboychakov, M.Yu. Kagan, S.L. Ogarkov, Physica B. (2008). doi:10.1016/j.physb.2007.10.148
34. D.I. Khomskii, K.I. Kugel, Phys. Rev. (2003). doi:10.1103/PhysRevB.67.134401; J. Magn. Magn. Mat. (2003). doi:10.1016/S0304-8853(02)01044-2
35. D.V. Efremov, D.I. Khomskii, Phys. Rev. B. (2005). doi:10.1103/PhysRevB.72.012402
36. M.V. Mostovoy, D.I. Khomskii, Phys. Rev. Lett. (2004). doi:10.1103/PhysRevLett.92.167201; Phys. Rev. Lett. (2002). doi:10.1103/PhysRevLett.89.227203
37. A. Daoud-Aladine, J. Rodríguez-Carvajal, L. Pinsard-Gaudart, M.T. Fernández-Díaz, A. Revcolevschi, Phys. Rev. Lett. (2002). doi:10.1103/PhysRevLett.89.097205
38. E. Saitoh, S. Okamoto, K.T. Takahashi, K. Tobe, K. Yamamoto, T. Kimura, S. Ishihara, S. Maekawa, Y. Tokura, Nature (2001). doi:10.1038/35065547
39. S. Jandl, J. Laverdi re, A.A. Mukhin, V.Yu. Ivanov, A.M. Balbashov, Physica B. (2006). doi:10.1016/J.physb.2006.01.008

40. K.P. Schmidt, M. Grüninger, G.S. Uhrig, Phys. Rev. B. (2007). doi:10.1103/PhysRevB.76.075108
41. K. Kikoin, O. Entin-Wohlman, V. Fleurov, A. Aharony, J. Magn. Mat. (2003). doi:10.1016/J.jmmm.2003.12.1066
42. Y. Tanaka, A.Q.R. Baron, Y.J. Kim, K.J. Thomas, J.P. Hill, Z. Honda, F. Iga, S. Tsutsui, S. Ishikawa, C.S. Nelson, New J. Phys. (2004). doi: 10.1088/1367-2360/6/1/161
43. A. Yamasaki, F. Feldbacher, Y.F. Yang, O.K. Andersen, K. Held, Phys. Rev. Lett. (2006). doi: 10.1103/PhysRevLett.96.166401
44. Y.F. Yang, K. Held, Phys. Rev. B. (2007). doi: 10.1103/PhysRevB.76.212401
45. A.B. Harris, T. Yildirim, A. Aharony, O. Entin-Wohlman, I. Korenblit, Phys. Rev. B. (2004). doi: 10.1103/PhysRevB.69.035107
46. A. Aharony, O. Entin-Wohlman, I.Y.a. Korenblit, A.B. Harris, T. Yildirim, New J. Phys. (2005). doi:10.1088/1367-2630/7/1/049
47. D.V. Efremov, J.v.d. Brink, D.I. Khomskii, Nat. Mater. (UK). (2004). doi:10.1038/nmat1236
48. D.V. Efremov, J.v.d. Brink, D.I. Khomskii, Physica B. (2005). doi:10.1016/j.physb.2005.01.440
49. K.I. Kugel, K.I., Sboyshakov, A.O., Khomskii, D.I., J. Supercond. Nov. Magn. (2009). doi:10.1007/s10948-008-0380-6
50. D.I. Khomskii, Physics. (2009). doi:10.1103/Physics.2.20; J. Magn. Magn. Mater. (Netherlands) (2006). doi:10.1016/j.jmmm.2006.01.238
51. I.B. Bersuker, Ferroelectrics **164**, 75–100 (1995)
52. J.J. Borrás-Almenar, J.M. Clemente-Juan, E. Coronado, E. Palii, A.V., Tsukerblat, B.S., Chem. Phys. (2000). doi:10.1016/S0301-0104(00)00029-X
53. J.J. Borrás-Almenar, J.M. Clemente-Juan, E. Coronado, A.V. Palii, B.S. Tsukerblat, Chem. Phys. (2001). doi:10.1016/S0301-0104(01)00497-9; Chem. Phys. (2001). doi:10.1016/S0301-0104(01)00498-0
54. J.J. Borrás-Almenar, J.M. Clemente-Juan, E. Coronado, A.V. Palii, B.S. Tsukerblat, J. Solid St. Chem. (2001). doi:10.1006/jssc.2001.9156
55. B.S. Tsukerblat, S. Klokishner, A. Palii, *Jahn-Teller Effect in molecular magnetism: an overview*. Present book, (Springer, Heidelberg, 2009)
56. A.V. Palii, O.S. Reu, S.M. Ostrovsky, S.I. Klokishner, B.S. Tsukerblat, Z.M. Sun, J.G. Mao, A.V. Prosvirin, H.H. Zhao, K.R. Dunbar, J. Am. Chem Soc. (2008). doi:10.1021/J. a8050052
57. W.J.A. Maaskant, W.G. Haije, J. Phys. C, Solid State Phys. (1986). doi:10.1088/0022-3719/19/27/007
58. P. Ghigna, A. Carollo, G. Flor, L. Malavasi, G.S. Peruga, J. Phys. Chem B. **109**, 4365–4372 (2005)
59. I.B. Bersuker, *Electronic Structure and Properties of Transition Metal Compounds*. (Wiley, New York, 1996)
60. S. Muramatsu, N. Sakamoto, J. Phys. Soc. Jpn. (1978). doi:10.1143/J. PSJ..44.1640
61. F.S. Ham, in *Electron Paramagnetic Resonance*, ed. by S. Gecshwind (Plenum Press, New York, London, 1972), pp. 1–119
62. M.C.M. O'Brien, Proc. R. Soc. A. **281**, 323–339 (1964)
63. K.H. Höck, G. Schröder, H. Thomas, Physik B Cond Matter. (1978). doi:10.1007/BF01321093
64. W.J. Crama, W.J.A. Maaskant, Physica B & C. (1983). doi:10.1016/0378-4363(83)90145-6
65. A.J. Millis, Phys. Rev. B. (1996). doi:10.1103/PhysRevB.53.8434; also, see M.A. Ahmed, G.A. Gehring, Phys. Rev. B (2006). doi:10.1103/PhysRevB.74.014420

# Frustration Effect in Strongly Correlated Electron Systems with Orbital Degree of Freedom

Sumio Ishihara

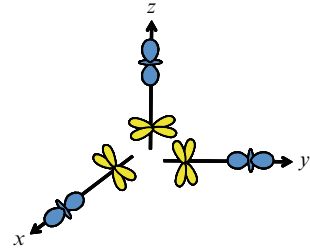
**Abstract** In a solid with orbital degree of freedom, an orbital configuration does not minimize simultaneously bond energies in equivalent directions. This is a kind of frustration effect which exists intrinsically in orbital degenerate system. We review in this paper the intrinsic orbital frustration effects in Mott insulating systems. We introduce recent our theoretical studies in three orbital models, i.e. the cubic lattice orbital model, the two-dimensional orbital compass model and the honeycomb lattice orbital model. We show numerical results obtained by the Monte-Carlo simulations in finite size systems, and introduce some non-trivial orbital states due to the orbital frustration effect.

## 1 Introduction

Orbital degree of freedom in strongly correlated electron system is one of the attractive and unresolved themes in recent solid state physics [1, 2]. Orbital implies the anisotropy of the electronic cloud and the electronic wave function in the transition metal ions, corresponding to the multiple moment. This degree of freedom often governs the magnetic, optical and transport properties in a solid with strong electron correlation. One of the well studied materials is the manganites with perovskite structure,  $R_{1-x}A_x\text{MnO}_3$  ( $R$ : a rare-earth ion,  $A$ : an alkaline-earth ion). At the concentration  $x = 0.5$ , an equal amount of  $\text{Mn}^{3+}$  and  $\text{Mn}^{4+}$  ions coexists, and the two ions spatially ordered. Since the electron configuration of a  $\text{Mn}^{3+}$  is  $(e_g)^1(t_{2g})^3$ , this ion has the  $e_g$  orbital degree of freedom. In the charge ordered phase in manganites, the orbital also shows the long range order where the  $d_{3x^2-r^2}$ - and  $d_{3y^2-r^2}$ -type orbitals are aligned alternately in the  $ab$  plane. This orbital order controls the optical anisotropy and the antiferromagnetic order. It is supposed that this charge/orbital orders and their melting by an applying magnetic field are responsible for the famous colossal magnetoresistance phenomena.

Although degenerate orbitals in an isolated ion are partially lifted in a molecule and in a solid, the degeneracy often partially remains in a crystal lattice with high symmetry. In a molecule, this degeneracy is lifted by ion distortions, i.e. the Jahn-Teller distortion. However, in a crystal lattice, an infinite number of degrees of

**Fig. 1** A schematic view of favored orbital configurations and the orbital frustration effect



freedom exist, and several interactions compete with each other. In particular, there are some equivalent bonds in a crystal. One orbital configuration which minimizes a bond energy in one direction is not always favored for other bond directions. Therefore, the bond energies in all directions are not able to be minimized simultaneously. This situation is schematically shown in Fig. 1. This is a certain kind of frustration, although this is not the usual geometrical frustration seen in, for example, the antiferromagnetic Heisenberg model in a triangular lattice. We term this the intrinsic orbital frustration effect. This effect provides several non-trivial phenomena in correlated system with the orbital degree of freedom.

In this paper, we review recent our theoretical studies in a viewpoint of the orbital frustration effect [3–7]. We introduce this effect in three different orbital models, i.e. the orbital model in a three-dimensional cubic lattice, that in a two-dimensional square lattice and that in a honeycomb lattice. We show numerical results obtained by the Monte–Carlo simulations in finite size systems. In some cases, non-trivial orbital states due to the orbital frustration effect are presented.

In Sect. 2, the microscopic model which describes the inter-site orbital interactions are introduced. In Sect. 3, the numerical study in the orbital model in a cubic lattice is presented. The non-trivial orbital states in the two-dimensional orbital compass model and the honeycomb lattice orbital model are introduced in Sects. 4 and 5, respectively. The last section is devoted to the summary of this paper.

## 2 Model

We start from the model Hamiltonian to describe the strongly correlated electron system with the  $e_g$  orbital degree of freedom. A system of the present interest is a Mott insulator where one electron occupies one of the doubly degenerate orbitals at each site in a simple cubic lattice. The doubly degenerate orbital degree of freedom is represented by the pseudo-spin operator with an amplitude of  $1/2$  defined by

$$\mathbf{T}_i = \frac{1}{2} \sum_{s\gamma\gamma'} c_{is\gamma}^\dagger (\boldsymbol{\sigma})_{\gamma\gamma'} c_{is\gamma'}, \quad (1)$$

where  $c_{is\gamma}$  is the electron annihilation operator at site  $i$  with spin  $s(=\uparrow, \downarrow)$ , and orbital  $\gamma(=d_{3z^2-r^2}, d_{x^2-y^2})$ , and  $\boldsymbol{\sigma}$  are the Pauli matrices. The angle  $\theta$  of  $\mathbf{T}_i$  in the  $T_z - T_x$  plane corresponds to a shape of the electronic cloud.

It is known that two dominant inter-site interactions between the orbitals in solids are the superexchange-type and the cooperative Jahn–Teller type interactions. The former is attributed to the virtual exchange of an electron under the strong on-site Coulomb interaction [8–11]. The explicit form of this interaction is given by

$$\begin{aligned} \mathcal{H}_{\text{exc}} = & -2J_1 \sum_{\langle ij \rangle} \left( \frac{3}{4} + \mathbf{S}_i \cdot \mathbf{S}_j \right) \left( \frac{1}{4} - \tau_i^l \tau_j^l \right) \\ & -2J_2 \sum_{\langle ij \rangle} \left( \frac{1}{4} - \mathbf{S}_i \cdot \mathbf{S}_j \right) \left( \frac{3}{4} + \tau_i^l \tau_j^l + \tau_i^l + \tau_j^l \right), \end{aligned} \quad (2)$$

where  $J_1$  and  $J_2$  are the positive coupling constants with the relation  $J_1 > J_2$ , and  $\mathbf{S}_i$  is the spin operator with an amplitude of  $1/2$ . We introduce the new orbital operator defined by

$$\tau_i^l = \cos\left(\frac{2\pi n_l}{3}\right) T_i^z + \sin\left(\frac{2\pi n_l}{3}\right) T_i^x, \quad (3)$$

where  $l (= x, y, z)$  indicates the bond direction connecting sites  $i$  and  $j$ , and  $(n_x, n_y, n_z) = (1, 2, 3)$ . This Hamiltonian is derived from the two-orbital Hubbard model where the intra-orbital Coulomb interaction  $U$ , the inter-orbital one  $U'$ , the Hund coupling  $I$ , and the electron transfer between NN sites  $t_{ij}^{\gamma\gamma'}$  are considered. Equation (2) is derived by the second-order perturbational calculation with respect to the electron transfer integral. The two terms in (2) correspond to the different two intermediate states in the perturbational processes. The first (second) term favors the ferromagnetic (antiferromagnetic) spin alignment with the antiferro-type (ferro-type) orbital one.

The cooperative Jahn–Teller type interaction is obtained by the orbital-lattice coupled model [12, 13]. Let us consider the Hamiltonian with the Jahn–Teller coupling  $g$ , the kinetic energy and the lattice potential for the Jahn–Teller phonon mode, the orbital-strain interaction, and the elastic-strain energy. The Jahn–Teller distortion mode  $Q_i$  around a metal site  $i$  is represented by the Jahn–Teller phonon coordinates  $q_{\mathbf{k}}$ . By introduce the canonical transformation for  $q_{\mathbf{k}}$ , the orbital and lattice degrees of freedom are separated. The final form of the interaction between the inter-site orbitals given by

$$\mathcal{H}_{\text{JT}} = J_{\text{JT}} \sum_{\langle ij \rangle} \tau_i^l \tau_j^l, \quad (4)$$

where  $J_{\text{JT}}$  is the positive coupling constant. Here we consider the perovskite crystal lattice and introduce the spring constant between the NN ligand and metal ions. Distortions of the ligand ions are assumed to be parallel to the NN ligand-metal bond. We also assume that the phonon coordinate and its canonical conjugate momentum  $p_{\mathbf{k}}$  are commutable with each other. Since a ligand ion is common for two NN metal ions in the perovskite crystal, this interaction favors the antiferro-type orbital alignment between the NN orbitals.

It is often useful to consider the orbital only model where we focus on the orbital degree of freedom in the ferromagnetic or paramagnetic spin states. By using the relation  $\sum_l \tau_i^l = 0$ , a sum of (2) and (4) is given by

$$\begin{aligned}
 \mathcal{H}_O &= J \sum_{\langle ij \rangle} \tau_i^l \tau_j^l \\
 &= J \sum_{\langle ij \rangle_z} T_i^z T_j^z \\
 &\quad + J \sum_{\langle ij \rangle_x} \left[ -\frac{1}{2} T_{iz} + \frac{\sqrt{3}}{2} T_{ix} \right] \left[ -\frac{1}{2} T_{jz} + \frac{\sqrt{3}}{2} T_{jx} \right] \\
 &\quad + J \sum_{\langle ij \rangle_y} \left[ -\frac{1}{2} T_{iz} - \frac{\sqrt{3}}{2} T_{ix} \right] \left[ -\frac{1}{2} T_{jz} - \frac{\sqrt{3}}{2} T_{jx} \right], \quad (5)
 \end{aligned}$$

with  $J = 3J_1/4 - J_2/2 + J_T$ . A symbol  $\langle ij \rangle_l$  implies a NN pair along the direction  $l$ . This model is termed the  $e_g$  orbital model in this paper. Some characteristics in this orbital model are listed below: (1) The orbital interaction is represented by the bond dependent operator  $\tau_i^l$ . That is, the interaction explicitly depends on the bond direction. Since  $J$  is positive, the different kinds of antiferro-type orbital configuration are favored in the three directions in the cubic lattice. A schematic view of the interaction is shown in Fig. 1. As mentioned in the previous section, it is impossible to minimize the bond energies along the three directions simultaneously. This implies a frustration effect which intrinsically exists in the orbital system in solid crystals. (2) The interaction does not have a continuous symmetry which is seen in the Heisenberg and XY spin models. (3) There is no macroscopic conserved quantity, such as the  $z$  component of the total spin angular momentum in the Ising model. The Hamiltonian is invariant under the simultaneous transformations of the  $120^\circ$  rotation in the pseudo-spin  $T_x - T_z$  plane and the permutation of the Cartesian coordinate in the real space.

Although the orbital model in (5) is derived in a simple cubic lattice, it is shown that, in general, the several orbital models are represented in similar forms of the Hamiltonian. This will be shown, in the following sections, for the orbital compass model in a two dimensional square lattice and the honeycomb lattice orbital model.

### 3 Cubic Lattice Orbital Model

First we examine the  $e_g$  orbital model in a simple cubic lattice introduced in the previous section. We introduce the Fourier transform of the orbital interaction and the orbital model in the momentum space,

$$\mathcal{H}_O = \sum_{\mathbf{k}} \psi_{\mathbf{k}}^t E(\mathbf{k}) \psi_{\mathbf{k}}, \quad (6)$$

**Fig. 2** Dispersion relation of the orbital interaction in (7) represented in the Brillouin zone for a simple cubic lattice

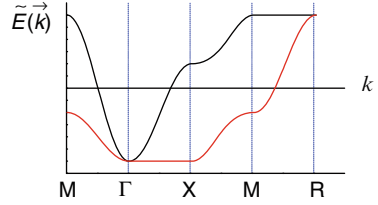
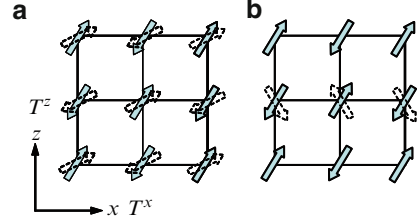


**Fig. 3** Schematic views of the degenerate states in the classical ground state. Arrows represent the orbital pseudo-spins in the  $T_x - T_z$  plane. (a) and (b) correspond to the type-I and II degenerate states (see text), respectively



where  $\psi_{\mathbf{k}} = [T_{\mathbf{k}}^z, T_{\mathbf{k}}^x]$  are the Fourier transforms of the orbital pseudo-spins. By diagonalizing the  $2 \times 2$  matrix  $E_{\mathbf{k}}$ , we obtain the following two eigen-values [14, 15]:

$$\tilde{E}(\mathbf{k})/J = c_x + c_y + c_z \pm \sqrt{c_x^2 + c_y^2 + c_z^2 - c_x c_y - c_y c_z - c_z c_x}, \quad (7)$$

where  $c_l = \cos ak_l$  with the lattice constant  $a$ . This dispersion relation is shown in Fig. 2. In the conventional antiferromagnetic Heisenberg model,  $E(\mathbf{k})/J = c_x + c_y + c_z$  which has its maximum point at  $\mathbf{k} = (\pi/a, \pi/a, \pi/a)$  indicating the antiferromagnetic long range order at this momenta. In (7),  $\tilde{E}(\mathbf{k})$  takes its maxima along  $\mathbf{k} = (\pi/a, \pi/a, \pi/a)$  (R-point) to  $(0, \pi/a, \pi/a)$  (M-point), and along other two equivalent lines. This result implies that, when we consider the classical ground state, a macroscopic number of orbital states are degenerate.

This degeneracy is classified into the following two types [16, 17]: (I) Let us consider a staggered-type orbital alignment with two sublattices, termed A and B, and momentum  $(\pi, \pi, \pi)$ . In the classical ground state, the pseudo-spin angles in the sublattices are given by  $(\theta_A, \theta_B) = (\theta, \theta + \pi)$  with any value of  $\theta$ . (II) Consider an orbital ordered state with the momentum  $(\pi, \pi, \pi)$  and  $(\theta_A, \theta_B) = (\theta_0, \theta_0 + \pi)$ , and focus on one direction in three-dimensional simple-cubic lattice, e.g. the  $z$  direction. The mean-field energy is preserved by changing all pseudo-spin in each layer perpendicular to the  $z$  axis independently as  $(\theta_0, \theta_0 + \pi) \rightarrow (-\theta_0, -\theta_0 - \pi)$ . These are schematically shown in Fig. 3. To determine the stable orbital configurations among them or examine a possibility of disordered states, further analyses beyond the mean-field approximation are necessary. This phenomenon originates from the directional nature of the orbital degree of freedom; the inter-site orbital interaction explicitly depends on the bond direction connecting the sites. When thermal and quantum fluctuations are taken into account, this degeneracy is lifted, and the long



range order appears [16–19]. This is the so-called order-by-fluctuation mechanism and has been studied by utilizing the spin wave analyses.

Here we demonstrate the degeneracy lifting and appearance of the long-range orbital order by the classical Monte–Carlo method in a finite size cluster system [3, 7]. We calculate the staggered orbital correlation function

$$M_{\text{OO}} = \frac{1}{N} \left\langle \left\{ \sum_i (-1)^i \mathbf{T}_i \right\}^2 \right\rangle^{1/2}, \quad (8)$$

and the angle correlation function

$$M_{\text{ang}} = \frac{1}{N} \left\langle \left\{ \sum_i (-1)^i \cos 3\theta_i \right\}^2 \right\rangle^{1/2}, \quad (9)$$

where  $\langle \dots \rangle$  represents the Monte–Carlo average. The orbital correlation at the momentum  $\mathbf{Q} = (\pi, \pi, \pi)$  is represented by  $M_{\text{OO}}$ , and the angle correlation  $M_{\text{ang}}$  takes one, when the orbital pseudo-spin angle is  $2\pi n/3$  with an integer number  $n$ . Therefore,  $M_{\text{OO}}$  and  $M_{\text{ang}}$  are monitors for lifting of the type-(II) and (I) degeneracies, respectively. Temperature dependences of  $M_{\text{OO}}$  for various size  $L$  are shown in Fig. 4a. With decreasing temperature, calculated results for all  $L$  show a sharp increasing around  $T/J = 0.35$ . This increasing becomes sharper with the system size  $L$ . An extrapolated value of  $M_{\text{OO}}$  toward  $T = 0$  is close to 0.5 which indicates that the type-(II) degeneracy is lifted and the orbital order with the momentum  $(\pi, \pi, \pi)$  is realized. Temperature dependences of  $M_{\text{ang}}$  presented in Fig. 4b increase monotonically toward one in the low temperature limit. Therefore, the type-(I) degeneracy is also lifted and the pseudo-spin angle is fixed. Both results indicate the long-range orbital order where the momentum is  $(\pi, \pi, \pi)$ , and the pseudo-spin angles are  $(\theta_A, \theta_B) = (\theta_0, \theta_0 + \pi)$  with  $\theta_0 = 2\pi n/3$ .

The temperature at which  $M_{\text{OO}}$  and  $M_{\text{ang}}$  change abruptly is around  $T/J = 0.33$  corresponding to the orbital ordering temperature  $T_{\text{OO}}$ . In more detail, this phase transition is determined by the finite-size scaling for the correlation length. The scaling relation for  $\xi$  is

$$\xi = LF \left[ L^{1/\nu} \{T - T_{\text{OO}}\} \right], \quad (10)$$

where  $\nu$  is the critical exponent for correlation length, and  $F$  is the scaling function. The correlation lengths  $\xi/L$  for various sizes cross with each other at  $T_{\text{OO}}$ . In Fig. 5, we plot  $\xi/L$  as a function of  $L^{1/\nu}[T - T_{\text{OO}}]$ . The scaling analyses work quite well for  $L = 10, 12$ , and  $14$ . The orbital ordering temperature  $T_{\text{OO}}$  and the critical exponent  $\nu$  are obtained as  $T_{\text{OO}}/J = 0.344 \pm 0.002$  and  $\nu = 0.69 - 0.81$ , although statistical errors are not enough to obtain the precise value of  $\nu$ .

**Fig. 4** (a) Temperature dependence of the orbital correlation function  $M_{OO}$ , and (b) that of the orbital angle function  $M_{ang}$  for several system sizes obtained by the classical Monte-Carlo simulation [3, 7]. The system size is given by  $L^3$

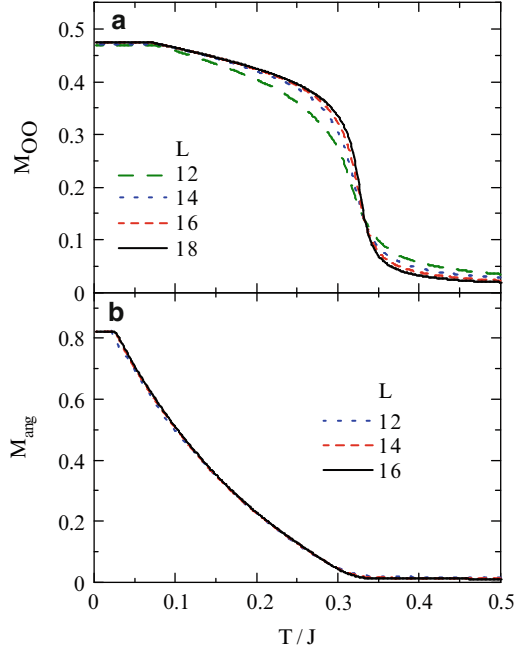
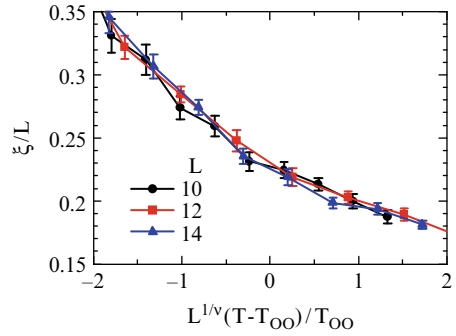


**Fig. 5** Scaling plot of the correlation length  $\xi$  for the staggered orbital correlation obtained by the classical Monte-Carlo simulation [3, 7]



## 4 Orbital Compass Model

As a different kind of orbital models with the intrinsic frustration effect, we introduce, in this section, the orbital compass model in the two-dimensional square lattice [16, 17, 20–22]. This model is given by

$$\mathcal{H}_{compass} = -2J \sum_{i,\ell=(x,z)} T_i^\ell T_{i+\ell}^\ell, \quad (11)$$

**Fig. 6** Dispersion relation of the orbital interaction of the two-dimensional orbital compass model in (11) represented in the Brillouin zone for the square lattice

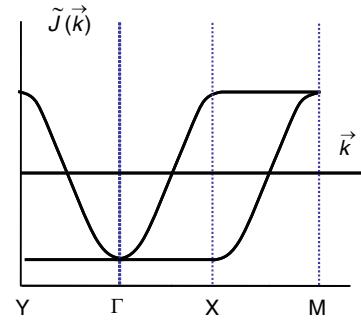
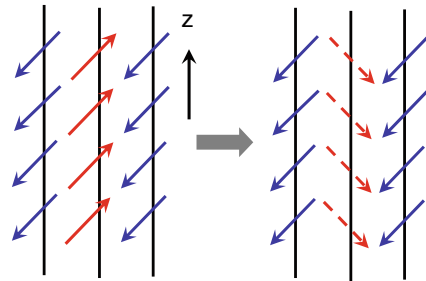


**Fig. 7** A schematic view of the symmetry operation under which the Hamiltonian is invariant



where  $J$  is defined to be positive. Along the  $x(z)$  direction in a two dimensional square lattice, the  $x(z)$  component of the pseudo-spin is concerned. This form of the interaction is similar to the  $e_g$  orbital model introduced in (5), when  $\tau^l$  is replaced by  $T^l$ . The momentum representation in the orbital interaction is shown in Fig. 6. The Fourier transformation of the effective interaction,  $\tilde{J}(\mathbf{k})$ , takes its maxima along the M-X line in the Brillouin zone as seen in the  $e_g$  orbital model in a cubic lattice. Thus, the orbital compass model is recognized as a two-dimensional version of the  $e_g$  orbital model in a three-dimensional cubic lattice. This model is also studied recently from the view point of the quantum computer and information.

This Hamiltonian is invariant under the following two-symmetry operations [16, 23]; (1) The global four-fold symmetry: the pseudo-spins at all sites and the crystal lattice are rotated by  $\pi/2$ , simultaneously, with respect to the  $y$  axis. (2) The local symmetry at each column and row: the  $z(x)$ -component of all pseudo-spins at each column (row) along the  $z(x)$  axis are flipped, i.e.  $T_{r_x, r_z}^{z(x)} \rightarrow -T_{r_x, r_z}^{z(x)}$  for each  $r_x$  ( $r_z$ ). This is schematically shown in Fig. 7.

Because of this symmetry, it is proven that the conventional long-range order is not realized. In spite of this, a kind of orbital order, termed the directional order [20, 23–25] is realized at finite temperature. A schematic picture of the directional order is presented in Fig. 8. In a one-dimensional chain along the  $z$  direction, the  $z$  component of the pseudo-spin is aligned ferromagnetically. However, there is no correlation between the chains. A similar order is possible along the  $x$  direction. This directional order is identified by the following order parameter,

**Fig. 8** A schematic view of the directional order

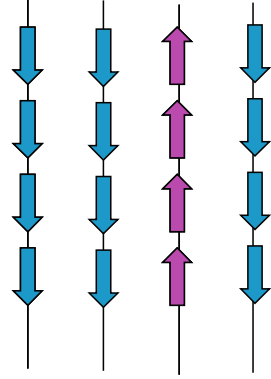
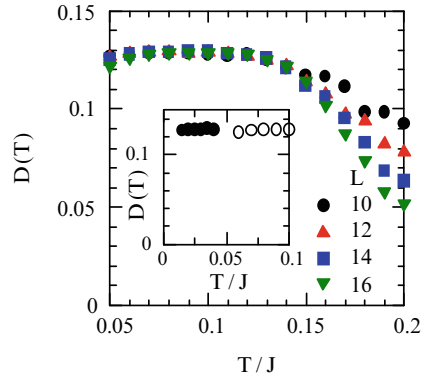


**Fig. 9** Temperature dependence of the directional order parameter obtained by the quantum Monte-Carlo simulation [4]



$$D = \frac{1}{N} \sum_i \left( T_i^x T_{i+\hat{x}}^x - T_i^z T_{i+\hat{z}}^z \right). \quad (12)$$

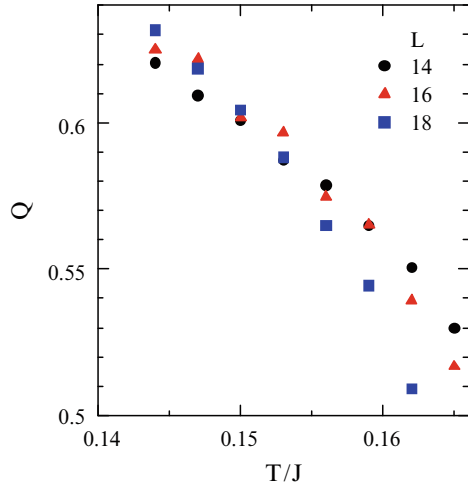
We examine the orbital compass model by utilizing the quantum Monte-Carlo method is a finite-size cluster [4]. The simulations have been performed on a square lattice of  $L \times L$  sites with periodic-boundary conditions.

First, we note that the site-diagonal order parameter

$$M = \frac{1}{N} \sqrt{\left\langle \left( \sum_{\mathbf{r}} \mathbf{T}_{\mathbf{r}} \right)^2 \right\rangle}, \quad (13)$$

decreases with increasing  $L$ . This is in contrast to the  $e_g$  orbital model introduced in the previous section. Temperature dependence of  $\sqrt{\langle D^2 \rangle} (\equiv D(T))$  for several  $L$  is presented in Fig. 9. Around  $T/J = 0.17$ ,  $D(T)$  grows with decreasing  $T$ , and is saturated to about 0.13 below  $T/J = 0.12$ . With increasing  $L$ , this dependence becomes steep, but the saturated value of  $D(T)$  at low  $T$  does not change much. We also present the temperature dependence of the Binder cumulant  $Q$  in Fig. 10. The

**Fig. 10** Temperature dependence of the Binder cumulant for several system size obtained by the quantum Monte–Carlo simulation [4]



Binder cumulant is defined by

$$Q = 1 - \frac{\langle D^4 \rangle}{3\langle D^2 \rangle^2}. \quad (14)$$

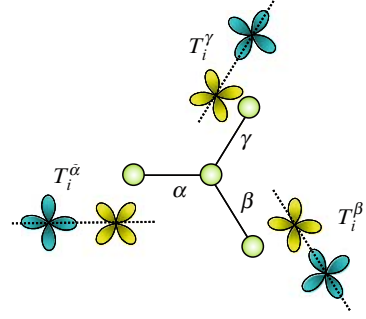
From this definition, we expect that, in the limit of  $L = \infty$ ,  $Q = 0$  in the high temperature limit, and  $Q = 2/3$  in the low temperature limit. It is known that  $Q - T$  curves for several system size  $L$  cross at the critical temperature. Thus, this cumulant is adopted to determine the ordering temperature of the directional order from the finite-size scaling analyses. The  $Q - T$  curves for the several system sizes cross around  $T/J = 0.15$  corresponding to the temperature where  $D(T)$  grows. That is, the directional order is realized in the quantum orbital compass model and  $T_{\text{DO}} = 0.150 \pm 0.003$ . The saturated value of  $D$  at low  $T$  is about half of the classical value of  $1/4$ . This reduction is much stronger than that in the quantum antiferromagnetic Heisenberg model with  $S = 1/2$  in a square lattice. This is due to large quantum fluctuations which induce correlations between columns or rows.

## 5 Honeycomb Lattice Orbital Model

In this section, we introduce another interesting orbital model with the frustration effect, termed the honeycomb lattice orbital model. We consider the model where the doubly degenerate orbitals, e.g. the  $d_{x^2-y^2}$  and  $d_{xy}$  orbitals, which are described by the pseudo-spin operator  $\mathbf{T}_i$ , are located at each site in a two dimensional honeycomb lattice. The explicit form of the model Hamiltonian is given by

$$\mathcal{H}_{\text{honeycomb}} = -J \sum_{i \in A} \left( \tau_i^\alpha \tau_{i+\mathbf{e}_\alpha}^\alpha + \tau_i^\beta \tau_{i+\mathbf{e}_\beta}^\beta + \tau_i^\gamma \tau_{i+\mathbf{e}_\gamma}^\gamma \right), \quad (15)$$

**Fig. 11** A schematic view of the orbital interaction in a two-dimensional honeycomb lattice



where  $\mathbf{e}_\eta$  is a vector connecting the NN sites along the direction  $\eta$ ,  $\sum_{i \in A}$  represents a sum of sites on the sublattice A, and  $J$  is the positive exchange constant. For the three-kinds of NN bonds,  $\eta = (\alpha, \beta, \gamma)$ , in a honeycomb lattice, we introduce the new pseudo-spin operator as

$$\tau_i^\eta = -\sin\left(\frac{2\pi n_\eta}{3}\right) T_i^z + \cos\left(\frac{2\pi n_\eta}{3}\right) T_i^x. \quad (16)$$

A numerical factor  $n_\eta$  is defined as  $(n_\alpha, n_\beta, n_\gamma) = (0, 1, 2)$ . The operator  $\tau_i^\eta$  represents a projection component of  $\mathbf{T}_i$  on the  $\eta$  bond direction. A schematic view of this interaction Hamiltonian is presented in Fig. 11. This Hamiltonian is rewritten as a following simple form

$$\mathcal{H}_{\text{honeycomb}} = \frac{J}{2} \sum_{i \in A, \eta} \left( \tau_i^\eta - \tau_{i+\mathbf{e}_\eta}^\eta \right)^2 - \frac{3}{2} J \sum_{i \in A} (T_i^{x2} + T_i^{z2}). \quad (17)$$

The second term is  $-3JN/16$ , when  $\mathbf{T}_i$  is a two-dimensional classical spin, and is  $-3JN/8$  in the quantum-spin case. A total number of sites is  $N$ . This model is proposed as a orbital state for the layered iron oxide, [5, 6, 26], and is also recently proposed in study of the optical lattice [27–29]. A similar orbital model in a honeycomb lattice termed the Kitaev model is recently well examined. [30, 31]

Let us introduce the Fourier transformation for the orbital pseudo-spin operator. The Hamiltonian (15) is represented in the momentum space, [5, 27]

$$\mathcal{H} = \psi^\dagger(-\mathbf{k}) \hat{J}(\mathbf{k}) \psi(\mathbf{k}). \quad (18)$$

We introduce a four-component vector defined as

$$\psi(\mathbf{k}) = [T_A^x(\mathbf{k}), T_A^z(\mathbf{k}), T_B^x(\mathbf{k}), T_B^z(\mathbf{k})], \quad (19)$$

and a  $4 \times 4$  matrix  $\hat{J}(\mathbf{k})$ . We obtain the eigen values of  $\hat{J}(\mathbf{k})$  are  $\pm 3J/4$  and  $\pm J [3 + 2 \cos \mathbf{k} \cdot \mathbf{a} + 2 \cos \mathbf{k} \cdot \mathbf{b} + 2 \cos \mathbf{k} \cdot (\mathbf{a} - \mathbf{b})]^{1/2} / 4$  where  $\mathbf{a}$  and  $\mathbf{b}$  are the primitive translation vectors. Numerical plot of  $\hat{J}(\mathbf{k})$  is presented in Fig. 12. The

**Fig. 12** Dispersion relation of the Fourier transformation of the orbital interaction in the honeycomb lattice orbital model

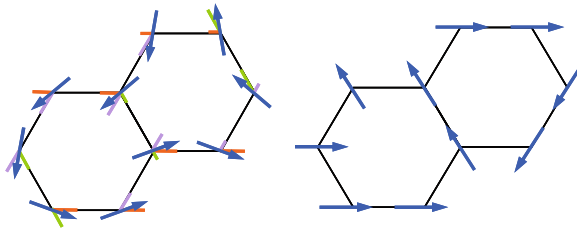
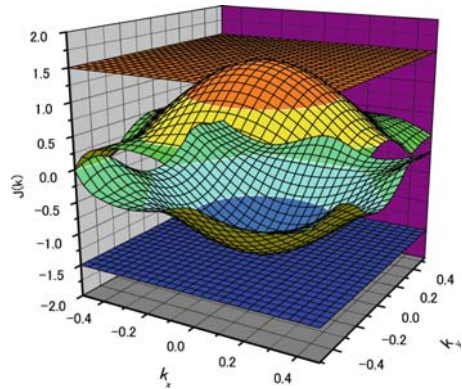


**Fig. 13** Two of the pseudo-spin configurations in the classical ground states

lowest eigen value is a momentum independent flat band of  $-3J/4$ . That is, the effective dimensionality for the lowest state is zero, and, in the classical ground state, stable orbital structures are not determined uniquely due to large fluctuation. The second eigen value touches the lowest band at the point  $\Gamma$ .

Orbital structure in the classical ground state is obtained from the Hamiltonian in (17). The ground state energy is  $-3J/16$ , when the pseudo-spins satisfy the following condition in all NN bonds; [5, 28, 29]

$$\tau_i^\eta = \tau_{i+\mathbf{e}_\eta}^\eta. \quad (20)$$

This relation implies that the projection components of pseudo-spins are equal with each other for all NN bonds. There is a macroscopic number of orbital structures which satisfy this condition. Two of them are shown in Fig. 13.

Now we introduce the numerical results obtained by the classical Monte–Carlo simulation [6]. First we present, in Fig. 14, temperature dependence of the specific heat  $C(T)$  for several system sizes. There is a sharp peak around  $0.005 - 0.01J$  which depends on system size. With increasing a system size, the peak shifts to a lower temperature side and becomes sharp. The peak position is denoted as  $T_O$  from now on. It is worth noting that this value of  $T_O$  is much smaller than the mean-field ordering temperature  $3J/8$ . To elucidate the orbital state below  $T_O$ , we calculate the

**Fig. 14** Temperature dependence of the specific heat for several cluster sizes obtained in the classical Monte–Carlo simulation [6]

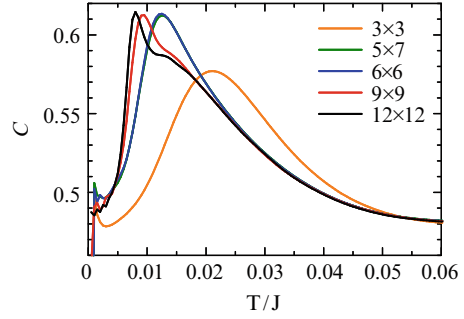
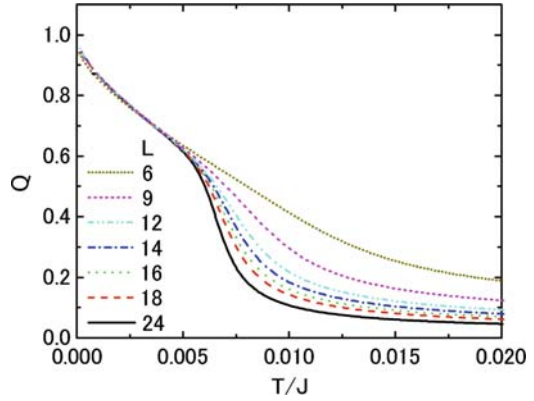


**Fig. 15** Temperature dependence of the angular parameter for several cluster sizes obtained in the classical Monte–Carlo simulation [6]



correlation functions for the pseudo-spin defined by

$$S^{lm}(\mathbf{k}) = \frac{4}{N^2} \sum_{ij} \langle T_i^l T_j^m \rangle e^{i\mathbf{k} \cdot (\mathbf{r}_i - \mathbf{r}_j)}, \quad (21)$$

where  $l$  and  $m$  take  $x$  and  $z$ , and  $\mathbf{r}_i$  is a position of site  $i$ . We calculate  $S^{zz}(\mathbf{k})$ 's for all possible momenta  $\mathbf{k}$  in a cluster. With increasing  $N$ , the values of  $S^{lm}(\mathbf{k})$  decrease rapidly, and in a  $2 \times 6 \times 6$  cluster, all  $S^{lm}(\mathbf{k})$ 's are less than 3% of their maximum value. We conclude that, below  $T_0$ , there are no conventional long-range order corresponding to the correlation functions given in (21).

Instead of the conventional orbital order, there is a remarkable enhancement of a physical parameter  $q$  for the pseudo-spin angle  $\theta_i$  defined by

$$q = \frac{1}{N} \sum_i \cos 3\theta_i. \quad (22)$$

When the angle  $\theta_i$  takes one of the three angles  $2n\pi/3$  [ $(2n+1)\pi/3$ ],  $q = 1$  ( $-1$ ). In Fig. 15, we plot the temperature dependence of the correlation function of  $q$  defined by



**Fig. 16** Two pseudo-spin configurations where the honeycomb lattice is covered by the NN bonds with the minimum bond energy

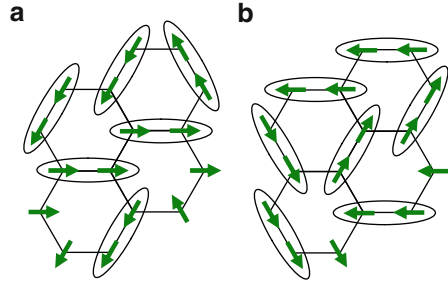
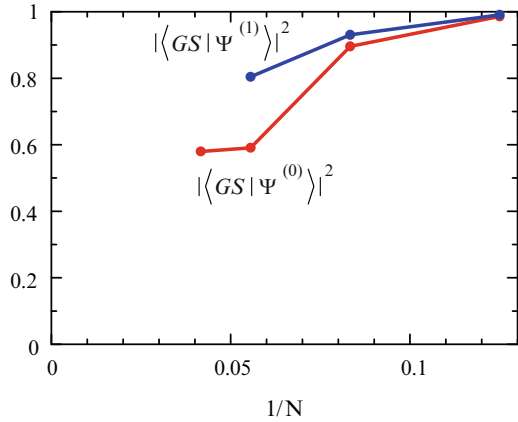


**Fig. 17** Cluster size dependence of the overlap integral between the ground state wave function  $|GS\rangle$  obtained by the Lanczos method and the trial wave function [6]. In the variational wave function  $|\Psi^{(1)}\rangle$ , the variational parameters are set to be equal, and in  $|\Psi^{(0)}\rangle$  the variational parameters are optimized



$$Q = \sqrt{\langle q^2 \rangle}. \quad (23)$$

This starts to increase around  $T_O$  and is saturated to the maximum value at the low temperature limit. With increasing the system size  $N$ ,  $Q$  abruptly increases around  $T_O$ . Stability of the  $q = \pm 1$  states is attributed to the low-lying excited states around the  $q = \pm 1$  states. The high density of the low-lying fluctuations around  $q = \pm 1$  states contributes to the entropy gain and stabilizes the  $q = \pm 1$  states at finite temperature.

Next we introduce the analyses of the Hamiltonian in (15) where the pseudo-spin is treated as a quantum spin operator with a magnitude of  $S = 1/2$  [6]. We use the exact diagonalization technique based on the Lanczos algorithm. The correlation functions defined in (21) are calculated for several momenta and system sizes. With increasing  $N$ ,  $S^{lm}(\mathbf{k})$ 's become almost momentum independent and all of the values are less than 25% of the maximum. Thus, the conventional long-range order characterized by the correlation functions does not exist, as we have shown in the classical model. We consider the trial pseudo-spin states where a honeycomb lattice is covered by the NN bonds with the minimum bond energy. Some examples are shown in Fig. 16. We construct the wave function as a linear combination of these states. This is given by

$$|\Psi\rangle = \mathcal{N} \sum_l \mathcal{A}_l |\psi_l\rangle, \quad (24)$$

where  $\mathcal{N}$  is a normalized factor,  $\mathcal{A}_l$  are variational parameters, and  $|\psi_l\rangle$  is the wave function for the  $l$ -th configuration which satisfy the condition explained above. Because of the off-diagonal matrix elements among some states in  $|\psi_l\rangle$ , certain kinds of resonance states are realized. Figure 17 shows the overlap integral  $W \equiv |\langle GS|\Psi\rangle|^2$  as a function of  $1/N$ . In a  $2 \times 2 \times 2$  size cluster, the ground-state wave function  $|GS\rangle$  is almost completely reproduced by the trial function. With increasing  $N$ , a value of  $W$  is gradually reduced. However,  $W$  is maintained around 0.8 even in the largest size cluster. Thus, at least within the present calculation, the ground-state wave function is well reproduced by the trial wave function where the honeycomb lattice is covered by NN bonds with the minimum bond energy.

## 6 Summary

We review in this paper the intrinsic orbital frustration effects in Mott insulating states with orbital degree of freedom. This effect is resulted from the directional nature of the orbital degree of freedom and the interaction between the inter-site orbitals, and is represented as a flat part of the dispersion relation in the effective orbital interaction in the Brillouin zone. As results, a macroscopic number of the orbital states are degenerated in the classical ground state, as seen in the frustrated magnets. In the cubic lattice orbital model, this degeneracy is lifted by thermal/quantum fluctuations, and the conventional long-range order is realized by the so-called order-by-fluctuation mechanism. In the two dimensional compass model, it is mathematically proved that no conventional long-range order is stabilized due to the local symmetry. Instead, the directional order occurs at finite temperature. In honeycomb lattice orbital model, it is numerically shown that the conventional long range orbital order does not occur. That is, the order-by-thermal/quantum fluctuation effect does not work. We find there is a certain kind of rule for the orbital pseudo-spin angle at each lattice site, although there is still a macroscopic number of degeneracy in the orbital configuration.

**Acknowledgements** The theoretical studies introduced in this paper have been done in collaboration with T. Tanaka (ISSP, University of Tokyo) and J. Nasu (Department of Physics, Tohoku University). The author would like to thank M. Matsumoto and K. Harada for their valuable discussions. This work was supported by JSPS KAKENHI (16104005), and TOKUTEI (18044001, 19052001, 19014003) from MEXT, NAREGI, and CREST.

## References

1. S. Maekawa, T. Tohyama, S.E. Barnes, S. Ishihara, W. Koshibae, G. Khaliullin, *Physics of Transition Metal Oxides* (Springer, Berlin, 2004)
2. Y. Tokura, N. Nagaosa, *Science* **288** 462 (2000)
3. T. Tanaka, M. Matsumoto, S. Ishihara, *Phys. Rev. Lett.* **95** 267204 (2005)
4. T. Tanaka, S. Ishihara, *Phys. Rev. Lett.* **98** 256402 (2007)
5. A. Nagano, M. Naka, J. Nasu, S. Ishihara, *Phys. Rev. Lett.* **99** 145263 (2007)
6. J. Nasu, M. Naka, A. Nagano, S. Ishihara, *Phys. Rev. B* **78** 024416 (2008)
7. T. Tanaka, S. Ishihara, *Phys. Rev. B* (2009).
8. K.I. Kugel, D.I. Khomskii, *Sov. Phys. Usp.* **25** 231 (1982)
9. S. Ishihara, J. Inoue, S. Maekawa, *Phys. Rev. B* **55** 8280 (1997)
10. L.F. Feiner, A.M. Oleś, J. Zaanen, *Phys. Rev. Lett.* **78** 2799 (1997)
11. R. Shiina, T. Nishitani, H. Shiba, *J. Phys. Soc. Jpn.* **66** 3159 (1997)
12. J. Kanamori, *J. Appl. Phys.* **31** 14S (1960)
13. S. Okamoto, S. Ishihara, S. Maekawa, *Phys. Rev. B* **65** 144403 (2000)
14. S. Ishihara, M. Yamanaka, N. Nagaosa, *Phys. Rev. B* **56** (1997) 686
15. S. Ishihara, S. Maekawa, *Phys. Rev. B* **62** 2338 (2000)
16. Z. Nussinov, M. Biskup, L. Chayes, J. van den Brink, *Euro. Phys. Lett.* **67** 990 (2004)
17. M. Biskup, L. Chayes, Z. Nussinov, *Commun. Math. Phys.* **255** 253 (2005)
18. J. van den Brink, P. Horsch, F. Mack, *Phys. Rev. B* **59** 6795 (1999)
19. K. Kubo, *J. Phys. Soc. Jpn.* **71** 1308 (2002)
20. A. Mishra, M. Ma, F.-C. Zhang, S. Guertler, L.-H. Tang, S. Wan, *Phys. Rev. Lett.* **93** 207201 (2004)
21. K.I. Kugel, D.I. Khomskii, *Sov. Phys. JETP* **37** 725 (1973)
22. D.I. Khomskii, M.V. Mostovoy, *J. Phys. A* **36** 9197 (2003)
23. J. Dorier, F. Becca, F. Mila, *Phys. Rev. B* **72** 024448 (2005)
24. C.D. Batista, Z. Nussinov, *Phys. Rev. B* **72** 045137 (2005)
25. B. Doucot, M.V. Feigel'man, L. B. Ioffe, A.S. Ioselevich, *Phys. Rev. B* **71** 024505 (2005)
26. M. Naka, A. Nagano, S. Ishihara, *Phys. Rev. B* **77** 224441 (2008)
27. C. Wu, D. Bergman, L. Balents, S. Das Sarma, *Phys. Rev. Lett.* **99** 070401 (2007)
28. C. Wu, *Phys. Rev. Lett.* **100** 200406 (2008)
29. E. Zhao, and W.V. Liu, *Phys. Rev. Lett.* **100** 160403 (2008)
30. A. Kitaev, *Ann. Phys.* **321** 2 (2006)
31. G. Baskaran, S. Mandal, R. Shankar, *Phys. Rev. Lett.* **98** 247201 (2007)

# Ultrasonic Consequences of the Jahn–Teller Effect

Vladimir Gudkov

**Abstract** Contribution of the Jahn–Teller system to the elastic moduli and ultrasonic wave attenuation of the diluted crystals is discussed in the frames of phenomenological approach and on the basis of quantum-mechanical theory. Both, resonant and relaxation processes are considered. The procedure of distinguishing the nature of the anomalies (either resonant or relaxation) in the elastic moduli and attenuation of ultrasound as well as generalized method for reconstruction of the relaxation time temperature dependence are described in detail. Particular attention is paid to the physical parameters of the Jahn-Teller complex that could be determined using the ultrasonic technique, namely, the potential barrier, the type of the vibronic modes and their frequency, the tunnelling splitting, the deformation potential and the energy of inevitable strain. The experimental results obtained in some zinc-blende crystals doped with  $3d$  ions are presented.

## 1 Introduction

What is the reason to use elastic waves, acoustic or ultrasonic, for investigating the Jahn–Teller effect? An elastic wave can be represented as a number of quasi-particles, named phonons, that can initiate electron transitions. The energy of phonons generated in an experiment is much lower than one of photons used in optics,  $\gamma$ -resonance, microwave absorption experiment, and electron spin resonance. Thus, the elastic wave technique broadens the facilities of the Jahn–Teller spectroscopy in its low energy part and provides new information mostly about the characteristics of the ground state and its tunneling splitting. Nuclear magnetic resonance (NMR) covers the frequency interval similar to one used in an ultrasonic experiment but NMR is observed in an external magnetic field and requires quite definite selection rules for the electron transitions. Acoustic waves have even lower frequency but still they can be used for investigating the quasi-static elastic moduli, which provide information about the symmetry of the crystal or the type of local distortions in a diluted crystal. Most of the experimental results was obtained at frequencies higher than  $10^4$  Hz, therefore we will focus our attention on ultrasonic wave propagation and on influence of the Jahn–Teller system on their phase velocity and

attenuation, or, in other words, real and imaginary components of the dynamic elastic moduli. The most evident reasons of ultrasonic technique application relate to structural phase transitions caused by the cooperative Jahn–Teller effect. The study of the temperature dependence of different components of the elastic moduli tensor provides information about critical temperature and the symmetry of new phase. Ultrasonic experiments deal with the cooperative Jahn–Teller effect were reviewed by Lüthi [1].

Another application of the ultrasonic technique is the investigation of diluted crystals, i.e., crystals with the impurity of low concentration. In this case, we do not observe a structural transition but we can register a tendency to it in a form of lattice instability. The instability manifests itself in softening of definite elastic modulus. This modulus indicates the character of the distortions of the Jahn–Teller complex and point out the type of vibronic mode. Ultrasonic attenuation gives additional information about the character of the electron-phonon interaction: either it is resonant, or relaxation one. The known experimental data support the statement that the relaxation process is observed. In the case of relaxation process, the procedure for reconstruction of the relaxation time was developed earlier by Sturge et al., described in [2] and recently it was generalized to be applicable to a low temperature experiment [3]. Simulation of the temperature dependence of the relaxation time can give us the magnitudes of the parameters of the Jahn–Teller complex, such as the potential barrier, the vibrational frequency, the deformation potential, the tunnelling splitting, etc. Since the cooperative Jahn–Teller effect was reviewed already [1], we will discuss the problems and the experimental results obtained in the diluted crystals.

## 2 Elastic Moduli. Phenomenological Approach

The parameters measured in an ultrasonic experiment are the amplitude and phase of the signal. They are determined by attenuation and phase velocity of a wave. In turn, the attenuation and phase velocity are associated with material constants. In our case they are elastic coefficients (or elastic moduli). These constants can be calculated using quantum-mechanical approach. Finally, we will obtain the expressions for the measured (phenomenological) parameters in terms of the microscopic ones. In the present section we will discuss the basics of the phenomenological elasticity theory and the microscopic description of the Jahn–Teller contribution to the elastic moduli will be discussed later.

Classical theory of elasticity (see, for example [4, 5]) contains the fundamental equations required to describe elastic waves propagation. Although real objects have atomic structure, the medium in which the waves propagate is regarded as a continuum. It means that the wavelength should be large enough with respect to the distance between molecules or atoms. Further we will discuss crystals, therefore, most of the variables will be tensors.

The principal equation of elasticity theory is the equation of motion, which relates the total force per unit volume  $\rho \ddot{u}_i$  to the gradient of the thermodynamic tensions  $\sigma_{ij}$  and the body force per unit volume  $f_i$ :

$$\rho \ddot{u}_i = \frac{\partial \sigma_{ij}}{\partial x_j} + f_i, \quad (1)$$

where  $\rho$  is the density of the medium and  $\mathbf{u}$  is the displacement of a volume element.  $\sigma_{ij}^0$  is defined as the force in  $\mathbf{e}_i$  direction applied to a unit square with normal vector parallel to  $\mathbf{e}_j$ . The thermodynamic tensions also can be defined so that the sum  $\sigma_{ij} d\varepsilon_{ij}$  equals the differential of the work per unit of original volume done by the non-dissipative part of the stress in stretching the medium [6]. Here

$$\varepsilon_{ij} = \frac{1}{2} \left( \frac{\partial u_i}{\partial x_j} + \frac{\partial u_j}{\partial x_i} \right) \quad (2)$$

is the strain tensor also known as the deformation tensor. Very often, the strain induces electric or magnetic fields and temperature variation. Therefore, other variables should be accounted. A complete description of a medium requires a set of 16 independent variables; for example, temperature  $T$ , components of electric induction  $D_k$ , magnetic induction  $B_k$ , and the strain tensor, whereas entropy  $S$ , components of  $\sigma_{ij}$ , electric field  $E_k$ , and magnetic field  $H_k$  may be regarded as their dependant variables. Using this set of variables, the differential of  $\sigma_{ij}$  has the form

$$\begin{aligned} d\sigma_{ij} = & \left( \frac{\partial \sigma_{ij}}{\partial \varepsilon_{kl}} \right)_{DBT} d\varepsilon_{kl} + \left( \frac{\partial \sigma_{ij}}{\partial D_k} \right)_{\sigma BT} dD_k \\ & + \left( \frac{\partial \sigma_{ij}}{\partial B_k} \right)_{\sigma DT} dH_k + \left( \frac{\partial \sigma_{ij}}{\partial T} \right)_{\sigma DB} dT. \end{aligned} \quad (3)$$

The first law of thermodynamics states that the change in the internal energy of a body equals the work done by the external forces plus the change in heat. In a more detailed form and for unit volume it is written as

$$dU = \sigma_{ij} d\varepsilon_{ij} + E_i dD_i + H_i dB_i + T dS. \quad (4)$$

Using the definition of the Helmholtz free energy  $F = U - TS$ , we have

$$dF = \sigma_{ij} d\varepsilon_{ij} + E_i dD_i + H_i dB_i - S dT. \quad (5)$$

The elastic (or stiffness) coefficients (moduli) are defined as the first derivatives of the tensions with respect to strain

$$c_{ijkl} = \frac{\partial \sigma_{ij}}{\partial \varepsilon_{kl}}, \quad (6)$$

or the second derivatives of the thermodynamic potentials

$$c_{ijkl}^{DBT} = \left( \frac{\partial^2 F}{\partial \varepsilon_{ij} \partial \varepsilon_{kl}} \right)_{DBT} , \quad (7)$$

$$c_{ijkl}^{DBS} = \left( \frac{\partial^2 U}{\partial \varepsilon_{ij} \partial \varepsilon_{kl}} \right)_{DBS} , \quad (8)$$

The ordinary or the second order elastic moduli represent the derivatives (7) and (8) calculated at  $\varepsilon_{ij} = 0$ . They enter the equations of linear with respect to deformation theory (the zero amplitude wave).

The  $n$ th-order elastic coefficients may be defined as the  $n$ th partial derivatives of the energy. The higher-order coefficients ( $n \geq 3$ ) should be included when the propagation of a finite amplitude waves (i.e., nonlinear phenomena) is under consideration.

We will restrict ourselves with consideration of small-amplitude waves and, therefore, use only the second-order moduli. Besides, we will discuss the phenomena in the zero electric and magnetic fields. It makes it possible to omit the superscripts and subscripts  $DB$ . In this case  $c_{ijkl}^S$  and  $c_{ijkl}^T$  will represent adiabatic and isothermal moduli, respectively. The first one does characterize very fast processes, while the second is a quasi-static modulus. Regardless of the definite form of the moduli (isothermal, adiabatic or another one) the equation of motion (1) at  $f_i = 0$  may be written in the form

$$\rho \ddot{u}_i = c_{ijkl} \frac{\partial^2 u_l}{\partial x_j \partial x_k} . \quad (9)$$

We will seek solution in the form of running wave

$$u_j = U_j \exp [i (\omega t - \mathbf{k} \cdot \mathbf{r})] , \quad (10)$$

where  $\omega$  is the radian frequency of the wave,  $t$  is time,  $\mathbf{k}$  is the wave vector, and  $\mathbf{r}$  is the radius-vector of the point where the wave is observed. Substitution into (9) gives

$$\left( c_{ijkl} \frac{k_j k_l}{k^2} - \rho v^2 \delta_{ik} \right) u_k = 0 , \quad (11)$$

where  $k^2 = |\mathbf{k}|^2$ , and  $\mathbf{v}$  is phase velocity defined by  $\mathbf{k} \cdot \mathbf{v} = \omega$ .

For nontrivial solutions the determinant of the coefficients of the system (11) vanishes

$$\left| c_{ijkl} \frac{k_j k_l}{k^2} - \rho v^2 \delta_{ik} \right| = 0 . \quad (12)$$

This equation determines  $\mathbf{v}$  as function of direction. Since it is cubic in  $v^2$ , there are three velocities associated with each direction. If we introduce the symmetric second-rank tensor

$$\lambda_{ik} = c_{ijkl} \frac{k_j k_l}{k^2}, \quad (13)$$

we see that  $\rho v^2$  are its eigenvalues, and the displacement vectors  $\mathbf{u}$  associated with distinct eigenvalues are mutually perpendicular. Thus for each direction of  $\mathbf{k}$  there can be three waves with mutually perpendicular displacement vectors and different (except in degenerate case) phase velocities

$$v_\beta = \sqrt{c_\beta / \rho}, \quad (14)$$

where  $\beta = s, f, \ell$  are the subscripts relating to these waves known as normal or eigen modes. If the waves propagate along the principal crystallographic axes, one of them has longitudinal ( $\ell$ ) polarization and two are shear polarized modes: fast ( $f$ ) and slow ( $s$ ) ones. The degenerate shear modes are observed if propagation occurs along the axis of high-order rotational symmetry (not less than three-fold). For an non-symmetrical direction the modes are quasi longitudinal and quasi shear.

Attenuation of a wave can be accounted with the help of either complex frequency  $\omega = \omega_1 + i\omega_2$  or complex wave vector  $\mathbf{k} = \text{Re}\mathbf{k} + i\text{Im}\mathbf{k}$ . We will consider frequency as a real value, while the wave vector as a complex one and use notation  $\mathbf{k} = (\omega/v - i\alpha)\mathbf{e}_k$ , where  $\mathbf{e}_k$  is the unit vector of  $\mathbf{k}$ -direction and attenuation coefficient  $\alpha$  describes the reduction of amplitude by the factor  $\exp(-\alpha\mathbf{e}_k \cdot \mathbf{r})$ . Thus the expression:

$$\mathbf{k}_\beta = \frac{\omega}{\sqrt{c_\beta / \rho}} \mathbf{e}_k \quad (15)$$

should be accepted as introduction of complex second-order moduli. These moduli can be still called as elastic ones since in most of the cases  $|\text{Re}(c_\beta)| \gg |\text{Im}(c_\beta)|$  but we must keep in mind that the imaginary part describes the energy loss, i.e., the anelastic behavior.

In the frames of phenomenological theory we cannot discuss the resonant effects and will restrict ourselves with relaxation processes only. We will follow an approach proposed by Zener [7]. For a small-amplitude wave equation (6) represents Hooke's law in terms of stress, strain and stiffness

$$c_{ijkl} = \frac{\sigma_{ij}}{\varepsilon_{kl}}. \quad (16)$$

It can be written in terms of stress, strain and compliance as well:

$$s_{ijkl} = \frac{\varepsilon_{kl}}{\sigma_{ij}}. \quad (17)$$

To describe the response of the medium on a stress suddenly applied to a solid and held constant, it was introduced unrelaxed (subscript  $U$ ) and relaxed (subscript  $R$ ) stiffness and compliance coefficients. The unrelaxed quantities relate to immediate response while the relaxed ones are the coefficients after relaxation occurs. The process of relaxation is characterized with the relaxation time  $\tau$ . Proposed by Zener



modification of the Hooke's law represents an expansion in the time derivatives of the stress and strain that retains only the lowest order derivatives:

$$\varepsilon_{kl} + \tau \frac{d\varepsilon_{kl}}{dt} = s_{ijkl}^R \sigma_{ij} + \tau s_{ijkl}^U \frac{d\sigma_{ij}}{dt} . \quad (18)$$

In the case of harmonic time-dependence of the variables (i.e.,  $\sigma_{ij}, \varepsilon_{kl} \propto \exp(i\omega t)$ ) and assuming small difference between the relaxed and unrelaxed compliances:

$$s_{ijkl}^R - s_{ijkl}^U \ll s_{ijkl}^R, s_{ijkl}^U = \frac{\varepsilon_{kl}}{\sigma_{ij}} , \quad (19)$$

solution of the (18) gives an expression for dynamic (i.e., frequency-dependent) moduli  $c_{ijkl}$ . Written for an appropriate liner combination that can be used in the expression (15), the solution has the form

$$c_\beta = c_\beta^U - \frac{c_\beta^U - c_\beta^R}{1 + \omega^2 \tau^2} (1 - i\omega\tau) , \quad (20)$$

or

$$c_\beta = c_\beta^R + \frac{c_\beta^U - c_\beta^R}{1 + \omega^2 \tau^2} (\omega^2 \tau^2 + i\omega\tau) . \quad (21)$$

In most of the cases, an ultrasonic wave propagates adiabatically, so the (20) looks more naturally: its right-hand side represents the adiabatic (non-relaxed) modulus and non-adiabatic contribution to the dynamic modulus. Recall that the relaxed (or isothermal) modulus should be regarded as quasi-static one. Figure 1 shows the frequency-dependent factor of non-adiabatic contribution as function of  $\omega\tau$ . One can see that transformation from isothermal-like to adiabatic-like propagation occurs in the vicinity  $\omega\tau = 1$ . The velocity of ultrasound is increased in this region, while the attenuation reaches its maximum value.

General relation between  $\mathbf{k}$  and  $c_\beta$  given by the (15) is often simplified for small deviation of the variables respectively certain initial reference values  $\mathbf{k}_0 \equiv \mathbf{k}_{\beta,0}$ ,  $v_0 \equiv v_{\beta,0}$ , and  $c_0 \equiv c_{\beta,0}$ . In other words we assume  $\mathbf{k}_{\beta,0} - \mathbf{k}_0 \equiv \Delta\mathbf{k}_{\beta,0}$ ,  $|\Delta\mathbf{k}_{\beta,0}| \ll |\mathbf{k}_{\beta,0}|$ ,  $v_{\beta,0} - v_0 \equiv \Delta v_{\beta,0}$ ,  $|\Delta v_{\beta,0}| \ll |v_{\beta,0}|$ ,  $c_\beta - c_{\beta,0} \equiv \Delta c_\beta$ ,  $|\Delta c_\beta| \ll |c_\beta|$ . In this case

$$\alpha_\beta = \frac{1}{2} k_0 \frac{\text{Im} c_\beta}{c_0} = \frac{1}{2} k_0 \frac{c_\beta^U - c_\beta^R}{c_0} \frac{\omega\tau}{1 + \omega^2 \tau^2} , \quad (22)$$

$$\frac{\Delta v_\beta}{v_0} = \frac{v_\beta - v_0}{v_0} = \frac{1}{2} \frac{\text{Re} \Delta c_\beta}{c_0} = -\frac{1}{2} \frac{c_\beta^U - c_\beta^R}{c_0} \frac{1}{1 + \omega^2 \tau^2} , \quad (23)$$

where  $k_0 = \omega/v_0$  and  $c_0 = \rho v_0^2$ . Note,  $\alpha$  is introduced so, that it characterizes attenuation of the amplitude, not energy:  $\alpha_\beta = -\text{Im}(k_\beta)$ .

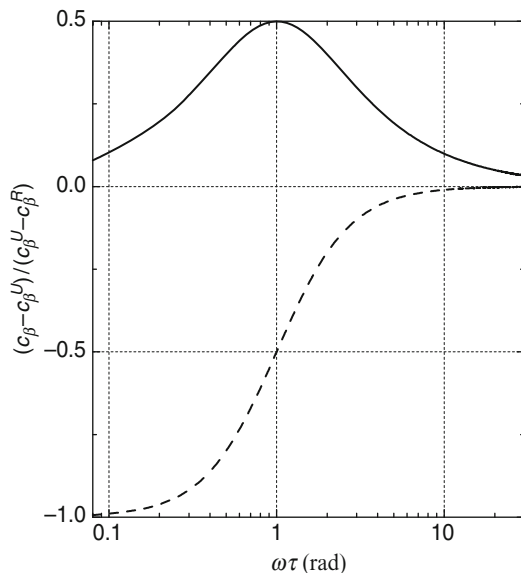


**Fig. 1** The frequency-dependent factor of the real [dash curve:  $(-1)/(1 + \omega^2\tau^2)$ ] and imaginary [solid curve:  $\omega\tau/(1 + \omega^2\tau^2)$ ] components of the non-adiabatic contribution to the dynamic elastic modulus

### 3 Manifestation of the Jahn–Teller Effect in an Ultrasonic Experiment

Because the energy state of a Jahn–Teller complex depends on the local lattice distortions, the macroscopic long-distant strain that produces an ultrasonic wave should influence it as well. The cross effect is: initiated by the Jahn–Teller complexes (1) the dispersion (i.e., frequency-dependent variation of phase velocity) and (2) attenuation of the wave. In terms of the elastic moduli it sounds as appearance (or account) of the Jahn–Teller contribution to the real and imaginary parts of the elastic moduli. For a small-amplitude wave it is a summand  $\Delta c_\beta$ . Obviously, interaction between the Jahn–Teller system and the ultrasonic wave takes place only if the wave, while its propagation in a crystal, produces the lattice distortions corresponding to one of the vibronic modes.

The Jahn–Teller effect requires quantum-mechanical description. Therefore, we will discuss the results obtained in a microscopic theory and later we will compare the expressions for ultrasonic absorption with one obtained in the phenomenological theory.

We will consider the effect in diluted crystals (i.e., in crystals with small concentration of the Jahn–Teller impurity so that the complexes are located far enough from each other and can be considered as independent).

### 3.1 *Quantum-Mechanical Description of the Jahn–Teller Effect in Diluted Crystals*

There are two ways in which interaction of the ultrasonic wave and the Jahn–Teller complex can occur: by resonant transition between two electron energy levels, or by relaxation between the different possible directions of the Jahn–Teller distortions.

#### 3.1.1 Resonance

Resonant process was considered by Bersuker [8] (see also the book [9]) under the assumption that  $\hbar\omega \ll \kappa T$ . We should note that the inequality is correct in most of the cases since the energy of phonons generated in an ultrasonic experiment is low enough. For example,  $\omega/2\pi = 10^8$  Hz corresponds to the energy in the temperature scale of  $\approx 5$  mK.

The expression for ultrasonic attenuation due to  $E \rightarrow A$  transition between the vibronic (tunnelling) levels of the  $E \otimes e$  problem for the system with a cubic-type symmetry was obtained in the following form

$$\alpha_{E \rightarrow A} = \frac{\pi}{6} \frac{n R^2 F_E^2 \omega^2}{\rho v_\beta^3 \kappa T} L g(\omega), \quad (24)$$

where  $\kappa$  is the Boltzmann constant,  $R$  is the minimal distance between the Jahn–Teller center and ligand,  $F_E$  is the linear vibronic constant,  $n$  is the concentration of the Jahn–Teller centers in the crystal,  $L$  is the factor accounting the propagation direction  $\mathbf{k}$  and the polarization of the wave  $\mathbf{U}$

$$L = \frac{1}{k^2 U^2} \left( \sum_i k_i^2 U_i^2 - \frac{1}{2} \sum_{i \neq j} k_i k_j U_i U_j \right), \quad (25)$$

$g(\omega)$  is the shape factor of the line,

$$\int_0^\infty g(\omega) d\omega = 1. \quad (26)$$

The shape factor can be expressed using the relaxation time as

$$g(\omega) = \frac{2}{\pi} \frac{\tau}{1 + (\omega - \omega_0)^2 \tau^2}, \quad (27)$$

where  $\hbar\omega_0$  is the tunnelling splitting. In our case  $\hbar\omega_0 = r\Gamma$ . Finally we can combine all the expressions (24)–(27) and obtain the following:

$$\alpha_{E \rightarrow A} = \frac{1}{3} k_0 \frac{n R^2 F_E^2 L}{c_\beta \kappa T} \frac{\omega \tau}{1 + (\omega - \omega_0)^2 \tau^2}. \quad (28)$$

We must point out that our expressions (24) and (28) differ from ones given in [8,9] by factor 1/2 because we discuss attenuation of amplitude, while in the mentioned references the expressions were obtained for the energy loss.

In this expression, the temperature dependent variables are  $R$ ,  $\nu_\beta$ ,  $\Gamma$ , and  $\tau$ . At low temperatures  $R$ ,  $\nu_\beta$ ,  $\Gamma$  can be regarded as temperature independent, whereas the relaxation time has strong temperature dependence. Thus, the shape factor given by the expression (27) has a maximum as a function of temperature. Its position,  $T_1$ , can be derived from

$$(\omega - \omega_0) \tau(T_1) = 1. \quad (29)$$

The temperature dependence of ultrasonic attenuation will also have a maximum but its location,  $T_m$ , should be shifted with respect to  $T = T_1$  due to the factor  $1/T$  in the expression (28).

### 3.1.2 Relaxation

The absorption due to relaxation between the possible directions of the Jahn–Teller distortions was observed initially in experiments done on the crystals of aluminum oxide (corundum), yttrium aluminum garnet, yttrium iron garnet, and lithium gallium spinel doped with  $3d$  ions [10, 11].

An easy way to obtain the formula for the relaxation-origin absorption is to consider the limit  $\omega \gg \omega_0$  in the expression (28). However, we will follow the approach suggested by Sturge et al. [11] and discussed in detail in [2], in which inevitable strain of a crystal was taken into account. It was supposed that at one particular site local strain lowered one of the adiabatic potential minima by amount  $u_0$  relative to others. If  $u_0 > \omega_0 = r\Gamma$ , the system will (at  $T = 0$ ) be localized in one of the valleys. At  $\kappa T \geq u_0$ , there will be thermal distribution among the minima.

Discussing the contribution of the Jahn–Teller system ( $\Delta c_{ijkl}^U - \Delta c_{ijkl}^R$ ) which enters expression (20), the authors stated that it should be calculated isothermally since adiabatic value  $\Delta c_{ijkl}^U$  vanishes. Thus

$$-(\Delta c_{ijkl}^U - \Delta c_{ijkl}^R) = \Delta c_{ijkl}^R. \quad (30)$$

Using the general expression for the relaxed (isothermal) modulus one can write

$$\Delta c_{ijkl}^R = \left( \frac{\partial^2 F}{\partial \varepsilon_{ij} \partial \varepsilon_{kl}} \right)_{\varepsilon=0} = n\kappa T \left( \frac{\partial^2 \ln Z}{\partial \varepsilon_{ij} \partial \varepsilon_{kl}} \right)_{\varepsilon=0}, \quad (31)$$

where  $Z$  is partition function of the Jahn–Teller ions.

In the case of  $E \otimes e$  problem for octahedral complex and the longitudinal wave propagation, the partition function has the following form

$$Z = 2 \exp(-\beta \varepsilon / \kappa T) + \exp[(u_0 + 2\beta \varepsilon) / \kappa T], \quad (32)$$

where

$$\beta^2 = 2A^2 \langle Q^2 \rangle, \quad (33)$$

where  $2A$  is the splitting of the  $E$  state per unit distortion (i.e., unit displacement not strain),  $\langle Q^2 \rangle$  equals  $R^2/6$  for propagation of the longitudinal wave in the direction of the  $[100]$  axis of the octahedron (in this case the splitting per unit strain  $b = 3\beta$ ) and equals  $R^2/24$  for the  $[110]$  axis. Finally, the contribution of the Jahn–Teller system to the modulus, which characterizes the longitudinal wave propagation in the  $[100]$  octahedron direction can be written as

$$\Delta c_\ell^R = -\frac{2n\beta^2}{\kappa T} f\left(\frac{u_0}{\kappa T}\right). \quad (34)$$

Function  $f(x)$  satisfies  $f(0) = 1$ ,  $f(\pm\infty) = 0$ . Considering small inevitable strain  $u_0 \ll \kappa T$  and assuming  $f(u_0/\kappa T) = 1$ , attenuation due to the Jahn–Teller system was derived as

$$\alpha_\ell = \frac{1}{2}k_0 \frac{(-\Delta c_\ell^R)}{c_0} \frac{\omega\tau}{1 + \omega^2\tau^2} = \frac{k_0n\beta^2}{c_0\kappa T} \frac{\omega\tau}{1 + \omega^2\tau^2}. \quad (35)$$

Like before, this expression describes the attenuation of the amplitude but not the energy loss as it is discussed in [2].

In most the cases,  $\tau(T)$  is a monotonous function, moreover, it is reducing with temperature increase. Keeping in mind that other variables in the expression (35) can be assumed as temperature-independent at least at low temperatures, one can see that the relaxation attenuation has maximum at a certain temperature  $T = T_m$ . Similar to the resonant attenuation, its position is shifted due to the the factor  $1/T$  with respect to  $T = T_1$  which is defined in this case with the condition

$$\omega\tau(T_1) = 1. \quad (36)$$

Discussing the relaxation time origin we will also follow [2]. Three mechanisms of relaxation can be accounted here: thermal activation over the potential barrier  $V_0$  (described with  $\tau_T$ ), tunnelling through the barrier accompanied by phonon emission ( $\tau_t$ ), and two phonon process analogous to Raman scattering ( $\tau_R$ ):

$$\tau^{-1} = \tau_T^{-1} + \tau_t^{-1} + \tau_R^{-1}. \quad (37)$$

The summands in the right-hand side of this expression are given by

$$\tau_T^{-1} = 2\nu_0 e^{-V_0/\kappa T}, \quad (38)$$

$$\tau_t^{-1} = \frac{6\Gamma^2\beta^2}{\pi\rho\hbar^4\nu_0^5} \frac{u_0}{\kappa T} \frac{(2 + e^{-u_0/\kappa T})}{(1 - e^{-u_0/\kappa T})}, \quad (39)$$

$$\tau_R^{-1} = \frac{9\Gamma^2\beta^4(\kappa T)^3}{\pi\rho^2\hbar^7\nu_0^{10}}, \quad (40)$$

where  $v_0$  is constant. It was called as the vibrational frequency in [11]. Actually it is the frequency of the deformations rotation which is always less than the frequency of radial vibrations (see p.171 in [9]).

Phase velocity  $v_\beta$  or corresponding real component of the dynamic modulus  $c_\beta$  can serve as object of study as well. According to the expression (23), they are also functions of  $c^U$ ,  $c^R$ , and  $\omega\tau$ . At low frequency or/and high temperatures (satisfying  $\omega\tau \ll 1$ ) one can observe softening of the modulus, i.e., reduction the velocity with lowering the temperature. Such a behavior is typical for an isothermal process. If  $\omega\tau \gg 1$ , the process will be close to an adiabatic one. Transformation from isothermal to adiabatic process occurs in the vicinity of  $T = T_1$ . Recall that  $T_1$  is defined from the condition  $\omega\tau(T_1) = 1$ . The factor  $1/(1 + \omega^2\tau^2)$  represents a smoothed step-function: it equals unity at  $\omega\tau \ll 1$  and vanishes at  $\omega\tau \gg 1$ .

Discussing contribution of the Jahn–Teller system to  $v_\beta$  we may use the expression (30)–(31) as well, and for particular case of  $E \otimes e$  problem for octahedral complex and the longitudinal wave propagation - the expressions (32)–(34). As a result:

$$\frac{\Delta v_\ell}{v_0} = \frac{1}{2} \frac{\Delta c_\ell}{c_0} = \frac{1}{2} \frac{\Delta c_\ell^R}{c_0} \frac{1}{1 + \omega^2\tau^2} = -\frac{n\beta^2}{c_0 k T} \frac{1}{1 + \omega^2\tau^2}. \quad (41)$$

The ordinary elastic moduli discussed above describe propagation of a small amplitude wave. In the case of large amplitude or pressure application the moduli (7), (8) should be considered as functions of distortions.

Averkiev et al. [12] investigated the softening of the lattice in  $p$ -GaAs:Cu. This crystal has a zinc-blende structure and the Jahn–Teller impurity is located in tetrahedral surrounding.

Discussing a zinc-blende crystal, it is convenient to consider two types of distortions:

$$\varepsilon_1 = \left[ \varepsilon_{33} - \frac{1}{2} (\varepsilon_{11} + \varepsilon_{22}) \right] \quad (42)$$

and  $\varepsilon_{12}$ . The first distortions are of tetragonal type (along the  $\langle 100 \rangle$  axes) and correspond to  $\epsilon$  vibronic mode. They are produced by the slow shear mode propagating in the  $\langle 110 \rangle$  direction with the polarization parallel to  $\langle 110 \rangle$ . The second - are trigonal distortions (along the  $\langle 111 \rangle$  axes) corresponding to  $\tau$  vibronic mode. They are initiated by the fast shear mode propagating in the same direction but polarized along  $\langle 100 \rangle$ . The phase velocities of these modes are determined by the elastic moduli  $c_s = (c_{1111} - c_{1122})/2$  and  $c_f = c_{1313}$ , respectively. Contributions of the Jahn–Teller system to the isothermal moduli ( $\Delta c^R$ ) should be in this case

$$\Delta c_s^R = \frac{3}{2} \frac{\partial^2 F}{\partial \varepsilon_1^2}, \quad \Delta c_f^R = \frac{\partial^2 F}{\partial \varepsilon_{12}^2}, \quad (43)$$

Note, the tetragonal distortion influence the  $c_s$  modulus exclusively, the trigonal - the  $c_f$  modulus. This fact can give us an instrument to determine the type of local distortions in an ultrasonic experiment carried out in a zinc-blende crystal: the distortions can be pointed out with the help of temperature dependences of the elastic moduli.

Interaction of the impurity with the  $\epsilon$  vibronic mode was considered [12] and, therefore, the local distortions have tetragonal type. The adiabatic potential in this case has three minima and the energy in the minima was introduced in the following form

$$E_1 = -b \left[ \epsilon_{33} - \frac{1}{2} (\epsilon_{11} + \epsilon_{22}) \right] = -b\epsilon_1, \quad E_{2,3} = b \left[ \frac{\epsilon_1}{2} \mp \frac{3}{4} (\epsilon_{11} - \epsilon_{22}) \right], \quad (44)$$

where  $b$  is the appropriate component of deformation potential tensor. Contributions of the Jahn–Teller system to the isothermal moduli ( $\Delta c^R$ ) those describe propagation of shear modes in the  $\langle 110 \rangle$  direction were written as

$$\Delta c_s^R = \frac{3}{2} \frac{\partial^2 F}{\partial \epsilon_1^2}, \quad \Delta c_f^R = \frac{3}{2} \frac{\partial^2 F}{\partial \epsilon_{12}^2}, \quad (45)$$

where the free energy was represented as

$$F = -\kappa T n \ln \left( e^{-E_1/\kappa T} + e^{-E_2/\kappa T} + e^{-E_3/\kappa T} \right). \quad (46)$$

Analyzing the expressions (44)–(46) one can easily see that non-zero contribution of the Jahn–Teller system to the elastic moduli takes place only to the  $c_s$  modulus (or to the velocity of the slow shear mode of the  $\langle 110 \rangle$  direction) and this contribution is

$$\Delta c_s^R = -\frac{27}{4} \frac{n b^2}{\kappa T} \frac{\cosh \left( \sqrt{\frac{3}{2}} \frac{b \epsilon_2}{\kappa T} \right) \exp \left( \frac{3}{2} \frac{b \epsilon_1}{\kappa T} \right)}{\left[ 2 \cosh \left( \sqrt{\frac{3}{2}} \frac{b \epsilon_2}{\kappa T} \right) + \exp \left( \frac{3}{2} \frac{b \epsilon_1}{\kappa T} \right) \right]^2}, \quad (47)$$

where

$$\epsilon_2 = \sqrt{\frac{3}{2}} (\epsilon_{11} - \epsilon_{12}) \quad (48)$$

In the mentioned paper [12], this expression was used for analysis the influence of the applied pressure on the luminosity of the  $p$ -GaAs:Cu crystal. As well, it can be useful for consideration of a small amplitude wave propagation in such a crystal. We should assume  $\epsilon_1 = \epsilon_2 = \epsilon_3 = 0$  and derive the following expression

$$\Delta c_s^R = -\frac{3}{4} \frac{n b^2}{\kappa T}, \quad (49)$$

which can be used for describing attenuation and phase velocity of the shear slow mode of the  $\langle 110 \rangle$  direction:

$$\alpha_s = \frac{1}{2} k_0 \frac{(-\Delta c_s^R)}{c_0} \frac{\omega \tau}{1 + \omega^2 \tau^2} = \frac{3}{8} \frac{k_0 n \beta^2}{c_0 \kappa T} \frac{\omega \tau}{1 + \omega^2 \tau^2}, \quad (50)$$

$$\frac{\Delta v_s}{v_0} = \frac{1}{2} \frac{\Delta c_s}{c_0} = \frac{1}{2} \frac{\Delta c_s^R}{c_0} \frac{1}{1 + \omega^2 \tau^2} = -\frac{3}{8} \frac{n\beta^2}{c_0 \kappa T} \frac{1}{1 + \omega^2 \tau^2}. \quad (51)$$

### 3.1.3 Approach of an Experimentalist

In this paragraph, we will discuss how the presented above can be used for analyzing the experimental data. We propose that we have one of the setups described, for example, in [13] or any other device that gives us an opportunity to measure temperature variation of the amplitude ( $A$ ) and phase ( $\Delta\varphi$ ) of the signal after passage of the running wave through a specimen. Some technique is based on measurement of the phase with the help of frequency balance of a bridge.

The relative change of the phase (or frequency  $f$ ), corresponding to the bridge balances obtained at  $T$  and  $T_0$ , is determined by phase velocity of ultrasonic wave and the distance of the wave passage  $\ell$  as follows

$$\frac{\Delta\varphi}{\varphi_0} = \frac{\Delta f}{f_0} = \frac{\Delta v_\beta}{v_0} - \frac{\Delta\ell}{\ell_0}, \quad (52)$$

where  $\varphi_0 = \varphi(T_0)$ ,  $f_0 = f(T_0)$ ,  $v_0 = v(T_0)$ , and  $\ell_0 = \ell(T_0)$ ,  $\Delta f = f(T) - f_0$ ,  $\Delta v_\beta = v_\beta(T) - v_0$ ,  $\Delta\ell = \ell(T) - \ell_0$ . Temperature variation of the specimen's dimension can be neglected at low temperatures. Therefore, we will omit the last term in (52) and the expression for the relative variation of phase velocity expressed in terms of the measured parameters is

$$\frac{\Delta v_\beta}{v_0} = \frac{\Delta\varphi}{\varphi_0} = \frac{\Delta f}{f_0}. \quad (53)$$

To obtain attenuation in  $\text{cm}^{-1}$  we should measure  $\ell_0$  in centimeters and use the following expression

$$\Delta\alpha_\beta = -\frac{1}{\ell_0} \ln \left[ \frac{A(T)}{A(T_0)} \right]. \quad (54)$$

Whenever we obtained the temperature dependence of attenuation and found a peak of absorption which we suppose is due to the Jahn–Teller effect, it is necessary to realize whether it has resonant or relaxation origin. The corresponding expressions are given by formulas (28) and (22), respectively.

One may see that a maximum of resonant attenuation should be observed at  $T = 0$  for  $(\omega - \omega_0)\tau \rightarrow 0$ . If  $(\omega - \omega_0)\tau \neq 0$  and  $\omega_0$  is a temperature-independent parameter, the function

$$f_1(\omega\tau, \Delta\omega\tau) = \frac{\omega\tau}{1 + (\Delta\omega\tau)^2} \quad (55)$$

has a maximum at  $|\Delta\omega|\tau = 1$ , but not at  $\omega\tau = 1$ , as is the case for the function

$$f_2(\omega\tau) = \frac{\omega\tau}{1 + (\omega\tau)^2} \quad (56)$$



which describes the relaxation attenuation given by (22). Here  $\Delta\omega \equiv (\omega - \omega_0)$ . Note that, if  $|\omega - \omega_0|/\omega < 1$ , the peak of  $f_1$  will be located at lower temperatures than that of  $f_2$ . If  $|\omega - \omega_0|/\omega > 1$ , the peak will be observed at higher temperatures, but its magnitude will be appreciably reduced due to the small value of  $\tau$ .

First we will consider a possible resonant origin of the attenuation maximum.

It is easy to determine experimentally which of the frequencies,  $\omega$  or  $\omega_0$ , is smaller, provided  $\tau$  is a monotonic function of  $T$  decreasing with temperature.

One can guess that, if  $\omega$  increasing leads to a shift of the attenuation peak to higher temperatures (what was reported in all the published papers those the author knows and illustrated in Fig. 2), the inequality  $\omega > \omega_0$  holds true. Note that the same shift should occur for relaxation attenuation, since it corresponds to an even stronger condition,  $\omega \gg \omega_0$ . If the peak is shifted to lower temperatures, the opposite inequality,  $\omega < \omega_0$  should be realized.

We will discuss the experimental procedure, consisting of measurements of  $\alpha_\beta^{(1)}(T)$  and  $\alpha_\beta^{(2)}(T)$  made with at least two fixed frequencies  $\omega_1$  and  $\omega_2$ , respectively. Using the expression for the resonant absorption in a more general form than it is given by (28), namely,

$$\alpha_\beta = \frac{k_0}{2} \frac{c_\beta^U - c_\beta^R}{c_0} \frac{\omega\tau}{1 + (\Delta\omega\tau)^2}, \quad (57)$$

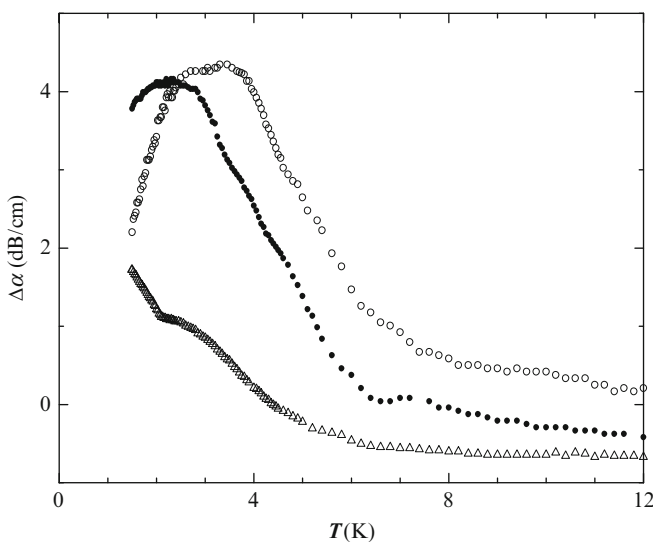


**Fig. 2** Temperature dependences of ultrasonic attenuation for longitudinal waves propagating in ZnSe:V<sup>2+</sup> along the [110] axis, measured at 270 MHz (*open circles*), 156 MHz (*filled circles*), and 52 MHz (*triangles*).  $\Delta\alpha = \alpha(T) - \alpha(T_0)$ ,  $T_0 = 16$  K. The plot for 52 MHz is shifted downward by 0.7 dB for clarity. Concentration of the dopant  $n_V = 5.6 \times 10^{18} \text{ cm}^{-3}$ . After Fig. 3 in [3]

we will write it the first time for an arbitrary temperature  $T$ , the second time for  $T_1$ , and derive the following system:

$$(\omega_1 - \omega_0)\tau(T) = F_1, \quad (58)$$

$$(\omega_2 - \omega_0)\tau(T) = F_2, \quad (59)$$

where

$$F_i = \frac{\alpha_\beta^{(i)}(T_1) \cdot T_1^{(i)}}{\alpha_\beta^{(i)}(T) \cdot T} \pm \sqrt{\left( \frac{\alpha_\beta^{(i)}(T_1) \cdot T_1^{(i)}}{\alpha_\beta^{(i)}(T) \cdot T} \right)^2 - 1}. \quad (60)$$

In this expression  $i = 1, 2$ ,  $T_1^{(i)}$  corresponds to  $(\omega_i - \omega_0)\tau = 1$ . Here  $\omega_0$  is assumed to be a temperature-independent parameter, or at least its temperature dependence should be sufficiently less pronounced than that of the relaxation time.

The system (58) and (59) can be solved with respect to  $\omega_0$  and  $\tau$ :

$$\omega_0 = \frac{\omega_1 F_2 - \omega_2 F_1}{F_2 - F_1}, \quad (61)$$

$$\tau(T) = \frac{F_2 - F_1}{(\omega_2 - \omega_1)}. \quad (62)$$

One important detail of the experiment should be mentioned here. Equation (57) describes resonant (or relaxation, if  $\omega_0 \rightarrow 0$ ) attenuation. However, total attenuation  $\alpha(T)$  is measured in the experiments. Therefore, the background attenuation  $\alpha_b(T)$  should be subtracted from the measured values.

The value of  $\alpha_\beta^{(i)}(T_1) T_1^{(i)}$  can be determined from the experimental data. If we multiply the left and right hand parts of equation (57) by  $T$ , the right hand part will represent the function  $f_1(\omega\tau, \Delta\omega\tau)$  [see (55)] multiplied by a temperature-independent coefficient. Obviously, the product reaches its maximum value precisely at  $(\omega - \omega_0)\tau = 1$ . We would outline that this procedure for determining  $T_1$  may be applied regardless of the attenuation type: it can be either resonant or relaxation. In the latter case  $T_1$  defines a maximum of  $f_2(\omega\tau)$ , given by (56), and corresponds to the condition  $\omega\tau = 1$ .

Such a procedure was applied for processing the data obtained in  $\text{ZnSe:V}^{2+}$ . The result of the application is shown in Fig. 3. Note, the measurements done in a certain temperature interval gave a statistical distribution characterizing their accuracy.

Sometimes the temperature  $T_1$  can be determined even when the maximum of  $\Delta\alpha(T)$  is located at such a low temperature that is not accessible in the experiment. For example, the lowest temperature in [3] was 1.4 K and the attenuation maximum for the 52 MHz was not observed. However, the temperatures corresponding to  $(\omega - \omega_0)\tau = 1$ , obtained with the use of the procedure described above, was found as 1.85 K (see Fig. 4).

In the case of relaxation absorption, we can use (58) with the assumption that  $\omega_0 = 0$  and solve it for the relaxation time,

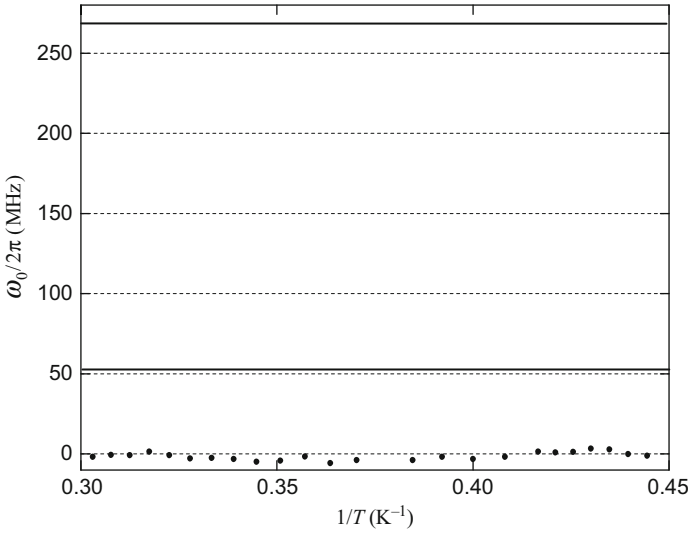


**Fig. 3** The parameter  $\omega_0/2\pi$  (circles) plotted as a function of inverse temperature for a  $\text{ZnSe}:\text{V}^{2+}$  crystal, using data taken at 52 and 270 MHz. Solid lines show the highest (270 MHz) and the lowest (52 MHz) frequencies used in the experiment. Concentration of the dopant  $n_V = 5.6 \times 10^{18} \text{ cm}^{-3}$ . After Fig. 4 in [3]

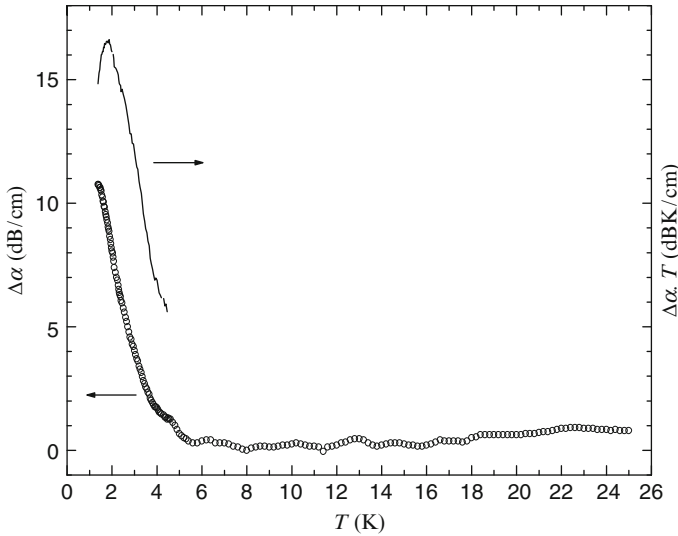


**Fig. 4** Temperature dependences of ultrasonic attenuation for fast shear mode propagating in  $\text{ZnSe}:\text{V}^{2+}$  along the [110] axis measured at 52 MHz (open circles).  $\Delta\alpha = \alpha(T) - \alpha(T_0)$ ,  $T_0 = 8 \text{ K}$ . Solid curve shows the dependence  $\Delta\alpha(T) \cdot T$ . Maximum of this curve corresponds to  $\Delta\omega\tau = 1$ . After Fig. 2 in [3]

$$\tau = \frac{1}{\omega} \left[ \frac{\alpha_\beta(T_1) \cdot T_1}{\alpha_\beta(T) \cdot T} \pm \sqrt{\left( \frac{\alpha_\beta(T_1) \cdot T_1}{\alpha_\beta(T) \cdot T} \right)^2 - 1} \right]. \quad (63)$$

This form of the expression differs from the one used in by Sturge [2]. We have replaced  $\alpha_m T_m$  by  $\alpha_1 T_1$ , and  $T_1$  is found as the temperature corresponding to the maximum of  $\Delta\alpha(T) \cdot T$  but not of  $\Delta\alpha(T)$ . The difference is the result of taking into account the temperature dependence of the pre-factor  $(c_\beta^U - c_\beta^R)/c_0 \propto 1/T$  in the expression (57). The necessity to account the temperature dependence of this pre-factor was pointed out by Schad and Lassmann [14]

Whenever the dependence  $\tau(T)$  is reconstructed, we can simulate it and fitting will give us the magnitudes of the potential barrier,  $V_0$ , the tunnelling splitting,  $r\Gamma$ , the vibrational frequency,  $\nu_0$ , the deformation potential,  $b$ , and the energy of inevitable strain,  $u_0$ . For a doubly degenerate states one can use the expressions (38)–(40).

The magnitude of attenuation measured at  $T = T_1$

$$\alpha_\beta(T_1) = k_0 \frac{\Delta c_\beta^U - \Delta c_\beta^R}{c_0} \approx -k_0 \frac{\Delta c_\beta^R}{c_0} \quad (64)$$

can give us the value of of the product  $nb^2$ , provided the frequency,  $\omega$ , density,  $\rho$ , and the reference phase velocity,  $\nu_0$ , are known: two definite expressions for relaxed moduli are given by the (34) and (49) relating to tetragonal distortion in the octahedral and tetrahedral Jahn–Teller complexes, respectively. One may propose that the concentration of the impurities,  $n$ , is a known parameter characterizing the specimen. It is correct in most of the cases. However, if  $n$  is very small, the procedure of its measurement can be not so easy. For example, the acoustic loss due to the Jahn–Teller effect was observed in  $\text{Al}_2\text{O}_3:\text{Ni}^{3+}$  with 0.004% of the dopant [10]. Therefore, concentration of the Jahn–Teller centers may be an additional parameter which is required to define independently in an ultrasonic experiment. In this case, the deformation potential  $b$  should be determined at the stage of  $\tau(T)$  fitting.

Now we will discuss a procedure of reconstruction the temperature dependence of the relaxed and unrelaxed elastic moduli. We proposed before that the unrelaxed modulus, which describes the Jahn–Teller contribution, vanishes. Actually, the dynamic modulus measured in an experiment is the total one containing the contribution of the Jahn–Teller system as a summand. So, even the dynamic modulus which contains the unrelaxed Jahn–Teller contribution should be non-zero and can have a certain temperature dependence that is not associated with the Jahn–Teller impurities. As well, the relaxed modulus for this reason can differ from one described with the expression (45). To deal with the impurity's contribution only, we can measure the temperature dependence of the dynamic modulus for an un-doped crystal and subtract it from one obtained for the the doped crystal. But it requires two specimens (doped and un-doped) and two experiments. More easy is to reconstruct the relaxed and unrelaxed moduli with the help of the data relating to the doped crystal. To derive the necessary expressions we will use the (20) and (21) and

solve them respectively  $c_\beta^U$  and  $c_\beta^R$ . As a result we have

$$c_\beta^U = \operatorname{Re} c_\beta + 2 \frac{\alpha_\beta}{k_0} \frac{\operatorname{Re} c_\beta}{\omega \tau}, \quad (65)$$

$$c_\beta^R = \operatorname{Re} c_\beta - 2 \frac{\alpha_\beta}{k_0} \operatorname{Re} c_\beta \omega \tau, \quad (66)$$

Accounting small variations of the dynamic modulus we can write the relative variation of  $c_\beta^U$  and  $c_\beta^R$  in terms of the reconstructed  $\tau$  and measured  $\alpha_\beta$  and  $v_\beta$  as follows

$$\frac{c_\beta^U - c_0}{c_0} = 2 \frac{\Delta v_\beta}{v_0} + 2 \frac{\alpha_\beta}{k_0} \frac{1}{\omega \tau}, \quad (67)$$

$$\frac{c_\beta^R - c_0}{c_0} = 2 \frac{\Delta v_\beta}{v_0} - 2 \frac{\alpha_\beta}{k_0} \omega \tau. \quad (68)$$

If the setup makes it possible to measure the ultrasonic velocity only (or the dynamic elastic modulus), a similar technique can be developed for reconstruction the relaxation time and all other parameters characterizing the Jahn–Teller system. In this case we need two temperature dependences  $v_\beta(T)$  (or  $c_\beta(T)$ ): the first one (denoted without superscript) obtained on the doped specimen and the second (superscript (2)) – on the un-doped. At high enough temperatures these dependences should be identical, while at low temperatures they should differ due to the Jahn–Teller effect. So, contribution of the Jahn–Teller system to the total dynamic modulus  $\Delta c_\beta$  may be written as

$$\Delta c_\beta = \delta c_\beta \equiv c_\beta - c_\beta^{(2)} = \Delta c_\beta^R \frac{1}{1 + \omega^2 \tau^2}. \quad (69)$$

Here we used the symbol  $\delta$  for indicating the difference between the moduli of different crystals, moreover, it is the difference between the measured moduli  $c_\beta(T)$  and  $c_\beta^{(2)}(T)$ . At high temperatures  $\Delta c_\beta$  should vanish, so it is convenient to consider the reference temperature  $T_0 \gg T_1$  and the reference modulus  $c_0 = c_\beta(T_0) = c_\beta^{(2)}(T_0)$ . Accordingly, we can introduce  $v_0 = (c_0/\rho)^{1/2}$  and write the relative difference between the measured velocities in the form of

$$\frac{\delta v_\beta}{v_0} \equiv \frac{v_\beta(T) - v_\beta^{(2)}(T)}{v_0} = 2 \frac{\delta c_\beta}{c_0} = 2 \frac{\Delta c_\beta^R}{c_0} \frac{1}{1 + \omega^2 \tau^2}. \quad (70)$$

We can rewrite this expression as

$$\frac{\delta v_\beta}{v_0} = 2 \frac{\eta}{\kappa T} \frac{1}{1 + \omega^2 \tau^2}, \quad (71)$$

where  $\eta$  is a constant with dimension of energy. The temperature  $T_1$ , defined by  $\omega \tau(T_1) = 1$ , can be found as the temperature corresponding to maximum of the derivative  $df/dT$ , where  $f(T) = (\delta v_\beta(T)/v_0) \cdot T$ . One can see that

$$\eta = \frac{\delta v_{\beta}(T_1) \cdot \kappa T_1}{v_0} . \quad (72)$$

The (71) can be presented in the form of

$$\frac{\delta v_{\beta}}{v_0} = 2 \frac{\delta v_{\beta}(T_1) T_1}{v_0 T} \frac{1}{1 + \omega^2 \tau^2} \quad (73)$$

and solved respectively  $\tau$ :

$$\tau = \pm \frac{1}{\omega} \sqrt{2 \frac{\delta v_{\beta}(T_1) \cdot T_1}{\delta v_{\beta}(T) \cdot T} - 1} . \quad (74)$$

The sign in the right hand part of this expression should be chosen so that  $\delta v_{\beta}(T) > \delta v_{\beta}(T_1)$  at  $T < T_1$  (adiabatic regime) and the opposite inequality should take place at  $T > T_1$  (isothermal regime for the Jahn–Teller system's contribution to the elastic modulus).

The next step is simulation of the relaxation time temperature dependence, the procedure similar to what was considered by Sturge [2]. As a result, one will obtain the magnitudes of the potential barrier,  $V_0$ , the tunnelling splitting,  $r\Gamma$ , the vibrational frequency,  $v_0$ , the deformation potential,  $b$ , and the energy of inevitable strain,  $u_0$ .

Concentration of the dopand could be determined as well, provided the definite form of  $\Delta c_{\beta}^R \propto n$  is known. The required expression follows from the (70) and can be derived from

$$\frac{\Delta c_{\beta}^R}{c_0} = \frac{\delta v_{\beta}(T_1)}{v_0} . \quad (75)$$

In the case of the doubly degenerate states in a tetrahedral surrounding, we may use the expressions (49) and have:

$$n = -\frac{16}{3} \frac{\delta v_{\beta}(T_1)}{v_0} \frac{c_0 \kappa T_1}{b^2} . \quad (76)$$

Note,  $\delta v_{\beta}$  is always negative, so  $n$  will be positive by all means as it should be.

Now we will overview some experiments that reveal the specificities of the Jahn–Teller effect in diluted crystals. First of all, we will discuss a justification of their relaxation origin. We have mentioned before that the first experiments were done on the crystals of aluminum oxide (corundum), yttrium aluminum garnet, yttrium iron garnet, and lithium gallium spinel doped with a number of  $3d$  ions [10, 11]. The main result was the discovery of attenuation maximum which was considered to be observed at  $\omega\tau \approx 1$  and reconstruction of the relaxation time temperature dependence. In some experiments reported later both the velocity and attenuation of ultrasound were measured as functions of the temperature. They were done on ZnSe and ZnTe crystals doped with transition metals. These crystals have the zincblende structure with the Jahn–Teller ion in tetrahedral coordination. The following

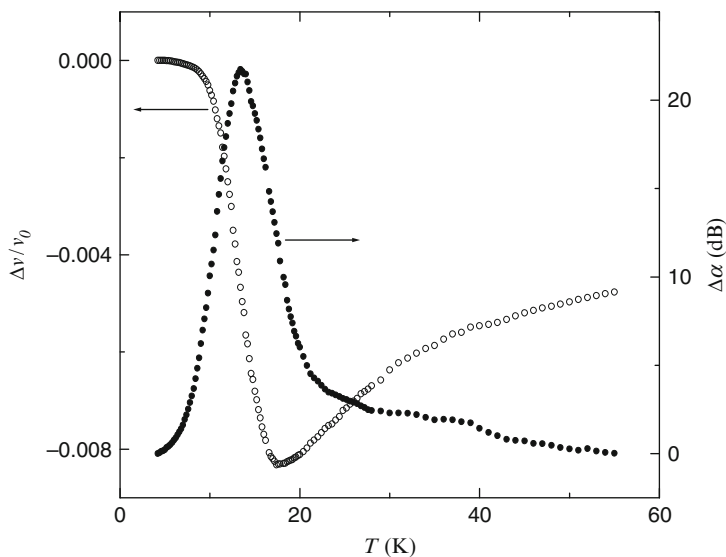


**Fig. 5** Temperature dependences of velocity [ $v_\ell(T) - v_\ell(4.2)/v_\ell(4.2)$ ] (*open circles*) and attenuation of ultrasound (*filled circles*) with respect to the level at  $T = 4.2$  K obtained in  $\text{ZnSe:Cr}^{2+}$  at 54.4 MHz. Concentration of the impurity  $n_{Cr} = 10^{20} \text{ cm}^{-3}$ . Longitudinal wave, ultrasound passage  $\ell = 0.717$  cm, propagation direction:  $[110]$ . After Fig. 1 in [17]

impurities were investigated:  $\text{Ni}^{2+}$  [15, 16],  $\text{Cr}^{2+}$  [17],  $\text{Fe}^{2+}$  [18],  $\text{Mn}^{2+}$  and  $\text{V}^{2+}$  [3] with concentration of  $10^{18} - 10^{21} \text{ cm}^{-3}$ . All the crystals which impurity has the orbitally degenerate states have exhibited: (1) a peak of attenuation and a step-like variation of the velocity at low temperatures (below 20 K, shown, e.g., for  $\text{ZnSe:Cr}^{2+}$  in Fig. 5), (2) shift of these anomalies to higher temperatures with frequency increase (Fig. 2), and (3) the lattice instability in the form of the modulus softening ( $c_s$  or  $c_f$ ) in a more wide temperature interval (Fig. 6). Such a behavior was not found for the crystal doped with  $\text{Mn}^{2+}$ . This ion has  ${}^6A_1(e^2t^3)$  high-spin ground state in tetrahedral environment [19], and, therefore, the Jahn–Teller effect should not be observed in this case.

Speaking about the relaxation origin of the low temperature anomalies, it is useful to show the temperature dependence of the wave number. It is useful because  $\text{Re}(\Delta k_\beta)/k_0 = -\Delta v_\beta/v_0$  and  $\text{Im}(\Delta k_\beta) = -\Delta\alpha_\beta$ , while  $\text{Re}(\Delta v_\beta)/v_0$  and  $\Delta\alpha_\beta$  are the parameters measured in an experiment. One can see that, in accordance with the expressions (15) and (20),  $\Delta k_\beta(T)/k_0$  should differ from  $\Delta c_\beta(T)/c_0$  by the factor of  $1/2$ :

$$\text{Im}\Delta k_\beta = -\Delta\alpha_\beta = -\frac{1}{2}k_0 \frac{\text{Im}\Delta c_\beta}{c_0} = -\frac{1}{2}k_0 \frac{c_\beta^U - c_\beta^R}{c_0} \frac{\omega\tau}{1 + \omega^2\tau^2}, \quad (77)$$

$$\text{Re}\Delta k_\beta = -\frac{1}{2}k_0 \frac{\text{Re}\Delta c_\beta}{c_0} = -\frac{1}{2}k_0 \frac{c_\beta^U - c_\beta^R}{c_0} \frac{1}{1 + \omega^2\tau^2}. \quad (78)$$

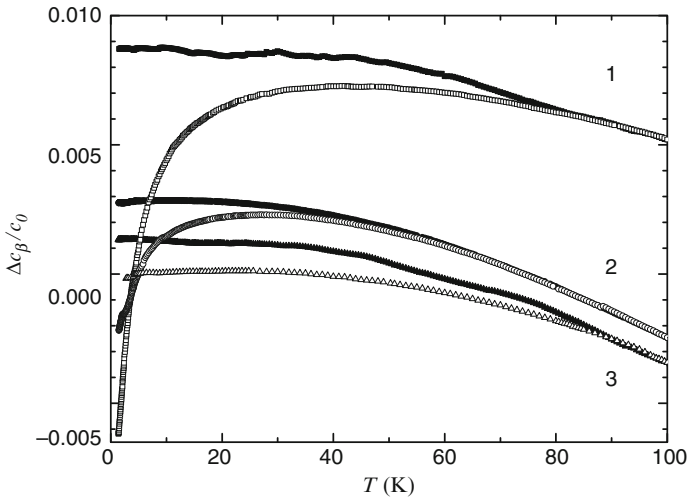


**Fig. 6** Temperature dependences of the elastic moduli in ZnSe:V<sup>2+</sup> and ZnSe:Mn<sup>2+</sup> ( $n_V = 5.6 \times 10^{18} \text{ cm}^{-3}$  and  $n_{Mn} = 9.4 \times 10^{20} \text{ cm}^{-3}$ ). Curves 1:  $\Delta c_f(T)/c_f(T_0)$  (open circles – ZnSe:V<sup>2+</sup>, filled – ZnSe:Mn<sup>2+</sup>, frequency 52 MHz for both plots); Curves 2:  $\Delta c_\ell(T)/c_\ell(T_0)$  (open circles – ZnSe:V<sup>2+</sup>, 52 MHz; filled – ZnSe:Mn<sup>2+</sup>, 55 MHz); and Curves 3:  $\Delta c_s(T)/c_s(T_0)$  (open circles – ZnSe:V<sup>2+</sup>, 52 MHz; filled – ZnSe:Mn<sup>2+</sup>, 55 MHz).  $\Delta c_i(T) = c_i(T) - c_i(T_0)$ ,  $T_0 = 4.2 \text{ K}$ . The plots for ZnSe:Mn<sup>2+</sup> were shifted to coincide with the corresponding plots for ZnSe:V<sup>2+</sup> at  $T = 100 \text{ K}$ . After Fig. 1 in [3]

Here  $\Delta k_\beta = k_\beta - k_0$ ,  $\Delta \alpha_\beta = \alpha_\beta - \alpha_0$ ,  $k_0$  and  $\alpha_0$  are the initial reference parameters determined at the lowest temperature (or as interpolation of the curve to  $T \rightarrow 0$ ).

The temperature dependence of the wave number obtained in ZnSe:Cr<sup>2+</sup> is given in Fig. 7, and it is typical for the mentioned diluted crystals. What do we see? We see the peak of  $\text{Im} \Delta k_\ell$  and the step-like variation of  $\text{Re} \Delta k_\ell$  in the interval of 6–20 K. The signs and the relative magnitudes of the variations correspond completely to what should be when the relaxation-origin anomalies take place. Remind,  $c^U - c^R \approx c^R < 0$ . The difference of the  $\text{Re} \Delta k_\ell$  (Fig. 7) and  $\text{Re} \Delta c_\beta$  (Fig. 1) is in the high-temperature region corresponding to  $\omega \tau < 1$ . This difference is due to the temperature dependence of the relaxed modulus  $c^R \propto 1/T$ . This dependence is clearly seen in Fig. 8, where the result is shown of reconstruction of  $c^U(T)$  and  $c^R(T)$  with the use of the formulas (67) and (68).

A typical temperature dependence of the relaxation time reconstructed according to the expression (63) is given in Fig. 9. The experiments done with the mentioned crystals proved that the curve  $\tau(T)$  for a given impurity does not depend on either the frequency or the polarization of the wave. Plotted logarithmically, it is represented by lines whose slopes change (indicated with the arrow in Fig. 9). The change of slope is interpreted [2] as a change in the relaxation mechanism: thermal activation over the potential barrier  $V_0$  at higher temperatures and tunnelling through the barrier at lower temperatures. The corresponding expressions for the contributions to the relaxation rate are given by the (38)–(40).



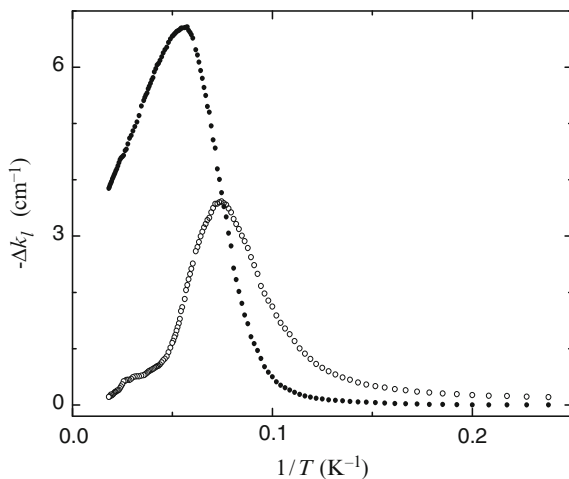


**Fig. 7** Real (*filled circles*) and imaginary (*open circles*) components of the complex wave number vs. inverse temperature obtained in  $\text{ZnSe:Cr}^{2+}$  at 54.4 MHz.  $\Delta k = k(T^{-1}) - k(T^{-1} \rightarrow \infty)$ . Concentration of the dopant  $n_{Cr} = 10^{20} \text{ cm}^{-3}$ . Longitudinal wave, propagation direction: [110]. After Fig. 2 in [17]

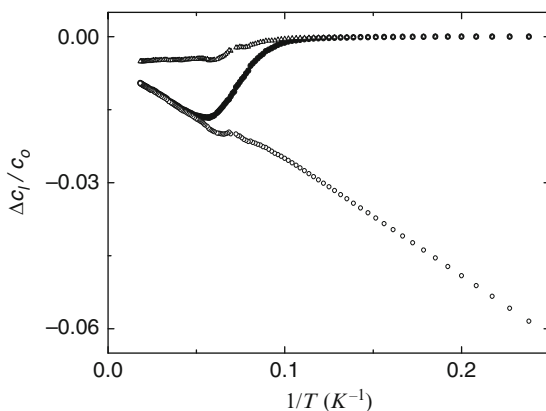


**Fig. 8** Elastic moduli  $c_\ell = (c_{1111} + c_{1122} + 2c_{1313})/2$  vs. inverse temperature obtained for 54.4 MHz in  $\text{ZnSe:Cr}^{2+}$  with concentration of the dopant  $n_{Cr} = 10^{20} \text{ cm}^{-3}$ . *Filled circles* represent the real part of the dynamic modulus  $(c_\ell - c_0)/c_0$ , *open circles* represent the relaxed modulus  $(c^R - c_0)/c_0$ , and *open triangles* represent the unrelaxed modulus  $(c^U - c_0)/c_0$ . The initial reference modulus  $c_0$  was taken as an extrapolation of  $c_\ell(T)$  to  $T = 0 \text{ K}$ . After Fig. 6 in [17]

The magnitudes of the some parameters of the Jahn–Teller complex determined in ultrasonic experiments are given in Table 1. Unfortunately, simulation of the reconstructed relaxation time was not completed for tunnelling regime of relaxation, and therefore, such parameters as the deformation potential  $b$ , the tunnelling splitting  $\Gamma$ , and the energy of inevitable strain  $u_0$  are not determined yet.

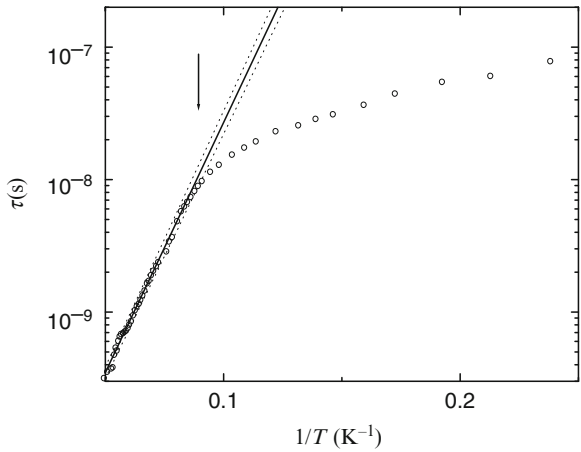


**Fig. 9** Relaxation time vs. inverse temperature in  $\text{ZnSe:Ni}^{2+}$  with concentration of the dopand  $n_{\text{Ni}} = 5.5 \times 10^{19} \text{ cm}^{-3}$ . *Open circles* show data obtained with fast shear waves at 56 MHz. The *lines* are plots of  $\tau = (2\nu_0)^{-1} e^{T_B/T}$ ; the *solid line* corresponds to  $T_B = V_0/\kappa = 87 \text{ K}$ , and the *dotted lines* to  $T_B = 87 \pm 2 \text{ K}$ ,  $\nu_0 = 11 \times 10^{10} \text{ sec}^{-1}$ . After Fig. 7 in [3]

**Table 1** Potential barriers  $V_0$ , softening moduli, active vibronic modes, and vibrational frequencies determined in ultrasonic experiments carried out on the zinc-blende crystals doped with  $3d$  ions

Crystal	Ground state of the impurity ion [19]	Softening modulus/active mode	Potential barrier, $V_0, \text{ cm}^{-1}$	Vibrational frequency, $\nu_0, 10^9 \text{ s}^{-1}$	Reference
$\text{ZnSe:Fe}^{2+}$	${}^5E(e^3t^3)$	$c_s^a / \epsilon$	24	10	[18]
$\text{ZnSe:Cr}^{2+}$	${}^5T_2(e^2t^2)$	$c_s / \epsilon$	38	7.6	[15]
$\text{ZnSe:V}^{2+}$	${}^4T_1(e^2t^1)$	$c_f^b / \tau$	5.6	4.8	[3]
$\text{ZnSe:Ni}^{2+}$	${}^3T_1(e^4t^5)$	$c_f / \tau$	60	110	[16]
$\text{ZnTe:Ni}^{2+}$	${}^3T_1(e^4t^5)$	$c_f / \tau$	21	600	[17]

<sup>a</sup>  $c_s = (c_{1111} - c_{1122})/2$

<sup>b</sup>  $c_f = c_{1313}$

## 4 Conclusion

Summarizing, we would like to say that ultrasonic technique could be very useful for investigation the the electronic ground states and their tunnelling splitting. First of all, the type of the vibronic mode (or local distortions) can be determined. The second, the potential barrier and vibrational frequency can be obtained with the help of the relaxation time reconstruction. The third, simulation of the reconstructed temperature dependence of the relaxation time can give the deformation potential, the tunnelling splitting, and the inevitable strain. The fourth, whenever the deformation potential is known, one can calculate the impurity concentration. Certainly, these parameters can be obtained from the experiments of another nature

by direct measurements or indirectly – with the help of appropriate simulation. But, anyway, ultrasonic experiment does represent one more independent source of information, sometime providing new information. As an example, we can mention the  $\text{ZnSe:Cr}^{2+}$  crystal. The results of ultrasonic experiment [17] clearly indicated the trigonal local distortions, while the optical experiment could not provide such definite information and both trigonal and tetragonal distortions were used for interpretation the absorption and emission spectra [20]. The possibility to determine the potential barrier is of particular interest. If we look at the Table 8.2 in [9], in which a number of the most important parameters of the Jahn–Teller system in various crystals (more than 30) are collected, we will see that this parameter is defined only for  $\text{CaO:Cu}^{23+}$ ,  $\text{Al}_2\text{O}_3:\text{Ni}^{3+}$ ,  $\text{CdF}_2:\text{Ni}^{2+}$ , and  $\text{CaF}_2:\text{Ni}^{2+}$ . Probably, this information will be obtained in the nearest future with the help of ultrasonic investigations.

## References

1. B. Lüthi, *Physical Acoustics in the Solid State*, 2nd edn. (Springer, Berlin, 2005), pp. 119–146
2. M.D. Sturge, in *The Jahn-Teller Effect in Solids*, ed. by S. Frederick, D. Turnbull, H. Ehrenreich. Solid State Physics, vol 20 (Academic, New York, 1967), p. 89
3. V.V. Gudkov, A.T. Lonchakov, V.I. Sokolov, I.V. Zhevstovskikh, V.T. Surikov, Phys. Rev. B **77** 155210 (2008)
4. L.D. Landau, E.M. Lifshitz, *Theoretical Physics: Theory of Elasticity*, vol.7 (Nauka, Moscow, 1987) (in English: Addison-Wesley, Reading, MA, 1959)
5. R.N. Thurston, in *Physical Acoustics: Principles and Methods*, ed. by W.P. Mason, vol 1A (Academic, New York, 1964)
6. C. Truesdell, R.A. Toupin, *Handbuch der Physik*, (Springer, Berlin, 1960), vol.III/1, pp. 226–793
7. C. Zeener, *Elasticity and Anelasticity of Metals*. (University of Chicago Press, Chicago, 1948)
8. I.B. Bersuker, Zh. Experm. I Teor. Fiz. **44** 1577 (1963); Sov. Phys. JETP (English Transl.) **17** 1060 (1963)
9. I.B. Bersuker, *The Jahn–Teller Effect*. (Cambridge University Press, Cambridge, 2006), p. 616
10. E.M. Gyorgy, M.D. Sturge, D.B. Fraser, R.C. LeCraw, Phys. Rev. Lett. **15** 19 (1965)
11. M.D. Sturge, J.T. Krause, E.M. Gyorgy, R.C. LeCraw, F.R. Merritt, Phys. Rev. **155** 218 (1967)
12. N.S. Averkiev, T.K. Ashirov, A.A. Gutkin, E.B. Osipov, V.E. Sedov, Fizika Tverdogo Tela **28** 2961 (1986); Sov. Phys. Phys. Solid State (English Transl.) **28** 2961 (1986)
13. V.V. Gudkov, *Magnetoacoustic Polarization Phenomena in Solids*. (Springer, Berlin, 2000), pp. 23–32
14. Hp. Schad, K. Lassmann, Phys. Let. **56A** 409 (1976)
15. V. Gudkov, A. Lonchakov, V. Sokolov, I. Zhevstovskikh, N. Gruzdev, Phys. Stat. Sol. (b) **242** R30 (2005)
16. V. Gudkov, A. Lonchakov, V. Sokolov, I. Zhevstovskikh, N. Gruzdev Jour. Korean Phys. Soc. (b) **52** 63 (2008)
17. V.V. Gudkov, A.T. Lonchakov, V.I. Sokolov, I.V. Zhevstovskikh, Phys. Rev. B **73** 035213 (2006)
18. V.V. Gudkov, A.T. Lonchakov, I.V. Zhevstovskikh, V.I. Sokolov, V. T. Surikov, Official Conference Book 25th International Conference on Low Temperature Physics (Amsterdam, Netherlands, August 6–13, 2008) p. 323; Physics of Low Temperatures **35** 99-102 (2009)
19. K.A. Kikoin, V.N. Fleurov *Transition Metal Impurities in Semiconductors: Electronic Structure and Physical Properties*, (World Scientific, Singapore, 1994), p. 163
20. G. Bevilacqua, L. Martinelli, E.E. Vogel, O. Mualin, Phys. Rev. B **70** 075206 (2004)

# Long Range Cooperative and Local Jahn-Teller Effects in Nanocrystalline Transition Metal Thin Films

Gerald Lucovsky

**Abstract** The group IVB transition metal (TM) elemental oxides,  $\text{TiO}_2$ ,  $\text{ZrO}_2$  and  $\text{HfO}_2$ , have emerged as candidate materials for advanced gate dielectrics for scaled Si microelectronics. Additionally, complex oxides, comprised of TM oxides and ordinary oxides, or TM and rare earth (RE) atom oxides are also being considered by the microelectronics community in the context of combining microprocessor and memory Si chip functions with additional types of functionality derived from complex oxides. This functionality includes ferroelectric and/or ferromagnetic storage or switching, which are generally enabled by Jahn-Teller (J-T) effects. The properties and reliabilities of both elemental and complex TM oxides are closely correlated with intrinsic TM-atom bonding defects, where J-T local bonding distortions are expected to be important. Defect centers can also be associated with impurity atoms, e.g., TM atoms that are not a constituent of the host TM oxide. J-T distortions in defect centers can manifest themselves in two ways: (1) adversely, as traps and/or charged defects that reduce carrier transport, or (2) positively, as centers which provide a pathway to control of nano-grain symmetry and thin film morphology, and promote changes in long range order as required for ferroelectric or ferromagnetic behavior.

This chapter will address two issues relevant to J-T structural distortions in elemental oxides: (1) cooperative J-T distortions in group IVB TM elemental oxides; and (2) localized J-T distortions in defect states in deposited thin film nanocrystalline TM elemental oxides. Each of these issues is addressed at two levels: (1) experimental determination of electronic structure, including valence band and final states, and band edge defects based on synchrotron O K edge X-ray absorption and soft X-ray photoelectron spectroscopies, and spectroscopic ellipsometry in the visible and vacuum UV; and (2) energy level diagrams based either on ab-initio calculations, or symmetry adapted linear combinations (SALC's) of TM and oxygen atomic states, including "text book" models that include the SALC's as a basis set.

## 1 Introduction

This chapter summarizes the research performed on group IVB TM elemental oxides by Professor Lucovsky and his research group at North Carolina State University (NCSU). These oxides had been targeted by the semiconductor industry

world wide, as candidate materials to replace non-crystalline silicon dioxide,  $\text{SiO}_2$ , and non-crystalline silicon oxynitride alloys  $(\text{Si}_3\text{N}_4)_x(\text{SiO}_2)_{1-x}$ , as replacement gate dielectrics for advanced metal-oxide-semiconductor (MOS) devices. These TM atom oxide devices are designed to significantly increase levels of integration, thereby providing increased functionality in circuits and systems on a single semiconductor integrated circuit chip. M. Houssa and M. Hyens have discussed the motivation for the introduction of the so-called high-k gate dielectric materials in [1]; and including the TM oxides of this chapter.

The group IVB TM oxides, in particular  $\text{ZrO}_2$  and  $\text{HfO}_2$ , and their respective silicates had initially emerged as materials of potential interest for these applications [1, 2]. Zr silicate was the first TM oxide that my group at NCSU investigated [3], and my introduction to the theoretical approaches to electronic structure for these high-k oxides was in a monograph authored by P.A. Cox [4]. This text indicated the importance of the J-T effect with respect to conduction band edge final states, and included the motivation for the approach taken in this chapter in addressing intrinsic monovacancy and divacancy defects.

This chapter has not been organized historically to trace research that has culminated world-wide in the introduction of high-k dielectrics into commercial advanced semiconductor devices, but instead is organized to describe the experiments and theory that underpin the importance of J-T effects in nano-crystalline thin film TM oxides, most importantly in the intrinsic bonding defects that limit device performance and reliability [1].

The majority of the experimental results presented are for nanocrystalline  $\text{TiO}_2$  and  $\text{HfO}_2$ , and have utilized thin films prepared by remote plasma enhanced chemical vapor deposition (RPECVD) on either Si substrates with a Si oxynitride interfacial transition passivation layer, or on plasma-nitrided Ge substrates [4, 5]. The  $\text{Y}_2\text{O}_3$  alloyed  $\text{ZrO}_2$  and  $\text{HfO}_2$ , cubic Zirconia and Hafnia, were prepared by reactive evaporation [6]. We have also studied samples of  $\text{HfO}_2$  prepared by atomic layer deposition [7], and for the same thickness, and post deposition annealing, the spectroscopic studies for these films yield results for conduction and valence band states and band edge defects that are essentially the same as the electronic structures in films prepared by RPECVD, establishing the intrinsic character of the electronic structure in general as well as these bonding defects.

## 2 Jahn-Teller Effects in Nano-Grain Thin Films

### 2.1 The Cooperative J-T Effect

In a Solid State Supplement, “*Long Range Order in Solids*” [8], the authors Robert M. White and Theodore H. Geballe, have pointed out that “in insulators comprised of ions with orbitally degenerate ground states,”; e.g., the TM oxides of this chapter, “it is possible to lower the electronic energy by splitting these degenerate levels

by means of a lower symmetry distortion”, and thereby removing the degeneracy. White and Geballe go on to state that, “such transitions are referred to as cooperative Jahn Teller distortions”. These transitions have also been discussed at length in a comprehensive review article [9]. It is important to note that cooperative J-T effects in crystals, whether they are a nanocrystalline scale,  $\sim 2\text{--}100\text{ nm}$ , or single crystals, depend primarily on breaking local site symmetry, and as such are fundamentally different than a Peierls distortion where the symmetry that is broken is translational.

The spectroscopic experimental evidence for cooperative J-T effects in the group IVB TM oxides,  $\text{TiO}_2$ ,  $\text{ZrO}_2$  and  $\text{HfO}_2$ , has been summarized in [4] and [5], in which degeneracy removal in conduction band final states has been observed in (1) synchrotron X-ray absorption spectroscopy (XAS) and X-ray photoelectron spectroscopy (XPS), and in (2) visible-vacuum-ultra-violet spectroscopic ellipsometry as well (vis-VUV SE). This paper focuses primarily on  $\text{HfO}_2$ , but includes data and analyses for  $\text{TiO}_2$  and  $\text{ZrO}_2$ , where the experimental results and interpretation in terms of electronic structure theory, including defects, provide increased insights into the relationships between the J-T effect and the accompanying changes in the local site symmetries.

$\text{HfO}_2$  (and also  $\text{ZrO}_2$ ) exist in three different crystallographic phases, monoclinic (m-) at room temperature with sevenfold coordinated Hf, tetragonal (t-) at intermediate temperatures with eightfold coordinated Hf, and finally a cubic (c-)  $\text{CaF}_2$  phase at high temperatures with eightfold coordinated Hf. The melting point of  $\text{HfO}_2$  from a cubic  $\text{CaF}_2$  structure is  $3887^\circ\text{C}$ , the transition into a tetragonal phase is at  $\sim 2200^\circ\text{C}$ , and the transition into a monoclinic phase is at  $\sim 1100^\circ\text{C}$ . The first phase to appear after quenching from a melt is the cubic  $\text{CaF}_2$  structure [9], in which Hf-atoms are eightfold coordinated, with the O-atoms fourfold coordinated. This structure is often described as in terms of planes of eightfold coordinated Hf-atoms separated by planes of fourfold coordinated O-atoms. The next phase is tetragonal with Hf-atoms remaining eightfold coordinated and O-atoms fourfold coordinated as well, but with local site symmetry reduced at the Hf-site by a tetragonal distortion, as well as a J-T vibronic distortion in both basal planes. Finally, the stable room-temperature phase is monoclinic with two significant changes in the local bonding: (1) the coordination of the Hf-atoms is reduced from eight to seven, and (2) the planes of O-atoms that bracket these Hf-atoms then alternate between threefold and fourfold coordinated to balance to sevenfold coordination of Hf. Films prepared by all of the deposition procedures identified below are inherently metastable, and as such they may have either monoclinic or tetragonal nano-grains, or be mixtures of monoclinic and tetrahedral nano-grains. Cubic phases have also be produced by stabilization with Y at low concentrations,  $>\sim 3\%$ , and extending up to  $\sim 20\%$ .

The first high temperature phase transition from the  $\text{CaF}_2$  is displacive, and is therefore a *classic* cooperative J-T distortion in which d-state degeneracies are lifted when the basal plane distortions are taken into account [7, 8]. The second transition represents a further and more significant reduction in local site symmetry. This symmetry is sufficiently low so that all d-state degeneracies are lifted, and in addition the local coordination of Hf is reduced from eightfold to sevenfold [9]. The definition of a cooperative J-T effect in [7] clearly includes the monoclinic phases of  $\text{HfO}_2$  and

ZrO<sub>2</sub>, even though they are separated by another J-T phase from the *parent* symmetric and cubic CaF<sub>2</sub> phase. In the spirit of [7], the monoclinic rutile and anatase phases of TiO<sub>2</sub> are also cooperative J-T phases, as well as other closely related phases of TiO<sub>2</sub>. These will not be addressed in the detail as for the HfO<sub>2</sub> phases [9].

The electronic structures of the cooperative J-T phases of all three group IVB transition metal oxides are always referenced to ideal structures, cubic rutile for TiO<sub>2</sub>, and cubic CaF<sub>2</sub> for HfO<sub>2</sub> and ZrO<sub>2</sub>. This approach parallels the seminal electronic structure calculations of the Robertson group at the University of Cambridge in which conduction band offset energies between Si and these TM oxides have been addressed in the context of *replacement or alternative* dielectrics for SiO<sub>2</sub> in advanced Si microelectronic devices [1, 10].

We apply an approach based on the local site symmetry that has been used in classic texts on molecular orbital theory [11, 12], and subsequently addressed in a more formal way for TM bonding in octahedral and tetrahedral arrangements, as for example in TiO<sub>2</sub>, and in cubic titanate and manganite perovskites by F.A. Cotton [13].

Figure 1 has been constructed from Fig. 8.13 of [13], as modified by Fig. 2.8 of [14] to illustrate how this approach is applied to TiO<sub>2</sub>. The 3d, 4s, and 4p atomic states of Ti, and the 2s and the 2p atomic states of O, are used to construct a set of symmetry adapted linear combinations (SALC's) of atomic orbitals that are consistent with the O<sub>h</sub> symmetry group of a regular, or undistorted octahedron as in an ideal cubic rutile structure. It is important to understand that other atomic states, e.g., the Hf 5f state symmetries can be introduced as well, and that the introduction of

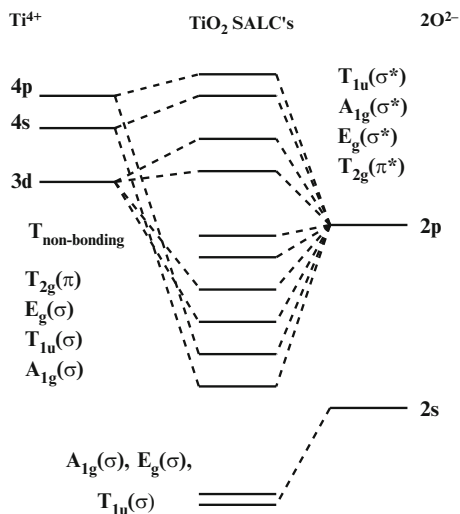


**Fig. 1** Schematic molecular orbital diagram for TiO<sub>2</sub>: sixfold-coordinated T<sup>4+</sup> ions, and threefold-coordinated O<sup>2-</sup> ions with covalent mixing of Ti and O atomic states in SALC's. Symmetry designations for occupied valence band states, the empty conduction band states, and the O-atom 2s shallow core state. Respective degeneracies for A, E and T states, are 1, 2 and 3 [13]

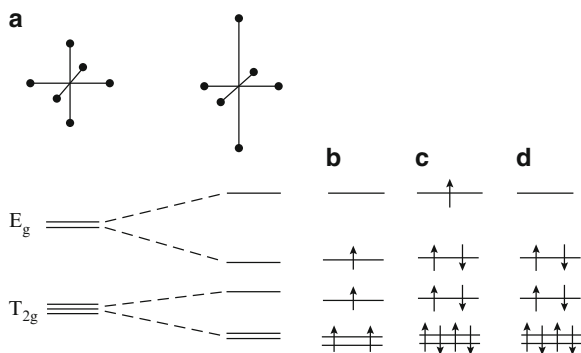
such states is not restricted to the so-called valence states of the particular transition metal atom. This is a very important distinction between *ab initio* molecular orbital theory and conventional wisdom as applied to other molecular orbital methods, such as the tight-binding LCAO method. The LCAO approach is more empirical and generally uses occupied valence state and symmetries in the respective basis sets of atomic wave functions for a diatomic oxide.

Figure 1 includes the 2s state of O for completeness; however, these states are essentially nonbonding, similar to the bonding in noncrystalline and crystalline  $\text{SiO}_2$  [15]. Figure 8.13 of [13] for the ionic limit, whereas, subsequent authors, e.g., Cox in [16] and Bersuker in [17], have modified the diagram to include covalent effects that effectively mix the TM atom and O-atom orbitals into a basis set of molecular orbitals that provide a pathway for comparison with experiment. This mixing underpins the discussions of new results presented later in this chapter; e.g., the *unambiguous* detection of Hf 5f states *virtual bound empty resonance states* in O K edge XAS spectra at X-ray energies  $>545$  eV. It is important to note these virtual or empty states are observed at X-ray photon energies above the energy threshold for the vacuum continuum, and are qualitatively different in detail than the antibonding states within the conduction band energies, that lie below the vacuum continuum level [7].

The electronic states of neutral O-atom vacancy defects have their atomic parentage in the TM atoms that border on the respective monovacancies or divacancies. The occupied and empty states of these defects fall within the forbidden energy gap, and it has been suggested in [4] and [5], that these states could be described in the context of trivalent ion states of the respective TM atoms. The occupied states of these mono- and divacancy defects are then isoelectronic to the occupied states of TM atoms in ionic states in which atomic d-states are occupied, rather than empty. Stated differently, the group IIIB and IVB TM elemental oxides are  $d^0$  oxides in the ionic limit [16], whereas in mono- and divacancy arrangements they are effectively trivalent ions with partial occupancy of their respective atomic d-states, in particular they are a  $d^1$  TM atom [14, 16, 17]. In addition, d-state occupancy in a vacancy bonding arrangement can either (1) result in a local J-T distortion, similar to what has been observed for divacancies in Si, where p-state, rather than d-state, degeneracy is at issue [18], or (2) alternatively simply reflect the J-T distortion of the host material.

We will use Fig. 2 as the basis for describing defects associated with octahedral coordination, e.g.,  $\text{TiO}_2$ , and complex oxide titanates and manganites as well. Figure 2 Schematic representation of d-state orbital energies for a regular octahedron, and tetragonally distorted octahedron. The regular octahedron in (a) is first applied to  $\text{TiO}_2$ , a  $d^0$  oxide in which none of the 3d-state orbitals is occupied [14]; however, as indicated in Fig. 1, these orbitals contribute the SALC's of Ti and O atoms, as required by the local  $O_h$  symmetry of the Ti atom and its six oxygen neighbors. In this  $d^0$  configuration, the lower energy  $T_{2g}$  state is triply degenerate, and the higher energy  $E_g$  state is doubly degenerate. The partial removal of these degeneracies for a tetragonal distortion in which the z-axis bonds are elongated is also a  $d^0$  state in the ionic limit; the degeneracy is completely removed for the  $E_g$  state, and the  $T_{2g}$  states is split in a doubly degenerate E-state, and a nondegenerate A-state. (b), (c)





**Fig. 2** Schematic representation of d-state orbitals (a) i) regular octahedron:  $T_{2g}$  state is triply degenerate,  $E_g$  state is doubly degenerate, and ii) tetragonal  $z$ -axis distortion: each of these has  $d^0$  occupancy, consistent with the ionic limit. (b), (c) and (d) represent respectively: high-spin  $d^4$ ,  $d^9$ , and a low-spin  $d^8$

and (d) are for other atomic species, e.g., Mn and Cu, where the number of occupied orbitals is a function of the ionic state [14, 16, 17]. (b) and (c), respectively are for *high-spin*  $d^4$  ion such as  $Mn^{3+}$  in (b), and a high spin  $d^9$  ion such as  $Cu^{1+}$  in (c). Finally (d) is for a *low-spin*  $d^8$  electron occupancy as in  $Cu^{1+}$ .

We will follow the procedure first used by the Robertson group [10], in which a cubic structure was used as a basis for addressing defects in  $HfO_2$  and  $ZrO_2$ , even for the thin film samples that have monoclinic, tetragonal, or a mixture monoclinic and tetragonal nano-grain distortions, including the removal of the  $E_g$  and  $T_{2g}$  state degeneracies. This approximation is validated experimentally by comparing conduction band edge defects in  $HfO_2$  and  $ZrO_2$ , with  $Y_2O_3$  stabilized cubic Hafnia and Zirconia, respectively [4, 5].

## 2.2 Local Bonding and J-T Effects in Mono- and Divacancy Defects

### 2.2.1 Intrinsic Bonding Defects

There have been two different proposals put forth for intrinsic bonding defects in  $HfO_2$  and  $ZrO_2$ . The first of these was that the defects in the upper half of the band gap observed experimentally [19, 20] were associated with unoccupied or partially-occupied O-atom monovacancies [21, 22]. The majority of these calculations were based on density function theory (DFT), with semiempirical approaches applied to estimate the band gaps, and the monovacancy energies in the forbidden band gap as well. It is significant to note that Professors Isaac Bersuker and Victor Pollinger, have expressed reservations about the application of DFT to transition metal oxides in general, and specifically for studies of defect states using this approach as well [23, 24]. The calculations in references 21 and 22 do not reflect the

strongly-correlated character of occupied TM states, and as such cannot be applied to defect states that associated with occupied TM atom states [13, 14].

Prior to the interest in  $\text{HfO}_2$  and  $\text{ZrO}_2$  for applications for advanced microelectronic devices, most of the experimental and theoretical studies dealing with defects in TM oxides focused on chemical defects associated first and second row TM atoms the were either octahedrally or tetrahedrally coordinated. These included applications to elemental oxides,  $\text{TiO}_2$  and  $\text{NiO}$ , as well as complex oxides such as the cubic perovskites, e.g.,  $\text{SrTiO}_3$  and other titanates and manganites [14, 17]. It is important to note that there are significant differences between the local bonding of O-atoms in  $\text{TiO}_2$ , where they are threefold coordinated, and in cubic perovskites where they are sixfold coordinated. In  $\text{SrTiO}_3$ , each O-atom has two Ti-neighbors, and 4 Sr-neighbors at a larger bond-length. These differences are important in the local bonding of monovacancy defects; however, the removal of an O-atom in  $\text{SrTiO}_3$  leads to two electrons being bonded three nearest-neighbor atoms. There are several ways to describe this arrangement. Since d-state occupancy is digital, the two O-atoms can be associated with two of the three Ti-atoms bordering on the monovacancy site. This would be designated a pair of coupled  $d^1$  states [14, 16]. Alternatively we could represent the bonding by a  $d^2$  electronic occupancy for an *equivalent* Ti atom, consistent with a Jahn-Teller distortion removing the degeneracy of these two states. The these two presentations, a pair of  $d^1$  states, or a single  $d^2$  states, are supported by the observation of two occupied valence band edge states in the soft XPS, SXPS spectra of  $\text{TiO}_2$  [4, 5]. The defect states in the gap for a monovacancy in  $\text{SrTiO}_3$  are assumed to be qualitatively similar to those in  $\text{TiO}_2$ .

For octahedrally-coordinated atoms such as Ti in either  $\text{TiO}_2$  or in cubic perovskites, the electronic structure for the intrinsic bonding defects are consistent with O-atom monovacancies, the concentrations of which can be varied by changing the growth or annealing O-atom over-pressures [16].

Figure 3 is a schematic representation the local bonding coordination at (1) a monovacancy in  $\text{TiO}_2$  in (a), (2) a monovacancy in  $\text{HfO}_2$  in (b), and (3) a divacancy in  $\text{HfO}_2$  (c) that is at the *face of the unit cell in contact with* the fourfold coordinated O-atoms in (c). To preserve charge neutrality after removal of a neutral

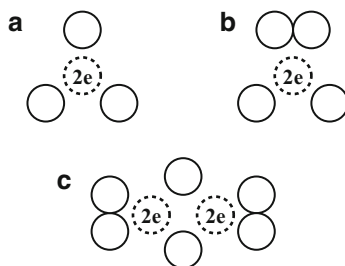


**Fig. 3** Schematic representation the local bonding coordination (a) a mono-vacancy defect in  $\text{TiO}_2$ , (b) a monovacancy defect in  $\text{HfO}_2$ , and (c) divacancy defect in  $\text{HfO}_2$ . Divacancy defect is equivalent to two monovacancies that are edge connected. Darker circles are Ti- and Hf-atoms, dashed circles are removed O-atoms: each contributes 2 electrons to defect bonding arrangements

O-atom, each of the monovacancies has two electrons that compensate the positive charge of the neighboring TM atoms, and thereby preserve overall charge neutrality for the removal of neutral O-atoms. The calculations in [21] assumed this charge is distributed over all of the TM atoms that were previously bonded to the removed neutral bonding atom. This redistribution of charge is expected to be valid for s- and p-states, but we suggest that is not consistent with the highly directional and localized character of the 3d-states of Ti, or the 5d-states of Hf. More importantly, defect states associated with impurity atoms that are localized in the forbidden band gap have three occupancy states: (a) empty, (b) singly occupied or (c) doubly occupied.

In the context of an ionic bonding limit, on average two of the three Ti atoms would be equivalent to  $\text{Ti}^{3+}$  ions, instead of  $\text{Ti}^{4+}$ ; however, this description is not consistent with the way the  $\text{Ti}^{3+}$  state has been treated in  $\text{Ti}_2\text{O}_3$  (see [15]). Following the approach of [14], these two atoms are represented in Fig. 4 and the electronic states of an *equivalent Ti* atom in a  $d^2$  configuration or equivalently, a pair of coupled  $d^1$  states“ it therefore reads” configuration, or equivalently, a pair of  $d^1$  states rather than the  $d^0$  configuration of the host crystal [14, 17]. This difference is significant, and will be applied to the experimentally determined electronic occupied and empty states within the monovacancy defect site in  $\text{TiO}_2$ . This description also applies to *virtual bound resonance states* that lie above the threshold for the vacuum continuum states [7], and will be addressed, and resolved by analysis of experimental results.

As noted in [4] and [5], and in the discussion above, the electronic structure of  $\text{Ti}^{3+}$  has been addressed for both  $\text{Ti}_2\text{O}_3$  [14], and the hydrated ion  $\text{Ti}(\text{H}_2\text{O})_6^{3+}$  complex [11]. However it is important understand these two applications are different. The  $d^1$  description applies exactly to each hydrated  $\text{Ti}^{3+}$  ion. In contrast, the  $d^2$  designation for the Ti-atoms in  $\text{Ti}_2\text{O}_3$  is based on a SALC molecular orbital representation of the  $\text{Ti}_2\text{O}_3$  electronic structure, in particular on overall and local charge neutrality.

An equivalent SALC molecular orbital description is also appropriate for the monovacancy defect in  $\text{HfO}_2$  in Fig. 3(b), and applies to  $\text{ZrO}_2$  monovacancies as well. As indicated in Fig 3(b) the *equivalent Hf ion* for this monovacancy is also

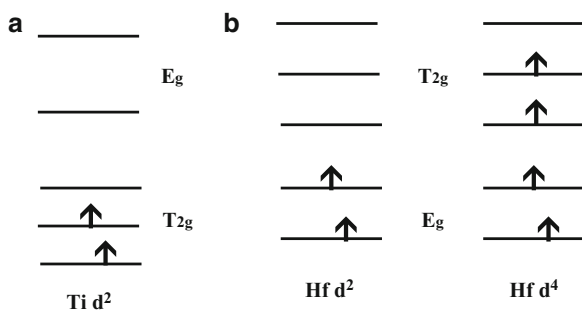


**Fig. 4** Schematic representation of orbital energies for: (a)  $\text{TiO}_2$  monovacancy in a monoclinically distorted octahedron with a  $d^2$  ion state; (b)  $\text{HfO}_2$  monovacancy and in a divacancy: monovacancy is  $d^2$  occupancy state, divacancy in a  $d^4$  occupancy state. Electron occupancies are all in high spin states

in an equivalent  $d^2$  configuration as well. This is easily recognized by a functional equalivance between a single  $d^2$  state, and a pair of interacting  $d^1$  states which are at different energies due to a Jahn-Teller distortion, as in the Si divacancy [8].

Figure 3(c), indicates the local bonding in the divacancy geometry described at the beginning of the last paragraph. This arrangement includes four charge compensating electrons, and is represented by the  $d^4$  d-state occupancy in Fig. 4(b), panel (3). As discussed above this equivalent  $d^4$  state is spectroscopically the same as 4  $d^1$  states in an  $S^2$  representation, with respect to states detected in pre-edge and vacuum continuum regions in O K edge XAS spectra.

It is significant to note that the same electronic state representation is basis for J-T distortions in many technologically important cubic and hexagonal perovskites. e.g., La and La,Sr manganites in which all of the Mn atoms in  $\text{LaMnO}_3$ , and the La fraction of  $(\text{La}, \text{Sr})\text{MnO}_3$ , are in  $\text{Mn}^{3+}$  ion states ( $d^4$ ). For the Sr fraction of  $(\text{La}, \text{Sr})\text{MnO}_3$ , in order to preserve local charge neutrality the Mn atoms are in  $\text{Mn}^{4+}$  ion states ( $d^3$ ). The interesting ferroelectric and ferromagnetic properties of  $(\text{La}, \text{Sr})\text{MnO}_3$  in point of fact derive from this combination of  $\text{Mn}^{3+}$  and  $\text{Mn}^{4+}$  ion states, that respectively balance the 3+ formal charge of La, and the 2+ formal charge of Sr in this *mixed valence* perovskite [14]. This includes a magnetic insulator to metal transition that takes place for 20% Sr [1]. The pre-edge, and vacuum continuum spectra associated with this occupied Mn states above the valence band edge are qualitatively similar to the defect states observed in the respective pre-edge and vacuum continuum spectral.

Figure 4(a) is a schematic representation of the relative orbital energies for Ti atoms in a  $d^2$  monoclinically distorted octahedral bonding arrangement and thereby promotes the complete removal of the  $T_{2g}$  and  $E_g$  state degeneracies. 4(b) indicates respectively the local electronic structure at a monovacancy or in a divacancy in monoclinically distorted  $\text{HfO}_2$  and  $\text{ZrO}_2$ . For these sevenfold-coordinated oxides, the symmetries are reversed, and we designate the twofold-degenerate state as  $E_g$ , based on its cubic parentage, and the threefold degenerate as  $T_{2g}$ . For the divacancy structure, the four electrons are in turn bonded to the divacancy site and represented by an equivalent Hf or Zr atom with a  $d^4$  ion high spin state or equivalently four coupled  $d^1$  states. This configuration, whether it be in periodic crystalline structure, or at a local defect site is a strong candidate for a J-T distortion that increases its stability. From this point on, no distinction will be made between a divacancy with a  $d^4$  configuration, and one or two pair of coupled  $d^1$  states. This in effect gives the Hf and Zr oxide divacancies an electronic structure similar to Si divacancies which display J-T distortions [18]. However, the Si divacancy has one electron/Si [18], where as the  $\text{HfO}_2$  divacancy has two-thirds of an electron/Hf atom.

These defect state electronic structures will be compared with experimental data in Sect. 4, and use the symmetry adapted linear combinations, SALC's, description of [13] as for assigning spectroscopic defect state signatures to equivalent molecular orbital states.

Inherent for this description of intrinsic bonding defects, it is important to note that the crystal field (C-F) splitting for a group IVB TM atom is characteristic of the atomic species, Ti, Zr and Hf, and is always less than the band gap for

stoichiometric oxide in the  $d^0$  state. This situation applies independent of the coordination of the TM atom. We will use the designation C-F, rather than the alternative *ligand field* (*L-F*) notation, even though the descriptive C-F was associated originally with an ionic model. The ionic model is at best qualitatively correct, and is not a reliable quantitative model for determining the C-F splittings for TM ions, even in strongly ionic oxide bonding environments [14].

## 2.2.2 Electronic Structure of Alloy and Dopant Atoms

The electronic structure TM alloy, impurity and/or dopant atoms in elemental oxides has been addressed in several *classic* texts that have treated TM oxides, e.g., [14, 16, 17]. This presentation is restricted to the group IVB TM elemental oxides,  $\text{TiO}_2$ ,  $\text{ZrO}_2$  and  $\text{HfO}_2$ . With reference to an ionic description in which the formal charge on Ti, Zr and Hf is  $+4$ , these atoms are in a  $d^0$  state in which two s-electrons, and two d-electrons are removed from the atom to form the  $+4$  ion. Thus, there are no additional electrons in the in 3d, 4d or 5d states associated with occupied d-states between the top of the valence band, and the bottom of the conduction band; i.e., within the forbidden energy gap [14]. This same situation prevails for isoelectronic group IVB alloys such  $(\text{Hf}, \text{Ti})\text{O}_2$ ,  $(\text{Zr}, \text{Ti})\text{O}_2$  and  $(\text{Hf}, \text{Zr})\text{O}_2$ , where the formal ionic charges are  $4+$  for both alloy cations. The atomic states symmetries available for bonding in these binary alloys include, Ti 4s, 4p, and 3d, Zr 5s, 5p and 4d and 4f, and Hf 6s, 6p and 5d, and also 5f. The respective 4f and 5f states contribute symmetries required for sevenfold coordination as monoclinic and monoclinic Hafnia and Zirconia, and eightfold coordination in cubic Hafnia and Zirconia. In this regard it is important to note that the respective 5p and 6p states of Zr and Hf, as well as the 4f and 5f states are not in the valence shell.

On the other hand, if a TM metal atom with *formal ionic valence* of more than 4, e.g., V, Cr, Mn, Fe, Co, Ni or Cu from the first row TM atoms, is an intentionally added impurity or alloy atom, and if this atom is resident on a group IV atom site that is fully-bonded to O, then additional occupied d-states can either be incorporated into the otherwise forbidden band gap between the occupied valence band states, and the empty conduction band states of the group IVB host and give rise to excited bound resonance states within the vacuum continuum. Additionally, if the TM d-states are more than half-occupied for a relevant ionic state, then occupied d-states associated with occupancy beyond five d-states sometimes drop into the valence band and are therefore present as bound state resonances [1]. The same description applies to 4f states in the lanthanide rare earth series. At the beginning of the series, there are occupied 4f states above the valence band edge. Later in the series, beyond Gd, a portion of these states drop into the valence band. By the time the third row of transition atoms begins, for example for Hf, the occupied 4f states are below the valence band.

If the impurity atom state resides in the band gap, and is additionally incorporated into a monovacancy or divacancy defect bonding arrangement, then the formal charge on that atom will be  $3+$ , and this changes the occupancy of occupied

impurity atom d-states within the forbidden band gap accordingly from incorporation into normal bonding site where the formal charge must be  $4+$ .

Group IVB atoms with a formal charge of  $+3$  in monovacancy and divacancy arrangements, as well as impurity and alloy atoms with a formal valence states greater than four, each introduce *virtual bound resonance localized states* in the continuum of states above the vacuum threshold [see page 268, Ref [7]]. These are effectively symmetry-induced antibonding states, and are qualitatively similar to the normally empty antibonding states associated with valence bond states. The virtual bond resonance states have been detected by a combination of (1) XAS spectroscopy, with SXPS and vis-VUV SE spectroscopies, and (2) discussed within the framework of the SALC formalism of [13] in Sect. 4 of this chapter.

### 3 Spectroscopic Studies of TM Elemental Oxides I

This section describes spectroscopic techniques that have been utilized in the studies of the intrinsic band edge electronic states of group IVB TM oxides by the Lucovsky group. These include (1) XAS, and SXPS, where the SXPS designation is used to differentiate studies using continuously variable energy monochromatic X-rays from a synchrotron source, with respect to discrete energy laboratory X-ray and vacuum ultra-violet sources used for XPS and UPS, respectively. Other spectroscopic techniques have been applied in this chapter and include (1) vis-VUV SE, and (2) depth-resolved cathodo-luminescence spectroscopy, or DRCLS.

These spectroscopic measurements were undertaken primarily to identify the intrinsic electronic structure, including valence and conduction states, as well as *intrinsic bonding defects*, defined here as those associated with the group IVB TM oxide atoms, but in defect, rather than ideal crystalline bonding arrangements. For example these measurements were used to assign the valence and conduction band states of  $\text{TiO}_2$  in the context of Fig. 1 for regular or ideal octahedral coordination as a basis for understanding changes in these states that are associated with the cooperative J-T effect as described in [7] and [8] [3,4,25].

The XAS measurements identify final conduction band, or *otherwise empty* antibonding states, with an emphasis on 3d states for Ti, 4d states for Zr, and 5d states for Hf. These states have also be designated as Rydberg states, defined in the context of the local symmetry, which is non-spherical. There is also an additional focus on determining the J-T splittings in the context of Fig. 2. The same studies have also revealed transitions that terminate in band edge defect states, and these have generally been identified by differentiation of the XAS spectra [4, 5]. We will continue to make a distinction between empty antibonding states, and virtual bound state resonances associated with occupied TM d-states in the otherwise forbidden band gap, e.g., in  $d^n$  configurations, with  $n > 0$ . These resonances occur in the vacuum continuum and are enabled by fundamental changes in their local symmetry from purely atomic to a symmetry that is consistent with their solid state neighbors, i.e., the local crystal-field, and SALC's of available atomic states of the host structure.

The SXPS measurements have identified the valence band bonding states, as well as occupied defects, again in the context of Figs. 1 and 2. The synchrotron X-ray beam lines and their relevant properties are described in [4, 5 and 25].

The visible and near ultra-violet (1–6 eV), and vacuum ultra-violet (4–8.5 eV) spectroscopic studies focus on transitions from the occupied states at the top of the valence band, primarily O 2p  $\pi$  nonbonding states to the conduction band states, primarily O 2p  $\pi$  and  $\sigma$  antibonding states that are mixed TM atomic states in the context of SLAC's. These spectra also include intra-d-state d-d' transitions between occupied ground states and empty excited states of band edge defects; these are not to be confused with d-d\* transitions that terminate in virtual bound resonance antibonding states within the vacuum continuum. In the context of many-electron theory as applied to X-ray measurements, these states are referred to respectively as “shake-up” and “shake-off” states. The SE instruments used in these studies were developed by D.E. Aspnes during his research studies at Bell Labs, and more recently at NCSU [4, 5].

FTIR and XPS measurements were used mainly to address the phase stability of Ti, Zr and Hf silicates, e.g.,  $(\text{TiO}_2)_x(\text{SiO}_2)_{1-x}$ , and Ti, Zr and Hf Si oxynitrides, e.g.,  $(\text{TiO}_2)_x(\text{SiO}_2)_y(\text{Si}_3\text{N}_4)_{1-x-y}$  [3, 4, 26, 27]. These studies will not be emphasized in this chapter, and the reader is directed to [26 and 27], which address, respectively, the silicates and Si oxynitride alloys of Zr. The spectrometers used in these studies were conventional laboratory instruments similar to those in most solid state and surface science laboratories.

The DRCLS studies were performed on a state of the art instrument developed by Professor L.F. Brillson at the Ohio State University. The instrumentation and experimental details are addressed in a recent publication that focuses on defect related DRCLS in as-deposited and annealed  $\text{HfO}_2$  [28].

This chapter provides an introduction to the way that XAS, SXPS, and vis-VUV SE spectroscopy provide important insights for the identification of cooperative J-T effects in group IVB TM oxides. Several specific areas are high-lighted: (1) spectroscopic confirmation of the length scale required for J-T distortions in nano-grain films, with the important role of kinetic as well as dimensional constraints based on  $\text{HfO}_2$ ; and (2) using  $\text{TiO}_2$  as a model TM oxide, the importance of local site symmetry, as exemplified by the SALC's approach of [13]. This has been used to correlate XAS, XPS, and vis-VUV SE spectroscopic studies with electronic structure, including degeneracy removal for the Ti 3d  $T_{2g}$  and  $E_g$  states; and the spectroscopic identification of (1) occupied valence band, and (2) empty conduction band edge and (3) continuum defect state features as well. In the spirit of (3) the experimental results for  $\text{TiO}_2$  also reveal two qualitatively different *virtual bound types of resonance states* above the vacuum continuum: (1) antibonding states associated with occupied d-states in monovacancy  $d^2$ , or equivalently pair  $d^1$ , bonding arrangements, and (2) relatively shallow core states, e.g., Ti 3p and O 2s.

### 3.1 Scales of Order For Cooperative J-T Degeneracy Removal

Since all of the samples of this study are deposited thin films, typically 1.8–6 nm thick, the concept of a cooperative J-T effect, and its role in removing d-state degeneracies must be revisited from this perspective, and in particular to identify both thickness dependent, and other processing dependent issues relative to the stabilization of cooperative J-T bonding arrangement distortions. In a bulk single crystal, or polycrystalline sample removal of d-state degeneracies must simply satisfy the conditions presented in [7 and 8], which assume no dimensional or thickness bonding constraints, and no kinetic limitations as well. However, in thin film materials in general, the film must be sufficiently thick for a cooperative J-T effect to take place in all three directions. The pathway for understanding a thickness constraint is the quantification of a scale of order required for a J-T vibronic distortion. Even though this associated with a local symmetry reduction, this symmetry reduction cannot take place in a single primitive unit cell, but instead involves a *larger electronic unit cell*; this is implicit in the definition and discussion in [7]. For molecules this can be linear, but for the TM elemental oxides it must be three-dimensional.

The issue of length scales was addressed in a seminal paper by Professor Isaac Bersuker published in 1975 [29]. In this paper it was demonstrated that in a linear chain of  $\text{Cu}^{+2}$  atoms,  $d^9$ , with a composition  $\text{Cu}(\text{NH}_3)_2\text{X}_2$ ,  $\text{X} = \text{Cl}$  or  $\text{Br}$ , a J-T vibronic distortion was stabilized when the chain contained at least seven (7) Cu atoms. This molecular stabilization corresponds to coupling seven primitive unit cells of  $\text{HfO}_2$  or  $\text{ZrO}_2$  before a J-T effect vibronic distortion can be stabilized and frozen in. Figure 2.12 of [13] provides insights in the microscopic mechanism in  $\text{HfO}_2$  and  $\text{ZrO}_2$  for a cooperative J-T effect. This figure has been reproduced in a modified form in this chapter as Fig. 5. Even though Fig. 5 and the length scale addressed in [29] are for a linear molecular structure, the concept of a length scale readily extends to three dimensions, and applies for the TM oxides. In the next paragraph, we point out that critical length for coherent bonding that supports a stable vibronic distortion is  $\sim 3$  nm. This length scale is applicable to film thickness,

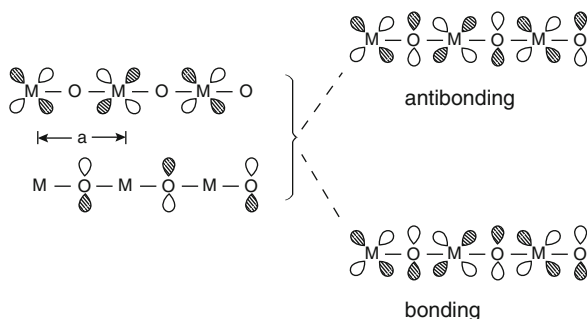


**Fig. 5** One-dimensional model for coherent  $\pi$ -bonding between metal atoms.  $\text{M} = \text{Hf}$ , and their O-atom neighbors utilizing Hf 5d-orbitals and O 2p  $\pi$  orbitals. Alternating phase establishes a coherence length equal to a sequence of 7 Hf atoms for enabling a cooperative J-T effect  $\text{Hf}(\text{Zr})\text{O}_2$  phase



e.g., the  $z$ -direction, but not apply for in-plane dimensions where transverse and lateral dimensions in the most aggressively scaled field effect transistors are more than 10–20 nm. However, it does apply to arrays of quantum dots and wires, and is a consideration to be addressed in designing and interpreting electrical results for quantum wire transistors.

This criterion of [29] corresponds to an *electronic unit cell* dimension or length scale for coherent  $\pi$ -bonding interactions of  $\sim 3$  nm [4,5]. In a paper presented at the recent XIX International Symposium in Heidelberg, DE on the J-T Effect, Professor Victor Polinger identified “inter-” or primitive (added for emphasis) “cell coupling as the driving mechanism for structural phase transitions in the above mentioned crystals”; i.e., in the TM elemental and complex oxides of this chapter. This leads to a dimensional constraint relative to thickness in thin film group IVB TM oxides identified in [4 and 5], and will be discussed below in the context of the detection of degeneracy removal in thin film samples of different thickness. Before this discussion, it is important to note that there is a second constraint associated with J-T effect distortions, and this relates the kinetics of the deposition process.

All of the thin films of this paper, and in many other studies of high- $k$  dielectrics, are generally deposited at low temperatures,  $< 500^\circ\text{C}$ . In this chapter the RPECVD process is performed at  $300^\circ\text{C}$  in order to minimize the formation, and subsequent incorporation of  $\text{OH}^{-1}$  impurity groups. At this temperature, and independent of the film thickness, the kinetics for organization of primitive unit cells into larger *electronic unit cells* is effectively suppressed, and J-T distortions cannot be observed independent of the film thickness.

Figure 6(a) indicates qualitative differences in the sharpness of spectral features in the O K edge XAS spectra of  $\text{HfO}_2$  films,  $\sim 4$  nm, thick as a function of processing temperature: as-deposited at  $300^\circ\text{C}$ , and after  $\sim 1$  min rapid thermal anneals in Ar at 500, 700 and  $900^\circ\text{C}$ . The spectral assignments will be discussed below; at this time, it is sufficient to note that the band edge Hf 5d,  $E_g$  (also sometimes designated as  $e_g$ ) feature sharpens between the 500 and  $700^\circ\text{C}$  anneals, and in differentiated spectra display a doublet structure indicative of a J-T splitting as well. These symmetry designations are referenced to a cubic system, the parentage of the phases with cooperative J-T effects, and have therefore been designated as  $E_g$  or  $T_{2g}$ . There are correlated increases in the Hf 6s and 6p features, and a sharpening the Hf 5d  $T_{2g}$  feature as well. Studies on other TM oxides, e.g., the complex oxide,  $\text{LaScO}_3$ , have indicated similar changes in the O K edge spectra for annealing temperatures higher than about  $700^\circ\text{C}$  as well [30].

Figure 6(b) indicates qualitative changes in the O K edge XAS spectra of  $\text{HfO}_2$  as a function of film thickness for films annealed at  $900^\circ\text{C}$ . All of the features in the 2 nm thick film are broad, and differentiation indicates no detectable J-T splittings in either the Hf 5d  $E_g$  or  $T_{2g}$  features. In contrast to the 2 nm thick film, all Hf features, the 5d  $E_g$  or  $T_{2g}$  absorptions, as well as the Hf 6s and 6p features are sharper in the 3 and 4 nm thick films. Differentiation of the Hf 5d features indicates complete degeneracy removal with two distinct minima for the  $E_g$  feature, and three for the  $T_{2g}$  feature. The major changes take place at a  $\sim 3$  nm film thickness consistent with the length scale approximated on the basis of the results in [29], and mechanism of  $\pi$ -bond coupling indicated in Fig. 5, and discussed in [4] and [5].

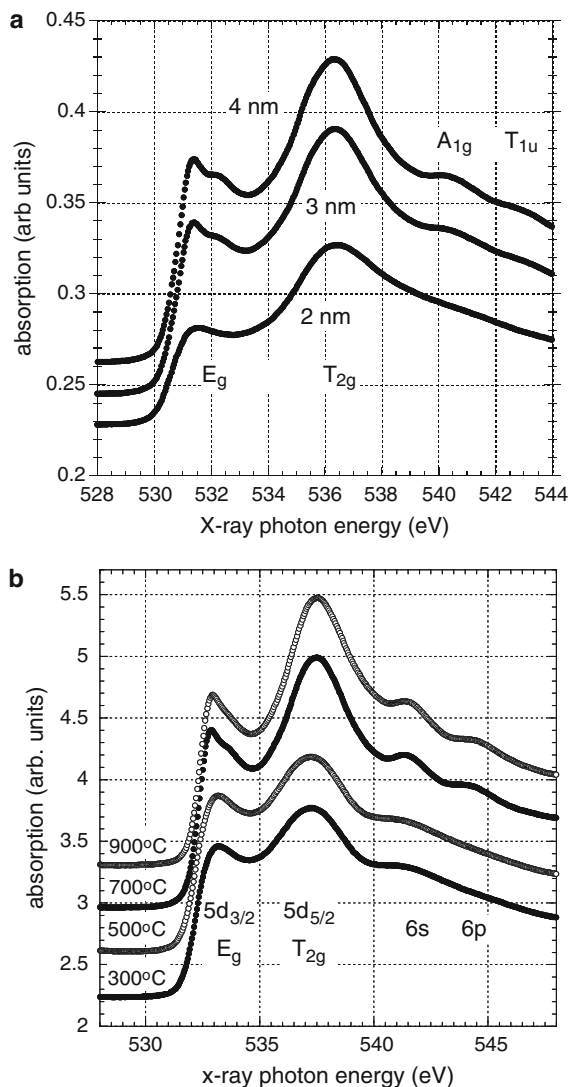


**Fig. 6** OK edge XAS spectra for empty conduction band states of nano-crystalline  $\text{HfO}_2$ : (a) as function of film thickness, and (b) for a fixed film thickness,  $>4$  nm, and as a function of processing temperature

### 3.2 Valence Band, and Conduction Band States: $\text{TiO}_2$

Figures 7(a) and (b) display, respectively, O K edge, and Ti  $L_3$  core level spectra for nanocrystalline  $\text{TiO}_2$ , with a thickness  $>4$  nm, and therefore not subject to dimensional constraint suppression of a J-T distortion. Additionally, and unless otherwise

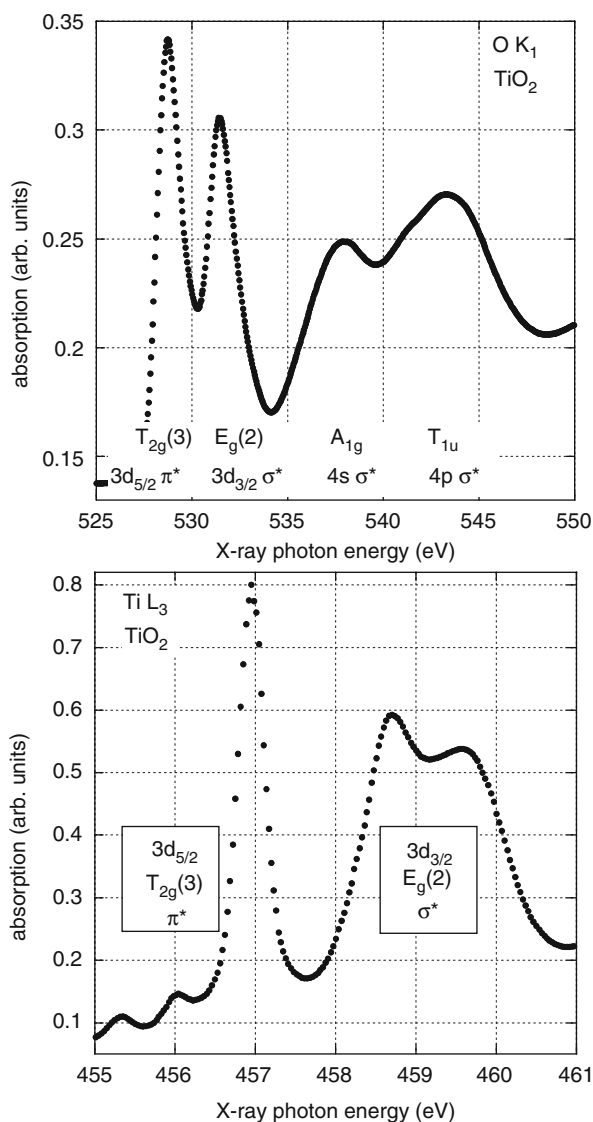


**Fig. 7** XAS spectra for  $\text{TiO}_2$  for films >4 nm thick, annealed in Ar at 900 °C. (a) OK edge spectrum for the empty conduction band states. (b) Ti L3 edge spectrum for intra-Ti transitions

indicated, all spectra displayed in this section, and the next are for nanocrystalline thin films that have been annealed in an inert nonoxidizing ambient of Ar at a temperature greater than 700 °C, and more generally 800 °C or 900 °C. Based on the discussions presented earlier, and in particular for Fig. 1, the O K spectra reflects X-ray absorptions that originate in the O 1s core state at ~543 eV (below the vacuum level), and in the spectral range up to about 545 eV terminate in final states below

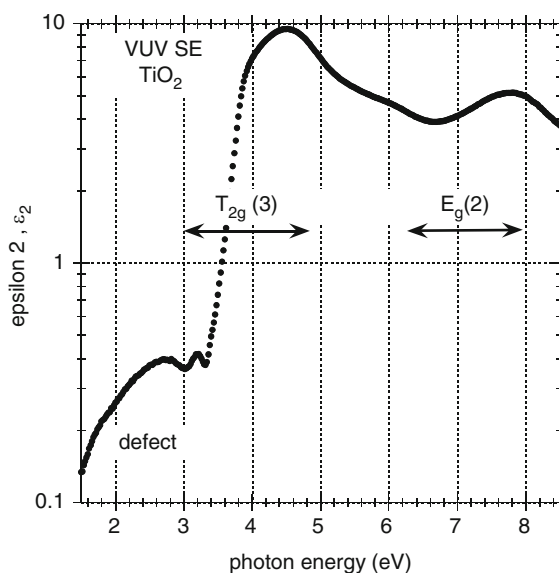
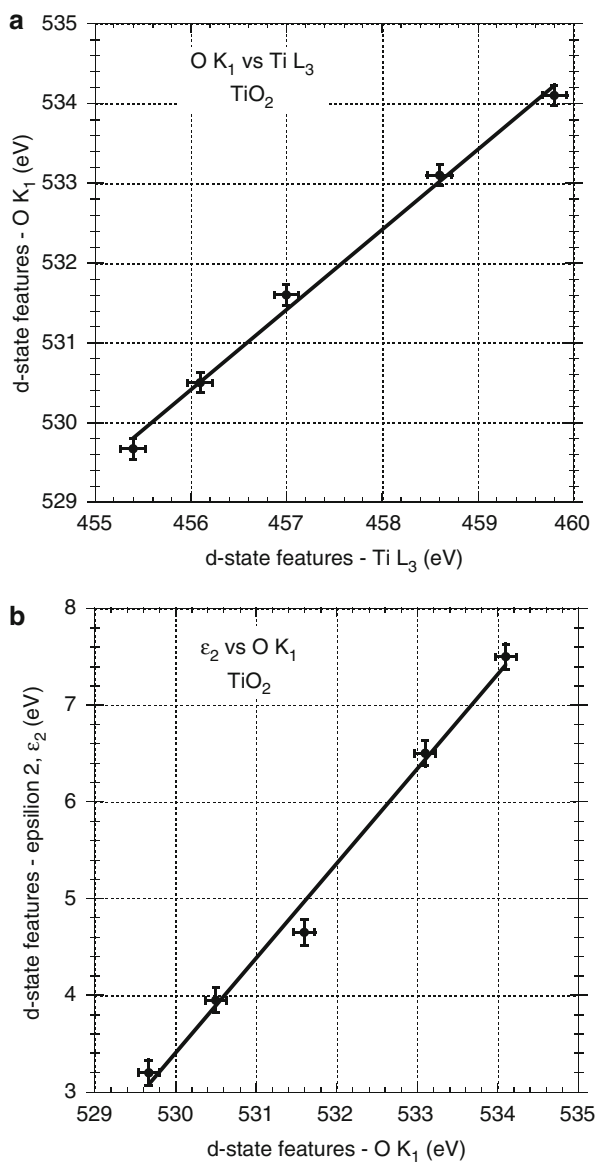


**Fig. 8** Log of epsilon 2 ( $\epsilon_2$ ) from vis-VUV SE for nanocrystalline  $\text{TiO}_2$ . Differentiation indicates five spectral features indicating complete removal 3d-state degeneracies

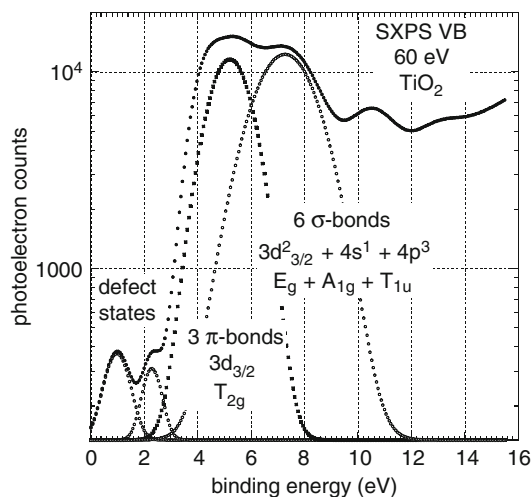
the vacuum level continuum. These states are O  $2p \pi^*$  antibonding states mixed in SALC molecular orbitals with empty, anti bonding Ti-atom 3d, 4s, and 4p states. In contrast, the Ti  $L_3$  core level spectra are intra-atomic, with transitions originating in relatively deep Ti  $2p_{3/2}$  states, and terminating in empty Ti 3d states. Upon differentiation, the O K edge and  $L_3$  spectra, indicate complete degeneracy removal for the Ti 3d  $T_{2g}$  and  $E_g$  features.

Figure 8 is a plot of the imaginary part of the complex dielectric constant  $\epsilon_2$  for  $\epsilon_c = \epsilon_1 + i\epsilon_2$ , as derived from the analysis of VUV SE data. The energies above 3 eV, including the very sharp feature at  $\sim 3.2$  eV are associated with empty conduction band states. The energies of the J-T term-split  $T_{2g}$  and  $E_g$  features have been extracted from these spectra by differentiation as well. These final 3d-state features display the same average C-F splitting between the average  $T_{2g}$  and  $E_g$  states, as well as the same J-T term splittings as the O K edge spectrum in Fig. 7 [30]. The relevant d-state energies are compared in Fig. 9(a) for the O K and Ti  $L_3$  edges, and in Fig 9(b), which includes a comparison between the O K edge and the  $\epsilon_2$  plot derived from analysis of the vis-VUV SE spectra.

Equally important, the spectral features in the conduction band states in the XAS spectrum, and the valence band states in the SXPS spectrum in Fig. 10 are qualitatively and quantitatively the same as those in (1) Fig. 8.13 of [13], and (2) a *morphing* of that figure into Fig. 1 of this paper. This morphed version *extends beyond* the ionic limit of Fig. 8.13, and has been simplified in detail similar to Fig. 2.8 of [14]. We will also use a more symbolic extension of Fig. 1, as a basis for discussing the d-state features in monoclinic, tetragonal and cubic  $\text{HfO}_2$  and  $\text{ZrO}_2$ .



**Fig. 9** Photon energies of Ti d-state features in  $\text{TiO}_2$ : (a) O  $K$  edge versus Ti  $L_3$  edge, and (b)  $\epsilon_2$  versus O  $K$  edge



**Fig. 10** SXPS spectrum of valence band for nanocrystalline  $\text{TiO}_2$ : log of photoelectron counts versus binding energy. Also includes are two band edge defects

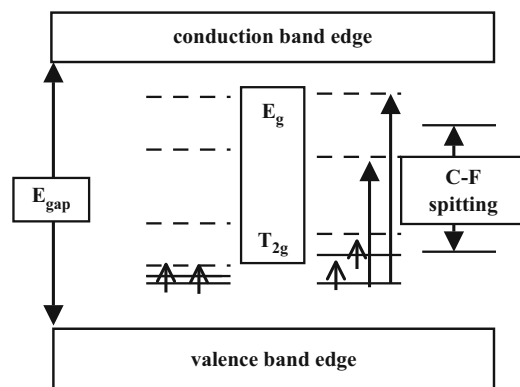


**Fig. 11**  $\text{Ti}^{3+}$   $d^2$  defect states for tetragonal (left) and monoclinic (right) distortions of cubic rutile. Band gap of  $\text{TiO}_2$  is 3.2 eV, and C-F splitting is  $\sim 2.7$  eV. Arrows indicate transitions from lower filled state to empty states. The solid lines are occupied states, and the dashed lines are empty final states

### 3.3 Band Edge Defects in $\text{TiO}_2$

Figure 11 indicates  $\text{Ti}^{3+}$   $d^2$  defect states for tetragonal and monoclinic distortions of cubic rutile. The band gap of  $\text{TiO}_2$  is 3.2 eV, and the C-F splitting is  $\sim 2.7$  eV. The solid arrows indicate transitions from the lower filled state to the two empty states for the monoclinic distortion. The experimental results presented below will be compared with the monoclinic distortion defect levels; i.e., a complete removal of the two and threefold degeneracies of the  $E_g$  and  $T_{2g}$  3d-states, respectively.

Consider first the valence band spectrum and the band edge defect state energies based on a linear extrapolation procedure used to estimate the energy of the top the valence band (see Fig. 10). These are J-T split states are occupied in a high-spin configuration of Fig. 11, and are at energies of  $0.5 \pm 0.15$  eV and  $1.5 \pm 0.15$  eV referenced to the linearly extrapolated valence band edge [25].

The existence of two states indicates a high spin configuration, suggests that the occupied defect states have the same symmetry as the nano-grain cooperative J-T effect; i.e., that these defect states do not display an additional *local* or *molecular scale* J-T effect. The energies for (1) d-state to d-state transitions between the C-F split J-T multiplets originating in these valence band edge occupied states, and for (2) transitions from the same ground state occupied valence band edge defects to states above the vacuum continuum will be determined experimentally. Following the definition put forth by Drs. White and Geballe in [7], p. 268: “(a) If the energy of a localized state” such as an occupied defect state at the valence band edge, “lies below the continuum of free electron states, we have a bound state. (b) If this energy lies within the free electron band,” what we shall call the vacuum continuum, “we have a *resonance* or a *virtual bound state*”, italics added for emphasis. We will designate the localized states observed spectroscopically within 30–50 eV of the vacuum continuum threshold in O K edge XAS spectra (at  $\sim 545$  eV) as *virtual bound states*, and underpin this definition with a description of these *virtual bound states* within the framework of the *SALC's of atomic states* approach of [13].

Returning to the experimental results in Figs. 7 and 8, the same relative conduction band features are present in both the XAS O K edge spectrum, and the VUV SE spectrum as indicated in Fig. 9(a). Consider first the VUV SE  $e_2$  spectrum in Fig. 8. The feature with a spectral peak at  $\sim 2.75$  eV with a shoulder detected in a differentiated spectrum at  $\sim 2$  eV identifies the energies for a transition from valence band edge defect states in the SXPS spectrum in Fig. 10, to final empty states; these are the d-state to d-state transitions between the C-F split J-T multiplets discussed above. The transition energy of 2.75 eV and the spectral half-width on the low eV side of  $\sim 0.5$  eV are essentially the same as the those obtained for the visible absorption spectrum of the  $[\text{Ti}(\text{H}_2\text{O})_6]^{3+}$  and are associated with similar d-d' transitions for the  $\text{Ti}^{3+}$  ion [11]. This gives an average C-F splitting of  $\sim 2.5$  eV, which is very close to the value calculated for the 2.36 C-F splitting in Table 2.2 of [13], and 2.4–2.5 eV of Table II of [30].

The defect states in nanocrystalline  $\text{TiO}_2$  have been examined in greater detail that goes beyond the scope of this article. The new experimental data and analysis of these results are addressed in [31]. One of the most important aspects of this study has been the possible identification of two types of monovacancy defects in nano-grain  $\text{TiO}_2$ , one associated with mono-vacancy defects that include all three Ti-atoms, and a second defect associated with mono-vacancy defects in which one of the three Ti-atoms is not present, e.g., on a grain-boundary or on the surface of a nano-grain. These two types of defects are observed in both the pre-edge spectra for X-ray energies  $< 530$  eV, and in the vacuum continuum regime for X-ray energies  $> 545$  eV. These O K edge regimes have been addressed in more detail in [31].

We will not address the densities of band edge defects until the discussion section of this chapter. The remainder of Sect. 3, and all of the research results discussed in Sects. 4 and 5 are effectively *x-axis physics*, the relatively easy, but yet important aspect of this study that is addressing symmetry changes associated with J-T effect bonding distortions that reduce the local symmetry to remove d-state degeneracies.

Returning now to spectroscopic studies of intrinsic defect states. The defect state energies discussed above are consistent with spectroscopic studies of intrinsic defects that have used the second derivative of the XAS O K edge absorption to study (1) empty band edge defects below the conduction band edge, and (2) *virtual bound state resonances* above the vacuum continuum. Figure 12 presents O K edge XAS 2nd derivative spectra for  $\text{TiO}_2$ : (a) d-d' transitions within the forbidden band gap; and (b) for two different types of virtual bound state resonances above the edge of the vacuum continuum. Consider first Fig. 12(a) which address the intra d-state d-d' transitions associated with occupied and empty *bound states*. Defect state features occur over a spectral range that includes empty states at both the valence and conduction band edges. The lower energy feature at  $\sim 522$  eV is assigned to an empty portion of higher energy state  $\text{T}_{2g}$  d-states in Fig. 11, and the feature at  $\sim 525$  eV is the lower energy 5d  $\text{E}_g$  symmetry defect state in state in Fig. 11 as well. The energy difference between these two features,  $\sim 3$  eV is close to the C-F splitting of  $\sim 2.5$  eV.

The two relatively narrow and sharp features in Fig. 12(b) have been assigned by to Ti 3d *virtual bound state resonances* that are in effect the antibonding ionization states associated with occupied Ti 3d states at the valence band edge (see Fig. 10). Based on the binding energy of the O 1s state relative to vacuum,  $\sim 543$  eV, we place the energy threshold for continuum states at  $\sim 545$  eV. The two spectral features at  $\sim 550$  and  $554$  are at energies above the continuum threshold; therefore *virtual bound state resonances* [7]. The virtual bound state resonances are enabled by the local symmetry at the defect site. To zeroth order these are in a  $d^2$  configuration, and their parentage are Ti  $3d_{3/2}$  atomic states. However in the atomic d-states are not a consistent with the local symmetry, and these states are *hybridized/mixed* within the SALC's approach of [13]. The mixing is the origin of an *antibonding resonance or virtual bound state* [7]. Two additional features have been identified in Fig 12(b). The transitions terminate in *virtual empty* resonance states. The local crystal field at these shallow core states reduces the respective Ti 3p and O 2s atomic symmetries by mixing them with O 2p  $\pi$  valence states to conform to the local site symmetry (see Fig. 1), and this mixing makes possible a nonvanishing matrix element for the observed transition to the *virtual bound* states that are marked in red in Fig. 12.

To the best of our knowledge this represents the first time these transitions to defect and core level associated *virtual states* have been identified spectroscopically using XAS from an O 1s level. As such, there was no motivation for theoretical calculations to determine the anticipated *virtual or empty state resonance* energies. Of more significance that the specific energies is the number of defect states detected. For nano-grain monoclinically distorted rutile  $\text{TiO}_2$ , it is equal to two the occupancy of electrons in monovacancy. The splitting between these virtual states is increased by about a factor of between 2.5 and 3 with respect to energy difference between the



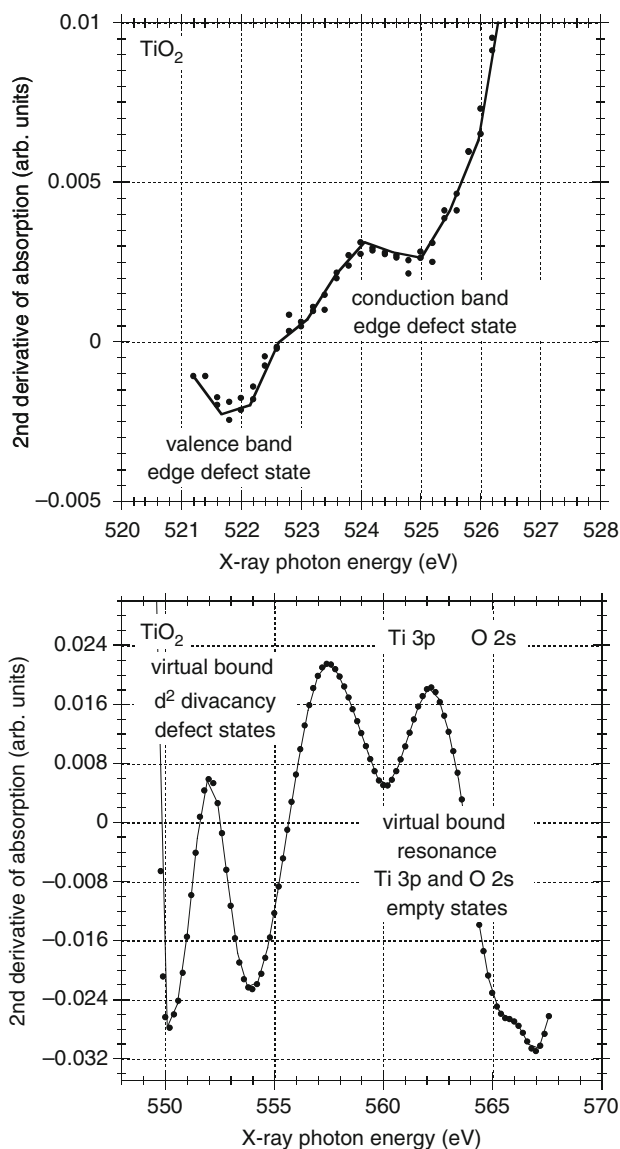


**Fig. 12** OK edge XAS 2nd derivative spectra for  $\text{TiO}_2$ : (a) conduction and valence band edge defects. (b) virtual bound resonance states: defect states; and shallow Ti and O core states

occupied band edge defects in the SXPS spectrum. Most importantly, the observance of *virtual absorptions* associated with band edge intrinsic defect states provides a way to settle an ongoing debate regarding the nature of the intrinsic defects in  $\text{HfO}_2$ , and  $\text{ZrO}_2$  as well; are these intrinsic bonding defects monovacancies, as in  $\text{TiO}_2$  with two virtual bound resonance states, as proposed in [21 and 22]?, or are

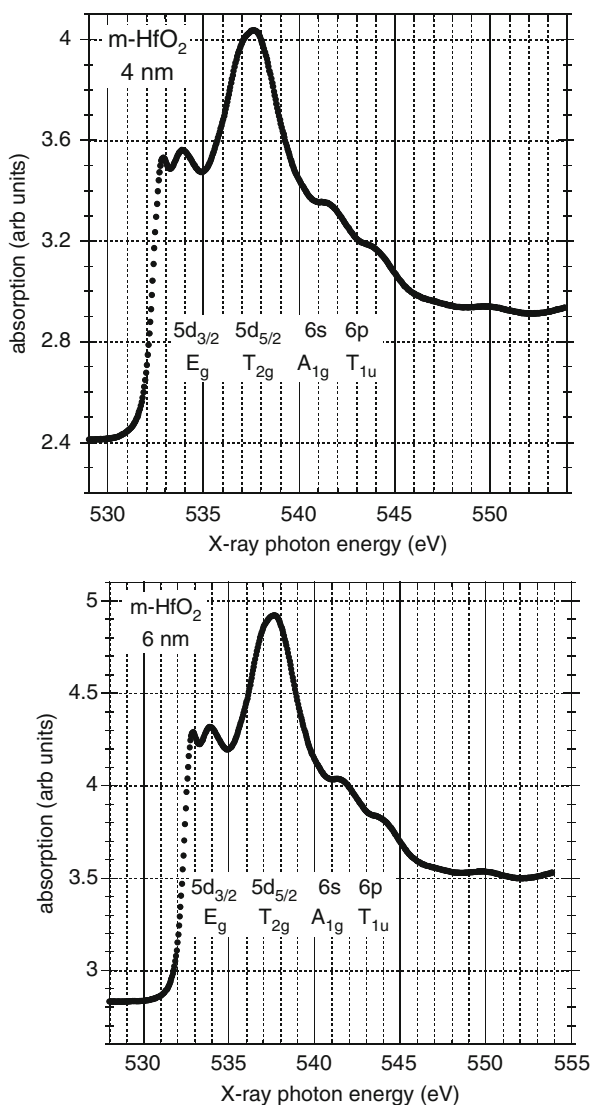
they divacancies as proposed in [4 and 5], with four virtual bound resonance states? This question will be resolved in Sect. 4, which presents spectroscopic results that indicates the intrinsic defect is a divacancy, rather than a monovacancy.

## 4 Spectroscopic Studies of TM Elemental Oxides II: Empty Conduction Band States and Band Edge Defects

This portion of the chapter focuses on spectroscopic results for nanocrystalline  $\text{HfO}_2$  thin films with a film thickness greater than, or equal to about 4 nm. Where appropriate, comparisons are made with spectroscopic results for cubic Hafnia, alloys of  $\text{HfO}_2$  with an approximate 15% atomic concentration of Y relative to  $\text{HfO}_2$ .

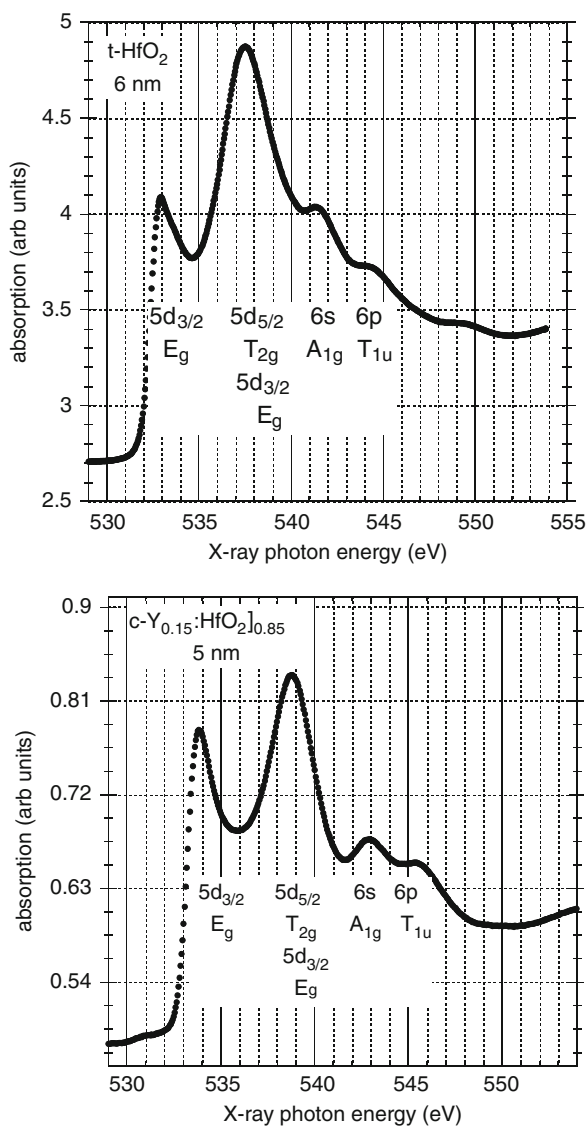
Figures 13(a) and (b) display respectively O K edge XAS spectra for the empty conduction band states of two nano-crystalline samples: in 13(a) a 4 nm thick m- $\text{HfO}_2$  film, and in Fig 13(b) a 6 nm thick m- $\text{HfO}_2$  film, each deposited on a nitrided Ge substrate and annealed in Ar to a temperature of 800 °C. The spectral features that are labeled are for transitions to O 2p  $\pi$  states, *mixed with* Hf 5d, 6s and 6p states to satisfy the local site symmetry, i.e., to meet the SALC criterion of [13]. We have used symmetry designations corresponding to parent cubic  $\text{CaF}_2$ , recognizing that the symmetries in these monoclinic films, and the tetragonal films to be addressed in Figs. 14(a) and (b) are different. These absorptions extend from the large increase in absorption just below the respective Hf 5d, E features, at  $\sim 532\text{--}533$  eV, to beyond the spectral peak assigned to Hf 6p states, and are below the vacuum continuum threshold between 545 and 550 eV. These absorptions are then identified as *bound resonance* states. The second derivative spectra of these films each indicate a complete removal of the degeneracies of the Hf  $E_g$  and  $T_{2g}$  d-states, and a C-F splitting of  $\sim 3.6 \pm 0.2$  eV consistent with a monoclinic nano-grain morphology [4, 5]. The Hf-atom coordination is sevenfold, and the Hf contributions to  $\sigma$ -bonding are the  $5d^3(T_2)$ ,  $6s^2(A_{1g})$  and  $6p^3(T_{1u})$  states, and the Hf contributions to  $\pi$ -bonding are the  $5d^2(E_g)$  states [4, 5]. It is also likely that there are also Hf 5f contributions to the  $s(\sigma)$ -bonding as well.

Figure 14 includes O K edge XAS spectra for the empty conduction band states of two other nanocrystalline thin films: (a) a 6 nm thick t- $\text{HfO}_2$  film with a tetragonal grain-morphology and (b) 5 nm thick cubic Hafnia, c- $\text{Y}_{0.15} : \text{HfO}_{20.85}$  film with a the disorder induced cubic nano-grain morphology. Each  $\text{HfO}_2$  spectrum in Fig. 14 displays only one Hf 5d  $E_g \pi^*$  feature, but four Hf 5d  $\sigma^*$  features, one  $E_g$  and three  $T_{2g}$ , consistent with the eightfold-coordination of Hf. The other four  $\sigma^*$  states are three Hf 6p  $T_{1u}$  states, and one Hf 6s  $A_{1g}$  state. It is significant to note that C-F splitting is larger for t- $\text{HfO}_2$  than for the m- $\text{HfO}_2$  films of Figs. 13(a) and (b). The C-F splitting is increased from  $3.6 \pm 0.2$  to  $\sim 4.2 \pm 0.2$  eV for the t- $\text{HfO}_2$  film in Fig. 14(a). The C-F splitting for cubic Hafnia is increased further to  $5.2 \pm 0.2$  eV in Fig. 14(b). The increased coordination from seven to eight accounts the increases with respect to m- $\text{HfO}_2$ , but can not explain relatively large difference of



**Fig. 13** OK edge XAS spectra for empty conduction band states of two nano-crystalline thin films (a) 4 nm m-HfO<sub>2</sub>, and (b) 6 nm m-HfO<sub>2</sub>

almost 1 eV between the t-HfO<sub>2</sub> and c-HfO<sub>2</sub> films. One possible explanation for the increased C-F splitting of the cubic Hafnia film is in the increased bond ionicity associated with the Y-atoms. A second difference relating to the alloy character of the cubic Hafnia, and the X-ray determined cubic symmetry. This aspect of the bonding in cubic Hafnia will be addressed below.



**Fig. 14** OK edge XAS spectra for empty conduction band states of two nano-crystalline thin films: (a) 6 nm  $t\text{-HfO}_2$ , and (b) 5 nm  $c\text{-Y}_{0.15}:\text{HfO}_2]_{0.85}$

Figure 15 compares second derivative O K edge XAS spectra in the spectral regime corresponding to the vacuum continuum for  $m\text{-HfO}_2$  and  $t\text{-HfO}_2$ , for two of the samples included in Figs. 13 and 14. Paralleling the discussion for the spectral features in Fig. 12, the four features between 545 and 547.6 eV are assigned to *antibonding states* of the occupied valence band edge defects that will be displayed later on in this chapter in Fig. 19. These states are above the estimated continuum

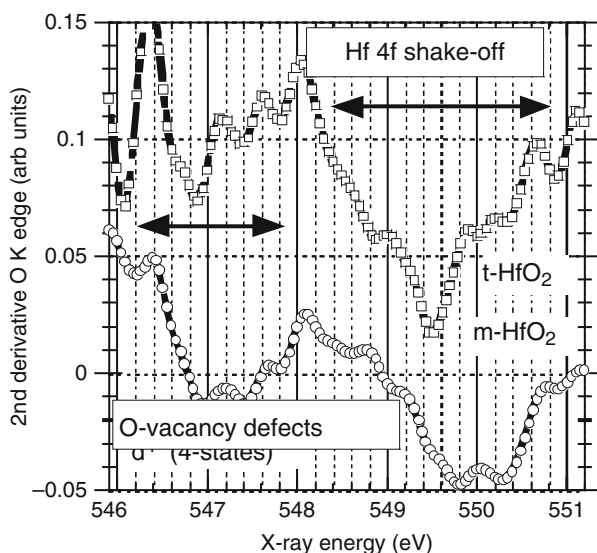


**Fig. 15** Derivative OK edge XAS spectra for four O-vacancy defect states and seven Hf 4f core level shake-off states in nano-crystalline t-HfO<sub>2</sub> and m-HfO<sub>2</sub>. The arrows indicate the widths of these two groups of 4+ and 7-states

threshold of  $\sim 545$  eV, and are therefore virtual bound resonance states in the spirit of the definition in [7]. The symmetry induced Hf 4f core level features are also virtual bound resonance states.

The assignments for the features marked in Fig. 15 parallel those discussed above for the spectrum in Fig. 12(b), but include significant qualitative and quantitative differences. First there are four, instead of two band edge defect features. Referring to Fig. 4, this confirms that the intrinsic defects in m-HfO<sub>2</sub> and t-HfO<sub>2</sub> are in a  $d^4$  configuration with four occupied d-states within the forbidden band gap. This establishes that they are in a divacancy bonding arrangement that is indicated symbolically in Fig. 3(c). The divacancy defect arrangement has a distorted octahedral character, but still displays an axial symmetry. The experiments of the Barklie group in Dublin have studied intrinsic bonding defects in TiO<sub>2</sub>, ZrO<sub>2</sub> and HfO<sub>2</sub> by electron spin resonance (ESR), and found that the line-shape of the respective ESR responses are consistent with an axial geometry [32], and refs. therein]. Alternatively, the four states may be associated with a monovacancy represented as a pair of couple  $d^1$  defects.

Additionally and equally significant, the spectral features assigned to the anti-bonding state of Hf 5f electrons display seven features indicating a completely removal of the Hf 4f<sub>5/2</sub> and Hf 4f<sub>7/2</sub> degeneracies of three and four, respectively. This is consistent with the local field induced symmetries of Hf 4f orbitals that are mixed with O 2p, and possibly O 2s states as well. This is the same mechanism that activated the Ti 3p and O 2s *virtual bound state resonance* absorptions in Fig. 12. The spectral widths of the Hf 5d<sup>4\*</sup> features (4 states) and Hf 4f\* features (7 states)

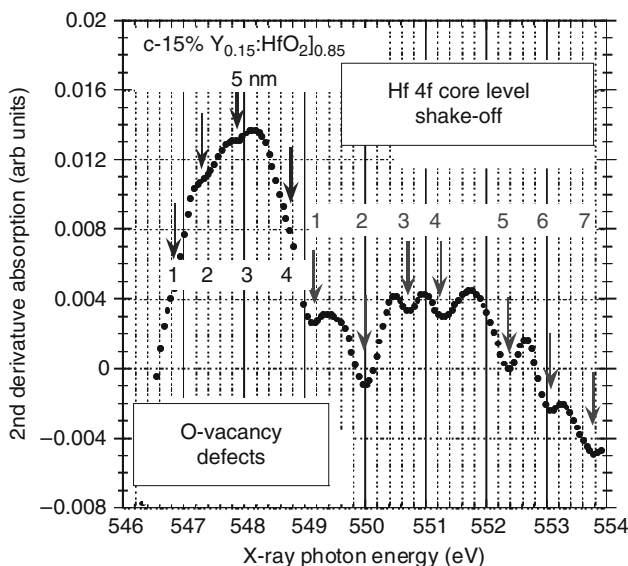


**Fig. 16** Derivative OK edge XAS spectra for four O-vacancy defect states and seven Hf 4f core level shake-off states in nano-crystalline Y-stabilized  $\text{HfO}_2$  5 nm thick

are essentially the same for both samples; However the symmetries are markedly different. O-vacancy defects and the seven Hf 4f core level shake-off states as well, display a higher symmetry that is consistent with a t- $\text{HfO}_2$ , including distortions in the top and bottom basal planes that derive from a J-T distortion. This is clearly evident in the position of the sharp local minimum for the t- $\text{HfO}_2$  traces.

The spectrum in Fig. 16 for cubic Hafnia displays a qualitatively different second derivative spectrum. We suggest that this derives from an observation that while X-ray diffraction (XRD) studies indicate a cubic, or  $\text{CaF}_2$  structure, the local bonding includes monovacancy defects compensating Y atom sites that are randomly introduced onto the Hf sublattice. This means that the XRD result is for a statistically averaged structure, and therefore qualitatively different that the *actual* eightfold-coordinated t- $\text{HfO}_2$  structure. We have included markers for band edge defects, and Hf 4f states respectively.

Figure 17 presents second derivative pre-edge O K edge XAS spectra the d-d' for the defect states just below the conduction band edge for nano-crystalline m- $\text{HfO}_2$  for two different film thickness. The 4 nm film displays a J-T splitting, whereas this is suppressed in the 2 nm thick film. Based on differences in defect densities, lower by  $10\times$  in the 2 nm thick film, and different nano-grain sizes discussed above, the features in the 4 nm thick film are to nanocrystallites 3 nm in size with J-T splittings, and those in the 2 nm film to small grains 2 nm in size and therefore with different inter-grain coupling as indicated by the absence of J-T term splittings.

Figure 18(a) is the second derivative O K edge XAS spectra for conduction band edge defects in nano-crystalline t- $\text{HfO}_2$  thin film 6 nm thick. The spectral features are different in detail than those in Figs. 17(a) and (b), and this is attributed to

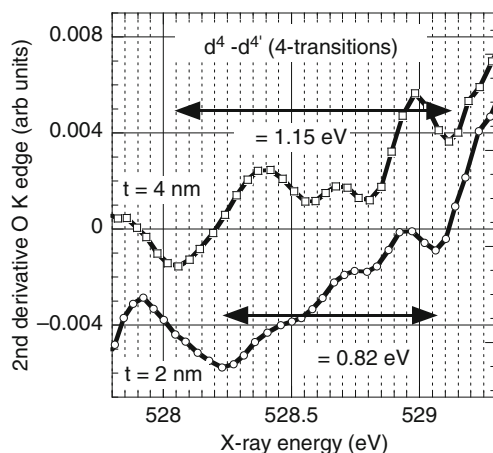


**Fig. 17** Derivative OK edge XAS spectra for conduction band edge empty defect states in nano-crystalline m-HfO<sub>2</sub> films: (a) 4 nm thick and (b) 2 nm thick. The arrows indicate the spectral width changes as a function of thickness, and therefore film morphology (see Fig. 6)

the eightfold-coordination of the Hf-atoms in the tetrahedral nano-grain structure. More importantly, the marked spectral width that includes one additional feature, not high-lighted in Fig. 15 is about 0.3 eV larger, consistent with an increase in the C-F splitting from about  $3.6 \pm 0.2$  eV in m-HfO<sub>2</sub> to  $4.2 \pm 0.2$  eV in t-HfO<sub>2</sub>. Referring to Figs. 19 and 20, the C-F splitting is expected to approximately equal to the spectral width in Fig. 17(a) or (b) plus the energy difference between the occupied spectral features at the valence band edge in the SXPS spectrum of m-HfO<sub>2</sub>. This is equal to 2.4 eV from Fig. 17 plus  $\sim 1.5$  eV from Fig. 19, or 3.9 eV compared with the C-F splitting of  $3.6 \pm 0.2$  eV. In a similar way, the spectral extent of the features for t-HfO<sub>2</sub> are expected to be increased with respect to that of m-HfO<sub>2</sub>, by the difference in the respective C-F splittings. This scaling applies qualitatively as noted above.

The spectrum for the divacancy defect is Fig. 18(b) is qualitatively different from that of the t-HfO<sub>2</sub> in Fig. 18(a), as well as those of m-HfO<sub>2</sub> in Figs. 17(a) and (b). This attributed to differences in the local atomic nano-grain structure that encapsulates the divacancy. In addition, the marked difference in the strength of the dominant derivative feature in Fig. 18(b) suggests that the intrinsic defects contain both Hf<sup>3+</sup> and Y<sup>3+</sup> atoms in the distorted octahedral arrangement that comprises the divacancy. A closer comparison between the band edge defect spectra between m-HfO<sub>2</sub> and cubic Hafnia, and m-ZrO<sub>2</sub> and cubic Zirconia, not shown in this chapter, but discussed in [32], indicates that one of the features in the monoclinic oxides, splits into a doublet in the respective cubic Hafnia and Zirconia, supported the argument for inclusion of Hf<sup>3+</sup> and Y<sup>3+</sup> atoms and Zr<sup>3+</sup> and Y<sup>3+</sup> atoms in these cubic thin films.

Figures 19(a) and (b) contain SXPS spectrum of nano-crystalline HfO<sub>2</sub>: log of photoelectron counts, versus binding energy for a m-HfO<sub>2</sub> thin film. The spectrum in Fig. 19(a) has been fit with seven Gaussian functions. The number of Gaussian

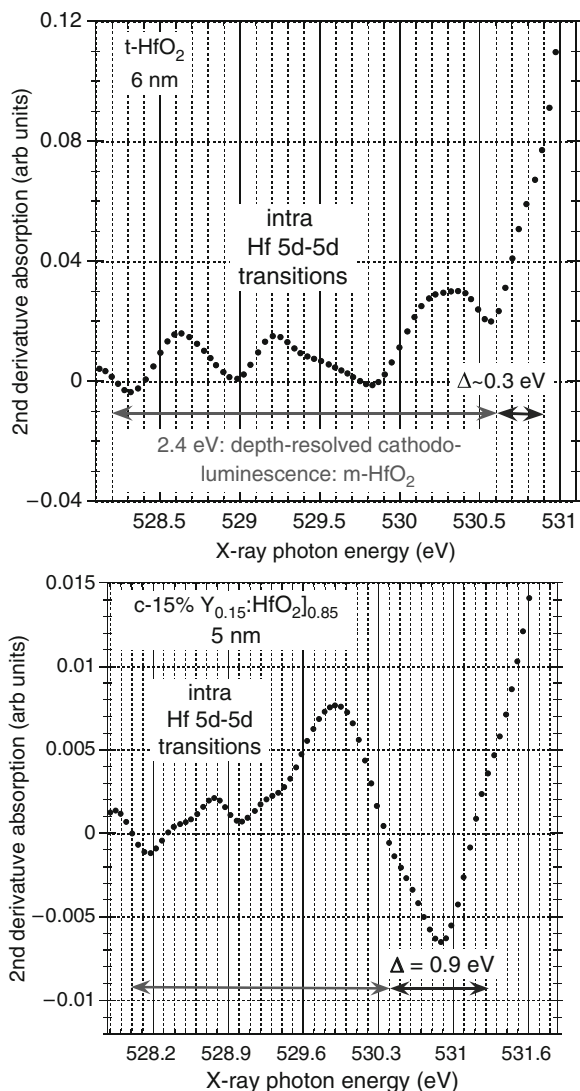


**Fig. 18** Derivative OK edge XAS spectra for conduction band edge empty defect states in (a) nano-crystalline  $t\text{-HfO}_2$  6 nm thick and (b)  $\text{Y:HfO}_2$  5 nm thick

features is consist with (1) the four SALC molecular orbitals, one  $\pi$ , Hf 5d  $E_g$ , and  $3\sigma$ , Hf 5d  $T_{2g}$ , Hf 6s ( $A_{1g}$ ) and Hf 6p ( $T_{1u}$ ), (2) the nonbonding O 2p  $\pi$  states at the valence band edge, and (3) two band edge occupied defect states. Also included in this figure are an expanded  $x$ -axis and  $y$ -axis plot for the spectral regime that corresponds to the two band edge defects; this plot includes the corresponding portion of the total SXPS response. On the basis of the four antibonding defect state features



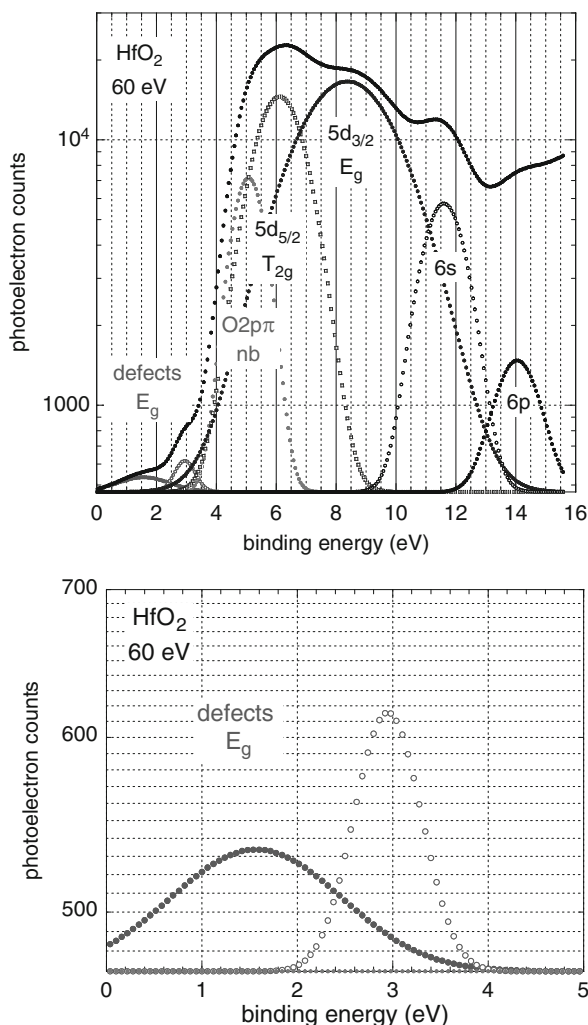


**Fig. 19** SXPS spectrum of nano-crystalline  $\text{HfO}_2$ : log of photoelectron counts, versus binding energy. (a) valence band and band edge defects. (b) expanded defect state plot

in Figs. 15(a) and (b), we would have expected to see four band edge defect features. Since the spectral width of each of the features in the Fig. 19(b) is  $>1\text{ eV}$ , we conclude that J-T term splittings can not be resolved due to intrinsic valence band broadening, and hence are not observed in this spectrum. This intrinsic broadening has been noted for the d-state contributions to the valence band states in  $\text{TiO}_2$  [25], where term-splittings are readily evident in O K edge spectra, but not in valence band spectra.

Figure 20 presents an SXPS spectra that is run at a higher UV photon energy, 130 eV compared with 60 eV for Figs. 17(a) and (b). These spectra are taken for

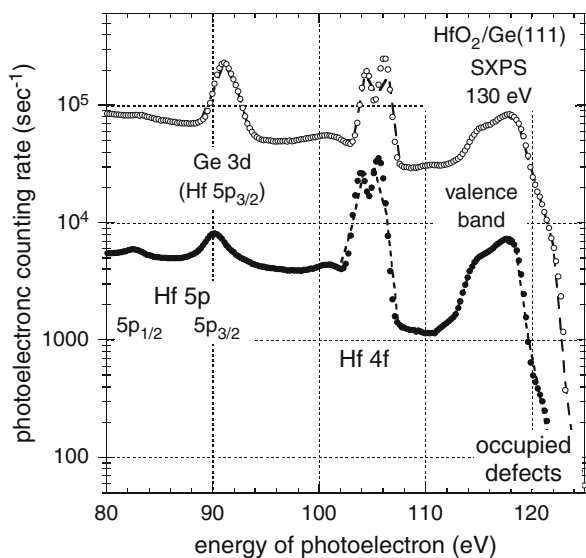


**Fig. 20** SXPS spectra: HfO<sub>2</sub> deposited onto Ge(111) as-deposited at 300 °C and after an 800 °C 1 min rapid thermal anneal in Ar

depositions of HfO<sub>2</sub> on nitrided Ge substrates, and displayed to illustrate two spectral features: (1) the width of the Hf 4f shallow core level, and (2) to verify that a substrate chemical reaction had taken place, and that Ge had been transported in the HfO<sub>2</sub> film. Changes in band edge defects as function of Ge-atom incorporation in the HfO<sub>2</sub> thin films have been discussed in [32 and 33]. The most important point relative to this discussion of spectral effects due to cooperative J-T distortions relates the width of that feature. The energy difference between the two peaks in the Hf 4f features in all four plots is  $\sim 2$  eV, consistent with the spin-orbit splitting of  $\sim 1.7$  eV [34], whereas the spectral width of the features in the antibonding Hf 4f states in Figs. 15(a), (b) and 16(a) have increased to  $>3$  eV, and is comparable to the maximum width of spectral features associated with intra 4f state absorptions in lanthanide series rare earth atoms, e.g., Ce<sup>4+</sup> [16].

Conduction band edge defects have been detected in VUV SE measurements [3, 4, 20, 33]. Additionally, the peaks in these spectra correspond to transition energies, so that it cannot be assumed that the final state energies of the transition region can be referenced to the top of the valence band. Recent vis VUV SE by our group places the defect state transition energies in HfO<sub>2</sub> at  $\sim 3.4$  eV and 4.6 eV [35]. These results are in excellent agreement with a recent as yet unpublished study by a group at Sematech. The development of an energy level diagram for band edge defects is addressed in the next section of this review.

The interpretation of this diagram, and the role it plays in differentiating between monovacancy and divacancy defects is supported by the interpretation of the spectra in Figs. 15, 16, 17 and 18, with the strongest evidence relating to the number of

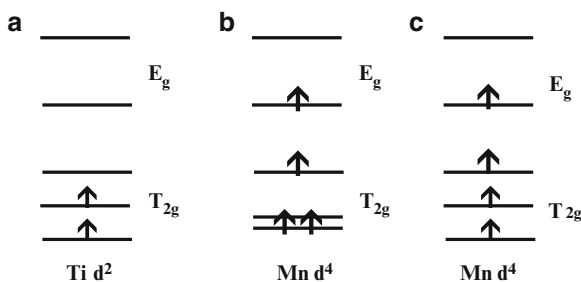


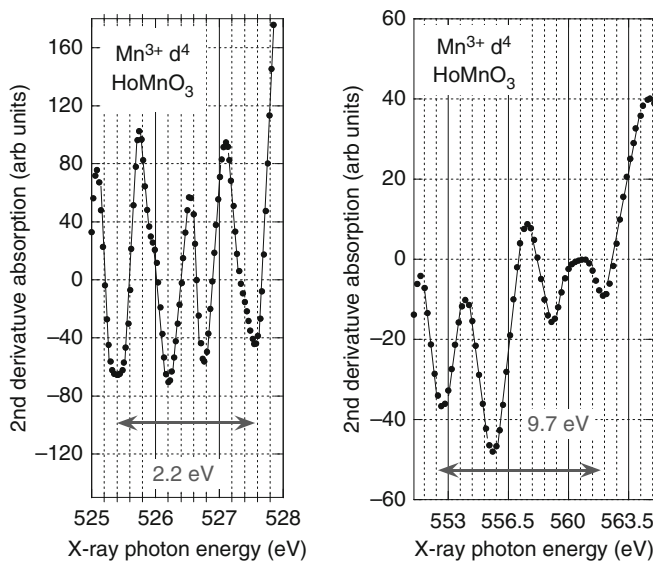
**Fig. 21** Energy level diagram for occupancy of  $Ti\ d^2$  and  $Mn\ d^4$  transition metal atom d-states within the forbidden energy gap. (a)  $Ti\ d^2$  occupied states in  $TiO_2$ . (b)  $Mn\ d^4$  occupied 3d states in a high spin tetragonal bonding arrangement [14]; and (c)  $Mn\ d^4$  occupied 3d states in a high spin bipyramidal bonding arrangement

antibonding states 5d states in the continuum energy regime  $>545\text{ eV}$ . Before proceeding to present and discuss this diagram, and we give additional support to the interpretation of these 5d-state spectra features in Figs. 17 and 18.

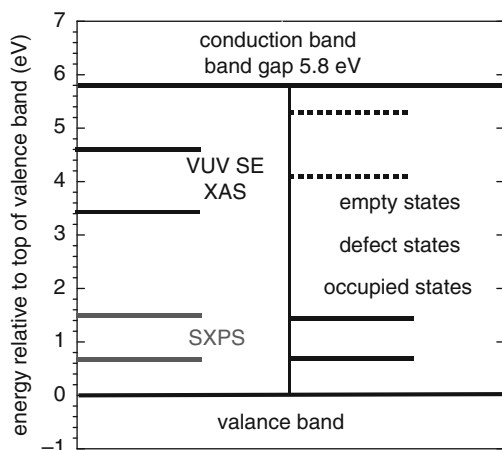
Figure 21 presents, and compares energy level diagrams for the occupancy of  $Ti\ d^2$  and  $Mn\ d^4$  transition metal atom d-states within the forbidden energy gap. Panel (a) is for the  $Ti\ d^2$  occupied states in  $TiO_2$  with a distorted rutile structure and complete removal of 3d-state degeneracies. Panel (b) is for the  $Mn\ d^4$  occupied 3d states in a high spin tetragonal bonding arrangement as in a cubic perovskite, e.g.,  $c\text{-}HoMnO_3$  [14]. Finally, Panel (c) is for the  $Mn\ d^4$  occupied 3d states in a high spin bipyramidal bonding arrangement as in a hexagonal perovskite; e.g.,  $h\text{-}YMnO_3$  or  $h\text{-}HoMnO_3$ .

Figure 22 presents derivative O K edge XAS spectra for d-states for the hexagonal perovskite,  $h\text{-}HoMnO_3$ , with a bipyramidal bonding arrangement for the Mn atoms that removes all d-state degeneracies [35]. Figure 21(a) addresses the conduction band edge occupied  $Mn^{3+}$  d-states, and Fig. 21(b), the antibonding  $Mn^{3+}$  3d states in the vacuum continuum above the antibonding conduction band states. Each of these spectra indicates four d-state features, consistent with the energy band diagram in Fig. 21, panel (c), and the  $d^4$  occupancy of the  $M^{3+}$  ion.

Finally, Fig. 23 presents a schematic energy level diagram that has been constructed on (1) the left from the experimental data from (a) the SXPS results, and (b) renormalized XAS and VUV SE results, and (2) on the right from an interpretation to consistent with the defect models addressed in Figs. 3 and 4. These data, and the analysis do not discriminate between mono- and divacancy models; each would have the same average C-F splitting between the average of the J-T split E and  $T_2$  states. However, most importantly, (1) the spectroscopic data for the continuum antibonding states in Figs. 12(b), 15(a) and (b), 16(a) and 21(b), and (2) the symbolic symmetry-determined energy level diagrams in Figs. 4, 11 and 20, unambiguously distinguish between two and four d-state occupancy, and as such resolve the issue in favor of divacancy, rather than monovacancy bonding in  $HfO_2$ , and  $ZrO_2$  as well [4, 5, 21, 22].



**Fig. 22** Derivative OK edge XAS spectra: (a) empty band edge  $d^4$  empty  $\text{Mn}^{3+}$  states for hexagonal perovskite,  $\text{h-HoMnO}_3$ ; and (b) virtual bound  $d^4$  resonance states of  $\text{Mn}^{3+}$  for hexagonal perovskite,  $\text{h-HoMnO}_3$



**Fig. 23** Summary of band edge defect energies derived from spectroscopic data: (a) energies of occupied and unoccupied d-state features in SXPS, and VUV SE and XAS, respectively. (b) occupied d-state features, and empty states determined by renormalizing VUV SE data for d-d' transition energies

## 5 Jahn-Teller Effects in Complex Oxides

Cooperative J-T effects also dominate to the properties of many of the complex oxides that have been addressed for introducing increased functionality in Si integrated circuits and systems. In particular, the insights into more general aspects of J-T effects in the group IVB elemental oxides,  $\text{TiO}_2$ ,  $\text{ZrO}_2$  and  $\text{HfO}_2$ , serve as a basis for identifying pathways to *design and optimization* of atomically engineered complex oxides with technologically significant properties. We define complex oxides as ternary and quaternary compound and/or alloy phases that include two, rather than one cations. Examples include  $\text{SrTiO}_2$ , where one of the cations is a simple metal Sr, and the other is a TM ion, Ti, as well as other samples such as  $\text{GdScO}_3$ , where one cation is lanthanide series rare earth atom, Gd, and the other a TM, Sc. These include similarities include cooperative J-T effects for host crystals as well intrinsic impurities and intentionally added TM alloy atoms. This has been illustrated in Fig. 21 [35], with more results forth coming shortly [36].

The advanced spectroscopic techniques that have been applied, XAS, vis-VUV SE, and SXPS carry over directly to complex oxides, as do the generalizations of the energy level diagrams based on SALCs. They are more complicated for complex oxides with two cations, where the local symmetries of these cations are inherently different. There is a further degree of freedom that involves the same TM atomic species, but in different ion states, as in  $\text{LaMnO}_3$ , where Mn is a  $3+$  ion with a  $d^4$  occupancy, and in  $\text{SrMnO}_3$  where it is a  $4+$  ion with  $d^3$  occupancy.

If we limit the discussion to perovskite complex oxides, then there are then two different classes of that oxides that form a basis set for complex oxides in general. The first and simplest class are  $d^0$  complex oxides, and this as illustrated schematically in Fig. 23 Their conduction and valence electronic structures at the respective band edges are qualitatively similar to those of the group IIIB or group IVB TM elemental oxides that they include. As indicated in [14], the band gaps of the group IVB complex oxides of this class and their respective group IVB elemental oxides do not differ significantly, with small increases in the titanates simply reflecting an increased average bond ionicity.

As an example, in the 0001 direction the  $\text{SrTiO}_3$  perovskite structure are alternating layers of SrO and  $\text{TiO}_2$ . In the ionic model, the formal charges on Sr and Ti respectively, are  $2+$  and  $4+$ , and these balance the formal charge of  $-2$  on O. This correspondence with respect to band edge electronic structure extends to the intrinsic defect structure as well, where the important defects are O atom mono-vacancies, each of which has two Ti neighbors, and four Sr neighbors. To a good

approximation, the electronic states occupied and empty states at the band edges, are qualitatively similar to the defects in  $\text{TiO}_2$ , and consequently their occupied and empty states in the band gap can also be described as having  $d^2$  occupancy as in Fig. 4. Therefore the same combinations of XAS, SXPS, and vis-VUV SE can be applied, including the extension of the XAS studies to include the virtual bound resonance states that effectively count the number of occupied d-states within the band gap.

The second class of complex oxides are constructed from elemental TM oxides that do not have  $d^0$  electronic structures. The seminal 1974 paper of the Falicov group identified the important role that occupied d-state levels play in defining the respective band edge states of these oxides, including NiO, and other first and second row examples [37]. Representative examples include, two different manganites, in which the formal electronic charges of Mn differ: (1) Ho, Y and La manganite, e.g.  $\text{LaMnO}_3$ , in which the formal charge on the Mn is  $3+$ , and (2) Sr manganite where it is  $4+$  as in  $\text{SrMnO}_3$ . These charges combined respectively with Ho, Y and La, or Sr simply balance the electronic charge of the O atoms.

Figure 24 includes the extension of Fig 23 to non  $d^0$  occupancy of  $\text{Mn}^{3+}$  within the ionic band gap in the context of [37], and Fig. 25 illustrates the antibonding conduction band states.

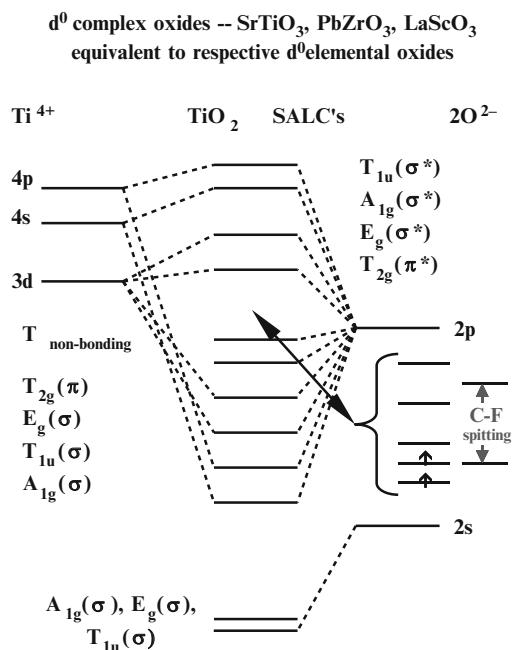


**Fig. 24** Schematic molecular orbital diagram of SALC's and band edge  $d^2$  defect for  $\text{SrTiO}_3$ , a  $d^0$  complex oxide

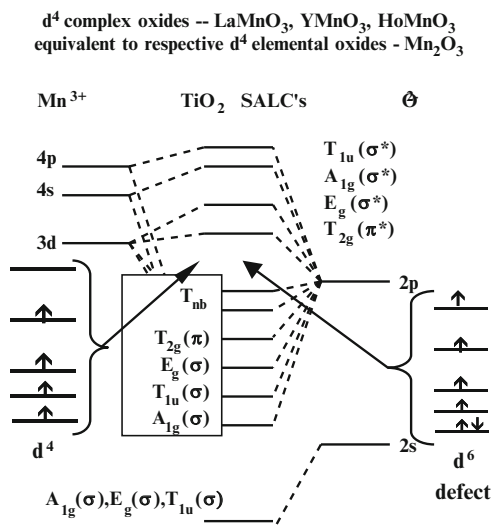


**Fig. 25** Schematic molecular orbital diagram of SALC's and band edge defects for La(Y,Ho)MNO<sub>3</sub>, a d<sub>4</sub> complex oxide, with d<sub>6</sub> band edge defects

## 6 Discussion and Summary

### 6.1 Discussion

This section addresses briefly the two most important points made with respect to J-T effects: (1) the cooperative J-T effect in the group IVB TM oxides, with an emphasis on HfO<sub>2</sub>; and (2) in band edge defects, wherein a significant issue regarding the applicability of monovacancy and divacancy models as the canonical intrinsic defects in HfO<sub>2</sub> is resolved by extending XAS spectroscopy of the O K edge into the vacuum continuum regime of X-ray photon energies. In final part of this Section, there is a bulleted summary of the most significant results.

The spectroscopic experimental evidence for cooperative J-T effects in the group IVB TM oxides, TiO<sub>2</sub>, ZrO<sub>2</sub> and HfO<sub>2</sub>, has been summarized in [4 and 5], in which degeneracy removal in conduction band final states has been observed in (1) synchrotron X-ray absorption spectroscopy (XAS) and X-ray photoelectron spectroscopy (XPS), and in (2) visible-vacuum-ultra-violet spectroscopic ellipsometry as well (vis-VUV SE). This paper focuses primarily on HfO<sub>2</sub>, but includes data and analyses for TiO<sub>2</sub> and ZrO<sub>2</sub>, where the experimental results and interpretation in terms of electronic structure theory, including defects, provide increased insights into the relationships between the J-T effect and the accompanying changes in the local site symmetry.

Prior to doing this we presented experimental data that established that there was a length scale for observing J-T term splittings spectroscopically (see Figs. 6(a)

and (b). The length scale was measured in units of a primitive unit cell, and based on a seminal paper of Professor Bersuker [29]. This scale corresponds to seven primitive unit cells which then comprise an electronic unit cell that is  $\sim 3$  nm in all directions, and defines a minimum film thickness for J-T term splitting. There is an additional kinetic limitation. To achieve this nano-grain size, films deposited at low temperature, e.g., room temperature to  $300^\circ\text{C}$ , must be annealed at a temperature of at least  $700^\circ\text{C}$  in Ar for J-T term splitting to be observable.

Nanocrystalline  $\text{TiO}_2$  has been used as prototypical elemental TM oxide with a distorted rutile phase. Most important are the spectra in Fig. 7 (XAS), Fig. 8 (VUV SE), and Fig. 10 (SXPS), and the comparisons of 3d-state splittings in Figs. 9(a) and (b). These assignments for Ti 3d, 4s and 4p atomic features in these spectra have been compared with the Symmetry Adapted Linear Combinations (SALC's) atomic states approach of F.A. Cotton in [13], and the modification of this to include covalency effects, in. [14 and 17].

We have used the experimental studies of  $\text{TiO}_2$ , and their interpretation as a basis for assigning spectral features in  $\text{HfO}_2$ , and  $\text{ZrO}_2$  as well. More importantly, the analysis of the defect spectra features in Fig. 13, subject to the energy level diagrams in Figs. 4 and 11 has enabled use to resolve an issue relative to the intrinsic bonding defects in  $\text{HfO}_2$ ; i.e., whether they are at monovacancy or divacancy bonding arrangements.

$\text{HfO}_2$  and  $\text{ZrO}_2$  exist in three different crystallographic phases, monoclinic (m-) at room temperature and up to  $\sim 1100^\circ\text{C}$  with sevenfold coordinated Hf, tetragonal (t-) at intermediate temperatures,  $\sim 1100^\circ\text{C}$ – $2200^\circ\text{C}$  with eightfold coordinated Hf, and finally a cubic (c-)  $\text{CaF}_2$  phase at temperatures  $> 2200^\circ\text{C}$  and up to the melting point of  $3387^\circ\text{C}$ , with eightfold coordinated Hf [9]. Films prepared by all of the deposition procedures identified below are inherently metastable, and as such they may have either monoclinic or tetragonal distortions, or be mixtures of monoclinic and tetrahedral nano-grains.

The results presented in Figs. 13(a) and (b), and Fig. 14(a) have distinguished between the monoclinic phase in Figs. 13(a) and (b), and the tetragonal phase in Fig. 14(a), on the basis of the multiplicity of d-state features in the respective O K edge conduction band edge XAS spectra. The primary factor is the coordination of Hf in the particular phase: (1) sevenfold-coordinated in m- $\text{HfO}_2$ , and (2) eightfold-coordinated in t- $\text{HfO}_2$ . The  $E_g$  feature includes a J-T term split doublet in m- $\text{HfO}_2$ , and in contrast a single contribution for t- $\text{HfO}_2$ . This criterion of multiplet counting is supported by comparing the O K edge XAS spectrum of t- $\text{HfO}_2$  in Fig. 14(a) with the O K edge XAS spectrum of cubic Hafnia in Fig. 14(b). The discriminating factor in this comparison is presence, or absence of a J-T term splitting the band edge  $E_g$  state. It is a single relatively narrow feature in each of these spectra simply because of the eightfold-coordination in the tetragonal and cubic phases, independent of the differences in the remaining d-state features; (1) the second d-state feature requires contributions from eight Hf atomic states,  $5d^1 E_g$ ,  $5d^3 T_{2g} + 5d^1 E_g$ ,  $6s_2 A_{1g}$  and  $6p^3 T_{1u}$ ; however (2) the degeneracy in the d-state features is removed completely for t- $\text{HfO}_2$ , but not for cubic Hafnia.



The majority of O K edge XAS spectra of TM elemental and complex oxides have addressed only the dominant features of these spectra, generally in a spectral range for X ray energies between about 525 eV and 545 eV. In point of fact the majority of our earlier studies, identified in [4] and [5], also follow this approach. However, in the past few years, we have also differentiated these XAS spectra, and found (1) additional features below the sharp rise in absorption, typically  $\sim 527\text{--}528$  eV for  $\text{TiO}_2$ , and complex titanates, and  $531\text{--}533$  eV for  $\text{HfO}_2$  and  $\text{ZrO}_2$ , that correspond to final states for intraimpurity absorption, and (2) more recently, and reported for the first time in this review, for energies greater than about 545 eV; these absorption reveal antibonding states associated with either monovacancy or divacancy defects, as well as Hf 4f spectral features.

The multiplicity of the antibonding defect state absorptions has provided a basis for distinguishing between monovacancy and divacancy defect state bonding arrangements. Based on this criterion, and compared with the energy band models in Figs. 4 and 11, this has identified the band edge defects in  $\text{TiO}_2$  as being incorporated into a monovacancy, and therefore have a  $d^2$  electronic with two occupied states at the valence band edge, and two antibonding states in the vacuum continuum. The spectral resolution, and more importantly the inherent broadening valence band states is not sufficient to reveal J-T multiplets, and two band defects are also observed in the SXPS spectrum in Fig. 19; however, the second derivative spectra for both m- $\text{HfO}_2$  and t- $\text{HfO}_2$  for (1) conduction band edge empty states in Figs. 17 and 18, and (2) antibonding states in Figs. 15 and 16 unambiguously reveal four features, establishing a  $d^4$  electronic state in a divacancy bonding arrangement.

This approach to determining the number of occupied TM d-states in above the valence band edge, and below the threshold for absorption to empty conduction band states has been validated for the  $\text{Mn}^{3+} d^4$  ion in  $\text{HoMnO}_3$  in Fig. 21. However, recent measurements, discussed below, indicate that four transitions in the pre-edge shake-up, and continuum shake-off regimes, can also occur for coupled  $d^1$  states associated with a monovacancy.

## 6.2 *Bulleted Summary*

The bulleted summary of this sub-section reflects the more recent results which have changed the interpretation of spectral data regarding the distinction between mono- and divacancy defects.

1. The occupied valence band states, and empty conduction band states for nanocrystalline  $\text{TiO}_2$  films with a physical thickness  $>4$  nm, and annealed at a temperature of at least  $700^\circ\text{C}$  (a) in qualitative and quantitative agreement with the ionic energy level approach of Cotton in [13] using SALC's of atomic states as a basis set, and (b) display a complete removal of J-T d-state degeneracies.
2. The band edge intrinsic defects, identified in XAS, SXPS and vis-VUV SE in  $\text{TiO}_2$  are consistent with monovacancy bonding arrangements, and are described

by a  $d^2$  occupied d-state electronic structure. The  $d^2$  character has been confirmed by spectroscopic identification of the antibonding states of the occupied valence bond defect states.

3. The length scale of order for observing J-T term splittings in TM elemental oxides length has been determined in units of a primitive unit cell, and is based on a seminal paper of Professor Bersuker [29]. This scale corresponds to seven primitive unit cells defining an *electronic unit cell* that is  $\sim 3$  nm in all directions, and defines a minimum film thickness for J-T term splitting. There is an additional kinetic constraint for films deposited at relatively low temperature, e.g., room temperature to  $300^\circ\text{C}$ ; these require annealing in Ar or another inert ambient at temperature of at least  $700^\circ\text{C}$ .
4. There are two phases of  $\text{HfO}_2$  that are cooperative J-T distortions of a parent  $\text{CaF}_2$  structure: (a) t- $\text{HfO}_2$  with eightfold-coordinated Hf, and basal plane distortions which are associated with a J-T effect distortion that removes all Hf 5d-state degeneracies, and (b) m- $\text{HfO}_2$  with sevenfold-coordinated Hf. These phases are readily distinguish by number of features in the band edge Hf 5d Eg symmetry state: one for t- $\text{HfO}_2$  and two for m- $\text{HfO}_2$ .
5. Intrinsic defects have been observed at the conduction band edge: (a) directly by vis-VUV SE, and (b) by differentiation of XAS; and at the valence band edge by (b) SXPS. Confirmation of the divacancy defect state bonding geometry was obtained from differentiation of the continuum regime of the XAS spectrum for X-ray photon energies  $>545$  eV; four shake-off features are observed corresponding to a pair of coupled  $d^1$  states. In a complimentary manner four shake-up features are also found in the pre-edge regime of the differentiated XAS spectra.
6. The derivative O K edge XAS spectra the hexagonal perovskite, h- $\text{HoMnO}_3$ , has a bipyramidal bonding arrangement of the Mn atoms that removes all d-state degeneracies [35]. The conduction band edge spectrum indicates four occupied  $\text{Mn}^{3+}$  d-states, and the vacuum continuum above the antibonding conduction band states indicates four antibonding antibonding  $\text{Mn}^{3+}$  3d. These are consistent with the  $d^4$  occupancy for the  $\text{Mn}^{3+}$  3d-state.
7. The approximate energies of occupied d-states of  $\text{HfO}_2$  are presented in Fig. 22. Each feature is equivalent to two states, which have not been resolved for either occupied states in the SXPS spectrum, or for empty states in the VUV SE spectra. The derivative XAS spectra, below and above the antibonding or empty states associated with the valence band, each are consistent with a pair of coupled  $d^1$  states occupancy.
8. The features above the top of the valence band in the SXPS spectra, and below the conduction band edge in the XAS and vis VUV SE spectra are associated with localized defects in the annealed film, and band-tail defects in the as-deposited film. There are inherent differences in the matrix elements for transitions for band to band, and impurity to impurity absorptions that result in differences in the band edge and defect absorption constants,  $\alpha$ , and  $e_2$ , as deduced from SE measurements. Therefore the relative strength in spectra must be adjusted according in the context of the N-sum rule [13]. The direct spectral estimates are factors of  $\sim 20$ – $50$ -fold higher than the actual defect densities, bringing the spectroscopic

results into good agreement with electrical I-V and C-V results. Typical defect densities in the high-temperature annealed films are in the regime of  $10^{12} \text{ cm}^{-2}$  or equivalently  $10^{18} \text{ cm}^{-3}$ .

### 6.3 *Noted added in proof*

Based on recent experimental studies since the J-T conference in Heidelberg in 2008 [31], and the application of many-electron theory [14,38], the intrinsic bonding defects in  $\text{TiO}_2$  and  $\text{HfO}_2$  have been assigned to monovacancies, with no definitive evidence for divacancies in  $\text{HfO}_2$  or  $\text{ZrO}_2$ . The electronic structure of Ti and Hf atoms bordering vacancies is described by a local site symmetry many-electron theory as applied to occupied d-states of these atoms [38]. The many electron  $d^n$  notation is used to describe the electronic states of Hf and Ti atoms that border on a monovacancy (hereafter vacancy) in  $\text{HfO}_2$ ,  $\text{ZrO}_2$  and  $\text{TiO}_2$  [13]. There are several different oxides of Ti;  $\text{TiO}$ ,  $\text{Ti}_2\text{O}_3$  and  $\text{TiO}_2$ , that illustrate the  $d^n$  notation. In the ionic model the formal valence states for Ti atoms in these oxides are obtained by setting the charge on O-atoms to -2. Neutral atomic states of Ti and Hf are described by s and d-shell occupancies: Ti as  $4s^2 3d^2$  and Hf as  $6s^2 5d^2$  [13]. Since the s-states have higher energies with respect to vacuum, they are removed first in ion formation. Formal charges on the respective Ti oxide atoms are  $\text{Ti}^{2+}$ ,  $\text{Ti}^{3+}$  and  $\text{Ti}^{4+}$ .  $\text{TiO}$  is a metallic  $d^2$  oxide,  $\text{Ti}_2\text{O}_3$  is a narrow band semiconductor d1 oxide, and  $\text{TiO}_2$  is a  $d^0$  insulator oxide. The ground state strongly correlated electronic configurations for oxides with occupied d-states,  $d^n$  with  $n > 1$ , explain their markedly different properties. Based on octahedral coordination of Ti, the ground state is a doublet  ${}^2T_{2g}$  for the d1 oxide,  $\text{TiO}$  and a triplet  ${}^3T_{2g}$  for the  $d^2$  oxide,  $\text{Ti}_2\text{O}_3$  [13,39]. Occupied electron states are above the valence band edge and the basis for systematic changes in oxide character [13].

In strongly correlated systems, the removal of a neutral O-atom reduces the average ionic charge in  $\text{TiO}_2$  and  $\text{HfO}_2$  below +4. This removal is better described by a local model using two populated of  $\text{Ti}^{3+}$  ionic states per removed O. Based on Pauli exclusion, or equivalently Hund's rule [13,38], the lowest energy configuration is a high spin  $d^1$  state with in  ${}^2T_{2g}$  configuration. The formalism for treating intra-atomic d-state transitions in  $d^n$  configurations [38] is the basis for defining the electronic spectra associated with intrinsic bonding defects in  $\text{HfO}_2$  and  $\text{TiO}_2$ . A monovacancy is represented by two inequivalent and coupled  $d^1$  states, and a divacancy by four coupled d1 states, where the coupling removes the degeneracy of these states. SXPS results, and more recently obtained XAS defect spectra for  $\text{HfO}_2$  and  $\text{TiO}_2$  [39] establish that intrinsic defects in  $\text{HfO}_2$  and  $\text{TiO}_2$ , and  $\text{ZrO}_2$  as well are monovacancies. The coupling of the two d1 states generates the four features observed in pre-edge shake-up spectra, and the continuum shake-off spectra as well [40].

**Acknowledgements** The author acknowledges the contributions of his most recent Ph.D. students, Sanghyun Lee, Hyuntak Seo, Joseph P Long, and Jinwoo Kim, and his most recent post doctoral fellows, Les Fleming, Kwun-Bum Chung and Relja Vasic in contributing to the film deposition and spectroscopy studies. He also acknowledges the important discussions relative to theory with Professors Jerry Whitten and Mike Whangbo of the Department of Chemistry at NCSU. He also acknowledges collaborations relative to (1) vis-VUV SE with Professor Dave Aspnes at NCSU, and (2) depth resolved cathodoluminescence with Professor Len Brillson of The Ohio State University. He also acknowledges an ongoing collaboration with Professor Darrell Scholm of Pennsylvania State University, soon to be moving to Cornell University in preparing complex oxides. On going collaboration in XAS and SXPS studies with Marc Ulrich of ARO, and an adjunct faculty at NC State is also gratefully acknowledged. Finally, it is a pleasure to acknowledge collaborations with Jan Luning and Dennis Nordlund of the Stanford Synchrotron Research Laboratory (SSRL) for their assistance in mentoring me, my graduate students, and post doctoral fellows in the acquisition of XAS data, and the mounting of samples as well at Beam-Line 10-1 of SSRL. The research results presented in this review have been supported in part by the Semiconductor Research Corporation, the Air Force Office of Scientific Research sponsorship of a MURI program that is Administered and Lead by Vanderbilt University, the National Science Foundation, and the Defense Threat Reduction Agency. Finally, the author appreciates a collaboration with Professors Theodore H. Geballe and Robert M. White that dates back to the mid-1979's when the author was a Senior Research Fellow and Laboratory Manager at the Xerox Palo Alto Research Center (Xerox PARC), and Professor White was a Principal Scientist and Area Manager at Xerox PARC as well. This collaboration addressed transition metal dichalcogenides in groups VB, and VIB as well as group IVB and introduced me to the first, second and third row transition metal dichalcogenides, and the differences that a few additional electrons could make in the infra-red effective charges.

The features above the top of the valence band in the SXPS spectrum are associated with localized defects in the annealed film, and band-tail defects in the as-deposited film. There are inherent differences in the matrix elements for transitions for band to band, and impurity to impurity absorptions that result in differences in the band edge and defect absorption constants,  $a$ , and  $e_2$ , as deduced from SE measurements. Therefore the relative strength in spectra must be adjusted according in the context of the N-sum rule [13]. The direct spectral estimates are factors of  $\sim 20$ – $50$ -fold higher than the actual defect densities, bringing the spectroscopic results into good agreement with electrical I–V and C–V results. Typical defect densities in the high-temperature annealed films are in the regime of  $10^{12}$  cm $^{-2}$  or equivalently  $10^{18}$  cm $^{-3}$ .

## References

1. M. Houssa, M.M. Hyens, in *High-K gate dielectrics*, ed. by M. Houssa (Institute of Physics, Bristol, 2004) Chap 1.1
2. G.D. Wilk, R.M. Wallace, J.M. Anthony, J. App. Phys. **87**, 484 (2000)
3. G. Lucovsky, et al., Mat. Res. Soc. Symp. Proc. **567**, 343–348, (1999)
4. G. Lucovsky, H. Seo, S. Lee, et al., Jpn. J. Appl. Phys. **46**, 1899 (2007)
5. G. Lucovsky, J. Mol. Struct. **838**, 187 (2007)
6. C.C. Fulton, G. Lucovsky, R.J. Nemanich, Appl. Phys. Lett. **84**, 580 (2004)
7. R.M. White T.H. Geballe, *Long Range Order in Solids, Solid State Physics Supplement*, vol. 15, (Academic Press, New York, 1979) Chap IV
8. G.A. Gehring, K.A. Gehring, Rep. Prog. Phys. **38**, 1 (1975)
9. R.W.G. Wyckoff, *Crystal Structures*, vol.2 (Interscience, New York, 1968)
10. P.W. Peacock, J. Robertson, J. App. Phys. **92**, 4712 (2002)
11. H.B. Gray, *Electrons and Chemical Bonding*. (Benjamin, New York, 1965) Chap. IX
12. C.J. Ballhausen, H.B. Gray, *Molecular Orbital Theory*. (W.A. Benjamin, New York, 1964) Chap. 8

13. F.A. Cotton, *Chemical Applications of Group Theory*. 2nd edn. (Wiley Interscience, New York, 1963) Chapter 8
14. P.A. Cox, *Transition Metal Oxides*, (Oxford, UK: Clarendon Press, 1992)
15. D.J. Chadi, R.B. Laughlin, J.D. Joannopoulos, in *The Physics of SiO<sub>2</sub> and Its Interfaces*, ed. by S.T. Pantelides (Pergamon, New York, 1978), p. 55
16. D.S. McClure, *Electronic Spectra of Molecules and Ions in Crystals* (Academic Press, New York, 1959)
17. I. Bersuker, *Electronic Structure and Properties of Transition Metal Compounds: Introduction to the Theory*. (Wiley, New York, 1996)
18. G.D. Watkins J.W. Corbett, Phys. Rev. **138**, A543 (1965)
19. J.L. Autran, D. Munteanu, M. Houssa, in *High-K Gate Dielectrics*, ed. by M. Houssa (Institute of Physics, Bristol, 2004) Chap. 3.4
20. H. Takeuchi, D. Ha, J. T-J King, Vac. Sci. Technol. A. **22**, 1337 (2004)
21. K. Xiong et al., Appl. Phys. Lett. 87, **183505**, (2005)
22. J.L. Gavartin, et al., Appl. Phys. Lett. 89, **082908**, (2006)
23. I.B. Bersuker, J. Comput. Chem. **18**, 260 (1997)
24. V.Z. Pollinger, unpublished
25. L. Fleming, C.C. Fulton, G. Lucovsky, et al., Appl. Phys. 120, **033707**, (2007)
26. G. Lucovsky, C.C. Fulton, et al., Radiat. Phys. Chem. **75**, 159 (2006)
27. G.B. Rayner et al., J. Vac. Sci. Technol. B. **20**, 1748 (2002); J. Vac. Sci. Technol. B. **21**, 1783 (2003)
28. Y.M. Strzhemechny, M. Bataiev, S.P. Tumakha et al., J. Vac. Sci. Technol. B. **26**, 232 (2008)
29. I.B. Bersuker, J. Struct. Chem. **16**, 863 (1975) (transl. from Zh. Srukt. Khim. 16, 935 (1975); (see also Ref. 16, Chapter 9)
30. F.M.F. de Groot, et al., Phys. Rev. B. **40**, 5715 (1989)
31. G. Lucovsky, K.B. Chung, J.W. Kim et al., Microelectron. Eng. **86**, 1676 (2009)
32. S. Wright, S. Feeney, R.C. Barklie, Microelectron. Eng. **84**, 2378 (2007)
33. G. Lucovsky, in *SiGe, Ge, and Related Compounds 3: Materials, Processing, and Devices*, ed. by D Haramé, et al. (The Electrochemical Society, Pennington, 2008), p. 381
34. K.B. Chung et al., Appl. Phys. Lett. 93, **182903**, (2008)
35. R. Vasic, M.D. Ulrich, G. Lucovsky, unpublished data
36. R. Vasic, M.D. Ulrich, G. Lucovsky, to be presented at the American Physical Society March Meeting (2009)
37. B. Koiller, L. Falicov, J. Phys. C: Solid State Phys. **7**, 299 (1974)
38. R. de Groot, A. Kotani, *Core Level Spectroscopy of Solids* (CRC Press, Boca Raton, 2008) chap 4
39. G. Lucovsky in *Physics Status Solids (C)* (2009), in press
40. B.K. Teo, *EXAFS: Basic Principles and Data Analysis* (Springer Verlag, Berlin. 1986) chap 5
41. H.R. Philipp, H. Ehrenreich, Phys. Rev. **129**, 1550 (1963)

**Part VII**  
**Jahn-Teller Effect and High-Tc**  
**Superconductivity**

# Jahn–Teller Polarons, Bipolarons and Inhomogeneities. A Possible Scenario for Superconductivity in Cuprates

Joaquin Miranda Mena

**Abstract** Some of the early models of high temperature superconductivity (HTS) in cuprates dismissed a pairing mechanism based on electron–phonon (e–ph) interactions. One of the arguments against the e–ph theories was the negligible isotope effect on the critical temperature,  $T_c$ . Other arguments were based on approximations performed near the strong e–ph interaction regime in which HTS might take place<sup>1</sup>. This leads to the conclusion that an e–ph pairing is inoperative. As a result, pure electron correlations, excitonic mechanisms and spin fluctuations have attracted most of the attention, overshadowing the e–ph approaches. However, some of the features shown by copper oxides seem to validate the e–ph models, in particular those which concern small bipolarons and the Jahn–Teller (JT) effect. For instance, these materials have a bandwidth within a range where the strength of JT coupling is important. Nonadiabatic effects cannot be ignored when high frequency phonons are coupled to itinerant charges. Therefore, theories based on on-site or intersite bipolarons, JT bipolarons and different mechanisms of carrier dynamics, such as Bose-Einstein condensation and tunneling-percolation, have been proposed. However, our discussion is centered on the JT models and the intriguing possibility that HTS could be driven by JT forces. The JT models have several distinctive features: they deal with a multidimensional electron basis coupled to symmetric phonon degrees of freedom. Moreover, JT polarons exhibit strong anharmonicity. The review highlights these local constraints and their consequences for the dynamics of polaron formation, the appearance of an inhomogeneous state and charge transport properties. In addition, the broken local symmetry at the thermodynamic limit of interacting JT polarons, when it is combined with long range Coulomb interactions, leads to specific macroscopic manifestations. Thus, cooperative effects go beyond standard structural transitions, and a novel organization of nanoscopic textures is manifested. Here we also address this issue and its connection with HTS, e.g. whether the so-called pseudogap observed in cuprates is related to the energy scale of the JT-bipolaron formation and the phase-segregation phase.

---

<sup>1</sup> See [47] regarding the isotope effect, and for a discussion of the *e-ph* approximation see for example E. G. Maksimov and O. V. Dolgov *Physics – Uspekhi* 50 (9) 933–937 (2007) and A. S. Alexandrov *Europhys. Lett.* 56, 92–98 (2001).

## 1 Introduction

In general it is agreed that the parent compounds of HTS copper oxides exhibit a strong electronic correlation. But it is also known that across their entire phase diagram various energy scales coexist. All the energy crossover regions give the impression that this is a very intricate problem; all the energy scales could be, in principle, a good starting point for the description of the phenomena. Then the fundamental question arises: what is the energy scale that drives the cuprates into superconductivity (SC)? Among these energy scales, there is one associated with JT instabilities and charge inhomogeneity. In this chapter we address their mutual relations and possible connection with HTS.

The chapter is organized as follows. The first section recalls that the germinal idea behind the discovery of SC in oxide superconductors was the JT effect. Afterwards we present some of the well established electronic properties of these materials (Sect. 3). It is important to recognize that the energy scale set by the electronic interactions led a substantial part of the scientific community to believe that HTS has its origin in purely electronic interactions. Therefore in Sect. 4 a brief review of models derived from these features is included. In Sect. 5 we illustrate the degree of controversy between e-ph and electron-based theories.

During the last two decades, diverse experimental techniques have provided evidence that links the HTS in copper oxides to self-organized JT-polarons. At the same time, advances in the development of powerful algorithms and solid theoretical foundations support the idea of an inhomogeneous phase as a basic element in cuprates for the SC transition. Due to the significant number of results from both areas, the community is reaching a consistent understanding of the interplay of inhomogeneities and lattice interactions and their key role for HTS. It is important to comment that the works presented are some of the most representative, but this chapter is not a detailed account of all the available literature. Rather, this chapter must be taken as a summary or a guide to these intertwined topics. The field is quite active and at the moment of finishing this book there are very exciting studies under development. Although the chapter is practically a theoretical revision, it includes an independent Sect. 6 dedicated to an experimental overview (the order of reading is optional, it can be done after reading Sects. 7 and 8). The selection was done on the basis of presenting information relevant for the discussion of the next sections. In this way we attempt to provide a more coherent presentation of the chapter. Before going into the formulation of JT-polarons and JT-bipolarons in the literature (Sect. 8), we outline some of the concepts of polarons and the achievements of bipolaron theory for cuprates (Sect. 7).

In Sect. 9 we present the JT effect as a mechanism for describing the type of inhomogeneities observed in cuprates. Special emphasis is placed on the long range Coulomb potential as a basic constituent of pattern formations. We close the chapter with Sect. 10 on the advances provided by JT models which use the concept of inhomogeneity as a basic element to predict HTS in doped copper oxides.



## 2 Superconductivity in Copper Oxides: The Original Concept

The strong JT distortion that perovskite oxides exhibit persuaded Bednorz and Muller to start a search for materials with higher  $T_c$ . Perovskites, like  $\text{SrTiO}_3$  and  $\text{LaAlO}_3$  [1], had shown signs of SC, but with a rather low  $T_c$ . Such low  $T_c$  came as no surprise, since they exhibit low carrier density, and according to the Bardeen-Cooper-Schrieffer (BCS) relation, a low temperature should be expected,

$$k_B T_c = 1.14 \omega_D e^{1/N_F V}. \quad (1)$$

Equation (1) is derived from the BCS theory; it relates  $T_c$  with the e-ph pairing potential,  $V$ , of electrons near the Fermi level, with  $N_F$  as their density of states (DOS). The Debye phonon cutoff is  $\omega_D$  and represents the average energy of the phonons involved in the process of pairing.

Nevertheless, following Muller and Bednorz, the e-ph interaction given by the strong JT effect in the  $\text{CuO}_6$  octahedral (Fig. 1a) in combination with a perovskite layer, could be the right condition for increasing  $T_c$ . In 1986 they published the highest  $T_c$  that had ever been measured ( $T_c = 35 \text{ K}$  [2]); it was registered in a doped  $\text{LaCuO}$  system (Fig. 1a):  $\text{La}_{1.85}\text{Ba}_{0.15}\text{CuO}_4$ . The discovery opened a completely new horizon, and ceramic oxides became some of the most studied materials. One

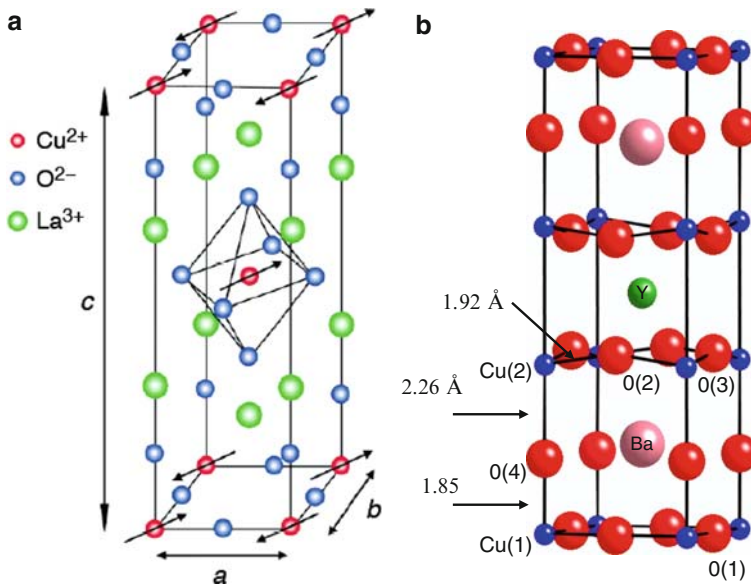


**Fig. 1** Two parent compounds of the family of ceramic oxides that under hole doping develop HTS. (a) In  $\text{LaCuO}$ , Lanthanum is substituted by Strontium or Barium. Ion valences, AF order, and the JT unit formed by the  $\text{CuO}_6$  octahedral are shown. (b)  $\text{YBaCuO}_{7-\delta}$  reaches HTS if oxygen is introduced into the Cu-O chains. The three lattice constants for the unit cell along the three axes are  $a = 3.81 \text{ \AA}$ ,  $b = 3.88 \text{ \AA}$  and  $c = 11.64 \text{ \AA}$ . Average Cu-O distances are indicated as well

year later, due to the efforts of M. Wu, P. Shu et al. [3],  $T_c$  was increased to 93 K. The new record was achieved by chemical substitution of Lanthanum by Yttrium, and the newest element in the family of HTS was YBaCuO<sub>7-8</sub> (Fig. 1b); the optimal chemical composition was Y<sub>1.2</sub>Ba<sub>0.8</sub>CuO. The highest  $T_c$  reached by 1995 [4] was under hydrostatic pressure and belongs to the compound HgBa<sub>2</sub>Ca<sub>2</sub>Cu<sub>3</sub>O<sub>8+8</sub>, with  $T_c = 168$  K.

### 3 Electronic Properties

One of the new paradigms that the copper oxides contributed to the phenomenon of SC is the notion of strong electronic correlations. On cuprates, charges have strong *repulsive and correlated* interactions, which are manifested by the failure of the Fermi liquid theory [5]. In principle the Fermi liquid theory is valid even if electrons have strong interaction; compounds like CeCu<sub>6</sub>, UBe<sub>13</sub> and CeAl<sub>3</sub>, which are known as heavy Fermions [6], are the best examples. These materials have electrons localized in *f*-shells and conduction electrons. Both classes of charges interact through a large Coulomb force. As a result the effective mass of the carriers is increased by three orders of magnitude; however the Fermi liquid theory is still valid. On the other hand, the Fermi liquid theory permitted one to deal with conventional superconductors. In the early days of SC the common wisdom was to start with a material with metallic properties (a metal or a metallic alloy). From the point of view of band theory, metals have partially filled bands. It was the core idea of BSC theory [7] to modify the metallic state in such a way that electrons end up in a coherent state, which gives rise to SC.

In the case of the parent compounds of the HTS, in addition to the strong interaction, there is a strong correlation that leads to the breakdown of the Fermi liquid theory. As result, band theory is no longer valid. They are referred to as Mott insulators [8, 9]. The term stems from the large Coulomb energy of double electron occupancy which blocks the possibility of having itinerant charges, even though the conduction band should exhibit metallic character. However, under doping (Fig. 2), this constraint is weakened, because electrons might find available sites where there is absence of a second electron. The variable  $U$  in (2) casts the strong local correlation. Another decisive factor in cuprates is the dimension where the SC takes place. Soon after their discovery it was pointed out that the CuO<sub>2</sub> plane and the CuO<sub>4</sub> plaque are the relevant units for tackling the new phenomena [10]. In addition, one of the first problems necessary to sort out was concerned with the orbital occupation of doped holes. Indeed it was expected that holes went into the Cu(3d) orbital, but X-ray absorption [11] confirmed that they occupy the *p* orbital of the in-plane oxygen instead. If holes are placed on this configuration, this introduces an extra level of energy because of the motion between copper and oxygen orbital levels. It was pointed out by Emery that the mid-gap observed in X-ray absorption is due to the opening of a new band created by the upper Cu and the *p*-O bands. According to the Allen-Sawatzky-Zaanen classification [12], the hole motion within the unit cell

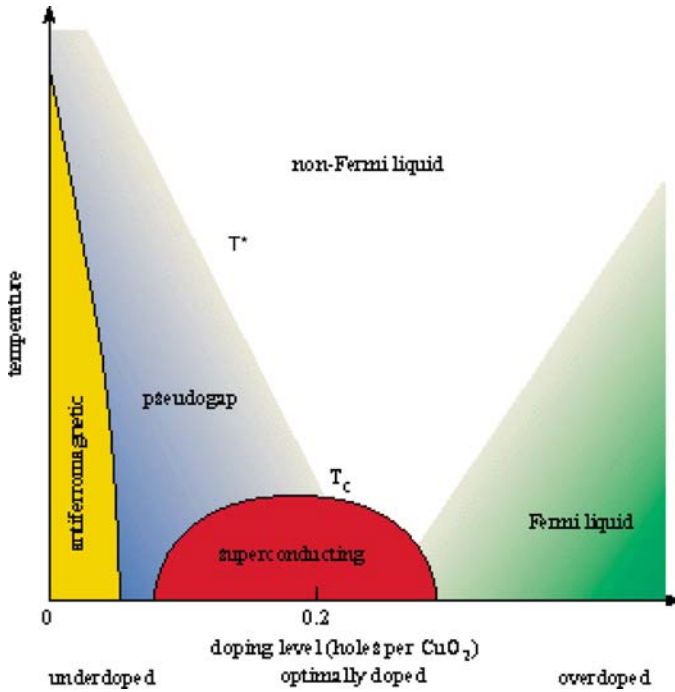


**Fig. 2** The phase diagram (temperature vs. hole doping) for the family of copper oxides. It shows the relevant regions and crossover lines often mentioned in this chapter

makes them charge-transfer insulators rather than Mott insulators. The following Hamiltonian reflects the rich electronic structure when the new level is taken into account:

$$\begin{aligned}
 H_{3\text{band.}} = & t \sum_{i,\sigma,\alpha} \left( d_{i,\sigma}^+ p_{i,\alpha,\sigma} + p_{i,\alpha,\sigma}^+ d_{i,\sigma} \right) + \varepsilon_p \sum_{i,\alpha} (n_{p,i,\alpha} - 1) \\
 & + \varepsilon_d \sum_i (n_{d,i} - 1) + U_p \sum_{i,\alpha} \left( n_{p,i,\alpha,\uparrow} - \frac{1}{2} \right) \left( n_{p,i,\alpha,\downarrow} - \frac{1}{2} \right) \\
 & + U_d \sum_i \left( n_{d,i,\uparrow} - \frac{1}{2} \right) \left( n_{d,i,\downarrow} - \frac{1}{2} \right) + V_{pd} \sum_{i,\alpha} (n_{p,i,\alpha,\uparrow} - 1)(n_{d,i} - 1).
 \end{aligned} \tag{2}$$

It is known as the three-band Hubbard Hamiltonian [13–15] and can describe the band structure of the parent compounds [16]. Here  $d^+$  ( $d$ ) and  $p^+$  ( $p$ ) are Fermionic operators for the bands  $d$  and  $p$  with orbital energy  $\varepsilon_d$  and  $\varepsilon_p$ , respectively. The energy of hopping for an electron (with spin  $\sigma = \uparrow, \downarrow$ ) from site  $i$  to site  $j$  is  $t$ . While  $U_p$  and  $U_d$  are Hubbard terms which are present if the occupation number operators ( $n_p$  or  $n_d$ ) are nonzero,  $V_{pd}$  is the intraband Coulomb repulsion.

It is common to reduce (2) into a single-band Hubbard Hamiltonian,

$$H_{\text{band.}} = t \sum_{i,j,\sigma} c_{i,\sigma}^{\dagger} c_{j,\sigma} + U \sum_i n_{i\uparrow}^{\dagger} n_{i\downarrow}, \quad (3)$$

with effective parameters given by  $t \approx t_{pd}^2/U$ ,  $U \approx \varepsilon_d - \varepsilon_p$ . Common values are  $U = 2.9 \text{ eV}$  (7 eV) and  $t = 0.33$  (0.5 eV) for  $\text{La}_2\text{CuO}_4$  and  $\text{YBaCuO}_{7-8}$  (E. Pickett 1989). Another effect of the strong Coulomb interaction is manifested by the anti-ferromagnetic (AF) order on the CuO plane (Fig. 1a). If  $U$  is large but finite, an additional scale of energy comes from the ability of charges to gain kinetic energy when they hop back and forward onto the oxygen ( $p$  orbital) that bridges two consecutive Cu ions. The process is known as virtual hopping. Although  $U$  inhibits doubly occupancy, this type of hopping may occur if the creation and destruction of these states happen simultaneously at the same site. The process gives rise to an effective AF correlation of spins (Fig. 2) with strength  $J$ , known as super exchange [16] and values near 0.3 eV.

## 4 Electronic Theories of High Temperature Superconductivity

Regardless of the type of formulation applied to explain HTS, the strong on-site repulsion set by  $U$  in (2) must be included. More puzzling could be the fact that such a term can by itself have the ability of pairing particles and ultimately organizing them into the SC state. In this section we give an account of some of the most influential models in the literature that have successfully surmounted these seemingly contradictory conceptions.

The same  $J$  term we mentioned at the end of last section has been pointed out as the dominant scale for SC. The interplay of the kinetic energy and the AF environment, where a hole is embedded, is captured in the so-called  $t - J$  model. A ferromagnetic background would make the problem far less complicated because holes would move easily; there would not be a compromise between the number of broken singlets and the gain of kinetic energy. From a descriptive view, if holes are strongly coupled to AF configurations, then two holes prefer to occupy adjacent sites, because it is energetically less costly: they break seven spin bounds, while two separate holes break eight. An alternative pairing is permitted if the holes are more weakly correlated to the spins. Here, one of the holes moves, freely tossing the spin arrangement, while the second follows the flipped path, restoring the original spin configuration. In this case the correlation length is larger. The model is formally derived from the Hubbard model (2) at the limit when  $U \gg t$ . Although there are several ways to deduce it [17], one that is widely used is the projection method onto a restricted Hilbert space where double occupancy is forbidden. However, any approximations introduced to make the model more tractable must retain the fundamental physics of the ground state and the low-lying excitations of the original Hubbard Hamiltonian. The traditional way to approximate the problem is to identify

a parameter and control it in a systematic fashion. The Hamiltonian capturing these features is:

$$H_{t-J} = t \sum_{\langle i,j \rangle, \sigma} \{c_{i,\sigma}^+ (1 - n_{i-\sigma}) (1 - n_{j-\sigma}) c_{j,\sigma} + h.c.\} + J \sum_{\langle i,j \rangle} S_i \cdot S_j, \quad (4)$$

where  $t$  represents the kinetic energy of holes with spin  $\sigma$ , moving from site  $i$  to site  $j$  (as long as  $j$  is not occupied),  $c^+$  ( $c$ ) are creation (annihilation) operators for Fermions occupying a site with spin  $\sigma$ , while  $n = c^+ c$  is the density of particles;  $J$  is the AF interaction and  $S$  is the quantum spin operator.

Similarly, in 1987, within the framework of his resonating valance bond (RVB) model, P. Anderson proposed an explanation of HTS, [11, 18]. The model works also in a reduced Hilbert space of single spins whose occupation number is one per  $\text{CuO}_4$  unit; the procedure is based on a projection technique onto a BCS-like paired wave function. The ground state of this wave function is formed by a linear superposition of all the possible ways of making up collective spin singlets. In this way, the pairing mechanism has its source in the AF order of the parent compound. The idea resembles the bonding mechanism of benzene molecules by electrons in a resonant orbital state, hence the name RVB. The key property is that, upon doping, holes are delocalized and even become SC carriers; the process involves a spin arrangement that goes from the long range AF order to a spin liquid order.

Systems near magnetic instabilities are subject to large spin susceptibility and thereby display a strong spin–spin interaction. The kind of AF order in cuprates has motivated researchers to introduce a model where this type of interaction is central for HTS. In the momentum space,  $k$ , the model takes the form (Moriya 1990, Pines (1990)):

$$H_{\text{SF}} = \sum_{\mathbf{k}, \sigma} \xi_{\mathbf{k}} c_{\mathbf{k}, \sigma}^+ c_{\mathbf{k}, \sigma} - \frac{1}{2} \sum_{\mathbf{q}} v(\mathbf{q}) \mathbf{S}_{\mathbf{q}} \cdot \mathbf{S}_{-\mathbf{q}}. \quad (5)$$

The nearest neighbor tight-binding band is denoted as  $\xi$ , the spin fluctuation as  $v$ , and  $S$  is the spin density contribution at momentum  $q$ . It is the second term that marks the importance of the spin interactions, as long as  $v$  is large. Computational simulations at a small level of doping showed that the magnetic susceptibility,  $\chi$ , which measures the AF fluctuations, goes from long to short correlation as the temperature is cooled down, and near  $q = (\pi, \pi)$  a large peak appears [19]. Using a diagrammatic technique, (random phase approximation, RPA), the relation between  $\chi$  and an effective electron–electron, ( $e - e$ ) interaction,  $u$ , is given by [20]

$$\chi(q) = \frac{\chi_0(q)}{1 - u\chi_0(q)}. \quad (6)$$

The Fourier transform to real space of the  $e - e$  interaction suggests that this interaction can lead to pairing if the potential changes sign every 90 degrees, which means that the pair potential must have a  $d_{x^2-y^2}$  symmetry. Therefore, holes must have a

particular spatial arrangement in order to avoid the strong Coulomb repulsion; the final shape of the potential has simultaneously attractive and repulsive regions.

An alternative approach is the Slave Boson approximation [21] where the Fermionic operators are defined as the product of Boson and spin operators. There is a constraint with the number of Fermions,  $n_f$ , and number of Bosons,  $n_b$  :  $n_f + n_b = 1$ . The spin part is treated with a RVB spin model and the charge as a Bose-Einstein condensation problem. These leads to a fractionalization of charges (holons) and spin (spinons), where uncondensed holons exist above the SC domain. The temperature crossover of the spinon pairing and the holon condensation, as a function of doping, is identified as peak in the SC domain.

Most of the HTS models rely on the notion of a pairing potential as the mechanism to achieve SC. However, there is a class of theories that see the phenomena from a different perspective. Generally speaking, the SC phase is achieved by lowering the total energy of the charges; this can be accomplished by either lowering the pair potential energy or lowering the kinetic energy of the particles. The models we have outlined so far belong to the first situation. The second situation has been put forward by J. Hirsch, and the dynamical Hubbard method has been the most widely used technique to embody the idea [22–24]. The physics behind is that carriers prefer to “bond”, because the kinetic energy is substantially reduced. This gives charges the ability to avoid all kind of possible interactions that could increase the sum of their individual kinetic energies. In other words, two particles traveling together through the obstacles in a material can move easily, otherwise the bouncing with the obstacles would slow them down. Some tentative predictions have been proposed; the most intriguing one is related to the shift frequency of the optical absorption [25].

The last electronic model we cite concerns the subject of the quantum critical point (QCP) [26] and its possible relation with HTS in copper oxides [27, 28]. The clue comes from the similarity between the phase diagram of the cuprates (Fig. 2) and the phase diagram of heavy Fermi systems. The explanation relies on the developing of magnetic fluctuation as doping is increased in the cuprates [29, 30]. A central issue in this type of models is that a well defined quasi particle (QP) must exist, which is the case for the heavy Fermi materials. The paramagnetic phase these materials exhibit is still a Fermi liquid, and its signatures are clearly shown in experiments. On the contrary, cuprates do not have well defined Fermi states if undoped, slightly doped, or even for optimal doping. Nevertheless, it has been proposed to treat the strong correlation as a perturbation to the Fermi liquid region (extreme right side of the T vs. doping phase diagram, Fig. 2). So far no evidence has been found in the experiments that can prove this proposal. A QCP is attainable at zero temperature by changing three of the following parameters: the level of doping, tuning an external magnetic field or applying pressure. Following the pseudogap ( $\Delta_p$ ) across temperature and doping, it would desirable that some experiment showed a signal of the QCP as one approximates optimal doping (near 0.15% of doping) at zero temperature. However, these experiments are quite complicated and the QCP is still elusive. One of the main reasons is the number of energy scales along the path

where that data must be collected, making it hard to distinguish whether it is a real quantum phase transition or a temperature crossover.

The electron-based theories presented explain two of the fundamental characteristics of HTS oxides readily, i.e. the  $d_{x^2-y^2}$  symmetry superconductor gap and the short correlation length of pairing, because in some way these features are built into the formulation. The situation in e-ph models is not so straightforward and requires a more careful formulation in order to remain compatible with the phenomenology. Other arguments that seem to validate the electronic models can be checked within the citations we made for each model.

## 5 Two Divergent Views

The electron-based models depend to a large extent on the electronic state called Zhang-Rice (Z-R) singlet. We will not go into details regarding its important function in these theories and related experiments. But the main reason to allude to it is because it is the point where we open the discussions about the definite issue that concerns us, the JT effect and its role in HTS. In 1988 Zhang and Rice proposed that holes occupying the O(2p) orbital are indeed delocalized around the Cu ion, taking any of the four bonds formed by Cu  $d_{x^2-y^2}$  and O-p orbitals [31]. The spin and the center hole at Cu is what is called Z-R singlet. Spin-polarized resonant photoemission measurements seem to show signals of such paired hole-spin configuration [32]. Despite a large number of publications supporting the existence of this singlet, recent molecular cluster calculations suggest that the concept should be revised. This task was performed by H. Koizumi [33], who studied the most stable configuration of a hole placed in two interacting CuO<sub>6</sub> JT active centers. The calculation showed that holes prefer occupy a mixture of single  $p$ -O orbital and two  $d$ -copper orbits. As a result, a polaron is formed by the lattice distortions of both CuO<sub>6</sub> octahedrons. In contrast, the Z-R singlet configuration exhibits a higher energy of stabilization. Moreover, the energy of the JT polaron was in agreement with both the EXAFS experiments for Cu-O bond distortions and the peak measured in photo-induced conductivity (both reviewed in the next section).

Another two subjects of controversy are the pairing symmetry and the bosonic mode that leads to the SC pairing. Since the middle of the 90s experiments with flux quantization and studies of phase order parameters probed by magnetic field modulations [34, 35] indicated that  $d$ -wave symmetry is present. This settled the dispute about the origin of the symmetry observed. On the one hand this property can easily be explained by pure electronic arguments [36, 37], but on the other hand it was demonstrated that  $d$ -wave symmetry might also arise from a phonon mechanism [38, 39]. Equally important is the extensive data provided by ARPES [40, 41]. This technique directly probes the QP energy dispersion and seems to be an ideal technique for monitoring the symmetry and energy of charges restricted to two dimensions – as is the case for CuO sheets that hold the SC carriers. Nevertheless the data has been interpreted in different ways and used as a battle ground to

test the different theories. Besides the  $d$ -wave symmetry also observed in this technique, the dispute has been extended to the ARPES amplitude and the kink observed in the energy dispersion. The energy where the kink develops should give an idea of the energy scale of the boson responsible pairing. But the assignation to the bosonic mode is a matter of debate, though. Some attribute it to a spin mode [42], while others favor a phonon mode [43].

An essential issue of debate, because it might be regarded as a precursor to the SC phase, is the origin of an appealing energy that emerges when the SC transition is approached above  $T_c$  at low doping (Fig. 2). The temperature range is denoted as  $T^*$  and the energy scale as  $\Delta_p$ . Some electronic theories identify  $\Delta_p$  as a spin gap. The basic idea behind this view is that, as the doped holes are introduced, they induce frustration on the spin alignments, and therefore break the long range spin order, with only interactions of short length remaining. Consequently, if the difference of energy between the ground state and the first excited state is due to the effect of spin frustration, the gap is a spin gap. But from the viewpoint of preformed pairs mediated by phonon interactions, the  $\Delta_p$  is related to the energy of charge confinement by lattice distortions.

It has also been argued that the  $\Delta_p$  energy is responsible for a type of organization related to an electronic order, whose origin could be due to spin or lattice interactions. In particular, at doping  $1/8$  a type of order has been a topic of intense debate; it is the stripe phase observed in diverse experiments (see for example J. Tranquada et al. (1995), Nature **375**, 561). Although there is consensus that such an order is present, there is no agreement whether the overall effect is in detriment to the SC. Neither is it clear what is the nature of the interaction dominating in the region of the phase diagram defined by  $T^*$ . For example, the spin gap nature of related kinds of orders was put forward in recent spin dynamics measurements [44] along with the predictions of a novel order state, emerging from magnetic interactions as found in the studies of Yamase et al. [45]. A comprehensive description involving lattice interactions will be given in the next sections.

## 6 Experimental Evidences of Polarons, Lattice-Charge Segregation, and the Isotope Effect: The Role of JT Distortions

At the end of the 80s, the first reports of carriers with a polaronic nature were measured with photo-induced absorption, optical conductivity and infrared reflexivity in  $\text{LaCuO}_{4+x}$  and  $\text{NdCuO}_{4-y}$  [46, 47]. The advocate idea was that with the assistance of absorbed light, polarons gain the ability to hop from one localized site to another. The origin of the mid-infra red peak oscillations that register on these experiments was linked to polarons. This picture was supported by related theoretical studies of polarons and bipolarons [48]. It is important to emphasize that these carriers were successfully modeled by Holstein-Hubbard and Holstein  $t - J$



polarons, which confirm their local character. Hence, the provided data stimulated more experiments aiming to test the importance of polaron mobility in cuprates.

At the same time, there was an improvement of the methods suited to probe the local structure, like for example EXAFS, whose high energy helped to resolve inter-atomic distances. This contrasts with traditional methods like X-ray diffraction that yield an average of the crystalline structure. Together with EXAFS, inelastic neutron scattering [49] became a primordial tool for studying the local environment of the single  $\text{CuO}_6$  octahedral, revealing anomalies in the atomic distributions. EXAFS analysis showed that the Cu-O apical in  $\text{YBaCuO}$  exhibits two distances, giving structural evidence of polarons in cuprates [50, 51]. The polarized X-rays along the  $c$ -axis found two equilibrium distances of 1.822 and 1.954 Å for the Cu(1)-O(4) (Fig. 1b), which differs from the average of 1.84 Å. This type of results is relevant for the JT effect. Since EXAFS can measure differences between the CuO apical and CuO planar distances, it can help to estimate the JT splitting and to determine whether the JT effect has to be treated as a pseudo JT effect. But, due to the time resolution of the technique, it cannot distinguish between dynamical and static JT distortions. Deeper conclusions from the EXAFS data came later on [52], when it was inferred that distorted domains coexist with undistorted domains at the scale of nanometers. The materials subject of study were  $\text{La}_{1.85}\text{CuO}_{4.1}$  and  $\text{La}_{1.85}\text{Sr}_{0.15}\text{CuO}_4$ , where two double distances appeared on the Cu-O layer and  $c$ -axis. The double distances are interpreted as the coexistence of two regions of  $\text{CuO}_6$  octahedra: one without deformation (16 Å of widths in the  $\text{La}_{1.85}\text{CuO}_{4.1}$  and 14.5 Å in  $\text{La}_{1.85}\text{CuO}_{4.1}$ ) and a second region with distorted octahedral (8 Å of width in the  $\text{La}_{1.85}\text{CuO}_{4.1}$  and 9.7 Å in  $\text{La}_{1.85}\text{CuO}_{4.1}$ ). All these results strongly suggest that copper oxides are not homogenous materials. More intriguing results came when the Cu-O pair distribution showed a broadening within the SC region as the doping was increased and the temperature kept fixed at  $T = 10$  K [53]. Similarly, the data collected at optimal doping and variable temperature shows a diffusive amplitude as the temperature approaches  $T_c$ , but suddenly peaks at  $T = T_c$  [54].

The rich interplay among time, energy and length scales has been successfully studied by a series of experiments using femto-second spectroscopy [55–58]. The technique is suitable to study the process of pair formation. The advantage of the technique resides in its characteristic time scale, which is within the time span that a QP requires to relax from the high energy state induced by a laser pulse to the low energy delimited by a bottom band where the QP exist, before it further relaxes and recombines. In the results presented in [55–58], the recombination time of the QP was attributed to the anharmonic life-time of the phonons that take part in the process. The technique also offers the opportunity to infer the length scale within which the process occurs and thereby exposes lattice-charge inhomogeneties, [59]. In addition, the coexistence of localized and free electronic states was confirmed. This has particular importance, since it has revived the two-component models, first proposed right after the discovery of HTS in cuprates. The group also extracted two different time scales of relaxation. One appears at  $T_c$  and is associated with the SC gap, with a life-time ranging from 0.1 to 3 ps. The second component, with a longer life time, is attributed to  $\Delta_p$  and the emergence of charge separation.

On another hand, the enormous improvement of scanning-tunneling microscopy (STM) in the last years has permitted to map the electronic DOS of some copper oxides, showing images with inhomogeneous charge distribution at the nanoscopic scale [60–64]. Although one problem that the technique faces is that the  $\text{Cu}_2\text{O}$  planes are not directly observed (this is due to fact that the cleaved process does not expose the CuO layers, but the Bi-O layer of Cu-O chains, for instance) However, it is considered to be one of the most influential techniques. The length scale measured by STM has also been confirmed by ion-channeling [65].

The isotope effect remains one of the most direct criteria to discriminate whether the vibrational modes of the ions are the constituent mechanism for superconductivity. In the case of cuprate special attention has been paid to substitution of  $^{16}\text{O}$  by  $^{18}\text{O}$ . The sign of the isotope shift detected in conventional superconductors persuaded Bardeen to establish an e-ph mechanism. In contrast, the relevance of phonon interaction in cuprates has long been debated, because of the negligible isotope effect on  $T_c$  [66]. However, advances in experimental techniques in recent years and carefully performed experiments have shown evidence of an isotope effect, but the signatures are not the usual ones, as those found in metals or alloys. Consequently, ceramics superconductors may also be regarded as unconventional superconductors, in the sense that the isotope effect is present, but in a subtle way. Furthermore in the BCS theory, the  $T_c$  dependence with the mass,  $m$ , of the ion involved in the phonon pairing is  $T_c = m^{-\alpha}$  with  $\alpha = 0.5$ . It is known that deviations from this value may depend on the type of interatomic potentials. This could be, for instance, a double well minimum potential corresponding to a polaron motion of an ion moving between two equivalent positions [67] or/and anharmonicity [68]. Hence, the JT tunneling between two degenerate or nearly degenerate states may be intimately related to this form of polaron, and therefore deviations from  $\alpha = 0.5$  should be expected.

One of the manifestations of the isotope effect is the huge isotope shift in the measurements done for the pseudogap,  $\Delta_p$ , regime. INS in  $\text{LaHSrCuO}$  showed an isotopic shift in the  $\Delta_p$  temperature of  $\Delta T^* = -10\text{ K}$ , here  $\Delta T^* = T^*(\text{O}_{16}) - T^*(\text{O}_{18}) = 60\text{K} - 70\text{K} = -10\text{ K}$ . In the case of  $\text{LaSrCuO}$   $T^*(\text{O}_{16}) = 110$  and  $T^*(\text{O}_{18}) = 170$ , with a  $\Delta T^* = 54.4\%$  of isotopic shift. As a matter of fact, the isotopic substitution was also performed for Cu ( $\text{Cu}_{63} \rightarrow \text{Cu}_{65}$ ), showing no isotopic shift and therefore confirming that the displacements involving the oxygens are the relevant modes [69, 70]. Thus, the isotope effect that does appear at the  $\Delta_p$  is strong evidence that the phonons, inhomogenities and preformed pairs are linked [71, 72].

Signatures of the isotope effect can be found in the studies of Kresin, Khasanov, H. Keller and Bussmann-Holder [73]. The normalized penetration depth and the superconducting gap show a linear tendency as a function of doping. The most significant feature in their discoveries is the negative correlation of the penetration depth at optimal doping and overdoped samples. An equally interesting result was given by the isotopic shift on magnetic transition temperatures at zero fields ( $\mu\text{SR}$ ); the experiments were performed for undoped  $\text{LaSrCuO}$ . Here, it was also demonstrated that light polaron carriers (corresponding to  $\text{O}_{16}$ ) have the ability to break the AF order more easily than the heavy polarons composed by  $\text{O}_{18}$ . All

these results fit into the particular interpretations made by Bussmann-Holder, Keller and Muller, which are based on a two-component band model with electron-lattice interactions [74, 75], where the nearest neighbors, second and third next-nearest neighbor-hopping in the CuO layers, as well as hopping for interlayers, was considered. The same approach used in [74, 75] was applied for a strain analysis. Because the effect of the strain changes the relative distance between oxygen and copper, one way to mimic the strain is through variation of the hopping integrals. It was found that the combination of nearest and next-nearest neighbors yields the optimal hopping parameters for an enhancement of  $T_c$ . Thus, when the strain is taken into account,  $T_c$  reaches a maximum for intermediate values of both values of hopping. Based on the isotope and strain effects, they conclude that the  $Q_2$  active JT mode, identified after the combination of such hopping parameters, has a prominent role in the SC properties.

Concerning strain experiments, only a few reliable studies exist. This is because strain must be tuned in a very controlled way, and the data interpretation is not straightforward. For instance, it is the aforementioned EXAFS technique that has proven to be a valuable tool when strain is applied to HTS samples; its importance resides in the fact that the changes in the lattice structure impinged by strain are accompanied by a modification of  $T_c$ . The  $\text{CuO}_6$  unit, which induces the JT effect, can be weakened or strengthened under tensile or compressive strain, respectively. Subsequently, the energy levels of the  $b_{1g}$  and  $a_{1g}$  electronic configurations are moving closer or further apart. Thereby, the hole motion can be tuned by the splitting energy between both electronic levels. Based on the EXAFS experiment, Oyanagui [76] proposed the interesting idea that can be summed up as follows: the superfluid density of holes with  $b_{1g}$  character is regulated by the level of inhomogeneities, which in turn depend on the applied strain. The details of how this occurs must be checked in [77]. We just give the relevant figures of the data collected by Oyanagui and coworkers. The  $\text{CuO}_6$  JT unit exhibits an elongation of 0.01 Å under tensile strain, which stabilizes static distorted regions, while the shortening of the JT unit, under compressive strain, makes the distorted regions dynamical. It is precisely these structural changes that make the latent carriers more extended or localized.

## 7 General Considerations of Polarons and Bipolarons

Before moving on to the formulation of the JT effect in the context of HTS, we need to briefly review some concepts regarding polarons, bi-polarons and their relation to e-ph coupling. It is of great importance to realize that the JT distortions we will discuss are directly related to these terms. It has to be recognized at the outset that it is necessary to have a strong e-ph coupling for an operating mechanism based on phonons. This is in part because of the strong on-site repulsion (Sect. 2) that charges need to overcome in order to form bounded particles. Any pair formation needs to meet the condition of a very short coherence length of pairing,  $\xi$ , present in these materials. One consequence of the strong e-ph coupling is the

deep deformation surrounding the lattice environment of a charge, giving rise to what is known in the literature as small polarons. In the most common definition, if the deformed region is of the same dimension as the lattice constant ( $a$ ), the polaron is called a small polaron. However, a proper definition is needed if one wants to know how the physical parameters of the material are involved. According to [78], if one defines the dimensionless coupling constant  $\lambda = E_p/E_a$  (where  $E_p$  is the energy for lattice relaxation due to a polaron and  $E_a = \hbar/2ma$  with  $m$  as the bare mass of the electron) then small polarons exist for values  $\lambda > 1$ . However, this criterion has to be modified for the formation of stable bipolarons, in which case  $\lambda > 0.5$  and the coupling constant can also be defined as  $\lambda = E_p/D$  (here  $D$  is used as the bare half-bandwidth). Bipolarons can be classified by the proximity of their two constituent charges. Generally, on-site bi-polarons refer to a situation in which the electrons are placed near the same site, while the term bi-polaron refers to electrons being in neighboring sites.

It is challenging to introduce a *bipolaron* mechanism that can achieve HTS in cuprates. For instance, in order to develop mobility, the polarons have to overcome the self-trapping effect. Another setback is due to the fact that the stable configuration is accomplished by overcrowded regions of polarons. One of the first attempts to use polarons as the source of pairing goes back to Ranninger and Alexandrov [79]; they used a real space representation of on-site or intersite bi-polarons with the purpose of generating charged bosons. The scenario proposed relies on polarons that, after pairing, create intersite bosons, which in turn undergo to a Bose-Einstein condensation transition. The bipolaron theory of HTS in cuprates finds solid grounding in the mathematical developments of Alexandrov and the late Mott [80,81], and some direct prediction in the normal state by Alexandrov, Mott and Kabanov [82].

The mechanism of bipolaron SC was also explored in 1981 by Y. Takada. Stimulated by the possibility to increase  $T_c$  using a bipolaron formalism in ionic crystals, he investigated the condition of pair formation in all possible spatial dimensions [83]. In his paper, Takada drew attention to the following facts. Although these materials display a low density of electrons, and the high lattice polarization reduces the electron attraction even at strong phonon coupling, the factor that makes possible the pairing is the dynamical interaction. He found that bipolarons, interacting through polar-optic phonons and repulsive Coulomb forces, are stable in one- and two-dimensional systems. Several authors have contributed to the study of polaron properties (for works related to cuprates, besides the ones presented in this chapter, consult T. Devrese, A. Firsov, S. Aubry and A. Trugman in [84], as well as A. Bishop).

The Holstein and the Frohlich polarons are two of the most studied types of polarons, typically the former are used for short range interactions and the latter for long range lattice interactions; in real space they are represented as:

$$H_{\text{pol.}} = -t \sum_{\langle i,j \rangle} c_i^\dagger c_j - g \sum_i f(i,j)(b_i^\dagger + b_i)n_i + \omega_0 \sum_i b_i^\dagger b_i, \quad (7)$$

where  $c^+$  ( $c$ ) are creation (annihilation) operators for Fermions at sites  $i$  and  $j$ ; while  $b^+$  ( $b$ ) are the respective operators for dispersionless phonon modes of bare frequency  $\omega$ ;  $n = c^+ c$  is the density of particles at site  $i$  and regulates the coupling with the phonons with a strength  $g$ . The nearest neighbor hopping,  $t$ , the mode  $\omega$  and coupling strength  $g$  are either in units of energy or without units. The space function  $f$ , distinguishes the Holstein phonon interaction,  $f = \delta_{i,j}$ , from the Frohlich phonon interaction,  $f(i, j) = [(i - j)^2 + 1]^{-3/2}$ . It is the imbalance of charge density, given in the second term, that activates the vibration of a phonon mode  $b$  and thereby the e-ph coupling.

The original idea that a considerable mobility of bipolarons could be realized in cuprates by short range movements is confirmed in the work of Hague et al. [85]. Two varieties of motion were studied for the case of Frohlich interactions on staggered geometries by means of a continuous Quantum Monte Carlo a “crawling-like” and a “crab-like” motion. This type of result rules out the misconceptions that polarons might not exhibit high mobility because they are strongly bound to distorted lattice regions. Although it is true that, in order to have very short SC coherence lengths in cuprates, a strong e-ph interaction is needed, the presence of the strong Coulomb repulsion helps to counterbalance it. As a result, the bipolaron mass is reduced. In the light of these results, it is now the turn of the JT bipolarons to clarify whether they offer a better standpoint.

## 8 Formulation of The Jahn–Teller Problem on Cuprates

The problem of JT in cuprates at very dilute concentrations is in essence a local problem; conceptually, it can be seen as an impurity center embedded in a crystal. In principle, various active modes are present, and in general each of the JT active modes can be studied individually. Whether all modes need to be considered depends in turn on the choice of the relevant mode for the problem. In the case of cuprates it is common to deal with the three dimensional character of the oxygens surrounding the Cu ion, or to take the two dimensional character of the four planar oxygens around the Cu ion (placed along the  $a - b$  crystallographic axis, see Fig. 1). If capital letters denote electronic states and small letters the vibrational modes, according to group theory, the  $\text{CuO}_4$  cluster can be described as an  $E \times E = A_1 + B_1 + B_2$  or a  $E \otimes (a_1 + b_{1g} + b_{2g})$  problem.  $E$  stands for the degenerate electronic state of the  $D_{4h}$  symmetry, and they are coupled to the asymmetric vibrational terms  $b_{1g}$  and  $b_{2g}$ . The electronic state represents the Cu wave function with  $x^2 - y^2$  or  $xy$  symmetries, and they are coupled to the  $b_{1g}$  mode. The  $b_{1g}$  represents the simultaneous motion of two opposite oxygens displacing towards the Cu center, while the other two oxygens move away from it. This displacement is commonly called half-breathing mode, in contrast to the breathing mode, which occurs when the four oxygens undergo a totally symmetric displacement. The two vibrational modes are pertinent to hybridization with the in-plane oxygen wave functions of  $p$  symmetry. If only the half-breathing mode is the subject of study, the problem is

referred to as an *Exb* problem and is the simplest model for holes with  $b_{1g}$  character moving along the CuO plane. Another important factor worth mentioning is the temperature at which the cuprates are studied, since some modes can be ignored if their phonon DOSs are low.

A more rigorous treatment is to consider the full CuO<sub>6</sub> octahedral; then the JT problem becomes  $Exe = A_I + E$  or  $E \otimes (a_I + e)$  [86]. In contrast to the CO<sub>4</sub> cluster, both the electronic states and the vibrational mode exhibit double degeneracy. The  $E$  term represents the  $3z^2 - r^2$  or the  $x^2 - y^2$  Cu orbital, which, together with the  $p$ -Oxygen orbitals, form the electronic degeneration. By this approach, the effect of the elongation along the crystallographic  $c$  axis can be added. The difference between the  $3z^2 - r^2$  bond energy and the  $x^2 - y^2$  bond energy gives the JT split energy, which is also the scale energy that sets the problem as either a pure JT effect, or as a pseudo JT effect. At this point it has to be said that HTS oxides may not meet the conditions for a strict JT effect. For instance, due to the strongly layered structure, a highly symmetric environment (one of the basic requirements for the presence of the JT effect) might be absent [87]. Although not as strong as in the case of manganites [88], local probes offer some indication of local instabilities associated with a JT structure deformation in LaCuO and YBaCuO systems (see Sect. 6). However, a pseudo JT might remain. This raises a dilemma that the JT community often faces: how far apart need the two nearly-degenerate levels to be in order to treat the problem as a PJT? The discussion on this issue is beyond the scope of this review, but we refer to Bersuker in [86].

In order to address the properties of a JT-polaron, we compare it with the two classes of polarons we have already presented. We use the phonon interaction of the molecular Holstein or Frohlich Hamiltonian, given by (7) and we compare it with a JT Hamiltonian,

$$H_{\text{JT-pol}} = \sum_{\langle i,j \rangle, \alpha, \beta} \left( c_{i,\alpha}^+ c_{j,\beta} + hc. \right) - g \sum_i \left[ (n_{i,1} - n_{i,2}) (a_i^+ + a_i) + (c_{i,1}^+ c_{i,2} + c_{i,2}^+ c_{i,1}) (b_i^+ + b_i) \right] + \omega_0 \sum_i (a_i^+ a_i + b_i^+ b_i), \quad (8)$$

contrasting with (7), the electrons are interacting with two dispersionless degenerate phonon modes  $a$  and  $b$ . Besides that, there are two additional electronic orbitals, labeled as  $\alpha$  and  $\beta$ . Mode  $a$  is coupled with the charge density at site  $i$  while mode  $b$  couples, through hopping, to two different orbitals. The e-ph coupling  $g$  preserves the symmetry of the interaction. It is noticed that, with this formulation, the coupling is more complex than that described by (7). The difference of charge density in the two orbitals activates coupling to the  $a$  modes, while the coupling to the  $b$  modes requires an electronic transition between orbitals.

The first numerical results from a strictly quantum mechanical calculation were given a few years ago [89]. In particular, P. Kornilovitch formulated a path integral representation of a three-dimensional JT polaron. Applying a QMC algorithm, he calculated the energy of the ground state, the DOS and the effective mass of a single

JT polaron, and compared them with the computed values of a Holstein polaron. The two types of polarons showed similar behavior, except at the intermediate and strong coupling, where the JT polaron was lighter and developed a peaked DOS. That same year, in 2000, Y. Takada published an analytical paper, in which he proved that JT polarons should be lighter due to the fact that the vertex corrections are less effective in JT polarons than in Holstein polarons [90]. However, one year after Takada's publication, an analytical work carried out by H. Barentzen [91] showed that such differences in the two types of polarons may not be as pronounced as it is predicted in [90]. Similarly, for the one-dimensional case a comparative study of JT polarons and Holstein polarons was made by Shawish, Bonza et al. [92]; they used an advanced algorithm to compute the optical conductivity, the effective mass and the spatial extension. In addition, they included the strong Hubbard term for electrons placed either in the same orbital or in different orbitals. The results in the strong coupling regime showed that the JT interactions reduce the effective mass of the polarons and bi-polarons, while at weak coupling the two types of polarons display no differences. The same tendency as a function of coupling was observed in the radial extension of the polarons.

In summary, JT-polarons are good candidates as charge carriers in cuprates, and their ultimate consequences for the transport properties are worth exploring. Nevertheless, the JT polarons by themselves may not lead to SC, and some other considerations are needed. So far we only discussed isolated JT centers; the problem is more complex when the concentration of JT active centers is increased: The higher the doping, the larger the possibility that the JT centers start to interact, and the assumption of two equivalent displacements in a JT center is no longer valid [93]. In other words, the presence of JT neighbors affects the degeneracy, provoking that one of the configurations is more likely to be present. This leads to the cooperative JT effect. In the simplest case this would happen if the centers are close enough and their respective lattice distortions overlap. Another type of cooperative interaction occurs when the JT centers are viewed as sources of virtual phonons that are being exchanged through the medium offered by the lattice. The importance of the cooperative JT effect, for our purposes, is that it gives rise to inhomogeneity when it is counterbalanced by long range repelling forces. Next, we discuss how these elements are combined in such a way that they might generate the right conditions for the SC transition.

## 9 From Jahn–Teller Polarons to Mesoscopic Inhomogeneities

Now we focus on the charge phase separation as an important component for the salient physics of cuprates. The viewpoint presented here is that above a certain temperature  $T^*$  a gas of weakly interacting polarons exists, and below this temperature polarons have an energy that promotes them to form bound particles and charge agglomerations (Fig. 3). In this manner, the  $\Delta_p$  energy coincides with the emergence of inhomogeneities, and its scaling dependence is intimately related to



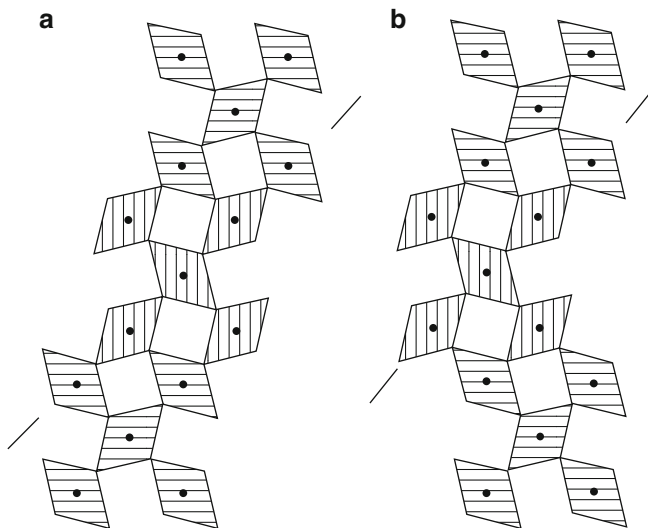


**Fig. 3** (a) Favorable and (b) unfavorable stripe arrangement of JT distorted regions, as a result of cooperative JT interactions. The illustration corresponds to patterns on a CuO sheet of a copper oxide. After Bersuker and Goodenough [94]

the scaling dependence of  $T^*$ . The proposal is that, upon doping, the charges self-organize due to forces exerted by lattice instabilities of the JT type. These lattice deformations offer two features that seem suitable for the stripes and HTS: they display anisotropic interactions, and they can create Cooper pairs of short range order,  $\xi$ .

Firstly, the JT polaron concept has been used explicitly in the pseudogap physics of the copper oxides since this scale of energy assumed a larger importance in the 90s. For example in [95] R. Markiewicz proposed a possible explanation of this crossover region present in the phase diagram of the cuprates (Fig. 2). He made the observation that the temperature and doping dependence of  $\Delta p$  could be directly related to an intermediate step, which involves coupled JT centers, during the structural phase transition from a high-temperature tetragonal (HTT) phase to the low-temperature orthorhombic (LTO) phase and a low-temperature tetragonal (LTT) phase. It would be a sort of dynamical JT coupling among different octahedra (see Fig. 1), mediated by planar oxygens. The intermediate stage (composed of tilted Octahedra between 0 and 45° with respect to the Cu-O bond) would be the result of the composition of the two phases HTT and LTO; the doping and temperature would play the role of tune parameters to reach this mixed phase. More important is that the transition is triggered by local dynamics which leads to modifications in the Cu-O bond length and, at the same time, induces e-ph couplings. What is essential to remark in this type of works is that the notion of the structural phase transition present in cuprates might elude an ordinary classification of structural transitions, and some valuable physics could be missed if one does not pay attention to the



short-range order as well. Thus, the predicted curves in his calculation as a function of these two tuned parameters are based on the identification of a scale dependence  $T_{LTO} = T^*/2$ , where  $T_{LTO}$  is the temperature identified as the crossover temperature to the LTO phase.

On another hand, not long after the discovery of the cuprates, the phenomenon of charge separation was predicted independently by J. Zaanen, V. Emery and L. Gorkov [96]. Later on, a discussion in terms of lattice deformations was presented by Alexandrov-Kabanov-Mott, Kusmartsev, Bishop-Shenoy-Lookman, and more recently further studies were published by Spivak-Kivelson-Emery, Miranda-Kabanov, Ortix-Di Castro-Lorenzana, Castro-Morais, and Boris-Egami. In these works, minimal conditions for the phase separation were set. Some of them also address the role of phonon interaction as a mechanism that can trigger the phase separation. One way of clarifying this issue is being aware of what type of phonon mechanism one has in mind when the term *phonon interaction* is invoked, and what limit of coupling strength is referred to. Although an e-ph interaction could be one of the main factors that drive the charge separation, it is necessary to make some distinctions. For instance, in some regions of e-ph coupling Frohlich polarons (in the adiabatic and antiadiabatic regimes) show a homogeneous phase. Similarly, a Holstein model results in a liquid state of bipolarons.

We should also mention that, due to the character of the JT effect, one might intuitively anticipate that lattice instabilities might form domains with a local symmetry breaking obeying the JT restrictions. But any attempt to formulate a microscopic origin of JT pairing should be able to reconcile different aspects, like the existence of JT domains with mesoscopic scale, predict specific charge transport properties in the normal state, and explain the SC itself. The possibility of an attractive potential created by the anharmonic tunneling of JT distortions was already suggested in 1987 by Johnson [97, 98], and multi-JT interacting centers as a mechanism of JT nanostructuring in 1997 by Moskvina [99]. A proposal which includes some of these elements is the one introduced by Bersuker and Goodenough [94]. Another work that includes the JT effect and stripes is found in the work of R. Markiewicz, where he supports his analysis on the Van Hove singularity [100].

In the early 90s, Shou and Goodenough explained their thermo power measurements, made in a wide range of doping and temperature, through polaron interactions. The system under scrutiny was the single layer  $\text{La}_{2-x}\text{Sr}_x\text{CuO}_4$ , which facilitates the interpretation of the type of experiments they performed, because the material is single-layered [101]. The experiments provided data that approximated the size of deformed region around the Cu ion. These clues lead Bersuker and Goodenough [94] to establish a more elaborate model, which utilizes the JT effect as a primordial mechanism to predict the heterogeneity, make an estimation of the polaron mobility, predict the temperature dependence of the resistivity and give some insights for achieving high  $T_c$ . They proposed to deal with the polaron domains within the JT scheme as a  $(A_{I_g} + B_{I_g}) \otimes (a'_{I_g} + a_{I_g} + b_{I_g})$  problem. Thus, the interaction matrix for a JT center located at site  $i$  is,

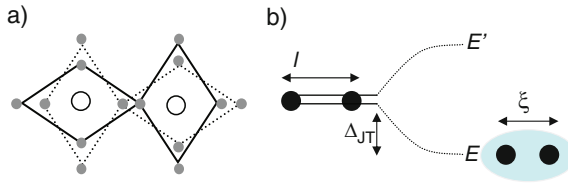


**Fig. 4** Schematic representation of: a) an inter-site JT-bipolaron and its two equivalent configurations (white and grey circles represent copper and oxygen sites respectively); b) two electrons (in a doubly degenerated energy level and separated one from each other by  $l$ ) lowering their energy by a magnitude of  $\Delta_{JT}$  (related to  $\Delta_p$ ), when they interact through a lattice instability of JT-type. Here  $\xi$  represent the coherence length of a pair, while  $E$  and  $E'$  are two lifted energies.

$$H_v(i) = \begin{pmatrix} V_A Q_A(i) + \Delta/2 & V_B Q_B(i) \\ V_B Q_B(i) & V_A Q_A(i) - \Delta/2 \end{pmatrix}. \quad (9)$$

The vibronic constants  $V_A$  and  $V_B$  represent the coupling between  $A_{1g}$  ( $B_{1g}$ ) with the displacements  $a_{1g}$  ( $b_{1g}$ ), respectively, and  $\Delta$  is the energy splitting between electronic levels, while  $Q_{\Gamma=A,B}$  stands for the symmetric nuclear displacements. For  $i = 1, 2, \dots, n$  JT centers surrounding a polaron, the Hamiltonian is,

$$H_{JTP} = \frac{1}{2} \sum_{i, \Gamma=A,B} P_{\Gamma}^2(i) + \frac{1}{2} \sum_{i,j} \omega_{i,j}^2(\Gamma) Q_{\Gamma}(i) Q_{\Gamma}(j) + \sum_i H_v(i); \quad (10)$$

$\Gamma = A, B$

where  $P_{\Gamma}$  is the momentum conjugated to  $Q_{\Gamma}$ ,  $(\omega_{i,j})^{-2}$  is an inverse elastic constant for  $b_{1g}$  vibrations, which has the function of coupling two JT centers. Each site  $i$  can have two equivalent distortions, whose magnitude is given by

$$Q_0 = \pm \left[ V_B^2 (\omega_{11}^{-2}(B, B))^2 - \left( \frac{\Delta}{2V_B} \right)^2 \right]^{1/2}. \quad (11)$$

Within this scheme, the energy of pairing is the difference between the energy of two interacting multimode JT polarons and the energy of a single JT polaron. The symmetry of the JT interaction is crucial for pairing; the relative position of the two holes gives rise to a pairwise potential which can be either attractive (pairing) or repulsive. The vibrational mode  $b_{1g}$  is responsible for this type of dependence; thus, while two  $b_{1g}$  distortions in the opposite direction lead to pairing, two parallel distortions lead to antipairing. If several JT centers are allowed to interact, the model leads to cluster formation, with six polaron centers arranged in an antiferrodistortive fashion. More interesting is the fact that the clusters acquire a stripe shape. The model also predicts the most stable stripe configuration on the CuO sheet (Fig. 3). The authors concluded their work with an analysis of the motion of polarons occupying

the edge of the formed cluster. The type of movement that the polaron develops is a crawling movement with a mobility of  $1\text{--}10\text{ cm}^2\text{ Vs}^{-1}$ .

A step forward in the evaluation and the implications of the JT effect is found in a series of publications by Mihailovic, Kabanov and coworkers. The theory incorporates JT polaron interactions through the length of their lattice distortions. A JT Hamiltonian formulated either in real space [102] or equivalently in  $k$ -space [103] embodies these ideas. The model incorporates a  $k$  dispersion on the phonon's mode of coupling. This contrasts with models that set  $k = 0$  for the interaction; they foresee the SC emerging from a homogeneous state. The model's aim is to achieve an inhomogeneous state that leads to SC. Some similarities are found with the model proposed in [94], in the sense that both consider an anisotropic interaction of the strain type. In contrast, Mertelj et al. [104] incorporated explicitly the long range Coulomb interaction. The  $\text{La}_{2-x}\text{Sr}_x\text{CuO}$  in [102] and  $\text{YBa}_3\text{CuO}_8$  in [103] are the two chosen materials to exemplify the concepts. One of the most important results is that the most stable configurations are for clusters with even number of particles. Quite remarkably, in [104–106] it was proven that the combination of the anisotropic JT interaction and the three dimensional Coulomb interaction, whose repelling force is acting among charges confined to the CuO plane, are enough elements to give rise to stripe formation. The full Jahn–Teller–Coulomb Hamiltonian which incorporates this sort of competing forces is described by means of a lattice gas model. Miranda et al. extracted further conclusions, e.g. the DOS [107], charge transport properties [108] and strain effects. In the calculated DOS a suppression of energy states (gaps) was observed as the temperature was lowered. The opening of those gaps (up to three gaps) coincides with the emergence of stripes. The formation of each of the gaps corresponds to the breaking of the bonds created by cooperative JT distortions, which could be referred to as a JT-gap. Thus the lowest energy JT-gap corresponds to the breaking of a single bond; the second gap is due to two bonds and so on. However, the calculations never showed more than three gaps, even at high doping [107]. This observation was attributed to the fact that stripes have an average width of one or two sites at most; therefore charges are rarely surrounded by more than three nearest neighbors. Further calculations confirmed that multiple gaps are related to the energy formation of a JT bipolaron and JT domains.

## 10 Towards HTS

After the above considerations in the last sections, it is expected that they lead to the ultimate goal of this review: the explanation of the HTS in cuprates. For this purpose we end with an overview of the proposals of a few authors, whose opinion is that the origin HTS might be found in a proper combination of the elements we have brought into this chapter: strong  $e$ – $e$  correlations, a significant  $e$ –ph coupling of the JT type, and inhomogeneities.

Stimulated by the particular layered composition of the cuprates and the arrangement of dopants at random, J. Philips has established a three dimensional filamentary

theory of SC in copper oxides. The theory foresees the motion of the carriers through distinctive paths connected by topological constraints. By all means, the theory is a percolative picture of HTS. The segments of the filament trajectory are composed by (Metallic path 1)-(bridge)-(Metallic path 2), where the two metallic paths are not necessarily of the same origin. The metallic paths, for instance in YBaCuO, could be a Cu-O chain and a CuO plane, while in ceramics like LaCuO (no Cu-O chains) the two metallic regions would be only within the CuO planes. The model strongly relies on the existence of metallic strings in the CuO sheets. The key point is that JT distortions play the role of bridges, forcing the carriers to cross the two metallic regions by resonant tunneling and doing so as an impurity state. In addition, the concentration of bridges and the number of metallic paths modulate the location of  $T_c$  on the doping axis of the phase diagram. For the optimal  $T_c$ , it corresponds to a nearly perfect match between the number of metallic paths and JT joints, the underdoped corresponds to fewer JT bridges with respect to the paths, and the overdoped would correspond to an overpopulation of JT joints. Because the filament current is occurring at regions connected in series, Phillips estimated that  $T_c = \sqrt{T_B T_R} \approx 100$  K, for the case of a two-temperature component contribution: a CuO planar region, ( $T_B \approx 25$  K) and a Cu ion vibration near an oxygen impurity, ( $T_R \approx 350$  K). For details the original paper of 1987 should be consulted [109], and for a more extended version and update work, the recent publication ref. [110].

A hybrid theory that combines the local nature of the JT effect and the local character of the AF spin interactions, is the one proposed in 1989 by Kamimura and Suwo [111]. The theory considers the lower and upper levels energies given by the  $a_{1g}$  wave function and  $b_{1g}$  wave function of a hole moving in two alternate type of environments. One environment is created by a JT deformation of the CuO<sub>6</sub> Octahedral and the other is an antiparallel spin host with respect to the moving carrier. According to Kamimura and Suwo, the hole takes on a Zhang-Rice singlet character, and if it is in the  $b_{1g}$  state, it interacts through super exchange interactions with other nearest neighbors. When the hole is in the  $a_{1g}$  form, it is coupled locally by Hund's rule, and the local spins form a triplet state. In this view, the carriers preserve the AF order; at the same time a metallic property can be achieved. The important point in the model is how the JT distortion is affected by doping. Introducing holes by substitution of Sr in LSCO has the result that the apical oxygens in the CuO<sub>6</sub> cluster reduce their distances. This effect is called anti-JT effect, and it has consequences for the energy splitting between the  $a_{1g}$  and  $b_{1g}$  levels. The interplay of the Sr concentration and energy splitting controls the correlation length where holes can move at the Fermi level. According to an effective one-electron band calculation, the hole in this coherent state couples to Hund's state in relation to the Z-R singlet with a magnitude of 1–5 eV. However, the model seems to be valid only at dilute concentrations. The way the e-ph interaction is spin dependent plus the momentum space correlation creates zones with either pair hole attraction or pair hole repulsion. The final shape of the pair potential is a  $d_{x^2-y^2}$  gap.

A similar strategy considered by Bussmann-Holder and H. Keller is to divide the CuO plane into two regions, one made up of JT distortions, and the second region of AF spins [74, 75]. The model includes explicitly the size domain of the

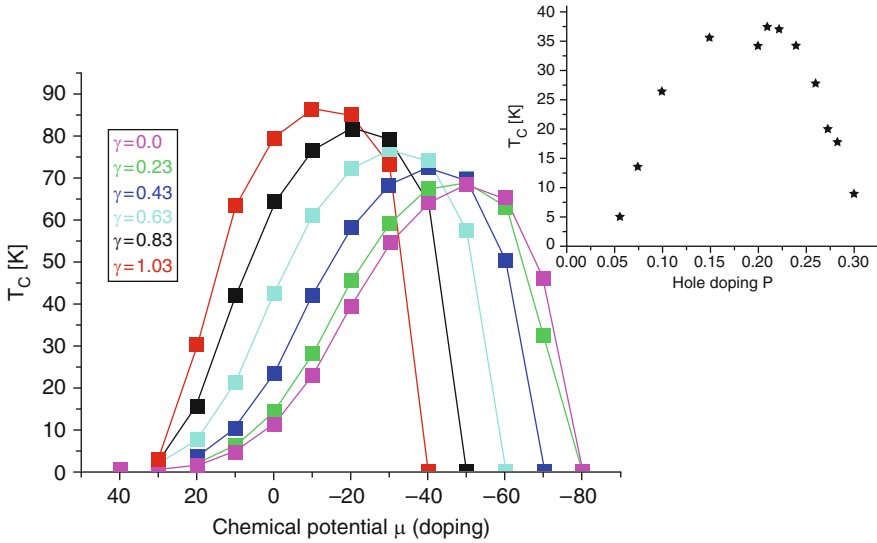


**Fig. 5**  $T_c$  predicted on the multicomponent SC model, and  $T_c$  measured on  $\text{La}_{2-x}\text{Sr}_x\text{CuO}_4$  (inset). After [87]

different phase separation regions. In addition, the lattice displacement lying on the border of both areas is responsible for the coupling of charges belonging to the two different regions. This leads to an interband interaction that appears together with a shift in the energy due to the polaron coupling of holes and JT vibrational modes. The result of such a type of electron interaction makes the model a multi band treatment that facilitates an enhancement of  $T_c$ . In fact, the results of the isotope and strain effects reviewed in Sect. 6 were deduced under these assumptions. A notable concept in the Hamiltonian introduced in ref. [87] is the inclusion of an intraband potential. It comprises on-site pairing and two extra terms with  $s$  and  $d$  wave pairing. Noteworthy is the similarity of the calculated  $T_c$  dependence with the  $T_c$  observed in experiments (Fig. 5).

In reference [112], it was [112] developed a theory that uses the inhomogeneities themselves as the primary elements for HTS. The lattice distortions, induced by the charges, create JT regions that help the carriers to move coherently. After crossing the paths, charges tunnel among other distorted regions in a Josephson-type of tunneling. In this sense the model is also a percolative description, with a threshold set at the doping where cuprates become SC (6% of doping). The distinctive feature of this percolative model is that JT bipolarons not only help to build the paths, but they are also one component for the carrier dynamics, while the second component is of Fermi character. The percolative theory explains why a maximum  $T_c$  is reached at the optimal doping, and then decays as more charges are introduced: it is the balance between pairs and stripes that give the optimal  $T_c$ . On the one hand stripes pave the metallic regions, on the other hand they also reduce the number of available pairs for SC because the carries have been used up. So, stripes enhance or hinder the SC transition.

A novel approach to quantum criticality in HTS in cuprates was proposed by A. Bianconi. His view differs from the QCP driven by quantum magnetic fluctuation whose features were briefly commented upon in Sect. 4. Following Bianconi, the variable that would control the proximity to a QCP would be the tensile microstrain,  $\varepsilon$ , and that together with the doping defines the QCP near  $T_c$  [113, 114]. Two nearly degenerate ground states fluctuate around this QCP: an inhomogeneous phase of JT polarons arranged in stripe-like structures, and free charge carriers. The tensile microstrain could originate in the mismatch between the  $\text{CuO}_2$  layer and the rock-salt layer in cuprate perovskites. This mismatch depends on the variation in the sum of the radius of the metal-ion in the rock-salt layer and the radius of  $\text{O}^{2-}$  in the  $\text{CuO}_2$  plane. This leads to variations of the  $\text{Cu-O}$  bond length and thus modifies transport and other properties from those of a system that does not exhibit a microstrain. The arguments were supported by some of the results we already reviewed in the context of EXAFS in Sect. 6. The lattice mismatch provokes that the  $\text{CuO}_4$  plaques rotate, tilt and dimple, changing the  $\text{CuO}$  bond distance. Using this distance, the value of  $\varepsilon$  can be estimated by the relation  $\varepsilon = 197 < \text{Cu-O} > / 197$  and related to  $T_c$ . The critical bond length ( $\text{Cu-O} = 1.89 \pm 0.5$ ) gives a critical value of  $\varepsilon_c = 4 \pm 0.3\%$ , while the critical value of doping, the second control parameter, is 16% of the hole concentration. A very suggestive plot of  $T_c$  against the two control parameters reaches its maximum  $T \approx 140$  K (Fig. 6). Bianconi concludes that “e-ph coupling is controlled by the chemical pressure, is the variable that drives

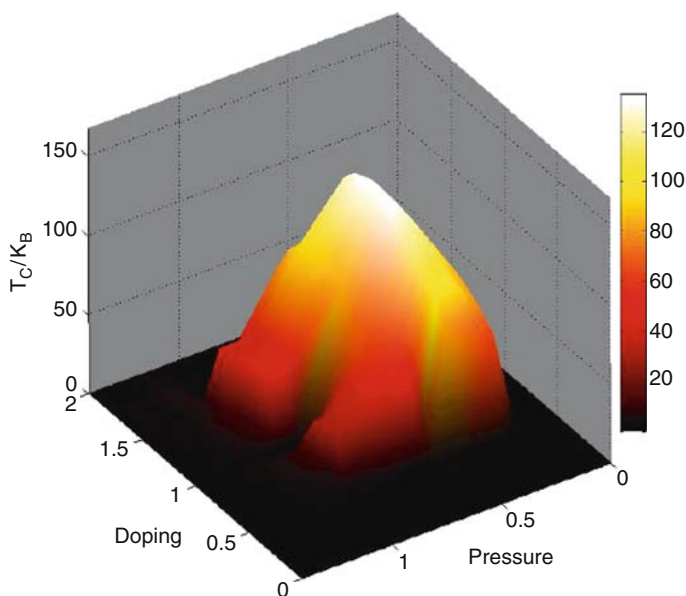


**Fig. 6** The competition between pseudo JT polarons (structured in stripes) and free quasi-particles gives rise to the QCP at  $T_c$ , which is found at the normalized critical doping  $= \delta/\delta_c = 1$  and normalized critical pressure  $= \varepsilon/\varepsilon_c = 1$ . Here  $\delta_c = 0.25$  belongs to the doping for stripe formation, and  $\varepsilon_c = 0.4$  is the optimal microstrain at a maximum  $T_c$  inferred from EXAFS data. After [113]

the system to localization, and there is a QCP where an electronic solid with long range order competes with the SC order”. By an exact diagonalization of the Hamiltonian designed for bipolaron formation, Miranda et al. [115] proved that, indeed, parameters relevant to  $T_c$  are modified under strain. Thus, it was proved that the polaron tunneling is importantly modified by the uniaxial strain. Secondly, there is a maximum of isotopic shift, i.e. substitution of  $O^{16}$  by  $O^{18}$ , for intermediate val-

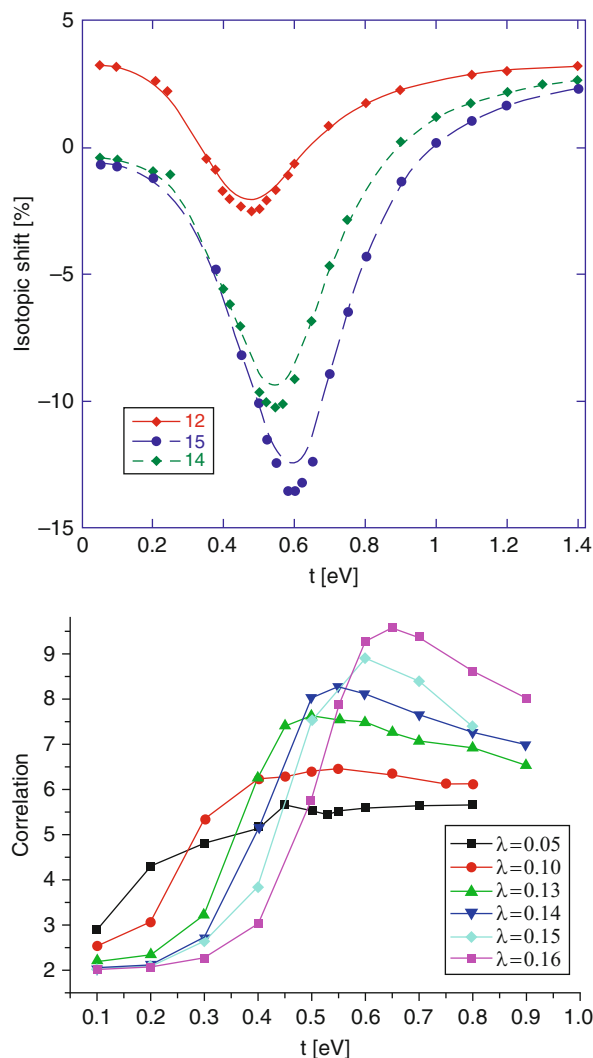


**Fig. 7** According to bi-polaron model of [115], the isotopic shift shows the largest signal only for intermediate values of hopping,  $t$ , which were carefully chosen to mimic the microstrain. It is for e-ph couplings,  $\lambda$ , above  $\lambda = 12$  where the isotopic shift takes negative values, and this is possibly connected to the relevant properties of HTS (Upper panel). Conversely, the isotopic change of the polaron correlation shows a maximum for a given value of  $\lambda$  (Lower panel), [116]

ues of hopping (Fig. 7). In addition, it was shown that the polaronic correlation is strongest at similar values of hopping, where the isotopic shift is at a maximum [116]. The results take on more relevance due to the fact that this polaron Hamiltonian was successfully used to model local distortion in the EXAFS experiments performed by Mustre et al. (Sect. 6). Moreover, they might be closely related to the type of isotopic effects mentioned in the same section and in ref [69, 70]. However, further studies should be done, either with this type of approach or in a similar direction, in order to provide supplementary information about the properties that link free carriers, localized JT polarons, and the SC transition.

## 11 Conclusions

The problem of HTS in cuprates has been resolved by no means, and there is no universal theory accepted by the scientific community. At the beginning of the chapter we depicted this situation with the controversial analyses of experiments and the highly debated results of calculations. Models based on the JT effect, when combined with the notion of inhomogeneity, have proved that a high  $T_c$  is attainable. Hopefully, after being exposed to this scenario, the reader has been convinced that such models are no less legitimate than other mainstream models. It seems that the problem of SC in cuprates is an issue of energy scale. All the models we presented, though eloquently formulated, rely on some assumptions that can be validated only by experiments. In this regard, we showed that there is compelling evidence that lattice effects cannot be ignored, therefore challenging the idea proposed soon after their discovery of ceramic oxides that phonons are not relevant. Although our explanation of the experiments is unavoidably biased, what remains are the facts of the plain data, and the clear signature of the scale energy should be free of interpretations. However, the experiments are faced with their own problems, because the possible driving forces are close in temperature and energy ranges; this makes it difficult to distinguish which dominate and which are accidentally present. Perhaps after 23 years of polarized debate, started by the old theories and increased by the latest, we are still missing an ingredient that will allow us to put all the pieces together and renovate the perspectives of HTS in cuprates.

## References

1. K.A. Muller, in *Structural Phase Transition and Soft Modes*, ed. by E.J. Samuelsen, E. Anderson, J. Feder (Universitetsforlag, Oslo, 1971) p. 85
2. J.G. Bednorz, K.A. Muller, *J. Phys. Condens. Matter* **64**, 189 (1986)
3. K.M. Wu et al., *Phys. Rev. Lett.* **58**, 908 (1987)
4. P. Dai, B.C. Chakoumakos, G.F. Sun, K.W. Wong, Y. Xin, D.F. Lu, *Physica C:Superconductivity* **243**(3–4), 201–206 (1995)
5. A.A. Abrikosov, I.M. Khalatnikov, *Rep. Prog. Phys.* **22**, 329–367 (1959)



6. F. Steglich, J. Aarts, C.D. Bredl, W. Leike, D.E.M.W. Franz, H. Schafer Phys. Rev. Lett. **43**, 1892 (1976)
7. J. Bardeen, L.N. Cooper, J.R. Schrieffer, Phys. Rev. **106**, 162 **108**, 1175 (1957)
8. N.F. Mott, R. Peierls, Proc. Phys. Soc. Lond. **49**, 72 (1937)
9. N.F. Mott, Proc. Phys. Soc. Lond. Series A **62**, 416 (1949)
10. P.W. Anderson, *The theory of superconductivity in the High  $T_c$  Cuprates* (Princeton University Press, Princeton NJ, 1997)
11. C.T. Chen et al., Phys. Rev. Lett. **66**, 104, (1991)
12. J. Zaanen, G.A. Sawatzky, J.W. Allen, Phys. Rev. Lett. **55**, 418, (1985)
13. V.J. Emery, Phys. Rev. Lett. **58**, 2794 (1987)
14. V.J. Emery G. Reiter, Phys. Rev. B **38**, 4632 (1988)
15. C.M. Varma, S. Schmitt-Rink, Solid state Com. **62**, 681 (1987)
16. F. Mattheiss, Phys. Rev. Lett. **58**, 1028, (1987)
17. P.W. Anderson, Phys. Rev. **79**, 350–356 (1950)
18. P.W. Anderson, G. Baskaran, Z. Zou, T. Hsu, Phys. Rev. Lett. **58**, 2790 (1987) For recent review see Paramekanti 2001, 2003
19. C. Gross, R. Joynt, T.M. Rice, Phys. Rev. B. **68**, See also E. Dagotto, *Int. J. Mod. Phys.* **5** **77** (191)(1987)
20. A. Moreo et al., Phys. Rev. B. **41**, 2313 (1990)
21. N.F. Berk, J.R. Schrieffer, Phys. Rev. Lett. **17**, 433 (1966)
22. G. Kotliar, P.A. Lee, N. Read, Physica C: Superconductivity. 153–155, 1538 (1988)
23. F. Marsiglio, J. E. Hirsch Phys. Rev. B **41**, 6435–6456 (1990)
24. J.E. Hirsch Phys. Rev. Lett. **87**, 206402 (2001)
25. D.N. Basov et al., Science. **283**, 49 (1999)
26. S. Sachdev, *Quantum Phase Transitions*. (Cambridge University Press, New York, 1999)
27. P. Coleman, A.J. Schofield, A.M. Tsvelik, Phys. Rev. Lett. **76**, 1324–1327 (1996)
28. P. Krotkov, A.V. Chubukov, Phys. Rev. B **74**, 014509 (2006)
29. A.J. Millis, H. Monien, D. Pines, Phys. Rev. B. **42**, 167 (1990)
30. D. Pines. Physica B **163**, 78 (1990)
31. F.C. Zhang, T.M. Rice, Phys. Rev. B. **37**, 3759 (1988)
32. L.H. Tjeng, et al., Phys. Rev. Lett. **78**, 1126 (1997)
33. S. Miyaki, K. Makoshi, H. Koizumi, J. Phys. Soc. Jpn. **77**, 034702 (2008)
34. D.A. Wollman, D.J. Van Harlingen, J. Giapintzakis, D.M. Ginsberg, Phys. Rev. Lett. **74**, 797 (1995)
35. C.C. Tsuei, et al., Phys. Rev. Lett. **73**, 593 (1994)
36. G. Kotliar, J. Liu, Phys. Rev. B. **38**, 5142 (1988)
37. C. Gros Phys. Rev. B **38**, 931 (1988)
38. J.P. Hague, Phys. Rev. B. **73**, 060503 (R) (2006)
39. M. Grilli, C. Castellani Phys. Rev. B **50**, 16880 (1994)
40. Z.X. Shen et al., Phys. Rev. Lett. **70**, 1553 (1993)
41. Z.H. Damascelli, Z.X. Shen, Rev. Modern Phys. **75**, 473, (2003)
42. H. Matsui, T. Sato et al., Phys. Rev. B. **67**, 060501 (2003); Physica C: Superconductivity **460–462**, 862 (2007)
43. A. Lanzara et al., Nature **412**, 510 (2001)
44. V. Hinkov et al., Science **319**, 597 (2008)
45. H. Yamase, W. Metzner, Phys. Rev. B. **73**, 214517 (2006)
46. D. Mihailovic, C.M. Foster, K. Voss, A.J. Heeger, Phys. Rev. B. **42**, 7989 (1990)
47. J.P. Falck, A. Levy, M.A. Kastner, R.J. Birgenau, Phys. Rev. Lett. **69**, 1109 (1992); Phys. Rev. B **48**, 4043 (1993)
48. D. Emin, Phys. Rev. B. **45**, 5525 (1992)
49. S.J. Bilinge, T. Egami, Rev. B. **47**, 14386 (1993)
50. J. Mustre de León, I. Batistic, A.R. Bishop, S.D. Conradson, S.A. Trugman, Phys. Rev. Lett. **68**, 3236 (1992)
51. M. Salkola, A.R. Bishop, J. Mustre de Leon, S.A. Trugman. Phys. Rev. B **49** 3671 (1994)
52. A. Bianconi et al., Phys. Rev. Lett. **76**, 3412 (1996)

53. E.S. Bozin et al., Phys. Rev. Lett. **84**, 5856 (2000)
54. J. Mustre de Leon, M. Acosta-Alejandro, S.D. Conradson, A. Bishop, J. Supercond. Nov. Magn. **15**(5) (2002)
55. C. Gianneti, G. Coslovich et al. Phys. Rev. B. **79**, 224502 (2009)
56. G. Coslovich, C. Gianneti, et al. Lectures on the physics of strongly correlated systems XIII, edited by A. Avella and F. Mancini. (2009)
57. V.V. Kabanov, J. Demsar, D. Mihailovic Phys. Rev. Lett. **95**, 147002 (2005)
58. P. Kusar, V.V. Kabanov, J. Demsar, T. Mertelj, S. Sugai, D. Mihailovic Phys. Rev. Lett. **101** 227001 (2008)
59. D. Mihailovic, Phys. Rev. Lett. **94**, 207001 (2005)
60. D.J. Derro et al., Phys. Rev. Lett. **88**, 097002 (2002)
61. S.H. Pan et al., Nature **413** 282 (2001)
62. McElroy et al., Nature **422**, 592 (2003)
63. K. Gomes et al., Nature **477**, 569 (2007)
64. A. Pasupathy et al., Science **320**, 196 (2008)
65. C. Howald et al., Phys. Rev. B. **67**, 014533 (2003)
66. B. Batlogg, et al., Phys. Rev. Lett. **58**, 2333 (1987)
67. J. Mustre de Leon, R. de Coss, A.R. Bishop, S.A. Trugman, Phys. Rev. B. **49**, 3671 (1994)
68. K.A. Müller, Z. Phys. B. **80**, 193 (1990)
69. R. Temprano et al., Phys. Rev. Lett. **84**, 1999 (2000) see also Phys. Rev. B **66**, 184506 (2002)
70. A. Lanzara et al., Cond. Matt **11**, L254 (1999)
71. G.H. Gweon et al., Nature **430**, 187 (2004)
72. V.Z. Kresin, S.A. Wolf, Phys. Rev. B **49**, 3652 (1994)
73. R. Khasanov, et al., Phys. Rev. B. **77**, 104530 (2007); Phys. Rev. Lett. **98**, 057007 (2007); Phys. Rev. Lett. **99**, 237601 (2007); Phys. Rev. Lett. (2007) **98**, 057007
74. A. Bussmann-Holder, H. Keller, Eur. Phys. J. B. **44**, 487 (2005)
75. A. Bussmann-Holder, et al., Europhys. Lett. **72**, 423 (2005)
76. H. Oyanagi, A. Tsukada, M. Naito, N.L. Saini, Phys. Rev. B. **77**, 024511 (2007)
77. M. Abrecht, et al., Phys. Rev. Lett. **84**, 057002 (2003)
78. A.S. Alexandrov, N. Mott, Polarons, Bipolarons, Edit. World Scientific (1995)
79. A. Alexandrov, J. Ranninger, Phys. Rev. B. **24**, 1164 (1981)
80. A.S. Alexandrov, N.F. Mott, Phys. Rev. Lett. **71**, 1075 (1993)
81. A.S. Alexandrov. Phys. Rev. B **77**, 094502 (2008); Phys. Rev. B **61**, 12315 (2000)
82. A.S. Alexandrov, V.V. Kabanov, N.F. Mott, Phys. Rev. Lett. **77**, 4796 (1996)
83. Y. Takada, Phys. Rev. B. **26**, 1223 (1982)
84. A.S. Alexandrov, Polarons in advanced materials. *Springer Series in materials science 103*, edit. Springer (2007)
85. J.P. Hague, P.E. Kornilovitch, J.H. Samson, A.S. Alexandrov, Phys. Rev. Lett. **98**, 037002 (2007)
86. I.B. Bersuker, *The Jahn-Teller Effect Edit.* (Cambridge University Press, Cambridge, 2006)
87. E. Warren, Picket Rev. Mod. Phys. **61**, 433 (1989)
88. T.A. Tyson, M. Leon, et al., Phys. Rev. B. **53**, 13982 (1996)
89. P.E. Kornilovitch, Phys. Rev. Lett. **84**, 1551 (2000)
90. Y. Takada, Phys. Rev. B. **61**, 8631 (2000)
91. H. Barenzten, Eur. Phys. J. **24**, 197 (2001)
92. S. El Shawish, J. Bonča, K.u. Li-Chung, S.A. Trugman, Phys. Rev. B. **67**, 014301 (2003)
93. M.D. Kaplan, B.G. Vekheter, *Modern inorganic chemistry*. Series editor P. Fackler, Jr. (Plenum Press, New York, 1995)
94. J.B. Goodenough, J.S. Zhou, J. Chart, Phys. Rev. B. 475275 (1993)
95. R.S. Markiewicz, Physica C. **255**, 211 (1995)
96. J. Miranda, V. Kabanov, J. Supercond. Nov. Magn. **22**, 287 (2009) and references therein. Also in "charge inhomogeneities in strongly correlated systems" by A. Castro and C. Morais in the book "Strong interaction in low dimensions systems", edit. Springer (2004)
97. K.H. Johnson et al., Physica C. **153**, 1165 (1988)
98. K.H. Jonhson, D.P. Clougherty, M.E. McHenry, Mod. Phys. Lett. **B3** 867 (1989)

99. A.S. Moskvina, A.S. Ovchinnikov, O.S. Kovalev, Phys. Solid State. **39**(11) 1742 (1997)
100. R. Markiewicz, C. Kusko, V. Kidambi, Phys. Rev. B. **60**, 627 (1999)
101. G. Bersuker, J.B. Goodenough, Physica C. **274**, 267 (1997)
102. D. Mihailovic, V.V. Kabanov, Phys. Rev. B. **63**, 054505 (2001)
103. V.V. Kabanov, D. Mihailovic, Phys. Rev. B. **65**, 212508 (2002)
104. T. Mertelj, V.V. Kabanov, D. Mihailovic, Phys. Rev. Lett. **94**, 147003 (2005)
105. R.J. McQueeney, Y. Petrov, T. Egami, M. Yethiraj, G. Shirane, Y. Endoh, Phys. Rev. Lett. **82**, 628 (1999)
106. H.A. Mook, F. Dogan, Nat. Lond. **401**, 145 (1999)
107. T. Mertelj, V.V. Kabanov, J. Miranda Mena, D. Mihailovic, Phys. Rev. B. **76**, 054523 (2007)
108. J. Miranda, T. Mertelj, V.V. Kabanov, D. Mihailovic, J. Supercond. Nov. Magn. **20**, 587 (2007)
109. J. Miranda, T. Mertelj, V.V. Kabanov, D. Mihailovic, J. Supercond. Nov. Magn. **22**, 281 (2009)
110. J.C. Phillips, Phys. Rev. B. **75**, 214503 (2007)
111. J.C. Phillips, Phys. Rev. Lett. **19**, 856 (1987)
112. D. Mihailovic, V.V. Kabanov, K.A. Muller, Europhys. Lett. **57**(2), 254–259 (2002)
113. A. Bianconi, N.L. Saini, S. Agrestini, D. Di Castro, G. Bianconi, Int. J. Mod. Phys. **14**, 3342 (2000)
114. A. Bianconi, S. Agrestini, G. Bianconi, D. Di Castro, N.L. Saini 2001. J. Alloys Compounds **317–318**, 537 (2000)
115. J. Miranda, M.de Leon, A.R. Bishop, Supercond. Nov. Magn. **20**, 603 (2007)
116. M.de Leon, J. Miranda, A.R. Bishop, J. Phys. Conf. Series. **108**, 012020 (2008)

# Polarons and Bipolarons in Jahn–Teller Crystals

Chishin Hori and Yasutami Takada

**Abstract** A review is made on the developments in the last two decades in the field of the Jahn–Teller effect on itinerant electrons in Jahn–Teller crystals. Special attention is paid to the current status of the researches on the fullerene superconductors and the manganite perovskites exhibiting the colossal magnetoresistance. Present knowledge about the polarons and bipolarons in the typical Jahn–Teller model systems is also summarized, together with some original results of our own.

## 1 Introduction

Physics and chemistry of the Jahn–Teller (JT) effect started from the theory in 1930s [1], investigating structural instabilities of high-symmetry configurations in molecules. The theory has been developed further and sophisticated in the next several decades to provide a very general quantum-mechanical framework for treating a particular type of electron–vibrational (or electron–phonon) coupling in molecules or solids in which two or more orbitally degenerate (or pseudodegenerate) electronic states are mixed nonadiabatically through ionic (or lattice) vibrational modes.

Due to its intrinsic complexity arising from the orbital multiplicity, the researches in this field have been almost exclusively concerned with the JT effect in rather simple systems like molecules, small clusters, and a single JT impurity center in solids in which itinerant electrons do not play an important role [2,3]. Even if the JT crystals, in which an infinite number of such JT centers occupy regular positions in a lattice, are considered in the context of the cooperative JT effect, relevant electrons in the system have usually been assumed to be localized [4].

A surge of a new sort of interest in the JT effect occurred in the late 1980s when high-temperature superconductivity (HTSC) was discovered in the copper oxides [5]. Because these compounds may be regarded as a class of the JT crystals, people began to pay much attention to *the JT effect on itinerant electrons*. In 1990s the interest in the JT effect in metals was intensified by both the discovery of superconductivity in the alkali-metal-doped fullerenes of the type  $A_3C_{60}$  with  $A = K, Rb, Cs$  (or their combinations) [6] and the subsequent one of the colossal magnetoresistance (CMR) in the manganite perovskites [7,8].

As for the current status of the researches on these materials, a rather comprehensive review was given by Bersuker in Sect. 8.4 of [3] from the standpoint of elucidating the roles of the JT effect. Therefore it would not be necessary to reiterate a similar kind of review here, particularly for the issue of HTSC for which Bersuker made a very detailed account, but it might be appropriate for us to make some supplementary comments or remarks on the issues of the CMR and the fullerene superconductors from our perspective that is reflecting the experience of one of the authors (Y.T.) who was engaged in the studies on those issues in 1990s.

The CMR is a technical term to indicate the phenomenon of a strong variation of the electric resistance with the change of applied magnetic fields, as observed, for example, in  $\text{La}_{1-x}\text{Ca}_x\text{MnO}_3$  with  $x$  in the range between 0.2 and 0.4. The conduction electrons in these compounds are composed of the Mn  $e_g$  orbitals with the density of  $1 - x$  electrons per Mn ion, implying that the system can be regarded as a JT crystal of the canonical  $E \otimes e$  type. It is widely believed that the double-exchange (DE) mechanism associated with the Hund's-rule coupling between the Mn  $t_{2g}$  localized core spins and the mobile  $e_g$  electrons [9–11] plays a crucial role in making a qualitatively correct explanation of the CMR, but an important claim was made that the JT coupling was also needed for its quantitatively accurate description [12]. This claim has been confirmed by both experiment using the state-of-the-art photospectroscopy [13] and theory based on the first-principles calculation of the electronic band structure and the electron–phonon coupling constant [14, 15]. Thus the CMR can be regarded as the outcome of the interplay among spin, charge, orbital, and phonon degrees of freedom, as emphasized in several review articles on the manganites [16–22].

This complicated interplay has made the physics of manganites very rich and we can enumerate several fascinating proposals of new physics in relation to these compounds, including (1) *the cooperative JT effect mediated by electron hopping* rather than by phonons (or lattice distortions) [14], (2) *the phase-separation scenario* for the CMR in the manganites, in which the Coulomb correlation is considered to be a more important competitor with the DE mechanism than the electron–phonon coupling [17], (3) *the concept of the complex-orbital ordering*, in which linear superposition of basic orbitals,  $d_{x^2-y^2}$  and  $d_{3z^2-r^2}$ , with complex coefficients is suggested [23], (4) *the topological-phase scenario* for the formation of the stripe and the charge-ordered states, in which the key notion is the winding number (the Chern integers) associated with the Berry-phase connection of an  $e_g$  electron parallel transported through the JT centers along zigzag one-dimensional paths in an antiferromagnetic environment of the  $t_{2g}$  core spins [24, 25], and (5) *the concept of the geometric energy* which is defined as the difference in energy caused by the change in the winding number [26]. This is a concept proposed in analogy to the exchange energy (or the spin singlet-triplet energy splitting) in the case of spin degrees of freedom.

This complication in the manganites, however, has also a negative side, because it obscures the actual role of the JT effect on the CMR. In fact, what is actually confirmed so far is that the conduction electron should not be treated as a bare band electron but a rather small polaron in order to obtain the CMR in the experimentally

observed magnitude, if we try to explain the CMR in terms of a one-conduction-electron picture. This polaron motion can be realized not only through the  $E \otimes e$  coupling (or the *off-diagonal vibrational coupling* in degenerate electronic-state representation) but also through the conventional Holstein model [27] in which a nondegenerate electronic orbital ( $A$ ) is coupled to a nondegenerate non-JT phonon ( $a$ ), leading to the “ $A \otimes a$ ” problem with the *diagonal vibrational coupling*. In this respect, we do not know to what extent the JT effect is an indispensable factor in bringing about the CMR. In order to give a definite answer to this question, we need to know, first of all, more detailed information about the similarities and the differences in the polaronic nature between the  $E \otimes e$  JT and the  $A \otimes a$  Holstein models. Section 3 of this article addresses this issue by comparing the results of the one-electron problem in various theoretical models, each of which is described by the Hamiltonian introduced in Sect. 2.

The fulleride is an insulating molecular crystal in which narrow threefold conduction bands (with the bandwidth  $W$  of the order of 0.5 eV) are derived from the triply-degenerate  $t_{1u}$  LUMO orbitals of a  $C_{60}$  molecule. With the doping of three alkali atoms per one  $C_{60}$ , we obtain the metallic compound  $A_3C_{60}$  in which the conduction bands are half-filled. This compound exhibits superconductivity with the transition temperature  $T_c$  over 30K and the short coherence length  $\xi_0$  of only a few times the  $C_{60}$ - $C_{60}$  separation. The conduction electron interacts with various intramolecular phonons (two nondegenerate  $a_g$  modes and eight fivefold degenerate  $h_g$  multiplets), but the high-energy ( $\omega_0 \approx 0.2$  eV) tangential  $h_g$  modes couple most strongly to the electron, as suggested by the first-principles calculations [28–31], implying that  $A_3C_{60}$  can be modeled as a JT crystal of the  $T_{1u} \otimes h_g$  type.

As discussed in many review articles [32–39], superconductivity in  $A_3C_{60}$  is generally understood in terms of a simple BCS picture of the  $s$ -wave pairing driven by these high-energy  $h_g$  intramolecular JT phonons. This understanding is based on, among others, the observation of the isotope effect on  $T_c$  by the substitution of  $^{13}C$  for  $^{12}C$  [40–43] and also on the reproduction of the observed  $T_c$  by using the McMillan’s formula [44, 45]

$$T_c = \frac{\omega_0}{1.2} \exp \left[ -\frac{1.04(1 + \lambda)}{\lambda - \mu^*(1 + 0.62\lambda)} \right], \quad (1)$$

in which the nondimensional electron–phonon coupling constant  $\lambda$  is evaluated to be in the range 0.5 – 1 [28–30] and the Coulomb pseudopotential  $\mu^*$  is taken as about 0.2. In particular, the characteristic dependence of  $T_c$  on the lattice constant of the crystal  $a_0$  is well reproduced in this BCS scenario [46].

A closer look at this system, however, reveals that the present situation is not so clear and simple. In fact, it is far from being settled for the reasons given in the following: (1) The McMillan’s formula is derived based on the Migdal–Eliashberg (ME) theory for superconductivity [47] which is valid only when the parameter  $\omega_0/E_F$  (with  $E_F$  the Fermi energy) is small enough to neglect the vertex corrections [48]. In  $A_3C_{60}$ , however, this parameter is not small, owing to the fact that  $E_F (\approx W/2)$  is about the same as  $\omega_0$ . Thus we need to consider the contribution

from the vertex corrections [49]. (2) In the case of  $E_F \approx \omega_0$ , the concept of  $\mu^*$  is not applicable, either [50], requiring that the electron–electron and electron–phonon interactions should be treated on an equal footing. Actually, the Coulomb repulsion between electrons  $U$  (or the Coulomb correlation) is strong in the  $C_{60}$  molecule, rendering the interplay of this repulsion including the Hund’s-rule coupling  $J$  with the phonon-mediated attraction  $-U_{ph}$  as a matter of intense research even in a single-site  $T_{1u} \otimes h_g$  JT system [51–55]. (3) As mentioned before, the isotope effect for the completely substituted  $A_3^{13}C_{60}$  can be explained quantitatively well with resort to the McMillan’s formula, but it is concluded [56] that the formula can never explain the intriguing experiment done by Chen and Lieber who observed the large difference in  $T_c$  between the atomically substituted  $Rb_3(^{13}C_x^{12}C_{1-x})_{60}$  and the molecularly substituted  $Rb_3(^{13}C_{60})_x(^{12}C_{60})_{1-x}$  [57, 58].

In order to overcome these difficulties, Han, Gunnarsson, and Crespi have calculated the on-site pairing susceptibility in the dynamical mean-field theory (DMFT) [59] and claimed that the JT phonons in both  $E \otimes e$  and  $T_{1u} \otimes h_g$  systems bring about a local (intramolecular) Cooper pair which does not suffer much from the effect of large  $U$ , in contrast to the non-JT phonons in the Holstein ( $A \otimes a$ ) model [60]. They have also claimed that with the change of the parameters such as  $U$ ,  $\lambda$ , and the conduction-electron density  $n$ , the obtained  $T_c$  behaves much differently from that predicted in the McMillan formula (or in the ME theory), leading to a qualitative explanation of the interesting  $T_c$  versus  $n$  dependence as observed in  $Na_2Cs_xC_{60}$  and  $K_{3-x}Ba_xC_{60}$  compounds [61]. These interesting results, however, are still open to debate, partly because the effect of the Hund’s-rule coupling  $J$  is not considered in their work, though it is evident that  $J$  works to destroy the intramolecular (or on-site) Cooper pair, and partly because there is a completely opposite claim that the ME theory is very robust in the JT systems [62, 63].

In relation to the Hund’s-rule coupling  $J$ , there is another controversial claim that the dynamical feature of the JT phonons is not crucial at all in such a strongly-correlated system as  $A_3C_{60}$ , especially in the situation near the Mott–Hubbard transition [64, 65] or the antiferromagnetic (AF) state [66]. According to their claim, the only role that the JT phonons can play is to make  $J$  effectively negative, leading to the multi-band Hubbard model with the on-site strong repulsion  $U$  and an additional inverted Hund’s-rule coupling, based on which superconductivity in the fullerenes is addressed [67, 68].

A further simplification of the system is pursued by arguing that even the band-multiplicity is not crucial, either, as long as the physical parameters are chosen appropriately. What really matters is only *the strong competition between the phonon-mediated attraction  $-U_{ph}$  and the local Coulomb repulsion  $U$* . Actually, by adopting the Hubbard–Holstein model (or the  $A \otimes a$  system with the on-site Coulomb repulsion  $U$ ) and exploiting the fact that the coherence length  $\xi_0$  is very short [70], the calculations of  $T_c$  have been done, with the electron–electron and electron–phonon interactions treated on an equal footing, to find that the experimental results, including (a) the relations between  $T_c$  and  $a_0$  in both fcc and simple cubic lattices [36, 69], (b) the experiment by Chen and Lieber on the anomalous isotope effect [57, 71], and (c) the relation between  $T_c$  and  $n$  [36, 61], are all successfully

reproduced in a coherent fashion. The point here is the consideration of the off-site pairing (leading to the extended  $s$ -wave nature) composed of not the bare electrons but the (phonon fully-dressed) polarons in order to avoid the strong on-site repulsion [72].

To summarize, much more works, with taking various aspects into account, are needed to obtain a full understanding of the mechanism of superconductivity in  $A_3C_{60}$ . Even in the  $E \otimes e$  and  $T_{1u} \otimes h_g$  model systems, setting aside the fullerenes, the JT effect on superconductivity, especially in the presence of the Coulomb effect including the Hund’s-rule coupling, is not known well. To some extent we shall address this issue in the model JT systems in Sect. 4 of this article.

Incidentally, in any kind of the strong-coupling electron–phonon systems, there is always a subtle argument on the competition between the two scenarios for the occurrence of superconductivity; one for the formation of a Cooper pair of two polarons and the other for bipolaron superconductivity [73–78]. In the former, the pair formation and superconductivity occur simultaneously, while in the latter, the bipolaron is formed first and then its Bose-Einstein condensation (BEC) brings about superconductivity. At the present stage of the theoretical investigations in this field, there is no precise knowledge about the conditions to make the one scenario dominate the other, but it is usually presumed that the second scenario will apply, if the electron–phonon coupling  $\lambda$  is large enough. Therefore we shall be mainly concerned with this situation and treat the bipolaron formation and its BEC in Sect. 4. In the rest of this article, we shall employ units in which  $k_B = \hbar = 1$ .

## 2 Preliminaries

### 2.1 Models for JT Crystals

Let us imagine a lattice composed of  $N$  JT centers at which electronic and phononic states are, respectively,  $N_e$ - and  $n_{ph}$ -fold degenerate. In general, we may decompose the Hamiltonian  $H$  for this system as

$$H = \sum_{\mathbf{j}} H_{\mathbf{j}} + H_t + H_{\text{elastic}} + H_V, \quad (2)$$

where  $H_{\mathbf{j}}$  is the part containing all the possible terms defined at site  $\mathbf{j}$ ,  $H_t$  describes the inter-site hoppings of electrons,  $H_{\text{elastic}}$  represents the elastic interactions between neighboring sites (or the inter-site phonon–phonon interactions), and  $H_V$  takes care of the inter-site Coulomb repulsions. In the fullerenes, we need not consider  $H_{\text{elastic}}$  from the outset and  $H_V$  will not be crucial. In the manganites, on the other hand,  $H_{\text{elastic}}$  may be important [14] and  $H_V$  may also be important in considering the nanoscale phase separation, but because we are not primarily concerned with either the cooperative JT effect mediated by phonons or the phase-separation scenario, we shall forget both  $H_{\text{elastic}}$  and  $H_V$  altogether in this article.



With the assumption that electrons hop only between nearest-neighbor sites, we may write  $H_t$  in second quantization as

$$H_t = - \sum_{\langle \mathbf{j}, \mathbf{j}' \rangle} \sum_{\gamma, \gamma'=1}^{N_e} \sum_{\sigma} t_{\mathbf{j}\mathbf{j}'}^{\gamma\gamma'} \left( c_{\mathbf{j}\gamma\sigma}^{\dagger} c_{\mathbf{j}'\gamma'\sigma} + c_{\mathbf{j}'\gamma'\sigma}^{\dagger} c_{\mathbf{j}\gamma\sigma} \right), \quad (3)$$

where  $t_{\mathbf{j}\mathbf{j}'}^{\gamma\gamma'}$  is the overlap integral between the electron orbital  $\gamma$  at site  $\mathbf{j}$  and the other  $\gamma'$  at site  $\mathbf{j}'$  and  $c_{\mathbf{j}\gamma\sigma}^{\dagger}$  ( $c_{\mathbf{j}\gamma\sigma}$ ) creates (annihilates) an electron at site  $\mathbf{j}$  with orbital  $\gamma$  ( $= 1, \dots, N_e$ ) and spin  $\sigma$  ( $= \uparrow, \downarrow$ ). The actual values for  $t_{\mathbf{j}\mathbf{j}'}^{\gamma\gamma'}$  can be determined in a concrete manner [25], once the crystal structure is specified, but if we are not concerned with some specific situation, we shall take

$$t_{\mathbf{j}\mathbf{j}'}^{\gamma\gamma'} = \begin{cases} t & \text{for a nearest-neighbor pair } \langle \mathbf{j}, \mathbf{j}' \rangle \text{ and } \gamma = \gamma', \\ 0 & \text{otherwise,} \end{cases} \quad (4)$$

which is the simplest choice for this hopping matrix.

The site term  $H_j$  consists of the chemical-potential term  $H_e^{(j)}$ , the electron–electron interaction term  $H_{ee}^{(j)}$ , the phononic term  $H_{ph}^{(j)}$ , and the electron–phonon coupling term  $H_{e-ph}^{(j)}$ . (The coupling with the  $t_{2g}$  core spins is needed in the manganites, but it is neglected here.) The first and second terms are written as

$$H_e^{(j)} = -\mu \sum_{\gamma\sigma} n_{j\gamma\sigma}, \quad (5)$$

$$\begin{aligned} H_{ee}^{(j)} = & U \sum_{\gamma} n_{j\gamma\uparrow} n_{j\gamma\downarrow} + \frac{1}{2} U' \sum_{\gamma \neq \gamma'} \sum_{\sigma\sigma'} n_{j\gamma\sigma} n_{j\gamma'\sigma'} \\ & + \frac{1}{2} J \sum_{\gamma \neq \gamma'} \sum_{\sigma\sigma'} c_{j\gamma\sigma}^{\dagger} c_{j\gamma'\sigma'}^{\dagger} c_{j\gamma\sigma'} c_{j\gamma'\sigma} + \frac{1}{2} J' \sum_{\gamma \neq \gamma'} \sum_{\sigma} c_{j\gamma\sigma}^{\dagger} c_{j\gamma-\sigma}^{\dagger} c_{j\gamma'-\sigma} c_{j\gamma'\sigma}, \end{aligned} \quad (6)$$

where  $\mu$  is the chemical potential and  $n_{j\gamma\sigma} (= c_{j\gamma\sigma}^{\dagger} c_{j\gamma\sigma})$  denotes the electron number operator. The on-site Coulomb interaction is prescribed by the parameters  $U$ ,  $U'$ ,  $J$ , and  $J'$ , which represent, respectively, the magnitudes of the intra-orbital repulsive, the inter-orbital repulsive, the orbital-exchange (or the Hund's-rule coupling), and the pair-exchange interactions. These parameters are related to each other through

$$U = U' + J + J' = U' + 2J. \quad (7)$$

In (7), rotational symmetry in the degenerate-orbital space leads to the first equality, while we can derive the second one (or  $J = J'$ ) by comparing the concrete analytical expressions for  $J$  and  $J'$  [20].

With use of the phonon energy  $\omega_0$ , the phononic term is given simply as

$$H_{\text{ph}}^{(\text{j})} = \omega_0 \sum_{\nu=1}^{n_{ph}} a_{\text{j}\nu}^{\dagger} a_{\text{j}\nu}, \quad (8)$$

with  $a_{\text{j}\nu}^{\dagger}$  ( $a_{\text{j}\nu}$ ) the local-phonon creation (annihilation) operator at site  $j$  with mode  $\nu (= 1, \dots, n_{ph})$ . Finally, the coupling term  $H_{\text{e-ph}}^{(\text{j})}$  is described as

$$H_{\text{e-ph}}^{(\text{j})} = g_{N_e \otimes n_{ph}} \sum_{\nu} \sum_{\gamma\gamma'} \sum_{\sigma} V_{\gamma\gamma'}^{(\nu)} c_{\text{j}\gamma\sigma}^{\dagger} c_{\text{j}\gamma'\sigma} (a_{\text{j}\nu} + a_{\text{j}\nu}^{\dagger}), \quad (9)$$

where  $g_{N_e \otimes n_{ph}}$  is the electron–phonon coupling constant characterizing the  $N_e \otimes n_{ph}$  JT center and  $V_{\gamma\gamma'}^{(\nu)}$  is its coupling matrix element. Its concrete form will depend on the type of the JT system. For example, in the  $E \otimes e$  system in which the electronic orbitals are  $d_{x^2-y^2}$  and  $d_{3z^2-r^2}$  for  $\gamma = 1 (= \epsilon)$  and  $2 (= \theta)$ , respectively, the results for  $V^{(\nu)} \equiv (V_{\gamma\gamma'}^{(\nu)})$  with  $\nu = 1 (= \epsilon)$  and  $2 (= \theta)$  are written as

$$V^{(1)} = \begin{pmatrix} 0 & 1 \\ 1 & 0 \end{pmatrix} \text{ and } V^{(2)} = \begin{pmatrix} 1 & 0 \\ 0 & -1 \end{pmatrix}. \quad (10)$$

In the  $T \otimes t$  system, on the other hand, they are given as

$$V^{(1)} = \begin{pmatrix} 0 & 0 & 0 \\ 0 & 0 & 1 \\ 0 & 1 & 0 \end{pmatrix}, V^{(2)} = \begin{pmatrix} 0 & 0 & 1 \\ 0 & 0 & 0 \\ 1 & 0 & 0 \end{pmatrix}, \text{ and } V^{(3)} = \begin{pmatrix} 0 & 1 & 0 \\ 1 & 0 & 0 \\ 0 & 0 & 0 \end{pmatrix}, \quad (11)$$

while in the  $T \otimes h$  system, they are obtained as

$$V^{(1)} = \frac{\sqrt{3}}{2} \begin{pmatrix} 0 & 0 & 0 \\ 0 & 0 & 1 \\ 0 & 1 & 0 \end{pmatrix}, V^{(2)} = \frac{\sqrt{3}}{2} \begin{pmatrix} 0 & 0 & 1 \\ 0 & 0 & 0 \\ 1 & 0 & 0 \end{pmatrix}, V^{(3)} = \frac{\sqrt{3}}{2} \begin{pmatrix} 0 & 1 & 0 \\ 1 & 0 & 0 \\ 0 & 0 & 0 \end{pmatrix},$$

$$V^{(4)} = \frac{\sqrt{3}}{2} \begin{pmatrix} 1 & 0 & 0 \\ 0 & -1 & 0 \\ 0 & 0 & 0 \end{pmatrix}, \text{ and } V^{(5)} = \frac{1}{2} \begin{pmatrix} -1 & 0 & 0 \\ 0 & -1 & 0 \\ 0 & 0 & 2 \end{pmatrix}. \quad (12)$$

Of course,  $V^{(1)} = 1$  for the  $A \otimes a$  system.

In considering electron motion in a crystal, it is convenient to introduce momentum representation which is the Fourier transform of site representation as

$$c_{\mathbf{k}\gamma\sigma} = \frac{1}{\sqrt{N}} \sum_{\mathbf{j}} e^{-i\mathbf{j}\cdot\mathbf{k}} c_{\text{j}\gamma\sigma} \text{ and } a_{\mathbf{k}\nu} = \frac{1}{\sqrt{N}} \sum_{\mathbf{j}} e^{-i\mathbf{j}\cdot\mathbf{k}} a_{\text{j}\nu}. \quad (13)$$

In this representation,  $H_t$  can be diagonalized. In particular, under the assumption of (4), we obtain

$$H_t + \sum_{\mathbf{j}} H_e^{(\mathbf{j})} = \sum_{\mathbf{k}\gamma\sigma} (\epsilon_{\mathbf{k}} - \mu) c_{\mathbf{k}\gamma\sigma}^\dagger c_{\mathbf{k}\gamma\sigma}, \quad (14)$$

with  $\epsilon_{\mathbf{k}}$  the single-electron dispersion relation, which is given by

$$\epsilon_{\mathbf{k}} = -2t \sum_{i=1}^d \cos k_i, \quad (15)$$

for a simple cubic lattice in  $d$  dimensions. Though the results will not be given here, other parts of the Hamiltonian can be rewritten accordingly in this representation.

## 2.2 Conservation of Pseudospin Angular Momentum

In the  $E \otimes e$  JT system, we can define  $T_{\mathbf{j}}$  the operator to rotate *pseudospin* at site  $\mathbf{j}$  by

$$T_{\mathbf{j}} = i \left( a_{\mathbf{j}\epsilon}^\dagger a_{\mathbf{j}\theta} - a_{\mathbf{j}\theta}^\dagger a_{\mathbf{j}\epsilon} \right) - \frac{i}{2} \sum_{\sigma} \left( c_{\mathbf{j}\epsilon\sigma}^\dagger c_{\mathbf{j}\theta\sigma} - c_{\mathbf{j}\theta\sigma}^\dagger c_{\mathbf{j}\epsilon\sigma} \right). \quad (16)$$

As easily checked, this operator commutes with  $H_{\mathbf{j}}$ , leading to the local conservation law of “pseudospin angular momentum” in the electron–phonon coupled system. If (4) is assumed, the total pseudospin rotation operator  $T (\equiv \sum_{\mathbf{j}} T_{\mathbf{j}})$  is conserved in the entire crystal.

In order to better exploit this local conservation law, we shall change the representation in which the one-body basis functions are the eigen functions of both the Hamiltonian and  $T_{\mathbf{j}}$ . This can be accomplished by the following canonical transformation from the basis functions  $(\epsilon, \theta)$  to those  $(\alpha, \beta)$  as

$$\begin{pmatrix} d_{\mathbf{j}\alpha\sigma} \\ d_{\mathbf{j}\beta\sigma} \end{pmatrix} = \frac{1}{\sqrt{2}} \begin{pmatrix} 1 & -i \\ 1 & i \end{pmatrix} \begin{pmatrix} c_{\mathbf{j}\epsilon\sigma} \\ c_{\mathbf{j}\theta\sigma} \end{pmatrix} \text{ and } \begin{pmatrix} b_{\mathbf{j}\alpha} \\ b_{\mathbf{j}\beta} \end{pmatrix} = \frac{1}{\sqrt{2}} \begin{pmatrix} -i & 1 \\ i & 1 \end{pmatrix} \begin{pmatrix} a_{\mathbf{j}\epsilon} \\ a_{\mathbf{j}\theta} \end{pmatrix}. \quad (17)$$

In this new representation,  $H_{e-\text{ph}}^{(\mathbf{j})}$  and  $T_{\mathbf{j}}$  are, respectively, rewritten as

$$H_{e-\text{ph}}^{(\mathbf{j})} = \sqrt{2} g_{E \otimes e} \sum_{\sigma} \left[ (b_{\mathbf{j}\alpha} + b_{\mathbf{j}\beta}^\dagger) d_{\mathbf{j}\alpha\sigma}^\dagger d_{\mathbf{j}\beta\sigma} + (b_{\mathbf{j}\alpha}^\dagger + b_{\mathbf{j}\beta}) d_{\mathbf{j}\beta\sigma}^\dagger d_{\mathbf{j}\alpha\sigma} \right], \quad (18)$$

$$T_{\mathbf{j}} = b_{\mathbf{j}\alpha}^\dagger b_{\mathbf{j}\alpha} - b_{\mathbf{j}\beta}^\dagger b_{\mathbf{j}\beta} + \frac{1}{2} \sum_{\sigma} \left( d_{\mathbf{j}\alpha\sigma}^\dagger d_{\mathbf{j}\alpha\sigma} - d_{\mathbf{j}\beta\sigma}^\dagger d_{\mathbf{j}\beta\sigma} \right). \quad (19)$$

Equation (18) for  $H_{\text{e-ph}}^{(j)}$  explicitly expresses the characteristic feature of *the off-diagonal electron–phonon coupling*, in contrast to the *the diagonal electron–phonon coupling* in the  $A \otimes a$  Holstein model [27], in which  $H_{\text{e-ph}}^{(j)}$  is described as

$$H_{\text{e-ph}}^{(j)} = g_{A \otimes a} \sum_{\sigma} \left( a_j^{\dagger} + a_j \right) c_{j\sigma}^{\dagger} c_{j\sigma}. \quad (20)$$

The existence of the conserved pseudospin rotation is not a common feature among the JT systems. In fact, we cannot define an operator corresponding to  $T_j$  in both  $T \otimes t$  and  $T \otimes h$  systems. Mathematical analysis of the continuous group invariances in each JT system determines the presence/absence of such an operator [79]; the  $SO(2)$  invariance in the  $E \otimes e$  system generates the operator  $T_j$ , while there are no such invariances in the  $T \otimes t$  system. In Sect. 3, we shall find an unexpected consequence of this mathematical structure of the JT system in the behavior of the polaron mass.

### 2.3 Theoretical Tools

There are various theoretical tools to investigate the polaron and bipolaron problems. In the weak-coupling region, the standard method is the perturbation-theoretic approach including the Green’s-function method. In the strong-coupling region, on the other hand, the canonical transformation due to Lang and Firsov [80] is commonly used. This is a method very similar to the Lee–Low–Pines unitary transformation [81] developed for the Fröhlich model [82] and provides a very useful trial wavefunction for many types of variational approaches.

These are basically analytic methods, but in recent years numerical methods play a major role. Among them, the simplest one is exact diagonalization in which the Hamiltonian matrix obtained with an appropriate expansion basis is numerically diagonalized. This is very elementary, but due to the bosonic character of phonons, the size of the Hamiltonian matrix increases exponentially as  $N$  and/or  $N_e$  increase. Thus it is not easy to treat the  $E \otimes e$  system with more than two sites by this method.

In order to take care of larger systems, more sophisticated methods have been employed. For example, path-integral quantum Monte Carlo (PIQMC) [83] is a powerful method in which bosonic degrees of freedom are analytically integrated out to provide an effective self-interaction working on an electron and the remaining integral is performed through quantum Monte Carlo (QMC) simulations. Since the polaron problem does not suffer from the notorious negative-sign problem, we can hope to obtain accurate results for a lattice of very large  $N$  and arbitrary dimensions by using QMC. Other advanced methods include; (1) density-matrix renormalization group (DMRG) [84], (2) the large-scale variational method called “variational exact diagonalization (VED)” [85,86], (3) dynamical Mean-field theory (DMFT) [87], and (4) diagrammatic Monte Carlo (DMC) [88]. It is very fortunate that useful textbooks on these methods have recently been published [89,90]. We suggest interested readers to consult them for details.

### 3 Polaron: Single-Electron Problem

In the polaron problem (or the single-electron system coupled with phonons), both spin degrees of freedom and the electron–electron interaction as described by  $H_{ee}^{(j)}$  are irrelevant. The first work on the JT polaron was done by Höck et al. [91] on the  $E \otimes b$  system [92] which, unfortunately, possesses a too simple internal structure to provide qualitatively different features from those of the  $A \otimes a$  system. Several works have treated the second simplest  $E \otimes e$  system and found a quantitative difference in the polaron effective mass from that in the  $A \otimes a$  system [63, 93–98]. The  $T \otimes t$  JT polaron has also been studied and the difference from that in the  $E \otimes e$  system is revealed [99–101].

Let us start with the  $E \otimes e$  JT polaron in the weak-coupling region (or for the case of small  $g_{E \otimes e}$ ), in which the perturbation approach in momentum representation is useful. The thermal one-electron Green's function  $G_{\mathbf{k}\gamma\sigma}(i\omega_n)$  with  $\omega_n$  the fermion Matsubara frequency is defined at temperature  $T$  by

$$G_{\mathbf{k}\gamma\sigma}(i\omega_n) = - \int_0^{1/T} d\tau e^{i\omega_n\tau} \langle T_\tau d_{\mathbf{k}\gamma\sigma}(\tau) d_{\mathbf{k}\gamma\sigma}^\dagger \rangle. \quad (21)$$

This function is related to the self-energy  $\Sigma_{\mathbf{k}\gamma\sigma}(i\omega_n)$  through the Dyson equation as  $G_{\mathbf{k}\gamma\sigma}(i\omega_n)^{-1} = i\omega_n - \epsilon_{\mathbf{k}} + \mu - \Sigma_{\mathbf{k}\gamma\sigma}(i\omega_n)$ . In Fig. 1, diagrammatic representation for  $\Sigma_{\mathbf{k}\gamma\sigma}(i\omega_n)$  are given, together with the formal expansion series for the vertex function  $\Gamma_{\gamma'\sigma',\gamma\sigma}(\mathbf{k}'i\omega_{n'}, \mathbf{k}i\omega_n)$ . Using the self-energy analytically continued on the real frequency axis, we can determine the polaron (renormalized) dispersion relation  $E_{\mathbf{k}}$  by the solution of  $E_{\mathbf{k}} = \epsilon_{\mathbf{k}} + \Sigma_{\mathbf{k}\gamma\sigma}(E_{\mathbf{k}}) - \mu$ . The bare band mass  $m$  and the polaron effective mass  $m^*$  are derived from the curvatures of  $\epsilon_{\mathbf{k}}$  and  $E_{\mathbf{k}}$  at  $\mathbf{k} = \mathbf{0}$ , respectively. Of course, the polaron stabilization energy  $E_{\text{JT}} (\approx -g_{E \otimes e}^2/\omega_0)$  is obtained as the shift of  $\mu (= -E_{\text{JT}})$ .

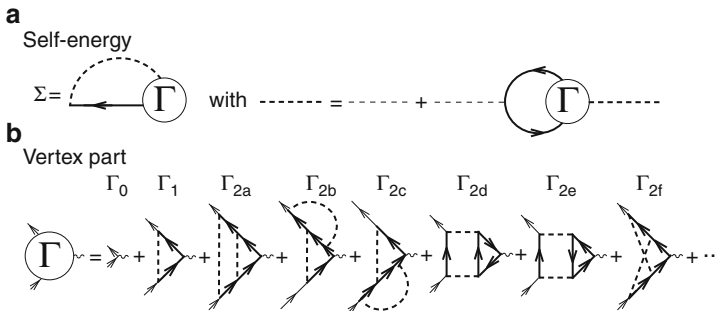


**Fig. 1** (a) Self-energy in diagrammatic representation. (b) Expansion series for the vertex  $\Gamma$  up to  $g^4$ . Thick solid, thick dashed, and thin dashed lines indicate, respectively, the electron Green's function, the dressed phonon, and the bare phonon propagators

In the weak-coupling region, we may replace  $G_{\mathbf{k}\gamma\sigma}(i\omega_n)$  by the bare one  $(i\omega_n - \epsilon_{\mathbf{k}} + \mu)^{-1}$  in Fig. 1 and take  $\Gamma_{\gamma'\sigma',\gamma\sigma}(\mathbf{k}'i\omega_{n'}, \mathbf{k}i\omega_n)$  as unity or the first term  $\Gamma_0$  in Fig. 1b. Then we obtain the result for the mass ratio  $m^*/m$ , the most fundamental quantity in the polaron physics, as

$$\frac{m^*}{m} = 1 + 2 \left( \frac{g_{E\otimes e}}{\omega_0} \right)^2. \quad (22)$$

Similar calculations can be done for  $A \otimes a$ ,  $T \otimes t$ , and  $T \otimes h$  to find

$$\frac{m^*}{m} = 1 + \left( \frac{g_{A\otimes a}}{\omega_0} \right)^2, \frac{m^*}{m} = 1 + 2 \left( \frac{g_{T\otimes t}}{\omega_0} \right)^2, \text{ and } \frac{m^*}{m} = 1 + \frac{5}{3} \left( \frac{g_{T\otimes h}}{\omega_0} \right)^2, \quad (23)$$

from which we see that it is exactly the same mass enhancement factor in all the cases, if we normalize the coupling constants in the following way:

$$g_{A\otimes a} = g, g_{E\otimes e} = \frac{1}{\sqrt{2}} g, g_{T\otimes t} = \frac{1}{\sqrt{2}} g, \text{ and } g_{T\otimes h} = \sqrt{\frac{3}{5}} g. \quad (24)$$

In fact, there is no qualitative difference between the JT polaron and the Holstein polaron in this region. Even quantitatively, they are exactly the same, as long as the coupling constants are normalized according to (24).

In the strong-coupling limit, a polaron will be completely localized at a single site, indicating  $m^*/m = \infty$ , and the problem is reduced to a *single-site system* in which the polaron stabilization energy is a main issue [102]. For a finite but very large coupling, the localized polaron will begin to hop between sites, but the hopping in this case is a very rare event. Thus physics connected with such a hopping can be well captured by just considering a *two-site system*. The same is true for the anti-adiabatic case in which  $t$  is very small, implying that the hopping is a very rare event from the outset.

Now, we need to know a formula to evaluate  $m^*/m$  from the eigen-state energies in a finite-site system. For this purpose, let us consider a one-dimensional ( $d = 1$ ) infinite chain first. By making an expansion of the bare dispersion  $\epsilon_k$  in (15) around  $k = 0$ , we see that  $t = 1/2m = [\max\{\epsilon_k\} - \min\{\epsilon_k\}]/4$ , where  $\max/\min\{\epsilon_k\}$  is the maximum/minimum value of  $\epsilon_k$  in the entire Brillouin zone. With the introduction of the electron–phonon interaction,  $t$  will be modified effectively into  $t^*$ . Then we can follow a similar argument to reach the relation of  $t^* = 1/2m^* = [\max\{E_k\} - \min\{E_k\}]/4$ . By taking the ratio of these results, we obtain an interesting result as  $m^*/m = [\max\{\epsilon_k\} - \min\{\epsilon_k\}]/[\max\{E_k\} - \min\{E_k\}]$ . In this derivation, we have assumed one dimensionality, but exactly the same result can be obtained even if we consider in both 2D and 3D, indicating that  $m^*/m$  can be evaluated only through the polaron bandwidth,  $\max\{E_k\} - \min\{E_k\}$ , irrespective of dimensionality.

The total polaron bandwidth can be estimated by calculating  $E_k$  in finite-site systems where some discrete values of  $k$ 's are available. In the two-site problem, if we write the ground-state wavefunction for a polaron localized at site  $\mathbf{j}$  as  $\Psi_{\mathbf{j}}$ , the

ground- and the first-excited-state wavefunctions in a two-site ( $\mathbf{j} = 1$  or  $2$ ) system are well represented by  $\Psi_+ = (\Psi_1 + \Psi_2)/\sqrt{2}$  and  $\Psi_- = (\Psi_1 - \Psi_2)/\sqrt{2}$ , respectively, in the region under consideration. The former corresponds to the bonding state ( $k = 0$ ) with energy  $E_+$  and the latter to the anti-bonding one ( $k = \pi$ ) with energy  $E_-$ . Then, since  $\epsilon_\pi - \epsilon_0 = 2t$  in the two-site calculation, we obtain  $m^*/m$  through the relation

$$\frac{m^*}{m} = \frac{2t}{E_- - E_+}. \quad (25)$$

Note that the result  $m^*/m$  obtained through (25) does not depend on the value  $t$  in the strong-coupling and/or anti-adiabatic region.

With use of (25), a rigorous analytical result has already been obtained for the  $E \otimes e$  JT polaron as [93]

$$\frac{m^*}{m} = I_0(g_{E \otimes e}^2/\omega_0^2) + I_1(g_{E \otimes e}^2/\omega_0^2) \approx \frac{2}{\sqrt{\pi}} \frac{\omega_0}{g} \exp\left[\frac{1}{2} \left(\frac{g}{\omega_0}\right)^2\right], \quad (26)$$

where  $I_i(x)$  is the modified Bessel function of  $i$ th order and (24) is used in arriving at the last equation. Compared to  $m^*/m = \exp[(g/\omega_0)^2]$  the Holstein's famous factor for the  $A \otimes a$  system, we come to realize that  $m^*/m$  becomes much less enhanced in the  $E \otimes e$  polaron than that in the Holstein model.

By comparing the result of  $m^*/m$  for the infinite-site system obtained by VED [96] (see, Fig. 2), we are confident that the two-site calculation provides a reasonably good result for  $m^*/m$  in the whole range of  $g$  at least in the anti-adiabatic region of  $t/\omega_0$ . The relevance of the two-site calculation has also been seen in the Holstein model [78]. Thus we can expect that the same is true for the  $T \otimes t$  JT polaron. In Fig. 3, we show the result of  $m/m^*$  for the  $T \otimes t$  system (*solid curve*) which is obtained in the anti-adiabatic region by implementing an

**Fig. 2** Inverse of the polaron mass enhancement factor,  $m/m^*$ , as a function of  $g^2/\omega_0^2$  for the  $A \otimes a$  (HP: Holstein polaron) and the  $E \otimes e$  JT polaron. In the latter, the result in the infinite chain ( $d = 1$ ) is compared with that in the two-site system as well as the analytic result in (26). The anti-adiabatic condition of  $\omega_0/t = 5$  is assumed

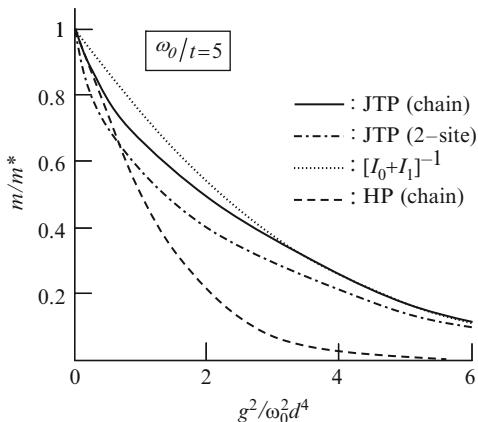
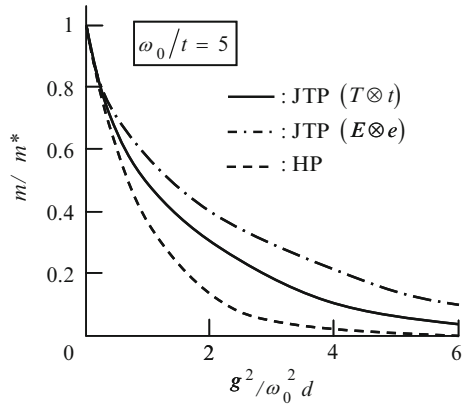


**Fig. 3** Inverse of the mass enhancement factor,  $m/m^*$ , as a function of  $g^2/\omega_0^2$  with  $d = 1$  for the  $T \otimes t$  (solid curve) and the  $E \otimes e$  (dotted-dashed curve) JT polarons in comparison with the Holstein one (dashed curve). All the results are obtained by exact diagonalization applied to the two-site Hamiltonian in the anti-adiabatic region



exact diagonalization study of the two-site Hamiltonian [100, 101]. This result is situated between the corresponding ones for the  $E \otimes e$  JT (dotted-dashed curve) and the  $A \otimes a$  Holstein (dashed curve) polarons.

Physically the polaron mass enhancement is brought about by the virtual excitation of phonons. In the  $A \otimes a$  Holstein model no restriction is imposed on exciting multiple phonons, implying that all the terms in Fig. 1b for the vertex function contribute, while in the  $E \otimes e$  JT model, there is a severe restriction due to the existence of the conservation law intimately related to the  $SO(2)$  rotational symmetry in the pseudospin space. Actually, among the first- and second-order terms for the vertex function, only the term  $\Gamma_{2f}$  contributes, leading to the smaller polaron mass enhancement factor  $m^*/m$  than that in the Holstein model in which the correction  $\Gamma_1$  is known to enhance  $m^*/m$  very much. In this way, the applicable range of the Migdal's approximation [48] becomes much wider in the  $E \otimes e$  JT system [63].

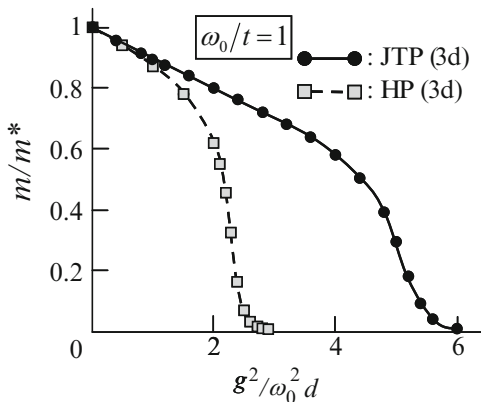
In order to understand the reason why the result for  $m^*/m$  in the  $T \otimes t$  JT system comes between those in the  $A \otimes a$  and  $E \otimes e$  systems, we shall rewrite  $H_{e-ph}^{(j)}$  in (9) for the  $T \otimes t$  system as [101]

$$\begin{aligned}
 H_{e-ph}^{(j)} = & \sqrt{\frac{2}{3}} g T \otimes t \left[ (b_{j1}^+ + b_{j2})(d_{j1\sigma}^+ d_{j3\sigma} + d_{j3\sigma}^+ d_{j2\sigma} - 2d_{j2\sigma}^+ d_{j1\sigma}) \right. \\
 & + (b_{j1} + b_{j2}^+)(d_{j3\sigma}^+ d_{j1\sigma} + d_{j2\sigma}^+ d_{j3\sigma} - 2d_{j1\sigma}^+ d_{j2\sigma}) \\
 & \left. + (b_{j3}^+ + b_{j3})(2d_{j3\sigma}^+ d_{j3\sigma} - d_{j1\sigma}^+ d_{j1\sigma} - d_{j2\sigma}^+ d_{j2\sigma}) \right], \quad (27)
 \end{aligned}$$

by introducing an appropriate unitary transformation. The first two terms in (27) has a structure very similar to that in (18) representing the feature of *the off-diagonal electron–phonon coupling*, which makes many terms in the vertex correction vanish. On the other hand, the last term in (27) has the feature of *the diagonal electron–phonon coupling* as in the  $A \otimes a$  system. In this respect, the system  $T \otimes t$  may be regarded as  $T \otimes (a \oplus e)$ , an intermediate character.



**Fig. 4** Inverse of the mass enhancement factor,  $m/m^*$ , for the  $E \otimes e$  JT polaron as a function of  $g^2/3\omega_0^2$  in the simple cubic lattice, in comparison with the corresponding result in the Holstein polaron [94]



The reduction of  $t \rightarrow a \oplus e$  can also be ascertained by considering the adiabatic potential energy surface for the  $T \otimes t$  system. The potential contains four equivalent wells for sufficiently large  $g_{T \otimes t}$  [103–105], but the wells are not isotropic and the vibrational  $t$ -mode splits into an  $a$ -mode of energy  $\omega_0$  and two  $e$ -modes of energy  $\sqrt{2/3} \omega_0$ .

In Fig. 4,  $m/m^*$  for the  $E \otimes e$  JT polaron in the intermediate-adiabaticity region is given in comparison with the corresponding one for the Holstein polaron in the simple cubic lattice ( $d = 3$ ). The results are obtained by PIQMC [94] and the physical message is just the same as the one we have already explained.

In concluding this section, we emphasize an amazing fact that the internal mathematical structure of the JT center determines the magnitude of the polaron effective mass. This implies that there will be an intrinsic difference in  $m^*$  between the manganese oxides  $\text{La}_{1-x}\text{Sr}_x\text{MnO}_3$  with  $e_g$  electrons and the titanium ones  $\text{La}_{1-x}\text{Sr}_x\text{TiO}_3$  with  $t_{2g}$  electrons, as may be observed by the difference in the transport mass or the  $T$ -linear coefficient in the low-temperature electronic specific heat  $C_v(T)$  [101]. The experimental result on  $C_v(T)$  obtained by Tokura's group [106] may be relevant to this issue.

## 4 Bipolarons: Problems with Two or More Electrons

### 4.1 Bipolaron Formation

If there are two or more electrons in the system, we should take the Coulomb correlation into account by considering  $H_{ee}^{(j)}$  given in (6). In the case of the  $E \otimes e$  system, using (7) and (17), we can rewrite (6) into

$$\begin{aligned}
H_{ee}^{(j)} &= (U' + J) \sum_{\gamma} n_{j\gamma\uparrow} n_{j\gamma\downarrow} + (U' + J) \sum_{\sigma} n_{j\alpha\sigma} n_{j\beta-\sigma} \\
&\quad + (U' - J) \sum_{\sigma} n_{j\alpha\sigma} n_{j\beta\sigma} + 2J \sum_{\sigma} d_{j\alpha\sigma}^{\dagger} d_{j\beta-\sigma}^{\dagger} d_{j\alpha-\sigma} d_{j\beta\sigma} \\
&= \frac{\bar{U}}{2} n_j (n_j - 1) - 2J \sum_{\sigma} n_{j\alpha\sigma} n_{j\beta\sigma} + 2J \sum_{\sigma} d_{j\alpha\sigma}^{\dagger} d_{j\beta-\sigma}^{\dagger} d_{j\alpha-\sigma} d_{j\beta\sigma}, \quad (28)
\end{aligned}$$

where  $\bar{U} \equiv U' + J$  and  $n_j \equiv \sum_{\gamma\sigma} n_{j\gamma\sigma}$ .

In addition to the Coulomb interaction, the phonon-mediated interactions  $U_{\text{ph}}$  work on the electrons. In the weak-coupling and anti-adiabatic region, the lowest-order perturbation calculation provides  $U_{\text{ph}} = \sum_j U_{\text{ph}}^{(j)}$  with  $U_{\text{ph}}^{(j)}$  obtained as

$$U_{\text{ph}}^{(j)} = 2 \frac{g_{E \otimes e}^2}{\omega_0} \sum_{\sigma} n_{j\alpha\sigma} n_{j\beta\sigma} - 2 \frac{g_{E \otimes e}^2}{\omega_0} \sum_{\sigma} d_{j\alpha\sigma}^{\dagger} d_{j\beta-\sigma}^{\dagger} d_{j\alpha-\sigma} d_{j\beta\sigma}, \quad (29)$$

in the  $E \otimes e$  system. By comparing (29) with (28), we notice that the phonon-exchange effect makes  $J$  decrease, while  $\bar{U}$  unchanged at least up to this order of perturbation. This result is somewhat different from the one in the single-band system. In fact, in the case of the  $A \otimes a$  system with the Hubbard- $U$  interaction  $H_U (= U \sum_j n_{j\uparrow} n_{j\downarrow})$ , the corresponding  $U_{\text{ph}}$  is obtained as

$$U_{\text{ph}} = -2 \frac{g_{A \otimes a}^2}{\omega_0} \sum_j n_{j\uparrow} n_{j\downarrow}, \quad (30)$$

indicating that the Coulomb repulsion  $U$  itself is reduced by the phonon-induced attraction. Of course, the electron–phonon interaction shifts both the hopping integral  $t$  and the chemical potential  $\mu$  as well.

The formation of a bipolaron (or a bound pair of two polarons) is established, if the ground-state energy of the two-electron system is lower than twice the ground-state energy of a polaron. This issue has been studied rather intensively for the Holstein bipolaron [78], but it is not the case for the JT bipolaron. In [96], the electron–electron correlation function and the effective mass of an  $E \otimes e$  bipolaron was studied in one dimension in comparison with the corresponding results for the Holstein bipolaron [107]. In Fig. 5, we plot the phase diagram for the bipolaron formation, from which we find that the JT bipolaron is less stable than the Holstein one.

## 4.2 Two-Site Four-Electron $E \otimes e$ System

Due to huge dimensions of the Hilbert space for JT systems, it is quite difficult to treat many JT polarons even with state-of-the-art supercomputers. Therefore we

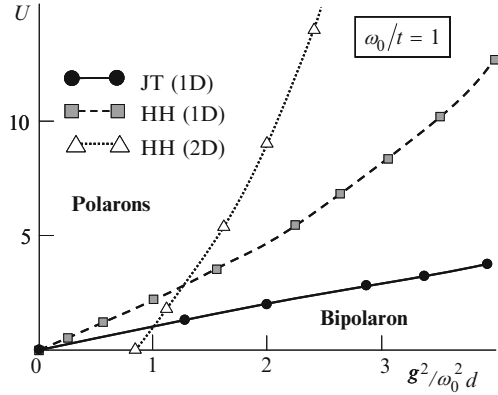


**Fig. 5** Phase boundary for the bipolaron formation [96, 107]. The spatial dimension of the system is indicated by  $d$

have to be satisfied with studying small clusters, if we resort to exact diagonalization or its marginal refinements.

Here we present our results of the two-site  $E \otimes e$  JT model at half-filling (two electrons per site on average) at which the competition between the Coulomb repulsion and the JT-phonon induced attraction becomes very eminent, because both the Hund's-rule coupling and the pair-exchange interaction work only if two electrons exist at the same site. This two-site calculation is of particular relevance to the physics of a crystal in the anti-adiabatic and/or strong-coupling region, but we may claim that studying this system is generally the first and important step towards a full understanding of the physics connected with the electron hopping effect in JT crystals due to the fact that a two-site system is a minimal model containing electron hopping terms in the presence of various kinds of competing interactions.

As a work preceding to ours, Han and Gunnarsson [108] treated three kinds of one- and two-site JT models ( $E \otimes a$ ,  $E \otimes e$ , and  $T \otimes h$ ) in considering the metal-insulator transition (MIT) in  $A_nC_{60}$  with  $n = 3$  or 4. They were mainly concerned with the parameters in the region of

$$g \ll \omega_0 \ll W \ll U \text{ and } J \sim g^2/\omega_0 \ll W, \quad (31)$$

in which the effects of the Hund's-rule and the JT couplings manifest themselves as merely first- and second-order perturbation, respectively. Here  $W$  denotes the bare bandwidth. Then, as mentioned before, the effect of the JT coupling simply cancels that of the exchange integral  $J$ , excluding more subtle physics driven by the competition of the JT and Hund's-rule couplings. We shall discuss this subtle physics by relaxing the parameter space from the conditions specified in (31).

Before discussing the calculated results, let us consider the two limiting cases first. One is the limit of  $g(= \sqrt{2}g_{E \otimes e}) \rightarrow \infty$ , in which four electrons form two bipolarons with each localized at a different site due to the fact that the  $E \otimes e$  coupling favors the spin-singlet electron pair per site. The structure of the electronic wave function corresponding to this situation is shown schematically in Fig. 6. Due

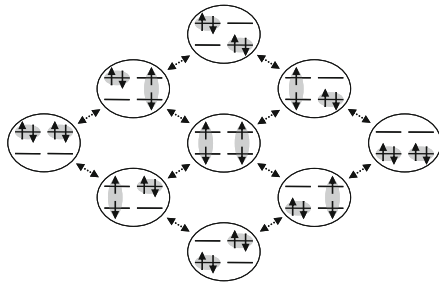


**Fig. 6** Structure of the electronic wave function for the two-site  $E \otimes e$  system at half-filling. This structure schematically represents “the intra-site singlet state”. Double-sided arrows indicate the connection of the matrix elements of the wave function via the  $E \otimes e$  coupling

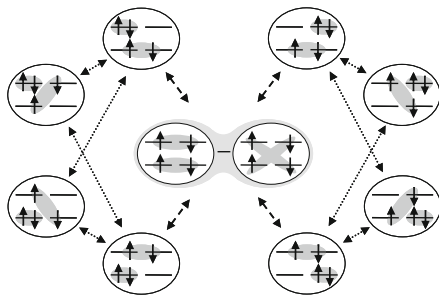


**Fig. 7** Similar schematic view of the Structure of the electronic wave function for the two-site  $E \otimes e$  system at half-filling. This structure represents the state dominated by “the inter-site singlet state”. In this case, double-sided arrows indicate the connection of the matrix elements of the wave function via both the  $E \otimes e$  coupling and the usual inter-site hopping

to large  $g$ , the effective hopping amplitude  $t^*$  is virtually zero, making the system insulating. In particular, in the limit of  $g \rightarrow \infty$ , the ground state is characterized by *an orbital ordering*. In the intermediate-coupling region, however, it can be an insulator without the orbital ordering or a *nonmagnetic JT Mott insulator*, as suggested by Fabrizio and Tosatti [109]. The detail of the orbital ordering depends on the choice of  $t_{ij}^{\gamma\gamma'}$ : In the diagonal hopping ( $t_{ij}^{\gamma\gamma'} = t\delta_{\gamma\gamma'}$ ), an antiferro-orbital (AFO) ordering is more favorable than a ferro-orbital one.

Another limit is to take  $J \rightarrow \infty$  with keeping  $U'/J$  fixed.<sup>1</sup> Due to large  $U'$  and  $J$ , each site is occupied by two electrons with parallel spins, but the total spin of the ground state  $S$  is not two but zero owing to the superexchange interaction, suggesting an antiferromagnetic or a spin density wave (SDW) state the structure of which is schematically shown in Fig. 7.

<sup>1</sup> In view of the fact that  $U'$  and  $J$  are, more or less, of the same order of magnitude in actual materials, we consider this condition to be reasonable.

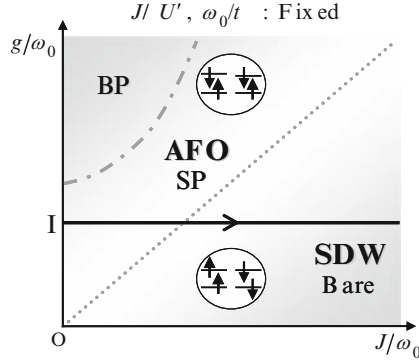


**Fig. 8** Schematic phase diagram for the two-site  $E \otimes e$  system at half-filling in the  $(g, J)$  space. AFO and SDW indicate, respectively, antiferro-orbital ordering and spin density wave states. The electronic state is specified by either the bare electron (Bare), the single-polaron (SP), or the bipolaron (BP). Parameters  $g$ ,  $\omega_0/t$ , and  $J/U'$  are, respectively, chosen as 1, 1, 0.5 along the line I

In Fig. 8, a schematic phase diagram is shown to connect the above two limits by changing the parameters  $g$  and  $J$ . We shall focus our attention on the intermediate-coupling region along the line I in this figure, where a strong competition between  $g$  and  $J$  is expected. This competition is investigated by the calculation of various physical quantities with use of exact diagonalization. Along the line I, the parameters  $g$ ,  $\omega_0/t$ , and  $J/U'$  are set equal to be 1, 1, 0.5, respectively. These values are chosen in reference to the manganites.

The calculated quantities include charge density wave (CDW), spin density wave, antiferro-orbital ordering, and electron-pairing response functions. The corresponding operators are the density operator  $A^c$ , the spin density operator  $A^s$ , the antiferro-orbital operator  $A^o$ , and the singlet pairing operator  $\Phi$ , all of which are defined in terms of the original orbitals of  $\epsilon (= d_{x^2-y^2})$  and  $\theta (= d_{3z^2-r^2})$  as

$$A^c = \frac{1}{2} \sum_{\gamma\sigma} (c_{1\gamma\sigma}^\dagger c_{1\gamma\sigma} - c_{2\gamma\sigma}^\dagger c_{2\gamma\sigma}), \quad (32)$$

$$A^s = \frac{1}{2} \sum_{\gamma} [(c_{1\gamma\uparrow}^\dagger c_{1\gamma\uparrow} - c_{1\gamma\downarrow}^\dagger c_{1\gamma\downarrow}) - (c_{2\gamma\uparrow}^\dagger c_{2\gamma\uparrow} - c_{2\gamma\downarrow}^\dagger c_{2\gamma\downarrow})], \quad (33)$$

$$A^o = \frac{1}{2} \sum_{\sigma} [(c_{1\epsilon\sigma}^\dagger c_{1\epsilon\sigma} - c_{1\theta\sigma}^\dagger c_{1\theta\sigma}) - (c_{2\epsilon\sigma}^\dagger c_{2\epsilon\sigma} - c_{2\theta\sigma}^\dagger c_{2\theta\sigma})], \quad (34)$$

$$\Phi = \sum_{k,\gamma,\gamma'} \Delta_k(\gamma, \gamma') c_{k\gamma'\downarrow} c_{k\gamma\uparrow}, \quad (35)$$

where the operator  $c_{k\gamma\sigma}$  is defined as

$$c_{k\gamma\sigma} = \frac{1}{\sqrt{2}} \left( c_{1\gamma\sigma} + e^{ik} c_{2\gamma\sigma} \right), \quad (36)$$

where  $k$  is either 0 or  $\pi$ ,<sup>2</sup> and  $\Delta_k$  is a complex parameter to be determined variationally under the normalization and the antisymmetric conditions

$$\sum_{k,\gamma,\gamma'} |\Delta_k(\gamma, \gamma')|^2 = 1 \text{ and } \Delta_k(\gamma, \gamma') = \Delta_k(\gamma', \gamma). \quad (37)$$

With using the operator  $A^c$ , we can define the charge response function as

$$\chi^c(\omega) = -i \int_0^\infty dt e^{i\omega t - 0^+ t} \langle [A^c(t), A^c(0)] \rangle. \quad (38)$$

Similarly, we can define other response functions  $\chi^s$  and  $\chi^o$  in terms of  $A^s$  and  $A^o$ , respectively. We can also define the pairing response function by

$$\chi^p(\omega) = -i \int_0^\infty dt e^{i\omega t - 0^+ t} \langle [\Phi(t), \Phi^\dagger(0)] \rangle. \quad (39)$$

In calculating  $\chi^p(\omega)$  at  $\omega \rightarrow 0^+$  (static limit), we optimize the parameters  $\Delta_k(\gamma, \gamma')$  so as to maximize the absolute value of  $\chi^p(0)$ , through which we can automatically determine a favorable types of electron pairing for given set of parameters  $U'$ ,  $J$ , and  $g$ . More specifically, we can find the better pairing between the two possibilities; one is the pairing with their total electronic pseudospin  $T = 0$  (SCP0) and the other is the pairing with  $T = 1$  (SCP1). We denote the former by  $\chi^{p0}$  and the latter by  $\chi^{p1}$ .

The response functions in the noninteracting two-site four-electron system are easily calculated to give  $\chi^c(0) = \chi^s(0) = \chi^o(0) = 2\chi^p(0) = -1/t$ . We shall normalize the static response functions by the corresponding values in the noninteracting system;  $\tilde{\chi} \equiv -t\chi(0)$  for  $A^c$ ,  $A^s$ , and  $A^o$ , while  $\tilde{\chi} \equiv -2t\chi(0)$  for  $\Phi$ .

Now we shall show our calculated results along the line I in Fig. 8. For the sake of convenience, let us divide the values of  $J$  into three regions; weak-coupling ( $0 \lesssim J/t \lesssim 0.5$ ), intermediate-coupling ( $0.5 \lesssim J/t \lesssim 1$ ), and strong-coupling ( $J/t \gtrsim 1$ ). The ground-state and the first-excited-state energies are shown in Fig. 9. In the entire region of the phase diagram, the ground state is always characterized by  $S = T = 0$ . In the weak-coupling region where the effect of  $g$  dominates that of  $J$ , the electrons form an intra-site singlet state and the first-excited state is specified by  $S = 0$  and  $T = 1$ , suggesting the dominance of orbital fluctuations. In the intermediate-coupling region, on the other hand, the electrons begin to form spin-triplet states at both sites due to the Hund's-rule coupling, but  $S$  remains to be zero

<sup>2</sup> Note that we define  $k$  modulo  $2\pi$ , indicating that  $-k = k$ .

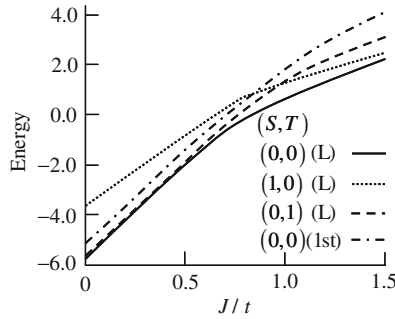


**Fig. 9** Ground-state and first-excited-state energies in units of  $\omega_0$  of the two-site four-electron  $E \otimes e$  system for  $t = \omega_0$ ,  $g = \omega_0$ , and  $J/U' = 0.5$ .  $S$  and  $T$  denote the total spin and pseudospin of the system, respectively. Solid curve ((0, 0) (L)) indicates the lowest energy in the  $(S, T) = (0, 0)$  sector; dotted curve ((1, 0) (L)) the lowest energy in the sector with  $(S, T) = (1, 0)$ ; dashed curve ((0, 1) (L)) the lowest energy in the sector with  $(S, T) = (0, 1)$ ; dashed-dotted curve ((0, 0) (1st)) the first-excited-state energy in the sector with  $(S, T) = (0, 0)$

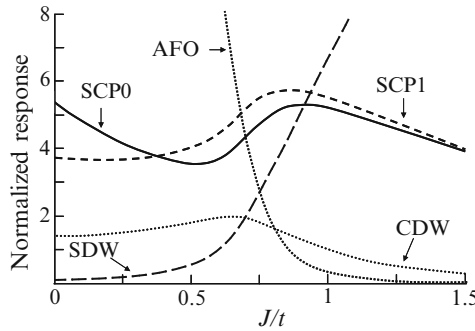


**Fig. 10** The normalized response functions for  $t = \omega_0$ ,  $g = \omega_0$ , and  $J/U' = 0.5$ . SCP0 is the response of the singlet Cooper pairing with pseudospin zero ( $\tilde{\chi}^{p0}$ ), SCP1 that of the singlet Cooper pairing with pseudospin one ( $\tilde{\chi}^{p1}$ ), AFO the antiferro-orbital ordering ( $\tilde{\chi}^o$ ), SDW ( $\tilde{\chi}^s$ ), and CDW ( $\tilde{\chi}^c$ ). Note that the results for SCP0, SCP1, and CDW are given in ten times magnification

brought about by the electron hopping term or the superexchange antiferromagnetic interaction. From this viewpoint, this phase should be regarded as an inter-site singlet state rather than a local-triplet state. Finally in the strong-coupling region, the first-excited state changes into the one with  $S = 1$ , implying the dominance of spin fluctuations.

The results for the response functions are plotted in Fig. 10 in which a sharp crossover and the concomitant enhancement of SCP0 and SCP1 are seen. (The total number of excited phonons in the system was cut off at sixteen, which is enough for convergence.)

In the weak-coupling region, the AFO response is largest, as expected from the result of  $T = 1$  for the first-excited state (see Fig. 9) and the electrons form local singlet states with either the total-pseudospin-zero state (P0) described by

$(d_{j\alpha\uparrow}^\dagger d_{j\beta\downarrow}^\dagger - d_{j\alpha\downarrow}^\dagger d_{j\beta\uparrow}^\dagger)/\sqrt{2}$  or the total-pseudospin-one state (P1) described by either  $d_{j\alpha\uparrow}^\dagger d_{j\alpha\downarrow}^\dagger$  or  $d_{j\beta\uparrow}^\dagger d_{j\beta\downarrow}^\dagger$ . The weight of the P0 state is larger than that of the P1 state, leading to the larger response in SCP0 than that in SCP1. As  $J$  is gradually turning on, both AFO and SCP response functions begin to decrease, reflecting the gradual breaking of the local singlet pairing.

In the intermediate-coupling region, SCP0 and SCP1 cease to decrease and then increase; each has a peak in the vicinity of the crossover from AFO to SDW states. This enhancement corresponds to the growth of the inter-site pairing, as seen by inspecting the forms for P0 and P1. In this region, P0 is represented by either  $(d_{1\alpha\uparrow}^\dagger d_{2\beta\downarrow}^\dagger - d_{1\alpha\downarrow}^\dagger d_{2\beta\uparrow}^\dagger)/\sqrt{2}$  or  $(d_{1\beta\uparrow}^\dagger d_{2\alpha\downarrow}^\dagger - d_{1\beta\downarrow}^\dagger d_{2\alpha\uparrow}^\dagger)/\sqrt{2}$ , while P1 by either  $(d_{1\alpha\uparrow}^\dagger d_{2\alpha\downarrow}^\dagger - d_{1\alpha\downarrow}^\dagger d_{2\alpha\uparrow}^\dagger)/\sqrt{2}$  or  $(d_{1\beta\uparrow}^\dagger d_{2\beta\downarrow}^\dagger - d_{1\beta\downarrow}^\dagger d_{2\beta\uparrow}^\dagger)/\sqrt{2}$ . Then the diagonal hopping makes SCP1 dominate over SCP0.

In the strong-coupling region, the SDW response dominates, as expected from the result of  $S = 1$  for the first-excited state (see Fig. 9). The decrease of the SCP0 and SCP1 responses can be understood in terms of the Lehmann representation of  $\chi^p$  as

$$\lim_{\omega \rightarrow 0} \chi^p(\omega) = - \sum_n \frac{|\langle 2, n | \Phi | G \rangle|^2 + |\langle 6, n | \Phi^\dagger | G \rangle|^2}{E(2, n) + 2\mu - E_G}, \quad (40)$$

where  $|G\rangle$  is the ground state,  $|N, n\rangle$  denotes the  $n$ th excited state of the  $N$ -electron system,  $E(N, n)$  is its energy. (In deriving (40), we have exploited particle-hole symmetry.) In the two-electron system, each electron becomes localized at a different site as  $J$  increases, leading to the saturation of the ground-state energy  $E(2, 0)$ , but the situation is different in the four-electron system;  $E_G$  does not saturate but increases almost linearly with  $U' - J$ . Thus the energy denominator  $E(2, n) + 2\mu - E_G$  becomes large as  $J$  and  $U'$  increase with keeping  $J/U'$  fixed, resulting in the decrease of the SCP0 and SCP1 responses. Physically, the period of antiferromagnetic order is comparable to the coherence length of the spin-singlet Cooper pair and these two orders do not coexist in this situation.

We have also explored the situation in which  $g$  is increased with other parameters kept fixed. The qualitative behaviors of the response functions are almost the same as those along the line I, except for the sharpness of the crossover, as illustrated in Fig. 11 for the number of excited phonons associated with each electron.

### 4.3 Two-Band Hubbard Model with Hund's-rule coupling

Inspired by fullerene superconductors, Capone et al. [68] studied a two-band (or two-orbital) Hubbard model, defined by the Hamiltonian  $H$  described as



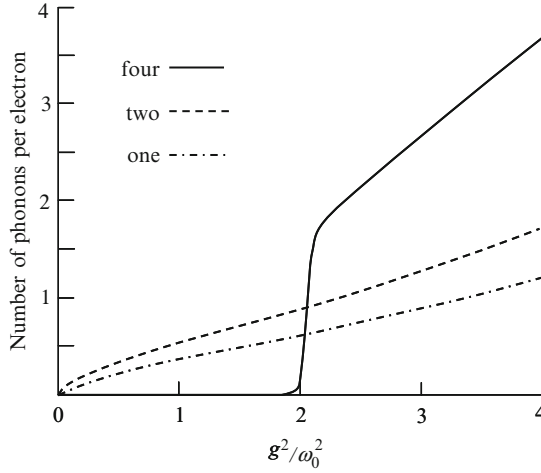


**Fig. 11** The number of phonons per electron of the two-site  $E \otimes e$  system for  $t = \omega_0$ ,  $U' = 3\omega_0$ , and  $J = 1.5\omega_0$ . The *solid curve* (four) represents the result for the four-electron system, the *dashed curve* (two) for the singlet two-electron system, and the *dashed-dotted curve* (one) for the single-electron system. (We have achieved convergence by cutting off the total number of excited phonons at thirty-two in this four-electron system)

$$\begin{aligned}
 H = & -t \sum_{\langle j, j' \rangle} \sum_{\gamma\sigma} \left( d_{j\gamma\sigma}^\dagger d_{j'\gamma\sigma} + d_{j'\gamma\sigma}^\dagger d_{j\gamma\sigma} \right) \\
 & + \frac{\bar{U}}{2} \sum_j n_j(n_j - 1) + 2\bar{J} \sum_{j\sigma\sigma'} d_{j\alpha\sigma}^\dagger d_{j\beta\sigma'}^\dagger d_{j\alpha\sigma'} d_{j\beta\sigma}, \quad (41)
 \end{aligned}$$

with  $\bar{U} \geq 0$  and  $\bar{J} \leq 0$ . Note that (1) the sign of  $\bar{J}$  is *negative*, and (2) this Hamiltonian can be regarded as an effective Hamiltonian for the  $E \otimes e$  molecular-crystal model in the anti-adiabatic and *weak-coupling* regime of  $g$ , but the effect of  $g$  dominates over the Hund's-rule coupling. The ground state of this model was analyzed around half-filling by means of DMFT. Since the electrons locally form a singlet state due to the inverted Hund's-rule coupling, this system goes to a *local-singlet Mott insulator* in the limit of  $\bar{U} \rightarrow \infty$  at half-filling. Attention was paid to the physics near this Mott transition.

Using DMFT, Capone et al. calculated the  $s$ -wave superconducting gap  $\Delta$  as a function of  $\bar{U}$  and obtained an intriguing ground-state phase diagram in the  $(\bar{U}/W, \delta)$  space, shown in Fig. 12, where  $\delta$  is the doping concentration. It is remarkable that in the very weak-coupling region of  $\bar{J}$  ( $|\bar{J}|/W = 0.05$  with  $W$  the bare bandwidth),  $\bar{U}$  enhances the Cooper pairing close to the Mott transition ( $\bar{U}/W \sim 0.8$ ), as called *the strongly correlated superconductivity* (SCS). Another DMFT analysis by Han [110], based on the  $E \otimes e$  molecular crystal model without the usual Hund's-rule coupling, supported the emergence of this SCS.

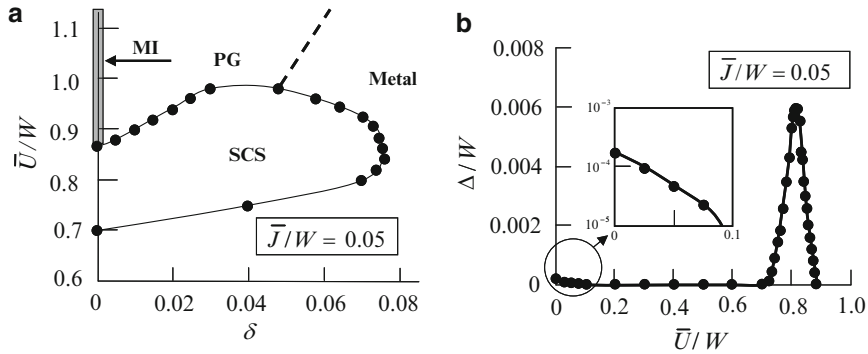


**Fig. 12** (a) Ground-state phase diagram for the model with inverted Hund's-rule coupling with  $\delta$  the doping concentration. (b) Superconducting gap at half filling as a function of  $\bar{U}/W$  [112]. MI, PG, and SCS indicate Mott insulating, pseudogap, and strongly-correlated superconducting phases, respectively

The scenario leading to SCS is explained as follows: In the Hamiltonian (41), there are two interactions,  $\bar{U}$  and  $\bar{J}$ .  $\bar{J}$  is an attraction responsible for the Cooper pairing, while  $\bar{U}$  is a repulsive interaction to renormalize  $W$  into the narrower effective bandwidth  $W^*$ , which is given by  $W^* = zW$  with  $z$  the renormalization factor. Since  $\bar{J}$  is not anticipated to be renormalized by  $\bar{U}$  [67], the ratio  $|\bar{J}|/W^*$  becomes larger as  $\bar{U}$  increases. As is suggested by studies on the attractive Hubbard model [111],  $\Delta$  may become large, if the effective bandwidth and the attraction become comparable, leading to the peak structure in  $\Delta$  as a function of  $\bar{U}$  for  $|\bar{J}|/W^* \sim 1$ .

In real systems, the effectively negative  $\bar{J}$  inevitably indicates the rather strong  $g_{E \otimes e}$  in competition with the bare Coulombic orbital-exchange interaction  $J$ . Then, as shown in Fig. 11, there would appear the effects of  $g_{E \otimes e}$  that are not included in the simple reduction leading to  $\bar{J}$ . Study of the  $E \otimes e$  JT system with fully including the dynamic phonon effects and faithfully treating the Hund's-rule coupling is an important challenge.

#### 4.4 Bipolaron Superconductivity

Although the intermediate-coupling region is realistic and most interesting, it is also most difficult to treat accurately. Before considering this difficult problem, it would be helpful to investigate extreme situations of weak- and strong-coupling regions.

In the former region, an electron–phonon interaction brings about an attraction between electrons, leading to superconductivity in the BCS scenario. In this sense, it is a well-explored region. In the strong-coupling region, on the other hand, it is not the case, although the concept of bipolaron superconductivity is

believed to be basically correct. In fact, the scenario of Bose–Einstein condensation (BEC) of many bipolarons is not matured enough, because many issues including the mass enhancement/renormalization and the repulsion between bipolarons are not satisfactorily solved yet. In this subsection, we shall touch on this bipolaron superconductivity.

Let us start with the  $A \otimes a$  Holstein model. In the strong-coupling region, it is usually the case to employ the Lang-Firsov transformation [80], defined as

$$\tilde{c}_{j\sigma} = e^{-iS} c_{j\sigma} e^{iS} = e^{\lambda(a_j - a_j^\dagger)} c_{j\sigma}, \text{ and } \tilde{a}_j = e^{-iS} a_j e^{iS} = a_j - \lambda n_j, \quad (42)$$

where  $\lambda = g_{A \otimes a} / \omega_0$  and

$$S = i\lambda \sum_j n_j (a_j - a_j^\dagger). \quad (43)$$

Then the original Holstein Hamiltonian  $H_H$  is rewritten with these new variables by

$$\begin{aligned} H_H = & -t \sum_{(j,j')\sigma} (c_{j\sigma}^\dagger c_{j'\sigma} + c_{j'\sigma}^\dagger c_{j\sigma}) + \omega_0 \sum_j \tilde{a}_j^\dagger \tilde{a}_j \\ & - 2\lambda^2 \omega_0 \sum_j \tilde{n}_{j\uparrow} \tilde{n}_{j\downarrow} - (\mu + \lambda^2 \omega_0) \sum_j \tilde{n}_j. \end{aligned} \quad (44)$$

Treating the first two terms in the right hand side of (44) within second-order perturbation, we obtain

$$H_{\text{eff}} = -\tilde{t} \sum_{(j,j')} (B_j^\dagger B_{j'} + B_{j'}^\dagger B_j) + 2\tilde{V} \sum_{(j,j')} \rho_j \rho_{j'} - 2\tilde{\mu} \sum_j \rho_j, \quad (45)$$

where the the quasi-boson operator  $B_j^\dagger$  and its density operator  $\rho_j$  are defined as

$$B_j^\dagger = \tilde{c}_{j\uparrow}^\dagger \tilde{c}_{j\downarrow}, \text{ and } \rho_j = \tilde{n}_{j\sigma} = \frac{1}{2} \tilde{n}_j, \quad (46)$$

respectively. The various parameters in (44) have been defined by

$$\tilde{t} = \frac{2t^2}{\omega_0} e^{-2\lambda^2} \sum_{nm} \frac{(-1)^{n+m}}{n!m!} \frac{\lambda^{2(n+m)}}{n+m+2\lambda^2}, \quad (47)$$

$$\tilde{V} = \frac{2t^2}{\omega_0} e^{-2\lambda^2} \sum_{nm} \frac{1}{n!m!} \frac{\lambda^{2(n+m)}}{n+m+2\lambda^2}, \quad (48)$$

$$\tilde{\mu} = \mu + 2\lambda^2 \omega_0 + \frac{1}{2} z \tilde{V}, \quad (49)$$

where  $z$  is the coordination number.

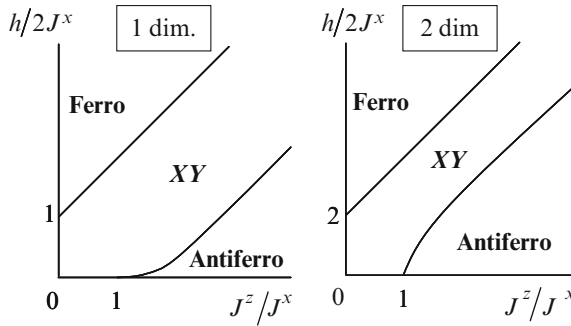


**Fig. 13** Schematic ground-state phase diagram for the spin-1/2  $XXZ$  model in the magnetic field in one [115] and two dimensions [119]. The line of  $h = 0$  corresponds to the half-filling in the Holstein model. Antiferromagnetic, ferromagnetic, and  $XY$  phases correspond, respectively, to charge density wave, band insulating, and superconducting states in the Holstein model

Now, by exploiting the similarity of the commutation relations of  $[B_j, B_j^\dagger] = (1 - 2\rho_j)\delta_{jj'}$  and  $[S_j^-, S_j^+] = -2S_j^z\delta_{jj'}$ , we can introduce *the exact mapping* of the operators  $B_j^\dagger$  and  $\rho_j$  to the spin 1/2 operators through

$$B_j^\dagger \rightarrow S_j^+, \text{ and } \rho_j \rightarrow S_j^z + 1/2. \quad (50)$$

With this exact mapping, we can transform  $H_H$  to the Hamiltonian  $H_{XXZ}$  representing the spin-1/2 quantum  $XXZ$  model [113, 114], written by

$$H_{XXZ} = 2 \sum_{\langle j,j' \rangle} \left( J^x S_j^x S_{j'}^x + J^y S_j^y S_{j'}^y + J^z S_j^z S_{j'}^z \right) - h \sum_j S_j^z, \quad (51)$$

where the parameters  $J^x$ ,  $J^y$ ,  $J^z$ , and  $h$  are, respectively, defined by<sup>3</sup>

$$J^x = J^y = \tilde{t}, J^z = \tilde{V}, \text{ and } h = 2\mu + 4\lambda^2\omega_0. \quad (52)$$

The spin-1/2  $XXZ$  model has been extensively investigated, especially for the case of one dimension by both the Bethe–ansatz approach [115] and field-theoretic methods [116]. In Fig. 13, the ground-state phase diagram is shown in the  $(h/2J^x, J^z/J^x)$  space. In the regions specified by “Ferro” and “Antiferro”, the ground state is characterized by a finite energy gap excitation, indicating that the corresponding state in the mapped Holstein system is an insulator. More specifically, the former corresponds to a band insulating state, while the latter to a CDW phase. In the region indicated by “ $XY$ ”, the gapless ground state appears, implying the

<sup>3</sup> The sign of  $J^x$  can be changed by a canonical transformation without changing those of  $h$  and  $J^z$ , and is not essential. The ratios of  $J^z/J^x$  and  $h/J^x$  are relevant.

appearance of a conducting state. According to Leggett [117], the conducting phase in a pure Bose system is assumed to be always superfluid at zero temperature.

In two dimensions, the ground-state phase diagram has been obtained by quantum Monte Carlo simulation [118, 119]. There is a little difference in the vicinity of the Heisenberg point ( $J^x = J^z$ ) from that in one dimension, but they are qualitatively quite similar.

The  $XXZ$  model is equivalent to a hard-core Bose–Hubbard model with only nearest-neighbor hopping and interaction. Recently the Bose–Hubbard model has been investigated, but exact phase diagrams have not been obtained so far in three or larger dimensions. It is hoped that DMFT will clarify the phase diagram in infinite dimensions.

Finally we consider the JT bipolarons. In the original  $E \otimes e$  model, two vibrational modes are doubly-degenerate. Instead, we treat the  $E \otimes (b_1 + b_2)$  model, the Hamiltonian of which reads

$$H = - \sum_{\langle j,j' \rangle} \sum_{\sigma \gamma \gamma'} t_{\gamma \gamma'} \left( c_{j\gamma\sigma}^\dagger c_{j'\gamma'\sigma} + c_{j'\gamma'\sigma}^\dagger c_{j\gamma\sigma} \right) - \mu \sum_j n_j + \sum_j \sum_{l=1,2} \omega_l a_{jl}^\dagger a_{jl} \\ + g_1 \sum_j (n_{j\alpha} - n_{j\beta}) (a_{j1} + a_{j1}^\dagger) + g_2 \sum_{j\sigma} \left( c_{j\alpha\sigma}^\dagger c_{j\beta\sigma} + c_{j\beta\sigma}^\dagger c_{j\alpha\sigma} \right) (a_{j2} + a_{j2}^\dagger). \quad (53)$$

When  $g_1 = g_2$  and  $\omega_1 = \omega_2$ , this model is reduced to the  $E \otimes e$  JT system. For simplicity, we assume that  $g_1/\omega_1 \gg g_2/\omega_2$  and treat the  $g_2$  term within second-order perturbation. By adopting a similar method in treating the Holstein model, we can map the  $E \otimes (b_1 + b_2)$  model into the effective spin model as

$$H = 2 \sum_{\langle j,j' \rangle} \sum_{\gamma \gamma'} \sum_p J_{\gamma \gamma'}^p S_{j\gamma}^p S_{j'\gamma'}^p + 2 \sum_{j\mathbf{p}} J_{\perp}^p S_{j\alpha}^p S_{j\beta}^p - h \sum_{j\gamma} S_{j\gamma}^z, \quad (54)$$

where  $h = 2\mu$  and other parameters are given as

$$J_{\gamma \gamma'}^x = J_{\gamma \gamma'}^y = \frac{2t_{\gamma \gamma'}^2}{\omega_1} e^{-2\lambda_1^2} \sum_{nm} \frac{(-1)^{n+m}}{n!m!} \frac{\lambda_1^{2(n+m)}}{n+m+2\lambda_1^2}, \quad (55)$$

$$J_{\gamma \gamma'}^z = \frac{2t_{\gamma \gamma'}^2}{\omega_1} e^{-2\lambda_1^2} \sum_{nm} \frac{1}{n!m!} \frac{\lambda_1^{2(n+m)}}{n+m+2\lambda_1^2}, \quad (56)$$

$$J_{\perp}^x = J_{\perp}^y = \frac{2g_2^2}{\omega_1} e^{-4\lambda_1^2} \sum_n \frac{1}{n!} \frac{(-1)^n (2\lambda_1)^{2n}}{n+2\lambda_1^2+\omega_2/\omega_1}, \quad (57)$$

$$J_{\perp}^z = 4\lambda_1^2 \omega_1 + \frac{2g_2^2}{\omega_1} e^{-4\lambda_1^2} \sum_n \frac{1}{n!} \frac{(2\lambda_1)^{2n}}{n+2\lambda_1^2+\omega_2/\omega_1}. \quad (58)$$

Note (1) there are two kinds of spins  $S_\alpha$  and  $S_\beta$  per site and (2)  $J_{\perp}^z$  is much larger than the other interaction parameters.

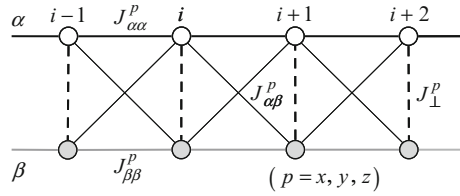


**Fig. 14** Schematic representation of the effective spin model for the  $E \otimes (b_1 + b_2)$  molecular crystal system in one dimension.  $J_{\gamma\gamma'}^p$  ( $\gamma, \gamma' = \alpha, \beta$ ;  $p = x, y, z$ ) denotes the interaction between nearest-neighbor spins  $\gamma$  and  $\gamma'$ .  $J_{\perp}^p$  is the on-site interaction between  $\alpha$  and  $\beta$  at the same site

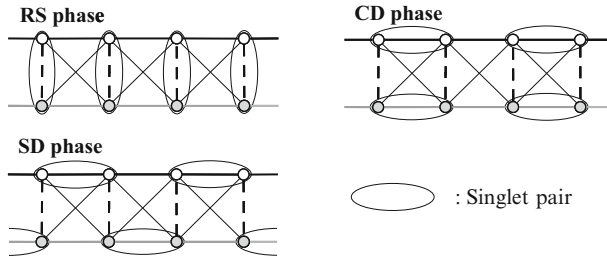


**Fig. 15** Schematic pictures for three phases that may exist in the relevant parameter region at half-filling. RS denotes rung singlet, CD columnar dimerization, and SD staggered dimerization, respectively. There may be other possible phases

In one dimension, this spin model is represented by a two-leg ladder system [120] as shown in Fig. 14 and examples of possible phases are schematically given in Fig. 15. In two dimensions, we may think of the effective spin model as shown in Fig. 16. As we see, those spin models are the subject of intense researches in relation to HTSC and at present we cannot give a further reliable information.

## 5 Conclusions and Future Prospects

We have reviewed the recent developments in the field of the Jahn–Teller effect on itinerant electrons in Jahn–Teller crystals. In Sect. 1, we have summarized the current status of the researches on the fullerene superconductors and the manganite perovskites exhibiting the colossal magnetoresistance and concluded that, although various impressive findings have been made in relation to those oxides, there still remain many challenging problems, reflecting the intrinsic complexities of those materials. In Sect. 2–4, we have focused on the model JT systems, in particular, the canonical  $E \otimes e$  model, and discussed some of the interesting features of polarons and bipolarons in the JT crystals, including our own original contributions.

In concluding this review, we have to admit that the researches on the JT effect on itinerant electrons are still in a very early stage, considering the richness of the

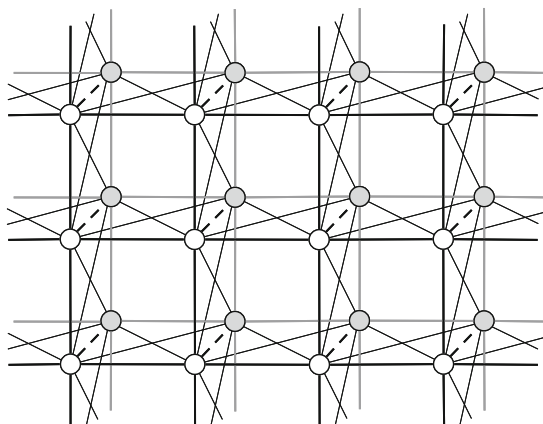


**Fig. 16** Schematic representation of the effective spin model for the  $E \otimes (b_1 + b_2)$  molecular crystal system in two dimensions. The two-leg ladders, each of which represents a one-dimensional  $E \otimes (b_1 + b_2)$  crystal, are piled in the direction of  $z$  axis

problem concerning the interplay among spin, charge, orbital, and phonon degrees of freedom. We would presume that this field of research will pose very good challenging projects for the next-generation supercomputers and hope that such heavy numerical works will open a new rich field of physics and chemistry.

**Acknowledgements** This work was partially supported by Global COE Program “the Physical Sciences Frontier”, the Ministry of Education, Culture, Sports, Science, and Technology (MEXT), Japan as well as by a Grant-in-Aid for Scientific Research in Priority Areas “Development of New Quantum Simulators and Quantum Design” (No.17064004) of MEXT, Japan. We would like to thank M. Kaplan, H. Koizumi, T. Hotta, and H. Maebashi for useful discussions for years.

## References

1. H.A. Jahn, E. Teller, *Proc. R. Soc. Lond.* **A161**, 220 (1937)
2. R. Engleman, *The Jahn–Teller Effect in Molecules and Crystals* (Wiley, New York, 1972)
3. I.B. Bersuker, *The Jahn–Teller Effect* (Cambridge University Press, Cambridge, 2006)
4. M.D. Kaplan, B.G. Vekhter, *Cooperative Phenomena in Jahn–Teller Crystals* (Plenum, New York, 1995)
5. J.G. Bednorz, K.A. Müller, *Z. Phys. B* **64**, 189 (1986)
6. A.F. Hebard, M.J. Rosseinsky, R.C. Haddon, D.W. Murphy, S.H. Glarum, T.T.M. Palstra, A.P. Ramirez, A.R. Kortan, *Nature* **350**, 600 (1991)
7. S. Jin, T.H. Tiefel, M. McCormack, R.A. Fastnacht, R. Ramesh, J.H. Chen, *Science* **264**, 413 (1994)
8. Y. Tokura, Y. Tomioka, H. Kuwabara, A. Asamitsu, Y. Moritomo, M. Kasai, *J. Appl. Phys.* **79**, 5288 (1996)
9. C. Zener, *Phys. Rev.* **82**, 403 (1951)
10. P.W. Anderson, H. Hasegawa, *Phys. Rev.* **100**, 675 (1955)
11. P.-G. de Gennes, *Phys. Rev.* **118**, 141 (1960)

12. A.J. Millis, P.B. Littlewood, B.I. Shariman, Phys. Rev. Lett. **74** 5144 (1995)
13. N. Mannella, A. Rosenhahn, C.H. Booth, S. Marchesini, B.S. Mun, S.-H. Yang, K. Ibrahim, Y. Tomioka, C.S. Fadley, Phys. Rev. Lett. **92** 166401 (2004)
14. Z. Popovic, S. Satpathy, Phys. Rev. Lett. **84** 1603 (2000)
15. C. Ederer, C. Lin, A.J. Millis, Phys. Rev. B **76** 155105 (2007)
16. A.P. Ramirez, J. Phys. : Condens. Matter **9**, 8171 (1997)
17. A. Mareo, S. Yunoki, E. Dagotto, Science **283** 2034 (1999)
18. Y. Tokura, in *Colossal Magnetoresistive Oxides*, ed. by Y. Tokura (Gordon & Breach, Amsterdam, 2000)
19. Y. Tokura, N. Nagaosa, Science **288** 462 (2000)
20. E. Dagotto, T. Hotta, A. Moreo, Phys. Rep. **344** 1 (2001)
21. M.B. Salamon, M. Jaime, Rev. Mod. Phys. **73** 583 (2001)
22. Y. Takada, T. Hotta, Int. J. Mod. Phys. B **15** 4267 (2001)
23. J. van den Brink, D. Khomskii, Phys. Rev. B **63** 140416(R) (2001)
24. T. Hotta, Y. Takada, H. Koizumi, Int. J. Mod. Phys. B **12** 3437 (1998)
25. T. Hotta, Y. Takada, H. Koizumi, E. Dagotto, Phys. Rev. Lett. **84** 2477 (2000)
26. Y. Takada, T. Hotta, H. Koizumi, Int. J. Mod. Phys. B **13** 3778 (1999)
27. T. Holstein, Ann. Phys. **8** 325 (1959)
28. C.M. Varma, J. Zaanen, K. Raghavachari, Science **254** 989 (1991)
29. M. Schluter, M. Lannoo, M. Needels, G.A. Baraff, D. Tomanek, Phys. Rev. Lett. **68** 526 (1992)
30. I.I. Mazin, S.N. Rashkeev, V.P. Antropov, O. Jepsen, A.I. Liechtenstein, O.K. Andersen, Phys. Rev. B **45** 5114 (1992)
31. S. Suzuki, K. Nakao, Phys. Rev. B **52** 14206 (1995)
32. A.P. Ramirez, Superconduct. Rev. **1** 1 (1994)
33. M.P. Gelfand, Superconductivity Review **1** 103 (1994)
34. O. Gunnarsson, Rev. Mod. Phys. **69** 575 (1997)
35. L. Degiorgi, Adv. Phys. **47** 207 (1998)
36. Y. Takada, T. Hotta, Int. J. Mod. Phys. B **12** 3042 (1998)
37. B. Sundqvist, Adv. Phys. **48** 1 (1999)
38. S. Suzuki, S. Okada, K. Nakao, J. Phys. Soc. Jpn. **69** 2615 (2000)
39. O. Gunnarsson, *Alkali-Doped Fullerenes* (World Scientific, Singapore, 2004)
40. T.W. Ebbesen, J.S. Tsai, K. Tanigaki, J. Tabuchi, Y. Shimakawa, Y. Kubo, I. Hirosawa, J. Mizuki, Nature **355** 620 (1992)
41. A.P. Ramirez, A.R. Kortan, M.J. Rosseinsky, S.J. Duclos, A.M. Muijsce, R.C. Haddon, D.W. Murphy, A.V. Makhija, S.M. Zahurak, K.B. Lyons, Phys. Rev. Lett. **68** 1058 (1992)
42. A.A. Zakhidov, K. Imaeda, D.M. Petty, K. Yakushi, H. Inokuchi, K. Kikuchi, I. Ikemoto, S. Suzuki, Y. Achiba, Phys. Lett. A **164** 355 (1992)
43. C.-C. Chen, C.M. Lieber, J. Am. Chem. Soc. **114**, 3141 (1992)
44. W.L. McMillan, Phys. Rev. **167** 331 (1968)
45. P.B. Allen, R.C. Dynes, Phys. Rev. B **12** 905 (1975)
46. T. Yildirim, J.E. Fischer, R. Dinnebier, P.W. Stephens, C.L. Lin, Solid State Commun. **93** 269 (1995)
47. G.M. Eliashberg, Sov. Phys. JETP **11** 696 (1960)
48. A.B. Migdal, Sov. Phys. JETP **7** 996 (1958)
49. Y. Takada, J. Phys. Chem. Solids **54** 1779 (1993)
50. O. Gunnarsson, G. Zwirnagl, Phys. Rev. Lett. **69** 957 (1992)
51. N. Manini, E. Tosatti, A. Auerbach, Phys. Rev. B **49** 13008 (1994)
52. L.F. Chibotaru, A. Ceulemans, Phys. Rev. B **53** 15522 (1996)
53. C.C. Chancey, M.C.M. O'Brien, *The Jahn–Teller Effect in C<sub>60</sub> and Other Icosahedral Complexes* (Princeton University Press, Princeton, 1997)
54. S. Wehrli, M. Sigrist, Phys. Rev. B **76** 125419 (2007)
55. Y. Wang, R. Yamachika, A. Wachowiak, M. Grobis, M.F. Crommie, Nat. Mater. **7** 194 (2008)
56. D.M. Deaven, D.S. Rokhsar, Phys. Rev. B **48** 4114 (1993)
57. C.-C. Chen, C.M. Lieber, Science **259** 655 (1993)



58. M. Riccò, F. Gianferrari, D. Pontiroli, M. Belli, C. Bucci, T. Shiroka, Europhys. Lett. **81** 57002 (2008)
59. A. Georges, G. Kotliar, W. Krauth, M.J. Rozenberg, Rev. Mod. Phys. **68** 13 (1996)
60. J.E. Han, O. Gunnarsson, V.H. Crespi, Phys. Rev. Lett. **90** 167006 (2003)
61. T. Yildirim, L. Barbedette, J.E. Fischer, C.L. Lin, J. Robert, P. Petit, T.T.M. Plastr, Phys. Rev. Lett. **77** 167 (1996)
62. E. Cappelluti, P. Paci, C. Grimaldi, L. Pietronero, Phys. Rev. B **72**, 054521 (2005)
63. Y. Takada, Physica C **364-365** 71 (2001)
64. J.E. Han, E. Koch, O. Gunnarsson, Phys. Rev. Lett. **84** 1276 (2000)
65. J.E. Han, O. Gunnarsson, Phys. B **292** 196 (2000)
66. Y. Iwasa, H. Shimoda, T.T.M. Palstra, Y. Maniwa, O. Zhou, T. Mitani, Phys. Rev. B **53** R8836 (1996)
67. M. Capone, M. Fabrizio, C. Castellani, E. Tosatti, Science **296** 2364 (2002)
68. M. Capone, M. Fabrizio, C. Castellani, E. Tosatti, Phys. Rev. Lett. **93** 047001 (2004)
69. K. Tanigaki, I. Hirose, T.W. Ebbesen, J. Mizuki, J.S. Tsai, J. Phys. Chem. Solids **54** 1645 (1993)
70. Y. Takada, Int. J. Mod. Phys. B **21** 3138 (2007)
71. Y. Takada, J. Phys. Soc. Jpn. **65** 3134 (1996)
72. Y. Takada, J. Phys. Soc. Jpn. **65** 1544 (1996)
73. M.R. Schafroth, S.T. Butler, J.M. Blatt, Helv. Phys. Acta **30** 93 (1957)
74. J.M. Blatt *Theory of Superconductivity* (Academic, New York, 1964)
75. A.S. Alexandrov, J. Ranninger, Phys. Rev. B **23** 1796 (1981)
76. A.S. Alexandrov, J. Ranninger, Phys. Rev. B **24** 1164 (1981)
77. Y. Takada, Phys. Rev. B **26** 1223 (1982)
78. A.S. Alexandrov, N.F. Mott, *Polarons and Bipolarons* (World Scientific, Singapore, 1995)
79. D.R. Pooler, J. Phys. A: Math. Gen. **11** 1045 (1978)
80. I.G. Lang, Yu. A. Firsov, Sov. Phys. JETP **16** 1301 (1963)
81. T.D. Lee, F.E. Low, D. Pines, Phys. Rev. **90** 297 (1953)
82. H. Fröhlich, Phys. Rev. **79** 845 (1950)
83. P.E. Kornilovitch, Phys. Rev. Lett. **81** 5382 (1998)
84. E. Jeckelmann, S.R. White, Phys. Rev. B **57** 6376 (1998)
85. J. Bonča, S.A. Trugman, I. Batistič, Phys. Rev. B **60** 1633 (1999)
86. J. Bonča, T. Katrašnik, S.A. Trugman, Phys. Rev. Lett. **84** 3153 (2000)
87. S. Ciuchi, F. de Pasquale, S. Fratini, D. Feinberg, Phys. Rev. B **56**, 4494 (1997)
88. A.S. Mishchenko, N.V. Prokof'ev, A. Sakamoto, B.V. Svistunov, Phys. Rev. B. **62** 6317 (2000)
89. A.S. Alexandrov (Ed.), *Polarons in Advanced Materials*: Springer series in materials science **103** (Canopus Publishing and Springer GmbH, Bath, UK, 2007).
90. H. Fehske, R. Schneider, A. Weiße (Eds.), *Computational Many-Particle Physics* (Springer, Heidelberg, 2008)
91. K. -H. Höck, H. Nickisch, H. Thomas, Helv. Phys. Acta **56** 237 (1983)
92. K. Ziegler, Phys. Rev. B **72** 075120 (2005)
93. Y. Takada, Phys. Rev. B **61** 8631 (2000)
94. P.E. Kornilovitch, Phys. Rev. Lett. **84** 1551 (2000)
95. H. Barentzen, Eur. Phys. J. B **24** 197 (2001)
96. S. El Shawish, J. Bonča, L.-C. Ku, S.A. Trugman, Phys. Rev. B **67**, 014301 (2003).
97. S.A. Trugman, L.-C. Ku, J. Bonča, J. Supercond. **17**, 193 (2004)
98. R. Ramakumar, S. Yarlagadda, Phys. Rev. B **69** 104519 (2004)
99. H. Barentzen, J. Phys.: Condes. Matter **17** 4713 (2005)
100. Y. Takada, M. Masaki, J. Mol. Struct. **838** 207 (2007)
101. Y. Takada, M. Masaki, J. Supercond. Nov. Magn. **20** 629 (2007)
102. H.C. Longuet-Higgins, U. Öpik, M.H.L. Pryce, R.A. Sack, Proc. R. Soc. Lond. **A244** 1 (1958)
103. W. Moffitt, W. Thorson, Phys. Rev. **108** 1251 (1957)
104. M.C.M. O'Brien, J. Phys. A: Math. Gen. **22** 1779 (1989)
105. Y.M. Liu, C.A. Bates, J.L. Dunn, V.Z. Polinger, J. Phys.: Condens. Matter **8** L523 (1996)

- 106. T. Okuda, A. Asamitsu, Y. Tomioka, T. Kimura, Y. Taguchi, Y. Tokura, Phys. Rev. Lett. **81** 3203 (1998)
- 107. A. Macridin, G.A. Sawatzky, M. Jarrell, Phys. Rev. B **69**, 245111 (2004)
- 108. J.E. Han, O. Gunnarsson, Phys. B **292** 196 (2000)
- 109. M. Fabrizio, E. Tosatti, Phys. Rev. B **55** 13465 (1997)
- 110. J.E. Han, Phys. Rev. B **70** 054513 (2004)
- 111. R. Micnas, J. Ranninger, S. Robaszkiewicz, Rev. Mod. Phys. **62** 113 (1990)
- 112. M. Schiró, M. Capone, M. Fabrizio, C. Castellani, Phys. Rev. B **77** 104522 (2008)
- 113. J.E. Hirsch, E. Fradkin, Phys. Rev. B **27**, 4302 (1983)
- 114. J.K. Freericks, Phys. Rev. B **48** 3881 (1993)
- 115. M. Takahashi, *Thermodynamics of One-dimensional Solvable Models* (Cambridge University Press, Cambridge, 1999)
- 116. D.C. Cabra, P. Pujol, in *Quantum Magnetism*, ed. by U. Schollwöck, J. Richter, D.J.J. Farnell, R.F. Bishop. Lect. Notes Phys. **645** (Springer, Heidelberg, 2004), p. 253
- 117. A.J. Leggett, Phys. Fenn. **8** 125 (1973)
- 118. F. Hébert, G.G. Batrouni, R.T. Scalettar, G. Schmid, M. Troyer, A. Dorneich, Phys. Rev. B, **65**, 014513 (2001)
- 119. G. Schmid, S. Todo, M. Troyer, A. Dorneih, Phys. Rev. Lett. **88**, 167208 (2002).
- 120. G.-H. Liu, H.-L. Wang, G.-S. Tian, Phys. Rev. B **77**, 214418 (2008) and references therein

# Vibronic Polarons and Electric Current Generation by a Berry Phase in Cuprate Superconductors

Hiroyasu Koizumi

**Abstract** High temperature superconductivity in cuprates occurs upon hole doping in half-filled antiferromagnetic insulating parent compounds. This insulating state is often called, a “Mott insulator” state, in which strong on-site Coulomb repulsion is the origin of the insulating behavior. Superconductivity occurs upon hole (or electron) doping in this state. In addition to the strong on-site Coulomb repulsion, a number of experimental and theoretical results indicate that strong hole-lattice interactions are present; the interactions are so strong that doped-holes become small polarons at low temperatures. In this review, we discuss the small polaron formation and its consequences in the superconductivity in cuprates. First, we will present some experimental and theoretical results that indicate the presence of strong interactions between doped-holes and the underlying lattice; especially, it is worth mentioning that a recent EXAFS experiment on  $\text{La}_{1.85}\text{Sr}_{0.15}\text{Cu}_{1-x}\text{M}_x\text{O}_4$  ( $\text{M} = \text{Mn}, \text{Ni}, \text{Co}$ ) reveals a direct connection between the local lattice distortion and superconductivity. When small polarons are formed, the mobility of the holes becomes very small; then, the system behaves as an “effectively half-filled Mott insulator (EHMI)” to an external perturbation whose interaction time is much shorter than the hole-hopping life-time. We argue that this EHFMI state is adequate for explaining the magnetic excitation spectrum in the cuprate; actually, the “hourglass-shaped magnetic excitation spectrum” is explained due to spin-wave excitations in the presence of spin-vortices with their centers at hole-occupied sites. The spin-wave excitations are composed of two types: the first (Mode I) is the one exhibits antiferromagnetic dispersion for high energy excitations, and the other (Mode II), which is a novel one, is the one has a sharp commensurate peak at the maximum excitation energy, and a broadened dispersion at energies below; this novel spin-wave excitations explain the Drude-like peak in the optical conductivity. Next, we will present a novel current generation mechanism that is compatible with the small polaron and spin-vortex formations. The unit of the current is a loop current around each spin-vortex; and a macroscopic current is generated as a collection of loop currents. The existence of such loop currents in the cuprate is supported by the fact that the enhanced Nernst signal observed in the pseudogap phase is explained by the flow of the loop currents. Lastly, we present an implication of the new current generation mechanism in the cuprate superconductivity; we will show that the superconducting transition in the underdoped cuprate is explained as an order-disorder transition of the loop currents.

# 1 Introduction

High temperature superconductivity in cuprates occurs upon hole doping in half-filled antiferromagnetic insulating parent compounds. More than 20 years has passed since the discovery of the high temperature superconductivity in cuprates [1]. Despite very extensive and intensive researches, the mechanism for it is still not elucidated.

A family of materials called “cuprates” contain  $\text{CuO}_2$  planes (Fig. 1); the electron conduction for superconductivity is believed to occur in these planes.

The parent compounds ( $x = 0$  in Fig. 2) are antiferromagnetic insulators known as Mott insulators where an insulating behavior with an antiferromagnetic spin-order occurs due to strong Coulomb repulsion [2]. This insulating state is different from the band insulator where the transport theory based on Bloch electrons is applicable. Upon hole doping ( $x > 0$ ), the long-range antiferromagnetic order disappears, and an anomalous metallic phase appears between the pseudogap temperature  $T^*$  and superconducting transition temperature  $T_c$  (Fig. 2). This metallic phase is called, the “pseudogap phase” since many phenomena associated with an energy gap formation is observed, and the elucidation of anomalous behaviors in this phase is one of the key issues to understand the cuprate.

To investigate the hole-doping effect, the optical conductivity has been measured [3] (Fig. 3). An energy gap of about 2 eV is observed in the parent compound; it is well understood as arising from an energy gap between the ground state and an excited state in which charge is transferred between a Cu atom and surrounding oxygen atoms (this peak is called the “charge-transfer peak”). Upon hole-doping, the spectral weight of the charge transfer peak decreases, and two new peaks appear; one is a Drude-like peak centered around 0 eV; the other is a mid-IR peak with its

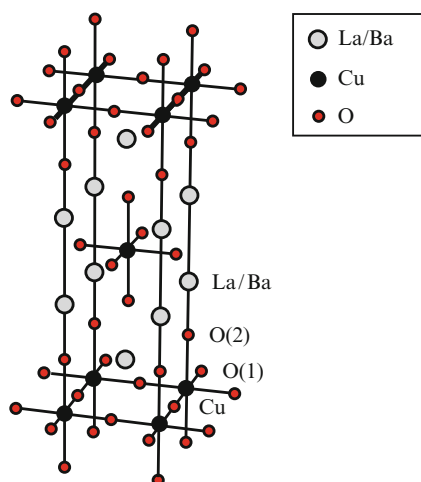
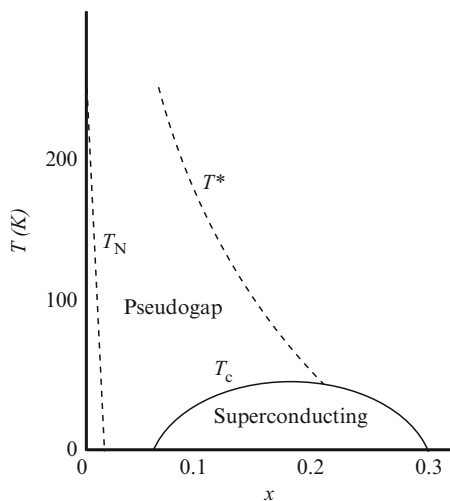
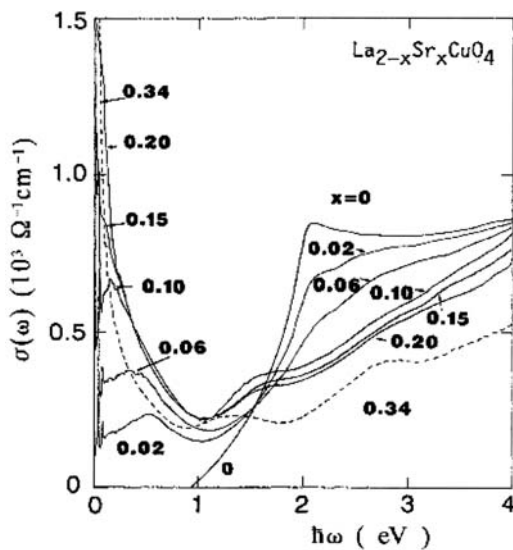


Fig. 1 The unit cell of a cuprate superconductor  $\text{La}_{1-x}\text{Ba}_x\text{CuO}_4$



**Fig. 2** A schematic phase diagram of  $\text{La}_{1-x}\text{Sr}_x\text{CuO}_4$  (LSCO).  $T_N$ ,  $T_c$ , and  $T^*$  indicate the Neel, superconducting, and pseudogap temperatures, respectively



**Fig. 3** Optical conductivity of LSCO [3]

center at around 0.5 eV for the  $x = 0.02$  sample, and shifts to lower energies as the hole concentration is increased.

The Drude-like peak may be attributed to the coherent motion of doped-holes. This assignment is based on the assumption that the conventional transport theory is applicable in the cuprate although a number of experiments indicate that metallic

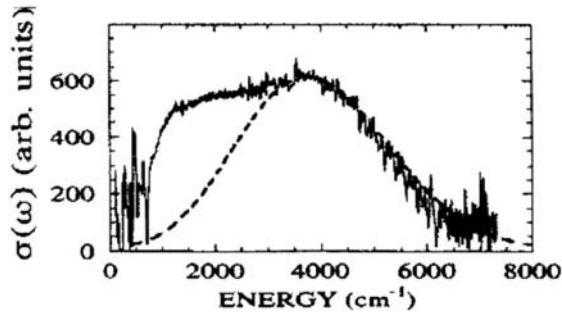


**Fig. 4** The photoinduced infrared conductivity (*solid line*) in the insulator precursor of LSCO. The *dotted line* indicates a simulation based on the small polaron transport theory [4]

phase of the cuprate is completely different from the conventional band metal; thus, this assignment is not conclusive. Nevertheless, it is the most popular assignment at present.

The mid-IR peak has been explained due to the small polaron formation since the early days of the cuprate research. A support for this assignment is the photoinduced conductivity measurement [4]; the photoinduced conductivity in LSCO (Fig. 4) shows a very similar peak to the mid-IR peak of the optical conductivity in the  $x = 0.02$  sample. It is also qualitatively explained by the small polaron transport theory [4]. However, this mid-IR peak assignment contradicts the assignment that the Drude-like peak is due to the coherent motion of holes since the former assumes that the hole-lattice interaction is so strong that doped holes become small polarons, while the latter does opposite. Therefore, if we assign that the mid-IR peak is due to small polaron formation, we have to abandon the assignment that the Drude-like peak is due to the coherent motion of doped-holes.

As is explained above, even the assignment of major peaks in the optical conductivity is unsettled even today. This fact seems to indicate that we need the transport theory that goes beyond the conventional one. Actually, there are a number of other anomalous behaviors in the pseudogap phase that strongly suggest the need for a new transport theory. In the following, we list the four most important anomalous behaviors:

1. *The metallic conductivity much less than the Ioffe-Regel-Mott limit is observed* [5](Fig. 5).

At high temperatures, the resistivity shows a positive dependence with the increase of temperature. This is a typical metallic behavior; however, the magnitude of the resistivity is much larger than the so-called, “Ioffe-Regel-Mott limit” [2]. Thus, it is suggested that the origin of the metallic behavior here may not be due to the coherent motion of doped-holes.

2. *Local spin correlation survives* [6, 7] (Fig. 6).

The magnetic excitation spectrum has an “hourglass shape”. The dispersion at high energies is very similar to the one arising from antiferromagnetic spin-wave

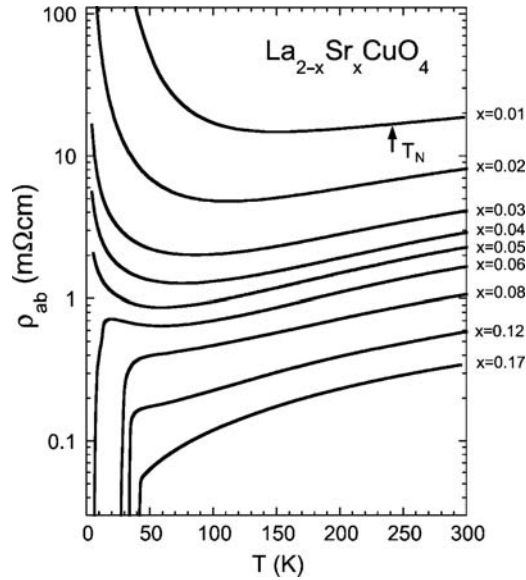


**Fig. 5** The temperature dependence of the resistivity in the  $\text{CuO}_2$  plane of LSCO [5]

excitation; thus, it is suggested that the antiferromagnetic spin-order remains locally in the underdoped cuprates. At low energies, the spectrum is significantly deviated from that of the antiferromagnetic spin-waves, where the splitting of the so-called commensurate peak  $((h, k) = (1/2, 1/2))$  into four peaks is observed.

3. *Disconnected arc-shaped “Fermi surface” is observed in the angle-resolved photoemission spectroscopy experiments* [9] (Fig. 7).

It is unusual that a Fermi surface is disconnected. Besides, it appears even at a very low doping  $x = 0.03$  where the system is an insulator [10].

4. *Large Nernst signals are observed in Nernst effect experiments* [11–13] (Fig. 8).

Very large Nernst signals are usually associated with the flow of Abrikosov vortices of superconductors. But the observed Nernst signals occur much higher temperatures than  $T_c$ ; thus, it can not be simply explained by the usual fluctuation effect of superconductivity.

The theory of the cuprate superconductivity must explain all above experimental facts, and the mechanism of the superconductivity itself. The strong Coulomb repulsion is certainly a very important ingredient as is manifested by the fact that parents compounds are Mott insulators. However, we will show that, in addition to it, strong hole–lattice interactions are also very important. In this review, we will present explanations for some of the above anomalies by including the strong hole–lattice interactions.

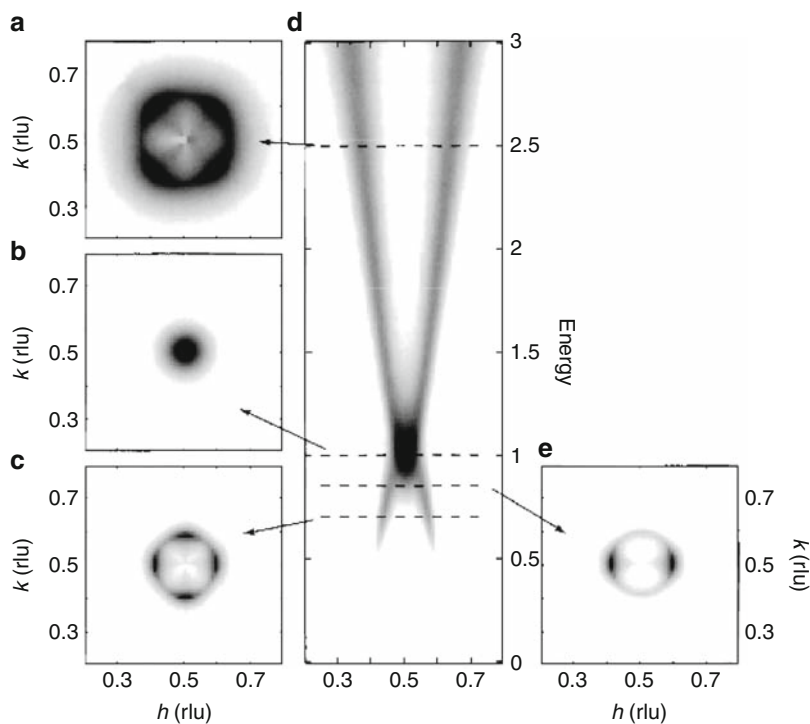


**Fig. 6** Schematic plots intended to represent neutron scattering measurement of  $\chi''(\mathbf{Q}, \omega)$  in superconducting  $\text{YBa}_2\text{Cu}_3\text{O}_{6+x}$  [8]

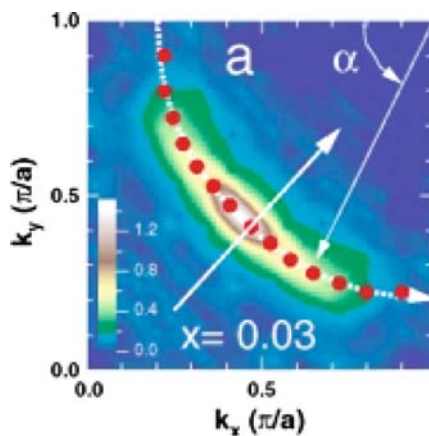


**Fig. 7** Disconnected Fermi surface, the "Fermi-arc" observed in LSCO with  $x = 0.03$  [10]



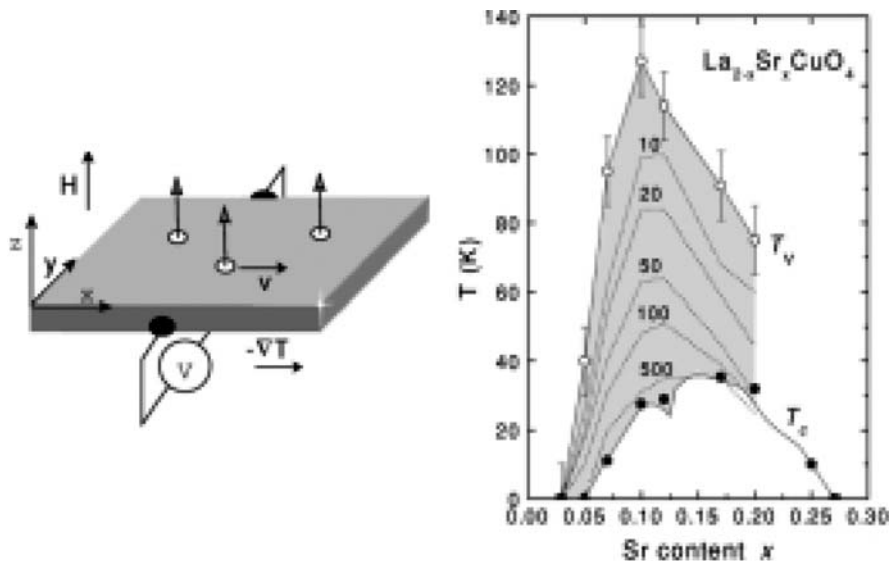


Fig. 8 Left: experimental setup for the Nernst experiment. Right: the measured Nernst signals [11]

## 2 Vibronic Character of Doped-Holes: Small Polaron Formation

Using the EXAFS method, Cu–O bond length fluctuations in  $\text{La}_{2-x}\text{Sr}_x\text{CuO}_4$  ( $x = 0.15$ ) have been measured [14] (Fig. 9). They exhibit splittings of the Cu–O distances from the average at temperatures below about 100 K (it is close to  $T^*$ ). The observed peaks of the short and long Cu–O lengths in the  $\text{CuO}_2$  plane are around 1.87 and 1.96 Å, respectively; those of apical Cu–O lengths are around 2.29 and 2.43 Å, respectively.

The local lattice instability by the hole-doping has been studied by the *molecular orbital cluster method* [15]. In this method a part of a solid, “cluster”, is embedded in a model potential that mimics the crystal environment; and the molecular orbital calculation is only performed on the cluster. The advantage of this method is that strong-electron correlation is systematically handled. However, the cluster size is rather limited, thus, a care must be taken whether it really reflects the bulk property.

Multiconfiguration molecular orbital calculations are performed on clusters with two copper atoms,  $(\text{Cu}_2\text{O}_{11})^{18-}$  and  $(\text{Cu}_2\text{O}_{11})^{17-}$ , embedded in a crystal environment for  $\text{La}_{2-x}\text{Ba}_x\text{CuO}_4$  (a crystal environment for  $\text{La}_{2-x}\text{Sr}_x\text{CuO}_4$  is essentially the same), where the former corresponds to the parent undoped cluster and the latter to the one-hole doped cluster.

In Fig. 10 potential energy curves for R2 deformation (the definition of it is given in the figure) are depicted. Some other deformations were also considered but this one is the best one to explain experimental results. As is seen, the parent cluster

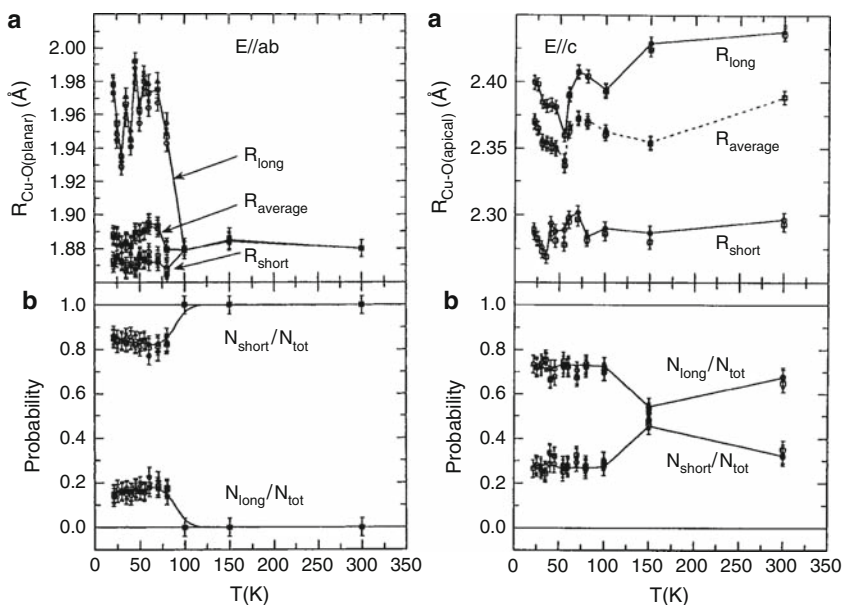


**Fig. 9** Temperature dependence of the Cu–O distances and their relative probability measured by the EXAFS experiments [14]

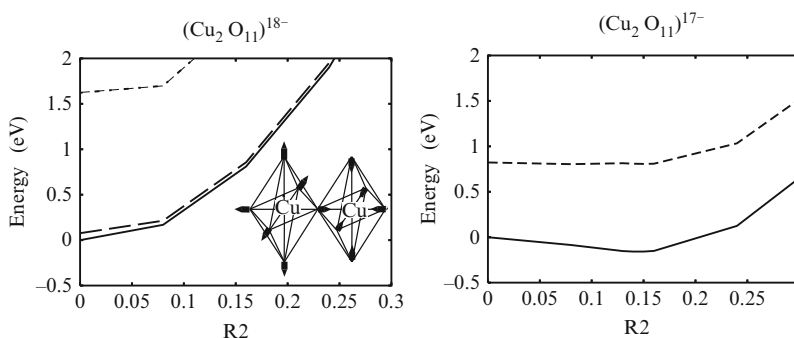


**Fig. 10** Potential energies for a local lattice deformation,  $R2$ , of  $(\text{Cu}_2\text{O}_{11})^{18-}$  and  $(\text{Cu}_2\text{O}_{11})^{17-}$ . For the unit  $R2$  deformation (anti-phase combination of the breathing vibration around the two Cu atoms), oxygen atoms move 1 (a.u.) in the directions indicated by the arrows. *Left:*  $(\text{Cu}_2\text{O}_{11})^{18-}$ ; solid, dashed, and dotted lines are used for the singlet ground, triplet ground, and singlet first excited states, respectively. *Right:*  $(\text{Cu}_2\text{O}_{11})^{17-}$ ; solid and dashed lines are used for the doublet ground and first excited states, respectively [15]

does not show any lattice instability, but the hole doped cluster does. The magnitude of the deformation is calculated as  $R2 = 0.14$  and the stabilization energy is 0.21 eV. This energy is reasonably close to the peak value observed in the photoinduced absorption spectra in Fig. 4 [4]; thus, the present results seem to support the argument that the peak is the evidence that doped holes become small polarons.

At  $R2 = 0.14$ , the Cu–O lengths in the  $\text{CuO}_2$  plane are 1.82 and 1.96 Å, respectively; these values are comparable with the experimental values, 1.87 and 1.96 Å, respectively. At  $R2 = 0.14$ , the apical Cu–O distances are 2.34 and 2.49 Å, respectively; they are close to the experimental values, 2.29 and 2.43 Å, respectively. The agreement between the calculated and experimental values is very good.

The charge-transfer energy gap is also obtained from the cluster calculation. The energy difference between the ground and first excited states in the parent cluster is about 1.6 eV, which is close to the energy gap observed in the optical conductivity [3]. By examining the wave function, the excited state is verified to be a charge-transferred one [15].

In the hole-doped cluster, the excitation energy from the ground state to the first excited state is obtained as 0.97 eV at  $R2 = 0.14$ . Actually, this value is close to a peak in the energy loss function observed in the optical conductivity (Fig. 11) [3]. Usually, a peak in the energy-loss function arises from the plasma mode excitation or a mode that strongly couples with the plasma mode. The present result suggests that it corresponds to the electronic excitation within the hole-doped cluster; this mode is expected to couple strongly with the plasma oscillation since it creates the longitudinal charge oscillation by the  $R2$  motion in the excited potential energy surface. The experimental result shows an almost fixed peak position; only its amplitude increases with the increase of  $x$ . This is in accordance with the above assignment since the number of the hole-doped clusters increases with the increase of  $x$ ; on the other hand, the peak position is fixed because the hole-doped cluster unit is unchanged by the increase of  $x$ .

Very recently, experimental results that indicate a direct connection between the local Cu–O bond fluctuation and occurrence of superconductivity have been obtained (Fig. 12) [16]. The mean squared relative displacement (MSRD) of Cu–O bond lengths in the  $\text{CuO}_2$  plane,  $\sigma_{\text{Cu-O}_p}^2$ , shows an anomalous increase below  $T^*$  and a sudden decrease around  $T_c$ . The 5% substitution of Cu by magnetic atoms, Co or Ni, suppresses superconductivity completely, and so does the anomalous behavior

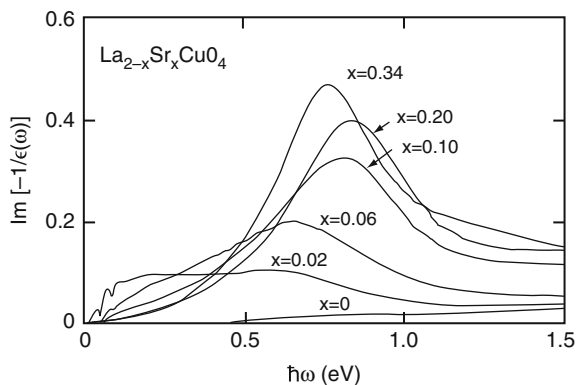


**Fig. 11**  $x$  dependence of energy-loss function [3]

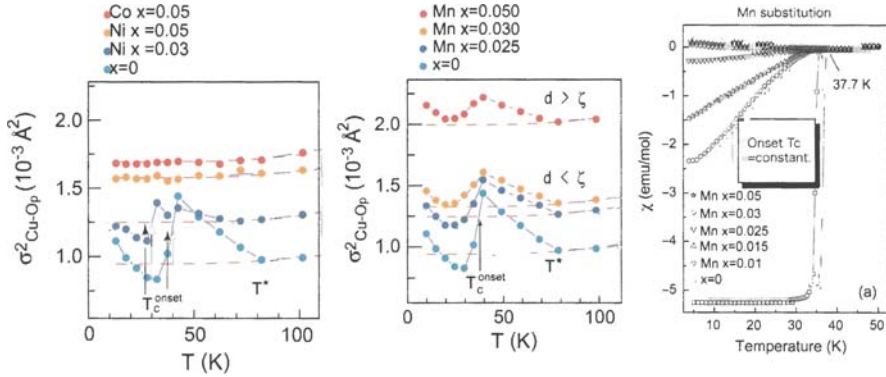


**Fig. 12** Temperature dependence of the in-plane Cu–O bond MSRD  $\sigma^2_{\text{Cu-O}_p}$  and magnetic susceptibility ( $\mathbf{B} \perp \text{CuO}_2$  plane) for  $\text{La}_{1.85}\text{Sr}_{0.15}\text{Cu}_{1-x}\text{M}_x\text{O}_4$  ( $\text{M} = \text{Mn}, \text{Ni}, \text{Co}$ ) samples [16]

in the MSRD. On the other hand, the substitution by Mn gradually suppresses the superconductivity with keeping the onset temperature and the anomalous MSRD behavior. This result clearly indicates a direct connection between the anomalous MSRD behavior and superconductivity since the lattice anomaly and the occurrence of superconductivity coincide. The lattice anomaly is most likely caused by small polaron formation; thus, a direct involvement of small polarons in superconductivity is strongly suggested.

### 3 Spin-Wave Spectrum in the Presence of Spin Vortices: The Origin of an Hourglass-Shaped Magnetic Excitation Spectrum

In the previous section, we have presented the evidence that the small polaron is an important ingredient of the cuprate superconductivity. In this section, we show that the spin–vortex is another important ingredient.

Using the inelastic neutron scattering, magnetic excitations in cuprates are measured [6, 7] (Figs. 6 and 13). They exhibit an hourglass-shaped dispersion (Fig. 6); the high energy part is essentially that of spin-wave excitations of an antiferromagnet; the low energy part exhibits four peaks distributed around the antiferromagnetic commensurate position at  $(h, k) = (1/2, 1/2)$ .

In order to explain the observed spectrum, the *stripe model* has been extensively used. This model assumes a phase separation of the system into charge-rich stripe regions, and remaining antiferromagnetic insulating regions (Fig. 14). This model explains a rough feature of the hourglass-shaped dispersion. However, the obtained constant-energy slices show peaks with rectangular distributions in disagreement with the experimental circular distributions. Besides, the stripe-model calculations

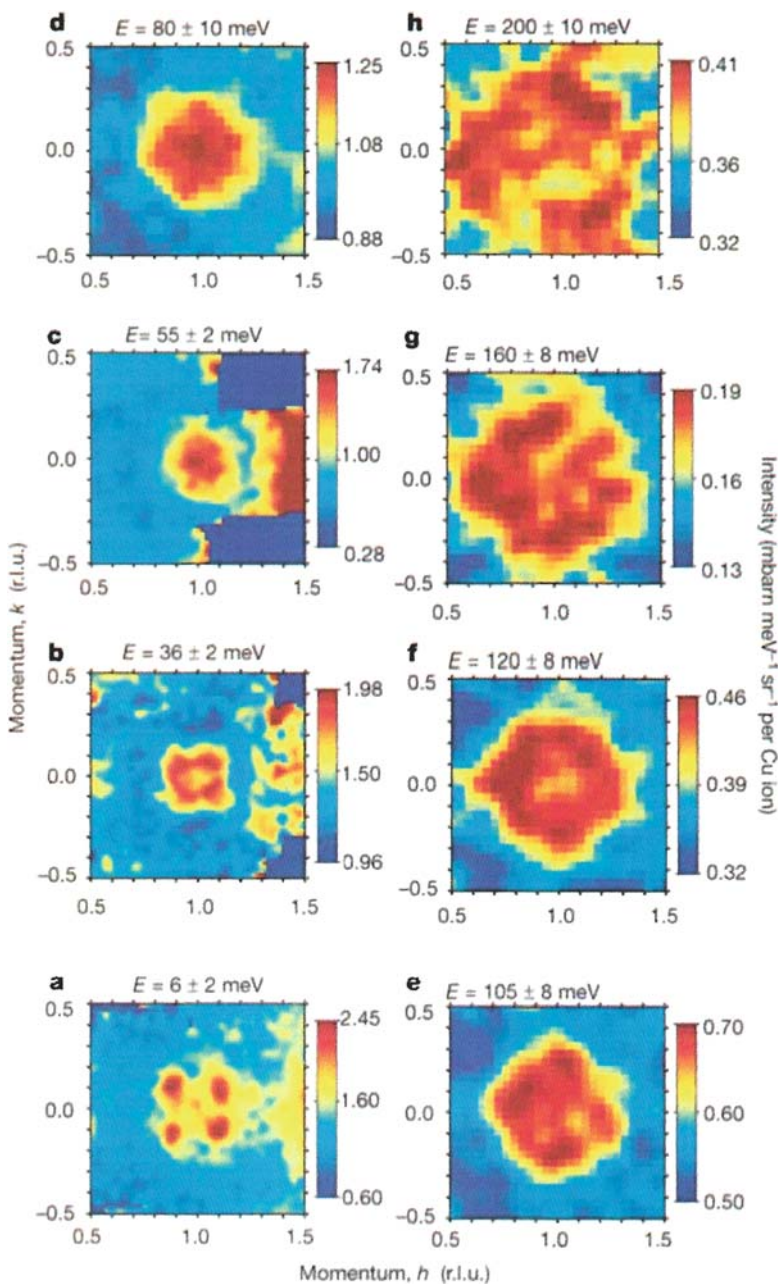


**Fig. 13** Constant-energy slices through the experimentally measured magnetic scattering from  $\text{La}_{1.875}\text{Ba}_{0.125}\text{CuO}_4$  [7]. The  $h$  and  $k$  directions are rotated by  $\pi/4$  from the usual directions

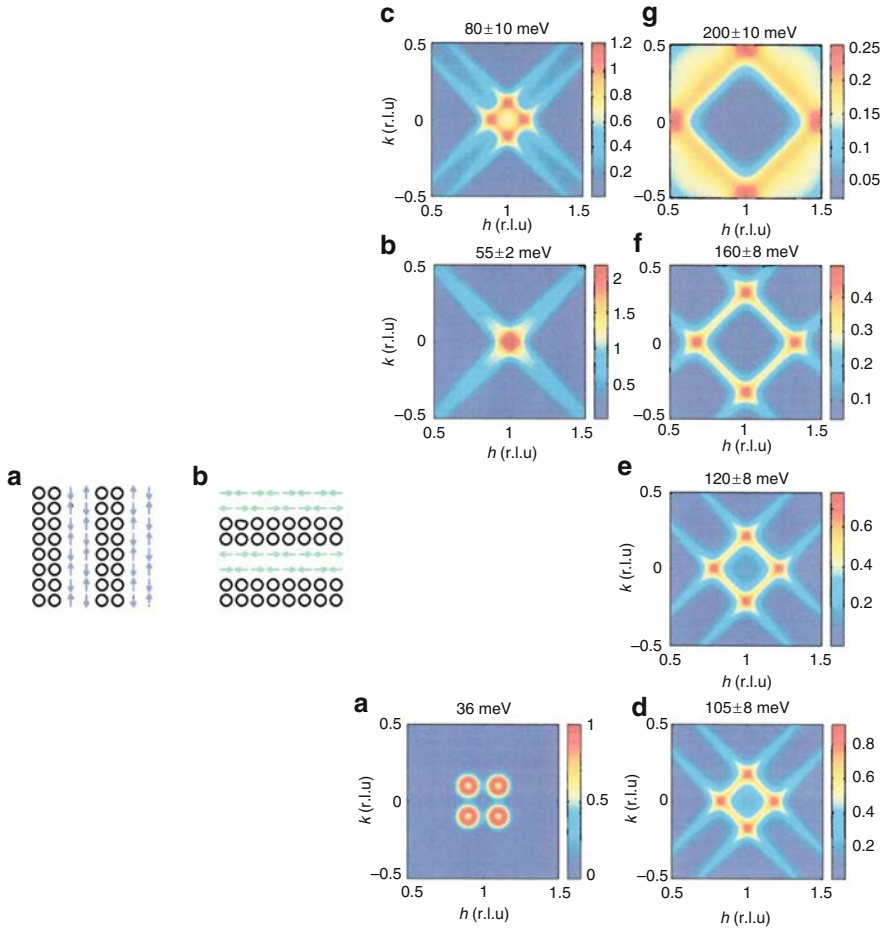


**Fig. 14** *Left*: Schematic diagrams of the stripe model (a: vertical stripes, b: horizontal stripes). Circles indicate Cu sites in hole-doped stripes, and arrows indicate magnetic moments on undoped Cu sites. *Right*: Simulations of the constant-energy slices using the stripe model [7]. The  $h$  and  $k$  directions are rotated by  $\pi/4$  from the usual directions

are performed on static stripes that are known to be insulators; thus, the stripe model is not successful in providing a consistent explanation for the magnetic excitations.

Another model that has been used to explain the magnetic excitations is the *spin-vortex model* [17]. In the following, we simulate the magnetic excitation spectra using the spin-vortex model. We will show that it gives circular peak distributions that agree with the experiment [18]; besides, it provides a new assignment for the Drude-like peak in the optical conductivity [23], thus, consistent assignments are given to the three major peaks in the optical conductivity.

The spin-vortex model assumes the existence of spin-vortices with their centers at small polarons. It is also assumed that the system response to the incident

neutrons is that of the effectively half-filled Mott insulator (EHMI). Let us consider the EHFMI using the Hubbard model given by

$$H = - \sum_{i,j,\sigma} t_{ij} c_{i\sigma}^\dagger c_{j\sigma} + U \sum_j c_{j\uparrow}^\dagger c_{j\uparrow} c_{j\downarrow}^\dagger c_{j\downarrow}, \quad (1)$$

where the first and second terms describe electron hopping and on-site Coulomb interaction, respectively. For now, we take  $t_{ij}$  to be  $t$  if  $i$  and  $j$  are nearest-neighbor sites, and zero otherwise. When holes are doped, we assume that they become small polarons due to strong hole-lattice interaction. The hole-lattice interaction is not included in the Hamiltonian in (1), but is present in the total Hamiltonian for the electron-lattice system. The hopping rate of the small polarons are very small; thus, the system is in an “effectively half-filled Mott insulator (EHFMI) state” where electrons are in an effectively half-filled situation in which doped-holes can be treated as almost immobile vacancies. If we consider the limiting case where small polarons are immobile, the Hamiltonian in (1) can be used as an approximation for the total Hamiltonian; in this case polaron occupied sites are removed from hopping accessible sites. We use this approximation in the following.

In the strongly-correlated case, parameters satisfy the condition  $U \gg t$ . Then, the Coulomb interaction term,

$$H_U = U \sum_j c_{j\uparrow}^\dagger c_{j\uparrow} c_{j\downarrow}^\dagger c_{j\downarrow}, \quad (2)$$

is the dominant one, and the hopping term

$$K = - \sum_{i,j,\sigma} t_{ij} c_{i\sigma}^\dagger c_{j\sigma}. \quad (3)$$

is a perturbation.

To describe the EHFMI state, it is convenient to introduce new annihilation operators  $a_j$  and  $b_j$  that are related to the original as

$$\begin{pmatrix} a_j \\ b_j \end{pmatrix} = e^{i\frac{\chi_j}{2}} \begin{pmatrix} e^{i\frac{\xi_j}{2}} \cos \frac{\theta_j}{2} & e^{-i\frac{\xi_j}{2}} \sin \frac{\theta_j}{2} \\ -e^{i\frac{\xi_j}{2}} \sin \frac{\theta_j}{2} & e^{-i\frac{\xi_j}{2}} \cos \frac{\theta_j}{2} \end{pmatrix} \begin{pmatrix} c_{j\uparrow} \\ c_{j\downarrow} \end{pmatrix}. \quad (4)$$

In the zeroth order approximation, the ground state is given by

$$|0\rangle = \prod_{j \in \text{occ.}} a_j^\dagger |\text{vac}\rangle, \quad (5)$$

where the product runs through electron-occupied sites.

The zeroth order expectation values of electron spin is calculated as



$$\begin{aligned}
S^x(j) &= \frac{1}{2} \langle 0 | c_{j\uparrow}^\dagger c_{j\downarrow} + c_{j\downarrow}^\dagger c_{j\uparrow} | 0 \rangle = \frac{1}{2} \cos \xi_j \sin \theta_j, \\
S^y(j) &= \frac{i}{2} \langle 0 | -c_{j\uparrow}^\dagger c_{j\downarrow} + c_{j\downarrow}^\dagger c_{j\uparrow} | 0 \rangle = \frac{1}{2} \sin \xi_j \sin \theta_j, \\
S^z(j) &= \frac{1}{2} \langle 0 | c_{j\uparrow}^\dagger c_{j\uparrow} - c_{j\downarrow}^\dagger c_{j\downarrow} | 0 \rangle = \frac{1}{2} \cos \theta_j,
\end{aligned} \tag{6}$$

thus, we may identify  $\xi_j$  and  $\theta_j$  as azimuth and polar angles of the spin direction.

A phase factor  $\exp(i\chi_j/2)$  introduced in (4) is a very important one; it is added to ensure the single-valuedness of the transformation matrix. Although  $\xi_j$  and  $\xi_j + 2\pi$  are physically equivalent, the sign-change occurs for  $\exp(\pm i\xi_j/2)$  when  $\xi$  is shifted by  $2\pi$ . The added factor  $\exp(i\chi_j/2)$  compensates this sign-change; we may take  $\chi = \xi$  for this purpose, but other choices are also possible. It is also worth noting that  $\chi/2$  is a Berry phase arising from spin vortices. The Berry phase [19], (also known as the quantum geometric phase [20]) here is similar to the one first found in the  $E \otimes e$  Jahn–Teller system [21] since it also arises from two-component character of the wave function: in the  $E \otimes e$  Jahn–Teller case, the two components arise from the doubly-degenerate  $E$  state, and a crossing point of adiabatic potential surface is the source of a Berry phase and a fictitious magnetic field [22]; in the present case, the two components correspond to two spin-states, and a spin vortex is the source of a Berry phase and a fictitious magnetic field.

It is well-known that the ground state of a half-filled system of the  $t \ll U$  Hubbard model is an antiferromagnetic insulator. The antiferromagnetic conditions are given by

$$\xi_i - \xi_j = \pi; \quad \theta_i + \theta_j = \pi, \tag{7}$$

where  $i$  and  $j$  are nearest neighbors. In the following, we consider the spin vortex formation that violates the condition  $\xi_i - \xi_j = \pi$  while retaining the condition  $\theta_i + \theta_j = \pi$ . Actually, we adopt  $\theta_j = \pi/2$  for all sites and take the  $z$ -axis normal to the two-dimensional  $\text{CuO}_2$ .

Using new annihilation and creation operators, the hopping terms are written as

$$K = K_a + K_b + K_{ab}, \tag{8}$$

where

$$\begin{aligned}
K_a &= -\sum_{k,j} t_{kj} e^{\frac{i}{2}(\chi_k - \chi_j)} \cos \frac{\xi_k - \xi_j}{2} a_k^\dagger a_j, \\
K_b &= -\sum_{k,j} t_{kj} e^{\frac{i}{2}(\chi_k - \chi_j)} \cos \frac{\xi_k - \xi_j}{2} b_k^\dagger b_j, \\
K_{ab} &= -i \sum_{k,j} t_{kj} e^{\frac{i}{2}(\chi_k - \chi_j)} \sin \frac{\xi_k - \xi_j}{2} (a_k^\dagger b_j + b_k^\dagger a_j).
\end{aligned} \tag{9}$$



Spin vortices are described by adopting the following functional form for  $\xi_j$ ,

$$\xi_j = \pi(j_x + j_y) + \sum_M W(j, M) - \sum_A W(j, A), \quad (10)$$

where the first term in the r.h.s.,  $\xi_j = \pi(j_x + j_y)$ , describes the antiferromagnetic spin configuration, and the second and third terms are those for spin vortices with winding number  $+1$  (called, “meron”), and  $-1$  (called, “antimeron”) [17], respectively; the function  $W(j, M)$  given by

$$W(j, M) = \tan^{-1} \frac{j_x - M_x}{j_y - M_y} \quad (11)$$

is a harmonic function that describes winding of spin directions.  $j$ ,  $M$ , and  $A$ , respectively, indicate two-dimensional coordinates for the  $j$ th site, the center of a meron, and the center of an antimeron; their coordinates are given by  $j = (j_x, j_y)$ ,  $M = (M_x, M_y)$ , and  $A = (A_x, A_y)$ , respectively. All centers of merons and antimerons are assumed to be at hole occupied sites.

Now we construct effective Hamiltonians that act in the space of state vectors that allow only single-electron-occupancy at every site except those occupied by small polarons. The single occupancy means that we may use the relation

$$a_j^\dagger a_j + b_j^\dagger b_j = 1 \quad (12)$$

if the  $j$ th site is not occupied by a hole. If we take  $H_U$  as the zeroth Hamiltonian and  $K_{ab}$  as a perturbation, the effective Hamiltonian is obtained as

$$\begin{aligned} H_{\text{eff}}^{(1)} &= -\frac{1}{U} \sum_{k,j} t_{jk}^2 \sin^2 \frac{\xi_j - \xi_k}{2} \left( a_j^\dagger b_k + b_j^\dagger a_k \right) \left( a_k^\dagger b_j + b_k^\dagger a_j \right) \\ &= \frac{1}{U} \sum_{k,j} t_{jk}^2 \sin^2 \frac{\xi_j - \xi_k}{2} \left( \tilde{S}_k^- \tilde{S}_j^- + \tilde{S}_k^+ \tilde{S}_j^+ - 2\tilde{S}_k^Z \tilde{S}_j^Z - \frac{1}{2} \right), \end{aligned} \quad (13)$$

where spin operators,  $\tilde{S}_j^+$ ,  $\tilde{S}_j^-$ , and  $\tilde{S}_j^Z$  are defined as

$$\tilde{S}_j^+ = b_j^\dagger a_j; \quad \tilde{S}_j^- = a_j^\dagger b_j; \quad \tilde{S}_j^Z = \frac{1}{2} (b_j^\dagger b_j - a_j^\dagger a_j). \quad (14)$$

The commutation relations among them are given by

$$[\tilde{S}_j^Z, \tilde{S}_j^\pm] = \pm \tilde{S}_j^\pm; \quad [\tilde{S}_j^+, \tilde{S}_j^-] = 2\tilde{S}_j^Z. \quad (15)$$

$H_{\text{eff}}^{(1)}$  is basically that of an antiferromagnet; it describes the antiferromagnetic spin-wave dispersion observed at high energies.

Now, let us take  $K_a + K_b$  as a perturbation. The effective Hamiltonian is obtained as

$$\begin{aligned} H_{\text{eff}}^{(2)} &= -\frac{1}{U} \sum_{k,j} t_{jk}^2 \cos^2 \frac{\xi_j - \xi_k}{2} \left( a_j^\dagger a_k + b_j^\dagger b_k \right) \left( a_k^\dagger a_j + b_k^\dagger b_j \right) \\ &= \frac{1}{U} \sum_{k,j} t_{jk}^2 \cos^2 \frac{\xi_j - \xi_k}{2} \left( \tilde{S}_k^- \tilde{S}_j^+ + \tilde{S}_k^+ \tilde{S}_j^- + 2\tilde{S}_k^Z \tilde{S}_j^Z - \frac{1}{2} \right). \end{aligned} \quad (16)$$

This Hamiltonian does not arise in the usual derivation of the spin Hamiltonian from the Hubbard model since in the usual derivation  $\xi_j - \xi_k$  is taken to be  $\pi$ , thus, we have  $\cos^2[(\xi_j - \xi_k)/2] = 0$ . It gives rise to “ferromagnetic” spin-wave excitations, in which excitations such as  $\tilde{S}_j^+|0\rangle$  propagates. As the number of spin-vortices increases, the contribution from this Hamiltonian increases. This mode is also considered as an excitation propagation mode, which probably connects to the coherent electron motion in the overdoped region.

Finally, the total spin Hamiltonian is obtained as the sum of the two;

$$H_{\text{spin}} = H_{\text{eff}}^{(1)} + H_{\text{eff}}^{(2)}. \quad (17)$$

There are two ways to calculate dispersions; one is the Holstein-Primakoff method, and the other is the equations of motion method. Usually, these two methods yield similar results. However, in the presence of spin-vortices, the latter method yields a new-type mode that is not obtained by the former method. In the following we employ the latter method [18, 23].

In order to obtain spin-wave dispersions, we use the following approximations;

$$\tilde{S}_k^Z \approx \langle 0' | \tilde{S}_k^Z | 0' \rangle \approx \langle 0 | \tilde{S}_k^Z | 0 \rangle = -\frac{1}{2}, \quad (18)$$

where  $|0'\rangle$  denotes the exact ground state to linearize equations.

Then, equations of motion are obtained as

$$\begin{aligned} -i\dot{\tilde{S}}_k^+ &= [H_{\text{spin}}, \tilde{S}_k^+] \approx \frac{2}{U} \sum_j t_{kj}^2 \sin^2 \frac{\xi_j - \xi_k}{2} (\tilde{S}_j^- + \tilde{S}_k^+) \\ &\quad - \frac{2}{U} \sum_j t_{kj}^2 \cos^2 \frac{\xi_j - \xi_k}{2} (-\tilde{S}_j^+ + \tilde{S}_k^+). \end{aligned} \quad (19)$$

We write spin-wave excited states as

$$|f\rangle = \frac{1}{\sqrt{2}} \sum_j (C_j^X(f) - iC_j^Y(f)) \tilde{S}_j^+ |0'\rangle + \frac{1}{\sqrt{2}} \sum_j (C_j^X(f) + iC_j^Y(f)) \tilde{S}_j^- |0'\rangle, \quad (20)$$

where  $C_j^X(f)$  and  $C_j^Y(f)$  are parameters to be determined.

If we use (19) with Heisenberg representations of operators, we obtain

$$\begin{aligned} \frac{d}{dt} \langle 0' | -i \tilde{S}_k^+ | f \rangle e^{-i\omega_f t} &= \frac{2}{U} \sum_j t_{kj}^2 \sin^2 \frac{\xi_j - \xi_k}{2} \langle 0' | \tilde{S}_j^- + \tilde{S}_k^+ | f \rangle e^{-i\omega_f t} \\ &\quad - \frac{2}{U} \sum_j t_{kj}^2 \cos^2 \frac{\xi_j - \xi_k}{2} \langle 0' | -\tilde{S}_j^+ + \tilde{S}_k^+ | f \rangle e^{-i\omega_f t}, \end{aligned} \quad (21)$$

where  $\omega_f$  is the excitation energy from  $|0'\rangle$  to  $|f\rangle$ .

Substituting the state vector  $|f\rangle$  in (20), the above equations provide the relations among  $C_j^X(f)$  and  $C_j^Y(f)$ . There are two ways to couple the two components  $C_j^X(f)$  and  $C_j^Y(f)$ . If we couple the  $X$  component to the nearest-neighbor  $Y$  component and vice versa, we obtain a set of eigenvalue equations given by

$$\text{(Mode I)} \begin{cases} i\omega_f C_k^X(f) = \frac{2}{U} \sum_j t_{kj}^2 \cos(\xi_j - \xi_k) (C_j^Y(f) - C_k^Y(f)) \\ i\omega_f C_k^Y(f) = -\frac{2}{U} \sum_j t_{kj}^2 (C_j^X(f) - \cos(\xi_j - \xi_k) C_k^X(f)) \end{cases}; \quad (22)$$

if we connect the  $X$  component to a nearby  $X$ , and the  $Y$  to a nearby  $Y$  component, we obtain another set,

$$\text{(Mode II)} \begin{cases} \omega_f C_k^X(f) = -\frac{2}{U} \sum_j t_{kj}^2 (C_j^X(f) - \cos(\xi_j - \xi_k) C_k^X(f)) \\ \omega_f C_k^Y(f) = -\frac{2}{U} \sum_j t_{kj}^2 \cos(\xi_j - \xi_k) (C_j^Y(f) - C_k^Y(f)) \end{cases}. \quad (23)$$

The Mode II does not arise in the Holstein-Primakoff calculation. This is the new mode that arises due to the existence of spin-vortices. We obtain the excited state vector  $|f\rangle$  and its excitation energy  $\omega_f$  by numerically solving the above equations.

The spin-wave dispersion is calculated using the zero temperature structure factor given by

$$S(\mathbf{k}, \omega) = \sum_f \sum_{p=x,y,z} |S_f^p(\mathbf{k})|^2 \delta(\omega - \omega_f), \quad (24)$$

where  $S_f^p(\mathbf{k})$  are related to  $S_j^p(f)$  through the Fourier transformation as

$$S_f^p(\mathbf{k}) = \frac{1}{\sqrt{N_s}} \sum_j S_j^p(f) e^{-i\mathbf{k}\cdot\mathbf{r}_j}; \quad (25)$$

$S_j^x(f)$ ,  $S_j^y(f)$ , and  $S_j^z(f)$  are given by  $C_j^X(f)$  and  $C_j^Y(f)$  as

$$S_j^x(f) = \sin \xi_j C_j^Y(f); \quad S_j^y(f) = -\cos \xi_j C_j^Y(f); \quad S_j^z(f) = -C_j^X(f). \quad (26)$$

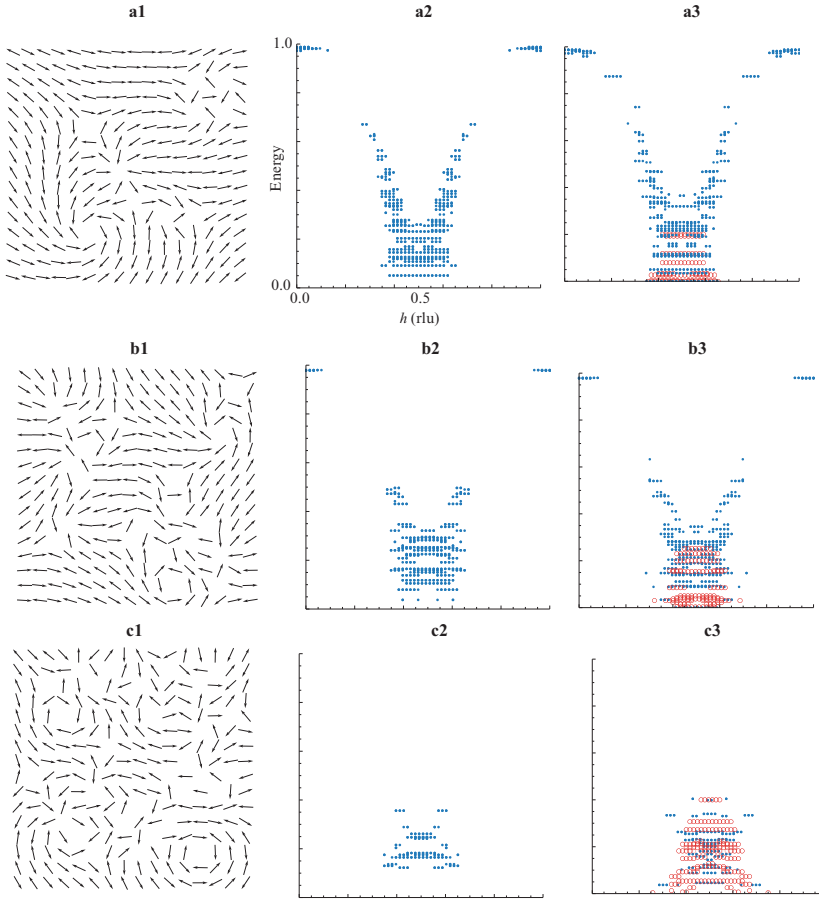


**Fig. 15** Plots of magnetic excitation dispersion. Calculations are performed for a two-dimensional  $16 \times 16$  square lattice with open boundary conditions. Parameters are  $U = 8t$ , and  $t$  is the unit of energy. **a1**: Spin configuration for a 10-hole case. The configuration is one gives the lowest energy among randomly generated configurations; the energy is estimated by the classical Heisenberg model. **a2**: The dispersion obtained by the Holstein–Primakoff method for the spin configuration in **a1**. **a3**: The dispersion obtained by the equations of motion method for the spin configuration in **a1**; (filled dots are for Mode I, and open circles are for Mode II). **b1**: The same as **a1** but for a 20-hole case. **b2**: The same as **a2** but for the spin configuration in **b1**. **b3**: The same as **a3** but for the spin configuration in **b1**. **c1**: The same as **a1** but for a 30-hole case. **c2**: The same as **a2** but for the spin configuration in **c1**. **c3**: The same as **a3** but for the spin configuration in **c1**

In Fig. 15, magnetic excitation spectra calculated by the spin–vortex model are depicted. Results obtained by the Holstein–Primakoff method are also depicted. The dispersions exhibit hourglass-shapes. As the number of spin–vortices are increased, the peaks of the dispersion become blur. The neck energy increases with the increase of the number of holes in agreement with experiment.

Some constant-energy slices are plotted in Fig. 16. The peak distributions are circular in agreement with the experimental result.

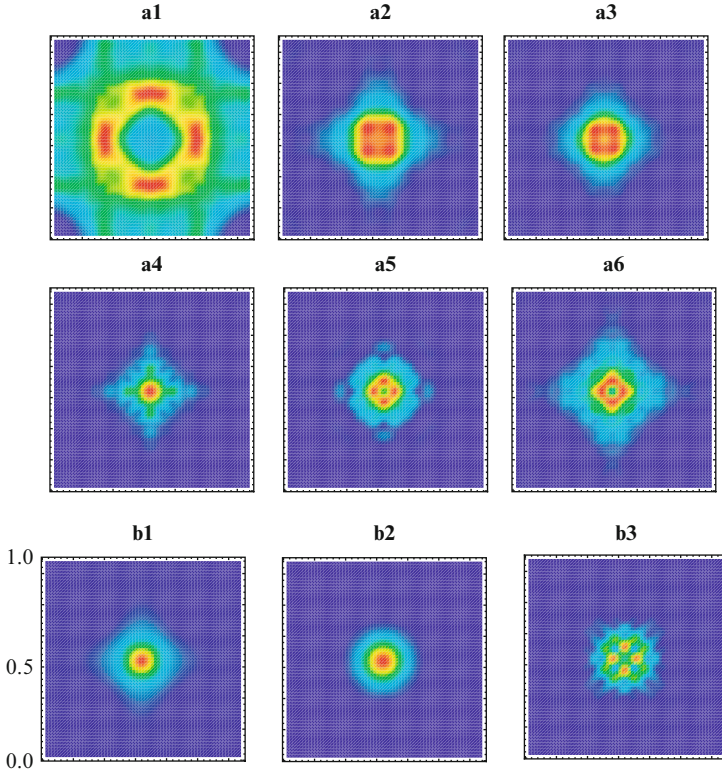


**Fig. 16** Constant-energy slices of the magnetic excitation spectrum. The spin configuration is given in Fig. 15b1. **a1**: Contour plot of a cross section of the energy dispersion in Fig. 15b2. It is an average of the 100–110th states (energy range is  $0.737t$ – $0.700t$ ). **a2**: The same as **a1** but it is an average of the 200–205th states (energy range is  $0.306t$ – $0.275t$ ). **a3**: The same as **a1** but of the 206th–210th states (energy range is  $0.260t$ – $0.225t$ ). **a4**: The same as **a1** but the plot of the 215th state (energy is  $0.165t$ ). **a5**: The same as **a1** but the plot of the 218th state (energy is  $0.130t$ ). **a6**: The same as **a1** but the plot of the 222th state (energy is  $0.0967t$ ). **b1**: Contour plot of a cross section of the energy dispersion in Fig. 15b3 with *open circles*. It is the plot of the first state (energy range is  $0.254t$ ). **b2**: The same as **b1** but the plot of the 5th state (energy is  $0.1549t$ ). **b3**: The same as **b1** but the plot of the 10th state (energy is  $0.0438t$ )

The new-type spin-wave mode, Mode II, actually accounts for the Durude-like peak observed in the optical conductivity. Let us calculate the real part of optical conductivity given by

$$\text{Re } \sigma(\omega) = \frac{e^2 \pi}{N_s} \sum_f \frac{|\langle f | \hat{j}_x | 0' \rangle|^2}{\omega} \delta(\omega - \omega_f), \quad (27)$$

where  $N_s$  is the number of sites in the system, and  $\hat{j}_x$  is the  $x$ -component of the current operator.

In order to use (27), the ground state vector,  $|0'\rangle$ , is needed. Instead of an exact ground state vector, we use an approximate one given by  $|0'\rangle \approx |0\rangle + |1\rangle$ , where the first-order correction in  $K_{ab}$  to  $|0\rangle$ , denoted as  $|1\rangle$ , is given by

$$|1\rangle = \sum_{m,j} \frac{it_{mj} b_m^\dagger a_j |0\rangle}{U} e^{\frac{i}{2}(\chi_m - \chi_j)} \sin \frac{\xi_m - \xi_j}{2}. \quad (28)$$

Then, the leading-order contributions come from transitions by the current operator from  $K_b$  given by

$$\hat{j}_x^b = it \sum_l \left( e^{\frac{i}{2}(\chi_{l+x} - \chi_l)} \cos \frac{\xi_{l+x} - \xi_l}{2} b_{l+x}^\dagger b_l - \text{h.c.} \right), \quad (29)$$

where  $l+x$  denotes the nearest-neighbor site of  $l$  in the  $x$ -direction.

The final expression for the optical conductivity is given by

$$\text{Re } \sigma(\omega) = \frac{\pi e^2 t^4}{2U^2 N_s} \sum_f \sum_{\alpha=x,y} \frac{|\sum_l (C_{l+\alpha}^X(f) + C_l^X(f)) \sin(\xi_{l+\alpha} - \xi_l)|^2}{\omega} \delta(\omega - \omega_f), \quad (30)$$

where the conductivity is averaged over in the  $x$ - and  $y$ -directions by assuming the equivalence of the  $x$ - and  $y$ -directions.

In Fig. 18, the effective density of carriers defined by

$$N_{\text{eff}} = \int_0^\infty d\omega' \text{Re} \sigma_{\text{II}}(\omega') \quad (31)$$

is plotted; optical conductivity here is calculated by including only Mode II spin-wave excited states since the contributions of Mode I excited states are negligible. The calculated  $N_{\text{eff}}$  is roughly equal to the number of spin vortices. In the experiment [3] (Fig. 19), the effective carrier number from the Drude-like peak is roughly proportional to the number of doped holes [3]; thus, the present result explains the experiment if most of the doped holes become centers of spin vortices.

## 4 A New Electric Current Generation Mechanism by a Berry Phase from Spin Vortices

By now, we have identified three important ingredients in the cuprate superconductivity; strong on-site Coulomb repulsion, small polaron formation, and spin-vortex formation. With all these ingredients, however, the conventional transport theory based on Bloch electrons will predict that the system is an insulator. In order to

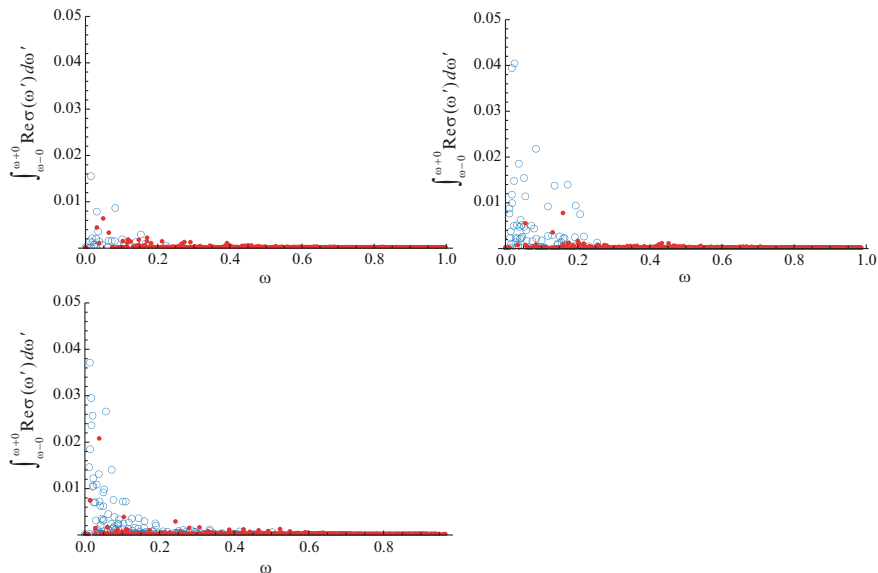


**Fig. 17** Plots of  $\int_{\omega-0}^{\omega+0} \text{Re}\sigma(\omega') d\omega'$  vs.  $\omega$ . The units with  $\hbar = e = t = 1$  are used. The system is a two-dimensional square lattice with  $N_s = 16 \times 16 = 256$ ; the parameter  $U$  is  $8t$ . Red dots are those from Mode I, and blue open-circles are those from Mode II. Plots are superpositions of results from nominally 5 lowest energy states among randomly generated states in which energy is estimated by the classical Heisenberg model. All doped-holes are either centers of merons or antimerons. *Left*: results for five merons and five antimerons. *Center*: results for ten merons and ten antimerons. *Right*: results for 15 merons and five antimerons

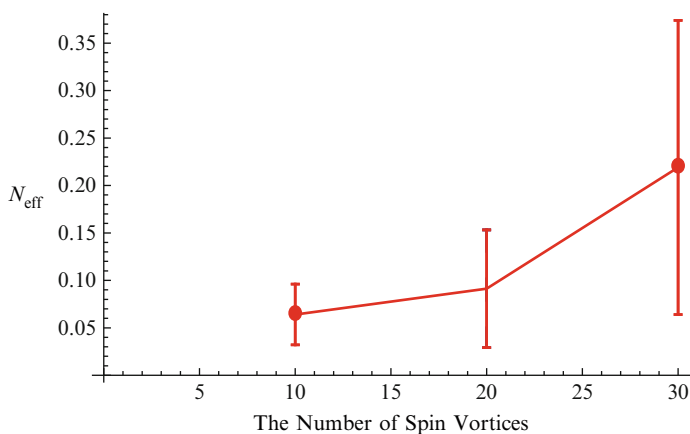


**Fig. 18** Effective density of carriers  $N_{\text{eff}}$  vs. the number of spin vortices. Error bars indicate standard deviations of  $N_{\text{eff}}$  calculated from five nominally lowest energy states used in the calculations for Fig. 17

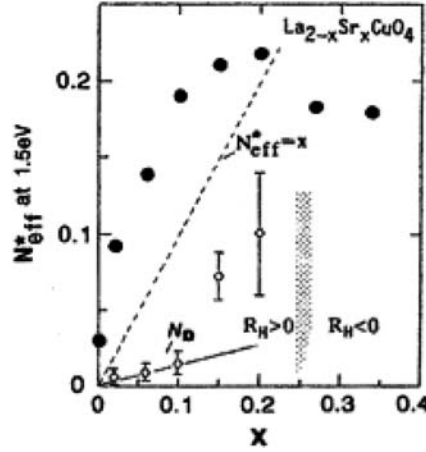


**Fig. 19** Effective electron number at 1.5 eV (solid circles) as a function of  $x$ . The dashed straight line indicates  $N_{eff}^* = x$ . The open diamond with an error bar represents a free-carrier contribution estimated from a Drude fit to the optical conductivity [3]

explain a metallic conductivity in the underdoped cuprate, a novel current generation mechanism is necessary. Recently, the present author proposed a new current generation mechanism that utilizes a Berry phase from spin vortices [24]. In this section, we very briefly explain this new mechanism.

The effect of a magnetic field  $\mathbf{B} = \nabla \times \mathbf{A}$ , where  $\mathbf{A}$  is an electromagnetic vector potential, can be included in the Hamiltonian in (1) by modifying transfer integrals as

$$t_{kj} \rightarrow t_{kj} \exp \left( i \frac{q}{c\hbar} \int_j^k \mathbf{A} \cdot d\mathbf{r} \right), \quad (32)$$

where  $c$  is the speed of light and  $q$  is the charge.

Then, the appearance of factors

$$e^{\frac{i}{2}(\chi_k - \chi_j)} = e^{\frac{i}{2} \int_j^k \nabla \chi \cdot d\mathbf{r}} \quad (33)$$

in (9) can be interpreted that a “fictitious magnetic field”

$$\mathbf{B}_{\text{fic}} = \nabla \times \mathbf{A}_{\text{fic}} \quad (34)$$

with a vector potential

$$\mathbf{A}_{\text{fic}} = \frac{c\hbar}{2q} \nabla \chi \quad (35)$$

exists in the system.



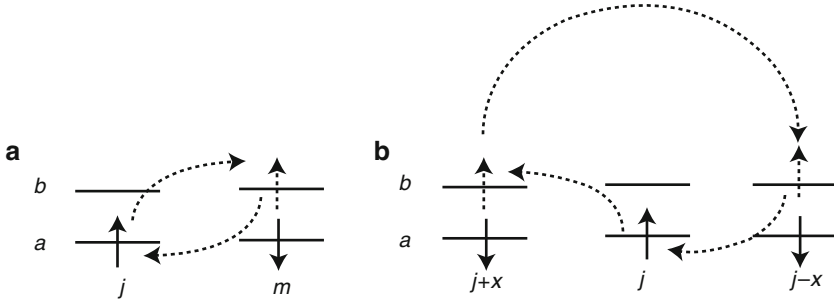


**Fig. 20** Appearance of extended single-particle states by spin-vortices. **(a)** An antiferromagnetic order without spin-vortices case. Only  $K_{ab}$  is nonzero. All electrons are localized. **(b)** A spin configuration with spin-vortices.  $K_a$  and  $K_b$  become nonzero around spin-vortices; extended single-particle states appear around spin-vortices

Although the zeroth order state  $|0\rangle$  is currentless, states with perturbations from hopping terms  $K_b$  and  $K_{ab}$  are current-carrying. As is schematically shown in Fig. 20, in the absence of spin-vortices  $K_b = K_a = 0$ , thus, only hopping by  $K_{ab}$  is possible. In this situation electrons are localized. When spin-vortices are present, the hopping term  $K_b$  allows extended single-particle states around the vortices. Furthermore, due to the fictitious magnetic field produced by the spin Berry phase, a state with loop currents around them becomes the minimal energy one.

In Fig. 21, the result from numerical calculations using a mean-field theory is depicted. It indicates that the fictitious magnetic field produces current roughly given by

$$\mathbf{j} = -C\hbar\nabla\chi, \quad (36)$$

where  $C$  is a constant [24]. Each spin vortex is accompanied a loop current due to the single-valuedness condition in the unitary transformation in (4). Note that the conservation of charge requires that  $\chi$  to be a harmonic function, i.e., it satisfies  $\nabla^2\chi = 0$ .

In Fig. 22a, an example of a spin configuration with two spin vortices is depicted. Different current patterns are possible for the same spin configuration by different  $\chi$ 's. Although each loop current is rather localized around each center of the vortices, a macroscopic current can be generated as a collection of loop currents if the number of loop currents is large enough (Fig. 22d).

## 5 Fictitious Electric Field and Enhanced Nernst Effect

In the previous section, a new current generation mechanism is presented. It is based on the theoretical observation that loop currents should be generated around spin-vortices as a Berry phase effect. In this section, we present experimental evidence

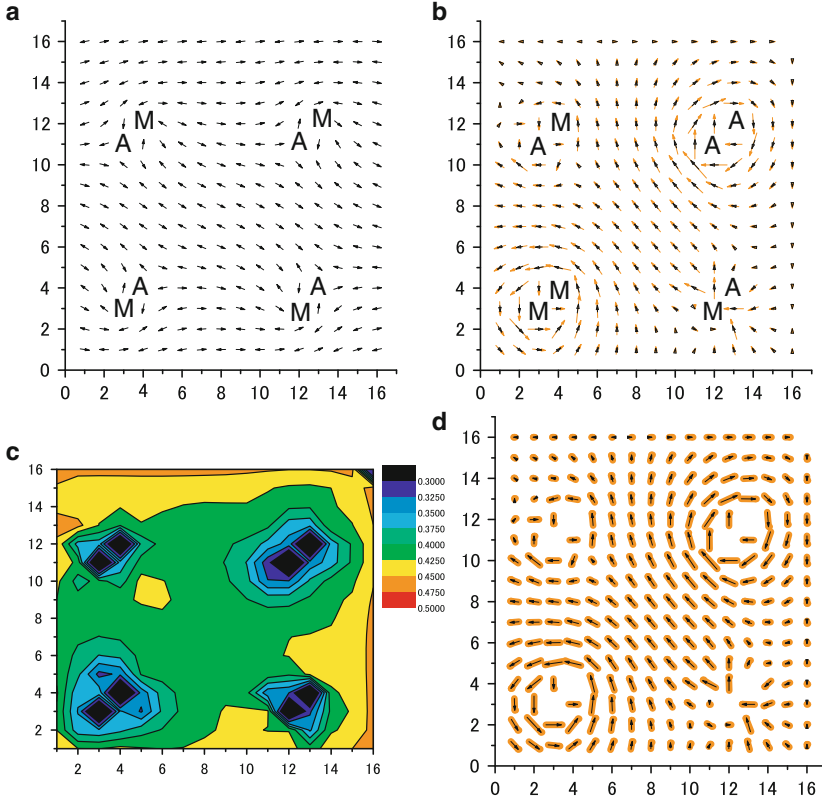


**Fig. 21** Plots obtained by mean-field calculations for an EHFMI [24]. Calculations are performed for a two-dimensional  $16 \times 16$  square lattice with open boundary conditions. Parameters used are  $U = 8t$  and  $t' = -0.2t$  ( $t'$  denotes the second nearest neighbor transfer integrals  $t_{jk}$ ). The number of doped holes is 8; half of them are centers of merons and the rest are centers of antimerons. (a) Plot for spin configuration. Centers of spin vortices are indicated as “M” for a meron (winding number  $+1$  spin vortex) and “A” for an antimeron (winding number  $-1$  spin vortex), respectively. (b) Plot for current density  $\mathbf{j}$  (short black arrows) and  $\nabla\chi$  (long orange arrows). “M” and “A” here indicate centers of counterclockwise and clockwise loop currents, respectively; (c) Plot for  $D(\mathbf{x})$ , which connects  $\mathbf{j}(\mathbf{x})$  and  $\nabla\chi(\mathbf{x})$  as  $|\mathbf{j}(\mathbf{x})| = D(\mathbf{x})|\nabla\chi(\mathbf{x})|$ ; (d) Plot for  $2\mathbf{j}$  (thick orange line; arrows are not attached but directions are the same as those of the black arrows) and  $2D(\mathbf{x})\nabla\chi(\mathbf{x})$  (black arrows)

for the existence of such loop currents; we argue that enhanced Nernst signals in the pseudogap phase [11–13] are due to the flow of such loop currents [25].

Let us derive the formula for the Nernst signal arising from the flow of loop currents.

When  $\mathbf{A}_{\text{fic}}$  is time-dependent, it gives rise to a fictitious electric field [26] given by

$$\mathbf{E}_{\text{fic}} = -\frac{1}{c} \frac{\partial \mathbf{A}_{\text{fic}}}{\partial t} = -\frac{\hbar}{2q} \nabla \dot{\chi}. \quad (37)$$

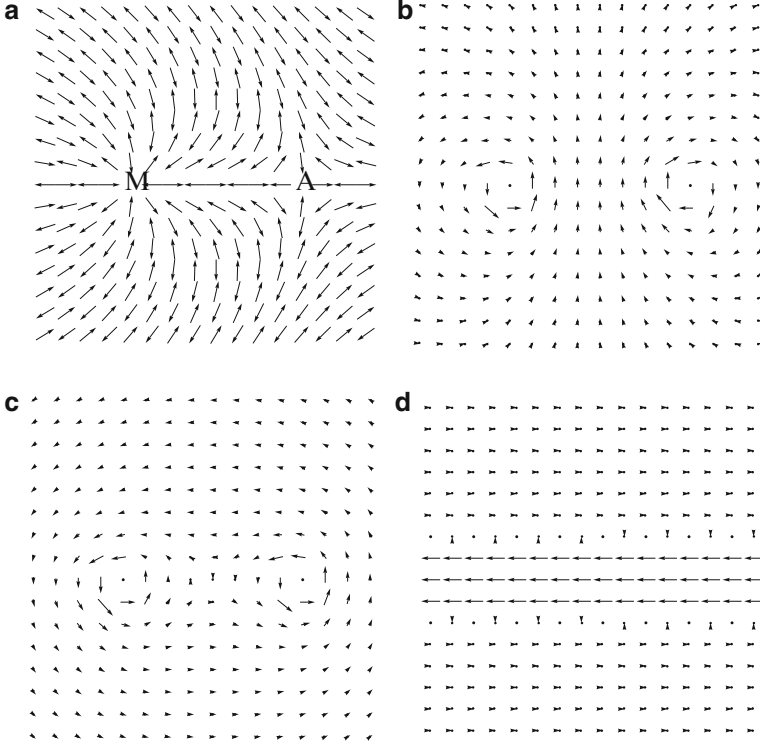


**Fig. 22** Spin vortices and current generated by them [25]. (a) Two spin vortices embedded in the antiferromagnetic background. The spin polarization direction at  $j$ th site in the  $x$ - $y$  plane is given by  $(\cos \xi_j, \sin \xi_j)$ , where  $\xi_j = \pi(j_x + j_y) + \tan^{-1} \frac{j_y - M_y}{j_x - M_x} - \tan^{-1} \frac{j_y - A_y}{j_x - A_x}$  ( $(j_x, j_y)$  is the coordinate of the  $j$ th site,  $(M_x, M_y)$  and  $(A_x, A_y)$  are coordinates of centres of spin vortices at  $M$  and  $A$ , respectively). (b) A collection of loop currents given by  $\mathbf{j} = -\hbar C \nabla \chi$ , where  $C$  is a positive constant, and  $\chi_j = -\tan^{-1} \frac{j_y - M_y}{j_x - M_x} + \tan^{-1} \frac{j_y - A_y}{j_x - A_x}$ . (c) The same as (b) but for the current pattern given by  $\chi_j = -\tan^{-1} \frac{j_y - M_y}{j_x - M_x} - \tan^{-1} \frac{j_y - A_y}{j_x - A_x}$ . (d) A macroscopic current flow generated by a collection of loop currents; loop currents with winding number  $+1$  and those with  $-1$  are aligned in parallel lines. The definition of the winding number is given in (58). The total number of loop currents is 16 in the figure. Between the two lines, a directional current flow is realized with almost zero current outside

When a temperature gradient exists, flow of small polarons occurs; then,  $\chi$  becomes time-dependent, and a fictitious electric field appears.

The Nernst signal is measured by an experimental setup shown in Fig. 23a; a temperature gradient  $\nabla T$  is created in the  $x$ -direction, and a magnetic field  $\mathbf{B}$  is applied in the  $z$ -direction. Due to the flow of loop currents,  $\mathbf{E}_{\text{fic}}$  appears in the  $y$ -direction and exerts force on electrons; then, a real electric field develops to balance the fictitious electric field ( $\mathbf{E} = -\mathbf{E}_{\text{fic}}$ ) as in the Hall effect measurement. The Nernst signal is defined as the developed electric field in the  $y$ -direction,  $E_y$ , divided by

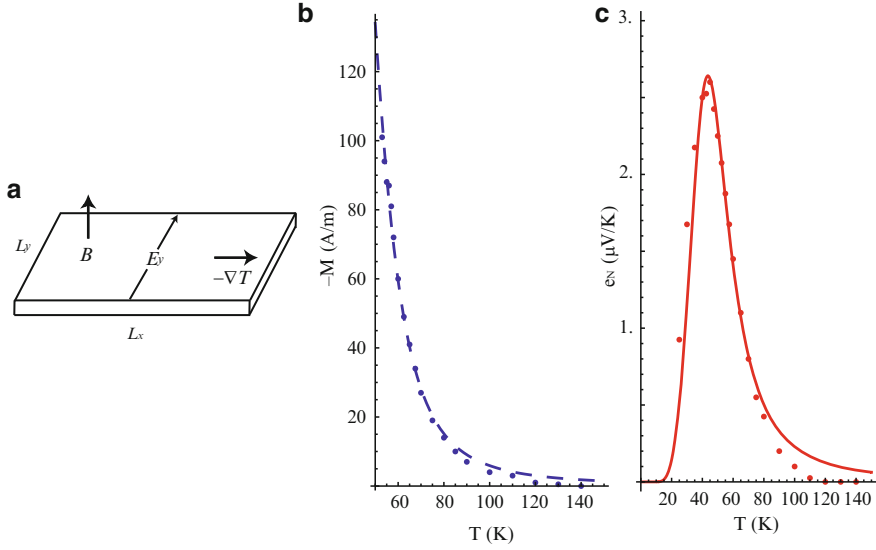


**Fig. 23** Temperature dependences of magnetization  $M$  and Nernst signal  $e_N$  for the underdoped  $\text{Bi}_2\text{Sr}_2\text{CaCu}_2\text{O}_{8+\delta}$  (Bi2212,  $T_c = 50$  K) [25]. **(a)** Experimental setup. **(b)** Temperature dependence of  $M$ ; it is fitted by (46) with  $c_1 = 300$ ,  $c_2 = 10$ , and  $W_p/k_B = 300$  K. **(c)** Temperature dependence of  $e_N$ ; it is fitted by (49) with  $c_3 = 5200$ . Dots are experimental results [12]

the temperature gradient in the  $x$ -direction as

$$e_N = \frac{E_y}{|\partial_x T|}. \quad (38)$$

Let us consider a rectangular system shown in Fig. 23a and derive a formula for the Nernst signal  $e_N$ . The system has a length  $L_x$  in the  $x$  direction ( $0 \leq x \leq L_x$ ), and a width  $L_y$  in the  $y$  direction ( $0 \leq y \leq L_y$ ). Using (37),  $E_y$  at  $x = L_x/2$  is calculated as

$$E_y = \frac{\hbar}{2qL_y} \int_0^{L_y} dy \frac{\partial}{\partial y} \dot{\chi} \left( \frac{L_x}{2}, y \right) = \frac{\hbar}{2qL_y} \left[ \dot{\chi} \left( \frac{L_x}{2}, L_y \right) - \dot{\chi} \left( \frac{L_x}{2}, 0 \right) \right] \quad (39)$$

Diamagnetic currents arise around spin vortices given by (36). Then, after the vortex flow from  $x = 0$  to  $x = L_x$ , the phase change of  $\chi$  for is given by

$$\Delta\chi = \chi(L_x/2, L_y) - \chi(L_x/2, 0) = -2\pi N_m, \quad (40)$$

where  $N_m$  is the number for loop currents.

We denote an average velocity of the small polaron flow by  $v$ ; then,  $\Delta t = L_x/v$  will be the average time for the flow from  $x = 0$  to  $x = L_x$ . The time-derivative of the phase difference is approximately given by

$$\frac{\Delta\chi}{\Delta t} = -\frac{2\pi N_m}{L_x}. \quad (41)$$

Then, substituting (41) and  $q = -e$  in (39),  $E_y$  is obtained as

$$E_y = \frac{h\nu n_m}{2e}, \quad (42)$$

where  $n_m$  is the surface density of loop currents given by  $n_m = N_m/L_x L_y$ . Finally, the Nernst signal is given by

$$e_N = \frac{h\nu n_m}{2e|\partial_x T|}. \quad (43)$$

A large magnetization is also observed in the Nernst effect experiment [12]. If it is produced by loop currents around spin vortices, it should be roughly proportional to  $n_m$ . Then, the temperature dependence of  $M$  is essentially that of  $n_m$ .

In order to obtain the temperature dependence of  $n_m$ , we consider the situation where small polarons coexist with “large polarons” of effective mass  $m^*$  [27]. The equilibrium condition between “large polarons” and small polarons may be given by

$$\frac{x - n_m}{n_m} = \frac{2\pi m^* k_B T}{n_s h^2} e^{-W_p/k_B T}, \quad (44)$$

where  $W_p$  is the polaron stabilization energy and  $n_s$  is the density of sites. Here, the lattice constant of the two-dimensional square lattice of the  $\text{CuO}_2$  plane is taken to be the unit of distance.

A formula for  $M$  is

$$M = -\gamma d n_m, \quad (45)$$

where  $\gamma$  is the average magnitude of a magnetic moment for a loop current and  $d$  is the distance between  $\text{CuO}_2$  planes. Using  $n_m$  obtained from (44), the result is

$$-M = c_1/(1 + c_2 T e^{-W_p/k_B T}), \quad (46)$$

where  $c_1 = x\gamma d$  and  $c_2 = 2\pi m^* k_B/(n_s h^2)$ . In Fig. 23b, experimentally observed  $M$  and its fit by treating  $c_1$ ,  $c_2$ , and  $W_p$  as fitting parameters are depicted. It is seen that the fitting by (46) follows experimental data quite well.

From (43), it is seen that the Nernst signal is proportional to a product of  $n_m$  and  $v$ . Since  $v$  is proportional to the mobility  $\mu$  as

$$v = \mu|\nabla T|, \quad (47)$$

$e_N$  should be proportional to a product of  $n_m$  and  $\mu$ .

For the activation-type small polaron hopping [2],  $\mu$  is expressed as

$$\mu = \mu_0 T^{-1} e^{-W_H/k_B T}; \quad (48)$$

where  $W_H$  is the activation energy for the polaron hopping, and  $\mu_0$  is a constant. Note that  $W_H$  may be related [2] to  $W_p$  as  $W_H = 0.5W_p$ .

Overall, the Nernst signal is expressed as

$$e_N = c_3 T^{-1} e^{-0.5W_p/k_B T} / (1 + c_2 T e^{-W_p/k_B T}), \quad (49)$$

where  $c_3 = xh\mu_0/2e$  is a constant.

In Fig. 23c, experimentally observed  $e_N$  and its fit are depicted. The fit is very good except at high temperatures; at those temperatures, the mobility given in (48) is probably too simple. The good agreement between the theory and experiment suggests that the above formula for  $e_N$  captures essentials of the temperature dependence of the Nernst signal. We may take this good agreement as a support for the existence of loop currents with their centers at small polarons in cuprates.

## 6 Implications of the New Electric Current Generation Mechanism in Superconductivity

When both real magnetic field  $\mathbf{B} = \nabla \times \mathbf{A}$  and the fictitious magnetic field  $\mathbf{B}_{\text{fic}} = \nabla \times \mathbf{A}_{\text{fic}}$  are present, the electric current becomes

$$\mathbf{j}_e = -q\hbar C \left( \nabla\chi + \frac{2q}{\hbar c} \mathbf{A} \right). \quad (50)$$

For the gauge transformation

$$\mathbf{A}' = \mathbf{A} + \nabla f \quad (51)$$

electron operators are modified as

$$c_{j\sigma} \rightarrow c_{j\sigma} \exp\left(-i \frac{q}{\hbar c} f_j\right), \quad (52)$$

which, according to (4), means that  $\chi$  is modified as

$$\chi'_j = \chi_j - \frac{2q}{\hbar c} f_j. \quad (53)$$

Therefore, it is seen that

$$\nabla\chi + \frac{2q}{\hbar c} \mathbf{A}; \quad (54)$$

is gauge invariant. Thus,  $\mathbf{j}_e$  is gauge invariant, and should describe an observable current.

From (50), the energy increase due to loop currents is obtained as

$$U = \frac{C\hbar}{4} \int d^2r \left( \nabla\chi + \frac{2q}{\hbar c} \mathbf{A} \right)^2; \quad (55)$$

it is constructed so that the electric current density is given by

$$\mathbf{j}_e = -c \frac{\delta U}{\delta \mathbf{A}}. \quad (56)$$

It is suggested that at temperature around  $T_c$  spin vortices are created around all doped holes [23]. We express  $\nabla\chi$  as a sum of contributions from loop currents,

$$\nabla\chi = \sum_i \nabla\chi(i), \quad (57)$$

where  $\chi(i)$  is the phase introduced to compensate the sign-change caused by a single spin vortex at the  $i$ th site.

The winding number for the  $i$ th loop current is defined by

$$w_i = \frac{1}{2\pi} \oint_{C_i} \nabla\chi(i) \cdot d\mathbf{r} \quad (58)$$

with  $C_i$  being a closed path encircling the  $i$ th site.

Then, by setting  $\mathbf{A} = 0$ , (55) is simplified as

$$U = \frac{\pi C\hbar}{2} \sum_i w_i^2 \ln \frac{R_c}{a_c} + \frac{\pi C\hbar}{2} \sum_{i \neq j} w_i w_j \ln \frac{R_c}{r_{ij}} \quad (59)$$

where  $R_c$  and  $a_c$  are upper- and lower-cutoff-radii of each loop current, respectively;  $r_{ij}$  denotes the distance between centers of loop currents at sites  $i$  and  $j$ .

If the magnetic field is absent, loop currents with winding number  $\pm 1$  are created with the total sum of them being zero. We consider this situation below. For simplicity, we only retain adjacent pairs in the second sum  $\sum_{i \neq j}$  in (59); we replace  $r_{ij}$  by its average value given by  $1/\sqrt{\pi x}$ , and consider a square lattice of a lattice constant  $1/\sqrt{\pi x}$ . As a result, the following very simple interaction potential for loop currents is obtained;

$$U_{\text{loop}} = \frac{\pi C\hbar}{2} \ln \frac{x}{x_0} \sum_{\langle i,j \rangle} w_i w_j, \quad (60)$$

where  $x_0$  is introduced through

$$R_c = \frac{1}{\sqrt{\pi x_0}}, \quad (61)$$

and the sum is taken over nearest neighbor pairs.

The interaction potential  $U_{\text{loop}}$  is equivalent to an Ising model for antiferromagnets if the hole concentration satisfies  $x > x_0$ ; two loop currents  $w_i = +1$  and  $w_i = -1$  correspond, respectively, to up- and down-spin states. Then,  $T_c$  is obtained as the order-disorder transition temperature expressed as

$$T_c = T_0 \ln \frac{x}{x_0}, \quad (62)$$

where  $T_0 = 1.14\pi C\hbar$  is a constant.

In Fig. 24, doping dependence of  $T_c$  in the underdoped region is depicted. The experimental data for La214 [28] shows anomalous depression of  $T_c$  around  $x = 1/8$  and the agreement is not good around there; otherwise the formula in (62) fits the experimental data very well.

If an applied magnetic field is present, a loop current pattern that is different from that for the “antiferromagnetic” loop-current order mentioned above will be realized. If we denote the wave function for the “antiferromagnetic” pattern by  $\Psi$ , the wave function for the different current pattern is given by

$$\Psi' = \exp\left(-i \sum_{k=1}^{N_e} g_k\right) \Psi, \quad (63)$$

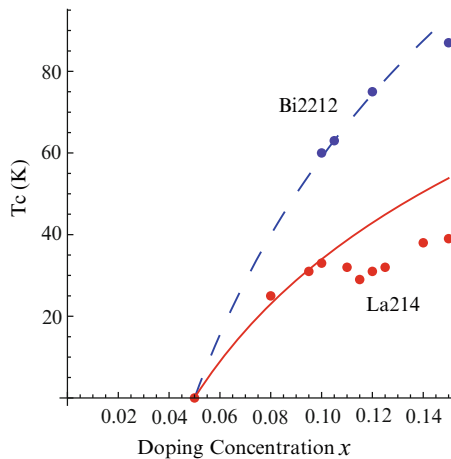


**Fig. 24** Doping concentration dependence of the transition temperature  $T_c$  [25]. Experimental data are fitted by (62) with  $x_0$  and  $T_0$  as fitting parameters.  $x_0$  is taken to be 0.05 for all. Solid line is the result for  $\text{Bi}_2\text{Sr}_2\text{CaCu}_2\text{O}_{8+\delta}$  (Bi2212) with  $T_0 = 85$  K. Dashed line is the result for  $\text{La}_{2-x}\text{Sr}_x\text{CuO}_4$  (La214) with  $T_0 = 49$  K. Dots are experimental results [28]



where  $N_e$  is the number of electrons; the phase  $g$  is given by

$$g_j = \sum_{M'} \tan^{-1} \frac{j_x - M'_x}{j_y - M'_y} - \sum_{A'} \tan^{-1} \frac{j_x - A'_x}{j_y - A'_y}; \quad (64)$$

in the sum over  $M'$ , sites of loop currents whose winding number is changed from  $+1$  to  $-1$  are included; and in the sum over  $A'$ , sites of loop currents whose winding number is changed from  $-1$  to  $+1$  are included. The flexible change of loop current pattern by (63) and (64) will explain very sensitive response of the supercurrent against an external magnetic field.

## 7 Concluding Remarks

If a long-range coherence of a collection of loop currents generated by spin vortices is established, a macroscopic persistent current will be realized. From the fitting to experimental data, we obtain  $x_0 = 0.05$ . This value corresponds to  $R_c = 2.5$ , which suggests that if the distance between nearby holes is less than 5 times of the lattice constant, interaction between loop currents is strong enough to establish a long-range order.

We may construct a nano-structure that generates persistent current from the above observation. An example is depicted in Fig. 25, where a directional current is

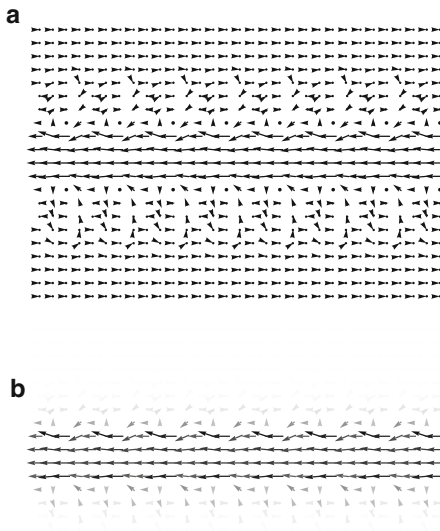


**Fig. 25** A macroscopic directional current generated by lines of loop currents [25]. Centers of loop currents are marked by 16 dots in (a); the directional current flows between two lines of loop current centers. In (b) the same directional current given in (a) is depicted with its magnitude indicated by the gray scale

created between two lines of centers of loop currents. The situation here is analogous to a magnetic field produced in a solenoid; the magnetic field inside the solenoid corresponds to the directional current, and electric current in the wire of the solenoid corresponds to vorticity of the loop currents.

In the cuprate, holes are expected to exist at each center of loop currents; thus, if we arrange holes in this way artificially, a persistent current will be generated, even if the hole concentration is  $x < 0.05$ . Instead of holes, we may use some atoms (for example, Mn may be appropriate as is suggested by the result in [16]) as centers of loop currents. In this way, we may obtain an enhanced stability in spin vortices. If we find a way to construct such a spin–vortex structure that is similar to one given in Fig. 25, and which is robust even at room temperatures, a room temperature superconductivity may be realized.

## References

1. J.G. Bednorz, K.A. Müller, *Z. Phys.* **B64**, 189 (1986)
2. N.F. Mott, *Metal-Insulator Transitions*, 2nd edn. (Taylor & Francis, London, 1990)
3. S. Uchida, T. Ido, H. Takagi, T. Arima, Y. Tokura, S. Tajima, *Phys. Rev. B* **43**, 7942 (1991)
4. D. Mihailovic, C.M. Foster, K. Voss, A.J. Heeger, *Phys. Rev. B* **42**, 7989 (1990)
5. Y. Ando, A.N. Lavrov, S. Komiya, K. Segawa, X.F. Sun, *Phys. Rev. Lett.* **87**, 017001 (2001)
6. S.M. Hayden, H.A. Mook, P. Dai, T.G. Perring, F. Doğan, *Nature* **429**, 531 (2004)
7. J.M. Tranquada, H. Woo, T.G. Perring, H. Goka, G.D. Gu, G. Xu, M. Fujita, K. Yamada, *Nature* **429**, 534 (2004)
8. J.M. Tranquada, in *Handbook of High-Temperature Superconductivity*, ed. by J.R. Schrieffer, J.S. Brooks (Springer, Berlin, 2007), p. 260
9. M.R. Norman, H. Ding, N. Randeria, J.C. Campuzano, T. Yokoya, T. Takeuchi, T. Takahashi, T. Mochiku, K. Kadowaki, P. Guptasarma, D.G. Hinks, *Nature (London)* **392**, 157 (1998)
10. T. Yoshida, X.J. Zhou, T. Sasagawa, W.L. Yang, P.V. Bogdanov, A. Lanzara, Z. Hussain, T. Mizokawa, A. Fujimori, H. Eisaki, Z.-X. Shen, T. Kakeshita, S. Uchida, *Phys. Rev. Lett.* **91**, 027001 (2003)
11. Y. Wang, Z.A. Xu, T. Kakeshita, S. Uchida, S. Ono, Y. Ando, N.P. Ong, *Phys. Rev. B* **64**, 224519 (2001). 257003 (2002)
12. Y. Wang, L. Li, M.J. Naughton, G.D. Gu, S. Uchida, N.P. Ong, *Phys. Rev. Lett.* **88**, 247002 (2005)
13. Y. Wang, L. Li, N.P. Ong, *Phys. Rev. B* **73**, 024510 (2006)
14. A. Bianconi, N.L. Saini, A. Lanzara, M. Messori, T. Rossetti, H. Oyanagi, H. Yamaguchi, K. Oka, T. Ito, *Phys. Rev. Lett.* **76**, 3412 (1996)
15. S. Miyaki, K. Makoshi, H. Koizumi, *J. Phys. Soc. Jpn.* **77**, 034702 (2008)
16. C.J. Zhang, H. Oyanagi, *Phys. Rev. B* **79**, 094521 (2009)
17. M. Berciu, S. John, *Phys. Rev. B* **69**, 224515 (2004)
18. H. Koizumi, *J. Phys. Soc. Jpn.* **77**, 104704 (2008)
19. M.V. Berry, *Proc. Roy. Soc. London A* **392**, 45 (1984)
20. A. Bohm, A. Mostafazadeh, H. Koizumi, Q. Niu, J. Zwanziger, *The Geometric Phase in Quantum Systems* (Springer, Berlin, 2003)
21. H.C. Longuet-Higgins, U. Öpik, M.H. Pryce, R.A. Sack, *Proc. Roy. Soc. London A* **244**, 1 (1958)
22. C.A. Mead, D. Truhlar, *J. Chem. Phys.* **70**, 6090 (1982)
23. H. Koizumi, *J. Phys. Soc. Jpn.* **77**, 123708 (2008)
24. H. Koizumi, *J. Phys. Soc. Jpn.* **77**, 034712 (2008)

25. H. Koizumi, to appear in J. Chem. Phys. A (2009)
26. H. Koizumi, Y. Takada, Phys. Rev. B **65**, 153104 (2002)
27. H. Sumi, J. Phys. Soc. Jpn. **33**, 327 (1972)
28. T. Matsuzaki, M. Ido, N. Momono, R.M. Dipasupil, T. Nagata, A. Sakai, M. Oda, J. Phys. Chem. Solids **62**, 29 (2001)

# Index

- Absorption bands, 609–611  
Activation energy, 900  
Adiabatic approximation, 101–104, 108–110  
Adiabatic correction, 205, 219–220, 228, 233  
Adiabatic potential energy, 690, 691  
Adiabatic potential energy surfaces (APES),  
283, 286, 287, 293, 297, 298,  
305, 490–492, 507, 691, 714–716,  
720, 722  
Adiabatic potentials, 562  
Adiabatic representation, 216  
Adiabatic surfaces, 561–562  
Adiabatic-to-diabatic transformation (ADT),  
283, 284  
Amplitudes, 217, 218, 221–223, 230–233  
Angular overlap model (AOM), 378, 397, 399,  
407, 409–411, 480, 692, 719  
Anharmonic, 375, 376, 392, 408  
Anthracene radical cation, 278–280, 301–306  
Anti-adiabatic, 851–853, 855, 856, 862  
Antiferrodistortive ordering, 696, 698, 699  
Antiferro-orbital ordering (AFO), 857, 858,  
860, 861  
Antimeron, 887, 893, 896  
Aromatic hydrocarbons, 277, 278, 291  
Atomic vibronic coupling constant (AVCC),  
110, 114–115  
Attenuation  
relaxation, 744, 747, 752, 755–757  
resonant, 744, 747, 750, 752, 755–757  
ultrasonic, 744, 750, 751, 756, 758  
  
Backward, 220, 231  
Benzene, 182, 184, 188–193, 277, 289–291,  
293, 296, 301, 306  
Benzene cation, 240, 241, 243–245, 252, 259,  
260, 263, 271  
Berry phase, 873–904  
Berry phase factor, 21  
  
Berry pseudo-rotation, 324, 335, 340  
Binuclear metal clusters, 708  
Bipolarons  
high temperature superconductivity (HTS),  
812–814, 816–819, 821, 823, 824,  
826, 828, 831–836  
JT bipolarons, 811–836  
mobility, 824, 825  
superconductivity (SC), 811–836  
Bohr magneton, 80  
Bond-centered electron density, 707  
Bond covalence, 471, 475, 478, 479  
Bond lengths, 381, 383, 385, 406, 407  
Born–Oppenheimer approximation, 101,  
103–106, 201, 204, 210, 234  
Bose-Einstein condensation (BEC), 845, 864  
Branching space, 171–173, 175, 176, 178–181  
Breit-Pauli Hamiltonian, 80, 87  
Breit-Pauli operator, 78–80, 85, 87, 91  
  
C<sub>60</sub>  
and charge-transfer, 521, 523–524, 531  
HOMO, 529  
Hückel molecular orbital (HMO), 532–533  
LUMO, 523, 528, 529, 531, 544  
STM Images of, 521, 530, 535, 538  
Caesium titanium alum, 397–401  
Canonical shift transformation, 657, 664, 668  
CaO WCu<sup>2C</sup>, 386, 387  
Charge ordering, 701, 706  
Charge transfer, 462, 471, 478, 481  
Charge-transfer energy gap, 881  
Charge-transfer peak, 874  
Chemical bonding, 687, 688, 697, 710,  
719, 722  
Chemical potential, 120, 123  
Cobaltocene (CoCp<sub>2</sub>), 132, 137, 138, 154,  
157, 160, 161  
Colossal magneto resistance, 705

- Complete active space self-consistent field (CASSCF), 321, 323, 329, 330, 333, 334, 339, 340
- Complexes, transition metal
  - CuII-FeIII, 631, 641
  - cyanide, 621, 622, 631, 645
  - dinuclear, 631, 642, 648
  - [Fe(CN)<sub>6</sub>]3-, 630–631
  - oligonuclear, 622, 631, 646
- Computational studies, 311, 316, 320–322, 326–341
- Configuration coordinate approach, 348
- Configuration interaction, 629, 630
- Conical intersection (CI), 4, 14, 169–173, 176–184, 186, 191, 192, 195, 196, 201, 204, 206, 207, 209, 214, 215, 219, 226, 233, 235, 240, 246, 258, 259, 263, 269, 270, 277–280, 284, 285, 292, 296–301, 303, 305, 306
- Cooperative, 492, 495, 499–501
- Cooperative JT effect, 685–723
- Cooperative pseudo JT effect, 707
- Coriolis splitting, 12
- Corner sharing octahedrons, 712
- Coupled cluster calculations, 247, 273
- Coupling, 201–235
  - exchange, 622, 623, 631, 632, 634, 635, 639, 643, 645–648
  - ferromagnetic, 623, 633, 642, 645
  - isotropic, 631–634, 643, 646
  - Jahn-Teller, 621–648
  - spin-orbit, 622, 628–629, 635, 639, 640, 642–648
  - vibronic, 623, 628, 630–632, 634, 640
- Cross sections
  - differential, 202, 217, 233
  - Integral, 202, 222, 233, 234
- Crude adiabatic approximation, 103–104, 106, 107
- Crystal field
  - cubic, 349–357, 366
  - effects, 367
  - energy levels, 356
  - Hamiltonian, 349
  - interaction, 348
  - splitting, 356, 394
  - strength, 358, 360, 362
  - symmetry, 349
  - theory, 358
- Cubic crystal
  - field, 350
  - states, 350
- Cu(II) doped MgO, 388, 404
- CuO<sub>6</sub>, 813, 819, 821, 823, 826, 832
- Cuprates, 811–836, 873–904
- Curie temperature, 701
- Cyclopentadienyl radical (C<sub>5</sub>H<sub>5</sub>), 132, 146–149, 160
- Deformation potential, 744, 754, 759, 761, 764, 765
- Degeneracy analysis, 558–560
- Delocalized electronic pair, 584–586
- Density, 99–128
- Density functional theory (DFT), 132, 136, 137, 140, 141, 143–158, 160, 161, 417, 418, 427, 433–440, 442, 443, 451, 458–460, 466–468, 472, 473, 475, 477, 478, 622, 627–631, 633, 639, 647
  - Multideterminantal DFT, 132, 141, 146–148, 152, 154
- Density function theory (DFT), 772
- Diabatic (state, representation), 242, 243, 247, 252, 255, 257, 266, 267, 269, 272, 273
- Diabatic and adiabatic representation, 216
- Diabatic electronic states, 283, 288
- Diabatic representation, 207, 215, 216, 219, 220, 223–227
- Diabatic vibronic Hamiltonian, 303
- Diagonalization of Hamiltonian matrix, 283, 288, 289, 293, 295, 299, 300, 304
- Differential, 202, 210, 217, 224–225, 233, 234
- Difficult, 424, 428
- Diffraction, 493, 496, 498, 502, 503, 506, 507, 509, 510
- Diffuse interstellar bands, 277, 280
- Difluorobenzene cation, 268–269
- Dimensionless normal coordinates, 285, 286, 296, 303
- Dipolar instabilities, 421
- Dirac-Coulomb Hamiltonian, 79
- Dirac equation, 78
- Directional order, 734–736, 741
- Direct product representation, 58, 61, 68, 70
- Displacement operator method, 656
- Distortions
  - Jahn-Teller, 743, 744, 749–751
  - lattice, 744, 749, 753
  - tetragonal, 753, 754, 759
  - trigonal, 753, 766
- Drude-like peak, 874–876, 884, 892
- Durude-like peak, 891
- Dynamic, 492, 495, 497, 499, 500
- Dynamical matrix, 692, 694, 696
- Dynamic JT effect, 108–110, 520, 542, 549

- Dynamic vibronic problem
  - tautomeric compounds, 607–608
  - valence tautomeric system, 608–609
- $E \otimes b_1$ , 689, 692, 694
- $E \otimes b_{1g}$ , 696, 698, 715, 716
- $E \otimes b_{2g}$ , 716
- $E \otimes \varepsilon$ , 538–543, 549
- $E \otimes e$ , 696
- $E \otimes e$  case, 690, 718
- $E \otimes e_g$ , 711, 715–717
- $E \otimes e$  Jahn–Teller system, 886
- $E \otimes e$  vibronic hamiltonian, 371–372
- Easy axis, 708, 709
- Effective density of carriers, 892, 893
- Effective involving, 431
- Effectively half-filled Mott insulator (EHMI), 885
- Elastic coupling, 686, 687, 693, 711, 712, 714
- Elastic energy, 690–692, 713
- Elastic intercell coupling, 718, 720, 722
- Elasticity theory, 745
- Elastic modulus
  - adiabatic, 746, 748, 749, 751, 754
  - dynamic, 744, 748, 749, 753, 759, 760, 764
  - isothermal, 746, 748, 751, 753, 754, 761
  - relaxed, 748, 751, 759, 763, 764
- Elastic order, ferrodistorive, 457
- Elastic properties, 661
- Electron energy bands, 702, 703
- Electron hopping, 696, 701–707, 714, 719
- Electronically excited molecules, 306
- Electronic basis, 101–103
- Electronic correlations, 812, 814, 816–819, 831
- Electronic coupling, 565
- Electronic function, 98, 117
- Electronic Hamiltonian function, 102, 111
- Electronic Raman, 386–388, 401–403
- Electronic spectra, 318, 319
- Electronic wavefunction, 102, 104, 111–114, 117
- Electron paramagnetic resonance, 630
- Electron–phonon interaction, 367
  - coupling, 359
  - interaction, 348
- Electron pockets, 703, 704
- Electron-strain interaction, 665, 667
- Elementary excitations, 662, 664
- Encirclement, 234
- Energy
  - exchange, 633, 634, 642, 645, 647
  - free, 745, 754
  - internal, 745
- Energy loss function, 881
- E-ph coupling, 823, 825, 826, 828, 829, 831, 834, 835
- Epikernel, 332, 333, 339–341
- Epikernel principle, 47, 59, 61, 62, 67–69, 71, 73–75, 311, 332, 376
- Epikernel subgroup, 55
- EPR spectra, 388, 398
- Equations of motion method, 888, 890
- Exchange
  - anisotropic, 631, 645–647
  - antisymmetric, 632, 633
  - ising, 644, 648
  - isotropic, 631–634, 643, 645–647
  - magnetic, 361, 622
  - symmetric, 632, 633, 647
- Exchange coupling
  - double, 702, 708
  - Heisenberg, 701, 708, 709
  - Kramers–Anderson superexchange, 708
  - magnetic, 686, 696, 701, 702, 708–709
  - orbital, 686, 695, 697, 700, 708, 709, 711, 712, 714, 717, 718, 722
  - phonon-mediated orbital, 717
  - vibronic, 720, 721
- Exchange interactions, 558–560
- Excitons, 703
- $E \times E$  Jahn–Teller effect, 81–85, 91
- Extended X-ray absorption fine structure (EXAFS), 420, 879, 880
- Face sharing octahedrons, 710
- Femtosecond UV laser excitation, 324
- Fermi surface, 703, 877, 878
- Ferro- and antiferroelectricity, 666–669
- Ferrodistorive ordering, 693, 696, 698, 699
- Ferroelastic ordering, 658
- Ferroelectricity, vibronic theory of, 707
- Ferro-electric phase transitions, 417
- Ferromagnetic effect, 567
- Feynman path integral, 203, 230
- Fictitious magnetic field, 886, 894, 895, 900
- Flat band, 738
- Fluorescence dynamics, 241, 269–271
- Foldy–Wouthuysen transformation, 78
- Forward, 220, 225, 231
- Franck–Condon factor, 17
- Franck–Condon transitions, 569, 570
- Frustration, 727–741
- Fullerene
  - anions, 15
  - ions, 123–126

- Fulleride, 489–512  
 $K_3C_{60}$ , 518, 531  
 $K_4C_{60}$ , 518, 531  
 STM of, 518  
 Fulvene, 170, 171, 173, 181–184, 192  
 Functions to be multivalued, 207
- Gauge invariant, 901  
 Gauge transformation, 900  
 Generalized gradient approximation (GGA), 433–435, 441, 443  
 Geometric, 201–235  
 Geometric phase, 85, 89, 91, 201–235  
 Guanidinium Vanadium Sulphate, 401–403
- Ham, 347–349, 356, 360–362, 366, 368–369  
 effect, 347, 349, 360–362, 366, 371, 394–403  
 parameter, 361  
 quenching, 356  
 reduction factor, 347, 361, 368–369  
 theory, 361
- Hamiltonian, 347–355, 357, 358, 360–362, 366, 367  
 crystal field, 348  
 diagonalize, 349  
 effective, 348, 357, 361  
 effective first- and second-order SO, 351  
 effective second-order SO Hamiltonian, 351  
 effective second-order spin, 347  
 eigenvalues, 357  
 free ion, 349  
 matrix, 350, 353  
 matrix elements, 355  
 parameters, 353, 361  
 second-order effective SO, 360  
 second-order effective spin, 366  
 second order effective spin Hamiltonian, 355  
 spin-orbit, 349  
 vibronic, 367
- Harmonic function, 887, 895  
 Harmonics, 210, 211  
 Heisenberg-Dirac-Van Vleck (HDDVV), 558  
 Helicoidality, 659, 681  
 Hellmann-Feynman theorem, 110, 112–113  
 Hidden JTE (HJTE), 3–22  
 Higher-order terms, 375  
 High-spin/low-spin, 451–485  
 crossover, 453, 460, 462, 463, 471  
 equilibrium, 451, 460  
 non-adiabatic separation energy, 459, 469  
 vertical separation energy, 456, 462, 466  
 High temperature superconductivity (HTS), 812–814, 816–819, 821, 823, 824, 826, 828, 831–836  
 Holstein bipolaron, 855  
 Holstein polaron, 852, 854  
 Holstein-Primakoff method, 888–890  
 Homotopes, 231  
 Hourglass-shaped dispersion, 876, 882, 890  
 Hourglass-shaped magnetic excitation spectrum, 876, 882–892  
 Huang-Rhys factor, 359, 362  
 Hund energy, 702  
 Hund's-rule coupling, inverted, 844, 862, 863  
 Hydrogen-Exchange reaction, 202, 203, 219  
 Hyperfine constants, 572–576  
 Hyperoctahedron, 44–47  
 Hyperspherical coordinates, 207, 231  
 Hyperspherical formalism, 209–211  
 Hyperspherical harmonics, 210, 211
- Icosahedral system, 543  
 Icosahedron, 32, 36, 40–44, 48  
 Impurity  
 centres, 348  
 ion, 353, 357–359, 367  
 isolated, 348  
 Inelastic, 202, 216–218, 221, 233  
 Inelastic scattering, 216–218, 233  
 Instability, 416, 418, 419, 422, 426, 429, 430, 434–441  
 Instant nuclear configuration, 562  
 Intercell elastic coupling, 686, 687, 693, 711, 712, 714  
 Intermediate-spin state, 466  
 Intersection Space Hessian, 176–183  
 Intrinsic reaction coordinate, 154, 163  
 Ioffe-Regel-Mott limit, 876  
 IR spectroscopy, 317–318, 321  
 Isotope effect, 820–823  
 Isotropic exchange, 567  
 Itinerant electrons, 841, 867
- Jacobi coordinates, 207, 212, 217, 219  
 Jahn-Teller  
 active, 360  
 active coordinate, 52, 57–59, 68, 70, 71, 73–75  
 active modes, 367  
 active normal mode, 355  
 coupling constant, 83

- distortion, 364
- effect, 347–369
- energy, 349, 360–362
- Hamiltonian, 84, 88
- instability, 686–692, 696, 698, 700, 711, 716
- interaction, 349, 361, 562–565
- intraction, 348
- mode, 360
- radius, 376, 383
- selection rules, 86, 87
- splittings, 777, 780, 793
- stabilization energy, 347, 360, 362–365, 687, 713, 719
- theorem, 26–29, 51, 89
- Jahn–Teller and pseudo Jahn–Teller (PJT), 241
- Jahn–Teller effect (JTE), 4, 5, 7–13, 15, 18, 20–22, 77, 78, 81, 86, 91, 277, 284, 416, 429–432, 491–493, 495, 497–503, 507–509, 512
- C–F splittings, 775, 776, 783, 785–787, 789, 790, 794, 798
- complex oxides, 800–802
- cooperative, 768–772
- distortion, 769, 771, 773, 775, 778–781, 787, 793, 797, 805
- exchange interactions and degeneracy analysis, 558–560
- ground state and adiabatic surfaces, 561–562
- influence, 562–565
- intrinsic bonding defects, 772–776
- molecular magnetism, 556–557
- MV cluster, 565–601
- vibronic interaction, 560–561
- Jahn–Teller problem ( $H \times (g + 2h)$ ), 42
- JT bipolaron,  $E \otimes e$ , 855
- JT polarons, 705, 709, 717, 722
  - $E \otimes e$ , 850, 852–854
  - $T \otimes t$ , 850, 852
- Keggin structure, 584–586
- Kernel group, 54, 55, 74
- Kernel subgroup, 54
- Kitaev model, 737
- Kramers degeneracy, 85, 89
- Kugel–Khomskii model, 686, 722
- Large polarons, 899
- Lattice, 415–429, 432–438, 441, 442
- Lattice distortions, 819, 820, 827, 831, 833
- LCAO method, 771
- Ligand field
  - d-d spectra, 456, 458, 466, 467, 471, 473, 475–477
  - parameters, 458, 462, 463, 467, 471, 473, 475, 482
- Ligand field theory (LFT), 630
- Linear vibronic constant, 750
- Linear vibronic coupling, 107, 116, 124, 286
- Local density approximation (LDA), 433
- Local phase transitions, 425
- Loop currents, 895–904
- Magnetic anisotropy, 708
- Magnetic exchange, 686, 695, 701, 702, 708–709
- Magnetic memory cells, 706
- Magnetic ordering, 705, 708, 709
- Magnetic polarons, 701
- Magnetism, single molecular, 621–623
- Magnetoelectricity, 676–682
- Magneto- or (and) electrostriction, 669
- Magnetoresistance, 671, 673, 674, 676, 682
- Magnons, 705, 706
- Manganites, 703, 721
- Mass enhancement factor, 851–854, 864
- MATI spectra, 260–264
- M–CO Bonding, 312–315
- Mean-field, 693, 695
- Mean field approximation, 693, 695
- Mean-square displacement, 383
- Mean squared relative displacement (MSRD), 881, 882
- Meron, 887, 893, 896
- Metaelasticity, 670, 671, 675
- Metamagnetoelasticity and metamagnetism, 670–674
- Method, öpic and price, 625
- Mexican hat, 89, 691, 715
- Mid-IR peak, 874, 876
- Mixed-valence (MV), 452, 465, 468, 471, 481
  - charge and structural ordering, 587–591
  - double exchange, 566–568
  - electronic coupling, 565
  - multimode Jahn–Teller problem, 580–586
  - Piepho–Krausz–Schatz model, 568–571
  - Robin and Day classification, 568–571
  - vibronic coupling, 565
  - vibronic effects, 576–580
- Mobility, 899, 900
- MO diagrams, 313
- Molecular orbital cluster method, 879
- Monofluorobenzene cation, 241, 259, 268, 270
- Mössbauer spectra, 595



- Mott insulators, 874, 877  
 Mott-Jahn-Teller insulator, 492, 502, 508, 509, 512  
 Multi-configuration time-dependent Hartree (MCTDH), 241, 249–251, 264, 265, 288, 294, 297, 299, 304  
 Multiferroics, 679, 681, 682  
 Multimode JT Effect, 132, 133, 147, 148, 152, 156–161, 432  
 Multi-state vibronic (coupling) Hamiltonian, 240, 241, 245–246, 271  
 Multivalued basis functions, 202  
  
 Nano-grain thin films, 768–777  
 Naphthalene radical cation, 278–280, 301–306  
 Néel temperature, 700, 701  
 Nephelauxetic effect, 464, 474, 475, 482  
 Nernst signals, 877, 879, 896–900  
 Nesting, 703, 704  
 Neutron, 493  
 Non-adiabatic coupling, 101, 104–106, 108, 110, 201–205, 282, 284, 291, 292, 295, 297–299, 304–306  
 Non-Berry pseudo-rotation, 319, 324, 333, 335, 340, 341  
 Nonmagnetic JT Mott insulator, 857  
 Nonradiative decay, 277, 280, 301–306  
 Nonreactive, 218, 222, 230, 234  
 Nonreactive scattering amplitudes, 218, 222  
 Normal coordinates, 87  
 Normal mode, 107, 121, 126–128  
 Nuclear magnetic resonance (NMR), 421, 424, 428  
  
 Off-centre displacement, 416–419, 423, 425, 426, 436, 440, 442  
 Off-diagonal coupling, 104, 105, 110  
 One-photon absorption, 325, 329  
 Optical absorption, 420, 423–426  
 Optical spectra, 348  
 Orbital compass model, 728, 730, 733–736  
 Orbital degeneracy, 25, 40  
 Orbital disorder, 697  
 Orbital disproportionation, 3, 10, 14–18, 21, 22  
 Orbital exchange, 686, 695–698, 700, 709, 711–717, 719, 720, 722, 723  
 Orbitally degenerate metal ions, 576–580  
 Orbital ordering, 685–723  
 Orbital ordering approach (OOA), 685–723  
 Orbital ordering temperature, 732  
 Orbital pseudo spin, 697, 708, 717, 718, 722  
  
 Orbiton liquid, 705  
 Orbitons, 705, 706  
 Orbit, splitting, 366  
 Order-by-fluctuation, 732, 741  
 Ordering of orbitals, 654, 673, 675, 676  
 Ordering patterns  
   antiferro, 695, 711  
   antiferrodistortive, 696–699  
   antiferromagnetic, 697  
   antiferromagnetically, 703  
   ferrodistortive, 693, 697, 699  
   ferroelectric, 706  
   ferromagnetic, 697, 703, 705  
   ferro type, 695, 711  
   helical, 710, 711  
   orbital, 695, 698–700, 708, 709, 711, 712  
   spin-canted, 708  
 Order parameter, 659, 661, 669, 672  
 Other subtler properties, 432  
 Outer valence Green's functions, 287  
 Overlap integrals, 688, 689, 702, 712  
 Ozone, 3, 10–12  
  
 Pairing, 813, 816–820, 822, 824, 830, 833  
 Particle-exchange symmetry, 220–222  
 Partitioning, 714, 719, 722, 723  
 Partitioning the Hilbert space, 719  
 Pauli spin matrices, 80  
 Permutation groups, 44  
 Perovskites, 687, 698, 699, 702, 705–707, 709–711, 719, 721  
 Perturbation theory, 52, 57, 58, 75  
 PES extremal points, 57, 58, 60  
 Phase, 207, 211, 212, 220–222, 225, 232–234  
 Phase separation, 701  
 Phase transition, 457, 492, 500, 505, 507  
   magnetic, 695, 700, 701  
   metal-insulator, 702, 705  
   structural, 686, 698, 700, 701, 706, 710, 712, 721  
 Phase velocity, 743, 744, 746, 749, 753–755, 759  
 Phenide anion, 277, 289–292, 296  
 Phenylacetylene, 277, 279, 289–301  
 Phenylacetylene radical cation, 277, 279  
 Phenyl radical, 277, 279, 289–301  
 Photoactive coordinates, 185–187  
 Photochemistry, 169–198  
 Photochromic effect, 601–602  
 Photoelectron spectra, 240, 241  
 Photophysics, 169–198  
 Photostability, 277–280, 301, 304, 306

- Piepho-Krausz-Schatz model, 568–571  
PKS vibronic coupling, 572  
 $p^n \otimes h$ , 544  
Point defects, 348  
Point groups  
  icosahedral, 496  
  of symmetry, 52–55, 61  
Polaron effective mass, 850  
Polarons  
  J-T polaron, 811–836  
  mobility, 821, 825, 829, 831  
Polycyclic aromatic hydrocarbons, 277, 279  
Polymerization, 510–512  
Potential barrier, 744, 752, 759, 761, 763, 765, 766  
Potential energy curves, 459  
Potential energy surface (PES), 55–57, 349, 357, 360, 362, 364, 366, 368, 375–378, 389, 393, 394, 406, 408–411  
Predissociation, 202, 204, 206, 216, 218, 225–230, 233, 234  
Primitive lattice, 697, 704, 706, 709, 711, 719, 722, 723  
Pseudogap, 818, 822, 828  
Pseudogap phase, 874–876, 896  
Pseudo Jahn–Teller (PJT) effect, 4, 333–337, 340, 416, 432  
Pseudo Jahn–Teller problem  
  adiabatic potentials, 604–606  
  Mössbauer spectra, 595–601  
  photochromic effect, 601–602  
  vibronic model, 602–604  
Pseudorotation, 491, 493, 494, 497, 498, 501, 507, 508, 541–543, 546, 547  
Pseudo spin, 848–849, 853, 859–861  
  orbital, 695, 697, 705, 708, 717, 718, 722  
  vibronic, 709, 718, 720–723  
Pseudo-spin operator, 728, 736, 737  
  
Quadratic, 375, 377, 387  
Quadrupole-quadrupole coupling, 712  
Quadrupole-quadrupole intersite interaction, 711  
Quantum dynamics, 278, 302, 306  
Quantum geometric phase, 886  
Quasidynamical model, 591–595  
  
Radiationless transitions, 17  
Radical, 132, 137, 161  
Random strains, 426  
Rare-earth compounds, 686, 712  
  
Reaction paths, 231, 235  
Reactive scattering amplitude, 218, 222, 223, 230  
Reduction factors, 709, 718  
Reference configuration, 100, 103  
Reference state, 100, 117  
Relaxation, 17, 18  
Relaxation time, 744, 747, 750–752, 757, 761, 763–765  
Renner coupling constant, 91  
Renner effect, 77, 91  
Renner Hamiltonian, 90  
Renner–Teller effects (RTE), 4, 5  
Reorganization energy, 108, 116  
Resolved vibronic spectrum, 277, 291, 296, 304  
Resonances, 203, 218, 226, 228–230, 234  
Resonance states, 741  
Rydberg states, 216, 218, 225–230, 234  
  
Scanning tunnelling microscopy (STM), 517–525, 528–543, 546–550  
Scattering  
  amplitudes, 217, 222, 223, 230, 233  
  inelastic, 202, 216–218, 221, 233  
  non reactive, 218, 222  
  reactive, 202–204, 206, 210, 212, 215–223, 227, 228, 230–233  
Schrödinger equation, 101, 103  
Seams  
  curvature, 171  
  intersection, 169–176, 180, 183, 184  
Sears resonances, 91  
Second-Order Analysis, 169–176  
Segregation, 510–511  
Shift operator, 715  
Shift transformation, 715, 716  
Side sharing octahedrons, 712  
Single molecule magnets (SMM), 556  
Small polarons, 876, 879–882, 884, 885, 887, 892, 897–900  
Solids, 417, 418, 421, 432, 433, 443  
Spectral broadening, 289  
Spectroscopy  
  electron spin resonance, 510  
  energy loss, 494  
  gas-phase, 493  
  infrared, 506  
  mid-infrared, 505, 508  
  near infrared, 494, 505, 507, 509  
  nuclear magnetic resonance, 493  
  Raman, 494, 499, 506  
Spin-based qubits, 558

- Spin Berry phase, 895
- Spin crossover, 16–18, 22
- Spin density wave (SDW), 857, 858, 860, 861
- Spin double group, 81, 88, 90, 94
- Spin-flip, 455, 458, 459, 471, 478, 484, 485
- Spin-frustrated metal clusters, 557–565
- Spin-frustrated triangular system, 560–561
- Spin Hamiltonian, 888
- Spin-orbit coupling, 78, 81–85, 89–91, 348
- Spin-orbit interaction, 78, 347–350
- Spin-orbit operator, 78–80, 83, 85, 86, 89–94
- Spin-orbit splitting, 91, 348, 349
- Spin ordering, 686, 695, 708
- Spin vortex, 882, 884, 886, 890, 892, 895, 896, 901, 904
- Spin vortices, 882–899, 901, 903, 904
- Spin-wave excitations, 876–877, 882, 888
- Spontaneous polarization, 706, 707, 723
- Square-planar system, 703, 704
- Standard orientation, 496, 498, 502
- State-to-state differential cross sections, 202, 234–235
- Step-by-step descent in symmetry, 71, 75
- Steric strain, 408
- Strain, 745, 747–749, 751, 752, 759, 761, 764, 765
  - binding, 484
  - elastic, structural, 484
- Stripe model, 882, 884
- Stripes, 820, 828–831, 833, 834
- Structural phase transitions, 654–656, 658–661, 664–666, 668, 669, 673, 675
- Superconductivity (SC), 479–482, 811–836
- Superhyperfine, 419, 429, 436, 438
- Superstructures, 701
- Surface hopping, 334, 335, 337
- Surfaces, 517–550
- Susceptibility, 424, 428
- SXPS, 773, 777, 778, 783, 785, 786, 789, 794–801, 803–807
- Symmetry-adapted group orbitals, 688, 691
- Symmetry adapted linear combinations (SALC), 770, 771, 774, 775, 777, 778, 783, 786, 787, 789, 795, 800–804
- Symmetry breaking, 7
- Symmetry-breaking instability, 688, 689
- Symmetry characters, 53, 54, 58, 59
- Symmetry considerations, 207–209
- Symmetry descent paths, 60–67, 74
- Symmetry selection rule, 245
- Tautomeric compounds, 607–608
- $T_d$ , 339, 340
- $T \otimes e_g$ , 716
- Tensor
  - exchange, 633, 646, 647
  - g-tensor, 628, 629, 632, 634, 641, 642, 644, 646, 647
  - magnetic susceptibility, 644–646
  - zero-field splitting, 632, 633, 644, 646
- Tetrachlorovanadium(IV) ( $\text{VCl}_4$ ), 132, 139, 141–146, 157, 160
- Tetrahedron, 31, 32, 34, 35
- $T \otimes h$ , 536
- Time-dependent electronic population, 264–265
- Time-reversal operator, 81, 84, 85, 88, 90, 96
- Time-reversal symmetry, 79
- Timescale, 381, 386
- $\text{TiO}_2$ , transition metal (TM)
  - band edge defects, 785–789
  - valence and conduction band, 781–785
- Topological (Berry) phase, 12
- Topology, 231
- Transition metals, 761
- Transition states, 203, 230, 231, 235
- Tricorne, 715
- Trifluorobenzene cation, 241, 246, 253, 254, 268, 270, 271
- Triptycene, 390–394
- $T \otimes t_2$ , 721
- Tunnelling, 417, 421, 424, 426
- Tunnelling splitting, 706, 720–721, 750, 752, 759, 761, 763–765
- Tutton salts, 403–407
- Two-photon absorption, 325, 327, 329
- $T \times T$  Jahn–Teller effect, 86
- Ultrafast electron diffraction, 323
- Ultrafast nonradiative dynamics, 279
- Ultrafast relaxation, 322–327
- Ultrasound measurements, 662
- Valence tautomeric system, 608–609
- Vector coupling coefficients, 371–373, 397
- Vector potential approach, 202, 207, 211–214, 221–223
- Vertex corrections, 844, 853
- Vertex function, 853
- Vertex-sharing octahedrons, 699
- Vibration 6 (C–C stretch), 149
- Vibrational, 349–357, 368
  - energy, 347
  - frequencies, 357, 744, 753, 759, 765

- interaction, 362
- modes, 347, 349–357
- state, 355
- Vibrations, 489–491, 493–499, 508, 510, 512
- Vibron, 705, 717
- Vibronic
  - amplification, 718, 723
  - angular momentum operator, 109, 110
  - coupling, 277–286, 288–306, 565
  - effects, 576–580
  - interaction, 560–561
  - model, 602–604
  - parameters
  - spectra, 279, 297, 303
- Vibronic coupling, 416, 418, 420, 429–432, 437, 440, 443
  - dynamic, 457, 474
  - first order-JT, 452
  - Hamiltonian, 333, 337
  - higher order-JT, 453, 454
  - model, 242, 258
  - pseudo-JT, 452, 455
- Vibronic coupling density analysis
  - Fukui and nuclear Fukui function, 119–123
  - structures, 117–119
- vibronic energy levels, 380–382, 386–394
- Vibronic Hamiltonian, 170
- Vibronic Hamiltonian coupling, 99–101, 123, 124, 127
- Vibronic interaction, 239–241, 270, 271
- Vibronic mode, 744, 749, 753, 754, 765
- Vibronic reduction factor, 709, 718
- Vice-versa, 332
- Vide supra, 322–326
- Virtual bound resonance, 774, 777, 778, 788, 789, 792, 801
- Virtual phonon exchange, 654, 656–659, 667, 673, 675, 677, 682
- Virtual phonons, 716–720
- von Neumann and Wigner, 172–174, 180
- Wave
  - acoustic, 743, 759
  - elastic, 743, 744
  - longitudinal, 747, 751–753, 756, 762, 764
  - running, 746, 755
  - shear, 747, 765
  - ultrasonic, 743, 748–750, 755, 756
- Wavepacket dynamics, 287, 335, 338, 341, 342
- Wave vector, 746, 747
- Wigner–Eckart theorem, 107, 111, 137, 372–373
- Winding number, 887, 896, 897, 901, 903
- XANES, 704, 707
- X-ray, 493, 498, 507, 510
- X-ray absorption fine structure (XAFS), 385, 406, 407
- X-ray absorption spectroscopy (XAS), 769, 771, 775, 777, 778, 780–783, 786–795, 798–807
- X-ray crystal structure, 692
- X-ray diffraction, 704, 707
- X-ray scattering, 700
- Zeeman energy pattern, 564
- Zeeman splitting, 563
- Zener polaron, 705
- zero-point vibrational, 17, 18
- ZnSe
  - $\text{Cr}^{2+}$ , 762, 763, 766
  - $\text{Fe}^{2+}$ , 762
  - $\text{Mn}^{2+}$ , 762
  - $\text{Ni}^{2+}$ , 762
  - $\text{V}^{2+}$ , 757, 762
- ZnTe: $\text{Ni}^{2+}$ , 765